

*See CRDI
for Kadish*

Outer Continental Shelf Environmental Assessment Program

Final Reports of Principal Investigators
Volume 26 **November 1984**



U.S. DEPARTMENT OF COMMERCE
National Oceanic and Atmospheric Administration
National Ocean Service
Office of Oceanography and Marine Assessment
Ocean Assessments Division
Alaska Office



U.S. DEPARTMENT OF THE INTERIOR
Minerals Management Service

"Outer Continental Shelf Environmental Assessment Program Final Reports of Principal Investigators" ("OCSEAP Final Reports") continues the series entitled "Environmental Assessment of the Alaskan Continental Shelf Final Reports of Principal Investigators."

It is suggested that sections of this publication be cited as follows:

Galt, J. A., and G. Watabayashi. 1984. Modeling report to OCSEAP. U.S. Dep. Commer., NOAA, OCSEAP Final Rep. 26: 1-61.

Overland, J. E., and T. R. Hiester. 1984. A synoptic climatology for surface winds along the southern coast of Alaska. In J. A. Galt, J. E. Overland, C. H. Pease, and R. J. Stewart, Numerical Studies--Pacific Marine Environmental Laboratory, p. 525-607. U.S. Dep. Commer., NOAA, OCSEAP Final Rep. 26.

OCSEAP Final Reports are published by the U.S. Department of Commerce, National Oceanic and Atmospheric Administration, National Ocean Service, Office of Oceanography and Marine Assessment, Ocean Assessments Division, Alaska Office, Anchorage, and printed by the General Services Administration Printers in Juneau, Alaska.

Requests for receipt of OCSEAP Final Reports on a continuing basis should be addressed to:

NOAA-OMA-OAD
Alaska Office
701 C Street
P.O. Box 56
Anchorage, AK 99513

OUTER CONTINENTAL SHELF
ENVIRONMENTAL ASSESSMENT PROGRAM

FINAL REPORTS OF PRINCIPAL INVESTIGATORS

VOLUME 26

NOVEMBER 1984

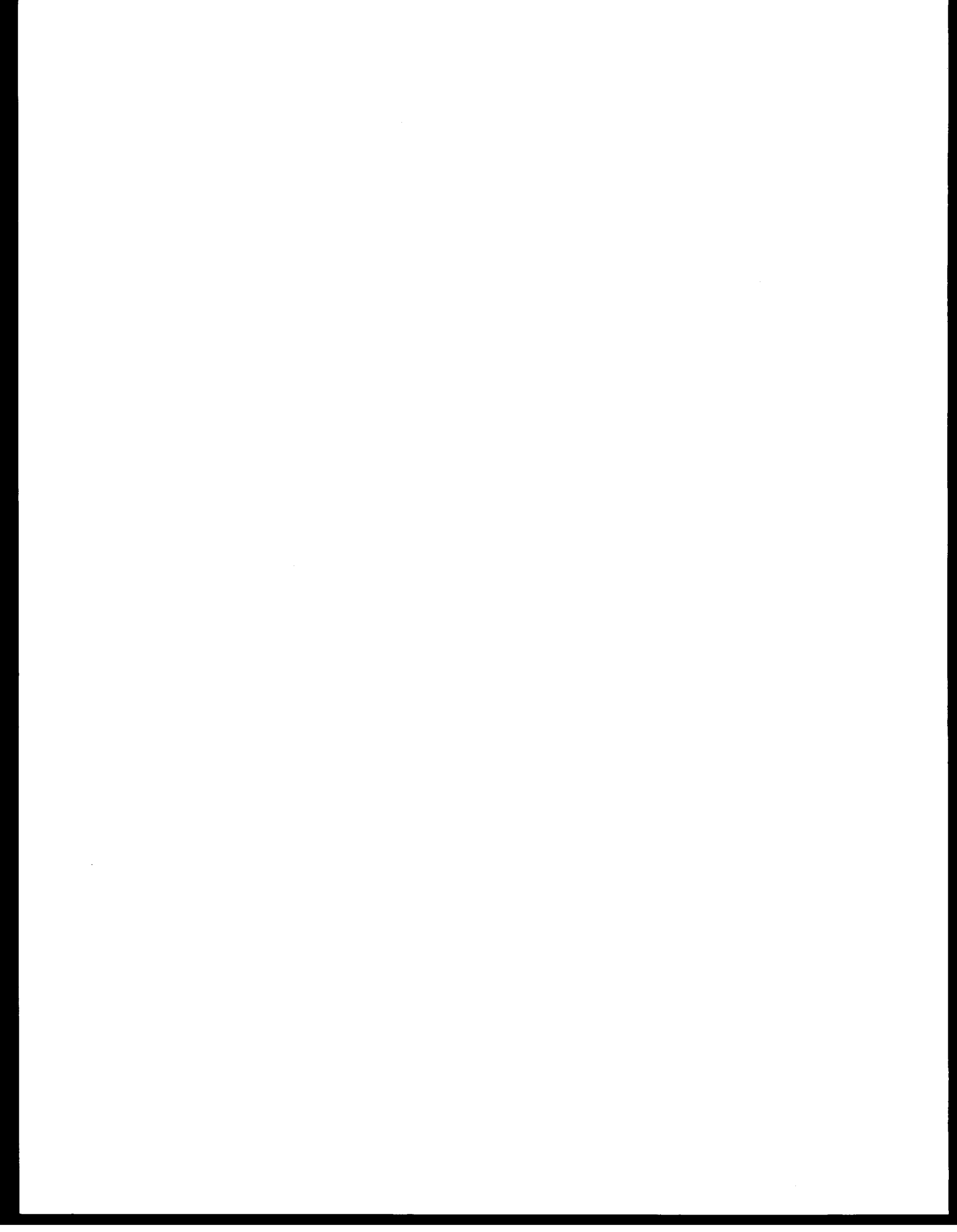
U.S. DEPARTMENT OF COMMERCE
NATIONAL OCEANIC AND ATMOSPHERIC ADMINISTRATION
NATIONAL OCEAN SERVICE
OFFICE OF OCEANOGRAPHY AND MARINE ASSESSMENT
OCEAN ASSESSMENTS DIVISION
ALASKA OFFICE

ANCHORAGE, ALASKA



The facts, conclusions, and issues appearing in these reports are based on research results of the Outer Continental Shelf Environmental Assessment Program (OCSEAP), which is managed by the National Oceanic and Atmospheric Administration, U.S. Department of Commerce, and primarily funded by the Minerals Management Service, U.S. Department of the Interior, through interagency agreement.

Mention of a commercial company or product does not constitute endorsement by the National Oceanic and Atmospheric Administration. Use for publicity or advertising purposes of information from this publication concerning proprietary products or the tests of such products is not authorized.



Outer Continental Shelf Environmental Assessment Program
Final Reports of Principal Investigators

VOLUME 26

NOVEMBER 1984

C O N T E N T S

J. A. GALT AND G. WATABAYASHI: Modeling report to OCSEAP.	1
J. A. GALT, J. E. OVERLAND, C. H. PEASE, AND R. J. STEWART: Numerical studies--Pacific Marine Environmental Laboratory	63

MODELING REPORT TO OCSEAP

by

J. A. Galt and G. Watabayashi

U.S. Department of Commerce
National Oceanic and Atmospheric Administration
Environmental Research Laboratories
Pacific Marine Environmental Laboratory
3711 15th Avenue N.E.
Seattle, Washington 98105

Current address:
Hazardous Materials Response Branch (N/OMA34)
Ocean Assessments Division
Office of Oceanography and Marine Assessment
National Ocean Service, NOAA
BIN C15700
7600 Sand Point Way N.E.
Seattle, Washington 98115

Final Report
Outer Continental Shelf Environmental Assessment Program
Research Unit 140

January 1980
(Minor revisions, November 1984)

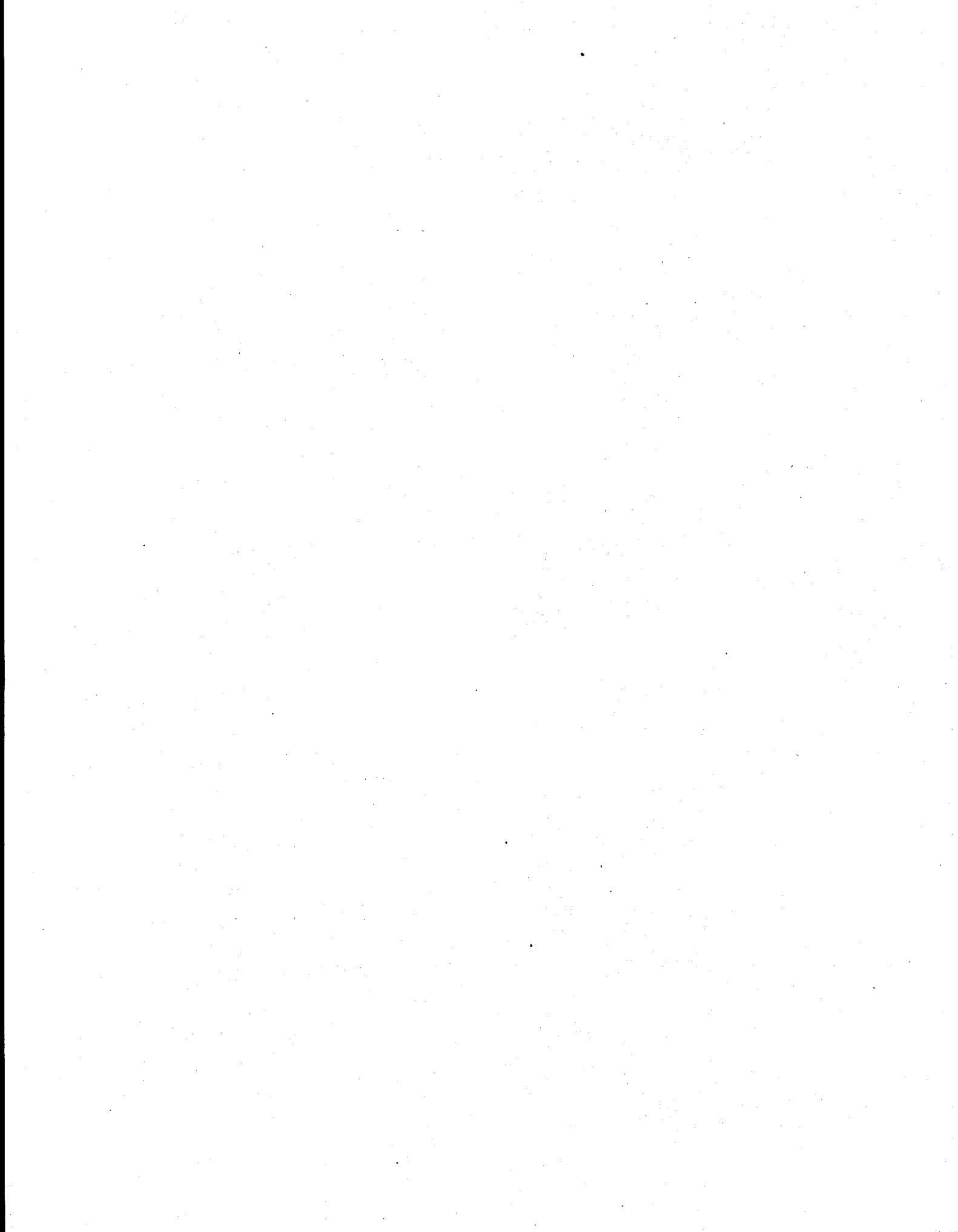


TABLE OF CONTENTS

	Page
I. INTRODUCTION.	5
II. KODIAK REGIONAL STUDY	7
Barotropic Mode	10
Baroclinic Mode	13
Averages of Baroclinic Modes.	21
Composite Currents.	27
Comparison of Observed Current Features and Model Results	38
III. FAIRWEATHER GROUND STUDY.	41
Barotropic Mode	44
Baroclinic Mode	45
Composite Regional Currents	51
IV. CONCLUSIONS	54

[The page contains extremely faint and illegible text, likely bleed-through from the reverse side of the document. No specific content can be transcribed.]

I. Introduction

Over the last year modeling experiments have been carried out for two areas of the Alaskan Outer Continental Shelf as part of the work done on RU 140. The first study area was in the vicinity of Kodiak Island; the second study area covered the Fairweather Ground region. Both of these studies made use of oceanographic data obtained in other components of the OCSEAP program and a diagnostic circulation model developed previously under RU 140.

The circulation model and its use have been described elsewhere (RU #140 - Report to OCSEAP September 1978) so a detailed description of those procedures will not be presented here. To briefly summarize the techniques for obtaining current estimates, we proceed as follows:

- 1) The flow is assumed to be quasi-steady;
- 2) The dynamics are assumed to be controlled by a combination of geostrophic and Ekman flows;
- 3) The geostrophic flow is separated into two components;
- 4) The first component is baroclinic and is forced by the internal mass distribution and, as such, requires oceanographic data. The resolution will depend upon available station spacing and may be noisy in the sense that detailed current features may be poorly resolved or aliased;
- 5) The second geostrophic component is barotropic and represents the large-scale effect of wind set-up of the sea surface. This component of the flow is density independent and is assumed to be in dynamic balance with the regional wind.
- 6) These two components of the geostrophic flow added together with a simple non-divergent surface Ekman layer are then assumed to represent the regional surface currents.

The diagnostic circulation model is solved using a finite element technique and a bases set of first order triangular elements. The

dependent variable is the elevation of the sea surface. Results are presented as either vector arrows over the region in question or maps of sea surface elevation which can then be taken to represent streamlines of the surface flow.

II. Kodiak Regional Study

The Kodiak Regional Study covered the continental shelf area surrounding Kodiak Island. It extended from the Kenai Peninsula in the northeast to Chirikof Island in the southwest. Within this regional study special emphasis was put on the area just offshore and east from Kodiak Island. This is a complex region of banks and troughs which is identified as Portlock Bank, Marmot Bank, and Albatross Bank. This particular section of the continental shelf has extremely complex topography, and thus, required a high resolution system of grid points or triangular finite elements to resolve the region in sufficient detail. To cover the region over 400 vertices were used with subsections being run independently and then analytically combined. Figure 1 represents the general area of the study and Figure 2 represents the bathymetric features which were resolved within the model. For purposes of description, we see that the northeast section of the region is covered by Portlock Bank. Stevenson Entrance leads in towards Cook Inlet and around to Shelikof Strait, which separates Kodiak Island from the mainland. Offshore from Kodiak is a series of complex banks which are collectively referred to as Marmot and Albatross Banks. To the southeast of Kodiak Island are the Trinity Islands and beyond that, the outflow from Shelikof Strait which moves toward Chirikof Island.

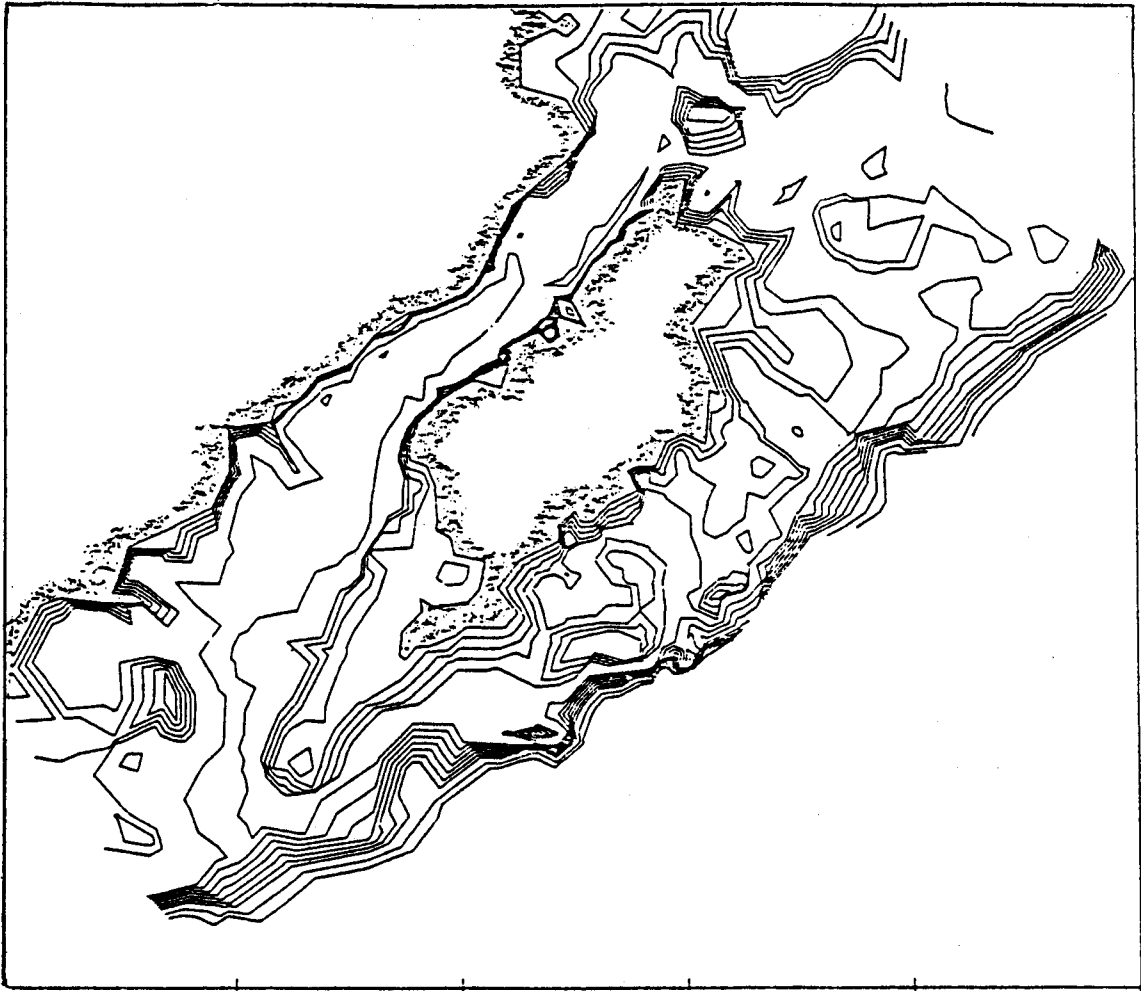


Figure 2. Shelf bathymetry resolved during the barotropic mode studies for the Kodiak region. Shaded areas represent the coastline of Kodiak Island and the Alaskan Peninsula. Contour intervals (m) (20, 40, 601200)

Barotropic Mode

The first component of the flow to be considered is the barotropic circulation. It is assumed that this flow results from the set-up of the sea surface by the regional winds. In this case, the regional wind stress was assumed to be in bathystrophic balance along the north-east boundary of the model with the sea surface sloping upwards toward the Kenai Peninsula. With this as boundary conditions, the four regional sub-models were run and the results combined to derive the current pattern shown in Figure 3. Figure 3a shows the computed vector arrows at triangle centroids and Figure 3b shows the current vectors evaluated on the standard cartesian grid. This is representative of the flow patterns that can be expected given this large-scale regional forcing. The actual magnitude associated with these currents will depend on the magnitude of the wind stress. For moderate to strong wind cases, characteristic velocities are on the order of 1 knot. From a study of this figure, a number of features of the barotropic flow can be identified:

- 1) A general flow is seen to be southwest through Shelikof Strait. This is fed in part by flow from Cook Inlet, and in part from flow through Stevenson Entrance;
- 2) In the vicinity of Portlock Bank flow is generally to the southwest along the coast. Major cross-shelf intrusions of water are identified with the trough regions. Onshore flow is along the eastern and deeper part of the trough, then there is a subsequent offshore flow along the western edge of this trough. Further to the southeast, between Portlock Bank and Marmot Bank, cross-shelf flow is again seen in the trough that separates these two areas;
- 3) In the area of Albatross Bank just offshore from Kodiak the current is again seen to reflect the bank and trough bathymetry. The flow is seen to move onshore along the northeast side of the troughs, and offshore along the southwest section of the troughs. This is a region where a deep channel exists close to the shore and a coastal current is seen to flow toward the southwest through this region;

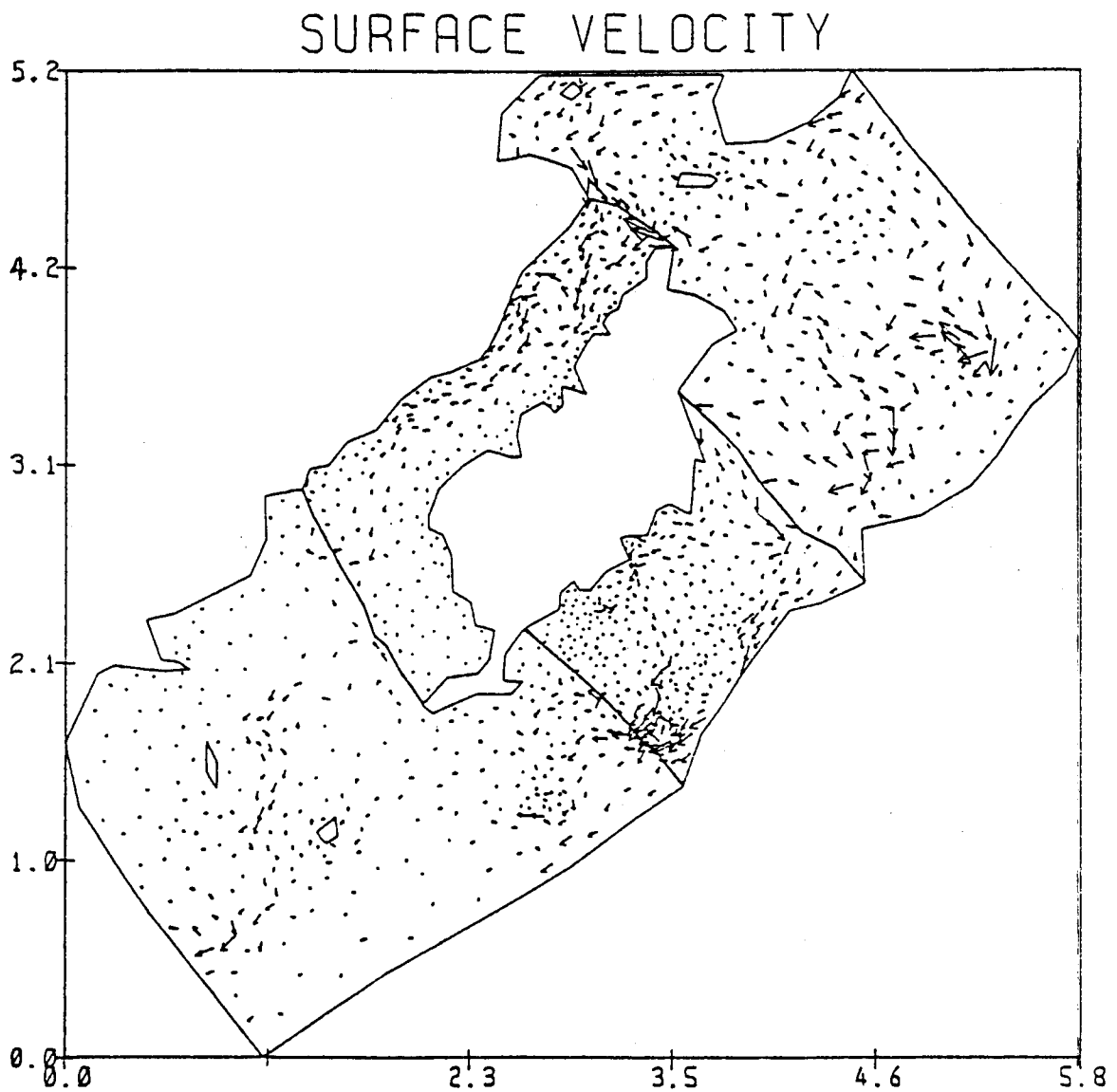


Figure 3a. A delineation of the four subregions used in the Kodiak Island study with vector arrows plotted at the centroids of the triangular bases set. The arrow spacing gives an indication of the resolution used in various parts of the model.

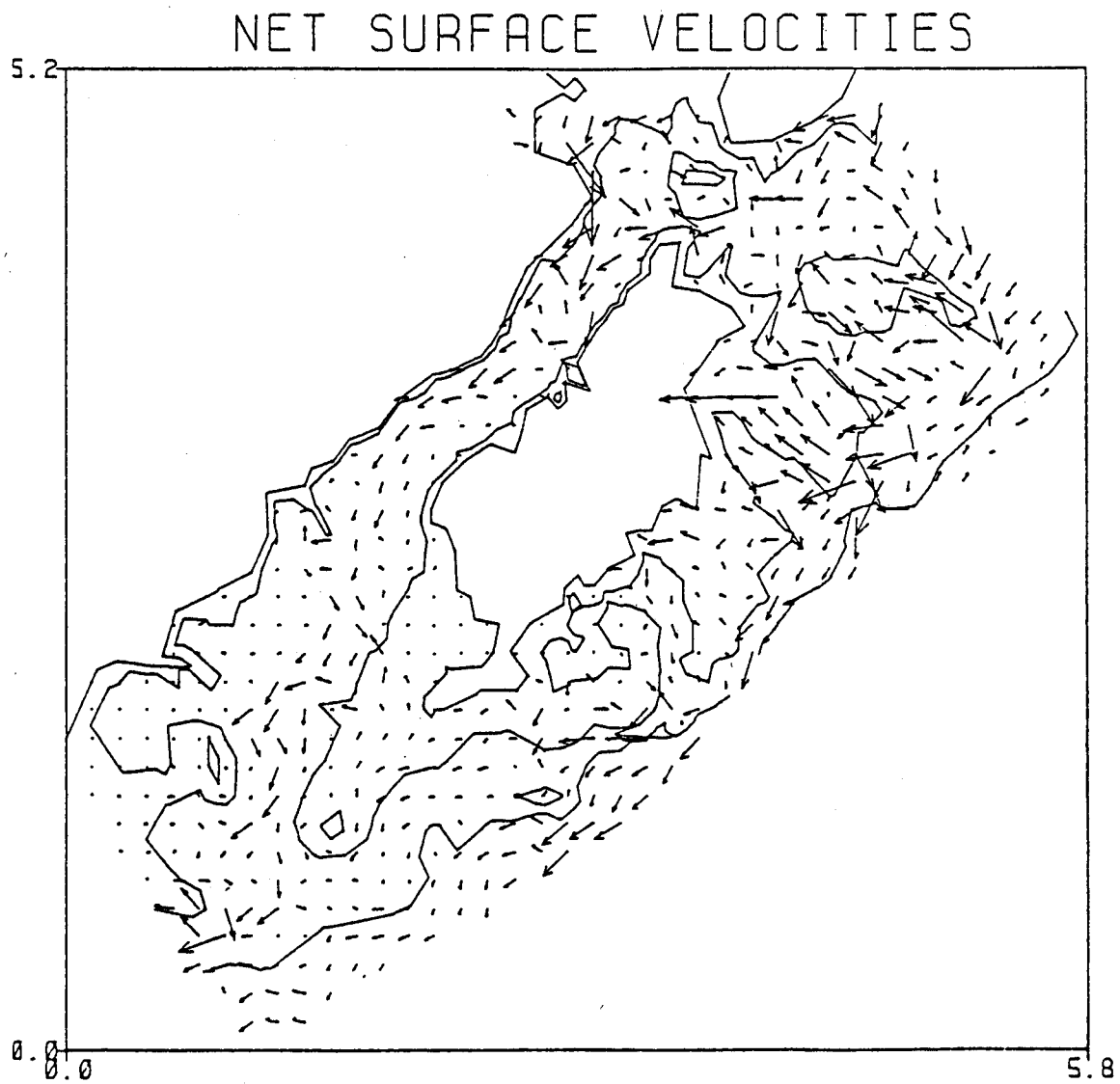


Figure 3b. Barotropic current vector arrows evaluated on a regular cartesian grid for the Kodiak Island study area.

- 4) To the southwest of Kodiak Island the flow is seen to continue in a southwest direction and be joined by the outflowing currents from Shelikof Strait.

Baroclinic Mode

The baroclinic component of the geostrophic flow was estimated using data from oceanographic cruises. For the Kodiak region, six cases were available. These cases cover the periods:

1. May 1976
2. September 1977
3. November 1977
4. April 1978
5. May 1978
6. June 1978

Each of these oceanographic cruises covered slightly different areas and has variable station spacing. For the model study, they were considered separately and, in each case, the baroclinic component of the current was calculated for regions where it was defined by sufficient oceanographic data. For purposes of comparison, all cases have been plotted on the same overall map with currents evaluated on a regular cartesian grid which has been superimposed over the triangular bases sets used computationally in the model. Figure 4 shows the results of these baroclinic studies.

Figure 4a shows the results from the May 1976 cruise. Of the six cases studied, this one had the most general coverage and the most complete set of oceanographic data. One can notice a strong baroclinic current southwest through Shelikof Strait and strong currents along the outer continental shelf edge offshore from Kodiak Island. Previous model studies have indicated a sensitivity in the model results due to poorly resolved information along the shelf edge, and it is possible that these strong currents seen along the outer edge of the model may represent noise in the data.

NET SURFACE VELOCITIES

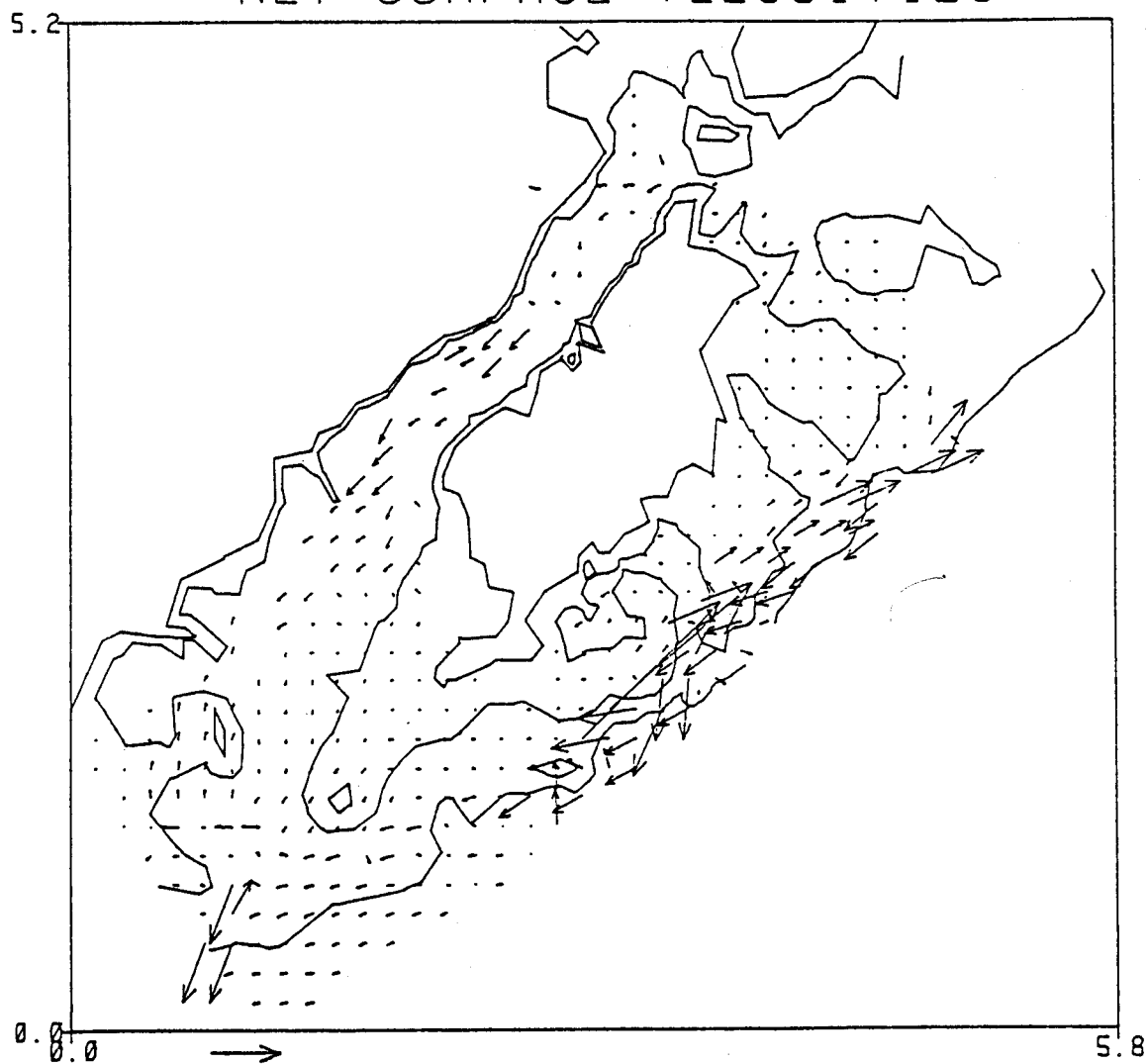


Figure 4a. Baroclinic current vectors plotted on a regular cartesian grid derived from data collected during May 1976. Scale arrow indicates 1 m/sec current.

It is also obvious that the strong currents shown in the extreme southwest corner of the model domain are the result of one hydrograph station that appears to have anomalous density data. As these vector arrows are questionable and at the extreme limit of the calculations they should be disregarded for future composites of currents.

Figure 4b represents the baroclinic currents resulting from the September 1977 oceanographic data. This study covered the Portlock Bank and northeast section of Albatross Bank. A general southwest set to the baroclinic currents over the continental shelf is seen and, once again, stronger currents along the outer edge of the continental shelf with the possibility of poorly resolved eddies or streams.

Figure 4c shows the results of November 1977 oceanographic data concentrating on the Albatross Bank region. Once again, a general southwesterly baroclinic component to the current is seen over the shelf with higher velocities seen along the outer edge of the shelf.

The next three figures result from data collected during the spring of 1978. These figures run through the sequence April-May-June. Figure 4d represents the April data and covers Portlock Bank and along the outer edge of Kodiak down to approximately the area of the Trinity Islands. The April case shows very little baroclinic current over the shelf itself. Marmot Bank and Albatross Bank are nearly devoid of baroclinic flow. Along the outer edge of the shelf, stronger currents are observed, particularly offshore from the Trinity Islands region. In detail, these stronger currents appear as a clockwise eddy but it is also obvious that the spatial pattern is poorly resolved by the data.

Figure 4e shows the same region the following month (May 1978). In this, it can be seen that baroclinic currents are beginning to develop over

NET SURFACE VELOCITIES

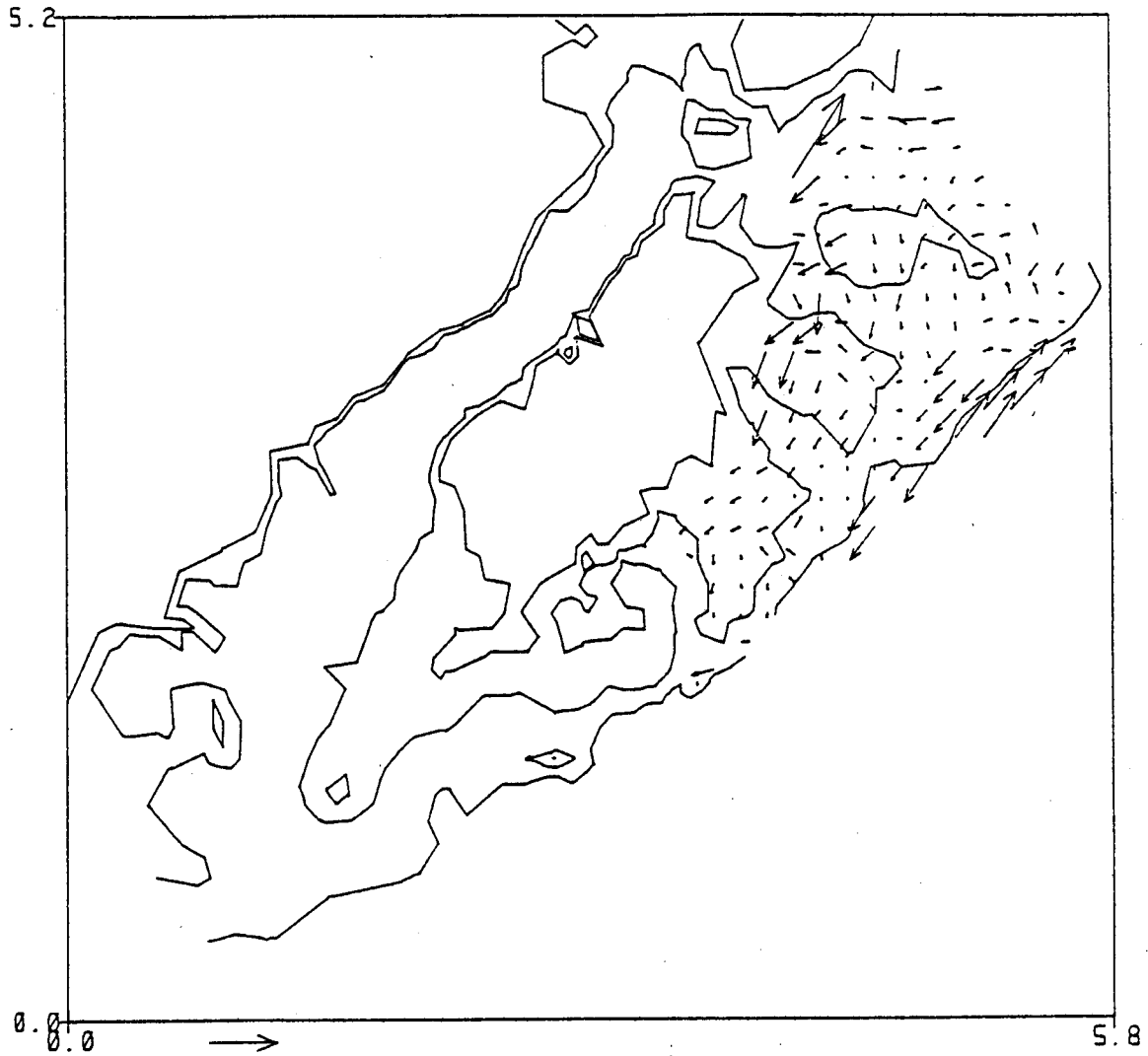


Figure 4b. Baroclinic current vectors plotted on a regular cartesian grid derived from data collected during September 1977. Scale arrow indicates 1 m/sec current.

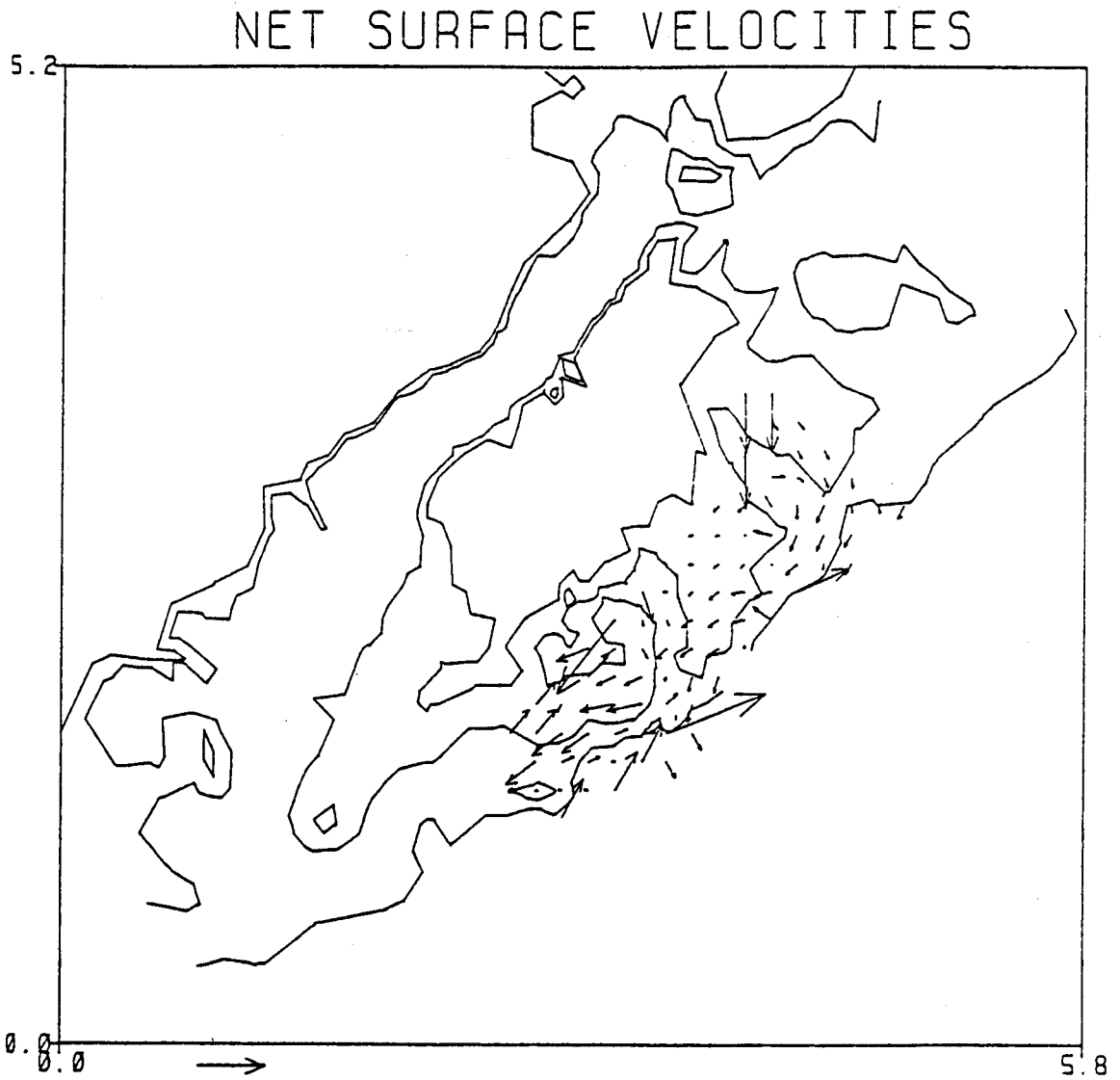


Figure 4c. Baroclinic current vectors plotted on a regular cartesian grid derived from data collected during November 1977. Scale arrow indicates 1 m/sec current.

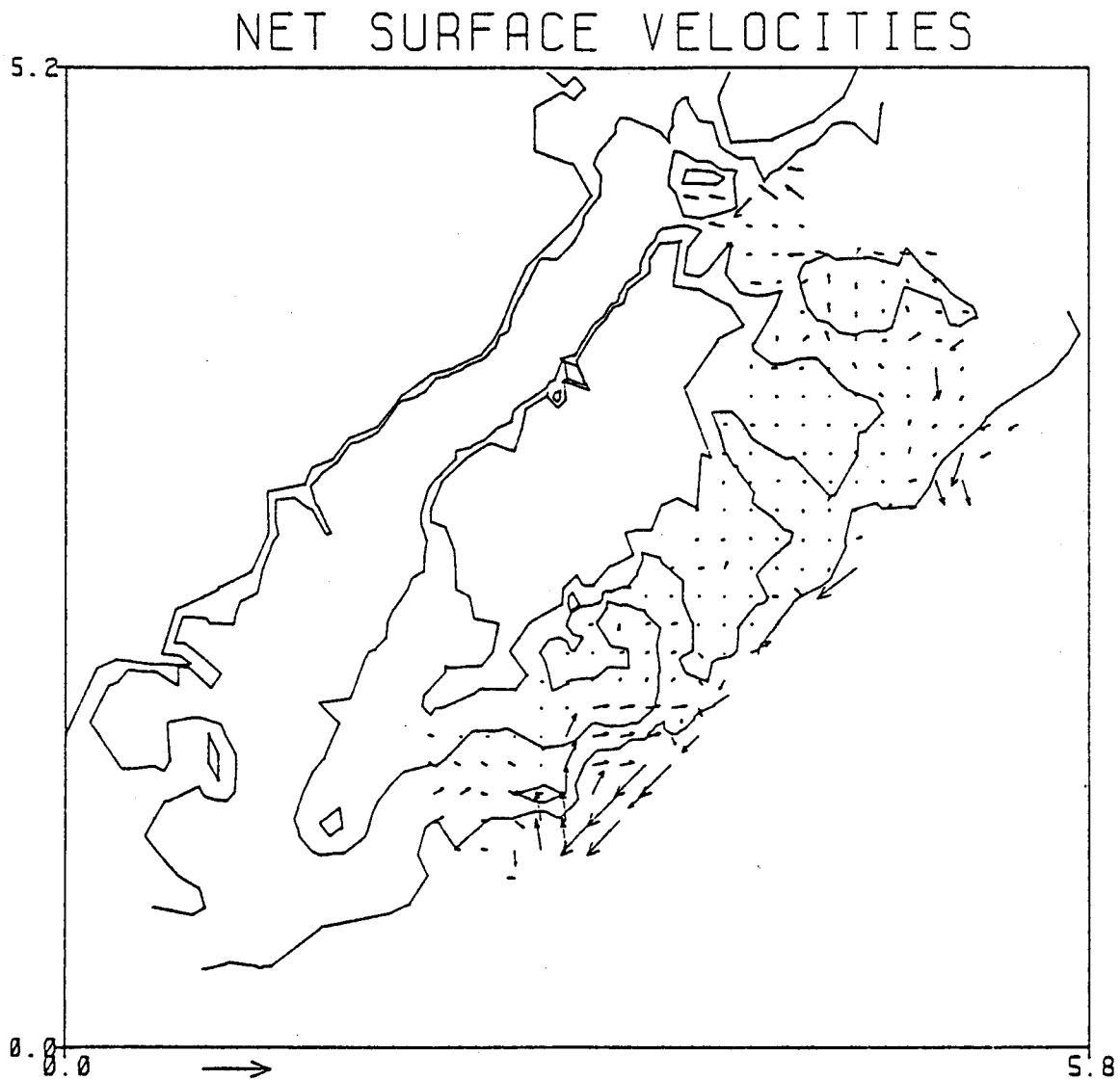


Figure 4d. Baroclinic current vectors plotted on a regular cartesian grid derived from data collected during April 1978. Scale arrow indicates 1 m/sec current.

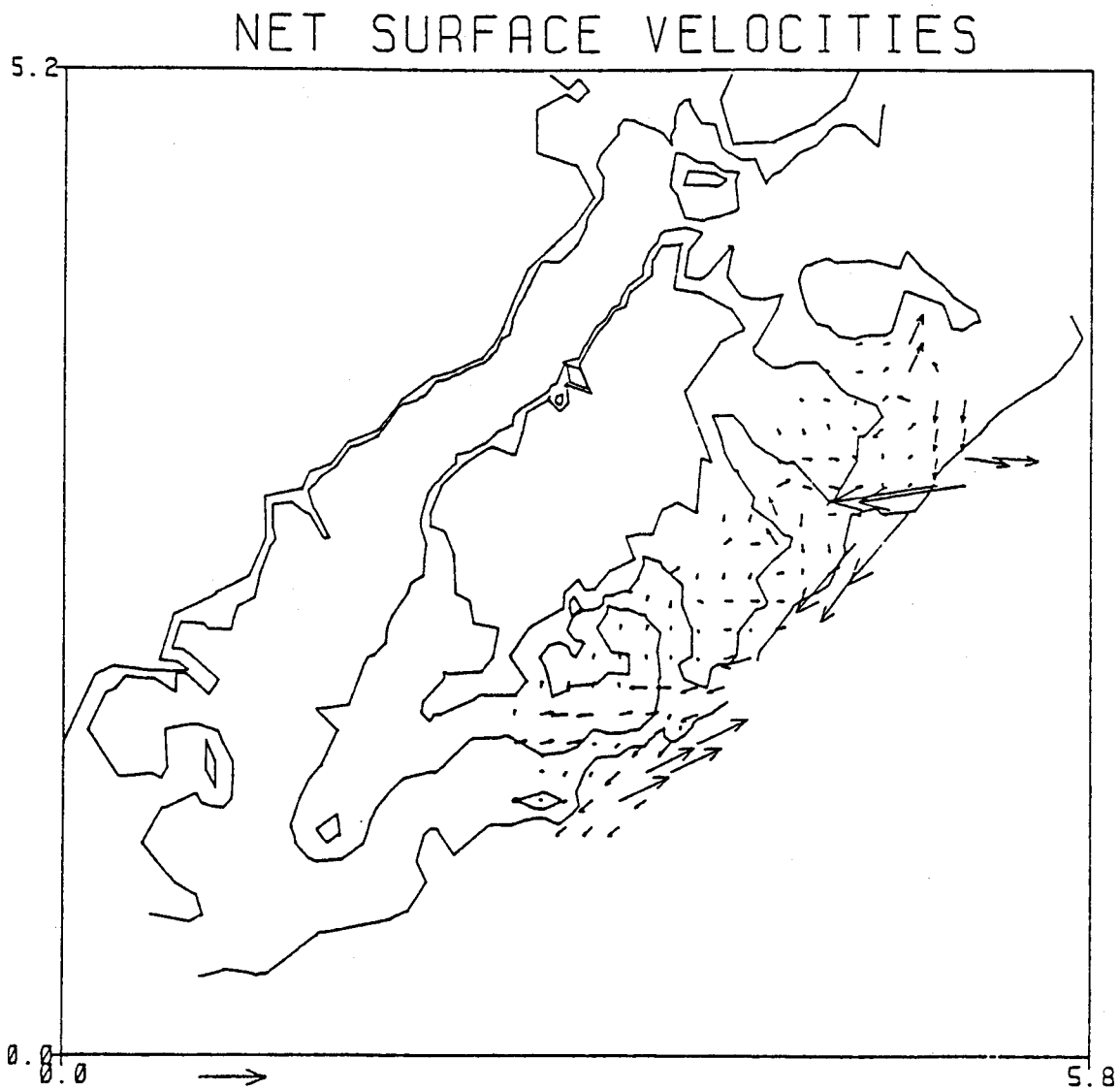


Figure 4e. Baroclinic current vectors plotted on a regular cartesian grid derived from data collected during May 1978. Scale arrow indicates 1 m/sec current.

NET SURFACE VELOCITIES

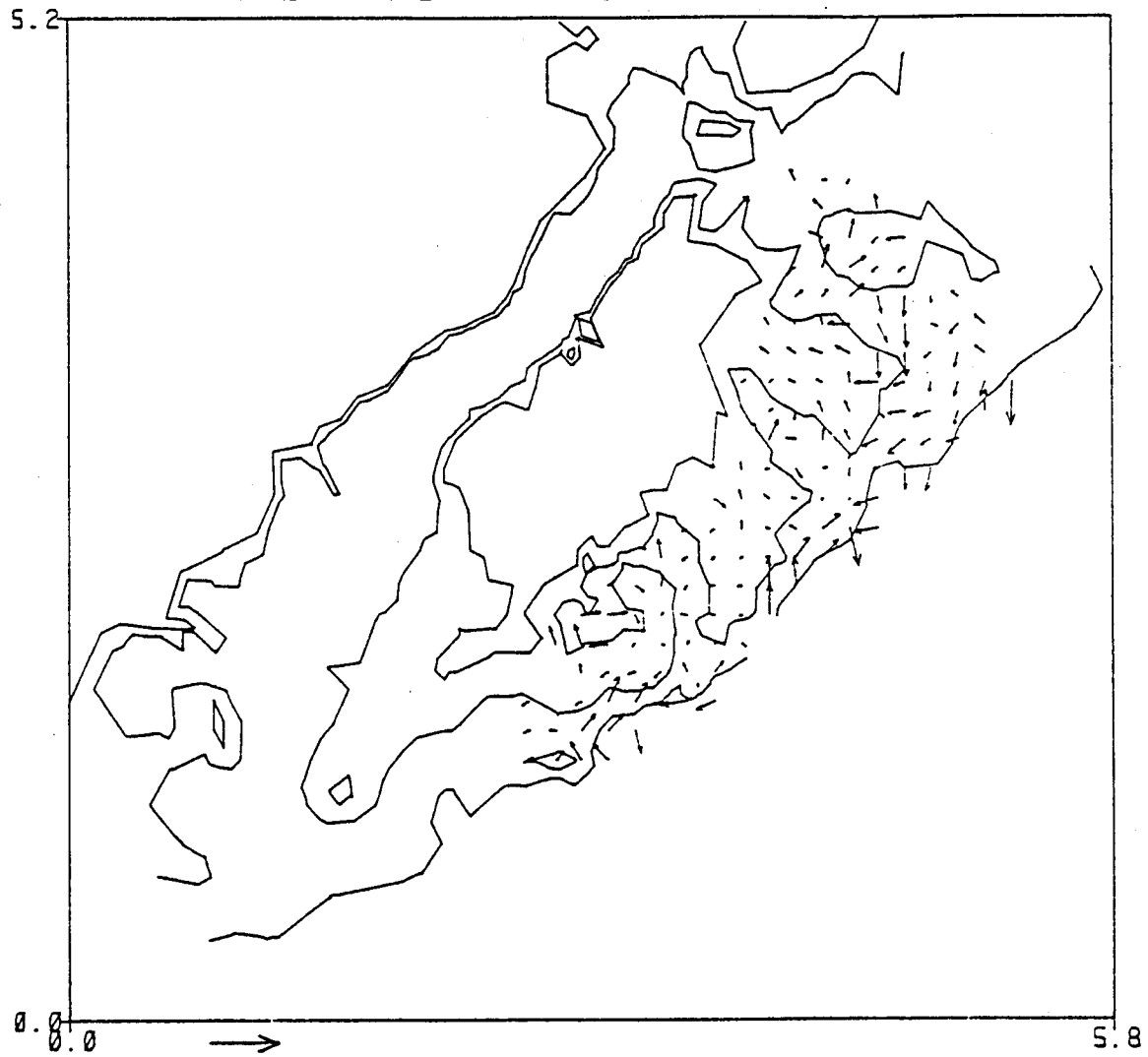


Figure 4f. Baroclinic current vectors plotted on a regular cartesian grid derived from data collected during June 1978. Scale arrow indicates 1 m/sec current.

the shelf itself, and circulation is seen over the trough area between Marmot and Albatross Banks. In addition, some baroclinic flow is seen over the southwest edge of Albatross Bank. Stronger currents are once again observed along the outer edge of the shelf, but they do not appear to be coherent with the pattern seen a month earlier.

Figure 4f shows the results of June 1978 data and covers essentially the same region as the previous two cases. By this time, the baroclinic currents are even stronger over the shelf region with an onshore component in the vicinity of Marmot Bank and a general clockwise circulation seen over Kiliuda Trough and the southwest edge of Albatross Bank.

Having looked at a number of cases of baroclinic flow certain characteristics of the regional dynamics have become apparent. There appears to be seasonal differences between the baroclinic flow over the shelf; stronger baroclinic currents are observed during the fall while decreased baroclinic currents are observed during the spring. In addition, the data collected does not appear to be able to resolve the details of the stronger flows seen along the edge of the outer continental shelf.

Averages of Baroclinic Modes

In order to get a better understanding of how the actual mean flows may look, it is instructive to consider averaging the baroclinic fields from these six cases. By doing this the stronger currents, due to poorly resolved baroclinic signatures along the edge of the shelf, should average out and a more realistic mean flow can be expected. To consider this problem in more detail, we can look at Figure 5, which indicates the area of coverage shown in the six cases considered in Figure 4. From this, it can be seen that all six of the cases cover the region between Portlock Bank and the



Figure 5. Composite overlays of the coverage from each of the six baroclinic data sets presented in Figure 4. Scale arrow indicates 1 m/sec current.

Trinity Islands. The Kiliuda Trough-Albatross Bank region is, in fact, covered by all six cases: whereas the Shelikof Strait and southwest section of the model was only covered once, in May of 1976. Figure 6a represents the total baroclinic flow or the average of all six cases. This was calculated by taking the total number of estimates for each grid location and dividing by the number of estimates. Regions where there was only one case (as in the Shelikof Straits) were computed as the value given from the May 1976 data whereas regions over Kiliuda Trough were the average of all six cases. As expected, Figure 6a shows smoother flow with southwest currents through Shelikof Straits and a general southwest drift over the outer continental shelf region. The region of the outer continental shelf break is once again an area of stronger currents, but appears definitely less noisy than before. It is interesting to note that even with all six of the cases averaged, a counterclockwise circulation region is seen along the shelf edge offshore from the Trinity Islands.

Figure 6b shows the average of the two fall cases (September and November 1977). These two cases show the flow as southwest over most of the region with stronger current nearshore in the vicinity of Marmot Bank and weaker currents over the central area of Albatross Bank. It is interesting to note that the fall case shows a relatively strong baroclinic signature over the shelf. This appears to reflect the increase in baroclinic structure that develops over the summer period.

Figure 6c represents the average of the spring cases (May 1976 and April-May-June 1978). From this data the flow is seen to be generally weak over the shelf with stronger currents along the shelf break. In this case the relatively weak signature seen in the spring is presumably the result of a general breakdown of baroclinic structure over the continental shelf in the wintertime.

NET SURFACE VELOCITIES

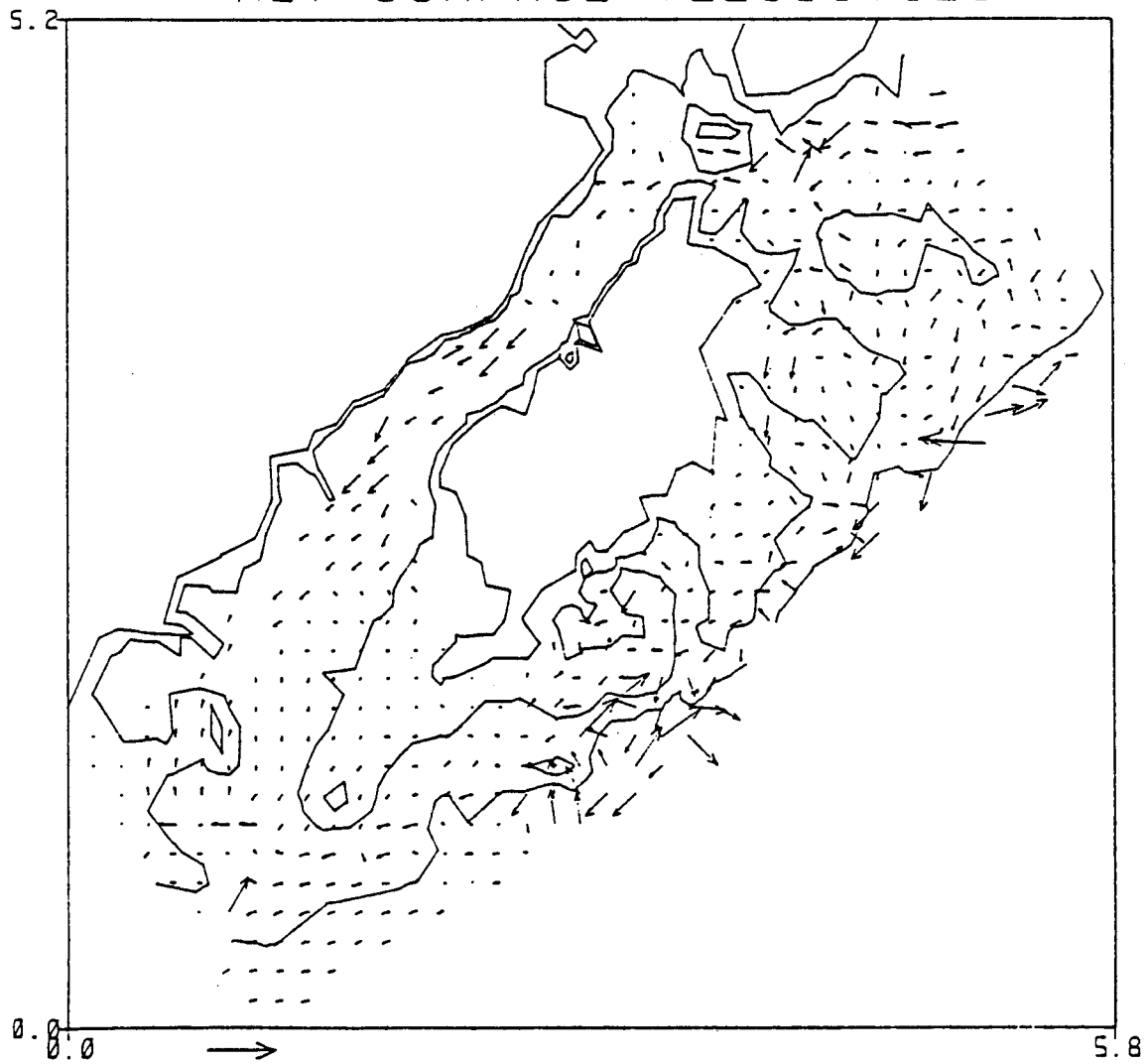


Figure 6a. Average baroclinic currents derived from all six baroclinic data sets. Scale arrow indicates 1 m/sec current.

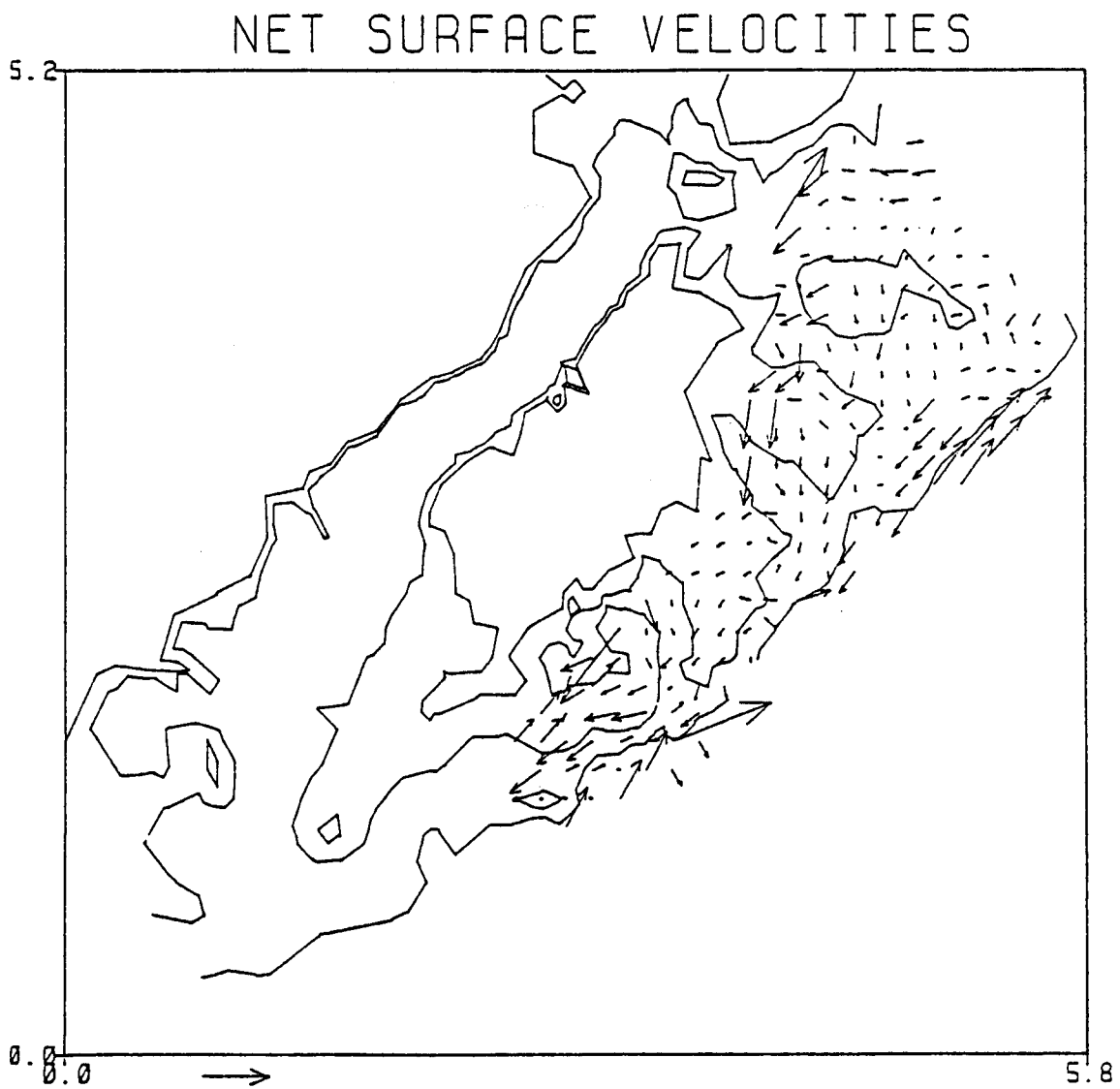


Figure 6b. Fall average baroclinic currents derived from September 1977 and November 1977 data. Scale arrow indicates 1 m/sec current.

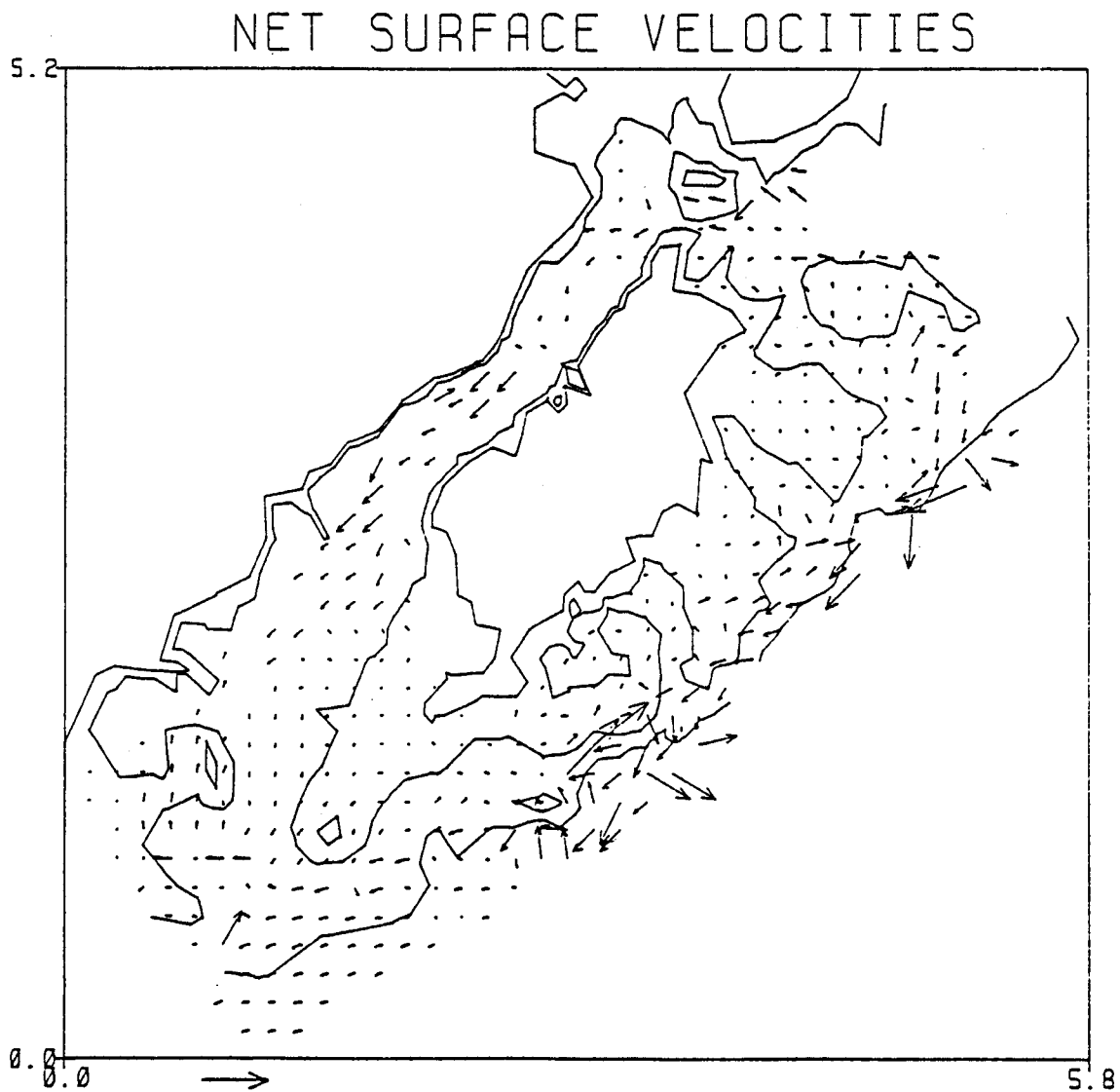


Figure 6c. Spring average baroclinic currents derived from May 1976 and April, May, and June 1978 data. Scale arrow indicates 1 m/sec current.

Composite Currents

We are now in a position to consider the total surface current estimates for the Kodiak region. The total current will be the algebraic sum of the baroclinic modes and the barotropic pattern. To combine these currents, we must assign a magnitude to the barotropic component of the flow. This can be done based on estimates of the winds set up along the coast; a number of different cases are considered. Figures 7a, 7b, and 7c represent examples of the barotropic mode plus the average baroclinic flow. Figure 7a represents a moderate wind case that results in the onshore set-up of the sea surface. This would correspond to a large-scale wind pattern which had a southwest component to the wind. Such patterns are relatively common in the Gulf of Alaska, and are associated with low pressure and cyclonic atmospheric circulation over the central Gulf.

Figure 7b shows the expected pattern for increasing southwest wind components. This would be like the previous case but for a stronger wind regime.

Figure 7c is present for completeness and indicates what would be expected for a wind condition that depressed, or set down, the sea surface. This would correspond to a large-scale weather pattern that led to northeast winds along the coast.

Figure 8 represents the composite currents derived from the averaged fall data and the pattern information from the barotropic study. Figure 8a represents a moderate set-up of the sea surface associated with cyclonic circulation in the Gulf. Figure 8b represents an increased wind event or flow driven by stronger southwest winds. Figure 8c represents the set-down conditions associated with cyclonic flow over the Gulf or a weak northeast wind along the coast.

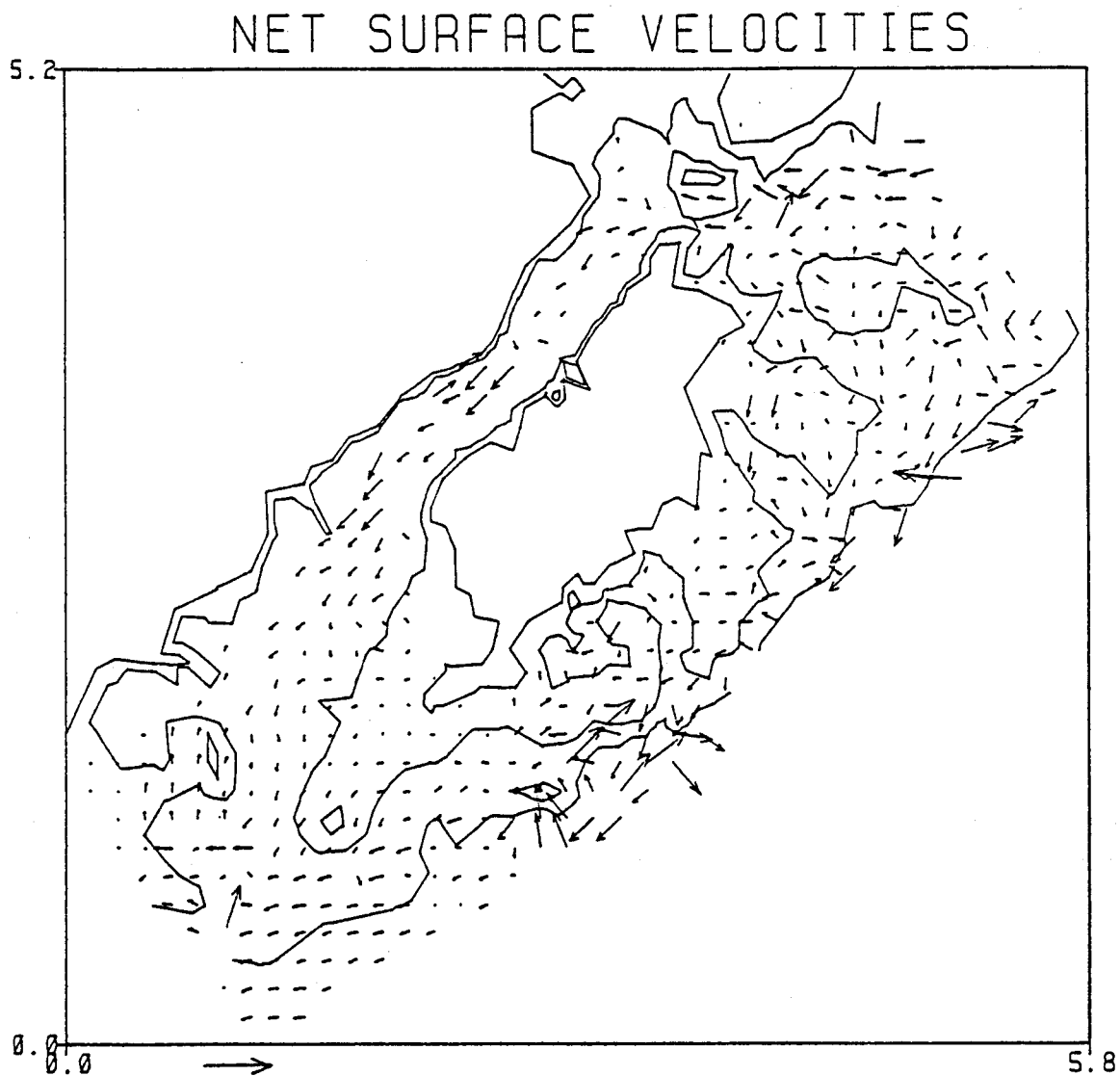


Figure 7a. Composite current vectors showing the sum of the average baroclinic mode and a moderate barotropic mode. Scale arrow indicates 1 m/sec current.

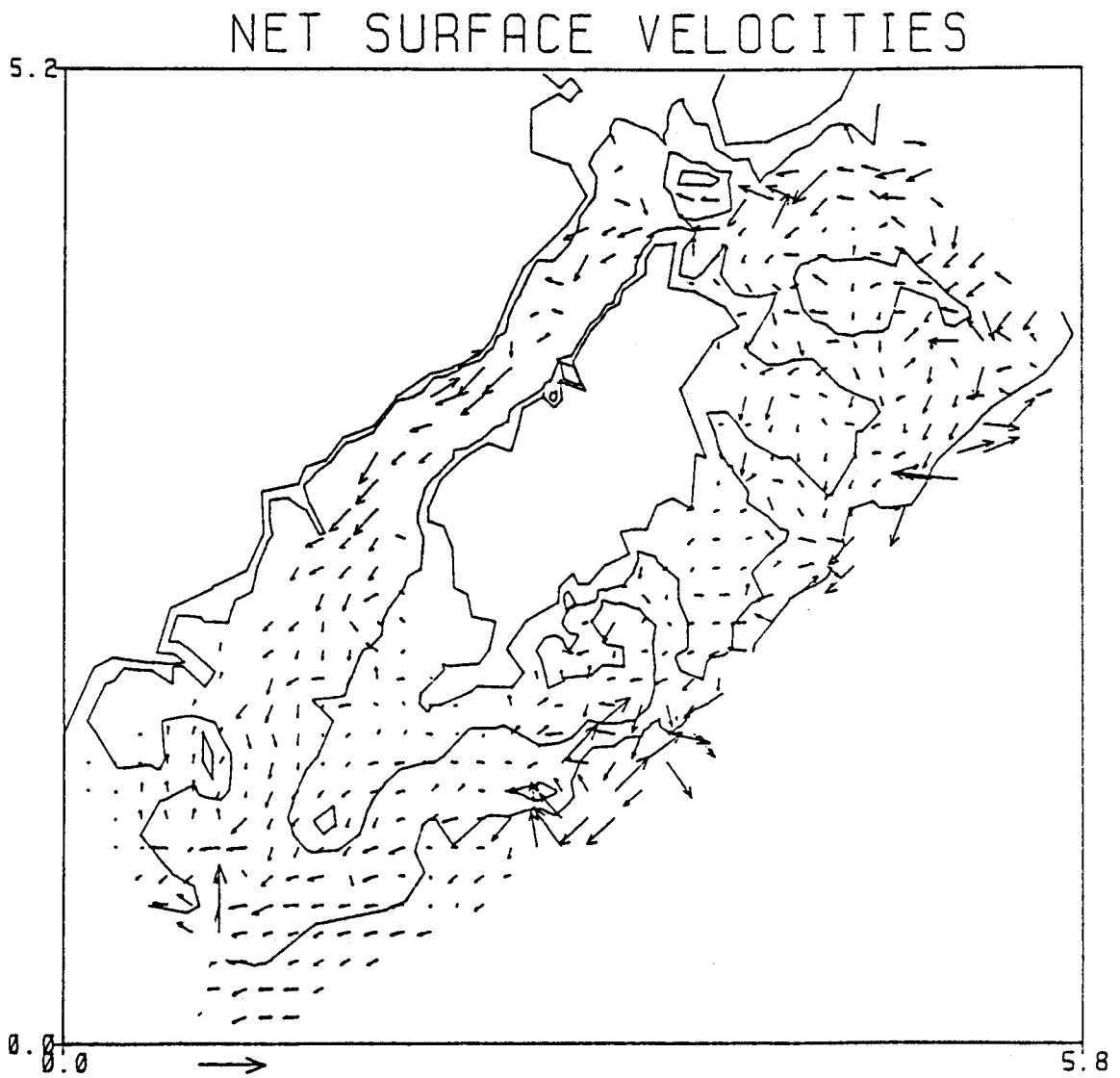


Figure 7b. Composite current vectors showing the sum of the average baroclinic mode and a large to intermediate barotropic mode. Scale arrow indicates 1 m/sec current.

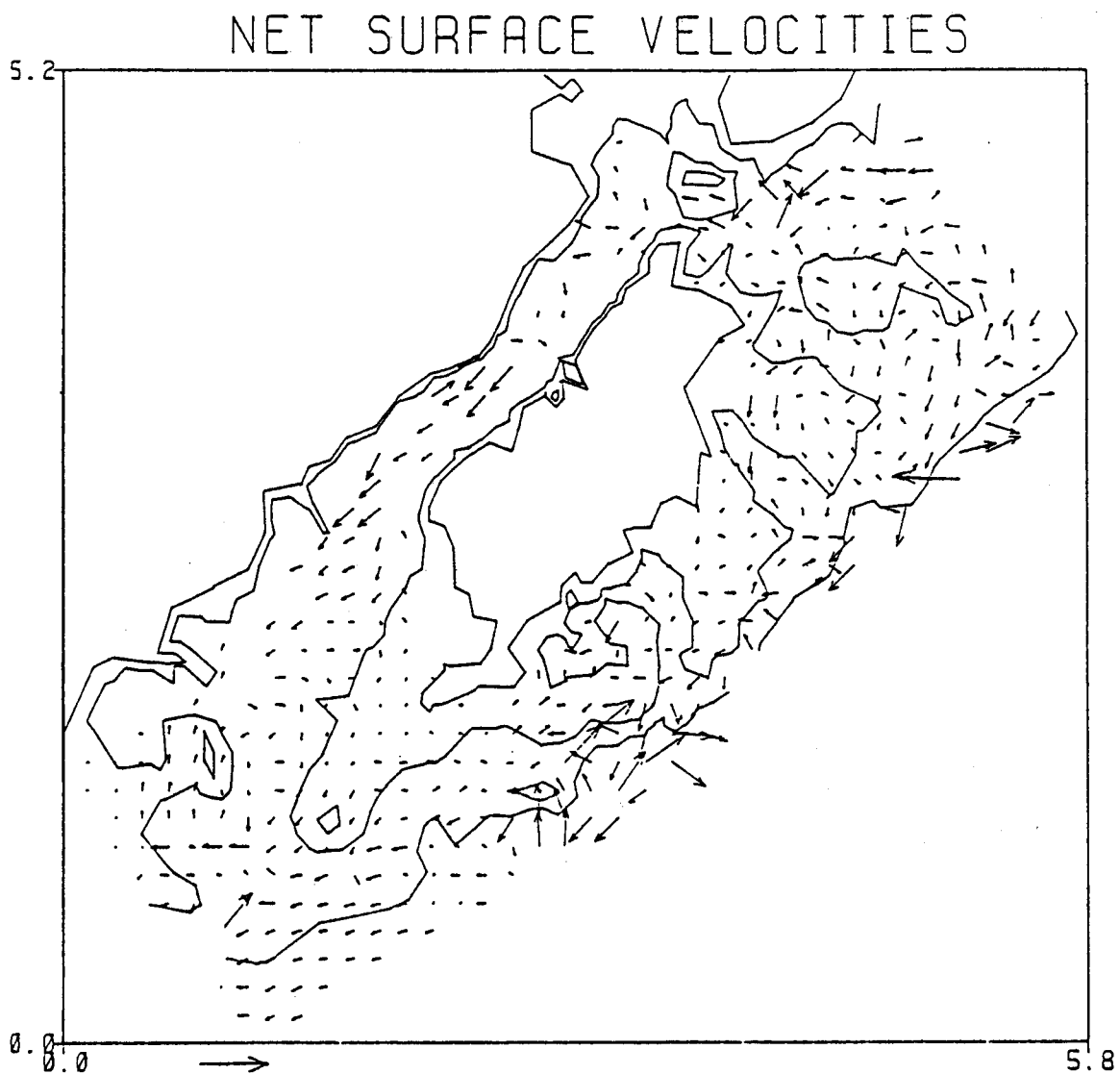


Figure 7c. Composite current vectors showing the sum of the average baroclinic mode and a weak negative barotropic mode. Scale arrow indicates 1 m/sec current.

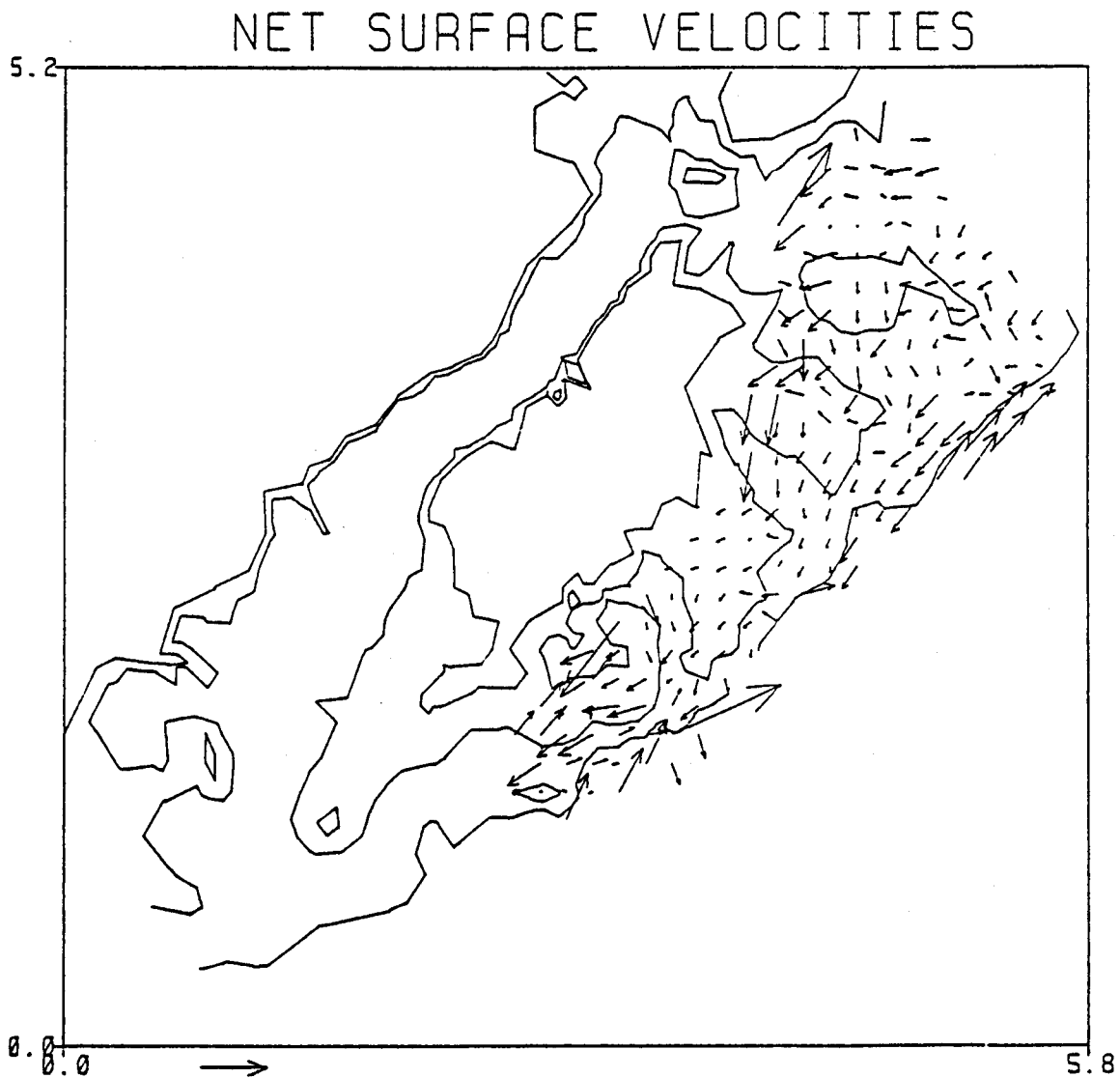


Figure 8a. Composite current vectors showing the sum of the fall average baroclinic mode and a moderate barotropic mode. Scale arrow indicates 1 m/sec current.

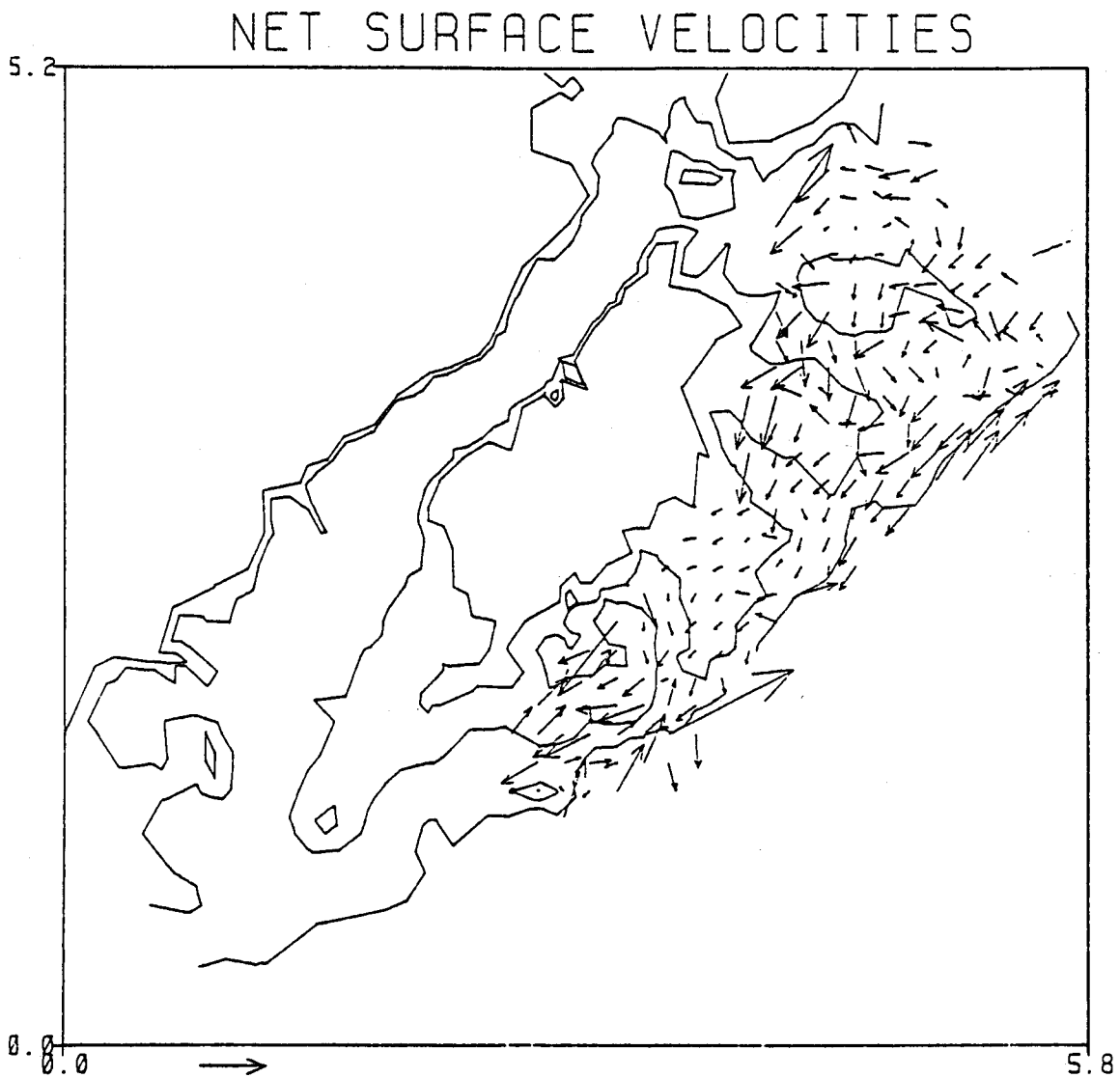


Figure 8b. Composite current vectors showing the sum of the fall average baroclinic mode and a large to intermediate barotropic mode. Scale arrow indicates 1 m/sec current.

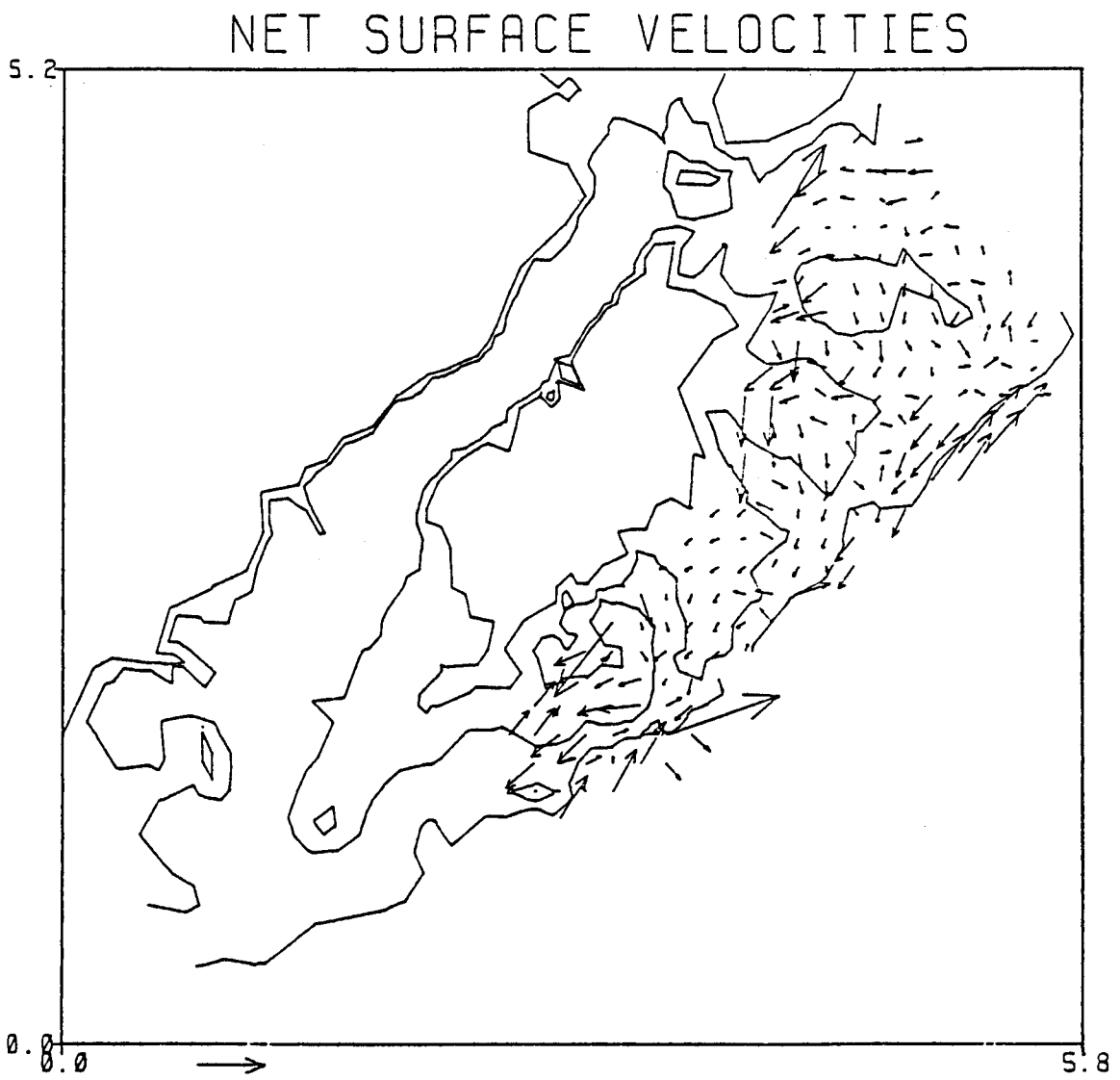


Figure 8c. Composite current vectors showing the sum of the fall average baroclinic mode and a weak negative barotropic mode. Scale arrow indicates 1 m/sec current.

Figure 9 is a composite of the four springtime baroclinic fields and the barotropic pattern information. Figure 9a represents a moderate cyclonic circulation pattern for the region (winds towards the southwest over the Kodiak region at approximately 10 knots), and Figure 9b represents the results of a stronger cyclonic wind event (winds toward the southwest over the Kodiak region at approximately 20 knots). Finally, Figure 9c represents the weak northeast winds along the coast (winds towards the northeast over the Kodiak region at approximately 10 knots).

The model studies of the Kodiak region have produced current patterns which include the baroclinic data from a number of different oceanographic observation sets, as well as the dynamic constraints that are associated with the barotropic set-up of the sea surface along the coast. Although this is an extremely complicated domain, a number of features of the flow have been identified, and appear to be consistent with observations and recognized regional dynamics. A persistent southwest flow through Shelikof Strait appears to be fed jointly from outflow from Cook Inlet and flow northwest through Stevenson Entrance. Along the outer edge of Kodiak Island the currents set to the southwest with major perturbations and convolutions in the flow pattern associated with the complex bank and trough topography. In particular, the troughs between Portlock Bank, Marmot Bank, and the various components of Albatross Bank, are all seen to affect the flow. The dynamics of this appear to be related primarily to the barotropic mode where the planetary vorticity interacts with the bathymetry. This suggests that the model dynamics represent an appropriate way to extrapolate current information over this complex region. The baroclinic data is seen to be generally consistent when averaged over seasonal values but flow along the outer edge of the continental shelf is apparently not resolved by the available data.

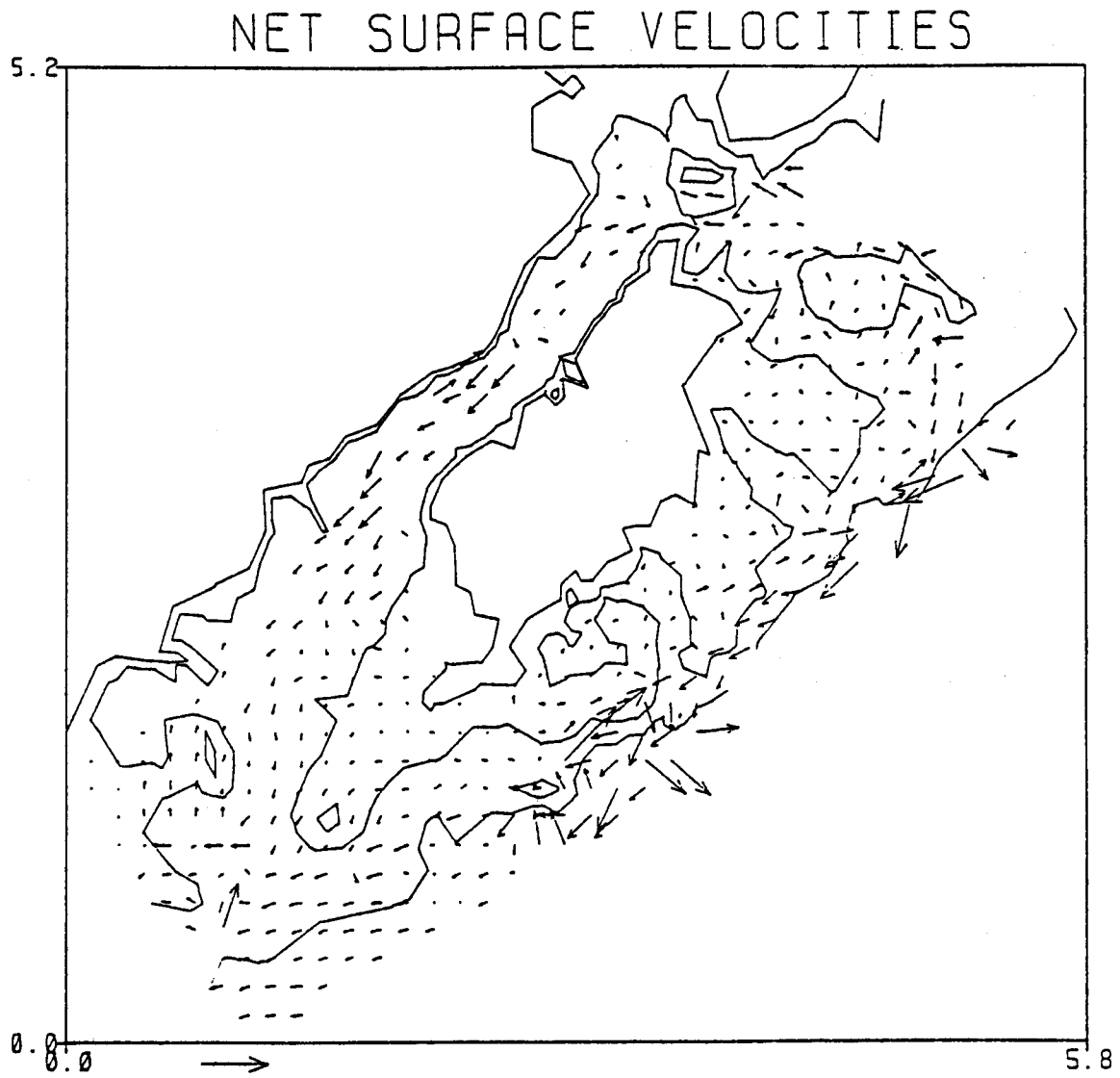


Figure 9a. Composite current vectors showing the sum of the spring average baroclinic mode and a moderate barotropic mode. Scale arrow indicates 1 m/sec current.

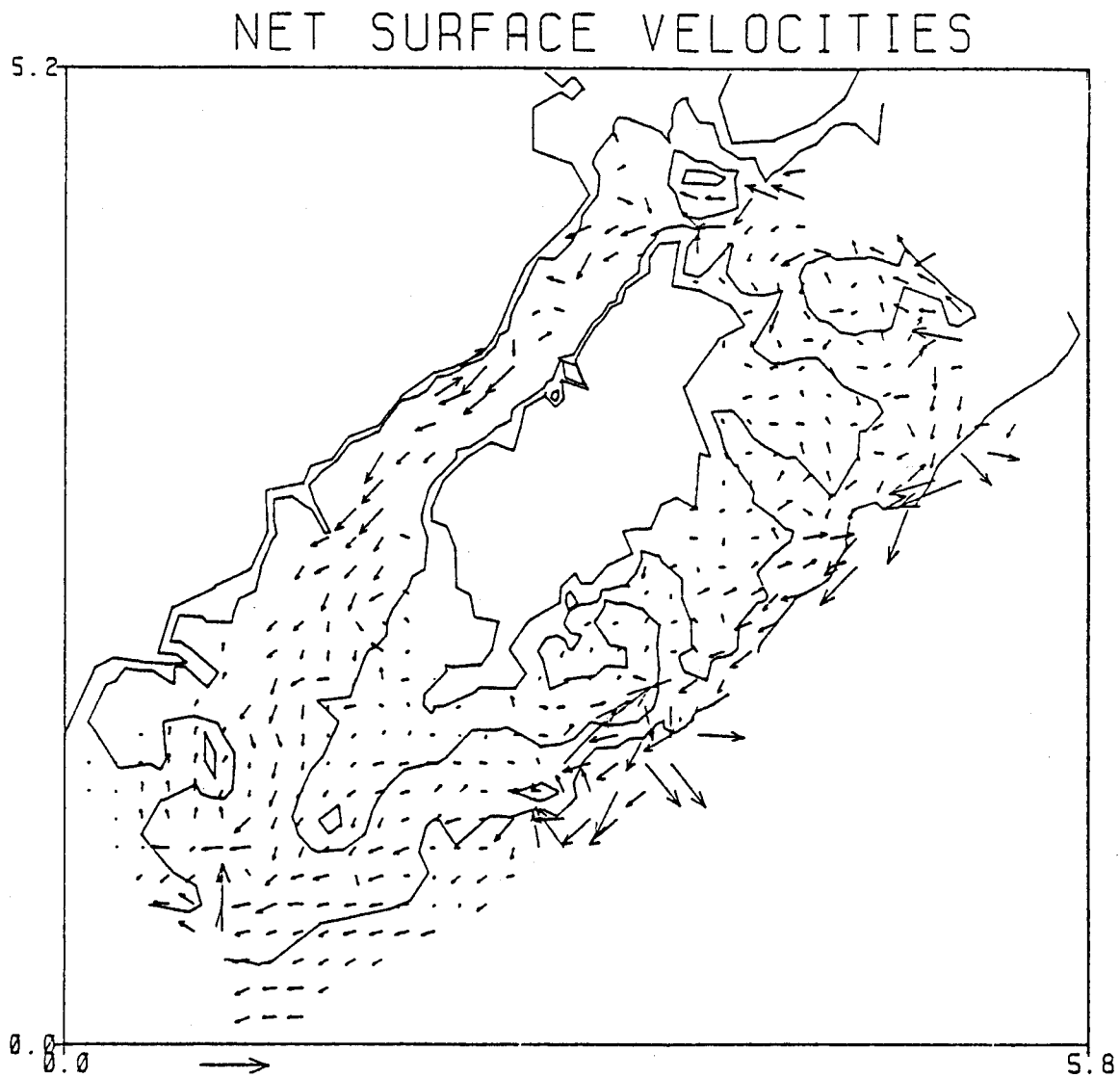


Figure 9b. Composite current vectors showing the sum of the spring average baroclinic mode and a large to intermediate barotropic mode. Scale arrow indicates 1 m/sec current.

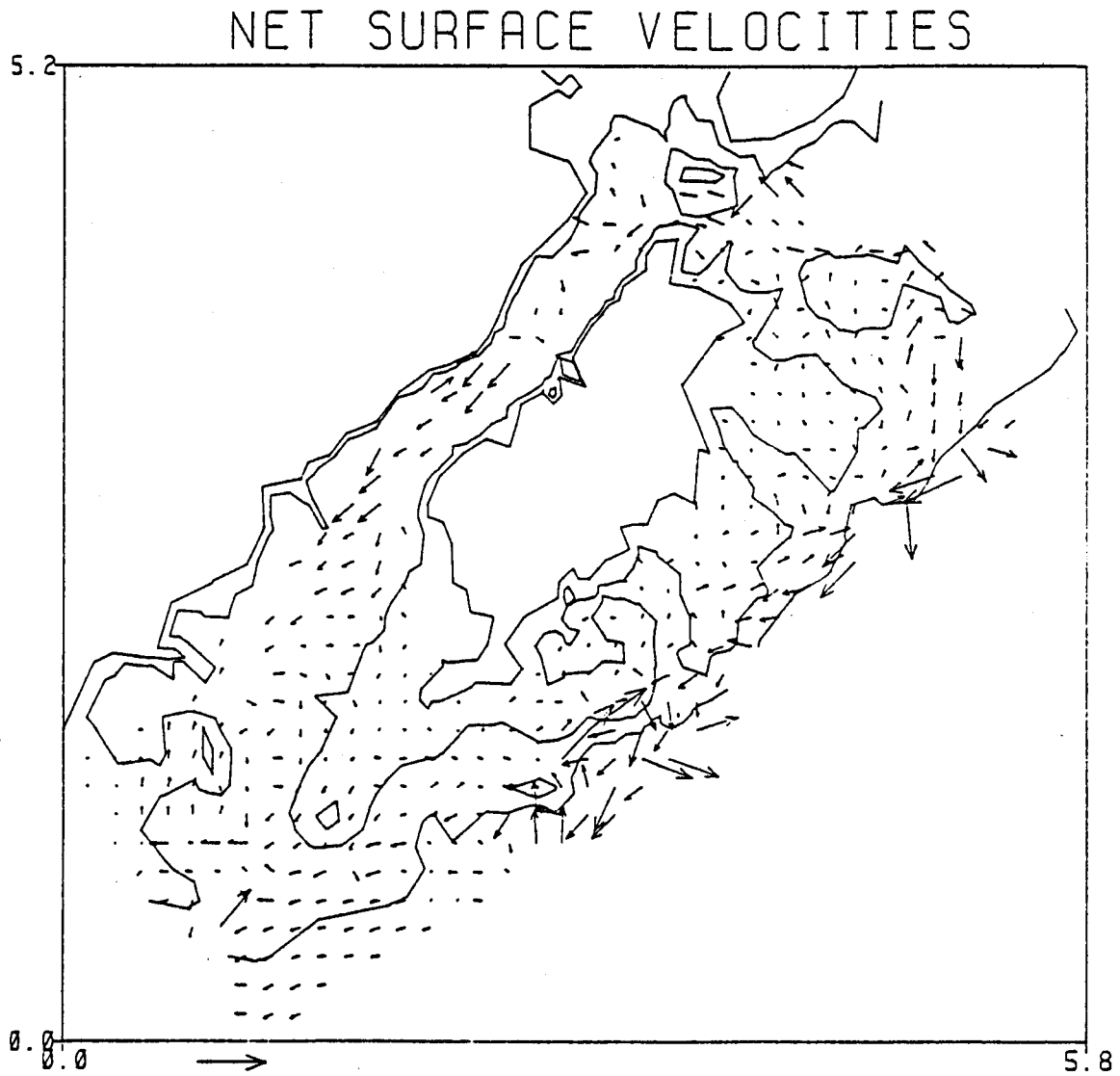


Figure 9c. Composite current vectors showing the sum of the spring average baroclinic mode and a weak negative barotropic mode. Scale arrow indicates 1 m/sec current.

The baroclinic data is seen to separate into summer and winter cases with the build-up of baroclinic currents throughout the summertime reflecting higher stratification for the region over the shelf. As the baroclinic fields develop, they tend to enhance the southwest flow over the shelf region off Kodiak, and this flow adds on to the barotropic mode which is basically in the same direction. In summary, Figures 8 and 9 represent the present best estimates of the expected circulation patterns for the Kodiak region. These composites should represent the regional response over a large variety of wind cases and seasonal baroclinic adjustments.

All of the individual baroclinic current patterns as well as the barotropic current pattern for the Kodiak region were forwarded to the USGS' assessment modelers (K. Landfear, USGS, Reston, Va.) for input into their impact statement considerations. These could obviously be combined into whatever linear combinations make the most sense in the context of their model.

Comparison of Observed Current Features and Model Results

It is of some interest to compare the results of these model studies to observational data that has been collected for the Kodiak region. As a point of departure we may consider the work of Favorite and Ingraham (On Flow in Northwestern Gulf of Alaska, May 1972, Journal of the Oceanographic Society of Japan, Vol. 33, No. 2). In this work, the authors examine the results of an oceanographic cruise and consider some sea bed drifter returns.

The first conclusion of Favorite and Ingraham's work is that the Alaska stream occurs as a strong but narrow current over the outer part of the continental shelf. Average currents are a knot with two knots as the maximum.

The currents are baroclinic and as such would show up in the baroclinic calculations. Earlier studies with the diagnostic model (Third Annual Report to OCSEAP on RU 140, pp. 3-19) specifically considered Favorite and Ingraham's data and completely reproduced this feature, which is not surprising since the baroclinic mode in the diagnostic model degenerated into the classical dynamics heights calculation for deep water cases and the two techniques should give identical results when using the same data. Comparing those earlier results to Figure 6c, it can be seen that for the six cases considered, the data does not extend seaward enough to adequately define the features of the strong Alaska Stream.

A second feature of the regional circulation identified by Favorite and Ingraham relates to the movement of sea bed drifters and their implication on bottom currents. Their Figure 6 indicates the release and recovery points of drifters over Portlock Bank, Marmot Bank, and the northeast sector of Albatross Bank. With the decomposition of the diagnostic model as defined in last year's RU 140 report (Appendix C), the barotropic mode contains all of the bottom currents and the appropriate figure to refer to is Figure 3b. From this we see the model predicts onshore movement over all the banks, consistent with all of the observations. In addition, releases off Dangerous Cape would be projected to move southwest and onshore with good qualitative agreement between the model and observational results. The only bottom drifter release that showed a northeast trend was in the trough south of Marmot Island. In this vicinity the model shows weak bottom flow with a divergence. Close to Marmot Island the flow is predicted to be northeast whereas closer to Kodiak and Chiniak Bay the bottom flow trends southwest.

A third feature identified by Favorite and Ingraham is a gyre over the continental slope south of Albatross Bank. Looking at Figures 6a, 6b, and 6c

it can easily be seen that this feature appears in various averages of the baroclinic data and corroborates the results derived from the May 1972 data.

A second study of circulation in the Kodiak region (Circulation and Hydrography Near Kodiak Island September and November 1977, NOAA Technical Memorandum ERL PMEL-13, J. D. Schumacher, R. K. Reed, M. Grigsby, and D. Dreves) can be compared briefly with the model results. This work by Schumacher et al. notes irregular gyre-like patterns over the troughs separating the various sections of Albatross Bank. Figures 3a and 3b clearly show the influence of these features with the general southwest flow over the shelf interrupted by the troughs. In the model results the dynamics associated with these meanders is related to conservation of potential vorticity and closed gyres are not seen. In particular, the flow tends to follow f/d contours with some cross isobath flow due to friction. Within the expected accuracy of either the hydrographic coverage or the model these detailed differences are not resolvable. The general aspects of the flow, however, do agree.

A second observation made by Schumacher et al. described a relatively strong baroclinic current along the Kenai Peninsula. The model did not have data covering that region so no additional insights can be added to their information due to these model studies.

A third study of circulation in the Kodiak Island area (Winter Circulation and Hydrography Over the Continental Shelf of the Northwest Gulf of Alaska, NOAA Technical Report ERL 404-PMEL 31, J. D. Schumacher, R. Sillcox, D. Dreves, and R. D. Muench) presented data on flow through Shelikof Strait and around the complex trough and bank region.

Considering the flow through Shelikof Strait, Schumacher et al. suggest a strong southwest flow that is barotropic. Model results support this view.

Figure 4a indicates that in the spring the baroclinic mode in the northeast sector of the straits is weakly developed, while Figures 3a and 3b show a strong down straight barotropic flow. The amplitude on the barotropic mode is arbitrary and depends on the assumed set-up of the bathystrophic cross shelf pressure gradient. The pattern information, however, is correctly represented and it can be seen from Figure 3a that the magnitude of the flow through Shelikof Strait is comparable to flows over the outer continental shelf, which are known to be on the order of one half to one knot.

Schumacher et al. also discussed current meter observations from Kiliuda Trough and concluded that flow tended to follow isobathic contours (Figure 10). As mentioned earlier, this is also a feature of the model-generated currents.

In summary, the key features of the three observational studies were all supported in the model results where the data covered the region or period of comparison. The basic dynamics and formulation of the model for the Kodiak region appears to successfully reproduce much of the observed flow characteristics as well as offer a means of interpolating the results to regional patterns.

III. Fairweather Ground Study

The second area studied with numerical modeling techniques this year on the Alaskan outer continental shelf was the Fairweather Ground region. The studied area extended from Cross Sound to Yakutat Bay. This section includes a fairly straight but high and rugged coastal region. The shelf varies in width with the major feature being the shallow Fairweather Ground which is made up of a shore area extending some 40 nautical miles offshore. To the northwest of the Fairweather Ground region, a deep trough cuts across the shelf with the hundred fathom isobath coming to within ten miles of shore. Figure 11 indicates the general study area.

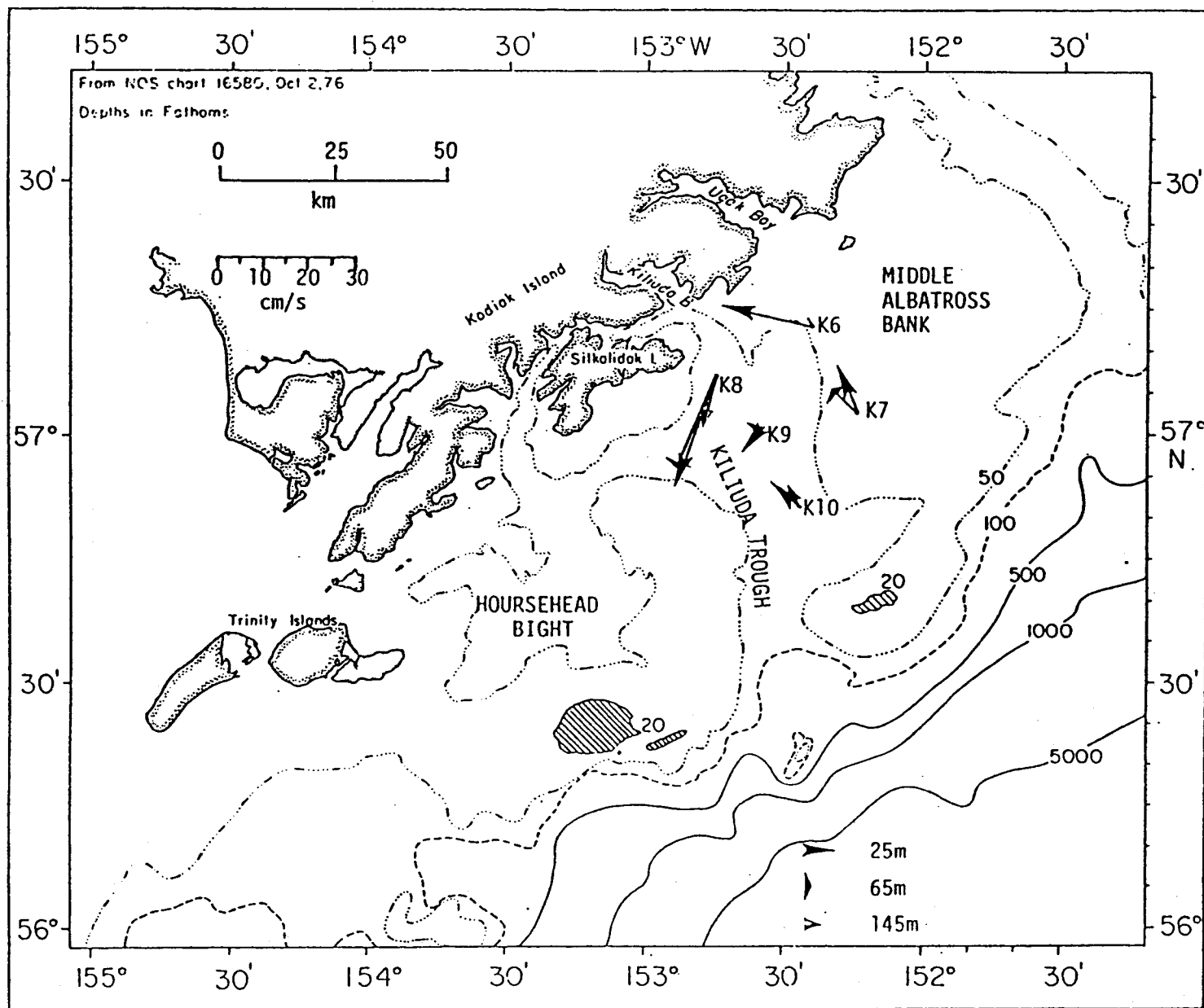


FIGURE 10 MEAN FLOW VECTORS FOR OBSERVED CURRENTS: OCTOBER 1977 - MARCH 1978.

Barotropic Mode

The first aspect of the Fairweather Ground study was to obtain estimates of the barotropic current. To do this, a number of vertices were placed over the area to resolve the major bathymetric features and provide the triangular bases for the finite element mode. To do this, a grid of 132 vertices was utilized. The typical or characteristic station spacing was less than five nautical miles. On this grid, a wind set-up perpendicular to the coast was assumed to be in bathystrophic balance. The actual line along which this boundary condition was applied extends perpendicular to the shore cutting off a small section the southeast corner of the domain. This condition resulted in an alongshore circulation pattern which satisfied the basic model dynamics and accounted for the flow over the complex bathymetry. In previous model studies carried out in both real and hypothetical domains questions have arisen as to the fundamental balance between the frictional dissipation in the model and the constraints imposed by conservation of potential vorticity. As one might expect under conditions of strong friction, the flow is smooth and small details in the bathymetry are not significant in causing variations in the flow. A secondary and more fundamental aspect of increasing friction is the decrease in sea surface elevation along the shoreline. Under conditions of high friction, the sea surface will drop as one moves in an along-current direction down the coast. This alongshore gradient in the pressure is probably a fundamental characteristic of the regional flow and plays an important role in determining how to impose the bathystrophic balance conditions for the model.

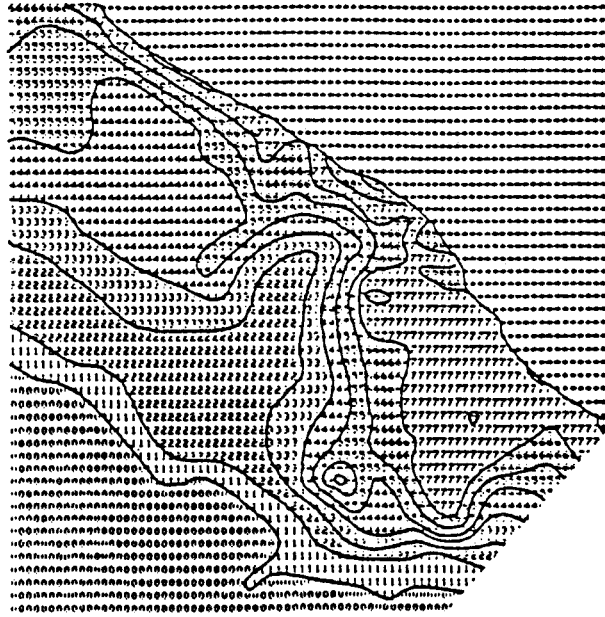
For the present model study the relative effect of the frictional parameter and the alongshore pressure gradient was investigated in a series of tests. This was done by running the model repeatedly with

variations in the frictional parameter. The results of the flow can easily be seen in the surface elevation contour plots presented in Figure 12. Figure 12a represents the surface elevation contours plotted for the minimum frictional case. Figures 12b, 12c, and 12d each represent successively higher frictional values. Several characteristics of the flow are immediately obvious. For the low friction case, the flow has considerably more spatial details and small scale variations in the bathymetry results in perturbations of the flow direction. Some regions of the bathymetry cause closed eddies or gyres. This is particularly apparent south of the Fairweather Ground. A second aspect of the increased frictional cases is the drop in sea surface elevation as you progress from southeast to northwest along the coastline. A third aspect of the barotropic flow patterns is the general tendency for northerly flow across the Fairweather Bank region followed by a loop in the current nearshore which turns in a counterclockwise direction and then leads offshore along the northern edge of Alsek Strath. This northerly flow across the Fairweather Ground and return flow appears to be independent of the frictional parameter and is a consistent feature for any reasonable value.

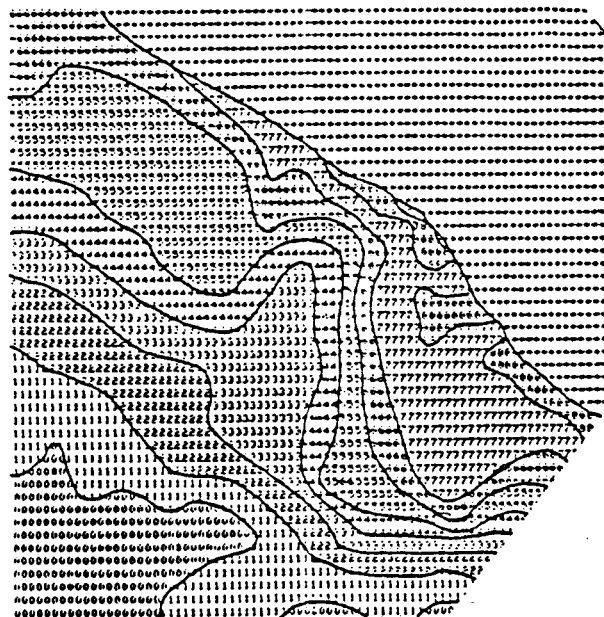
Figure 13 shows a vector plot corresponding to the sea surface elevation contours shown in Figure 12. Figure 13a represents the minimum frictional case with Figures 13b, 13c, and 13d corresponding to increasing frictional values. It is obvious that increasing the frictional parameterization leads to smoother flow patterns and the northerly flow across the Fairweather Ground and recirculation or counterclockwise circulation around Alsek Strath is clearly seen for all cases.

Baroclinic Mode

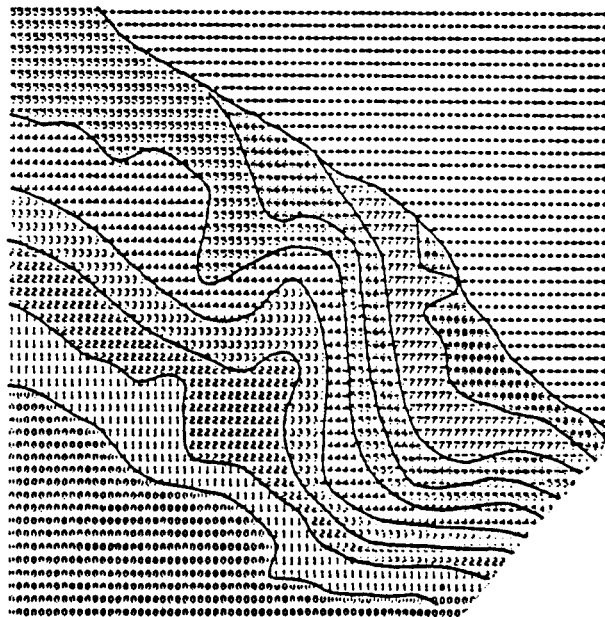
To estimate the baroclinic component of the flow for the Fairweather



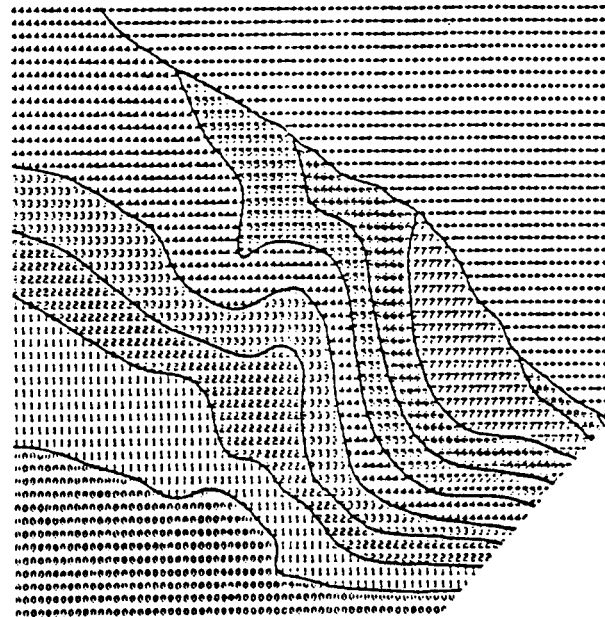
(a)



(b)



(c)

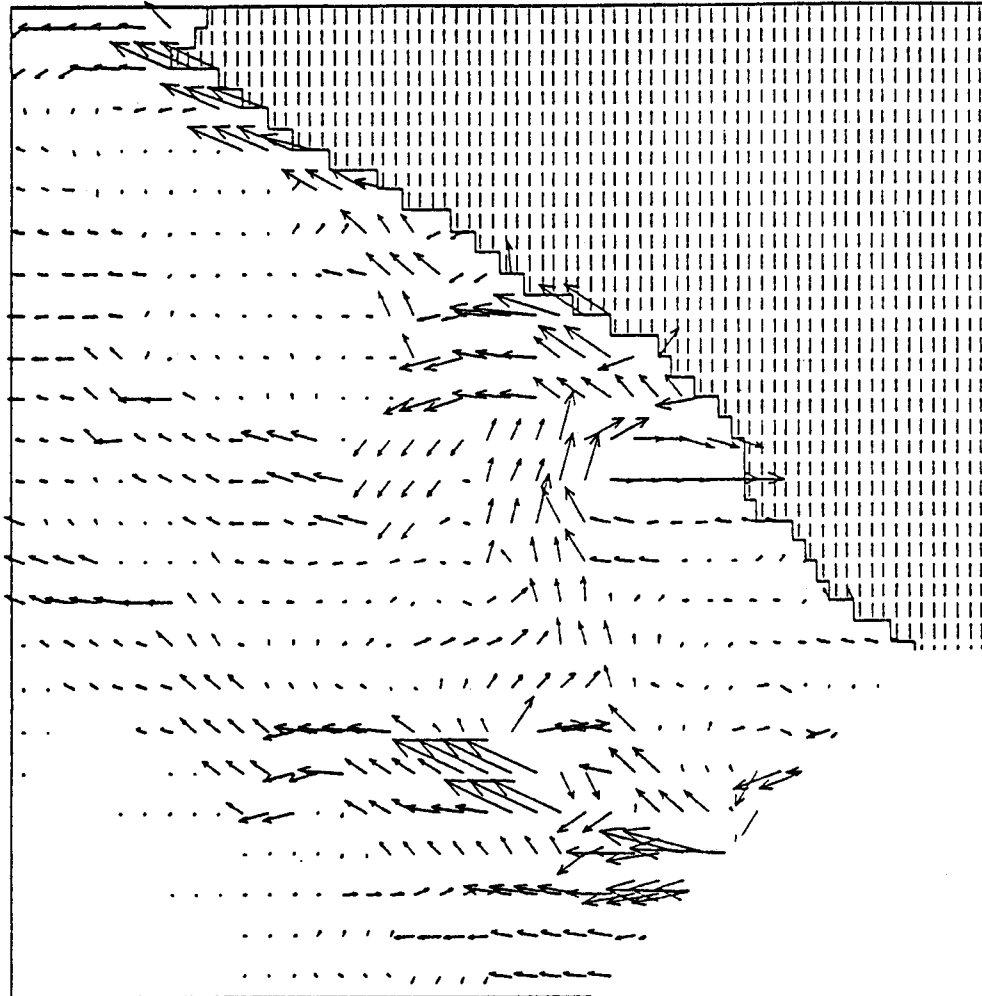


(d)

Figure 12

Sea surface elevation contours for the Fairweather Ground barotropic mode. The four figures correspond to increasing frictional effects with the minimal friction seen in case a and the maximum friction seen in case d.

LATITUDE 59 37.3
LONGITUDE 149 25.8

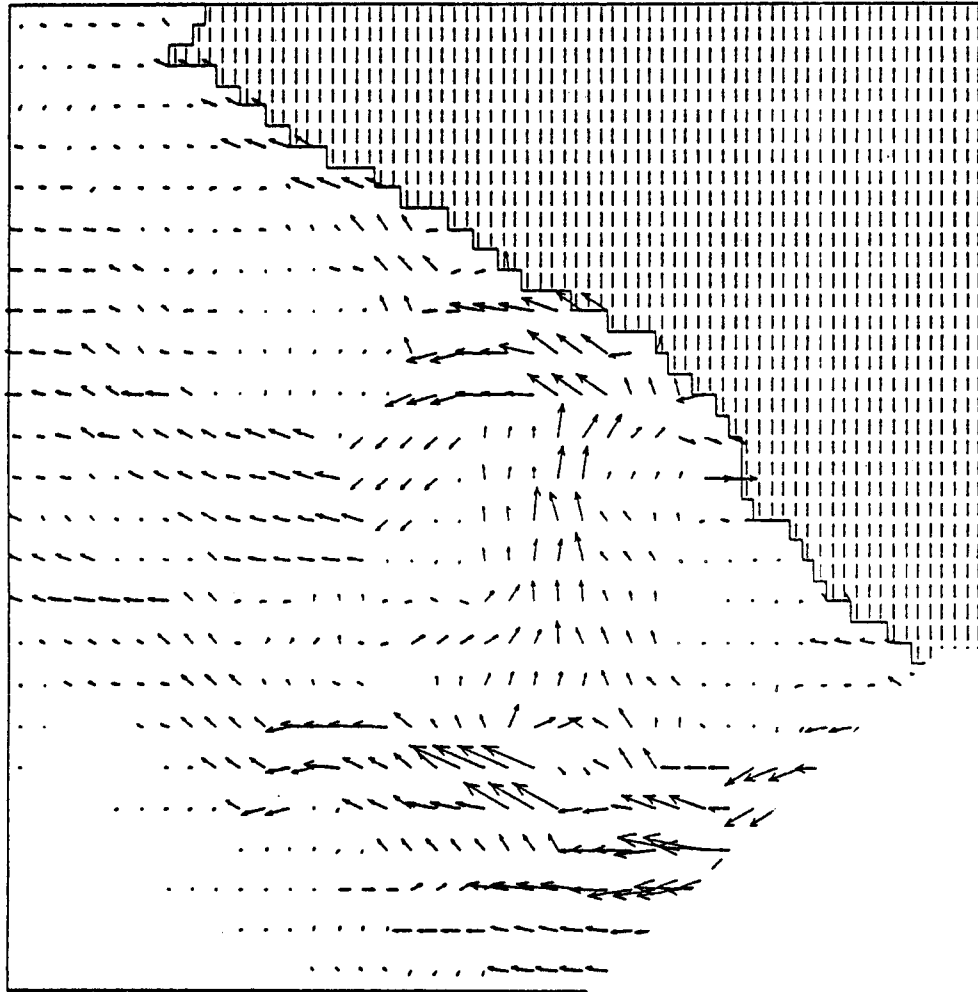


24.67 KM

LATITUDE 57 53.5
LONGITUDE 137 4.5

Figure 13 a. Current vector arrows for the Fairweather Ground barotropic mode minimum frictional case.

LATITUDE 59 37.3
LONGITUDE 148 25.8

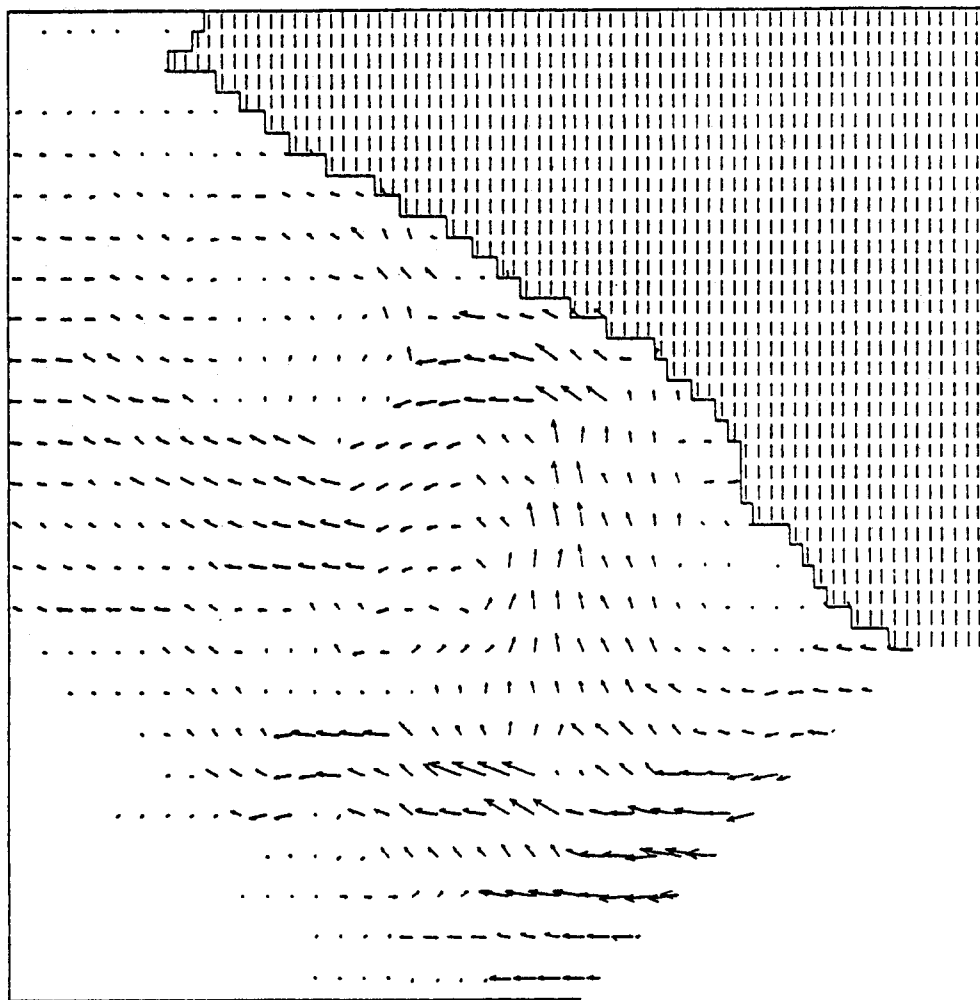


24.67 KM

LATITUDE 57 53.5
LONGITUDE 137 4.5

Figure 13b. Current vector arrows for the Fairweather Ground barotropic mode low frictional case.

LATITUDE 59 37.3
LONGITUDE 148 25.0



24.67 KM

LATITUDE 57 53.5
LONGITUDE 137 4.5

Figure 13c. Current vector arrows for the Fairweather Ground barotropic mode moderate frictional case.

LATITUDE 59 37.3
LONGITUDE 148 25.0

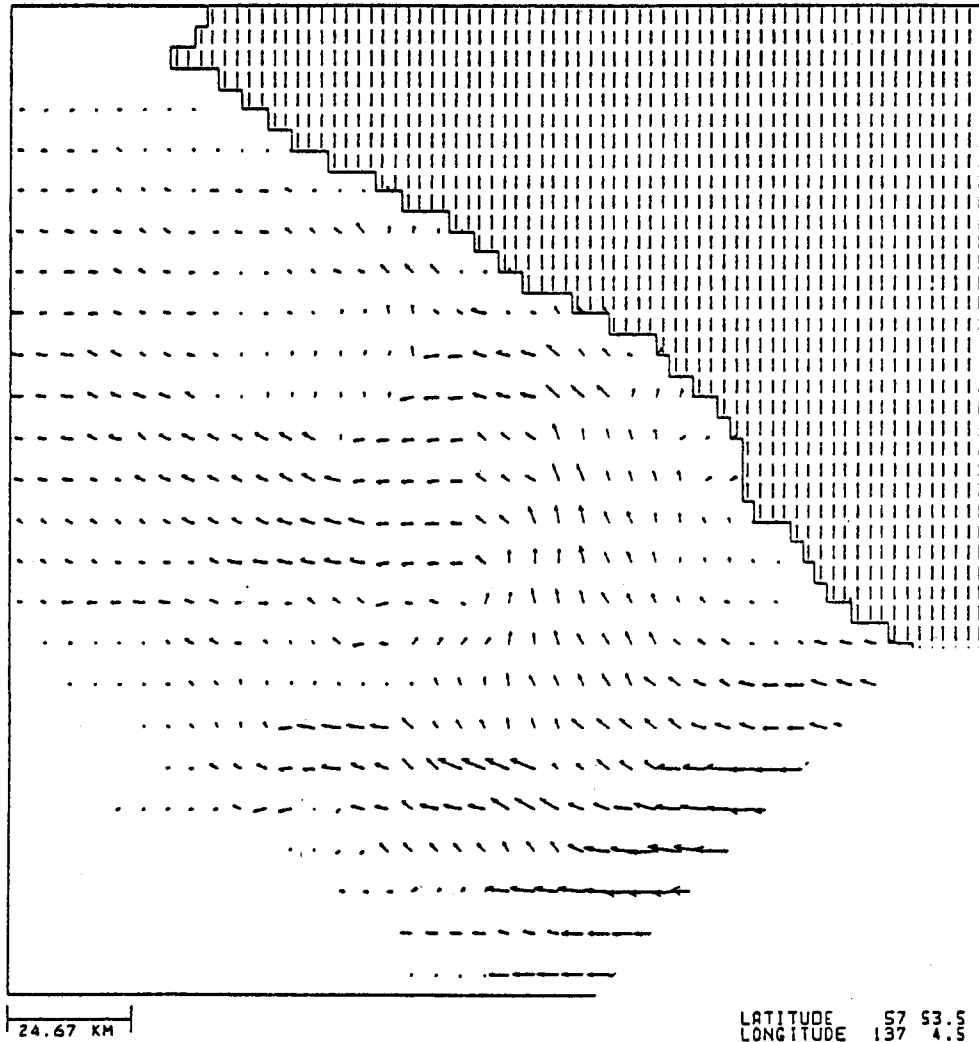


Figure 13d. Current vector arrows for the Fairweather Ground barotropic mode maximum frictional case.

Bank region, a data set from March 1979 was used. At the time of the study, this was the only available set of density stations. One hundred and seven stations were available and their relative coverage and the finite element triangular mesh associated with this data set are shown in Figure 14. Calculations of the baroclinic components of the current are shown in Figure 15. Several characteristics of this flow may be noted: 1) The Alaskan Stream is clearly evident in the southwest corner of the region. Here, a fairly uniform current is seen to move to the northwest along the outer edge of the shelf region and over the continental slope. Typical speeds of this current appear to be in excess of one knot; 2) Over the shelf region itself flow is generally weak but baroclinic currents do appear to develop over the Alek Strath region with a general tendency for anti-cyclonic flow to the north of the Strath and cyclonic flow south of the Strath and cyclonic flow south of the Strath and in the vicinity of the Fairweather Bank region; 3) A third characteristic of the baroclinic flow pattern is the relatively noisy appearance of the current along the shelf break region. As noted in previous studies, it is difficult to obtain sufficient data to resolve the strong baroclinic field and bathymetric interactions that take place along the shelf break.

Composite Regional Currents

The composite current for the Fairweather Ground region will be represented by a combination of the baroclinic and barotropic fields. The barotropic pattern information was seen to depend on a choice of frictional parameter which related to the relative balance between the bottom frictional effects and the constraints associated with conservation of potential vorticity. These also depended on the alongshore pressure gradient.

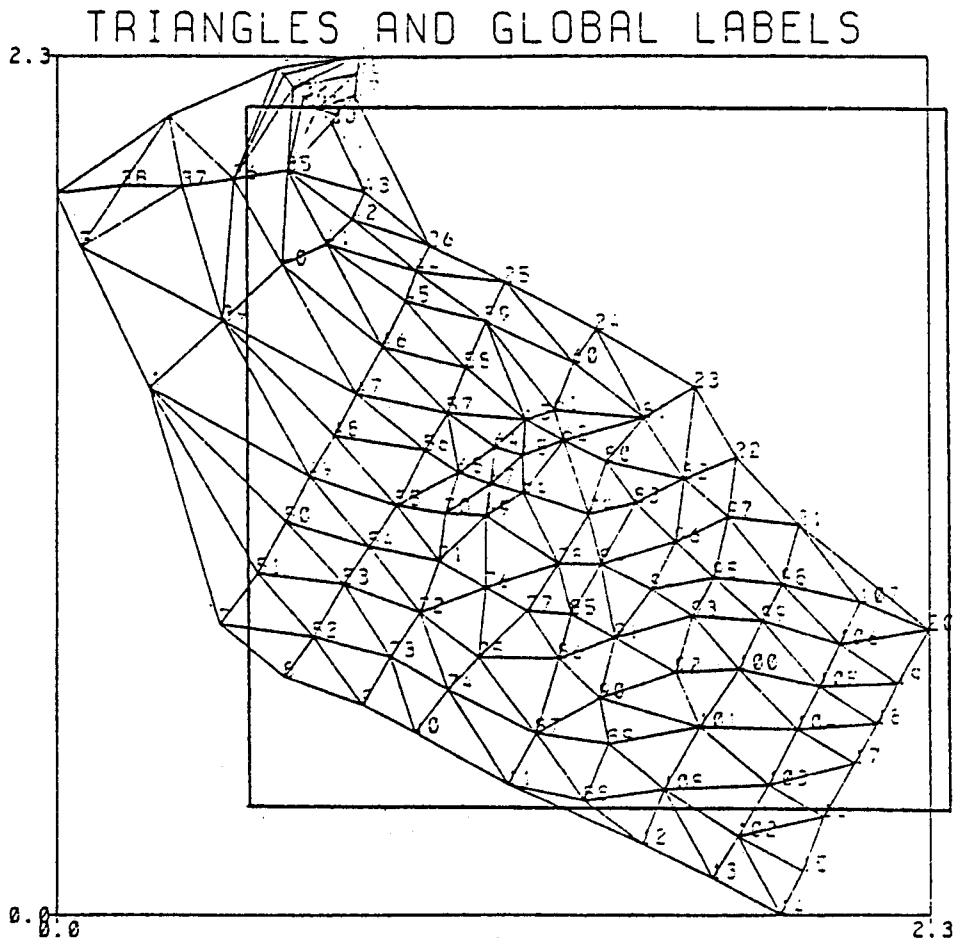


Figure 14. Representation of triangular grid used to calculate baroclinic currents for Fairweather Ground study area. Inner rectangle shows area covered by barotropic mode calculations.

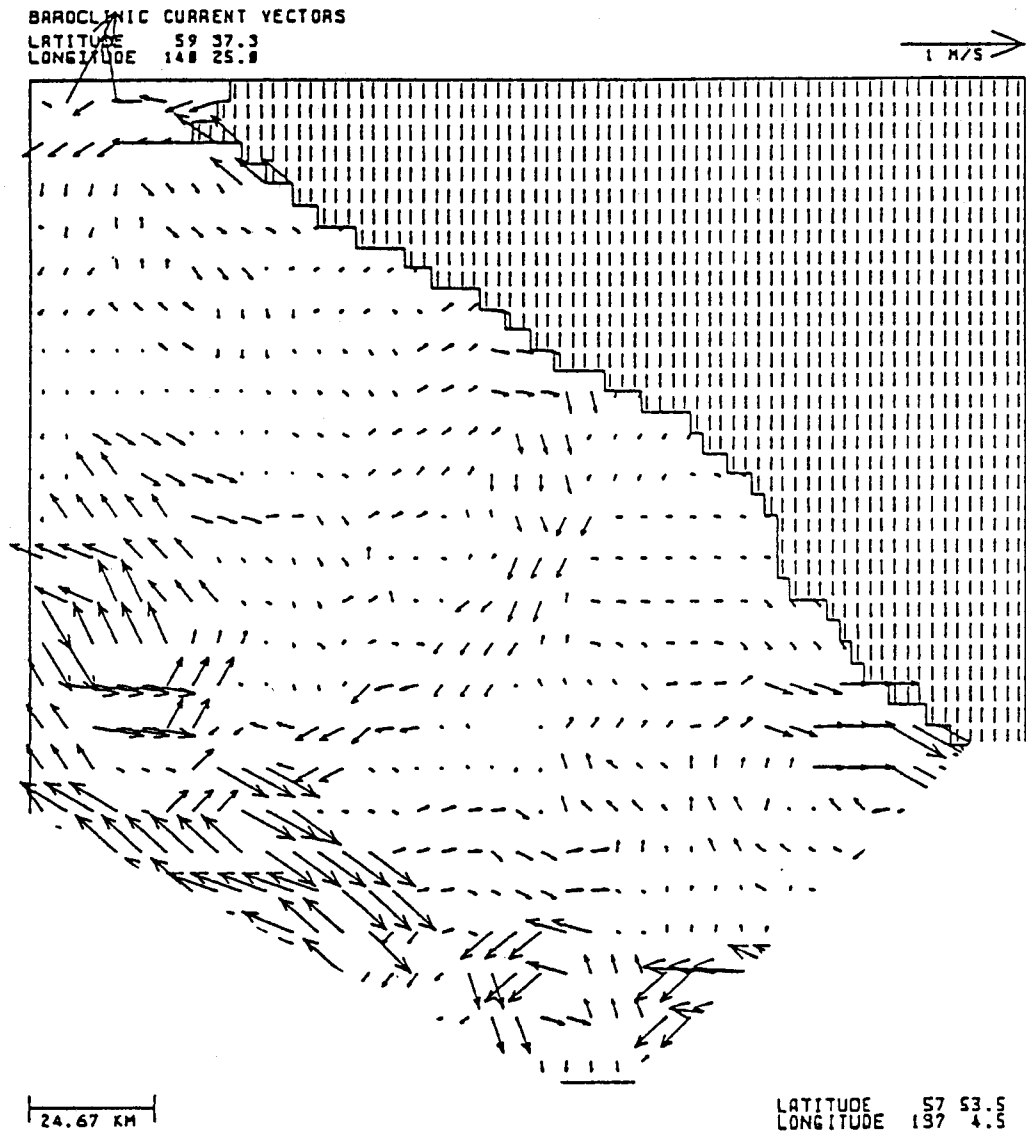


Figure 15. Baroclinic current vector arrows for Fairweather Ground study region based on March 1979 data.

For the present study, it was assumed that the flow pattern represented in Figures 12c and 13c was the most realistic realization for the barotropic current field. Figure 16 represents a combination of this barotropic pattern and the baroclinic information shown in Figure 15. Figure 16a corresponds to an onshore set-up of the sea surface as would be typical of a wind stress to the northwest along the coast. The implied bathystrophic balance at the southeast edge of the model indicates an upslope along the model edge as one proceeds onshore. Figures 16b and 16c correspond to decreasing wind stress cases. These are obtained by decreasing the amplitude of the barotropic pattern as it is algebraically added to the baroclinic flow pattern. Figure 16d represents a wind case where the alongshore component of the wind stress is to the southeast. To relate these figures back to more characteristic weather patterns the flow shown in Figures 16a, 16b, and 16c would correspond to a typical cyclonic circulation over the Gulf of Alaska that would be characterized by an atmospheric low pressure over the central Gulf. Figure 16d would correspond to a weaker, possibly summertime pattern associated with anti-cyclonic flow in the atmosphere over the Gulf of Alaska. In general, these composite current fields shown in Figure 16 can be taken as current estimates which span the likely variations expected in the flow. For pollutant trajectory work these current patterns represent the total surface flow less whatever Ekman or Stokes drift is assumed appropriate for the pollutant in question.

IV. Conclusions

Modeling studies have been carried out for two outer continental shelf regions of Alaska. Techniques developed over the five year history of RU 140 were applied to obtain estimates of the flow suitable for trajectory assessment experiments.

The general circulation patterns developed for the Kodiak Island region include information from six oceanographic cruises. These data sets appear to give a reasonable definition of the baroclinic mode for the flow during spring and fall periods. In addition, a three month series of cruises in the spring of 1978 gives an indication of the summer buildup of the regional baroclinic fields. The general cycle of the baroclinic flow for the region is seen to build up during the springtime with higher stratification effects in the late summer or early fall. During the wintertime, the baroclinic structure breaks down with lower baroclinic currents occurring in the late winter or early spring. Repeated sets of data indicate a clockwise gyre in the vicinity of the shelf break south of the Trinity Islands. The general direction of the baroclinic flow tends to be southwest at the surface over the region of the continental shelf offshore of Kodiak Island. This flow direction tends to enhance the barotropic mode for the region.

The barotropic mode for the Kodiak Island region was studied with a high resolution finite element mesh. In general, the alongshore flow is controlled by the bathymetry with the bank and trough system as the dominant steering features. The general flow is to the southwest with onshore meanders in the currents associated with the northwest or leading edge of the troughs. As the stream continues, offshore flow is seen on the downstream or southwest regions of the troughs. This is particularly apparent over the Kiliuda Trough region which is situated southwest of Middle Albatross Bank.

West of the Marmot Bank region, a deeper trough extends parallel to the shore of Kodiak Island. A southwesterly current is seen to be present here under the dominant influence of cyclonic atmospheric conditions in the Gulf of Alaska.

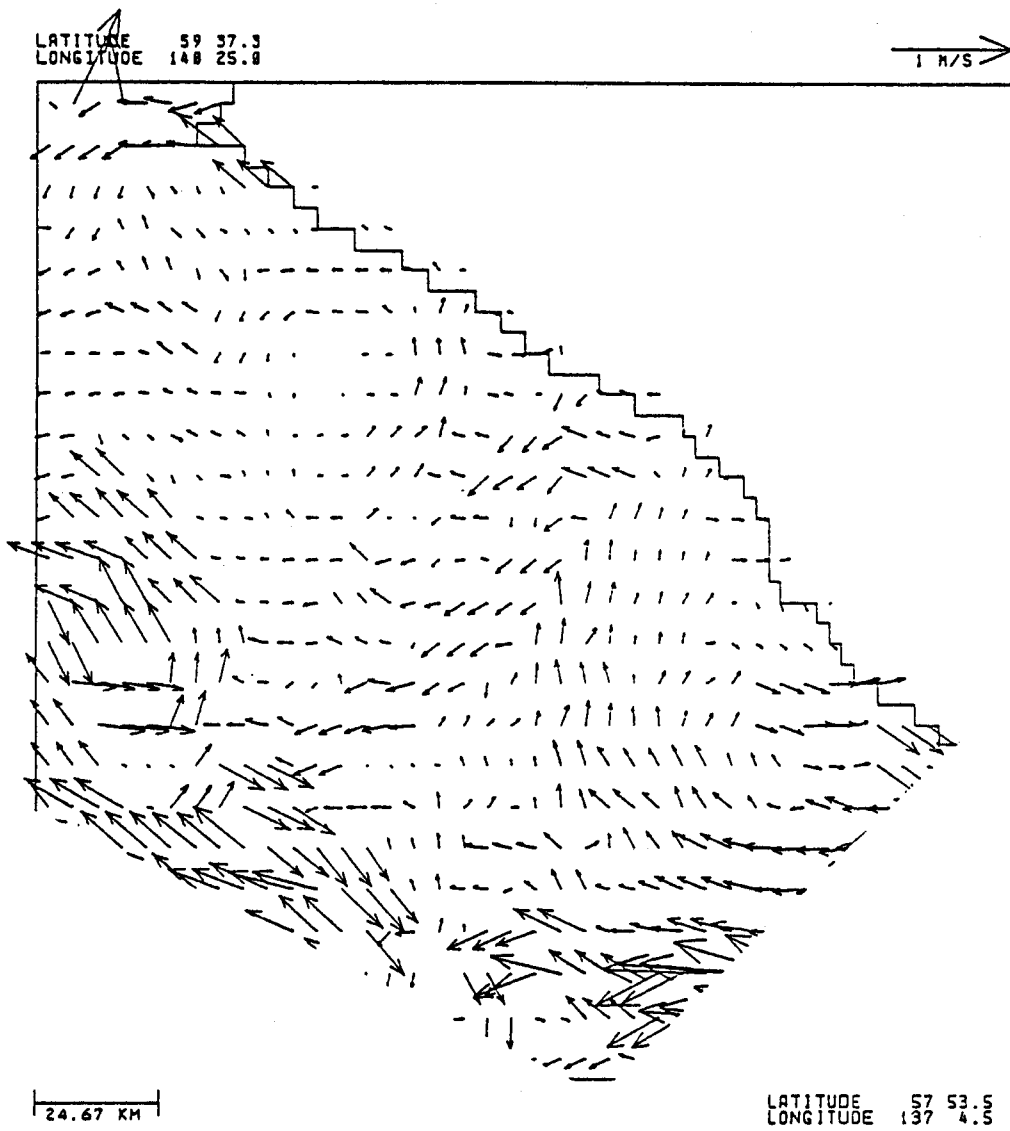


Figure 16a. Composite current vector arrows showing the sum of the baroclinic mode for March 1979 plus the strong barotropic mode.

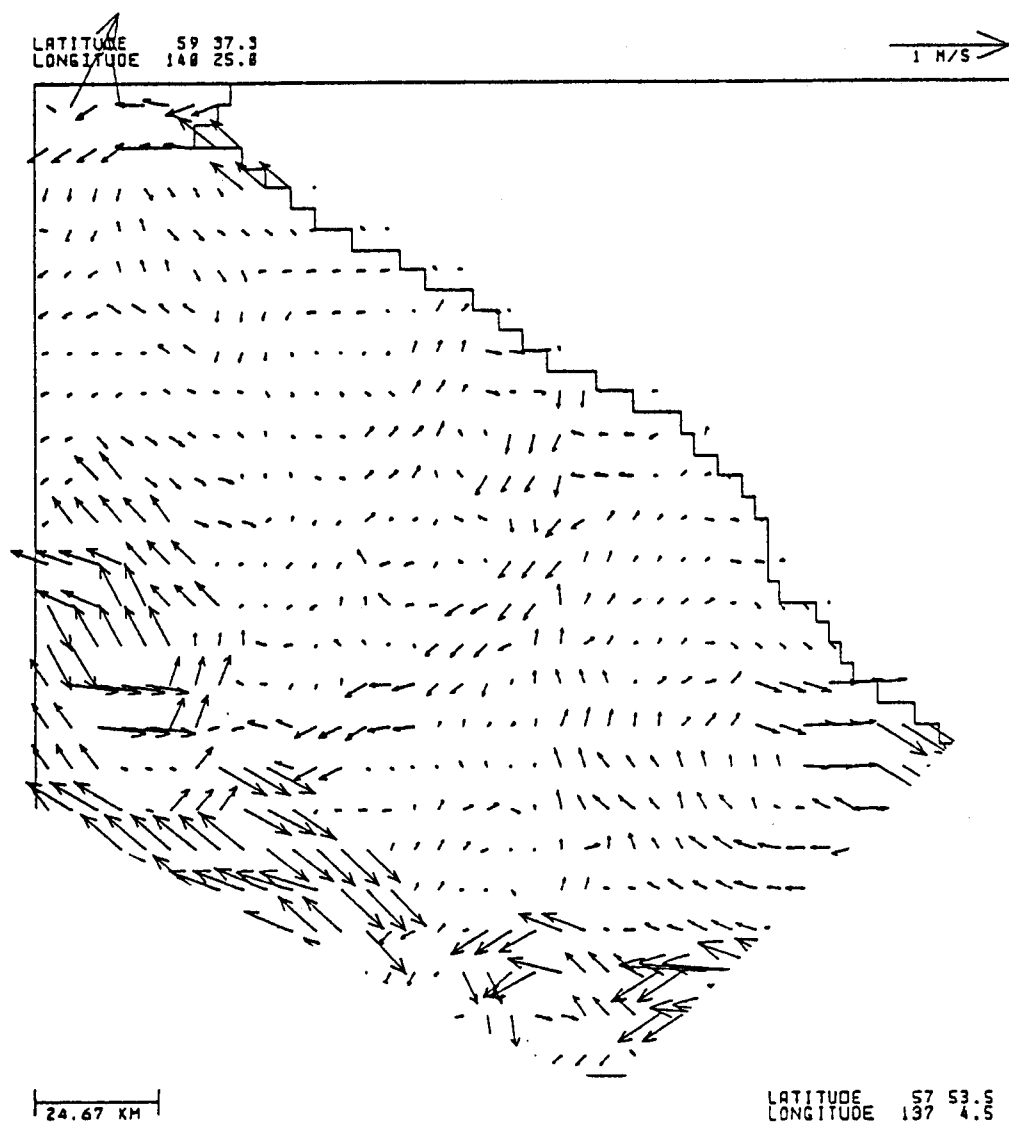


Figure 16b. Composite current vector arrows showing the sum of the baroclinic mode for March 1979 plus the moderate barotropic mode.

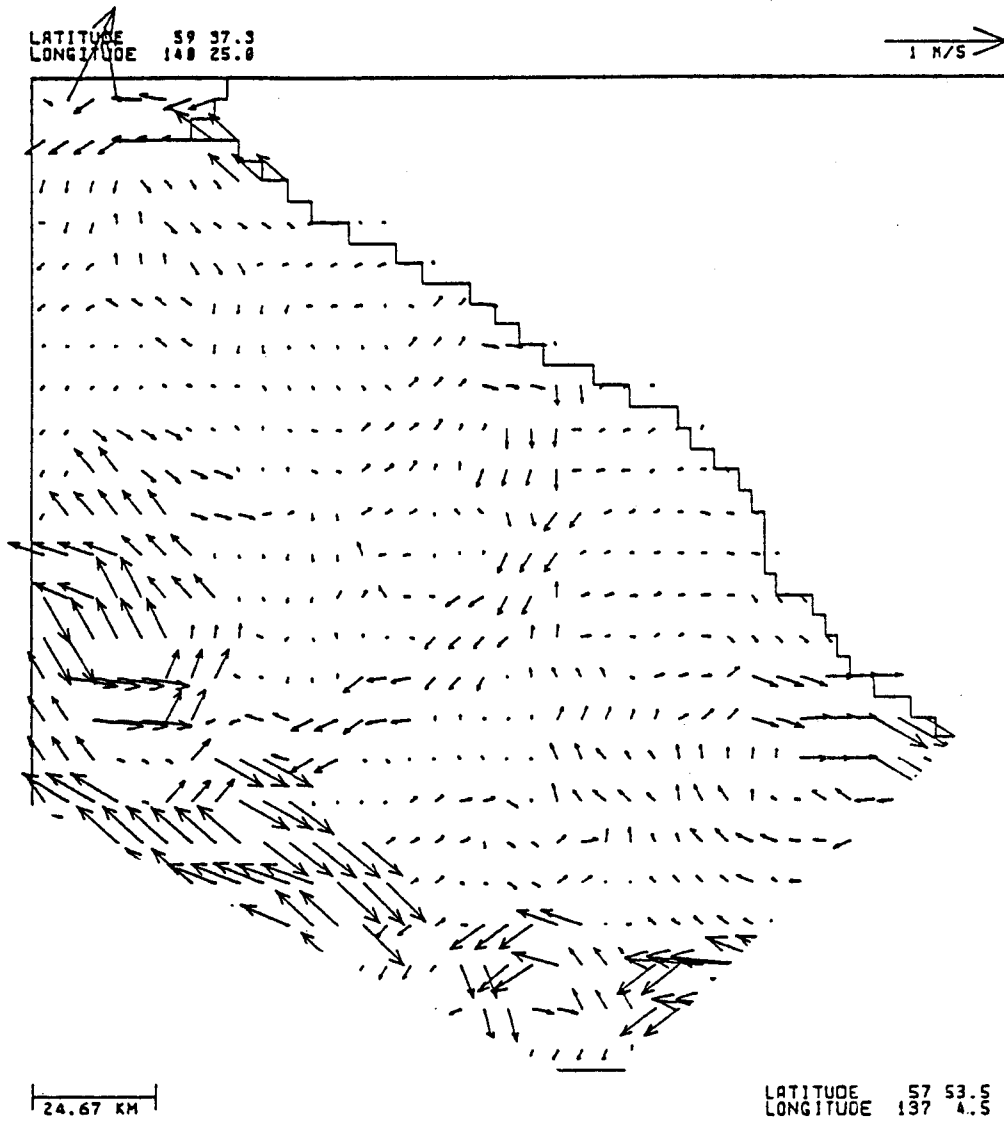


Figure 16c. Composite current vector arrows showing the sum of the baroclinic mode for March 1979 plus the weak barotropic mode.

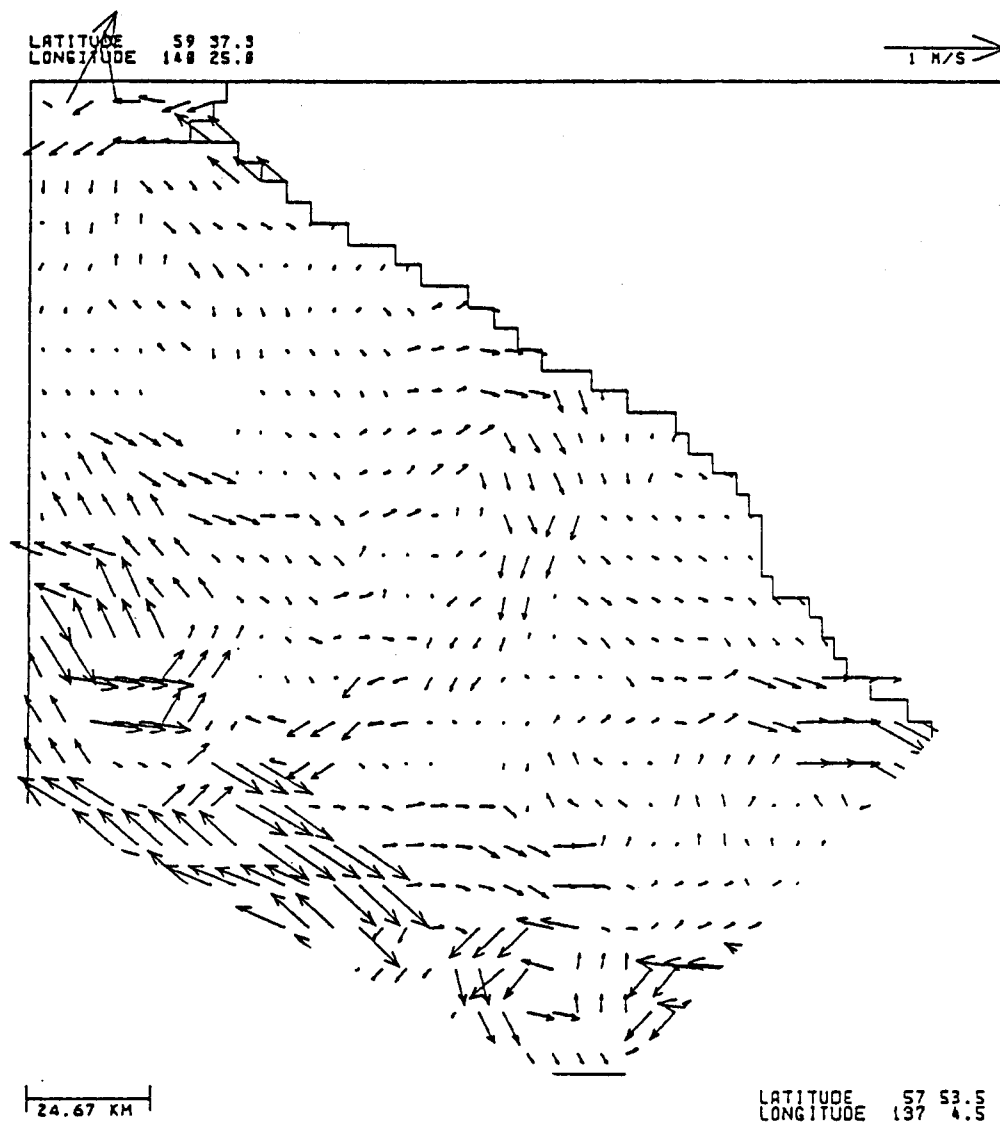


Figure 16d. Composite current vector arrows showing the sum of the baroclinic mode for March 1979 plus the small negative barotropic mode.

The amplitude associated with the barotropic mode depends on the regional wind stress. The dominant or characteristic flow direction is to the southwest resulting from low atmospheric pressure in the Gulf of Alaska. In general, the winter patterns are expected to be stronger than the summertime patterns because of the increased intensity of this characteristic low pressure circulation in the atmosphere over the Gulf of Alaska. This tends to compensate for the decreased baroclinic mode which weakens during the winter period. The general balance, then, appears to be dominated by barotropic flow conditions during the winter period and a combination of baroclinic and barotropic forcing during the summertime. Under nearly all conditions, the flow tends to be to the southwest and the influence of the bank and trough bathymetry is clearly seen.

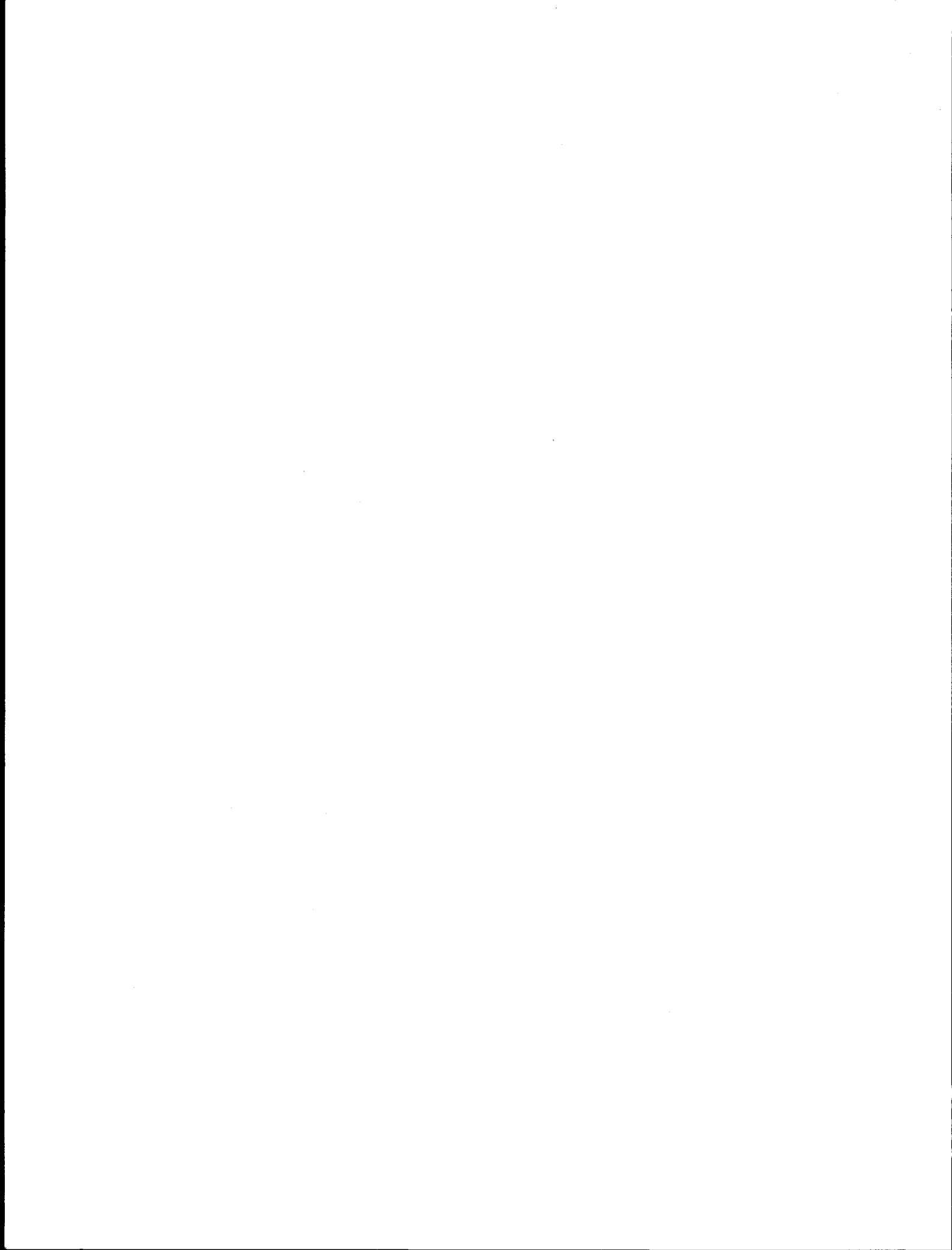
Comparisons of observational studies and model output indicate that mean flows in the Kodiak area are well represented by the derived patterns.

The Fairweather Ground region was studied with the use of one set of oceanographic data which was collected during the spring of 1979. The baroclinic field was dominated by the Alaskan Stream which flowed to the northwest along the outer edge of the continental shelf. A secondary baroclinic circulation was seen to result in a clockwise circulation over the Alsek Strath and northern section of the Fairweather Ground.

The barotropic mode for the Fairweather Ground was studied with a parametric exploration of the effects of friction on the flow patterns. It was seen that the relative importance of the frictional terms could be related to the alongshore gradient in the pressure. For all of the cases considered, a northerly flow was seen over the Fairweather Ground region. This extended towards the inshore end of Alsek Strath, at which point a counterclockwise circulation develops in the flow. This counterclockwise curvature extends

the current around the end of the Strath and back out across the shelf to the north. For the one case studied, the baroclinic mode tended to dominate the flow along the outer edge of the continental shelf with the barotropic mode dominating over the shelf proper and in the vicinity of the Fairweather Ground and Alsek Strath region.

Current estimates for the Fairweather Ground region have now been processed in OSSM (On-Scene-Spill-Model) which is used routinely for trajectory model experimental studies. In this format, the data can be easily used to study pollutant distributions for the region.



NUMERICAL STUDIES--
PACIFIC MARINE ENVIRONMENTAL LABORATORY

by

J. A. Galt, J. E. Overland,
C. H. Pease, and R. J. Stewart

U.S. Department of Commerce
National Oceanic and Atmospheric Administration
Environmental Research Laboratories
Pacific Marine Environmental Laboratory
3711 15th Avenue N.E.
Seattle, Washington 98105

Final Report
Outer Continental Shelf Environmental Assessment Program
Research Unit 140

September 1978
(Minor Revisions, November 1984)

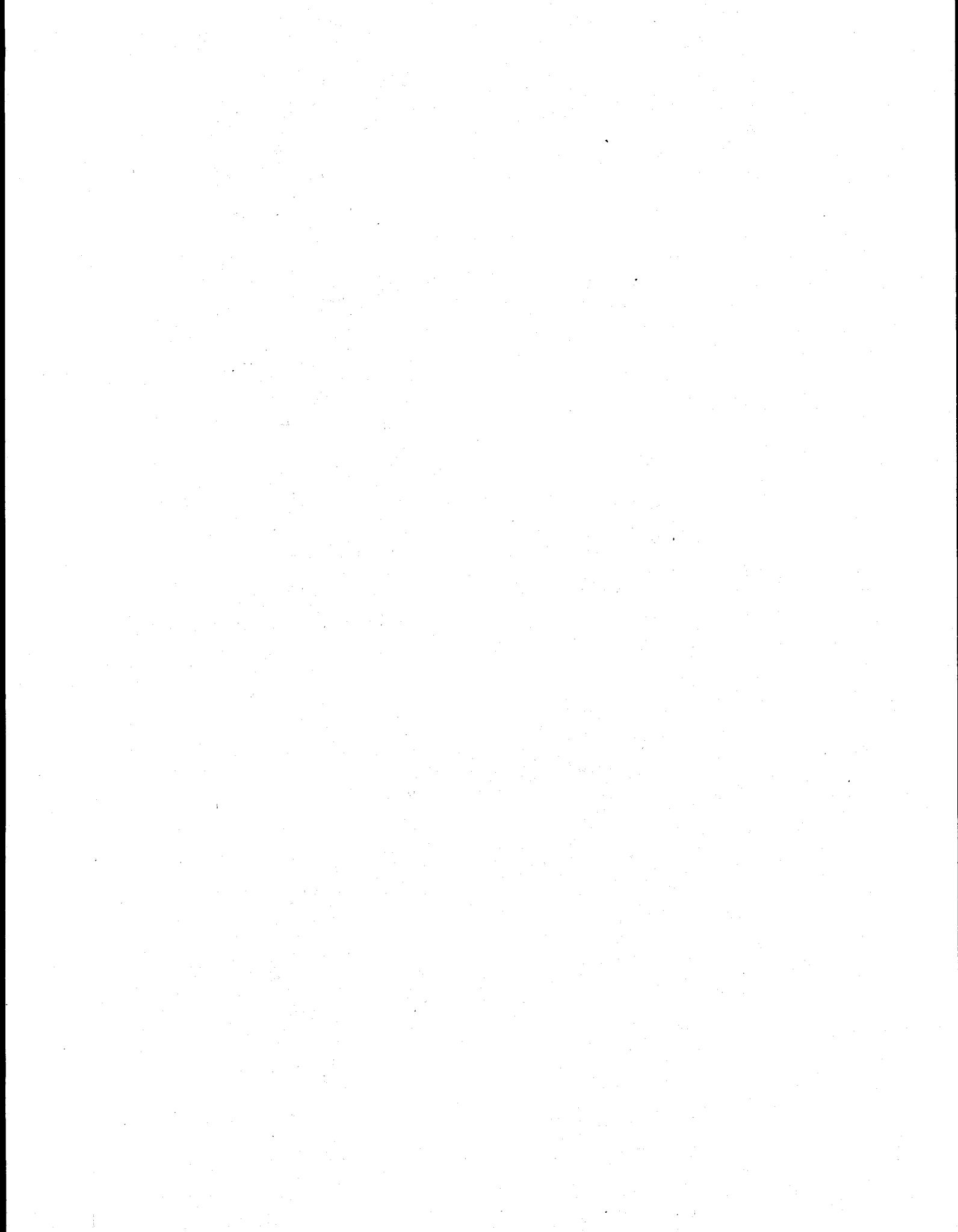


TABLE OF CONTENTS

	Page
PREFACE	67
1. INTRODUCTION.	73
2. NORTHEAST GULF OF ALASKA (NEGOA) WIND FIELDS.	79
2.1 Introduction	79
2.2 The Six Surface Weather Type Patterns.	82
2.3 Local Wind Fields for NEGOA.	86
2.4 Weather Typing for the Trajectory Calculations	97
3. ANALYSIS OF NORTHEAST GULF OF ALASKA CURRENT PATTERNS	117
3.1 Introduction	117
3.2 Model Decomposition.	122
3.3 Wind Set-up Response Patterns.	128
3.4 Density Driven Response.	153
3.5 Composite Current Patterns	174
3.6 References	175
4. DEVELOPMENT OF THE ENVIRONMENTAL LIBRARY.	177
4.1 Introduction	177
4.2 Model Design and Data Structure.	177
4.3 Interface Programs	179
4.4 Selection of the Prototype NEGOA Model Runs.	184
5. TIME SERIES SIMULATION AND VALIDATION	188
6. TRAJECTORIES.	201
7. CONCLUSIONS	248
APPENDIX A. Development of a Simplified Diagnostic Model for Interpretation of Oceanographic Data.	251

TABLE OF CONTENTS (continued)

	Page
APPENDIX B. A Finite Element Solution Technique for a Diagnostic Shelf Circulation Model.	301
APPENDIX C. The Linear Decomposition of a Diagnostic Shelf Circulation Model and Discussion of Alternate Boundary Condition Formulations	449
APPENDIX D. A Synoptic Climatology for Surface Winds Along the Southern Coast of Alaska.	525
APPENDIX E. The Regional Meteorological Model Status Report. . . .	609
APPENDIX F. A Numerical Investigation of the Bering Sea Circulation Using a Linear Homogenous Model	697
APPENDIX G. Trajectory Model Listing	737

PREFACE

Numerical studies have been a part of OCSEAP research since the program began in July of 1974. During the four and one-quarter years of funding for research unit #140, a number of research projects have been undertaken in support of the overall goal of describing the surface transport processes for specific OCS regions. These studies have been carried out by a number of different investigators and have been coordinated with many other studies and agencies. In particular, the numerical studies have been strongly influenced by the observational oceanographic field programs and by data collected by the Spilled Oil Research Team of OCSEAP. Related pollutant trajectory work has been carried out by the Marine Ecosystems Analysis Program, by NOAA Marine Services studies, and by PMEL base funded research. In addition to developing specific products associated with numerical descriptions of transport phenomena, research group members have taken an active role in the planning, coordination and information transfer for the larger-scope physical oceanographic studies being carried out by OCSEAP. For example, during the fifty-one months of the project to date, group members have traveled over seventy times on business directly related to oil trajectory research. About one-fourth of this travel was for overall program planning. Another fourth was for research planning and for coordination with other OCSEAP investigators. Four different times the group has presented data at OCSEAP physical oceanography principal investigators' meetings (which we originally instigated). On eleven different occasions group members have presented briefings of research results (three times to NOAA senior management, five times directly to BLM or DOI personnel - including the transfer of computer algorithms for use in their assessment models, and three

times to national advisory boards). Group personnel have taken part in seven or more different observational field programs and have described their research results to the Juneau Project Office at seven different briefings.

Research results from group members have also been presented at six national meetings and at three special workshops, with the contributions being published for four of these.

Papers by group members relating to oil trajectory analysis are represented by the following:

Regional Meteorological Model for Mountainous Coastal Regions,
PMEL Technical Report (in press), J. Overland, M. Hitchman
and Y.-J. Han.

Comments on "Numerical Simulation of Cold Easterly Circulation Over
the Canadian Western Plains Using a Mesoscale Boundary Layer
Model", Boundary Layer Meteorology, 1978 (14): 433-434, J. Overland.

Tankers in U.S. Waters, (1977), Oceanus 20(4), Robert J. Stewart.

Bayesian Hypothesis Tests of Sampling Function Form, Robert
J. Stewart (submitted to JASA for publication).

Estimating Tanker Spill Risks in U.S. Waters, Proceedings of
the 1978 Joint Statistical Meeting, San Diego, Calif., Robert
J. Stewart.

Estimating Oil Spill Risks for Offshore Development, Proceedings
of the 1978 Joint Statistical Meetings, San Diego, Calif.
Robert J. Stewart.

Physical Oceanography and Dynamics of the NE Gulf of Alaska,
Proceedings AINA Conference, Anchorage, 16-17 October, 1975,
J.A. Galt and Thomas T. Royer.

The Use of a Diagnostic Circulation Model for Oil Trajectory Analysis,
EPA/API/USCG Oil Spill Conference, New Orleans, March 7-11, J.A.
Galt and Carol H. Pease. (1977)

Circulation Studies on the Alaska Continental Shelf Off the Copper
River Delta, NOAA/ERL Technical Report, March 1976, J.A. Galt.

Investigation of Physical Processes, J.A. Galt, The AMOCO CADIZ
Oil Spill, NOAA/ERL Report, Wilmot N. Hess, Editor. (1978)

A Numerical Investigation of the Bering Sea Circulation Using a
Linear Homogeneous Model, NOAA Draft Technical Report, Y. J.
Han and J.A. Galt.

Development of a Simplified Diagnostic Model for the Interpretation
of Oceanographic Data, NOAA Technical Report ERL 399-PMEL-25,
1975, J.A. Galt.

A Finite Element Solution Technique for a Diagnostic Shelf Circulation
Model, NOAA/ERL/PMEL Technical Report (submitted) G. Watabayashi
and J.A. Galt.

A Linear Decomposition of a Diagnostic Shelf Circulation Model and
Discussion of Alternate Boundary Condition Formulations, NOAA/ERL/
PMEL Technical Report (submitted), J.A. Galt and G. Watabayashi.

A Synoptic Climatology for Surface Winds Along the Southern Coast
of Alaska, NOAA/ERL.PMEL (Draft Tech Report), J.E. Overland and
T.R. Hiester.

Since some of these papers are still in draft form, and thus not generally available, they have been included as appendices to this report. This collection covers selected aspects of the spill trajectory investigations that have been carried out by the Numerical Studies group. A more complete coverage of their activities carried out under RU#140 is

contained in the annual reports of the last four years.

The first of these, "Physical Oceanography Contribution to the First Annual Report" by J.A. Galt (July, 1975), was an attempt to collect the contributions of D. Barrick (WPL), D. Halpern (PMEL), S. Hayes (PMEL), R.M. Reynolds (PMEL), T. Royer (IMS) and J. Schumacher (PMEL) to produce an initial synthesis from the NEGOA area, concentrating on a description of regional dynamic processes.

The next annual report, "Numerical Studies of Alaska Region" RU#140, 146, 149, 31 (June 1976) by J.A. Galt, describes the conceptual design of a general oil spill trajectory model, a stochastic dispersion experiment based on NEGOA winds, the ice problem in the Beaufort Sea, initial diagnostic model experiments for NEGOA, and some results from preliminary modeling studies in the Bering Sea. A study of the circulation off the Copper River and a bibliography of sea ice papers were also included as part of that report.

The third annual report by J.A. Galt, J.E. Overland, C.S. Smyth, Y. J. Han and C.H. Pease (June 1977) describes a conceptual advanced trajectory model, a series of trajectory modeling experiments run for the NEGOA area, initial diagnostic model studies of the Kodiak region, an investigation of the use of small scale planetary boundary layer models to predict surface wind patterns, additional results from modeling studies of the Bering Sea circulation, and an analysis of computer requirements for a trajectory graphics system.

The fourth annual report "Alaska Numerical Modeling" by J.A. Galt, J.E. Overland, R.J. Stewart, C.H. Pease and M. Hitchman (May 1978), described the continuing analysis of the diagnostic circulation model, concentrating on the formal decomposition of the linear model equations. In addition,

available data sets for running NEGOA trajectory analysis studies were identified, and strategies for forming environmental libraries were described. That report also discussed weather typing experiments being carried out for the Alaska region.

The four years of numerical studies that have been carried out have seen the development of a consistent and balanced approach for the study of pollutant trajectories. This approach combines both theoretical work and empirical data so that the underlying dynamics responsible for particular physical response can be clearly identified. It is now possible to assemble the various components and to carry out a serious analysis of regional trajectories for an OCS region. The following report is a demonstration of the techniques developed in RU#140 applied to the investigation of trajectories in the Northeast Gulf of Alaska.

In addition to the principal authors of this report significant support was given by other Numerical Studies personnel: Clifford Fridlind, Gary Torgrimson, Debra Payton, Curtis Mobley, Jon Nestor and Y. J. Han. Contract help was received from Thomas R. Hiester and Betty-Ann Morse. Students also contributed to individual sections, including Eric Raisters, Glen Watabayashi, Matthew Hitchman, John DeVault, Rita Chin and Mark Bjornson. We would also like to acknowledge help from Carl Pearson (Coastal Physics, PMEL) in the preparation of field data for model input.

1. The first part of the document discusses the importance of maintaining accurate records of all transactions and activities. It emphasizes that proper record-keeping is essential for ensuring transparency and accountability in financial reporting.

2. The second part of the document outlines the various methods and techniques used to collect and analyze data. It highlights the need for a systematic approach to data collection and the importance of using reliable sources of information.

3. The third part of the document focuses on the analysis and interpretation of the collected data. It discusses the various statistical and analytical tools that can be used to identify trends and patterns in the data.

4. The fourth part of the document discusses the importance of communicating the results of the analysis to the relevant stakeholders. It emphasizes the need for clear and concise reporting and the importance of providing context and interpretation of the findings.

5. The fifth part of the document discusses the various challenges and limitations associated with data collection and analysis. It highlights the need for a thorough understanding of the data and the importance of being transparent about any limitations or biases that may be present.

6. The sixth part of the document discusses the various ethical considerations that must be taken into account when collecting and analyzing data. It emphasizes the need for transparency and accountability in the data collection process and the importance of protecting the privacy and confidentiality of the data.

7. The seventh part of the document discusses the various applications and uses of the collected data. It highlights the importance of using the data to inform decision-making and to identify areas for improvement and innovation.

8. The eighth part of the document discusses the various future trends and developments in data collection and analysis. It highlights the importance of staying up-to-date on the latest research and technology in the field and the need for a continuous learning and development mindset.

1. Introduction

The following report documents a series of studies that have been carried out as part of OCSEAP, RU #140. This research represents a multi-year effort that has been carried out by scientists in the Numerical Studies group at the Pacific Marine Environmental Laboratory of NOAA/ERL. The general subject addressed by OCSEAP Research Unit #140 is best described as numerical, or computer oriented, techniques for the interpolation and synthesis of environmental data to present a composite analysis of pollutant trajectories. In carrying out this work many different approaches have been used. Fundamental research in meteorology, oceanography, statistics and computer science have all played a part. Additional use has been made of empirical data sets made available through the continuous efforts of other OCSEAP investigators and their predecessors. In all of these component studies underlying dynamic principles have been identified. Formal solutions have been combined with observational information in such a way as to yield optimum coverage of expected environmental situations. It has been felt that this approach offers the best opportunity, using regional information, to obtain a consistent and conceptually balanced bases for trajectory analysis.

As with any research, not all of the proposed paths lead directly to the objectives. Thus some of the studies carried out during this project do not see their way into the final synthesis. Also to be considered is that alternate dynamic formulations are often considered while zeroing in on a useful regional representation. The final procedures and combinations of dynamics and data will be chosen from the available techniques so as to focus on the immediate area of concern. The following chapters of this report are a detailed case study of pollutant trajectory analysis for a specific region, the Northeast Gulf of Alaska.

Among the processes that are likely to control the movement and spreading of spilled oil, some of the first thought to come into play are due to the wind. The wind actually enters the problem in several distinct ways. The wind generates a local surface wind drift, which advects any floating pollutants. In addition the local wind transfers momentum to floating oil indirectly through wave and stress interactions. Although neither one of these local wind effects is completely understood, the net movement of the oil can be reasonably well parameterized in terms of the wind. The wind also enters the trajectory problem through the regional forcing of the shelf circulation. Here the wind across the shelf sets up the sea surface slope, creating a pressure gradient that drives the flow. To fulfill these requirements for both regional wind patterns and for detailed local wind vectors, a meteorological study of the NEGOA region was carried out and is described in the second section of this report. In developing these NEGOA wind patterns a number of techniques were applied to various data sets, with the results converging towards the development of a single set of patterns capable of representing all the meteorological situations that could be expected for the region.

Starting with large scale pressure data, as represented on synoptic weather maps, an investigation was carried out to identify the dominant weather types. This was done subjectively by a visual comparison of a large number of daily maps. Upon completing this phase of the study, the results were compared to previous subjective typing studies that had been carried out for the entire Alaska region. Then objective typing techniques were considered, with the eventual choice of pattern correlation methods over other methods of pattern recognition (empirical orthogonal functions and factor analysis) primarily because of time constraints.

Small scale local wind patterns have been investigated by concentrating on the processes that modify the larger scale synoptic patterns in the planetary boundary layer and in coastal regions. Included in these studies were the results of one- and two-dimensional boundary layer models, as well as the results of observational studies of coastal winds. The final wind patterns chosen to represent the NEGQA region are based on the large synoptic patterns (types), with local wind vectors derived by the careful subjective application of the information obtained from the boundary layer studies.

After establishing the required characterizations of the representative wind patterns for NEGQA, the determination of regional current patterns can be made. Currents enter into the pollutant trajectory problem as a process that simply advects floating material. The description of the regional currents must include considerations of the bathymetry, stratification and major dynamic forcing. To include these effects, a diagnostic shelf circulation model has been used. This model assumes that the currents are a combination of geostrophic and Ekman flows. The density field, bottom topography, and winds are the independent variables; the model solves for the sea surface elevation.

The application of the diagnostic model is greatly simplified by the decomposition of the resulting flow into density-driven and wind-driven components. This procedure and its application to the NEGQA region are described in section three of this report. The partitioning of the model dynamics makes it possible to easily identify the regional response associated with each of the individual forcing mechanisms. A bathystrophic balance between the regional winds and the sea surface set-up is assumed and with this assumption it is possible to derive

regional current patterns corresponding to each of the climatological wind patterns described in Section Two. This approach insures that the currents have two very important characteristics. First that they are directly related to the large scale climatological forcing, for which long historical records are available. And second, that when used in conjunction with the wind patterns in a pollutant trajectory analysis, the appropriate wind-current correlations for the region are preserved. The correct representation of these correlations is essential for obtaining realistic trajectory statistics for regional assessment investigations.

The pollutant trajectory model used in the study of the NEMO region is a series of algorithms which incorporates the regional wind, current and geography information into appropriate parameterizations. The model predicts the sequential displacements of a floating mass of hydrocarbons, and presents the results in a suitable graphical format. The algorithms require various time series records for the specific periods of time for which investigations are desired. These records contain a progression of climate types, as well as wind and current data, from single keying (or scaling) stations. Conceptually, all of the wind, current and time series data can be thought of as a regional environmental library which the trajectory algorithms must access. The actual numerical development of this library, with a description of file structure and data packing strategy, is described in the fourth section of this report.

Both the wind pattern and current pattern information have been developed in terms which describe the flow only in a relative sense. To obtain the absolute winds or currents it is first necessary to identify the pattern that most closely represents the synoptic situation. Then

the observed winds from a station within the model region are used to scale the entire wind pattern; the currents are scaled by the square of the wind speed, consistent with the bathystrophic assumptions used in the diagnostic model decomposition. This procedure yields a consistent series of wind and current data for every location within the model domain and reflects the appropriate climatology as well as the smaller scale region dynamics. What is not included in these pattern keying strategies is the higher frequency variations (which are unresolved by the 12 hour weather maps). Such time dependent scales of motion are not dynamically represented in either the wind or current model studies, and their effects must be modeled as uncertainties, or pseudo-random displacements. The higher frequency information from wind and current records is compared with model predictions, and the deviations are taken as a measure of uncertainty. The details of this keying strategy application and the statistics of the observed residual winds and currents are examined in section five of this report.

The sixth section of the report documents examples of pollutant trajectory investigations. Two specific time periods are considered: summer, 1974 and winter, 1975. These are presented as examples of the model and library concept and make no attempt to present a statistical assessment. The components are complete and such a study could be carried out with the existing meteorological data. The analysis incorporates all of the system components described in the previous sections of the report. The examples use climate pattern sequencing from weather maps during the period in question, with the definition of local winds and currents corresponding to the synoptic situation scaled by observations at Middleton Island. High frequency variations in the observed records,

which are not explicitly included in the model formulation are incorporated into the trajectory algorithms and give a realistic estimate of composite uncertainty in the analysis.

The final section in the report presents conclusions and recommendations based on the numerical studies carried out in RU #140 and in the NEGOA study.

2.0 NEGOA Wind Fields

2.1 Introduction

This section describes a synoptic climatology to estimate surface winds over NEGOA for trajectory calculations coupled with the ability to provide frequency of occurrence information from the meteorological record. It is an abbreviated version of the appended draft technical report (Overland and Hiester, 1978). A synoptic climatology is a collection of generalized quasi-steady states of the atmosphere which are frequently observed or a continuum of states along particular storm tracks. Weather types aim to maintain the range of synoptic variability while grouping daily weather maps which have the same basic meteorological structure but slightly different locations or intensities. A synoptic climatology differs from calculation of means in that it specifies specific type patterns, such as a high or low pressure center, which could occur on any given day rather than forming an average over several possibly different sequential daily maps.

It should be recalled that atmospheric modes are continuous in time and that synoptic systems differ in size and intensity throughout their individual life cycle and from one storm to the next. Given the assumption that classification is possible, our approach regards patterns of weather circulation as implicit functions of the static sea level pressure distribution (Barry, 1972). It differs from a kinematic approach in which synoptic weather maps are classified in terms of principal storm tracks. The former approach is most appropriate in regions where a proportion of features form and/or decay in situ or are persistent. Since the Gulf of Alaska is often the decay center for storms in the Pacific, the static approach is taken as a working hypothesis. Western Europe and the East

Coast of the United States are examples where a kinematic approach would be more appropriate.

There are two approaches to map typing which can be referred to as objective (or at least automated) and subjective. Objective typing can be considered a pattern recognition problem involving digitized weather maps. Such techniques are generally based upon principal component analysis, factor analysis and their close relatives (Kendall and Stuart, 1972), or pattern correlation techniques (Lund, 1963). General objective techniques are being investigated as a companion study to the research reported here. The subjective approach involves assigning daily weather maps into different categories by a synoptic meteorologist. A rationale for subjective typing is that in order for patterns to be successful the underlying meteorological processes leading to these patterns should be recognizable.

Six subjectively derived weather types have been established for the Northeast Gulf of Alaska (NEGOA) - Kodiak Island region, which are subdivided into twelve subtypes. These six patterns were derived from combining and modifying patterns from two previous studies by Sorkina (1963) and Putnins (1966), subjective analysis of fall 1977 - summer 1978 sea level pressure charts from the National Meteorological Center, and post modification of patterns based upon daily typing of candidate patterns. Post analysis indicated the necessity of including subtypes. Subtypes within a type contain the same general distribution of features and meteorological basis but represent slight variations in locations of features which cause changes in the orientation of the geostrophic wind at the central location of the NEGOA coastline.

The digitized sea level pressure grids for the northern hemisphere produced by the National Meteorological Center (Jenne, 1975) are an additional

source for this study. These fields are available for 1968-1975.

Each subjective subtype was digitized on the same mesh as the Meteorological Center grid for twenty-four common points. A daily map may then be quickly typed by computing its correlation with each of the subjective types. Such a procedure forms the basis for percent coverage and transition probability calculations for various types.

The second approach to typing considered in this report consists of applying the pattern correlation technique (Lund, 1963) to the digitized daily weather maps. The pattern correlation technique consists of forming the correlation of each day with all the other days during the year. The days with the highest number of correlations greater than a prescribed cutoff value with type A are removed and the procedure is repeated to find type B; the analysis is continued until the data are exhausted. This procedure is applied to NEGQA as an independent check on the subjective typing.

The relations of the surface wind fields over coastal waters of Alaska to geostrophic winds are complicated by coastal blocking, extensive air mass modification and mesoscale features induced by coastal topography. The available density of station data does not provide the resolution of the spatial variation of the wind field over the water for input to trajectory calculations. As an alternative we have developed local wind fields on a $7\frac{1}{2}$ minute latitude by 15 minute longitude grid which are the assumed local winds that occur with each synoptic scale subtype. These local patterns use a single point planetary boundary layer model proposed by Cardone (1969) to compute surface stress from the geostrophic wind, including corrections for thermal influence, and modify the near shore wind field based upon the field program of Reynolds, et al. (1978).

2.2 The Six Surface Weather Type Patterns

The six types represented by twelve subtype patterns as described in the attached draft technical report are summarized by Table 2-1. All 22 of Putnins' patterns can be incorporated into these slightly more general patterns, and most of the 77-78 surface maps subjectively resemble one or another of the twelve subtypes.

To determine pattern frequencies automated sea level pressure analyses over the northern hemisphere produced at the National Meteorological Center (NMC) were obtained for 1968-1975. A subset of 24 grid points was extracted from each 12 hour map for the NEGOA region. Each subjective subtype was also digitized to provide sea level pressure values at each of the 24 grid point locations. The correlation was then computed between each map and the twelve subtypes to determine the pattern for each 12 hour weather map:

$$r_{it} = \left(\sum_{m=1}^{24} P_{im} P_{tm} \right) \left(\sum_{m=1}^{24} P_{im}^2 \sum_{m=1}^{24} P_{tm}^2 \right)^{-1/2}$$

where P_{im} and P_{tm} represent the deviation of pressures from the map average for date i and type t at grid point m . The weather type with the largest correlation is assigned to that map. The magnitude of the correlation is recorded along with the type.

The percent of occurrence of each type by year and season are listed in Table 2.2 and graphed in Figure 2-1. The Aleutian low (pattern 2.0) is dominant in all seasons. Pattern 3.0 (high in the interior of Alaska) is confirmed as a winter pattern and the east Pacific high pressure as a summer pattern. Lows to the north (pattern 4) peak in summer and lows to the southeast (pattern 6) peak in winter. The same tables also list

TABLE 2.1

Type	Description	Sorkina Type	Putnins Type	Dominant Season
I	Low in Gulf of Alaska	4c	A', A ₁ , G, H	Winter
II	Aleutian Low	5b	A, C, E, A _C	Winter, Spring, Fall
III	High pressure in Alaskan Interior	6a	D, B, D	Winter
IV	Low pressure center over Central Alaska	1a	A'', A ₃ , F	Summer
V	Pacific Anticyclone	1b, 5a	A''', A ₂ , E', E' ₁	Summer
VI	Stagnating low off of Queen Charlotte Islands	7a	D', E'', E ₁ , F ₁	Spring, Fall

TABLE 2.2

TRANSITIONS FROM INITIAL TYPE TO FOLLOWING TYPE
Based on 12 Hourly Analyses 1968-1974

	Initial Type	% Occurrence of Initial Type	% of Initial Type Followed by Following Type					
			1	2	3	4	5	6
Y E A R	1	16	47	17	6	13	2	15
	2	31	12	71	6	7	3	1
	3	9	14	15	56	1	1	13
	4	18	8	11	~0	60	16	5
	5	12	~0	24	1	15	59	1
	6	14	15	3	9	8	3	62
W I N T E R	1	23	57	15	6	6	1	15
	2	26	13	71	8	6	1	1
	3	19	10	10	70	~0	1	9
	4	7	19	14	1	42	13	11
	5	4	0	29	5	14	52	0
	6	21	14	2	9	4	1	70
S P R I N G	1	16	43	17	6	16	1	17
	2	37	11	73	6	7	2	1
	3	8	16	21	47	0	0	16
	4	16	8	14	1	54	16	7
	5	9	0	35	2	10	52	1
	6	14	16	4	8	10	4	58
S U M M E R	1	8	34	20	4	27	5	10
	2	30	8	68	5	9	8	2
	3	3	27	20	29	2	7	15
	4	26	4	7	0	67	20	2
	5	27	~0	19	0	12	68	1
	6	6	14	7	4	15	7	52
F A L L	1	18	45	18	6	14	1	16
	2	30	15	68	6	8	2	1
	3	8	16	18	43	3	1	19
	4	22	9	12	~0	60	13	6
	5	7	1	27	0	34	37	1
	6	15	15	2	10	9	3	61

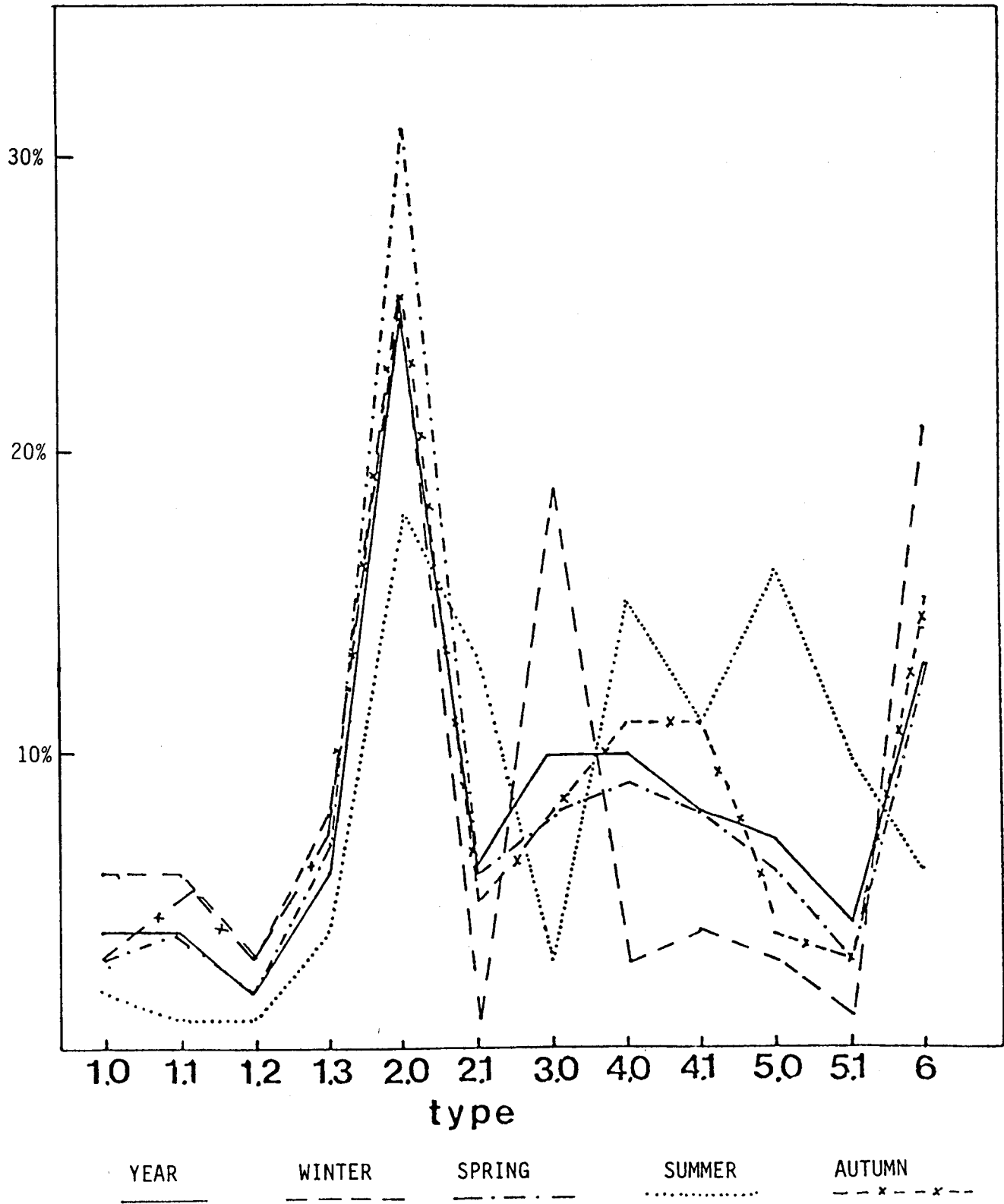


Figure 2-1. Percentage of occurrence of synoptic weather type by season.

transition probabilities. The large diagonal components, many over 50% are an indication of persistence of each pattern.

Figure 2-2 plots the percentage of days from the 1968-1973 record which could be typed by at least one of the patterns at a given threshold value of the correlation coefficient. Approximately 75% of the record can be typed by subjective patterns with a correlation of 0.7 or better. The figure also shows results for types generated by the pattern correlation technique applied to 1974 data. The final curve is typing the 1968-1973 data against ten daily maps drawn at random from 1974.

2.3 Local Wind Fields for NEG OA

This section discusses the generation of local wind fields from surface pressure pattern types described in section 2. For use in the oil spill trajectory calculations all local wind speeds within a pattern will be scaled against an anemometer record. Therefore, the primary aim is to produce wind fields showing local direction and relative magnitude. Computation began by computing gradient wind speeds and directions from the patterns on a uniform set of grid points over the localized area. The grid consisted of 800 boxes; each box was $7\frac{1}{2}$ minutes in latitude by 15 minutes in longitude. At 60°N the boxes were 13.89 km on a side.

We assumed a thermal structure for the marine planetary boundary layer (PBL) so that the baroclinicity of the PBL was consistent with an ideal storm structure and climatology. Isotherms were drawn to reproduce the climatological large scale temperature gradient from the OCSEAP atlas (Brower, 1977) and then distorted to be consistent with storm structure packing the isotherms in frontal zones. Actual fronts were not created so as not to over-specify the generalized storm. From the isotherms, the magnitude and direction (relative to the surface geostrophic wind)

12 SUBJ. 8 RANDOM. .8. AND .7 CUTS

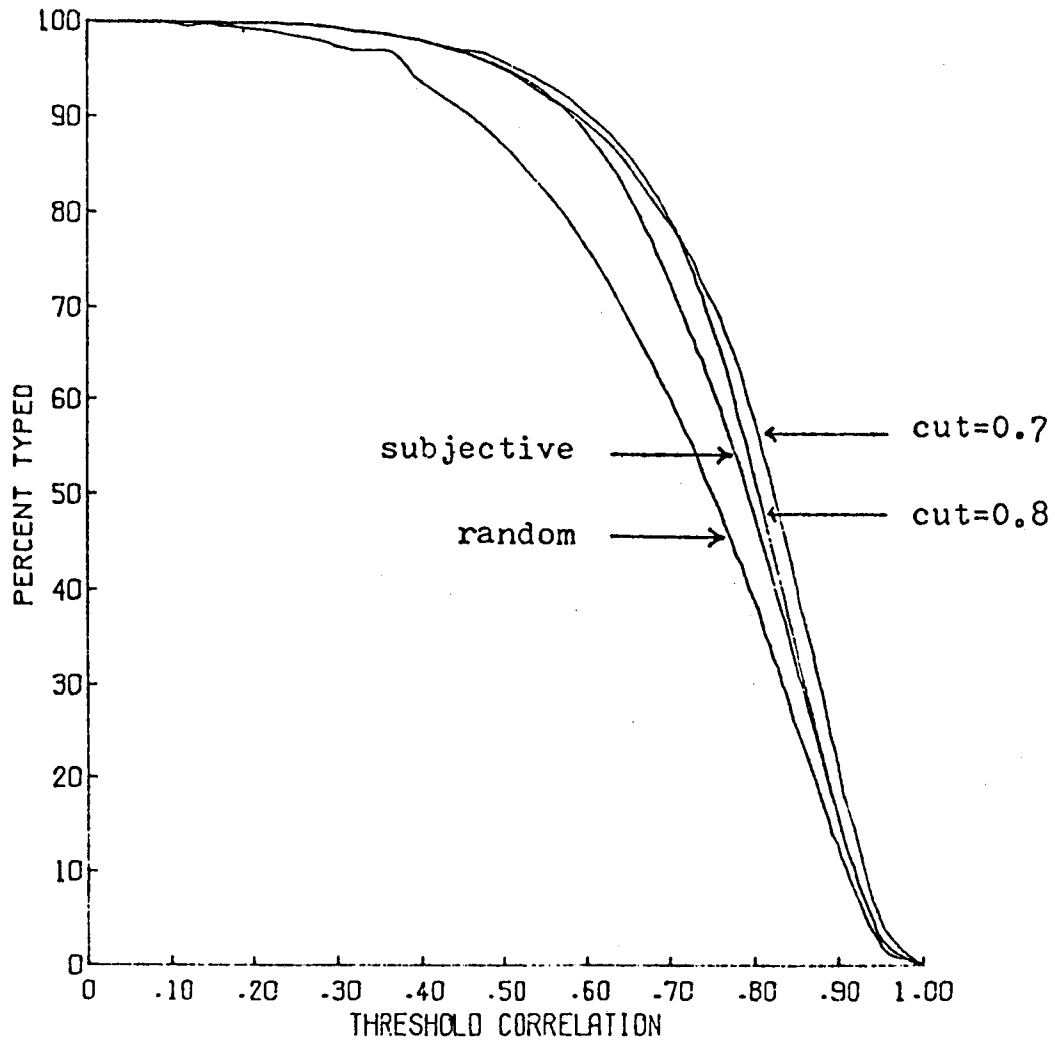


Figure 2-2. Percentage of 12 hour NMC pressure fields typed by the subjective approach, the two pattern correlation types and the average of eight sets of ten maps drawn at random from the NMC data set for 1974.

of the baroclinic field (thermal wind) were determined. The distribution of air-sea temperature difference was also assumed for each pattern, also drawing on idealized storm structure and climatology.

Cardone's (1969) Ekman layer model was used to provide the friction velocity u_* and cross isobar flow angle α . The inputs required are the gradient wind speed, G , the magnitude of the PBL horizontal temperature gradient, \sqrt{T} , the angle between the surface geostrophic wind and the thermal wind, η , and the air-sea temperature difference $\Delta\theta$.

Surface stress was converted to a neutral stratification 10 m surface layer wind speed. Only constant drag coefficients or drift factors should be used with these winds as wind speed and stability corrections are already included.

By comparing the baroclinic, stability dependent 10 m wind field with a wind field based on a constant $u_*/G = 0.025$ for pattern type 1.0, the effects of stability and baroclinicity are about 15%.

Within 50 - 100 km of the coast where Cardone's model is inappropriate, primary guidance was taken from actual measurements and descriptions of coastal processes reported in the draft NOAA Technical Report, "Coastal Meteorology in the Gulf of Alaska, Icy Bay to Yakutat Bay" (Reynolds, Hiester, Macklin, 1978). That report dealt only with the Icy Bay to Yakutat coastline but the following principles of that area were applied to the remainder of the NEGOA coastline.

Planetary boundary layer air piles up against the sides of coastal mountains when the incident winds are obliquely onshore. A pressure gradient forms normal to the coastline which establishes a longshore geostrophic flow. This orographic forcing is part of the reason the low pressure systems stagnate in the Gulf of Alaska. The length scale

of the seaward extent that the deviation from the incident geostrophic flow is discernible is poorly understood. The length scale probably depends on the angle between the initial geostrophic flow and the coast, and the speed of an impinging pressure system. There are indications that the length scale may sometimes exceed 100 km.

Near the surface and nearshore, the winds are not in geostrophic balance and blow at an angle to the coastline. Within 20 km of the coast, the winds can have an offshore katabatic component due to drainage of denser air from the mountain valleys and glaciers. This is an almost permanent feature in winter but occurs mainly at night in the summer. Winds nearshore also respond to the coastal discontinuity in frictional drag creating an offshore wind component when there are longshore easterlies in NEGOA and an onshore component for longshore westerlies.

Figure 2-3 shows the wind speed and direction measured from an aircraft in a line directly offshore of the Malaspina Glacier. Nearshore winds were blowing from the NNE, slightly offshore and out of Yakutat Bay, while 50 km offshore, the winds were from the SE. Where the offshore and the onshore winds merged, the flow accelerated and formed a coastal jet 10 to 30 km offshore and parallel to the shore. That was the best example measured, but we believe the jet is a frequently occurring feature. The sensitivity of the jet to variations in meteorological parameters remains unknown.

In winter the winds nearshore are persistently offshore but in summer the drainage winds are weak and easily overcome by an onshore push. There is a deceleration as the shore is approached. Data from EB-70, EB-43, and an anemometer at Pt. Riou (on the shore at the western tip of the Malaspina Glacier) were used to scale these decelerations.

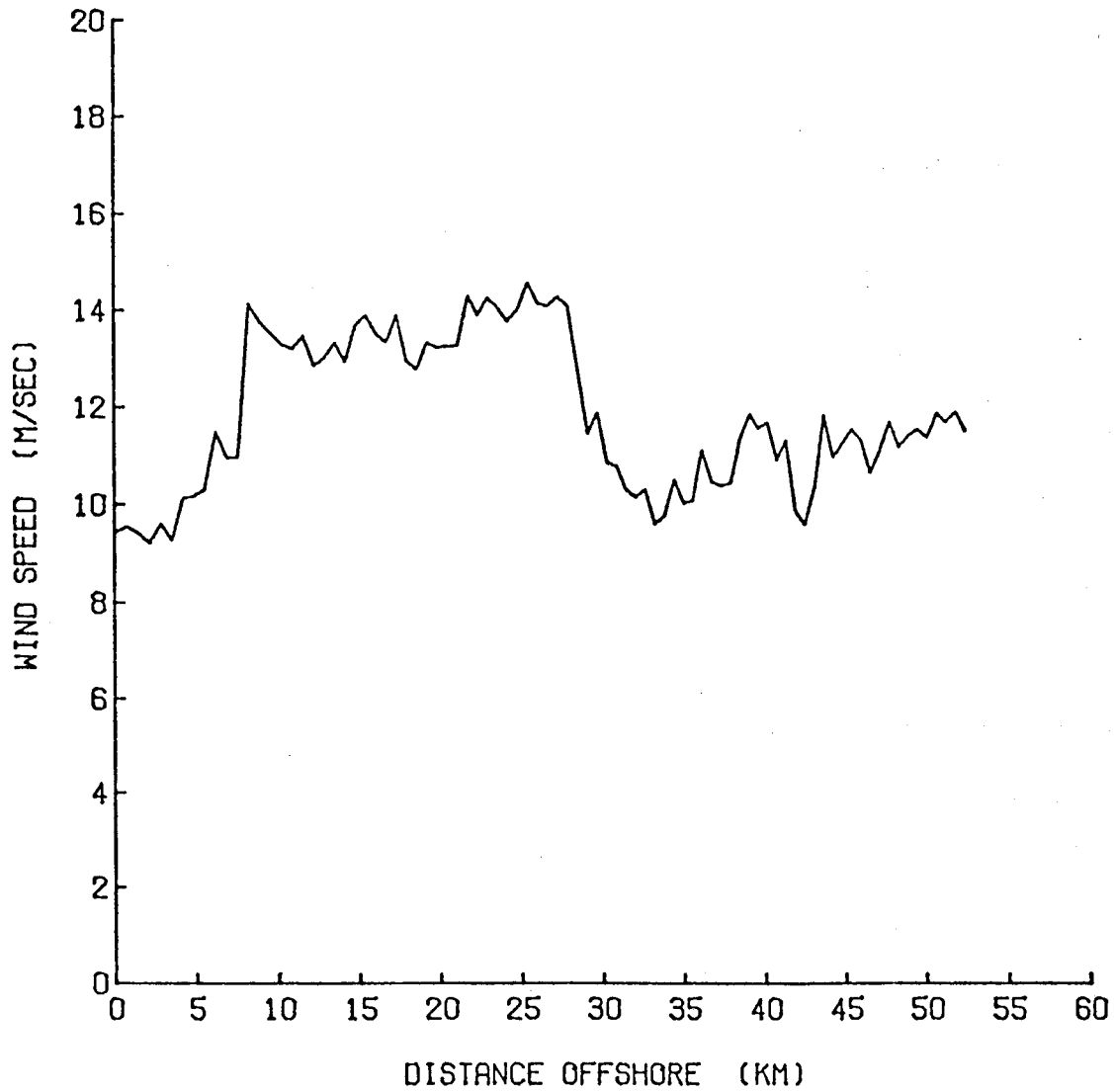


Figure 2-3(a). Wind speed as a function of offshore distance

ALASKAN COASTAL METEOROLOGY
OFFSHORE DISTRIBUTION AT 30 M

YAKUTAT 1977
24 FEBRUARY

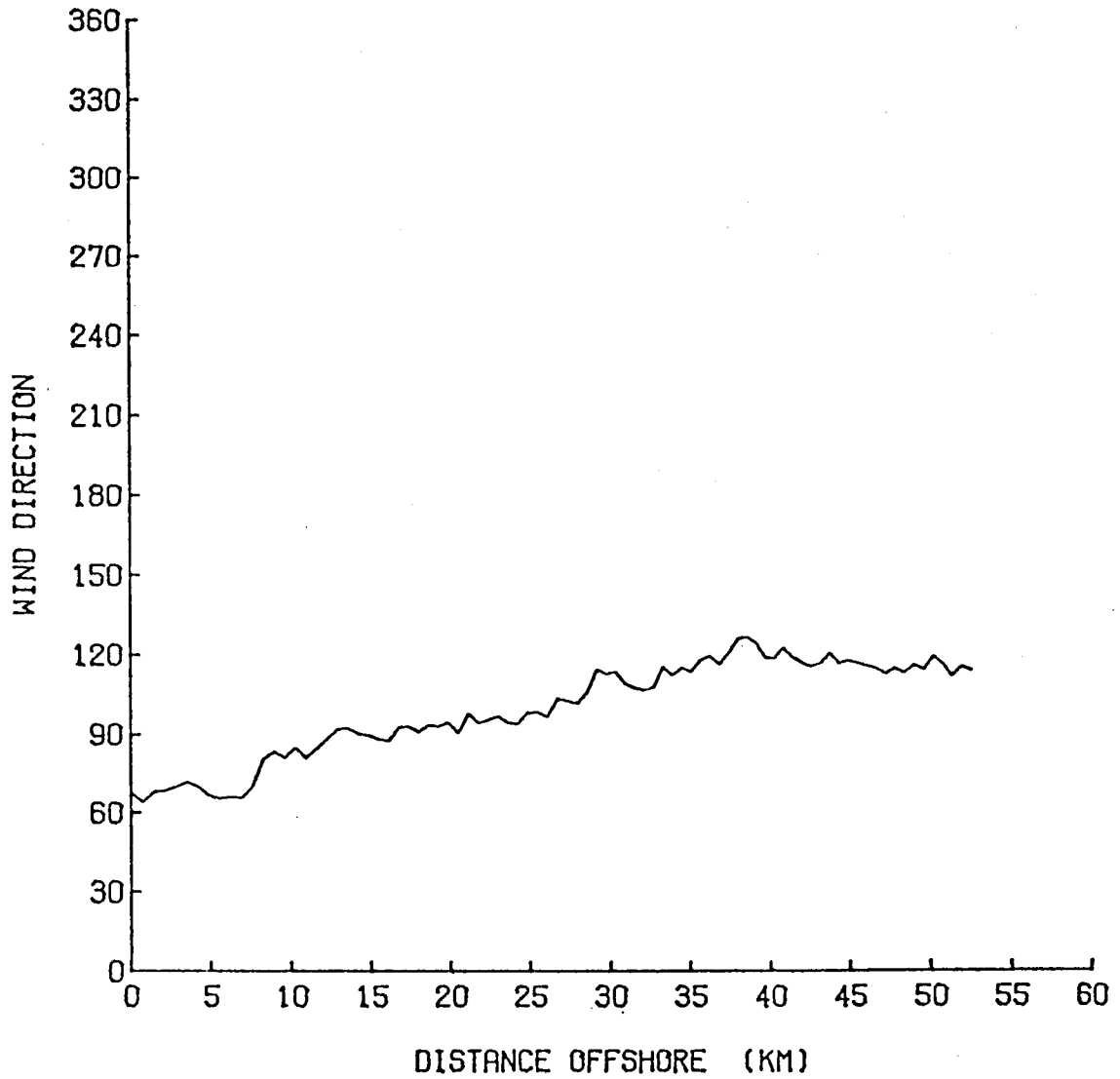


Figure 2-3(b). Direction of the 30 meter wind as a function of offshore direction.

After using the above principles to modify the coastal winds, the wind fields were smoothed. A nine point smoother was used on all grid boxes that were at least one box away from the shore.

Finally, the divergence at each grid point was computed for every wind field. The contours of the divergence field ($\times 10^5$) for type 1.0 are shown in figure 2-4. The values at the coastline cannot be taken too literally as the wind vectors only represent the over water wind. The figure provides confidence in the overall method. There is convergence (of sensible magnitude) at the center of the storm, divergence behind the cold front, and convergence just off the coast where onshore flow meets katabatic flow.

Thirteen velocity fields for the synoptic subtypes described in section 2 are shown at the end of this section as figures A through M. The length of each arrow is a measure of the relative wind speed, and each arrow points downwind.

Synoptic pattern 1 represents a low pressure system contained within the Gulf of Alaska by coastal mountains. This pattern was broken down into four subtypes corresponding to four positions of the storm center as it migrates through the Gulf. Figure 2D is the vector plot for type 1.3 with the storm center at 57°N and 152°W , just east of Kodiak Island. The topographical forcing of the boundary layer is not yet strong so the flow near shore, in the mid to western portions of our grid is onshore. Near the shoreline and at the surface (not necessarily representative of the entire depth of the PBL) there is offshore katabatic flow. Fed by surrounding tributaries, the drainage flow is deeper in the estuaries such as Yakutat Bay and hence dominates the wind fields in those regions. Whenever flow encounters land it decelerates and turns toward lower pressure.

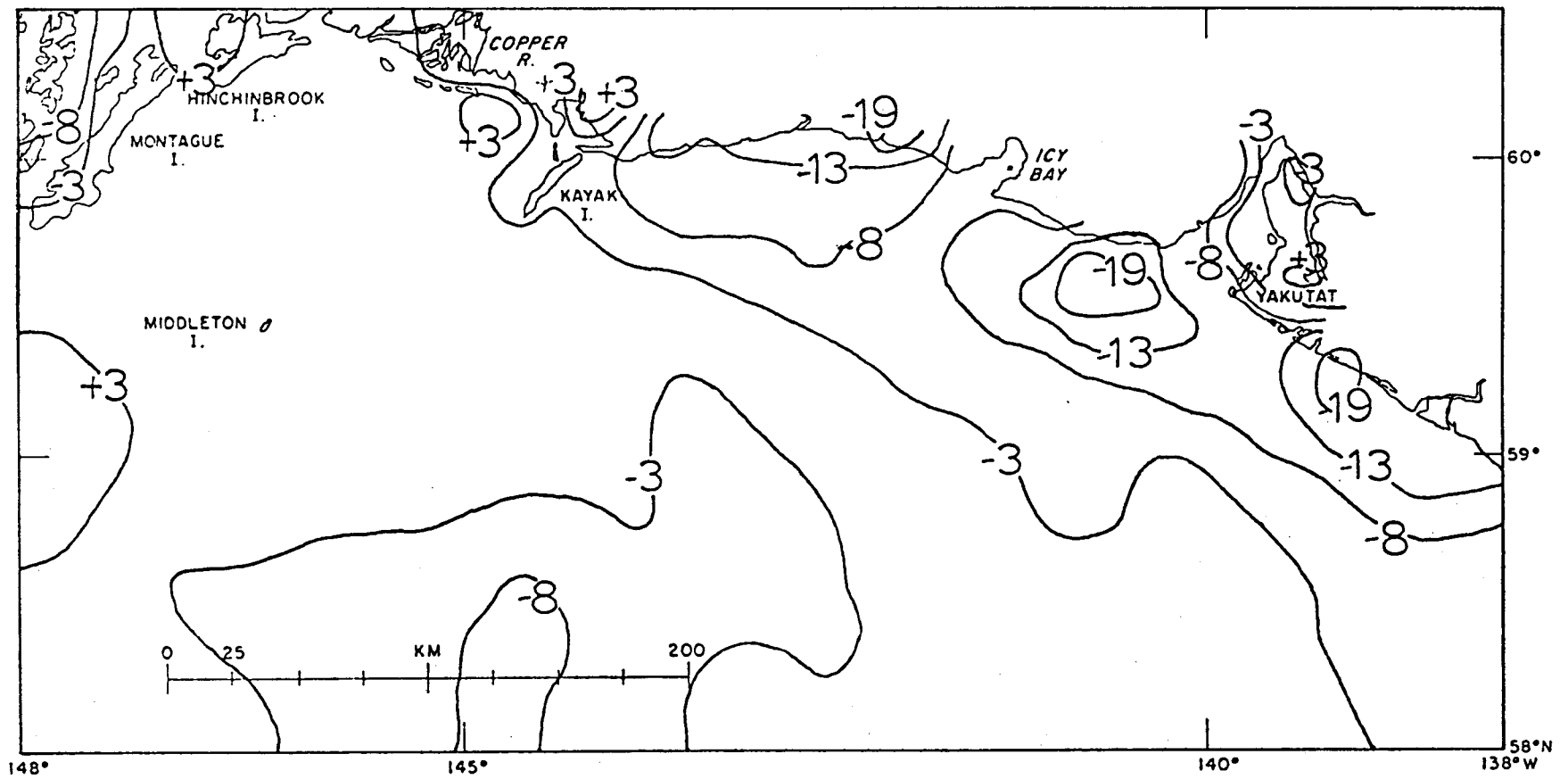


Figure 2-4. Divergence field calculated from the local wind field for type 1.0.

For example, the winds that blow across Kayak Island are retarded and deflected to the south. The air accelerates around the southern tip of the island to rejoin undisturbed flow on the lee side. The winds are also generally slowed by the landforms at the entrances to the Copper River Delta and Prince William Sound, however some passes channel and accelerate the flow.

Figure 2B is the wind field for type 1.1 when the storm is centered at about 50°N , 148°W . The considerations are similar to those documented for type 1.3.

The archetype for this series, type 1.0, is shown in figure 2A. As the storm moves eastward into this position the orographic forcing of the PBL becomes strong, especially in the Yakutat to Kayak Island region. There the offshore flow (katabatically, frictionally and topographically forced) meets the onshore flow and the two form an alongshore jet. The winds blowing offshore in the western portion of the grid accelerate from their nearshore speeds up to their open ocean speeds, causing some divergence there.

Figure 2C shows the wind field for type 1.2. The storm is at its eastern extreme; at about 58°N , 141°W . The alongshore jet is mostly east of our grid region but is visible entering the region at the eastern border. The jet quickly dissipates in the diffluent region in the northwest quadrant of the storm.

Type 2 represents an Aleutian low. The local wind field is shown in figure 2E. There is also an alongshore jet for this type. Since the flow in the eastern part of the grid is roughly alongshore, there is no alongshore acceleration there. The jet forms between Icy Bay and Kayak Island where the geostrophic flow is more directly onshore. The confluence at the mouth of the Yakutat Bay and the deceleration windward

of Kayak Island cause those areas to be convergence centers. There is relief behind Kayak Island where the winds turn northward to almost be in geostrophic-frictional balance before encountering the drainage winds in the Copper River area. The winds are slowed by the land masses in the Cape Hinchinbrook region, but are not blocked by them. Figure 2F represents an autumn case of type 2.1 with a remanant of high pressure to the east.

We have split the synoptic type 3 into two cases. Type 3.0 (figure 2G) is the usual case where the anticyclone over the Yukon dominates the NEGOA area. This is typically a time of clear skies. Radiational cooling of the land surfaces causes katabatic flow, especially off of the Bering, Malaspina, and Hubbard Glaciers. East of Yakutat, the winds accelerate offshore making it a region of divergence. From Yakutat Bay to Kayak Island there is convergence of katabatic and alongshore winds. West of the Bering Glacier is another region of divergence. The winds blowing from the Copper River delta hit Hinchinbrook and Montague Islands quite obliquely, so we show the air blowing roughly parallel to those shores and around the islands to the south rather than making the more energy consuming trip over the tops as in the previously described types. The eastern shores of these islands are, therefore, in a covergent region.

Type 3.1 (figure 2H) allows for the reported cases of very strong (50 to 100 knots) winds near shore along the NEGOA coast. The surface pressure pattern is virtually indistinguishable from that of type 3.0. The air northeast of the coastal mountains is very cold throughout a very deep layer; i.e., the 1000-500 mb thickness is less northeast of the mountains than in the Gulf. When the reservoir of cold air gets deep enough, the cold air spills through the mountain passes like water

over a dam. The low temperature is somewhat maintained (against adiabatic warming during descent) by flow over the radiationally cooled icefields. Large velocities build up as the air drains out of the prominent valleys. We have allowed strong winds to blow out of the Alsek River Valley, Yakutat Bay, Icy Bay, off the Bering Glacier, and from the Copper River Valley.

The Icy Bay winds are strongest and actually blow off the Malaspina Glacier just east of Icy Bay. Guidance for this location came from a preliminary meteorological model run (Overland, et al. 1977). We assumed the core of strong winds would totally mix with the ambient air about 100 km downstream of the shore. Most cores turn to the right as they mix with the ambient flow. The Bering Glacier and Copper River winds meet and mutually interfere.

Synoptic pattern 4 is a summertime case when a large low pressure system over central Alaska dominates with the Pacific high retreating to the south. It is also observed if the Aleutian low (type 2) drifts north. In the local wind fields (figure 2I and 2J) we weaken the katabatic flow off the ice (the land surfaces may be warmer than the ocean), and the land-sea frictional differences encourage onshore flow. The winds also blow up estuaries, unlike previously described cases.

Synoptic pattern 5 represents the predominant summer case of the Pacific anticyclone. The local wind fields, shown in figure 2K and 2L were treated similarly to type 4. There is some topographical forcing, however, as the isobars are slightly packed on the eastern side of the high. The central area of the high is divergent with the onshore flow at the coast being convergent.

Synoptic type 6 represents the low pressure center west of the Queen Charlotte Islands. Frequently this low stagnates and fills in place,

but it also may move NNW into the Gulf of Alaska and become type 1.2. The local wind field (figure 2M) is divergent over most of the NEG OA grid. Guidance in scaling the small horizontal variations for this pattern was taken from aircraft measurements made under similar synoptic conditions, reported in the Reynolds et al. report.

2.4 Weather Typing for the Trajectory Calculations

July-August 1974 and February-March 1975 are the two periods for the sample trajectory calculations. The hand drawn sea level pressure analyses from the National Meteorological Center were visually typed every twelve hours through these periods (Table 2.3 and 2.4).

Figure 2-5 shows the direction of the local wind (meteorological) at Middleton Island for each weather type as inferred from figures 2A - 2M. For comparison the anemometer record at Middleton Island during the sample periods was stratified by synoptic type. Vector mean winds were then computed within each type and plotted for the winter period on figure 2-5 and for the summer period in figure 2-6. A similar plot for winds at EB-33 in winter is shown in figure 2-7. A discussion of wind residuals as compared to Middleton Island and EB-33 winds is presented in section 5.

Table 2.3

(SUMMER)

SUBJECTIVE TYPING

DAY	TIME (GMT)	TYPE	DAY	TIME (GMT)	TYPE	DAY	TIME (GMT)	TYPE
<u>JULY, 1974</u>								
1	00	1.3	23	00	1.3	13	00	5.1
1	12	1.3	23	12	2.1	13	12	5.1
2	00	4.1	24	00	1.1	14	00	5.1
2	12	2.1	24	12	4.0	14	12	5.1
3	00	4.1	25	00	4.0	15	00	5.1
3	12	4.0	25	12	1.1	15	12	5.1
4	00	5.0	26	00	5.0	16	00	5.1
4	12	5.1	26	12	5.1	16	12	5.0
5	00	5.1	27	00	5.1	17	00	5.1
5	12	1.1	27	12	5.1	17	12	5.1
6	00	1.1	28	00	5.0	18	00	1.0
6	12	5.1	28	12	5.0	18	12	4.1
7	00	5.1	29	00	4.0	19	00	5.1
7	12	5.0	29	12	5.0	19	12	5.1
8	00	5.1	30	00	5.1	20	00	4.1
8	12	5.0	30	12	5.1	20	12	1.1
9	00	5.1	31	00	5.1	21	00	4.1
9	12	5.1	31	12	4.0	21	12	4.0
10	00	5.1	<u>AUGUST, 1974</u>			22	00	4.0
10	12	1.1	1	00	3.0	22	12	4.0
11	00	1.1	1	12	2.0	23	00	1.1
11	12	1.3	1	12	2.0	23	12	4.1
12	00	1.1	2	00	1.3	24	00	4.1
12	12	1.1	2	12	1.3	24	12	5.0
13	00	2.1	3	00	1.1	25	00	1.3
13	12	2.0	3	12	1.1	25	12	1.3
14	00	4.0	4	00	1.1	26	00	1.0
14	12	5.1	4	12	6.0	26	12	4.0
15	00	5.1	5	00	5.0	27	00	2.1
15	12	5.1	5	12	4.0	27	12	2.0
16	00	4.0	6	00	2.1	28	00	2.1
16	12	5.1	6	12	2.1	28	12	2.1
17	00	4.1	7	00	2.1	29	00	2.1
17	12	5.1	7	12	1.3	29	12	2.1
18	00	5.0	8	00	1.1	30	00	2.1
18	12	4.0	8	12	4.0	30	12	2.1
19	00	4.0	9	00	5.0	31	00	5.1
19	12	2.1	9	12	5.0	31	12	4.0
20	00	2.1	10	00	5.0			
20	12	2.0	10	12	5.1			
21	00	2.0	11	00	5.1			
21	12	1.3	11	12	5.1			
22	00	1.3	12	00	5.1			
22	12	1.1	12	12	5.1			

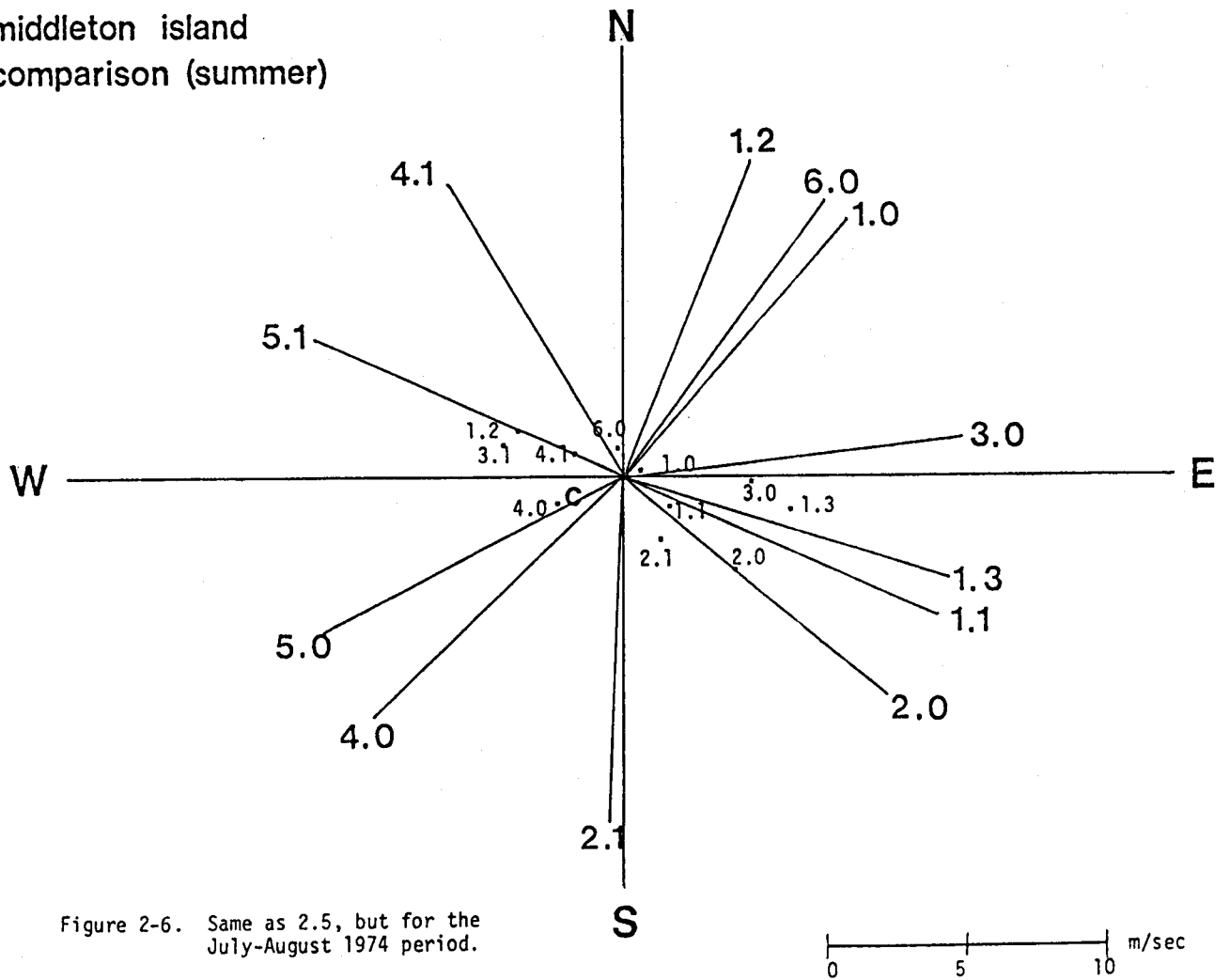
Table 2.4

(WINTER)

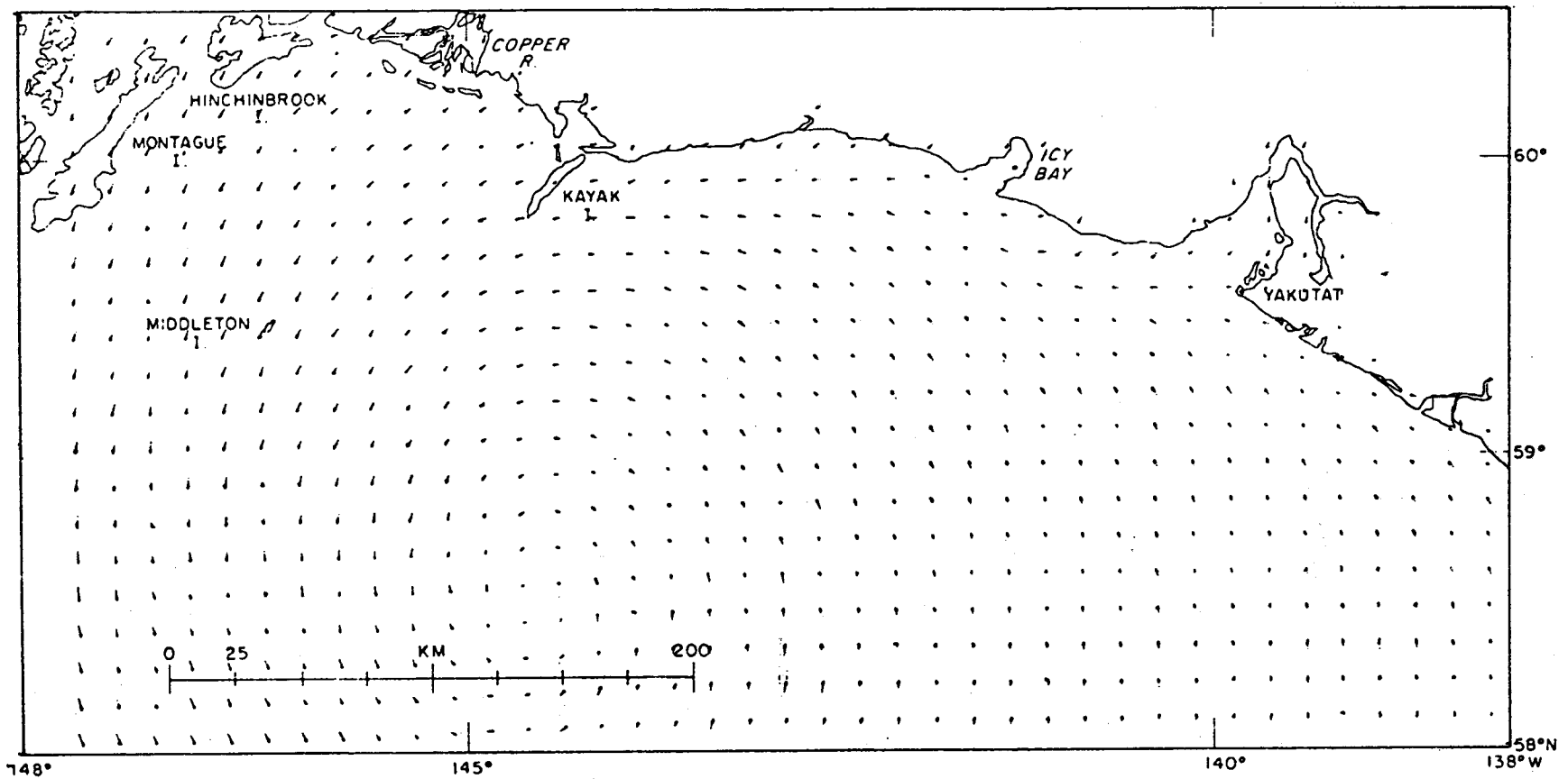
SUBJECTIVE TYPING

DAY	TIME (GMT)	TYPE	DAY	TIME (GMT)	TYPE	DAY	TIME (GMT)	TYPE
<u>FEBRUARY, 1975</u>								
1	00	6.0	23	00	2.0	16	00	3.0
1	12	6.0	23	12	5.0	16	12	1.3
2	00	6.0	24	00	4.0	17	00	1.3
2	12	6.0	24	12	2.1	17	12	6.0
3	00	6.0	25	00	1.3	18	00	6.0
3	12	6.0	25	12	2.0	18	12	6.0
4	00	6.0	26	00	1.3	19	00	6.0
4	12	5.1	26	12	2.0	19	12	1.0
5	00	5.1	27	00	4.0	20	00	5.0
5	12	5.1	27	12	2.1	20	12	4.0
6	00	3.0	28	00	5.0	21	00	2.1
6	12	6.0	28	12	5.0	21	12	4.0
7	00	6.0	<u>MARCH, 1975</u>			22	00	4.1
7	12	1.2	1	00	6.0	22	12	1.2
8	00	2.0	1	12	6.0	23	00	1.1
8	12	2.0	2	00	5.1	23	12	1.1
9	00	4.1	2	12	3.0	24	00	1.1
9	12	6.0	3	00	6.0	24	12	4.0
10	00	6.0	3	12	5.0	25	00	4.1
10	12	6.0	4	00	2.1	25	12	4.1
11	00	6.0	4	12	2.0	26	00	1.3
11	12	1.0	5	00	1.3	26	12	1.3
12	00	1.0	5	12	1.0	27	00	2.0
12	12	1.0	6	00	1.0	27	12	2.0
13	00	1.1	6	12	1.2	28	00	2.0
13	12	1.1	7	00	6.0	28	12	3.0
14	00	1.1	7	12	6.0	29	00	2.0
14	12	2.0	8	00	5.1	29	12	4.1
15	00	4.0	8	12	1.2	30	00	5.1
15	12	4.0	9	00	1.0	30	12	5.0
16	00	5.0	9	12	2.0	31	00	1.3
16	12	2.0	10	00	3.0	31	12	5.0
17	00	1.3	10	12	2.0			
17	12	4.0	11	00	2.0			
18	00	2.0	11	12	4.0			
18	12	2.1	12	00	5.0			
19	00	2.0	12	12	2.0			
19	12	4.1	13	00	3.0			
20	00	4.0	13	12	2.0			
20	12	4.1	14	00	1.3			
21	00	2.0	14	12	1.2			
21	12	2.0	15	00	1.3			
22	00	2.0	15	12	1.1			
22	12	4.0						

middleton island
comparison (summer)



ARCHETYPE LOW IN GOR. LOW CENTERED AT 59.5N, 144.5W CASE 1.0

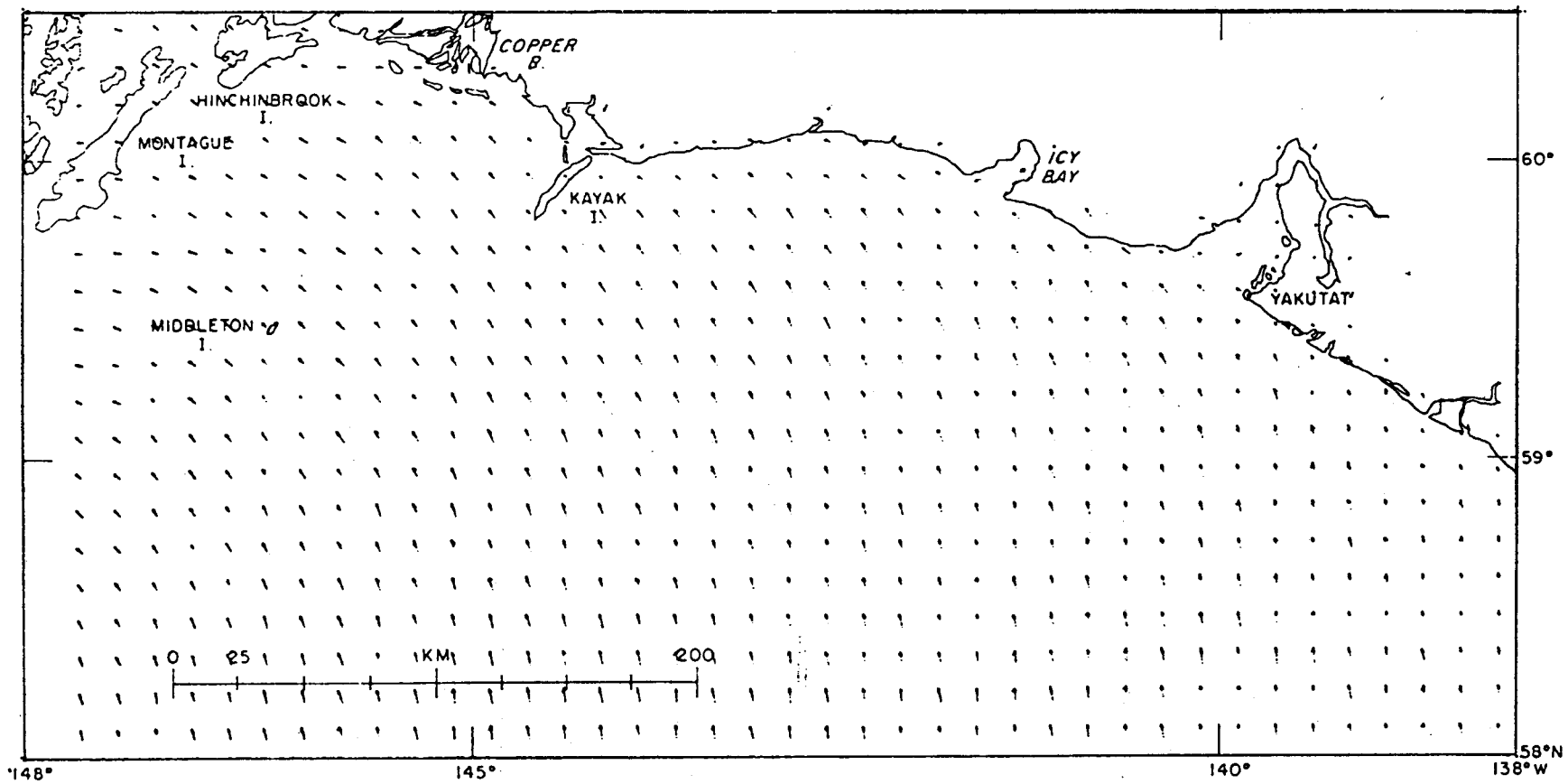


103

Figure 2A

LOW IN GOA. CENTERED AT 50N, 148W

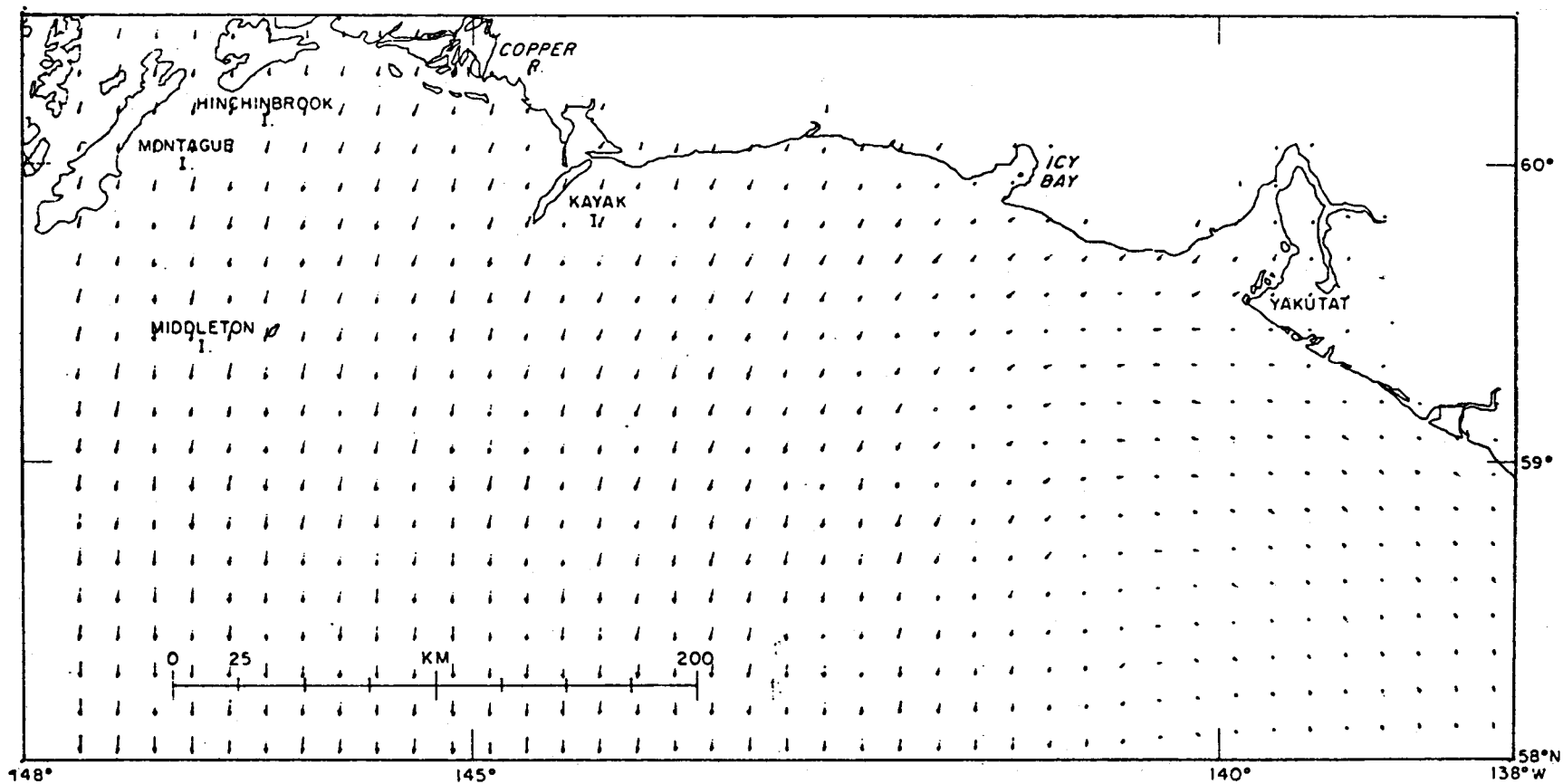
CASL 1.1



104

Figure 2B

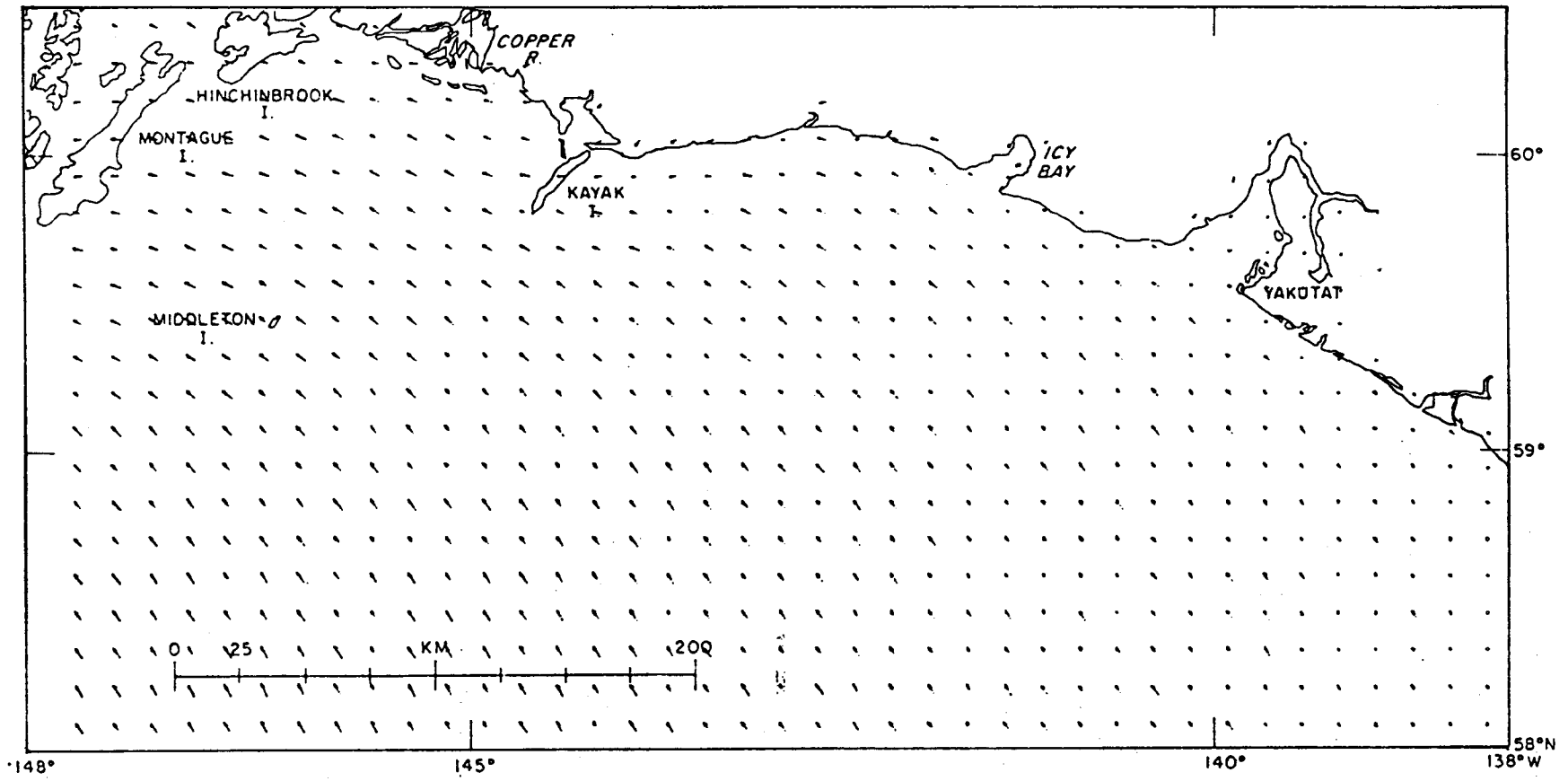
EASTERN EXTREME OF TYPE 1 LOWS CENTERED AT 58N, 141W CASE 1.2



105

Figure 2C

WESTERN EXTREME OF TYPE I LOWS CENTERED AT 57N, 152W (EAST OF KODIAK) CASE 1.3

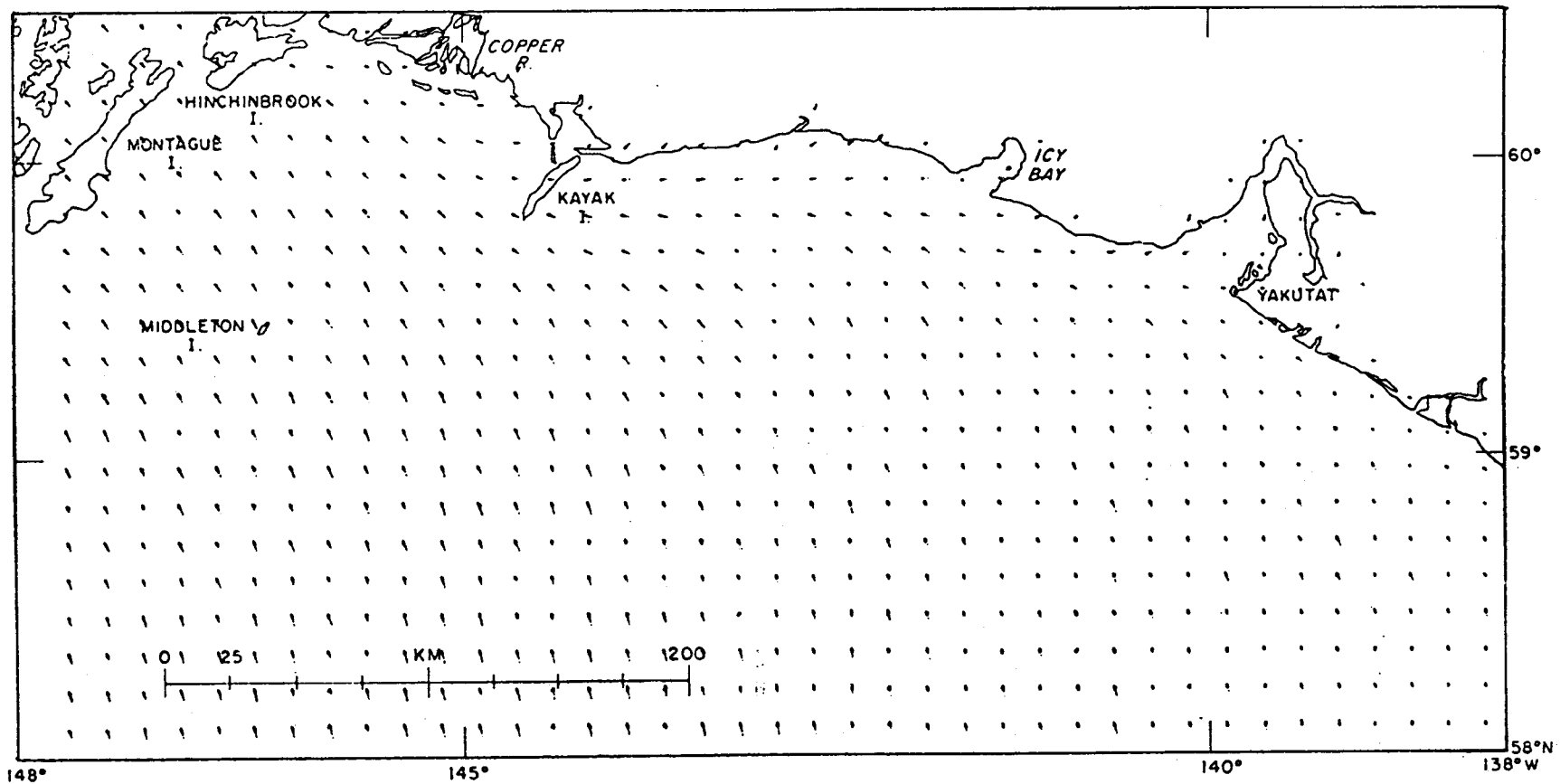


106

Figure 2D

ALEUTIAN LOW

CASE 2.0

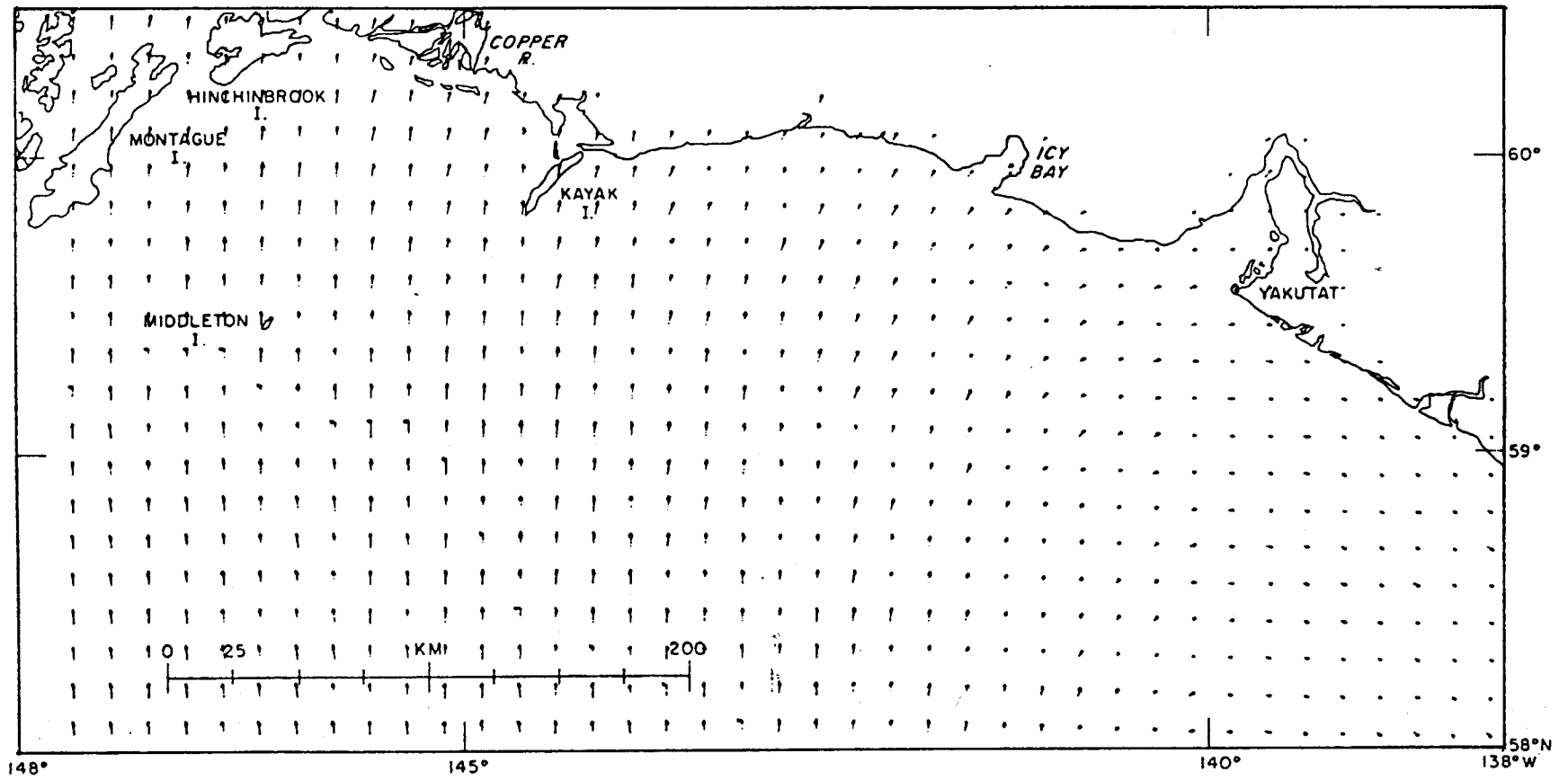


107

Figure 2E

ALEUTIAN LOW IN SUMMER

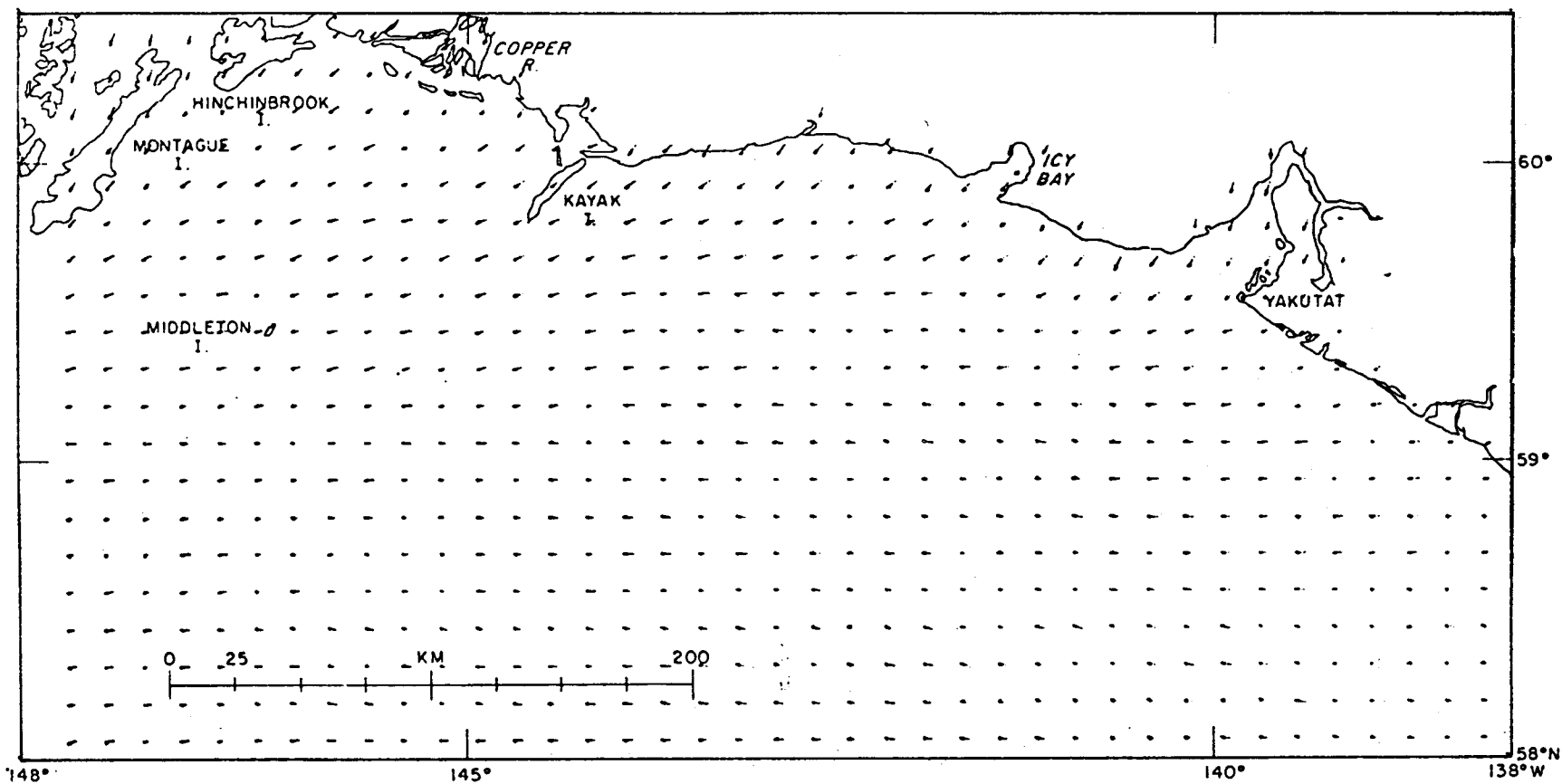
CASE 2.1



108

Figure 2F

HIGH OVER YUKON CAUSING EASTERLY WINDS OVER NEGOR CASE 3.0



109

Figure 2G

SAME SURFACE PRESSURES AS 3.0 BUT HIGH (>50KTS) KATABATIC WINDS

PAGE 3.1

110

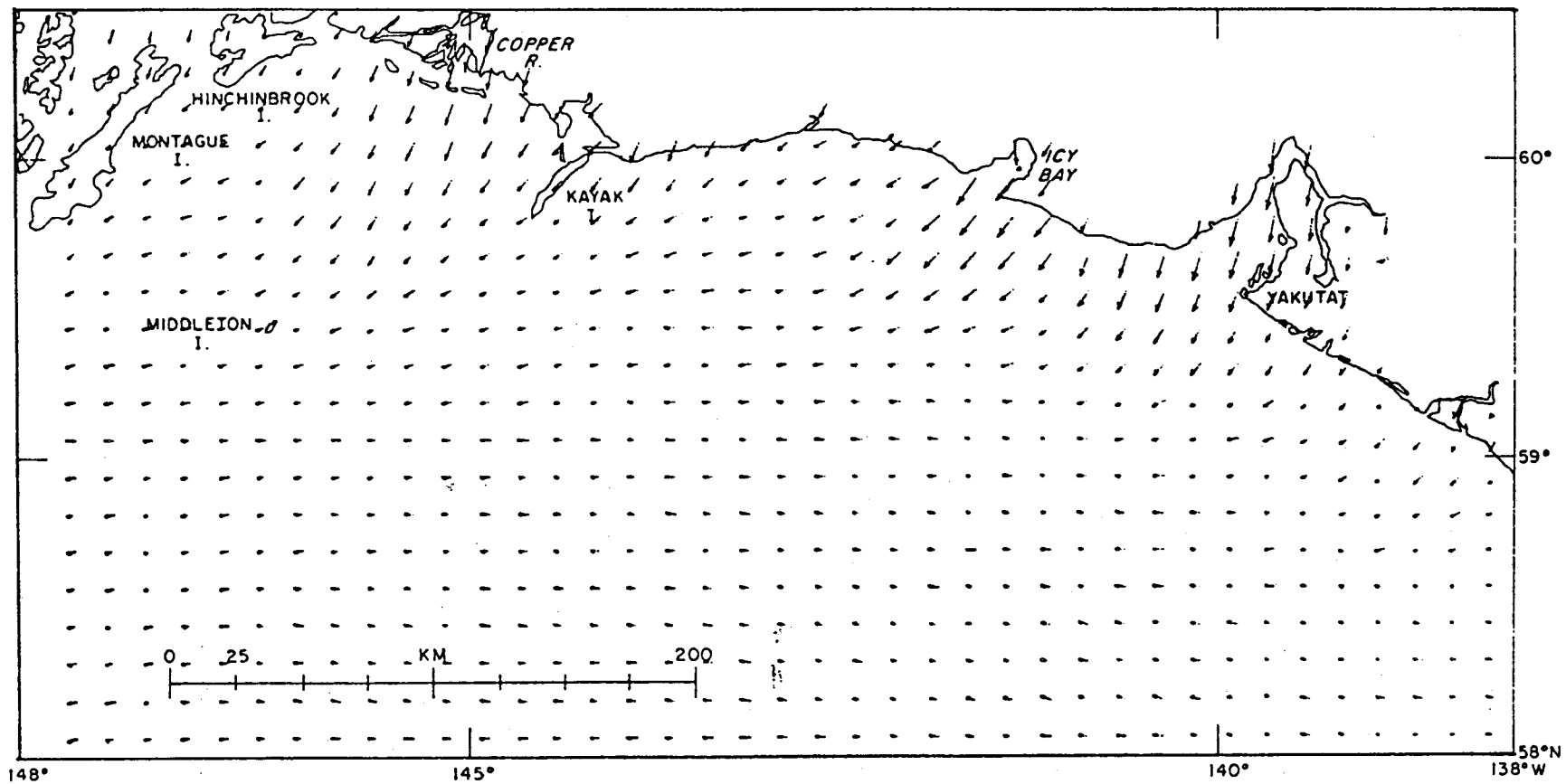
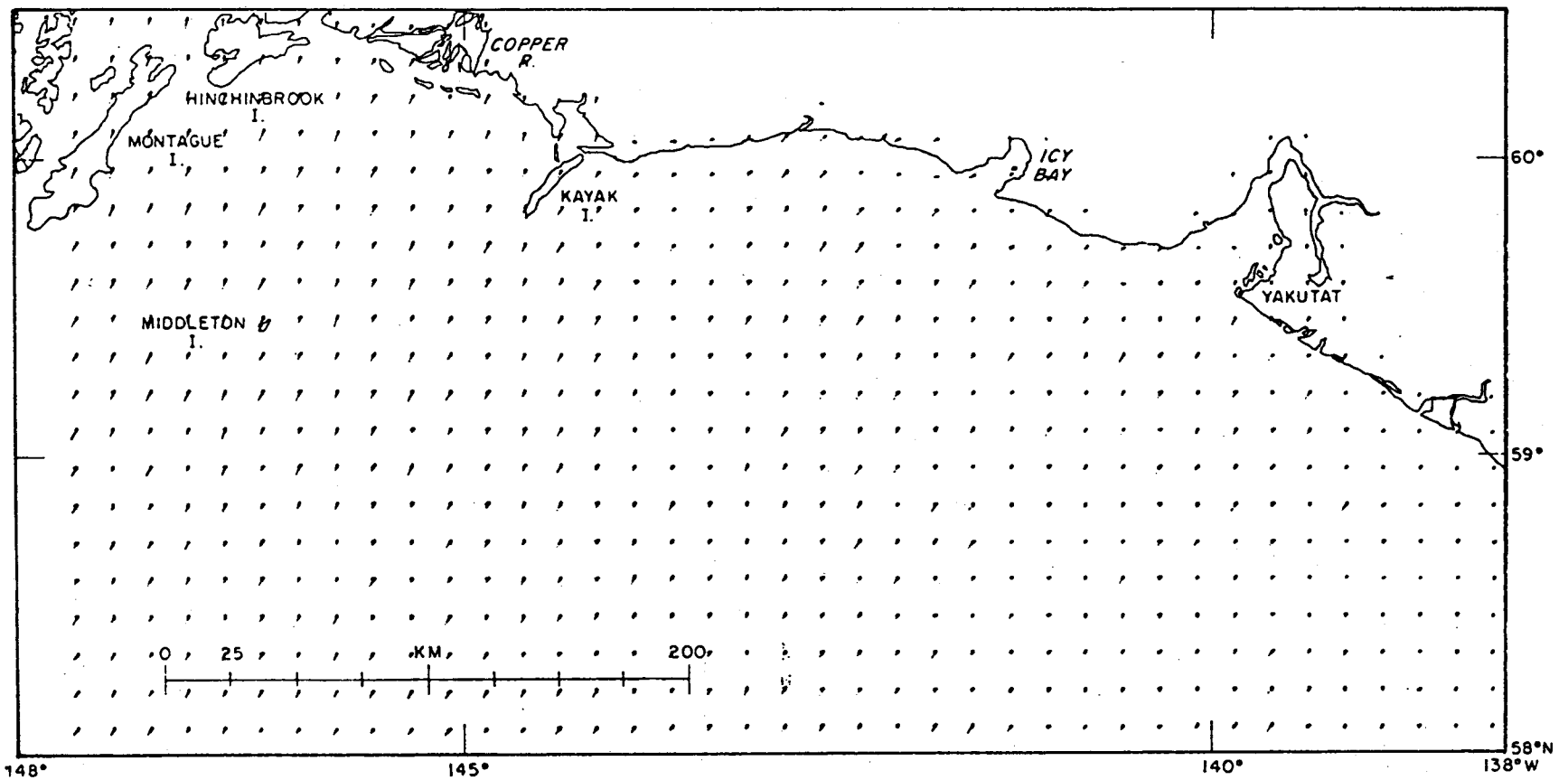


Figure 2H

SUMMER LOW OVER CENTRAL ALASKA

CASE 4.0

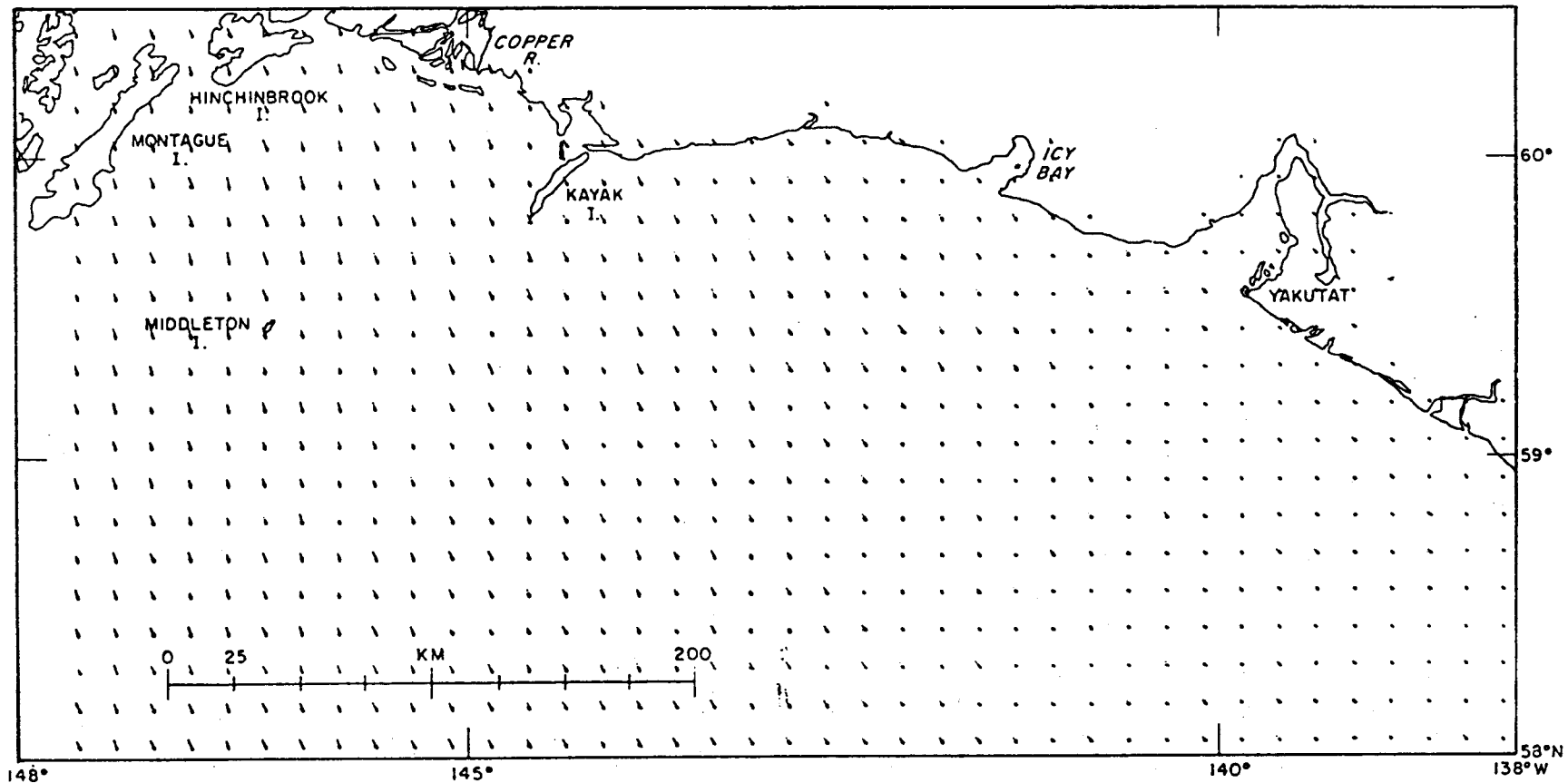


111

Figure 2I

SUMMERTIME INTERIOR LOW OVER YUKON

CASE 4.1

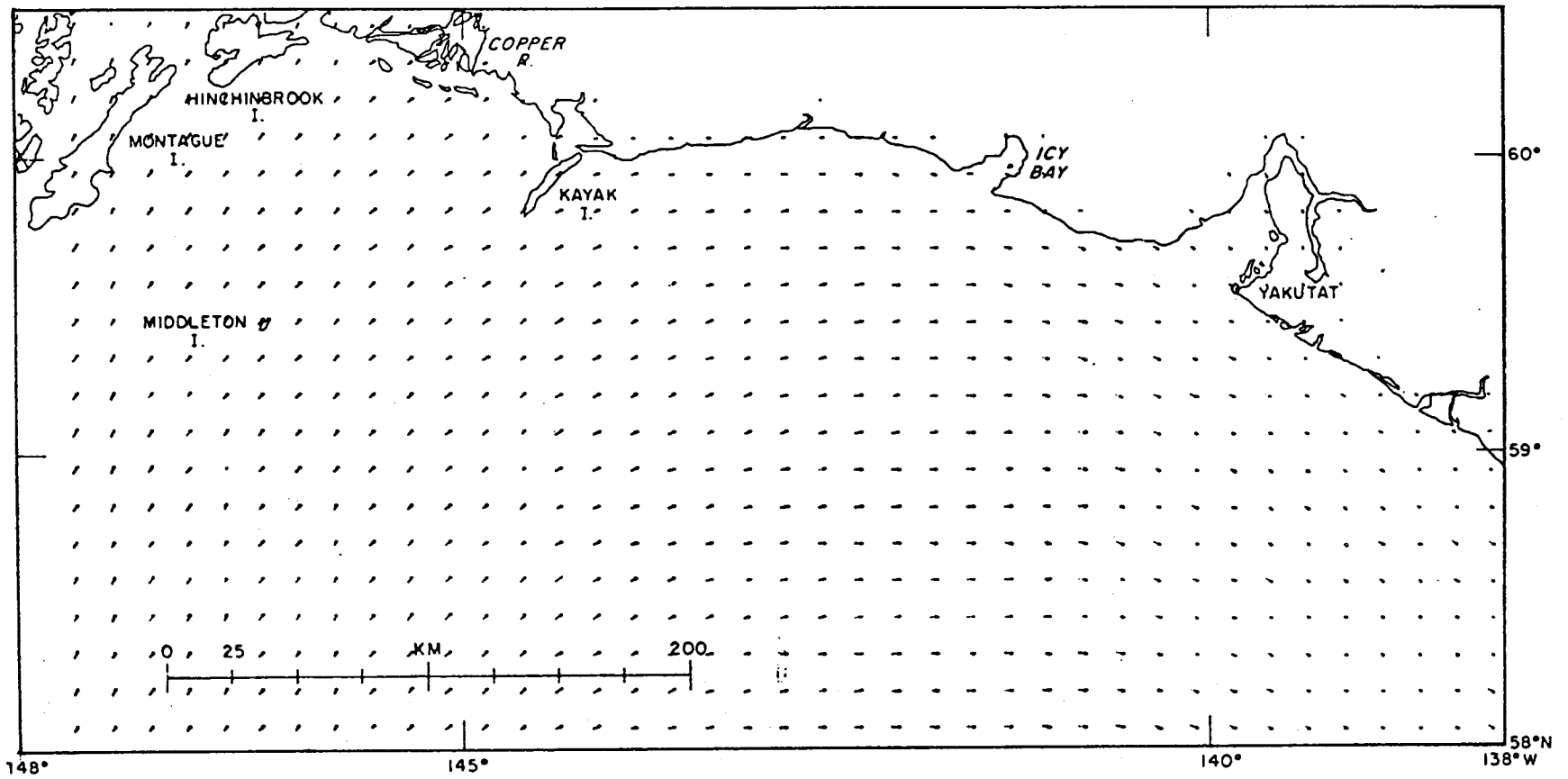


112

Figure 2J

SUMMER PACIFIC ANTICYCLONE

CASE 5.3

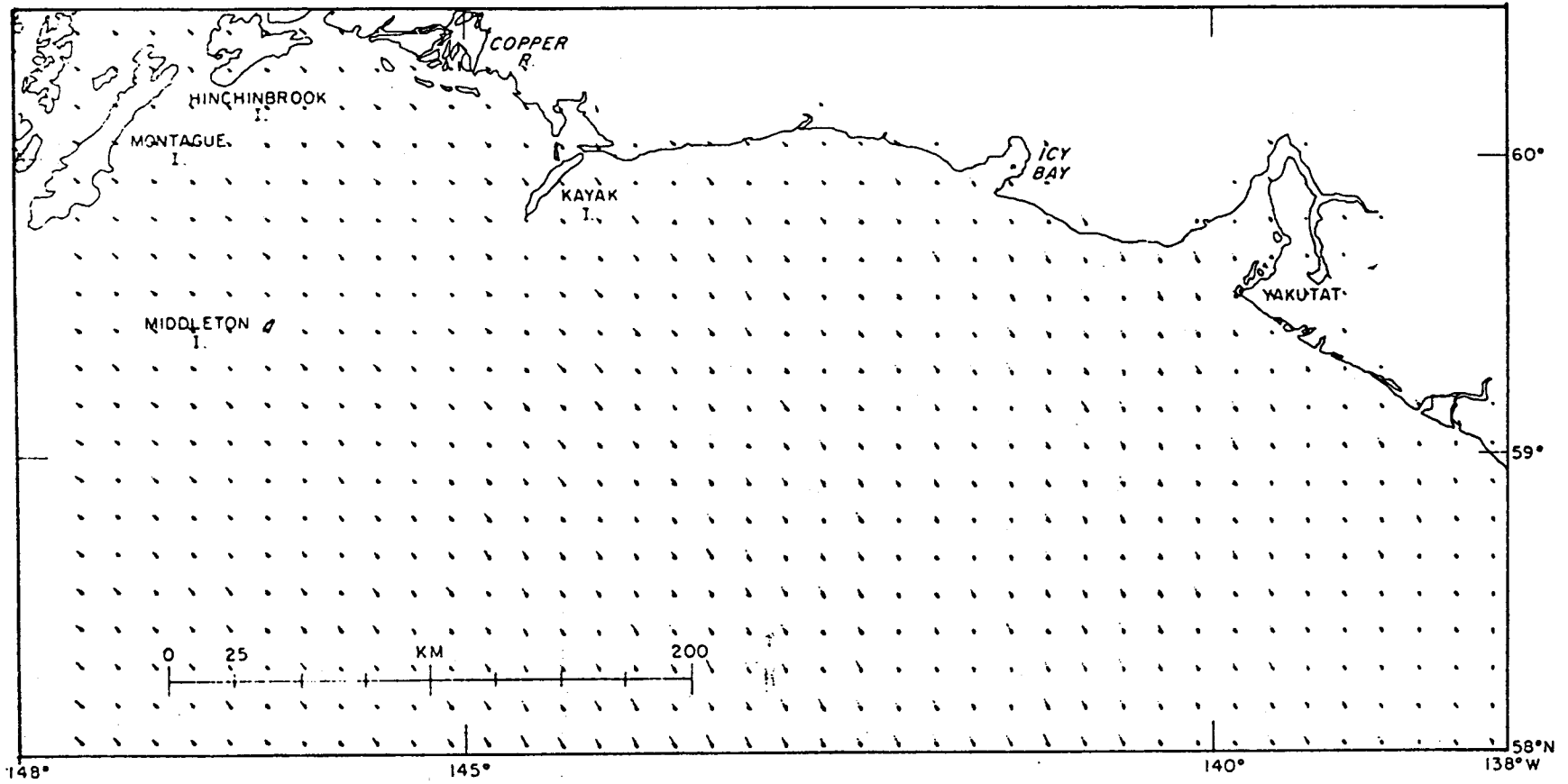


113

Figure 2K

SUMMERTIME PACIFIC HIGH DISPLACED TO WEST

CASE 5.1



114

Figure 2L

LOW STAGNATING JUST OFF COAST WEST OF QUEEN CHARLOTTE ISLANDS

CASL 6.3

115

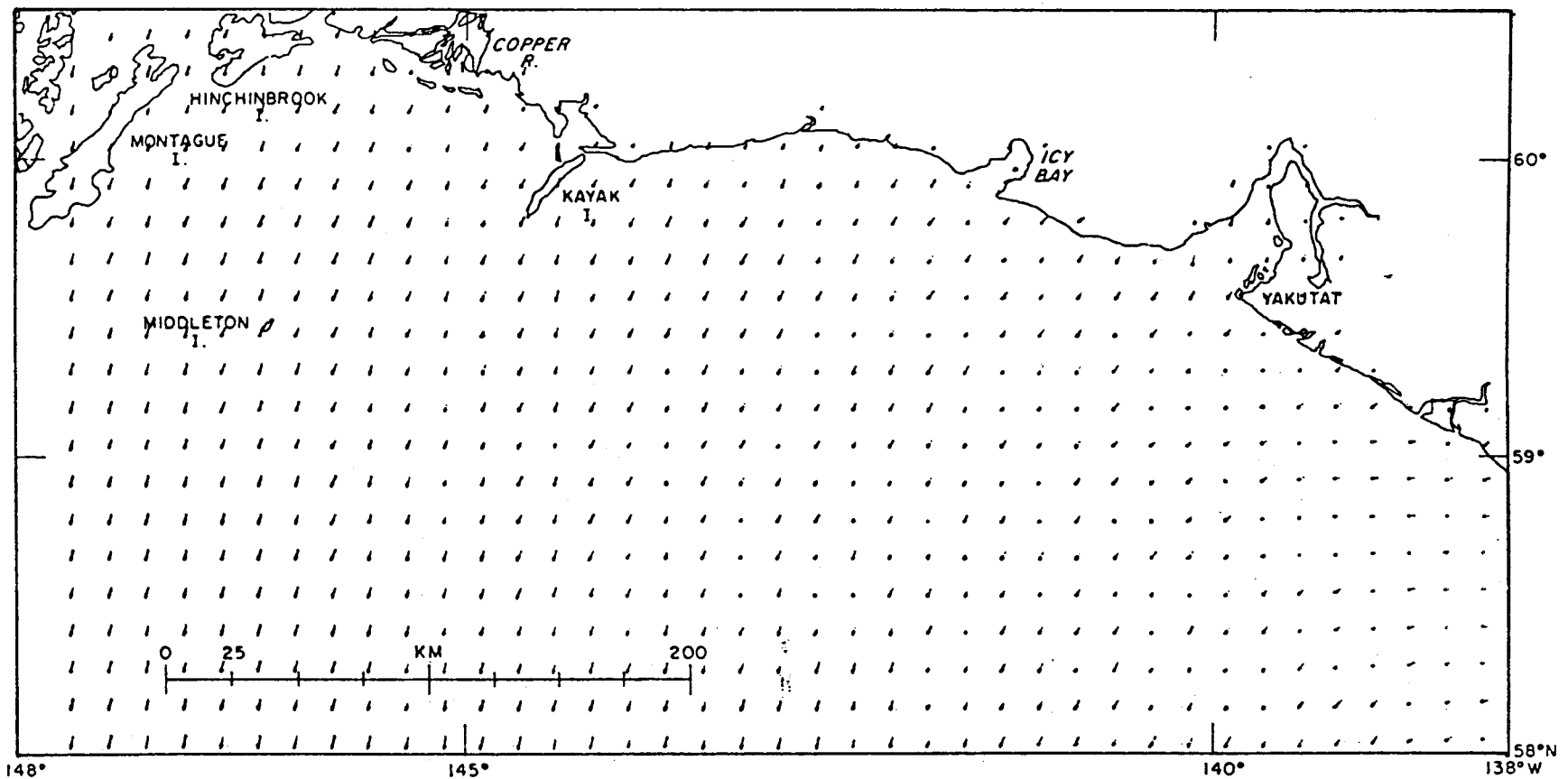


Figure 2M

REFERENCES

- Barry, R.G. and A.H. Perry (1973): Synoptic Climatology, Methods and Application. London: Methuen & Co. 553 pp.
- Brower, W.A.Jr., H.F. Diaz, A.S. Prechtel, H.W. Searby and J.L. Wise. (1977): Climatic Atlas of the Outer Continental Shelf waters and coastal regions of Alaska: Vol. 1, Gulf of Alaska, National Climate Center, Environmental Data Service, NOAA, Ashville, N.C. 439 pp.
- Cardone, V.J. (1969): Specification of the wind distribution in the marine boundary layer for wave forecasting. Report GSL TR69-1 New York University School of Engineering Science, 131 pp.
- Jenne, R.L. (1975): Data sets for meteorological research. NCAR Tech Note NCAR-TN/1A, 194 pp.
- Kendall, M.G. and A. Stewart (1975): The Advanced Theory of Statistics, Vol. 3. New York, N.Y., Hafner Press, 585 pp.
- Lund, I.A. (1963): Map pattern classification by statistical methods. J. Appl. Meteor. 2, p 56-65.
- Overland, J.E. and Thomas R. Hiester (1978): A Synoptic Climatology for Surface Winds Along the Southern Coast of Alaska. NOAA/ERL/PMEL, Tech. Report (draft).
- Overland, J.E., M.H. Hitchman and Y.-J. Han (1978): A Regional Surface Wind Model for Mountainous Coastal Areas PMEL/ERL/NOAA Technical Report (in press).
- Putnins, P. (1966): The sequence of baric pressure patterns over Alaska. Studies on the meteorology of Alaska 1st Interim Report, Washington D. C., Environmental Data Service, ESSA, 57 pp.
- Reynolds, R.M., T.R. Hiester and S.A. Macklin (1978): Coastal Meteorology of the Gulf of Alaska Icy Bay to Yakutat Bay. PMEL/ERL/NOAA Tech. Report (In press).
- Sorkina, A.I. (1963): Tipy atmosfernoi tsirkuliatsii, Israel Program for Scientific Translations, Jerusalem, 247 pp.

3.0 Analysis of Northeast Gulf of Alaska Current Patterns

3.1 Introduction

The Northeast Gulf of Alaska (NEGOA) area is situated in the northern bight of the Gulf of Alaska, with the present area of interest centered on the continental shelf between Yakutat and Montague Island (figure 3-1). The shelf topography is quite complex with many small and intermediate scale features (5-50 km). On a large scale the shelf is relatively narrow east of Kayak Island and comparatively broad west of that point. The shelf break as indicated by the 100 fa. contour (figure 3-1) is irregular and gives the shelf domain a very complex shape. The coastal morphology is dominated by mountains, and the weather patterns and coastal winds show evidence of significant orographic influence. For many years this region saw very little in the way of systematic oceanographic studies, but with the advent of potential offshore gas and oil development a series of studies was initiated. These have included the repeated mapping of state variables with CTD or STD cruises, moored current meter deployments, Lagrangian drifter studies, installation of bottom mounted pressure gauges, coastal meteorological studies, and the placement of large weather buoys within the study area.

Early studies have shown the relationship of the NEGOA area to the larger scale current of the Gulf of Alaska (Favorite, et al. 1976). More detailed studies of the shelf circulation proper were presented by Galt (1976) and regional hydrology has been discussed by Royer (1975), Galt and Royer (1975), and Royer (1978). The relationship between the bottom pressure distribution across the shelf off Icy Bay and the local currents has been investigated by Hayes and Schumacher (1976) and Hayes (1979).

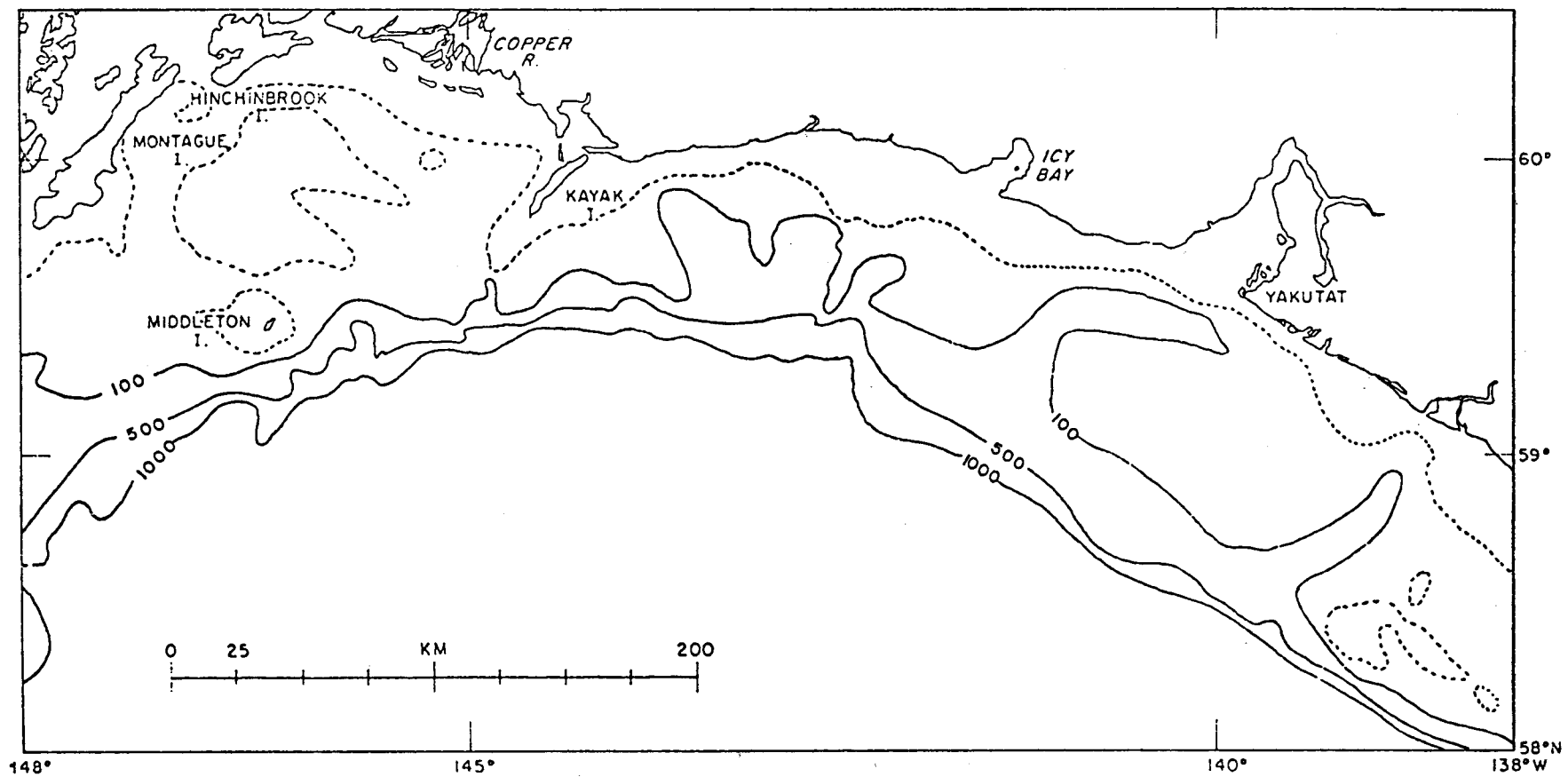


Figure 3-1. Northeast Gulf of Alaska study area. Depth contours shown in fathoms. Dotted contour represents 50 fathom curve.

The Lagrangian current measurements from drogue studies have been described by Royer, et al. (1978). In addition to these recent oceanographic studies, the regional meteorology has also come under scrutiny. The coastal region has been investigated by Reynolds, et al. (1978) with particular attention being directed towards the description of the nearshore wind regime. Starting with earlier work by Putnins (1966), Overland and Hiester (1977) extended the climatology for the Gulf of Alaska with weather typing studies concentrating on the definition of a set of inclusive patterns for the synoptic scale pressure field and their relationship to the regional wind fields.

All in all a great deal of new information has become available about the NEGOA region within the last few years, and it is now possible to qualitatively describe many of the features of the general flow. In addition a number of dynamic processes have been identified and in some cases can be quantitatively documented. The off shelf region is under the continuing influence of the general Gulf of Alaska circulation, and its baroclinic signature is clearly evident over the continental slope and shelf break. Coastal run-off and precipitation also induce baroclinic fields that are clearly seen to influence the near shore region over the shelf. Over the shelf proper the regional winds set up a barotropic response which has a much shorter adjustment period than is evident in the internal density field and in the resulting density driven currents. In all cases the irregular bathymetry appears to have a significant effect by channeling the flow.

Despite our greatly improved documentation of the Northeast Gulf of Alaska region and the contributions that many of the authors have made, there are still some significant gaps in the overall understandings

of regional dynamic processes and in the description of the currents. The object of this study is to address one particular facet of this problem: the spatial distribution of the surface currents. Most of the oceanographic information that has been gathered for NEGOA has been Eulerian in nature, giving dense temporal coverage at a single location. The regional studies have, for the most part, concentrated on the definition of dynamic processes and not on the deliniation of flow patterns. Two exceptions were the Lagrangian drifter experiments (Royer, et al. 1978) and the numerical trajectory experiments (Galt, 1976), but these were limited in coverage.

In this report a more general approach to the study of Northeast Gulf of Alaska current patterns is attempted using a numerical circulation model. The model is a finite element diagnostic formulation developed by Galt (1975). The details of the numerical techniques and program for the model solution are described by Watabayashi and Galt (1978). The dynamic partitioning of the model and recommended strategies for its use, along with an example, are presented by Galt and Watabayashi (1978). The model dynamics are a simple linear combination of geostrophic and Ekman currents formulated for an arbitrarily shaped continental shelf region. The geostrophic flow is made up of both barotropic and baroclinic (internal and external) modes, and the Ekman dynamics leads to the inclusion of both upper and lower frictional boundary layers.

The dynamics included in this formulation has been the subject of many studies in the past. The problem for homogeneous water and enclosed basins was first addressed by Welander (1956). More recent studies for simplified geometries have been carried out by Pedlosky (1974) and Csanady (1978). Pedlosky's work introduces the possibility of coastal boundary layers subject to a more complex dynamics than is represented by the

simple formulation considered in this study. For regions that are dominated by these side wall boundary layers one may expect the present results to be deficient. Scale analysis suggests that the influence of these layers is confined to within a few tens of kilometers of the coast, and by implication there is a corresponding band in which the solutions may be considered incomplete. A finite difference formulation of a diagnostic model for shelf circulation has been developed by Hsueh and Peng (1978). Their results are applicable to relatively simple shelf configurations for which the dynamic influence of depth variations is limited to one dimension, normal to the coast line. In addition, however, these authors do present a section discussing the time dependent form of the equations, where the terms responsible for shelf waves are scaled.

In this work it will be assumed that the steady state form of the diagnostic model equations is valid. This implies a number of things. To start with the density field, which is specified by a set of hydrographic cruises, is assumed to give synoptic distributions which can be considered fixed for time periods on the order of a month. This assumption is amenable to test, both in the NEGOA data and through related diagnostic model studies carried out by Hann (1978). In general it seems that the baroclinic shears are well represented by the fields for periods of a week or so and can be considered as representative, but not correct in detail, for longer periods. The barotropic wind set-up response of the region is also assumed to be in steady state balance, but not necessarily the same for all time. This brings in the second set of assumptions about the modeled current patterns. The adjustment of the barotropic response to the regional wind patterns (sea surface set-up) is assumed to be continuous. This means two things. First of all the flow is quasi-geostrophic

at all times (except within the Ekman layers). And second, the adjustment process is smooth enough so that energetic shelf waves are not generated. This second assumption is somewhat more restrictive than the first. An examination of smoothed current meter records (Galt, 1976) from the NEGOA region show directional oscillations around the mean flow that may well be related to shelf wave phenomena. These oscillations are not represented by the diagnostic model formulation, but they do not appear to dominate the flow. And to the extent that they are linear, the oscillations will not even interact with the dominant and most energetic patterns that the model does represent.

The following sections will present the diagnostic model analysis of Northeast Gulf of Alaska current patterns subject to the caveats that (1) only time scales in excess of what are needed for quasi-geostrophic assumptions are considered, (2) shelf waves are not represented, (3) baroclinic shears may not be correct in detail beyond a few weeks of the time they were observed, and (4) within the immediate vicinity of the shoreline additional side wall boundary layers may contribute significant components to the flow.

3.2 Model Decomposition

In this section the linear decomposition of the diagnostic model equations will be briefly reviewed, and the relationship of these component flows to the input data and assumptions will be outlined. A more detailed description of the linear aspects of model formulation and the rationale for this partitioning are presented by Galt and Watabayashi (1978).

The basic governing equation for the diagnostic model describes the dependent variable, the surface elevation as follows:

$$N_2 \nabla^2 \xi - J(\xi, d) + N_1 N_2 \nabla^2 \alpha - N_1 J(\alpha, d) - k \cdot \nabla x \tau = 0 \quad (3-1)$$

where

ξ = surface elevation

d = depth

α = the integral of the density from the bottom to the surface

$k \cdot \nabla \times \tau$ = curl of the surface wind stress

N_1 = stratification parameter

N_2 = bottom friction parameter

All of the terms in this vorticity equation are scaled and nondimensional. The first term represents the vorticity stretching caused by the barotropic mode, (depth independent) flow created by pressure forces related to variations in the sea surface elevation driving a bottom Ekman layer. The second term represents the interaction of the barotropic flow with the bottom and describes the vorticity stretching caused by the flow crossing isobaths. The third term represents vorticity stretching of the baroclinic mode evaluated at the bottom (flow created by the pressure forces related to the internal mass distribution) driving a bottom Ekman layer. The fourth term represents the vorticity induced by the joint baroclinic and bathymetric interaction and is seen to relate to the stretching caused by the baroclinic component of the flow crossing isobaths. The last term is the curl of the wind stress, or the vorticity added by the wind.

To solve this equation it may be noted that the system is linear, so that a decomposition is possible. Doing this, the following two problems can be considered:

$$N_2 \nabla^2 \xi_1 - J(\xi, d) - k \cdot \nabla \times \tau = 0 \quad (3-2)$$

and

$$N_2 \nabla^2 \xi_2 - J(\xi_2, d) + (N_1 N_2 \nabla^2 \alpha - N_1 J(\alpha, d)) = 0 \quad (3-3)$$

The total solution is just the sum of these two component solutions,
i.e.

$$\xi = \xi_1 + \xi_2 \quad (3-4)$$

The problem defined by the first of these equations will be referred to as the wind set-up component. The problem defined by the second equation will be referred to as the density driven component.

Turning first to the wind set-up component of the flow, it is necessary to define appropriate boundary conditions and to apply the finite element solution technique described by Watabayashi and Galt (1978). To develop these boundary conditions for the NEGOA area a number of assumptions is made.

As a point of departure the curl of the wind stress will be considered negligible for the region. This is done for two reasons, first, that the actual data available on regional wind stress curl on this scale is practically nil (Bakun, 1973), and second, that the direct local set-up of the cross shelf sea surface slope by along-shore winds is the dominant wind forcing. To parameterize the relationship between the wind and the cross shelf component of the sea surface slope, a bathystrophic balance will be hypothesized. This assumes that the along-shore component of the wind stress is locally balanced by the along-shore component of the water stress, and that the normal component of the sea surface gradient is in geostrophic balance with the along-shore current. For the linear stress law hypothesized by the Ekman dynamics this is represented by

$$\frac{\partial \xi}{\partial n} = c(w)^2 \cos(\theta_s) , \quad (3-5)$$

i.e., the sea surface slope normal to the coast is proportional to the square of the wind speed times the cosine of the angle between the wind and the coastline.

With this suggested balance it now remains to specify how this relationship is to be applied as boundary conditions. We know that the sea surface slope imposed at the boundary does not extend seaward indefinitely, but is confined to the shelf area. As a first approximation it will be assumed that the forced component of the slope is uniform for a band extending from the coast to the vicinity of the shelf break. Along the coast line a zero transport normal to the coast is imposed and along any open cross shelf boundaries the differential equation is applied right up to the boundary without additional constraints (the so called finite element method natural boundary conditions). For a more detailed discussion refer to Galt and Watabayashi (1978). Thus the wind set-up forcing is envisioned as a simple linear profile where the sea surface is undisturbed in deep water, but slopes up or down uniformly across the shelf (with the slope proportional to the along-shore wind speed squared), as if hinged at the shelf break. Such a response has been suggested for other areas in the past (Beardsley and Butman, 1974). In specific studies of the NEGOA area, Hayes (1979) suggested that such a linear cross shelf hinge profile accounts for a major segment of the variance observed in the bottom pressure measurements.

The question of where to apply this hinge profile to drive the wind set-up response of the model requires careful thought. Obviously the wind acts as a continuum along the coast line, and at any coastal boundary point we could impose a uniform slope through a line of stations leading away from the shore. Solving the model with this single imposed hinge profile will give the regional response to this type forcing. To combine a number of these is straightforward, since it is possible to consider any single hinge profile as the Green's function response to an imposed

bathystrophic profile at that point.

For example, suppose that

$$R(x, y, S_0)$$

is the model response to a unit amplitude hinge imposed on the coastline at point S_0 , and that

$$W(S)$$

is the distribution of alongshore wind specified along the coastline, with S being simply distance along the coast. Then the total wind set-up response will be the superposition

$$\xi_1(x, y) = \int_{\text{coast}} C R(x, y, S) W(s) \cos(\theta_s) ds \quad (3-6)$$

For the present NEGOA study the numerical approximation to this integral formulation will be made with six simple hinge modes, each of which is seen to influence specific segments of the shelf domain.

It should be pointed out that the Green's function formulation outlined here does not result in a composite pattern that has a uniform cross shelf profile everywhere. Instead each cross shelf profile is influenced by its neighbors, taking into account alongshore variations in the wind, bathymetry, and model dynamics.

A final point to consider with the wind set-up response is that alternate strategies are possible for determining the relative hinge weights in the composite patterns. For example, if sea surface elevations were available at n locations along the coast, the Green's function integral could easily be inverted to solve for the coefficients associated with n independent hinge modes, whose composite would satisfy the observed coastal distribution, consistent with the model dynamics.

It is now possible to consider the second partition of the diagnostic mode, the density driven response. This is represented by equation (3-3). In this equation it can be seen that the density distribution acts as forcing through two terms: the baroclinic bottom Ekman layer, and the joint baroclinic - bathymetric interaction. Both of these can be seen to induce vorticity to the barotropic flow either through cross isobath flow or through stretching of the water column. This ξ_2 component of the sea surface displacement (barotropic mode) can be thought of as required by the fact that any given density driven flow will in general result in some stretching of the water column through these bottom interactions. In the presence of this stretching some barotropic adjustment is required to satisfy model dynamic constraints, even in the absence of wind set-up or forcing.

An examination of equation (3-3) shows that

$$\xi_2 + N_1 \alpha^* = \text{constant} \quad (3-8)$$

is a solution for the interior of the domain, where α^* is the pressure deviation defined for any region as

$$\alpha(x, y, z) = \alpha'(z) + \alpha^*(x, y)$$

The solution given by (3-8) has a number of characteristics of interest. Galt and Watabayashi (1978) have shown that this solution corresponds to a minimum potential energy of the sea surface distribution ξ_2 that is consistent with the model dynamics over an extended open shelf domain. This minimum barotropic mode forced by the density field has the physical significance that for an unforced region, with a fixed density distribution, one would expect the sea surface to relax, or set-down, as much as possible,

consistent with the dynamic vorticity constraints. It can also be seen that (3-8) yields a solution which gives a terrain following level of no motion because the baroclinic and barotropic flow just cancel out at the bottom over the entire domain. This then is a natural extension of the level of no motion concepts that are routinely applied in deep water off of the shelf. Thus the minimum potential energy barotropic mode can also be seen to represent the minimum bathymetric interaction mode. It should also be noted that (3-8) is the only possible inviscid solution to equation (3-3), and that as such it is the only possible unforced, steady state solution that could be expected.

For the NEGOA region we expect a number of patterns which are linear superpositions of the following responses: (1) wind set-up responses, which are determined by the wind pattern only (and thus are independent of the density distribution and are valid for all seasons), and (2) density driven responses (one response for each density distribution), which yield a minimum barotropic mode.

3.3 Wind Set-up Response Patterns

The wind set-up response for the NEGOA area will be given by the solution to equation (3-2). This will be composed of a number of hinge modes. Each of these will assume a bathystrophic balance over a single across shelf profile. The coastal boundary will be subject to a no net transport condition, and off shore in deep water the surface elevation remains unperturbed. A high resolution grid with approximately two hundred vertices covers the shelf region between Yakutat and Seward (figure 3-2) giving increased resolution of the complex bathymetric features. Within the area of particular interest between Yakutat and Montague Island six individual hinge modes are investigated (figure 3-2). These have been

TRIANGULAR MESH FOR DIAGNOSTIC MODEL

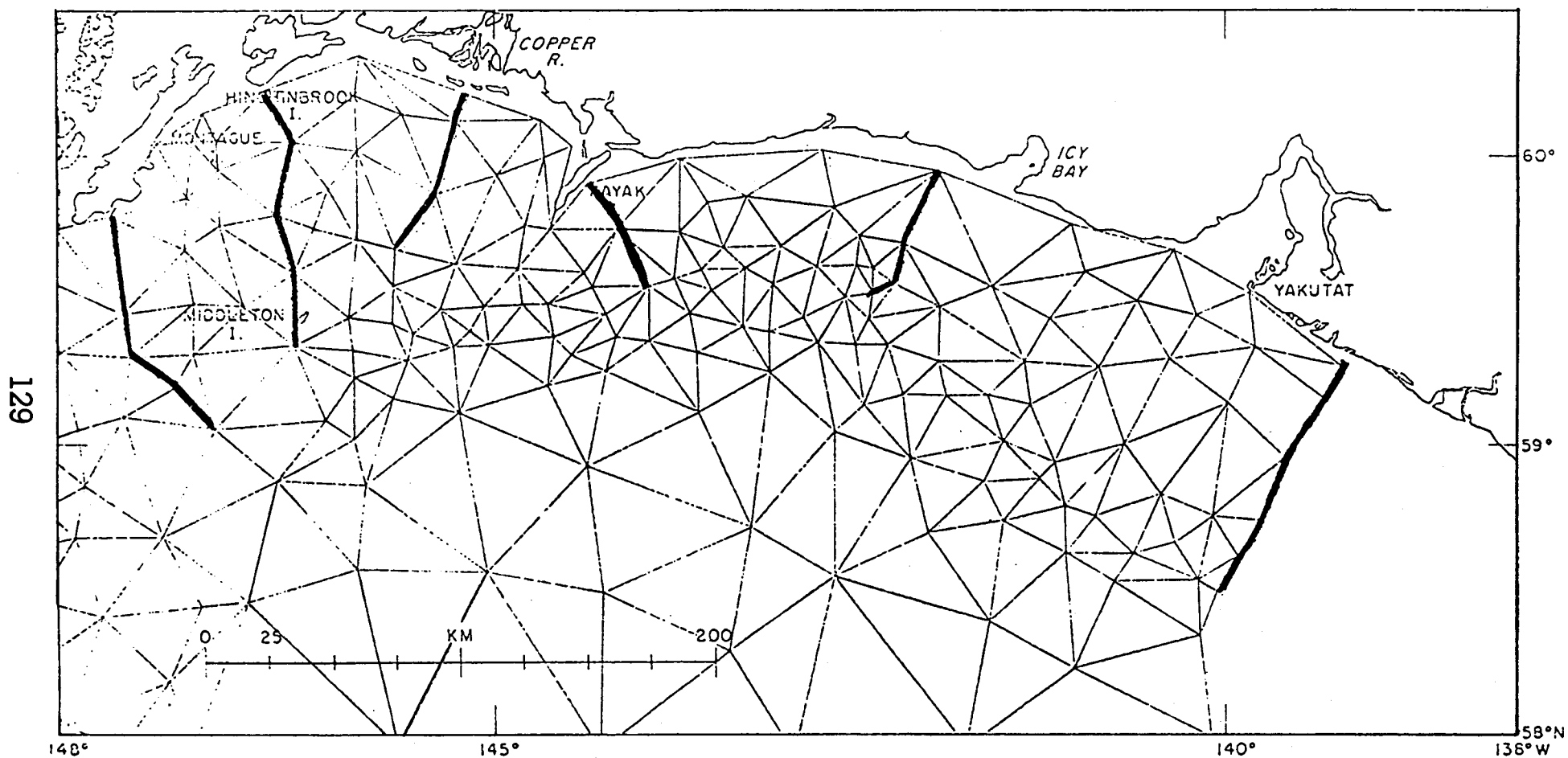


Figure 3-2. Triangle mesh used for Northeast Gulf of Alaska wind set-up study. Heavy lines represent positions of bathymorphically balanced hinge modes.

chosen in such a way as to obtain a fundamental set that cover the domain. They are not unique and alternate choices are certainly possible. Nonetheless, these suitably cover the region of interest and do not show excessive overlap, so each can be considered to represent the local influence of coastal winds. Actual scale analysis and the rationale for choosing various hinge configurations are discussed in Galt and Watabayashi (1978). The six hinge response modes for the area of interest are shown in figures (3-3) through (3-8). These six patterns give the independent degrees of freedom that comprise the wind set-up for this section of shelf. The magnitudes associated with these patterns are arbitrary; only the relative spacial distributions associated with the set-up hinges are shown. The vector arrows in these figures have been transformed from the finite element triangular domain onto a regular cartesian grid for ease in interpretation and in subsequent computer library storage.

For any particular distribution of surface winds the six basic hinge modes described above are combined to give the composite wind set-up corresponding to that wind pattern distribution. The basic wind patterns that will be considered are those that have been obtained from the NEGOA meteorological analysis carried out by Overland and Hiester (1978). Their research, based on climate typing techniques and local analysis, has identified six dominant weather types, with a total of thirteen patterns including sub-types.

For each of these patterns the relative weight factors for the various hinges are obtained from the square of the wind (scaled to the value at Middleton Island, since the wind patterns are also arbitrary) at each hinge point times the cosine of the angle between the local wind vector and the coastline. In evaluating these relative weighting factors, the

BAROTROPIC HINGE 1

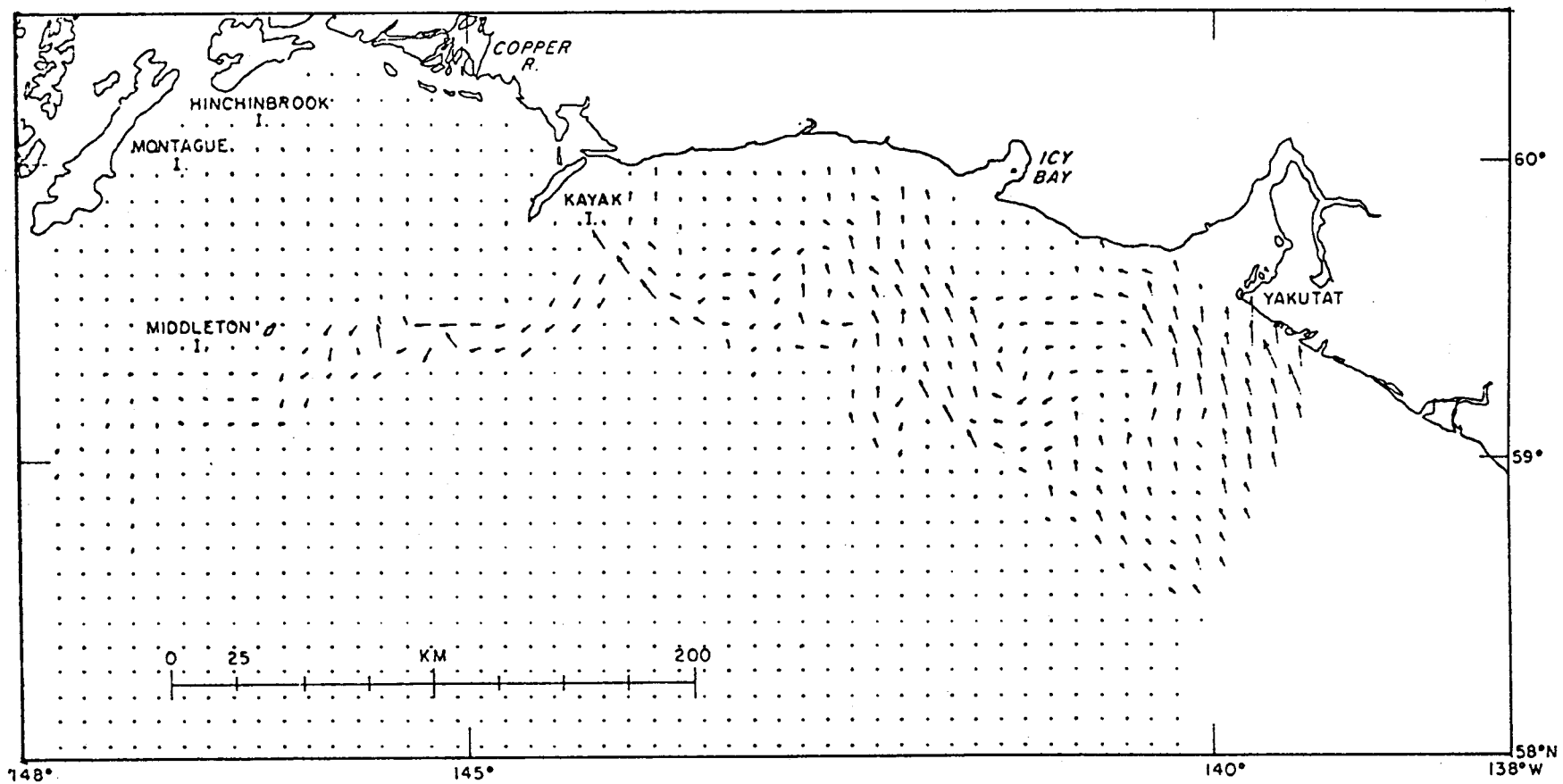
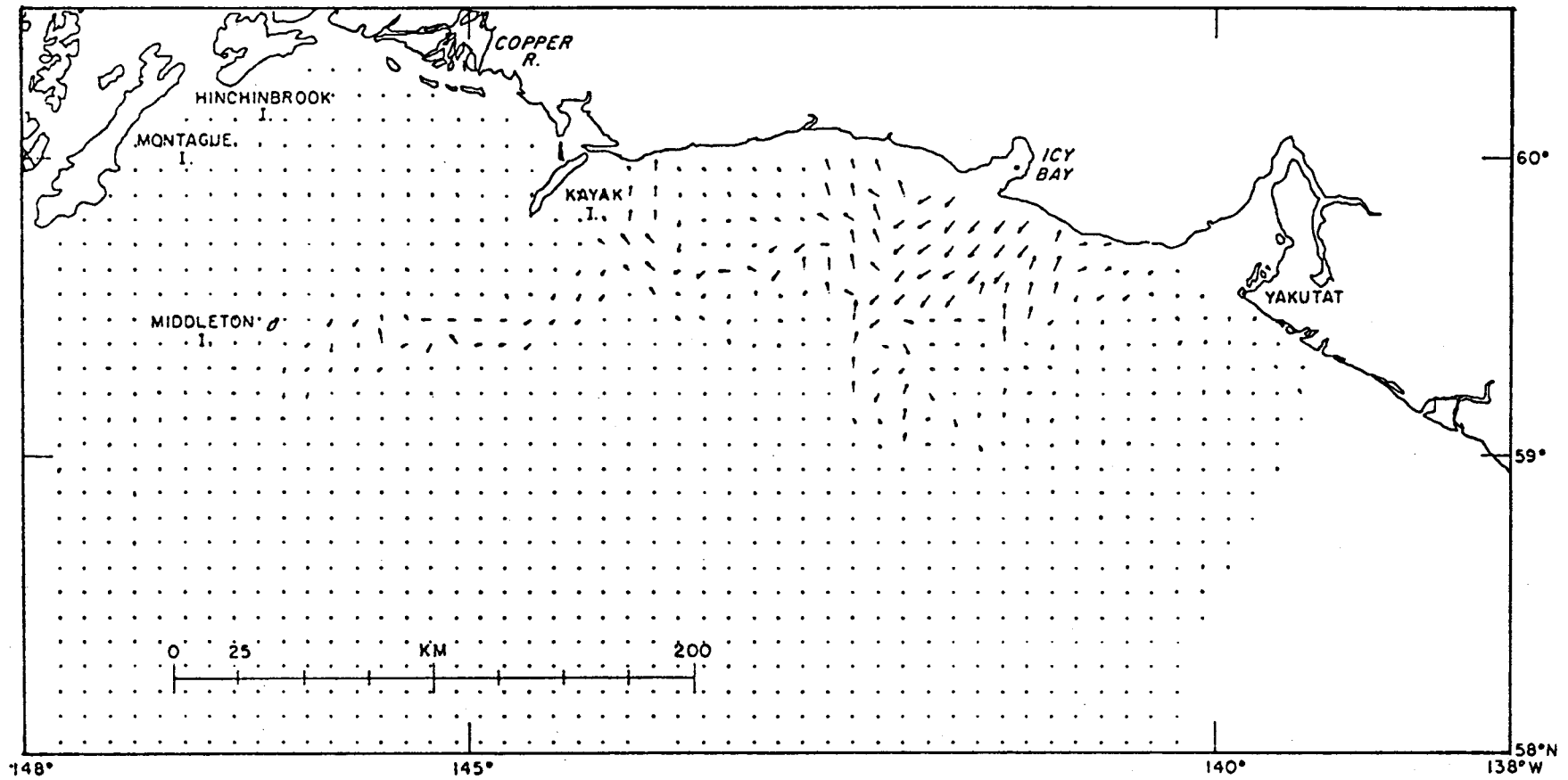


Figure 3-3. Bathystrophic wind set-up, or hinge mode one (Yakutat).

BAROTROPIC HINGE 2



132

Figure 3-4. Bathystrophic wind set-up, or hinge mode two (Icy Bay).

BAROTROPIC HINGE 3

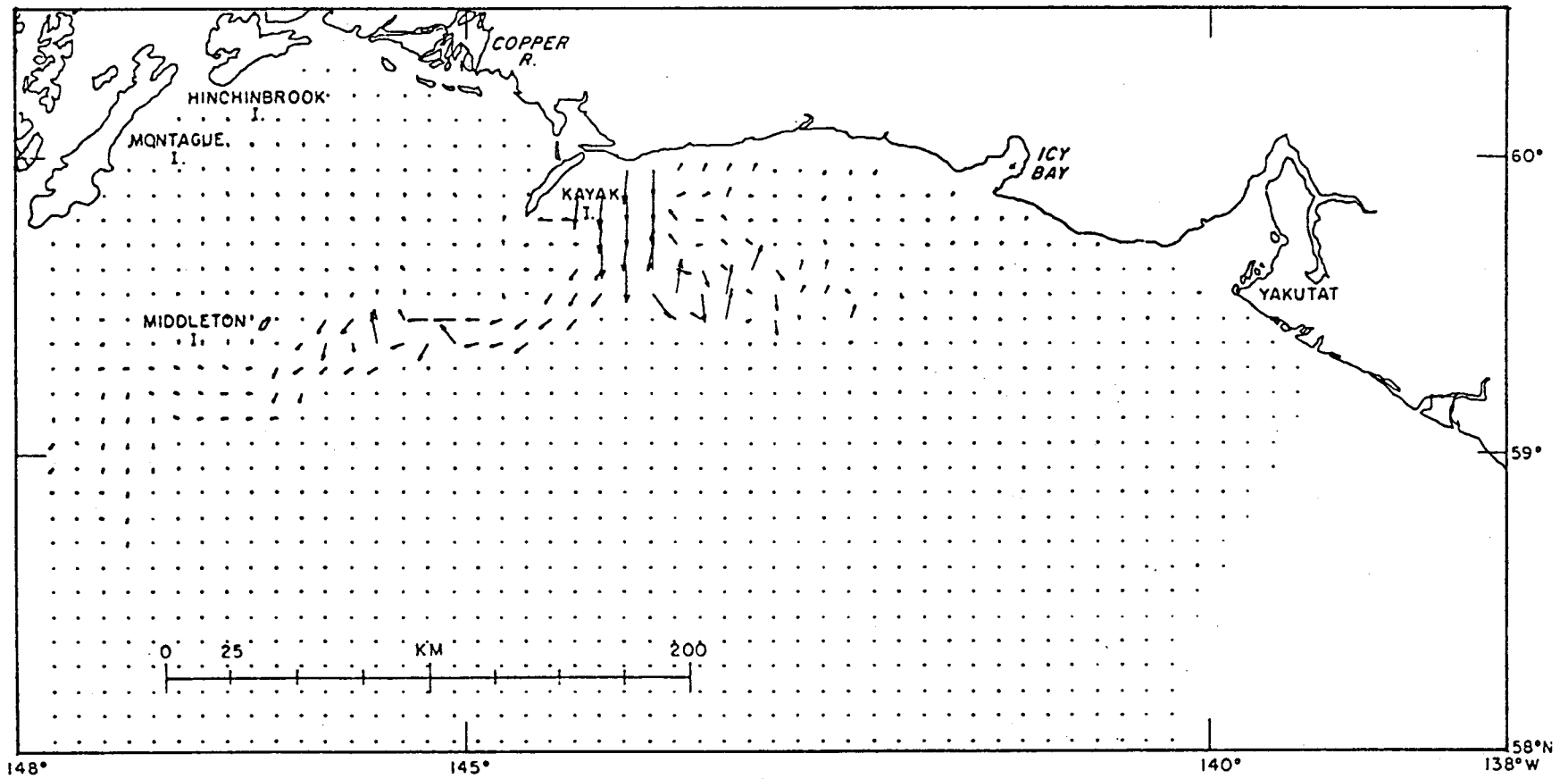
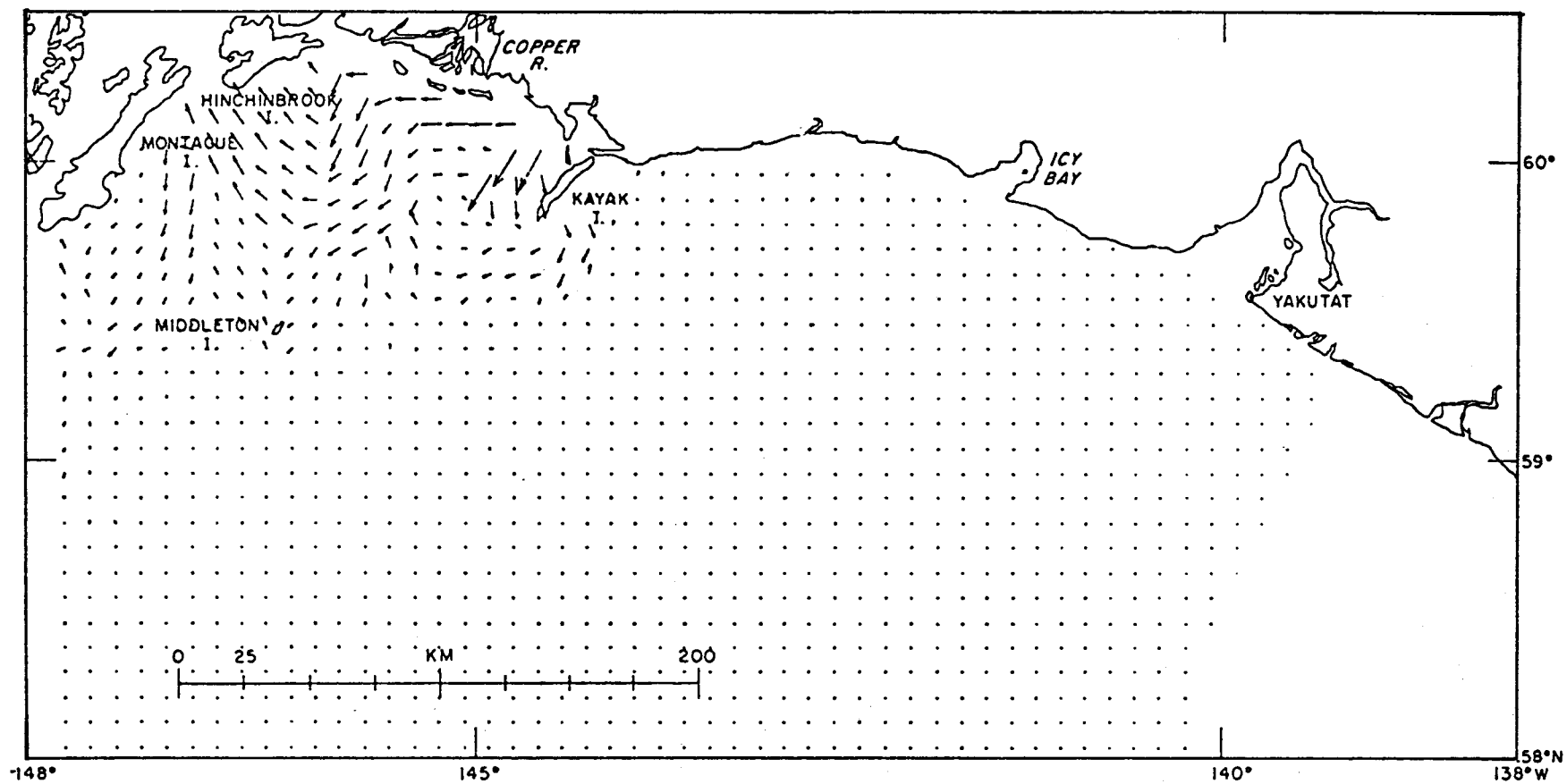


Figure 3-5. Bathystrophic wind set-up, or hinge mode three (Kayak Island).

BAROTROPIC HINGE 4



134

Figure 3-6. Bathystrophic wind set-up, or hinge mode four (Copper River).

BAROTROPIC HINGE 5

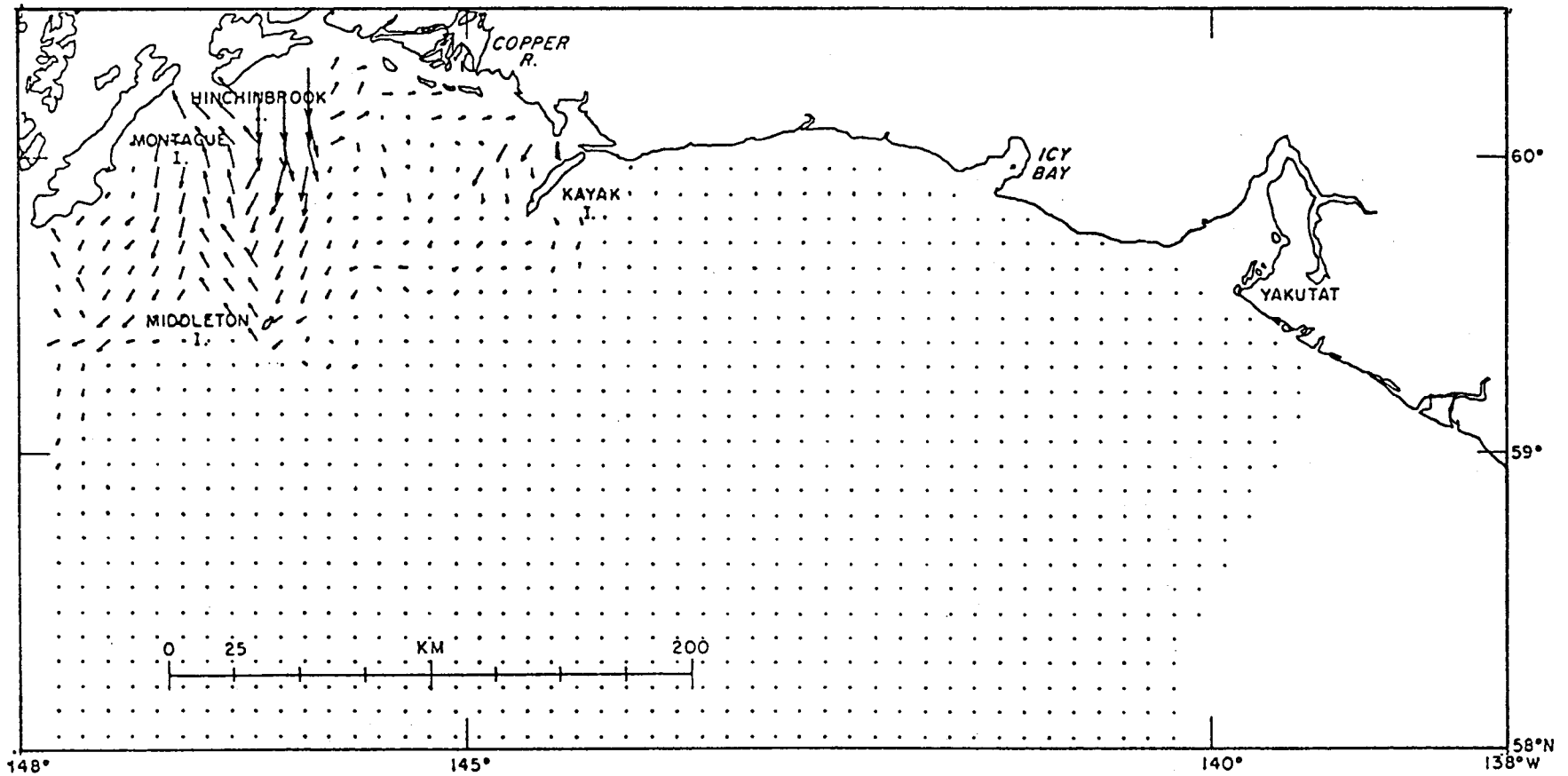
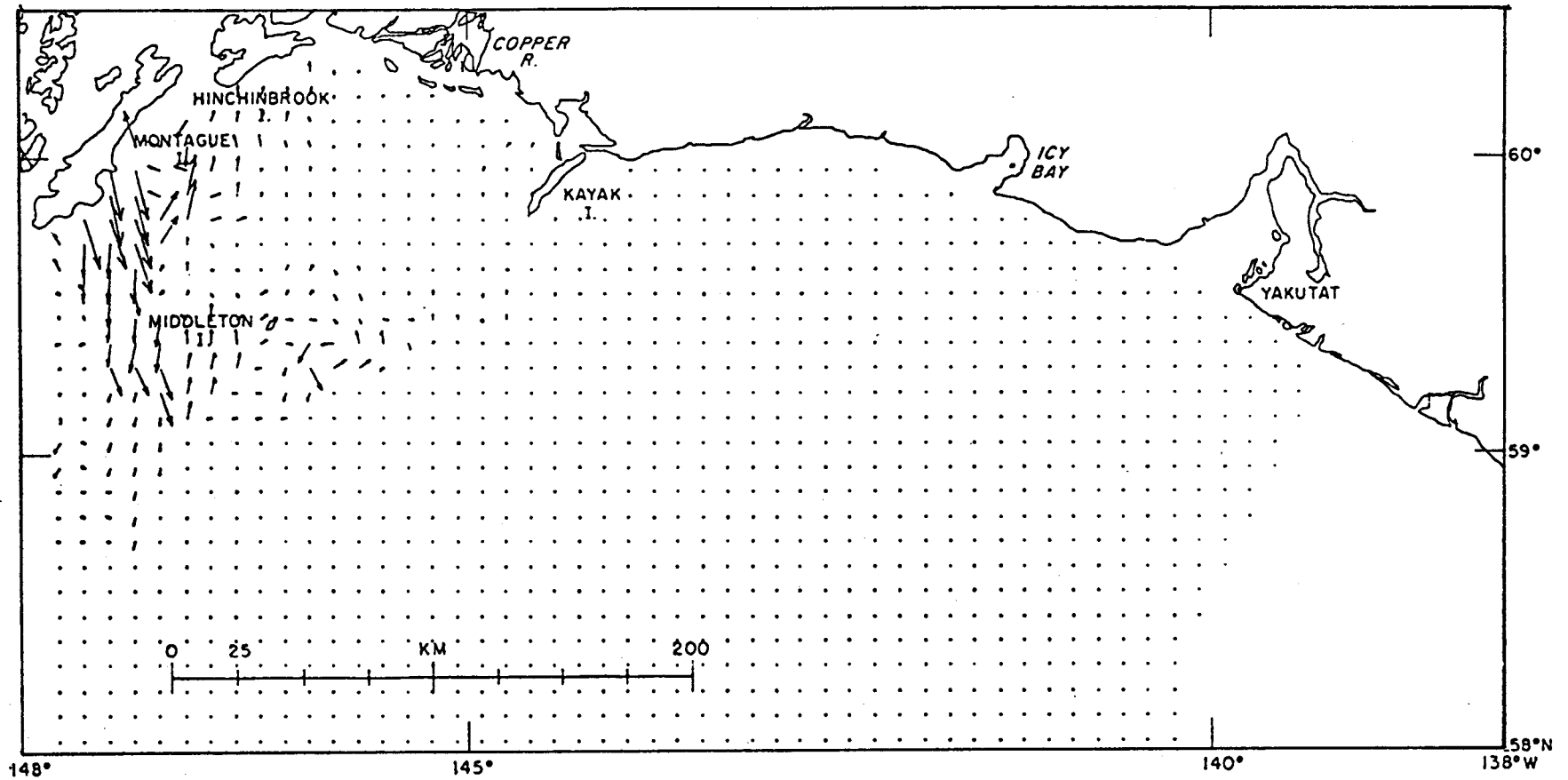


Figure 3-7. Bathystrophic wind set-up, or hinge mode five (Hinchinbrook Island)

BAROTROPIC HINGE 6



136

Figure 3-8. Bathystrophic wind set-up, or hinge mode six (Montague Island).

vector winds were averaged over the inner shelf region of individual hinges, in order to get winds which were more representative than the actual coastal value. Table 3-1 gives the relative weighting factors for the thirteen patterns described by Overland and Hiester (1978).

The coefficients from Table 3-1 are used to form linear combinations of the basic patterns for each of the wind patterns. The resulting current patterns are shown in figures (3-9) through (3-21). Once again the magnitudes of these current patterns are arbitrary, with the vector arrows only giving relative pattern information. Assuming that the bathystrophic assumptions are correct, the magnitudes for the currents associated with these patterns should be scaled as proportional to the square of the wind speed at Middleton Island.

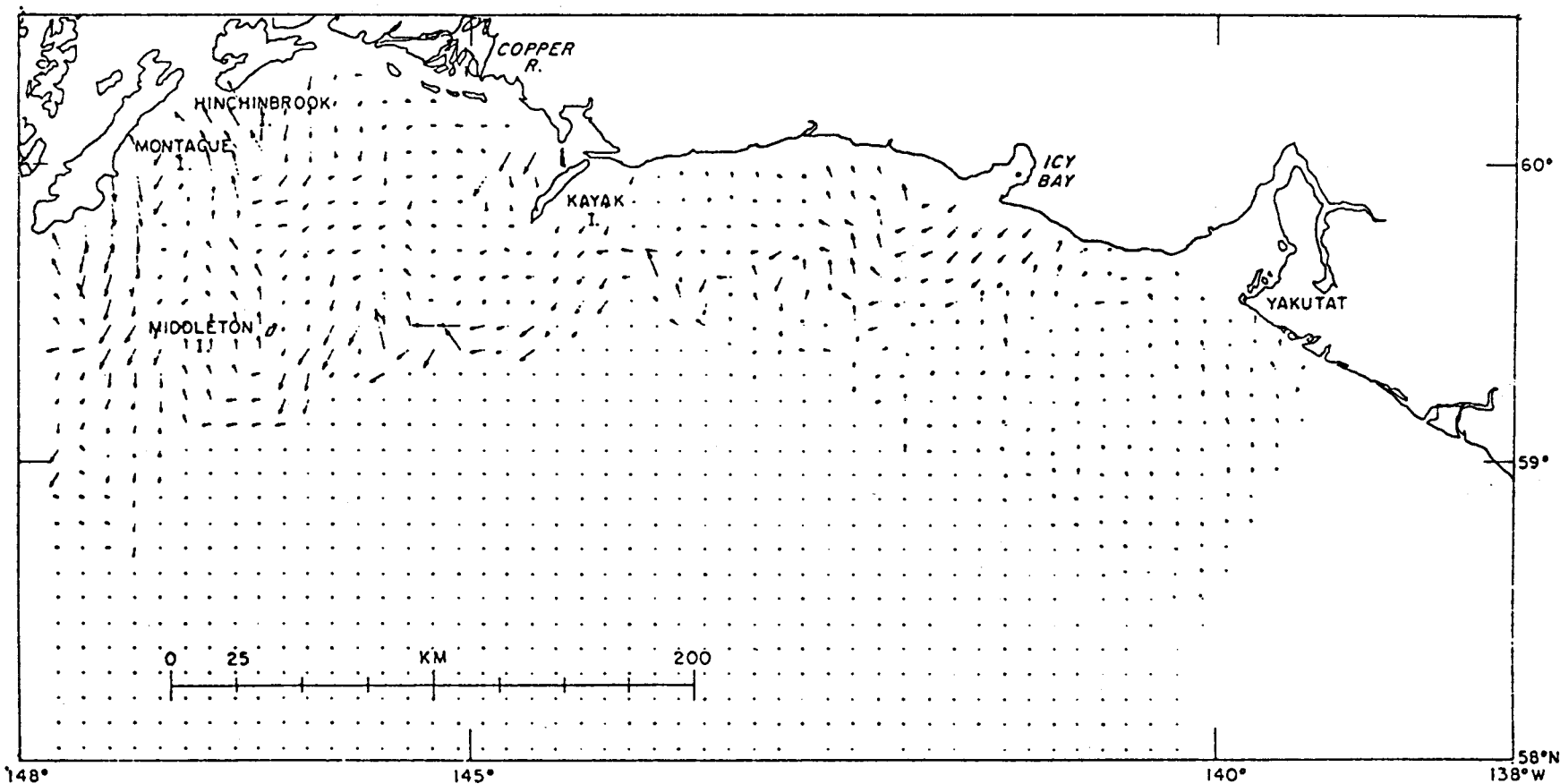
The first four current patterns, figures (3-9) through (3-12), correspond to weather patterns dominated by low pressure systems situated in the Gulf of Alaska. The first of these (wind pattern 1.0) can be thought of as the prototype. The currents are seen to move generally east to west across the shelf. The effects of bathymetric influence on the currents are evident. The deep segment of the shelf off of Yakutat shows reduced current magnitudes with the general tendency for the flow to follow isobaths. The complex topography on the shelf to the west of Icy Bay also is clearly reflected in the current directions. The general tendency for enhanced flow along the shelf break is also clear. The large submarine canyon that cuts across the shelf break east of Middleton Island causes a meander in the shelf break flow with the potential for the formation of an eddy associated with this topographic feature. Other regions of enhanced flow are seen in the lee of Kayak Island and are associated with the sea valley leading into Prince William Sound between Hinchinbrook and Montague Island. The second wind pattern (1.1)

TABLE 3-1

RELATIVE AMPLITUDES FOR THE FUNDAMENTAL HINGE MODES CORRESPONDING TO THE
WIND PATTERNS DESCRIBED BY OVERLAND AND HIESTER (1978)

Wind Pattern	Hinge Coefficients					
	1	2	3	4	5	6
1.0	.77	1.73	.76	.74	.88	.93
1.1	.78	1.27	.42	1.00	.59	.94
1.2	.63	.24	.55	.13	.29	.55
1.3	.43	.69	.41	.67	.73	.60
2.0	.55	.94	.91	.81	.64	.71
2.1	.65	.39	.64	-.20	.39	.42
3.0	.74	.66	1.15	.77	.79	.80
3.1	.50	2.05	1.59	.39	.79	.79
4.0	-.05	-.51	-.55	-.27	-.75	-.80
4.1	-.67	-1.07	.41	.89	.22	.19
5.0	-.97	-.80	-.77	-.50	-.94	-.85
5.1	-1.28	-.98	-.49	-.70	-.92	-.65
6.0	.24	.31	.60	.28	.64	.77

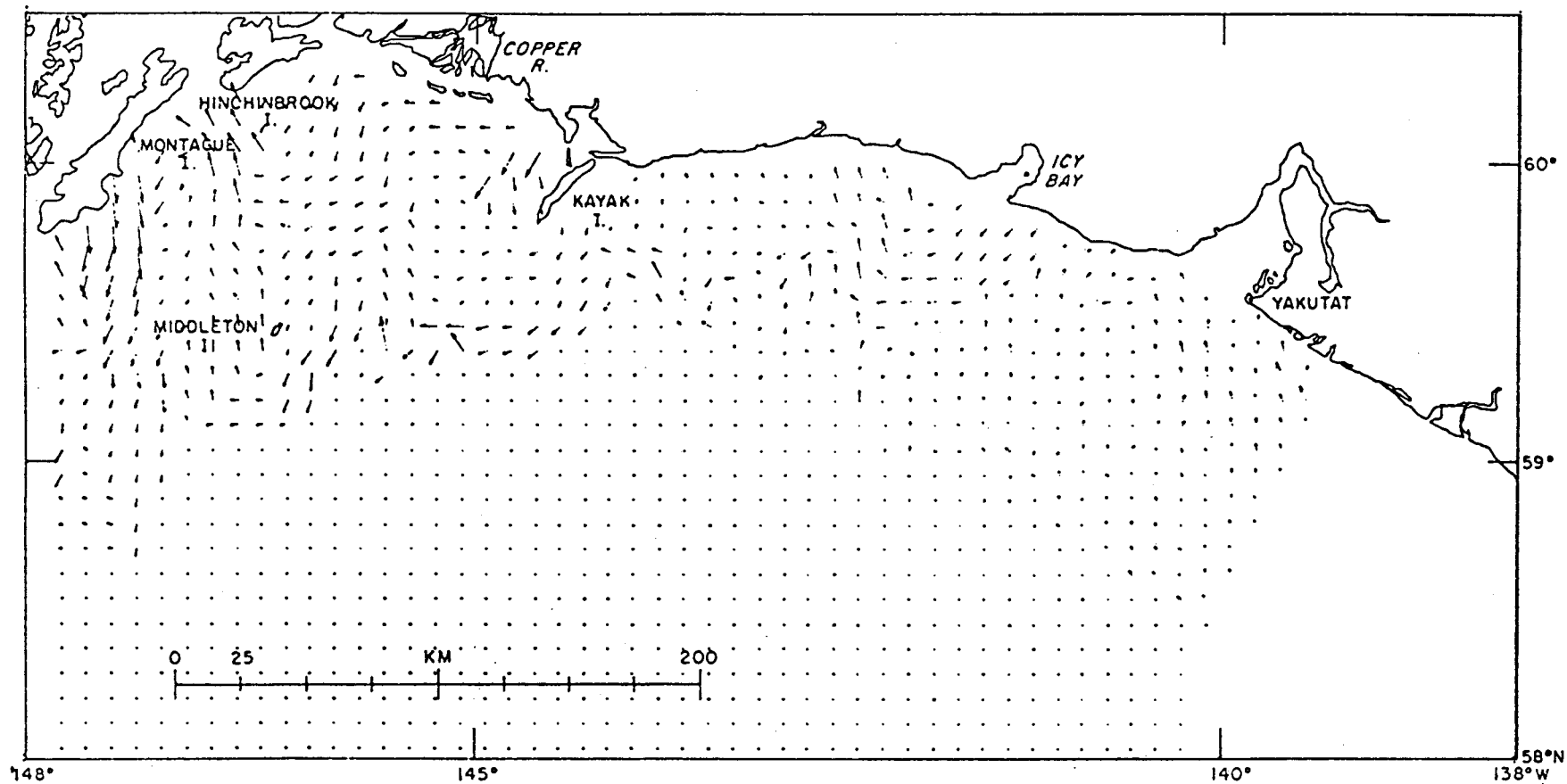
BAROTROPIC CURRENT RESPONSE TO WIND PATTERN 1.0



139

Figure 3-9. Composite wind set-up response for Northeast Gulf of Alaska weather type 1.0.

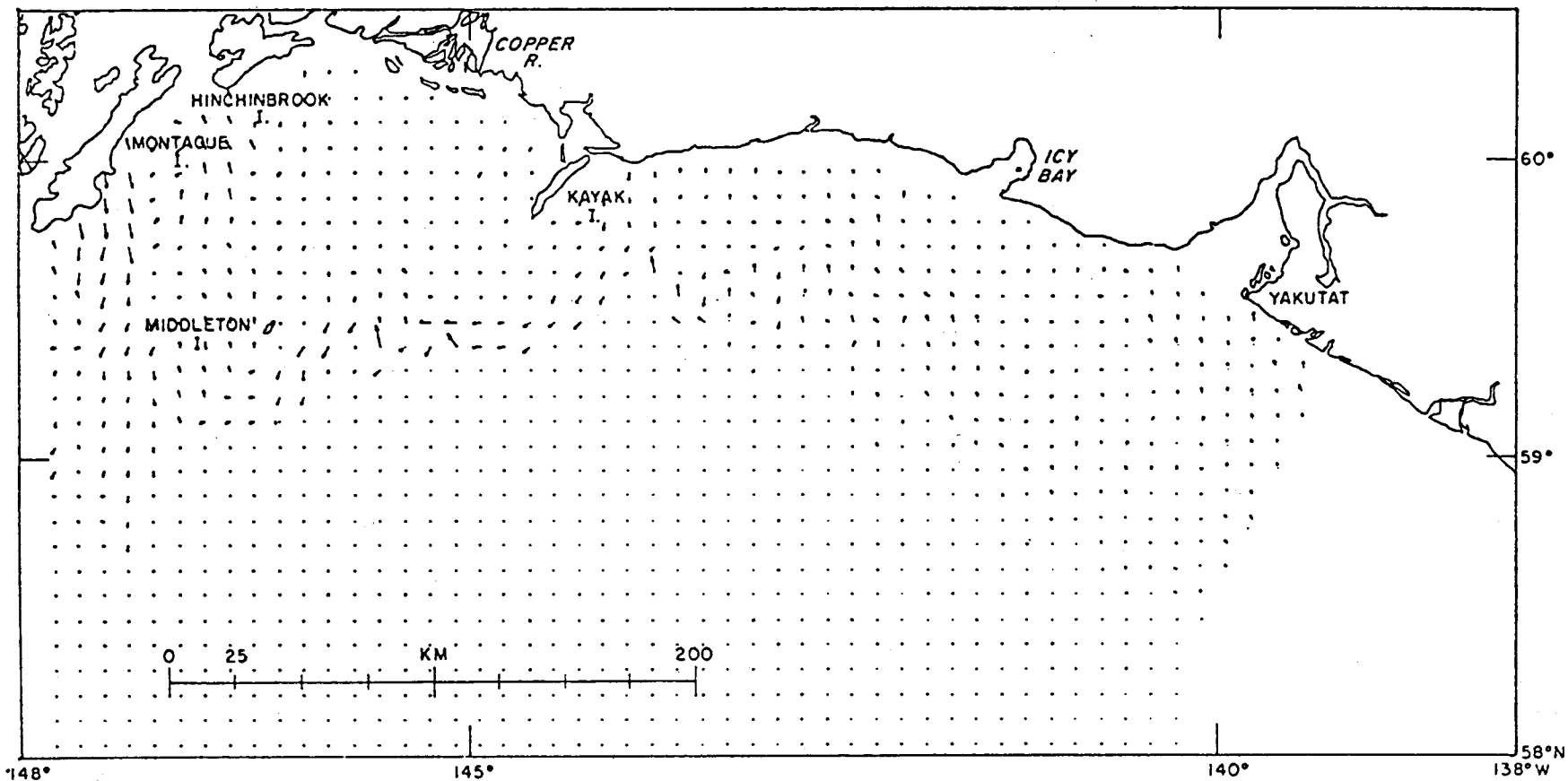
BAROTROPIC CURRENT RESPONSE TO WIND PATTERN 1.1



140

Figure 3.10. Composite wind set-up response for Northeast Gulf of Alaska weather type 1.1.

BAROTROPIC CURRENT RESPONSE TO WIND PATTERN 1.2



141

Figure 3-11. Composite wind set-up response for Northeast Gulf of Alaska weather type 1.2.

BAROTROPIC CURRENT RESPONSE TO WIND PATTERN 1.3

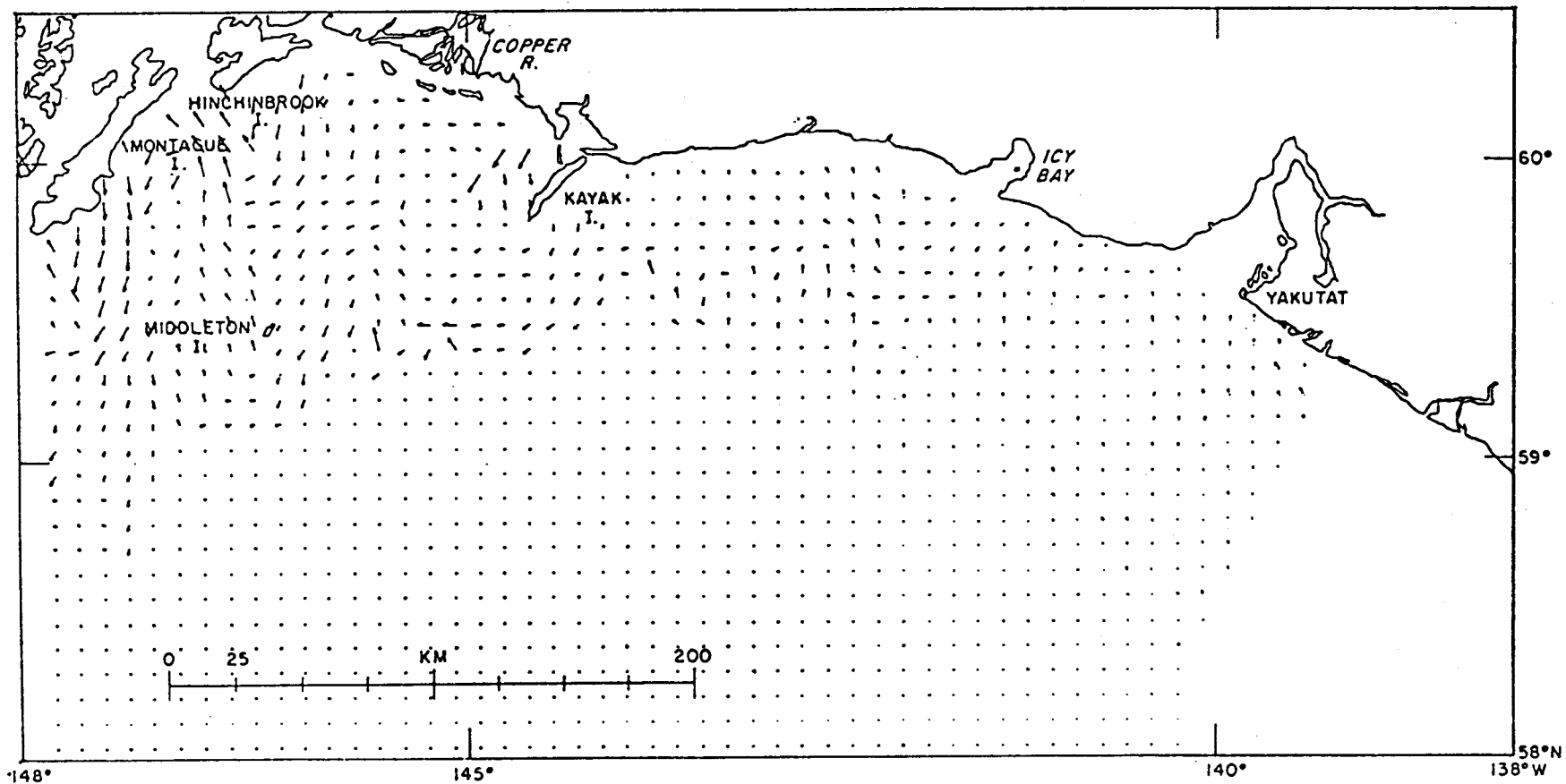
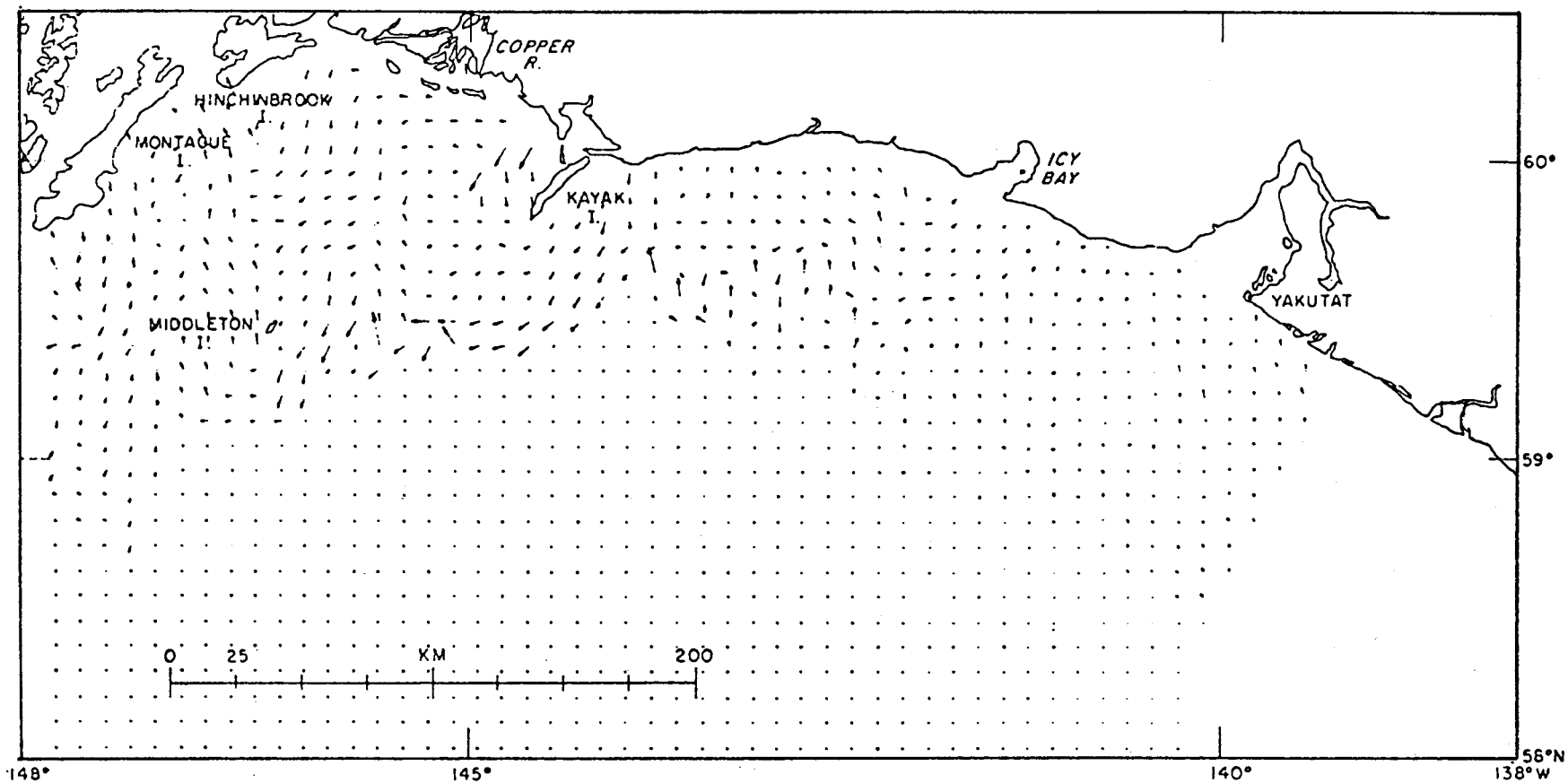


Figure 3-12. Composite wind set-up response for Northeast Gulf of Alaska weather type 1.3.

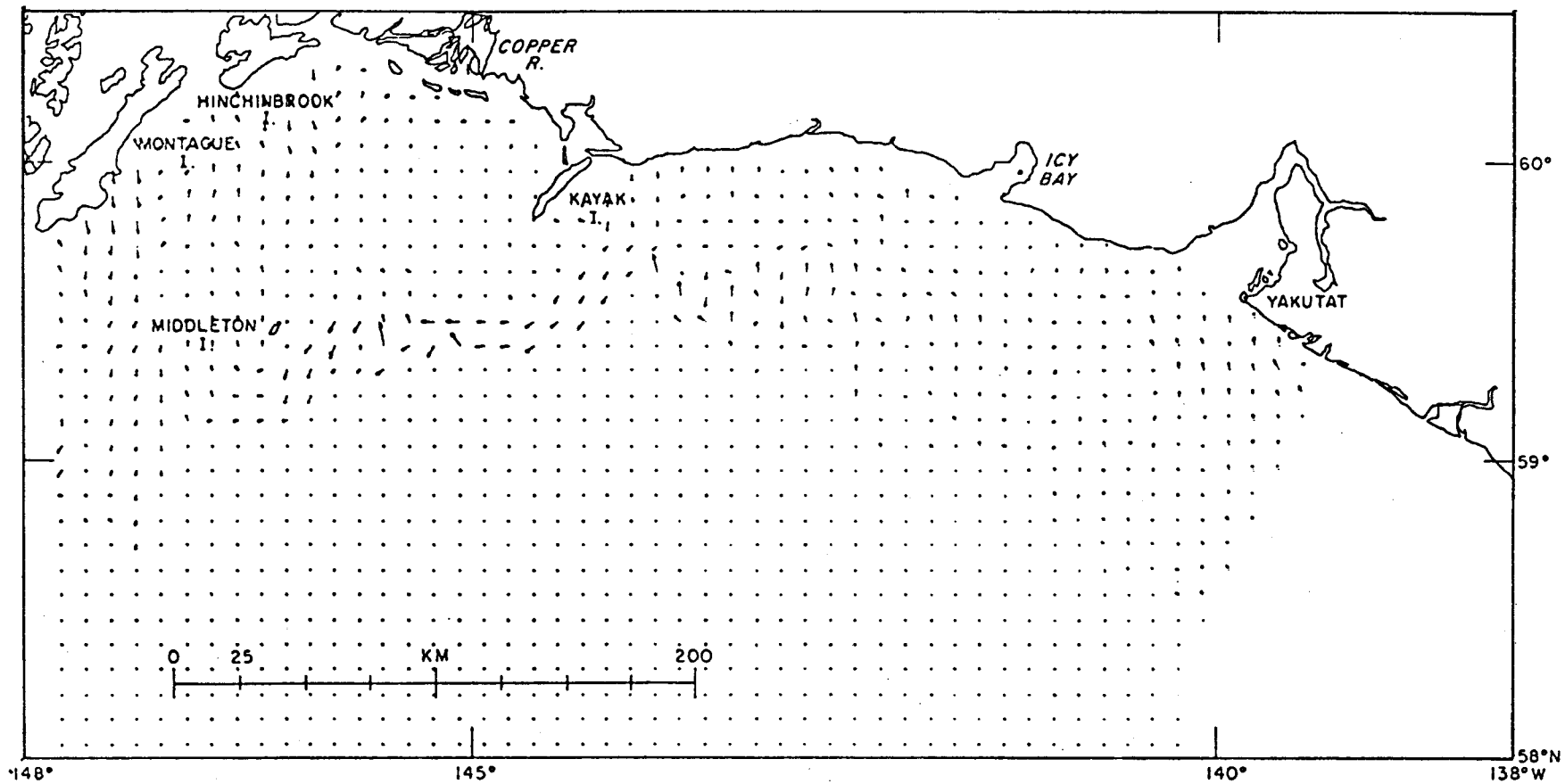
BAROTROPIC CURRENT RESPONSE TO WIND PATTERN 2.0



143

Figure 3-13. Composite wind set-up response for Northeast Gulf of Alaska weather type 2.0.

BAROTROPIC CURRENT RESPONSE TO WIND PATTERN 2.1



144

Figure 3-14. Composite wind set-up response for Northeast Gulf of Alaska weather type 2.1.

BAROTROPIC CURRENT RESPONSE TO WIND PATTERN 3.0

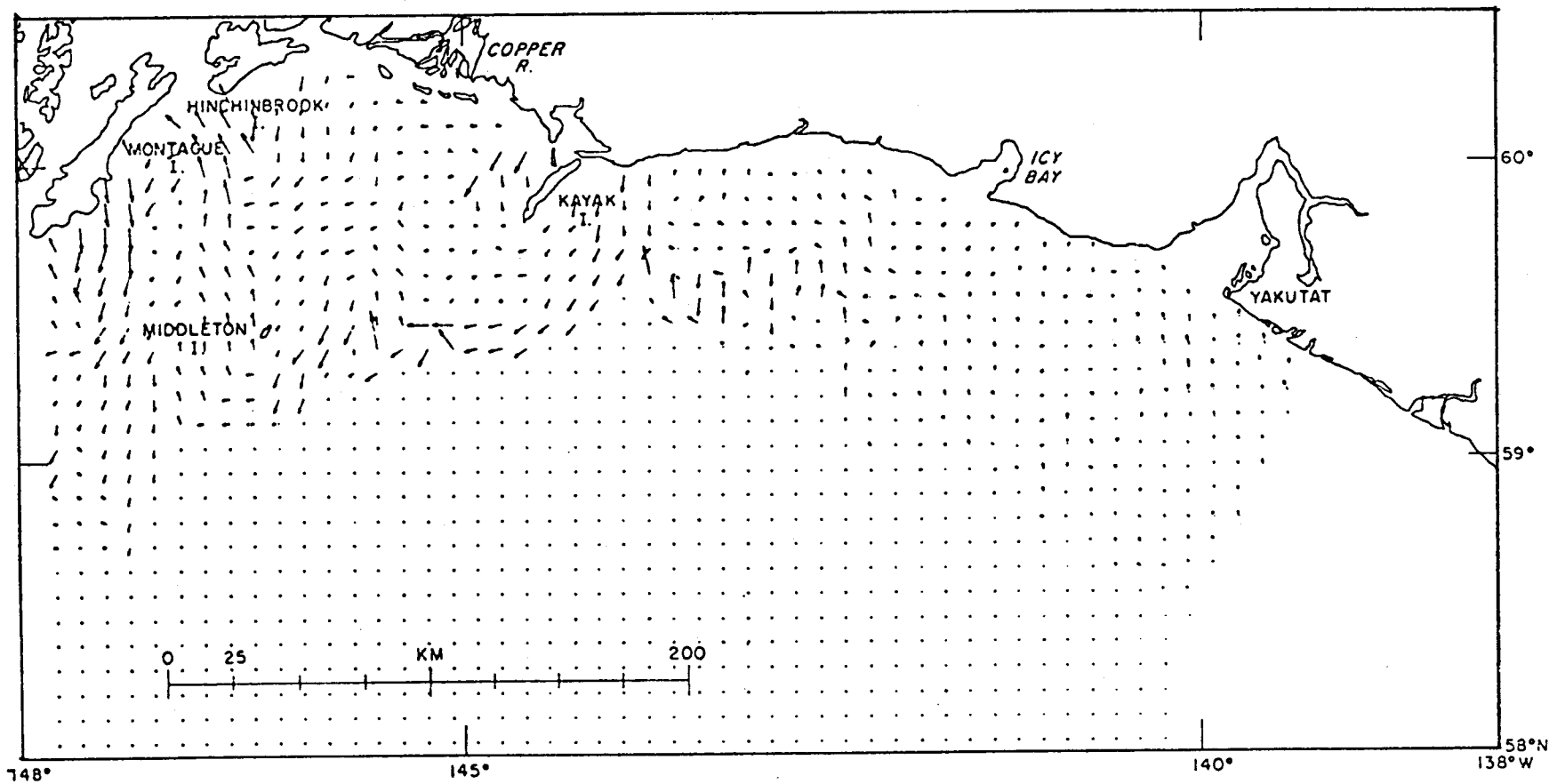


Figure 3-15. Composite wind set-up response for Northeast Gulf of Alaska weather type 3.0.

BAROTROPIC CURRENT RESPONSE TO WIND PATTERN 3.1

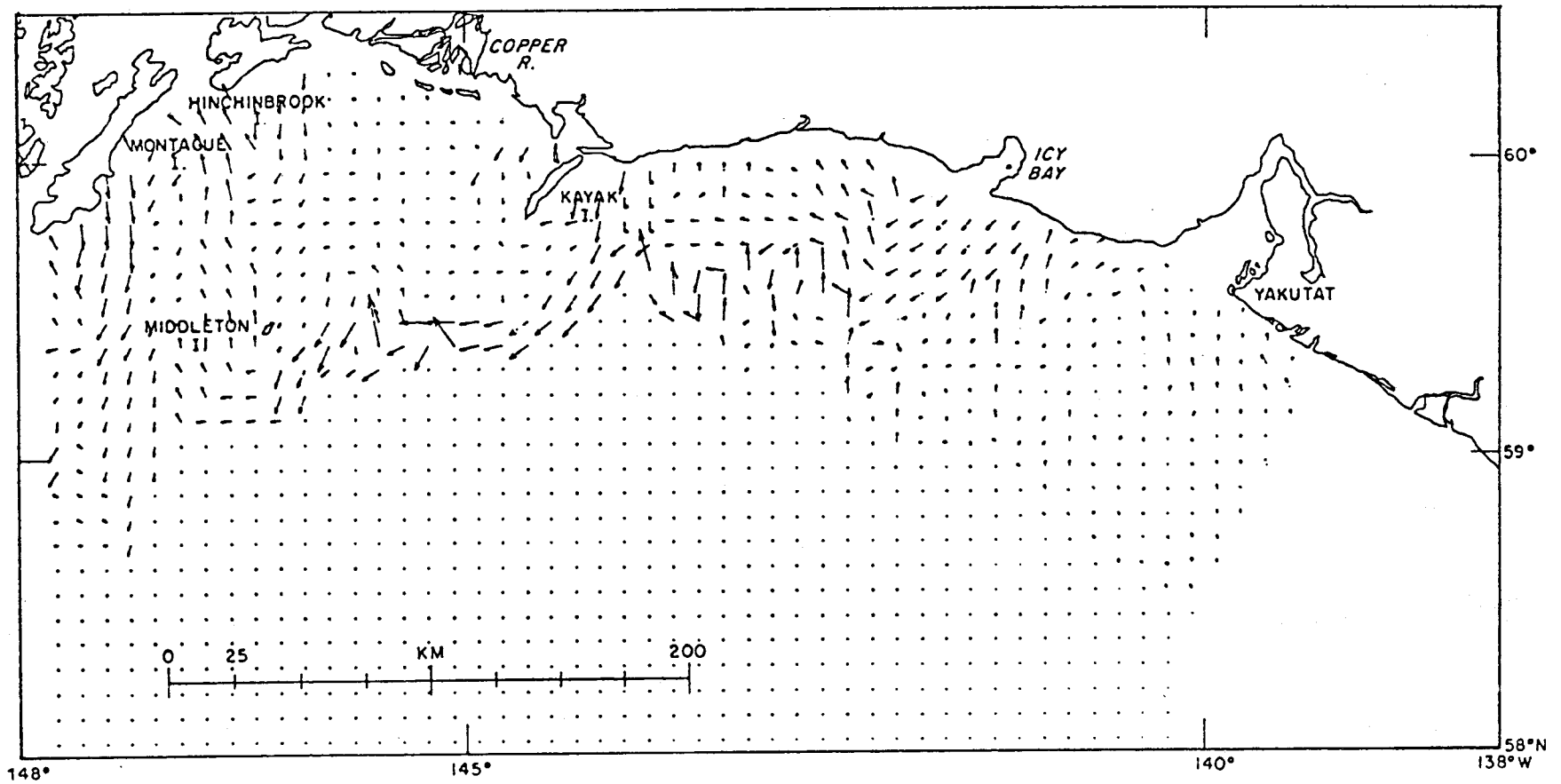
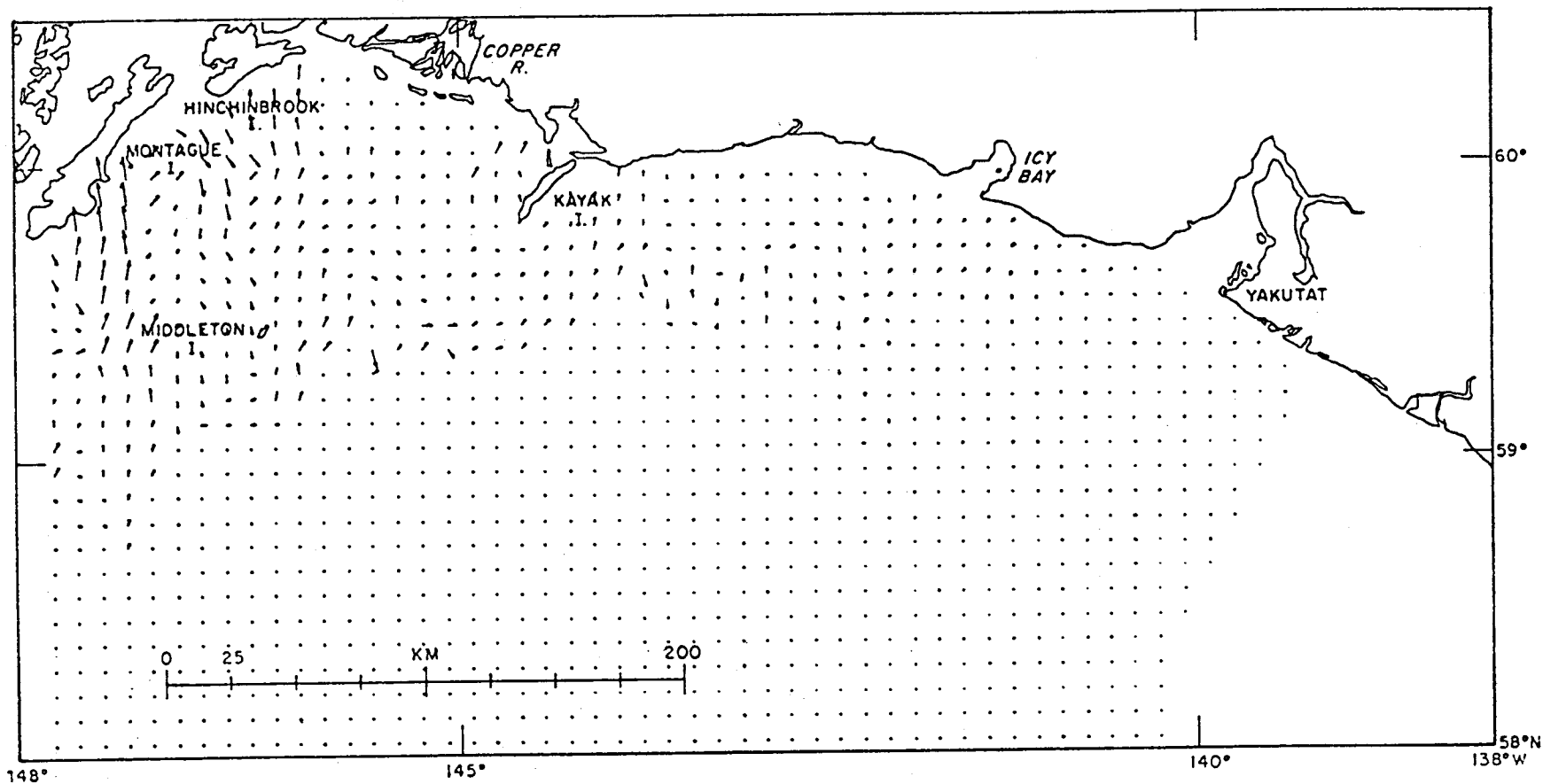


Figure 3-16. Composite wind set-up response for Northeast Gulf of Alaska weather type 3.1.

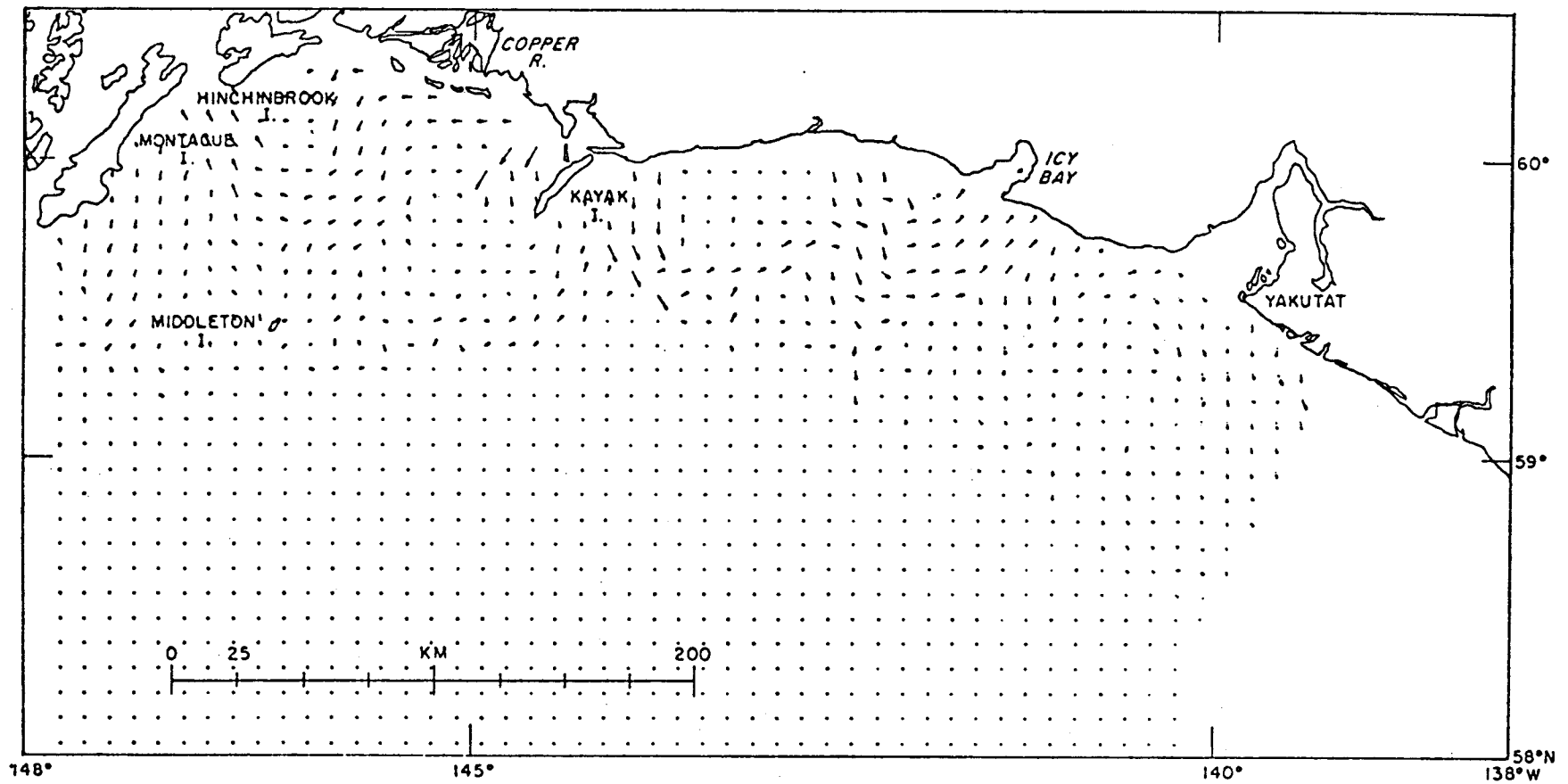
BAROTROPIC CURRENT RESPONSE TO WIND PATTERN 4.0



147

Figure 3-17. Composite wind set-up response for Northeast Gulf of Alaska weather type 4.0.

BAROTROPIC CURRENT RESPONSE TO WIND PATTERN 4.1



148

Figure 3-18. Composite wind set-up response for Northeast Gulf of Alaska weather type 4.1.

BAROTROPIC CURRENT RESPONSE TO WIND PATTERN 5.0

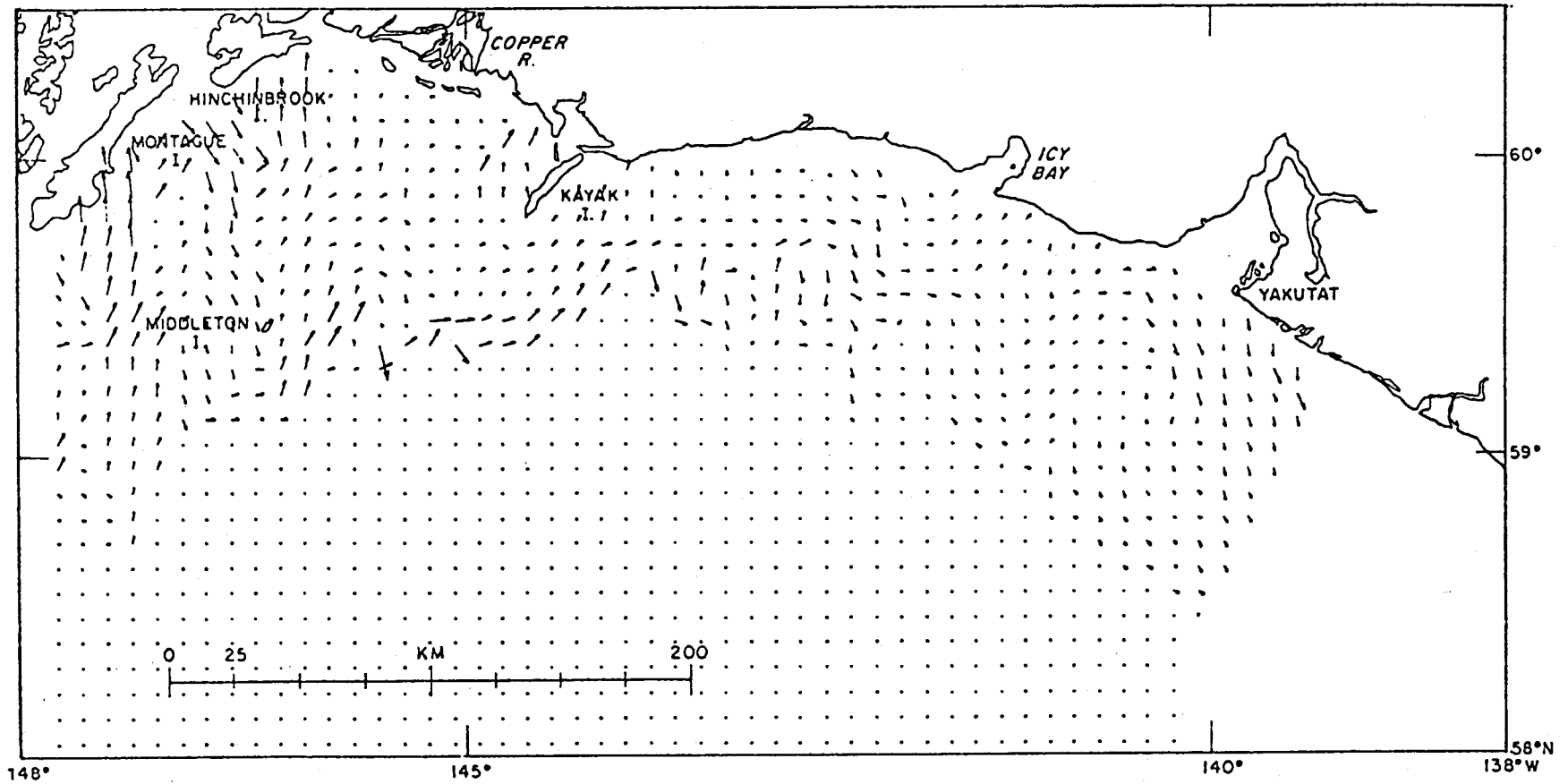


Figure 3-19. Composite wind set-up response for Northeast Gulf of Alaska weather type 5.0.

BAROTROPIC CURRENT RESPONSE TO WIND PATTERN 5.1

150

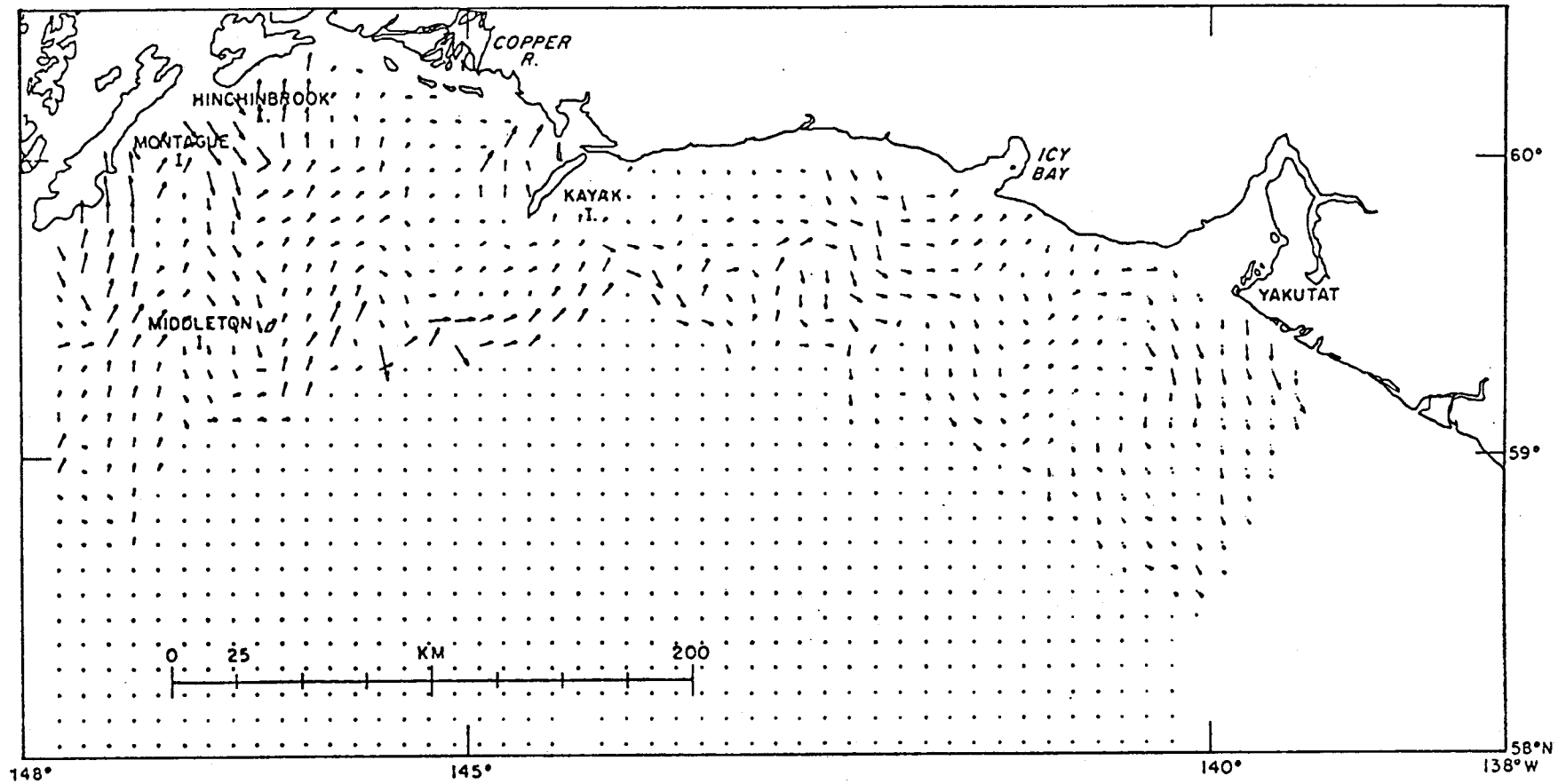


Figure 3-20. Composite wind set-up response for Northeast Gulf of Alaska weather type 5.1.

BAROTROPIC CURRENT RESPONSE TO WIND PATTERN 6.0

151

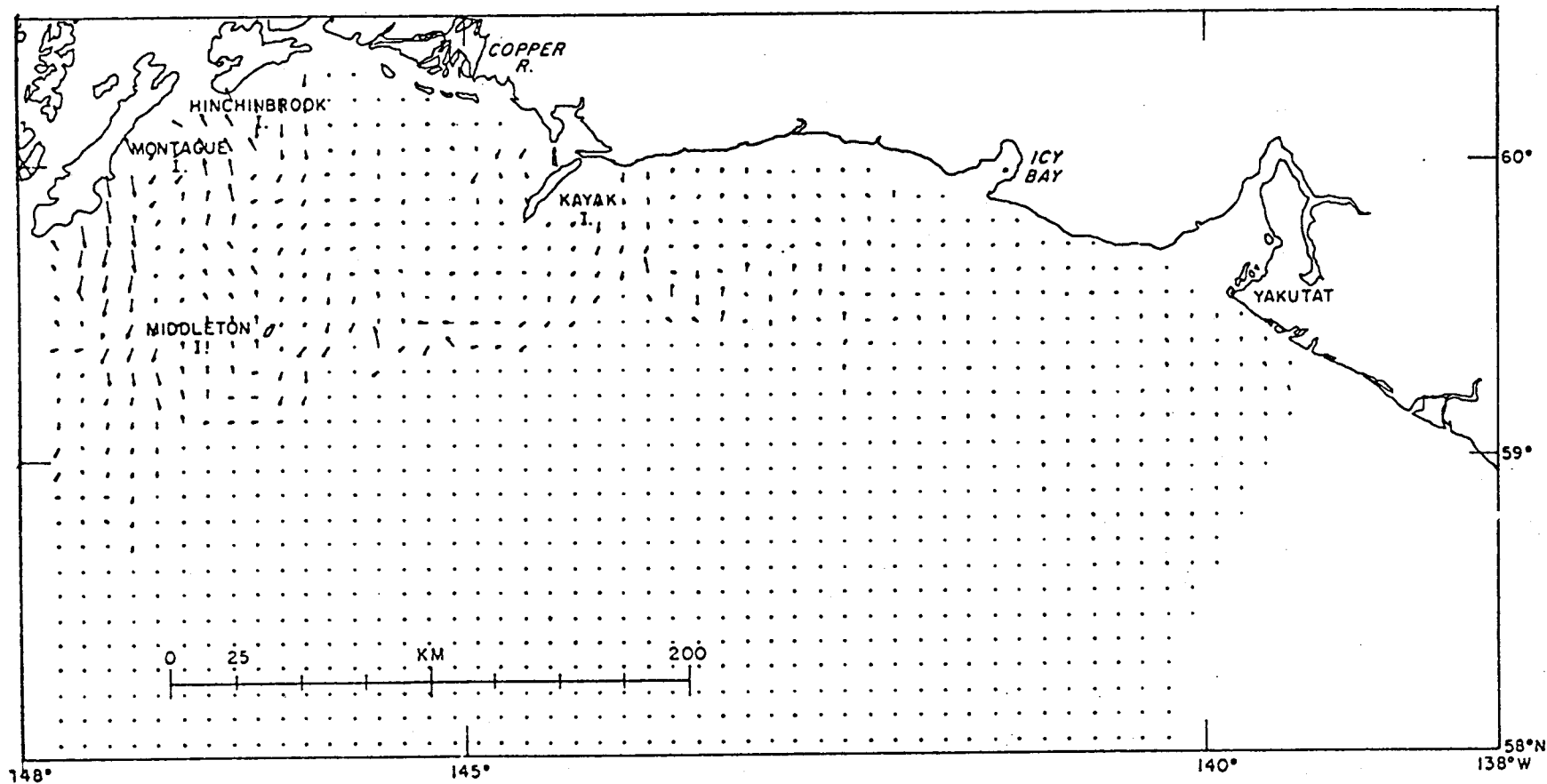


Figure 3-21. Composite Wind set-up for Northeast Gulf of Alaska weather type 6.0.

is similar to the first, except that the wind pattern is displaced to the west, causing a subsequent reduction of the currents in the eastern part of the region. The third current pattern in response to wind pattern (1.2), an eastward displacement of the low, shows significantly reduced flow over much of the area, since the coastal winds are directed more nearly perpendicular to the coast over the study area. The fourth pattern for the Gulf of Alaska low positioned to the extreme west (figure 3-12 - wind pattern 1.3) shows even more pronounced reduction of the currents in the eastern portion of the region.

Figures (3-13) and (3-14) show the current response to wind patterns (2.0) and (2.1), corresponding to an Aleutian low. The first of these is similar to (3-12), showing again a reduction of currents over the eastern half of the NEGOA shelf region. Figure (3-14)(for the summer case) shows continuation of flow along the shelf break, but significantly weaker flows over the shelf proper, with particularly quiescent conditions off of the Copper River region.

Figures (3-15) and (3-16) give the current response to wind patterns (3.0) and (3.1), which represent a high pressure situated over the Yukon, with the second including a katabatic outbreak in the winds over the Icy Bay and Copper River regions. Comparing the two current patterns clearly shows the results of these intense coastal winds. The first shows what might be considered the normal westward drift for the region. The second shows significantly increased flow over the eastern shelf region and along the shelf break, but a reduction of currents off the Copper River, since the along-shore component of the wind (bathystrophic forcing) is actually reduced in this region.

Figures (3-17) and (3-18) show the response to wind patterns (4.0) and (4.1), which represent summer positions of inland lows over Alaska.

Both show a general reversal of the shelf circulation, with the first giving stronger currents in the western NEGOA region and the second more intense flow along the east portion between Kayak Island and Yakutat.

Figures (3-19) and (3-20) shows the response to two alternate positions of the east Pacific high represented by wind patterns (5.0) and (5.1). Both show nearly identical eastward flowing currents over the entire NEGOA shelf region. These appear to be nearly opposite to the flow given in figure (3-9).

The final current pattern shown in figure (3-21) is the response of the region to a stagnating low off of the Queen Charlotte Islands. This shows generally weak flow over the shelf, with moderate westward currents along the shelf break off of Kayak Island and along Montague Island.

Subject to the assumptions that are inherent in the original weather typing and in the bathystrophic development of hinge responses along the coast, the thirteen current patterns shown represent a complete set, which should be capable of describing all the possible wind responses to be expected for the NEGOA shelf region. More importantly these current patterns are directly related to regional wind forcing, which in turn is related to large scale pressure maps. Such maps have been available for a long period of time so that reliable climatologies can be developed. Using these to key a sequence of current patterns, it becomes possible for the first time to develop regional "current climatologies" directly linked to the forcing and meteorological data base.

3.4 Density Driven Response

The density driven response to the NEGOA region will be given by the solution to equation (3-3). Input data for a density response current pattern must come from a mapping of the internal density field. This

data is collected on standard hydrographic cruises. A number of hydrographic studies have been carried out for the NEGOA region, and at this time seven independent sets are available which have a sufficient number of stations to cover the area. These data sets cover the following periods:

July, 1974

February, 1975

June, 1975 S

June, 1975 A

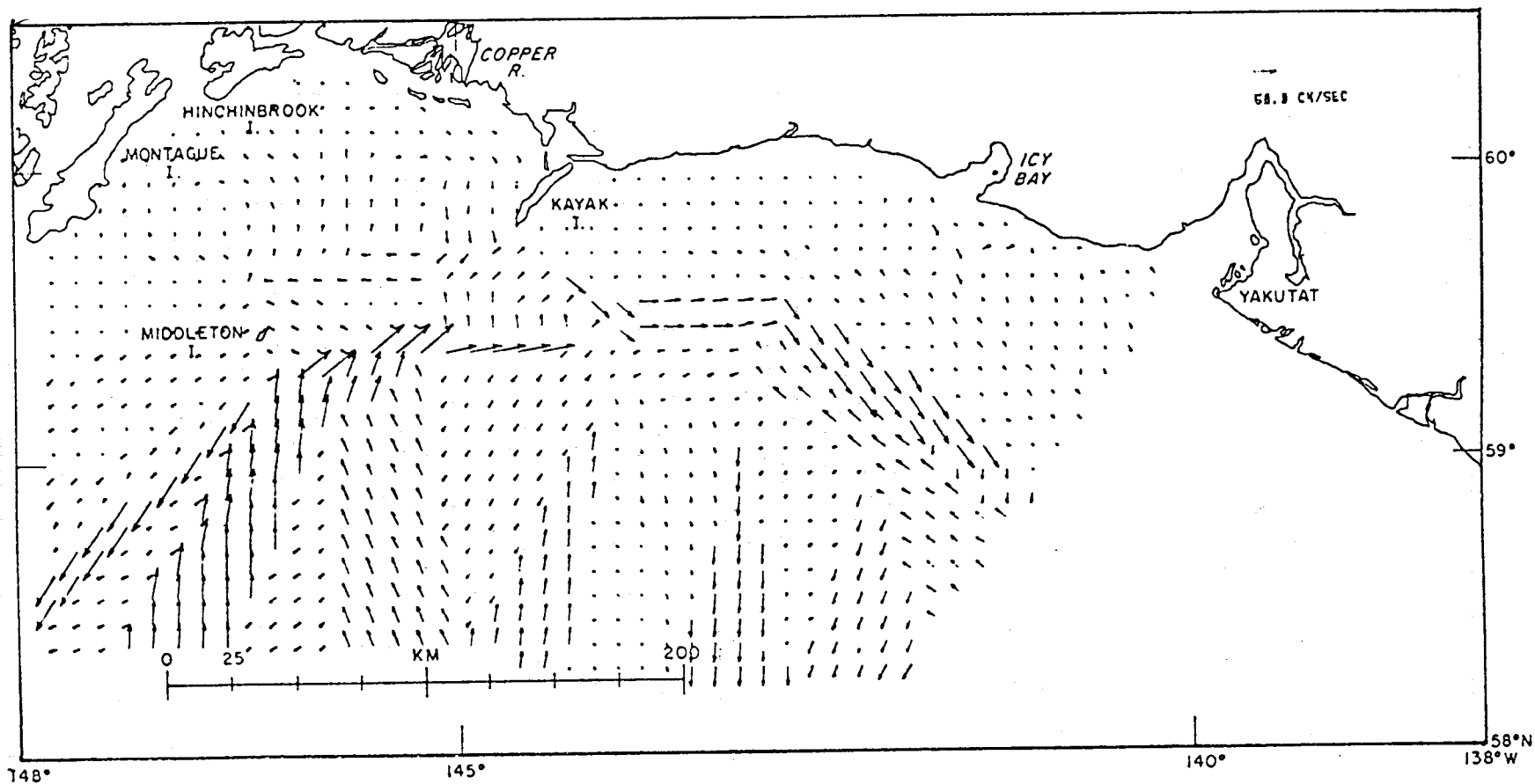
October, 1975

February, 1976

April, 1976

Once again it should be reiterated that the solution to equation (3-3) yields a minimum barotropic mode which is in reality a minimum bathymetric interaction mode consistent with the model dynamics, density distribution and bathymetry. In terms of a more classical approach this gives the dynamic height of the sea surface, assuming that the region has a terrain following level of no motion. As a practical matter for stations beyond the shelf, a level of no motion is assumed at 1200 meters. Subject to these conditions the density driven response patterns for the above data sets are shown in figures (3-22) through (3-28). Once again the vector arrows have been transformed from the triangular finite element grid to a regular cartesian grid for ease in computer storage and graphic representation. It should also be noted that these patterns are not of arbitrary magnitude, but give absolute velocities related to the shear induced by the baroclinic fields.

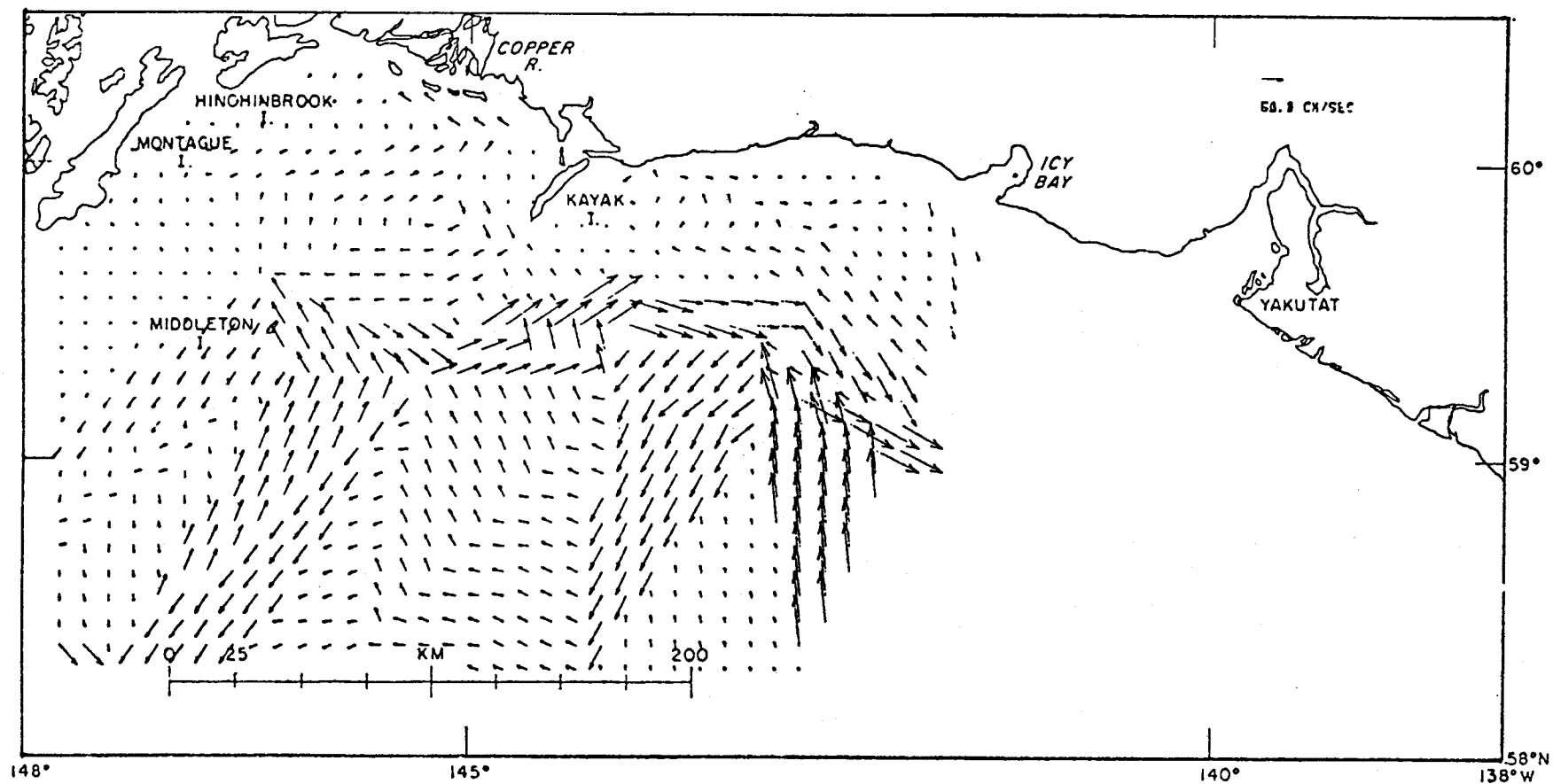
BAROCLINIC CURRENT FIELD - JULY 1974



155

Figure 3-22. Density driven response currents for the Northeast Gulf of Alaska from data collected in July 1974.

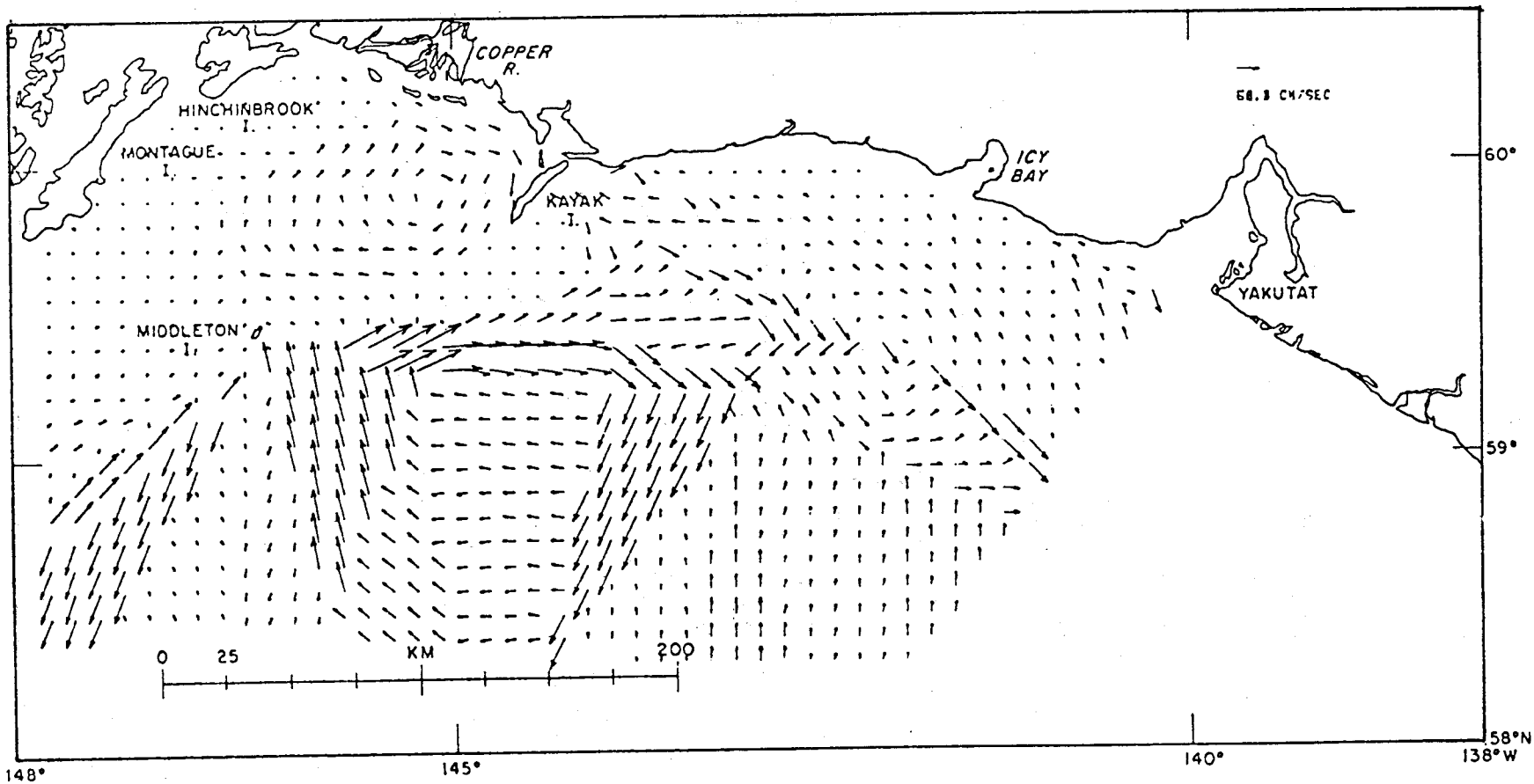
BAROCLINIC CURRENT FIELD - FEBRUARY 1975



156

Figure 3-23. Density driven response currents for the Northeast Gulf of Alaska from data collected in February 1975.

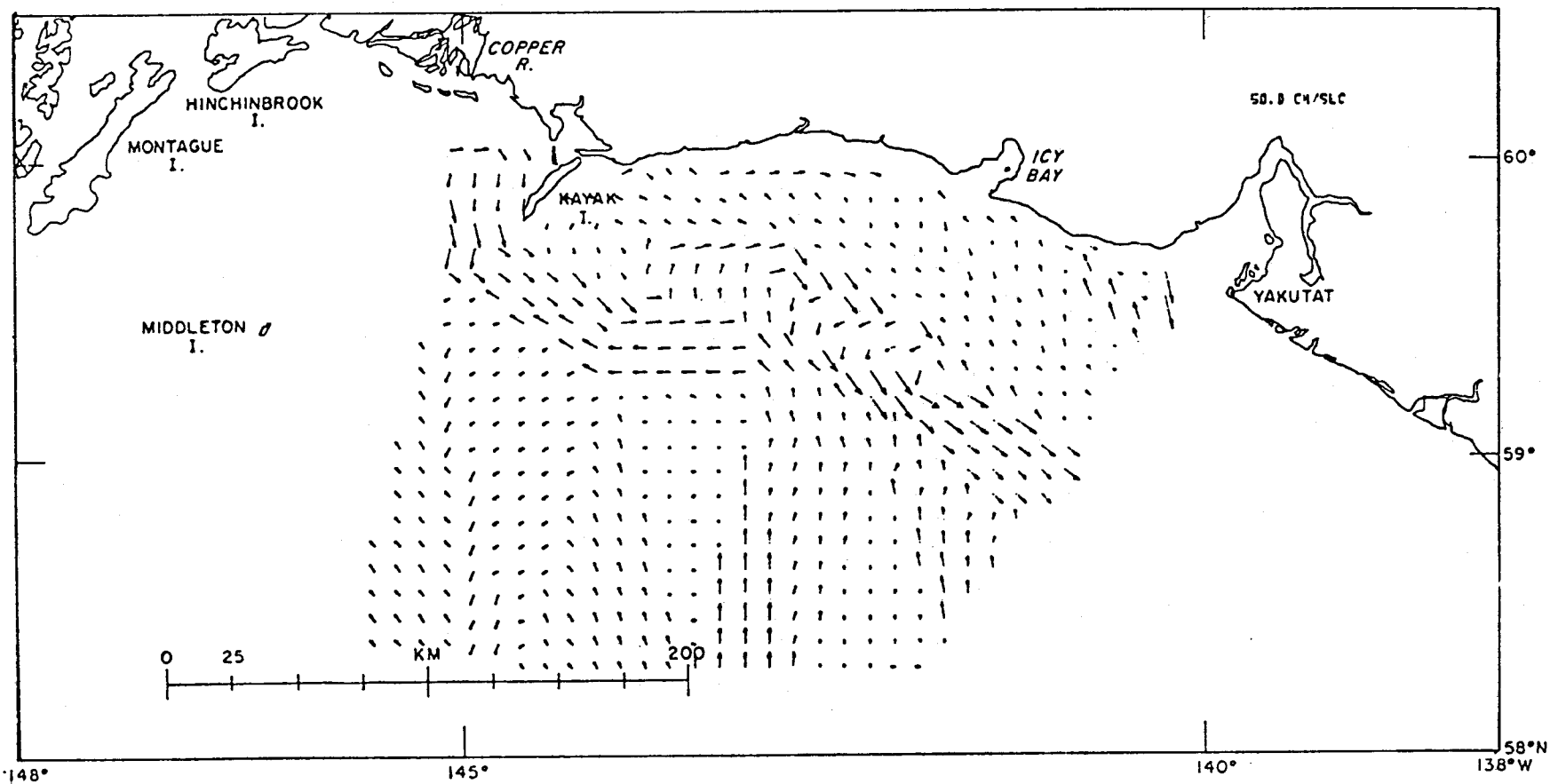
BAROCLINIC CURRENT FIELD - JUNE 1975



157

Figure 3-24. Density driven response currents for the Northeast Gulf of Alaska from data collected in June 1975 (NOAA Ship Surveyor).

BAROCLINIC CURRENT FIELD - JUNE 1975



158

Figure 3-25. Density driven response currents for the Northeast Gulf of Alaska from data collected in June 1975 (R/V Acona).

BAROCLINIC CURRENT FIELD - OCTOBER 1975

159

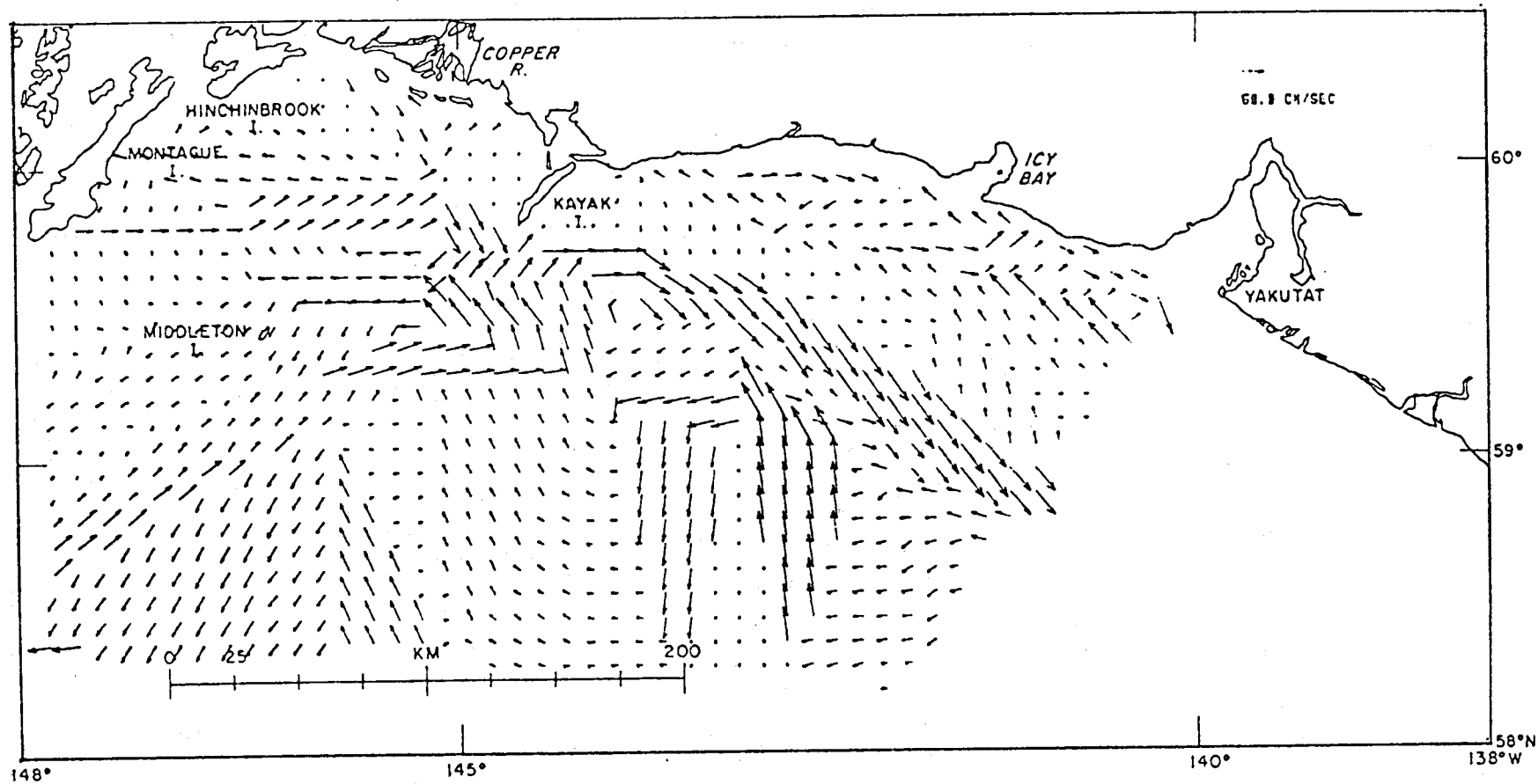
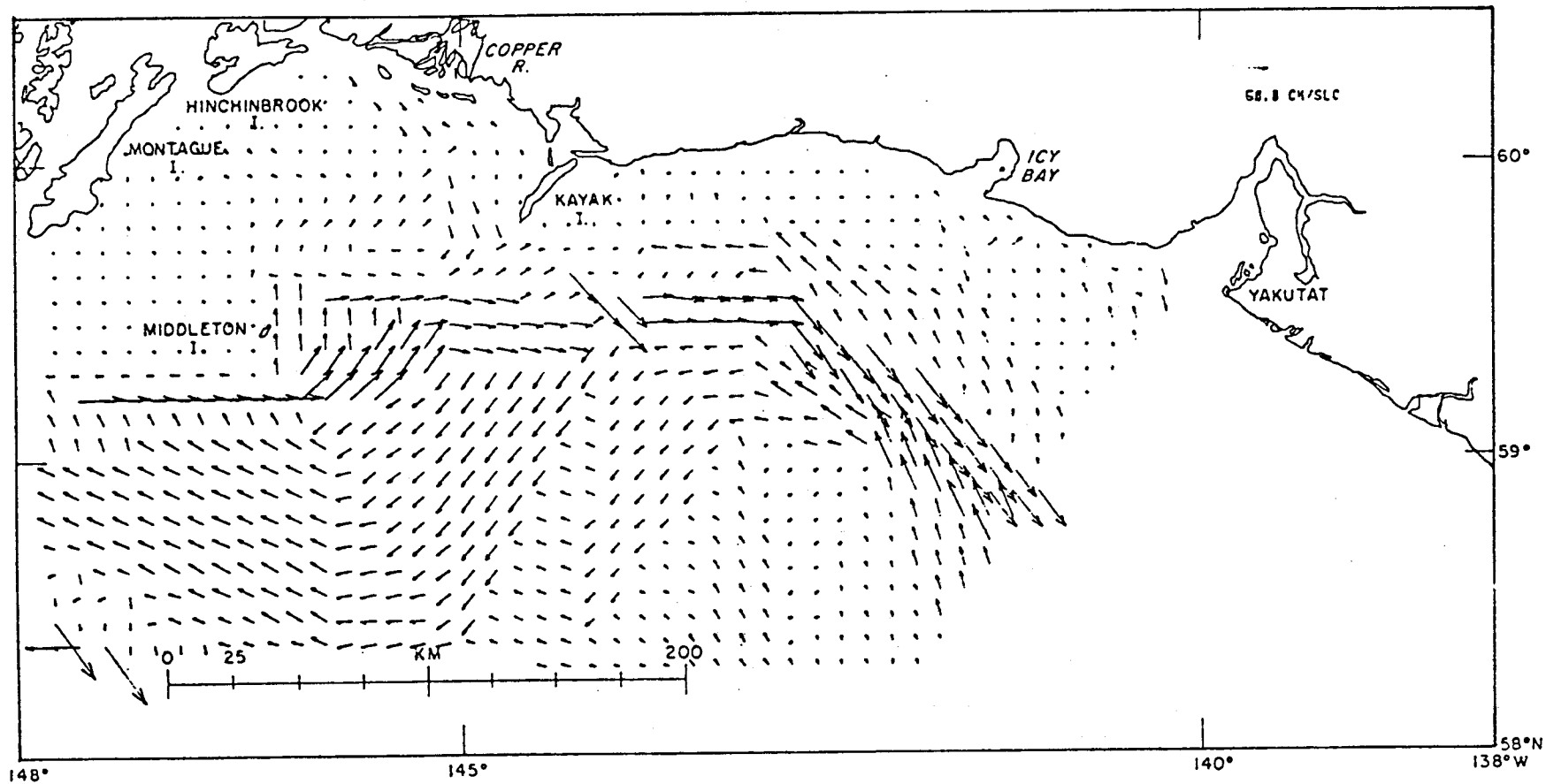


Figure 3-26. Density driven response currents for the Northeast Gulf of Alaska from data collected in October 1975.

BAROCLINIC CURRENT FIELD - FEBRUARY 1976 CASE A



160

Figure 3-27. Density driven response currents for the Northeast Gulf of Alaska from data collected in February 1976.

BAROCLINIC CURRENT FIELD - APRIL 1976

191

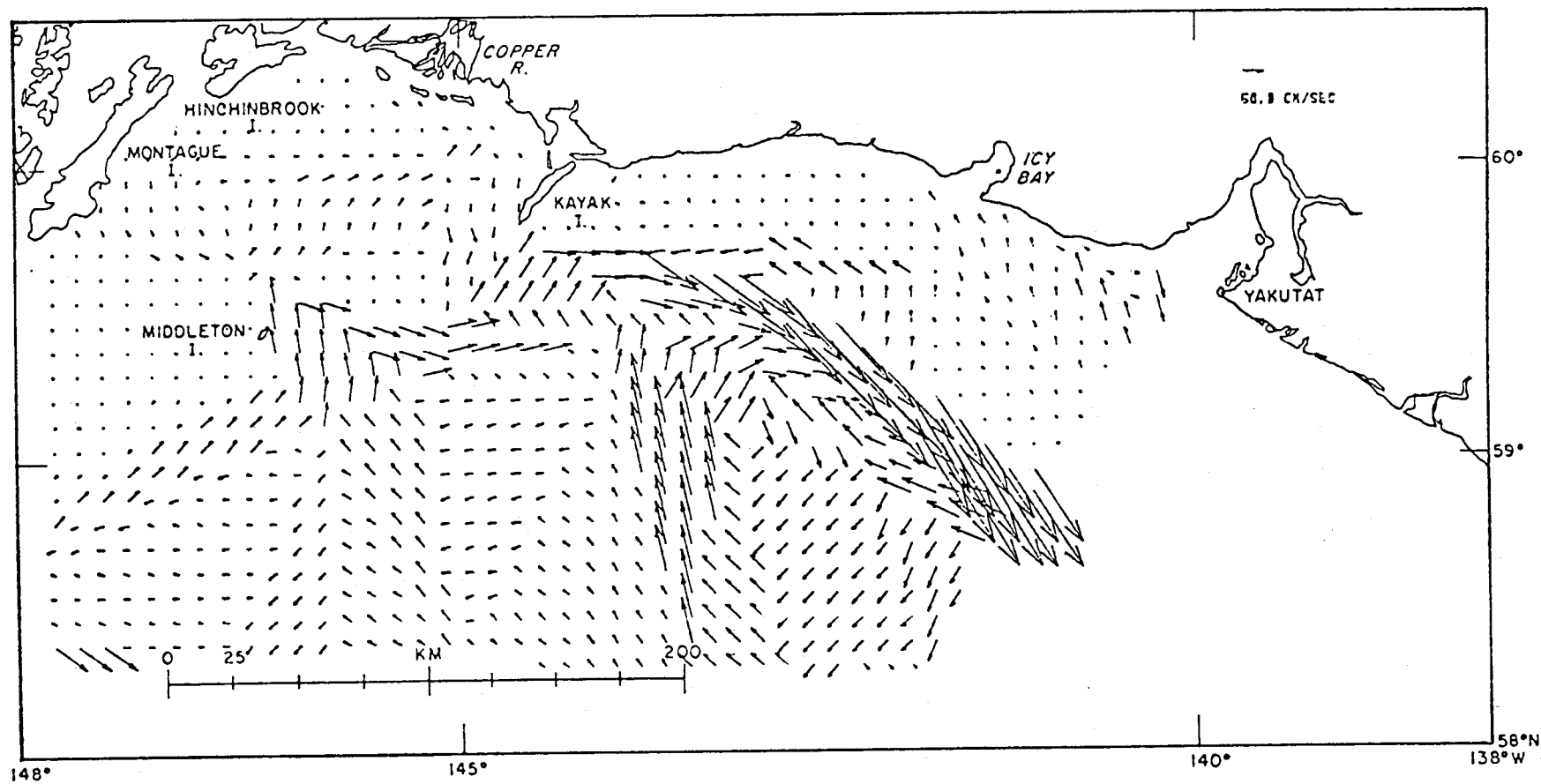


Figure 3-28. Density driven response currents for the Northeast Gulf of Alaska from data collected in April 1976.

An examination of the density driven response patterns reveals several immediate points. The first of these is that on the shelf proper the currents are considerably smaller than the ones seen off of the shelf. As a second point the off-shelf currents appear to be associated with large-scale (>200 km) eddies that are present in all the data sets. It is significant to note that although the position of these mesoscale baroclinic eddies varies from one cruise to the next, they are always present to some extent.

In an attempt to discuss the density driven response patterns in a systematic order, the on-shelf and off-shelf flow will be discussed separately.

Concentrating first on the on-shelf patterns, figure (3-22) indicates the density driven response for July, 1974. On the shelf ($d < 100$ fa.) the currents are generally weak (< 10 cm/sec) with little organized flow except for an anticyclonic gyre to the west of Kayak Island and a westward flowing current NE of Middleton Island. There is also evidence of a slightly weaker cyclonic gyre NNW of Middleton Island, but it is less clear. The gyre or eddy behind Kayak Island has been discussed previously (Galt, 1976) and compared to other observational evidence.

Figure (3-23) shows the density driven response for data collected in February, 1975. On the shelf the currents are generally somewhat more energetic than during the previous summer. The anticyclonic gyre to the west of Kayak Island is still evident along with a westward flowing current along the coast off of the Copper River. There is also a generally consistent westward flow along the outer edge of the shelf which moves at about 40 cm/sec.

Figure (3-24) shows the density driven response for data collected

in June, 1975. In this case the gyre west of Kayak Island is particularly well developed with speeds of nearly a knot. In addition it appears that offshore the eddy S and SW of Kayak Island has moved into the region where the shelf narrows, and a fairly strong coastal current to the west is evident. As in the previous summer the southern extreme of the gyre west of Kayak Island appears to border on a westward flow to the NE of Middleton Island.

Figure (3-25) is particularly interesting in that it shows the density driven response from a partial field that was collected on a second cruise in June, 1975, approximately a week after the one shown in figure (3-24). Several significant changes are evident. First of all the currents south and east of Kayak Island have been deformed. Secondly, the large offshore gyre south of Kayak Island does not appear to have been sampled by the station spacing.

Figure (3-26) shows the density driven response currents for data collected in October, 1975. This appears to be an unusual pattern. Flow on the shelf is relatively energetic with bands of eastward flow particularly along the coast west of Icy Bay and east of the southern end of Montague Island. There is an indication of anticyclonic flow to the WSW of Kayak Island but the pattern is considerably deformed compared to previous realizations of this feature.

Figure (3-27) shows the density driven response for data collected in February, 1976. Once again this indicates the development of an anti-cyclonic gyre west of Kayak Island. Interestingly, just south of Kayak Island the flow is eastward as in the second June, 1975 pattern. Southeast of Icy Bay along the outer edge of the shelf (100 fa. contour) relatively strong NW flow is seen. The offshore pattern SE of Middleton Island

is clearly seen to penetrate onto the shelf.

Figure (3-28) shows the density driven response for April, 1976. West of Kayak Island the anticyclonic flow pattern is evident with a weaker cyclonic flow to the east of Montague Island. Once again it appears that the offshore circulation penetrates onto the shelf to the SE of Middleton Island and the SE of Kayak Island.

It is now necessary to focus attention on the offshore segments of the density driven current patterns. In doing this it is obvious from figures (3-22) through (3-28) that the sampling scale offshore is too coarse to accurately resolve the mesoscale eddies that are present. In addition the predicted currents are often large, with speeds in excess of two knots. For this deep region the model results are just what would be obtained from classical dynamic height calculations, and as such a more common presentation is the sea surface elevation contours. These are shown in figures (3-29) through (3-35) for the seven data sets previously considered. From the surface elevation contours the eddy nature of the patterns is more clearly seen, with an offshore length scale of approximately 200 km. The questions concerning origin and initial movement of these mesoscale features are of obvious oceanographic interest, but will not be addressed in the present study. It is enough to point out that they seem to be common for the Gulf of Alaska bight region and are an ubiquitous feature in the data.

A more pressing question concerning these mesoscale eddies is how they interact with the continental slope and shelf break area. Since the object of the present study is the NEGOA shelf region, it is this dynamic exchange and current description that are needed.

To address the eddy-slope interaction problem it is useful to first consider a baroclinically balanced, symmetric, anticyclonic gyre moving

BAROCLINIC SEA SURFACE ELEVATION - DENSITY DRIVEN RESPONSE

JULY 1974

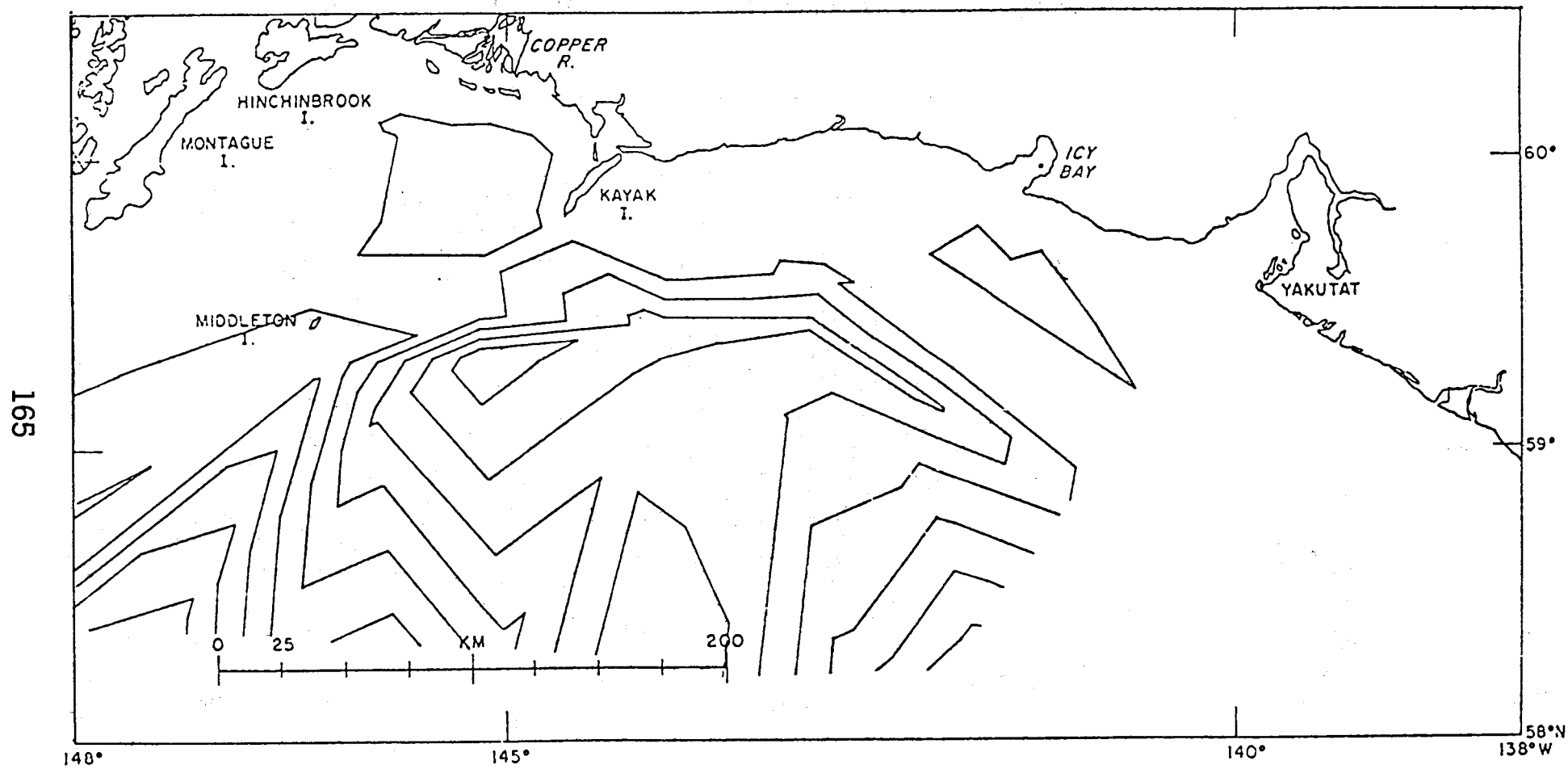


Figure 3-29. Sea surface elevation contours for Northeast Gulf of Alaska from data collected in June 1974. Contour interval is 4 cm/sec.

BAROCLINIC SEA SURFACE ELEVATION - DENSITY DRIVEN RESPONSE

FEBRUARY 1975

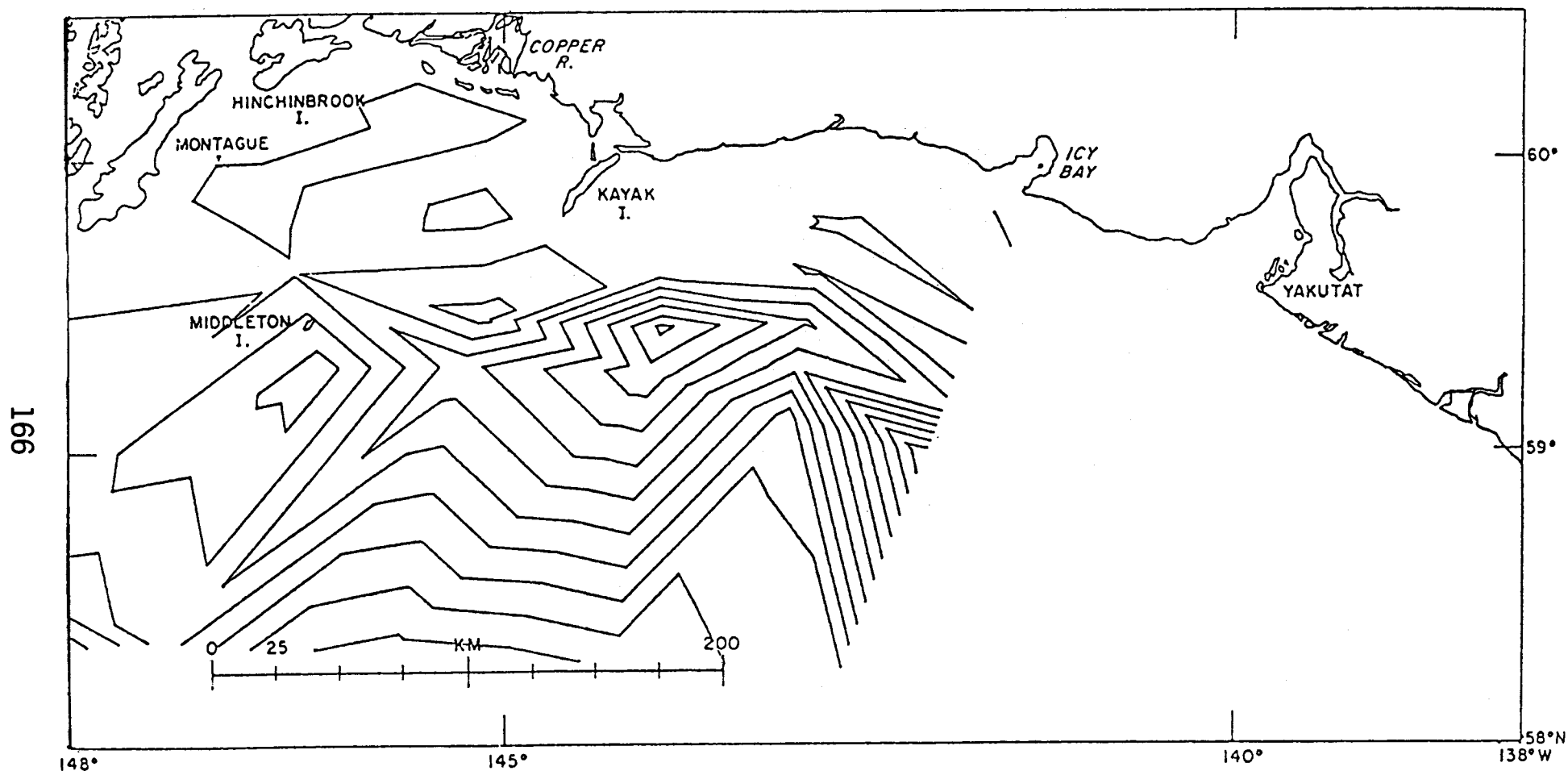


Figure 3-30. Sea surface elevation contours for Northeast Gulf of Alaska from data collected in February 1975. Contour interval is 4 cm/sec.

BAROCLINIC SEA SURFACE ELEVATION - DENSITY DRIVEN RESPONSE

JUNE 1975

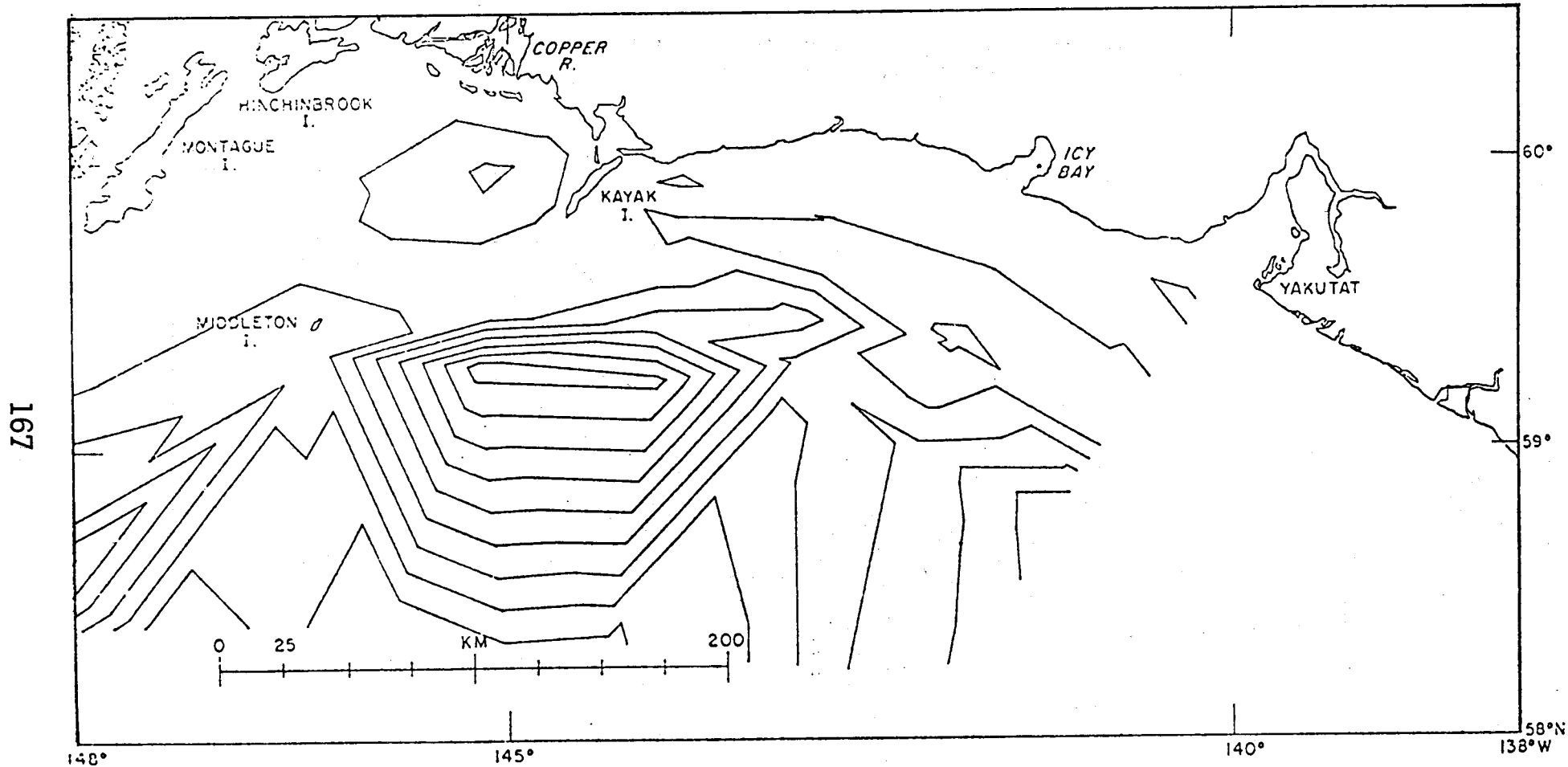
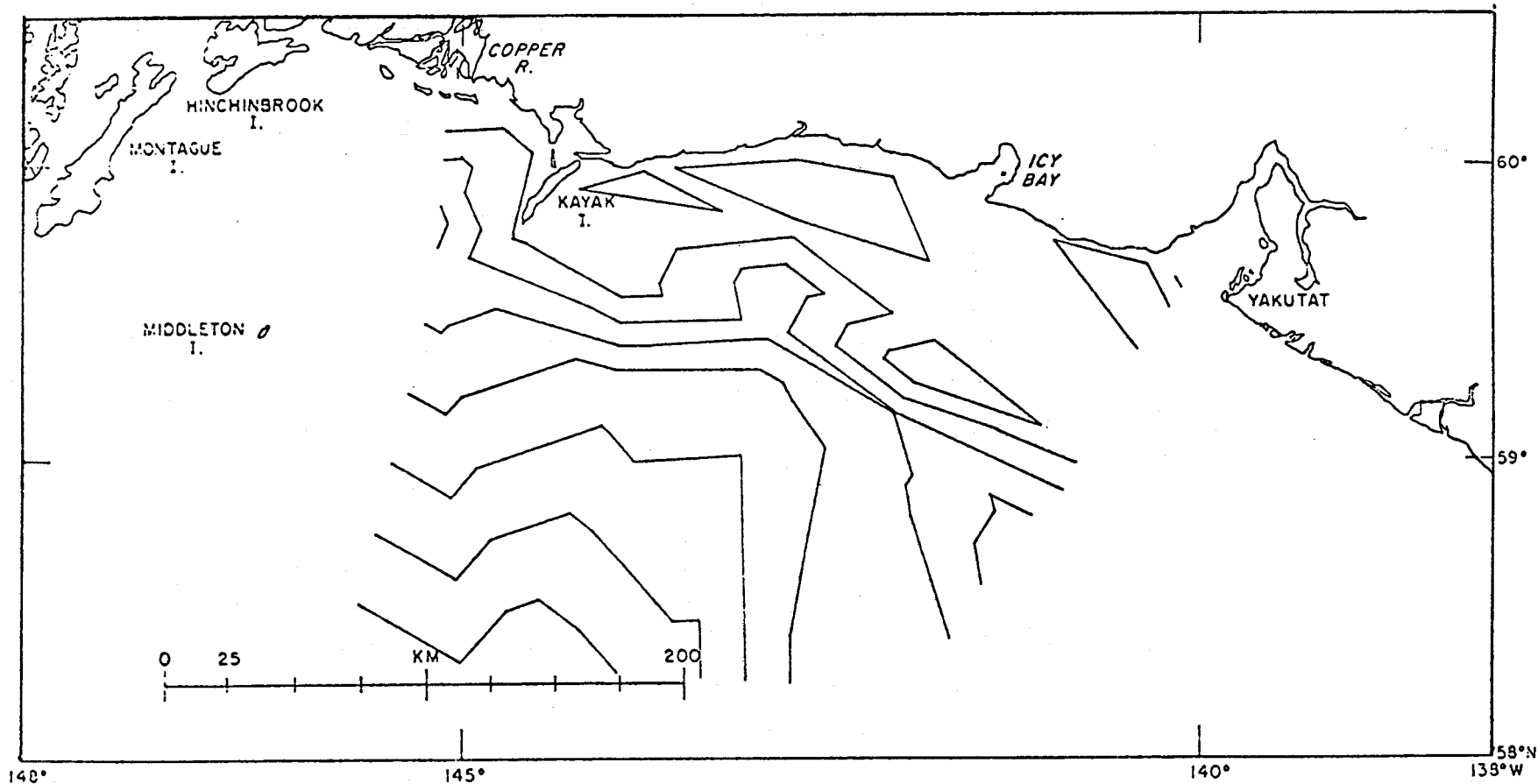


Figure 3-31. Sea surface elevation contours for Northeast Gulf of Alaska from data collected in June 1975 (NOAA Ship Surveyor). Contour interval is 4 cm/sec.

BAROCLINIC SEA SURFACE ELEVATION - DENSITY DRIVEN RESPONSE

JUNE 1975



168

Figure 3-32. Sea surface elevation contours for Northeast Gulf of Alaska from data collected in June 1975 (R/V Acona). Contour interval is 4 cm/sec.

BAROCLINIC SEA SURFACE ELEVATION - DENSITY DRIVEN RESPONSE

OCTOBER 1975

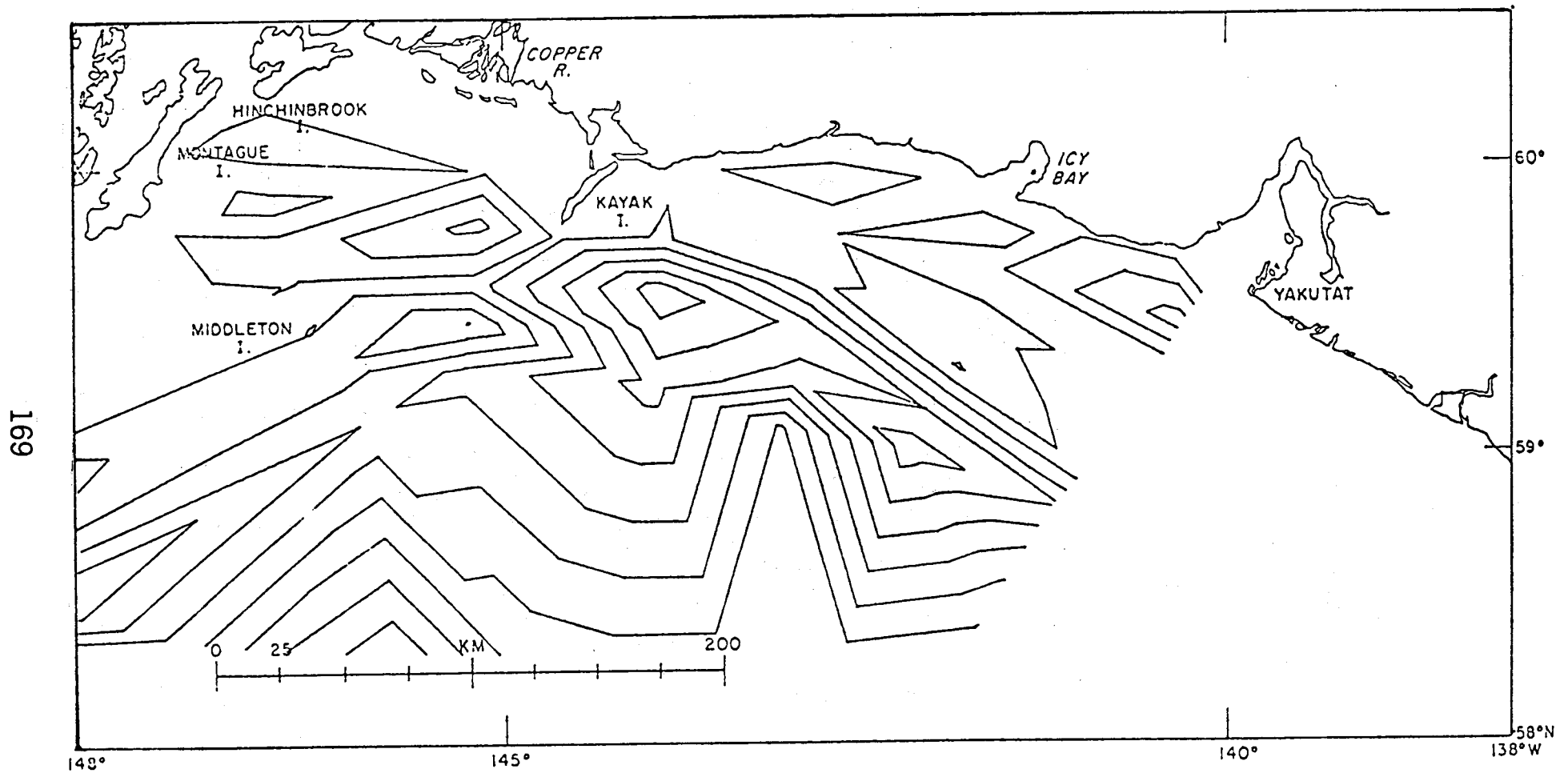


Figure 3-33. Sea surface elevation contours for Northeast Gulf of Alaska from data collected in October 1975. Contour interval is 4 cm/sec.

BAROCLINIC SEA SURFACE ELEVATION - DENSITY DRIVEN RESPONSE

FEBRUARY 1976 A

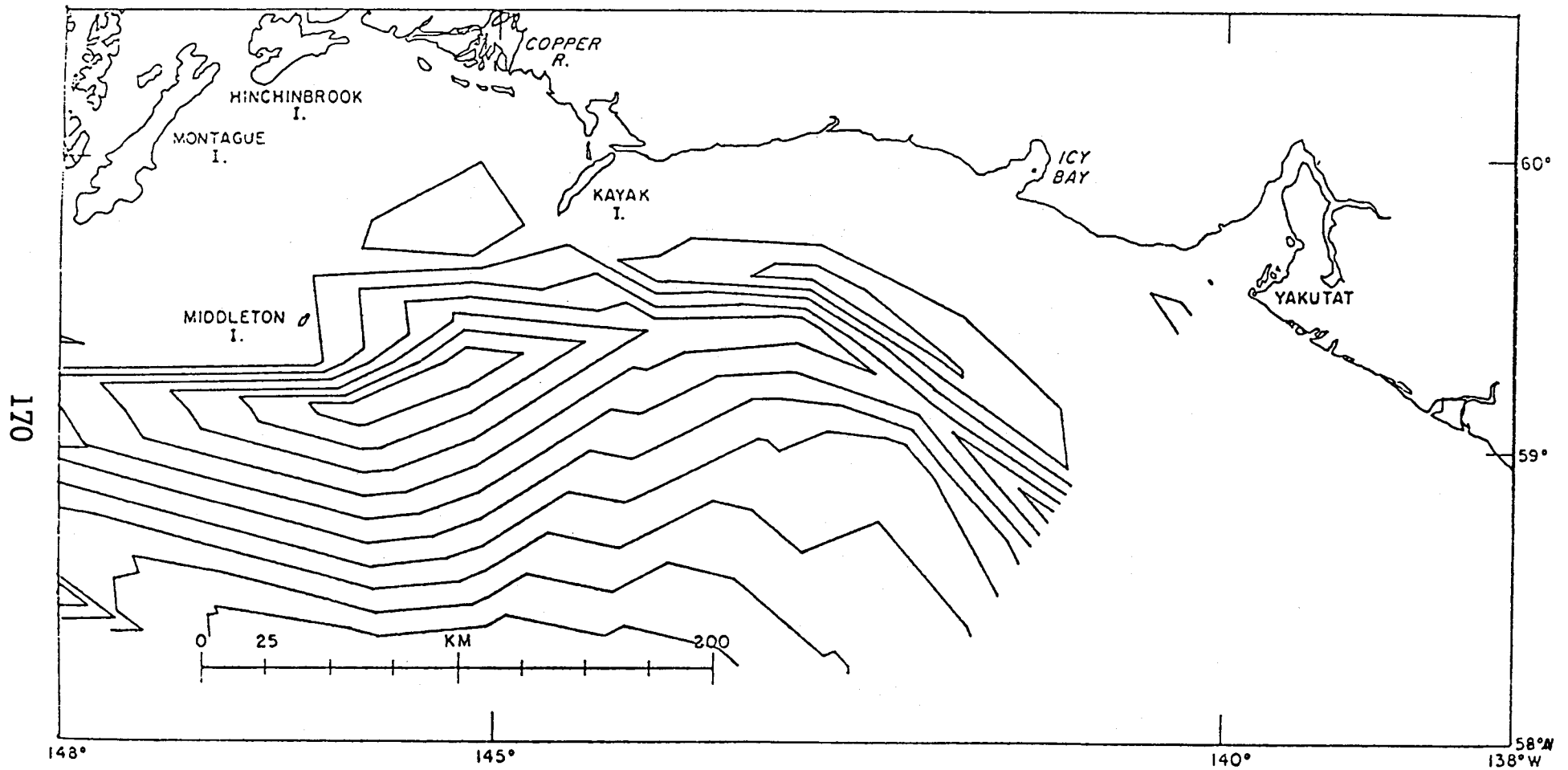


Figure 3-34. Sea surface elevation contours for Northeast Gulf of Alaska from data collected in February 1976. Contour interval is 4 cm/sec.

BAROCLINIC SEA SURFACE ELEVATION - DENSITY DRIVEN RESPONSE

APRIL 1976

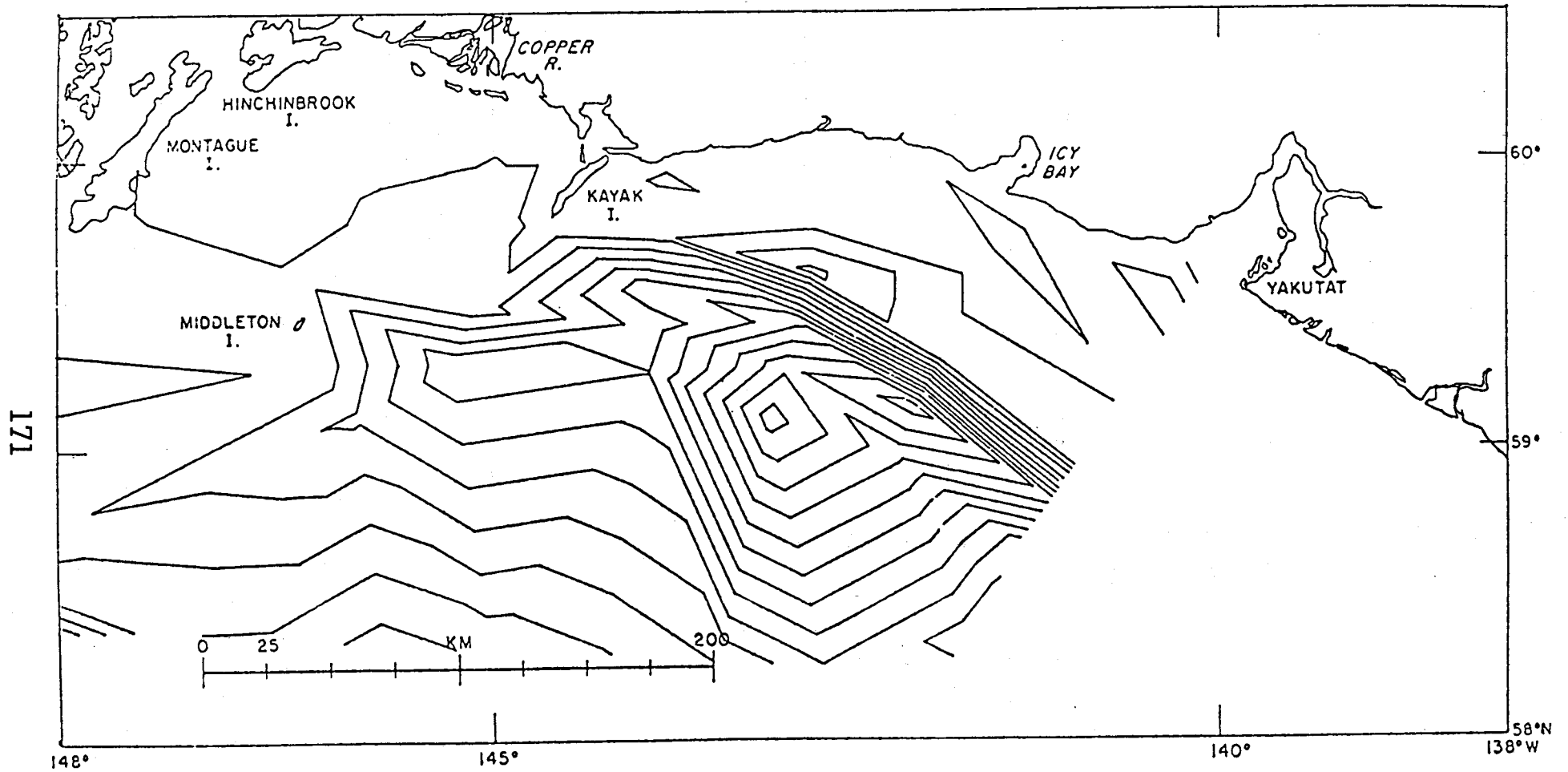


Figure 3-35. Sea surface elevation contours for Northeast Gulf of Alaska from data collected in April 1976. Contour interval is 4 cm/sec.

from deep water towards the slope (figure 3-36). As the gyre first encounters the bottom influence, pressure variations will be induced along the isobaths that the gyre is crossing. In particular, the center of its path will show higher pressure along any particular isobath than off to either the right or left. Under these conditions a careful examination of the $J(\alpha, d)$ term in equation (3-3) shows that the area to the left of the center line of the eddy must develop additional negative circulation, while the area to the right must compensate with the development of positive circulation. Putting these results together, the qualitative pattern must be deformed as is shown in figure (3-36). It is interesting to note that similar flow-bathymetry interactions have been described by Csanady (1978) under somewhat different initial conditions and referred to as arrested barotropic waves.

A close examination of figures (3-29) through (3-35) reveals that many of the eddies present appear to be compressed along the continental slope and show the characteristic extension to the east that is suggested in figure (3-36).

Offshore of the NEGOA shelf region mesoscale eddies commonly occur in deep water. As they encounter the continental slope they are dynamically modified through the action of the joint baroclinic - bathymetric term in the vorticity balance. When this happens, the onshore edge of the eddy is significantly compressed with a subsequent intensification of the currents. As this develops, a characteristic flattened loop pattern appears, which in extreme cases will appear as a banded pattern. This is a region where potentially strong currents may be expected over the shelf and shelf break region. From the NEGOA data it appears that these eddy related shelf edge currents do extend over the shelf break, at least in certain areas - in particular, SE of Middleton Island, SE of Kayak Island and SW of Icy Bay. The prediction, in even a statistical

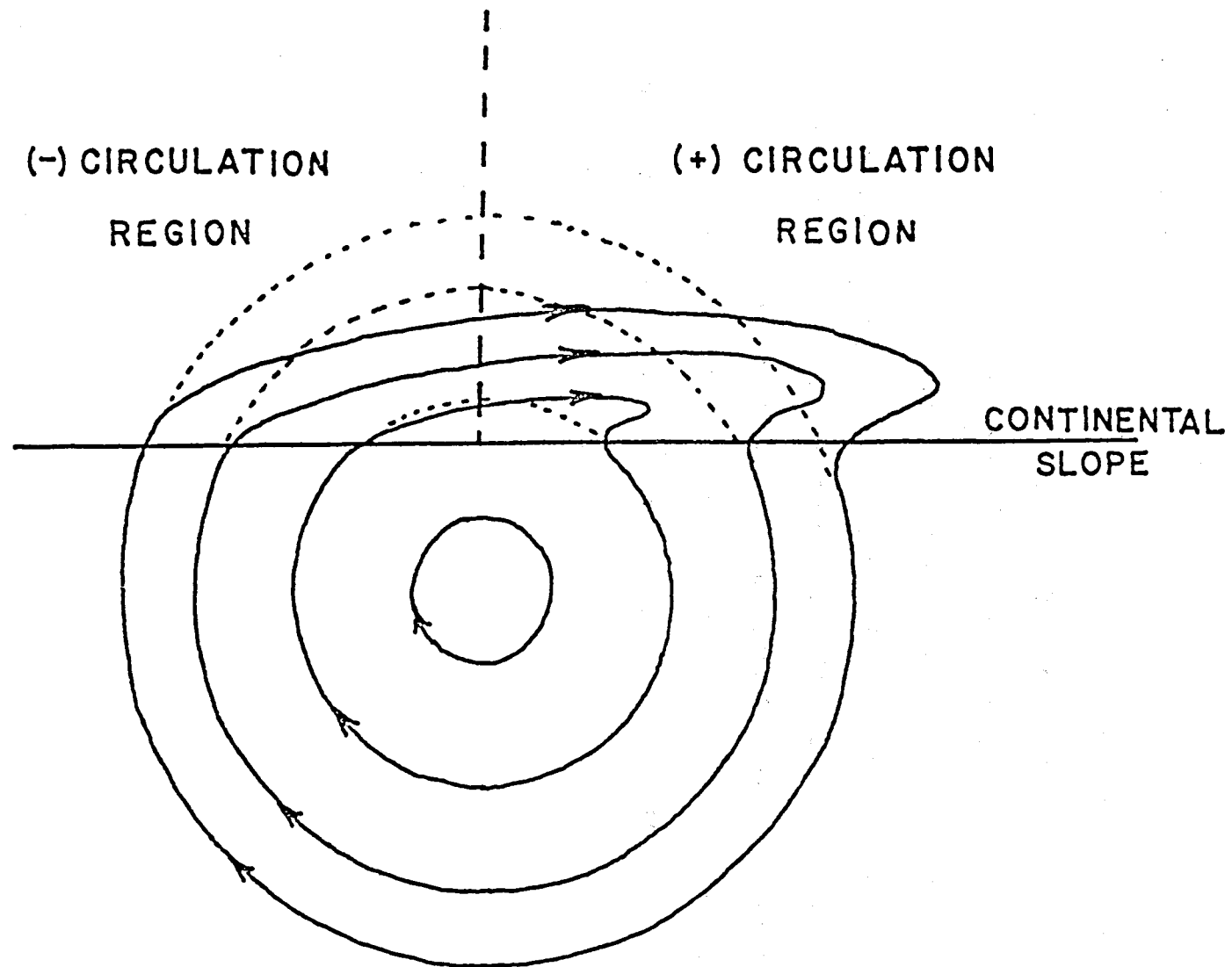


Figure 3-36. Representation of a deepwater mesoscale eddy and its deformation as it dynamically interacts with the continental slope.

sense, of these current patterns must be coupled to a more complete understanding of the distribution and movement of these offshore mesoscale eddies.

3.5 Composite Current Patterns

The total currents for the Northeast Gulf of Alaska will be represented by a simple linear superposition of the wind response component and the density driven response. How these are combined and what sequences are chosen to represent particular climatological periods depends on keying strategies which will be the subject of other NEGQA studies. The important point to be made here is that given the model dynamics, bathystrophic wind set-up, weather types and specific density fields, the totality of all possible, consistent current patterns is represented by the patterns shown here.

3.6 REFERENCES

- Bakun, A. (1973): Coastal upwelling indices: West coast of North America. NOAA Tech. Report, NMFS SSRF - 671, 103 pp.
- Beardsley, Robert C. and Bradford Butman (1974): Circulation on the New England continental shelf: Response to strong winter storms, Geophy. Res. Letters 1 (4), pp 181-184.
- Csanady, G.T. (1978): Arrested Topographic Wave, J. Phy. Oc. 8(1), pp 47-62.
- Favorite, F., A.J. Dodimeand and K. Nasu, (1976): Oceanography of the Sub-arctic Pacific region, 1960-71. Bull. Int. N. Pac. Fish. Comm., 33, 187 pp.
- Galt, J.A. (1975): Development of a simplified diagnostic model for the interpretation of oceanographic data, NOAA Tech. Report ERL 339-PMEL 25 NOAA, U.S. Department of Commerce, Wash. DC, 36 pp.
- Galt, J.A. (1976): Circulation studies on the Alaskan continental shelf off the Copper River, NOAA, U.S. Department of Commerce, Wash. DC, 46 pp.
- Galt, J.A. and Thomas C. Royer (1975): Physical oceanography and dynamics of the NE Gulf of Alaska. Proceedings of the Symposium on Science, Resources and Technology in the Gulf of Alaska, Oct. 16-17, 1975, AINA
- Galt, J.A., and Glen Watabayashi (1978): The linear decomposition of a diagnostic shelf circulation model and discussion of alternate boundary condition formulations, NOAA/ERL/PMEL (Draft Tech. Report).
- Hann, Greg (1978): Diagnostic Model of Water and Oxygen Transport in the New York Bight. NOAA professional paper - Oxygen Depletion and Associated Mass Mortality in the NYB, 1976. Editor, R.L. Swanson.
- Hayes, S.P. (1979): Variability of currents and bottom pressure across the continental shelf in the Northeast Gulf of Alaska, Journal Phy. Oc. (in press).
- Hayes, S.P. and J.D. Schumacher (1976): Description of wind, current and bottom pressure variations on the continental shelf in the Northeast Gulf of Alaska, from February to May, 1975. JGR 81 (36), pp 6411-6419.
- Hsueh, Y. and Chich Yuan Peng (1978): A diagnostic model of continental shelf circulation. JGR 83(C6), pp 3033-3041.
- Overland, J.E. and Thomas R. Hiester (1978): A Synoptic Climatology for Surface Winds Along the Southern Coast of Alaska. NOAA/ERL/PMEL, Tech. Report (draft).
- Pedlosky, J. (1974): Longshore currents, upwelling and bottom topography, Jour. Phy. Oc. 4(2), pp 214-226.

Putnins, P. (1966): Studies on the Meteorology of Alaska, Environmental Data Service, Silver Spring, MD, 90 pp.

Reynolds, R. Michael, Thomas R. Hiester and S.A. Macklin (1978): Coastal meteorology of the Gulf of Alaska, Icy Bay to Yakutat Bay, PMEL/ERL/NOAA, Tech. Report (in press).

Royer, T.C. (1975): Seasonal variations of waters in the northern Gulf of Alaska, DSR 22, pp 403-416.

Royer, T.C. (1978): On the effect of precipitation and runoff on coastal circulation in the Gulf of Alaska, J.P.O. (in press).

Royer, T.C., Donald V. Hansen and David J. Pashinski (1978): Coastal flow in the Gulf of Alaska as observed by dynamic topography and drogued drift buoys, (draft manuscript).

Watabayashi, G. and J.A. Galt (1978): A finite element solution technique for a diagnostic shelf circulation model. NOAA/ERL/PMEL Tech. Report (in review).

Welander, Pierre (1956): Wind action on a shallow sea: some generalization of Ekman's theory. Tellus 9(1), pp 45-52.

4. Development of the Environmental Library

4.1 Introduction

The oil spill trajectory model was designed for the implementation of a batch mode program on the ERL-owned CDC 6600 in Boulder, Colorado. The disk space associated with this machine is partitioned into user areas on a public disk pack. The trajectory model and graphics elements were written and are stored in one user area and the data package was assembled and is stored in another area. The separation of these functions allows the model to remain relatively independent of region. By dedicating a user area to environmental data endemic to a given region such as NEGOA, standardized procedures and file names can be used without confusion caused by duplicity of file names or by storage limitations.

In addition to the role as storage bin, the data library acts as an interface between sundry data sources and the program. Thus the library must contain routines necessary to convert both field data from the meteorological grids and the diagnostic model, and time series data from current meter records and anemometer records into formats palatable to the trajectory model. Conversions required such details as fitting area data to proper grids, making hourly averages on time series, and compacting real formatted velocity pairs into integer words to reduce core requirements. The library also contains programs to plot vectors of field data and stick plots of time series used in the verification and interpretation of model results.

4.2 Model Design and Data Structure

The Boulder computer system has a number of attributes which influenced the model design and concomitant data structure requirements. These at-

tributes deserve consideration because future users may wish to modify the design to effectively utilize a different computing system or size of data set.

A major consideration in the model construction is the management of large numbers of words of data. For the NEGOA prototype model runs we needed; a) thirteen wind patterns (u and v) on a 40 x 20 grid; b) thirteen barotropic current patterns (u and v) on a 60 x 30 grid; c) two baroclinic current patterns (u and v) on the same grid; d) two current meter and two anemometer records (u and v) for ideally 90 days, 24 per day; and e) two pattern sequences for 90 days and twice per day. These sum to approximately 92,000 decimal words of data. The standard available core at Boulder is 256,000 octal or approximately 89,000 decimal words. Since the number of words is over the normal machine limit and since we must also allow for program core and other space requirements, we cannot load the entire data set at once in this format. Thus we must consider some alternatives.

In some systems, random access disk files could be used with a simple look-up algorithm added to the model program. This method would avoid loading the pattern data into core more than a few words at a time. I/O requirements would increase only moderately since random access reads are usually efficient. The Boulder facility does not have a random access capability so we are constrained to sequentially accessed files.

The costing algorithms on many machines are based on per second useage of the various systems resources including CPU time and I/O time. The Boulder system has relatively low I/O time limits and costs are high for I/O because the system runs near saturation. These factors eliminate the possibility of manipulating sequential files through repeated FORTRAN reads and rewinds at Boulder.

Another possibility for dealing with the mass of data is to reduce the size of the data set. There are a couple of alternatives. One is to reduce the number of words required to run the model by only loading those sets actually employed for a given model run. This was considered unacceptable since it meant reassembling the data set for every run, a cumbersome and error inducing exercise at best. A second alternative is to reduce the number of words required by simply packing the data. An asset of a CDC computer is it's word size; an integer word can have up to ten characters. We took advantage of this by packing the two velocity components into one integer word for each grid point of the field data and time step of the series. The core requirements were approximately halved which brought the program well within machine core limits. The disadvantage of this method is that the data must be unpacked as needed for each calculation. The method we chose was straightforward (described in the following section) and moderately quick (total model CP compilation is 3.5 seconds plus on the order of 20. seconds execution time per trajectory run, exclusive of plotting). Other packing algorithms may be more efficient, but not others were explored since this one worked so well.

4.3 Interface Programs

Because every source seems to introduce its own problems, the number of interface programs appears to be proportional to the number of different types of data that are to be used. The routines presently available are described in this section and are abstracted in Table 4.1. The name of the procedure file which runs the program follows the program name in parentheses. The data files they call or create are summarized in Table 4.2.

The diagnostic model output includes surface u,v pairs and three vertex numbers for each triangle, and for each vertex number the location is given in a km based scaling system. The program REGRID (RUNGRID) decodes the position of the vertices into latitude and longitude. Then it maps u and v onto a regular grid by finding which triangle contains each point and assigning the associated triangle u and v to the regular grid point. If no data exists for a given grid point, then -999. is the value given u and v. No smoothing or interpolating is done. The output records contain I, J, U, V, and the triangle number and have the format (1X,2I5,2F10.3,I5). The output files are named either BOCnmm for baroclinic runs where nn is year and mm is month, or RHINGEn for the barotropic single hinge cases where n is the case number.

The wind fields are recorded as wind speed and direction. The program MODWIND (RUNMOD) copies the case number and title for the wind case and then computes u and v at each grid point. If no data exists for a given grid point then 999. is the value given u and v. The output contains first a record with the case number and title with the format (1X,F3.1,6X,7A10), then the remaining records contain I, J, U, V and a sequence number and the format is (1X,2I5,2F10.3,I5). The output files are named WINDnn, where nn is the case number multiplied by ten.

The program SUMGRID (RUNSMGD) needs to be implemented to make the summed barotropic fields described in section 3. The inputs are the barotropic single hinge cases RHINGEn. The coefficients are supplied by means of a data statement which must be offered for each summed field run. The output is in exactly the same format as REGRID output. The output files are called BWPnn where nn is the case number without the decimal point of the corresponding wind field.

It is important to verify the velocity fields before trying to make trajectory calculations, so a routine called PLOTVEC (RUNPLOT) was written to draw vectors on the same scale background as the trajectories. This routine can use any of the field data files as input since they are all formatted the same (BOCmmnn, RHINGEn, BWPnn, and WINDnn). The operating requirements are two-fold. The sense switches in the data statement at the beginning of the program must be properly set for either the current or wind case. Instructions for this are located in comment cards adjacent to the data statement. Also the title must be entered in a data statement. For the current runs the title must be supplied and for the wind runs the title must be set to blanks. The output of these runs are CALCOMP type plot commands. Examples of these plots can be seen in sections 2 and 3.

The final effort for preparing the field data for the trajectory model is the packing of the u, v pairs into integer words. This is accomplished by REPACK (RUNPACK). Each velocity component is rounded to the nearest tenth, multiplied by ten, fixed as an integer and added to a positive increment. This increment is chosen so that the entire set of numbers will be positive. Then both the integer versions of u and v are written into one word by multiplying the u value by twice the increment and adding the v value. As an example, for the NEGQA currents we used an increment of 5000, so the effect was to take UU.u and VV.v and make 5UUu5VVv an eight digit integer word. For the winds we used an increment of 500 so we made six digit words. If u and v were -999., then -999 was stored in

the integer word. The output records were written 10I8 for the currents and 10I6 for the winds. Instructions for setting the sense switches for either the current or wind case are located in comment cards at the beginning of the program. The output files are called WNDnn for the wind cases, and CURmmnn for the baroclinic currents, and CURnn for the barotropic currents. The thirteen NEGOA wind files were appended through a systems routine into one file called WINDXY for the trajectory model read. The order of the cases is just the numerical order of the pattern numbers. Similarly, the thirteen barotropic current files and the two baroclinic current files were appended into one file called CURRXY in the numerical order of the case numbers for the barotropic fields, followed by the chronological order for the baroclinic fields.

The next major undertaking is the treatment of the time series data. The program MAKECUR (RUNCUR) reads data from current meter tapes supplied by the Coastal Physics group from PMEL, averages the data automatically over every hour (not a running mean) and writes records containing date, time, u, v and a counter with the format (1X,A10,A5,2F8.3,I5). The output file names are CURnn1 where nn1 is the current meter station number.

The routine CONVOL (RUNCVL) makes running averages of any specified length on time series data. It calls files like CURnn1 and writes files like FCRnn1 with the same format.

The program STICK (RUNSTIK) makes stick plots of current time series data. It can attach either CURnn1 or FCRnn1 type files and outputs CALCOMP type plot commands. Examples of these plots can be seen in section 2. This program requires a reasonable effort on the operator's part and some prior knowledge of the data set, since the titles and date cutoffs need to be present at the beginning of the routine.

Following a similar sequence of preparation as with the pattern data,

we are now ready to pack the current meter data. Program PACKET (RUNPKCM) stores the u, v pairs as a single integer word in the same method as discussed in program REPACK. The output of PACKET is written on CURMnn, where nn is an abbreviated current meter label. The format of the output is 8I8.

The Middleton Island wind data came from a card deck supplied by the Institute of Marine Sciences (T. Royer). The card image file was given the name MIDISX. Program RDMISIS (LOADAT), converts from speed and direction to u and v, linearly interprets between data points to fill in gaps in the record, and packs the u, v pairs into single integer words. The output is written in 12I6 on the file called WM1km, where k is the beginning month, l is the ending month, and m is the year, as in 197m. The integer sequence of wind patterns was appended to the end of WMklm and was stored in 30I2 format.

The remaining function of the library is to help with the interpretation of the trajectory model results. A second version of the stick plot routine, STICK2 (RUNSTK2), was written to plot up time series like output from the trajectory model. The output file contains records of u, v pairs of the following quantities: the observed current at some station; the observed winds at Middleton Island, the baroclinic current at the spill, the total simulated current at the spill, and the total simulated wind at the spill. These records are written in 10F8.3 format. STICK2 reads these for one trajectory sequence and outputs CALCOMP type plot commands. This version of the stick plot routine is much more automatic than the other, since titles are consistent from run to run and the time axis progresses as hours since the beginning of the spill instead of being fixed to some particular dates. Examples of this type of plot can be seen in section 6.

4.4 Selection of the Prototype NEGOA Model Runs

The two study choices for NEGOA are July-August 1974 for a summer case and February-March 1975 for a winter case. Weather pattern maps were available from January 1974 through December 1975. The maps for 1976 have been ordered but were not available for weather typing for this report. The Middleton Island wind data is available for 24 May 1972 through 31 January 1977. CTD data for running the baroclinic cases of the diagnostic model were available for the following dates: July, 1974; February, 1975; June, 1975; October, 1975; February, 1976; and April, 1976. The latter three of these cases were not completed in time to be considered for the trajectory calculations because of difficulties experienced in obtaining the data sets. These problems have been detailed in previous reports.

The availability of CTD data limited our trajectory cases to three possible choices: summer 1974, winter 1975, and summer 1975. Current meter station 60A chronologically coincided well with the July 1974 CTD data set. Current meter station 62B fit well with the February 1975 CTD data set. Current meters 62C and 64 came before the June 1975 CTD data set and 62D came after. Thus the two best choices are February-March 1975 and July-August 1974. It should be noted that these cases are not representative of all possible winters and all possible summers. They are two particular seasonal cases and, as such, only represent the conditions in their own years.

TABLE 4.1
INTERFACE PROGRAM FILE DIRECTORY

File Name (Procedure File Name)	Description	Input File(s)	Output File(s)
REGRID (RUNGRID)	Finds u,v on rectangular grid from diagnostic triangular mesh	(Diagnostic model output files)	- BOCnmm - RHINGEn
MODWIND (RUNMOD)	Converts speed and direction to u,v for wind field	TYPEnn (card images)	- WINDnn
SUMGRID (RUNSMGD)	Sums single hinge diagnostic fields according to wind case	RHINGEn	- BWPnn
PLOTVEC (RUNPLOT)	Plots vector field over scaled area	WINDnn BOCmnn BWPnn RHINGEn	- - (plot files) -
REPACK (RUNPACK)	Packs field data from real u,v pairs into single integer words	WINDnn BOCmnn BWPnn	- WNDnn - CURnmm - CURnn
MAKECUR (RUNCUR)	Chooses current meter data from tape and makes hourly averages	(Data tapes from Coastal Physics)	- CURnn1
CONVOL (RUNCVL)	Makes running averages on time series data	CURnn1	- FCRnn1
STICK (RUNSTIK)	Makes stick plots from time series data	FCRnn1 CURnn1	- (plot files)
PACKET (RUNPKCM)	Packs current meter data from real u,v pairs into single integer words	CURnn1	- CURMnn
RDIDIS (LOADAT)	Fills gaps in wind record and packs data from real u,v pairs into single integer words	MIDISX (card images)	- WMk1m
STICK2 (RUNSTK2)	Makes stick plots of model data output	VELSTnn	- (plot files)

TABLE 4.2
DATA FILE TYPE DIRECTORY

File Name	Description	Format
RHINGEn	Diagnostic model barotropic field based on hinge numbered n. (I,J,U,V,ITRI)	(1X,2I5,2F10.3,I5)
BOCnmm	Diagnostic model baroclinic field based on CTD casts taken MONTH mm, YEAR nn (I,J,U,V,ITRI)	(1X,2I5,2F10.3,I5)
BWPnn	Diagnostic model barotropic field based on RHINGEn files due to wind case nn (I,J,U,V,ICOUNT)	(1X,2I5,2F10.3I5)
WINDnn	Meteorological field data for case nn (I,J,U,V,ICOUNT)	(1X,2I5,2F10.3,I5)
WNDnn	Meteorological field data for case nn (W(I,J))	(10I6)
CURnn	Barotropic current field data for case nn (V(I,J))	(10I8)
CURnmm	Baroclinic current field data for case nmm (V(I,J))	(10I8)
CURnn1	Current meter data from station nn1 (DATE,TIME,U,V,ICOUNT)	(1X,A10,A5,2F8.3,I5)
FCRnn1	Filtered current meter data from station nn1 (DATE,TIME,U,V,ICOUNT)	(1X,A10,A5,2F8.3,I5)
CURMnn	Packed current meter data (V(t))	(8I8)
WMI1km	Packed wind series from Middleton Island (V(t))	(12I6)
VELSTnn	Model output for plotting time series (U1,V1,U2,V2,U3,V3,U4,V4,U5,V5) (see text for description)	(10F8.3)

TABLE 4.3
AVAILABLE DATA SOURCES

Date	Weather Pattern Maps	Middleton Island Wind Data	CTD Data for Diagnostic Model Runs	Current Meter Records
1/74	*	*(24 May 1972)		
2	*	*		
3	*	*		
4	*	*		
5	*	*		
6	*	*	*	60A *
7	*	*		*
8	*	*		61 *
9	*	*		*
10	*	*		62A *
11	*	*		
12	*	*		
1/75	*	*	*	*
2	*	*		62B *
3	*	*		*
4	*	*		64 *
5	*	*		62C
6	*	*	*	
7	*	*		
8	*	*		62D *
9	*	*		
10	*	*	*	
11	*	*		
12	*	*(31 January 1977)		

5. Time Series Simulation and Validation

The model elements up to this point include arrays of wind and current velocities and a time series that sequences the wind and current patterns. The wind and current velocity arrays were derived using both physical insight and numerical models. In the case of the diagnostic model, for example, physical insight was used to simplify the dynamics of the modeled system. This simplification resulted in a set of equations that was amenable both to linearization and numerical solution. Both facets of this dynamical simplification were exploited in the solution technique. The wind field, in a similar fashion, was initially analyzed numerically using highly approximate formulas incorporating very simple dynamics. It was then modified using both experimental observations and the results of numerical studies of wind impinging on an idealized coastline. Finally, the sequence of wind patterns was determined by a variety of means, including some simple statistical methods, an examination of the surface wind observations from Middleton Island and EB33 and consideration of regional influences on the large scale baric patterns.

The idea underlying all this work was that the resultant product was to be used to calculate oil spill trajectories. Because of this goal, we considered both the requirement that the wind and current velocities be specified over space and the requirement that the temporal variability of these fields be modeled. In our judgement, the elements discussed up to this point represent the limit of state-of-the-art, deterministic techniques for achieving these goals. It now remains to be shown whether the model elements do, in fact, resemble the physical world. And, as a related task, we need to characterize statistically those departures between the model and the real world. These departures will both qualify the trajectory

results and identify the main priorities for subsequent work.

Because the principal dynamical omission in the current model was the acceleration term, and because the wind pattern typing was based on the idea of persistence, which is an obvious approximation, it is natural to consider the departure of actual time series observations from the modeled time series. It would be most desirable to do this at a variety of locations within the region, thereby providing a spatial dimension to the time series departures. However, we were limited in this study by the availability of wind and current observations. As we pointed out in the library section, the summer case includes one station each of wind and current measurements, and the winter case includes two anemometer stations and one current meter station (both seasons, of course, also include complementary hydrographic measurements). This is hardly an overwhelming empirical basis on which to judge the model elements. Further, these data are not independent of the model results as the winds, at least, were used in the weather typing. Thus, we are limited to characterizing the model departure at single points in the region, and these characterizations are not easily analyzed statistically due to the interplay of data and the selection of model parameters.

Figure 2-5 through 2-7 showed the average wind velocity (a vector quantity) for Middleton Island and EB33 as sorted by pattern type. The Middleton Island data, Figures 2-5 and 2-6, readily suggest that the directional specification for the wind patterns is very good for the majority of cases at Middleton Island. We have not calculated the statistical confidence limits for this direction parameter. This is due in part to the fact that the direction statistic is of a complicated functional form. More important than this functional complexity, however, are the facts that the time series data is not a sequence of independent values, but rather it exhibits correlations over considerable time lags; and the fact that this data was considered

in the pattern selection. These make analysis difficult. However, it is our subjective judgement that the correspondence shown in Figures 2-5 and 2-6 is not simply fortuitous. We believe it reflects a firm linkage between the model and the real world.

The EB33 data, on the other hand, is not so supportive of this assertion, Figure 2-7. However, even here we can see some tendency in the angular departures for the wind field to be flattened along the axis of the coast. The fact that the perturbations exhibit a pattern of this type is suggestive that the model is related to the observations, but that some unknown factor has entered the problem. There is no simple explanation for the phenomena, but further study may reveal the cause of this deviation. It might be a simple artifact in the sea surface pressure field, or it might represent some complex meteorological phenomena; both avenues should be explored. In the meantime we believe that this result simply implies our patterns are slightly off and not that the typing procedure is in question.

It is generally accepted that the higher frequency perturbation in the wind will be proportional to some longer time average of the wind. In the case at hand, the good correspondence in average wind direction shown in Figures 2-5 and 2-6 suggests that we might decompose the hourly perturbations into components lying along the pattern vector and normal to it. If the pattern changes, then we can consider a decomposition along a series of direction pairs that evolve linearly from the initial pattern direction to the subsequent pattern direction. If we then assume that the perturbations are nearly independent over several hours, it is possible to estimate the pattern amplitudes at the beginning and end of the transition using centered wind velocity averages at the time of the pattern measurement. With these assumptions, it is possible to attempt to further decompose

the variance associated with the sorted wind categories based on the amplitude and direction properties. This decomposition is illustrated in Figure 5-1.

The hypothesis underlying this decomposition is that the wind is composed of both a low frequency component that is measured by the sea surface pressure maps, and a higher frequency component that is superimposed on the fundamental flow. This higher frequency component should exhibit low time-wise correlation if our amplitude estimating technique is to be valid.

A simple test of this hypothesis was performed. The variances of the along and normal-to perturbations measured as in Figure 5-1 are shown plotted against the low frequency wind amplitude in Figures 5-2 and 5-3. Both summer and winter cases are shown. Notice that no dependency is suggested for the summer case, but that a strong dependency appears in the winter case. We suspect that the summer case variance is a measure of the intrinsic variability associated with the measurement technique. It might, for example, be associated with high frequency aliasing of the anemometer record. The winter case variance, however, is seen to grow with pattern strength. This variance may well be due to important meteorological phenomena that are of too small a scale to be resolved in the analysis underlying the sea level pressure maps.

We also examined the covariance between these perturbation components and found them to be uncorrelated. The principal axis of the perturbation was, therefore, in the normal direction (since this had the larger variance in both spring and summer) and the minor axis lay in the direction of the smoothly rotating wind pattern vector.

We know from Figures 2-5 and 2-6 that the average of the normal perturbation must be nearly zero for each of the wind patterns at Middleton Island.

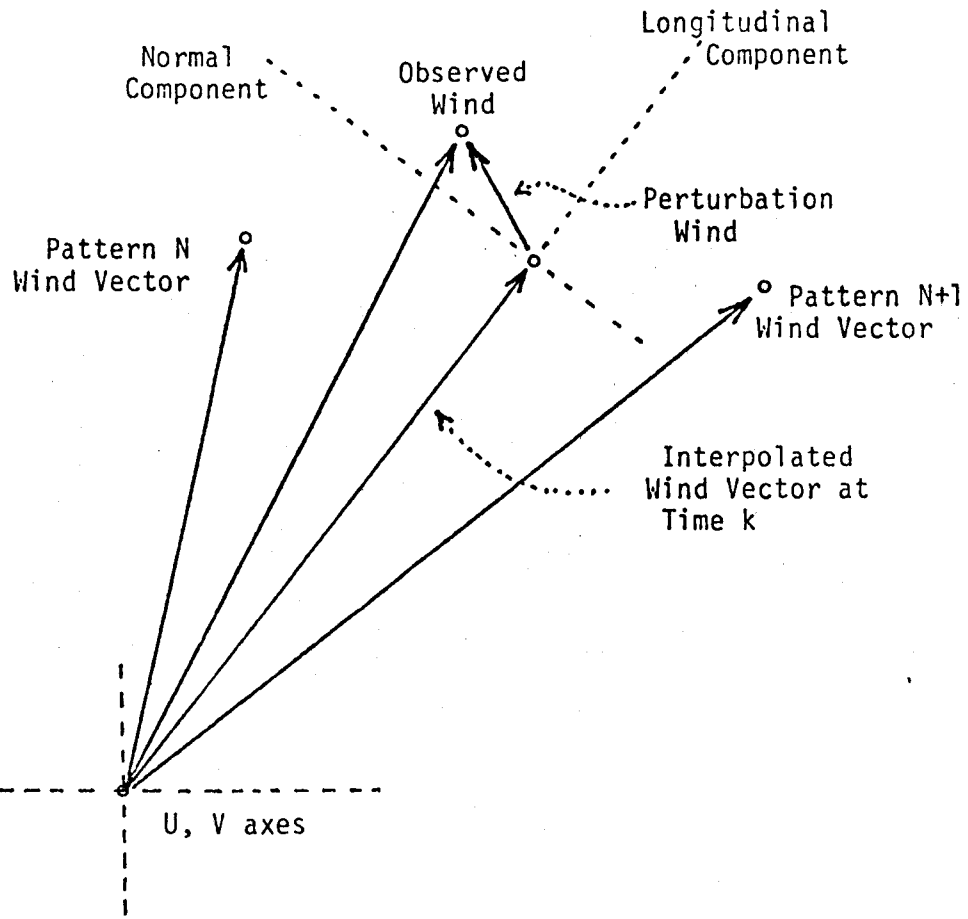


Figure 5-1. Vector plot of relationship between model predicted winds, measured winds and wind perturbation.

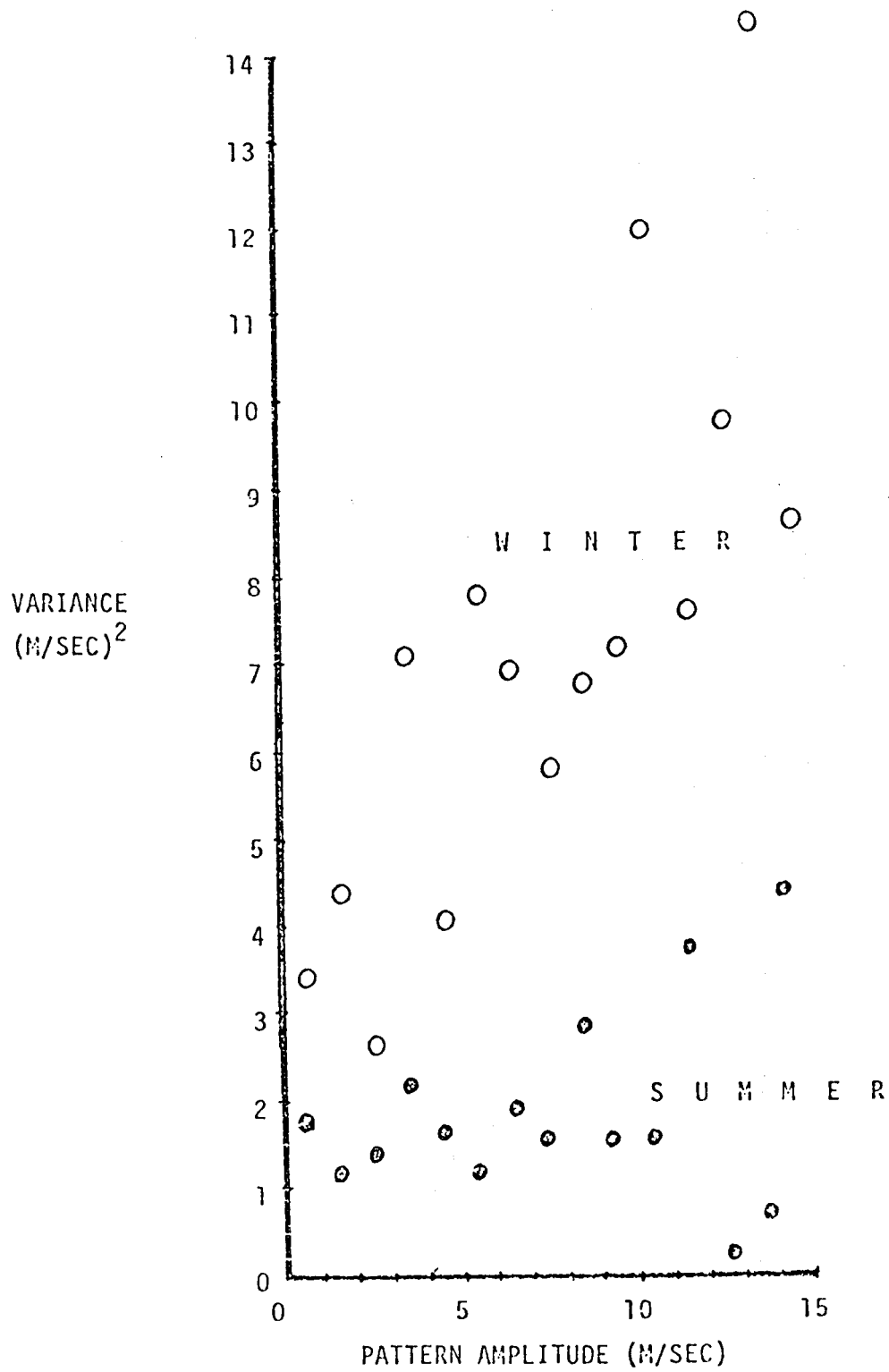


Figure 5-2. Variance of the Longitudinal Wind Velocity Perturbations.

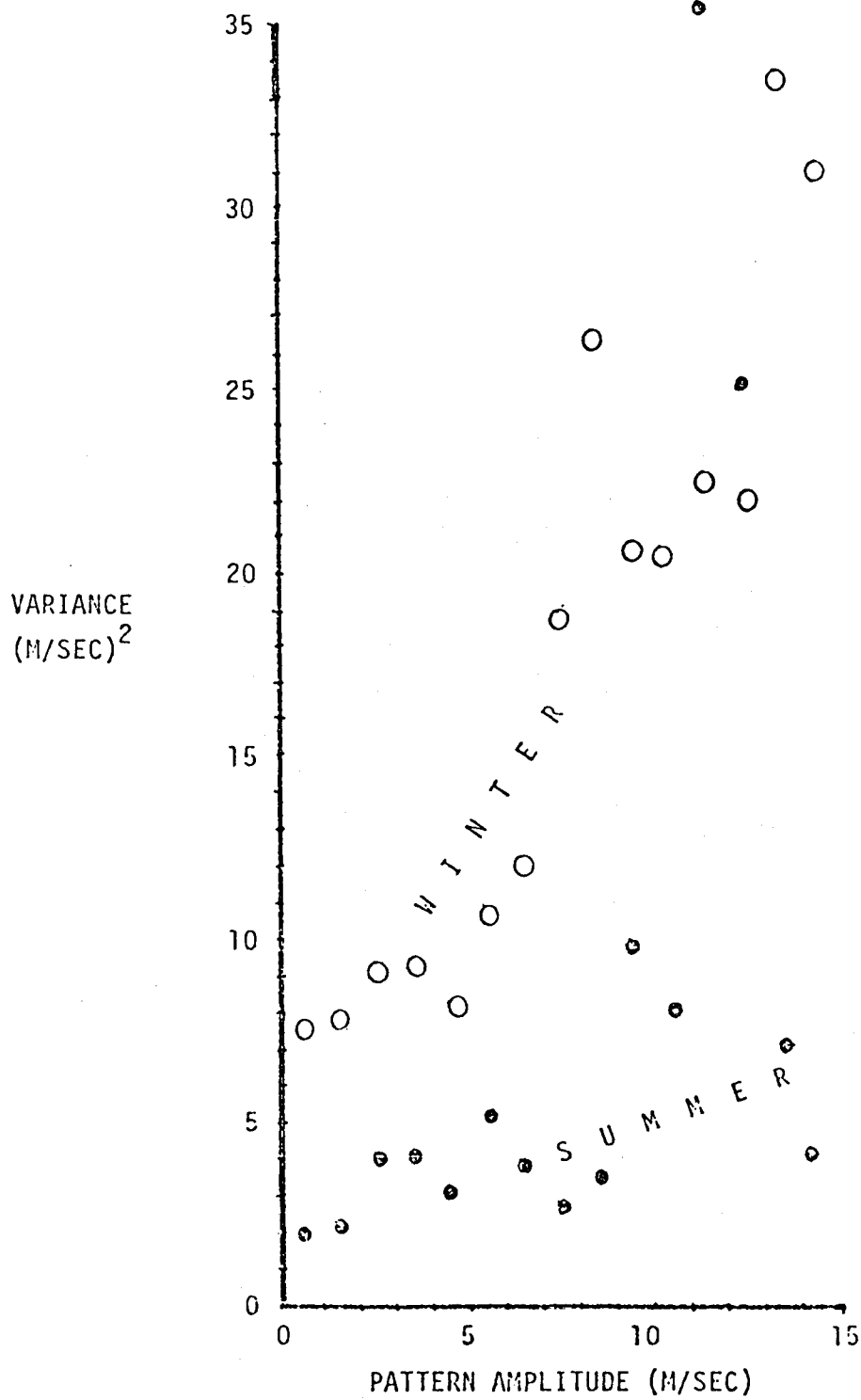


Figure 5-3. Variance of the Transverse Wind Velocity Perturbation.

If they exhibited a nonzero average of large magnitude, the vector averages would not lie in the vicinity of the pattern direction. The existence of large non-zero averages may be considered evidence of bias in the wind field patterns. Figure 5-4 shows the average of the along and normal-to perturbations as a function of low frequency wind amplitude. The summer case shows no important bias over the range of wind speeds studied. The winter case, however, suggests that the pattern vectors are rotated too far to the right by 5° or 10° at wind speeds of around 10 m/sec. Again, a statistical interpretation of this result is very difficult. We have sketched the 1σ confidence intervals assuming the data is independent. In fact, the zones should be larger. Nevertheless, the strong pattern shown in the figure leads us to believe that this result is significant, and it therefore merits further study.

We also examined the time-correlation of the along and normal-to perturbations. The correlations of the dimensional perturbation velocity components were very similar to those found in first order autoregressive processes. Typical time scales were on the order of $2\frac{1}{2}$ hours for the along components and 3.8 to 4.8 hours (summer and winter respectively) for the transverse component. When these perturbations were normalized by dividing by the pattern amplitude, the new variate showed almost no correlation over lags of one hour.

These observations suggest several things. First, the wind model can be considered a useful analog of the real surface wind. It is a practical solution to the problem even though we know it has imperfections. The data from EB33, for example, showed that the model may have errors in the specification of the wind direction that range from near zero to as high as 45° , with a typical estimate being 10° to 15° . Errors of this type are

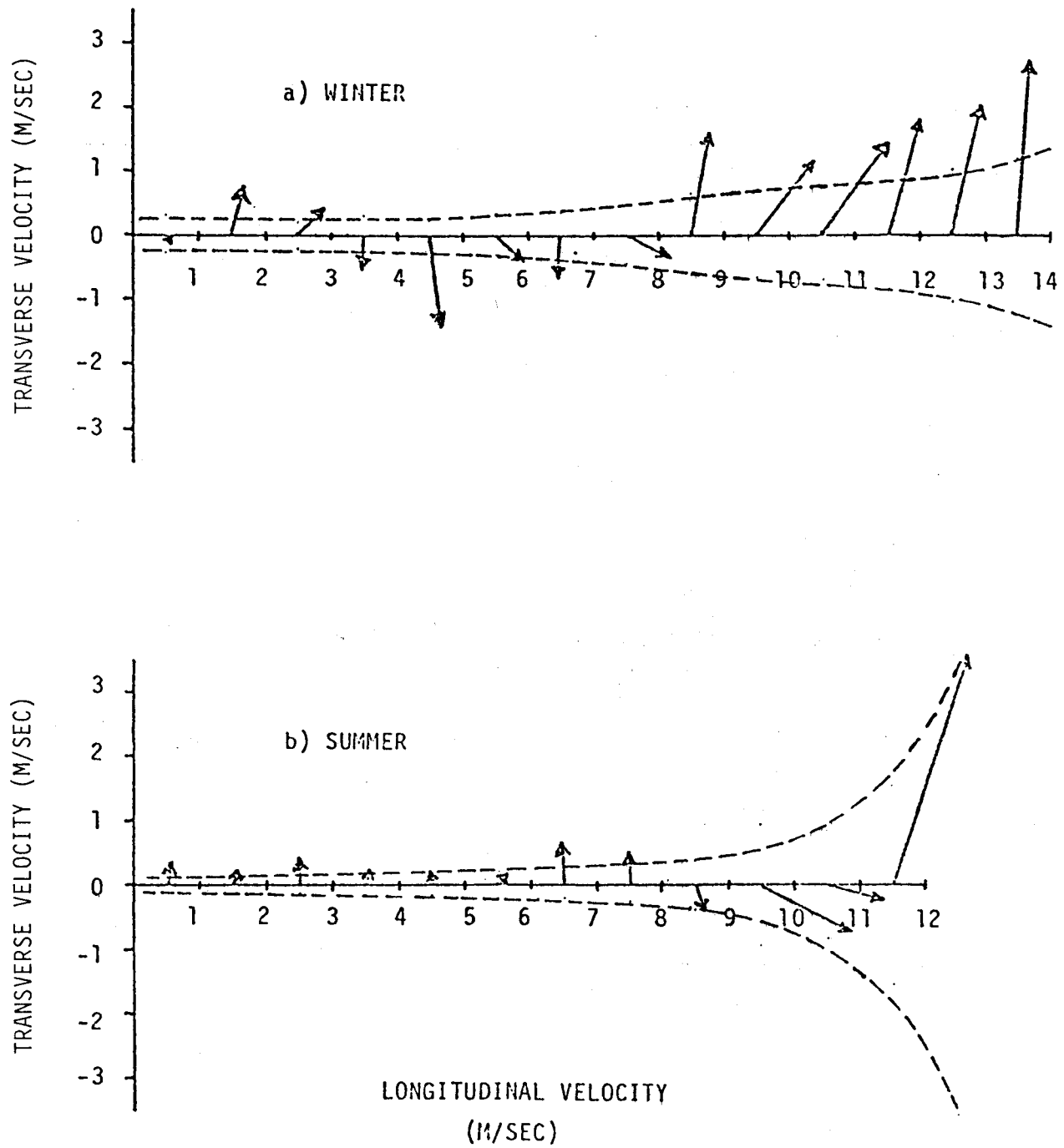


Figure 5-4. Observational Bias in the Wind Perturbation as a Function of Pattern Amplitude.

probably a function of position in the region. These nominal, and in principle correctable errors are to be compared with the much larger errors that would accompany a uniform direction model such as those used in past trajectory studies.

It is also apparent that a large portion of the wind velocity's variance can be explained by transitions between wind patterns. Further, the remaining variance can be explained in terms of longitudinal and transverse components with magnitudes that are proportional to the wind pattern strength in winter, and constant in summer. If this decomposition can be substantiated using other data sets in the NEGOA region, it presents the important possibility that the wind field could be completely synthesized using just the sea surface pressure maps. This would open the door to a true climatological analysis since the requisite pressure map data is available for very long periods of time.

We have not examined the relative amplitude information contained in the wind patterns. This analysis will require several simultaneous time series coupled with a more thorough understanding of the velocity perturbation problem including its spatial dependencies. It is a logical follow-on to the present study.

The current model was also examined. The important questions were whether the decomposition into barotropic and baroclinic geostrophic modes was justified; whether the assumption that the time variability was simply linked to the applied stress pattern; and whether these perturbations were well modeled by the transitions of barotropic modes.

Although our data base is rather limited, it appears that the decomposition into a baroclinic (and minimum barotropic) mode was a useful simplification. Figure 5-5 shows the long term, vector average current at stations 60 and 62B for the summer and winter seasons respectively. This

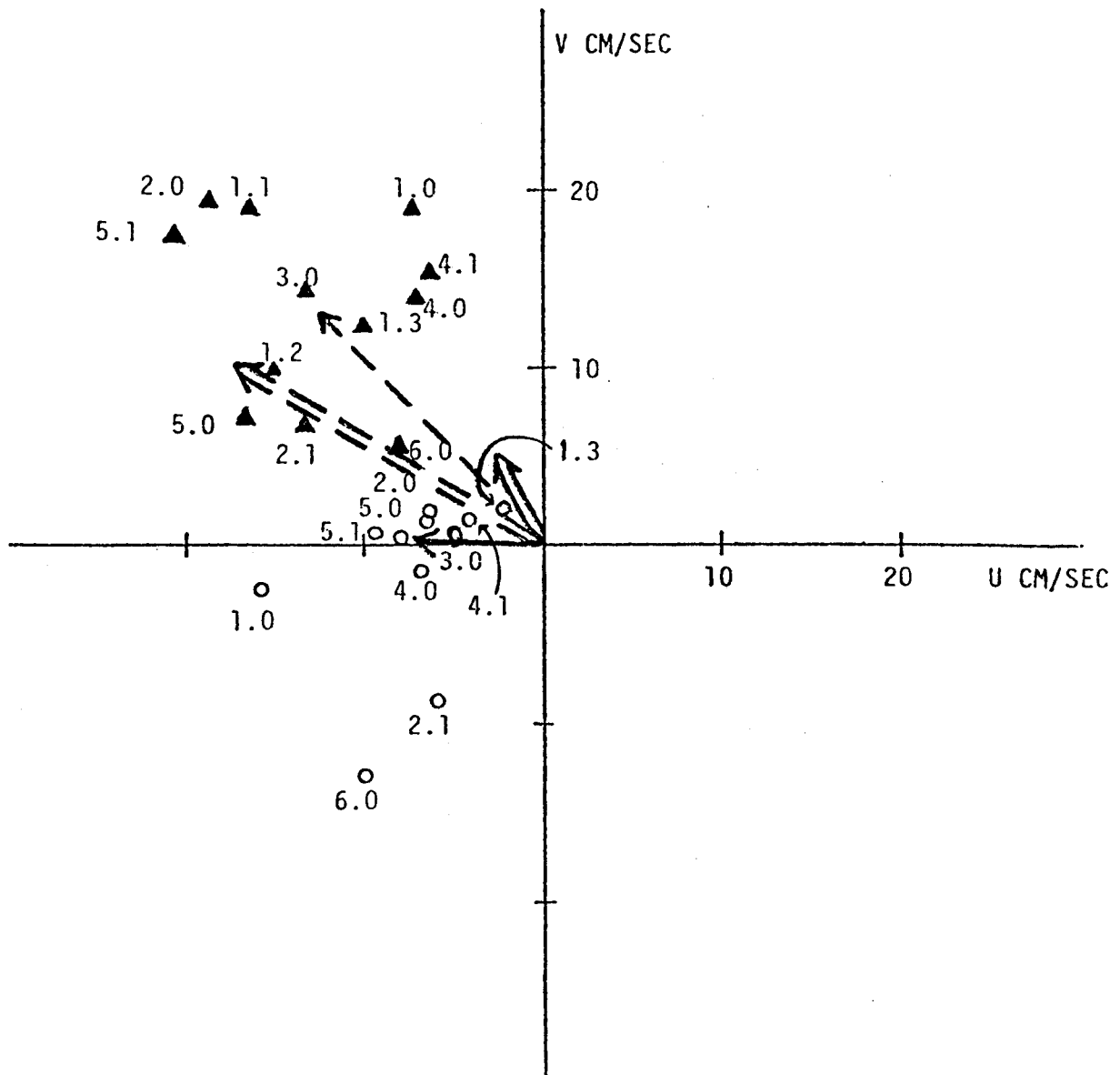


Figure 5-5. Comparison of observed currents by pattern type for winter station 62 (▲) and summer station 60 (○). Single line and double line vectors represent the mean observed current and the baroclinic component respectively; dashed for winter, solid for summer.

long term average should correspond to the baroclinic mode under the assumptions that the density field is reasonably constant over the period in question and that the average, wind-driven barotropic component is nearly zero. This long term average current is also shown in Figure 5-5. It is readily seen in Figure 5-5 that the baroclinic current exhibits some angular error, with respect to the long term average current in both cases, with the most pronounced error occurring at Station 60, which is in the Copper River gyre. The error in direction at Station 60 might be associated either with the coarse resolution provided off the Copper River gyre by the hydrographic stations, or it might represent some net contribution from the wind-driven barotropic modes. Despite this angular error, however, we can see that the magnitudes of the baroclinic velocities are approximately correct for both cases. It is our judgement that these results are in sufficient agreement to warrant preliminary acceptance of the decomposition techniques.

The second question was whether the current perturbations could be usefully sorted based on the weather pattern. Figure 5-5 also addresses this question. It shows the average observed currents sorted by pattern type. The standard deviations for these averages were typically on the order of 1 to 3 cm/sec assuming the samples were independent. Correcting this range upwards to account for the probable correlation between samples, we find that the analysis does not support grouping of current observations by weather patterns, since all the groups are close to the overall mean current vector. We have also performed an analysis in which the currents lagged the wind patterns and found a similar lack of support for the simple wind-driven hypothesis. We believe this is caused by strong high frequency oscillations in the data associated with tidal motions, shelf waves, and other phenomena not considered in our model formulation.

Because the sorting by pattern type was not successful, it is premature to compare the individual barotropic current modes with the current meter observations sorted by weather type. A logical follow on to the present work would be to examine the filtered data to see both if it could be usefully sorted by pattern type and if the residual exhibits properties like those predicted by the barotropic modes.

For the purposes of the trajectory model it appears that we can reasonably expect the baroclinic currents to be well modeled. The remainder is best treated as a stochastic residual. It is not realistic to expect this residual to be constant over the spatial domain. Bottom topography and other effects will undoubtedly channel and amplify the perturbations. As an approximate, but theoretically somewhat justifiable approach, we therefore will use the barotropic response to scale and direct the perturbations. The exact algorithm is discussed in the following chapter.

6. Trajectories

In physical terms, the trajectory model is composed of several FORTRAN programs and a variety of data sets that depict the spatial and temporal variability of the wind and current. The main trajectory program, AMCTRAJ (Appendix G), calculates the boundary location of an oil spill given wind and current time series, wind and current patterns, and starting date and locations. The output from this program is then converted to graphical plots of the trajectories using the program PICTUR and loadsets specific to our plotting equipment. An auxiliary output is also available from AMCTRAJ which can be used to generate the stick plots of the wind and current time series as seen at the wind and current stations and at the simulated spill.

The principal considerations for the design of the program AMCTRAJ were the storage requirements for the extensive spatial fields of the wind and current. Approximately 46,000 words were required for storage in the program. These problems were discussed above in the description of the environmental libraries. The numerical algorithm that uses these fields to calculate a simulated oil spill trajectory is relatively simple and will be described below. This functional portion of the program required a relatively small amount of core, about 24,000 CDC words.

The important conceptual function of the trajectory model is that it implements a number of hypotheses by which we synthesize the available environmental information into a simulated oil spill trajectory. Although the hypotheses relating to our description of the environment have been discussed separately in the various sections above, it is useful to reiterate them here.

1. We have assumed that the surface wind field can be related to large scale synoptic sea level pressure maps. The calculation of the surface wind field was done using accepted procedures, but it has not been verified for NEGOA with independent data, although preliminary results suggest reasonable correspondence. These maps are our only data incorporating both spatial and temporal variability.

2. We have assumed that the sea level pressure maps exhibit characteristic features with sufficient regularity that they can be approximated with a small set of generic patterns. Our preliminary analysis indicates that this assumption is probably acceptable.

3. We have assumed that the current field can be completely decomposed into barotropic and baroclinic geostrophic components. We explicitly neglect tidal and inertial currents, consigning all such currents to simulation via a scaled and rotated perturbation term.

4. We assume the baroclinic current field is constant throughout the simulation period. This is probably a rather weak assumption because there is much evidence suggesting the presence of transient mesoscale eddies along the shelf break.

5. We assume that the barotropic modes are established instantaneously and without lag in response to surface stress applied by the large scale wind pattern. We further assume that the magnitude of these currents will be proportional to the square of the surface wind speed (i.e., proportional to surface stress).

Within this hierarchy of assumptions, it appears that the wind related assumptions are the least suspect in so far as they appear to yield realistic wind behavior. The current assumptions, on the other hand, appear to be rather crude. Not surprisingly, perhaps, the baroclinic current appears

to be the best modeled current component. It fits the long term average current fairly well at stations 60 and 62B. This baroclinic component incorporates data from the quasi-synoptic hydrographic measurements in the region and so in a sense it is analogous to the derivation of the wind field from the surface level pressure. This is to say that the baroclinic current is based on a lot of data that can be combined in a dynamically consistent model. The barotropic current, however, had no directly measured input term, but was in fact calculated from the derived wind fields for the hypothesized generic wind field patterns. Being twice removed from actual data, it is not surprising that it was poorly substantiated by the current meter records.

Because of the poor state of our measurements of currents in the region, these hypotheses should not be judged solely on the basis of how well they fit our very limited data. Hypotheses, in fact, are constructed mainly for the purpose of reducing the data required, and so any data-poor study must rely heavily upon assumptions in the form of hypotheses. The question then becomes whether the hypothesis was sufficiently simple to allow future verification and whether there was any theoretical basis for the hypothesis that might endow it with intrinsic credibility. In the case at hand, the assumption of non-inertial dynamics does allow the theoretical decomposition of the current problem into baroclinic and barotropic portions. There is good reason to suggest that these geostrophic components are important in the net transport problem. Further, the assumption is subject to easy validation given more extensive current meter records than those examined here. Thus, the assumption provides a practical first step towards grappling with the larger problems.

In addition to hypotheses regarding the synthesis of the environmental data, the model is also dependent upon an hypothesized oil transport equation.

It is beyond the scope of this report to detail the uncertainties we presently face regarding the mechanisms responsible for oil spill transport on the ocean. However, it should be pointed out that there is neither a substantial theoretical basis for the oil-on-water problem, nor is there a data base of sufficient size to suggest an empirical basis. In these circumstances we have simply assumed that the velocity of the oil will be given by the vector sum of the current velocity and three percent of the wind velocity. This is a formulation that is generally accepted and which has some empirical evidence to support it.

Figure 6.1 shows the method used to synthesize the local wind velocity. The surface wind fields were utilized to provide the relative magnitude and the direction of the local wind. The absolute magnitude of the local wind was obtained from the time series data by comparing the twelve hourly centered average of the time series data to the wind field magnitude at the anemometer station. The factor formed from the ratio of these numbers was then applied to the local wind velocity. Thus, if the wind field showed a wind velocity of 12 m/sec to the NW at the local coordinate, and if the nominal wind speed at the anemometer location was 10 m/sec whereas the twelve hourly average was 5 m/sec in the time series data, the wind field would be scaled by $(5 \div 10)$, resulting in a modeled wind of 6 m/sec to the NW at the local coordinate.

Hourly perturbations were then added to the scaled wind field velocity to simulate the higher frequency changes. These perturbations were calculated by first determining the differences between the hourly time series velocity and the scaled wind field velocity at the anemometer location. This perturbation was then resolved into components lying along and normal to the vector of the wind field velocity. These components were then scaled by the ratio

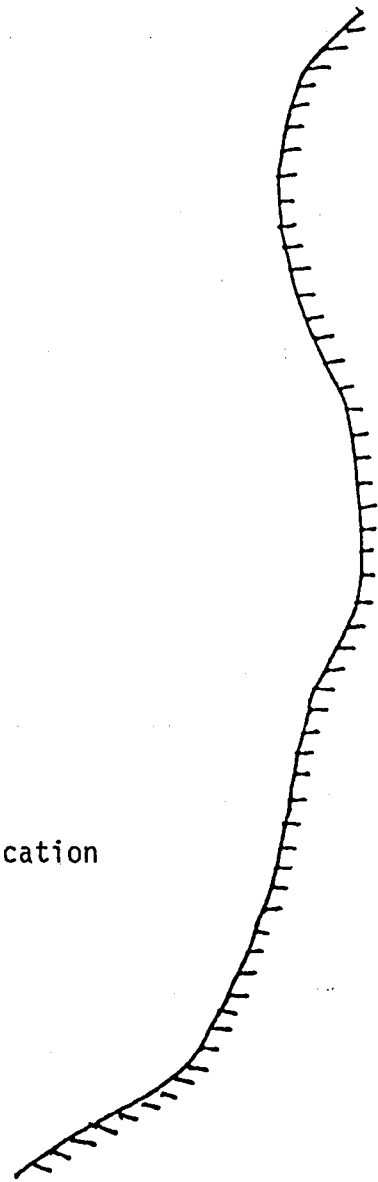
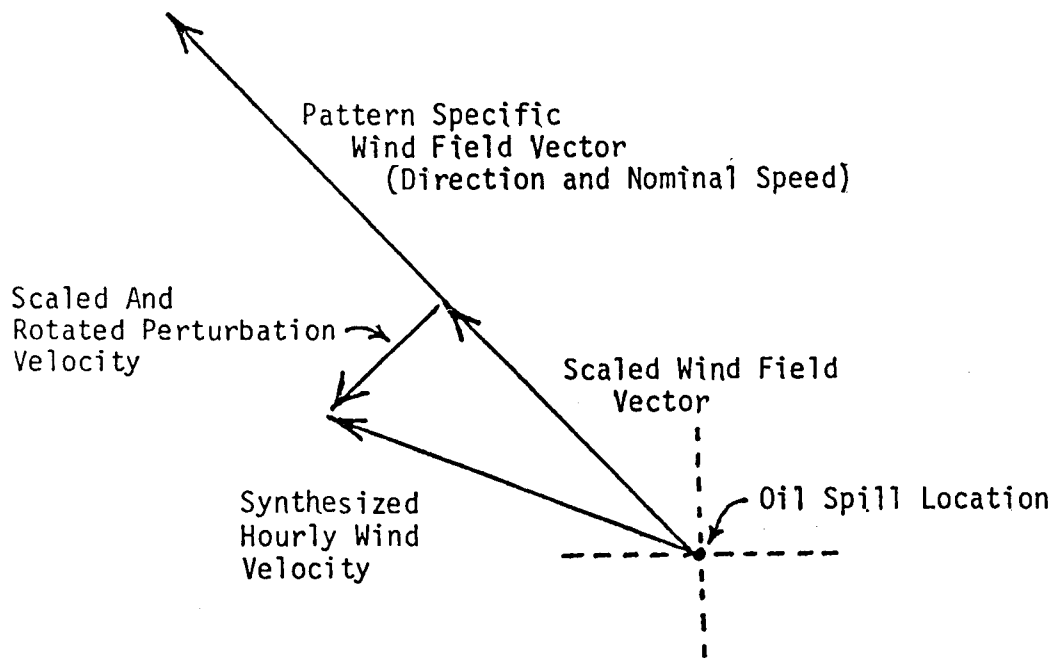
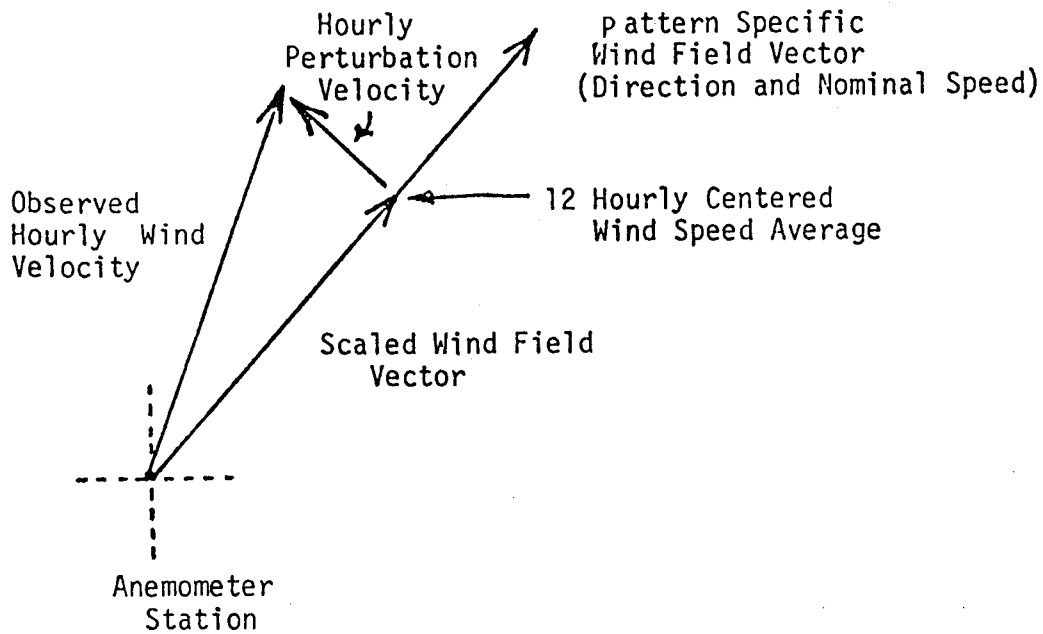


Figure 6-1. Vector representation of method used to calculate magnitude of local winds and perturbations in the wind field.

of the wind field speed at the local position and the wind field speed at the anemometer. Finally, the perturbations were then added in the along and normal to direction relative to the local wind velocity. Thus in the example above a perturbation of 1 m/sec lying to the left perpendicular of the wind field velocity at the anemometer station would be scaled by $(12 \div 10)$ and added to the local velocity in the left perpendicular direction. In this case, the direction of the perturbation is towards the SW since the field velocity was to the NW, and the amplitude would be 1.2 m/sec.

Figure 6-2 shows the technique used to synthesize the current velocity. This technique was related to that used for the winds. However, under the assumption of geostrophic motion, the dynamical balance governing the currents will require the perturbations to nearly follow the bottom topography. Although this quasi-steady assumption will not be valid for high frequency motions, we felt it plausible to require that the perturbations be oriented with respect to the axis of the barotropic current velocity. Therefore, the baroclinic component is first subtracted from the observed (hourly) current at the current meter location. A perturbation velocity is then determined by subtracting the barotropic current component from the residual. This perturbation is then resolved into along and left perpendicular components relative to the barotropic current direction. These perturbations are then added to the local barotropic current in coordinates rotated to coincide with the local barotropic direction. The barotropic current is scaled by the square of the wind field strength. The perturbation components are scaled by the ratio of the local barotropic current to the barotropic current at the current meter location. Thus periods of strong winds in the time series data will induce strong barotropic motion and locations with low relative barotropic current velocities will have correspondingly small current perturbations.

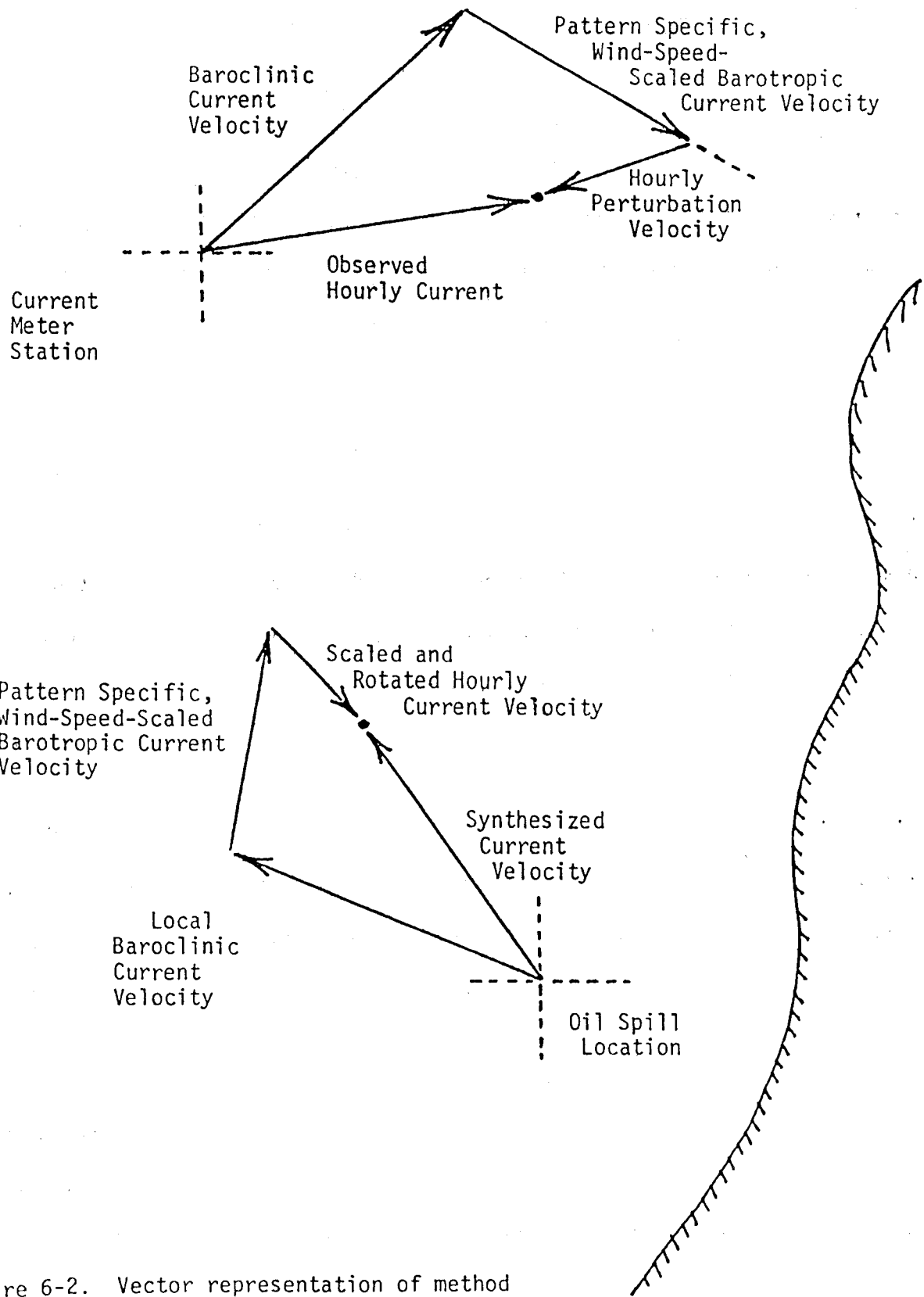


Figure 6-2. Vector representation of method used to calculate magnitudes for local wind-set-up currents and cumulative current perturbation velocities.

It should be noted that the perturbation incorporated into the wind set-up current mode is a measure of the cumulative errors that are seen in the entire current prediction process. Errors in the current meters, wind field typing errors, errors in the bathystrophic assumption, errors associated with the baroclinic current resolution and errors induced by the model dynamics are all lumped at this point. In this sense the perturbations are a measure of the total system errors and should not be associated with the single barotropic wind-set mode.

The combined model is now available to carry out trajectory analysis for the NEGOA region. For purposes of this demonstration seven release sites have been chosen (figure 6-3). A summer period of July and August, 1974 and a winter period of February and March, 1975 are investigated. At each site a release is hypothesized every five days and the trajectory is continued until it either exits the model or exhausts the two month study period.

The summer period will be considered first. The baroclinic data for this period was collected in July, 1974 and is described in section three of this report. This component of the flow is dominated by the mesoscale currents induced by eddies along the continental slope. On the shelf proper the baroclinic currents are generally weak, but the anticyclonic gyre to the west of Kayak Island is evident. The winds for the period are usually weak with types 4 and 5 present throughout the record. The perturbations in the currents are obtained from NEGOA current station 60 which is located just off shore from the Copper River. It is useful to note that this is an area where the predicted currents are quite weak and variable. Since these observations will determine the scale and relative directional stability of the predicted currents throughout the model we can expect that the choice of this current meter as a keying station will lead to a relatively

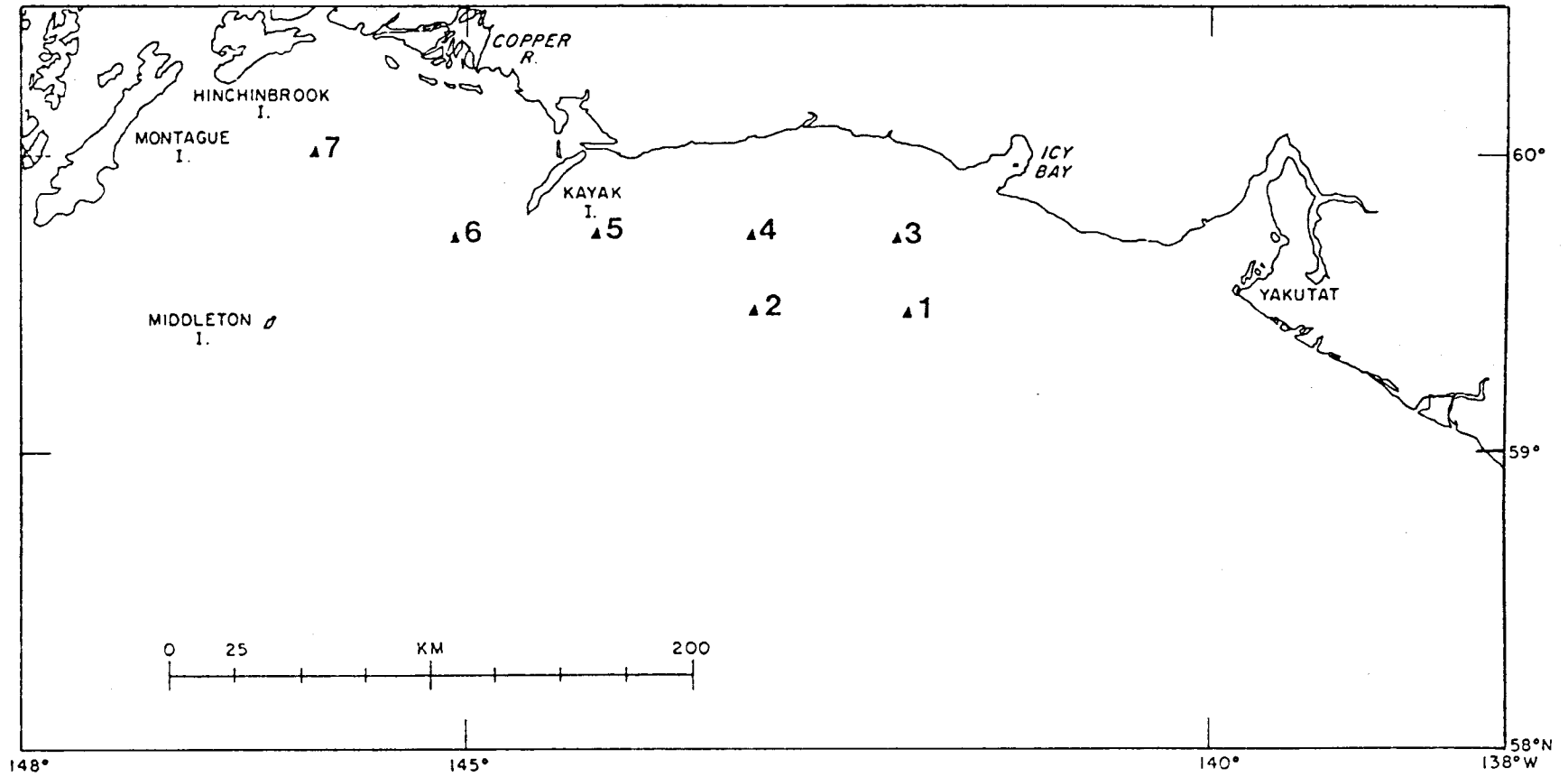


Figure 6-3. Chart of release sites for NEGQA trajectory studies.

high level of uncertainty. This will be reflected in the trajectories as increased scatter. In retrospect, current station 60 would not be considered an optimal choice and had model results been available prior to deployment alternate locations should have been considered. Despite the problem of this station placement it should be clear that the model results will still be correct within the context of the formulation and accurately represent the uncertainty inherent in the input data.

The trajectories from release location one are shown in figure 6-4. This release point is located on the outer continental shelf southwest of Icy Bay. From this point the trajectories are seen to move towards shore with a potential threat to about 150 km of the coastline. Over this region of shelf both winds and currents are weak and hundreds of hours are typical for transit times to shore.

Trajectory releases from site two are shown in figure 6-5. This location is in the vicinity of the continental slope mid-way between Icy Bay and Kayak Island. These trajectories show a quite different behavior than was seen in releases from site one. They are immediately under the influence of the relatively strong baroclinic current that is due to an offshore eddy interacting with the continental slope. This carries them rapidly to the southwest. Under the influence of onshore winds most of them are eventually moved out of the current onto the shelf, where many are seen to move in a clockwise arch following the deep valley that cuts across the shelf southwest of Yakutat. This example also shows several interesting exceptions. Two trajectories move quickly onto the shelf and progress more or less directly onshore. Two other trajectories are seen to move out of the southwesterly baroclinic current in an offshore direction and their movement is then dominated by the offshore baroclinic circulation.

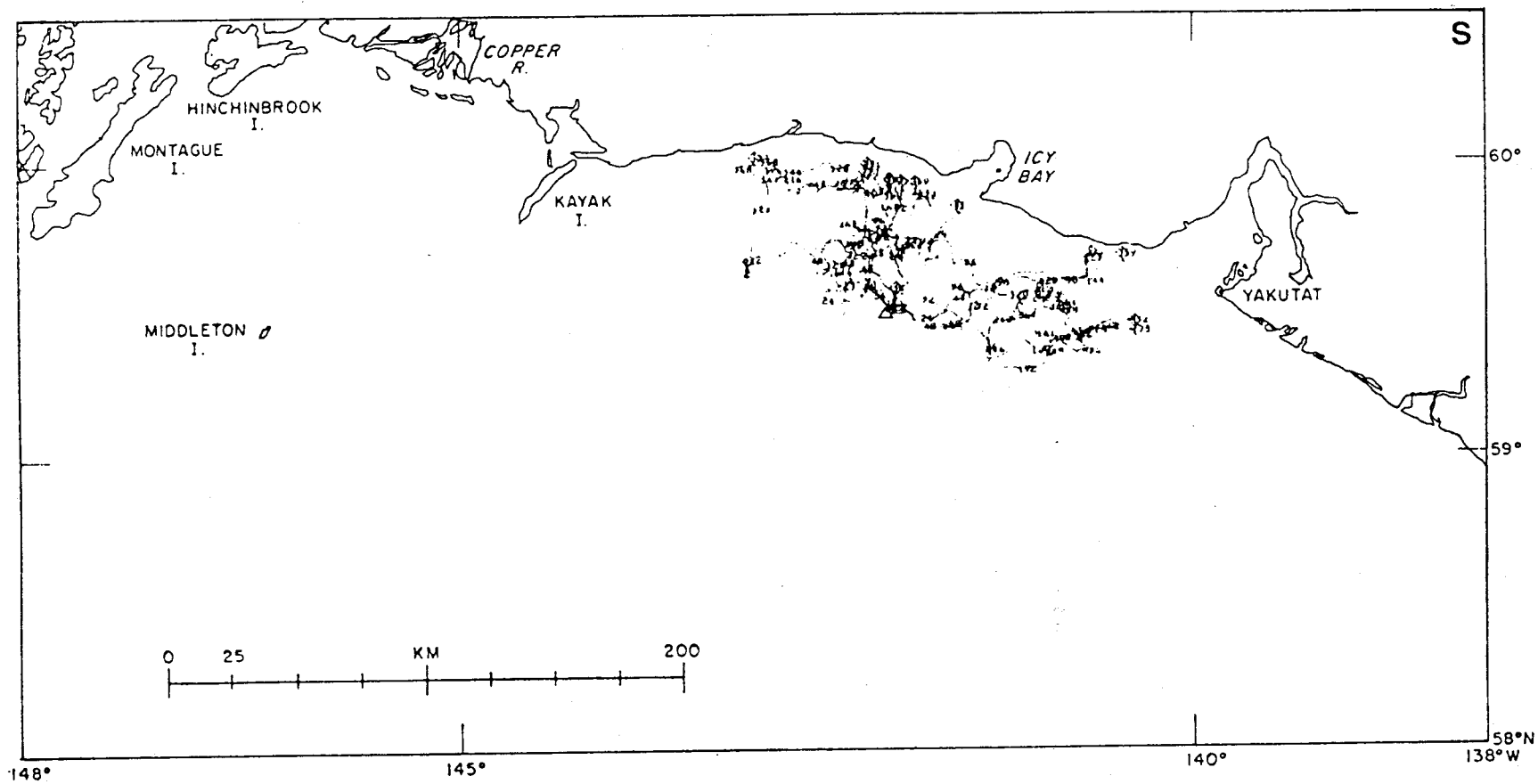


Figure 6-4. Summer trajectories of releases from site one.

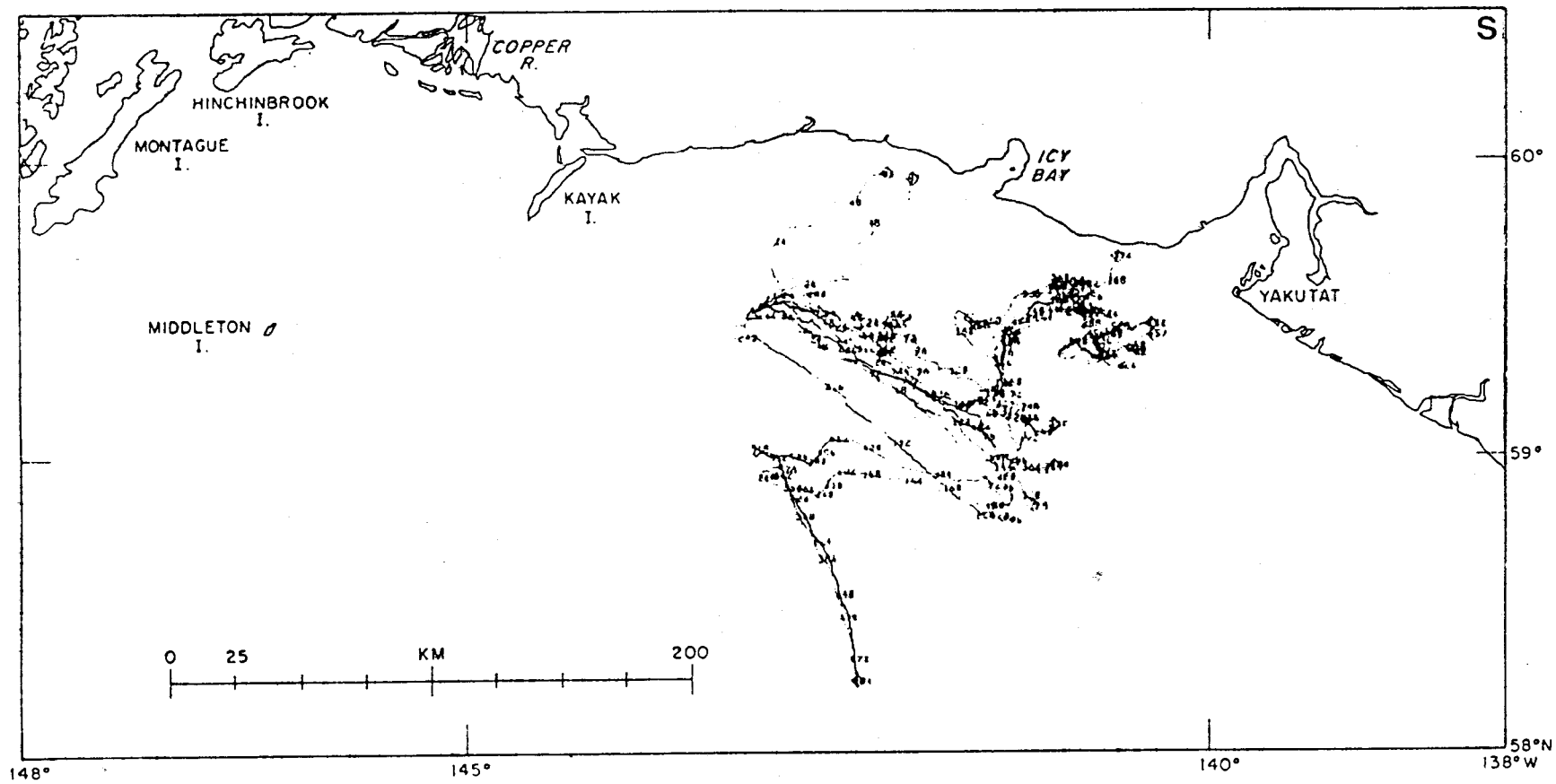


Figure 6-5. Summer trajectories of releases from site two.

It is interesting to note that a satellite tracked drogoue released from the spill of the ARGO MERCHANT seemed to follow a similar sort of dynamic path associated with a baroclinic Gulf Stream eddy.

Release site three is on the shelf southwest of Icy Bay. Trajectories leading from this point are shown in figure 6-6 and for the most part move directly towards the coast with the exception of a couple that move towards the east, apparently dominated by weather types 5.0 and 5.1.

Release site four is on the shelf mid-way between Icy Bay and Kayak Island. Trajectories from this location are shown in figure 6-7. This is a region of complex bathymetry and although the trajectories generally lead north and northwest wide variations are seen both in pathways and transit times.

Release site five is on the shelf southeast of Kayak Island. Trajectories from this site are shown in figure 6-8. Most of the trajectories tend towards the coast, but this is once again a complex area where the shelf is quite narrow. Some of the trajectories are seen to lead offshore and come under the influence of the baroclinic currents along the continental slope, traveling nearly two hundred kilometers before being blown out of the stream back onto the shelf.

Release site six is southwest of Kayak Island and the trajectories from this point are seen in figure 6-9. From these the anticyclonic gyre west of Kayak Island is seen to dominate the pathways with most of the trajectories showing long residence times and eventually moving towards the Copper River region. A secondary area where these trajectories tend to concentrate is towards the northwest and Hinchinbrook and Montague Islands. One trajectory diverges from the pattern and is seen to move east for about three days eventually going ashore halfway to Icy Bay.

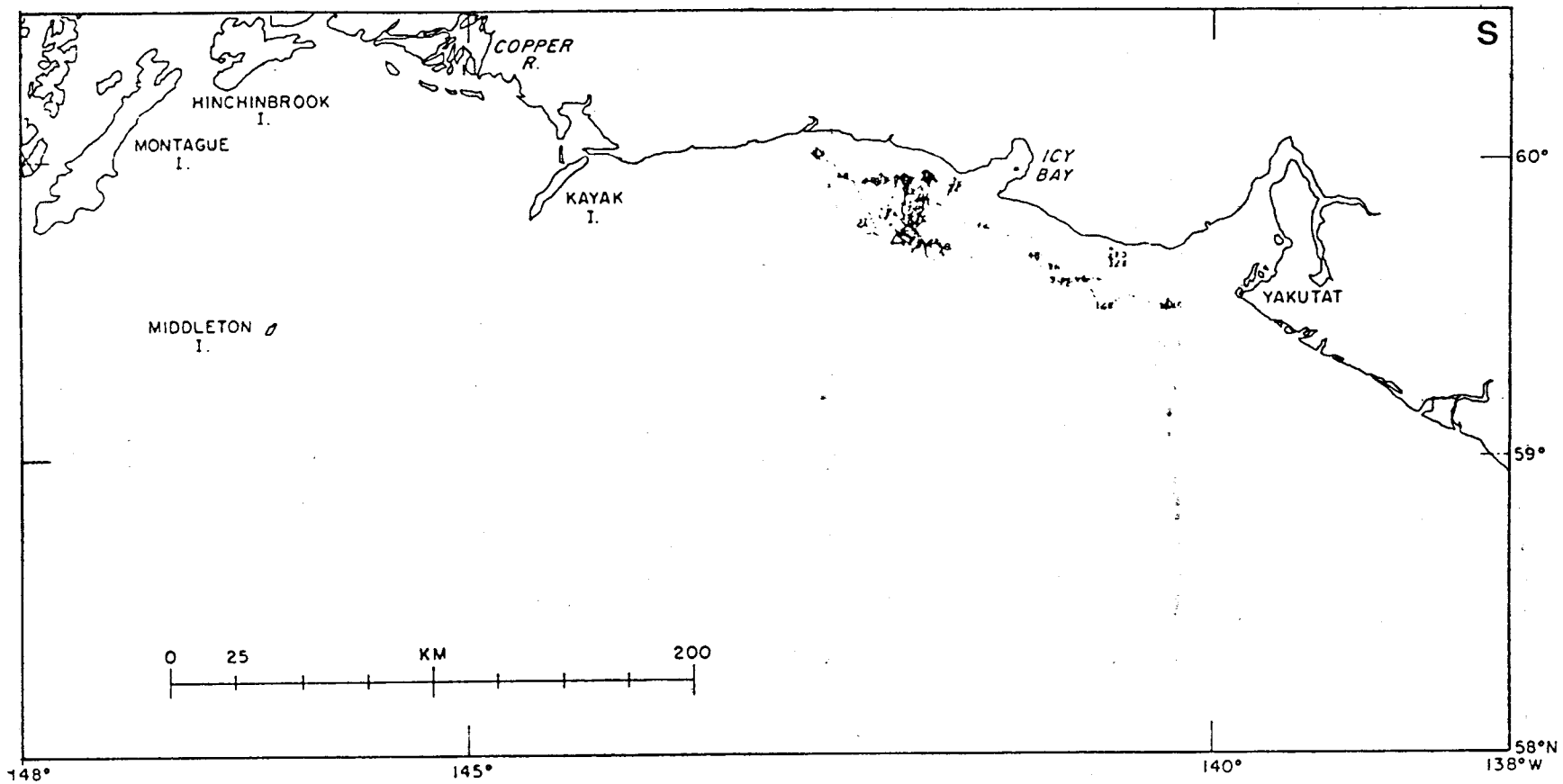


Figure 6-6. Summer trajectories of releases from site three.

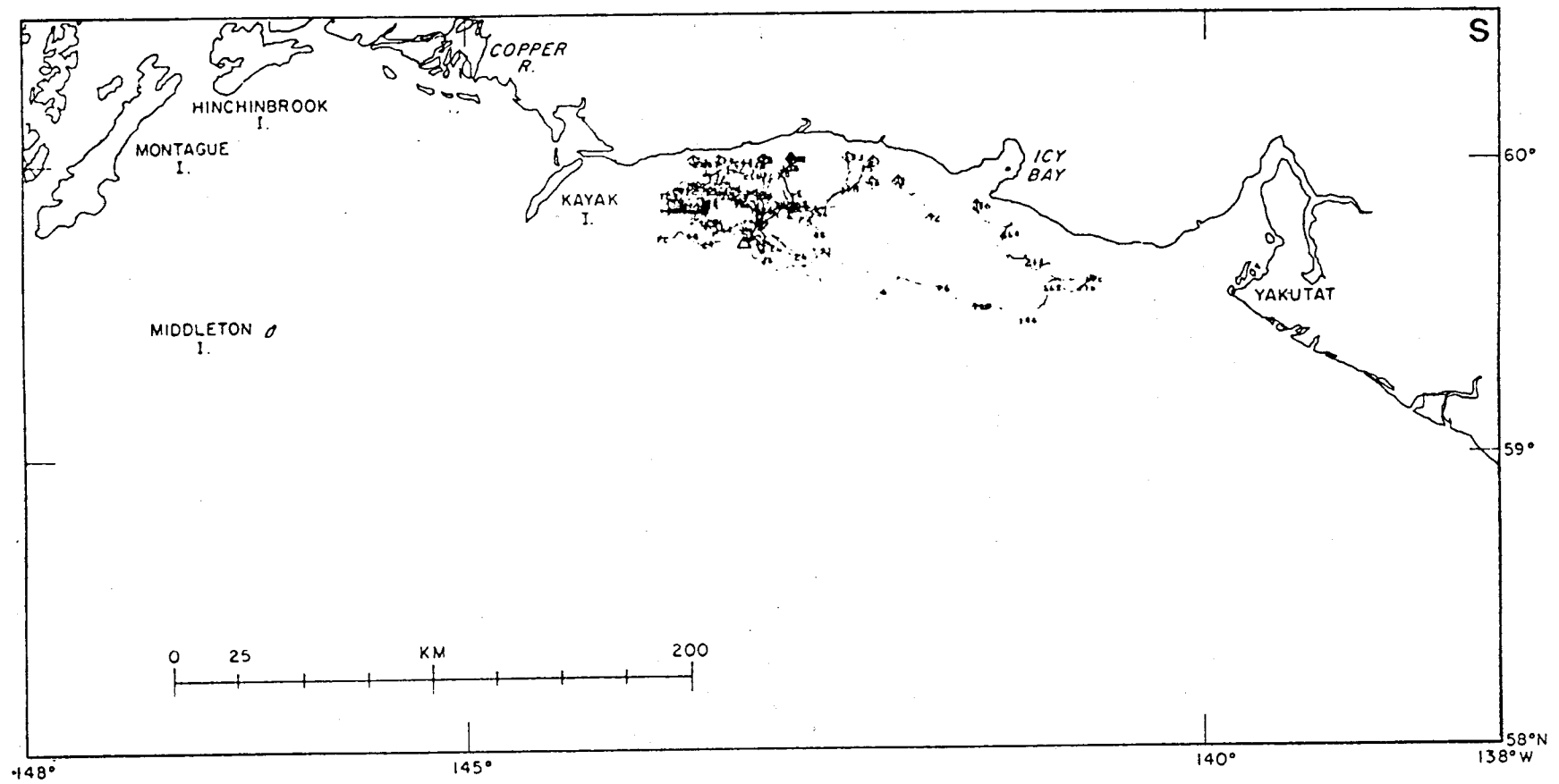


Figure 6-7. Summer trajectories of releases from site four.

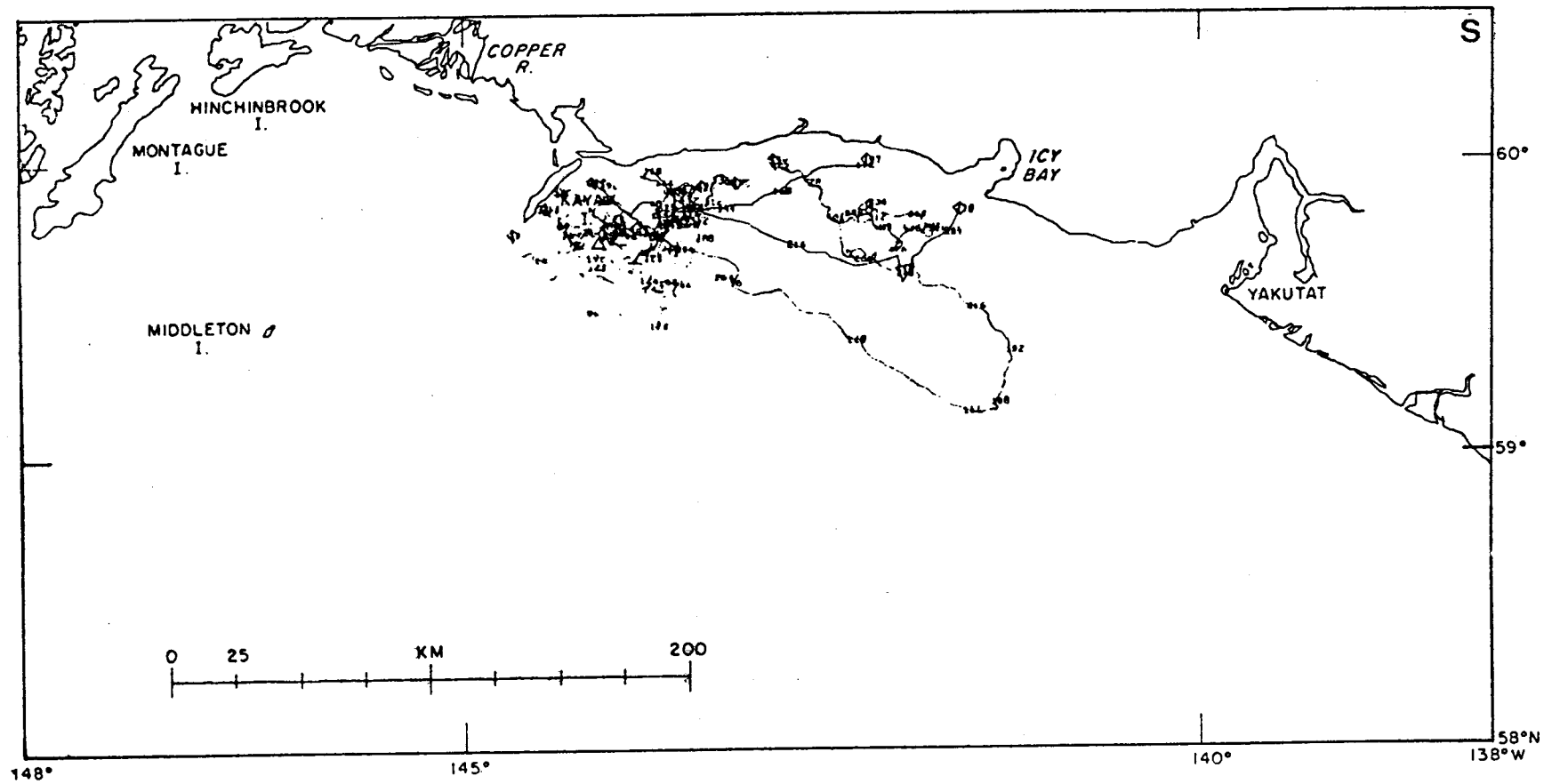


Figure 6-8. Summer trajectories of releases from site five.

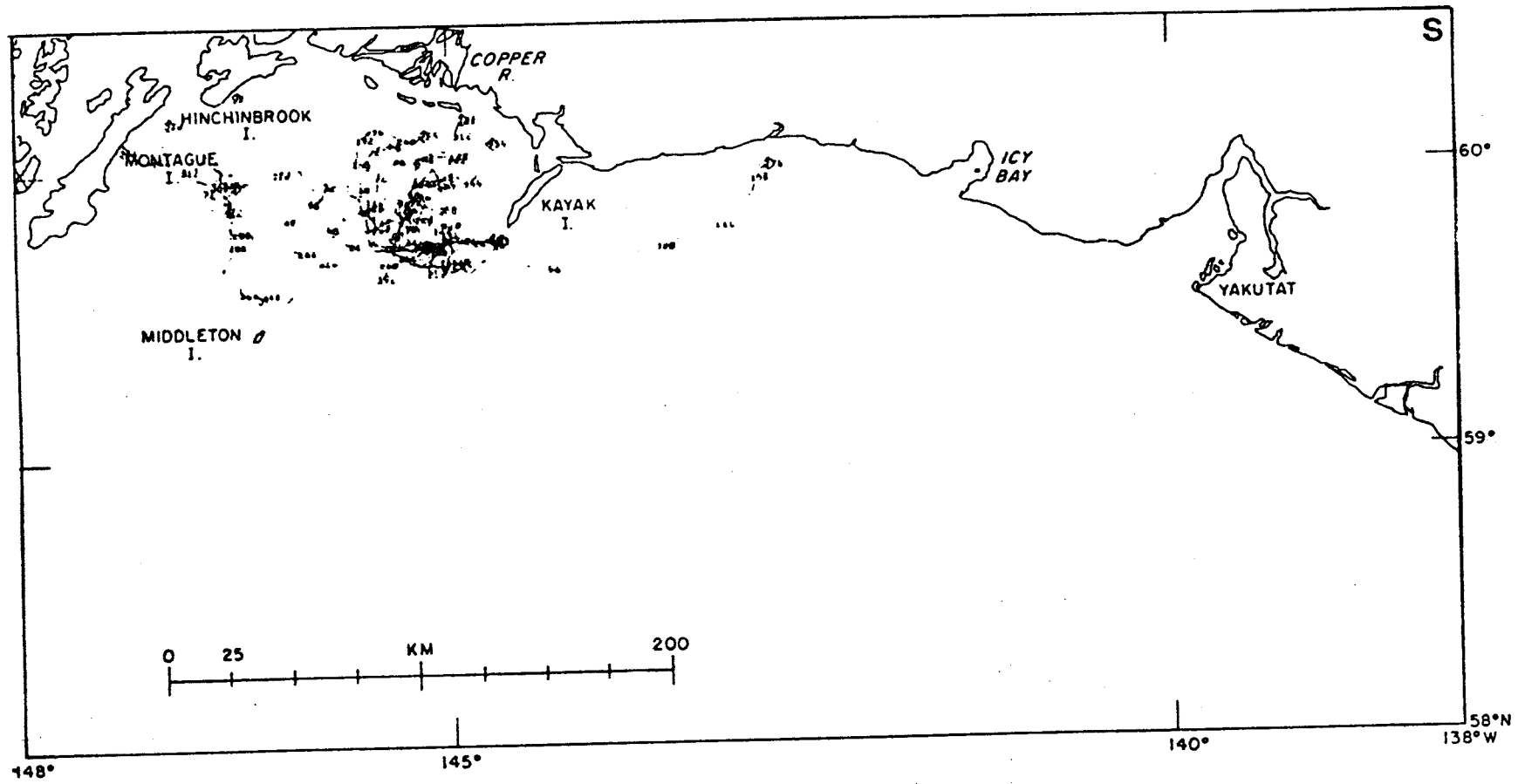


Figure 6-9. Summer trajectories of releases from site six.

Trajectories from the last release site (seven) are shown in figure 6-10. This location is in the region known as Tarr Bank and is situated southeast of Hinchinbrook Island. Releases from this point move onshore and potentially threaten a long section of coast from the Copper River to Montague Island.

A second series of releases were considered for each of the above locations under conditions appropriate for the following winter. The climate types that represented the February and March 1975 period showed proportionately more 1, 2 and 6 patterns corresponding to oceanic lows in various positions. These in turn lead to dominant westerly flow predicted in the wind set-up modes over the shelf. The winds at Middleton Island that were used to scale the model were more energetic than for the previous summer and as a result predicted displacements were generally more rapid. The density data used to describe the baroclinic mode were obtained in February 1975. The field shows strong flows along the continental slope associated with mesoscale eddies offshore. The anticyclonic eddy to the west of Kayak Island is well developed and a generally westward drift is seen along the outer edge of the shelf. This data set does not extend to the east beyond Icy Bay and this sets the limit of the overall model domain. The current meter station used to scale the residual currents was at station 62B which was located near the edge of the shelf southwest of Icy Bay in a region of large bathymetric gradients. This was once again not an optimal choice for a current meter reference station. In this case the predicted currents were significant, but its location near the edge of the shelf put it in an area of strong baroclinic activity and the response to set-up modes was not very sensitive to alternate patterns since it showed strong evidence of bathymetric constraints. Once again the use of this current meter station:

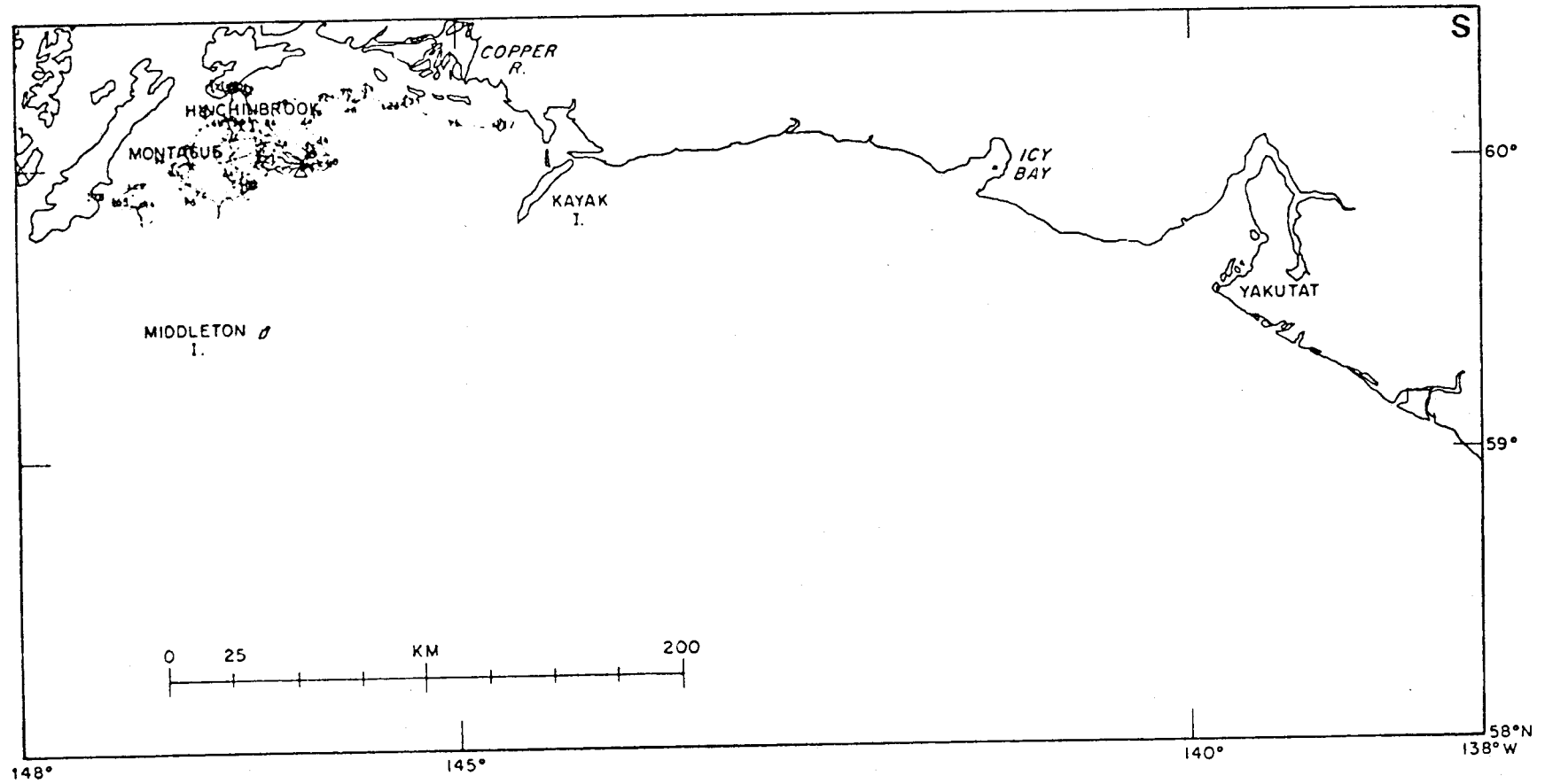


Figure 6-10. Summer trajectories of releases from site seven.

location for scaling the modeled current residual will be correctly represented by a higher level of uncertainty in the trajectories.

Trajectories released from site one are shown in figure 6-11. The majority of these are seen to move northwest across the shelf, although several come under the influence of the offshore eddy south-southwest of Kayak Island. This release site appears to threaten a large section of coast in both summer and winter examples.

Releases from site two are shown in figure 6-12. As before, this location is strongly influenced by the baroclinic currents along the slope and lead to initial displacements to the east. Trajectories that move north out of this current under the influence of the wind appear to establish a northerly movement trending towards the coast. Interestingly, one trajectory pathway escapes south of the gyre located over the slope and reverses the apparent trend by consistently moving out to sea.

Trajectories released from site three southwest of Icy Bay are shown in figure 6-13. The majority of these move onshore covering a seventy kilometer front along the coast. Three exceptions are seen to move offshore where they are clearly influenced by baroclinic flow. Two of the three stay in the current band flowing west along the outer edge of the shelf and end up at Kayak Island. The third track moves even farther offshore and is carried southeast by the continental slope eddy.

Trajectories from site four are shown in figure 6-14. This location shows a wide scatter (recall that it is a region of complex bathymetry) with all but one of the trajectories trending north and west threatening a wide section of coastline. As with site three, one trajectory leads offshore and comes under the influence of the continental slope baroclinic gyre.

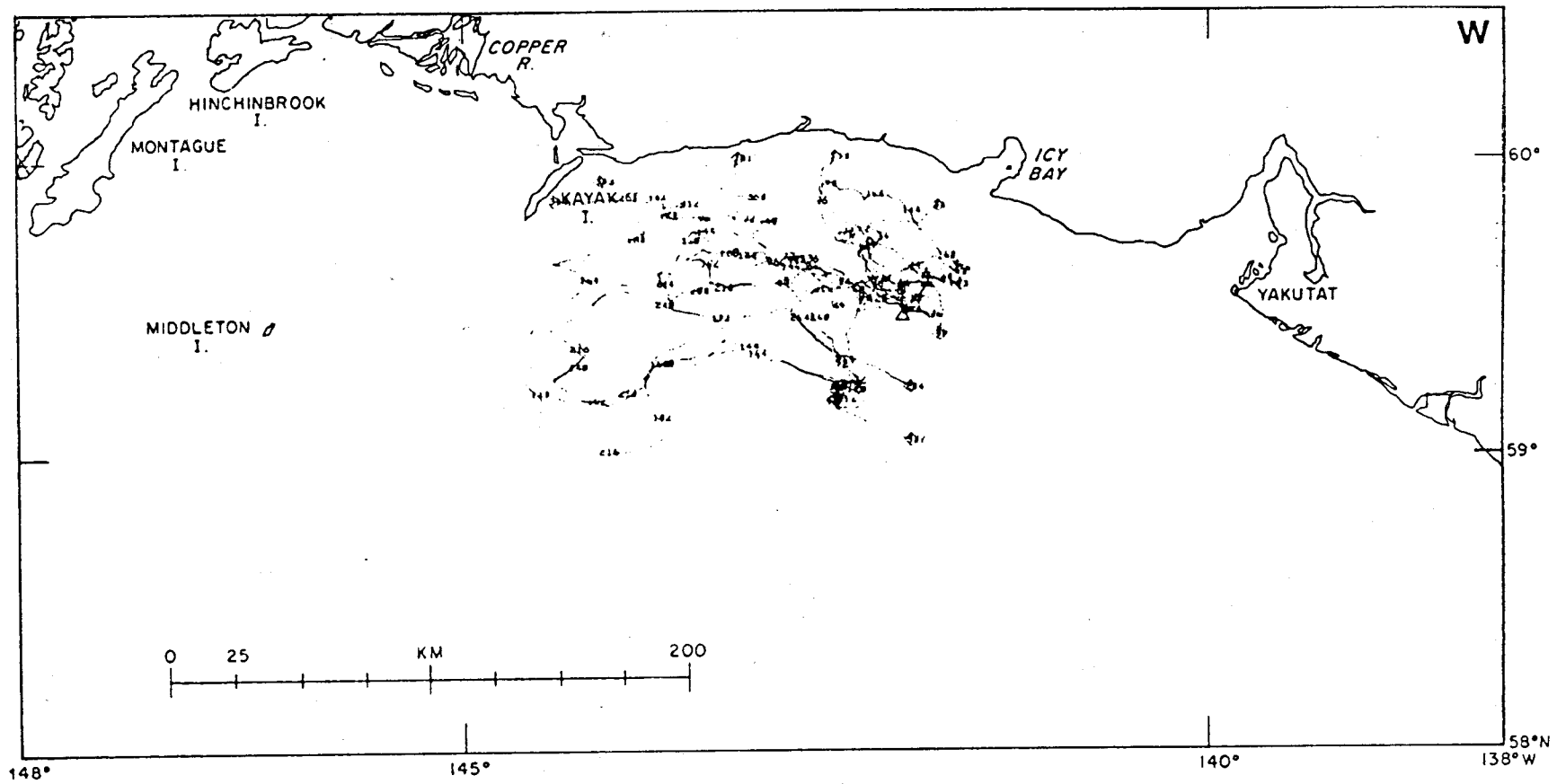


Figure 6-11. Winter trajectories of releases from site one.

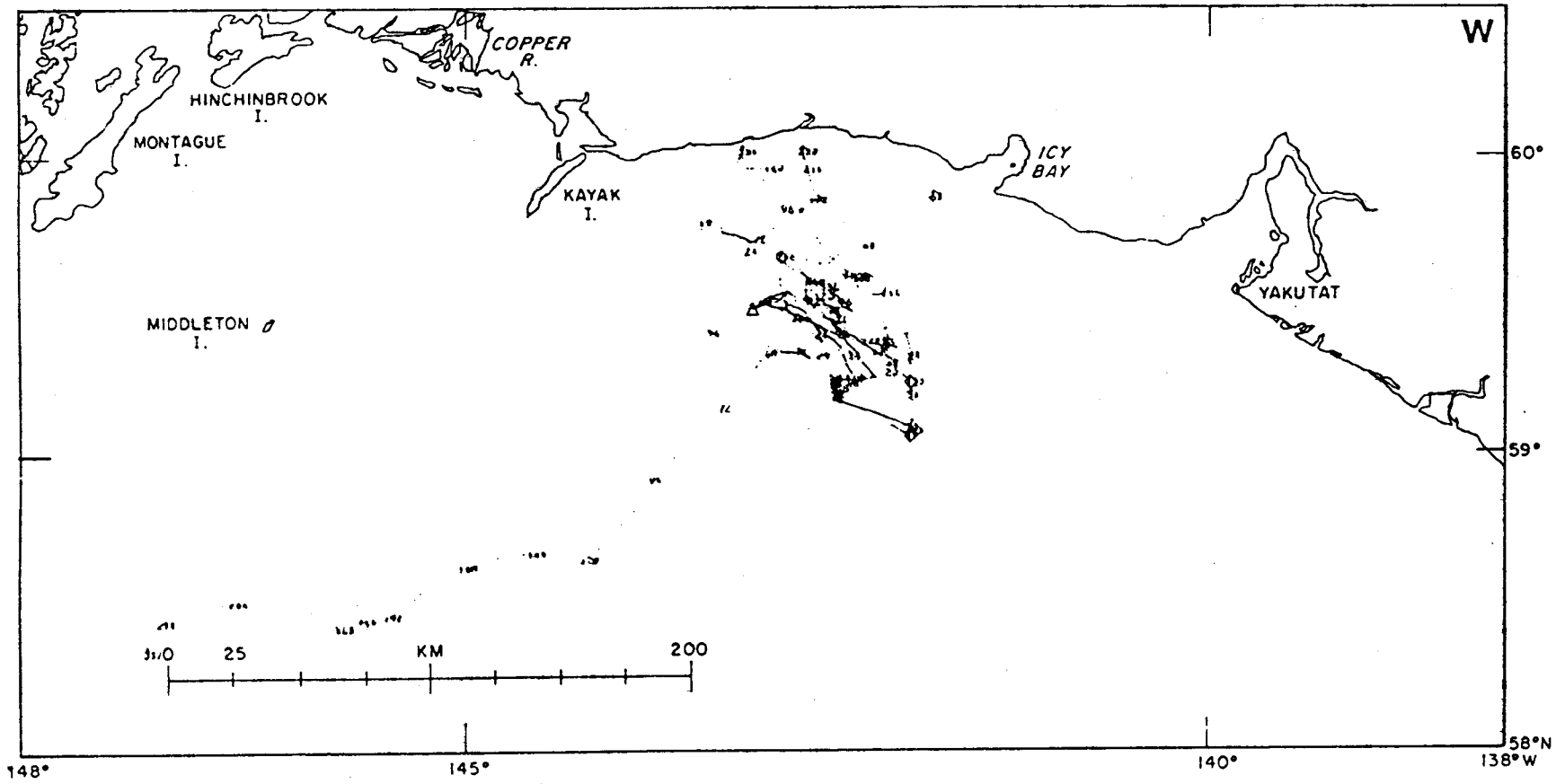


Figure 6-12. Winter trajectories of releases from site two.

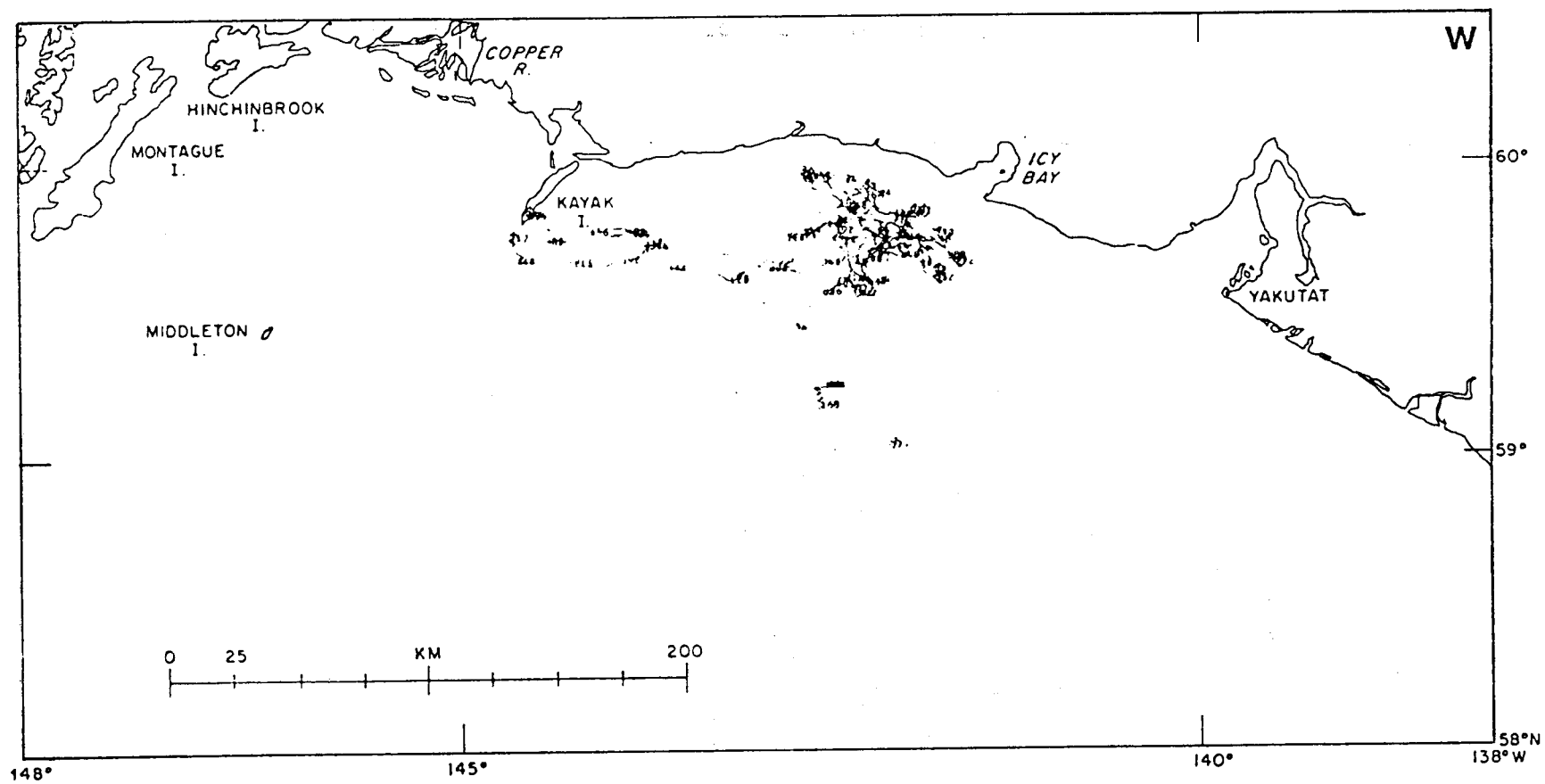


Figure 6-13. Winter trajectories of releases from site three.

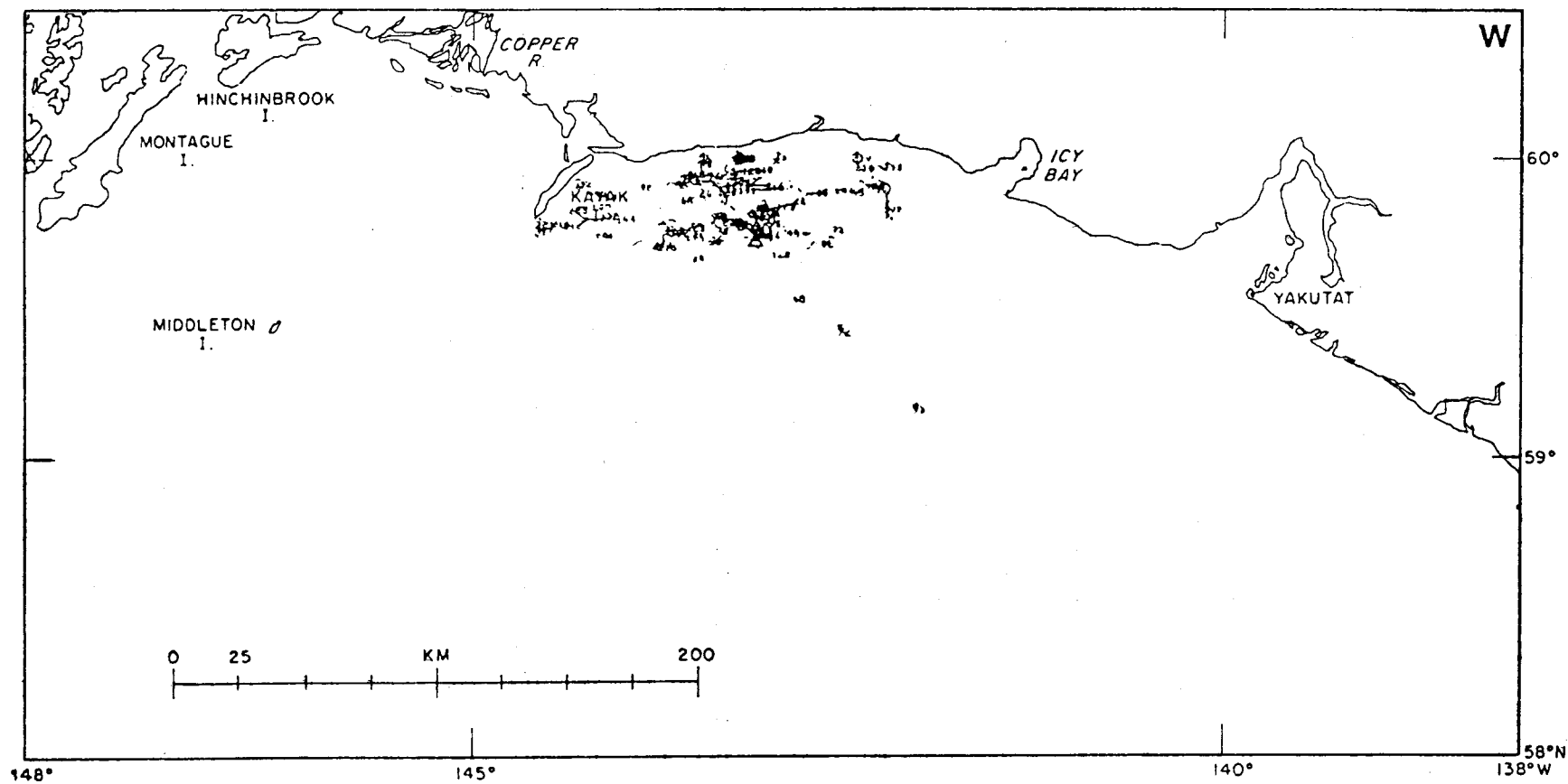


Figure 6-14. Winter trajectories of releases from site four.

The releases from site five southwest of Kayak Island are shown in figure 6-15. Most of these move north impacting the southeast coast of Kayak Island. Two exceptions are seen. The first of these moves offshore and follows the now familiar, but still minority drift to the southwest under the influence of baroclinic currents. Another pathway is seen to move southwest, round Kayak Island, and eventually end up at the Copper River.

Trajectories from site six are shown in figure 6-16 and show a wide scatter, but appear to fall into several classes. The majority appear to be trapped in the gyre circulation west of Kayak Island and eventually end on the west coast of Kayak Island and along the Copper River delta. A second class moves west north of Middleton Island and then northwest towards Hinchinbrook Island. A subclass of the pathways that initially move west appear to travel south in the vicinity of Middleton Island and then move east or west subject to influence of the shelf edge baroclinic currents.

Releases from site seven are shown in figure 6-17. From this location the majority of the tracks move northwest towards Hinchinbrook Island and the entrance to Prince Williams Sound.

Thus far this analysis has concentrated on collections of spills from various locations with comments being confined to general characteristics. The dynamic decomposition of the model and component reconstruction make it possible to examine trajectories in much more detail. The individual displacements associated with direct wind drift, baroclinic currents and wind set-up plus residual currents can each be monitored throughout the calculations. To demonstrate this five individual trajectories from the summer and winter periods are examined in detail. First, considering the July and August 1974 period, two trajectories have been selected from release

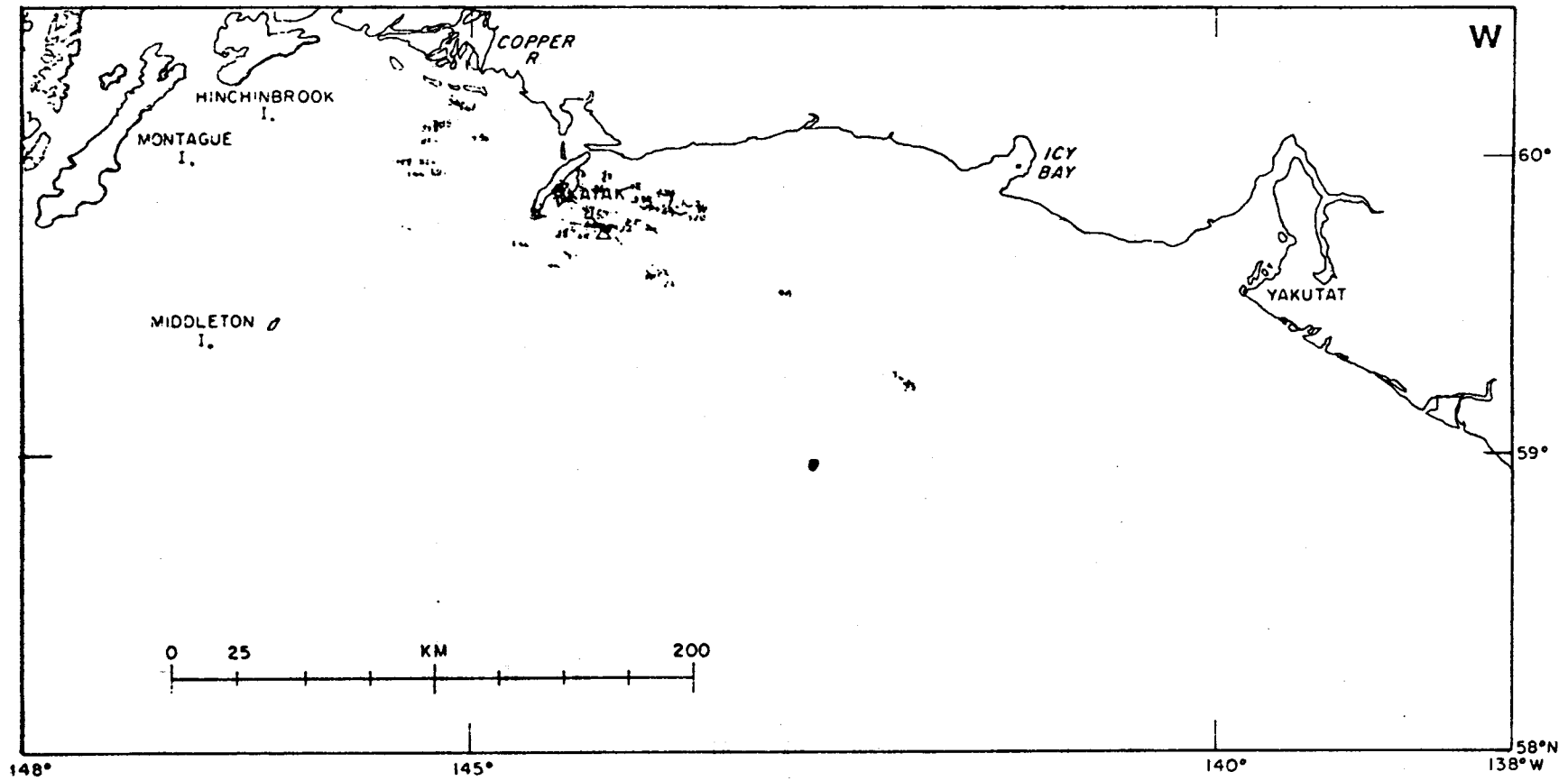


Figure 6-15. Winter trajectories of releases from site five.

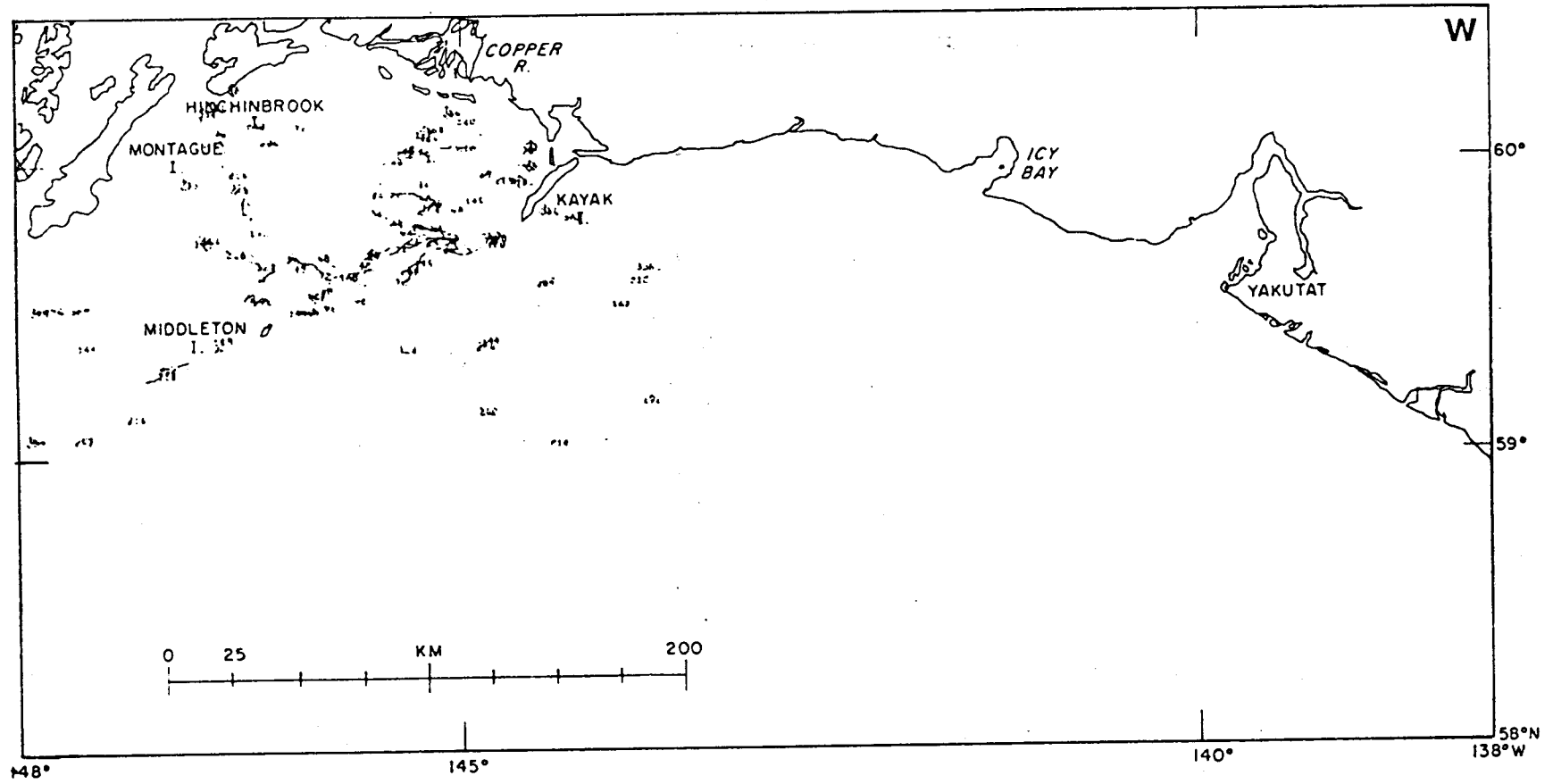


Figure 6-16. Winter trajectories of releases from site six.

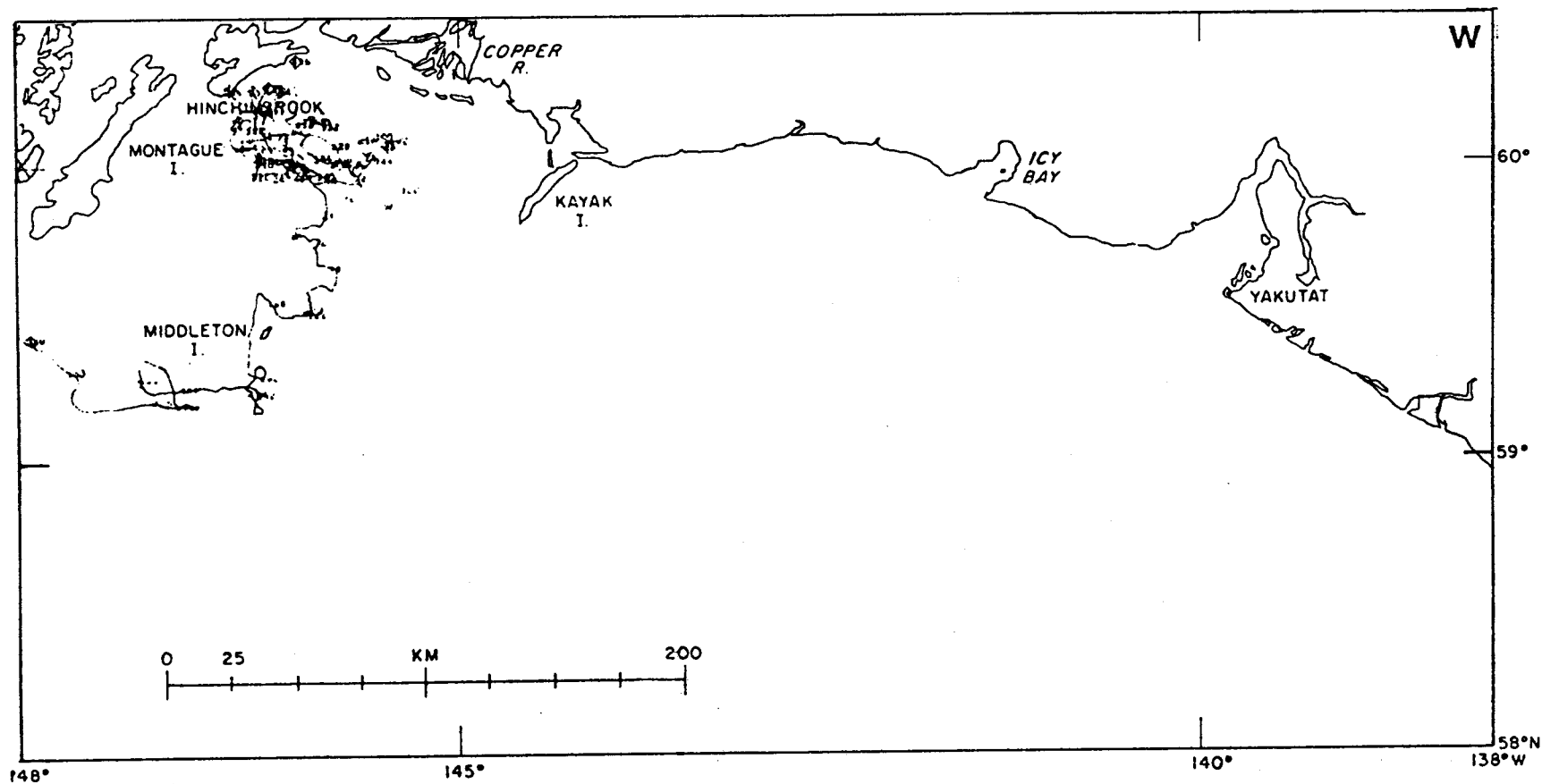


Figure 6-17. Winter trajectories of releases from site seven.

site two (figure 6-18) and three trajectories have been selected from release site six (figure 6-19).

Trajectory s1 is seen to move generally northwest from spill site two. The specific components responsible for this motion are shown in figure 6-20. This particular track was initiated on the 16th of August. Figure 6-20 shows five different time series vector stick plots. The first two represent the observed currents and winds that are used to scale the pattern and current residual. The last three time series vector stick plots represent the conditions as predicted from the model within the Lagrangian frame of reference following the path of the trajectory. The first two keying stations are basically Eulerian data. Many trajectory estimates in the past have been based on progressive vector diagrams derived from such data. These clearly will not reflect the appropriate pattern information; that is, progressive vector diagrams can't represent trajectories unless the fields have no spatial derivatives. The next three plots indicate the spatial pattern information incorporated into the model. These plots can be thought of as data collected from a drifting platform, collecting wind, current and density data. Also included are the uncertainties suggested by a comparison of model predictions and observational data at the location of the current keying station. This analysis shows that the direct wind forcing and baroclinic currents did not contribute significantly to the movement of this trajectory. The total simulated current was clearly responsible for this trajectory's movement.

The second summer trajectory (s2) selected for study was initiated on the 17th of July. The components responsible for this trajectory are shown in figure 6-21. Initially (up to about 150 hours) the baroclinic currents dominate the movement and the trajectory trends southeast. From about 200 to 300 hours the total current moves the path south out of the

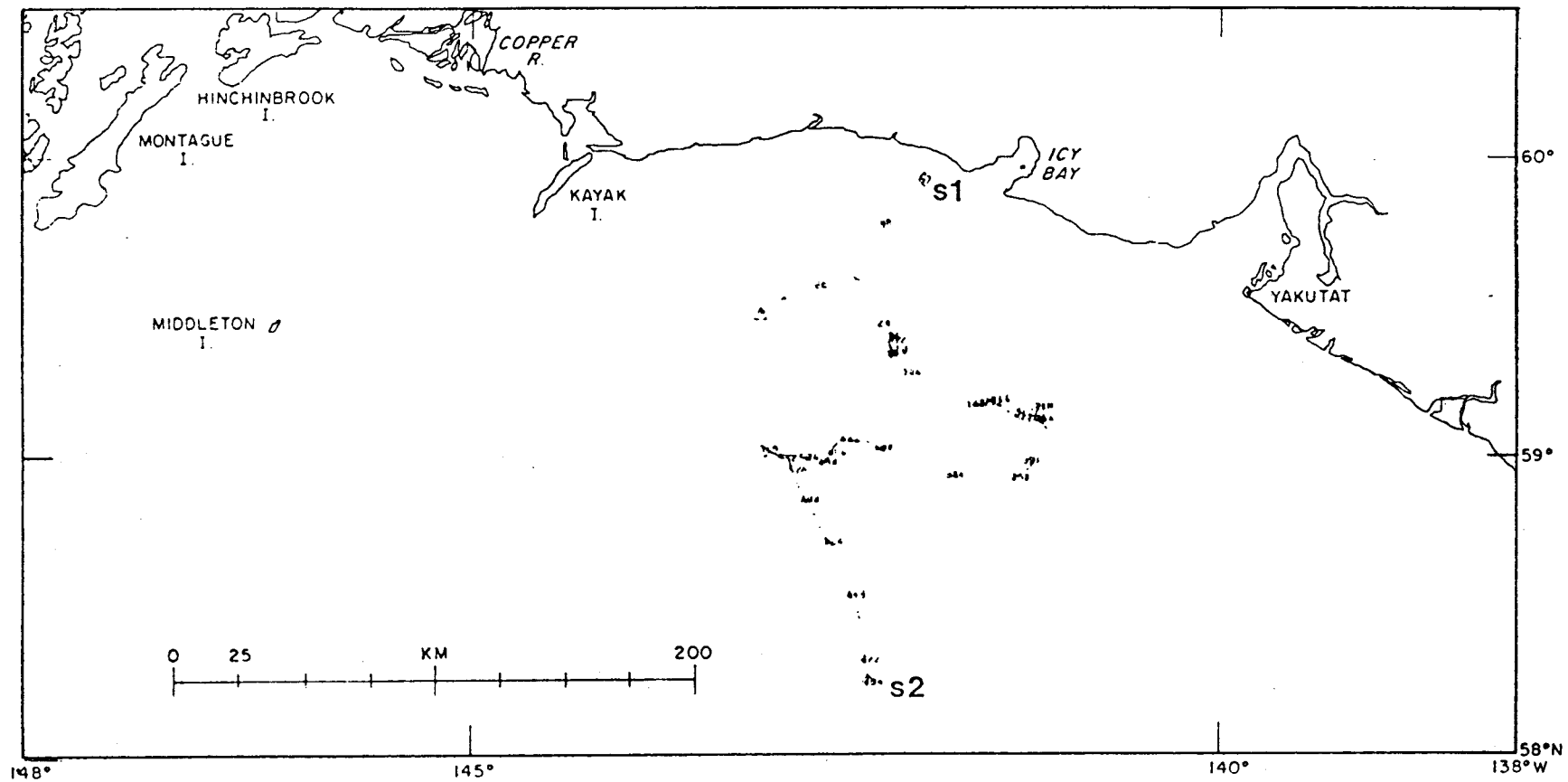


Figure 6-18. Individual summer trajectories s1 and s2 of releases from site two.

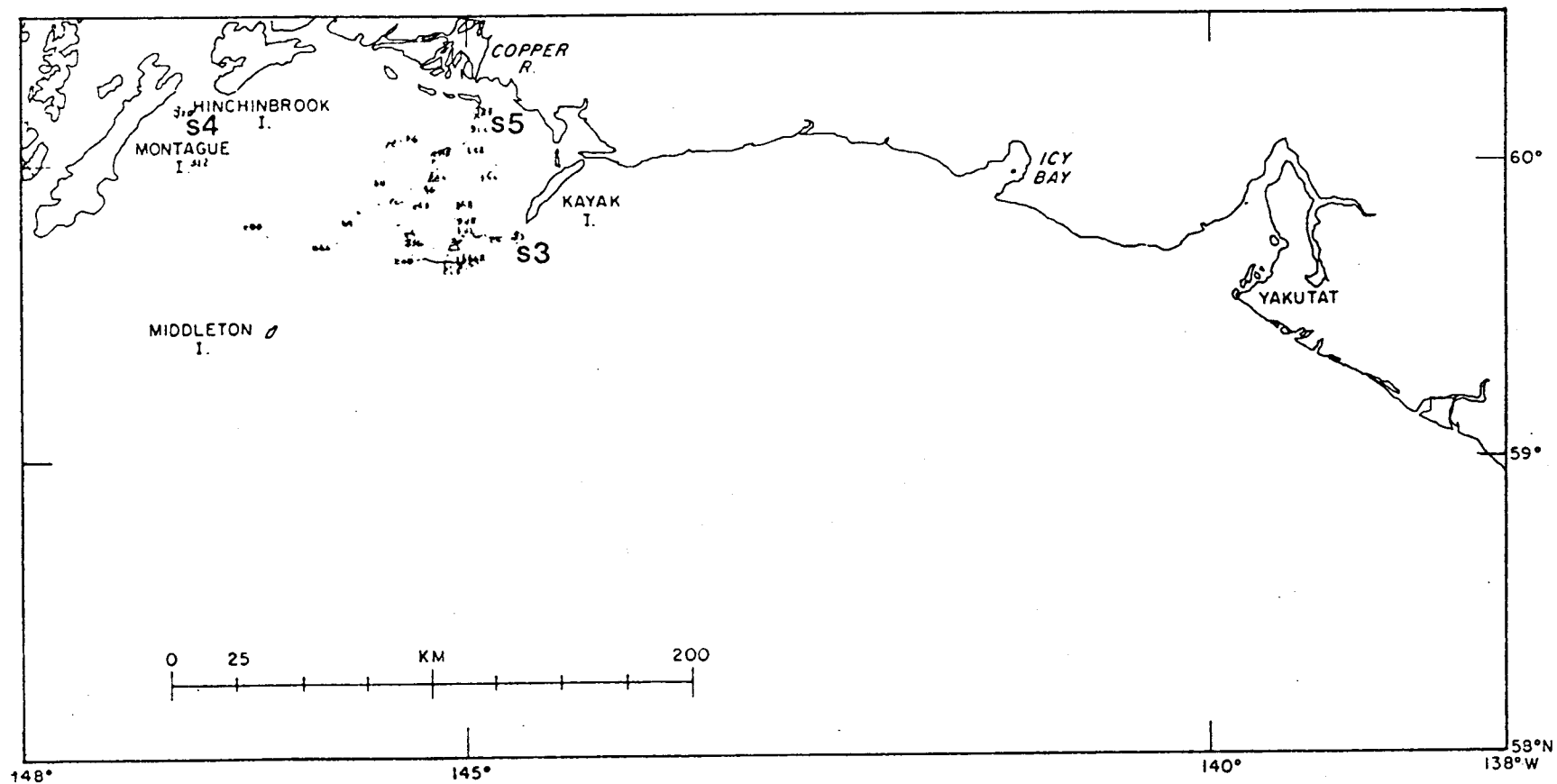


Figure 6-19. Individual summer trajectories s3, s4, and s5 of releases from site two.

s1

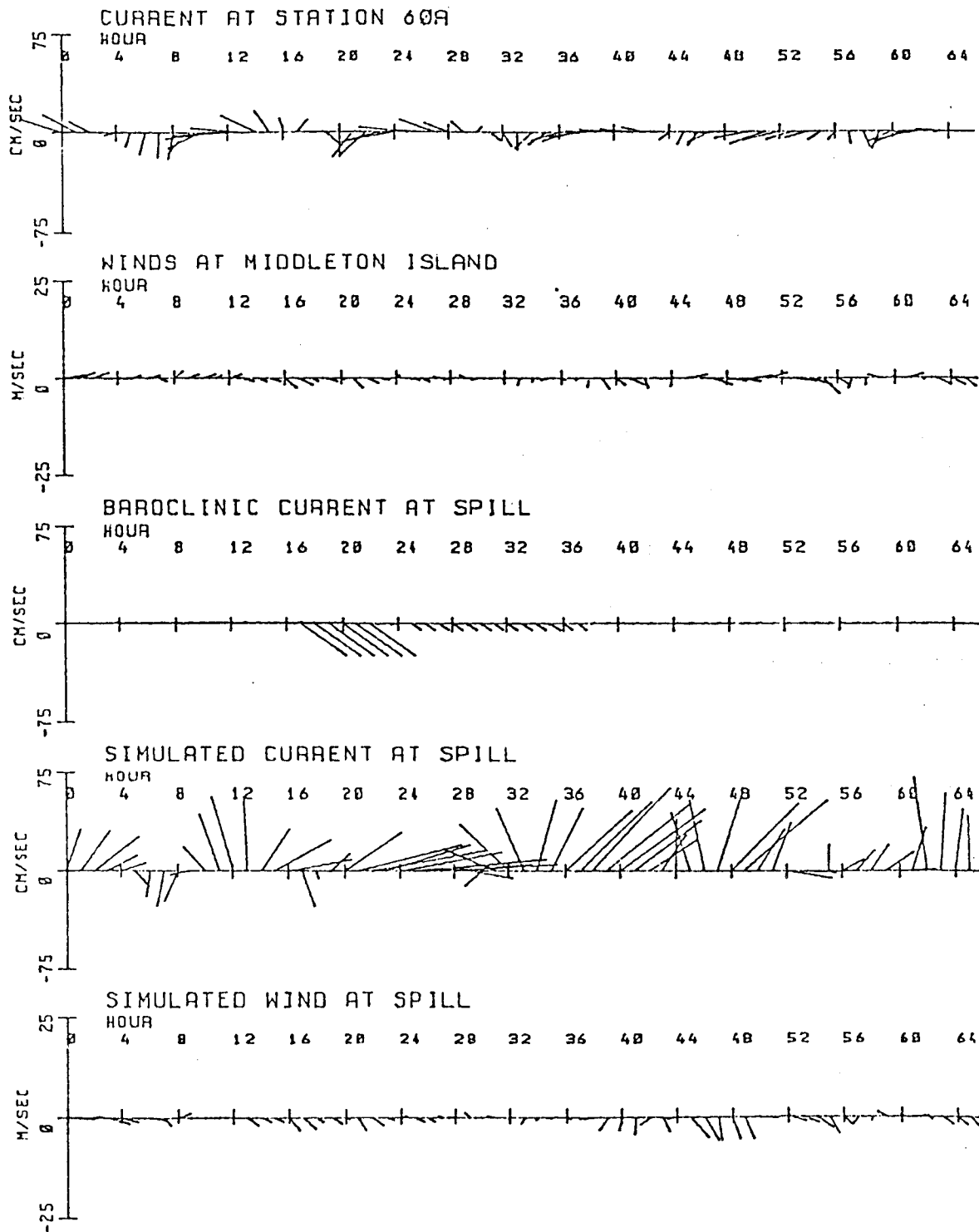


Figure 6-20. Detailed analysis of trajectory s1.

s2

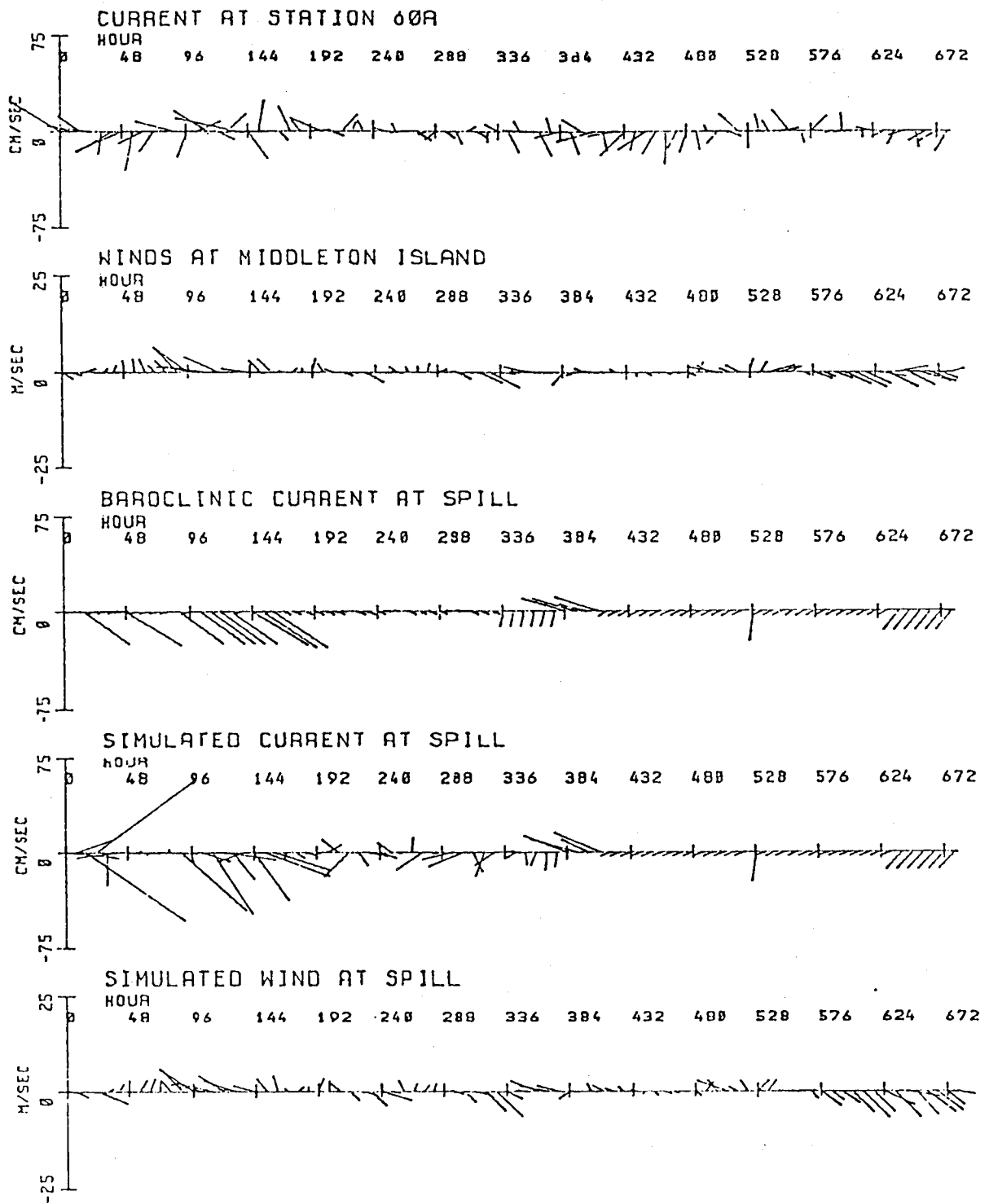


Figure 6-21. Detailed analysis of trajectory s2.

dominant slope current. After 300 hours baroclinic currents are again seen to dominate the movement (the trajectory is beyond the shelf edge and influence of the hinge set-up modes). Towards the end of this case study, after 480 hours the general winds increase and are seen to result in a significant southeasterly component to the trajectory movement.

The third summer study (s3) is of a short trajectory released from site six on the 7th of July. This trajectory leads quickly to the west, towards Kayak Island. The results of this analysis are shown in figure 6-22. The baroclinic currents for this trajectory are consistently to the south representing part of the gyre to the west of Kayak Island. This is countered by hinge set-up flow to the north such that the total currents have a steady easterly component. The wind drift is never dominant, but steadily to the east. The net result of these factors is a direct path to the east.

The fourth summer trajectory to be studied (s4) was released from site six on the 22nd of July. The results of this analysis are seen in figure 6-23. For the entire 300 plus hours of this drift the direct wind contribution was small. For the first 130 hours this trajectory is within the Kayak Island gyre pattern with the movement first north then east and finally south. After about 144 hours the path has lead back nearly to its original position. At this point several strong southerly excursions carry the path out of the gyre to the westerly flowing region. After 200 hours the currents carry the trajectory steadily west and finally north, encountering quite strong currents in the vicinity of the sea valley leading in towards Hinchinbrook just before it goes ashore.

The last summer trajectory (s5) investigated left site six on the 6th of August and the results of this analysis are shown in figure 6-24.

s3

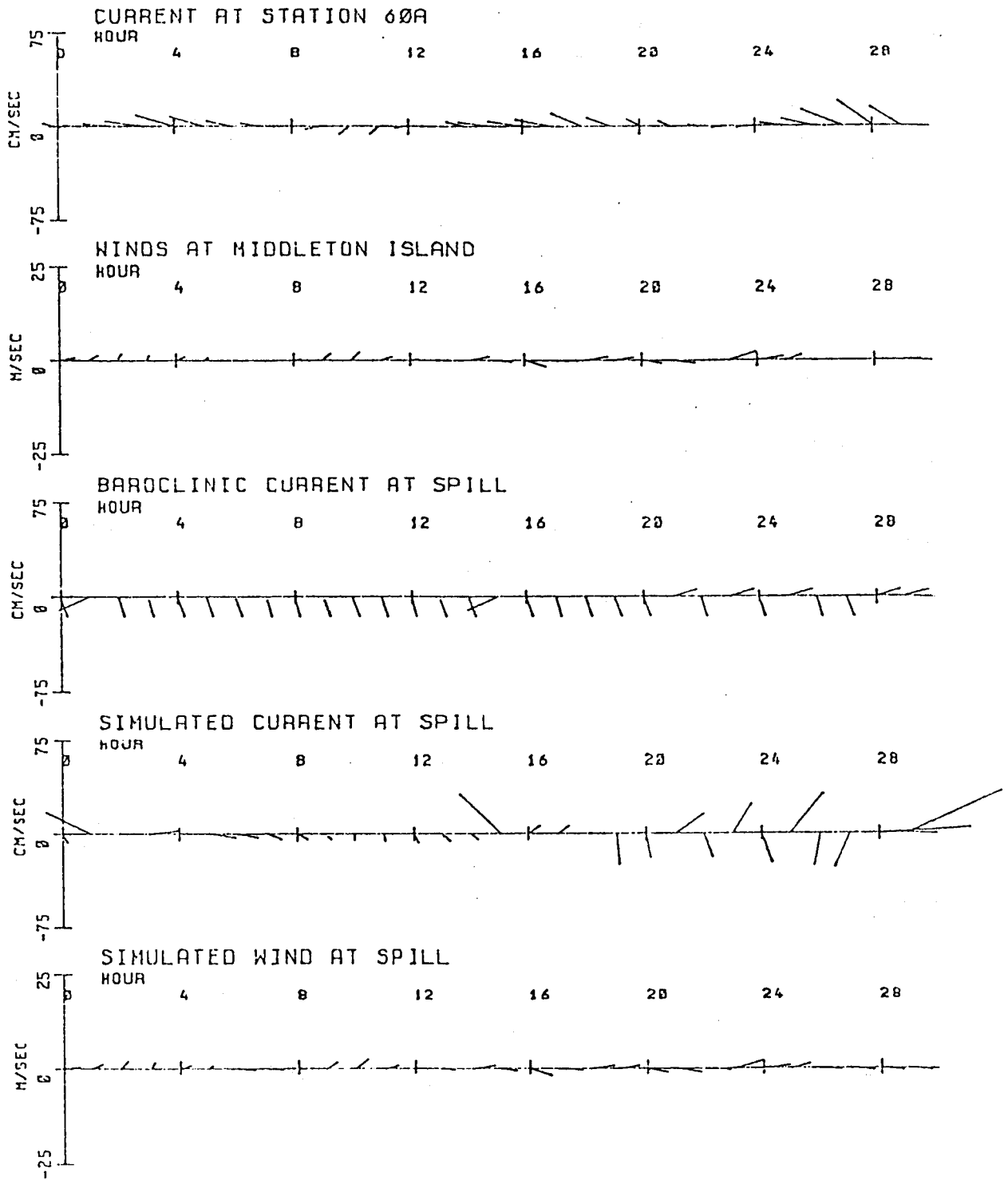


Figure 6-22. Detailed analysis of trajectory s3.

s4

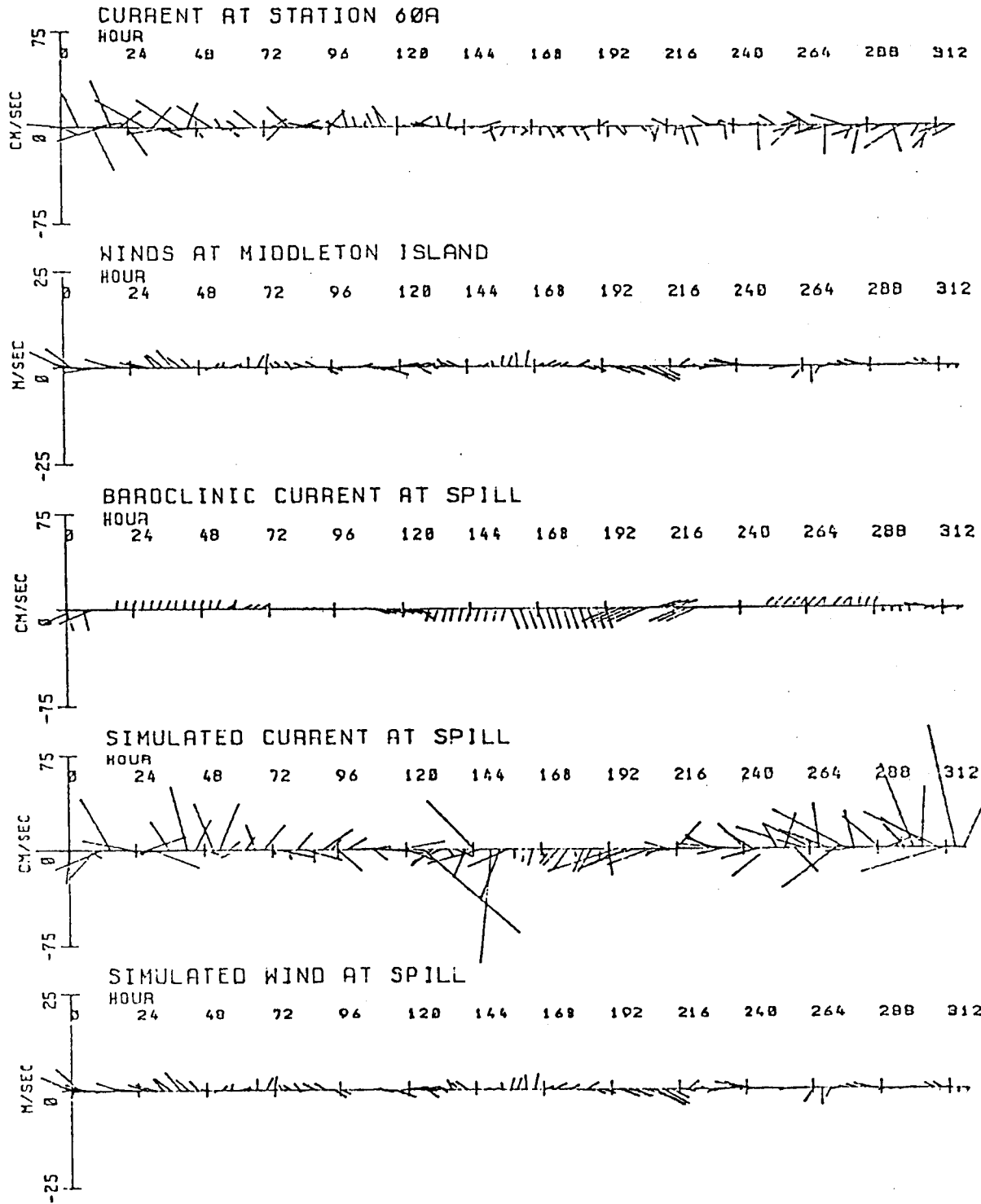


Figure 6-23. Detailed analysis of trajectory s4.

s5

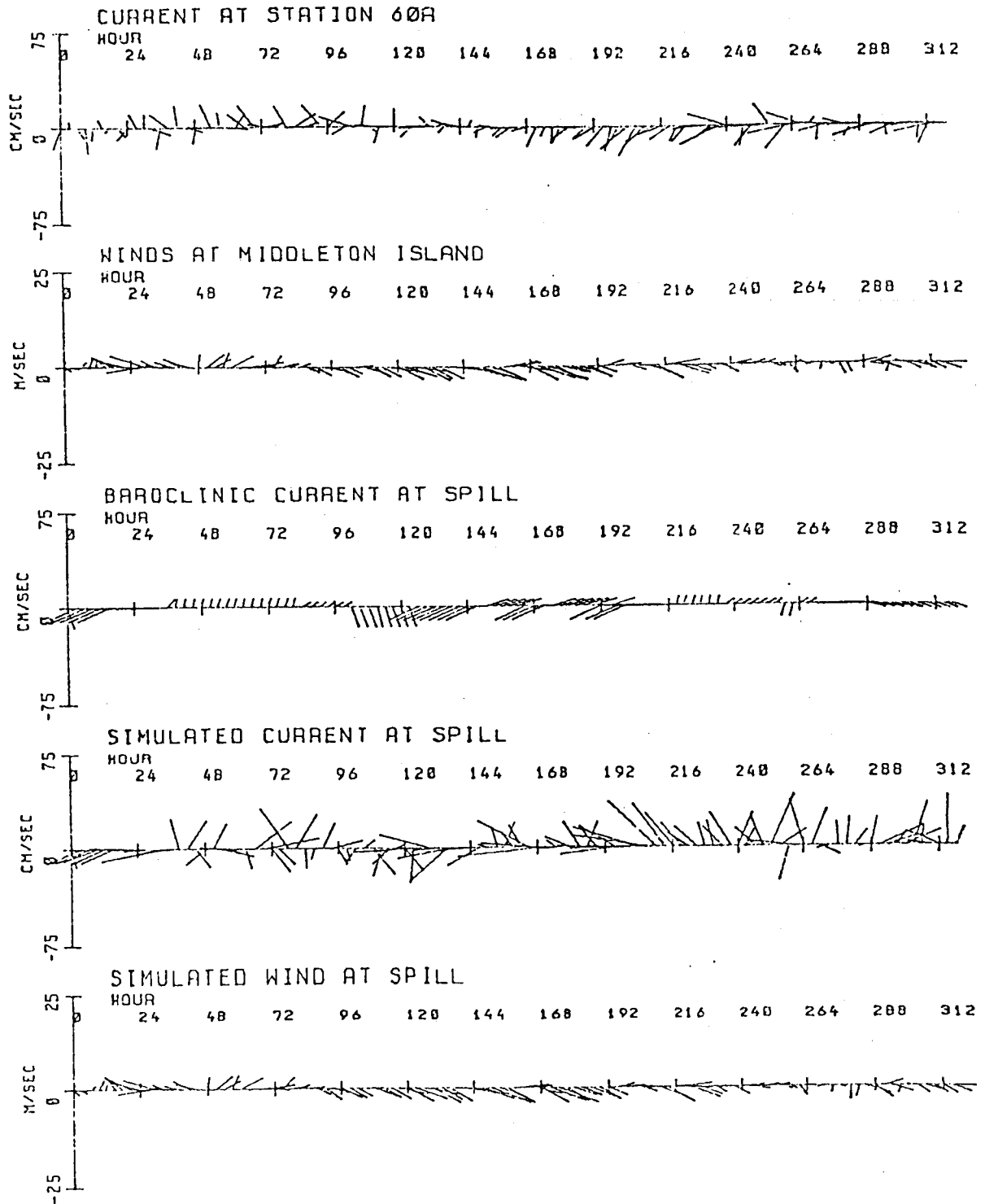


Figure 6-24. Detailed analysis of trajectory s5.

Once again the direct wind contribution is small although it is steadily to the east and slightly south. The currents (both baroclinic and total) show evidence of the Kayak Island gyre, moving north for about 100 hours, south for another 60 and then more or less steadily north till the path leads ashore near the Copper River. Like the last example, this trajectory leads back to its point of origin, but did not receive a short southerly push necessary to escape the gyre circulation.

Of the five winter trajectories studied in detail three originated from site five southeast of Kayak Island (figure 6-25) and two originated from site seven (figure 6-26).

The first winter trajectory (w1) left site five on the 2nd of February and proceeded rapidly (about 2 km per hour) to the east-southeast. The results of this analysis are shown in figure 6-27. During the first 18 hours the currents carried the path strongly to the south under the influence of weather type 6.0. This was able to move the trajectory into the area where baroclinic currents along the continental slope dominate the movement, as can be seen from the currents after about 20 hours. The winds, although never really a major factor, pick up after about 20 hours and remain in the same general direction as the currents contributing to the large overall drift.

The second winter trajectory (w2) left site five on the 27th of February and is quite different from the case considered above (figure 6-28). The first three days both the currents and winds are seen to carry the path to the east with the currents adding a slight northerly component. This carries the trajectory onto a shelf region where baroclinic currents are continually weak. Up until about 220 hours the path wanders around with the winds and currents often counter to each other. At around 230 hours a strong wind event is seen to develop local winds in excess of 20

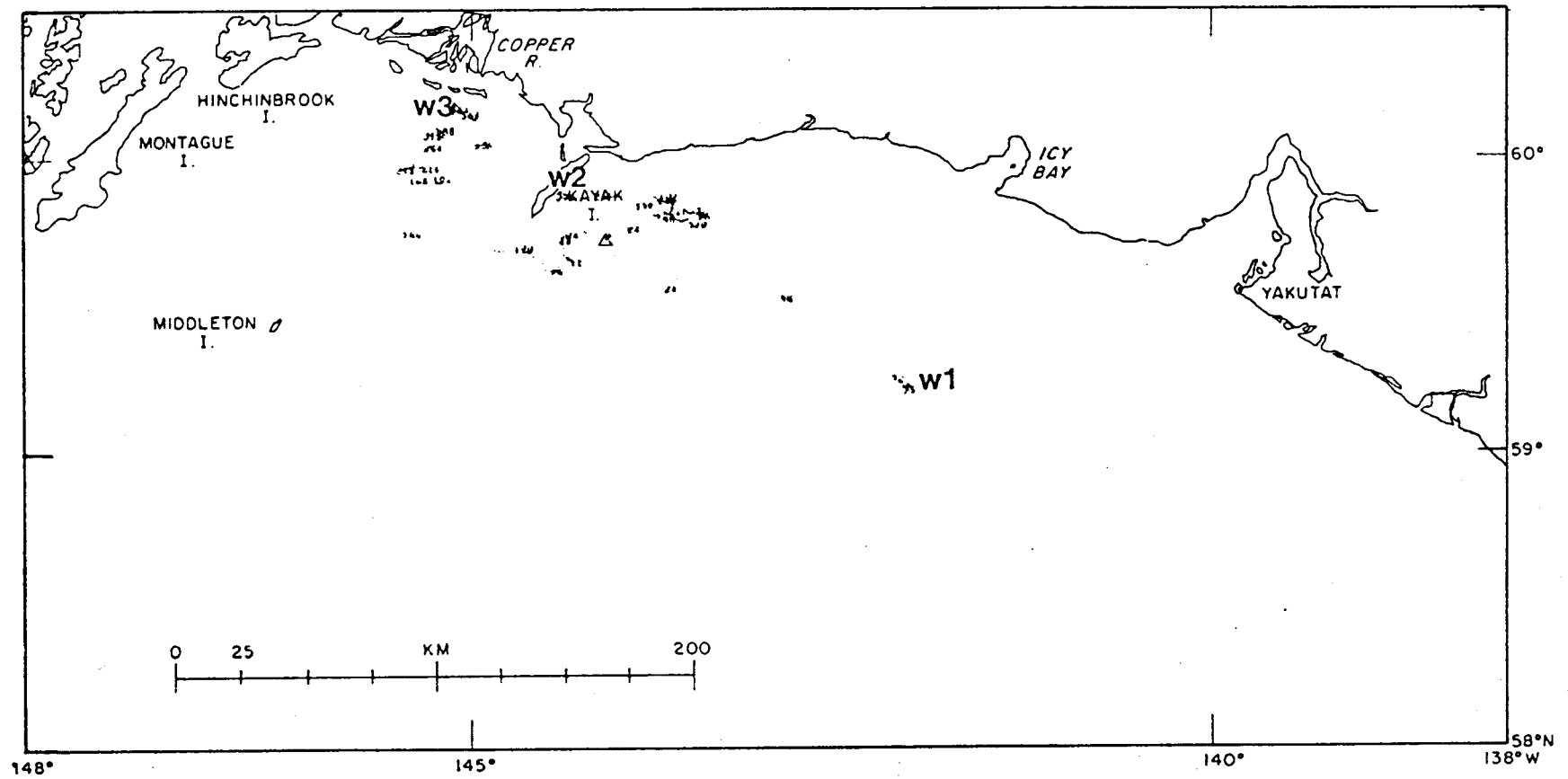


Figure 6-25. Individual winter trajectories w1, w2, and w3 of releases from site five.

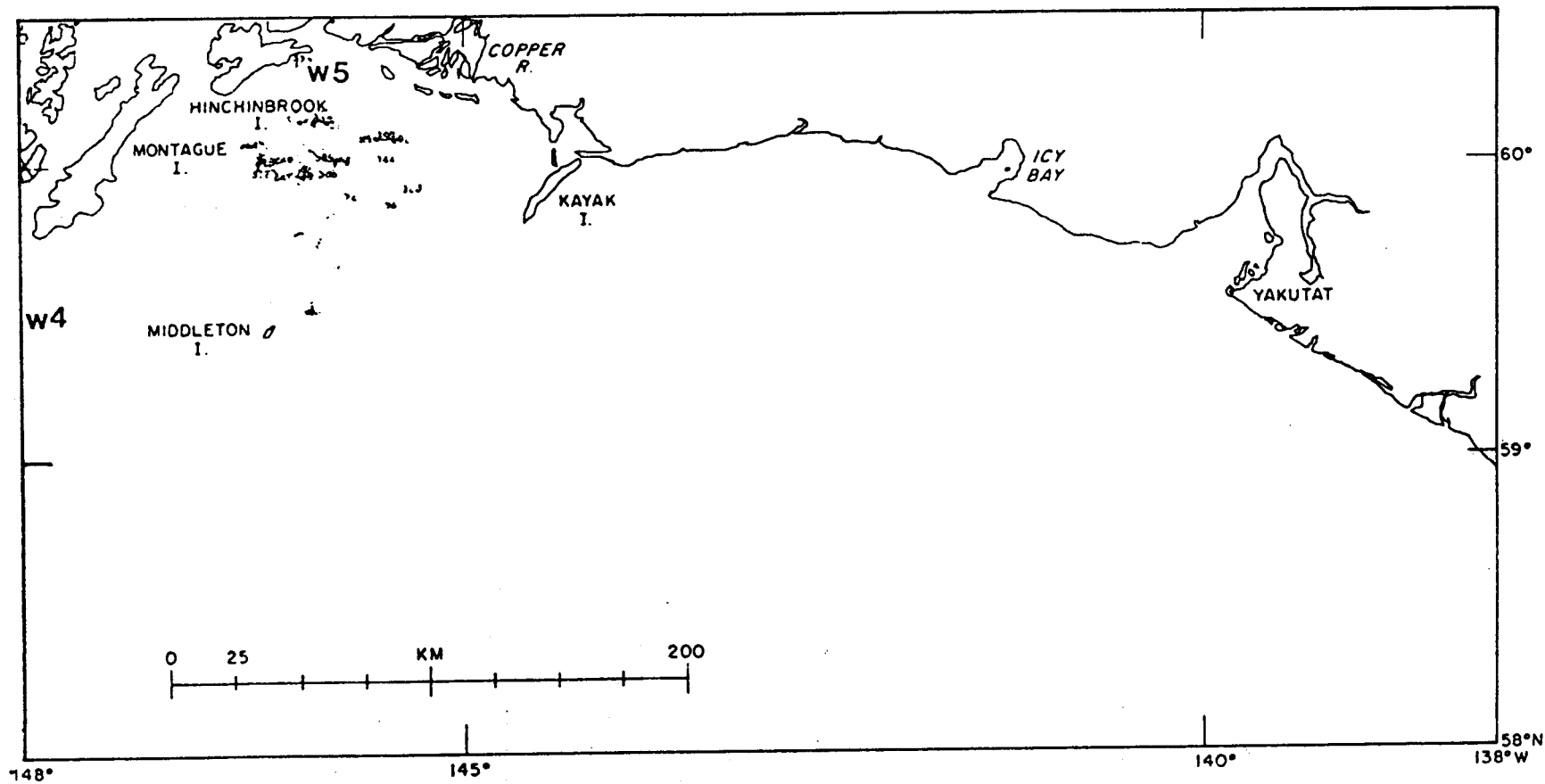


Figure 6-26. Individual winter trajectories w4 and w5 of releases from site seven.

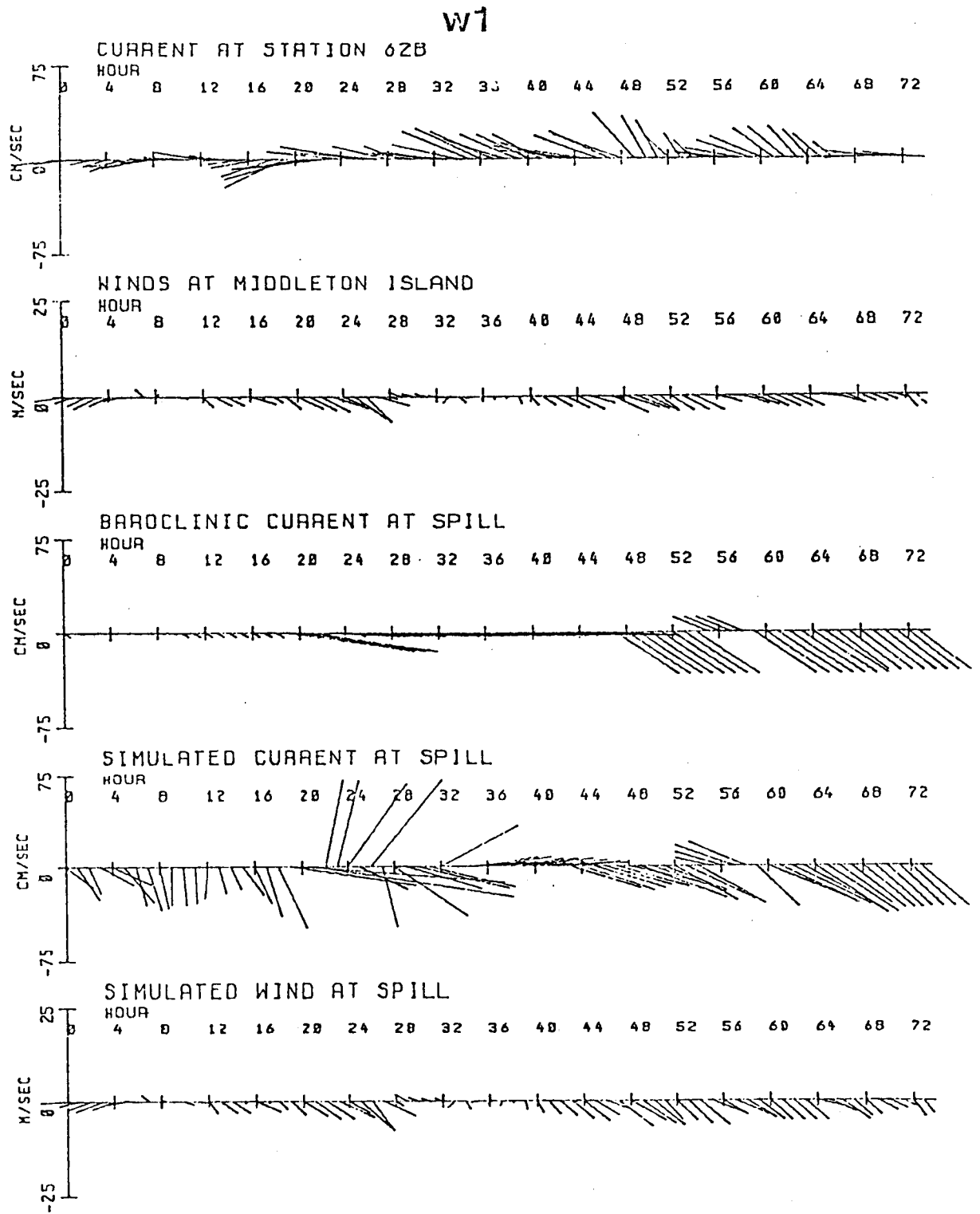


Figure 6-27. Detailed analysis of trajectory w1.

w2

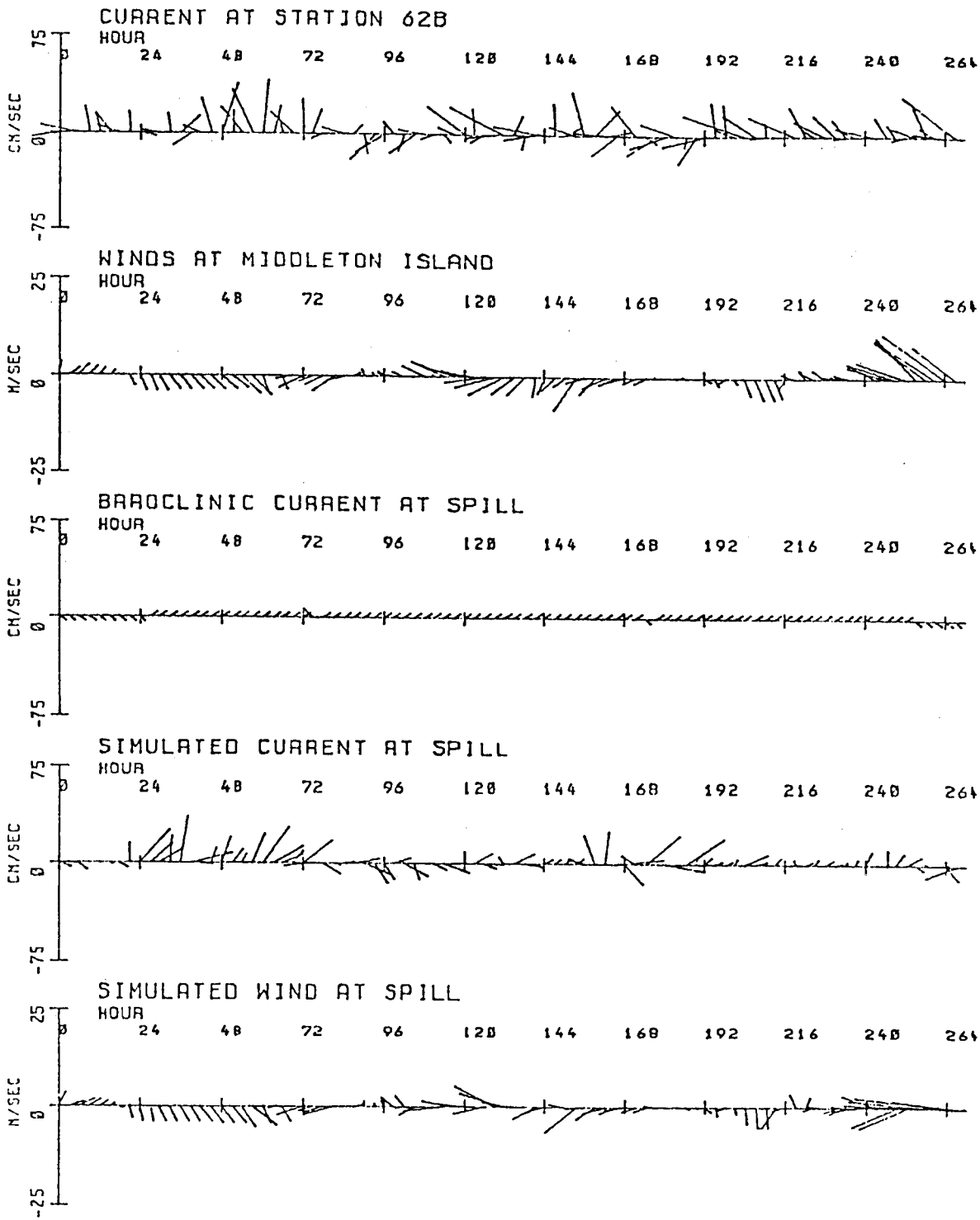


Figure 6-28. Detailed analysis of trajectory w2.

m/sec driving the trajectory westward into Kayak Island.

The third trajectory studied from the winter data (w3) left site five on March 4th. The results of this investigation are seen in figure 6-29 and show an interesting series of exchanges between dominant processes. For the first 24 hours the wind kicks the path off to the west. On the third day the total current advects to the south. From 72 to 110 hours the baroclinic and wind currents are mostly at odds resulting in a slow movement to the northwest. About hour 120 a strong wind event sends the trajectory off to the west. After hour 150 the winds and currents, although strong, are pretty much balancing each other and the net drift is north as indicated by the baroclinic currents.

These last three trajectories, all from site five, indicate the significance of early movements and their role in moving the trajectory into different advective regimes.

The fourth winter trajectory to be studied (w4) in detail left site seven on the 2nd of February (figure 6-30). For the first 100 hours the winds, although not as strong as the currents, are more persistent and lead to a net southerly drift. After about 120 hours the baroclinic currents are relatively large and influence the overall currents. Their influence is particularly evident in the direction reversal seen north of Middleton Island (figure 6-26). From 200 hours onward the wind and currents are highly variable and a number of loops and meanders are seen in the trajectory.

The last trajectory studied (w5) was released from site seven on the 4th of March and the results are shown in figure 6-31. For the entire duration of this trajectory the baroclinic currents are small. For

approximately 300 hours the currents and winds are both large, but often counter each other and the trajectory oscillates east and west. After about 300 hours both develop northerly components and the resultant path quickly moves north to hit the coast on Hinchinbrook Island.

w3

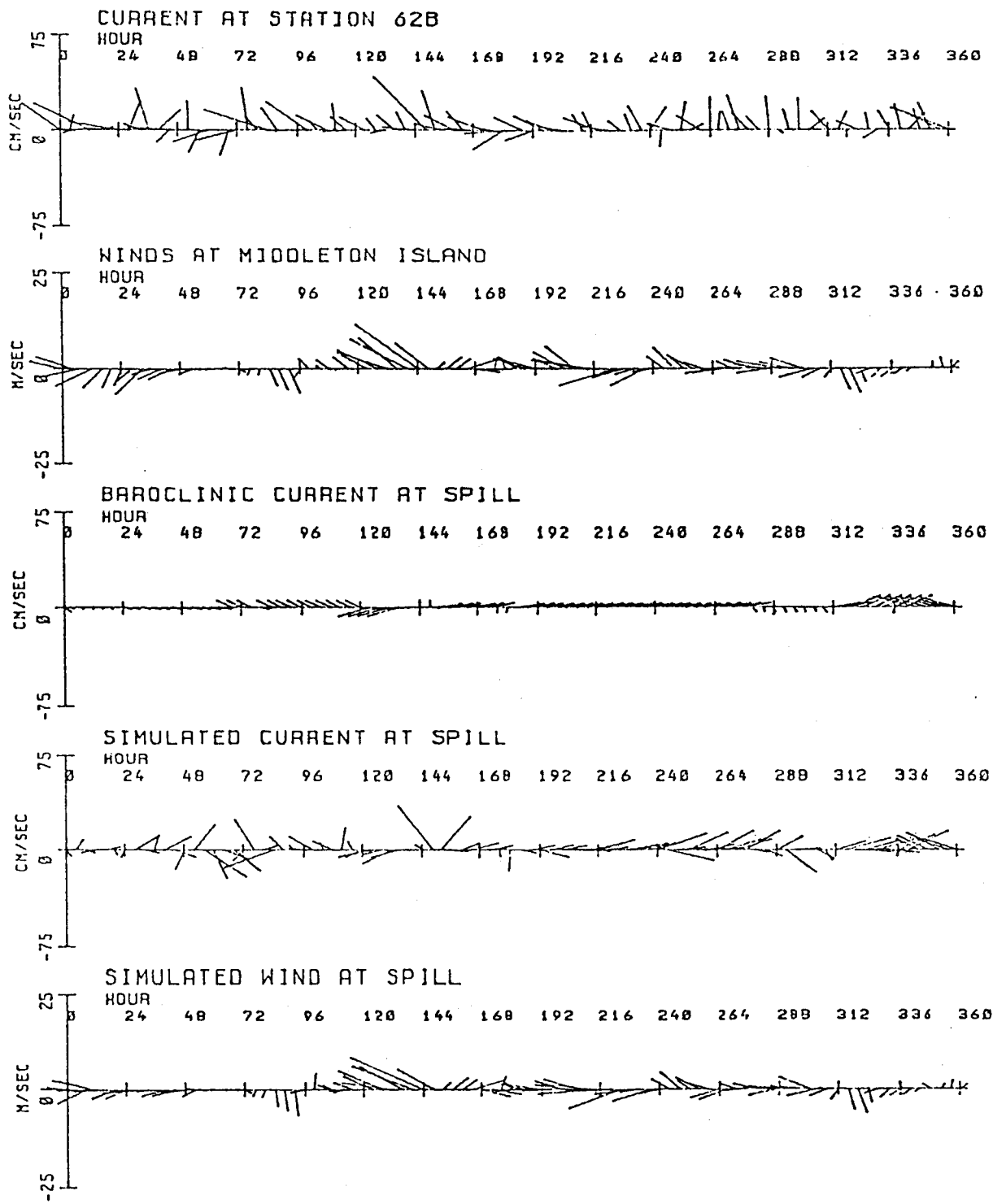


Figure 6-29. Detailed analysis of trajectory w3.

w4

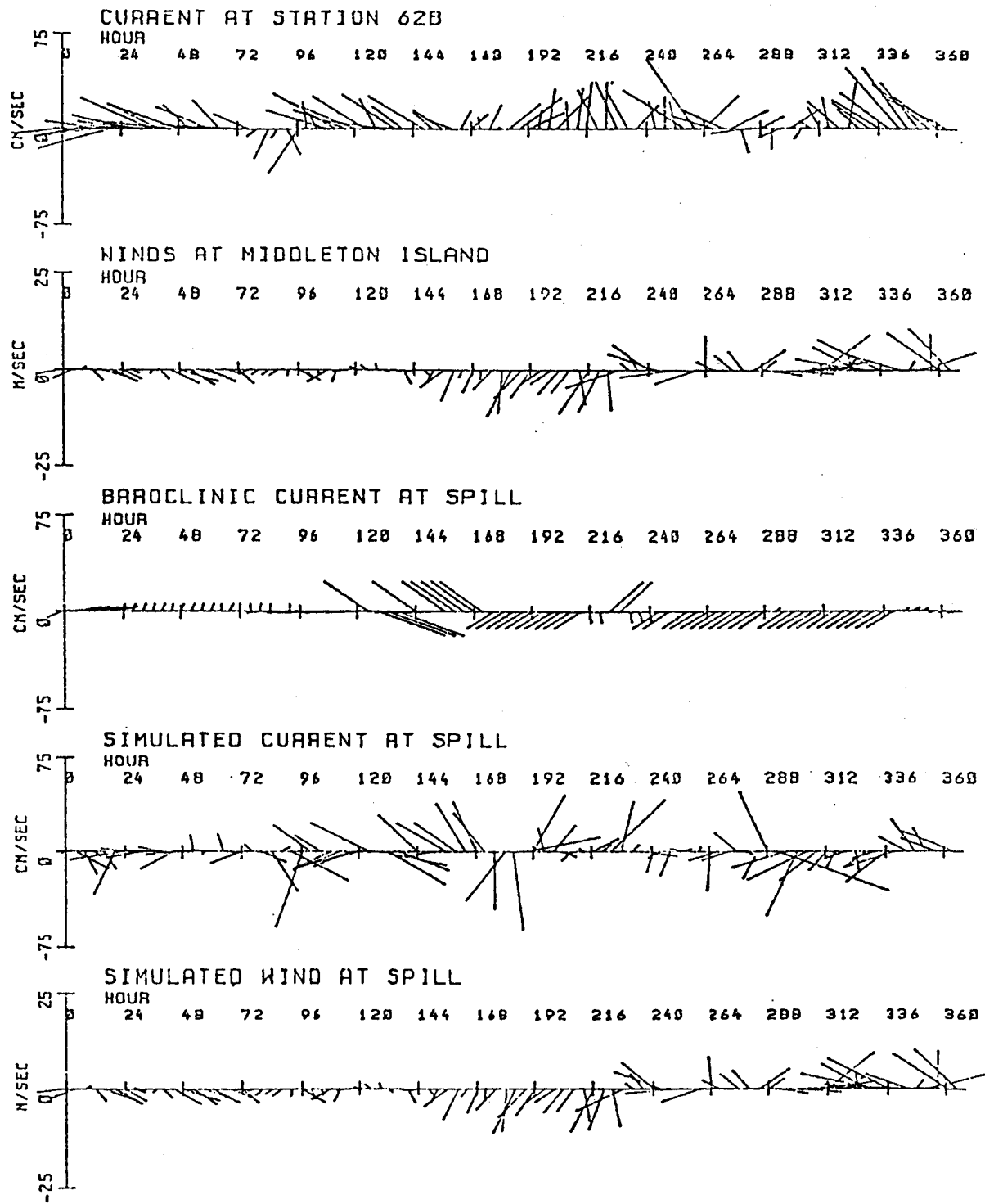


Figure 6-30. Detailed analysis of trajectory w4.

w5

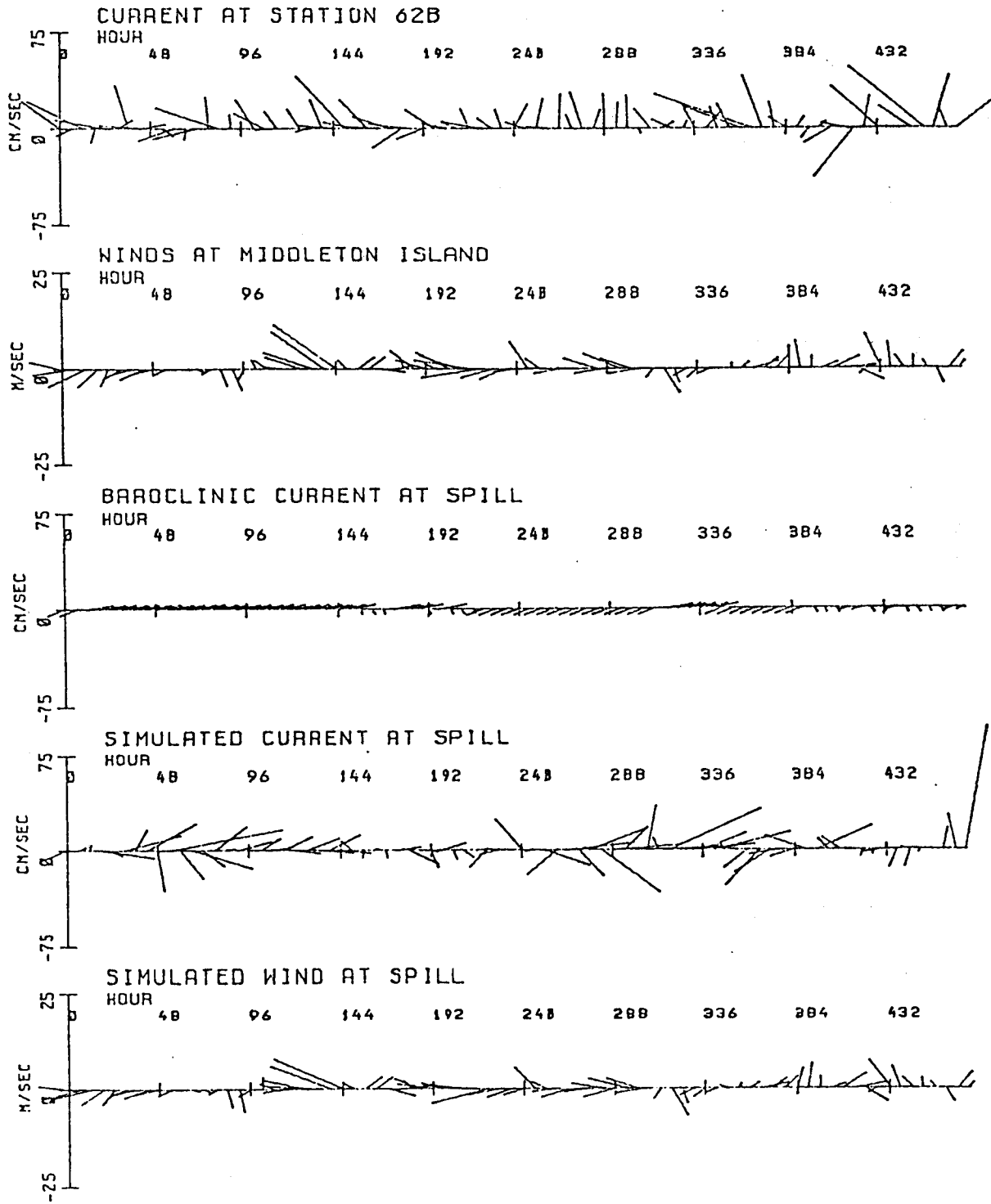


Figure 6-31. Detailed analysis of trajectory w5.

In this section a demonstration of trajectory analysis techniques has been presented using NEGQA data. In this the model synthesized the results of the components described in the earlier chapters of this report. The integration and graphic presentation of all the component segments as well as a detailed analysis of selected trajectories is documented in a representative presentation.

7. Conclusions

A comprehensive trajectory model has been developed for NEGOA with the following features:

The model includes three elements - surface wind drift, barotropic currents (wind driven) and baroclinic currents (density driven). The elements form a physically consistent set with approximately the same level of sophistication in each component. The formulation explicitly couples wind and current variations as suggested by observational shelf studies.

Synoptic meteorological data drive a set of local wind fields and the barotropic component of a diagnostic model of coastal currents. The set of local wind and current fields are chosen to represent the observed range of atmospheric variability. The data set for the baroclinic component of the diagnostic model is the available hydrographic survey data.

The linear decomposition of the diagnostic model into density and wind driven components makes it possible to identify the regional response associated with each of the forcing mechanisms.

The Green's function solution for the barotropic current response for NEGOA is complete for any arbitrary wind field. The diagnostic model need not be run on a case by case basis for the barotropic component in future trajectory calculations.

A method for treating the uncertainty in the input data to trajectory calculations is included. The difference between a current meter record and the cumulative model response is treated as a residual. The residual is applied throughout the field, scaled by the ratio of the barotropic response at each location to the response at the current meter. The result represents a dispersive element in the family of trajectories which accounts for both unresolved high frequencies in the current field and cumulative model uncertainty.

The input to the trajectory calculations are the available long time series of sea level pressure charts and, at present, a surface current meter and anemometer time series. The possibility exists to remove the dependence on the current meter and anemometer through a stochastic treatment of residuals.

This report has presented sample trajectory calculations for July-August 1974 and February-March 1975. It does not include the climatological assessment of spill possibilities in NEGOA. Such

an assessment may now be undertaken based upon available data. Conclusions about current circulation in NEGOA which have been derived from RU#140 to date are:

Baroclinic response, particularly the encroachment of mesoscale eddies, dominates the currents at the shelf break.

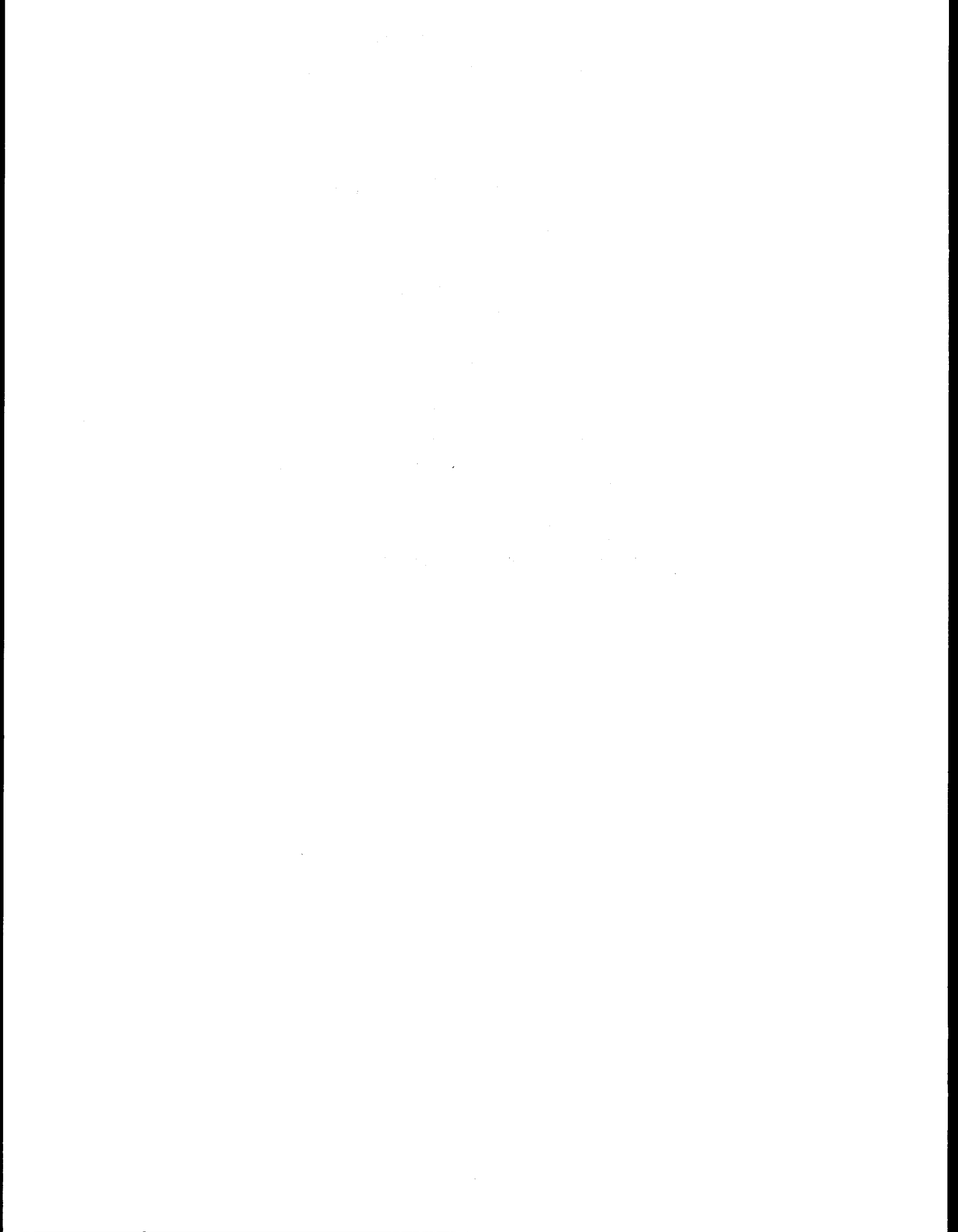
In general, surface wind drift and barotropic response dominate currents on the shelf.

The major exception is the baroclinic gyre behind Kayak Island, which occurs in 6 of 7 density data sets.

The results of the diagnostic model infer that the coherence length scale of currents on the shelf is on the order of 30 km, the diffusive scale, and is order 300 km at the shelf break, controlled by conservation of potential vorticity along isobaths.

To measure currents in NEGOA certain locations are much more desirable than others, relative to their horizontal coherence, magnitude and variability.

Dispersion of trajectories is quite large and bimodal. Temporal variation of wind plays an important role as well as the spatial variations of the relative magnitude of wind driven and density driven drift.



APPENDIX A

Development of a Simplified Diagnostic Model
for Interpretation of Oceanographic Data

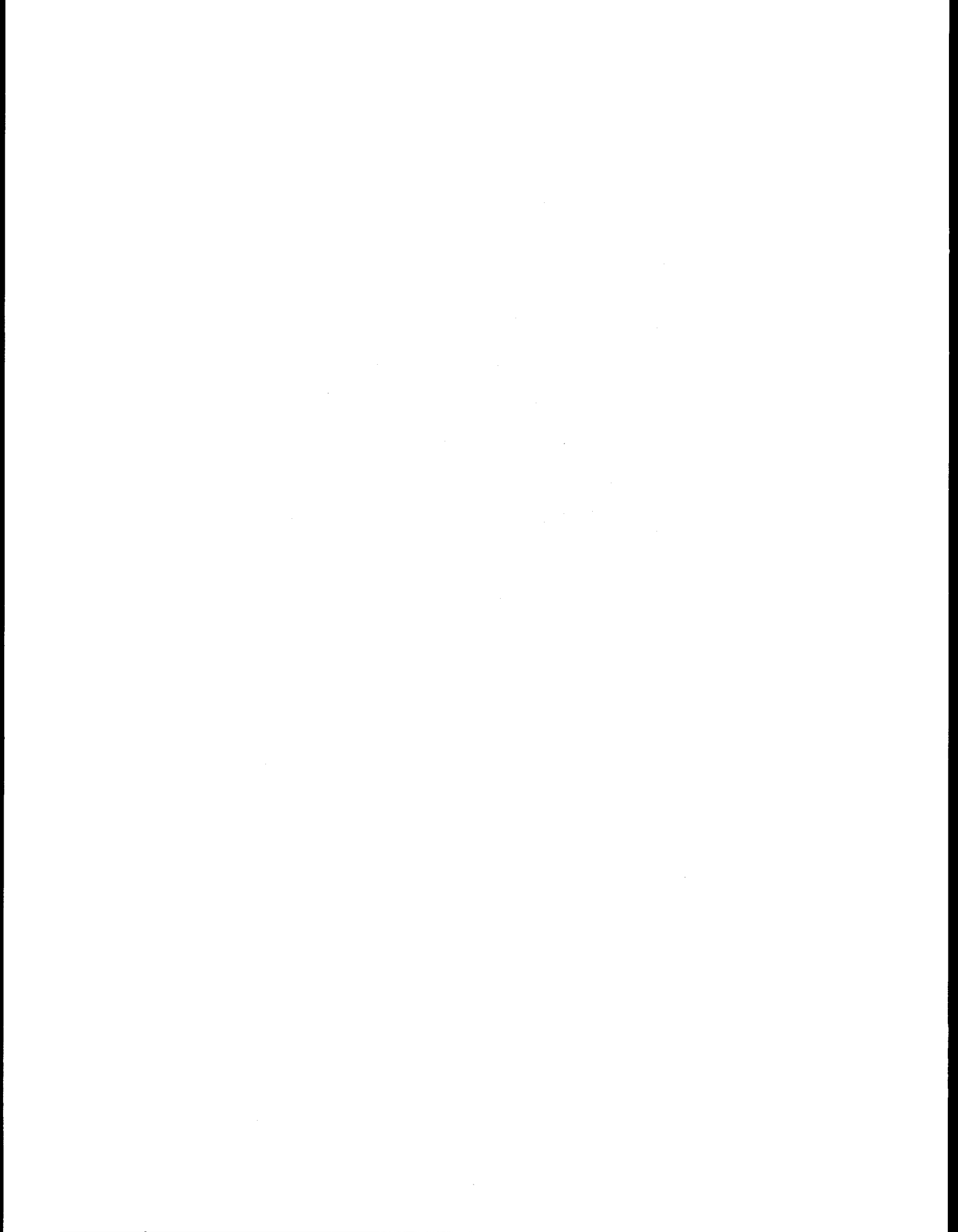
by

J. A. Galt

(Reprint of: Galt, J. A. 1975. Development of a simplified diagnostic model for interpretation of oceanographic data. U.S. Dep. Commer., NOAA Tech. Rep. ERL 339-PMEL 25.)

TABLE OF CONTENTS

	Page
LIST OF SYMBOLS	255
ABSTRACT.	257
1. INTRODUCTION.	257
2. DEVELOPMENT OF MODEL EQUATIONS.	264
2.1 Surface Elevation as Dependent Variable.	272
2.2 Transport Stream Function as a Dependent Variable.	273
3. BOUNDARY CONDITIONS AND DATA REQUIREMENTS	274
4. NON-DIMENSIONAL FORMULATION OF THE MODEL EQUATIONS.	290
5. APPLICATION OF MODEL EQUATIONS.	295
6. ACKNOWLEDGMENTS	298
7. REFERENCES.	298



LIST OF SYMBOLS

- Λ, B, C, D variable coefficients, known functions of position
- d vertical position of ocean bottom
- f Coriolis parameter - vertical component of Earth's rotation vector
- f_0 regional average Coriolis parameter
- g acceleration of gravity
- H constant used to scale the depth
- J Jacobian differential operator $J(a, b) = \left(\frac{\partial a}{\partial y} \frac{\partial b}{\partial x} - \frac{\partial a}{\partial x} \frac{\partial b}{\partial y} \right)$
- K eddy coefficient for diffusion of momentum
- \vec{k} unit vector in the positive z direction
- L a scale length for horizontal dimensions
- N eddy coefficient for diffusion of density
- N_1 non-dimensional scaling parameter $\frac{g\epsilon H}{\rho_0 f_0 U L}$
- N_2 non-dimensional scaling parameter $\frac{\gamma}{\rho_0 H}$
- N_3 non-dimensional scaling parameter $\frac{\beta L}{f_0}$
- n, s Locally orthogonal coordinate axes with s along a given curve
- P pressure
- $P(A)$ atmospheric pressure
- $P(d)$ pressure at the bottom of the ocean $z = d$
- $P(\zeta)$ pressure on the surface $z = 0$
- R radius of the Earth
- T_n integrated mass transport normal to a given boundary
- T_x integrated mass transport in the x direction
- T_y integrated mass transport in the y direction
- t time-independent variable

u x -component of fluid velocity and horizontal velocity scale factor
 $u(d)$ x -component of the geostrophic velocity at the bottom
 \vec{V} vector fluid velocity
 v y -component of fluid velocity
 v_D y -component of the geostrophic velocity at the bottom
 x, y, z Coordinate axes - independent variables
 α vertical integral of fluid density
 $\alpha(d)$ definite integral of fluid density from the surface to the bottom
 β gradient of the Coriolis parameter
 γ bottom friction coefficient
 Δ definite integral of α from the surface to the bottom
 ϵ constant used to scale density variations
 ∇ del operator $(\frac{\partial}{\partial x} \vec{i} + \frac{\partial}{\partial y} \vec{j})$
 ζ vertical position of the sea surface
 ϕ latitude
 ρ fluid density
 ρ_0 constant representative fluid density
 $\vec{\tau}$ horizontal component of wind stress at the surface
 τ_x x -component of surface wind stress
 τ_y y -component of surface wind stress
 ψ mass transport stream function
 $\vec{\Omega}$ Earth's rotation vector

DEVELOPMENT OF A SIMPLIFIED DIAGNOSTIC MODEL
FOR INTERPRETATION OF OCEANOGRAPHIC DATA

J. A. Galt

A steady state numerical model of ocean circulation is formulated to include geostrophic and Ekman dynamic balances as well as the effects of bathymetric variations. The model is diagnostic in that certain segments of the flow are determined from field data. In particular the baroclinic portion of the geostrophic mode is obtained from in situ density measurements and the surface wind driven layer is determined from wind stress data. The model solves for the required barotropic mode and subsequent bottom frictional layer that satisfies continuity and the assumed boundary conditions.

The dependency of the model solution on input data and boundary conditions is discussed. For the case where bottom friction is not included the model reduces to a first order, ordinary differential equation that can be solved along characteristic (f/d) contours. For preliminary model studies this simplified formulation is recommended with a combination of moored current meter data and dynamic height calculations for boundary conditions.

1. INTRODUCTION

In doing oceanographic studies, one has traditionally been faced with the task of estimating circulation. This has proved a formidable undertaking and success has been limited even in restricted areas. Direct measurements have proved particularly difficult. Stable platforms that can survive the ocean environment for extended periods are hard to engineer and recording current meters are expensive. Once the direct

measurements are obtained, problems in analysis are common, with typical measurements showing significant energy at higher frequencies. These energetic fluctuations make it difficult to calculate significant mean currents, or obtain coherent flow patterns over even very short distances without averaging quite long records. For many applications it is just this mean flow that is needed and the effects of higher frequency fluctuations could be adequately represented by eddy coefficients.

Since direct current measurements are so difficult to make and apply to regional oceanographic studies, it is reasonable to attempt a theoretical description of currents. To do this, equations representing the flow must be formulated and solved. The Navier-Stokes equation is basically an expression of Newton's second law that can be applied to geophysical fluids. Combining this with equations for continuity and the distribution of density, a closed set of equations is obtained that is theoretically capable of solution. This set of equations may be written in the following form which is appropriate for large-scale oceanic flows:

$$\frac{\partial \vec{v}}{\partial t} + (\vec{v} \cdot \nabla) \vec{v} + 2\vec{\Omega} \times \vec{v} = - \frac{1}{\rho} \nabla \rho + \nabla (K \nabla \vec{v}) - g \vec{k} \quad (1)$$

$$\nabla \cdot \vec{v} = 0 \quad (2)$$

$$\frac{\partial \rho}{\partial t} + (\vec{v} \cdot \nabla) \rho = \nabla (N \nabla \rho) \quad (3)$$

where

\vec{v} vector velocity

$\vec{\Omega}$ rotation vector of the Earth

ρ density

p pressure

g acceleration of gravity

\vec{k} unit vector in the vertical direction

K eddy coefficients for the diffusion of momentum

N eddy coefficients for the diffusion of density - note:

formulating the equations in terms of the diffusion of density eliminates the equation of state.

These equations have been simplified to some degree already; nevertheless they do represent a relatively general formulation of the circulation and solutions can be attempted. Problems arise, however, since this set of equations is extremely rich in solutions. In addition, nonlinear effects make general solutions impossible in analytic form, and even with numerical approximations only limited ranges or scales of flow can be investigated. To get around these mathematical difficulties additional approximations can be introduced. These limited formulations can consistently represent certain classes or parts of the flow that are thought to be dominant. Even in these simplified forms major difficulties still stand in the way of a purely theoretical description of the flow. In particular, the advection of the density field by the currents leads to mathematically complex expressions. If both the fluid velocity and the

density are dependent variables then even the simplified forms of the equations are nonlinear. The idea of diagnostic modeling is to get around this particular difficulty.

In a diagnostic model the density is not taken as a dependent variable. It is obtained by direct measurements in the field or region of interest. The direct measurements are then used as coefficients to linearize the theoretical equations. Looking at this in a slightly different light, a diagnostic model solves for the velocity field subject to some observed density distribution and the equations of motion. In this sense it is a combination of direct observations and theoretical solutions. It should be pointed out, however, that the direct observations required are of the density field. (In the ocean this requires temperature and salinity measurements.) These are much easier to obtain on a routine basis than direct measurements of the actual currents. In its simplest form, then, a diagnostic model analyzes the observed temperature and salinity distribution of a region and supplies the current implied by them.

Diagnostic modeling is not new to meteorology or oceanography. The standard geostrophic calculation of currents using the dynamic method (Forman, 1964) is a form of diagnostic modeling. Russian scientists have been particularly active in the development of very general diagnostic models and in applying them to large-scale oceanic circulation. An interesting review and discussion is presented by Sarkisyan and Keondjiyan (1972). Bryan (personal communication) has also investigated large-scale ocean circulation using diagnostic formulations in the initialization of

more complex prognostic modeling experiments. Peng and Hsueh (1974) have applied a relatively complete diagnostic model to a coastal zone as part of the CUE study. The initial dynamic processes included in their work are similar to those proposed in this study, i.e., geostrophic plus Ekman flow. This is a quite common point of departure for linear circulation models. In their work Peng and Hsueh carry out relatively detailed scale analysis for the special case where the bottom slope provides the dominant gradient in the potential vorticity. In applying their model a somewhat idealized coastal configuration was used.

The object of the present work is to formulate a simplified diagnostic model that can readily be used in the interpretation of data from coastal and continental shelf regions. Optional sets of boundary conditions and computational techniques will be presented. A detailed derivation of the model equations will be presented in the following section. Before this, a brief outline will be given of the types of flow included in the formulation.

Scale analysis of the equations of motion for open ocean flows indicate that accelerations are small and that Coriolis and pressure forces nearly balance each other. If this balance is assumed, a geostrophic current is represented. The equation for this is

$$\vec{f} \times \vec{v} = -\frac{1}{\rho} \nabla p, \quad (4)$$

where \vec{f} = vertical component of the Earth's rotation, or Coriolis parameter.

For these same scales of motion the relationship between the pressure and the density is hydrostatic, i.e.,

$$\frac{\partial P}{\partial z} = - \rho g , \quad (5)$$

where z = vertical coordinate axis,

g = acceleration of gravity.

To obtain a diagnostic relationship between the density and velocity equation (4) is differentiated with respect to z and equation (5) is substituted for the pressure term. This results in the so-called "thermal wind" equation:

$$f \times \frac{\partial \vec{v}}{\partial z} = \frac{1}{\rho} \nabla P . \quad (6)$$

From this equation the geostrophic velocity can be obtained to within a constant of integration providing the horizontal gradients in the density are known.

Near the surface of the ocean a wind-driven layer (Ekman layer) is superimposed on the geostrophic flow. The dynamics of the flow are represented by a balance between the Coriolis force and shear stress. This results in the equation:

$$f \times \vec{v} = \frac{\partial}{\partial z} \left(K \frac{\partial \vec{v}}{\partial z} \right) , \quad (7)$$

and boundary conditions

$$K \frac{\partial \vec{v}}{\partial z} \text{ surface} = \vec{\tau} , \text{ and } \vec{v} \text{ bottom} = 0 \quad (8)$$

where $\vec{\tau}$ = the surface wind stress

Equation (7) is also in a diagnostic form in that the wind-driven currents can be determined once the surface stress distribution is

known. The simple linear sum of equations (4) and (7) then represents a wind-driven baroclinic regime. Moreover, a recent study by Beardsley and Butman (1974) suggests that this relatively simple formulation can describe a significant portion of the observed flow in some continental shelf regions.

The Ekman plus geostrophic formulation can easily be extended to include bottom stress and a subsequent bottom Ekman layer. Given the density distribution and the wind stress the flow is then completely determined to within the constant of integration that results from equation (6). Traditionally this constant has been evaluated using the assumption that horizontal velocities go to zero at great depth (level of no motion), or equivalently, that the slope of the sea surface is known. While this may be a reasonable assumption in deep water, it is quite clearly not true in the shallower regions over the continental shelf. In this case an alternate method of obtaining the constant of integration must be considered. One straightforward approach is to set continuity constraints on the transport. Typically these will require that the divergence of the total horizontal flow is zero. A classical open ocean model incorporating this type of dynamics was done by Sverdrup (1947). In shallower regions over the continental shelf and slope, the circulation may interact strongly with the sloping bottom. Satisfying an integral condition on the transport has the additional advantage of allowing the flow to couple appropriately with the bathymetry; thus this formulation satisfies potential vorticity constraints and includes the important

Joint Effects of Baroclinicity And bottom Relief (JEBAR) (Sarkisyan and Ivanov, 1971; Holland, 1973).

From this relatively simple theory a diagnostic model can be developed that includes wind-driven currents, geostrophic flow (barotropic and baroclinic modes), frictionally controlled currents along bottom, and the effects of complex bathymetry. This model will then be used to describe the flow along coastal and continental shelf regions using relatively easy to obtain wind and density data as input.

2. DEVELOPMENT OF MODEL EQUATIONS

We may begin by considering a coordinate system in the northern hemisphere, as shown in Figure 1. The x and y axes are horizontal and at the mean elevation of sea level; x points to the east and y to the north. The z axis is positive up giving a right-handed Cartesian coordinate system; $\zeta(x, y)$ defines the vertical position of the free surface, and $d(x, y)$ gives the vertical position of the bottom.

Making the assumption that the pressure is hydrostatic gives

$$\frac{\partial P}{\partial z} = - \rho g \quad , \quad (9)$$

and, integrating this, gives the pressure at any depth as

$$P(z) = P(A) - g \int \rho dz \quad , \quad (10)$$

where $P(A)$ is the local atmospheric pressure at sea level. Assuming that the ocean adjusts to this atmospheric pressure as an inverted barometer, there will be no associated steady-state flow. Without any loss in

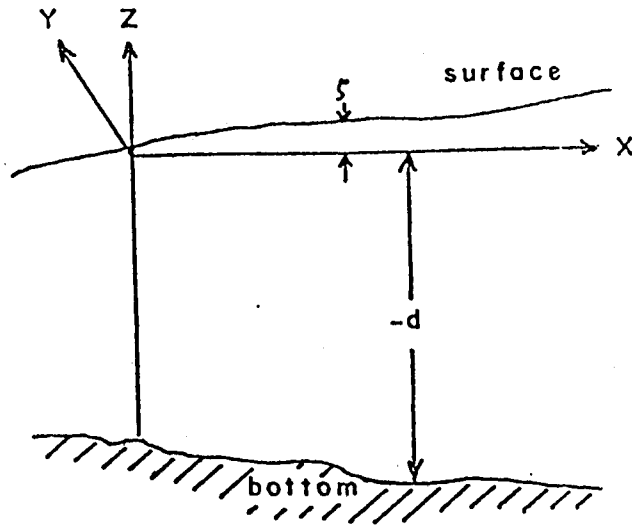


Figure 1. Coordinate system used for model equations.

generality, $P(A)$ will be taken as zero. We may now obtain horizontal components to the pressure gradients by differentiation of (10), i.e.,

$$\frac{\partial P}{\partial x} = - \frac{\partial}{\partial x} \left(g \int_{\zeta}^z \rho dz \right) = \frac{\partial}{\partial x} \left(g \int_0^{\zeta} \rho dz \right) + \frac{\partial}{\partial x} \left(g \int_z^0 \rho dz \right). \quad (11)$$

Using Leibniz's rule for interchanging the order of differentiation and integration in the first term on the right-hand side gives

$$\frac{\partial P}{\partial x} = (g\rho_0) \frac{\partial \zeta}{\partial x} + g \int_0^{\zeta} \frac{\partial \rho}{\partial x} dz + \frac{\partial}{\partial x} \left(g \int_z^0 \rho dz \right), \quad (12)$$

where $\rho(\zeta)$ is replaced by ρ_0 , a characteristic constant density. The second term on the right-hand side is negligible compared with the typical values for the other two terms. It represents the baroclinic contribution to the pressure gradient of something less than the top meter of

water. For a homogeneous upper layer this would be identically zero and will be assumed zero in this model. Both of these assumptions will be clearly appropriate when the equations are scaled and nondimensionalized in a following section of this report; thus equation (12) becomes

$$\frac{\partial p}{\partial x} = g\rho_0 \frac{\partial \zeta}{\partial x} + g \frac{\partial \alpha}{\partial x} , \quad (13)$$

where

$$\alpha(z) = \int_z^0 \rho dz . \quad (14)$$

The first term on the right-hand side gives the barotropic contribution to the pressure gradient, i.e., that part caused by the slope of the sea surface. It is obviously independent of depth and with present technology cannot be measured at sea. The second term on the right-hand side gives the baroclinic contribution to the pressure gradient, i.e., that part caused by the internal distribution of mass in the ocean. This can be obtained from standard oceanographic stations using a Nansen bottle or STD data.

Using the same arguments, the y component of the pressure gradient can be written as

$$\frac{\partial p}{\partial y} = \rho_0 g \frac{\partial \zeta}{\partial y} + g \frac{\partial \alpha}{\partial y} . \quad (15)$$

We may now consider an ocean region where the currents are the sum of a surface Ekman layer driven by the wind, a geostrophic interior driven by barotropic and baroclinic pressure gradients, and a bottom Ekman layer that matches a zero slip condition along the bottom. The equations to represent this flow are as follows:

$$-f\rho v = -\frac{\partial p}{\partial x} + \frac{\partial}{\partial z} \left(\kappa \frac{\partial u}{\partial z} \right) , \quad (16)$$

$$f\rho u = -\frac{\partial p}{\partial y} + \frac{\partial}{\partial z} \left(\kappa \frac{\partial v}{\partial z} \right) , \quad (17)$$

where u and v are the x and y components of velocity, respectively. Integrating these equations from d to ζ and using Leibniz's rule gives

$$-fTy = -\frac{\partial}{\partial x} \int_d^\zeta P dz + P(\zeta) \frac{\partial \zeta}{\partial x} - P(d) \frac{\partial d}{\partial x} - \tau_x(d) + \tau_x(\zeta) , \quad (18)$$

$$fTx = -\frac{\partial}{\partial y} \int_d^\zeta P dz + P(\zeta) \frac{\partial \zeta}{\partial y} - P(d) \frac{\partial d}{\partial y} - \tau_y(d) + \tau_y(\zeta) , \quad (19)$$

where T_x and T_y are the x and y components of the mass transport, $\tau_x(d)$ and $\tau_y(d)$ are the x and y components of the stress evaluated at the bottom, and $\tau_x(\zeta)$ and $\tau_y(\zeta)$ are the x and y components of the wind stress acting on the surface of the water.

By cross differentiating equations (18) and (19) and subtracting, the following vorticity equation is obtained: (assuming $f = f_0 + \beta y$)

$$-\beta T_y - f \nabla^2 \vec{T} = J(P(\zeta), \zeta) - J(P(d), d) + \vec{k} \cdot \nabla_x \vec{\tau}(d) - \vec{k} \cdot \nabla_x \vec{\tau}(\zeta) . \quad (20)$$

Setting the divergence of the total transport equal to zero means that the last term on the left-hand side is identically zero. In addition, making the Boussinesq approximation the surface layer is assumed homogeneous and the first term on the right-hand side is zero. This leaves the following vorticity equation:

$$-\beta T_y = -J(P(d), d) + \vec{k} \cdot \nabla_x \vec{\tau}(d) - \vec{k} \cdot \nabla_x \vec{\tau}(\zeta) . \quad (21)$$

The stress at the bottom can be evaluated using Ekman theory. (Neumann and Pierson, 1966, p. 200). Assuming that the depth of water is greater

than the depth of frictional influence, the stress will be linearly related to the geostrophic velocity at the bottom. In Peng and Hseuh's (1974) model this assumption is not made and the more general case where the water depth can be smaller than the Ekman layer thickness ($\pi\sqrt{\frac{K}{\rho f}}$) is included. This leads to more complex coefficients in the final formulation and it is not particularly clear that it extends the usefulness of the model very much. In particular, if the water is shallower than 20-30 meters the linear dynamics become highly questionable. Proceeding with the assumption that the depth is greater than the Ekman depth,

$$\tau_{x_d} = f\gamma(u(d) - v(d)) , \quad (22)$$

$$\tau_{y_d} = f\gamma(u(d) + v(d)) , \quad (23)$$

where $u(d)$ and $v(d)$ are the geostrophic velocity components evaluated at the bottom and γ is a dimensional factor proportional to an eddy coefficient.

The geostrophic velocity can be obtained from the horizontal components of the pressure gradient, i.e.,

$$-f\rho v = -\frac{\partial P}{\partial x} ,$$

$$f\rho u = -\frac{\partial P}{\partial y} .$$

To simplify this the density on the left-hand side of these equations may be taken as the representative constant value. This is equivalent to making a Boussinesq approximation and gives the following results:

$$\tau_{x(d)} = \frac{\gamma}{\rho_0} \left(-\frac{\partial P(d)}{\partial y} - \frac{\partial P(d)}{\partial x} \right) , \quad (24)$$

$$\tau_{y(d)} = \frac{\gamma}{\rho_0} \left(-\frac{\partial P(d)}{\partial y} + \frac{\partial P(d)}{\partial x} \right) . \quad (25)$$

Cross differentiating these two components gives the curl of the bottom stress as

$$\vec{k} \cdot \nabla \vec{x} \tau(d) = \frac{\gamma}{\rho_0} \nabla^2 P(d) . \quad (26)$$

Substituting (26) into (21) yields

$$-\beta T_y = -J(P(d), d) + \frac{\gamma}{\rho_0} \nabla^2 P(d) - \vec{k} \cdot \nabla \vec{x} \tau(\zeta) .$$

In the absence of significant variations in the Coriolis parameter (i.e., where horizontal length scale is small compared with the radius of the Earth), this equation can be solved for the single dependent variable, bottom pressure. A more useful form of the equation can be obtained by substituting from equations (13) and (15) into the above. Doing this gives the following equation in the two unknowns, surface elevation and y -component of transport:

$$-\beta T_y = -g\rho_0 J(\zeta, d) - gJ(\alpha(d), d) + g\gamma \nabla^2 \zeta + \frac{g\gamma}{\rho_0} \nabla^2 \alpha(d) - \vec{k} \cdot \nabla \vec{x} \tau(\zeta) . \quad (27)$$

This equation specifies the complete vorticity balance represented in the model, and it may clarify the physics a bit to identify the significance of each term. The left-hand side of the equation gives the so-called β -effect or planetary tendency associated with variations in the Coriolis parameter. The first two terms on the right-hand side of the equation represent the joint interaction of the flow with the bathymetry. These are the JEBAR terms with the first of the pair giving the contribution from the barotropic mode and the second giving the baroclinic contribution. One can note that for homogeneous water the second term would be identically zero and the first would give the familiar

stretching term in the conservation of potential vorticity. On the other extreme, if a complete baroclinic adjustment resulted in no net horizontal pressure gradient at depth, these terms would identically cancel each other. The third term on the right-hand side represents the vorticity contribution by the barotropic mode caused by bottom friction. The fourth term gives the vorticity added through the baroclinic mode by bottom friction. Finally, the last term in equation (27) is the vorticity added to the flow by the wind stress.

To solve equation (27) we must come up with an additional relationship between the transport and the surface elevation. This can easily be done by enumerating the components to the total transport. To begin with, the transport in the surface Ekman layer is given by

$$T_y(\text{Ekman}) = -\frac{\tau_x}{f}(\zeta), \quad (28)$$

subject to the condition that the water depth is greater than the Ekman layer thickness. Next the barotropic velocity is independent of depth and given by

$$pv = \frac{g\rho_0}{f} \frac{\partial \zeta}{\partial x},$$

and, integrating this from d to 0 , gives

$$T_y(\text{barotropic}) = -\frac{g\rho_0 d}{f} \frac{\partial \zeta}{\partial x}. \quad (29)$$

The baroclinic velocity is given by

$$pv = \frac{g}{f} \frac{\partial \alpha}{\partial x},$$

and, integrating this from d to 0 , gives

$$\begin{aligned} \tau_y (\text{baroclinic}) &= \frac{g}{f} \int_d^0 \frac{\partial \alpha}{\partial x} dz & (30) \\ &= \frac{g}{f} \left(\frac{\partial}{\partial x} \int_d^0 \alpha dz + \alpha(d) \frac{\partial d}{\partial x} \right) \\ &= \frac{g}{f} \left(\frac{\partial \Delta}{\partial x} + \alpha(d) \frac{\partial d}{\partial x} \right), \end{aligned}$$

where Δ is the definite integral

$$\Delta = \int_d^0 \alpha dz \quad (31)$$

The transport in the bottom Ekman layer will be given by:

$$\tau_y (\text{d-Ekman}) = \frac{\tau_x(d)}{f}, \quad (32)$$

again subject to the condition that the water depth is greater than the Ekman layer thickness, and substitution into this from (13), (15) and (24) gives

$$\tau_y (\text{d-Ekman}) = -\frac{\gamma g}{f} \left(\frac{\partial \zeta}{\partial x} + \frac{\partial \zeta}{\partial y} \right) - \frac{\gamma g}{\rho_0 f} \left(\frac{\partial \alpha(d)}{\partial x} + \frac{\partial \alpha(d)}{\partial y} \right) \quad (33)$$

The total mass transport in the y direction can now be written as the sum of equations (28), (29), (30) and (33), i.e.,

$$\begin{aligned} \tau_y &= -\frac{\tau_x(\zeta)}{f} - \frac{g \rho_0 d}{f} \frac{\partial \zeta}{\partial x} + \frac{g}{f} \left(\frac{\partial \Delta}{\partial x} + \alpha(d) \frac{\partial d}{\partial x} \right) & (34) \\ &\quad - \frac{\gamma g}{f} \left(\frac{\partial \zeta}{\partial x} + \frac{\partial \zeta}{\partial y} \right) - \frac{\gamma g}{\rho_0 f} \left(\frac{\partial \alpha(d)}{\partial x} + \frac{\partial \alpha(d)}{\partial y} \right). \end{aligned}$$

For completeness the x -component of the mass transport will be written as

$$\begin{aligned}
 \tau_x = & + \frac{\gamma y(\zeta)}{f} + \frac{g\rho_0 d}{f} \frac{\partial \zeta}{\partial y} - \frac{g}{f} \left(\frac{\partial \Delta}{\partial y} + \alpha(d) \frac{\partial d}{\partial y} \right) \\
 & - \frac{\gamma g}{f} \left(\frac{\partial \zeta}{\partial x} - \frac{\partial \zeta}{\partial y} \right) - \frac{\gamma g}{\rho_0 f} \left(\frac{\partial \alpha(d)}{\partial x} - \frac{\partial \alpha(d)}{\partial y} \right)
 \end{aligned} \quad (35)$$

Equations (27), (34) and (35) now give three equations in the three unknowns τ_x , τ_y and ζ . From these it is possible to obtain a single equation for the elevation of the free surface, or for the transport (expressed in terms of a stream function). Sarkisyan and Keondjiyan (1972) discuss the relative merits of each formulation in some detail. In this work some attention will also be given to the following alternate forms.

2.1 Surface Elevation as Dependent Variable

For the present section the free surface elevation will be chosen as the dependent variable, thus focusing attention on the near surface currents. Substituting equation (34) in (27) and rearranging terms gives

$$\begin{aligned}
 & + g\gamma \nabla^2 \zeta + \frac{g\gamma}{\rho_0} \nabla^2 \alpha(d) - g\rho_0 J(\zeta, d) - gJ(\alpha(d), d) - \vec{k} \cdot \nabla_{x1} \tau(\zeta) \\
 & - \frac{\beta}{f} \tau_x(\zeta) - \frac{g\rho_0 d \beta}{f} \frac{\partial \zeta}{\partial x} + \frac{g\beta}{f} \left(\frac{\partial \Delta}{\partial x} + \alpha(d) \frac{\partial d}{\partial x} \right) - \frac{\gamma g \beta}{f} \left(\frac{\partial \zeta}{\partial x} + \frac{\partial \zeta}{\partial y} \right) \\
 & - \frac{\gamma g \beta}{\rho_0 f} \left(\frac{\partial \alpha(d)}{\partial x} + \frac{\partial \alpha(d)}{\partial y} \right) = 0
 \end{aligned} \quad (36)$$

This, then, is a final model equation. It is elliptic in the single unknown ζ . It represents a diagnostic model in that the variable coefficients are all given in terms of known constants, the depth distribution and the observed density field. Solving this equation is equivalent to

finding the barotropic mode that satisfies continuity, subject to a given baroclinic mode, wind stress driven Ekman layer and assumed Ekman dynamics in a bottom Ekman layer.

2.2. Transport Stream Function as a Dependent Variable

In this section a diagnostic equation for the total transport will be derived. This option tends to focus attention on the integrated flow and in some cases leads to more natural, or easier to interpret, boundary conditions. To develop this form of the equation (34) and (35) can be solved for the gradient components of the surface elevation. These values are then differentiated and the results substituted into (27). For the general case the algebra involved is quite tedious and the resulting formulation so unwieldy that it is not of any practical value. One special case is quite useful, however, and this will be developed. In particular, if the frictional drag on the bottom is zero (formally $\gamma = 0$), equations (34) and (35) no longer require simultaneous solution, and we may proceed directly as follows:

$$g\rho\frac{\partial\zeta}{\partial x} = -\frac{fTy}{d} - \frac{\tau_x(\zeta)}{d} + \frac{g}{d}\left(\frac{\partial\Delta}{\partial x} + \alpha(d)\frac{\partial d}{\partial x}\right), \quad (37)$$

$$g\rho\frac{\partial\zeta}{\partial y} = \frac{fTx}{d} - \frac{\tau_y(\zeta)}{d} + \frac{g}{d}\left(\frac{\partial\Delta}{\partial y} + \alpha(d)\frac{\partial d}{\partial y}\right), \quad (38)$$

and substituting these into equation (27), again with the assumption that $\gamma = 0$, and introducing a stream function for the total mass transport such that

$$\tau_y = \frac{\partial\Psi}{\partial x} \quad \tau_x = -\frac{\partial\Psi}{\partial y}, \quad (39)$$

the following equation is obtained:

$$J(\psi, \frac{f}{a}) = -\frac{g}{a} J(\alpha, d) - \frac{g}{a^2} J(\Delta, d) + \frac{1}{a^2} \vec{k} \cdot \nabla d \vec{x} \tau(\zeta) - \frac{1}{a} \vec{k} \cdot \nabla x \tau(\zeta). \quad (40)$$

Here again we have a diagnostic model with the total transport stream function as the dependent variable expressed in terms of the density distribution, bathymetry and the surface wind stress distribution. The solution will yield the transport that satisfies the integrated continuity constraints subject to a measured baroclinic mode, surface wind-driven Ekman layer and bathymetric distribution.

3. BOUNDARY CONDITIONS AND DATA REQUIREMENTS

In the preceding section two diagnostic equations were derived: Equation (36) giving the surface elevation or barotropic mode and (40) giving the total integrated mass transport. To make use of these equations a method of solution must be introduced and appropriate boundary conditions applied. In this section a number of specific cases will be considered and the demands for input data and boundary conditions will be discussed.

The first case to be considered will be the one represented in equation (36). This form is relatively general in that it includes both surface and bottom Ekman layers, geostrophic flow (including barotropic and baroclinic modes), the effects of bathymetry, and the variation of the Coriolis parameter with latitude. The equation can be written in the following form:

$$A \nabla^2 \zeta + B \frac{\partial \zeta}{\partial x} + C \frac{\partial \zeta}{\partial y} + D = 0, \quad (41)$$

where the non-constant coefficients are known functions of the independent variables, i. e.,

$$A = \gamma g , \quad (42)$$

$$B = g\rho_0 \left(\frac{\partial d}{\partial y} - \frac{\beta d}{f} - \frac{\beta \gamma}{f\rho_0} \right) , \quad (43)$$

$$C = g\rho_0 \left(\frac{\partial d}{\partial x} - \frac{\beta \gamma}{f\rho_0} \right) , \quad (44)$$

$$D = \frac{\gamma g}{\rho_0} \nabla^2 \alpha(d) - gJ(\alpha(d), d) - \frac{\gamma g \beta}{f\rho_0} \left(\frac{\partial \alpha(d)}{\partial x} + \frac{\partial \alpha(d)}{\partial y} \right) , \quad (45)$$

$$\frac{g\beta}{f} \left(\frac{\partial \Delta}{\partial x} + \alpha(z) \frac{\partial d}{\partial x} \right) = \vec{k} \cdot \nabla_x \vec{\tau}(\zeta) - \frac{\beta \tau_x(\zeta)}{f}$$

The variable part of these coefficients depends on the depth, the density distribution and the wind stress field.

The depth distribution can be obtained with satisfactory accuracy from standard hydrographic charts. In virtually all cases the quantity and quality of the bathymetric data is better than any of the other required input data. It is only necessary to digitize chart data and develop some appropriate method for interpolating and differentiating the results. Once this is done it is a relatively simple task to calculate the depth and gradient of the depth at whatever numerical grid points are desired.

The density information that is required is contained in the values of $\alpha(d)$ and Δ introduced in (14) and (31). These are specified by the density as follows:

$$\alpha(z) = \int_z^0 \rho dz , \quad (46)$$

which is clearly related to the pressure in a hydrostatic fluid. This integral would typically be done numerically after obtaining values for the integrand at discrete depths from Nansen bottle or STD data. Numerically this is quite similar to the type of procedure that is routinely done to calculate specific volume anomaly and dynamic heights. Once this is done the two required definite integrals can also be calculated, i.e.,

$$\alpha_d = \int_d^0 \rho dz \quad \Delta = \int_d^0 \alpha dz = \int_d^0 \int_z^0 \alpha(z') dz' dz = \int_d^0 (z-d)\rho(z) dz$$

These would also be integrated numerically. A physical interpretation of these terms is perhaps now more apparent. The first obviously relates to the pressure or mean density and the second represents the first moment of the density around the bottom depth. After the field of α_d and Δ is obtained, horizontal derivatives must be calculated at required grid spacings. This would once again require the development of some interpolation scheme. It should be noted that in deep water α_d and Δ may turn out to be very large numbers and that the gradients will be given as relatively small differences between these large numbers. This can lead to the loss of significant figures and subsequent numerical difficulties. For typical oceanic depths (> 4000 m) this can be a serious problem, and even the best quality data may need to be artificially smoothed before reasonable results can be obtained. In shallower water over the continental shelf and slope this accuracy problem tends to be less troublesome for two reasons. First of all the depth is much less, typically several hundred meters; and secondly, the density gradients

are often greater than in the open ocean. It appears then that the classical method of calculating currents by dynamic heights and diagnostic models complement each other. In deep water, baroclinic compensation is likely to take place, and the assumption of a stationary reference level is not altogether improbable. This is just the point where inaccuracies in the integrated transport make it difficult to apply continuity constraints, and hence diagnostic modeling techniques are difficult to apply. Conversely, in shallower water baroclinic adjustment is not likely to take place and interactions between the flow and the bathymetry are significant. This then will make a reference level concept unworkable and leaves diagnostic modeling as a strong alternative since the numerical problems associated with the transport constraints will be reduced and this method can include the effects of complex topography.

Another potential source of error in the density field measurements must also be considered. These do not depend on numerical errors, but rather on sampling schemes that are typically used to collect the data. The dynamics of the model assume the flow to be geostrophic, hydrostatic, and steady. To the extent that these conditions are not met and are reflected in the data, the model will introduce erroneous results. Two obvious sources of potential error come quickly to mind. First of all, if there are strong internal tides in the region of interest these may well alias the density field. To test for this eventuality a local study that can resolve internal tides would seem prudent. For example, a few 24-hr series of STD casts at one location

should indicate the typical magnitude of density perturbations introduced into the data. Secondly, a problem could develop if the density data is not truly synoptic. Typically a single ship could gather density field data in something like a week. If this is the case, a regional baroclinic current with time scales of a week or less would tend to distort the density field and errors in the calculated gradients may result. The most likely currents to alias the data in this manner are quasi-geostrophic shelf waves. To minimize this difficulty, the regional data should be collected as quickly as possible. In addition, long-term current records can be analyzed to estimate the potential magnitude of these errors.

Both of the problems mentioned above could be minimized by using density fields that represent the average of an ensemble collection of data. This would require the analysis of historical data, and, if enough is available to construct a reasonably smooth mean density field for whatever periods are of interest, would be an attractive option.

The final independent variable input needed for the model is the surface wind stress. For most oceanographic studies, wind data are notoriously poor. Under the best circumstances one might expect to have a few strategically located shore stations and moored buoys that report winds. In cases where this is not available it is possible to estimate the wind stress field using atmospheric pressure data (Aagaard, 1969, 1970). If pressure maps are not available on a synoptic basis it is often possible to use climatological data. In most cases the spatial

resolution of the wind field is minimal and only the general characteristics of the wind forcing can be included in the model. Even at this minimal level the wind effect can significantly modify the flow patterns in coastal areas and important additions to the flow dynamics are represented by including them. For example, the barotropic setup along the coastlines caused by Ekman transport is included in the dynamics of the model, and the resulting coastal currents will be simulated.

It now remains to specify the boundary conditions necessary to uniquely solve (41). The form is clearly elliptic, so there are several optional sets of boundary conditions that would close the problem. Because the dependent variable is surface elevation, Dirichlet type boundary conditions will be relatively easy to interpret (Sneddon, 1957), i.e., specification of the surface elevation around the perimeter of the domain will be sufficient to completely determine the solution. Since the sea surface along the boundary gives the normal component of the barotropic mode, this is equivalent to specifying the distribution of barotropic flow into the region. This is represented schematically in Figure 2.

In a mathematical sense the problem is now formally closed, but to make much use of the model a bit more detail on the implications of various boundary value specifications seems in order. In addition, some thought should be given to how the actual boundary values might be obtained in a consistent manner.

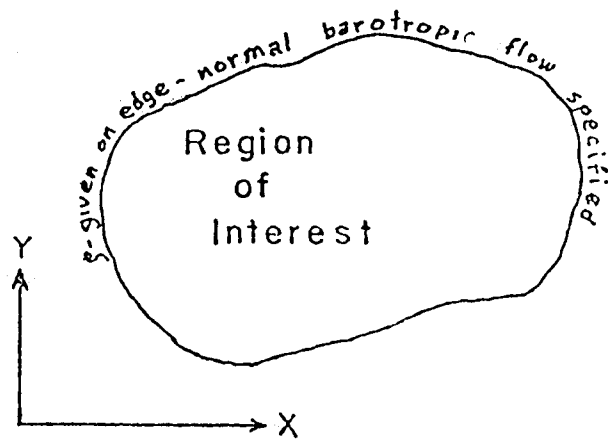


Figure 2. Dirichlet type boundary conditions for region of interest.

To begin with, we may note that the barotropic transport across a unit length of boundary (where s is distance measured along a prescribed line) is given by:

$$T_n = - \frac{g\rho_0 d}{f} \frac{\partial \zeta}{\partial s},$$

and across any section of the boundary:

$$\int T_n = - \frac{g\rho_0 d}{f} \int \frac{\partial \zeta}{\partial s} ds$$

If the depth is constant along a closed path of integration (i.e., the boundary), then the net barotropic transport into the region is identically zero (unless the region is large enough so that variations in f are significant). The same will be true for the total geostrophic transport, and thus for the baroclinic mode and barotropic mode, individually. This can also easily be seen from (30), assuming d and f are constants, meaning that for flat bottom regions or closed bathymetric contours the

geostrophic flow cannot directly contribute to the net advection of either mass or vorticity into the domain. For this particularly simple case any wind-driven convergence in the surface Ekman layer must be balanced by divergence in the bottom layer. Assuming Ekman dynamics for the lower layer, any divergence will be proportional to the negative curl of the geostrophic flow. From this, the dependence of the solution on the forcing and boundary conditions can easily be seen, i.e., the rotational component of the flow is determined by the wind stress distribution. In addition, an incompressible component is added to satisfy the given boundary values. It is also clear that the problem will become degenerate as the frictional coefficient for the bottom layer approaches zero (equation 41). Physically the geostrophic vorticity will approach infinity and mathematically the higher order terms drop out and the equation goes from an elliptic form to a first order partial differential equation. This important special case will be considered in more detail later.

We may now consider a more general situation where there is a variable depth region to be investigated. Once again, if the surface elevation is given around the perimeter, the inflow (outflow) of the barotropic mode is determined. In this case it is possible, in fact likely, that the barotropic mode will give some net advection of mass or vorticity into the domain. In general, the only case where the barotropic mode does not add any net contribution to either the mass or vorticity is where water enters and exits the model region on the same bathymetric contour. This of course satisfies the conditions for conservation of

potential vorticity in a homogeneous geostrophic fluid (a limited subset of the physics included in the model formulation).

One of the major difficulties in formulating the model boundary conditions should now be clear. The divergence in the surface Ekman layer and the baroclinic mode are given by the diagnostic input data (i.e., wind stress and density field). In addition, the boundary conditions specify the net divergence of the barotropic mode. If these do not sum to zero, the only alternative available to the model is to satisfy continuity with the secondary flow in the bottom frictional layer. If the imposed boundary conditions are accurate then there is no difficulty. If, on the other hand, the balance is not correct, extraneous circulation in the barotropic mode around the boundary will result. In particular, a clockwise boundary circulation will give divergence in the bottom layer and a counterclockwise boundary current will give a net convergence in the bottom layer (fig. 3). In addition, we can see that the secondary flow required for the continuity balance is coupled to the geostrophic currents with the bottom frictional coefficient. If this is reduced, the couple becomes weaker, and much stronger boundary currents are required. Much the same kinds of arguments can be made about the vorticity balance within the model. This type of behavior is not uncommon in the solutions to differential equations where the highest order terms are multiplied by a small parameter, and boundary layers can be anticipated (Cole, 1968). This leads to the troubling conclusion that for small values of bottom friction coefficient the model may be very sensitive to the boundary conditions.

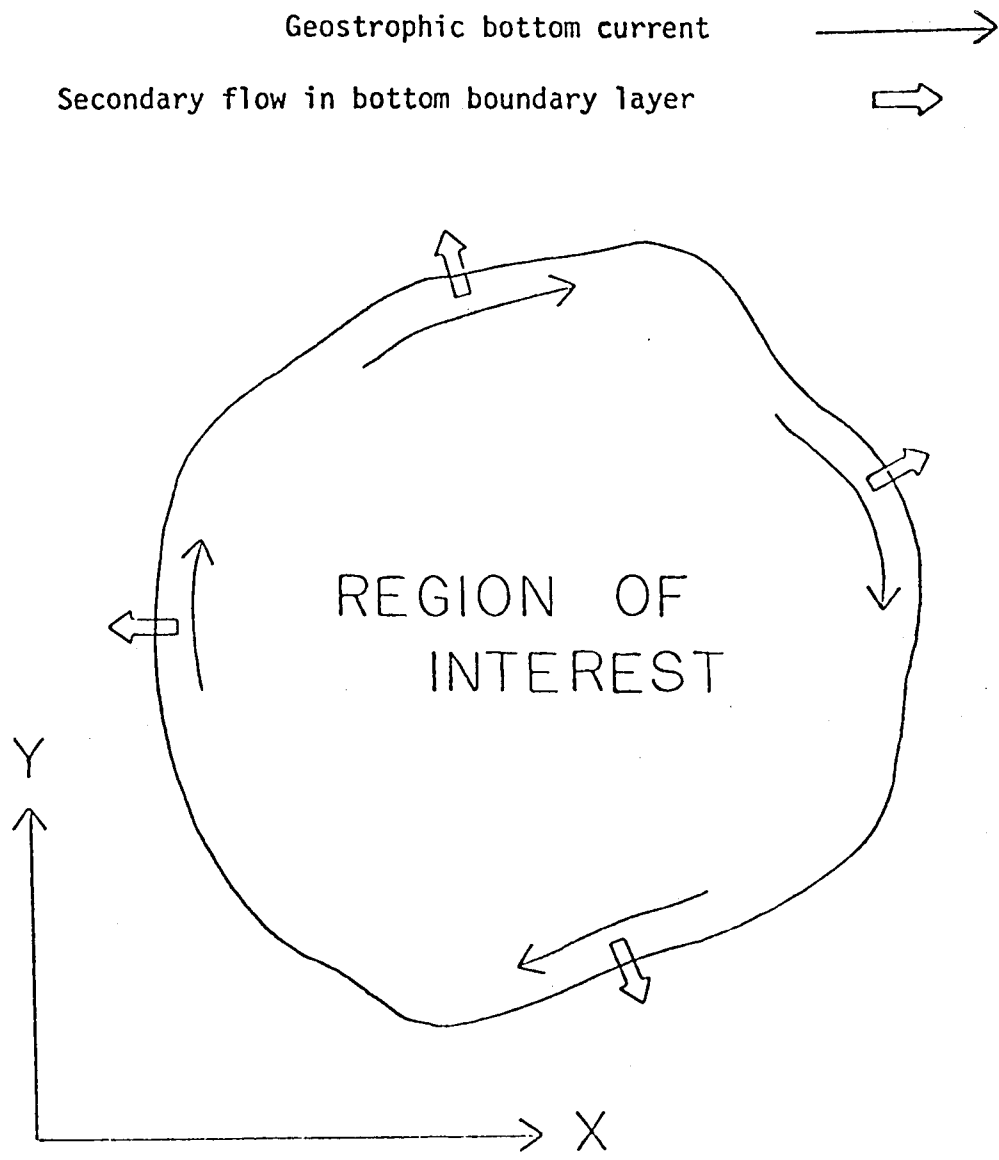


Figure 3. Net divergence within the area due to transport in secondary bottom boundary currents.

It should perhaps be pointed out that many partial basin models, both prognostic and time dependent, allow a steady geostrophic solution and are subject to these same potential difficulties. In some cases, this does not seem to be clearly understood, and insufficient care in the specification of boundary conditions has made model results difficult to interpret.

In other model studies, the effect of boundary currents is reduced by making the solution area larger than the actual area of interest. In this way it is hoped that errors near the model boundaries will not seriously affect the solution in the area of interest. This appears to be fairly successful in some cases but adds considerable complexity to the problem and is not consistent with the present goal of coming up with an operational easy-to-apply regional model.

To approach the problem of boundary conditions from a different and slightly more optimistic point of view, we can consider the equations without bottom friction and look at the implications of how the flow will be modified by introducing the small secondary flow associated with weak bottom friction.

In many respects this is in line with intuitive ideas of ocean currents. In general, it seems that bottom friction is not a dominant factor in the dynamics even in shallow water currents, and in deeper water the effects of bottom friction are essentially negligible.

Proceeding along this line, we may rewrite (36) assuming that γ is zero:

$$\begin{aligned}
 & -g\rho_0 J(\zeta, d) - gJ(\alpha(d), d) - \frac{g\rho_0 d \beta}{f} \frac{\partial \zeta}{\partial x} + \frac{g\beta}{f} \left(\frac{\partial \Delta}{\partial x} + \alpha(d) \frac{\partial d}{\partial x} \right) \\
 & - \vec{k} \cdot \nabla_x \vec{\tau}(\zeta) - \frac{\beta}{f} \tau_x(\zeta) = 0
 \end{aligned} \tag{47}$$

Multiplying this equation by f/d^2 and collecting terms gives

$$g\rho_0 J(\zeta, \frac{f}{d}) = \frac{g\beta}{d^2} J(\alpha(d), d) - \frac{g\beta}{d^2} (\frac{\partial \Delta}{\partial x} + \alpha(d) \frac{\partial d}{\partial x}) + \frac{f}{d^2} \vec{k} \cdot \nabla_x \vec{\tau}(\zeta) + \frac{\beta}{d^2} \vec{\tau}_x(\zeta) \quad (48)$$

This is now a first-order partial differential equation, and the appropriate boundary conditions are quite different from those required for (41). To get some indication of what these are and how they will determine the solution, we may consider the simplified case of a barotropic fluid with no surface wind. Under these assumptions the density is a function of z only, i.e.,

$$\rho = \rho(z) .$$

This results in the first two terms on the right-hand side of (48) being zero. With no stress the last two terms on the right-hand side are also zero, leaving:

$$J(\zeta, \frac{f}{d}) = 0 . \quad (49)$$

Physically the problem has been reduced to the familiar conservation of potential vorticity where the flow follows f/d contours. In a mathematical sense the most general solution to equation (49) is

$$\zeta = w(\frac{f}{d}) \quad (50)$$

where $w(\frac{f}{d})$ is an arbitrary function (Courant and Hilbert, 1962). Clearly, then, the solution for the entire domain is known once w is determined. To do this, the value of ζ must be given along any line that runs monotonically from the lowest value of f/d in the region to the highest (fig. 4). Even in the baroclinic case, the f/d contours will represent

characteristics for the differential equation, which means that along any of the f/d contours the partial differential equation can be written as an ordinary differential equation. To clarify this a bit, we may rewrite the Jacobian in a local orthogonal right-handed coordinate system where the n -axis is normal to f/d contour and the s -axis is along the contour (fig. 5). In this form, (48) becomes

$$\frac{\partial \zeta}{\partial n} \frac{\partial}{\partial s} \left(\frac{f}{d} \right) - \frac{\partial \zeta}{\partial s} \frac{\partial}{\partial n} \left(\frac{f}{d} \right) = RHS \quad (51)$$

where RHS just represents the right-hand side of (48) divided by $g\rho_0$. Next we see that the choice of coordinate systems makes the first term on the left-hand side equal to zero, and we are left with an ordinary differential equation:

$$\frac{d\zeta}{ds} = - \frac{RHS}{\frac{\partial}{\partial n} \left[\frac{f}{d} \right]} \quad (52)$$

From a numerical point of view this is now a straightforward problem. The right-hand side of (52) is given in terms of known quantities. Starting from the known point (boundary condition) on each f/d contour the equation can be integrated along the contour in either direction. In most cases a simple desk-top computer could handle the problem after some initial data analysis. Qualitatively the model reduces to about the same level of difficulty as the problem of calculating geostrophic currents using dynamic heights.

From the form of (52) we can also clearly see the physical significance of the right-hand side terms in (48). They represent the components of cross contour flow associated with the baroclinic (first two

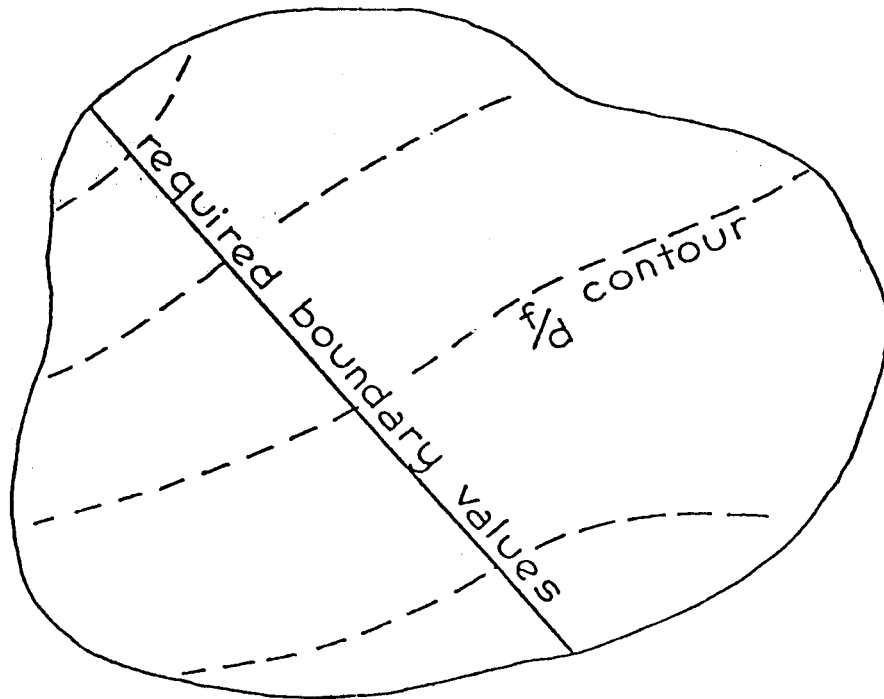


Figure 4. Required boundary conditions and characteristics for formulation without bottom friction.

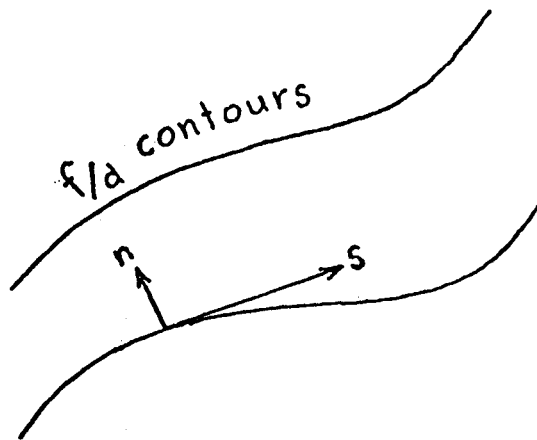


Figure 5. Orthogonal coordinate system related to f/d contours.

terms) and Ekman wind-driven modes (last two terms). The change of ζ along the contour physically represents the barotropic component of cross-contour flow, and to conserve the potential vorticity in the water column this barotropic stretching effect must just balance the contributions from the baroclinic and Ekman flow. In this context it is also obvious what happens in a region where the f/a gradient vanishes. The required stretching from the barotropic mode is impossible and a vorticity balance cannot be obtained. As was mentioned before, in a uniform depth region the geostrophic modes are non-divergent and a non-geostrophic component to the flow is required for solution, unless the curl of the wind stress is zero and it has no meridional component. In the context of the present model this non-geostrophic component would be the bottom frictional layer.

We are now in a position to work back to the full model including the effects of weak bottom friction. Starting with wind and density data, for some region, the surface elevation along any line running from the shallow to deep extremes is required. These data can be obtained in a variety of ways. In deeper regions a level of no motion assumption and dynamic height calculations might provide reasonable estimates. In shallower segments a line of moored current meter arrays across the f/a gradient should yield the most useful data, particularly if simultaneous measurements of bottom pressure are also obtained. If all else fails, a judicious guess could provide a point of departure for the careful numerical exploration of the implications of a given wind and density field.

Once the input data is accumulated the first phase of the model would solve for the simplified physics represented in equation (52).

From this the values of ζ around the entire boundary could be obtained, and the second phase of the model would use these with the full information given in equation (41). Obviously the potential for problems associated with the boundary conditions still exists, but for small values of bottom friction this method should prove a useful point of departure. It is likely that careful testing and qualitative iterations on the boundary values will give useful insights into model results.

As a final point, the stream function representation of the model given in equation (40) has the same mathematical form as equation (48) and can be solved in much the same way. These two equations represent identical physical processes and the choice of which one to use is essentially a matter of emphasis.

The boundary conditions required along a closed boundary are obvious when the transport stream function is the dependent variable. A no-flux condition requires a constant value for the stream function along the boundary. With the surface elevation as the dependent variable, the formulation is not quite so straightforward. For that case the change in surface elevation along the boundary must give a barotropic current that just balances the contribution across the boundary from the baroclinic and Ekman modes. These components to the flow must be calculated from the local values of input data for the model, and once again, if bottom friction is included boundary currents may be expected if net transport conditions are not met.

4. NON-DIMENSIONAL FORMULATION OF THE MODEL EQUATIONS

The actual solution of the model equations and their application to a geophysical situation will be greatly simplified if they are written in a consistently scaled non-dimensional form. This will also make it possible to come up with at least order-of-magnitude estimates for the relative significance of various terms and in some cases to suggest alternate formulations.

As a first step the pressure distribution and its gradient will be non-dimensionalized. This can be done by defining the following non-dimensionalized (primed) variables and constant dimensional scaling factors:

$$x = L(x') , \quad (53)$$

$$P = \rho_0 g z + \rho_0 f_0 U L (P') , \quad (54)$$

$$\rho = \rho_0 + \epsilon(\rho') , \quad (55)$$

where clearly the pressure is divided into a component which is hydrostatic with-respect to the typical density and a variable part that depends somehow on the density variations. It is likewise assumed that the density is made up of an average part and a fluctuating part. Also considering typical ocean situations, $\epsilon \approx O(10^{-3} \text{ g/cm}^3) \ll \rho_0 \approx O(1 \text{ g/cm}^3)$, it should be obvious that when considering variations in α and Δ , only the $\epsilon(\rho')$ component will contribute and that this partitioning will reduce the loss of significant figures that could result if the entire density field were scaled with a single constant. The depth variations

will also be scaled in two parts, reflecting the basic partitioning of the pressure gradient terms into barotropic and baroclinic parts. For elevation of the sea surface the following non-dimensional variable is used:

$$\zeta = \frac{f_0 U L}{g} (\zeta') \quad , \quad (56)$$

and for depths within the water column,

$$z = H(z') \quad . \quad (57)$$

These definitions may now be substituted into (11) and, applying Liebniz's rule, yield

$$\begin{aligned} \rho_0 f_0 U \left(\frac{\partial P'}{\partial x'} \right) &= [\rho_0 + \epsilon(\rho')] f_0 U \left(\frac{\partial \zeta'}{\partial x'} \right) + \epsilon f_0 U \int_0^{\zeta'} \frac{\partial \rho'}{\partial x'} dz' \\ &+ \frac{g \epsilon H}{L} \int_{z'}^0 \rho' dz' \quad , \end{aligned}$$

and dividing through by $\rho_0 f_0 U$ gives

$$\begin{aligned} \frac{\partial P'}{\partial x'} &= \left[1 + \frac{\epsilon}{\rho_0} (\rho') \right] \frac{\partial \zeta'}{\partial x'} + \left(\frac{\epsilon}{\rho_0} \right) \int_0^{\zeta'} \frac{\partial \rho'}{\partial x'} dz' \\ &+ \left(\frac{g \epsilon H}{\rho_0 f_0 U L} \right) \frac{\partial}{\partial x'} \int_{z'}^0 \rho' dz' \quad (58) \end{aligned}$$

Since all of the non-dimensional terms are now scaled to be $o(1)$ and $\epsilon/\rho_0 o(10^{-3})$, it is clear that the ϵ/ρ_0 terms can be neglected; thus

$$\frac{\partial P'}{\partial x'} = \frac{\partial \zeta'}{\partial x'} + \left(\frac{g \epsilon H}{\rho_0 f_0 U L} \right) \frac{\partial \alpha'}{\partial x'} \quad , \quad (59)$$

where

$$\alpha'(z') = \int_{z'}^0 \rho' dz' \quad . \quad (60)$$

Equation (59) is the non-dimensional form of (13), and the assumptions that were made can now clearly be identified as dropping terms that are typically three orders of magnitude smaller than the dominant terms. The non-dimensional constant coefficient (which from now on will simply be referred to as N_1) obviously represents the ratio of the baroclinic component of the pressure gradient to the barotropic component of the pressure gradient. For typical continental shelf situations we can estimate the magnitude of this coefficient as follows:

$$\begin{aligned}
 g &= 10^{-3} \text{ cm/sec}^2 & L &= 10^7 \text{ cm} \\
 \epsilon &= 10^{-3} \text{ g/cm}^3 & H &= 2 \times 10^4 \text{ cm} \\
 \rho_0 &= 1 \text{ g/cm}^3 & U &= 20 \text{ cm/sec} \\
 f_0 &= 10^{-4} \text{ sec}^{-1}
 \end{aligned}$$

which gives

$$N_1 = \frac{g\epsilon H}{\rho_0 f_0 U L} \approx 1 \quad (61)$$

Equation (15) may now also be written in non-dimensional form as:

$$\frac{\partial P'}{\partial y'} + \frac{\partial \zeta'}{\partial y'} + N_1 \frac{\partial \alpha'}{\partial y'} \quad (62)$$

To non-dimensionalize the vorticity balance, the following additional non-dimensional variables are defined:

$$f = f_0 + \beta L (y'), \quad (63)$$

$$\tau = \rho_0 f_0 U H (\tau'), \quad (64)$$

$$T = \rho_0 U H (T') \quad (65)$$

It should perhaps be pointed out that the non-dimensionalization used for the stress (eq. 64) results in a non-dimensional numerical value that

is typically not order one, but somewhat smaller. An alternate approach would be to scale the stress with the Ekman depth instead of the total depth. This would bring the numerical value back in line, but leaves an Ekman number dependence in the final form of the vorticity equation that is misleading. The curl of the wind stress term (eq. 36) physically represents the divergence or convergence in the surface Ekman layer and this of course is independent of Ekman number, providing only that it is not zero. To have this term multiplied by some power of the Ekman number implies a dependence on the eddy coefficient that simply is not there. To avoid this potential difficulty it is preferable to deal with stress values that are numerically smaller.

Substituting these and the previously defined non-dimensional variables into (27) and then dividing by $\rho_0 f_0 UH/L$ yields

$$\begin{aligned}
 -N_3 \nabla^2 y' = & -J(\zeta', \beta') - N_1 J(\alpha'(d'), d') + N_2 \nabla^2 \zeta' \\
 & + N_1 N_2 \nabla^2 \alpha'(d') - \vec{k} \cdot \nabla \times \tau'(\zeta'), \quad (66)
 \end{aligned}$$

where two more non-dimensional coefficients have been defined as

$$N_2 = \frac{\gamma}{\rho_0 H} \quad \text{and} \quad N_3 = \frac{\beta L}{f_0} . \quad (67)$$

Once again it is possible to estimate the order of magnitude of these coefficients. For a bottom stress of a dyne per centimeter squared, equation (22) can be used to show

$$\gamma = \frac{\tau}{UH} = 5 \times 10^{-2} \text{ g/cm}^2 .$$

And this then suggests that

$$N_2 = \frac{\gamma}{\rho_0 H} \approx 2 \times 10^{-2} . \quad (68)$$

To evaluate N_3 , we note that

$$\beta = \frac{\partial f}{\partial y} = \frac{f}{R \tan \phi} ,$$

where ϕ is the latitude and R is the radius of the Earth. Substituting this into the expression for N_3 and evaluating it for a latitude of 60° gives

$$N_3 = \frac{L}{R \tan \phi} \approx 2 \times 10^{-2} . \quad (69)$$

It is now necessary to non-dimensionalize (34) and substitute the results into (66). This can be carried out by the straightforward substitution of the defined non-dimensional variables and gives

$$\begin{aligned} T y' = & - \tau x' - d' \frac{\partial \zeta'}{\partial x} + N_1 \left(\frac{\partial \Delta'}{\partial x'} + \alpha' (d') \frac{\partial d'}{\partial x'} \right) - N_2 \left(\frac{\partial \zeta'}{\partial x'} + \frac{\partial \zeta'}{\partial y'} \right) \\ & - N_1 N_2 \left(\frac{\partial \alpha'}{\partial x'} (d') + \frac{\partial \alpha'}{\partial y'} (d') \right) . \end{aligned} \quad (70)$$

Substituting this into (66) gives the final non-dimensional form of the model equation

$$\begin{aligned} N_2 \nabla^2 \zeta' + N_1 N_2 \nabla^2 \alpha' (d') - J(\zeta', d') - N_1 J(\alpha' (d'), d') \\ - \vec{k}' \cdot \nabla_{\mathbf{x}'} \vec{\tau}' (\zeta') - N_3 \tau x' - N_3 d' \frac{\partial \zeta'}{\partial x'} + N_1 N_3 \left(\frac{\partial \Delta'}{\partial x'} + \alpha' (d') \frac{\partial d'}{\partial x'} \right) \\ - N_2 N_3 \left(\frac{\partial \zeta'}{\partial x'} + \frac{\partial \zeta'}{\partial y'} \right) - N_1 N_2 N_3 \left(\frac{\partial \alpha'}{\partial x'} (d') + \frac{\partial \alpha'}{\partial y'} (d') \right) = 0 . \end{aligned} \quad (71)$$

In this form the equation can be easily attacked using numerical techniques, and the consequences of the geophysical scaling are clearly evident.

5. APPLICATION OF MODEL EQUATIONS

Thus far, the model has been derived and its demands for boundary conditions and input data have been considered. In this section the proposed application of the model to a real geophysical situation will be outlined. The actual detailed results of that application will be the subject of the next technical report in this series.

The region first to be studied with this model is a portion of the Continental Shelf in the Gulf of Alaska. Within this region, roughly 80 by 150 miles, a series of oceanographic stations have been laid out in an inner and outer array. The inner array extends well into deep water (fig. 6). Obviously the inner array was designed to attempt some minimal resolution of the complex bathymetry associated with the shelf break and the outer array is anticipated to supply offshore boundary conditions. STD casts will be made at each of these stations approximately six times within a year. For each of these, α and Δ will be calculated and used as input into the model. Wind data will be compiled from daily weather maps prepared by the National Weather Service regional office in Anchorage. Monthly values will be summarized and a representative stress field calculated. All input data will be reduced to values at station locations. Each of the variable fields will be interpolated assuming continuous linear variations over the triangular elements whose vertices are the station location (fig. 7).

The first solution will use the formulation given in (71), and for the first model tests N_3 will be assumed to be zero. The necessary boundary conditions will initially be estimated from assumed transports

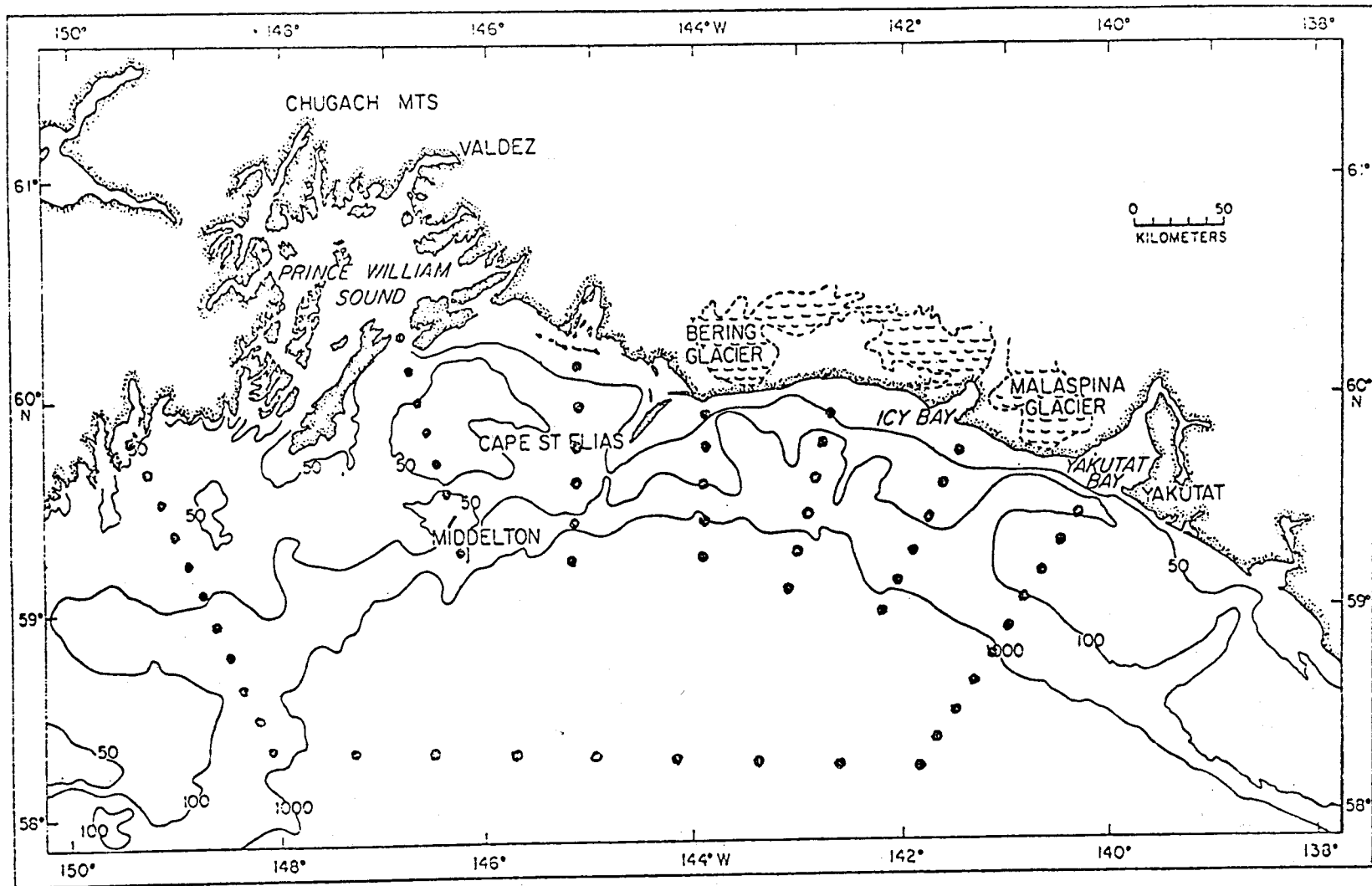


Figure 6. Test study area in the Gulf of Alaska.

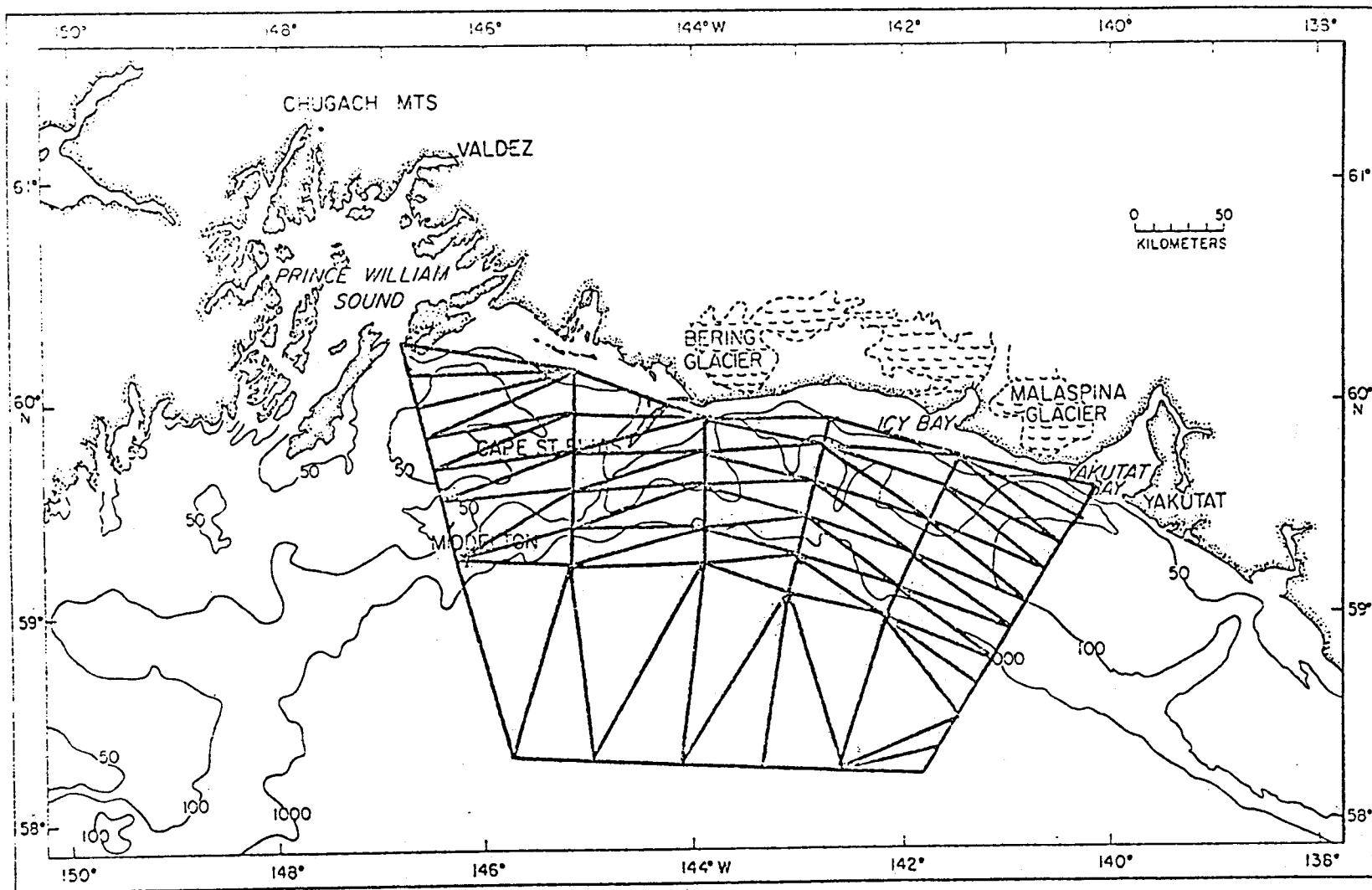


Figure 7. Triangular elements used for interpolation of field data.

along a line roughly perpendicular to the coastline. Later phases of the study will use data from moored current meter arrays and pressure gauge records within the study area (fig. 8) for boundary conditions. The effects of various boundary formulations will be carefully investigated using some range of values for the parameter N_2 .

6. ACKNOWLEDGMENTS

This report is presented as part of the ongoing Pacific Marine Environmental Labs estuarine and near shore research program and has been carried out as part of the Bureau of Land Management sponsored Gulf of Alaska Continental Shelf Study.

7. REFERENCES

- Aagaard, Knut (1969), Relationship between geostrophic and surface winds at weather ship M, Jour. Geophy. Res. 74(13):3440-3442.
- Aagaard, Knut (1970), Wind driven transports in the Greenland and Norwegian seas, Deep Sea Res. 17(2):281-291.
- Beardsley, Robert C. and Bradford Butman (1974), Circulation on the New England continental shelf; response to strong winter storms, Geophy. Res. Letters 1(4):181-184.
- Cole, Julian (1968), Perturbation Methods in Applied Mathematics, Blaisdell, New York, 260 pp.

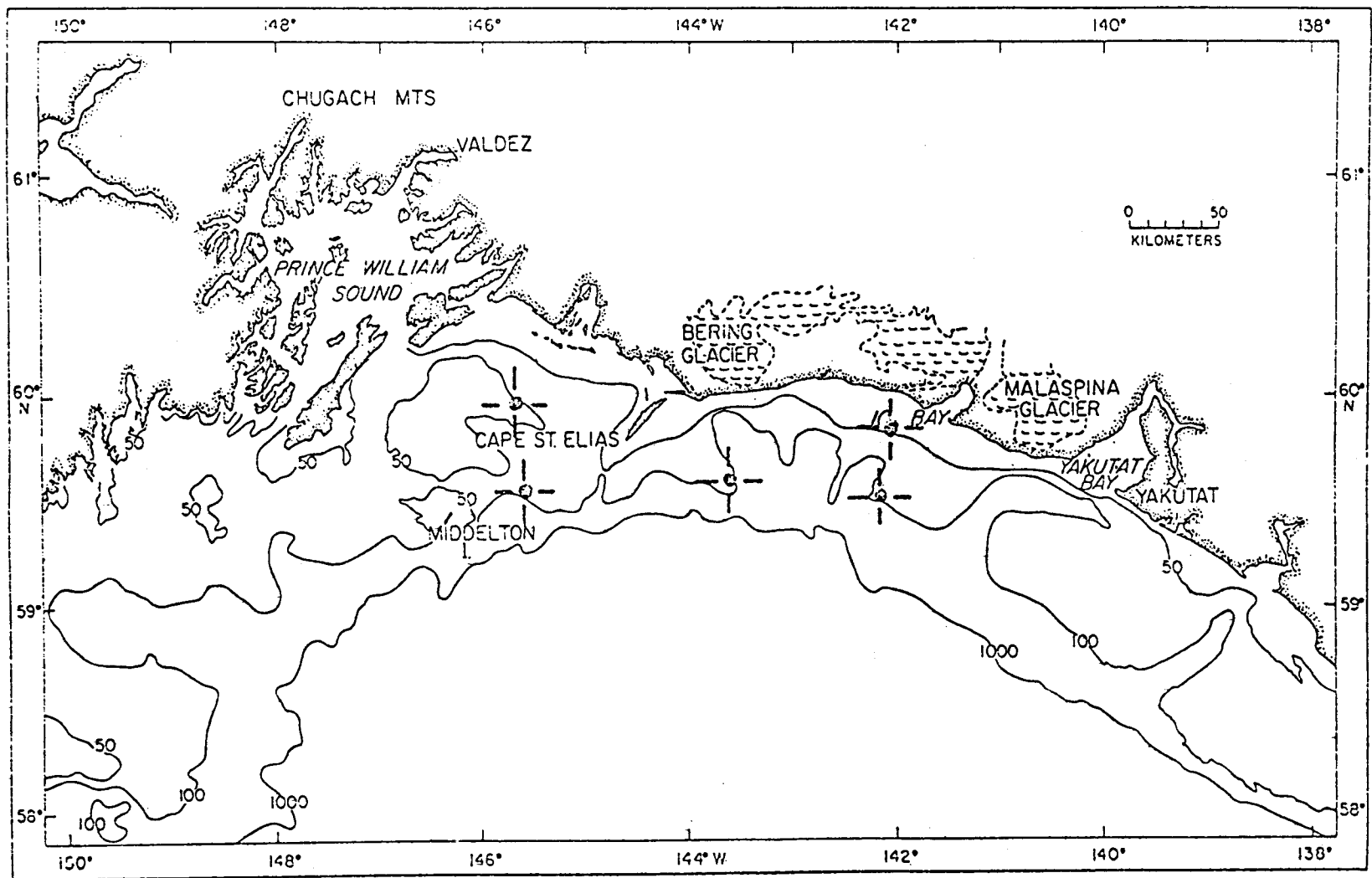


Figure 8. Positions of moored current meter arrays for use in the formulation of boundary conditions.

- Courant, R. and D. Hilbert (1962), Methods of Mathematical Physics,
Vol. II, Interscience Publishers, New York, N.Y., 830 pp.
- Formin, L.M. (1964), The Dynamic Method in Oceanography, Elsevier,
New York, 211 pp.
- Holland, William R. (1973), Baroclinic and topographic influences on the
transport in the western boundary currents, Jour. Geophys. Fluid Dyn.
4(3):187-210.
- Neumann, Gerhard and Willard J. Pierson, Jr. (1966) Principles of Physical
Oceanography, Prentice-Hall, Englewood Cliffs, N.J., 545 pp.
- Peng, Chich-Yuan and Ya Hsueh (1974), A diagnostic calculation of conti-
nental shelf circulation, Dept. of Oceanography, Florida State
Univ., Tallahassee, Florida, August 1974.
- Sarkisyan, A.A. and V.F. Ivanov (1971), Joint effect of baroclinicity
and bottom relief as an important factor in the dynamics of sea
currents, Bull. Acad. Sci. USSR, Atmos. and Oceanic Phy., 7:(173-188)
(English Trans. p 116)
- Sarkisyan, A.A. and V.P. Keondjiyan (1972), Review of numerical ocean
circulation models using observed density field. NAS - Numerical
Ocean Modeling Symposium - Durham, N.H., Oct. 1972.
- Sneddon, Ian N. (1957), Elements of Partial Differential Equations,
McGraw-Hill, New York, 327 pp.
- Sverdrup, H.U. (1947), Wind driven currents in a baroclinic ocean; with
applications to the equatorial currents of the eastern Pacific.,
Proc. of Nat. Acad. Sc. 33(11):318-326.

APPENDIX B

A Finite Element Solution Technique
for a Diagnostic Circulation Model

by

G. Watabayashi and J. A. Galt

September 1978

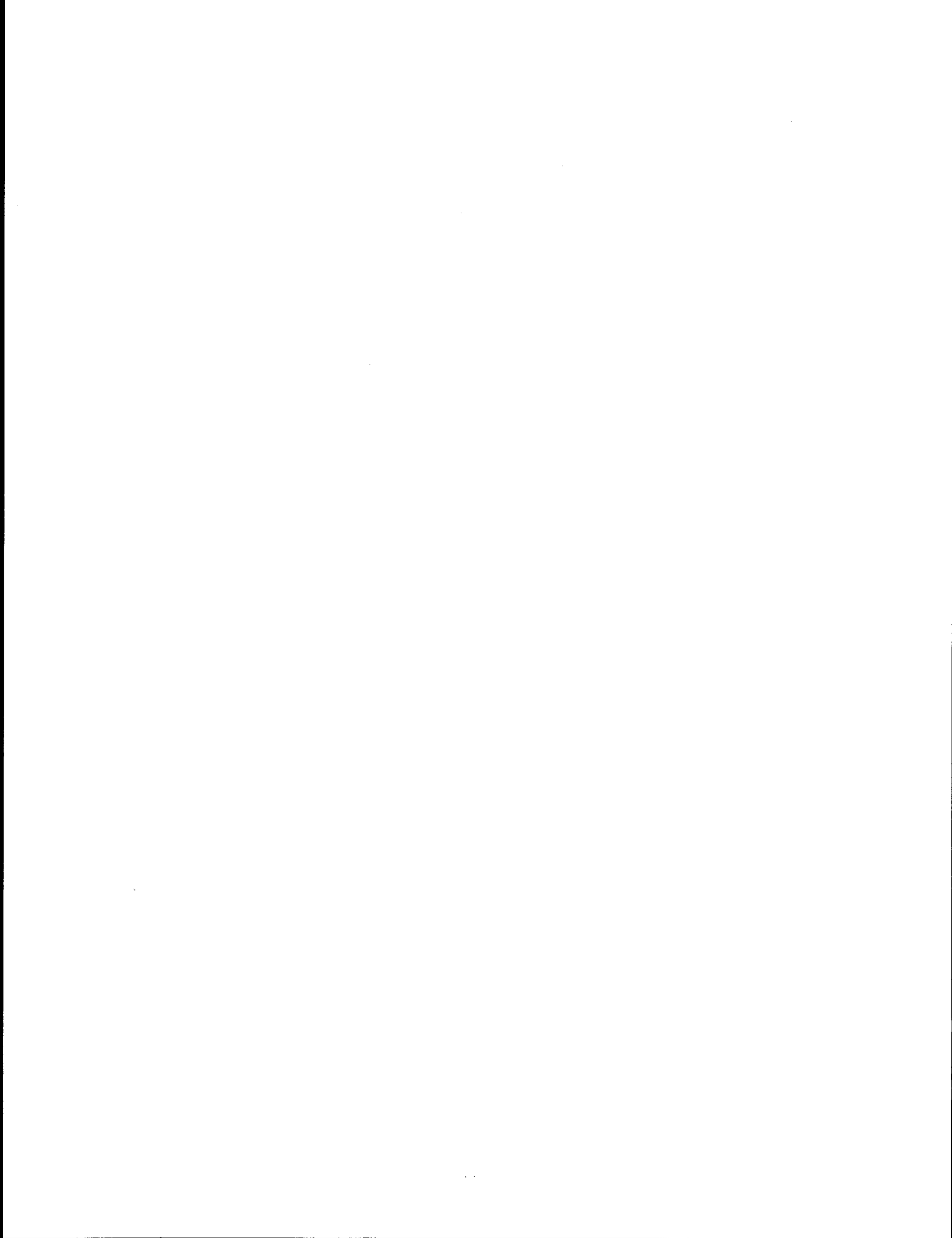
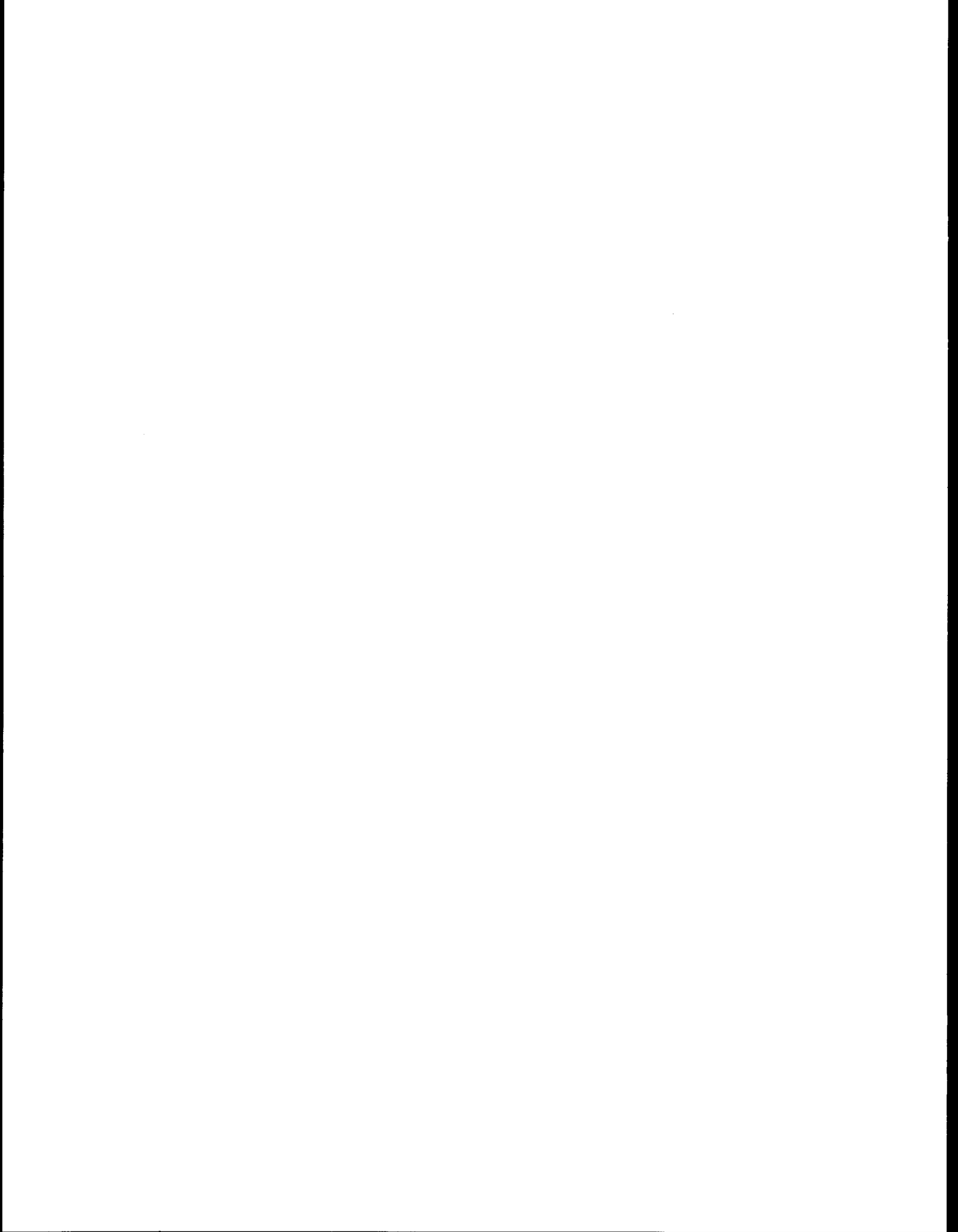


TABLE OF CONTENTS

	Page
ABSTRACT	305
1. INTRODUCTION	305
2. THE FINITE ELEMENT TECHNIQUE	307
3. THE PROGRAM	317
4. RESULTS	333
5. CONCLUSION	340
ACKNOWLEDGMENTS	341
REFERENCES	342
FIGURES	343
Appendix I. Revised Flow Chart of Diagnostic Model	357
Appendix II. Listing	359
Appendix III. Sample Cards	440
Appendix IV. Triangle Scheme	443
Appendix V.	446
Appendix VI	447



A FINITE ELEMENT SOLUTION TECHNIQUE
FOR A DIAGNOSTIC SHELF CIRCULATION MODEL

Glen Watabayashi and J. A. Galt

Pacific Marine Environmental Laboratory, ERL/NOAA
Seattle, Washington 98105

ABSTRACT. A linear diagnostic shelf circulation model developed by Galt (1975) is implemented using the Finite Element Method. The model solves a second-order non-homogeneous elliptic vorticity equation for the surface elevation within the region of interest. Solutions are obtained using finite element techniques, with elemental areas determined by available STD station spacing. After obtaining the surface elevations, velocities are calculated.

The model was initially tested on several simple contrived cases to help demonstrate the physics and the numerical techniques involved. Results from these tests indicate that, physically, the model generates a barotropic flow within the region of interest such that water and vorticity are conserved through the bottom Ekman layer. Numerically, the model approximates the analytical solution by piecewise linear functions. Therefore, if the analytical solution is not linear numerical errors occur which depend upon the mesh size.

The computer model has been written up in Standard Fortran and requires a set of STD station data and wind-stress data. The model is configured so that it can be economically run on intermediate size computers (100-150K core).

1. INTRODUCTION

The purpose of this study is to develop an economic and easily used flow model for continental shelf areas to help study the distribution of offshore pollutants. This report documents the program and demonstrates its use for simple test cases. A geostrophic model appropriately formulated for time scales of a few days is attempted. Most geostrophic flow models in the past have been developed for flow in deep water where a level of no motion is specified. At this reference level the net horizontal pressure gradient is assumed

to be zero (Sverdrup et al., 1942; Formin, 1964). From this hypothesized level, the relative isopycnal slopes can be calculated from STD observations. Over shelf areas, however, a level of no motion is improbable, and a different kind of model is needed.

The model developed here for shelf areas is a linear steady-state model requiring a set of STD and wind-stress data. The model incorporates baroclinic contributions, a variable depth, a wind-driven surface Ekman layer, and a geostrophically driven bottom Ekman layer into a vertically integrated vorticity equation. Continuity is invoked; the coriolis parameter is taken to be a constant, and the final result is a nonhomogeneous elliptic equation for the surface elevation. (A similar formulation for the homogeneous case is presented by Welander, 1957.) This equation is solved using a finite element technique with a triangular mesh system which can be adjusted to a region of arbitrarily located stations. Once the surface elevations are obtained, estimates of surface and bottom velocities are computed.

The actual computer model calls a set of subroutines which can easily be bypassed, altered, or used elsewhere. For example, the model has a subroutine to convert geographic coordinates into a nondimensional x, y Cartesian grid, and another to normalize the raw station data in terms of arbitrary dimensions read in by the user.

This report will concentrate on the finite element technique used, the development of the mathematics and physics of the model has been published by Galt (1975). A companion report will discuss the details of the boundary conditions formulation and suggest strategies for model use.

2. THE FINITE ELEMENT TECHNIQUE

We now turn our attention to solving the elliptic model equation for the surface elevation. This equation is solved numerically using a finite element technique. The finite element approach copes with randomly spaced discrete data within a region, and the finite element grid fits odd-shaped regions well.

The finite element approach approximates the solution as a linear combination of "shape functions". These functions are inserted into the differential equation and the residual, or error, is minimized. For example, the equation to be solved is

$$N_2 \nabla^2 \xi - J(\xi, d) - N_1 J(\alpha, d) + N_1 N_2 \nabla^2 \alpha - \nabla x \vec{\tau} = 0 \quad . \quad (1)$$

This can be written in the following operator form

$$L(\xi) = F \quad , \quad (2)$$

where

$$L(\xi) = N_2 \nabla^2 \xi - J(\xi, d) \quad , \quad (3)$$

$$F = N_1 J(\alpha, d) - N_1 N_2 \nabla^2 \alpha + \nabla x \vec{\tau} \quad . \quad (4)$$

The solution, ξ , can be approximated in the following way:

$$\xi = \sum_{i=1}^{NVRTX} \psi_i C_i \quad , \quad (5)$$

where

NVRTX = number of points at which the equation will be solved
(No. of stations);

$\psi_i = \psi_i(x, y)$, "shape function";

c_i = value of solution at specified locations.

The shape functions used here will be piecewise continuous and take on the value of one at node "i", and zero at neighboring nodes. The exact nature of the shape functions and the strategy behind them is explained in the following section. At this point, the ψ 's are a linearly independent bases set of functions used to approximate the solution.

The next step is to substitute the approximate solution into equation (2) to give

$$L \left(\sum_{i=1}^{NVRTX} \psi_i C_i \right) - F = E, \quad (6)$$

where

E = error introduced due to approximation.

The error is minimized by the Galerkin technique (Zienkiewicz, 1971). The method requires that the error be orthogonal to the space spanned by the bases set of functions. This is expressed by the following equation:

$$\iint_D E \cdot \psi_j dx dy = 0 \text{ for } j = 1, 2, \dots, NVRTX, \quad (7)$$

where

D = domain of interest.

Writing this as a system of NVRTX equations and substituting the expression for E from (6) into the above gives

$$\sum_{j=1}^{NVRTX} \iint_D \left(L \left(\sum_{i=1}^{NVRTX} \psi_i C_i \right) - F \right) \psi_j dx dy = 0 . \quad (8)$$

Since the operator, L, is linear, and the C_i 's are constants, this can be written as

$$\sum_{j=1}^{NVRTX} \sum_{i=1}^{NVRTX} C_i \iint_D L(\psi_i) \psi_j dx dy = \sum_{j=1}^{NVRTX} \iint_D F \psi_j dx dy . \quad (9)$$

This can be written in matrix form as

$$AC = R , \quad (10)$$

where

$$A_{ij} = \iint_D \psi_j L(\psi_i) dx dy , \quad (11)$$

$$R_j = \iint_D F \psi_j dx dy . \quad (12)$$

Substituting the operator from (3) into (11) gives

$$A_{ij} = \iint_D \left[N_2 \psi_j \left(\frac{\partial^2 \psi_i}{\partial x^2} + \frac{\partial^2 \psi_i}{\partial y^2} \right) - \psi_j \left(\frac{\partial \psi_i}{\partial y} \frac{\partial d}{\partial x} - \frac{\partial \psi_i}{\partial x} \frac{\partial d}{\partial y} \right) \right] dx dy . \quad (13)$$

The shape functions, ψ , will be made up of linear functions of x and y , and are piecewise continuous across element boundaries. Thus the second derivative terms are not well-defined along the boundaries and the integration shown in equation (13) cannot be completed. To avoid this problem, the second derivative terms are integrated by parts (for details, see Appendix V), giving

$$A_{ij} = -N \iint_D \left(\frac{\partial \psi_i}{\partial x} \frac{\partial \psi_j}{\partial x} + \frac{\partial \psi_i}{\partial y} \frac{\partial \psi_j}{\partial y} \right) dx dy \quad (14)$$

$$- \iint_D \psi_j \left(\frac{\partial \psi_i}{\partial y} \frac{\partial d}{\partial x} - \frac{\partial \psi_i}{\partial x} \frac{\partial d}{\partial y} \right) dx dy + \int_s \psi_j \left(\frac{\partial \psi_i}{\partial x} l_y + \frac{\partial \psi_i}{\partial y} l_x \right) ds ,$$

where

s = boundary of the domain,

l_x, l_y = directional cosines along the boundary.

Similarly, R_j may be obtained by substituting from (4) into (12):

$$R_j = \iint_D N_1 \psi_j \left(\frac{\partial \alpha}{\partial y} \frac{\partial d}{\partial x} - \frac{\partial \alpha}{\partial x} \frac{\partial d}{\partial y} \right) - N_1 N_2 \psi_j \left(\frac{\partial^2 \alpha}{\partial x^2} + \frac{\partial^2 \alpha}{\partial y^2} \right)$$

$$+ \psi_j \left(\frac{\partial \tau_y}{\partial x} - \frac{\partial \tau_x}{\partial y} \right) dx dy . \quad (15)$$

Once again integrating the second derivative term by parts gives

$$R_j = N \iint_D \psi_i \left(\frac{\partial \alpha}{\partial y} \frac{\partial d}{\partial x} - \frac{\partial \alpha}{\partial x} \frac{\partial d}{\partial y} \right) dx dy + N_1 N_2 \iint_D \left(\frac{\partial \psi_j}{\partial x} \frac{\partial \alpha}{\partial x} + \frac{\partial \psi_j}{\partial y} \frac{\partial \alpha}{\partial y} \right) dx dy$$

$$+ \iint_D \psi_j \left(\frac{\partial \tau_y}{\partial x} - \frac{\partial \tau_x}{\partial y} \right) dx dy - N_1 N_2 \int_s \psi_j \left(\frac{\partial \alpha}{\partial x} l_y + \frac{\partial \alpha}{\partial y} l_x \right) ds . \quad (16)$$

Equations (14) and (16) now define the matrix equations which must be solved.

Now consider the geometrical problem of calculating A_{ij} and R_j . First the domain is divided into triangular vertices. The five-station case is an example in figure 1. At each station, the position, depth, α , Δ , and wind stress components are given as

$s(N)$, $y(N)$, depth (N), alpha (N), delta (N), tau_x (N), tau_y (N),
 where N refers to the global label of the station.

Within each triangle, the bases functions and independent variables are all assumed to be linear functions of x and y. This means that within each triangle the independent variables are represented as

$$\text{depth}_{TN} = D_x \cdot x + D_y \cdot y + D_0 \quad ,$$

$$\text{alpha}_{TN} = \alpha_x \cdot x + \alpha_y \cdot y + 0 \quad ,$$

$$\text{tau}_{xTN} = \tau_x \cdot x + \tau_x \cdot y + \tau_x \cdot 0 \quad ,$$

$$\text{tau}_{yTN} = \tau_y \cdot x + \tau_y \cdot y + \tau_y \cdot 0 \quad .$$

The coefficients are determined by matching values at the vertices.

For example, to solve for D_x , D_y , and D_0 in triangle T1, we solve the following set of equations:

$$\text{depth (I)} = D_x \cdot x(I) + D_y \cdot y(I) + D_0 \quad ,$$

$$\text{depth (III)} = D_x \cdot x(III) + D_y \cdot y(III) + D_0 \quad ,$$

$$\text{depth (V)} = D_x \cdot x(V) + D_y \cdot y(V) + D_0 \quad .$$

Each triangle contributes to the value of the shape function at each of its vertices. For example, triangle T1 contributes to the value of the shape function of points I, III, and V. The contributing elements to the shape functions are defined as follows:

$$\begin{aligned}
 \psi_I^{TN} &= \psi_x(1) \cdot x + \psi_y(1) \cdot y + \psi_0(1) , \\
 \psi_J^{TN} &= \psi_x(2) \cdot x + \psi_y(2) \cdot y + \psi_0(2) , \\
 \psi_K^{TN} &= \psi_x(3) \cdot x + \psi_y(3) \cdot y + \psi_0(3) ,
 \end{aligned}
 \tag{17}$$

where

TN = triangle number,

I, J, K = vertex number.

The coefficients, ψ_x , ψ_y , and ψ_0 are determined in such a way that

$\psi_I^{TN} = 1$ at I and zero at vertices J and K. As an example, in triangle T1, to obtain $\psi_x(1)$, $\psi_y(1)$, and $\psi_0(1)$, the following set of equations is solved:

$$\begin{aligned}
 1 &= \psi_x(1) \cdot x(1) + \psi_y(1) \cdot Y(1) + \psi_0(1) , \\
 0 &= \psi_x(1) \cdot x(2) + \psi_y(1) \cdot Y(2) + \psi_0(1) , \\
 0 &= \psi_x(1) \cdot x(3) + \psi_y(1) \cdot Y(3) + \psi_0(1) .
 \end{aligned}
 \tag{18}$$

Within each triangle the shape functions and independent variables are planar segments. Over the entire region, the shape functions and independent variables are piecewise continuous.

The next step is to assemble the matrix and right-hand side of equation (10) one triangle at a time. Since the independent variables and shape function are linear, all the first derivatives are constants. Therefore, A_{ij} can be rewritten as

$$A_{ij} = - N_2 \iint_{DTN} (\psi_x(K_i) \cdot \psi_x(K_j) + \psi_y(K_i) \cdot \psi_y(K_j)) dx dy \quad (19)$$

$$- \iint_{DTN} \psi_i (\psi_y(K_i) \cdot D_x - \psi_x(K_i) \cdot D_y) + \oint \psi_j \left(\frac{\partial \xi_j}{\partial x} \ell_y + \frac{\partial \xi_j}{\partial y} \ell_x \right) ds ,$$

where

DTN = Domain of triangle TN,

K_i, K_j = refers to the global coefficient associated with points i and j .

R_j becomes

$$N_1 \iint_j (\alpha_y D_x - \alpha_x \cdot D_y) dx dy + N_1 N_2 \iint_{DTN} ((\psi_x)_i \alpha_x + (\psi_y)_j \alpha_y) dx dy$$

$$+ \iint_{DTN} (\psi_j (\tau_y)_x - (\tau_x)_y) dx dy - N_1 N_2 \oint_s \psi_j (\alpha_x \cdot \ell_y + \alpha_y \ell_x) ds. \quad (20)$$

Notice that the line integrals contribute only to the points which lie on the boundary of the entire domain. In the five-point example, the line integrals are zero unless both i and j do not equal V .

To evaluate A_{ij} and R_j , three types of integrals have to be evaluated for each triangle:

$$\begin{aligned}
\text{(a)} & \iint_{DTN} dx dy , \\
\text{(b)} & \iint_{DTN} \psi dx dy , \\
\text{(c)} & \oint_s \psi ds .
\end{aligned}$$

The first is simply the area of the triangle. The second is one-third the area of the triangle (see Appendix VI), and the third equals the length of the triangle sides adjacent to the boundary point divided by two. A_{ij} and R_j can now be rewritten as:

$$\begin{aligned}
A_{ij} = & -N_2(\psi_x(K_i) \cdot \psi_x(K_j) + \psi_y(K_i) \cdot \psi_y(K_j)) \cdot \text{Area} \\
& - (\psi_y(K_i) \cdot D_x - \psi_x(K_i) \cdot D_y) \cdot 1/3 \text{ Area} \\
& + (\psi_x(K_i) \cdot \ell_y + \psi_y(K_i) \cdot \ell_x) \cdot \oint \psi_j ds ,
\end{aligned} \tag{21}$$

$$\begin{aligned}
R_j = & N_1(\alpha_y \cdot D_x - \alpha_x \cdot D_y) \cdot 1/3 \text{ Area} + N_1 N_2(\psi_x(K_j) \cdot \alpha_x \\
& + N_1 N_2(\alpha_x \cdot \ell_y + \alpha_y \cdot \ell_x) \oint \psi_j ds .
\end{aligned} \tag{22}$$

The matrix and right-hand side are now ready to be assembled by adding the contributions from each triangle. In our test case, we begin with triangle T1. All the gradients are calculated along with the area of the triangle. Then the contributions to R_j and A_{ij} are calculated and placed in their appropriate locations. For T1, $i = 1, III, V$, and $j = I, III, V$; the contributions to A_{ij} would be at $A_{11}, A_{13}, A_{15}, A_{31}, A_{33}, A_{35}, A_{51}, A_{53},$ and A_{55} , while the contributions

to R_j would be to R_1 , R_3 , and R_5 . The line integral terms contribute only when i and j are boundary points. After T1 is completed, the system is repeated for T2. For the second triangle A_{15} and A_{51} already have values from the previous triangle, so we add on to the existing values.

After all the triangles are covered, the boundary conditions are considered. The solution vector components c_i are the surface elevations at the triangle vertices which are known along the boundary. To incorporate the boundary conditions where the elevation is given, the rows associated with the boundary points are set to zero except for the diagonal element which is set to 1. Then the element of the right-hand side associated with this row is set to the boundary value. Along island or coastline boundaries a no net transport condition is added on to the assembled matrix. Along these boundaries we require:

$$-d \frac{\partial \xi}{\partial s} + N_2 \left(\frac{\partial \xi}{\partial n} - \frac{\partial \xi}{\partial s} \right) = - N_1 \left(\frac{\partial \Delta}{\partial s} + \alpha \frac{\partial d}{\partial s} \right) + \tau_s - N_1 N_2 \left(\frac{\partial \alpha}{\partial n} - \frac{\partial \alpha}{\partial s} \right) \quad (23)$$

Where \bar{n} is a unit vector normal to the coast pointing offshore and \bar{s} is a unit vector given by $\bar{k} \times \bar{n} = \bar{s}$, where \bar{k} is positive up. To see how this is incorporated into the assembled matrix consider the following triangle with a coastal boundary (figure 3)

We see:

$$\bar{n} = n_x \bar{z} + n_y \bar{a} \quad (24)$$

$$= \left[\frac{(y_m - y_\ell)}{(x_m - x_\ell)^2 + (y_m - y_\ell)^2} \right] \bar{z} + \left[\frac{-(x_m - x_\ell)}{(x_m - x_\ell)^2 + (y_m - y_\ell)^2} \right] \bar{a}$$

$$\bar{s} = s_x \bar{z} + s_y \bar{a} \quad (25)$$

$$= \left[\frac{(x_m - x_\ell)}{(x_m - x_\ell)^2 + (y_m - y_\ell)^2} \right] \bar{z} + \left[\frac{(y_m - y_\ell)}{(x_m - x_\ell)^2 + (y_m - y_\ell)^2} \right] \bar{a}$$

Within this triangle all variables are expressed in terms of the three shape functions, i.e.,

$$\xi = C_\ell \psi_\ell + C_m \psi_m + C_n \psi_n$$

$$d = d_\ell \psi_\ell + d_m \psi_m + d_n \psi_n$$

$$\alpha = \alpha_\ell \psi_\ell + \alpha_m \psi_m + \alpha_n \psi_n$$

$$\Delta = \Delta_\ell \psi_\ell + \Delta_m \psi_m + \Delta_n \psi_n$$

And the shape functions are defined by

$$\psi_\ell = (\psi_\ell)_x x + (\psi_\ell)_y y + (\psi_\ell)_o$$

$$\psi_m = (\psi_m)_x x + (\psi_m)_y y + (\psi_m)_o$$

$$\psi_n = (\psi_n)_x x + (\psi_n)_y y + (\psi_n)_o$$

With these normal and tangential derivatives can be defined by

$$\begin{aligned} \frac{\partial \xi}{\partial n} = & (C_{\ell}(\psi_{\ell})_x + C_m(\psi_m)_x + C_n(\psi_n)_x) n_x \\ & + (C_{\ell}(\psi_{\ell})_y + C_m(\psi_m)_y + C_n(\psi_n)_y) n_y \end{aligned} \quad (26)$$

Using these forms we can substitute into equation (23) to get a relationship between known triangle parameters and the nodal values of the dependent variable. The error in this equation is then required to be orthogonal to the bases set of functions integrated along the coastal or island boundary. These constraints are added on to the matrix which has already been assembled using the differential equation.

Details are shown in the program listing given in Appendix II.

3. THE PROGRAM

The FORTRAN program making up the model satisfies several specifications. First and foremost, the program can be easily utilized by anyone who has a set of standard STD station data and an available computer. Second, the program has several options as to what is read, computed, and printed. Third, parts of the program are easily changeable, bypassed, or omitted without affecting other parts of the program. The program is basically written as a collection of overlays and subroutines. In the main program, the user specifies what type of data is to be read, what is to be computed, and what is to be printed. The main program subsequently activates the appropriate set of overlays and subroutines.

Before dealing with the program in detail, it would be helpful to briefly summarize the program. It begins by reading in several control parameters which dictate what is to be computed, listed, punched, and plotted. The program has the option to list whatever is read and computed, and to punch whatever is computed. This allows data to be easily echo-checked, and computed values need not be recomputed for future runs using the same source deck. The first set of control parameters deals with normalizing the station data. If raw station data is read in with corresponding geographic coordinates, the program will transform the positions onto a scaled x-y Mercator grid and normalize the station data according to scale parameters which are also read in. The normalized data can be punched onto cards for later runs. The next set of options concerns the triangular mesh used for interpolation and as the finite element mesh. The user has the option of either reading in the triangular mesh or using a set of subroutines in the program to create the triangles. Then the boundary values are read in. If the triangles are internally generated, the triangles external to the region are eliminated. The program proceeds to generate and solve the finite element matrix and right-hand side vector subject to the boundary conditions. The solution yields the surface elevation at each station, and with this information, the transport, mean velocity, surface slope velocity, wind-driven surface velocity, and the geostrophic velocity at the bottom for each triangle are calculated. Finally, there is a set of plotting option which will draw and contour the results.

Appendix I is a flow chart of the main program and overlay structure with explanations of the key routines. A listing of the complete program is given in Appendix II.

3. Documentation

3.1 Section I

The program begins by reading the control parameters. These parameters determine what the program will do and how it will function. There are three types of control parameters. The first allows the user to bypass an option. For example, if NOGRID is set to 0, the program will not generate a Mercator grid; instead, it will read the grid. The second type of control parameter allows one to list whatever is read or calculated. These parameters all begin with the letter L. For example, if LTRI is set to 1, the program will list the triangle vertices. The third type of control parameter begins with the letters IP and determines if the program will punch the results on cards. For example, if IPNORM is set to 1, the program will punch the normalized station data. A detailed explanation of each option is given in the program itself (see Appendix II). If any control parameter is set to 1, the option will be executed and, if it is 0, the option will be bypassed. In addition to the list, punch, and bypass options, there are parameters which allow the user to alter the boundary conditions during the given run, store the decomposed matrix on a file for later use, and smooth the alpha and delta field to a least squares fit over the data.

3.2 Section II

This section deals with the input of station data. There are several options available. The first is to set NORMAL and NOGRID to 1 and read the raw station data. The program will then generate a Mercator grid and normalize the station data. Another choice is to read in normalized station data with geographic coordinates, or raw station data with Mercator coordinates. In the last two cases, either NOGRID or NORMAL is set to 0. The last option is to read normalized station data with Cartesian coordinates for the station locations. In this case, both NOGRID and NORMAL are set to 0. If more than one run is made on the same set of data, the last option should be exercised after generating a data deck of the normalized data and Mercator grid from the initial run.

Raw station data is read using format 10. An example is given in Appendix III.

3.4 Section III

The scale parameters which control the scaling and nondimensionalizing are read in here, they are as follows:

- USCALE: Velocity scale in meters per second;
- DSCALE: Depth scale in meters;
- ALSCALE: Horizontal length scale in meters;
- G : Gravity in meters per second squared;
- E : Perturbation density in grams per centimeter cubed;
- Q : Constant density in grams per centimeter cubed;
- GAMMA : Bottom friction coefficient in grams per centimeter squared.

3.5 Section IV

In this section, geographic coordinates are transformed into Mercator x-y grid. Notice that the routine works only for the northern hemisphere and west longitude. The subroutine finds the maximum and minimum values of latitude and longitude. The minimum latitude becomes the $y = 0$ axis. The y coordinate value of each station is obtained by calculating its distance from the $y = 0$ axis and scaling the distance by the horizontal length scale. For example, if a station is 100 km north of the $y = 0$ line and the length scale is 100 km, the y coordinate value of the station is one unit. The x coordinate is computed in a slightly different manner because the distance between a station and the $x = 0$ line is a function of its longitude and latitude. The program finds the mean latitude and calculates the distance in the x direction that the station is from the $x = 0$ longitude and the longitude of the station at the mean latitude.

The Mercator grid can be scaled so the output overlays standard hydrographic charts. The transformations are as follows:

$$X(I) = -(R * \lambda - \lambda_{\min})$$

$$Y(I) = R * A \text{LOG}(\text{TAN}(\vartheta/2. + \pi/4) - \text{TAN}(\frac{\vartheta_{\min}}{2} + \pi/4))$$

where:

R = Radius of Earth + (ALSCALE * COS (ϑ average)) this makes each nondimensional unit in the horizontal direction one scale (ALSCALE) length at the mean latitude.

λ = Longitude

λ_{\min} = Western most longitude to become x = 0 line

\emptyset = Latitude

\emptyset_{\min} = minimum latitude to become y = 0 line

The radius, R, is listed by the routine and if a plot is to be made to fit another Mercator projection, the x and y axis can be scaled appropriately. For example on a typical Mercator chart there will be a statement that the scale of the projection is 1:N on reference latitude \emptyset ref. Then if R is entered as:

$$R = \frac{\text{Radius of the earth (meters)}}{N} * \text{COS}(\emptyset_{\text{REF}})$$

The plots will be correctly scaled to overlay the chart.

The data for this routine is read with the raw station data. The degrees of latitude and longitude are read into two integer arrays and the minutes of latitude and longitude into two decimal places are read into two real arrays. The x and y coordinates returned from this subroutine are stored into the real arrays, and the original latitude and longitude of the stations are lost.

3.6 Section V

This routine calculates the mean coriolis value, F0, by averaging the maximum and minimum coriolis values of the region.

3.7 Section VI

The raw station data is normalized according to the scale parameters read in by Section III. In the following, the primed values are the

normalized, nondimensional values:

$$\begin{aligned}\text{ALPHA}' &= (\text{ALPHA} - \text{Q} * \text{DEPTH}) / (\text{E} * \text{DSCALE}); \\ \text{DELTA}' &= (\text{DELTA} - \text{Q} * \text{DEPTH} * \text{DEPTH} / 2) / (\text{E} * \text{DSCALE} * \text{DSCALE}); \\ \text{DEPTH}' &= \text{DEPTH} / \text{DSCALE} \\ \text{TAUX}' &= (1 / (\text{FO} * \text{USCALE} * \text{Q} * \text{DSCALE})) * \text{TAUX}; \\ \text{TAUY}' &= (1 / (\text{FO} * \text{USCALE} * \text{Q} * \text{DSCALE})) * \text{TAUY}; \\ \text{CURL}' &= (1 / (\text{FO} * \text{USCALE} * \text{Q} * \text{DSCALE} * \text{ALSCALE})) * \text{CURL}.\end{aligned}$$

The normalized values are stored in the arrays where the raw data was stored.

3.8 Section VII

In this section, a least squares fit is made over the alpha and delta fields. A third-order polynomial in the z direction is fit to both the alpha and delta data.

$$\begin{aligned}\text{ALPHA} &= A_0 + A1 * Z + A2 * Z * Z + A3 * Z * Z * Z \\ \text{DELTA} &= D_0 + D1 * Z + D2 * Z * Z + D3 * Z * Z * Z\end{aligned}$$

The coefficients are returned by the subroutine to be used later to calculate the alpha and delta gradients. The subroutine is a general least squares fit program, and the basis set of functions used for the least squares interpolation can be changed. The user also has the option of smoothing the alpha and delta fields. For example, if the parameter "SMOOTH" is set to 1.5, the program will smooth data over 1.5 standard deviations away from the least squares fit back to 1.5 standard deviations.

3.9 Section VIII

In this section, the nondimensionalized run parameters are either read in or calculated:

$$\text{CONST1} = (\text{G} * \text{E} * \text{H}) / (\text{Q} * \text{FO} * \text{USCALE} * \text{ALSCALE});$$

$$\text{CONST2} = \text{GAMMA} / (\text{Q} * \text{DSCALE}).$$

3.10 Section IX

Here the program either reads in the triangles or generates them. The triangle information is stored in an array, $\text{IP}(\text{I}, \text{N})$, where N is the number of the triangle and I is the local vertex number (1, 2, or 3). The value of IP is the global number of the particular point. See figure 4 for an example.

If the triangles are to be read in, integer format 5 is used (see Appendix III for an example). A brief explanation of how the triangles are generated is given in Appendix IV.

3.11 Section X

The boundary values are read in this section. If the triangles are generated internally, the external boundary values must be read in counter-clockwise order. This will allow the program to determine what triangles are inside or outside of the domain. The boundary values needed are the surface elevations of the boundary stations in centimeters. Coastal and island boundary points must be identified. A discussion of the strategy used to obtain boundary values is given in the comparison report in this series. See Appendix III for an example of how the boundary values should be read.

3.12 Section XI

This section is used only if the triangles are generated internally. The subroutine FINDBP stores the number of boundary points that each triangle has, rearranges the local vertex numbers of the boundary triangles so the boundary points are the lead vertices in counterclockwise order, and finally checks to see that the boundary points are ordered consistently. This section sets up the boundary triangles for the next routine which eliminates the triangles external to the region (see figure 5).

3.13 Section XII

Again, this option is needed only if the triangles are generated internally. Subroutine ELIM is used to eliminate the triangles external to the region. This will be the case for concave domains (see figure 6) and islands. Each triangle with three boundary points is tested to see if it is external or internal to the region (see figure 6).

The final mesh of the triangles to be used for the finite element technique and the number of triangles, NTRI, are products of this section.

3.14 Section XIII

Subroutine SETMAT zeros the global matrix and right-hand side. The subroutine also has the option of eliminating the triangles with three boundary points from the finite element mesh. If the second option is activated, the last parameter in the call, IELI, is set to 1.

3.15 Section XIV

The assembly of the global matrix starts here. K is the number of the triangle being operated on.

3.16 Section XV

The triangle vertices are identified in terms of their global labels. The first vertex of triangle K has global label J, the second, L, and the third, M.

3.17 Section XVI

The three-by-three location matrix is set and used to calculate the area of the triangle and all the gradients within the triangle. For example, the first row of the matrix contains the x and y coordinates of the first local vertex of triangle K.

3.18 Section XVII

Now the area of the triangle is calculated. Subroutine TRIAREA calculates the determinant of the location matrix A, and multiplies it by a half. The absolute value of this quantity becomes the area of the triangle.

3.19 Section XVIII

The gradients needed for the triangle are calculated with the exception of the alpha gradients. The alpha gradients are calculated in the next section. The other forcing function gradients are obtained here using the position matrix as a coefficient matrix and setting the right-hand side vector, B(1), B(2), B(3), equal to the particular values of the forcing function at vertices 1, 2, and 3. For example, for the depth we have:

$$\begin{bmatrix} A \end{bmatrix} \begin{bmatrix} \frac{d}{x} \\ \frac{d}{y} \\ d_0 \end{bmatrix} = \begin{bmatrix} B(1) \\ B(2) \\ B(3) \end{bmatrix} = \begin{bmatrix} \text{Depth at vertex 1} \\ \text{Depth at vertex 2} \\ \text{Depth at vertex 3} \end{bmatrix}$$

The three-by-three system is solved by Kramer's Rule in subroutine SOLVE which calls TRIAREA to compute the determinants.

The shape function gradients are also calculated in the same manner by solving the following set of equations:

$$\begin{bmatrix} A \end{bmatrix} \begin{bmatrix} \frac{d \text{ shape } (I)}{dx} \\ \frac{d \text{ shape } (I)}{dy} \\ c \text{ shape } (I) \end{bmatrix} = \begin{bmatrix} B(1) \\ B(2) \\ B(3) \end{bmatrix} = \begin{bmatrix} 1 \\ 0 \\ 0 \\ I=1 \end{bmatrix} \quad \text{or} \quad \begin{bmatrix} 0 \\ 1 \\ 0 \\ I=2 \end{bmatrix} \quad \text{or} \quad \begin{bmatrix} 0 \\ 0 \\ 1 \\ I=3 \end{bmatrix}$$

The subscript I tells you which vertex the particular gradient is associated with.

3.20 Section XIX

The alpha gradients are calculated differently than the other gradients. A simple linearization of the alpha field introduces errors which are unacceptably large, so a more detailed description of the density field is needed than the bottom alpha values at the triangle vertices. Therefore, a third-order least squares fit to the alpha field is generated (see Section VII) and used to obtain alpha values at the triangle vertices for the centroid depth.

$$\begin{aligned} \text{Alpha (at centroid depth)} &= \text{alpha (at bottom)} + \frac{\partial(\text{alpha})^*}{\partial z} \delta z \\ &+ \frac{\partial^2(\text{alpha})^{**}}{\partial z^2} \frac{\delta z^2}{2} + \frac{\partial^3(\text{alpha})^{***}}{\partial z^3} \frac{\delta z^3}{6} \end{aligned}$$

In the above calculations, the alpha gradients are obtained by differentiating the least squares function of alpha. Once the alpha values

at the centroid depth are obtained over each vertex, subroutine GRAD is called to calculate the horizontal alpha gradients. The delta gradients needed for the transports are calculated in the same manner.

3.21 Section XX

The triangle's contribution to the global matrix and right-hand side is added in here. Each triangle contributes to particular rows and columns of the global matrix determined by the global label of the triangle vertices (figure 7).

$$\begin{array}{ccc}
 & 3 & 4 & 5 \\
 3 & \begin{bmatrix} x & & \\ & x & \\ & & x \end{bmatrix} & & \\
 4 & \begin{bmatrix} & x & \\ & & x \\ & & & x \end{bmatrix} & & \\
 5 & \begin{bmatrix} & & x \\ & & & x \\ & & & & x \end{bmatrix} & & \\
 & & \begin{bmatrix} \\ \\ \\ \end{bmatrix} C & = & \begin{bmatrix} x \\ x \\ x \end{bmatrix} & & \begin{array}{l} 3 \\ 4 \\ 5 \end{array}
 \end{array}$$

is zeroed. Then the diagonal element of that row is set to 1, and the element in the right-hand side associated with that row is set equal to the boundary value. For example, suppose a four-by-four system of equations was assembled as shown:

$$\begin{bmatrix}
 GM(1,1) & GM(1,2) & GM(1,3) & GM(1,4) \\
 GM(2,1) & GM(2,2) & GM(2,3) & GM(2,4) \\
 GM(3,1) & GM(3,2) & GM(3,3) & GM(3,4) \\
 GM(4,1) & GM(4,2) & GM(4,3) & GM(4,4)
 \end{bmatrix}
 \begin{bmatrix}
 C(1) \\
 C(2) \\
 C(3) \\
 C(4)
 \end{bmatrix}
 =
 \begin{bmatrix}
 RHS(1) \\
 RHS(2) \\
 RHS(3) \\
 RHS(4)
 \end{bmatrix}$$

Then suppose that C(1) and C(2) are known boundary values. Subroutine BC alters the system into the following:

$$\begin{bmatrix}
 1 & 0 & 0 & 0 \\
 0 & 1 & 0 & 0 \\
 GM(3,1) & GM(3,2) & GM(3,3) & GM(3,4) \\
 GM(4,1) & GM(4,2) & GM(4,3) & GM(4,4)
 \end{bmatrix}
 \begin{bmatrix}
 C(1) \\
 C(2) \\
 C(3) \\
 C(4)
 \end{bmatrix}
 =
 \begin{bmatrix}
 BV(1) \\
 BV(2) \\
 RHS(3) \\
 RHS(4)
 \end{bmatrix}$$

Coastal and island boundary vertices have a no net flux boundary constraint added to the assembled matrix.

3.23 Section XXII

The system of equations is now solved by subroutine SOLN. This matrix solving routine programmed by Steve Smyth from Knuth (1968, 1973) takes advantage of the sparseness of the matrix by not storing zero values, and a second to tell us where in the matrix the nonzero values occur. The program is set to solve a 200 by 200 system with each row containing no more than 20 nonzero elements and another array, INTP (4900) keeps

track of where the nonzero elements belong in the matrix. If a larger matrix is to be solved, the two arrays can be increased in a manner described within the program itself. The routine begins by reducing the global matrix into the product of an upper triangular and lower triangular system. Partial pivoting on the columns is used and the triangular matrices are stored into the original global matrix. The lower triangular system is solved first, then the upper triangular system is solved for vector C.

$$\begin{bmatrix} \text{GM} \end{bmatrix} \text{ becomes } \begin{bmatrix} & \text{U} \\ \text{L} & \end{bmatrix}$$

The system now can be written as

$$\begin{bmatrix} & \text{O} \\ \text{L} & \end{bmatrix} \begin{bmatrix} & \text{U} \\ \text{O} & \end{bmatrix} \zeta = \text{RHS} .$$

Let

$$\begin{bmatrix} & \text{U} \\ \text{O} & \end{bmatrix} \zeta = \gamma .$$

now solve the following system:

$$\begin{bmatrix} & \text{O} \\ \text{L} & \end{bmatrix} \gamma = \text{RHS} .$$

Once γ is obtained, the following system is solved for C:

$$\begin{bmatrix} & \text{O} \\ \text{U} & \end{bmatrix} \zeta = \gamma .$$

The decomposed global matrix and right-hand side are saved. If different sets of boundary conditions are to be tested, the same decomposed global matrix is used and the right-hand side is adjusted accordingly.

3.24 Section XXIII

Here surface velocities and bottom geostrophic velocities are calculated for the centroid of the triangles.

3.25 Section XXIV

This is an option to calculate the terms of the vorticity equation. The values are calculated at the triangle centroids and are as follows:

$$\text{Barotropic torque} = J(\xi, d),$$

$$\text{Baroclinic torque} = N_1 J(\alpha, d),$$

$$\text{Wind stress} = \nabla \times \vec{\tau}^W,$$

$$\text{Bottom friction} = -(\text{barotropic torque} + \text{baroclinic torque} + \text{wind stress}).$$

3.26 Section XXV

The plotting is executed in this section. The plotting is basically handled by several subroutines which draw and label the triangles, label the vertices, and contour any parameter defined at the vertices. A separate program is used to take the punched velocity data from the model and plot velocity arrows at the centroids of the triangle.

3.27 Section XXVI

This is the option to alter the right-hand side of the global system of equations to take into account new boundary conditions. The user determines the input for this subroutine for each set of boundary conditions. Basically, the routine changes the specific boundary values

in the right-hand side vector. Once this is done, the program returns to SOLN and resolves the system of equations using the decomposed global matrix, subject to the new boundary conditions. With this system, numerous sets of boundary conditions can be tested at minimal cost.

4. RESULTS

Once the theory and software for the model was developed, operational testing was carried out. The model was run on simple contrived test cases. These runs were made to develop a better understanding of the physics involved to test the finite element method which is regularly used in engineering studies but is relatively new to oceanography. A summary of the results along with a discussion of the problems encountered will be presented here.

4.1 Test Cases

The test cases were designed to give a clear idea of how the model reacts to different physical conditions. Four simple cases were analyzed. In the first two, the finite element technique yielded exact linear solutions. In the last two cases, the analytical solutions could not be exactly represented by the first-order bases set and the accuracy of the numerical solution depended upon the resolution yielded by the mesh system.

The first test case was run on a regular six by six grid with a mesh of 50 triangles. The boundary elevations increased uniformly to the north from zero to 5 cm and the wind stress was zero. The depth and density were constant, and the nondimensional parameters were: $CONST1 = 1.00$, and $CONST2 = .025$. The vorticity equation reduces to Laplace's

equation subject to the linear boundary conditions. Physically, the geostrophic flow is forced only by the surface slope and is unidirectional and nondivergent. The geostrophically driven bottom Ekman layer is also nondivergent and is transporting water from north to south. The analytical solution to the vorticity equation is $\xi = ky$ where k is a constant determined by the boundary elevation slope. The numerical solution for this case is exact since the finite element solution approximates the solution with piecewise linear functions and is accurate to the first order (fig. 8).

The second test case is nearly identical to the first. The boundary conditions were the same and once again, there was no stratification or wind forcing. For this case, however, the depth was decreased uniformly toward the north from 1200 m to 200 m.

In this case the vorticity equation becomes

$$N^2 \nabla^2 \xi + \frac{\partial d}{\partial y} \frac{\partial \xi}{\partial x} = 0 ,$$

and the resulting geostrophic flow is unchanged from the previous case. The surface slope once again drives a unidirectional, nondivergent current which has no shear except in the bottom Ekman layer. Mass and vorticity are conserved within the region by having the geostrophic flow follow isobaths. The solution once again is $\xi = ky$, and the numerical solution is exact (fig. 9).

In the third case, baroclinicity was introduced into the model by taking the density as a linear function of y . The bottom depth, wind stress and boundary conditions were identical to those of case 2. Alpha, the integrated density, became a second-order function of y . The vorticity

equation for this case reduces to:

$$N_2 \nabla^2 \xi + \frac{\partial d}{\partial y} \frac{\partial \xi}{\partial x} = N_1 N_2 \nabla^2 \alpha = \text{const.}$$

Now, the linear basis set of functions used to approximate the solution cannot fit the exact solution and numerical errors are expected. Physically, the density field, depth, and boundary conditions are only functions of y and the resulting barotropic and baroclinic flows are in the x direction and nondivergent. The baroclinic mode increases with depth and flows counter to the barotropic mode. This results in a level of no motion at the mean depth of 700 m. Above the level of no motion, the boundary forced barotropic mode dominates, and the geostrophic flow is to the west. This in turn drives a bottom Ekman layer to the south. Below the level of no motion, the baroclinic mode dominates, and the geostrophic flow is to the east. This forces a bottom Ekman layer to the north (Fig. 10). Therefore, the bottom Ekman layer forced by the boundary conditions and baroclinic field is convergent. However, the total flow must be nondivergent, and the interior barotropic mode (specified by the dependent variable, surface height) must adjust over the prescribed bathymetry to compensate for the bottom Ekman convergence. In seeking the analytic solution, we first note the similarity between the reduced vorticity equation for this case and Stommel's model equation (1965).

Stommel's Equation

$$\nabla^2 \psi + \frac{D}{R} B \frac{\partial \psi}{\partial x} = \sin \frac{\pi y}{b}$$

$$\psi = 0 \text{ on Boundary}$$

Diagnostic Model, Case 3 Equation

$$\nabla^2 \xi + \frac{\partial d}{\partial y} \frac{\partial \xi}{\partial x} = N_1 \nabla^2 \alpha$$

$$\xi = K_y \text{ on Boundary}$$

This is a consequence of the integrated friction term being set proportional to the velocity in both models and the bathymetric stretching term for this case being of the same form as Stommel's beta term. If the boundary conditions for our vorticity equation were homogeneous, we would then expect the solution to be of the same form as Stommel's solution. The total solution in this case is just a linear combination of the solutions for the homogeneous equation solved for the nonhomogeneous boundary conditions (case 2; see equation A below) and the nonhomogeneous equation solved for the homogeneous boundary conditions (Stommel) type solution; (see equation B below).

Homogeneous Equation

$$N_2 \nabla^2 \xi + \frac{\partial d}{\partial y} \frac{\partial \xi}{\partial x} = 0$$

A

$$\xi = k_y \text{ on Boundary}$$

Nonhomogeneous Equation

$$N_2 \nabla^2 \xi + \frac{\partial d}{\partial y} \frac{\partial \xi}{\partial x} = N_1 N_2 \nabla^2 \alpha$$

B

$$\xi = 0 \text{ on Boundary}$$

Note the effect of the baroclinicity is to add a secondary flow onto the results obtained from the constant density case. Physically we

can expect the solution to show southward flow into deeper water to compensate for the converging bottom Ekman layer and then flow moving back to the north along the western boundary to satisfy the boundary conditions. The results of the total solution show wave-like oscillations which are unrealistic and not what was expected from the analytical solution. Haney (1975) describes similar oscillatory solutions when a numerical mesh cannot resolve a boundary layer. To see if this is the case, the secondary flow is examined by subtracting the results of the homogeneous equation subject to the nonhomogeneous boundary conditions, (i.e., case 2) from the total solution. Figure 11 indicates that the mesh system may have problems resolving the secondary flow. A western boundary current structure is evident but not clearly resolved. To show that this is the problem, the boundary layer size was increased by setting the nondimensional friction parameter, CONST2, equal to 1.25 from its original .025.

In case 3A the secondary flow in figures 12 and 13 is now well resolved. As expected, the secondary flow resembles Stommel's solution with a western boundary barotropic mode forcing water to the south to compensate for the convergent bottom Ekman layer and then moving back to the north along the Western boundary to satisfy the imposed boundary conditions. This confirms that the problem with the original solution for the third case was related to resolving the boundary layer.

The next step was to see if the triangles along the western boundary could be cut in half to increase the resolution of the secondary flow. The previous case (case 3) was run again on the same mesh with CONST2 equal to .25. From the results in Figures 14 and 15, it can be seen

that the numerical grid does not clearly resolve the boundary layer.

For case 3B, the mesh system was then altered such that the triangles along the western boundary were halved. The results are shown in Figure 16.

The solution is improved for Case 3C. It is more symmetrical and the surface elevation gradients are not as large. In general, a decrease in mesh size leads to more resolution, but the improvement is difficult to quantify because the finite element solution depends upon the triangle shapes as was the mesh size. For example, as the triangles become less equilateral, the global matrix becomes less conditioned (Strang and Fix, 1973).

For the fourth case, the density is once again set to a constant. The wind stress is still zero and the boundary condition is once again linear in the y direction. These are the same conditions as in the first case, but now the depth is made to be a linear function of both x and y (depth = Ax + By + C). See Figure 17.

The vorticity equation becomes:

$$N_2 \nabla^2 \xi + \frac{\partial d}{\partial y} \frac{\partial \xi}{\partial x} - \frac{\partial d}{\partial x} \frac{\partial \xi}{\partial y} = 0$$

The depth gradients are constants. Once again the linear basis set of functions used to approximate the solution cannot fit the exact solution and numerical errors are expected. In the interior, the flow attempts to follow isobaths but most deviate from the isobaths near the boundaries due to the boundary conditions. Along the north-south boundaries, the barotropic mode is not allowed to force water into or out of the region,

while the shallower water on the eastern boundary allows the barotropic mode to force less water into the region than is leaving on the western boundary. To compensate for this, a secondary flow with a boundary layer on the western side is set up. The secondary flow forces a convergent bottom Ekman layer to conserve water within the region.

In Figures 18 and 19 of the solution for case 4, clearly, the secondary flow and its boundary layer are not well-resolved. As in the previous case, the boundary layer thickness is increased by increasing the friction coefficient, CONST2, by an order of magnitude to .25.

In Figures 20 and 21, the solution for case 4A showing surface elevation and secondary flow, the large oscillations are gone and it is clear that the flow attempts to follow an isobath until it reaches the western boundary. The counterclockwise secondary flow and its western boundary layer is now well-defined. It forces a convergent bottom Ekman layer which compensates for the excess water the barotropic mode forces out of the region through the western boundary.

The next step is to increase the resolution along the western boundary by once again halving the triangle size along the western boundary.

In Figures 22 and 23 for case 4B, the difference in the solution yielded by the two different meshes is almost negligible. The current along the western boundary is better resolved, but the finer mesh results in only a slightly more symmetrical solution. The probable reason for this is that water is converging along the northern boundary and diverging along the southern boundary, and to improve the solution, more resolution along these boundaries is needed.

The results can be summarized by saying that the model physically compensates for continuity mismatches between the surface Ekman layer, boundary forced barotropic flow, and within the region which has either a convergent or divergent bottom Ekman layer. This secondary flow is similar to Stommel's model (1965) with a western boundary current and is a consequence of setting the vertically integrated friction terms proportional to the velocity. The model's inability to resolve the secondary flow due to too coarse a mesh was a problem in the test cases. Halving the mesh size along the western boundary improved the solution, but triangle shape as well as size affected the numerical solution.

The last test case indicates that care should be taken in setting the boundary conditions. If unrealistic boundary conditions are imposed, the model will compensate by forming a boundary layer which may degrade the results. The boundary layer thickness depends on the potential vorticity gradient (i.e., bottom slope) so the problem will be different for different geophysical settings.

5. CONCLUSION

A diagnostic shelf circulation model developed by Galt (1975) is implemented using the finite element method. The model is quasi-geostrophic and incorporates variable depth, baroclinicity, a surface Ekman layer, and a bottom Ekman layer. Physically, the model assumes a steady state, a small Rossby number flow. The depth scale is taken to be much less than the horizontal length scale, and the bottom Ekman layer is assumed to be driven by a geostrophic flow. The coriolis parameter is set to a constant and vorticity balance is required between the barotropic

and baroclinic stretching terms and the bottom and surface Ekman layers. The test cases indicate that the model accomodates the boundary conditions and forcing functions by creating a secondary barotropic flow within the region to conserved mass and vorticity through the bottom Ekman layer.

The model solves an integrated vorticity equation which is a second-order, nonhomogeneous, elliptic equation and is tested subject to Dirichlet boundary conditions. The dependent variable is the surface elevation solved for by the Finite Element Method. The program is written in Standard Fortran and is a collection of subroutines and overlays which can be easily altered, bypassed or used elsewhere. The input data requires standard STD station data, wind stress information, and the boundary surface elevations.

The major problems the model encounters are numerical. The spatial resolution of the model is limited and the exact position of current features cannot be predicted to any greater accuracy than the available input data. This means that although the model clearly recognizes the local dynamics, its resolution with respect to position, is no better than the station spacing, and this should be taken into consideration prior to taking stations. The stations must be spaced to create a mesh which can resolve both the secondary flow and forcing functions, particularly the density field, and depth.

ACKNOWLEDGEMENTS

The work described in this report has been sponsored in part by the Outer Continental Shelf Environmental Assessment Program under RU#140.

REFERENCES

- Formin, L.M., (1964): The dynamic method in oceanography. Elsevier, New York, 211 pp.
- Galt, J.A., (1975): Development of a simplified diagnostic model for the interpretation of oceanographic data. NOAA Technical Report ERL 339-PMEL 25, National Oceanic and Atmospheric Administration, U.S. Department of Commerce, Washington, D.C., 36 pp.
- Haney, R.L., and Wright, Jr. J.M., (1975): The relationship between the grid size and the coefficient of nonlinear lateral eddy viscosity in numerical ocean circulation models. J. Comp. Phys., 19, 257-266.
- Knuth, Donald E. (1968): The Art of Computer Programming, Vol. 1, Fundamental Algorithms. Addison-Wesley Publishing Company, Menlo Park, 634 pp.
- Knuth, Donald E., (1973): The Art of Computer Programming, Vol. 3, Sorting and Searching, Addison-Wesley Publishing Company, Menlo Park, 723 pp.
- Stommel, H., (1965): The Gulf Stream. University of California Press, Berkeley, 248 pp.
- Strang, G., and Fix, G., (1973): An analysis of the finite element method. Prentice Hall, Englewood Cliffs, N.J., 306 pp.
- Sverdrup, H.U., Johnson, M.W., and Fleming, R.H., (1942): The oceans: Their physics, chemistry and general biology. Prentice Hall, Englewood Cliffs, N.J., 1087 pp.
- Welander, P., (1957): Wind action on shallow sea: Some generalization of Ekman's Theory. Tellus, IX, 45-52.
- Zienkiewicz, O.C., (1971): The Finite Element Method in Engineering Science, McGraw-Hill, London, 521 pp.

FIGURE CAPTIONS

Figure

- #1 Five Station case where Roman numerals are global labels and triangles are labeled T1 to T4.
- #2 Illustration of a piecewise continuous hat function associated with node V.
- #3 Boundary triangle showing normal and alongshore directions.
- #4 Sample triangle with labeling.
- #5 Example of boundary triangles with labeling. Number of boundary points for each triangle:

$$\text{IBTRI} \quad (1) = 2$$

$$\text{IBTRI} \quad (2) = 1$$

$$\text{IBTRI} \quad (3) = 2$$

Relabeled local vertices so that boundary points lead in a counter-clockwise order:

$$\text{IP} (1,1) = 40; \quad \text{IP} (1,2) = 41; \quad \text{IP}(1,3) = 41$$

$$\text{IP} (2,1) = 41; \quad \text{IP} (2,2) = 43; \quad \text{IP}(2,3) = 42$$

$$\text{IP} (3,1) = 44; \quad \text{IP} (3,2) = 44; \quad \text{IP}(3,3) = 43$$

- #6 Example of a triangle external to the region of interest. If the outward normal to the boundary is in the triangle, then the triangle is external to the region. In this example the outward normal between vertices 1 and 2 fall inside triangle I so triangle I is outside of the domain and eliminated.
- #7 Two triangle examples.
- #8 Homogeneous water, flat bottom case, where the geostrophic flow is

- #8 nondivergent and toward the west and the bottom Ekman flow is
(cont) nondivergent and toward the east.
- #9 Homogeneous water, sloping bottom case, where the geostrophic flow is nondivergent and toward the west and the bottom Ekman flow is nondivergent and toward the south.
- #10 Baroclinic case with density and depth uniformly increasing toward the south and a level of no motion at the mean depth above the level of no motion.
- #11 Secondary flow for case 3 where the density is a linear function of y . The boundary layer is not resolved, resulting in numerical oscillation. Elevations are in centimeters.
- #12 Surface elevation contours for case 3 with boundary layer thickness increased ($CONST2 = 1.25$). Contours are in centimeters.
- #13 Secondary flow for case 3 with boundary layer thickness increased. Western boundary layer is now well resolved. Elevations are in centimeters. ($CONST2 = 1.25$).
- #14 Surface elevations for case 3 with $CONST2 = .25$. The boundary layer is not clearly resolved. Contours are .1 centimeter.
- #15 Secondary flow for case 3 where $CONST2 = .25$. The boundary layer is not clearly resolved. Contours are .1 centimeter.
- #16 Secondary flow for case 3 where the triangles along the western boundary are halved from previous case. The North-South symmetry of boundary layer is not yet fully resolved. Elevations are in centimeters. ($CONST2 = .25$)

- #17 Non-dimensional isobaths for case 4 where each unit is equivalent to 200 m.. Depth = $Ax + By + C$.
- #18 Surface elevations for case 4 where contours are in centimeters. The oscillations indicate that the boundary layer is not resolved.
- #19 Secondary flow for case 4 where contours are in centimeters and the boundary layer is not well resolved.
- #20 Surface elevations for case 4 where contours are in centimeters. CONST2 = .25.
- #21 Secondary flow for case 4 with CONST2 = .25. Elevations are in centimeters.
- #22 Surface elevations for case 4 with CONST2 = .25 and the triangles along the western boundary are halved.
- #23 Secondary flow for case 4 with CONST2 = .25 and the triangles along the western boundary have been halved from the previous case (figure 14). Elevations are in centimeters.

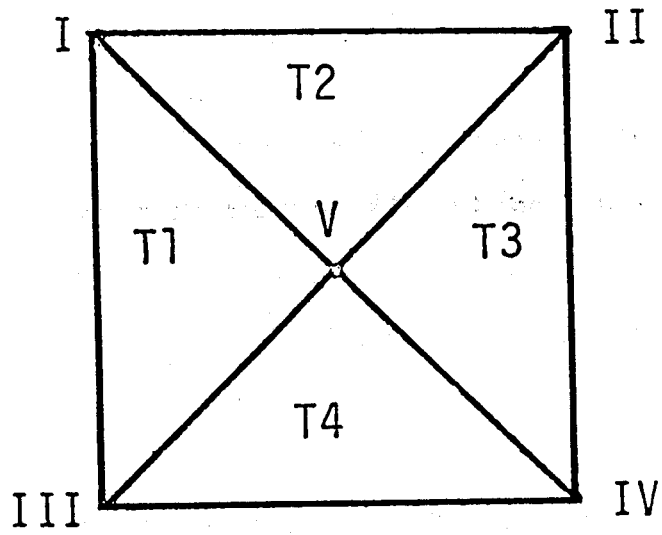


Figure 1.

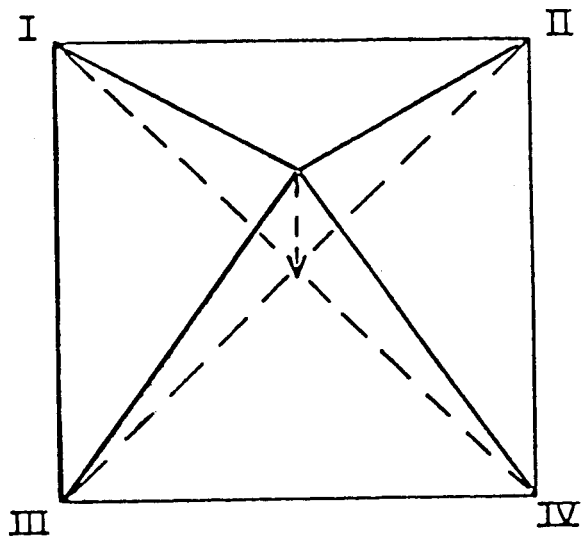


Figure 2.

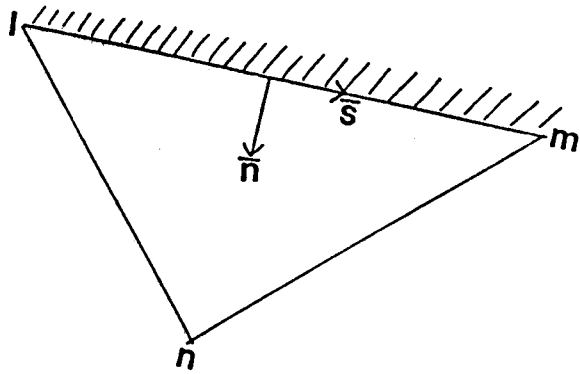


Figure 3.

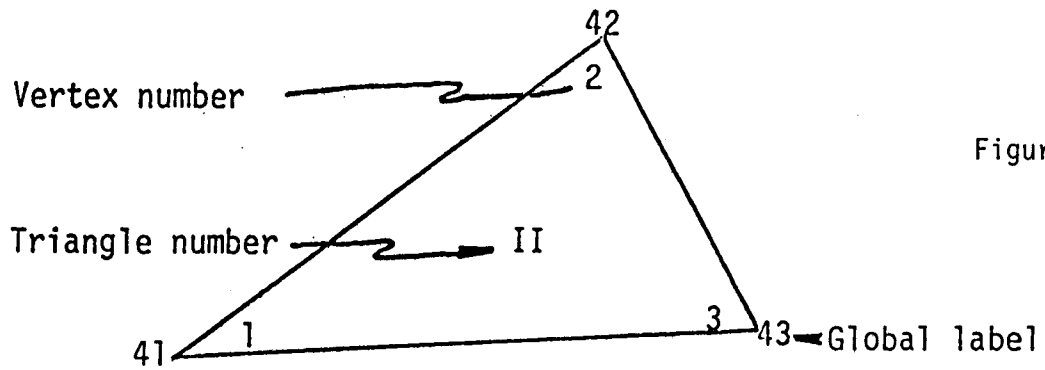


Figure 4.

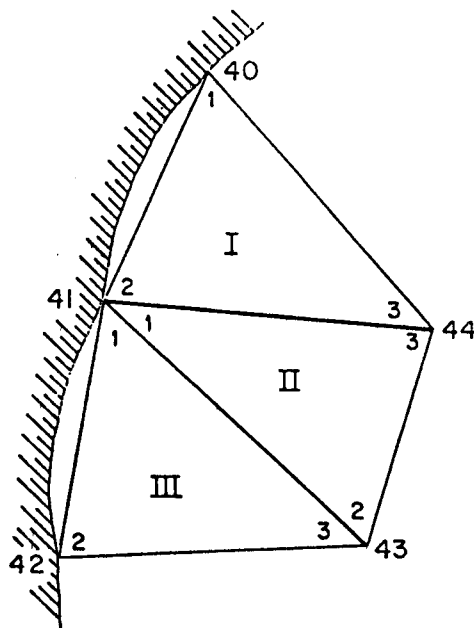


Figure 5.

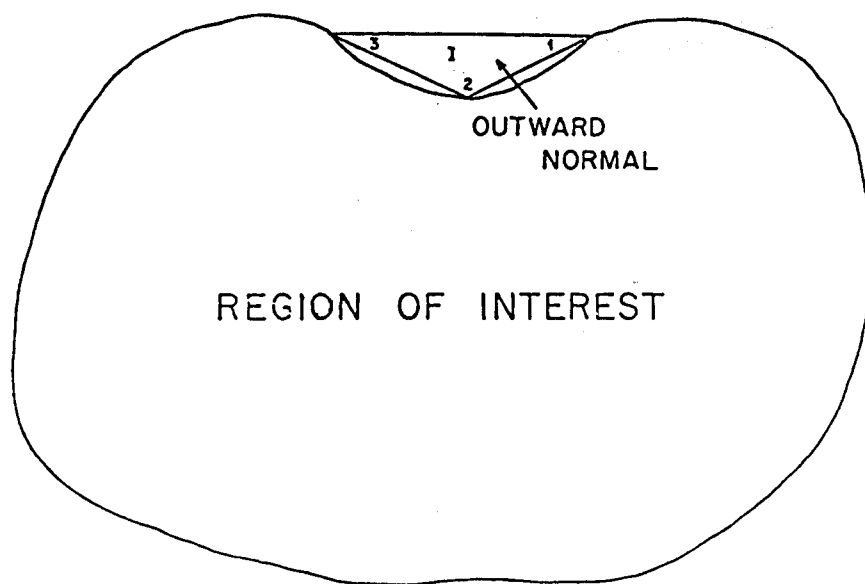


Figure 6.

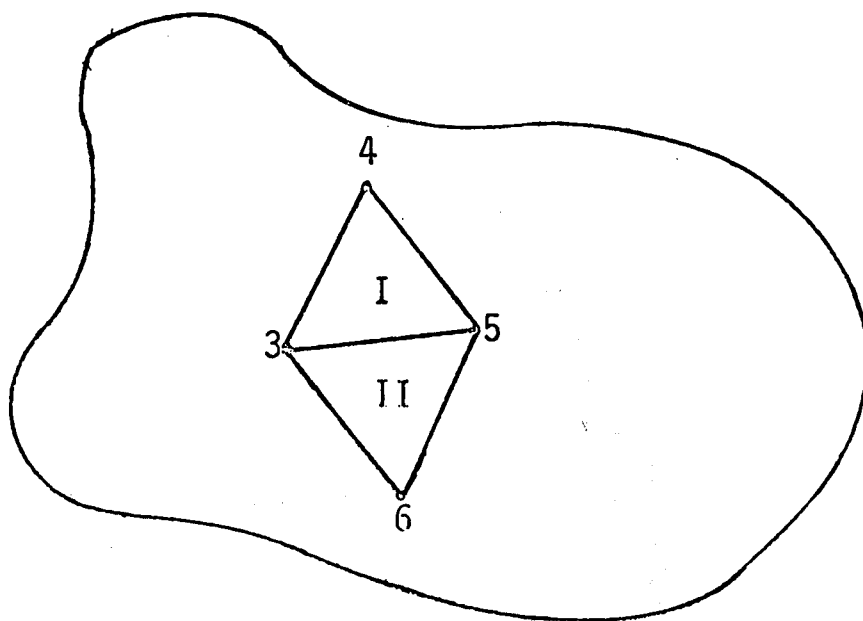


Figure 7.

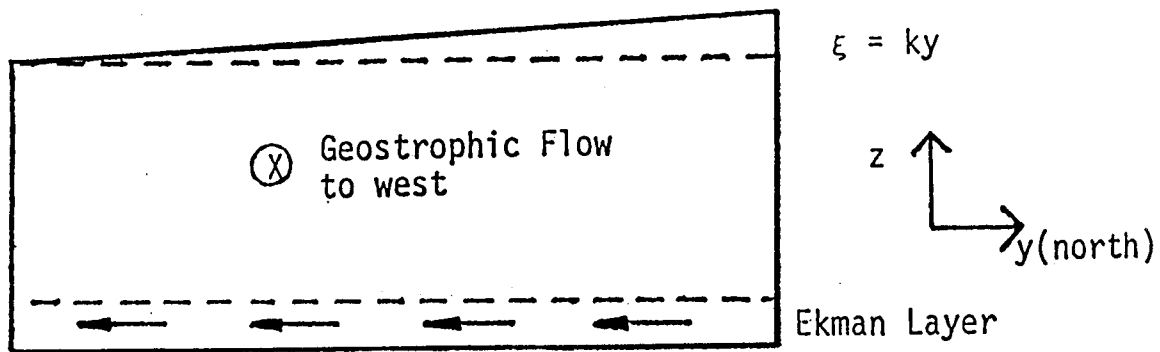


Figure 8.

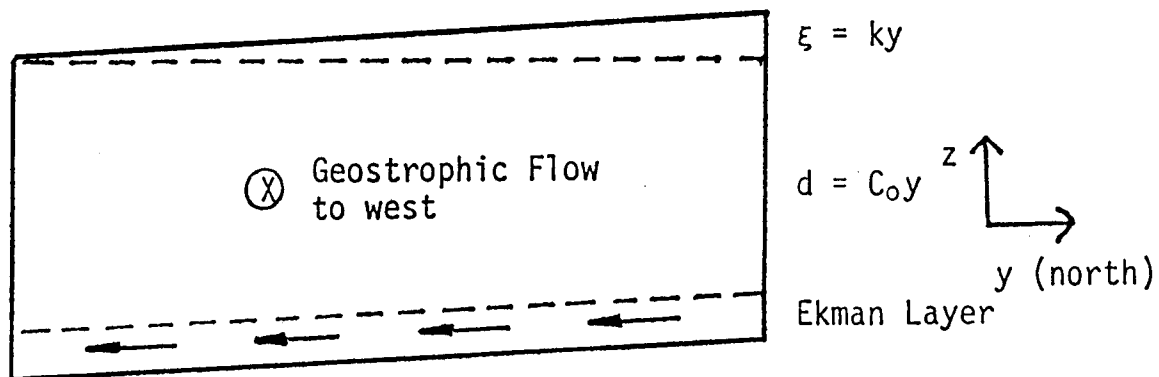


Figure 9.

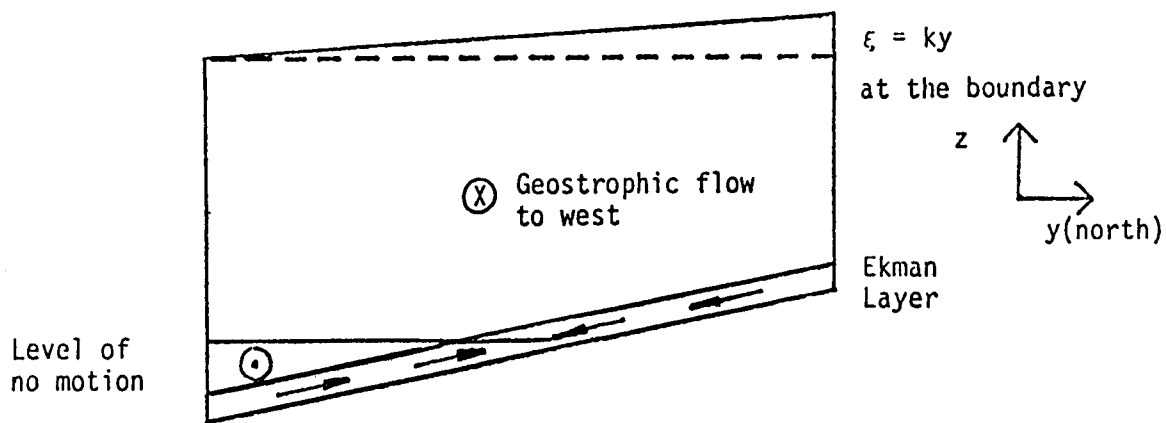


Figure 10.

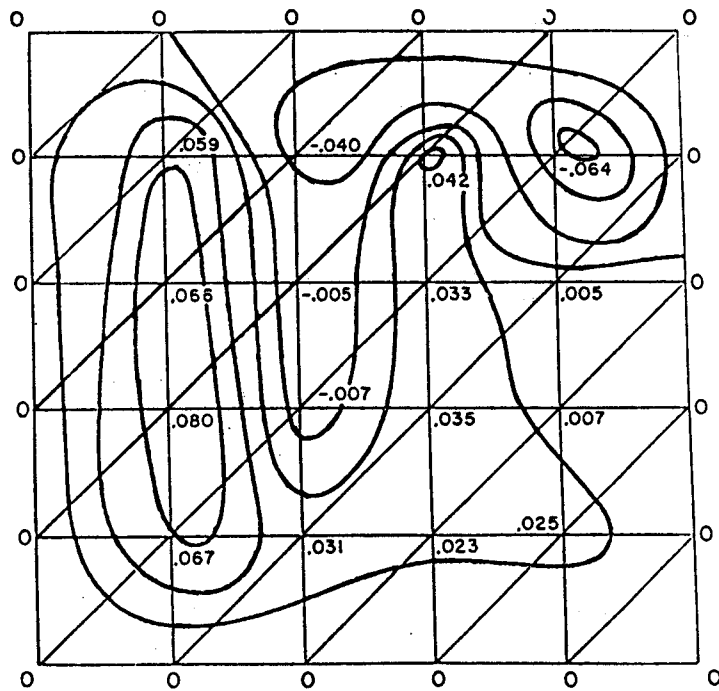


Figure 11.

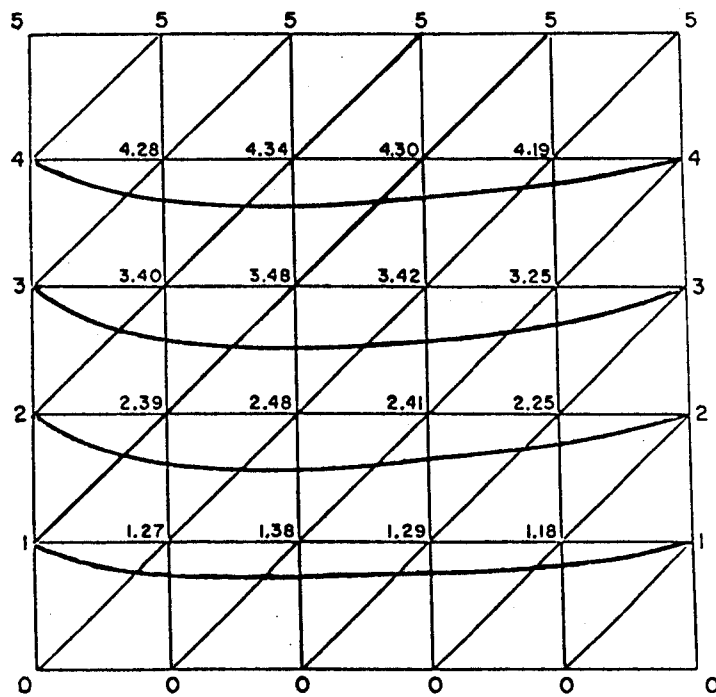


Figure 12.

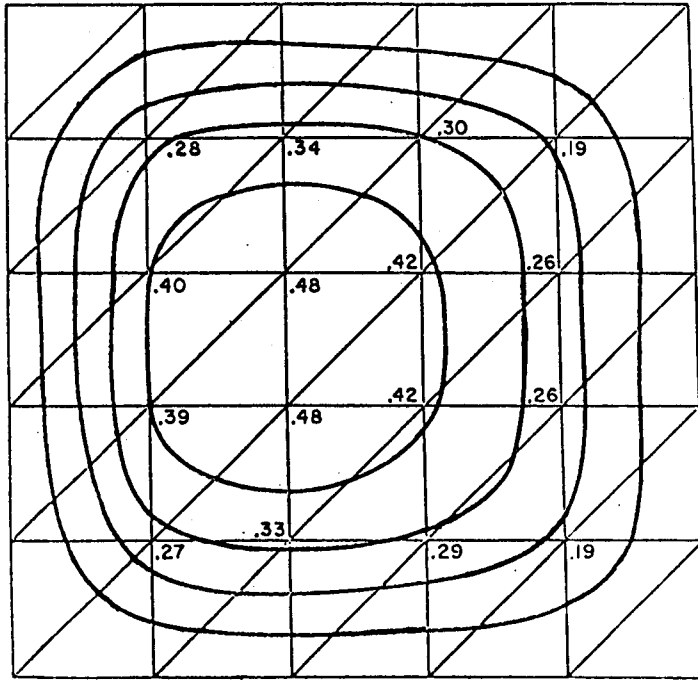


Figure 13.

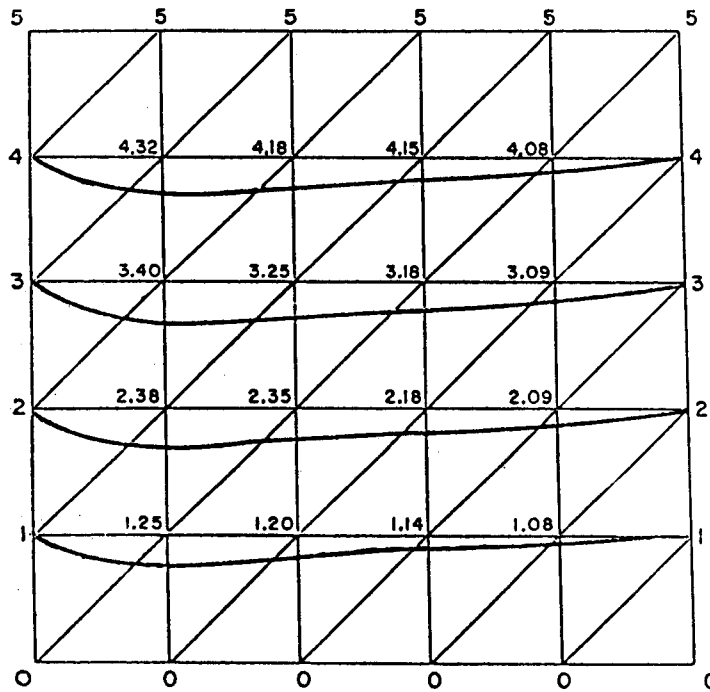


Figure 14.

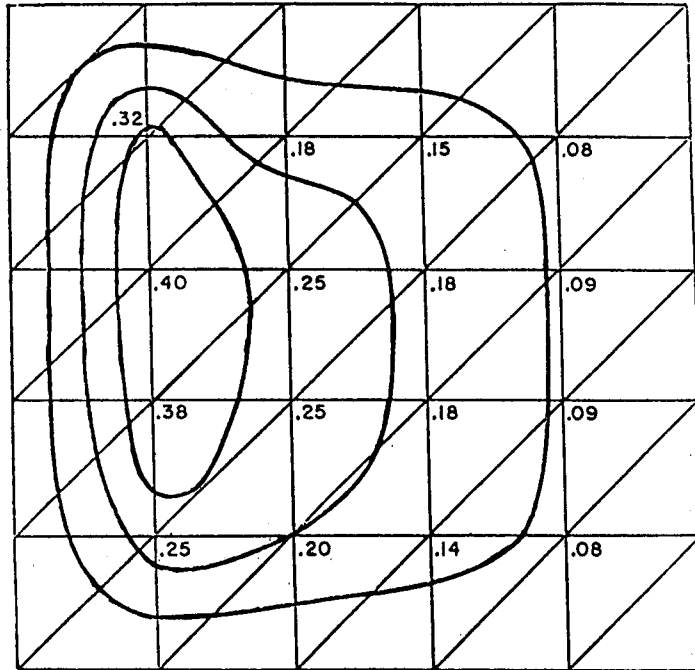


Figure 15.

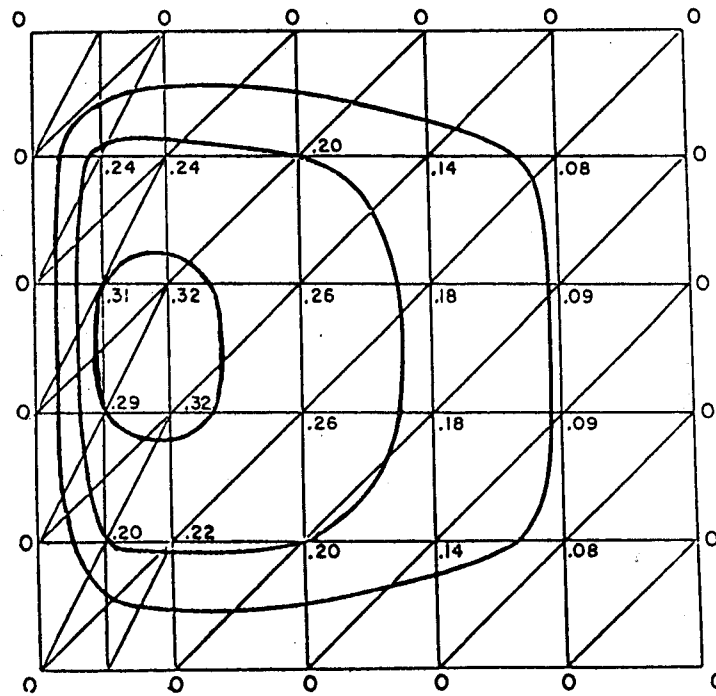


Figure 16.

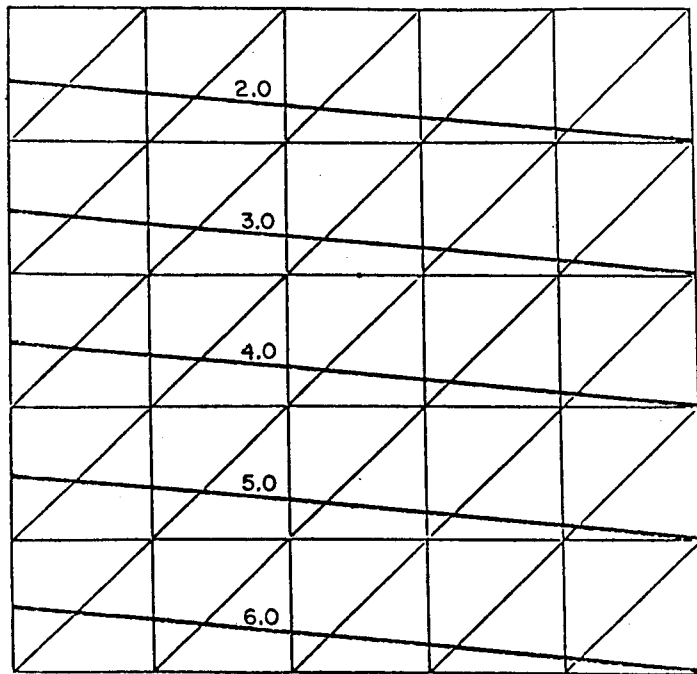


Figure 17.

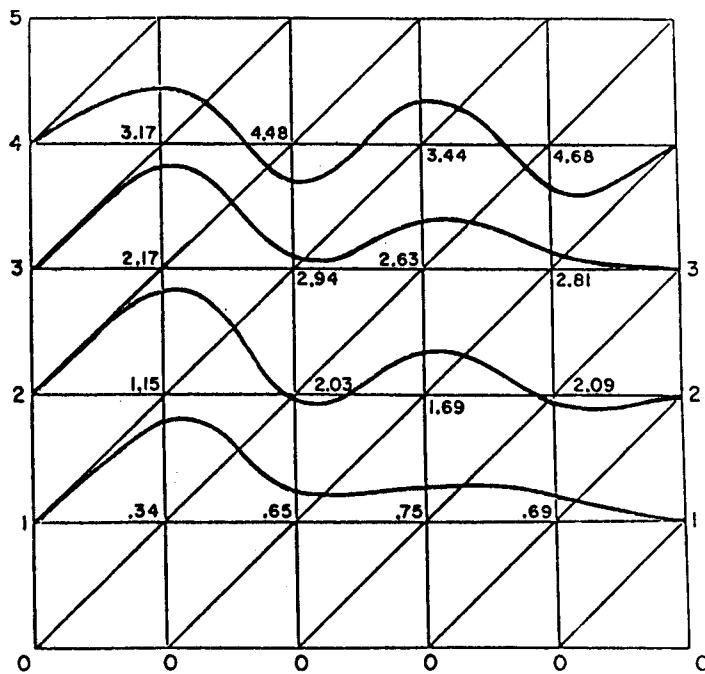


Figure 18.

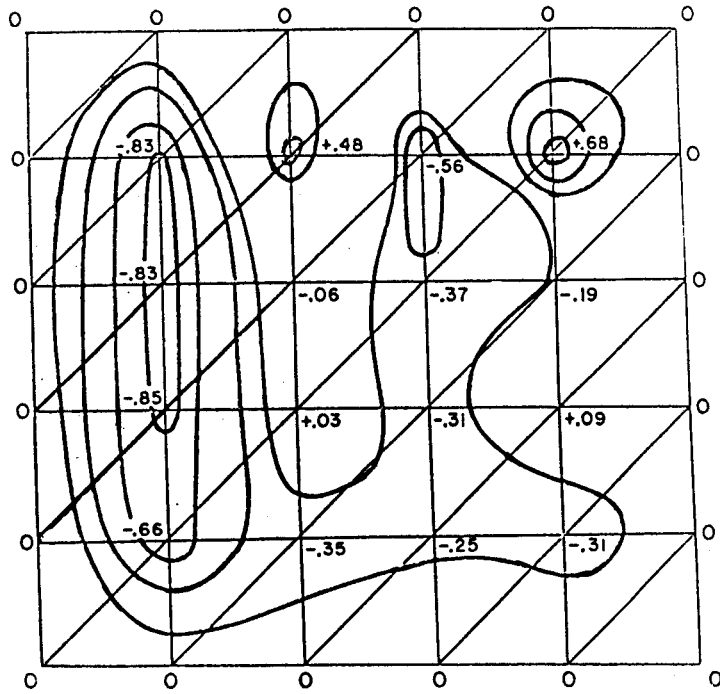


Figure 19.

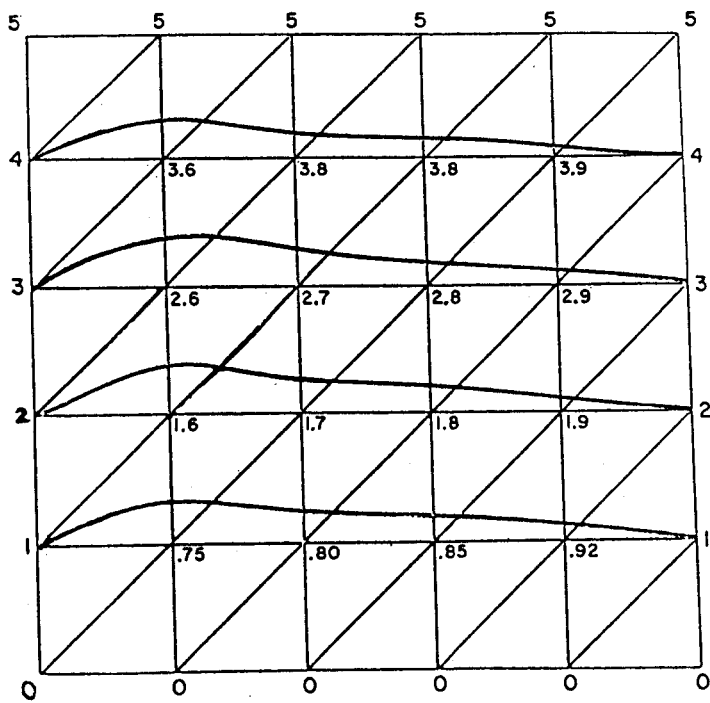


Figure 20.

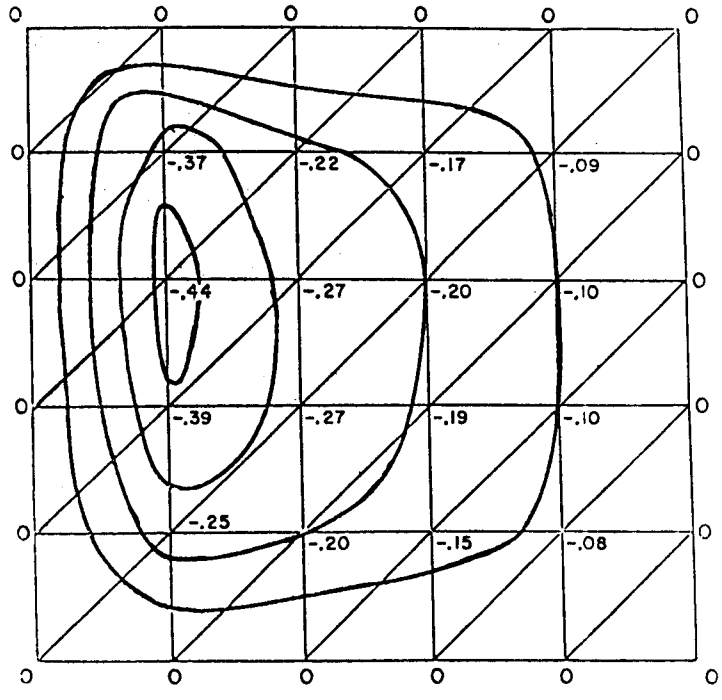


Figure 21.

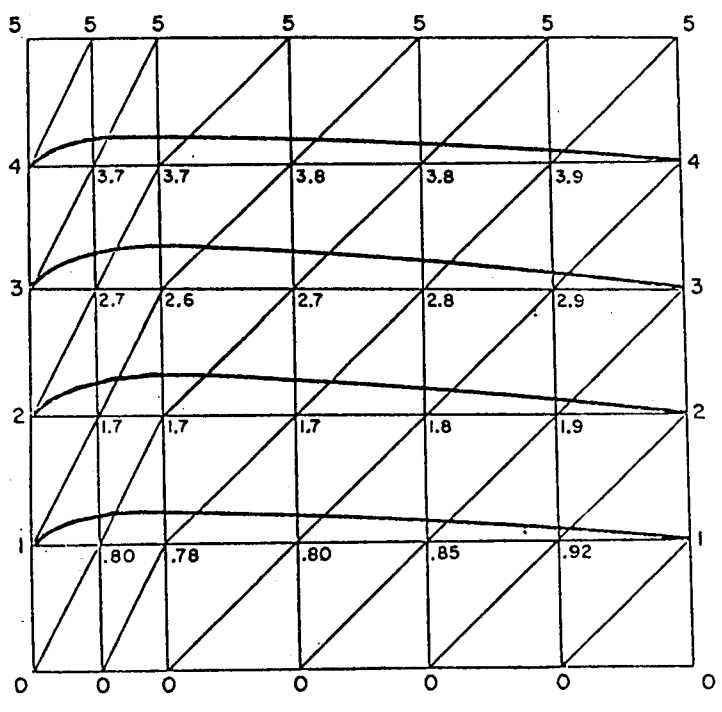


Figure 22.

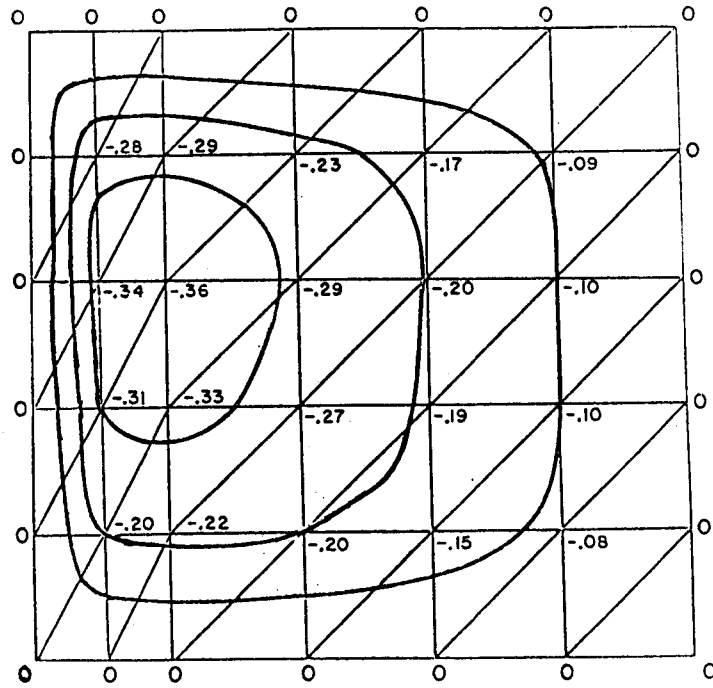
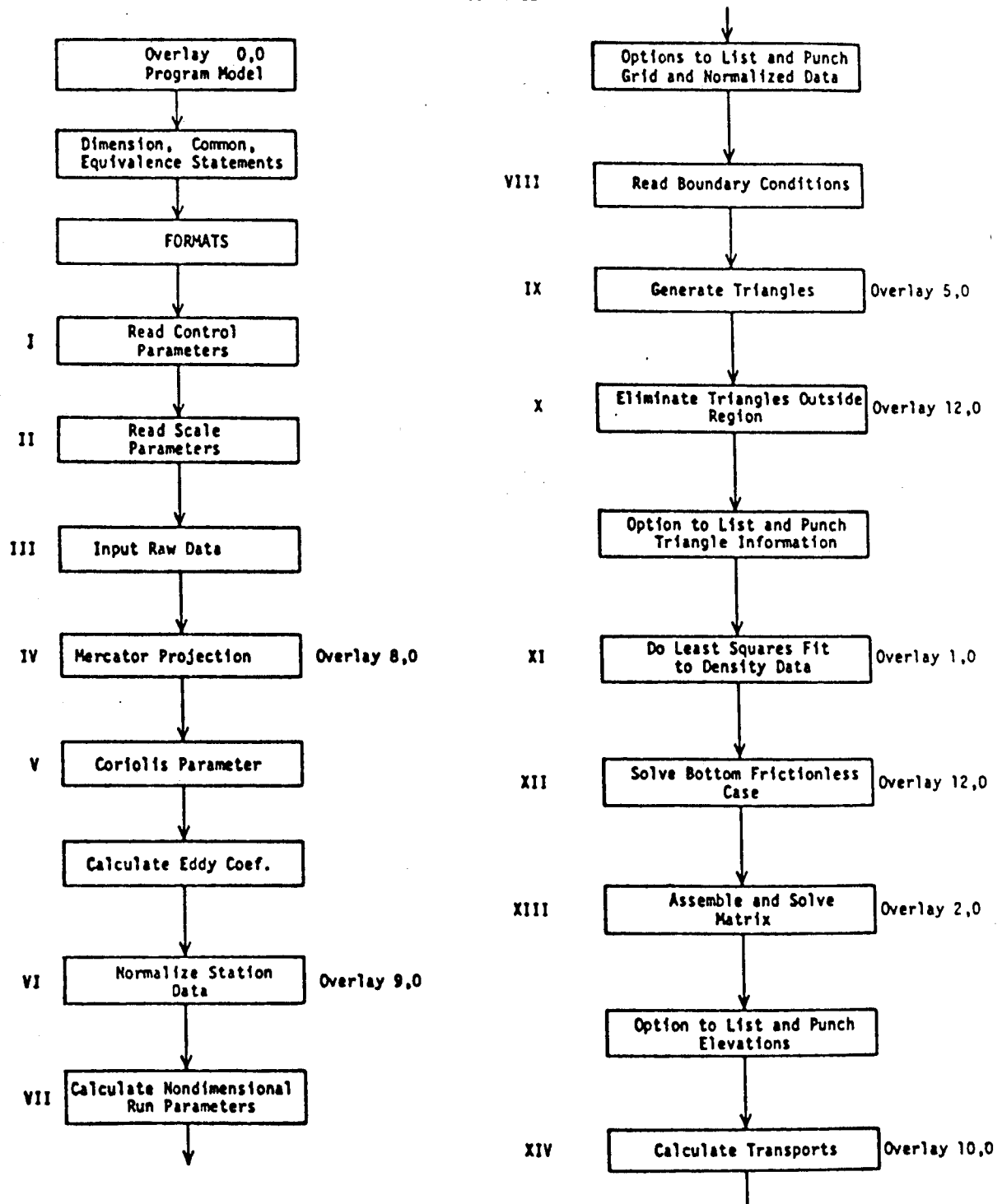
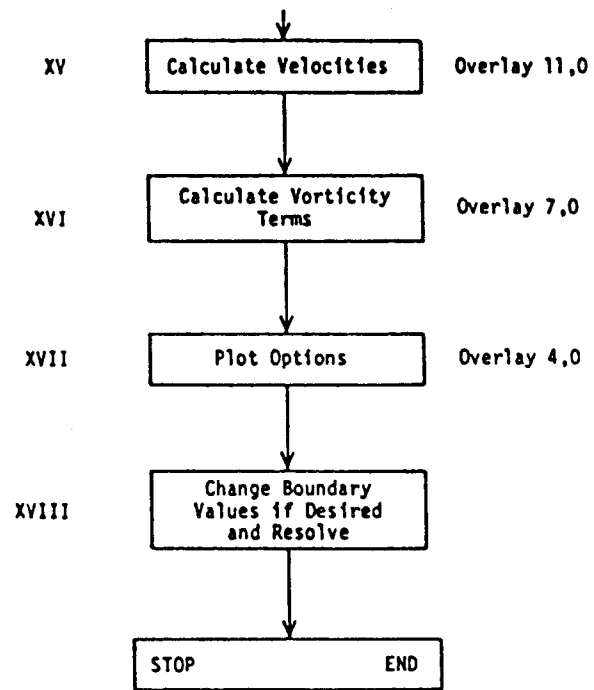


Figure 23.

Appendix 1
REVISED FLOW CHART OF
DIAGNOSTIC MODEL





APPENDIX II LISTING

KRONOS L419.39. 77/09/13.
 OPERATING SYSTEM
 JOB ORIGIN = BATCH.
 USER NUMBER/ID = GW
 JOBCARD NAME = GLENS00

NN	NN	EEEEEEEEEEEE	111	YY	YY	KK	KK
NNN	NN	EEEEEEEEEEEE	1111	YY	YY	KK	KK
NNNN	NN	EE	1 11	YY	YY	KK	KK
NN NN	NN	EE	11	YY	YY	KK	KK
NN NN	NN	EE	11	YY	YY	KK	KK
NN NN	NN	EE	11	YY	YY	KK	KK
NN NN	NN	EE	11	YYY	YYY	KK	KK
NN NN	NN	EEEEEEEE	11	YYY	YYY	KK	KK
NN NN	NNN	EEEEEEEE	11	YYY	YYY	KKKKK	
NN NN	NN	EE	11	YYY		KKKKK	
NN NN	NN	EE	11	YY		KK	KK
NN NN	NN	EE	11	YY		KK	KK
NN NN	NN	EE	11	YY		KK	KK
NN NN	NN	EEEEEEEEEEEE	111111111111	YY		KK	KK
NN NN	NN	EEEEEEEEEEEE	111111111111	YY		KK	KK

OUTPUT FOR: CLIFF FRIDLINO
 PACIFIC MARINE ENVIRONMENTAL LABORATORY
 3711 15TH AVE. N. E.
 SEATTLE, WASHINGTON 98105

FTS PHONE: 399-4850


```
OVERLAY(MODEL,0,0)
PROGRAM MODEL(FILE1,OUTPUT,FILE0,FILE1,TAPE5=FILE1,TAPE6=OUTPUT,TA
CPE7=FILE0,TAPE1=FILE1,TAPE99)
```

C
C
C
C
C
C
C
C

```
QUASI GEOSTROPHIC MODEL WITH AN EKMAN BOTTOM FRICTION LAYER
THE MAXIMUM NUMBER OF STATIONS THIS PROGRAM IS SET UP TO TAKE
IS 200. IF MORE STATIONS ARE ANALYSED, THE DIMENSION STATEMENTS
MUST BE INCREASED. THE PROGRAM AS IT STANDS TAKES ABOUT 75000 CH
OCTAL IF THE U. W. GRAFIX LIBRARY IS ATTACHED.
```

```
DIMENSION XS(100),YS(100)
DIMENSION ALAT(200),ALONG(200)
DIMENSION LAT(200),LONG(200)
COMMON/LSCOEF/SA(4),SD(4),STNOVA,STNOVD
```

C

```
COMMON/IALPHA/ALPHA(200)
COMMON/IDELTA/DELTA(200)
COMMON/IN/N(300)
COMMON/BOUND/IB(75),BV(75),NBV
COMMON/IA/A(3,3)
COMMON/EXTRA/EX(300)
COMMON/IB/B(3)
COMMON/CALC(CMP/XXMAX,YYMAX,ISTART,NBC
COMMON/IALP/ALPH(3)
COMMON/ICNST/CONST1,CONST2
COMMON/IDEPH/DEPTH(200)
COMMON/IGRAD/DALPHAX,DALPHAY,DOEPHDX,DOEPHXY,DEX,DEY,AREA
COMMON/IHEIGHT/HEIGHT(200)
COMMON/IIP/IP(3,350)
COMMON/INT/INTP(4500)
COMMON/IRHS/RHS(200)
COMMON/SCALES/USCALE,OSCALE,ALSCALE,G,E,Q,GAMMA,FO,EDDY
COMMON/HIND/TAUX,TAUY,CURL
COMMON/IWCRK/VALP(4500)
COMMON/IX/X(200)
COMMON/IY/Y(200)
COMMON/NUMB/NVRTX,NTRI,LIST,IPUNCH,NEWBV
COMMON/CUTOFF/NIBP,NFLX,NOMAT,JJ2,DEEP
```

C

```
COMMON/XYPLOT/XPLOT,YPLOT
COMMON/GDIV/X1(102),Y1(102),X2(102),Y2(102),NX,NY,XDIV,YDIV
COMMON/DEG/NDEC
COMMON/DEG/DEGREE
COMMON/CHSIZE/SIZE
COMMON/BLCK/IBLOCK
COMMON/OBJ/XRANGE,YRANGE,XMIN,YMIN,YBT,SLFT,YTP,XRGHT
COMMON/SUB/XLEFT,YBOT,XSCALE,YSCALE
COMMON/STNCH/NCHR
COMMON/LTYPE/NLINE
COMMON/NPT/NPTS
EQUIVALENCE(HEIGHT(1),LONG(1))
EQUIVALENCE(ALAT(1),Y(1))
```

EQUIVALENCE (ALONG(1),X(1))
EQUIVALENCE (IP(1,1),LAT(1))

C
C
C
C
C
C
C

*****WARNING. MIXED MODE OPERATIONS AROUND*****

WE BEGIN WITH ALL THE FORMATS WE NEED. NOTE THAT THE FORMAT
NUMBERS ARE ALL MULTIPLES OF 5.

5 FORMAT(15I5)
10 FORMAT(I3,I3,F6.2,I5,F6.2,F10.4,F14.4,F7.1,F6.3,F5.3,F6.3)
15 FORMAT(*1*)
20 FORMAT(*0*,*STAT*,5X,*LATITUDE*,5X,*LONGITUDE*,6X,*ALPHA*,11X,*DE
LTA,10X,*DEPTH*)
25 FORMAT(* *,I4,5X,I3,1X,F4.1,5X,I3,1X,F5.2,4X,F9.4,6X,F13.4,5X,F7.1
*,6X,F4.2,5X,F4.2,6X,F10.7)
30 FORMAT(*0*,*TRIANGLE NO.*,10X,*VERTEX 1*,10X,*VERTEX 2*,10X,*VERTE
X 3)
35 FORMAT(* *,4X,I3,19X,I3,14X,I3,15X,I3)
40 FORMAT(*0*,*TRIANGLE NO.*,35X,*VERTICES*)
45 FORMAT(* *,4X,I3,10X,*(*,F5.2,**,F5.2,*),10X,*(*,F5.2,**,F5.2,*
),10X,*(*,F5.2,**,F5.2,**)*)
50 FORMAT(I5,F20.3)
55 FORMAT(*0*,*BOUNDARY VAL. NO.*,10X,*GLOBAL LABEL*,10X,*BOUNDARY VA
LUE,9X,*CENTIMETERS*)
60 FORMAT(* *,8X,I3,29X,I3,18X,F7.3,15X,F8.3)
65 FORMAT(*0*,*PROGRAM TERMINATED, TRIANGLE*,2X,I3,2X,*HAS BOUNDARY P
OINTS,2X,I3,**,2X,I3,**,2X,*AND*,2X,I3,2X,*FOR VERTICES*)
70 FORMAT(1H0,*PROGRAM STOPPED TO CHECK NEW BOUNDARY CONDITIONS*)
75 FORMAT(*0*,5X,I3,14X,I3,I10,30X,I3)
80 FORMAT(*0*,*BOUNDARY VALUES*,/,*0*,*B.P.*,6X,*LATITUDE*,10X,*LONGI
TUDE,10X,*VALUE*)
85 FORMAT(* *,I3,7X,I3,1X,F4.1,10X,I3,1X,F4.1,11X,F5.2)
90 FORMAT(*0*)
95 FORMAT(*0*,*STAT NO.*,10X,*GLOBAL NO.*,10X,*X-COOR.*,10X,*Y-COOR*)
100 FORMAT(* *,2X,I3,15X,I3,13X,F6.2,10X,F6.2)
105 FORMAT(*1*,*RECHECK BOUNDARY TRIANGLE*,I3)
110 FORMAT(*1*,*STATION*,2X,I4,2X,*NOT ONE OF LISTED STATIONS*)
115 FORMAT(*0*,*GLOBAL LABEL*,10X,*X-COOR*,10X,*Y-COOR*,17X,*ELEVATION
NONDIM.,5X,*ELEVATIONS IN CM.*,/)
120 FORMAT(* *,4X,I3,15X,F6.2,10X,F6.2,20X,F9.5,12X,F10.5)
125 FORMAT(1H0,*RADIUS USED IN MERCATOR PROJECTION IS*,F10.5)
130 FORMAT(*1*,*BOUNDARY POINTS*,1X,I3,1X,*AND*,1X,I3,1X,*ARE IDENTICA
L)
135 FORMAT(* *)
140 FORMAT(7F10.2)
145 FORMAT(* *,*THIS LISTING IS BEFORE WE ELIMINATE TRIANGLES OUTSIDE
OF CUR DOMAIN)
150 FORMAT(7F10.3)
155 FORMAT(1H0,*X=0 LINE IS*,F7.4,1X,*RADIAN OF LONGITUDE WEST*)
160 FORMAT(1H ,*Y=0 LINE IS*,F7.4,1X,*RADIAN OF LATITUDE NORTH*)
165 FORMAT(* *,*STAT*,9X,*GL. LAB.*,9X,*ALPHA*,11X,*DELTA*,11X,*DEPTH

```

**)
170 FORMAT(1X,I3,12X,I3,9X,F9.5,6X,F11.5,7X,F9.5,10X,F9.4)
175 FORMAT(* *,*NORMALIZED VALUES*,/)
190 FORMAT(* *,*TRANSPORT AND MEAN VELOCITIES NONCIMENTIONALIZED*,/)
195 FORMAT(1X,2F10.2,50X,*STA.*,2X,I3)
200 FORMAT(F10.4,F15.4,F10.2,F10.4,F11.4,15X,*STA.*,2X,I3)
205 FORMAT(3I5,55X,*TRIA.*,1X,I4)
210 FORMAT(F10.4,60X,*HEIGHT*,1X,I3)
215 FORMAT(* *,*SCALE PARAMETERS*)
220 FORMAT(*0*,*VELOCITY*,7X,F6.3,1X,*METERS/SEC*,//,* *,*DEPTH*,10X,F
#7.1,1X,*METERS*,//,* *,*LENGTH*,9X,F8.1,1X,*METERS*,//,* *,*GRAVIT
#Y*,8X,F7.2,1X,*M/(SEC SQ)*,//,* *,*PERT. DENSITY*,2X,F6.4,1X,*GH/(
#CM CU)*,//,* *,*CONST. DENSITY*,1X,F7.3,1X,*GH/(CM CU)*,//,* *,*GA
#MMA*,10X,F7.1,1X,*GP/(CM SQ)*,//,* *,*CORIOLIS*,7X,F9.7,1X,*1/SEC*
#)
225 FORMAT(*0*,*NONDIMENSIONAL RUN PARAMETERS*,//,* *,*CONST1=GEH/QFUL
#=#,F5.2,//,* *,*CONST2=GAMMA/QH=#,F7.5)
230 FORMAT(* *,*VELOCITY IS IN CENTIMETERS PER SECOND*,/)
235 FORMAT(* *,*ELEVATION SCALE FACTOR IS*,F8.3,1X,*CM.*)
245 FORMAT(3F15.8)
250 FORMAT(F10.4,F15.4,F10.4,36X,*STA.*,1X,I3)
255 FORMAT(*MEAN CORICLIS IS*,F10.8)
260 FORMAT(*WIND STRESS AND CURL VALUES*,3F10.4)
265 FORMAT(* *,*RAW STATION DATA*,/, * *,*TAUX=#,F10.4,5X,*TAUY=#,F10.
#4,5X,*CURL=#,F10.4)
270 FORMAT(*ALPHA COEF.*,5F10.5)
275 FORMAT(*DELTA COEF.*,5F10.5)
280 FORMAT(*0*,*EDDY COEFFICIENT=#,F10.3,1X,*GH/(CM SEC)*
285 FORMAT(1H0,10H*****),2X,*GLOBAL MATRIX IS SINGULAR, PROBLEM
CTERMINATED*,10H*****))

```

```

C
C
C   HERE WE READ IN CONTRCL VALUES WHICH WILL TELL US WHAT WE WANT OUT
C   AND WHAT WE WANT DONE
C
C   IF ANY OF THE THE PARAMETERS IS SET TO 1, THE PROGRAM WILL EXECUTE
C   THAT OPTION. IF IT IS 0, THEN THE OPTION WILL BE BYPASSED
C   ALL LIST OPTIONS BEGIN WITH L, AND ALL PUNCH OPTIONS BEGIN WITH IP.
C
C   LRNOATA=1 MEANS THAT THE RAW DATA WILL BE LISTED. DATA 1
C
C   NOGRID=1 MEANS THAT THE CARTESIAN GRID WILL BE GENERATED. DATA 2
C   NOTE THAT IF THIS IS 0, THEN THE GRID IS READ IN.
C   LGRID=1 MEANS THAT THE CARTESIAN GRID WILL BE LISTED.
C   IPGRID=1 MEANS THAT THE CARTESIAN GRID WILL BE PUNCHED.
C
C   NORMAL=1 MEANS THAT THE RAW DATA WILL BE NORMALIZED. DATA 3
C   ONCE AGAIN IF THIS IS SET TO 0, THEN THE DATA WILL HAVE TO BE
C   READ IN.
C   LNORM=1 MEANS THAT THE NORMALIZED DATA WILL BE LISTED.
C   IPNCRP=1 MEANS THAT THE NORMALIZED DATA WILL BE PUNCHED.
C
C   MAKETRI=1 MEANS THAT THE TRIANGLES WILL GE GENERATED. DATA 3

```



```

C      IFILE=-1 MEANS THAT THE PROGRAM WILL PUT THE DECOMPOSED MATRIX      DATA 1
C      ONTO FILE1.
C      IFILE=0 MEANS THAT THE PROGRAM WILL DECOMPOSE THE MATRIX BUT NOT
C      PUT IT ONTO FILE.
C      IFILE=1 MEANS THAT THE PROGRAM WILL READ THE DECOMPOSED MATRIX
C      FRCH FILE1.
C      *****REMEMBER TO REQUEST FILE1 AND CATALOG IT IF THE MATRIX IS
C      PLACED ONTO FILE1. ALSO REMEMBER TO ATTACH THE FILE IF THE
C      THE MATRIX IS TO BE READ FROM THE FILE.*****
C
C      NIBF=NUMBER OF INTERICR(ISLAND) BOUNDARY POINTS YOU HAVE. ONE      DATA 1
C      ISLAND IS PERMITTED.
C      NFLX=NUMBER OF ONSHORE BOUNDARY POINTS YOU HAVE. THESE ARE THE
C      BOUNDARY POINTS WHICH DEFINE THE MAINLAND COASTLINE.
C
C      NOBCK=1 MEANS THAT THE PROGRAM WILL ALTER THE OPEN BOUNDARY      DATA 1
C      CONDITIONS BY SOLVING THE BOTTOM FRICTIONLESS CASE.
C      NOINTG=1 MEANS THAT THE INTEGRATION ALONG DEPTH CONTOURS WILL BE
C      DONE. THE ALTERNATIVE (NOINTG=0), IS TO READ IN THE
C      ELEVATION CHANGES ALONG THE DEPTH CONTOURS.
C      IPINTG=1 MEANS THAT THE ELEVATION CHANGES ALONG THE DEPTH CONTOURS
C      WILL BE PUNCHED OUT. NOTE THAT THE ELEVATION CHANGES ALONG
C      DEPTH CONTOURS ARE FUNCTIONS ONLY OF THE DEPTH, AND FORCING
C      FUNCTIONS, NOT OF THE BOUNDARY VALUES THEMSELVES.
C      IPBV=1 MEANS THAT THE NEWLY ADJUSTED BOUNDARY VALUES WILL BE
C      PUNCHED.
C      NOHCLT=1 MEANS THAT THE PROGRAM WILL BE TERMINATED AFTER THE
C      BOUNDARY VALUES HAVE BEEN ADJUSTED TO SEE IF THE BOUNDARY
C      CONDITIONS ARE REASONABLE.
C
C      DEEP=CUTOFF DEPTH AT WHICH THE BOUNDARY VALUES ARE OBTAINED FROM      DATA 1
C      DYNAMIC HEIGHT CALCULATIONS. THESE BOUNDARY VALUES WILL NOT
C      BE ALTERED.
C      THE QUANTITY DEEP IS READ IN NEGATIVE METERS.
C
C      READ(5,5)LRWDATA      DATA
C      READ(5,5)NOGRID,LGRID,IPGRID      DATA
C      READ(5,5)NORMAL,LNORM,IPNORM      DATA
C      READ(5,5)MAKETRI,LTRI,IPTRI,ISTOP      DATA
C      READ(5,5)NOCORY      DATA
C      READ(5,5)NOCONST,IPCONST      DATA
C      READ(5,5)LBV      DATA
C      READ(5,5)NOELEV,LELEV,IPELEV      DATA
C      READ(5,5)NOTRANS,IPTRANS      DATA
C      READ(5,5)NOVELO,IPVELO      DATA 1
C      READ(5,5)KCTERM      DATA 1
C      READ(5,5)NBC      DATA 1
C      READ(5,5)NOPLOT,INHAT      DATA 1
C      READ(5,5)LSF,LCCEF      DATA 1
C      READ(5,140)SMTHA,SMTHD      DATA 1
C      READ(5,5)IFILE      DATA 1
C      READ(5,5)NIBF,NFLX      DATA 1

```

```

READ(5,5)NOBCK,NOINTG,IPINTG,IPBV,NOHALT
READ(5,150)DEEP
DATA 1
DATA 1
C
NEHBV=1
ISTART=0
C
C
C WE NOW PROCEED TO READ IN THE SCALE PARAMETERS TO BE USED FOR OUR
NONDIMENSIONALIZED GRID AND OTHER SCALING.
C THE VELOCITY SCALE, #USCALE#, IS IN METERS/SEC. THE DEPTH SCALE,
C #DSCALE, IS IN METERS. THE HORIZONTAL LENGTH SCALE, #ALSCALE#,
C ALSO IS IN METERS.
C G, GRAVITY, IS IN METERS PER SECOND SQUARED
C E, THE PERTURBATION DENSITY, IS IN GM. PER CM. CUBED
C Q, THE CONSTANT DENSITY IS ALSO IN GM. PER CM. CUBED.
C GAMMA, THE BOTTOM FRICTION COEFFICIENT, IS IN GM. PER CM. SQUARED
C EDDY IS THE EDDY COEFFICIENT CALCULATED FROM GAMMA.
C
READ(5,150)USCALE,DSCALE,ALSCALE,G,E,Q,GAMMA
DEEP=DEEP/DSCALE
C
C NOW THE STATION DATA IS READ IN.
C ALPHA IS ENTERED IN (GM/CM**3)*METERS AND DELTA IS ALPHA*METER
C TAU, WIND STRESS, IS IN DYNES/(CM*CM)
C CURL IS READ IN AS CYNES PER CM. CUBED.
C
C AFTER THE LAST STATION DATA CARD IS READ, A CARD WITH STATION
C NUMBER ZERO IS READ IN TO INDICATE THAT NO MORE STATION DATA
C WILL BE INPUTED.
C
C NOTE***THE DEPTH, ALPHA, AND DELTA VALUES ARE POSITIVE QUANTITIES
C
C
C IF(NOGRID.EQ.0.AND.NORMAL.EQ.0) GO TO 111
C I=1
C 2 READ(5,10)N(I),LAT(I),ALAT(I),LONG(I),ALONG(I),ALPHA(I),DELTA(I),D
C #EPTH(I)
C DEPTH(I)=-DEPTH(I)
C IF(N(I).EQ.0) GO TO 4
C I=I+1
C GO TO 2
C
C 4 NVRTX=I-1
C READ(5,245)TAUX,TAUY,CURL
C
C WE EXIT FROM HERE WITH THE VALUE OF NVRTX, THE NUMBER OF VERTICES
C
C HERE THE STATION DATA IS ECHO CHECKED IF REQUESTED
C
C IF(LRWDATA.EQ.0) GO TO 8
C WRITE(6,15)
C WRITE(6,265)TAUX,TAUY,CURL
C WRITE(6,20)
C WRITE(6,90)

```

```

      DO 6 J=1,NVRTX
6     WRITE(6,25)N(J),LAT(J),ALAT(J),LONG(J),ALONG(J),ALPHA(J),DELTA(J),
      #DEPTH(J)
8     CONTINUE
C
C
111  CONTINUE
C
      IF(NOGRID.EQ.0) GO TO 12
      IPUNCH=IPGRID
      CALL CVERLAY(5HMOEEL,8,0,0)
      XMAX=DALPHAX
      YMAX=DALPHAY
      YMIN=DDEPTHX
      RADIUS=CDEPTHY
      XHIN=DEX
      GO TO 13
12  CONTINUE
C
C     *****NOTE THAT IF THE GRID SUBROUTINE IS BYPASSED, ONE NEEDS TO
C     READ IN YMIN,YMAX,YYMAX, AND XXMAX
C
      READ(5,5)NVRTX
      DO 3001 I=1,NVRTX
      READ(5,195)X(I),Y(I),N(I)
3001 CONTINUE
      READ(5,140)YMIN,YMAX,YYMAX,XXMAX
13  CONTINUE
C
C
C     NOW WE GO ON TO CALCULATE F KNOT, THE MEAN CORIOLIS VALUE.
C
      IF(NOCORY.EQ.0) GO TO 22
      CALL BETA1(YMIN,YMAX,FO)
      WRITE(7,255)FO
      GO TO 23
22  READ(5,255)FO
23  CONTINUE
C
      EDDY=GAMMA*GAMMA*2.*FC/Q
C
C     HERE THE STATION DATA IS NORMALIZED IF REQUESTED.
C
C
      IF(NORMAL.EQ.0) GO TO 24
      IPUNCH=IPNORM
      CALL CVERLAY(5HMOEEL,9,0,0)
      GO TO 6026
C
24  CONTINUE
      DO 1012 I=1,NVRTX
      READ(5,250)ALPHA(I),DELTA(I),DEPTH(I),N(I)
1012 CONTINUE

```

```

      READ(5,260)TAUX,TAUY,CURL
C
C
C
6026 CONTINUE
C   HERE WE LIST THE DIMENSIONAL COEFFICIENTS
C
      WRITE(6,15)
      WRITE(6,215)
      WRITE(6,220)USCALE,DSCALE,ALSCALE,G,E,Q,GAMMA,FO
      WRITE(6,280)EDDY
C
C   HERE WE HAVE THE OPTION TO GENERATE THE NON DIMENSIONAL RUN
C   PARAMETERS OR READ THEM IN
C   WE ALSO HAVE THE OPTION TO PUNCH THEM UP FOR FUTURE USE
C
      IF(NOCONST.EQ.1) GO TO 89
C
C   HERE NONDIMENSIONAL RUN PARAMETERS ARE READ IN
C   THESE ARE THE CONST COEFFICIENTS IN THE EQUATION
      READ(5,245)CONST1,CONST2
C
      GO TO 91
89 CONTINUE
      CONST1=(G*E*DSCALE)/(Q*FO*USCALE*ALSCALE)
      CONST2=GAMMA/(Q*DSCALE*100.)
91 CONTINUE
      WRITE(6,225)CONST1,CONST2
C
C   THIS IS AN OPTION TO OUTPUT GRID DATA
C
      IF(LGRID.EQ.0) GO TO 16
      WRITE(6,15)
      WRITE(6,95)
      WRITE(6,90)
      DO 14 I=1,NVRTX
      WRITE(6,100)N(I),I,X(I),Y(I)
14 CONTINUE
      WRITE(6,125)RADIUS
      WRITE(6,155)XMIN
      WRITE(6,160)YMIN
16 CONTINUE
C
C
C   THIS IS AN OPTION YC LIST THE NORMALIZED DATA
C
      IF(LNORM.EQ.0) GO TO 29
      WRITE(6,15)
      WRITE(6,175)
      WRITE(6,165)
      DO 27 I=1,NVRTX
      WRITE(6,170)N(I),I,ALPHA(I),DELTA(I),DEPTH(I)
27 CONTINUE

```

```

29 CONTINUE
C
C   THIS IS AN OPTION TO PUNCH NORMALIZED DATA
C
C   IF(IPCONST.EQ.0) GO TO 31
C   WRITE(7,245)CCNST1,CONST2
31 CONTINUE
C
C *****
C
C WE NOW PROCEED TO READ IN THE TRIANGLES IF NECESSARY.
C IF MAKETRI=0, THEN THE TRIANGLE VERTEX NUMBERS WILL BE READ IN
C AND NO TRIANGLES WILL BE GENERATED.
C
C IF(MAKETRI.EQ.1) GO TO 902
C HERE NTRI, THE NUMBER OF TRIANGLES ARE READ IN
901 READ(5,5)NTRI
C NOW TO READ IN THE GLOBAL LABELS OF EACH TRIANGLE VERTEX
C DO 903 I=1,NTRI
C   READ(5,5)(IP(J,I),J=1,3)
903 CONTINUE
902 CONTINUE
C
C
C WE NOW READ IN THE BOUNDARY VALUES AND THEIR STATION NUMBERS
C SURFACE ELEVATIONS ALONG THE BOUNDARY SHOULD BE IN CM.
C
C *****
C REMEMBER, IF AN ISLAND IS PRESENT, ITS BOUNDARY CONDITIONS SHOULD
C BE READ IN FIRST IN CLOCKWISE ORDER. THEN THE INSHORE BOUNDARY
C CONDITIONS SHOULD BE READ IN COUNTERCLOCKWISE ORDER. THESE
C ARE THEN FOLLOWED BY THE REST OF THE BOUNDARY CONDITIONS READ
C IN COUNTERCLOCKWISE ORDER.
C THE BOUNDARY ELEVATIONS FOR THE NO FLUX BOUNDARIES WILL BE
C CALCULATED RELATIVE TO THE FIRST NO FLUX STATION. THEREFORE,
C IF AN ISLAND IS PRESENT, THE ELEVATION OF THE FIRST ISLAND
C BOUNDARY POINT NEEDS TO BE DEFINED. THEN THE ELEVATION OF
C THE FIRST ONSHORE, COASTLINE BOUNDARY STATION MUST ALSO BE
C SPECIFIED. ALL OTHER NO FLUX BOUNDARY ELEVATIONS DONT NEED
C TO BE SPECIFIED.
C A BLANK CARD SHOULD BE READ IN AFTER ALL THE BOUNDARY CONDITIONS
C HAVE BEEN READ.
C *****
C
C DIM=G/(FO*USCALE*ALSCALE*Q*100.)
C I=1
58 READ(5,50) ISTAT,BVAL
C IF(ISTAT.EQ.0) GO TO 402
C DO 54 J=1,NVRTX
C   IF(ISTAT.NE.N(J)) GO TO 54
C   IB(I)=J

```

```

        BV(I)=BVAL*DIM
        I=I+1
        GO TO 58
    54 CONTINUE
        WRITE(6,110)ISTAT
        GO TO 2001
    402 CONTINUE
        62 NBV=I-1
C
C     HERE, WE EXIT WITH, NBV, THE NUMBER OF BOUNDARY POINTS
C
C
C     HERE WE HAVE AN OPTION TO ECHO CHECK THE BOUNDARY CONDITIONS
C
        IF(LBV.EQ.0) GO TO 746
        WRITE(6,15)
        WRITE(6,55)
        WRITE(6,90)
        DO 64 I=1,NBV
            BVV=BV(I)/DIM
            WRITE(6,60)I,IB(I),BV(I),BVV
    64 CONTINUE
    746 CONTINUE
C
C     NOW GENERATE THE TRIANGLES IF REQUESTED.
C
        IF(MAKETRI.EQ.0) GO TO 904
        IPUNCH=NIBP
        CALL OVERLAY(5HMODEL,5,0,0)
C
    904 CONTINUE
C
    401 CONTINUE
        IF(MAKETRI.EQ.0) GO TO 754
C
C     IF TRIANGLES WERE INTERNALLY GENERATED, WE WILL PROCEED TO
C     ELIMINATE THE TRIANGLES EXTERIOR TO THE REGION OF INTEREST.
C
        LIST=LTRI
        CALL OVERLAY(5HMODEL,6,0,0)
    754 CONTINUE
C
        IF(LTRI.EQ.0) GO TO 57
C
C     TRIANGLE NUMBERS ALONG WITH THE GLOBAL LABELS OF EACH VERTEX IS
C     LISTED AND ON THE NEXT PAGE, THE VERTEX COORDINATES ARE LISTED
C
        WRITE(6,15)
        WRITE(6,30)
        WRITE(6,90)
        DO 26 I=1,NTRI
    26 WRITE(6,35)I,(IP(J,I),J=1,3)
        WRITE(6,15)
        WRITE(6,40)

```

```

WRITE(6,90)
DO 28 I=1,NTRI
II=IP(1,I)
IL=IP(2,I)
IM=IP(3,I)
28 WRITE(6,45) I,X(II),Y(II),X(IL),Y(IL),X(IM),Y(IM)
57 CONTINUE
C
C THIS IS THE OPTION TO PUNCH THE TRIANGLE DATA
C
IF(IPTRI.EQ.0) GO TO 157
WRITE(7,5)NTRI
DO 156 I=1,NTRI
WRITE(7,205)IP(1,I),IP(2,I),IP(3,I),I
156 CONTINUE
157 CONTINUE
C
C
C WE NOW FIT THE ALPHA AND DELTA TO A THIRD ORDER POLYNOMIAL BY
C DOING A LEAST LEAST SQUARES FIT TO THE ALPHA AND DELTA FIELDS.
C
IPUNCH=LSF
LIST=LCOEF
SA(1)=SMTHA
SD(1)=SMTHD
CALL OVERLAY(5HMCCEL,1,0,0)
C
C
132 CONTINUE
*****
C
C NOW PROCEED TO ALTER THE BOUNDARY CONDITIONS BY SOLVING THE
C INVISCID CASE ALONG BOUNDARY DEPTH CONTOURS.
C
C
IF(NOBCK.EQ.0) GO TO 68
LIST=NOINTG
IPUNCH=IPINTG
CALL OVERLAY(5HMODEL,12,0,0)
IF(IPBV.EQ.0) GO TO 67
DO 66 I=1,NBV
BVV=BV(I)/DIM
J=IB(I)
66 WRITE(7,50)N(J),BVV
67 CONTINUE
IF(NOHALT.EQ.0) GO TO 68
WRITE(6,70)
GO TO 2001
68 CONTINUE
C
C IF THE LEAST SQUARES COEF. TO THE BAROCL. FIELD HAS GENERATED
C THEN WE WILL SAVE THE VALUES.

```

```

C      IF(LSF.EQ.0) GO TO 69
C      NOW PROCEED TO PUNCH THE VALUES UP SO WE DO NOT HAVE TO
C      REGENERATE THEM AGAIN.
C      WRITE(7,270)SA(1),SA(2),SA(3),SA(4),STNOVA
C      WRITE(7,275)SD(1),SD(2),SD(3),SD(4),STNOVD
69     CONTINUE
C
C      IF(ISTOP.EQ.1) GO TO 2999
C      *****
C
C      133 CONTINUE
C      WE NOW ASSEMBLE THE MATRIX
C
C      NOMAT=0
C      IF(NEWBV.GT.1) NOMAT=-1
C      IF(NOELEV.EQ.1) GO TO 164
C      DO 162 I=1,NVRTX
C      READ(5,210)HEIGHT(I)
162    CONTINUE
C      GO TO 134
164    CONTINUE
C      LIST=IFILE
C      CALL OVERLAY(5HMODEL,2,0,0)
C      IF(NVRTX.LT.0) GO TO 4001
C
C      134 CONTINUE
C
C      THIS IS AN OPTION TO LIST THE ELEVATION OF THE VERTICIES.
C
C      IF(LELEV.EQ.0) GO TO 178
C      WRITE(6,15)
C      ELEV=(FO*USCALE*ALSCALE/G)*100.
C      WRITE(6,235)ELEV
C      WRITE(6,115)
C      DO 176 I=1,NVRTX
C      DIM=HEIGHT(I)*ELEV
C      WRITE(6,120)I,X(I),Y(I),HEIGHT(I),DIM
176    CONTINUE
178    CONTINUE
C
C      THIS IS THE OPTION TO PUNCH THE ELEVATION DATA
C
C      IF(IPELEV.EQ.0) GO TO 159
C      DO 158 I=1,NVRTX
C      WRITE(7,210)HEIGHT(I),I
158    CONTINUE
159    CONTINUE
C
C      HERE WE HAVE THE OPTION TO CALCULATE THE TRANSPORT AT THE CENTROID
C      OF EACH TRIANGLE
C
C      IF(NCTrans.EQ.0) GO TO 184

```

```

      IPUNCH=IPTRANS
      CALL OVERLAY(5HMODEL,10,0,0)
C
184 CONTINUE
C
C      OPTION TO CALCULATE AND LIST EKMAN VELOCITY, BAROTROPIC VELOCITY
C      THEIR SUM, AND BOTTOM VELOCITY
C
      IF(NOVELO.EQ.0) GO TO 186
      IPUNCH=IPVELO
      CALL OVERLAY(5HMODEL,11,0,0)
185 CONTINUE
C
C      OPTION TO CALCULATE AND LIST THE DYNAMIC BALANCE TERMS.
C
      IF(NOTERM.EQ.0) GO TO 188
      CALL OVERLAY(5HMODEL,7,0,0)
188 CONTINUE
C      WE NOW HAVE THE OPTION OF PLOTTING THE TRIANGLES AND LABELING
C      THE VERTICIES WITH THEIR ELEVATIONS.
C      ONCE AGAIN THE UNIV. OF WASH.#S N.P.S. SYSTEM IS UTILIZED.
C
2999 CONTINUE
      IF(NOPLOT.EQ.0.AND.NBC.EQ.1) GO TO 2001
      IF(NOPLOT.EQ.0)GO TO 1999
C
C      WE NOW PROCEED TO PLOT THE SURFACE ELEVATIONS.
      LIST=IWHAT
      CALL OVERLAY(5HMODEL,4,0,0)
C
C
1999 CONTINUE
      IF(NEWBV.GE.NBC) GO TO 2001
      CALL NEWBVAL
      NEWBV=NEWBV+1
      IF(JJ2.EQ.0) GO TO 133
      GO TO 132
C
C
C      IF THE FORCING FUNCTIONS ARE ALTERED, THEN THE NEW VALUES ARE
C      READ IN SUBROUTINE NEWBVAL ALONG WITH ANY NEW BOUNDARY VALUES.
C      THEN ONE REASSEMBLES THE RIGHT HAND SIDE AND READJUSTS THE NEW
C      BOUNDARY VALUES BY SETTING JJ2 IN COMMON BLOCK CUTOFF TO 1 IN
C      SUBROUTINE NEWBVAL. THIS WILL SEND THE PROGRAM INTO BCHK. IF
C      ONLY THE BOUNDARY VALUES ARE CHANGED IN SUBROUTINE NEWBVAL, THEN
C      JJ2=0 AND ONLY THE NEW BOUNDARY VALUES ARE ALTERED AND NOT THE
C      ENTIRE RIGHT HAND SIDE.
C
C
4001 WRITE(6,285)
2001 STOP
      END

```

```

OVERLAY(MODEL,1,0)
PROGRAM LEAST
COMMON/NUMB/NVRTX,NTRI,LIST,IPUNCH
COMMON/IALPHA/ALPHA(200)
COMMON/IDELTA/DELTA(200)
COMMON/LSCOEF/SA(4),SD(4),STNDVA,STNDVD
COMMON/IHEIGHT/HEIGHT(200)
COMMON/IDEPH/DEPTH(200)
270 FORMAT(*ALPHA CCEF.*,5F10.5)
275 FORMAT(*ALPHA CCEF.*,5F10.5)
SMTHA=SA(1)
SMTHD=SD(1)
LSF=IPUNCH
IF(LSF.EQ.0) GO TO 166
LCOEF=LIST
CALL LQFIT(ALPHA,SA,STNDVA,LCOEF,NVRTX)
LCOEF=-LCOEF
CALL LQFIT(DELTA,SD,STNDVD,LCOEF,NVRTX)
C ****NOTE, THE COEFFICIENTS ARE STORED INTO SA, AND SD. SA HOLDS
C THE COEFFICIENTS FOR ALPHA AND SD FOR DELTA.
GO TO 167
166 CONTINUE
C HERE WE READ IN THE ALPHA AND DELTA COEFFICIENTS IF THEY WERE
C NOT GENERATED.
READ(5,270)SA(1),SA(2),SA(3),SA(4),STNDVA
READ(5,275)SD(1),SD(2),SD(3),SD(4),STNDVD
167 CONTINUE
C
C WE NOW HAVE THE OPTION OF SMOOTHING THE ALPHA AND DELTA FIELDS.
IF(SMTHA.EQ.-1.) GO TO 168
CALL SMOOTH(ALPHA,SA,SMTHA,STNDVA,NVRTX)
168 CONTINUE
IF(SMTHD.EQ.-1.) GO TO 169
CALL SMOOTH(DELTA,SD,SMTHD,STNDVD,NVRTX)
169 CONTINUE
END

```

```

OVERLAY(MODEL,2,0)
PROGRAM MATASS
COMMON/IN/N(300)
COMMON/IRHS/RHS(200)
COMMON/IWCRK/VALP(4500)
COMMON/INT/INTP(4500)
COMMON/LSCOEFS/SA(4),SD(4)
COMMON/IALPHA/ALPHA(200)
COMMON/IDPTH/DEPTH(200)
COMMON/IIP/IP(3,350)
COMMON/IA/A(3,3)
COMMON/IB/B(3)
COMMON/IY/Y(200)
COMMON/IX/X(200)
COMMON/NUMB/NVRTX,NTRI,IFILE,MASL,NEHBV
COMMON/WIND/TAUY,TAUX,CURL
COMMON/IALP/ALPH(3)
COMMON/SCALES/USCALE,DSCALE,ALSCALE,G,E,Q,GAMMA,FO,EDDY
COMMON/BOUND/IB(75),BV(75),NBV
COMMON/IHEIGHT/HEIGHT(200)
COMMON/ICNST/CONST1,CONST2
COMMON/IGRAD/DALPHAX,DALPHAY,DDEPTHX,DDEPTHY,DEX,DEY,AREA
COMMON/CUTOFF/NIBP,NFLX,JJ1,JJ2
C WE NOW PREPARE TO ASSEMBLE THE MATRIX BY SETTING IT TO ZERO
C AND BY SETTING THE INTEGER BOOK KEEPING ARRAY TO ZERO.
C
IF(JJ1.EQ.-1) GO TO 199
IF(NEHBV.GT.1) GO TO 201
CALL SETMAT(NVRTX,IFILE,MASL)
C
C
C WE NOW PROCEED TO CALCULATE GRADIENTS AND ASSEMBLE THE MATRIX
C
199 CONTINUE
CALL CVERLAY(5HMODEL,2,1,0)
C
201 CONTINUE
C
CALL CVERLAY(5HMODEL,2,2,0)
END

```

```

A(3,1)=X(M)
A(3,2)=Y(M)
A(1,3)=1.0
A(2,3)=1.0
A(3,3)=1.0
C
CALL TRIAREA(A,AREA)
AREA=ABS(AREA)
C
CALL GRAD(DEPTH(J),DEPTH(L),DEPTH(M),DDEPTHX,DOEPHTY,CDEPTH)
C
CALL ALPHX(K,DALPHAX,DALPHAY,ALPHA,SA,ALPH)
C
C
C
DO 104 I=1,3
DO 102 II=1,3
102 B(II)=0.
B(I)=1.
C
CALL GRAD(B(1),B(2),B(3),DSHAPEX(I),DSHAPEY(I),CSHAPE(I))
C
C
104 CONTINUE
C
CALL MATRIX(DSHAPEX,DSHAPEY,K,NVRTX,NTRI,IFILE,MASL)
C
C
C
128 K=K+1
IF(K.GT.NTRI) GO TO 132
GO TO 72
C
132 CONTINUE
C
NOW PROCEED TO ADD ON THE CONTRIBUTIONS FROM THE NO FLUX BOUNDARY
CONDITIONS.
C
C
CALL BASS(VALP,RHS)
C
HERE WE ADD THE PRESCRIBED BOUNDARY CONDITONS TO THE RIGHT HAND
SIDE.
C
CALL BC(NVRTX,NBV,IB,BV,MASL)
C
END

```

```

OVERLAY(MODEL,2,2)
PROGRAM SCLN
COMMON/NUMB/NVRTX,NTRI,IFILE,MASL,NEHBV
COMMON/INT/INTP(4500)
COMMON/IHEIGHT/HEIGHT(200)
COMMON/IWCRK/VALP(4500)
COMMON/BOUND/IB(75),BV(75),NBV
COMMON/IRHS/RHS(200)
100 FORMAT(E12.5,020)
NROW=NVRTX
NCOL=NVRTX
SMALL=.0000001
IF(NEHBV.GT.1) GO TO 1
IF(IFILE)2,2,4
2 CONTINUE

C
C   HERE THE MATRIX IS DECOMPOSED.
C
CALL DCPK(NROW,NCOL,IS,IR,IF,SMALL,INTP,VALP,MASL)
IF(IS.EQ.1) GO TO 10
IF(IFILE.EQ.0) GO TO 1

C
C   OPTION TO CREATE FILE
C
11 DO 6 I=1,4500
WRITE(1,100)VALP(I),INTP(I)
6 CONTINUE
GO TO 1

C
C   OPTION TO READ FROM FILE
C
4 DO 8 I=1,4500
JK=I-1
READ(1,100)VALP(I),INTP(I)
GO TO 1
8 CONTINUE

C
1 CONTINUE

C
C   WE NOW ADD THE BOUNDARY CONDITIONS IN. NOTE THEY MUST BE ADDED
C   INTO VALP AFTER THE MATRIX HAS BEEN DECOMPOSED.
DO 112 K=1,NRCW
VALP(K)=RHS(K)
112 CONTINUE

C
CALL SLVK(NROW,NCOL,IE,INTP,VALP)
IF(IE.EQ.1) GO TO 12
GO TO 21
10 WRITE(6,15)
15 FORMAT(*0*,*SING IS 1, MATRIX IS SINGULAR*)
NVRTX=-NVRTX
GO TO 301
12 WRITE(6,20)

20 FORMAT(*0*,*ERROR IS 1, DIVISION BY ZERO IN SLVK*)
NVRTX=-NVRTX
GO TO 301
21 CONTINUE
DO 22 I=1,NROW
J=I+NROW
22 HEIGHT(I)=VALP(J)
301 CONTINUE
END

```

```

OVERLAY (MODEL,4,0)
PROGRAM DRAW
COMMON/IRHS/RHS(200)
COMMON/BOUND/IB(75),BV(75),NBV
COMMON/SCALES/USCALE,OSCALE,ALSCALE,G,E,O,GAMMA,FO,EDDY
COMMON/IX/XA(200)
COMMON/IY/YA(200)
COMMON/IIP/IP(3,350)
COMMON/NUMB/NVRTX,NTRI,IHAT,IPUNCH,NEHBV
COMMON/IN/N(300)
COMMON/IHEIGHT/HEIGHT(200)
COMMON/CALCOMP/XXMAXA,YYMAXA,ISTART,NBC
DIMENSION CON(20)
DIMENSION TLABEL(3),X(200),Y(200)
C THIS SECTION IS FOR CALCOMP PLOTTING
C THE UNIVERSITY OF WASHINGTON'S NUMERICAL PLOTTING SYSTEM IS USED
C WE HAVE THE OPTION TO DRAW LABEL AND CONTOUR EACH POINT AND TRIANGLE
XXMAX=XXMAXA
YYMAX=YYMAXA
DIM=(FO*USCALE*ALSCALE)*100./G
C
DO 302 I=1,NVRTX
X(I)=XA(I)
Y(I)=YA(I)
302 CONTINUE
RATIO=XXMAX/YYMAX
YSIZE=6.
XSIZE=RATIO*YSIZE
XINC=XSIZE*5.
XINC=0.
YSTART=.5
XSTART=2.
IF(IHAT.EQ.1) GO TO 501
ENCODE(30,34,TLABEL)
34 FORMAT(27HTRIANGLES AND GLOBAL LABELS)
CALL SETUP(ISTART,1,XSIZE,YSIZE,TLABEL,1,0.,XXMAX,0.,YYMAX,05,05,X
#START,YSTART)
CALL DRTRI(X,Y,IP,NTRI,2,N)
DO 41 I=1,NVRTX
41 RHS(I)=FLCAT(I)
CALL ADVANC(0.,0.)
CALL TRILABL(X,Y,IP,NTRI,.112,1)
CALL ADVANC(0.,0.)
CALL VRTXLB(X,Y,RHS,0,NVRTX,.098,1)
IF(IHAT)2,3,2
3 CALL ADVANC(XINC,0.)
2 CONTINUE
ISTART=1
IF(IHAT.EQ.-1) GO TO 502
501 CONTINUE
ENCODE(30,33,TLABEL)
33 FORMAT(26HSURFACE ELEVATION CONTOURS)
CALL SETUP(ISTART,1,XSIZE,YSIZE,TLABEL,1,0.,XXMAX,0.,YYMAX,05,05,X
#START,YSTART)
DO 9 I=1,NVRTX
HEIGHT(I)=HEIGHT(I)*DIM
9 CONTINUE
CALL KONTRI(X,Y,IP,CON,NTRI,NVRTX,8,HEIGHT,1)
CALL FLTBND(X,Y,IB,NBV,1)
CALL VRTXLB(X,Y,HEIGHT,1,NVRTX,.091,3)
404 CONTINUE
ISTART=1
502 IF(NEHBV.LT.NBC) GO TO 1998
CALL EXITPL
GO TO 1
1998 CALL ADVANC(XINC,0.)
1 CCNTINUE
END

```

```

OVERLAY (MODEL,5,0)
PROGRAM MESH

C
C
C
HERE WE GENERATE THE MESH.

COMMON/IMCRK/P(204,2),VERT(402,6)
COMMON/INT/ISIDE(607,2),ITRI(403,3)
COMMON/IX/X(200)
COMMON/IY/Y(200)
COMMON/IIP/IP(3,350)
COMMON/NUMB/NVRTX,NTRI,LIST,NISP,HEWBV
COMMON/BOUND/IB(75),BV(75),NSV
COMMON/CALCOMP/XXMAX,YYMAX,ISTART,NSC

C
DO 101 I=1,NVRTX
P(I,1)=X(I)
P(I,2)=Y(I)
101 CONTINUE
CALL TRIAN(ISIDE,ITRI)
DO 2 I=1,NTRI
IS1=ITRI(I,1)
IS2=ITRI(I,2)
JP1=ISIDE(IS1,1)
JP2=ISIDE(IS1,2)
JP3=ISIDE(IS2,1)
IF (JP1.EQ.JP3 .OR. JP2.EQ.JP3) JP3=ISIDE(IS2,2)
IP(I,1)=JP1
IP(I,2)=JP2
IP(I,3)=JP3
2 CONTINUE

C
END

```

```

OVERLAY(MODEL,6,0)
PROGRAM OUTSIDE
COMMON/BOUND/IB(75),BV(75),NBV
COMMON/IIP/IP(3,350)
COMMON/NUPH/NVRTX,NTRI,LTRI,IPUNCH,NEHBV
COMMON/IWCRK/IBTRI(350)
COMMON/IX/X(200)
COMMON/IY/Y(200)

C
C CALCULATE THE NUMBER OF POINTS IN EACH TRIANGLE AND ORDER THE
C BOUNDARY POINTS. THE CODE IS AS FOLLOWS, THE VALUE OF IBTRI(K)
C WILL TELL US HOW MANY BOUNDARY POINTS TRIANGLE #K# HAS.
C
5 FORMAT(*1*,*WE HAVE FOUND A BAD TRIANGLE WITH IBTRI GT 3 IN
HPROGRAM OUTSIDE, TRI=#,I4)
10 FORMAT(* *,*THE GLOBAL LABELS ARE*,3I4)
15 FORMAT(*1*)
150 FORMAT(* *,*THIS LISTING IS DONE AFTER WE HAVE ELIMINATED TRIANGLE
#S OUTSIDE OF CUR DOMAIN*)
30 FORMAT(*0*,*TRIANGLE NO.*,10X,*VERTEX 1*,10X,*VERTEX 2*,10X,*VERTE
*X 3*)
90 FORMAT(*0*)
35 FORMAT(* *,4X,I3,19X,I3,14X,I3,15X,I3)
155 FORMAT(*1*,*PROGRAM IS TERMINATED BECAUSE OF FAULTY BOUNDARY TRIAN
#GLE#/,* *,*IBTRI WAS GREATER THAN 3*)
CALL FINDBP(IB,I=-IBTRI,NTRI,NBV)

C
C HERE WE HAVE THE OPTION TO ECHO CHECK THE BOUNDARY POINT SEQUENCES
C
DO 1 I=1,NTRI
IF(IBTRI(I).LT.4) GO TO 1
WRITE(6,5)I
WRITE(6,10)IP(1,I),IP(2,I),IP(3,I)
1 CONTINUE

C
C HERE WE MAKE ONE FINAL CHECK OF OUR BOUNDARY TRIANGLES.
C IF IBTRI IS GREATER THAN 3, THE PROGRAM IS KILLED.
C *****IT IS SUGGESTED THAT IBVCHK=1 UNTIL ONE GETS PAST THIS POINT.
C THIS WILL ALLOW ONE TO FIND THE BAD TRIANGLES.
C
DO 68 I=1,NTRI
IF(IBTRI(I).GT.3) GO TO 911
68 CONTINUE
GO TO 281
911 WRITE(6,155)
GO TO 754
281 CONTINUE

C
C THIS SECTION CHECKS TO SEE THAT ALL THE BOUNDARY TRIANGLES ARE
C INSIDE THE DOMAIN
C
C IF THERE ARE EXTRANEIOUS TRIANGLES OUTSIDE OF THE DOMAIN, THEY
C WILL BE ELIMINATED AND NTRI WILL BE ADJUSTED ACCORDINGLY
C
CALL ELIM(IBTRI,IP,X,Y,NTRI)

C
754 CONTINUE
END

```

```

OVERLAY(MODEL,7,0)
PROGRAM TERM
COMMON/NUMB/NVRTX,NTRI,LIST,IPUNCH,NEWSV
COMMON/IHEIGHT/HEIGHT(200)
COMMON/ICCNST/CONST1,CONST2
COMMON/LSCOEF/SA(4),SD(4)
COMMON/IALPHA/ALPHA(200)
COMMON/IIP/IP(3,350)
COMMON/IA/A(3,3)
COMMON/IB/B(3)
COMMON/IDEPH/DEPTH(200)
COMMON/WIND/TAUX,TAUY,CURL
COMMON/IX/X(200)
COMMON/IY/Y(200)
COMMON/IALP/ALP(3)
COMMON/IGRAD/DALPHAX,DALPHAY,DDEPTHX,DDEPTHY,DEX,DEY,AREA
WRITE(6,1)
1 FORMAT(*1*,*DYNAMIC BALANCE TERMS*)
WRITE(6,2)
2 FORMAT(*0*,*TRI*,8X,*BAROTROPIC TORQUE*,8X,*BAROCLINIC TORQUE*,7X,
/*CURL OF WIND*,5X,*BOTTOM FRICTION*)
DO 999 I=1,NTRI
J=IP(1,I)
K=IP(2,I)
L=IP(3,I)
A(1,1)=X(J)
A(1,2)=Y(J)
A(1,3)=1.0
A(2,1)=X(K)
A(2,2)=Y(K)
A(2,3)=1.0
A(3,1)=X(L)
A(3,2)=Y(L)
A(3,3)=1.0
CALL GRAD(DEPTH(J),DEPTH(K),DEPTH(L),DDEPTHX,DDEPTHY,CDEPTH)
CALL ALPHX(I,DALPHAX,DALPHAY,ALPHA,SA,ALP)
CALL GRAD(HEIGHT(J),HEIGHT(K),HEIGHT(L),DEX,DEY,CE)
CALL DYBALAN(BRT,BRC,CURL,BFRIC,CONST1)
WRITE(6,3)I,BRT,BRC,CURL,BFRIC
3 FCRMAT(* *,I3,11X,F10.4,14X,F10.4,12X,F10.4,9X,F10.4)
999 CONTINUE
END

```

```

OVERLAY(MODEL,10,0)
PROGRAM GRID
COMMON/IN/N(300)
COMMON/IGRAD/XMAX,YMAX,YMIN,RADIUS,XMIN,EXTRA(2)
COMMON/IX/X(200)
COMMON/IY/Y(200)
COMMON/IHEIGHT/HEIGHT(200)
COMMON/IIP/IP(3,350)
COMMON/NUMB/NVRTX,NTRI,LIST,IPUNCH,NEWBV
COMMON/CALCCMP/XXMAX,YYMAX,ISTART,NBC
COMMON/SCALES/USCALE,OSCALE,ALSCALE,G,E,Q,GAMMA,FO,EDDY
DIMENSION ALAT(200),ALONG(200),LAT(200),LONG(200)
EQUIVALENCE(HEIGHT(1),LONG(1))
EQUIVALENCE(ALAT(1),Y(1))
EQUIVALENCE(ALONG(1),X(1))
EQUIVALENCE(IP(1,1),LAT(1))
CALL CARTSN(LAT,ALAT,LONG,ALONG,NVRTX,ALSCALE,XXMAX,YYMAX,XMAX,YMA
X,YMIN,X,Y,RADIUS,XMIN)
IPGRID=IPUNCH
THIS IS THE OPTION TO PUNCH THE COORDINATE DATA UP
C
C
IF(IPGRID.EQ.0) GO TO 152
WRITE(7,5)NVRTX
5  FORMAT(15I5)
DO 151 I=1,NVRTX
WRITE(7,195)X(I),Y(I),N(I)
195  FORMAT(F10.3,F10.3,5X,*STA.*,2X,I3)
151  CONTINUE
WRITE(7,140)YMIN,YMAX,YYMAX,XXMAX,RADIUS
140  FORMAT(7F10.2)
152  CONTINUE
END

```

```

OVERLAY(MODEL,11,0)
PROGRAM NRHL
COMMON/IN/N(300)
COMMON/IALPHA/ALPHA(200)
COMMON/IDELTA/DELTA(200)
COMMON/IDEPH/DEPTH(200)
COMMON/WIND/TAUX,TAUY,CURL
COMMON/NUMB/NVRTX,NTRI,LIST,IPUNCH,NEWBV
CALL NORM(ALPHA,DELTA,DEPTH,TAUX,TAUY,CURL,NVRTX)
IPNCRM=IPUNCH
250  FORMAT(F10.4,F15.4,F10.4,36X,*STA.*,1X,I3)
260  FORMAT(*WIND STRESS AND CURL VALUES*,3F10.4)
IF(IPNCRM.EQ.0) GO TO 154
DO 153 I=1,NVRTX
WRITE(7,250)ALPHA(I),DELTA(I),DEPTH(I),N(I)
153  CONTINUE
WRITE(7,260)TAUX,TAUY,CURL
154  CONTINUE
END

```

```

OVERLAY(MODEL,12,0)
PROGRAM TRNS
COMMON/ICCNST/C1,C2
COMMON/IHEIGHT/HEIGHT(200)
COMMON/NUMB/NVRTX,NTRI,LIST,IPTRANS,NEWBV
COMMON/SCALES/USCALE,DSCALE,ALSCALE,G,E,Q,GAMMA,FO,EDDY
COMMON/IIP/IP(3,350)
COMMON/IX/X(200)
COMMON/IY/Y(200)
COMMON/IALPHA/ALPHA(200)
COMMON/IDELTA/DELTA(200)
COMMON/IDEPH/DEPTH(200)
COMMON/IGRAD/DALPHAX,DALPHAY,DDEPTHX,DDEPTHY,DELEVX,DELEVY,AREA
COMMON/WIND/TX,TY,CURL
COMMON/LSCOEF/SA(4),SD(4)
COMMON/IA/A(3,3)
COMMON/IB/B(3)
COMMON/IALP/ALP(3)
C
C SUBROUTINE TO CALCULATE TRANSPORTS AT CENTROID OF EACH TRIANGLE
C CX AND CY ARE THE LOCATIONS OF TRIANGLE CENTERS
C XTRANS AND YTRANS ARE THE TRANSPORTS IN THE X AND Y DIRECTIONS
C TTRANS IS THE TOTAL TRANSPORT
C
WRITE(6,15)
15 FORMAT(*1*)
DIM=USCALE*DSCALE**2
WRITE(6,240)DIM
240 FORMAT(* *,*TRANSPORT SCALE FACTOR IS*,F8.3,1X,*CUBIC METERS PER S
*COND PER SQUARE METER ASSUMING DENSITY IS ONE.*)
WRITE(6,230)
230 FORHAT(* *,*VELOCITY IS IN CENTIMETERS PER SECOND*,/)
WRITE(6,180)
180 FORMAT(* *,*TRIANGLE*,3X,*X-COOR*,4X,*Y-COOR*,7X,*X-TRANSP*,7X,*Y-
*TRANS*,5X,*TOT. TRANSP*,5X,*DEPTH*,6X,*U-MEAN*,4X,*V-MEAN*,5X,*V T
*OT*,/)
C
DO 100 I=1,NTRI
J=IP(1,I)
K=IP(2,I)
L=IP(3,I)
C
A(1,1)=X(J)
A(1,2)=Y(J)
A(1,3)=1.
A(2,1)=X(K)
A(2,2)=Y(K)
A(2,3)=1.0
A(3,1)=X(L)
A(3,2)=Y(L)
A(3,3)=1.
CALL GRAD(HEIGHT(J),HEIGHT(K),HEIGHT(L),DELEVX,DELEVY,CELEV)
CALL GRAD(DEPTH(J),DEPTH(K),DEPTH(L),DDEPTHX,DDEPTHY,CDEPTH)

```

```

C      CALL ALPHX(I,DALPHAX,DALPHAY,ALPHA,SA,ALP)
C      DELTA GRACIENTS ARE HANDLED LIKE THE ALPHA GRADIENTS
C      CALL ALPHX(I,DOELTAX,DOELTAY,DELTA,SD,ALP)
C
C      CX=(X(J)+X(K)+X(L))/3.
C      CY=(Y(J)+Y(K)+Y(L))/3.
C
C      DEP=(DEPTH(J)+DEPTH(K)+DEPTH(L))/3.
C
C      XTRANS=DELEVY*DEP-C1*DOELTAY+C2*(DELEVY-DELEVX)-C1*C2*(DALPHAX-DAL
C      PHAY)+TY
C
C      YTRANS=- (DELEVX*DEP)+C1*DOELTAX-C2*(DELEVY+DELEVX)-C1*C2*(DALPHAY+
C      DALPHAX)-TX
C
C      TRANS=(XTRANS*XTRANS+YTRANS*YTRANS)**.5
C
C      DEP=-DEP*200.
C      XTRANS=XTRANS*DIM
C      YTRANS=YTRANS*DIM
C      TRANS=TRANS*DIM
C      U=XTRANS/DEP*100.
C      V=YTRANS/DEP*100.
C      VT=TRANS/DEP*100.
C      WRITE(6,105)I,CX,CY,XTRANS,YTRANS,TRANS,DEP,U,V,VT
105  FORMAT(3X,I3,5X,F6.2,4X,F6.2,4X,F11.4,4X,F11.4,4X,F11.4,3X,F7.1,3X
C      ,F3.4,2X,F9.4,2X,F9.4)
C      IF (IPTRANS.EQ.0) GO TO 100
C      WRITE(7,260)XTRANS,YTRANS,TRANS,U,V,VT,I
260  FORMAT(6F10.3,10X,*TRANS*,2X,I3)
100  CONTINUE
101  CCNTINUE
C      END

```

```

OVERLAY (MODEL,13,0)
PROGRAM VELO
COMMON/HEIGHT/HEIGHT(200)
COMMON/NUMB/NVRTX,NTRI,LIST,IPVELO,NEWSV
DIMENSION ALPH(3)
COMMON/IGRAD/DALPHAX,DALPHAY,DDEPTHX,DDEPTHY,DEX,DEY,AREA
COMMON/LSCOEFS/SA(4),SD(4)
COMMON/SCALES/USCALE,OSCALE,ALSCALE,G,E,Q,GAMMA,FO,EDDY
COMMON/IIP/IP(3,350)
COMMON/IA/A(3,3)
COMMON/IB/B(3)
COMMON/IALPHA/ALPHA(200)
COMMON/IDEPH/DEPTH(200)
COMMON/HIND/TAUX,TAUY,CURL
COMMON/IX/X(200)
COMMON/IY/Y(200)
WRITE(6,1)
1 FORMAT(*1*,*COMPARATIVE VELOCITIES IN CM/SEC*)
WRITE(6,2)
2 FORMAT(*0*,16X,*EKMAN*,26X,*BAROTROPIC*,25X,*SURFACE*,26X,*BOTTOM*
*,/)
WRITE(6,4)
4 FORMAT(* *,*TRI*,5X,*U*,9X,*V*,7X,*TOTAL*,10X,*U*,9X,*V*,7X,*TOTAL
*,8X,* U *,5X,* V *,5X,*TOTAL*,10X,*U*,9X,*V*,7X,*TOTAL*,/)

```

C

```

DO 999 K=1,NTRI
I=IP(1,K)
J=JP(2,K)
L=LP(3,K)
A(1,1)=X(I)
A(1,2)=Y(I)
A(1,3)=1.
A(2,1)=X(J)
A(2,2)=Y(J)
A(2,3)=1.
A(3,1)=X(L)
A(3,2)=Y(L)
A(3,3)=1.

```

C

```

CALL GRAD(DEPTH(I),DEPTH(J),DEPTH(L),DDEPTHX,CDEPTHY,CDEPTH)
CALL ALPHX(K,DALPHAX,CALPHAY,ALPHA,SA,ALPH)
CALL GRAD(HEIGHT(I),HEIGHT(J),HEIGHT(L),DEX,DEY,CE)
CALL EKMAN(UE,VE,TOTE)
CALL BAROT(UB,VB,TOTB)
CALL SURF(UE,VE,U2,V8,US,VS,TOTS)
CALL BOTT(UBOT,VBOT,TOTBOT)
WRITE(6,5)K,UE,VE,TOTE,UB,VB,TOTB,US,VS,TOTS,UBOT,VBOT,TOTBOT
5 FORMAT(* *,I3,F8.3,2X,F8.3,2X,F8.3,5X,F8.3,2X,F8.3,2X,F8.3,5X,F8.3
*,2X,F8.3,2X,F8.3,5X,F8.3,2X,F8.3,2X,F8.3)
IF(IPVELO.EQ.0) GO TO 952
WRITE(7,105)K,US,VS,TOTS,UBOT,VBOT,TOTBOT
105 FORMAT(I5,6F10.3,2X,*VELOCITY*)
952 CONTINUE
999 CONTINUE
END

```

```

OVERLAY(MODEL,14,0)
PROGRAM BCHX

C
C
C
C
PROGRAM TO APPROXIMATE BOUNDARY CONDITIONS BY SOLVING
BOTTOM FRICTIONLESS CASE.

COMMON/EXTRA/XX(100),YY(100),DD(100)
COMMON/IGRAD/IFLG,IBEGIN,IEND,NIBP,NH
COMMON/IIF/IP(3,350)
COMMON/IX/X(200)
COMMON/IY/Y(200)
COMMON/ICNST/CONST1,CONST2
COMMON/IDPTH/DEPTH(200)
COMMON/IALPHA/ALPHA(200)
COMMON/BOUND/IB(75),BV(75),NBV
COMMON/WIND/TAUX,TAUY,CURL
COMMON/NUMB/NVRTX,NTRI,NOINTG,IPINTG,NEWBV
COMMON/IA/A(3,3)
COMMON/IB/B(3)
COMMON/IN/N(300)
COMMON/CUTOFF/IBP,NFLX,J1,J2,DEEP
COMMON/SCALE/USCALE,DSCALE,ALSCALE,G,E,Q,GAMMA,FO,EDDY
COMMON/LSCOEF/SA(4),SD(4)
COMMON/IHEIGHT/XI(100),YI(100)
COMMON/IRHS/DST(100),EI(100)

C
ISLAND=IBP
NIBP=IBP
LAND=NFLX
ESCALE=FO*USCALE*ALSCALE*Q*100./G
IF(NEWBV.GT.1) GO TO 198
IF(NOINTG.EQ.0) GO TO 201

C
C
C
ENTER OVERLAY TO OBTAIN ELEVATION CHANGES ALONG DEPTH CONTOURS.

CALL OVERLAY(5HMODEL,12,1)
GO TO 207
198 DO 199 I=1,NBV
    XI(I)=XX(I)
    YI(I)=YY(I)
199 EI(I)=BV(I)+DD(I)
    GO TO 207
201 DO 206 I=1,NBV
    J=IB(I)
    READ(5,200)X,N(J),XI(I),YI(I),DH
    XX(I)=XI(I)
    YY(I)=YI(I)
    DH=DH/ESCALE
    DD(I)=DH
206 EI(I)=BV(I)+DH
207 CONTINUE
    IBP=ISLAND
    NFLX=LAND

```

```

NIBP=ISLAND
C
C      RESULTS FROM SOLVER ARE LISTED HERE.
IF(NEBV.GT.1) GO TO 203
CALL WHIN(DST)
C
WRITE(6,25)
DO 21 I=1,NBV
BVV=BV(I)*ESCALE
J=IB(I)
DH=0.
DP=DEPTH(J)*DSCALE
CALL BYPASS(I,IYES)
IF(IYES.EQ.1) GO TO 19
CALL WHCUT(DST,XI(I),YI(I),EDST)
EEI=EI(I)*ESCALE
DH=EEI-BVV
GO TO 121
19 EDST=0.0
EEI=BVV
121 IF(IPINTG.EQ.0) GO TO 202
WRITE(7,200)I,N(J),XI(I),YI(I),DH
202 CONTINUE
21 WRITE(5,30)I,J,N(J),BVV,DP,X(J),Y(J),DST(I),XI(I),YI(I),EDST,EEI,0
#H
203 CONTINUE
C
C      THIS IS WHERE THE BOUNDARY ELEVATIONS ARE ALTERED ACCORDING
C      TO THE RESULTS FROM SOLVER.
C
CALL ALTER(XI,YI)
C
C      THE NEW BOUNDARY ARE LISTED HERE.
C
WRITE(6,35)
DO 41 I=1,NBV
J=IB(I)
BVV=BV(I)*ESCALE
41 WRITE(6,40)I,J,N(J),BVV
C
C      HERE THE NEW BOUNDARY VALUES ARE PLOTTED UP AS A FUNCTION OF
C      DISTANCE ALONG THE BOUNDARY.
C
CALL OVERLAY(5HMODEL,12,2)
C
5 FORMAT(3F10.2)
10 FORMAT(3I5,55X,*TRIA.*,I5)
15 FORMAT(I5,F10.2)
25 FORMAT(1H1,*BND.*,3X,*GLB.*,3X,*STA.*,4X,*ELEV.*,6X,*DEPTH*,5X,*EN
#TR. COOR. (DIST.)*,5X,*EXIT COOR. (DIST.)*,5X,*EXIT ELEV.*,5X,*ELEV.
#CHNG.*,/)
30 FORMAT(1H ,I3,3X,I4,3X,I3,5X,F6.2,4X,F6.0,5X,F5.2,*,*,F5.2,*(*,F5.
#2,*)*,5X,F5.2,*,*,F5.2,*(*,F5.2,*)*,5X,F8.4,7X,F8.4)
35 FORMAT(*1*,*BND. NO.*,5X,*GLB. NO.*,5X,*STA. NO.*,5X,*NEW ELEV.*,/
#)
40 FORMAT(* *,I5,8X,I5,8X,I5,8X,F9.4)
200 FORMAT(2I5,2F10.3,2F10.4)
205 FORMAT(F10.4,15X,F10.4)
210 FORMAT(47X,F10.4)
215 FORMAT(F15.7)
220 FORMAT(11X,4F10.4)
305 FORMAT(1X,F10.2,F10.2,54X,I5)
310 FORMAT(2F10.2)
END

```



```

SUBROUTINE NEWBVAL
C
C SUBROUTINE TO READ IN NEW BOUNDARY VALUES.
C
COMMON/IRHS/RHS(200)
COMMON/BOUND/IB(75),BV(75),NBV
COMMON/SCALES/USCALE,OSCALE,ALSCALE,G,E,Q,GAMMA,FO,EDDY
COMMON/WIND/TAUX,TAUY,CURL
COMMON/CUTOFF/NIBP,AFLX,NOMAT,JJ
ESCALE=G/(FO*USCALE*ALSCALE*Q*100.)
C
5 FORMAT(I5,F10.4)
10 FORMAT(3F10.4)
C
READ(5,10)TAUX,TAUY,CURL
WSCL=FO*USCALE*DSCALE*Q*10000.
TAUX=TAUX/WSCL
TAUY=TAUY/WSCL
CURL=CURL/(WSCL*ALSCALE*100.)
C
C WE HAVE JUST READ IN NEW WIND STRESS VALUES.
C
C DO 1 I=1,NBV
READ(5,5)IBN,BV(I)
BV(I)=BV(I)*ESCALE
1 CONTINUE
C
C WE HAVE READ IN THE NEW BOUNDARY VALUES ALONG WITH THEIR BOUNDARY
C NUMBERS, THEN PROCEEDED TO NONDIMENSIONALIZED THEM.
C
C WE NOW RETURN TO REASSEMBLE THE RIGHT HAND SIDE AND USE THE NEW
C BOUNDARY VALUES. THIS IS DONE BY SETTING NOMAT=-1.
C
JJ=1
C
RETURN
END

```

```

SUBROUTINE TRIAREA(A,AREA)
DIMENSION A(3,3)
AA=A(1,1)*A(2,2)*A(3,3)-A(2,3)*A(3,2)
BB=-A(1,2)*A(2,1)*A(3,3)-A(2,3)*A(3,1)
CC=A(1,3)*A(2,1)*A(3,2)-A(2,2)*A(3,1)
AREA=.5*(AA+BB+CC)
RETURN
END
132
134
136
138
140
142
144
146

```

SUBROUTINE SOLVE(A,B)	148
DIMENSION A(3,3),B(3),C(3),X(3)	150
CALL TRIAREA(A,AREA)	152
DO 2 J=1,3	154
DO 1 I=1,3	156
K=J-1	158
IF(J.NE.1) A(I,K)=C(I)	160
C(I)=A(I,J)	162
A(I,J)=B(I)	164
1 CONTINUE	166
CALL TRIAREA(A,X(J))	163
2 CCONTINUE	172
A(1,3)=C(1)	174
A(2,3)=C(2)	176
A(3,3)=C(3)	178
B(1)=X(1)/AREA	180
B(2)=X(2)/AREA	182
B(3)=X(3)/AREA	184
8 RETURN	186
END	188

SUBROUTINE GRAD(E,F,G,DX,DY,C)	190
	192
SUBROUTINE TO CALCULATE GRADIENTS	194
E,F, AND G ARE THE VALUES TO BE FILLED INTO THE B VECTOR	196
DX,DY AND C ARE THE SOLUTIONS TO BE RETURNED	198
	200
COMMON/IA/A(3,3)	202
COMMON/IB/B(3)	204
B(1)=E	206
B(2)=F	208
B(3)=G	210
CALL SOLVE(A,B)	212
DX=B(1)	214
DY=B(2)	216
C=B(3)	218
RETURN	220
END	222

C	SUBROUTINE BETA1(YMIN,YMAX,FO)
C	
C	THIS SUBROUTINE CALCULATES THE MEAN CORIOLIS VALUE FOR THE REGION
C	FO IS THE MEAN CORIOLIS VALUE
C	
C	OMEGA=.000072722052
	DEG=YMIN
	FO=2.*(OMEGA)*SIN(DEG)
	DEG=YMAX
	FM=2.*(OMEGA)*SIN(DEG)
	FC=(FO+FM)/2.
	RETURN
	END

```

SUBROUTINE ALPHX(I,DALPHAX,DALPHAY,ALPHA,S,ALPH)
DIMENSION ALPHA(3),ALPHA(1),S(1)
COMMON/IP/IP(3,350)
COMMON/IDEPH/DEPTH(200)
COMMON/IX/X(200)
COMMON/IY/Y(200)
COMMON/IA/A(3,3)
COMMON/IB/B(3)

C
C SUBROUTINE TO GET ALPHA AND DELTA GRADIENTS BY USING A THIRD ORDER
C LEAST SQUARES FIT TO THE ALPHA AND DELTA FIELDS.
C

J=IP(1,I)
K=IP(2,I)
L=IP(3,I)

C
RDEP=(DEPTH(J)+DEPTH(K)+DEPTH(L))/3.

C
C CHECK TO SEE IF ALL THE DEPTHS ARE EQUAL
C
IF(CEPTH(J).EQ.DEPTH(K).AND.DEPTH(J).EQ.DEPTH(L)) GO TO 3
GO TO 4
3 RDEP=DEPTH(J)
ALPH(1)=ALPHA(J)
ALPH(2)=ALPHA(K)
ALPH(3)=ALPHA(L)
GO TO 5
4 CONTINUE

C
C IF DEPTHS ARE NOT EQUAL, USE LSF FUNCTION TO GET ALPHA OR DELTA
C AT REFERENCE DEPTH.
C

DO 1 M=1,3
N=IP(M,I)
DO=DEPTH(N)
DZ=RDEP-DO
D1=3.*S(1)*DO*DO+2.*S(2)*DO+S(3)
D2=6.*S(1)*DO+2.*S(2)
D3=6.*S(1)
ALPH(M)=ALPHA(N)+D1*DZ+D2*(DZ*DZ/2.)+D3*(DZ*DZ*DZ/6.)
1 CONTINUE

C
C RESET A, THE POSITICN MATRIX AND GET HORIZONTAL GRADIENTS
C

5 CONTINUE
A(1,1)=X(J)
A(1,2)=Y(J)
A(1,3)=1.
A(2,1)=X(K)
A(2,2)=Y(K)
A(2,3)=1.
A(3,1)=X(L)
A(3,2)=Y(L)
A(3,3)=1.

C
CALL GRAD(ALPH(1),ALPH(2),ALPH(3),DALPHAX,DALPHAY,CALPHA)
RETURN
END

```

```

SUBROUTINE INVR ( A, N, B, M, DETERM, ISIZE, JSIZE )
C
C NAME: INVR
C PURPOSE: LINEAR EQUATION SOLUTION (MATRIX INVERSION)
C ALGORITHM: GAUSS-JORDAN ELIMINATION, FULL PIVOT SEARCH.
C SEE ANY NUMERICAL ANALYSIS TEXT FOR REFERENCE.
C AUTHOR: ORIGINAL VERSION, CIRCA 1966, AUTHOR UNKNOWN.
C RECOPIED, 1976, RIK LITTLEFIELD (U.W.), WITH
C STYLISTIC CHANGES AND MINOR BUG CORRECTIONS (NO
C ALGORITHM OR CALLING SEQUENCE CHANGES)
C USAGE: SEE U.WASH. COMPUTING INFORMATION CENTER DOCUMENT
C NUMBER W00042 FOR FULL DESCRIPTION. BASICALLY,
C A = INPUT: COEFFICIENT MATRIX, LOGICALLY (N,N),
C PHYSICALLY (ISIZE,*). OUTPUT: A-INVERSE.
C B = INPUT: RIGHT-HAND SIDE, LOGICALLY (N,M),
C PHYSICALLY (ISIZE,*). OUTPUT: SOLUTION MATRIX.
C DETERM = DETERMINANT OF A, 0. IF A APPEARS SINGULAR.
C JSIZE = CURRENTLY UNUSED, ORIGINALLY 2ND DIM. OF A.
C LIMITS: (100,100) SYSTEM. CHANGE DIMENSION STATEMENTS FOR
C LARGER SYSTEMS.
C TIMING: ORDER(N**3). TYPICAL .4 TO .5 SECONDS FOR (20,20),
C M=0, USING *RUN* FORTRAN COMPILER, CDC 6400.
C COMMENTS: THIS PARTICULAR IMPLEMENTATION OF THE ALGORITHM IS NOT
C THE BEST POSSIBLE - SEE ANY MATH SUBROUTINE LIBRARY
C (E.G., IMSL) FOR IMPROVED ROUTINES.
C
REAL A(ISIZE,1), B(ISIZE,1)
INTEGER PIVOT(100), INDEX(100,2)
INTEGER COLUMN, ROW
DO 10 J = 1,N
DETERM=1.
10 PIVOT(J) = 0
DO 130 I = 1,N
C
C *** FULL SEARCH FOR PIVOT ELEMENT (BRANCH OUT IF NO NON-ZERO
C *** PIVCT IS FOUND)
C
AMAX = 0.0
DO 30 I1 = 1,N
IF ( PIVOT(I1).NE.0 ) GO TO 30
DO 20 J = 1,N
IF ( PIVCT(J).NE.0 ) GO TO 20
IF ( ABS(A(I1,J)) .LE. AMAX ) GO TO 20
ROW = I1
COLUMN = J
AMAX = ABS(A(I1,J))
20 CONTINUE
30 CONTINUE
IF ( AMAX .EQ. 0.0 ) GO TO 200
PIVOT(COLUMN) = 1
C
C *** INTERCHANGE ROWS TO PUT PIVOT ELEMENT ON DIAGONAL
C

```

```

00100
00110
00120
00130
00140
00150
00160
00170
00180
00190
00200
00210
00220
00230
00240
00250
00260
00270
00280
00290
00300
00310
00320
00330
00340
00350
00360
00370
00380
00400
00410
00420
00430
00440
00450
00460
00470
00480
00490
00500
00510
00520
00530
00540
00550
00560
00570
00580
00590
00600
00610
00620

```

	IF (ROW .EQ. COLUMN) GO TO 60	00630
	DETERM = -DETERM	00640
	DO 40 J = 1,N	00650
	SWAP = A(RCH,J)	00650
	A(ROW,J) = A(COLUMN,J)	00670
40	A(COLUMN,J) = SWAP	00680
	IF (M.LE.0) GO TO 60	00690
	DO 50 J = 1,M	00700
	SWAP = B(ROW,J)	00710
	B(ROW,J) = B(COLUMN,J)	00720
50	B(COLUMN,J) = SWAP	00730
60	INDEX(I,1) = RCH	00740
	INDEX(I,2) = COLUMN	00750
	PVTELM = A(COLUMN,COLUMN)	00760
	DETERM = DETERM*PVTELM	00770
C	*** NORMALIZE PIVCT ROW (DIVIDE BY PIVOT ELEMENT)	00780
C		00790
C		00800
	A(COLUMN,COLUMN) = 1.0	00810
	DO 70 J = 1,N	00820
70	A(COLUMN,J) = A(COLUMN,J)/PVTELM	00830
	IF (M.LE.0) GO TO 90	00840
	DO 80 J = 1,M	00850
80	B(COLUMN,J) = B(COLUMN,J)/PVTELM	00860
C	*** REDUCE NON-PIVOT ROWS	00870
C		00880
C		00890
90	DO 120 I1 = 1,N	00900
	IF (I1.EQ.COLUMN) GO TO 120	00910
	T = A(I1,COLUMN)	00920
	A(I1,COLUMN) = 0.0	00930
	DO 100 J = 1,N	00940
100	A(I1,J) = A(I1,J) - A(COLUMN,J)*T	00950
	IF (M.LE.0) GO TO 120	00960
	DO 110 J = 1,M	00970
110	B(I1,J) = B(I1,J) - B(COLUMN,J)*T	00980
120	CONTINUE	00990
130	CONTINUE	01000
C	*** ELIMINATION DONE, INTERCHANGE COLUMNS TO COMPLETE INVERSE	01010
C		01020
C		01030
	DO 150 J = 1,N	01040
	L = N+1-J	01050
	IF (INDEX(L,1) .EQ. INDEX(L,2)) GO TO 150	01060
	ROW = INDEX(L,1)	01070
	COLUMN = INDEX(L,2)	01080
	DO 140 I = 1,N	01090
	SWAP = A(I,ROW)	01100
	A(I,ROW) = A(I,COLUMN)	01110
140	A(I,COLUMN) = SWAP	01120
150	CONTINUE	01130
	RETURN	01140
C		01150
C	*** SINGULAR MATRIX - ERROR EXIT	01160
C		01170
	200 DETERM = 0.0	01180
	RETURN	
	END	01200

```

SUBROUTINE SMOOTH(VAL,S,D,SD,NPTS)
COMMON/IDEPH/DEP(200)
DIMENSION VAL(1),S(1)
C
C
C
SUBROUTINE TO SMOOTH THE DATA ACCORDING TO LEAST SQUARES FIT.
DO 1 I=1,NPTS
V=S(1)*DEP(I)*DEP(I)+S(2)*DEP(I)*DEP(I)+S(3)*DEP(I)+S(4)
DD=VAL(I)-V
IF(DD.LT.-D) DD=-D*SD
IF(DD.GT.D) DD=D*SD
VAL(I)=DD+V
1 CONTINUE
RETURN
END

SUBROUTINE SETMAT(NVRTX,IFILE,MASL)
COMMON/IWCRK/VALP(4500)
COMMON/INT/INTP(4500)
COMMON/IRHS/RHS(200)
C
C
C
THIS SUBROUTINE SETS THE MATRIX AND RIGHT HAND SIDE TO 0 OPERATO
IF(IFILE.EQ.1) GO TO 15
DO 99 I=1,4500
VALP(I)=0.
99 INTP(I)=0
15 DO 16 I=1,200
RHS(I)=0.
17 CONTINUE
NROW=NVRTX
NCOL=NVRTX
MSZ=4500
C
C
C
HERE WE TELL THE SOLVING ROUTINE THAT WE ARE READY
CALL MINIT(INTP,NROW,NCOL,MSZ,MASL)
RETURN
END

SUBROUTINE NORM(ALPHA,DELTA,DEPTH,TAUX,TAUY,CURL,NVRTX)
COMMON/SCALES/USCALE,DSCALE,ALSCALE,G,E,O,GAMMA,FO,EDDY
DIMENSION ALPHA(1),DELTA(1),DEPTH(1)
*****
C
C
C
SUBROUTINE USED FOR NCRHALIZATION OF STATION DATA 49
C
C
C
ALPHA IS DENSITY INTEGRATED VERTICALLY (GM/CM**3)*M 50
C
C
C
DELTA IS ALPHA INTEGRATED VERTICALLY (GM/CM**3)*M**2 51
C
C
C
DEPTH IS CEPTH (M) 52
C
C
C
TAUX AND TAUY ARE WIND STRESS VALUES IN THE X AND Y DIRECTION 53
C
C
C
WIND STRESS UNITS ARE DYNES/CM*CM 54
C
C
C
DSCALE IS THE DEPTH SCALE (M) 55
C
C
C
USCALE IS THE HORIZCNTAL VELOCITY SCALE (M/SEC) 56
C
C
C
FO IS THE AVERAGE CORIOLIS PARAMETER 57
C
C
C
Q AND E ARE THE MEAN AND PERTURBATUON DENSITY RESPECTIVELY 58
C
C
C
NVRTX IS THE NUMBER OF STATIONS 59
C
C
C
***** 60
C
C
C
TO CALCULATE SCALE FACTORS 61
C
C
C
ALPH=E*DSCALE
DELTA=ALPH*DSCALE
DO 12 I=1,NVRTX 64
ALPHA(I)=(ALPHA(I)+DEPTH(I)*Q)/ALPH 65
DELTA(I)=(DELTA(I)-(DEPTH(I)*DEPTH(I)*Q)/2.)/DELTA 66
DEPTH(I)=DEPTH(I)/DSCALE 67
12 CONTINUE 68
C
C
C
STRESS=FO*USCALE*DSCALE*10000.*Q 69
TAUX=TAUX/STRESS
TAUY=TAUY/STRESS
STRESS=STRESS/(100.*ALSCALE)
CURL=CURL/STRESS
RETURN
END

```



```

SUBROUTINE MESH
C
C   HERE WE GENERATE THE MESH.
C
COMMON/INCRK/P(204,2),VERT(402,6)
COMMON/INT/ISIDE(607,2),ITRI(403,3)
COMMON/IX/X(200)
COMMON/IY/Y(200)
COMMON/IIP/IP(3,350)
COMMON/NUMB/NVRTX,NTRI,LIST,NIBP,NEWBV
COMMON/BOUND/IB(75),BV(75),NBV
COMMON/CALCOMP/XXMAX,YYMAX,ISTART,NBC
C
DO 101 I=1,NVRTX
P(I,1)=X(I)
P(I,2)=Y(I)
101 CONTINUE
CALL TRIAN
DO 2 I=1,NTRI
IS1=ITRI(I,1)
IS2=ITRI(I,2)
IS3=ITRI(I,3)
JP1=ISIDE(IS1,1)
JP2=ISIDE(IS1,2)
JP3=ISIDE(IS2,1)
IF(JP1.EQ.JP3.OR.JP2.EQ.JP3) JP3=ISIDE(IS2,2)
IP(1,I)=JP1
IP(2,I)=JP2
IP(3,I)=JP3
2 CONTINUE
C
RETURN
END

SUBROUTINE TRIAN
C
C   THE INFORMATION NEED TO RUN THE PROGRAM IS AS FOLLOWS,
C   AN INTEGER ARRAY T WHICH KEEPS TRACK OF WHAT THREE SIDES EACH
C   TRIANGLE HAS. THIS MUST BE A NTRI BY 3 ARRAY WHERE NTRI IS
C   THE MAXIMUM NUMBER OF TRIANGLES EXPECTED.
C   AN INTEGER ARRAY, S, WHICH RECORDS THE ENDPONTS OF EACH LINE.
C   THIS MUST BE AN NSIDE BY 2 ARRAY WHERE NSIDE IS THE MAXIMUM
C   NUMBER OF SIDES ONE EXPECTS.
C   NP, THE NUMBER OF POINTS ONE HAS.
C   NIBP, THE NUMBER OF INTERIOR BOUNDARY POINTS.
C   A REAL ARRAY, P, WHICH CONTAINS THE X AND Y COORDINATES OF EACH
C   POINT. THE X COORDIANTE GOES INTO THE P(NP,1) POSITION
C   AND THE Y COORDIANTE GOES INTO THE P(NP,2) POSITION.
C   THEREFORE P IS AN NP BY 2 ARRAY WHERE NP IS THE NUMBER OF
C   POINTS.
C   ALSO NEED ARE TWO WORKING ARRAYS, VERT(NT,3) AND IS(3)
C   VERT WILL STORE THE COORDIANTES OF EACH VERTEX OF EACH
C   TRIANGLES AS THEY ARE GENERATED. IS WILL CONTAIN THE SIDES.
C   *****NOTE*****
C   IF INTERIOR BOUNDARY POINTS ARE ENTERED (ISLAND), THEN THEY MUST
C   BE THE FIRST DATA CARDS READ IN AND THEY MUST BE READ IN
C   CLOCK WISE ORDER.
C   THE EXTERIOR BOUNDARY STATION NUMBERS ARE READ IN AFTER THE
C   X AND Y COORDIANTES OF EACH STATION HAS BEEN ENTERED, AND
C   THE EXTERIOR BOUNDARY STATION S ARE READ IN COUNTERCLOCK
C   WISE ORDER.
C
INTEGER S,T
DIMENSION IS(3)
COMMON/IHORK/P(204,2),VERT(402,6)
COMMON/INT/S(607,2),T(403,3)
COMMON/NUMB/NP,NT,LIST,NIBP,NEWBV
COMMON/CALCOMP/XMAX,YMAX,ISTART,NBC
COMMON/BOUND/IB(75),BV(75),NBV
C

```

```

C THE FIRST STEP IS TO FIND THE MAXIMUM DOMAIN COVERED BY THE POINTS
XMIN=0.
YMIN=0.
C
IF(XMIN.NE.XMAX) GO TO 101
XMAX=P(1,1)
XMIN=XMAX
YMAX=P(1,2)
YMIN=YMAX
DO 1 I=2,NP
IF(P(I,1).GT.XMAX)XMAX=P(I,1)
IF(P(I,1).LT.XMIN)XMIN=P(I,1)
IF(P(I,2).GT.YMAX)YMAX=P(I,2)
IF(P(I,2).LT.YMIN)YMIN=P(I,2)
1 CONTINUE
101 CONTINUE
C
C NOW THE OUTER LIMITS ARE SET.
C
DX=(XMAX-XMIN)*.1
DY=(YMAX-YMIN)*.1
P(201,1)=XMIN-DX
P(201,2)=YMIN-DY
P(202,1)=XMAX+DX
P(202,2)=P(201,1)
P(203,1)=P(202,1)
P(203,2)=YMAX+DY
P(204,1)=P(201,1)
P(204,2)=P(203,2)
C
C NOW THE INITIAL POINT OF REAL DATA IS USED TO FORM THE FIRST
C EIGHT SIDES AND FOUR TRIANGLES.
C
S(1,1)=201
S(1,2)=202
S(2,1)=202
S(2,2)=203
S(3,1)=203
S(3,2)=204
S(4,1)=204
S(4,2)=201
S(5,1)=201
S(5,2)=1
S(6,1)=202
S(6,2)=1
S(7,1)=203
S(7,2)=1
S(8,1)=204
S(8,2)=1
T(1,1)=1
T(1,2)=5
T(1,3)=6
T(2,1)=6
T(2,2)=7
T(2,3)=2
T(3,1)=3
T(3,2)=7
T(3,3)=8
T(4,1)=4
T(4,2)=5
T(4,3)=8
NS=8
NT=4
C
C THIS FILLS IN THE INITIAL VERTICES OF THE TRIANGLES
C
C NOW PROCEED TO LABEL THE X AND Y COORDIANES OF THE TRIANGLES
C
DO 2 I=1,4
2 CALL LOADVER(VERT,P,S,T,I)

```

```

C
C
C   THE REMAINING POINTS ARE NOW ADDED ONE BY ONE
C
C   DO 6 I=2,NP
C   X=P(I,1)
C   Y=P(I,2)
C   X AND Y BECOME THE NEXT POINT TO BE ADDED TO THE MESH
C   NOW PROCEED TO FIND OUT WHAT TRIANGLE X AND Y ARE IN
C
C   IFLAG=0
C   CALL INSIDE(VERT,X,Y,NT,ITRI)
C
C   ITRI IS NOW THE TRIANGLE THAT CONTAINS THE POINT I.
C
C   IF(ITRI.EQ.-2) GO TO 6
C   IF(ITRI.NE.0) GO TO 102
C   WRITE(6,200)I
200  FORMAT(*D*,*POINT*,IS,* IS NOT IN DOMAIN*)
C   GO TO 6
102  CONTINUE
C
C   HERE, THE NEW TRIANGLES AND SEGMENTS ARE ADDED.
C   WE BEGIN BY LABELING THE SIDES AND VERTICES OF THE FIRST TRIANGLE.
C
C   IS1=T(ITRI,1)
C   IS2=T(ITRI,2)
C   IS3=T(ITRI,3)
C   IP1=S(IS2,2)
C   IF(S(IS2,1).NE.S(IS1,1).AND.S(IS2,1).NE.S(IS1,2))IP1=S(IS2,1)
C   IP2=S(IS1,2)
C   IF(S(IS1,1).NE.S(IS2,1).AND.S(IS1,1).NE.S(IS2,2))IP2=S(IS1,1)
C   IP3=S(IS1,2)
C   IF(IP3.EQ.IP2)IP3=S(IS1,1)
C
C   NOW THE NEW LINE SEGMENTS ARE GENERATED.
C
C   S(NS+1,1)=IP1
C   S(NS+1,2)=I
C   S(NS+2,1)=IP2
C   S(NS+2,2)=I
C   S(NS+3,1)=IP3
C   S(NS+3,2)=I
C
C   NOW THE NEW TRIANGLES ARE CREATED
C
C   T(ITRI,1)=IS1
C   T(ITRI,2)=NS+2
C   T(ITRI,3)=NS+3
C   T(NT+1,1)=IS2
C   T(NT+1,2)=NS+1
C   T(NT+1,3)=NS+3
C   T(NT+2,1)=IS3
C   T(NT+2,2)=NS+1
C   T(NT+2,3)=NS+2
C
C   NOW THE VERTICES OF THE NEW TRIANGLES ARE LOCATED.
C
C   CALL LOADVER(VERT,P,S,T,ITRI)
C   II=NT+1
C   CALL LOADVER(VERT,P,S,T,II)
C   II=NT+2
C   CALL LOADVER(VERT,P,S,T,II)
C
C   NOW THE NUMBER OF TRIANGLES AND THE NUMBER OF LINES ARE UPDATED.
C
C   NT=NT+2
C   NS=NS+3
C

```

```

C     NOW THE TRIANGLES THAT SHARE SIDES, IS1,IS2, AND IS3 ARE EACH
C     CHECKED FOR POTENTIAL REORIENTATION.
C
IS(1)=IS1
IS(2)=IS2
IS(3)=IS3
DO 5 J=1,3
C     HERE TO FIND TWO NEIGHBORING TRIANGLES.
C
CALL NEIG(IS(J),T,JT1,JT2,NT)
C
C     NOW TO ORDER THE PAIR OF TRIANGLES.
C
IF(JT2.EQ.0) GO TO 5
JS1=IS(J)
JP1=S(JS1,1)
JP2=S(JS1,2)
C
DO 3 K=1,3
JST1=T(JT1,K)
JST2=T(JT2,K)
IF(S(JST1,1).EQ.JP1.AND.S(JST1,2).NE.JP2) JS2=JST1
IF(S(JST1,2).EQ.JP1.AND.S(JST1,1).NE.JP2) JS2=JST1
IF(S(JST1,1).EQ.JP2.AND.S(JST1,2).NE.JP1) JS3=JST1
IF(S(JST1,2).EQ.JP2.AND.S(JST1,1).NE.JP1) JS3=JST1
IF(S(JST2,1).EQ.JP1.AND.S(JST2,2).NE.JP2) JS4=JST2
IF(S(JST2,2).EQ.JP1.AND.S(JST2,1).NE.JP2) JS4=JST2
IF(S(JST2,1).EQ.JP2.AND.S(JST2,2).NE.JP1) JS5=JST2
IF(S(JST2,2).EQ.JP2.AND.S(JST2,1).NE.JP1) JS5=JST2
3 CONTINUE
C
JP3=S(JS3,1)
IF(JP3.EQ.JP2) JP3=S(JS3,2)
JP4=S(JS5,1)
IF(JP4.EQ.JP2) JP4=S(JS5,2)
C
C
C
C     THE TRIANGLES ARE NOW CHECKED TO SEE IF THEY FORM
C     A CONVEX REGION.
C
X1=P(JP4,1)
Y1=P(JP4,2)
X2=P(JP3,1)
Y2=P(JP3,2)
X3=P(JP1,1)
Y3=P(JP1,2)
X=P(JP2,1)
Y=P(JP2,2)
CALL INNER(X1,Y1,X2,Y2,X3,Y3,X,Y,IC)
IF(IC.EQ.1) GO TO 5
X3=X
Y3=Y
X=P(JP1,1)
Y=P(JP1,2)
CALL INNER(X1,Y1,X2,Y2,X3,Y3,X,Y,IC)
IF(IC.EQ.1) GO TO 5
C

```

C
C

```
      NOW CHECK FOR BOUNDARY SEGMENTS
      IF(JP3.GT.200.OR.JP4.GT.200) GO TO 5
      IF(JP1.GT.200.OR.JP2.GT.200) GO TO 4
      DO 307 KJ=1,NBV
      K1=IB(KJ)
      IF(JP1.NE.K1.AND.JP2.NE.K1) GO TO 307
      IMORE=KJ+1
      ILESS=KJ-1
      IF(ILESS.EQ.0) GO TO 331
      ILESS=IB(ILESS)
      IF(JP1.EQ.ILESS.OR.JP2.EQ.ILESS) GO TO 5
331  CONTINUE
      IF(IMCRE.GT.NBV) GO TO 332
      IMORE=IB(IMORE)
      IF(JP1.EQ.IMORE.OR.JP2.EQ.IMORE) GO TO 5
      GO TO 308
332  CONTINUE
307  CONTINUE
308  DO 309 KJ=1,NBV
      K1=IB(KJ)
      IF(JP3.NE.K1.AND.JP4.NE.K1) GO TO 309
      IMORE=KJ+1
      ILESS=KJ-1
      IF(ILESS.EQ.0) GO TO 431
      ILESS=IB(ILESS)
      IF(JP3.EQ.ILESS.OR.JP4.EQ.ILESS) GO TO 4
431  CONTINUE
      IF(IMCRE.GT.NBV) GO TO 432
      IMORE=IB(IMORE)
      IF(JP3.EQ.IMORE.OR.JP4.EQ.IMORE) GO TO 4
      GO TO 311
432  CONTINUE
```

C
C
C
C

```
      IN THIS SECTION, THE FLAGGED TRIANGLES ARE ELIMINATED AND THE
      LIST COMPACTED.  THE ACTUAL NUMBER OF TRIANGLES REMAINING IS
      RETURNED AS NT.
      T(NT+1,1)=0
      ITOP=NT+1
      IBEGIN=1
17  DO 10 I=IBEGIN,ITOP
      IF(T(I,1).NE.0) GO TO 10
      GO TO 16
10  CONTINUE
16  NEXT=I+1
      DO 9 J=NEXT,ITOP
      9  IF(T(J,1).NE.0) GO TO 13
      GO TO 18
13  INTV=J-I
      ITOP=ITOP-INTV
      DO 14 K=I,ITOP
      L=K+INTV
      DO 15 M=1,3
15  T(K,M)=T(L,M)
14  CONTINUE
      IBEGIN=I+1
      GO TO 17
18  CONTINUE
      DO 11 I=1,NT
      IF(T(I,1).EQ.0) GO TO 12
11  CONTINUE
12  NT=I-1
      RETURN
      END
```

```

SUBROUTINE LOADVER(VERT,P,S,T,I)
INTEGER S(607,2),T(403,3)
INTEGER P1,P2,P3,S1,S2
DIMENSION VERT(402,6),P(204,2)
S1=T(I,1)
S2=T(I,2)
P1=S(S1,1)
P2=S(S1,2)
P3=S(S2,1)
IF(P3.EQ.P1.OR.P3.EQ.P2)P3=S(S2,2)
VERT(I,1)=P(P1,1)
VERT(I,2)=P(P2,1)
VERT(I,3)=P(P3,1)
VERT(I,4)=P(P1,2)
VERT(I,5)=P(P2,2)
VERT(I,6)=P(P3,2)
RETURN
END

```

```

SUBROUTINE INNER(X1,Y1,X2,Y2,X3,Y3,X,Y,IC)
DIMENSION A(3,3)
CALL LOAD(A,X1,Y1,X2,Y2,X3,Y3)
CALL TRIAREA(A,AREA)
IF(AREA.EQ.0.) GO TO 8
CALL LOAD(A,X,Y,X2,Y2,X3,Y3)
CALL TRIAREA(A,AREA1)
CALL LOAD(A,X1,Y1,X,Y,X3,Y3)
CALL TRIAREA(A,AREA2)
AREA1=AREA1/AREA
IF(AREA1.LT.0.) GO TO 10
IF(AREA1.EQ.1) GO TO 9
AREA2=AREA2/AREA
IF(AREA2.LT.0.) GO TO 10
IF(AREA2.EQ.1) GO TO 9
AREA3=1.-AREA1-AEA2
IF(AREA3.LT.0.) GO TO 10
IF(AREA3.EQ.1) GO TO 9
IC=1
RETURN
10 IC=0
RETURN
9 CONTINUE
IF(X1.EQ.X) GO TO 11
IF(X2.EQ.X) GO TO 12
IF(X3.EQ.X) GO TO 13
GO TO 10
11 IF(Y1.EQ.Y) GO TO 14
GO TO 10
12 IF(Y2.EQ.Y) GO TO 14
GO TO 10
13 IF(Y3.EQ.Y) GO TO 14
GO TO 10
14 IC=-1
RETURN
8 CONTINUE
IC=2
RETURN
END

```

```

SUBROUTINE INSIDE(VERT,X,Y,NT,IPTRI)
DIMENSION VERT(402,6)
DO 1 I=1,NT
IF(AMIN1(VERT(I,1),VERT(I,2),VERT(I,3)).GT.X) GO TO 1
IF(AMAX1(VERT(I,1),VERT(I,2),VERT(I,3)).LT.X) GO TO 1
IF(AMIN1(VERT(I,4),VERT(I,5),VERT(I,6)).GT.Y) GO TO 1
IF(AMAX1(VERT(I,4),VERT(I,5),VERT(I,6)).LT.Y) GO TO 1
CALL INNER(VERT(I,1),VERT(I,4),VERT(I,2),VERT(I,5),VERT(I,3),VERT(
I,6),X,Y,IC)
IF(IC.EQ.1) GO TO 2
IF(IC.EQ.-1) GO TO 3
IF(IC.EQ.2) GO TO 4
1 CONTINUE
WRITE(6,5)X,Y
5 FORMAT(*0*,*POINT*,2F8.2,2X,*NOT IN ANY TRIANGLE*)
IPTRI=0
RETURN
2 IPTRI=I
RETURN
3 IPTRI=-2
WRITE(6,10)X,Y,I
10 FORMAT(*0*,*WE HAVE A DUPLICATE POINT*,2F8.2,I5)
RETURN
4 IPTRI=I
RETURN
END

```

```

SUBROUTINE LOAD(A,X1,Y1,X2,Y2,X3,Y3)
DIMENSION A(3,3)
A(1,1)=X1
A(1,2)=Y1
A(1,3)=1.
A(2,1)=X2
A(2,2)=Y2
A(2,3)=1.
A(3,1)=X3
A(3,2)=Y3
A(3,3)=1.
RETURN
END
SUBROUTINE CHKA(ITRI,VERT,IFLAG)
DIMENSION VERT(402,6),A(3,3)
X1=VERT(ITRI,1)
X2=VERT(ITRI,2)
X3=VERT(ITRI,3)
Y1=VERT(ITRI,4)
Y2=VERT(ITRI,5)
Y3=VERT(ITRI,6)
CALL LOAD(A,X1,Y1,X2,Y2,X3,Y3)
CALL TRIAREA(A,AREA)
IF(AREA.EQ.0.) GO TO 1
IFLAG=0
RETURN
1 IFLAG=1
RETURN
END

```

```

SUBROUTINE SWEEP(P,S,T,NT,ITIME,NIBP)
C
C THIS SUBROUTINE SWEEPS THROUGH THE TRIANGLES AND COMPARES
C NEIGHBORS FOR GOODNESS.
C
C P IS THE POINT ARRAY AS DESCRIBED IN TRIAN.
C S IS THE SIDE ARRAY AS DESCRIBED IN TRIAN.
C T IS THE TRIANGLE ARRAY AS DESCRIBED IN TRIAN.
C ITIME IS A COUNTER TELLING US HOW MANY TRIANGLES HAVE BEEN CHANGED
C NIBP IS THE NUMBER OF INTERIOR BOUNDARY POINTS.
C
C INTEGER S(607,2),T(403,3)
C COMMON/BOUND/IB(75),BV(75),NBV
C DIMENSION P(204,2)
C ITIME=0
C
C HERE THE SWEEP BEGINS.
C
C DO 100 I=1,NT
C DO 2 J=1,3
C
C BEGIN BY EXAMINING THE J SIDE OF TRIANGLE I
C
C IS=T(I,J)
C
C HERE WE LOCATE THE TWO NEIGHBORING TRIANGLES THAT HAVE SIDE IS.
C
C CALL NEIG(IS,T,JT1,JT2,NT)
C IF(JT2.EQ.0) GO TO 2
C
C PROCEED TO CODE THE POINTS OF THE NEIGHBORING TRIANGLES.
C
C JP1=S(IS,1)
C JP2=S(IS,2)
C IS1=T(JT1,1)
C IF(IS.EQ.IS1) IS1=T(JT1,2)
C JP3=S(IS1,1)
C IF(JP3.EQ.JP2.OR.JP3.EQ.JP1) JP3=S(IS1,2)
C IS1=T(JT2,1)
C IF(IS.EQ.IS1) IS1=T(JT2,2)
C JP4=S(IS1,1)
C IF(JP4.EQ.JP2.OR.JP4.EQ.JP1) JP4=S(IS1,2)
C
C NOW CHECK FOR CONVEX TRIANGLES.
C
C X1=P(JP4,1)
C Y1=P(JP4,2)
C X2=P(JP3,1)
C Y2=P(JP3,2)
C X3=P(JP1,1)
C Y3=P(JP1,2)
C X=P(JP2,1)
C Y=P(JP2,2)

```

```

C      CALL INNER(X1,Y1,X2,Y2,X3,Y3,X,Y,IC)
      IF(IC.EQ.1) GO TO 2
      X3=X
      Y3=Y
      X=P(JP1,1)
      Y=P(JP1,2)
C
      CALL INNER(X1,Y1,X2,Y2,X3,Y3,X,Y,IC)
      IF(IC.EQ.1) GO TO 2
C
C      NOW CHECK FOR BOUNDARY SEGMENTS
C
      IF(JP3.GT.200.OR.JP4.GT.200) GO TO 2
      IF(JP1.GT.200.OR.JP2.GT.200) GO TO 4
C
      DO 307 KJ=1,NBV
      K1=IB(KJ)
      IF(JP1.NE.K1.AND.JP2.NE.K1) GO TO 307
      ILESS=KJ-1
      IMORE=KJ+1
      IF(ILESS.EQ.0) GO TO 331
      ILESS=IB(ILESS)
      IF(JP1.EQ.ILESS.OR.JP2.EQ.ILESS) GO TO 2
331  CONTINUE
      IF(IMORE.GT.NBV) GO TO 332
      IMORE=IB(IMORE)
      IF(JP1.EQ.IMORE.OR.JP2.EQ.IMORE) GO TO 2
      GO TO 308.
332  CONTINUE
307  CONTINUE
308  DO 309 KJ=1,NBV
      K1=IB(KJ)
      IF(JP3.NE.K1.AND.JP4.NE.K1) GO TO 309
      ILESS=KJ-1
      IMORE=KJ+1
      IF(ILESS.EQ.0) GO TO 431
      ILESS=IB(ILESS)
      IF(JP3.EQ.ILESS.OR.JP4.EQ.ILESS) GO TO 4
431  CONTINUE
      IF(IMORE.GT.NBV) GO TO 432
      IMORE=IB(IMORE)
      IF(JP3.EQ.IMORE.OR.JP4.EQ.IMORE) GO TO 4
      GO TO 311
432  CONTINUE
309  CONTINUE
311  CONTINUE
C
C      NOW PROCEED TO CALCULATE AND COMPARE THE GOODNESS OF THE
      NEIGHBORING TRIANGLES.
C
      G1=GOOD(JP1,JP2,JP3,P)

```

```

G2=GOOD(JP1,JP2,JP4,P)
G3=GOOD(JP1,JP3,JP4,P)
G4=GOOD(JP2,JP3,JP4,P)
GW=AMIN1(G3,G4)
IF(G1.LT.GW) GO TO 4
IF(G2.LT.GW) GO TO 4
GO TO 2
4 CONTINUE

```

C
C
C
C

THIS IS WHERE THE SWITCHING OF THE TRIANGLES ARE DONE.
WE BEGIN BY LABELING THE SIDES FOR IDENTIFICATION.

```

JS1=IS
S(JS1,1)=JP4
S(JS1,2)=JP3
DO 200 K=1,3
JST1=T(JT1,K)
JST2=T(JT2,K)
IF(S(JST1,1).EQ.JP1.AND.S(JST1,2).NE.JP2) JS2=JST1
IF(S(JST1,2).EQ.JP1.AND.S(JST1,1).NE.JP2) JS2=JST1
IF(S(JST1,1).EQ.JP2.AND.S(JST1,2).NE.JP1) JS3=JST1
IF(S(JST1,2).EQ.JP2.AND.S(JST1,1).NE.JP1) JS3=JST1
IF(S(JST2,1).EQ.JP1.AND.S(JST2,2).NE.JP2) JS4=JST2
IF(S(JST2,2).EQ.JP1.AND.S(JST2,1).NE.JP2) JS4=JST2
IF(S(JST2,1).EQ.JP2.AND.S(JST2,2).NE.JP1) JS5=JST2
IF(S(JST2,2).EQ.JP2.AND.S(JST2,1).NE.JP1) JS5=JST2
200 CONTINUE

```

C
C
C
C
C

NOW THE TRIANGLES ARE ALTERED.
AND THE CHANGED RECORDED.

```

T(JT1,1)=JS1
T(JT1,2)=JS2
T(JT1,3)=JS4
T(JT2,1)=JS1
T(JT2,2)=JS3
T(JT2,3)=JS5
ITIME=ITIME+1
GO TO 100
2 CONTINUE
100 CONTINUE
RETURN
END

```

C
C

```

SUBROUTINE FINDBP(IB,IP,IBTRI,NTRI,NBV)
DIMENSION IB(1),IP(3,1),IBTRI(1)
THIS SUBROUTINE CALCULATES THE NUMBER OF POINTS IN EACH TRIANGLE
AND ORDERS THE BOUNDARY POINTS.
DO 1601 MN=1,NTRI
1601 ISTR1(MN)=0
DO 622 K=1,NBV
DO 622 J=1,NTRI

DO 621 I=1,3
IF(IB(K).NE.IP(I,J)) GO TO 621
IBTRI(J)=IBTRI(J)+1
I2=IBTRI(J)
NUM=IP(I2,J)
IP(I2,J)=IP(I,J)
IP(I,J)=NUM
GO TO 622
621 CONTINUE
622 CONTINUE

```

C
C

```

C   THIS SECTION CHECKS TO SEE IF THE BOUNDARY TRIANGLES AND NUMBERING
C   SYSTEM ARE CONSISTENT
C

```

```

DO 633 J=1,NTRI
NUM=IBTRI(J)-2
IF(NUM)633,634,643
634 DO 637 K=1,NBV
IF(IB(K).NE.IP(1,J)) GO TO 637
IJ=K+1
IF(IB(IJ).EQ.IP(2,J)) GO TO 633
IF(IP(1,J).EQ.IB(1).AND.IP(2,J).EQ.IB(NBV))GO TO 641
DO 734 H=IJ,NBV
IF(IB(H).EQ.IP(2,J)) GO TO 758
GO TO 734
758 IBTRI(J)=0
GO TO 633
734 CONTINUE
DO 736 H=1,NBV
IF(IB(H).EQ.IP(3,J)) GO TO 640
736 CONTINUE
GO TO 635
641 CONTINUE
NUM=IP(1,J)
IP(1,J)=IP(2,J)
IP(2,J)=NUM
GO TO 633
637 CONTINUE
635 IBTRI(J)=5

```

```

C   IBTRI(J)=5 INDICATES THAT NO BOUNDARY POINTS WERE FOUND IN THE
C   TRIANGLE EVEN THOUGH IBTRI WAS OVER 2 ORIGINALLY
C

```

```

FUNCTION GOOD(JP1,JP2,JP3,P)
DIMENSION AL(3),P(204,2)
DIMENSION X(2),Y(2)
X(1)=P(JP1,1)
X(2)=P(JP2,1)
Y(1)=P(JP1,2)
Y(2)=P(JP2,2)
AL(1)=ALENGTH(X,Y)
X(2)=P(JP3,1)
Y(2)=P(JP3,2)
AL(2)=ALENGTH(X,Y)
X(1)=P(JP2,1)
Y(1)=P(JP2,2)
AL(3)=ALENGTH(X,Y)
ALM=AL(1)
I=1
DO 2 J=2,3
IF(AL(J).GT.ALM) GO TO 1
GO TO 2
1 I=J
ALM=AL(J)
2 CONTINUE
RLL=C.
DO 3 J=1,3
IF(J.NE.I)RLL=RLL+AL(J)
3 CONTINUE
GOCC=RLL/ALM
RETURN
END

```

```

SUBROUTINE ELIM(IBTRI,IP,X,Y,NTRI)
DIMENSION IBTRI(1),IP(3,1),X(1),Y(1)
COMMON/IA/A(3,3)
COMMON/IB/B(3)
COMMON/INT/ISUM(300),IPROD(300)
C
C THIS SUBROUTINE ELIMINATES TRIANGLES OUTSIDE OF THE DOMAIN
C
DO 662 J=1,NTRI
IF (IBTRI(J).LT.2) GO TO 662
663 NN=IP(1,J)
M=IP(2,J)
L=IP(3,J)
664 DX=X(M)-X(NN)
DY=Y(M)-Y(NN)
DS=((DX**2.)+(DY**2.))**.5
DCOSX=DY/DS
DCOSY=-DX/DS
666 A(1,1)=X(L)
A(1,2)=Y(L)
A(1,3)=1.
A(2,1)=X(NN)
A(2,2)=Y(NN)
A(2,3)=1.
A(3,1)=X(M)
A(3,2)=Y(M)
A(3,3)=1.
B(1)=1.
B(2)=J.
B(3)=J.
CALL SOLVE(A,B)
667 DX=X(NN)+0.5*DX+0.01*DS*DCOSX
DY=Y(NN)+0.5*DY+0.1*DS*DCOSY
DS=B(1)*DX+B(2)*DY+B(3)
IF(DS.LT.0) GO TO 662
IBTRI(J)=6
662 CONTINUE
I=NTRI
262 DO 674 J=1,NTRI
IF (IBTRI(J).NE.6) GO TO 674
272 IF (J.EQ.I) GO TO 677
I=I-1
DO 676 K=J,I
L=K+1
IBTRI(K)=IBTRI(L)
IP(1,K)=IP(1,L)
IP(2,K)=IP(2,L)
676 IP(3,K)=IP(3,L)
IBTRI(NTRI)=0
IF (IBTRI(J).EQ.6) GO TO 272
674 CONTINUE
677 NTRI=I+1
DO 802 I=1,NTRI

GO TO 633
643 DO 649 K=1,NBV
IF (IB(K).NE.IP(1,J)) GO TO 649
IJ=K+1
IF (IB(IJ).EQ.IP(2,J)) GO TO 651
KK=NBV-1
IF (IP(1,J).EQ.IB(1).AND.IP(2,J).EQ.IB(KK)) GO TO 735
DO 737 M=IJ,NBV
737 IF (IB(M).EQ.IP(2,J)) GO TO 651
GO TO 635

```



```

SUBROUTINE WHOUT(DST,X1,Y1,EDST)
COMMON/BOUND/IB(75),BV(75),NBV
COMMON/IX/X(200)
COMMON/IY/Y(200)
DIMENSION DST(1)
CALL WHERE(X1,Y1,J1,J2)
I2=IB(J1)
ADD=((X(I2)-X1)**2.+(Y(I2)-Y1)**2.)**.5
EDST=DST(J1)+ADD
RETURN
END

```

```

SUBROUTINE WHIN(DST)
COMMON/BOUND/IB(75),BV(75),NBV
COMMON/IX/X(200)
COMMON/IY/Y(200)
DIMENSION DST(1)
DST(1)=0.
DO 9 I=2,NBV
J=IB(I)
L=I-1
K=IB(L)
DT=((X(K)-X(J))**2.+(Y(K)-Y(J))**2.)**.5
9 DST(I)=DST(L)+DT
RETURN
END

```

```

SUBROUTINE GUESS(X1,Y1,J1,J2,ELEV)
COMMON/BOUND/IB(75),BV(75),NBV
COMMON/IX/X(200)
COMMON/IY/Y(200)
COMMON/NUMB/NVRTX,NTRI,LIST,IPUNCH,NEWBV
I1=IB(J1)
I2=IB(J2)
DS1=((X(I1)-X1)**2.+(Y(I1)-Y1)**2.)**.5
DS2=((X(I2)-X1)**2.+(Y(I2)-Y1)**2.)**.5
DS=DS1+DS2
ELEV=(DS2/DS)*BV(J1)+(DS1/DS)*BV(J2)
RETURN
END

```

```

SUBROUTINE ALTER(XI,YI)

```

THIS ROUTINE ALTERS THE OLD BOUNDARY CONDITONS.

```

COMMON/IRHS/DST(100),EI(100)
COMMON/IDEPTH/DEPTH(200)
COMMON/BOUND/IB(75),BV(75),NBV
COMMON/IX/X(200)
COMMON/IY/Y(200)
COMMON/NUMB/NVRTX,NTRI,LIST,IPUNCH,NEWBV
COMMON/CUTCFF/NIBP,NFLX,J1,J2
DIMENSION XI(1),YI(1)
DO 10 I=1,NBV
CALL BYPASS(I,IYES)
IF(IYES.EQ.1) GO TO 10
9 DH=EI(I)-BV(I)
CALL WHOUT(DST,XI(I),YI(I),EDST)
IF(EDST.LT.DST(I)) GO TO 10
8 CALL WHERE(XI(I),YI(I),J1,J2)
CALL GUESS(XI(I),YI(I),J1,J2,ELEV)
BV(I)=ELEV-DH
10 CONTINUE
RETURN
END

```

```

SUBROUTINE BTH(X1,X2,Y1,Y2,X,Y,IYES)
IF(AHAX1(X1,X2).LT.X) GO TO 1
IF(AMIN1(X1,X2).GT.X) GO TO 1
IF(AHAX1(Y1,Y2).LT.Y) GO TO 1
IF(AMIN1(Y1,Y2).GT.Y) GO TO 1
IYES=1
RETURN
1 IYES=0
RETURN
END

```

```

SUBROUTINE WHERE(X1,Y1,J1,J2)
COMMON/IGRAD/IFLG,IBEGIN,IEND,NIBP,NH
COMMON/IX/X(200)
COMMON/IY/Y(200)
COMMON/BOUND/IB(75),BV(75),NBV
COMMON/NUPB/NVRTX,NTRI,LIST,IPUNCH,NEWBV
I=NIBP+1
I1=IB(I)
I=IB(NBV)
CALL BTH(X(I),X(I1),Y(I),Y(I1),X1,Y1,IYES)
IF(IYES.NE.1) GO TO 1
J1=NBV
J2=NIBP+1
RETURN
1 ISTCP=NBV-1
DO 2 I=1,ISTOP
J=I+1
K1=IB(I)
K2=IB(J)
CALL BTH(X(K1),X(K2),Y(K1),Y(K2),X1,Y1,IYES)
IF(IYES.EQ.0.) GO TO 2
J1=I
J2=J
RETURN
2 CONTINUE
WRITE(6,10)X1,Y1
10 FORMAT(*0*,2F10.2,3X,*NOT ON BOUNDARY*)
RETURN
END

```

```

SUBROUTINE INTG(X1,Y1,X2,Y2,ELEV1,ELEV2,I TRI,SA,DP)
DIMENSION SA(1)
COMMON/IALPHA/ALPHA(200)
COMMON/HIND/TAUX,TAUY,CURL
COMMON/ICCNST/CONST1,CONST2
COMMON/IIP/IP(3,350)
IF(X1.EQ.X2.AND.Y1.EQ.Y2) GO TO 1
DS=((X1-X2)**2.+(Y1-Y2)**2.)**.5
CALL JACOB(I TRI,DDX,DDY,AJ,SA)
CALL DDDN(X1,Y1,X2,Y2,DDX,DDY,DN)
IF(ABS(DN).LT..000001) GO TO 2
ELEV2=(CONST1*AJ+CURL)*DS/DN+ELEV1
RETURN
1 ELEV2=0.
RETURN
2 ELEV2=ELEV1
WRITE(6,10) I TRI
10 FORPAT(1H0,*WE HAVE RUN INTO A TRIANGLE WITH NO DEPTH GRADIENTS*,2
CX,I3^
RETURN
END

```

```

SUBROUTINE SOLVER(ELEV1,X1,Y1,ELEV2,X2,Y2,IGLB,SA)
C
C
C      THIS IS THE ROUTINE THAT SOLVES THE FIRST ORDER EQUATION.
COMMON/CUTOFF/IFINIS,NFLX,J1,J2
COMMON/IGRAD/IFLG,IBEGIN,IEND,NIBP,IDONE
COMMON/IDEPH/DEPTH(200)
COMMON/NUMB/NVRTX,NTRI,NOINTG,IPINTG,NEWBV
DIMENSION SA(1)
DP=DEPTH(IGLB)
IFINIS=0
IEND=0
IBEGIN=0
IFLG=0
IDONE=0
C
C      BEGIN BY LOCATING THE FIRST TRIANGLE WE WILL WORK WITH.
CALL FIRST(IGLB,ITRI,0)
IF(ITRI.NE.0) GO TO 1
X2=X1
Y2=Y1
ELEV2=ELEV1
RETURN
C
C      NOW FIND THE POINT ALONG THE TRIANGLE BOUNDARY WHICH HAS THE
C      SAME DEPTH AS THE POINT WE CAME FROM.
1 CALL FNDPT(X1,Y1,ITRI,X2,Y2,DP)
C
C      NOW INTEGRATE FROM THE ORIGINAL POINT TO THE SECOND POINT
C      WITHIN THE TRIANGLE.
CALL INTG(X1,Y1,X2,Y2,ELEV1,ELEV2,ITRI,SA,DP)
ELEV1=ELEV2
IEND=IEND+1
IF(IEND.EQ.NTRI) GO TO 7
C
C      NOW LOCATE THE NEXT TRIANGLE THE DEPTH CONTOUR ENTERS.
C      THEN GO BACK TO ONE AND FIND THE SECOND POINT AGAIN.
CALL EXTEND(X2,Y2,ITRI,NEWTRI)
IF(NEWTRI.EQ.0) RETURN
6 X1=X2
Y1=Y2
ITRI=NEWTRI
GO TO 1
7 WRITE(6,100)DP
100 FORMAT(1H0,*WE ARE LOST FOLLOWING*,1X,F6.2,1X,*DEPTH CONTOUR*)
RETURN
END

```

```

SUBROUTINE BETH(VAL,VAL1,VAL2,IYES)
COMMON/IGRAD/IFLG,IBEGIN,IEND,NN,NM
IFLG=0
IYES=0
IF(VAL.LE.VAL1.AND.VAL.GE.VAL2) GO TO 1
IF(VAL.GE.VAL1.AND.VAL.LE.VAL2) GO TO 1
RETURN
1 IYES=1
IF(VAL.EQ.VAL1) IFLG=1
IF(VAL.EQ.VAL2) IFLG=1
RETURN
END

```

```

SUBROUTINE FIRST(IGLB,ITRI,IOLD)
COMMON/CUTOFF/IFINIS,NFLX,IP1,IP2
COMMON/IGRAD/IFLG,IBEGIN,IEND,NIBP,IDONE
COMMON/IIP/IP(3,350)
COMMON/IX/X(200)
COMMON/IY/Y(200)
COMMON/IDEPH/DEPTH(200)
COMMON/NUMB/NVRTX,NTRI,LIST,IPUNCH,NEHBV
DO 2 I=1,NTRI
IF(I.EQ.ICLD) GO TO 2
IF(I.EQ.IFINIS) GO TO 2
IF(I.EQ.IDONE) GO TO 2
DO 1 J=1,3
K=IP(J,I)
IF(IGLB.EQ.K) GO TO 3
1 CONTINUE
GO TO 2
3 CONTINUE
I1=IP(1,I)
I2=IP(2,I)
I3=IP(3,I)
IF(IGLB.EQ.I1) GO TO 4
IF(IGLB.EQ.I2) GO TO 5
IF(IGLB.EQ.I3) GO TO 6
IF(IGLB.EQ.I1) GO TO 4
IF(IGLB.EQ.I2) GO TO 5
IF(IGLB.EQ.I3) GO TO 6
CALL BETH(DEPTH(IGLB),DEPTH(I1),DEPTH(I2),IYES)
IF(IYES.EQ.1) GO TO 6
GO TO 2
5 CONTINUE
IF(IGLB.EQ.I1) GO TO 4
IF(IGLB.EQ.I2) GO TO 5
IF(IGLB.EQ.I3) GO TO 6
CALL BETH(DEPTH(IGLB),DEPTH(I1),DEPTH(I3),IYES)
IF(IYES.EQ.1) GO TO 6
GO TO 2
4 CONTINUE
IF(IGLB.EQ.I2) GO TO 5
IF(IGLB.EQ.I3) GO TO 6
CALL BETH(DEPTH(IGLB),DEPTH(I2),DEPTH(I3),IYES)
IF(IYES.EQ.1) GO TO 6
GO TO 2
8 IBEGIN=0
2 CONTINUE
ITRI=0
RETURN
6 ITRI=I
IF(IFLG.EQ.0) GO TO 7
IBEGIN=IGLB
RETURN
7 IBEGIN=0
RETURN
END

```

```

SUBROUTINE VERTCH(X1,Y1,IOLD,IYES,IGLB)
COMMON/BOUND/IB(75),BV(75),NBV
COMMON/IIF/IP(3,350)
COMMON/IX/X(200)
COMMON/IY/Y(200)
COMMON/NUMB/NVRTX,NTRI,LIST,IPUNCH,NEWBV
IF(IOLD.LT.0) IOLD=-IOLD
DO 1 I=1,3
K=IP(I,IOLD)
DX=X1-X(K)
DY=Y1-Y(K)
DS=(DX*DX+DY*DY)**.5
IF(CS.LT..00000001) GO TO 2
1 CONTINUE
IYES=0
RETURN
2 IYES=1
DO 3 I=1,NBV
J=IB(I)
IF(J.EQ.K) GO TO 4
3 CONTINUE
IGLB=K
RETURN
4 IGLB=0
RETURN
END

```

```

SUBROUTINE EXTEND(X1,Y1,IOLD,NEWTRI)
COMMON/IIF/IP(3,350)
COMMON/IGRAD/IFLG,IBEGIN,IEND,NIBP,IDCNE
COMMON/CUTOFF/IFINIS,NFLX,J1,J2
COMMON/NUMB/NVRTX,NTRI,LIST,IPUNCH,NEWSV
CALL VERTCH(X1,Y1,IOLD,IYES,IGLB)
IF(IYES.EQ.1)GO TO 7
DO 5 I=1,NTRI
IF(I.EQ.IOLD) GO TO 5
DO 4 J=1,2
K=IP(J,I)
IF(K.NE.J1.AND.K.NE.J2) GO TO 4
JJ=J+1
DO 3 L=JJ,3
K=IP(L,I)
IF(K.NE.J1.AND.K.NE.J2) GO TO 3
NEWTRI=I
RETURN
3 CONTINUE
4 CONTINUE
5 CONTINUE
6 NEWTRI=0
RETURN
7 IF(IGLB.EQ.0) GO TO 6
RECCRD WHENCE WE CAME.
IFINIS=IOLD
CALL FIRST(IGLB,NEWTRI,IOLD)
RECCRD TO WHERE WE TREK.
IDONE=NEWTRI
RETURN
END

```

```

SUBROUTINE DDCN(X1,Y1,X2,Y2,DDX,DDY,DN)
DX=X2-X1
DY=Y2-Y1
DS=(DX*DX+DY*DY)**.5
DN=CX/DS*CDY-CY/DS*CDX
RETURN
END

```

```

SUBROUTINE JACOB(ITRI,DDX,DDY,AJ,SA)
COMMON/IALPHA/ALPHA(200)
COMMON/IDEPH/DEPTH(200)
COMMON/IIP/IP(3,350)
DIMENSION SA(1)
DIMENSION ALPH(3)
COMMON/IA/A(3,3)
I1=IP(1,ITRI)
I2=IP(2,ITRI)
I3=IP(3,ITRI)
CALL FILL(ITRI,A)
CALL ALPHX(ITRI,DAX,DAY,ALPHA,SA,ALPH)
CALL GRAD(DEPTH(I1),DEPTH(I2),DEPTH(I3),DDX,DDY,CC)
AJ=DAY*DDX-DAX*DDY
RETURN
END

```

```

SUBROUTINE INTERS(OP,X2,Y2,X1,Y1)
COMMON/IX/X(200)
COMMON/IY/Y(200)
COMMON/IIP/IP(3,350)
COMMON/IDEPH/DEPTH(200)
COMMON/CUTOFF/NIBP,NFLX,IP1,IP2
D1=DEPTH(IP1)
D2=DEPTH(IP2)
DS1=OP-D1
DS2=D2-OP
DS=D2-D1
W1=DS2/DS
W2=DS1/DS
IF(D1.NE.D2) GO TO 15
X2=X(IP2)
Y2=Y(IP2)
IF(X2.NE.X1.AND.Y2.NE.Y1) GO TO 20
X2=X(IP1)
Y2=Y(IP1)
20 RETURN
15 CONTINUE
X2=X(IP1)*W1+X(IP2)*W2
Y2=Y(IP1)*W1+Y(IP2)*W2
RETURN
END

```

```

SUBROUTINE FNDPT(X1,Y1,ITRI,X2,Y2,DP)
COMMON/IX/X(200)
COMMON/IY/Y(200)
COMMON/IIF/IP(3,350)
COMMON/IDEPTH/DEPTH(200)
COMMON/NUMB/NVRTX,NTRI,LIST,IPUNCH,NEWBV
COMMON/CUTOFF/NIBP,NFLX,IP1,IP2
IFLG=0
I1=IP(1,ITRI)
I2=IP(2,ITRI)
I3=IP(3,ITRI)
DO 10 I=1,3
IF(I.EQ.1) GO TO 9
IF(I.EQ.2) GO TO 8
IP1=I2
IP2=I3
CALL BETH(DP,DEPTH(IP1),DEPTH(IP2),IYES)
IF(IYES.EQ.0) GO TO 10
GO TO 7
9 IP1=I1
IP2=I2
CALL BETH(DP,DEPTH(IP1),DEPTH(IP2),IYES)
IF(IYES.EQ.0) GO TO 10
GO TO 7
8 IP1=I1
IP2=I3
CALL BETH(DP,DEPTH(IP1),DEPTH(IP2),IYES)
IF(IYES.EQ.0) GO TO 10
7 CALL INTERS(DP,X2,Y2,X1,Y1)
DX=(X1-X2)**2.
DY=(Y1-Y2)**2.
IF(DX.LT.1.0E-13.AND.DY.LT.1.0E-13) GO TO 10
RETURN
10 CONTINUE
WRITE(6,50) ITRI,X1,Y1,DP
50 FORMAT(*0*,*WE ARE LOST IN TRI.*,I5,2X,*FROM POINT*,2F7.3,2X,*DEPT
vH*,F6.3)
IFLG=1000
RETURN
END

```

```

SUBROUTINE PLOT(X,Y,NPTS,XSTRT,ysize,ysize,NOIV,NFL,NDEC,YMAX)
DIMENSION A(120),IX(200),IY(200),SYH(6),FRMT(3),TLAB(3),SB(30)
DIMENSION X(1),Y(1)
DATA SYH/1H ,1H*,1H0,1H-,1HX,1HI/

C
C
C AN ALL PURPOSE PRINTER PLOT ROUTINE WRITTEN IN STANDARD FORTRAN.
C
C X AND Y ARE COORDINATES OF POINTS TO BE PLOTTED.
C NPTS ARE NUMBER OF POINTS TO BE PLOTTED.
C XSIZE IS THE SIZE OF THE PLOT IN INCHES IN THE X DIRECTION.
C LIKewise FOR YSIZE.
C XSTRT IS THE VALUE OF THE THE MINIMUM X VALUE.
C NOIV IS THE NUMBER OF PARTITIONS THE X AXIS WILL BE DIVIDED INTO
C AND LABLED.
C NFL IS THE FIELD LENGTH OF THE LABEL IN F FORMAT.
C NDEC IS THE NUMBER OF DECIMAL POINTS THERE WILL BE IN THE FIELD
C LENGTH.
C YMAX IS CALCULATED.
C
C
C CALL SCALE(X,Y,IX,IY,NPTS,XSIZE,ysize,ypts,xmin,xmax,xpts,ymax)
C
C
C JX=IFIX(XSTRT/.1)
C IYPTS=IFIX(YPTS)
C IXPTS=IFIX(XPTS)
C IXTCT=IXPTS+JX
C NSKP=JX-NFL-1
C
C
C TOP LABEL.
C
C NCHR=23
C ENCODE(23,105,TLAB)
105 FORMAT(23HNEW BOUNDARY ELEVATIONS)
CALL TLB(TL#B,NCHR,IXPTS,JX)
C
C SIDE LABEL SET IN SUBROUTINE SLB.
C CALL SLB(SB,IS,IE,IYPTS)
C
C ENCODE(21,100,FRMT)NSKP,NFL,NDEC
100 FORMAT(5H(1H ,I2,4HA1,F,I1,1H.,I1,7H,110A1))
DO 6 I=1,JX
6 A(I)=SYH(1)
DO 1 I=JX,110
1 A(I)=SYH(4)
WRITE(6,5)(A(I),I=1,110)
5 FORMAT(1H ,110A1)
IC=1
DO 3 I=1,IYPTS
DO 2 IJ=1,110
2 A(IJ)=SYH(1)
IF(I.LT.IS.OR.I.GT.IE) GO TO 13
A(1)=SB(IC)

```

```

SUBROUTINE TOP(NDIV,XMIN,XMAX,A,NFL,NDEC,ISTR,NXPTS)
DIMENSION A(1),FRMT(3)
MRKS=NDIV+1
AINT=(XMAX-XMIN)/FLOAT(NDIV)
DO 1 I=1,MRKS
J=I-1
1 A(I)=FLCAT(J)*AINT+XMIN
RT=FLCAT(ISTR)-FLOAT(NFL)/2.
SKP=FLOAT(NXPTS)/FLOAT(NDIV)-FLOAT(NFL)
IRT=JFIX(RT)
NSKP=JFIX(SKP)
ENCCDE(22,100,FRMT)IRT,MRKS,NFL,NDEC,NSKP
100 FORMAT(5H(1H , ,I2,2HX , ,I2,2H(F,I1,1H , ,I1,1H , ,I2,3HX))
WRITE(6,FRMT)(A(I),I=1,MRKS)
RETURN
END

```

```

SUBROUTINE FILL(IT,A)
DIMENSION A(3,3)
COMMON/II/IP(3,350)
COMMON/IY/Y(200)
COMMON/IX/X(200)
I1=IP(1,IT)
I2=IP(2,IT)
I3=IP(3,IT)
A(1,1)=X(I1)
A(1,2)=Y(I1)
A(1,3)=1.
A(2,1)=X(I2)
A(2,2)=Y(I2)
A(2,3)=1.
A(3,1)=X(I3)
A(3,2)=Y(I3)
A(3,3)=1.
RETURN
END

```

```

SUBROUTINE SCALE(X,Y,IX,IY,NPTS,XSIZE,YSIZE,YPTS,XMIN,XMAX,XPTS,YX
v)
DIMENSION X(1),Y(1),IX(1),IY(1)
XMIN=X(1)
YMIN=Y(1)
XMAX=X(1)
YMAX=Y(1)
DO 2 I=2,NPTS
XMIN=AMIN1(XMIN,X(I))
YMIN=AMIN1(YMIN,Y(I))
XMAX=AMAX1(XMAX,X(I))
YMAX=AMAX1(YMAX,Y(I))
2 CONTINUE
IF(YX.GT.0.)YMAX=YX
XPTS=XSIZE/.1
YPTS=YSIZE/.167
XRANGE=XMAX-XMIN
YRANGE=YMAX-YMIN
XRES=XPTS/XRANGE
YRES=YPTS/YRANGE
DO 10 I=1,NPTS
IX(I)=IFIX((X(I)-XMIN)*XRES)
10 IY(I)=IFIX((Y(I)-YMIN)*YRES)
RETURN
END

```

```

      IC=IC+1
13  CONTINUE
      A(JX)=SYH(6)
      IFLG=0
      A(110)=SYH(6)
      DO 4 J=1,NPTS
      IF(IY(J).NE.I) GO TO 4
      N=IX(J)+JX
      A(N)=SYH(2)
      YLAB=Y(J)
      IFLG=1
      4  CONTINUE
      IF(IFLG.EQ.0) GO TO 11
      WRITE(6,FRMT)(A(L),L=1,NSKP),YLAB,(A(L),L=JX,110)
      GO TO 12
11  WRITE(6,5)(A(L),L=1,110)
12  CONTINUE
      3  CONTINUE
      DO 8 I=1,JX
      8  A(I)=SYH(1)
      DO 9 I=JX,110
      9  A(I)=SYH(4)
      WRITE(6,5)(A(I),I=1,110)
      CALL TOP(NDIV,XMIN,XMAX,A,NFL,NDEC,JX,IXPTS)
C
C      BOTTOM LABEL IS SET HERE.
C
      NCHR=22
      ENCODE(22,205,TLAB)
205  FORMAT(22HSURFACE ELEVATIONS CM.)
      CALL TLB(TLAB,NCHR,IXPTS,JX)
      RETURN
      END

```

```

SUBROUTINE SLB(S0,IS,IE,IYPTS)
DIMENSION SB(1)
NCHR=27
SB(1)=1HD
SB(2)=1HI
SB(3)=1HS
SB(4)=1HT
SB(5)=1H.
SB(6)=1H
SB(7)=1HA
SB(8)=1HL
SB(9)=1HO
SB(10)=1HN
SB(11)=1HG
SB(12)=1H
SB(13)=1HB
SB(14)=1HO
SB(15)=1HU
SB(16)=1HN
SB(17)=1HD
SB(18)=1HA
SB(19)=1HR
SB(20)=1HY
SB(21)=1H
SB(22)=1H1
SB(23)=1HO
SB(24)=1H
SB(25)=1HK
SB(26)=1HM
SB(27)=1H.
IH=IYPTS/2
JH=NCHR/2
IS=IH-JH
IE=IS+NCHR-1
RETURN
END

```

```

FUNCTION JFIX(R)
JFIX=IFIX(R)
D=R-FLOAT(JFIX)
IF(D.GE.5) JFIX=JFIX+1
RETURN
END

```

```

SUBROUTINE ISBNDRY(I,NO)
COMMON/CUTOFF/IBP,NFLX,JJ1,JJ2
COMMON/BOUND/IS(75),BV(75),NBV

```

C
C
C
C
C
C
C

SUBROUTINE TO TELL US IF WE ARE AT A BOUNDARY POINT, AND
WHAT TYPE OF BOUNDARY POINT.

```

NO=0, NOT A BOUNDARY POINT.
NO=-1, CIRCHLET BOUNDARY POINT, ON OPEN BOUNDARY.
NO=1, ONSHORE BOUNDARY POINT INCLUDING ISLAND.

```

```

NIBP=IBP
IF(NIBP.LT.0) NIBP=-IBP
IST=NFLX+NIBP+1
IEND=NIBP+NFLX
IS=NIBP+1
IF(IEND.EQ.0) GO TO 4
IF(NIBP.EQ.0) GO TO 2
DO 1 J=1,NIBP
K=IB(J)
IF(I.EQ.K) GO TO 8
1 CONTINUE
2 IF(NFLX.EQ.0) GO TO 4
DO 3 J=IS,IEND
K=IB(J)
IF(I.EQ.K) GO TO 7
3 CONTINUE
4 DO 5 J=IST,NBV
K=IB(J)
IF(I.EQ.K) GO TO 6
5 CONTINUE
NO=0
RETURN
6 NO=-1
RETURN
7 NO=1
RETURN
8 NO=1
RETURN
END

```

```

SUBROUTINE TLB(TLA9,NCHR,IXPTS,JX)
DIMENSION FRMT(3),TLAB(3)
JHALF=NCHR/2
IHAF=IXPTS/2
NSKP=JX+IHAF-JHALF
NC=10
ENCODE(16,100,FRMT)NSKP,NC
WRITE(6,FRMT)TLAB(1),TLAB(2),TLAB(3)
100 FORMAT(5H(1H , ,I2,4HX,3A,I2,1H))
RETURN
END

```

```

SUBROUTINE SCS(I1,I2,S,CS,DS)
COMMON/IX/X(200)
COMMON/IY/Y(200)
DX=X(I2)-X(I1)
DY=Y(I2)-Y(I1)
DS=(DX*DX+DY*DY)**.5
S=DY/DS
CS=DX/DS
RETURN
END

```

```

C SUBROUTINE MATRIX(DSHAPEX,DSHAPEY,K,NVRTX,NTRI,IFILE,MASL)
SUBROUTINE TO FORM GLOBAL MATRIX AND RIGHT HAND SIDE
DIMENSION DSHAPEX(1),DSHAPEY(1)
COMMON/IHEIGHT/N(200)
COMMON/ICCNST/CONST1,CONST2
COMMON/CUTOFF/NIBP,NFLX,NO,JNO
COMMON/IGRAD/DALPHAX,DALPHAY,DDEPTHX,DDEPTHY,DDELTA,DDELTA2,AREA
COMMON/INCRK/VALP(4500)
COMMON/INT/INTP(4500)
COMMON/IRHS/RHS(200)
COMMON/IIP/IP(3,350)
COMMON/HIND/TAUX,TAUY,CURL
NROW=NVRTX
DO 1 I=1,3
II=IP(I,K)
C
C IF(N(II).EQ.-1) GO TO 1
IF(N(II).EQ.1) GO TO 1
IF(NO.EQ.-1) GO TO 4
IF(IFILE)3,3,4
3 DO 2 J=1,3
JJ=IP(J,K)
CALL MNSRT(II,JJ,INTP,NB,NROW,MASL)
VALP(NB)=VALP(NB)+(+CCNST2*(DSHAPEX(I)*DSHAPEX(J)+DSHAPEY(I)*DSHAPEY(J))+1./3.*(DSHAPEY(J)*DDEPTHX-DSHAPEX(J)*DDEPTHY))*AREA
2 CONTINUE
4 CONTINUE
CHK=CONST1*(DALPHAY*DDEPTHX-DALPHAX*DDEPTHY)/3.
CHK1=CONST1*CONST2*(DSHAPEX(I)*DALPHAX+DSHAPEY(I)*DALPHAY)
RHS(II)=RHS(II)+(-CHK-CHK1-1./3.*CURL)*AREA
1 CONTINUE
900 FORMAT(*0*,*TRI.*,I3,5X,*VRTX.*,I5,5X,*JACOB.*,F10.4)
RETURN
END

```

```

103 CONTINUE
102 CONTINUE
  WRITE(6,200) I1,I2
200 FORMAT(*0*,*WE ARE LOST ALONG POINTS*,2I5,2X,*CAN NOT FIND BOUNDAR
  CY TRIANGLE IN MATRIX ASSEMBLY ROUTINE*)
  GO TO 101
C
C
  WE HAVE FOUND TRIANGLE, NOW TO GET GRADIENTS
C
104 DO 106 L=1,3
  M=IP(L,K)
  A(L,1)=X(M)
  A(L,2)=Y(M)
  A(L,3)=1.
106 CONTINUE
  CALL ALPHX(K,DALPHX,DALPHY,ALPHA,SA,ALPH)
  CALL ALPHX(K,DDELTX,DDELTY,DELTA,SD,ALPH)
  CALL SCS(I1,I2,S,CS,DS)
  HMEAN=(DEPTH(I1)+DEPTH(I2))/2.
  DDELTS=CS*DDELTX+S*DDELTY
  DALPHN=-S*DALPHX+CS*DALPHY
  DALPHS=CS*DALPHX+S*DALPHY
  TS=CS*TAUX+TAUY*S
C
  DO 107 L=1,3
  DO 108 M=1,3
108 B(M)=0.
  B(L)=1.
  CALL GRAD(B(1),B(2),B(3),DSHPX(L),DSHPY(L),CSHPE(L))
107 CONTINUE
C
C
  NOW ADD TO GLOBAL MATRIX
C
  II=I1
109 IF(NEHBV.GT.1) GO TO 111
  IF(IFILE)609,609,111
609 DO 112 L=1,3
  JJ=IP(L,K)
  CALL MNSRT(II,JJ,INTP,NB,NVRTX,MASL)
  DSHPN=-S*DSHPX(L)+CS*DSHPY(L)
  DSHPS=CS*DSHPX(L)+S*DSHPY(L)
  VALP(NB)=VALP(NB)-(CONST2*(DSHPN+DSHPS)-HMEAN*DSHPS)*DS/2.
112 CONTINUE
111 CONTINUE
C
C
  NOW ADD CONTRIBUTION TO RHS
C
  RHS(II)=RHS(II)-(CONST1*DDELTS-CONST1*CONST2*(DALPHN+DALPHS)-TS)*D
  CS/2.
  IF(II.EQ.I2) GO TO 101
  II=I2
  GO TO 109
101 CONTINUE

```

```
SUBROUTINE BC(NVRTX,NBV,IB,BV,MASL)
```

```
C  
C  
C  
C  
C  
C  
C
```

```
SUBROUTINE TO ADD ON BOUNDARY VALUE CONTRIEUTION
```

```
THE BOUNDARY ROWS HAVE ALREADY BEEN ZEROED DURING THE ASSEMBLY  
PROCESS. THEREFCRE WE PROCEED TO FILL THE RIGHT HAND SIDE  
VECTOR WITH THE BOUNDARY CONDITIONS AND SET THE DIAGNOL  
ELEMENTS TO ONE IF IT OCCURS IN A BOUNDARY ROW.
```

```
DIMENSION IB(1),BV(1)  
COMMON/CUTOFF/NIBP,NFLX,JJ1,JJ2  
COMMON/INT/INTP(4500)  
COMMON/IWORK/VALP(4500)  
COMMON/IRHS/RHS(200)  
NROW=NVRTX  
NSTP=NFLX+NIBP+1  
DO 10 K=NSTP,NBV  
J=IB(K)  
RHS(J)=BV(K)  
CALL MNSRT(J,J,INTP,NB,NROW,MASL)  
VALF(NB)=1.  
10 CONTINUE  
RETURN  
END
```

```
SUBROUTINE SETB(RHS,VALP)  
DIMENSION RHS(1),VALP(1)  
COMMON/INT/INTP(4500)  
COMMON/CUTCF/NIBP,NFLX,JJ1,JJ2  
COMMON/BCUND/IB(75),BV(75),NBV  
COMMON/NUMB/NVRTX,NTRI,IFILE,MASL,MEHBV  
IF(NIBP.EQ.0) GO TO 5  
KL=IB(1)  
RHS(KL)=BV(1)  
DO 1 I=1,NVRTX  
CALL MNSRT(KL,I,INTP,NB,NVRTX,MASL)  
VALF(NB)=0.  
IF(I.EQ.KL) VALF(NB)=1.  
1 CONTINUE  
5 ISTRT=NIBP+1  
I1=IB(ISTRT)  
RHS(I1)=BV(ISTRT)  
DO 7 I=1,NVRTX  
CALL MNSRT(I1,I,INTP,NB,NVRTX,MASL)  
VALF(NB)=0.  
IF(I1.EQ.I) VALF(NB)=1.  
7 CONTINUE  
RETURN  
END
```

```

SUBROUTINE BASS (VALP, RHS)
DIMENSION VALP(1), RHS(1)
DIMENSION DSHPX(3), DSHPY(3), CSHPE(3)
COMMON/ICCNST/CONST1, CONST2
COMMON/INT/INTP(4500)
COMMON/LSCOEF/SA(4), SD(4)
COMMON/IDELTA/DELTA(200)
COMMON/IALPHA/ALPHA(200)
COMMON/IDEPH/DEPTH(200)
COMMON/IY/Y(200)
COMMON/IIP/IP(3,350)
COMMON/IA/A(3,3)
COMMON/IB/B(3)
COMMON/IX/X(200)
COMMON/NUMB/NVRTX, NTRI, IFILE, MASL, NEWBV
COMMON/BOUND/IB(75), BV(75), NBV
COMMON/IALP/ALPH(3)
COMMON/WIND/TAUX, TAUY, CURL
COMMON/CUTOFF/NISP, NFLX, JJ1, JJ2

```

C
C
C
C

NOW IMPOSE THE NO FLUX BOUNDARY CONDITIONS.

BEGIN WITH ISLAND.

```

IF (NISP.EQ.0.AND.NFLX.EQ.0) RETURN
IF (NISP.EQ.0) GO TO 1
IST1=T=1
ISTCP=NIBP-1
GO TO 2
1 ISTART=1
  ISTCP=NFLX-1
  GO TO 2
3 ISTART=NIBP+1
  ISTCP=NIBP+NFLX-1
2 CONTINUE

```

C
C
C

NOW LOCATE BOUNDARY SIDE.

```

DO 101 I=ISTART,ISTOP
J=I+1
I1=IB(I)
I2=IB(J)

```

C
C
C

NOW LOCATE THE TRIANGLE WE ARE IN

```

DO 102 K=1,NTRI
KF=0
JF=0
DO 103 L=1,3
II=IP(L,K)
IF (II.EQ.I1) JF=L
IF (II.EQ.I2) KF=L
IF (KF.NE.0.AND.JF.NE.0) GO TO 104

```

```

SUBROUTINE SLVK(NROW,NCOL,ERROR,INTP,VALP)
C.....SOLUTION OF LINEAR SYSTEM AFTER QLUP DECOMPOSITION
C.....KNIUTH ORTHOGONAL LIST STORAGE SCHEME
C.....
C.....NROW IS NUMBER OF ROWS IN MATRIX
C.....NCOL IS NUMBER OF COLUMNS IN MATRIX
C.....ERROR IS AN INTEGER VARIABLE RETURNED AS 1
C.....IF AN ERROR OCCURS (ATTEMPTED DIVISION BY ZERO)
C.....OTHERWISE 2
C.....INTP IS AN INTEGER ARRAY OF LENGTH MSZ*((44/(NUMBER OF BITS
C.....PER INTEGER WORD)+1)...(SEE MINIT)
C.....VALP IS A REAL ARRAY OF LENGTH MSZ
C.....THE RIGHT HAND SIDE MUST BE STORED IN (VALP(I),I=1,2,...,NROW)
C.....AND THE SOLUTION IS RETURNED IN (VALP(I),I=NROW+1,NROW+2,...
C.....,NROW+NCOL)
C.....
C.....CAN ACCEPT A MATRIX WITH BOTH PERMUTED ROWS AND PERMUTED COLS
C.....**31APR75
      INTEGER INTP(1),ERROR
      REAL VALP(1)
      IP=IUP(INTP,1)
      IVS1=LEFT(INTP,NROW+1)+NROW
      VALP(IVS1)=VALP(IP)
      I=1
      80 IF(I-NCOL) 10,28,22
      10 I=I+1
      IP=IUP(INTP,I)
      IM1=I-1
      SUM=1.0
C.....ROW SCAN FROM COL 1 TO COL IM1
      ILFT=IP
      50 ILFT=LEFT(INTP,ILFT)
      KCOLS=ICOL(INTP,ILFT)
      IF(KCOLS) 60,60,30
      30 KCOLA=ICOL(INTP,KCOLS+NROW)
      IF(KCOLA-IM1) 70,70,50
      70 KCOLV=KCOLS+NROW
      SUM=SUM+VALP(ILFT)*VALP(KCOLV)
      GOTO 50
      60 IV=LEFT(INTP,I+NRCH)+NROW
      VALP(IV)=VALP(IP)-SUM
      GOTO 80
      20 IP=IUP(INTP,NCOL)
      NB=NBOX(IP,LEFT(INTP,NCOL+NROW),NROW,INTP)
      IF(NB) 100,100,110
      100 ERROR=1
      RETURN
      110 NV=LEFT(INTP,NROW+NCOL)+NROW
      VALP(NV)=VALP(NV)/VALP(NB)
C.....COLUMN SCAN FROM ROW NCOL-1 TO ROW 1
      I=NCOL
      170 IF(I-1) 150,150,160
      160 I=I-1

      IF(NIBP.EQ.0) GO TO 201
      J=NIBP-1
      IF(ISTOP.EQ.J) GO TO 3
      201 CALL SETB(RHS,VALP)
      RETURN
      END

```

```

SUBROUTINE DCPK(NROW,NCOL,SING,RANK,FILL,SMALL,INTP,VALP,MASL)
C.....QLUP DECOMPOSITION OF A REAL MATRIX
C.....KNUTH ORTHOGONAL LIST STORAGE
C.....
C.....NROW IS NUMBER OF ROWS IN MATRIX
C.....NCOL IS NUMBER OF COLUMNS IN MATRIX
C.....ROW SCALE FACTORS ARE STORED IN ROW BASE VALUES TEMPORARILY
C.....SING IS AN INTEGER VARIABLE RETURNING 1 IF MATRIX IS SINGULAR
C.....MEANING THAT RANK IS LESS THAN NCOL ... SING RETURNS 2 OTHERWISE
C.....RANK IS AN INTEGER VARIABLE RETURNING THE ROW RANK OF THE MATR
C.....FILL IS AN INTEGER VARIABLE RETURNING THE NUMBER OF ORIGINALLY
C.....ZERO MATRIX ELEMENTS THAT BECAME NONZERO DURING DECOMPOSITION
C.....MINUS THE NUMBER OF INITIALLY NONZERO ELEMENTS THAT BECAME
C.....ZERO DURING THE DECOMPOSITION PROCESS
C.....SMALL IS A REAL CONSTANT THAT SPECIFIES THE SMALLEST ABSOLUTE
C.....VALUE OF AN ELEMENT RELATIVE TO THE LARGEST ABSOLUTE VALUE
C.....OF ANY ELEMENT IN ITS ROW BEFORE DECOMPOSITION (THE ROW NORM)
C.....THAT WILL BE REPRESENTED BY MATRIX STORAGE ELEMENT
C.....INTP IS AN INTEGER ARRAY OF LENGTH MSZ*(44/(INTEGER WORD LENGT
C.....IN BITS))+1....(SEE MINIT SUBROUTINE)
C.....MASL IS A VARIABLE INITIALIZED BY MINIT
C.....ROWS AND COLUMNS ARE PERMUTED VIA ROW+COL BASES
C.....
C.....**31MAR76
C.....
      REAL VALP(1)
      INTEGER INTP(1),SING,RANK,FILL
      FILL=0
C.....FIND SCALE FOR EACH ROW =1.0/(MAX ABS VALUE IN ROW)
      I=0
      90 IF(I-NROW) 10,20,20
      10 I=I+1
      ROWNR=0.0
C.....START ROW I SCAN
      ILFT=I
      50 ILFT=LEFT(INTP,ILFT)
      IF(ICCL(INTP,ILFT)) 30,30,40
      40 ABV=ABS(VALP(ILFT))
      IF(ABV-ROWNR) 50,50,60
      60 ROWNR=ABV
      GOTC 50
      30 IF(ROWNR-SMALL) 70,70,80
      70 VALP(I)=0.0
      GOTC 90
      80 VALP(I)=1.0/ROWNR
      GOTO 90
      20 NM1=NCOL-1
C.....START COLUMN SCAN
      K=0
      240 IF(K-NM1) 100,110,110
      100 K=K+1
C.....SCAN LOWER RIGHT SUBMATRIX FOR COLUMN WITH LEAST NUMBER OF
C.....NONZERO ELEMENTS BYT AT LEAST ONE

```

```

SUBROUTINE PACK(I,J,VALP,VAL,INTP,NROW,MASL)
DIMENSION VALP(1),INTP(1)
CALL MNSRT(I,J,INTP,NB,NROW,MASL)
IF(MASL.EQ.-1) GC TC 10
VALP(NB)=VAL
RETURN
10 WRITE(6,5)I,J
5 FORMAT(*0*,*OVERFLOW OF VALP AT ENTRY*,I5,*,*,I3)
RETURN
END

```

```

GOTO 650
C.....TOO SMALL SO DELETE
690 CALL MDLET(IP,ICJRS,NROW,INTP,MASL)
    FILL=FILL-1
    GOTO 650
C.....NO MATCH SO FILL IM ONE
660 VAL=EM*VALP(JP)
C.....UNLESS TOO SMALL TO STORE
    IF(ABS(VAL)*SCALE-SMALL) 650,650,710
710 FILL=FILL+1
    CALL MNSRT(IP,ICJFS,INTP,NB,NROW,MASL)
C.....DETECT MEMORU OVERFLOW
    IF(NB) 720,720,730
730 VALF(NB)=VAL
    GOTO 650
C.....MEMORY OVERFLOW
C.....USER DETECTS THIS CONDITION IN CALLING PRIGRAM
C.....BY TESTING WHETHER MASL .LE. 0
720 K=1
    GOTO 180
110 IF(NBOX(IUP(INTP,NCCL),LEFT(INTP,NCOL+NROW),NROW,INTP))500,500,510
C.....RANK IS NCOL-1 IF DIAGONAL IS ZERO
500 K=NCCL
    GOTO 180
510 RANK=NCCL
    SING=2
    RETURN
    END

```

```

IP=IUP(INTP,I)
IP1=I+1
SUM=0.0
C.....ROW SACN FROM COL IP1 TO COL NCOL
    ILFT=IP
200 ILFT=LEFT(INTP,ILFT)
    KCOLS=ICOL(INTP,ILFT)
    IF(KCOLS) 180,180,190
190 KCOLA=ICOL(INTP,KCOLS+NROW)
    IF(KCOLA-IP1) 200,310,320
320 IF(KCOLA-NCOL) 310,310,200
310 KCOLV=KCOLS+NROW
    SUM=SUM+VALF(ILFT)*VALP(KCOLV)
    GOTO 200
180 NB=NBOX(IP,LEFT(INTP,I+NROW),NROW,INTP)
    IF(NB) 100,100,220
220 IV=LEFT(INTP,I+NROW)+NROW
    VALP(IV)=(VALF(IV)-SUM)/VALP(NB)
    GOTO 170
150 ERRCR=2
    RETURN
    END

```

```

SUBROUTINE SUP(INTP,NBOX,IUP)
INTEGER INTP(1)
CALL FAC(INTP(NBOX),20,35,IUP)
RETURN
END

```

```

      NEMAX=NCOL+1
      NPIV=0
      KA=K-1
820  IF(KA-NCOL) 800,810,810
800  KA=KA+1
      CALL FVSL1(KA,NROW,NCCL,INTP,VALP,IPIV,NE)
      IF(NE) 820,820,830
830  IF(NE-NEMAX) 840,820,820
840  NPIV=IPIV
      NEMAX=NE
      GOTO 820
810  IF(NPIV) 180,180,190
C.....NO PIVOT ON K-TH COLUMN
180  RANK=K-1
      SING=1
      RETURN
C.....PIVOT ON IPIV
190  KP=IRCH(INTP,NPIV)
      KC=ICOL(INTP,NPIV)
C.....ROW INTERCHANGE IF PIVOT NOT IN ROW K
      CALL HRXA(K,IROW(INTP,KP),NROW,INTP)
C.....COLUMN INTERCHANGE IF PIVOT NOT IN COLUMN K
      CALL MCXA(K,ICOL(INTP,KC+NROW),NROW,INTP)
      PIVCT=VALP(NPIV)
      I=K
230  IF(I-NROW) 220,240,240
220  I=I+1
      IP=I+(INTP,I)
      NB=NEOX(IP,LEFT(INTP,K+NROW),NROW,INTP)
      IF(NB) 230,230,250
250  EM=-VALP(NB)/PIVOT
      VALP(NB)=-EM
C.....START SCAN OF PIVOT ROW IN STORED ORDER
      JP=KP
      SKALE=VALP(IP)
650  JP=LEFT(INTP,JP)
      ICJPS=ICOL(INTP,JP)
      IF(ICJPS) 230,230,610
610  ICJPA=ICOL(INTP,ICJPS+NROW)
      IF(ICJPA-K) 650,650,630
630  IF(ICJPA-NCOL) 640,640,650
C.....TRY TO FIND ACTUAL SAME COLUMN IN WORK ROW
640  JR=IP
600  JR=LEFT(INTP,JR)
      ICJRS=ICOL(INTP,JR)
      IF(ICJRS) 660,660,670
670  ICJRA=ICOL(INTP,ICJRS+NROW)
      IF(ICJRA-ICJPA) 600,680,600
C.....FIND MATCH
680  VAL=VALP(JR)+EM*VALP(JP)
      IF(ABS(VAL)*SKALE-SMALL) 690,690,700
C.....STORE RESULT
700  VALP(JR)=VAL

```

```

SUBROUTINE MNSRT(KROW,KCOL,INTP,NB,NROW,MASL)
C.....INSERTS A MATRIX STORAGE ELEMENT AT ROW KROW AND COLUMN KCOL
C.....UNLESS THERE IS ALREADY AN ELEMENT ALLOCATED IN WHICH CASE
C.....THAT ELEMENT NUMBER IS RETURNED IN NB
C.....INTP IS AN INTEGER ARRAY
C.....(SEE MINIT)
C.....NB IS THE NEW ELEMENT NUMBER
C.....NROW IS THE NUMBER OF ROWS IN THE MATRIX
C.....MASL IS AN INTEGER VARIABLE INITIALIZED BY MINIT
C.....MASL=-1 IMPLIES OVERFLOW IN WHICH CASE NB
C.....RETURNS -1
C.....
      INTEGER INTP(1)
      IRGT=KROW
      30 ILFT=LEFT(INTP,IRGT)
         IF(ICCL(INTP,ILFT)-KCOL) 50,20,90
      90 IRGT=ILFT
         GOTO 30
      50 IBLW=NROW+KCOL
      150 IABV=IUP(INTP,IBLW)
         IF(IRCH(INTP,IABV)-KROW) 130,20,120
      120 IBLW=IABV
         GOTO 150
      130 IF(MASL) 60,60,70
      60 NB=-1
         RETURN
      70 NB=MCOL
         MASL=LEFT(INTP,MASL)
         CALL SLEFT(INTP,IRGT,NB)
         CALL SLEFT(INTP,NB,ILFT)
         CALL SUP(INTP,IBLW,NB)
         CALL SUP(INTP,NB,IABV)
         CALL SROW(INTP,NB,KROW)
         CALL SCOL(INTP,NB,KCOL)
         RETURN
      20 NB=ILFT
         RETURN
      END

```

```

SUBROUTINE SCOL(INTP,NBOX,ICCL)
INTEGER INTP(1)
CALL PAC(INTP(NBOX),48,59,ICCL)
RETURN
END

```

```

SUBROUTINE SRCH(INTP,NBOX,IRGW)
INTEGER INTP(1)
CALL PAC(INTP(NBOX),36,47,IROW)
RETURN
END

```

```

FUNCTION LEFT(INTP,NBCX)
INTEGER INTP(1)
CALL UNPAC(INTP(NBOX),4,19,LEFT)
RETURN
END

```

```

FUNCTION IUP(INTP,NBOX)
INTEGER INTP(1)
CALL UNPAC(INTP(NBOX),20,35,IUP)
RETURN
END

```

```

FUNCTION ICCL(INTP,NBOX)
INTEGER INTP(1)
CALL UNPAC(INTP(NBOX),48,59,ICOL)
RETURN
END

```

```

FUNCTION IRCW(INTP,NBOX)
INTEGER INTP(1)
CALL UNPAC(INTP(NBOX),36,47,IROW)
RETURN
END

```

```

SUBROUTINE MDLET(KROW,KCOL,NROW,INTP,MASL)
C.....DELETES MATRIX STORAGE ELEMENT AT IROW,ICCL IF ONE EXISTS
C.....NROW IS THE NUMBER OF ROWS IN THE MATRIX
C.....INTP IS AN INTEGER ARRAY (SEE MINIT)
C.....MASL IS AN INTEGER VARIABLE INITIALIZED BY MINIT
C.....*****020176*****
C.....
INTEGER INTP(1)
IABV0=NROW+KCOL
ILFT0=KROW
30 ILFT=LEFT(INTP,ILFT0)
IC=ICCL(INTP,ILFT)
IF(IC) 10,10,20
20 IF(IC-KCOL) 70,40,70
70 ILFT0=ILFT
GOTO 30
40 IABV=IUP(INTP,IABV0)
IR=IROW(INTP,IABV)
IF(IR) 10,10,50
50 IF(IR-KROW) 80,60,80
80 IABV0=IABV
GOTO 40
60 ILFT1=LEFT(INTP,ILFT)
CALL SLEFT(INTP,ILFT0,ILFT1)
IABV1=IUP(INTP,IABV)
CALL SUP(INTP,IABV0,IABV1)
CALL SLEFT(INTP,IABV,MASL)
MASL=IABV
10 RETURN
END

```

```

FUNCTION IRCW(INTP,NBOX)
INTEGER INTP(1)
CALL UNPAC(INTP(NBOX),36,47,IROW)
RETURN
END

```

```

      FUNCTION NBOX(KROW,KCOL,NROW,INTP)
C.....GETS MATRIX STORAGE ELEMENT NUMBER IF ONE EXISTS FOR ROW KROW
C.....AND COLUMN KCOL
C.....NROW IS HE NUMBER OF ROWS IN THE MATRIX
C.....INTP IS AN INTEGER ARRAY (SEE MINIT)
C.....NBOX RETURNS THE ELEMENT NUMBER UNLESS ONE DOESNT EXIST
C.....IN WHICH CASE IT RETURNS -1
C.....
      INTEGER INTP(1)
      ILFT=KROW
30  ILFT=LEFT(INTP,ILFT)
      IF(ICOL(INTP,ILFT)-KCOL) 10,20,30
10  NBOX=-1
      RETURN
20  NBOX=ILFT
      RETURN
      END

```

```

      SUBROUTINE SLEFT(INTP,NBOX,LEFT)
      INTEGER INTP(1)
      CALL FAC(INTP(NBOX),4,19,LEFT)
      RETURN
      END

```

```

      SUBROUTINE MRXA(KRA,JRA,NROW,INTP)
      INTEGER INTP(1)
      IF(KRA-JRA) 10,20,10
20  RETURN
10  KRS=IUP(INTP,KRA)
      JRS=IUP(INTP,JRA)
      CALL SUP(INTP,KRA,JRS)
      CALL SUP(INTP,JRA,KRS)
      CALL SROW(INTP,JRS,KRA)
      CALL SROW(INTP,KRS,JRA)
      RETURN
      END

```



```

SUBROUTINE MCXA(KCA,JCA,NROW,INTP)
INTEGER INTP(1)
IF(KCA-JCA) 10,20,10
20 RETURN
10 KCS=LEFT(INTP,KCA+NROW)
   JCS=LEFT(INTP,JCA+NROW)
   CALL SLEFT(INTP,JCA+NROW,KCS)
   CALL SLEFT(INTP,KCA+NROW,JCS)
   CALL SCCL(INTP,KCS+NROW,JCA)
   CALL SCCL(INTP,JCS+NROW,KCA)
   RETURN
END

```

```

SUBROUTINE SLCPE(X1,Y1,X2,Y2,SLOP,DIST)
DY=Y2-Y1
DX=X2-X1
IF(DX.EQ.0)DX=.0000001
SLCP=DY/DX
DIST=((DX*DX)+(DY*DY))**.5
RETURN
END

```

```

SUBROUTINE FINDSID(VAL1,VAL2,VAL3,VAL,IP1,IP2,IFLG)
DIMENSION IP1(2),IP2(2)
IFLG=0
J=1
IF(VAL1.EQ.VAL) GO TO 11
IF(VAL2.EQ.VAL) GO TO 12
IF(VAL3.EQ.VAL) GO TO 13
6 IF(VAL.LT.VAL1.AND.VAL.GT.VAL2) GO TO 1
IF(VAL.GT.VAL1.AND.VAL.LT.VAL2) GO TO 1
7 IF(VAL.LT.VAL2.AND.VAL.GT.VAL3) GO TO 2
IF(VAL.GT.VAL2.AND.VAL.LT.VAL3) GO TO 2
8 IF(VAL.LT.VAL1.AND.VAL.GT.VAL3) GO TO 3
IF(VAL.GT.VAL1.AND.VAL.LT.VAL3) GO TO 3
IF(IFLG.EQ.1) GO TO 4
WRITE(6,5)
5 FORMAT(*1*,*WE HAVE SCREWED UP IN FINDING THE TRIANGLE SIDE*)
GO TO 4
11 IP1(1)=1
   IP2(1)=2
   J=2
   IFLG=1
   GO TO 7
12 IP1(1)=1
   IP2(1)=2
   J=2
   IFLG=1
   GO TO 6
13 IP1(1)=2
   IP2(1)=3
   J=2
   IFLG=1
   GO TO 6
1 CONTINUE
IP1(J)=1
IP2(J)=2
IF(J.GT.1) GO TO 4
J=J+1
IFLG=0
GO TO 7
2 IP1(J)=2
   IP2(J)=3
   IF(J.GT.1) GO TO 4

```

```

J=J+1
IFLG=0
GO TO 8
3 IP1(J)=1
  IP2(J)=3
  IFLG=0
4 RETURN
END

```

```

SUBROUTINE SWITCH(A,B)
C=A
A=B
B=C
RETURN
END

```

```

SUBROUTINE FINDPT(VAL1,VAL2,VAL,X1,Y1,X2,Y2,X,Y,SLPE)
ISWITCH=0
IF(X2.GT.X1) GO TO 1
ISWITCH=1
CALL SWITCH(VAL1,VAL2)
CALL SWITCH(X1,X2)
CALL SWITCH(Y1,Y2)
1 CONTINUE
DIST12=VAL1-VAL2
DIST=VAL1-VAL
RATIO=DIST/DIST12
DIST12=X1-X2
DIST=Y1-Y2
DIST12=(DIST12**2+DIST**2)**.5
DIST=RATIO*DIST12
IF(X1.EQ.X2) GO TO 11
ANGLE=ATAN(SLPE)
DX=DIST*COS(ANGLE)
DY=DX*SLPE
GO TO 12
11 CONTINUE
DX=0.
IF(Y1.GT.Y2) DIST=-DIST
DY=DIST
12 CONTINUE
X=X1+DX
Y=Y1+DY
IF(ISWITCH.EQ.0) GO TO 2
CALL SWITCH(VAL1,VAL2)
CALL SWITCH(X1,X2)
CALL SWITCH(Y1,Y2)
2 RETURN
END

```

```

SUBROUTINE CHECK(VAL1,VAL2,VAL3,VAL,ICLK,IP1,IP2)
ICLK=1
IF(VAL1.EQ.VAL2.AND.VAL1.EQ.VAL) GO TO 1
IF(VAL2.EQ.VAL3.AND.VAL2.EQ.VAL) GO TO 2
IF(VAL1.EQ.VAL3.AND.VAL1.EQ.VAL) GO TO 3
ICLK=0
IP1=0
IP2=0
GO TO 4
1 IP1=1
  IP2=2
  GO TO 4
2 IP1=2
  IP2=3
  GO TO 4
3 IP1=1
  IP2=3
4 RETURN
END

```

```

SUBROUTINE KONTRI(X,Y,IP,CON,NTRI,NVRTX,NCON,VALUE,NPEN)
DIMENSION X(1),Y(1),IP(3,1),CON(1),VALUE(1),X1(2),Y1(2),II(2),JJ
(2),AX(2),AY(2)

```

```

C
C THIS IS A LINEAR CONTOURING ROUTINE USING THE TRIANGLES
C X AND Y ARE COORDINATES OF THE TRIANGLE VERTICES
C IP IS THE MATRIX(3 X NTRI) CONTAINING THE GLOBAL LABELS OF EACH
C TRIANGLE VERTEX
C CON IS THE VECTOR CONTAINING THE CONTOUR INTERVALS.
C NTRI IS THE NUMBER OF TRIANGLES
C NVRTX IS THE NUMBER OF GLOBAL POINTS
C NCON IS THE NUMBER OF CONTOURS YOU HAVE. IF THIS IS LESS THAN
C ZERO, THEN YOU ARE READING IN THE CONTOUR INTERVALS WITH
C THE NUMBER OF INTERVALS EQUAL TO ABS(NCON). IF NCON IS
C POSITIVE, THEN THE PROGRAM WILL GENERATE THE CONTOUR INTERVALS
C BY DIVIDING THE RANGE OF VALUES EVENLY INTO NCON INTERVALS.
C VALUE IS THE VECTOR CONTAINING THE VALUES TO BE CONTOURED AT EACH
C VERTEX
C NPEN IS THE PEN NUMBER YOU WANT TO USE FOR CONTOURING
CALL STPEN(NPEN)
IF(NCON.LT.0) GO TO 3
VMAX=0.
VMIN=1000000.
DO 1 I=1,NVRTX
VMAX=AMAX1(VMAX,VALUE(I))
1 VMIN=AMIN1(VMIN,VALUE(I))
CALL CONINT(VMAX,VMIN,NCON,CON)
3 NCON=IABS(NCON)
N=1
11 I=IP(1,N)
J=IP(2,N)
K=IP(3,N)
ALARG=AMAX1(VALUE(I),VALUE(J),VALUE(K))
ASHAL=AMIN1(VALUE(I),VALUE(J),VALUE(K))
IFIR=1
DO 6 L=1,NCON
IF(CON(L).LT.ASHAL.CR.CON(L).GT.ALARG) GO TO 6
IF(IFIR.GT.1) GO TO 4
CALL SLCRE(X(I),Y(I),X(J),Y(J),S12,DIS12)
CALL SLCPE(X(J),Y(J),X(K),Y(K),S23,DIS23)
CALL SLCPE(X(I),Y(I),X(K),Y(K),S13,DIS13)
IFIR=2
4 CALL CHECK(VALUE(I),VALUE(J),VALUE(K),CON(L),ICLK,II,JJ)
IF(ICLK.EQ.0) GO TO 5
II=IP(II,N)
JJ=IP(JJ,N)
X1(1)=X(II)
Y1(1)=Y(II)
X1(2)=X(JJ)
Y1(2)=Y(JJ)
CALL STNPTS(2)
CALL SLLILI(X1,Y1)
GO TO 6

```

```

SUBROUTINE CONINT(VMAX,VMIN,INT,C)
DIMENSION C(1)
INT=INT+1
DIFF=VMAX-VMIN
AINT=DIFF/FLOAT(INT)
INT=INT-1
DO 1 I=1,INT
C(I)=VMIN+FLOAT(I)*AINT
1 CONTINUE
WRITE(6,2)
2 FORMAT(*1*,*CONTOUR INTERVALS ARE*)
DO 4 I=1,INT
4 WRITE(6,3)I,C(I)
3 FORMAT(*0*,I5,3X,F10.2)
RETURN
END

```

```

SUBROUTINE SETUP(ISTART,IPRINT,XSIZE,YSIZE,TLABEL,IAXIS,XMIN,XMAX,
YMIN,YMAX,NDIVX,NDIVY,XSTRT,YSTRT)
DIMENSION TLABEL(3)
THIS IS A GENERAL SUBROUTINE TO SETUP AN NPS PROGRAM
C ISTART IS ZERO IF THIS IS THE FIRST TIME YOU CALL THE NPS ROUTINES
C IF YOU HAVE ALREADY CALLED PRNTO OR STCCON PREVIOUSLY, ISTART=1
C IPRINT=0 WILL CALL PRINTER PLOT
C IPRINT=1 WILL CALL STCCON
C SXIZE IS THE LENGHT OF PLOT IN INCHES IN X-DIRECTION
C YSIZE IS LENGHT OF PLOT IN INCHES IN Y-DIRECTION
C TLABEL IS ENCCDED IN MAIN PROGRAM WITH 30 SPACES AND DIMENSION 3.
C IT WILL BE THE TOP LABEL OF PLOT.
C IF YOU WANT AXIS DRAWN UP AND LABELED, IAXIS IS 1, OTHERWISE IT
C IS ZERO.
C XMIN,YMIN,XMAX,YMAX, ARE THE MAXIMUM AND MINIMUM X AND Y VALUES
C TO BE USED TO LABEL THE AXIS AND SET UP THE SUBJECT SPACE.
C NDIVX AND NDIVY ARE THE NUMBER OF DIVISIONS YOU WANT THE AXIS
C LABELING TO SHOW
C
IF(ISTART.EQ.1) GO TO 2
IF(IPRINT.EQ.1) GO TO 1
CALL PRNTO
GO TO 2
1 CALL STCCON(48HCALCOMP PLOT OF WHATEVER NEEDS TO BE PLOTTED
2 CONTINUE
CALL STPEN(1)
XADD=XSTRT+XSIZE
YADD=YSTRT+YSIZE
CALL STS2OB(XSTRT,XADD,YSTRT,YADD)
CALL STSUBJ(XMIN,XMAX,YMIN,YMAX)
CALL STNDIV(1,1)
CALL GOLILI
HEIGHT=XSIZE/30.
IF(HEIGHT.GT..49) HEIGHT=.49
CALL STCHSZ(HEIGHT)
CALL STNCHR(30)
CALL STLNR(0.)
CALL TITLET(TLABEL)
CALL AXLILI
IF(IAXIS.EQ.0) GO TO 3
CALL STNDIV(NDIVX,NDIVY)
HEIGHT=HEIGHT/2.
CALL STCHSZ(HEIGHT)
CALL STNDEC(1)
CALL NODLIB
CALL NODLIL
3 RETURN
END

```

```

5 CALL FINDSID(VALUE(I),VALUE(J),VALUE(K),CON(L),III,JJJ,IFLG)
IF(IFLG.EQ.1) GO TO 6
IA=III(1)
II=III(2)
JA=JJJ(1)
JJ=JJJ(2)
IF(IA.EQ.1.AND.JA.EQ.2) SLP1=S12
IF(IA.EQ.2.AND.JA.EQ.1) SLP1=S12
IF(II.EQ.1.AND.JJ.EQ.2) SLP2=S12
IF(II.EQ.2.AND.JJ.EQ.1) SLP2=S12
IF(IA.EQ.1.AND.JA.EQ.3) SLP1=S13
IF(IA.EQ.3.AND.JA.EQ.1) SLP1=S13
IF(II.EQ.1.AND.JJ.EQ.3) SLP2=S13
IF(II.EQ.3.AND.JJ.EQ.1) SLP2=S13
IF(IA.EQ.2.AND.JA.EQ.3) SLP1=S23
IF(IA.EQ.3.AND.JA.EQ.2) SLP1=S23
IF(II.EQ.2.AND.JJ.EQ.3) SLP2=S23
IF(II.EQ.3.AND.JJ.EQ.2) SLP2=S23
IA=IP(IA,N)
II=IP(II,N)
JA=IP(JA,N)
JJ=IP(JJ,N)
CALL FINDPT(VALUE(IA),VALUE(JA),CON(L),X(IA),Y(IA),X(JA),Y(JA),X1(
V1),Y1(1),SLP1)
CALL FINDPT(VALUE(II),VALUE(JJ),CON(L),X(II),Y(II),X(JJ),Y(JJ),X1(
V2),Y1(2),SLP2)
CALL STNPTS(2)
CALL SLLILI(X1,Y1)
6 CONTINUE
N=N+1
IF(N.GT.NTRI) GO TO 7
GO TO 11
7 RETURN
END

```

```

SUBROUTINE VRTXLB(X,Y,VAL,NDEC,NVRTX,HEIGHT,NPEN)
DIMENSION X(1),Y(1),VAL(1)
THIS SUBROUTINE LABELS THE POINTS
THE COORDIANATES OF THE POINTS ARE GIVEN BY X AND Y
THE VALUE AT EACH POINT IS GIVEN BY VAL
C
C
C
CALL STPEK(NPEN)
CALL STCHSZ(HEIGHT)
CALL STLNR(0)
CALL STNDEC(NDEC)
DO 1 I=1,NVRTX
CALL STLNST(X(I),Y(I))
CALL DECVAL(VAL(I))
1 CONTINUE
RETURN
END

```

```

SUBROUTINE DRTRI(X,Y,IP,NTRI,NPEN,N)
DIMENSION X(1),Y(1),IP(3,1),N(1),ZXX(2),ZYY(2)
C
C SUBROUTINE TO DRAW SUBROUTINES
C X IS X-ARRAY
C Y IS Y-ARRAY
C IP IS A THREE BY NTRI MATRIX GIVING THE GLOBAL LABELS OF EACH VRTX
C N IS A STORAGE ARRAY MAKING SURE WE DONT'T DRAW A LINE TWICE
C N SHOULD BE LARGER THAN THE AMOUNT OF LINES YOU HAVE
C NPEN IS THE PEN NUMBER YOU WANT TO USE
C
CALL STPEN(NPEN)
N(1)=0
M=1
LL=0
DO 1 I=1,NTRI
IX=1
IY=2
2 II=IP(IX,I)
IJ=IP(IY,I)
ZXX(1)=X(II)
ZYY(1)=Y(II)
ZXX(2)=X(IJ)
ZYY(2)=Y(IJ)
ICHECK=II*II+II+IJ*IJ+IJ+II*II+IJ*IJ+II+IJ
DO 4 L=1,M
IF(ICHECK.EQ.N(L)) GO TO 6
4 CONTINUE
M=M+1
IF(M.LT.301) GO TO 10
M=300
LL=LL+1
IF(LL.GT.300) LL=1
N(LL)=ICHECK
GO TO 11
10 CONTINUE
N(M)=ICHECK
11 CONTINUE
CALL STNPTS(2)
)4(RTXITS LLAC
C
CALL STTXTR(1)
CALL SLLILI(ZXX,ZYY)
6 IF(IY.EQ.3) GO TO 8
IY=3
GO TO 2
8 IF(IX.EQ.2) GO TO 1
IX=2
GO TO 2
1 CONTINUE
RETURN
END

```

```

SUBROUTINE DYEGLAN(BRT,BRC,CURL,BFRIC,CONST1)
COMMON/IGR/O/DALPHAX,DALPHAY,DDEPTHX,DDEPTHY,DEX,GEY,AREA
BRT=- (DEY*DDEPTHX-DEX*DDEPTHY)
BRC=- (DALPHAY*DDEPTHX-DALPHAX*DDEPTHY)*CONST1
BFRIC=-BRT-BRC-CURL
RETURN
END

```

```

SUBROUTINE TRILABL(X,Y,IP,NTRI,HEIGHT,NPEN)
DIMENSION X(1),Y(1),IP(3,1)

```

C
C
C
C
C
C
C

```

THIS SUBROUTINE LABELS THE TRIANGLES
X AND Y ARE RESPECTIVE COORDINATES
IP IS THE 3 X NTRI MATRIX CONTAINING THE GLOBAL LABELS OF THE VRTX
NTRI IS THE NUMBER OF TRIANGLES
HEIGHT IS THE HEIGHT OF THE NUMBERS IN INCHES
NPEN IS THE PEN NUMBER

```

```

CALL STPEN(NPEN)
CALL STCHSZ(HEIGHT)
DO 1 I=1,NTRI
  II=IP(1,I)
  IJ=IP(2,I)
  IK=IP(3,I)
  EX=(X(II)+X(IJ)+X(IK))/3.
  EY=(Y(II)+Y(IJ)+Y(IK))/3.
  XSHIFT=(HEIGHT/4.)*1.25
  YSHIFT=(HEIGHT/7.)*1.5
  EX=EX-XSHIFT
  EY=EY-YSHIFT
  CALL STNDEC(0)
  CALL STLNST(EX,EY)
  CALL DECVAL(FLOAT(I))
1 CONTINUE
RETURN
END

```

```

SUBROUTINE BAROT(U,V,TOT)
COMMON/IGRAD/DALPHAX,DALPHAY,DDEPTHX,DDEPTHY,DEX,DEY,AREA
COMMON/SCALES/USCALE,OSCALE,ALSCALE,G,E,Q,GAMMA,FO,EDDY
U=-DEY*USCALE
V=DEX*USCALE
U=U*100.
V=V*100.
TOT=(U*U+V*V)**.5
RETURN
END

```

```

SUBROUTINE EKMAN(U,V,TOT)
COMMON/WIND/TX,TY,CURL
COMMON/SCALES/USCALE,HSCALE,ALSCALE,G,E,Q,GAMMA,FO,EDDY
C=(EDDY*Q*FO)**(-.5)
U=C*(TX+TY)*USCALE*FO*HSCALE*Q
V=C*(-TX+TY)*USCALE*FO*HSCALE*Q
U=U*10000.
V=V*10000.
TOT=(U*U+V*V)**.5
RETURN
END

```

```

SUBROUTINE BOTT(U,V,TOT)
COMMON/IGRAC/DALPHAX,DALPHAY,DDEPTHX,DDEPTHY,DEX,DEY,C
COMMON/SCALES/USCALE,OSCALE,ALSCALE,G,E,Q,GAMMA,FO,EDDY
C=G/(FO*Q)
U=-C*(DALPHAY*E*OSCALE+DEY*FO*USCALE*Q*ALSCALE/G)/ALSCALE
V=C*(DALPHAX*E*OSCALE+DEX*FO*USCALE*Q*ALSCALE/G)/ALSCALE
U=U*100.
V=V*100.
TOT=(U*U+V*V)**.5
RETURN
END

```

```

SUBROUTINE SURF(UE,VE,UB,VB,U,V,TOT)
U=UE+US
V=VE+VB
TOT=(U*U+V*V)**.5
RETURN
END

```

```

* BITS I - J OF A ARE EXTRACTED
* IF I GT 5, N=60-(I-J-1)
* BITS I - 59, 0 - J OF A ARE EXTRACTED
* BIT J OF A ALWAYS GOES TO BIT 59 OF B
*

```

J. J. THOMAS 4/7/75

```

ENTRY UNPAC
VFD 42/0LUNPAC
IFEQ *F,2
VFD 18/UNPAC FTH ARGUMENT LINKAGE
UNPAC BSSZ 1
SB7 1 B7 = 1
SA2 A1+B7 GET ADDRESSES OF 1 - 9 IN X1 - X4
SA3 A2+B7
SA4 A3+B7
R MICRC 1,1,$X5
ELSE
IFNE *F,1,1
ERR NOT CALLED BY RUN OR FTH
VFD 18/4 RUN 2.3 ARGUMENT LINKAGE
UNPAC BSSZ 1
R MICRO 1,1,$B3
ENDIF
SA2 VRV.2 X2 = I
SA3 VRV.3 X3 = J
IX5 X3-X2 FIGURE NO. BITS - 1 TO EXTRACT FROM A
PL X5,J1
SX5 X5+60
J1 SB6 X2-60
SB5 X3+1
SB7 X5
MX0 1 MAKE MASK OF CORRECT LENGTH
SA1 VRV.1 X1 = A
AX0 B7
LX0 -B6 ALIGN MASK WITH CORRECT BITS OF A
BX6 X0*X1 EXTRACT BITS FROM A
LX6 B5 RIGHT-JUSTIFY THEM
SA6 VRV.4 STORE IN B
EQ UNPAC EXIT
END

```

```

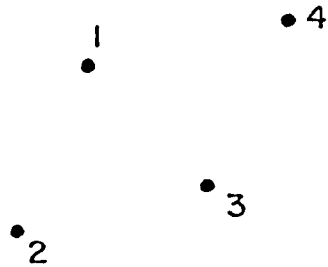
IDENT PAC CALL PAC(I,I,J,B)
* PACS THE N RIGHTMOST BITS OF B INTO A
* BITS ARE NUMBERED LEFT TO RIGHT FROM 0 - 59
* IF I LE J, N=J-I+1
* DESTINATION IS BITS I - J OF A
* IF I GT J, N=60-(I-J-1)
* DESTINATION IS BITS I - 59, 0 - J OF A
* BIT 59 OF B ALWAYS GOES TO BIT J OF A
*
J. J. THOMAS 4/7/75

ENTRY PAC
VFD 42/0LPAC
IFEQ *F,2
VFD 18/PAC FTN ARGUMENT LINKAGE
PAC BSSZ 1
SB7 1 B7 = 1 (CONSTANT)
SA2 A1+B7 GET ADDRESSES OF A - B IN X1 - X4
SA3 A2+B7
SA4 A3+B7
R MICRO 1,1,5X5
ELSE
IFNE *F,1,1
ERR NOT CALLED BY RUN OR FTN
VFD 18/4 RUN 2,3 ARGUMENT LINKAGE
PAC BSSZ 1
SB7 1 B7 = 1 (CONSTANT)
R MICRO 1,1,33?
ENDIF
SA1 VRV.1 X1 = A
SA2 VRV.2 X2 = I
SA3 VRV.3 X3 = J
SA4 VRV.4 X4 = B
IX5 X3-X2 FIGURE NO. BITS - 1 TO PAC INTO A
MX0 1
PL X5,J1
SX5 X5+60
J1 SB6 X5
AX0 B6 MAKE MASK OF CORRECT LENGTH IN RIGHT-MOST
SB7 B6+B7 PART OF WORD
LX0 B7
BX4 X0*X4 EXTRACT BITS FROM B
SB7 X3-59
LX0 -B7 ALIGN BITS FROM B AND MASK
LX4 -B7 WITH CORRECT BITS OF A
BX1 -X0*X1 INSERT BITS FROM B INTO A
BX6 X1*X4
SA6 A1 STORE A
EO PAC EXIT
END
IDENT UNPAC CALL UNPAC(A,I,J,B)
* EXTRACTS N BITS A AND PLACES THEM
* IN B, RIGHT-JUSTIFIED WITH ZERO FILL
* BITS ARE NUMBERED LEFT TO RIGHT FROM 0 - 59
* IF I LE J, N=J-I+1

```

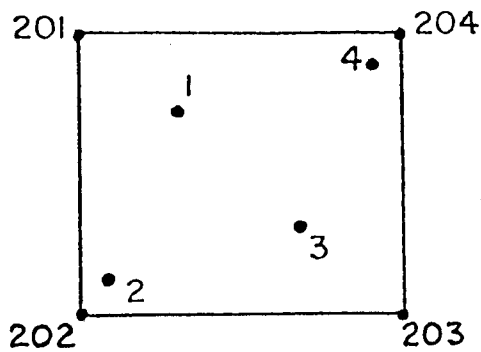

APPENDIX IV
TRIANGLE SCHEME

The triangle routine used was originally devised by Smyth (1975) and later simplified by Galt. To demonstrate how it works, we use a simple 4 station example, shown below:



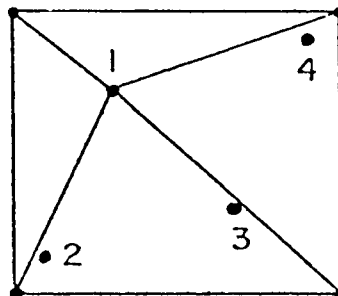
The 4 stations to be triangulated.

The first step is to enclose the region of interest by a rectangle:



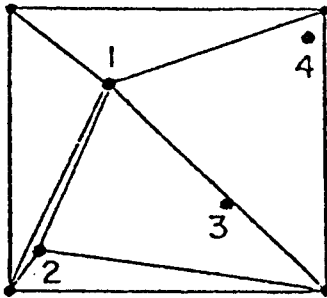
Rectangle defined by artificial points 201, 202, 203, and 204 enclose region of interest.

Next, take the first point and use that to subdivide the rectangle:



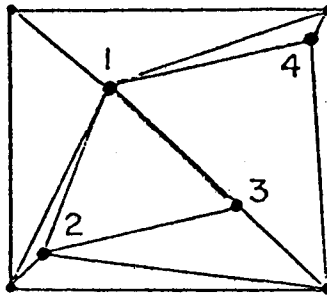
First subdivision of the initial triangle.

The second point is then used to subdivide the triangle it is in:



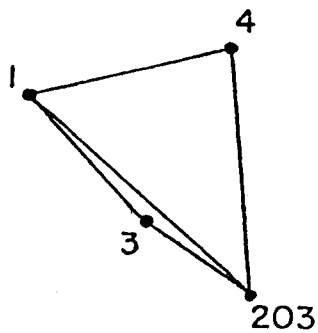
Second point used to subdivide the triangle.

After all of the points have been used to subdivide the larger triangles they lie in, we have:

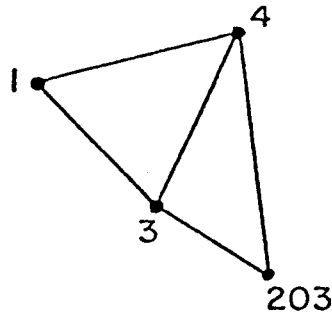


Mesh after all the subdivisions have been made.

Next, several sweeps are made to check the "goodness" of pairs of triangles. For example, the pair of triangles:

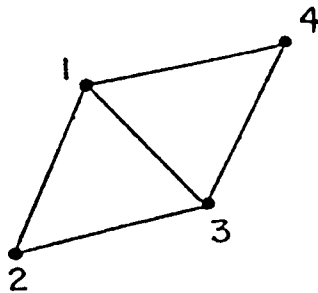


is checked to see if the triangles would be more equilateral if subdivided in the following way:



From tests run on a set of 130 stations and about 200 triangles, it was found that after about five sweeps through the entire mesh, the method converged and yielded a "best" mesh.

The last step in generating the mesh is to eliminate all triangles with corner vertices (201, 202, 203, 204). The final mesh is shown below:



Final mesh.

The routine has been written to accommodate up to 200 stations including one set of interior boundary points (an island). If there are interior boundary points, they must be read in first and in clockwise order.

APPENDIX V

To evaluate

$$N_2 \iint_D \phi_j \nabla^2 \phi_j \, dx dy, \quad (A1)$$

Begin by evaluating

$$N_2 \iint_D \phi_j \frac{\partial^2 \phi_j}{\partial x^2} \, dx dy.$$

First integrate

$$\int \phi_j \frac{\partial^2 \phi_j}{\partial x^2} \, dx \quad (A2)$$

by parts to get

$$\int \phi_j \frac{\partial^2 \phi_j}{\partial x^2} \, dx dy = \phi_j \frac{\partial \phi_j}{\partial x} - \int \frac{\partial \phi_j}{\partial x} \frac{\partial \phi_j}{\partial x} \, dx \quad (A3)$$

Now integrate by $\int dy$ to get

$$N_2 \iint_D \phi_j \frac{\partial^2 \phi_j}{\partial x^2} \, dx dy = N_2 \left[\int \phi_j \frac{\partial \phi_j}{\partial x} \, dy - \iint \frac{\partial \phi_j}{\partial x} \frac{\partial \phi_j}{\partial x} \, dx dy \right] \quad (A4)$$

The second term of (A1) can be integrated by parts also, to give

$$N_2 \iint_D \phi_j \frac{\partial^2 \phi_j}{\partial y^2} \, dx dy = N_2 \left[\int \phi_j \frac{\partial \phi_j}{\partial y} \, dx - \iint_D \frac{\partial \phi_j}{\partial y} \frac{\partial \phi_j}{\partial y} \, dy dx \right] \quad (A5)$$

Putting (A4) and (A5) together gives

$$N_2 \iint_D \phi_j \nabla^2 \phi_j \, dx dy = N_2 \left[\int \phi_j \frac{\partial \phi_j}{\partial x} \, dy + \int \phi_j \frac{\partial \phi_j}{\partial y} \, dx - \iint_D \left(\frac{\partial \phi_j}{\partial x} \frac{\partial \phi_j}{\partial x} + \frac{\partial \phi_j}{\partial y} \frac{\partial \phi_j}{\partial y} \right) \, dx dy \right] \quad (A6)$$

Now use the following substitution into the first two terms on the right-hand side:

$$dy = \frac{\partial y}{\partial s} \, ds, \quad dx = \frac{\partial x}{\partial s} \, ds, \quad (A7)$$

APPENDIX VI

To integrate $\int_{\Delta} \phi dx dy$

$$\phi = Ax + By + C \text{ such that}$$

$$\phi = 1 \text{ at } (X, Y) \text{ and}$$

$$\phi = 0 \text{ at } (0,0) \text{ and } (b,0)$$

Begin by integrating Part I first:

$$\phi = \left(\frac{y}{y_2}\right)$$

$$\delta x = \frac{x_2 - b}{y_2} y + (b - x_2)$$

$$\begin{aligned} \int_{\Delta I} \phi dx dy &= \int_0^{y_2} \left(\frac{y}{y_2}\right) \left(\frac{x_2 - b}{y_2} y + [b - x_2]\right) dy \\ &= (b - x_2) y_2 \frac{1}{6} \end{aligned}$$

Now to integrate Part II:

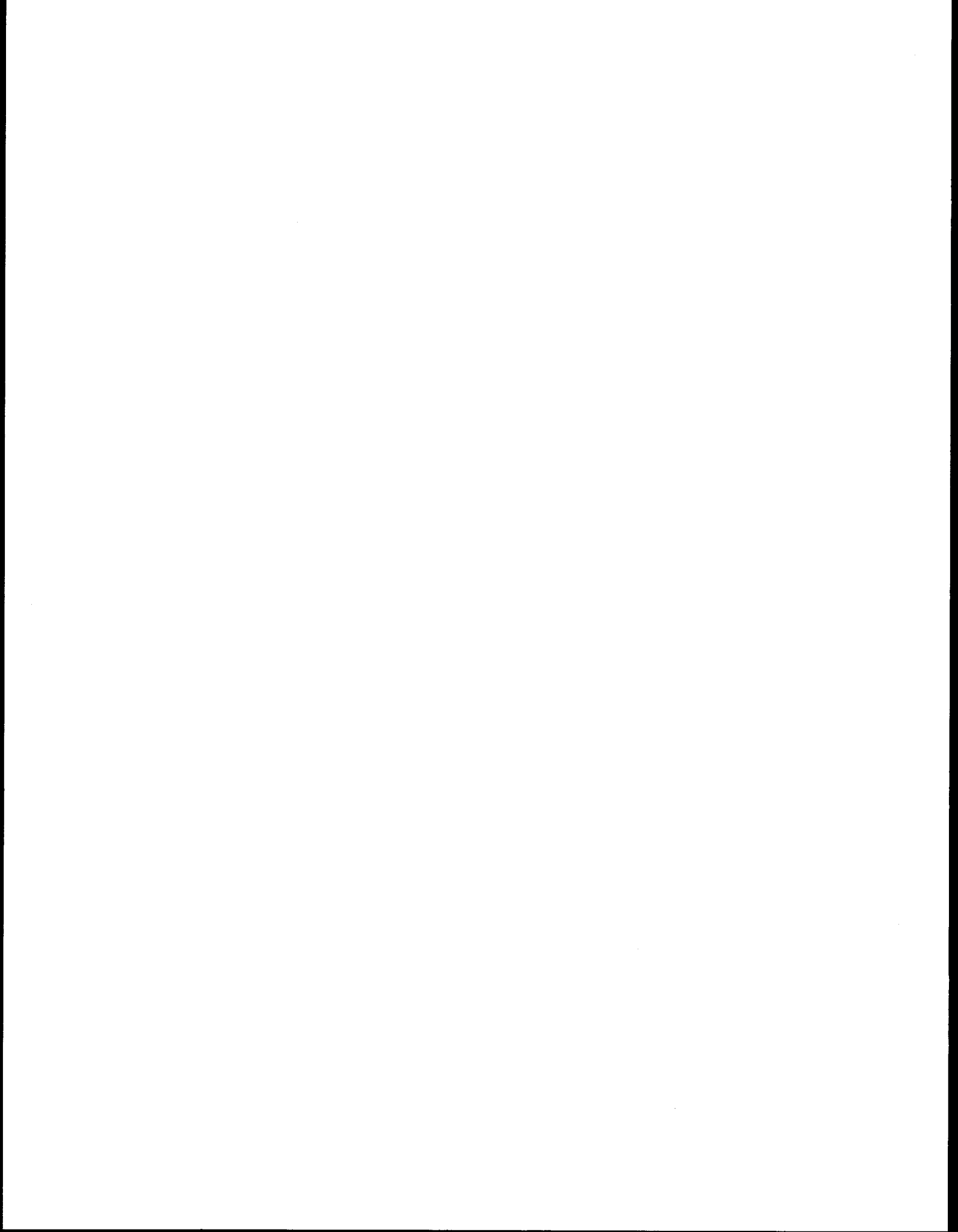
$$\phi = \frac{y}{y_2}$$

$$\delta x = \frac{x_2}{y_2} y + x_2$$

$$\begin{aligned} \int_{\Delta II} \phi dx dy &= \int_0^{y_2} \left(\frac{y}{y_2}\right) \left(-\frac{x_2}{y_2} y + x_2\right) dy \\ &= x_2 y_2 \frac{1}{6} \end{aligned}$$

The combined results give

$$\begin{aligned} \int_{\Delta} \phi dx dy &= \frac{1}{6} y_2 (b - x_2 + x_2) = \frac{1}{6} y_2 b \\ &= \frac{1}{3} (\text{area of triangle}). \end{aligned}$$



APPENDIX C

The Linear Decomposition of a Diagnostic
Shelf Circulation Model and Discussion of
Alternate Boundary Condition Formulations

by

J. A. Galt and G. Watabayashi

(Contribution No. 378 from the NOAA/ERL
Pacific Marine Environmental Laboratory.)

September 1978

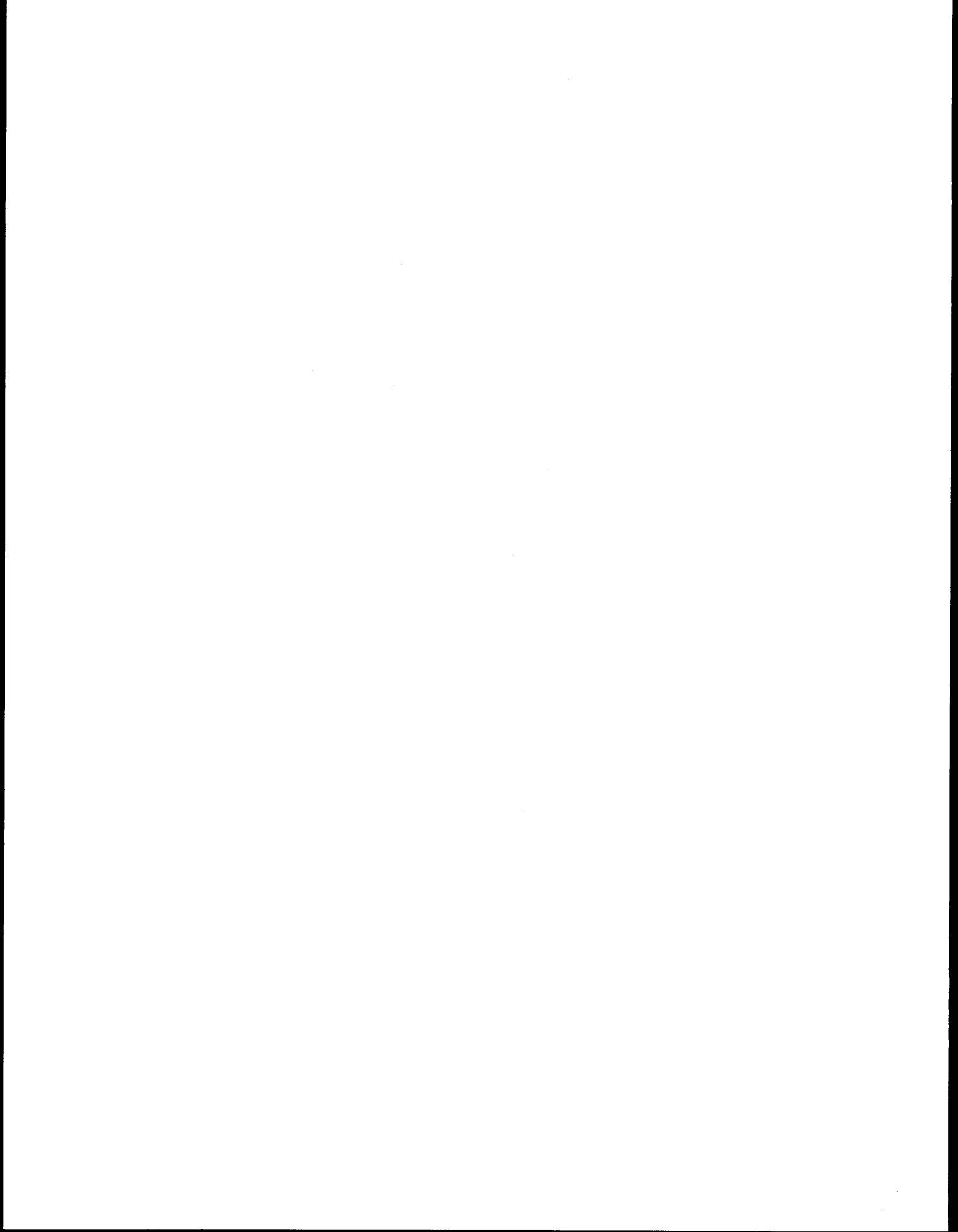
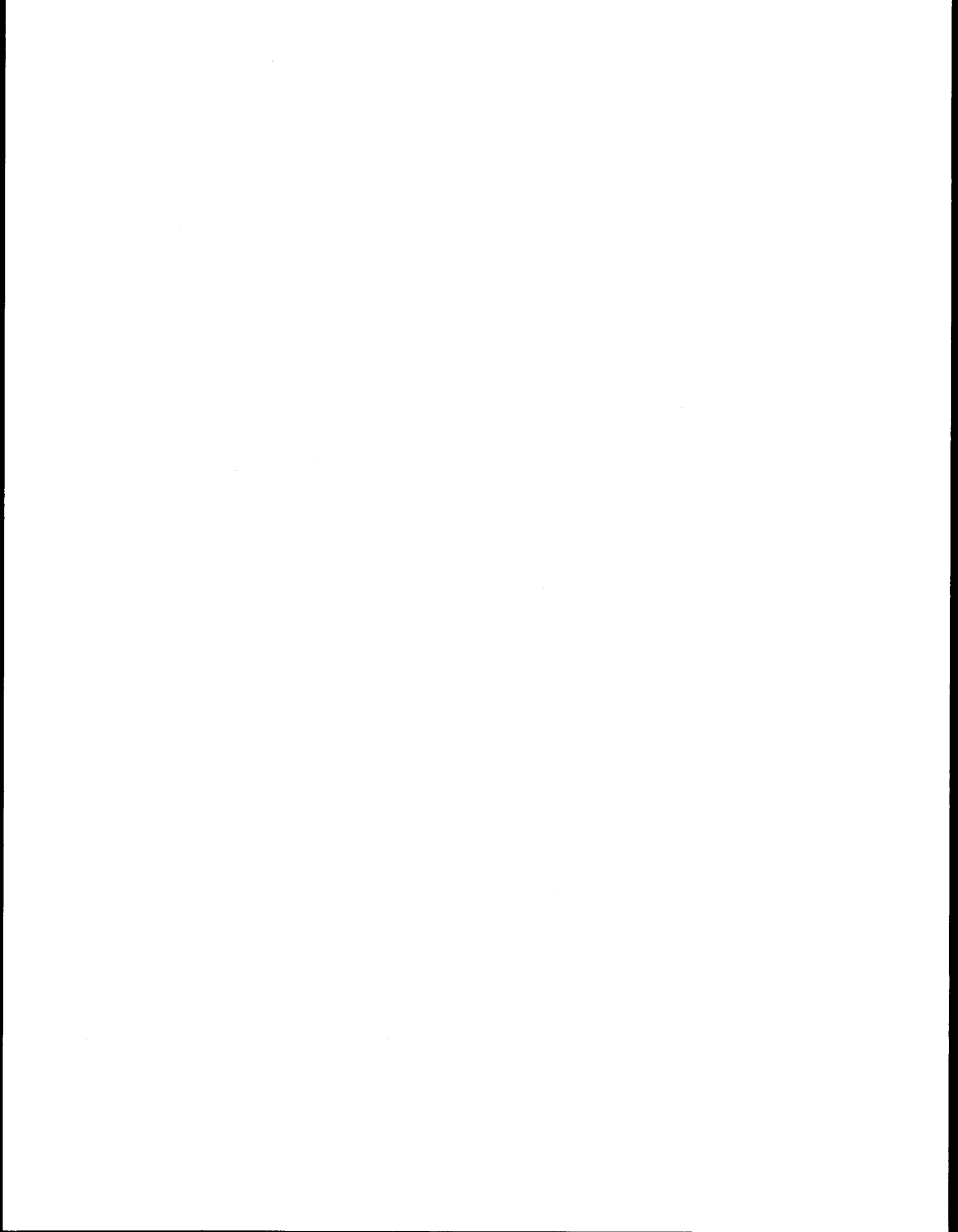


TABLE OF CONTENTS

	Page
ABSTRACT.	453
I. INTRODUCTION	453
II. DECOMPOSITION OF THE DIAGNOSTIC MODEL.	458
III. DENSITY-DRIVEN RESPONSE.	469
IV. WIND-DRIVEN RESPONSE	479
V. MODEL TEST	482
VI. DISCUSSION	487
VII. CONCLUSIONS.	497
ACKNOWLEDGEMENTS.	500
REFERENCES.	501
TABLE 1	503
FIGURES	504



The Linear Decomposition of a Diagnostic
Shelf Circulation Model and Discussion of Alternate
Boundary Condition Formulations*

J. A. Galt
Glen Watabayashi

Pacific Marine Environmental Laboratory
Environmental Research Laboratories
National Oceanic and Atmospheric Administration

ABSTRACT. This report will investigate the characteristics of the diagnostic model developed at PMEL and documented by Galt (1975) and Watabayashi and Galt (1978). The model is partitioned into density driven response and wind driven response components. The density driven response is shown to consist of the flow forced by the imposed density field and a minimum barotropic mode required to reconcile the density driven flow with the regional bathymetry. The wind driven response is associated with barotropic currents forced by the set-up of the sea surface across the shelf.

Alternate techniques used to determine the appropriate boundary conditions are herein investigated. A formal Green's function for the model equation provides useful insights into regional dynamics and clearly illustrates the dual elliptic and parabolic nature of the formulation. The model solution characteristics are demonstrated on a complex, analytic shelf domain.

I. INTRODUCTION

In this report we will look into the formulation of the boundary conditions and explore certain linear aspects of the diagnostic model equations described by Galt (1975). In contrast to past reports on the diagnostic

model (Galt, 1975; Galt, 1976; Watabayashi and Galt, 1978) that all concentrated on derivations, computer routines, and the study of circulation in a particular area, this report will have a more formal approach and will look at the decomposition of the equations into modes. We will discuss the implications of various boundary condition specifications in terms of these modes.

The basic derivation of the governing equations of the diagnostic model was presented by Galt (1975) and the equations have been described in detail in other places. Using the diagnostic model to study a particular area raises questions that are not directed at the model formulation, but rather at the choice of boundary conditions. The model formulation is a simple combination of geostrophic and Ekman modes, but the choice of boundary conditions is complicated by two factors. The first factor is that the model equations are second order due to a term which is small compared to the other terms in the dynamic balance. Because of this term, the boundary conditions required to solve the equation come close to overspecifying the flow; spurious solutions are a possible result. Secondly, when the model is used in open ocean regions, further difficulty associated with the boundary conditions results. The flow across the model boundaries is generally unknown, so various approximations are made, and the choice of these then leads to potential ambiguities in the solutions. The purpose of this report is to review the various approximations used to obtain boundary conditions in the past and to discuss possible ways of specifying a less arbitrary formulation for future studies.

Typically, whenever the diagnostic model is applied to a coastal region, one edge of the model lies along the coastline, another edge runs offshore

through deep water, with two lateral boundaries connecting these, from deep water across the shelf to the shore. The coastal boundary has a strong physical constraint associated with it which makes the formulation of the boundary conditions along the coast relatively easy. Physically, there is no flow through the coast. Along this coastal boundary four potential modes of flow are allowed: baroclinic and barotropic geostrophic components, Ekman modes at the surface, caused by wind stress, and at the bottom, caused by frictional drag. Setting the four of these to a net sum of zero involves a mixed Neumann type (Courant and Hilbert, 1962) boundary condition. The offshore boundary is typically located in deep water, a region where the classical dynamic height approximations tend to be valid. As a standard, we have simply imposed a dynamic height condition that allows for the flow to be zero at some fixed level, typically 1200 meters. To impose this boundary condition, we simply balance the barotropic and baroclinic geostrophic modes such that there is no flow at this depth.

Now we consider the two model boundaries which run normal to the coast. When the model was initially used, it was assumed that winds along the coast tended to set up the sea surface or push it down across the continental shelf by a mechanism suggested by Beardsley and Butman (1974). By assuming that the sea surface elevation across the shelf was represented by a simple wind dependent hinge, we were able to obtain solutions for the Northeast Gulf of Alaska region (NEGOA). The results of these initial studies appeared in the circulation study of the continental shelf off the Copper River Delta, Galt (1976). A moderate refinement on this study was to specify the inflow boundary condition of the flow along the eastern boundary as a simple hinge, adjusting the left hand boundary by hand so that a smoother set of streamlines was obtained along the outflow or western boundary. This was an admittedly

ad hoc approach to the problem, but the result did show some improvement. Galt and Pease (1977) presented flow patterns from this study using this method to simulate drift trajectories for a number of different wind conditions.

When the diagnostic model was applied to the area around Kodiak Island, Alaska, a problem arose with the use of a simple hinge concept. In the Kodiak region the topography is so complex that a simple hinge approach will not reflect the complex circulation occurring over the many banks and canyons that cut across the shelf. Hence we made use of the fact that a reduced inviscid set of model equations defines characteristics of a first order partial differential equation. These characteristics are very closely related to f/d contours where f is the Coriolis parameter and d is the depth. Along these contours the surface elevation is governed by a simple one-dimensional form of the differential equation. Using this method we generated a set of boundary conditions such that the inflow boundary was specified as a simple wind dependent slope, and the outflow boundary was related to the inflow boundary by using the characteristics that were defined by the simplified model equations. This approach led to circulation patterns which could then be related to wind conditions. Using this parameterization, a series of different cases was investigated; then the predicted currents from the model were compared to the scatter seen in current meter records from four different locations in the Kodiak area. The results of these studies were presented at a recent American Geophysical Union meeting (Galt, 1977). This characteristic technique was also used in the NEGOA area, and the results of these studies indicated the existence of several distinct domains within the NEGOA area that seemed to be strongly related to each other, (Royer, 1978). A final improvement in the combination hinge and characteristic

technique for determining boundary conditions was the introduction of a sea surface slope inversely proportional to depth to replace the hinge. This modified cross shelf profile meant that steeper sea surface slopes were obtained in shallower water along the coast assuming uniform wind, which tended to give a more realistic appearance to the current patterns, these techniques were applied in the Kodiak and NEGOA regions.

These techniques were characteristically applied to specific regions to obtain flow patterns for particular studies. They are also all derived in a heuristic way, which is typically labor intensive. The boundary conditions were tried; if they did not give reasonable results, alternate formulations were used. Although these empirical studies gave interesting current patterns, and in some cases appeared to accurately reflect direct observations, we still have reason to be skeptical of the results. In particular, location independent techniques might be derived, reflecting a more solid coupling of the fundamental physics to the model. Additionally, we are searching for a more formal way to approach the boundary problem as it relates to the diagnostic model.

In the next section we will discuss the decomposition of the model equations into a purely baroclinic mode, a minimum barotropic mode needed to satisfy continuity, and a barotropic wind driven mode. These various modes will be related to the kinds of data needed in order to solve the respective problems and to the number of degrees of freedom that are expected in the solutions. Next, we will discuss the types of boundary conditions to be imposed on each of the separate modes and ways to combine them to give a more general solution that would reflect the given density fields as well as the geometry of the specific region being studied. From these discussions we will derive a consistent approach for determining the boundary

conditions in a general study area.

In addition we will be able to determine the flow patterns that are likely to result from these particular sets of boundary conditions and relate them to observational data that can be obtained from CTD measurements and current meter data. To the extent that observational data do not fit the modal decomposition predicted by the model, we will also derive an objective way of determining whether or not the assumed boundary conditions are correct for the region.

II. Decomposition of the Diagnostic Model

The diagnostic model equations are linear. Therefore it is possible to decompose the governing equations into a number of different parts, each of which can be evaluated individually and then added up to give the total solution. The impetus for decomposing the model equations has come from two different problems. First of all, the simple hinge type boundary conditions that were used in a number of earlier studies led to a difficulty when the wind velocity approached zero. Under these conditions, the sea surface slope across the shelf also went to zero, thus, there was no barotropic transport across these particular boundaries. Nonetheless, the density field which was already specified gave a baroclinic transport that could be balanced only by invoking some rather exotic circulation patterns in the bottom Ekman mode. These results clearly indicated that some minimum barotropic mode had to exist to satisfy continuity in the presence of a non-uniform density field. A second reason for suggesting a decomposition of the model equations became apparent during an investigation of the number of degrees of freedom to be expected in the general class of solutions. Since the equations are linear, the number of degrees of freedom to be expected must be related to the number of degrees of freedom that are allowed

in specifying the boundary conditions. The hinge formulation introduced a single wind parameter; therefore, any similarity type distribution of sea surface elevation across the shelf would always lead to a single pattern in the flow. In order to better understand these patterns, we broke the boundary conditions into inhomogeneous parts related to the density field and a homogeneous and/or similarity part related to the set up by the wind. To see that this is possible, we may begin by looking at the diagnostic model equation.

$$N_2 \nabla^2 \xi - J(\xi, d) + N_1 N_2 \nabla^2 \alpha - N_1 J(\alpha, d) - k \cdot \nabla \times \tau = 0$$

where:

ξ = surface elevation, the dependent variable

d = depth

$k \cdot \nabla \times \tau$ = the curl of the surface wind stress

N_1 = non-dimensional stratification parameter

N_2 = non-dimensional bottom friction parameter.

A complete derivation of this non-dimensional form of the vorticity equation is given by Galt (1975). This can be separated into two parts such that

$$\xi = \xi_1 + \xi_2$$

where these new variables satisfy the following equations:

$$N_2 \nabla^2 \xi_1 - J(\xi_1, d) + N_1 N_2 \nabla^2 \alpha - N_1 J(\alpha, d) = 0$$

which is referred to as the density-driven response

$$N_2 \nabla^2 \xi_2 - J(\xi_2, d) - k \cdot \nabla \times \tau = 0$$

which is referred to as the wind-driven response.

Next we must consider the boundary conditions needed to solve these equations. To do this we will look at a typical model domain consisting of a coastline, shelf and deeper offshore section (see Fig. 1). The various segments of the boundary can be described in the following manner:

Segment a) This coastline boundary satisfies the physical condition that the net flux through the coast must be zero. To do this we simply sum the barotropic, baroclinic, surface Ekman and bottom Ekman modes in a non-dimensional form (Galt, 1975).

$$-d \frac{\partial \xi}{\partial s} + N_1 \left(\frac{\partial \Delta}{\partial s} + \alpha \frac{\partial d}{\partial s} \right) - \tau_s$$

$$+ N_2 \left(\frac{\partial \xi}{\partial n} - \frac{\partial \xi}{\partial s} \right) + N_1 N_2 \left(\frac{\partial \alpha}{\partial n} - \frac{\partial \alpha}{\partial s} \right) = 0$$

where \bar{n} is a unit vector normal to the coast pointing offshore; and \bar{s} is a unit vector given by $\bar{k} \times \bar{n} = \bar{s}$, where \bar{k} is positive up. These represent mixed Neumann type boundary conditions involving both normal and tangential derivatives of the dependent variable.

Segment b) This offshore or deep water boundary is assumed to be deep enough so that the concepts appropriate to classical dynamic heights can be used. To implement this in the diagnostic model we simply set the sea surface elevation at any station deeper than the level of no motion to:

$$\xi = -N_1 \alpha$$

Segments c & d) These cross shelf boundary regions require special attention. By specifying the surface elevation along this boundary, we supply Dirichlet type boundary conditions and determine the barotropic flow normal to the boundary. These nonhomogeneous conditions have been approximated in a variety of ways; to understand the rationale behind each potential problem we must look into these in some detail.

Basically the sea surface's departure from a level surface is caused by both thermohaline forcing and wind forcing. From a conceptual and computational point of view it is useful to separate these into a number of independent cases or modes. Before doing this, however, it is useful to outline the problems that are likely to occur if the boundary values are incorrectly specified.

In the model equation both geostrophic and Ekman flow are allowed and must be balanced to maintain continuity of mass. Moreover, around the boundary of the model most of the flow is determined by the independent variables (density, wind stress) or by the boundary conditions. In particular, the density data determines the baroclinic component of the geostrophic flow through the boundary; and the specification of the sea surface elevation determines the barotropic component of the geostrophic transport through the boundary. If these do not balance so that there is no net flow through the boundary, the model will establish a secondary flow in the bottom Ekman layer to complete the balance. To do this a strong barotropic current must flow parallel to the boundary. To get a better understanding of how this takes place, we may look at the following simple example (Fig. 2)

Model Domain: (assume y axis pointing North)

$$0 \leq x \leq l$$

$$0 \leq y \leq m$$

$$\text{depth : } d = -(2 - \frac{y}{m})$$

$$\alpha\text{-field: } \alpha = ax + by$$

$$\text{wind field: } \tau = 0$$

Substituting these into the governing equation gives:

$$N_2 \nabla^2 \xi + \frac{1}{x} \frac{\partial \xi}{\partial x} = -N_1 \frac{a}{m}$$

Boundary conditions will specify that flow enters from the right and exits from the left of the domain, i.e.;

$$\xi = y \text{ on } x = 0 \quad ; \quad 0 \leq y \leq m$$

$$x = l \quad ; \quad 0 \leq y \leq m$$

$$\xi = 0 \text{ on } 0 \leq x \leq l; \quad y = 0$$

$$\xi = y \text{ on } 0 \leq x \leq l; \quad y = m$$

To solve this we will use the homogeneous part of the equation to satisfy the non-homogeneous part of the boundary conditions. Thus

$$\xi = \xi' + \xi''$$

where ξ' satisfies

$$N_2 \nabla^2 \xi' + \frac{1}{m} \frac{\partial \xi'}{\partial x} = 0$$

subject to the boundary conditions given above. The solution for this part of the decomposition is easily seen to be:

$$\xi' = y$$

The remaining part of the solution will satisfy the full non-homogeneous equation subject to the homogeneous boundary conditions, i.e.;

$$N_2 \nabla^2 \xi'' + \frac{1}{l} \frac{\partial \xi''}{\partial x} = -N \frac{a}{m}$$

$$\xi''(0,y) = \xi''(l,y) = \xi''(x,0) = \xi''(x,m) = 0$$

This differential equation and boundary conditions are well known in the field of oceanography, as they are identical to the one proposed by Stommel

(1948) to represent general ocean circulation. For this secondary barotropic flow, the surface elevation contours will also be streamlines for the surface current (Fig. 3). This pattern shows a strong western boundary current analogous to general ocean circulation with the depth gradient taking the place of the β term and the baroclinic-bottom interaction term replacing the wind stress curl.

Several general characteristics of the model can be demonstrated from this simplified case. As previously stated the secondary flow is the result of a continuity imbalance. The basic barotropic mode $\xi' = y$ is nondivergent over the entire domain. The baroclinic forcing, on the other hand, is divergent. The density field will induce a flow, with both north and west components, which carries water from deep to shallow regions. This requires a secondary flow that results in a southerly drift and/or divergence in the bottom Ekman layer. We can see that this clockwise flow will support a bottom Ekman layer that transports water out of the domain, primarily through the strong western boundary current region. This strong asymmetry is another general characteristic of the secondary flow generated by the model. The coefficient N_2 is small; as a result, the leading and highest order term typically will not contribute significantly to the balance, except in boundary regions where the derivative in the independent variable can become large (Cole, 1968). For most of the interior and right hand boundary regions (to the right when facing from deep to shallow) the primary balance within the model is between the $J(\xi, d)$ term and the forcing terms. From this we may deduce two additional points. First, as the bottom friction ($\propto N_2$) becomes smaller, the western boundary current becomes more narrow and more intense. Secondly, for most of the model domain, the solution is totally dominated by the right hand boundary conditions and first order reduced equation. The intense western boundary current is clearly an artifact

of imposing additional boundary conditions, required by the second order equation, but redundant to the dominant first order dynamics. This explains the problem of picking appropriate boundary values across the c and d regions; they are coupled and generally cannot be set independently without expecting to get large, extraneous secondary flows.

With the problem demonstrated, we may now consider several techniques that can be applied in a systematic way to determine appropriate boundary values and define the degrees of freedom, or independent patterns, that can be expected from the model.

We will begin by considering the density driven response in the model, i.e.;

$$N_2 \nabla^2 \xi - J(\xi, d) + N_1 N_2 \nabla^2 \alpha - N_1 J(\alpha, d) = 0$$

To better understand how to proceed we will look only at what we know to be the dominant physics, i.e., the first order equation that remains when the bottom friction is negligible.

$$J(\xi, d) + N_1 J(\alpha, d) = 0$$

This corresponds to simple geostrophic flow over variable bathymetry.

Consider a triangular region of the ocean in which the depth, the sea surface elevation, and the vertical integral of the density can be approximated as linear functions of x and y. Thus if we define

$$\alpha = \int_d^0 \rho dz$$

we may write

$\alpha = A_1 \phi_1 + A_2 \phi_2 + A_3 \phi_3$	alpha field
$d = D_1 \phi_1 + D_2 \phi_2 + D_3 \phi_3$	depth
$\xi = Z_1 \phi_1 + Z_2 \phi_2 + Z_3 \phi_3$	surface elevation

where

$$\phi_1 = a_1x + b_1y + c_1$$

$$\phi_2 = a_2x + b_2y + c_2$$

$$\phi_3 = a_3x + b_3y + c_3$$

are the interpolating weight factors or shape functions associated with the triangle in question. (Zienkiewicz, 1971 and Fig. 4). The gradient in the α -field and thus the gradient in the bottom pressure will be:

$$\begin{aligned}\vec{\nabla}\alpha &= \left(\frac{\partial\alpha}{\partial x}\right)\vec{i} + \left(\frac{\partial\alpha}{\partial y}\right)\vec{j} \\ &= (A\cdot a)\vec{i} + (A\cdot b)\vec{j}\end{aligned}$$

Where the indicated three component vectors, A , a and b , are known from the geometry and from the density data given at the vertices. For the moment we will refer to $g\nabla\alpha$ as the baroclinic component of the pressure gradient where g is the acceleration of gravity. Given this assumption, we may define an internal velocity component, or the velocity at the bottom, due to the density variations as

$$\begin{aligned}\vec{v}_I &= \left(-\frac{g}{f\rho} \frac{\partial\alpha}{\partial y}\right)\vec{i} + \left(\frac{g}{f\rho} \frac{\partial\alpha}{\partial x}\right)\vec{j} \\ &= \frac{g}{f} (\vec{k}\times\vec{\nabla}\alpha) \\ &= \left(-\frac{g}{f\rho} (A\cdot b)\right)\vec{i} + \left(\frac{g}{f\rho} (A\cdot a)\right)\vec{j}\end{aligned}$$

This velocity component will be rotated 90° to the left of $\vec{\nabla}\alpha$. We may now look at the depth gradient which can be written as:

$$\begin{aligned}\bar{v}_d &= \left(\frac{\partial d}{\partial x}\right)\bar{i} + \left(\frac{\partial d}{\partial y}\right)\bar{j} \\ &= (D \cdot a)\bar{i} + (D \cdot b)\bar{j}\end{aligned}$$

In order to satisfy the continuity requirement that there be no flow through the bottom, we must require that the net horizontal bottom flow be along an isobath. Thus there is a minimum barotropic mode that must accompany the internal velocity V_I unless $\nabla\alpha$ and ∇d are co-linear. This minimal external or barotropic bottom velocity component will be parallel to the depth gradient and be given by (Galt, 1975, eq. 21)

$$\begin{aligned}\bar{V}_{EM} &= -\left(V_I \cdot \frac{\nabla d}{|\nabla d|}\right) \frac{\nabla d}{|\nabla d|} \\ &= \frac{g}{f \rho [(D \cdot a)^2 + (D \cdot b)^2]} \left[(A \cdot b)(D \cdot a)^2 - (A \cdot a)(D \cdot b)(D \cdot a) \right] \bar{i} \\ &\quad + \left[(A \cdot b)(D \cdot a)(D \cdot b) - (A \cdot a)(D \cdot b)^2 \right] \bar{j}\end{aligned}$$

This can be related to the sea surface elevations as follows:

$$\frac{\partial \xi}{\partial x} = \frac{f}{g} (V_{EM})_{\bar{j}} = (z \cdot a)$$

$$\frac{\partial \xi}{\partial y} = \frac{f}{g} (V_{EM})_{\bar{i}} = (z \cdot b)$$

where

$$(z \cdot a) = \frac{1}{\rho} \frac{[(A \cdot b)(D \cdot a)(D \cdot b) - (A \cdot a)(D \cdot b)^2]}{[(D \cdot a)^2 + (D \cdot b)^2]}$$

$$(z \cdot b) = \frac{-1}{\rho} \frac{[(A \cdot b)(D \cdot a)^2 - (A \cdot a)(D \cdot b)(D \cdot a)]}{[(D \cdot a)^2 + (D \cdot b)^2]}$$

and, with no loss of generality, we can set

$$z_1 = 0$$

These three equations can now be solved for the coefficients z_1 , z_2 , and z_3 to find the minimum barotropic mode.

It can be seen that the minimum barotropic mode is equivalent to specifying the component of the sea surface slope along an isobath, i.e., this determines the barotropic velocity normal to the depth contours. From a graphical viewpoint, the three conditions above are equivalent to placing vertex 1 of the triangle in the x-y plane and then rotating it around the vd axis until the slope is sufficient to give V_{EM} (Fig. 4).

Thus far we have determined only one component of the sea surface slope. It is also possible to rotate the solution plane for the sea surface elevation around the axes formed by the isobath. This can be done independently of the rotation around vd , physically it will result in a barotropic current that is parallel to the isobath, and thus have no effect on the continuity balance. This degree of freedom can be used to obtain a solution throughout a region composed of a number of triangular elements connected along an isobath or characteristic (Fig. 5). Specifying a slope for triangle 1 is equivalent to specifying the flow along the isobath and the single boundary condition needed to solve the first order partial differential equation. Triangle 2 can be rotated around the isobath until its two common vertices with triangle 1 match up, i.e., the solution plane for triangle 1 and for triangle 2 would be continuous along the common side AB. In a similar manner triangle 3 is rotated around the isobath and matched up along the common side with triangle 2. This process can be carried on through triangles as we follow an isobath or characteristic.

In order to get a better understanding of what is meant by this minimum barotropic mode, it is necessary to look into the physical implications of such a flow. For a single triangle this mode is clearly the barotropic component needed to align the bottom flow with the isobaths. This is an absolute minimum current; any other barotropic currents that are consistent with the density field and bathymetry will have components of the current along the isobath. These other cases would subsequently result in a sea surface slope with higher potential energy. When moving from one triangle to another along an isobath, continuity of flow across the boundary will determine the along isobath component of flow.

Why should we be interested in a sea surface distribution with minimum potential energy? We may note that this problem was considered by Wunsch (1977) in a different context. He discussed minimum energy solutions subject to a variety of conservation constraints, but none of his constraints happened to be bottom flow following f/d contours. He did, however, recognize this possibility. To answer the question in the context of the present problem, we recall that during the decomposition of the governing equation the density driven response did not include any wind forcing. Under these conditions the wind set up would relax and the sea surface would tend to decrease to the lowest energy level consistent with the dynamics represented by this component of the equations.

The next problem is to solve the density response partition of the diagnostic model equations, subject to the constraints that the surface elevation should be at a minimum potential energy and that there are no strong currents generated parallel to the boundary. Following this, we look for solutions to the wind driven response partition of the problem, assuming homogeneous water and some similarity profile for the wind set

up. The linear sum of these two solutions will be the total flow for the diagnostic model problem.

III. Density-Driven Response

The following is an investigation into the density driven response of the model. This will include the baroclinic mode and the minimum barotropic mode required for continuity. There are several ways to approach this problem, and included are outlines of three of them. Each way represents a somewhat different approach corresponding to various degrees of mathematical rigor. Obviously the computational effort required is quite different for each one of these and a comparison of results is of considerable practical interest.

3.1 Minimum Potential Along Characteristics

The coastal boundary segment previously labelled (a) (Fig. 1) must satisfy the "no net flux" condition. The deep water segment (b) will be represented by dynamic heights assuming a level of no motion on the order of 1000 - 1200. The remaining undetermined boundary values are for the segments (c) and (d) connecting the offshore and coastal regions. To evaluate these we will make use of the reduced invicid form of equation that represents the dominant physics, i.e.;

$$J(\xi, d) = -N_1 J(\alpha, d)$$

At each boundary point along these segments, the surface elevation is set to an unknown constant c . From this point we will integrate along a characteristic, satisfying the relationship obtained from the above equation:

$$\delta \xi = -N_1 \delta \alpha$$

Once the depth contour, or characteristic, is traced all the way across the model, the initial constant is adjusted to yield the minimum potential

energy for the surface profile along that path. A graphical interpretation for each triangle along the isobath is shown in Figure 6. The potential energy along this path can be written as:

$$PE_i = \int_0^{\delta s_i} \int_0^{\xi} \rho g z \, dz ds$$

This gives

$$PE_i = \int_0^{\delta s_i} \frac{1}{2} \rho g \xi^2 \, ds$$

where

$$\xi = (\xi_i + c) \left(\frac{\delta s_i - x}{\delta s_i} \right) + (\xi_{i+1} + c) \frac{x}{\delta s_i}$$

which leads to

$$\begin{aligned} PE_i &= (2\xi_i^2 + \xi_i \xi_{i+1} + 2\xi_{i+1}^2) \frac{\delta s_i}{6} \\ &+ (4\xi_i + (\xi_i + \xi_{i+1}) + 4\xi_{i+1}) \frac{\delta s_i}{6} c \\ &+ \frac{5}{6} \delta s \, c^2 \end{aligned}$$

Summing these contributions for each of the triangles connected by the isobath with the understanding that $\xi_1 = 0$, gives

$$\begin{aligned} \overline{PE} &= \frac{1}{12} \rho g \sum_{i=1}^{\Sigma} \delta s_i (2\xi_i^2 + \xi_i \xi_{i+1} + 2\xi_{i+1}^2) \\ &+ (4\xi_i + (\xi_{i+1} + \xi_i) + 4\xi_{i+1}) c + 5c^2 \end{aligned}$$

To obtain the minimum value for the potential energy along this path we differentiate with respect to c and set the result to zero, giving

$$c = \frac{\sum_{i=1}^{\infty} (\xi_{i+1} + \xi_2) \cdot \frac{\delta s_i}{2}}{\sum_{i=1}^{\infty} \delta s_i}$$

Once this is done for each of the points along the (c) and (d) boundaries, the interior solution for the full equation should give a minimum potential energy surface except for the contribution from the small bottom stress terms. A closer look, however, reveals several unresolved ambiguities and potentially degenerate cases.

This minimum potential energy approach will give elevations along segments (c) and (d) relative to other members of this set, but it does not suggest how to connect these sections to the offshore segments whose elevations are also only defined relative to other members of their sets. To resolve this problem we have adopted the convention that the offshore boundary segment be adjusted up or down by a constant amount so that the innermost line of stations (whose relative position is given by dynamic heights) is at a minimum potential energy relative to the $z = 0$ level. This same constant offset is then applied to the entire deep water region.

The degenerate cases that must be considered involve places along the boundary where neighboring points are at the same depth (characteristic runs along the boundary) or where the boundary point is a local maximum or minimum in the depth (characteristic does not penetrate the model domain). We set boundary values at these points by using a quadratic interpolation that fits a curve through two points on one side of the unknown point

and through one point on the other side. This procedure is done from both sides and averaged as shown in Figures 7 and 8.

We summarize this procedure as follows;

1) Coastal boundary points are set relative to each other using a "no net flux" constraint.

2) Deep water boundary points are set relative to each other by assuming level of no motion and using the dynamic heights method. In addition they are offset so that the innermost line of deep stations is also set at a minimum potential energy relative to $z = 0$.

3) Cross-shelf boundaries are set relative to each other by minimizing potential energy along characteristics, subject to the reduced form of the density-driven equation.

4) Degenerate cases are resolved by using interpolation techniques.

Once these steps have been done, the complete density-driven response is calculated giving a flow field including the effects of bottom friction. This solution can be expected to approximate the minimum potential energy solution (or most relaxed set-up) consistent with continuity considerations, the given density field, and the bathymetry.

3.2 Green's Function to Minimize Regional Potential Energy

In this section we will derive a technique for obtaining a complete solution to the minimum potential energy, density-driven response. To do this we will make use of the linearity of the diagnostic model equation.

We start with the general density drive equation:

$$N_2 \nabla^2 \xi - J(\xi, d) + N_1 N_2 \nabla^2 \alpha - N_1 J(\alpha, d) = 0$$

and consider the following series of problems:

1) The solution to the above equation subject to the following boundary conditions:

- a) no net flux through the coastal segment
- b) deep water boundary segment given by dynamic height and assumed level of no motion plus a constant offset
- c) all of the cross-shelf boundary values set to zero

2) The solution to the homogeneous equation is

$$N_2 \nabla^2 \xi - J(\xi, d) = 0$$

subject to the following boundary conditions:

- a) no net flux through the coastal segment
- b) all remaining boundary points are set equal to zero except one which is given a unit magnitude.

This second problem gives the numerical solution to the Green's function which represents the response of the system to a unit impulse from a particular boundary point. If there is a total of M boundary points along the cross-shelf boundary segments, we repeat problem two above with each point in turn acting as a source point for the Green's function.

In all we obtain $M+1$ solutions for each nodal point in the model plus the contribution from the variable density forcing terms with dynamic height values set offshore. After doing this we write the total solution as the linear sum

$$\xi^j = \xi_\rho^j + \sum_{i=0}^M C_i \xi_i^j$$

where the subscript i indicates those of Green's functions with which

the solution is associated, the superscript j indicates the nodal point value, and c_j is the 'as yet' undetermined amplitude associated with each of the Green's functions.

We will now determine the values of the c_j 's such that the potential energy for the total solution is a minimum. To do this we will consider a triangle with vertices l , m , and n and area Δ . With the shape functions ϕ_l , ϕ_m , and ϕ_n we define the surface elevation as

$$\xi = \xi^l \phi_l + \xi^m \phi_m + \xi^n \phi_n,$$

The potential energy of the surface relative to a flat surface at zero height (where the integration is over the triangle) is given by

$$\begin{aligned} PE &= \int dx \int dy \int_0^\xi \rho g z dz dy dx \\ &= \frac{1}{2} \rho g \int dx \int dy \xi^2 dx dy \end{aligned}$$

Substituting our expression for the surface elevation into this gives

$$PE = \frac{1}{2} \rho g \int dx \int dy (\xi^{l2} \phi_l^2 + \xi^{m2} \phi_m^2 + \xi^{n2} \phi_n^2 + 2\xi^l \xi^m \phi_l \phi_m + 2\xi^l \xi^n \phi_l \phi_n + 2\xi^m \xi^n \phi_m \phi_n) dx dy$$

To evaluate the integrals of these shape functions, we may use the formula given by Zienkiewicz (1971, page 120, eq. 7.34) which states

$$\int dx dy \phi_1^a \phi_2^b \phi_3^c dx dy = \frac{a!b!c!}{(a+b+c+2)!} 2\Delta$$

and the above integral becomes

$$PE = \frac{1}{12} \rho g (\xi^{l2} + \xi^{m2} + \xi^{n2} + \xi^l \xi^m + \xi^l \xi^n + \xi^m \xi^n) \Delta$$

Substituting our linear sum representation for ξ into the above gives

$$PE = \frac{1}{12} \left[\rho g \left(\xi_p^z + \sum_{i=0}^M C_i \xi_i^z \right)^2 + \left(\xi_p^m + \sum_{i=0}^M C_i \xi_i^m \right)^2 + \left(\xi_p^n + \sum_{i=0}^M C_i \xi_i^n \right)^2 \right. \\ \left. \left(\xi_p^z + \sum_{i=0}^M C_i \xi_i^z \right) \left(\xi_p^m + \sum_{i=0}^M C_i \xi_i^m \right) + \left(\xi_p^z + \sum_{i=0}^M C_i \xi_i^z \right) \left(\xi_p^n + \sum_{i=0}^M C_i \xi_i^n \right) \right. \\ \left. \left(\xi_p^m + \sum_{i=0}^M C_i \xi_i^m \right) \left(\xi_p^n + \sum_{i=0}^M C_i \xi_i^n \right) \right] \Delta$$

Expanding this out gives

$$PE = \frac{1}{12} \rho g \left[\left(\xi_p^z \right)^2 + \left(2 \xi_p^z \sum_{i=0}^M C_i \xi_i^z \right) + \left(\sum_{i=0}^M \sum_{j=0}^M C_i C_j \xi_i^z \xi_j^z \right) + \left(\xi_p^m \right)^2 \right. \\ \left. + \left(2 \xi_p^m \sum_{i=0}^M C_i \xi_i^m \right) + \left(\sum_{i=0}^M \sum_{j=0}^M C_i C_j \xi_i^m \xi_j^m \right) + \left(\xi_p^n \right)^2 + \left(2 \xi_p^n \sum_{i=0}^M C_i \xi_i^n \right) \right. \\ \left. + \left(\sum_{i=0}^M \sum_{j=0}^M C_i C_j \xi_i^z \xi_j^n \right) + \left(\xi_p^z \xi_p^m \right) + \left(\xi_p^z \sum_{i=0}^M C_i \xi_i^m \right) + \left(\xi_p^m \sum_{i=0}^M C_i \xi_i^z \right) \right. \\ \left. + \left(\sum_{i=0}^M \sum_{j=0}^M C_i C_j \xi_i^z \xi_j^m \right) + \left(\xi_p^z \xi_p^n \right) + \left(\xi_p^z \sum_{i=0}^M C_i \xi_i^n \right) + \left(\xi_p^n \sum_{i=0}^M C_i \xi_i^z \right) \right. \\ \left. + \left(\sum_{i=0}^M \sum_{j=0}^M C_i C_j \xi_i^z \xi_j^n \right) + \left(\xi_p^m \xi_p^n \right) + \left(\xi_p^m \sum_{i=0}^M C_i \xi_i^n \right) + \left(\xi_p^n \sum_{i=0}^M C_i \xi_i^m \right) \right. \\ \left. + \left(\sum_{i=0}^M \sum_{j=0}^M C_i C_j \xi_i^m \xi_j^n \right) \right] \Delta$$

This is once again the potential energy associated with a single triangle as a function of the Green's function contribution from each boundary point along the cross-shelf segment. The total potential energy for the

region will be the sum of this expression over each triangle. To minimize this we must differentiate with respect to each of the C's and set the resulting system of equations to zero, i.e., for $i = 0, 1, 2, \dots, M$

$$\Delta \left[2\varepsilon_\rho^l \varepsilon_i^l + 2\varepsilon_\rho^m \varepsilon_i^m + 2\varepsilon_\rho^n \varepsilon_i^n + \varepsilon_\rho^l \varepsilon_i^m + \varepsilon_\rho^m \varepsilon_i^l + \varepsilon_\rho^l \varepsilon_i^n + \varepsilon_\rho^n \varepsilon_i^l + \varepsilon_\rho^m \varepsilon_i^n \right. \\ \left. + \varepsilon_\rho^n \varepsilon_i^m + 2\varepsilon_i^l \left(\sum_{j=0}^M \varepsilon_j^l C_j \right) + 2\varepsilon_i^m \left(\sum_{j=0}^M \varepsilon_j^m C_j \right) + 2\varepsilon_i^n \left(\sum_{j=0}^M \varepsilon_j^n C_j \right) \right. \\ \left. + \varepsilon_i^l \left(\sum_{j=0}^M \varepsilon_j^m C_j \right) + \varepsilon_i^m \left(\sum_{j=0}^M \varepsilon_j^l C_j \right) + \varepsilon_i^l \left(\sum_{j=0}^M \varepsilon_j^n C_j \right) + \varepsilon_i^n \left(\sum_{j=0}^M \varepsilon_j^l C_j \right) \right. \\ \left. + \varepsilon_i^m \left(\sum_{j=0}^M \varepsilon_j^n C_j \right) + \varepsilon_i^n \left(\sum_{j=0}^M \varepsilon_j^m C_j \right) \right] = 0$$

This gives $M+1$ equations in the $M+1$ unknown C's, which can be written in the matrix form.

$$A c = \Gamma$$

Where

$$\Gamma_i = -[(\varepsilon_\rho^l + \varepsilon_\rho^m + \varepsilon_\rho^n)(\varepsilon_i^l + \varepsilon_i^m + \varepsilon_i^n) \\ + (\varepsilon_\rho^l \varepsilon_i^l + \varepsilon_\rho^m \varepsilon_i^m + \varepsilon_\rho^n \varepsilon_i^n)] \Delta$$

And

$$A_{ij} = [(\varepsilon_i^l + \varepsilon_i^m + \varepsilon_i^n)(\varepsilon_j^l + \varepsilon_j^m + \varepsilon_j^n) \\ + (\varepsilon_i^l \varepsilon_j^l + \varepsilon_i^m \varepsilon_j^m + \varepsilon_i^n \varepsilon_j^n)] \Delta$$

and where it is understood that these terms are summed over all the triangles.

Solving this system for the C_i 's, we then obtain the minimum potential energy solution for the density-driven response partition of the diagnostic model.

3.3 Natural boundary conditions for the Finite Element Solution

The third method of estimating the boundary conditions for the density-driven response to the model is by far the simplest and depends to some extent on serendipity. The basic procedure can be described as follows:

The density-driven response partition of the diagnostic equation is solved using the finite element technique and first-order linear shape functions subject to the following conditions:

- a) Along the coastal boundary segment a zero net flux condition is specified
- b) Along the deep water boundary segment the elevations are set using dynamic height considerations
- c) Along the cross-shelf boundaries no boundary conditions are imposed after the finite element matrix is assembled.

Surprisingly, a solution is then obtained without giving the elliptic problem explicit boundary conditions surrounding the domain. Furthermore, the resulting flow pattern appears to be very close to the one that was obtained using the technique of minimizing the potential energy along a characteristic or using the more complete Green's function minimization. To understand how this takes place we must first consider the finite element (FEM) method that is being used along with its bases set of functions. Next we will investigate the physical implications of these mathematical conditions and discuss why these should lead to a low or minimum potential energy state.

We start by observing that the differential operator represented by the diagnostic model equation is second order; we therefore expect the solution to come from the general function space of twice-differentiable functions. On the other hand, the interpolation functions which are used to make up the solution function space are only linear and piecewise continuous. This presents no particular problem in that the actual Galarkin formulation that is used to assemble the FEM solution matrix is in the "weak form" where higher derivatives in the operator are transformed to boundary constraints via integration by parts. When this is done, certain essential and natural type boundary conditions are identified (Strang and Fix, 1973). In the absence of the specification of essential boundary conditions (Dirichlet in this case) the solution will tend to optimize its approach to the natural boundary conditions (homogeneous Neumann type). In essence, when no boundary conditions are specified over some segment of the boundary, the normal derivative of the FE solution using first-order elements and the weak Galarkin form will tend to go to zero.

The sea surface slope normal to the boundary of the model corresponds to a barotropic flow along the edge of the domain. This type of circulation pattern has been previously identified as resulting from continuity mismatches around the boundary. It is at least plausible that by approaching natural type boundary conditions along the boundary segments crossing the shelf, the secondary flows will be small in some sense. Thus we can expect the total solution, constrained with essential conditions only around the deep water segment and the physically realistic non-flux conditions along the coast to approach a minimum energy state.

In this section we have presented three different approaches to solving the density driven response to the diagnostic model equations. Each rep-

resents a somewhat different point of view and requires different amounts of computational effort. These are investigated in section V to add formalism to the understanding of the model and to standardize the approach to its use. This is in strong contrast to previous explorations where trial and error and oceanographic intuition were major factors in model applications.

IV. Wind-Driven Response

In this section the wind-driven response of the model is considered by solving the partition of the diagnostic equation given by

$$N_2 \nabla^2 \xi - J(\xi, d) - k \cdot \nabla \times \tau = 0$$

This equation represents the wind forcing of the model region. The wind-driven effects can be conveniently divided into two separate components. The first of these is the surface Ekman flow, which enters into the vorticity equation as the curl of the wind stress (i.e., the local wind forcing caused by the winds within the model region.) The second category of wind forcing can be referred to as global. This is the result of large-scale wind patterns and is transmitted to the model through the set-up of the boundary points. Typical patterns associated with this process are modeled by imposing a slope across the continental shelf region that is proportional to the alongshore component of the wind stress. The assumed mechanism hypothesizes that the Ekman transport pushes water up against the coast inducing a barotropic set-up and subsequent alongshore currents. Such behavior has been qualitatively observed in many continental shelf areas and quantitatively documented by Beardsley and Butman (1974).

Looking more closely at the local wind forcing, we find that there are two ways in which the model can be forced directly by winds within

the model domain. The first of these is through the wind stress curl, which is small for typical length and time scales (100 km and days). For most cases, the open ocean, wind-driven convergence or divergence is a secondary contributor to the mass balance, or sea surface set-up. The second way that the local winds drive the model is through the mass convergence or divergence at the coastline. This effect enters through the no net flux boundary conditions. This direct forcing of the model covers all possible ways in which winds effect the dependent variable, i.e., sea surface elevation and subsequently the geostrophic currents at the surface. However, these effects do not include all of the wind-driven currents. Superimposed on this surface geostrophic current is the non-divergent component of the Ekman layer flow which is added onto the diagnostic model solution and clearly depends on local winds.

The global wind forcing to be used in the model presents two distinct problems. The first is theoretical, the second numerical. It is known that regional winds set up the sea surface. The details of how the physical processes operate in continental shelf regions with complex bathymetry and stratification are essentially unknown. Because of this, various assumptions have been made and tested with the model. The measure of success of these assumptions is a comparison of model results to current meter observations or Lagrangian drifter data. To date, only the simplest one parameter similarity profiles have been used, specifying either a uniform slope across the shelf or a slope inversely proportional to the depth. In these cases using the complete model, the density-driven and wind set-up effects were not clearly separated, and it was difficult to determine the actual degrees of freedom represented by the model or specified in the boundary formulation. The natural way to specify these

wind-driven elevation values across the shelf would be to have sea surface or bottom pressure measurements from a series of gages. Using this data, an observed cross-shelf profile could be used to drive the model. The pressure data would need to be filtered to remove non-geostrophic components. In addition it would be encouraging to find the appropriate geostrophic scale signal falling along a simple one-parameter cross-shelf profile.

When trying to key the wind-driven model response to various cross-shelf profiles, it is important to remember that the system is linear. For example, with n data points across the shelf, n different empirical orthogonal modes can be derived from the records. Then all possible profiles can be represented as linear combinations of these few model profiles. Thus, these studies can expect the most productive output by concentrating on empirically derived profiles.

An alternate technique for keying the wind-driven response of the model would be to develop a Green's function for various slope conditions between nodal points across the shelf. Methods would be similar to those presented in the preceding chapter and could be put together in linear combinations to represent any given cross-shelf profile.

The second general problem associated with the global wind forcing in the model is numerical and was discussed in section III of this report. As mentioned, the boundary layer nature of the governing equation and the dominant first-order physics associated with the bathymetric interaction term make it essential to consider the coupling between the right-hand and left-hand cross-shelf boundary segments. The two opposite boundary values must be related along bathymetric contours to avoid the presence of extraneous boundary currents in the secondary flow. There are several possible approaches to this problem; as discussed previously. The first

approach is to specify the surface elevation at only one point on each isobath and determine the second boundary value by using the reduced equation and integrating along the characteristic. The second approach makes use of the natural boundary condition behavior of the finite element solution technique. In this case, the elevation would be set on each characteristic and the remaining boundary conditions would remain unspecified to be determined by the solution technique so as to suppress extraneous boundary currents.

As a final point on the wind-driven response in the model, this partition of the model equation does not depend in any way on the density data. The initial finite element grid or nodal point positions were determined by the locations of CTD stations which supplied the density input. Commonly ship time and weather constraints limit the station coverage, and spatial distribution is not as detailed as one might like for resolving complex bathymetry. With the density- and wind-driven responses of the model partitioned as indicated, it is not necessary to restrict both partitions to the same finite element mesh. In fact, the wind driven response can be run once for any region on a grid as dense as needed to resolve the relevant topographic features.

V. Model Test

In order to get a better understanding of the model decomposition the model was tested on a relatively complex domain. Rather than go to a specific site and attempt to find data, a region was hypothesized with analytic bathymetry. The topographic features of the region are: a broad continental shelf, a bank or shoal region on the shelf, and a large submarine canyon. The actual model bathymetry is the sum of all these features

expressed in analytical non-dimensional form as follows:

$$\begin{aligned}
 d(x,y) = & D_0 - \frac{D_1}{(D_2 + \exp(D_3 y^2))} + D_{11} \frac{(Y-Y_2)}{(Y_3-Y_2)} \\
 & + D_4 \exp(-D_5(x-x_0)^2 - D_6(y-y_0)^2) \\
 & + D_9 \exp(-D_7(y-y_1)^2 - D_{10}(x-x_1)^2) (1 - \exp(D_{12} y^4) \cos(D_8(x-x_1)))
 \end{aligned}$$

Figure 9 shows the triangular grid system that was used on the 5 x 5 (non-dimensional units) domain. This corresponds to 143 stations with an increased density of points on the western boundary to avoid any resolution problems that might occur with the secondary boundary currents. Figure 10 shows a bathymetric contour map plotted from the station location data. We will refer to this as the GS (Gondwannaland Shelf) domain.

The density field will be given by a simple linear function of position at the surface that goes to a constant density at great depth, i.e.,

$$\rho = \rho_0 - (\delta\rho_1 x + \delta\rho_2 y + \delta\rho_3) \exp(D_{13} z)$$

This can be easily integrated from some depth z to the surface to give α , i.e.,

$$\alpha = \int_z^0 \rho dz = -\rho_0 z - \frac{(\delta\rho_1 x + \delta\rho_2 y + \delta\rho_3)}{D_{13}} (1 - \exp(D_{13} z))$$

From this the gradients in the α field and bottom pressure forces due to the baroclinic terms will be

$$\frac{\partial \alpha}{\partial x} = - \frac{\delta\rho_1}{D_{13}} (1 - \exp(D_{13} z))$$

$$\frac{\partial \alpha}{\partial y} = - \frac{\delta\rho_2}{D_{13}} (1 - \exp(D_{13} z))$$

Table 1 gives the non-dimensional values of the various depth and density coefficients used in the GS region parameterization. This relatively simple formulation retains analytic properties yet requires some cross-isobath flow in the minimum barotropic mode; thus it will be an informative example for the present study. Figure 11 shows the alpha field derivations plotted from the station data.

To round out the Gondwannaland Shelf domain data set, it is assumed that a number of pressure gages and meteorological data buoys have been deployed and have established the wind response characteristics of the region. For the present example this has reduced to the following: the sea surface elevation for any point along the coast (corrected for tide and barometric pressure) is a linear function of the alongshore component of the wind stress with the amplitude of the variation being roughly proportional to the width of the shelf. Then, for the purpose of this illustration, a linear bathystrophic forcing is hypothesized. In this the alongshore component of the flow is proportional to the alongshore component of the wind speed with the onshore/offshore component of the sea surface elevation in geostrophic balance with the alongshore current.

Given this GS domain data, we may now explore the regional circulation using the decomposition techniques outlined in the previous two sections of this report.

Starting with the density-driven response we will seek the baroclinic mode along with the minimum barotropic mode required for continuity. Three different methods of solution are suggested, and each will be investigated. The assumed level of no motion offshore will be taken as 1,000 m, thus the two outermost lines of stations will be set using dynamic height considerations.

The three methods are:

1) To obtain the boundary values using the minimization of potential energy along characteristics we proceed as outlined earlier. The surface elevation associated with the minimum barotropic mode for this case is shown in Figure 12a.

2) To solve for the density-driven flow using the Green's function approach we must calculate a number of different components to the flow. The first is the component forced by the offshore dynamic heights. This solution is shown in Figure 13a and can be thought of as the basic baroclinic forcing. Added to this will be a linear combination of the other Green's functions components. The first will be the constant elevation for the offshore region which corresponds to offshore adjustment necessary to minimize this region relative to the $z = 0$ level. This is shown in Figure 13b. The other Green's function components are all related to a unit displacement at some boundary point. An example is given in Figure 13c. Following the techniques outlined previously, the appropriate Green's function components are scaled and added to minimize the potential energy of the solution. The resulting surface elevation for the minimum barotropic mode is shown in Figure 12b.

3) The third technique for estimating the minimum barotropic mode is to use the finite element natural boundary condition formulation. Figure 12c shows the surface elevation predicted by the natural boundary condition case.

Figure 14 shows the surface velocity for the same three cases as seen in Figure 12. Figure 15 shows the corresponding bottom velocities for the three techniques. This differs from the surface currents by the

baroclinic shear that is introduced by the variable density.

We now turn our attention to the wind-driven response of our GS region. As previously stated, the assumed input data suggests a bathystrophic balance where the alongshore component of the wind is linearly related to a uniform sea surface slope across the shelf. This determines the boundary conditions that we will impose on the wind-driven component of the model decomposition.

Before considering the details of how to apply these conditions, we note that the wind-driven response does not depend in any way on the density data so that alternate grid systems are possible. To take advantage of this we will add stations in regions of particular interest for increased resolution of key bathymetric features. These additional stations will be added over the canyon, the shelf break and the shoal area. The more detailed grid system and new triangle mesh are shown in Figure 16.

The wind set-up forcing requires a uniform slope across the shelf of the GS domain. This forcing applied to any cross shelf section can be represented by a linear hinge. We set these with a slope of unity between the 1,000 m (non-dimensional depth 5) contour and the coast. In addition to these Dirichlet conditions we will assume the winds do not affect the deep offshore region so these values will be set to a constant equal to the value of the offshore extreme of the right-hand boundary. The coastal boundary segment will be subject to the usual "zero net flux" conditions. The complete wind set-up solution will be the linear sum of these forced hinge sections, each of which can be thought of as the Green's function response of the domain to an imposed bathystrophic balance across a particular shelf profile. For each of these hinge components,

the cross-shelf profile will be set; remaining cross-shelf model boundaries will be subject to the FEM natural boundary conditions.

The key question is; along which cross-shelf profile should the hinges be set? Where the bathymetric constraints dominate, either side should lead to the same result. On the flat nearshore segments of the shelf, however, the length scale is still determined by the elliptic terms in the equation and the influence of boundary values (or forced hinge) fall off with distance like the Green's function components. To explore these options three barotropic cases are run with the surface elevations shown in Figure 17 and the current vectors shown in Figure 18.

For each of these, alternate cross-shelf profiles would lead to alternate possible circulation patterns with the total number of degrees of freedom corresponding to the number of degrees of freedom in the specification of all of the cross-shelf profiles.

VI. Discussion

The GS numerical experiments can now be discussed, comparing first the density-driven response and the three different techniques that have been used to find the minimum barotropic mode. As discussed in section two of this report, a minimum barotropic mode is required because the given density distribution we have chosen is quite simple and the bathymetry is no more complex than that which might be expected of a typical shelf region, the joint interaction between these two fields becomes relatively complex. It is useful to examine the deviations in the alpha field along the bottom (Figure 11). Clearly the major bathymetric features and density field result in a complex pattern in the bottom pressure, or more specifically the lateral bottom pressure gradients. The details of how these interactions

effect the flow are represented as a $J(\alpha, d)$ torque term in the differential equation; this pattern of $J(\alpha, d)$ is shown in Figure 19. The resulting flow must satisfy both kinematic continuity constraints and conservation of vorticity conditions. The divergence in the flow (vertical stretching as the water moves over sloping bathymetry) interacts with the planetary vorticity and results in the development of shears and horizontal accelerations. In addition to these constraints, which are defined and controlled by the differential equation in the interior, we impose the boundary conditions that specify the form of the solution around the edge of the model. Our basic premise is that in the absence of wind set-up the sea surface should be at a low potential energy state, or that the flow's interaction with the bathymetry should be in some sense small; and that the solution should not show any strong or irregular currents along the open boundary regions across the shelf. Each of the three techniques used to obtain boundary conditions concentrate on obtaining low potential energy solutions overall, or on forcing a smooth boundary region. The general features of the flow can be seen in Figures 12, 14 and 15.

Looking first at minimizing the potential energy along reduced characteristics (Figures 12a, 14a and 15a) the general features of the density-driven flow are clear: 1) In general the flow is weak and energetic current bands do not develop, which is consistent with our initial premise. 2) As the forced onshore flow first encounters the steep continental shelf the baroclinic/bathymetric interaction term introduces a general turn to the east in the surface currents, with the bottom flow moving slowly to the original westward direction, paralleling the isobaths. 3) Over the shoal area on the eastern segment of the shelf a counterclockwise

circulation develops with intensified flow over the eastern slope of this positive bathymetric feature. 4) Over the canyon that cuts through the western segment of the shelf a clockwise circulation is observed, with the more intense currents found over the western slope of this negative bathymetric feature. 5) Along the shallow relatively flat coastal segment of the shelf region the flow is weak and generally to the east. Finally, 6) the offshore level of no motion and continental slope interaction region exhibits what appears to be a banded east-west current pattern that is particularly evident along the smooth eastern segment of the slope region. The bottom flow predicted by this approach is generally small (virtually zero over most of the shelf) and along isobaths, with the exception of a few boundary triangles right in the steepest region of the continental slope where the water that is forced onto the slope must exit the model. This is obviously an open boundary effect that the characteristic approach was not able to totally suppress.

We may now turn our attention to the more rigorous Green's function minimization of the potential energy. The results of this case study can be seen in Figures 12b, 14b and 15b. The numerical technique was verified to have actually obtained an overall minimum potential energy sea surface and the potential energy was found to be a quadratic function of the component amplitudes, as expected. The potential energy of the characteristic technique was 40% greater than the Green's function method. The general behavior of the solution can be discovered by looking at the individual components shown in Figure 13. Figure 13a is the basic baroclinic forcing and clearly shows that the interior is going to have baroclinic circulation associated with both the canyon and shoal regions. In addition a weak coastal current and the effects of the sharp discontinuity between

the offshore and interior region are evident. Figure 13b shows the barotropic model response associated with the elevation offset between the offshore and interior region. The major flow is along the continental slope, but the flow is also seen to extend into the canyon region and across isobaths, particularly in the shallow shelf region where the bottom friction plays a significant role. It is obvious that this can be combined with the baroclinic forcing (shown in Fig. 13a) in such a way as to largely cancel out the strong currents along the continental slope. Also pertinent to this Green's function component is the significant boundary layer that occurs on the western edge of the model. This is due to the cross-isobath flow that takes place gradually throughout the interior of the model and must be compensated for in the narrow return flow. Actually this is just a more complicated example of the flow which is described in section II and shown in Figure 3. The remaining Green's functions all show the model's barotropic response to elevation at a single boundary point (Fig. 13c). In the absence of strong bathymetry, the response is controlled by the elliptic terms in the model equation, and bottom friction sets the length scale.

In Figure 14b we see that the composite Green's function currents exhibit all of the six features of the interior flow that were enumerated for the results of the reduced characteristic technique. There are essentially no differences in the surface current vectors except in the western boundary region of the model where significant boundary layers are present. The bottom currents from the Green's function solution are uniformly very small except in the boundary region where some are surprisingly large. This approach clearly does not handle all of the extraneous boundary layers that occur, and some additional research would seem appropriate.

In re-examining the total potential energy of the model we may note that very strong boundary currents are possible with relatively minor potential energy changes in the small boundary triangles. In addition, when the large interior regions are included in the minimization, a very slight change over this area (representing a large potential energy) may balance a relatively extreme perturbation along the edge. At this point we should also invoke some of our fundamental understanding of how partial differential equations are solved and of the significance of boundary conditions in the construction of solutions. Basically the differential equation must specify the nature of the solution within the interior of the domain. Along the boundaries the nature of the solution must be imposed, and for these regions this is typically more significant than the control exerted by the differential equation. This all suggests that to minimize the potential energy over the entire model may be an incorrect strategy. It tends to specify the solution too rigidly over the interior and doesn't properly force the correct form of the solution in the critical boundary regions.

We can now examine the results of using the natural boundary condition technique shown in Figures (12c, 14c and 15c). The surface contour pattern appears to be very close to the one obtained by the characteristic and reduced equation technique. The six major features described in the previous cases are essentially unchanged by this technique.

Two interesting features do show up in the natural boundary condition case that were not seen in the characteristic or complete potential energy minimization/Green's function cases. First of all, there is no evidence of enhanced boundary currents. The total potential energy is 28% greater than for the Green's function minimization. This appears as a slight

offset over the interior with a much smoother surface in the boundary regions.

The second major feature of the natural boundary condition solution is that the bottom currents (Figure 15c) are zero, unlike the other cases. In this respect the solution appears to be a direct extension of the offshore dynamic heights methods adjusting the level of no motion to the bathymetry. Looking back at the basic differential equation it is clear that zero bottom currents (i.e., $\xi = -N_1\alpha$) $\xi^* = (\xi + N_1\alpha)$. Figures 4 and 5 illustrate the physical reason for the zero bottom flow condition over the entire domain produced by these boundary conditions. The zero bottom flow in boundary triangles leads to zero bottom flow along characteristics (as long as they are defined) and thus over the entire domain.

The three techniques used to estimate the density-driven partition of the flow can now be compared and evaluated in terms of our original objectives, i.e., to represent the baroclinic component of the flow along with the minimum barotropic mode (sea surface elevation) such that the bottom flow can be reconciled with the given density and topographic fields.

All three approaches lead to current patterns in the interior which are essentially indistinguishable. Differences occur in the boundary regions and in the small bottom currents. The method of minimizing potential energy along characteristics using the reduced equations leads to the highest overall potential energy of the three techniques. In terms of the obvious development of extraneous boundary currents the characteristic method is intermediate with boundary layers weaker than the Green's function solution, but with considerably stronger boundary layers in the natural boundary condition solutions. The characteristic method gives a relatively strong band of bottom currents along the face of the continental slope.

These currents are suspect and most likely are related to the way the offshore and cross-shelf segments are joined.

The Green's function technique gives a clear overall minimum potential energy solution. Interior bottom currents are very close to zero and seem to suggest that, away from the boundaries, the minimum set-up case consistent with the model dynamics results in quiescent bottom currents. The Green's function minimization of the entire regime does have the disadvantage that it generates energetic boundary currents which are obviously not realistic.

The natural boundary condition solution is computationally the simplest, and like the Green's function solution, the interior bottom currents are zero. In addition, this technique leads to essentially no boundary layers and extends the zero bottom flow throughout the entire domain, including boundary regions. With this it is possible to interpret the minimum barotropic mode in a somewhat different light. The unforced baroclinic response of a complex bathymetric region that has adjusted in such a way as to minimize the potential energy of the sea surface elevation will approach a zero bottom current condition. The natural boundary condition formulation best yields this "minimum barotropic" mode by a circulation that in fact creates a minimum (zero) bathymetric interaction. This differs from the absolute minimum potential energy flow only in the important open cross-shelf boundary regions, and here the natural boundary condition formulation leads to more realistic flow, free from what are known to be extraneous currents.

It is an interesting side note that, given an unforced geostrophic plus Ekman flow regime for any region, the only possible steady state circulation will be the case where the barotropic and baroclinic modes

combine in such a way as to yield a zero bathymetric interaction, which in essence turns off the frictional dissipation.

In Figures 17 and 18 we can see the GS region's response to indirect wind forcing. This includes the large-scale regional set-up of the sea surface but not local surface Ekman currents. An examination of these results reveal a number of interesting features and regional characteristics.

The use of the FEM natural boundary conditions allows for a smooth continuation of the solution through boundary regions, so that specifying surface elevations anywhere in the model results in a regional circulation pattern with what appears to be transparent boundaries. For example, in 17a and 18a a uniform surface slope is specified across the shelf on the eastern boundary and natural boundary conditions are used along the western boundary. Figures 17b and 18b show the flow that results when the cross-shelf elevations are determined across the middle of the model and both east and west boundaries are determined as the natural boundary conditions. Figures 17c and 18c show the corresponding case forced from the western boundary. It is interesting to note the differences between these cases. There is obviously a length scale associated with the region influenced by any of these cases. To understand these variations we may once again consider the Green's function components, which in turn represent just the regional dynamic response of the model. Along the shelf break where bathymetric controls are dominant the parabolic nature of the equations is evident, and extends across the entire model closely following f/d contours. In contrast, the shelf in the nearshore region is nearly flat and bottom friction, the elliptic nature of the equation dominant, and the diffusive character of the solutions are clearly seen. This diffusive scale is of special interest and can be estimated by a scale analysis

of the differential equation. The relevant term in the governing equation is

$$N_2 \nabla^2 \xi$$

Since in non-dimensional form ξ has been scaled to 0 (unity) this term will only be significant when

$$\frac{N_2}{L_2} \gg 0 \text{ (unity)}$$

This defines a length over which ξ variations must occur if the elliptic term is to be significant, i.e.,

$$L \propto (N_2)^{1/2}$$

This is the appropriate scale length for the Green's function response in relatively flat regions where elliptic nature of the differential equation dominates, i.e.,

$$|N_2 \nabla^2 \xi| > |J(\xi, d)|$$

It is also clear from these scaling considerations that the diffusive length scale $(N_2)^{1/2}$ determines the minimum size bathymetric feature that will be effective in the conservation of potential vorticity-dominated, parabolic model response. That is, in the presence of bathymetric variations the flow will follow f/d contours only down to a scale length where the diffusive processes become significant, at which point smoothing of the elevation contours will occur. Covering the entire cross shelf region, the solutions show a smooth gradation from one set of dynamic balances to the other. The same characteristics and length scales that are seen in the Green's function appear in our hinge solution.

As a final point, the three hinge modes are linearly independent and can be thought of as hinge influence functions. Then, assuming that we have sea surface elevation information at various points along the coast, these can be combined in a logical way. For each point along the coastal boundary (segment a - Fig. 1), a bathystrophic hinge response is calculated. A distribution of sea surface elevation along the coast will be associated with this hinge located at point n along the coast, i.e.,

$$E_n = f_n(s)$$

where $f(s)$ is just the value of the hinge response as a function of the distance s along the coast. Then given m locations along the coastline where the hinge amplitudes h_m are given, the following m equations can be developed:

$$h_m = \int_n c_n f_n(s_m)$$

For $m = n$ a solution is obviously possible, the appropriate weighting amplitudes for all the hinges are obtained in terms of the coefficients (c_n 's). If an infinite number of m locations are chosen, the above equation and formulation clearly degenerate to a continuum and once again give a formal Green's function solution to the model dynamics subject to a linear sea surface slope forcing (hinge mode) across the shelf.

For any particular shelf region or transect, the surface elevation will be the sum of a number of hinge modes; thus, it will not necessarily appear as a uniform cross-shelf profile. Instead it will reflect the appropriate dynamic distribution of the immediate location, plus the weighted contribution from neighboring locations. In a somewhat related study,

Csandady (1978) considered similar dynamics and the regional influence of local wind forcing and offshore circulation. His work was for a uniformly sloping wedge-shaped coastal region where the parabolic nature of the dynamics was uniformly dominant.

For the present study the three hinge modes shown in Figures 17 and 18 can be considered as an initial numerical approximation to the continuum Green's function. For these the influence function f_n falls off to essentially zero at adjacent hinge points and the weighting factors are locally determined, i.e.,

$$h_m = C_m$$

This means that each hinge coefficient will be set at the locally determined (bathystrophically balanced) value and the total solution will be the sum of the three hinge modes.

Having examined all of the various modes for the Gondwannaland Shelf region and considered the dynamics of the decomposition from a number of points of view, it is informative to look at the composite flow. We will combine the output of the density-driven and wind set-up responses. Figure 20 shows the results of the natural boundary condition solution for the density-driven response plus the sum of the hinge modes representing the coastal set-up case. Figure 21 shows the natural boundary condition solution for the density-driven response minus the sum of the hinge solutions representing a coastal set-down case. Assuming a simple hinge response for the shelf, all possible circulation patterns must be some linear combinations of the modes represented in 12c, 17a, and 17c.

VII. Conclusions

The linear diagnostic model equations have been formally decomposed into a density-driven response and a wind set-up response. These responses,

plus an additional non-divergent surface Ekman mode, make up the total flow that can be represented by the model. The density-driven response is made up of baroclinic currents driven by the imposed density field and by a minimum barotropic mode which orients the combined bottom currents in such a way as to satisfy the model's dynamic and kinematic constraints.

The model is tested on an analytic, but realistic domain (the Gondwanaland Shelf) which includes topographic features representing a broad shelf and continental slope with a shallower bank and large submarine canyon.

Three alternate approaches are used to obtain estimates of the minimum barotropic mode. The first, based on characteristic of the reduced model equations, is of historical interest in that it has been used in previous studies. The second solution technique obtains a minimizing potential energy for the sea surface, and thus shows the most relaxed overall regional state that is consistent with the bathymetry and density fields. The third method, which depends on the finite element technique, is computationally the simplest, and from a theoretical point of view should reduce the occurrence of extraneous open boundary currents.

All three of these techniques yield essentially identical interior flows. The finite element method using natural boundary conditions is seen to offer the best approximation to the minimum barotropic mode, in that it extends the formal minimum potential energy solution smoothly throughout the cross-shelf boundary regions. From a physical point of view, the minimum barotropic mode represents a "minimum bathymetric interaction" i.e., barotropic and baroclinic modes that give zero bottom flow. Conceptually this is a natural extension of the offshore level of no motion introduced by the dynamic heights method. In addition it can be seen that, given unforced barotropic, baroclinic and bottom Ekman modes, this is

the only possible steady inviscid circulation pattern. Within the context of the linear model formulation, the density-driven response contains all of the independent circulation information available from the density data. The development of the density-driven response can be carried out once for each set of STD or CTD data available for the study region, but beyond that no other independent density related circulation modes are possible.

The wind set-up response of the model can be represented by a number of hinge, or cross-shelf profile modes. The known profile can be applied anywhere within the model when the finite element method with natural boundary conditions is used. The region of influence of any single cross-shelf profile depends upon the topography and can be explained in terms of the joint elliptic and parabolic nature of the governing partial differential equation. This dependence can also be clearly demonstrated by the component Green's function responses that were developed. These domains of influence for the hinge or cross-shelf profile modes define the need for boundary input data and the spacial scale that must be resolved by observations.

Having developed the response characteristics of the model region, it is obvious that these patterns could be usefully employed to design the minimum resolution observational grid needed to study the area. For a linear system, the other relevant scale would be the length associated with the forcing (large-scale winds) that set up the cross-shelf profiles.

The total regional circulation for the model domain may now be represented by a simple linear combination of the density response mode and the various hinge or cross-shelf profile modes, plus a non-divergent surface Ekman drift. Since there is only one density response mode for each set

of STD or CTD data, and the wind response modes are all dependent only on the bathymetric characteristics of the region, the procedure of applying the model to a study region is greatly simplified. In addition to increased model efficiency, these modes are seen to represent fundamental physical processes that can be directly related to empirical data and can be used to obtain measures of success for predicted currents, as well as in the design of observation arrays.

Acknowledgements

The research described in this report has been funded in part by the BLM sponsored Outer Continental Shelf Assessment Program under RU #140. During the course of the work Dr. Robert J. Stewart has offered many helpful comments and his contribution is gratefully acknowledged.

REFERENCES

- Beardsley, Robert C. and Bradford Butman (1974): Circulation on the New England continental shelf; response to strong winter storms, Geophys. Res. Letters 1(4); pp 181-184.
- Cole, Julian (1968): Perturbation Methods in Applied Mathematics, Blaisdell, New York, 260 pp.
- Courant, R. and D. Hilbert (1962): Methods of Mathematical Physics, Vol. II, Interscience Publishers, New York, NY, 830 pp.
- Csanady, G.T. (1978): The Arrested Topographic Wave, JPO 8(1); pp 47-62.
- Galt, J.A. (1975): Development of a simplified diagnostic model for the interpretation of oceanographic data. NOAA Technical Report ERL 339-PMEL 25, National Oceanic and Atmospheric Administration, U.S. Department of Commerce, Washington, DC, 46 pp.
- Galt, J.A. (1976): Circulation studies on the Alaskan Continental Shelf off the Copper River Delta. National Oceanic and Atmospheric Administration, U.S. Department of Commerce, Washington, DC, 46 pp.
- Galt, J.A. (1977): A diagnostic circulation of the flow in the vicinity of Kodiak, EOS, Vol. 58, No. 12, p. 1173 (Abstract only).
- Galt, J.A. and C.H. Pease (1977): The use of a diagnostic circulation model for oil trajectory analysis, Proceedings of 1977 Oil Spill Conference, March 8-10, New Orleans, Louisiana, pp 447-454.
- Royer, T. (1978): Personal communication, manuscript in preparation.
- Stommel, H. (1948): The westward intensification of wind-driven ocean currents, American Geophysical Union, Transactions, Vol. 29, No. 2, pp 202-206.

- Strang, G. and G.J. Fix (1973): An Analysis of the Finite Element Method, Prentice-Hall Inc., Englewood Cliffs, NJ, 306 pp.
- Watabayashi, G. and J.A. Galt (1978): A finite element technique for a diagnostic shelf circulation model. NOAA Technical Report (in press).
- Wunsch, C. (1977): Determining the general circulation of the oceans: a preliminary discussion, Science, 196, pp 871-875.
- Zienkiewicz, O.C. (1971): The Finite Element Method in Engineering Science, McGraw-Hill Publishing Co., New York, NY, 521 pp.

TABLE 1 NONDIMENSIONAL CONSTANTS USED IN THE GONDWANNALAND SHELF

$$D0 = -100.$$

$$D1 = 50000$$

$$D2 = 49.$$

$$D3 = 7.00$$

$$D4 = 50.$$

$$D5 = 3.0$$

$$D6 = 1.5$$

$$D7 = 1.0$$

$$D8 = 3.14159/2.$$

$$D9 = -500.$$

$$D10 = 4.0$$

$$D11 = 80.$$

$$D12 = -1.0$$

$$X0 = 3.5$$

$$X1 = 1.5$$

$$Y1 = 1.0$$

$$Y2 = 2.0$$

$$Y3 = 5.0$$

$$Y0 = 2.5$$

$$DSHELF = D0 - D1 / (D2 + \exp(D3 * Y * Y)) + D11 * (Y - Y2) / (Y3 - Y2)$$

$$DBANK = D4 * \exp(-(D5 * (X - X0) ** 2. + D6 * (Y - Y0) ** 2.))$$

$$DCANYON = \exp(-D7 * (Y - Y1) ** -D10 * (X - X1) ** 2.) * \\ (\cos(D8 * (X - X1)) * D9 * (1. - \exp(D12 * Y ** 4.)))$$

$$RH00 = 1.032$$

$$A = .00025$$

$$B = .0005$$

$$C = 1./200.$$

$$RHO = RH00 - (A * X + B * Y) * \exp(C * Z)$$

$$ALPHA = RHO * D - (A * X + B * Y) * (1 - \exp(C * (-D))) / C$$

Figure Captions

- Figure 1 General configuration of typical continental shelf study region.
- Figure 2 Example of density field with cross isobath flow for use in an analytic example of model solutions.
- Figure 3 Surface elevation contours for secondary barotropic flow generated in response to cross isobath baroclinic forcing.
- Figure 4 Diagram of arbitrary triangle showing the relationship between the independent variables depth and density; their associated gradients ∇d and $\nabla \alpha$, and the geostrophic components of the bottom current.
- Figure 5 Series of triangles connected by an isobath, or characteristic for the reduced equation.
- Figure 6 Triangle intersected by an isobath with surface elevations determined at the ends of the transect.
- Figure 7 Demonstration of interpolation technique used to obtain boundary values for the case where f/d characteristics do not intersect the model except at one point.
- Figure 8 Demonstration of interpolation technique used to obtain boundary values for the case where f/d characteristic extends along the edge of the model for two or more boundary points.
- Figure 9 Grid system used for density driven response study on the GS region representing a square domain of 5×5 non-dimensional units.
- Figure 10 Bathymetric chart of the Gondwannaland shelf model domain showing the shelf section with a shoal to the east and a large submarine canyon to the west.
- Figure 11 Alpha field (bottom pressure) deviations along the bottom of the model domain.
- Figure 12 Contours of surface elevation indicating surface stream lines for the minimum barotropic mode. a) method of minimizing potential energy along the characteristics of the reduced equation. b) Green's function minimization of total potential energy. c) Finite element method of natural boundary conditions.
- Figure 13 Green's function components representing model response. a) non-homogeneous forced mode reflecting the density distribution and offshore dynamic heights. b) homogeneous model response to a uniform displacement of the offshore region relative to the shelf region. c) homogeneous response to a unit displacement of one boundary point.

- Figure 14 Surface current vectors for the density driven response with the minimum barotropic mode a) method of minimizing potential energy along the characteristics of the reduced equation. b) Green's function minimization of total potential energy. c) Finite element method natural boundary conditions.
- Figure 15 Bottom current vectors for the density driven response a) method of minimizing potential energy along the characteristics of the reduced equation. b) Green's function minimization of total potential energy. c) Finite element method natural boundary conditions.
- Figure 16 Triangular mesh used for the wind set-up partition of the GS region study.
- Figure 17 Surface elevation contours for the hinge response modes associated with the homogeneous wind set-up partition of the model equations a) eastern boundary set as hinge profile, b) central cross shelf transect set as hinge profile, c) western boundary set as hinge profile.
- Figure 18 Current vectors for the hinge response modes associated with the homogeneous wind set-up partition of the model equations. a) eastern boundary set as hinge profile. b) central cross shelf transect set as hinge profile. c) western boundary set as hinge profile.
- Figure 19 $J(\alpha, d)$ Baroclinic forcing in density driven response given by the joint baroclinic, bathymetric interaction. Shaded area indicates negative values.
- Figure 20 Sum of the density driven response and wind set-up response (hinge modes) for a case representing winds from the east. a) sea surface elevation contours. b) surface current vectors. c) bottom current vectors.
- Figure 21 Sum of density driven response and wind set-up response (hinge modes) for a case representing winds from the west. a) sea surface elevation contours. b) surface current vectors. c) bottom current vectors.

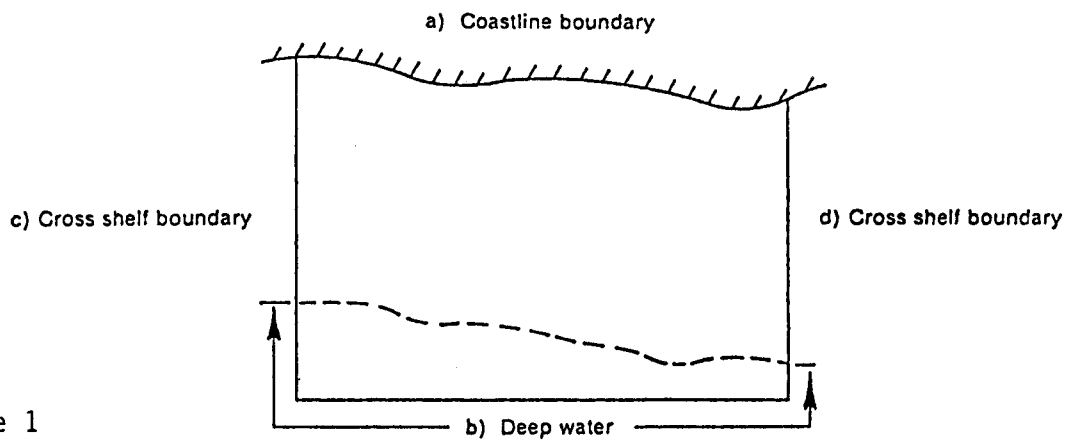


Figure 1

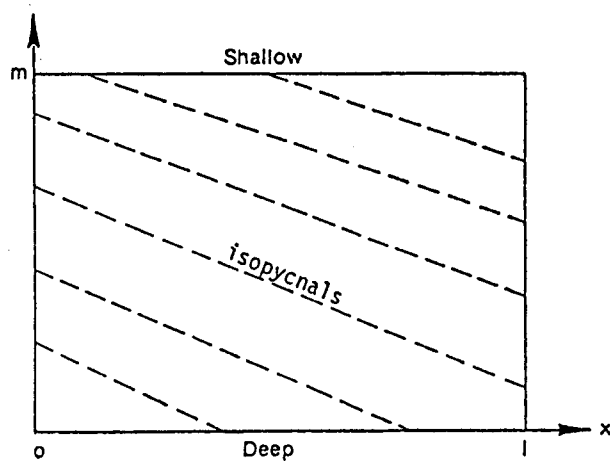


Figure 2

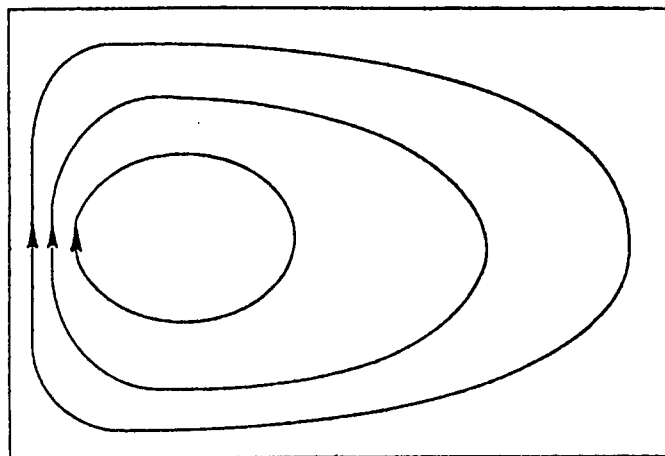


Figure 3

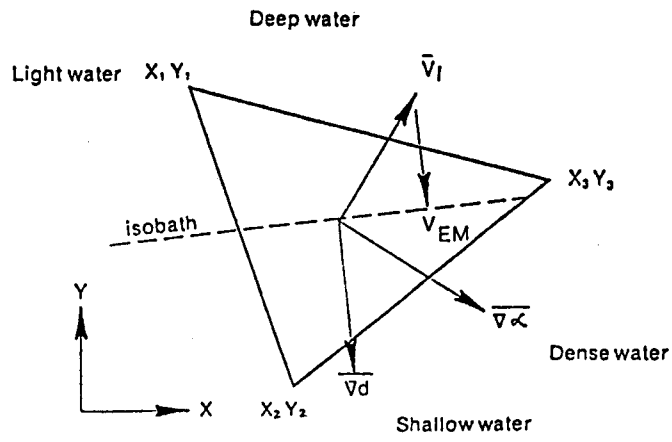


Figure 4

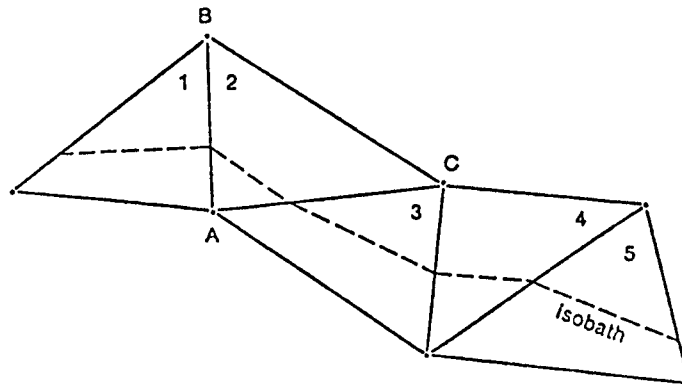


Figure 5

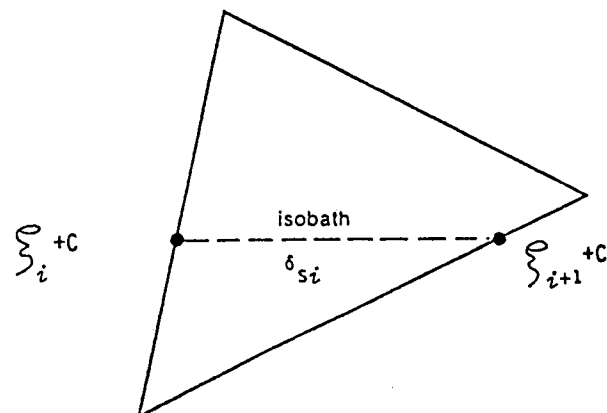


Figure 6

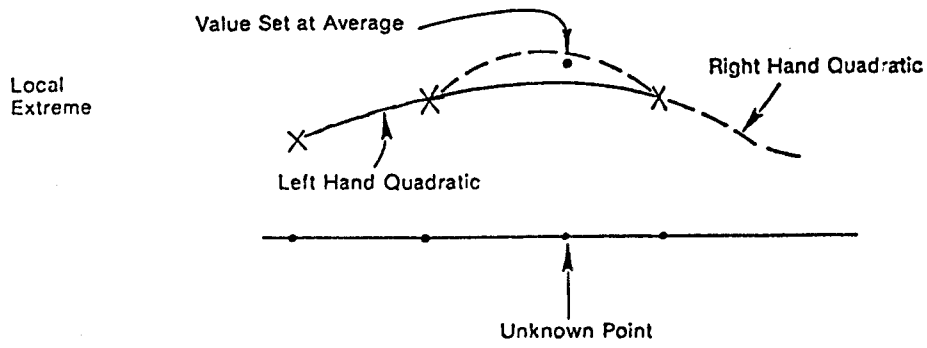


Figure 7

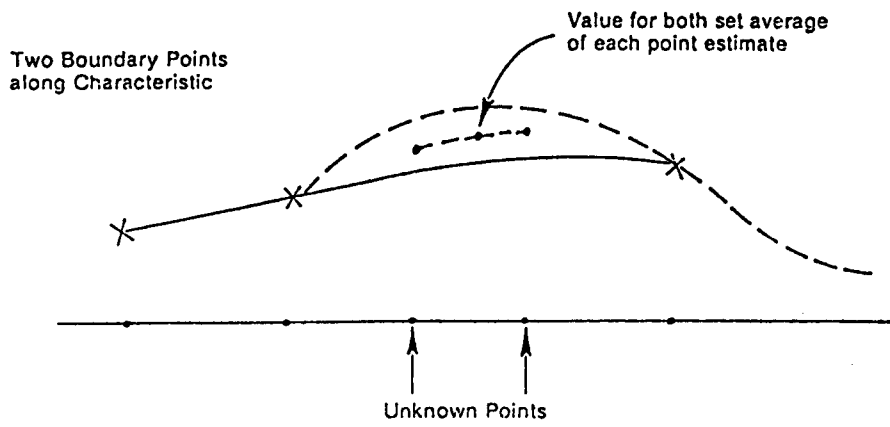


Figure 8

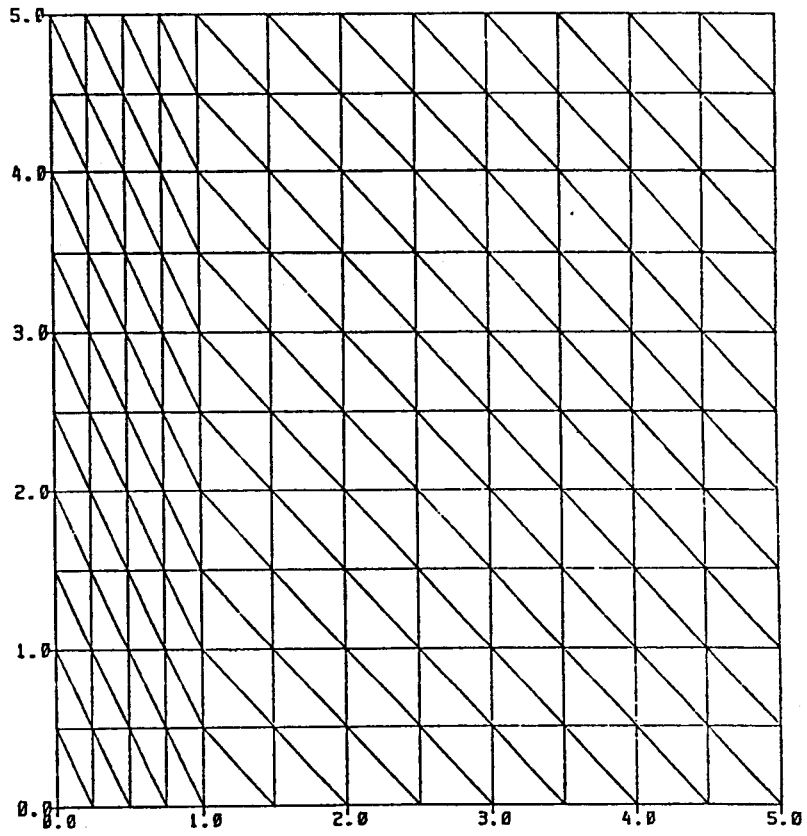


Figure 9

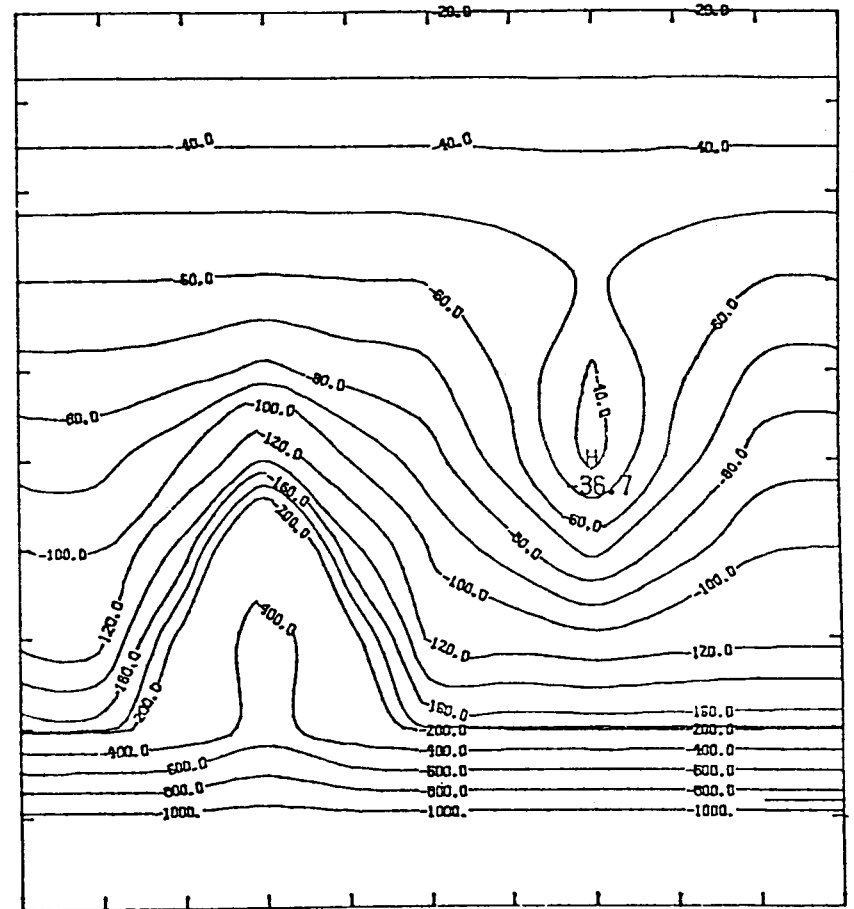


Figure 10

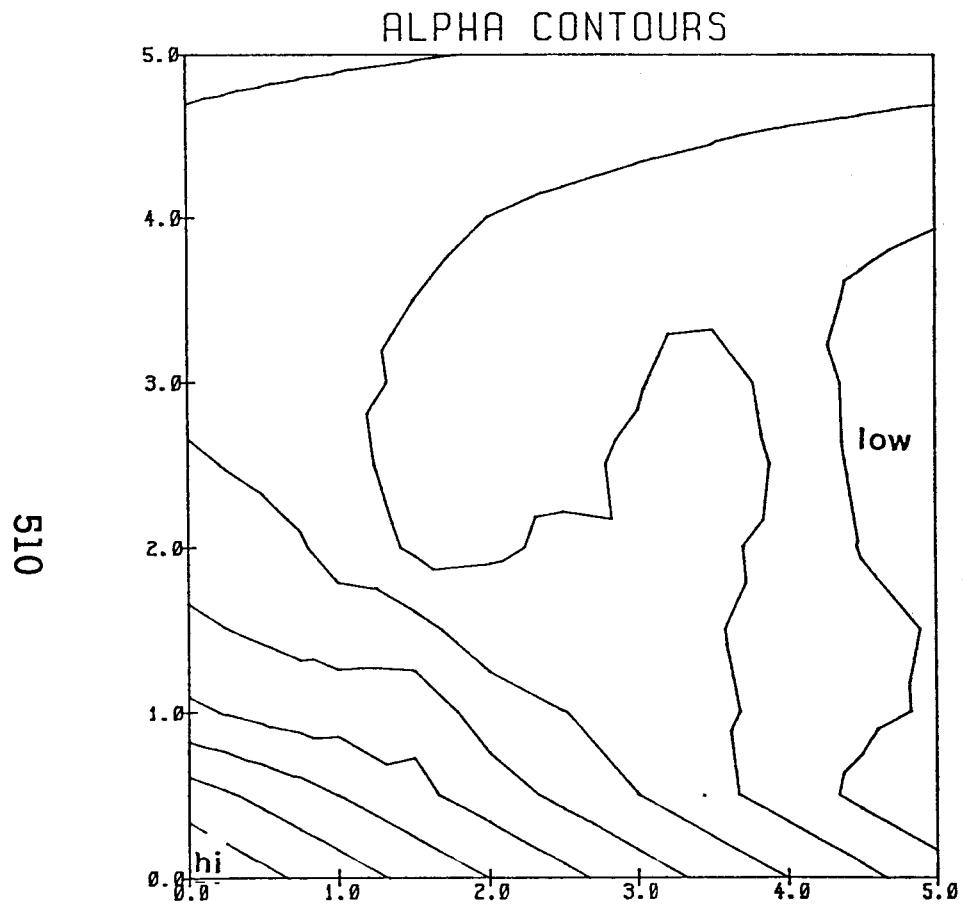


Figure 11

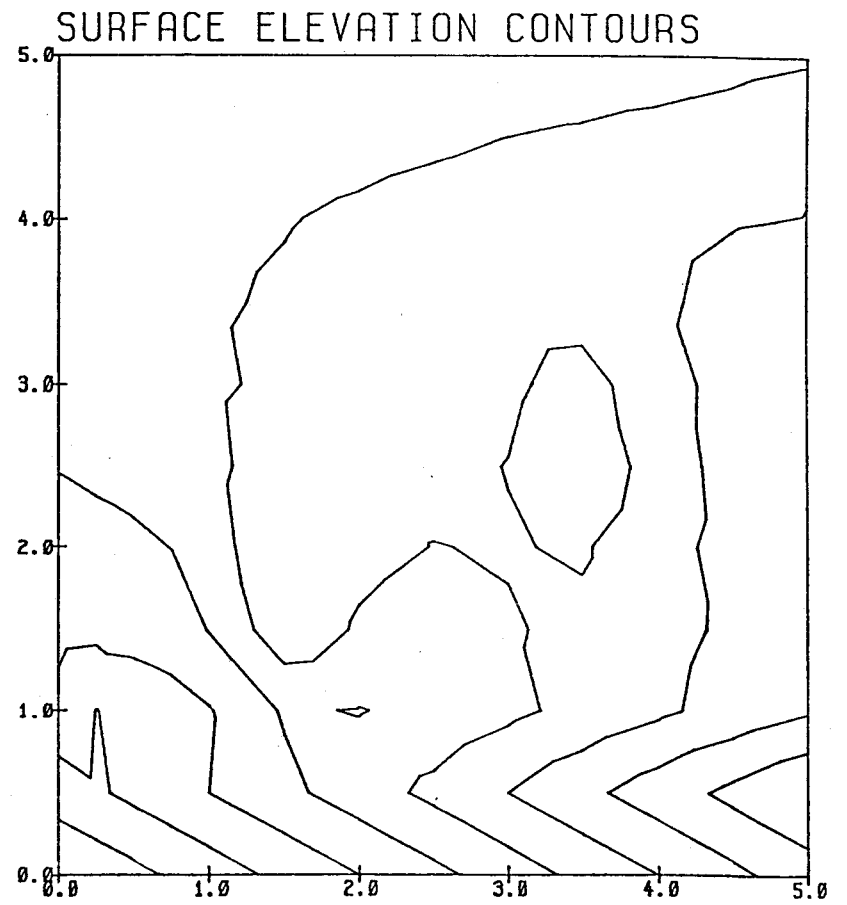


Figure 12a

511

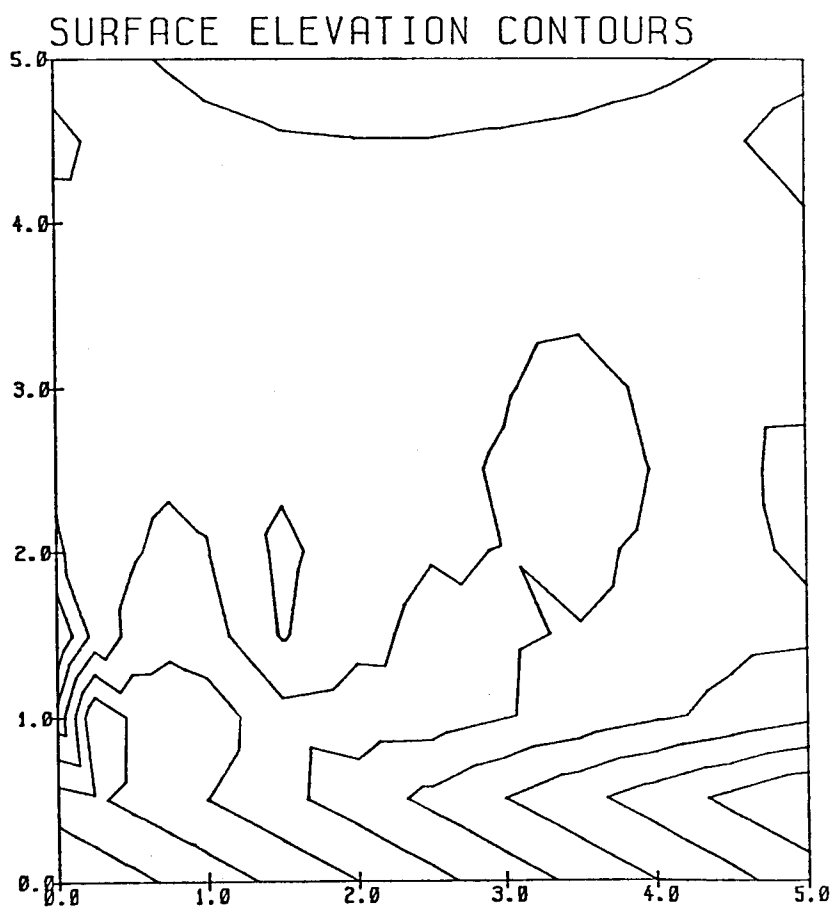


Figure 12b

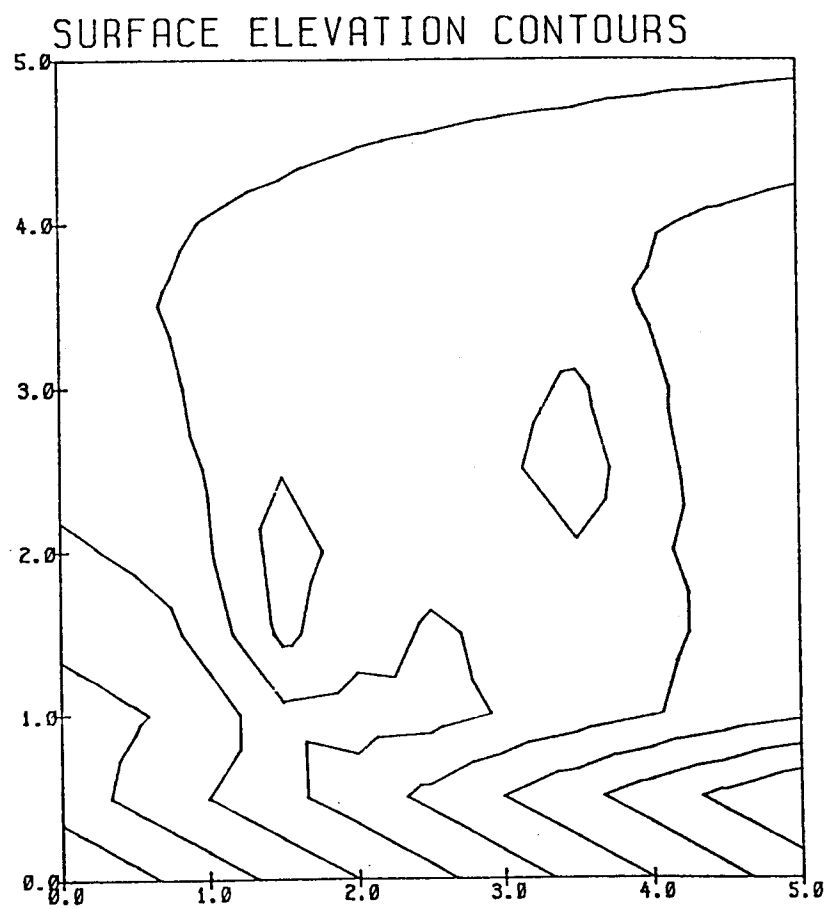


Figure 12c

512

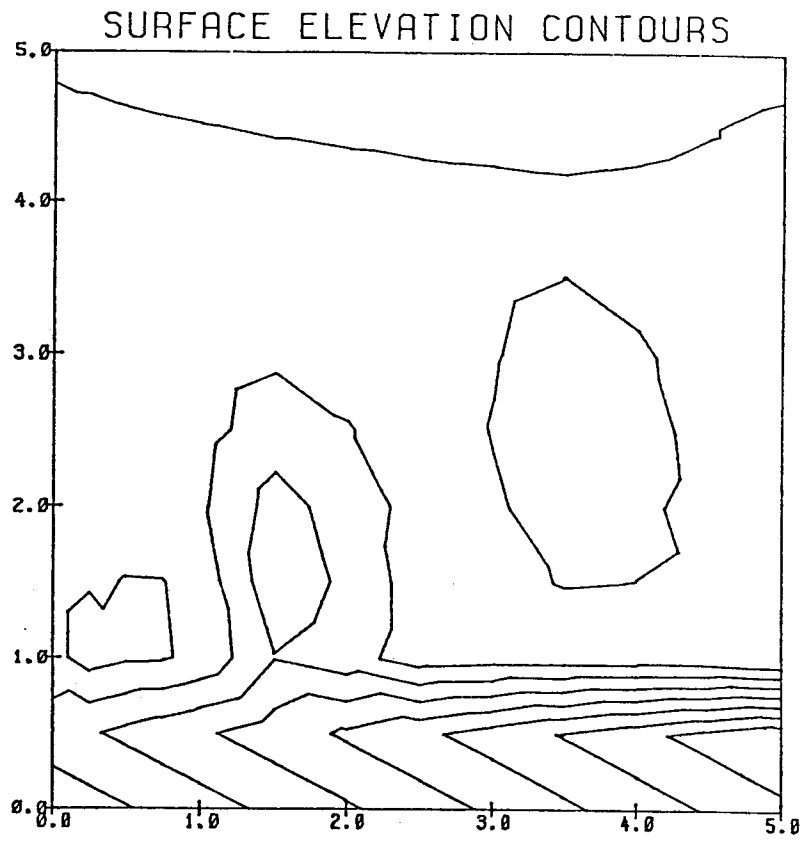


Figure 13a

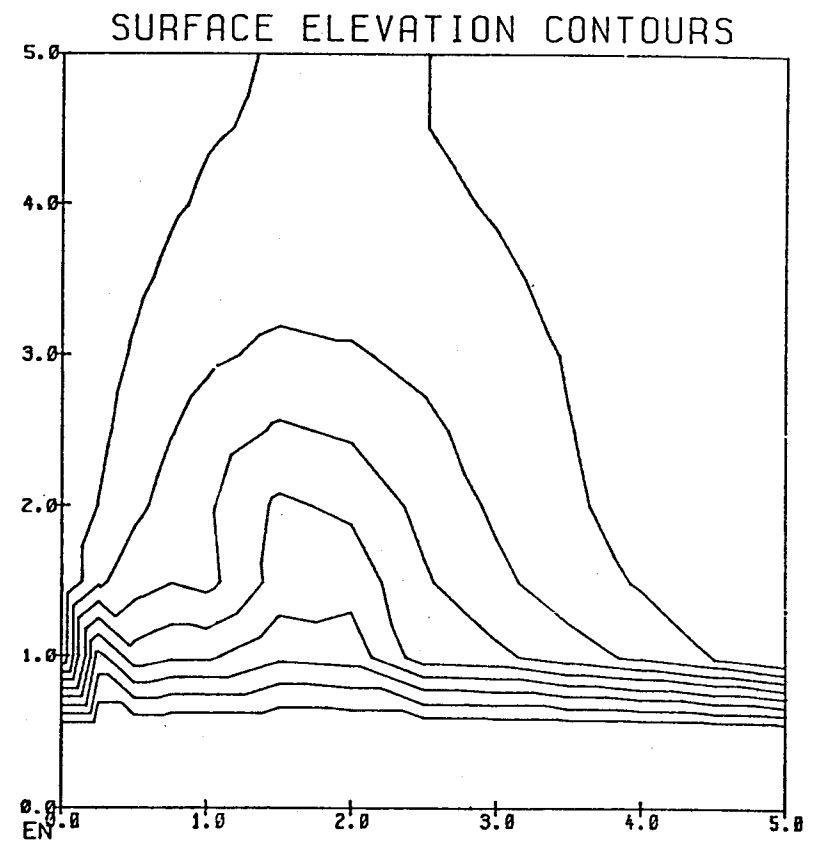


Figure 13b

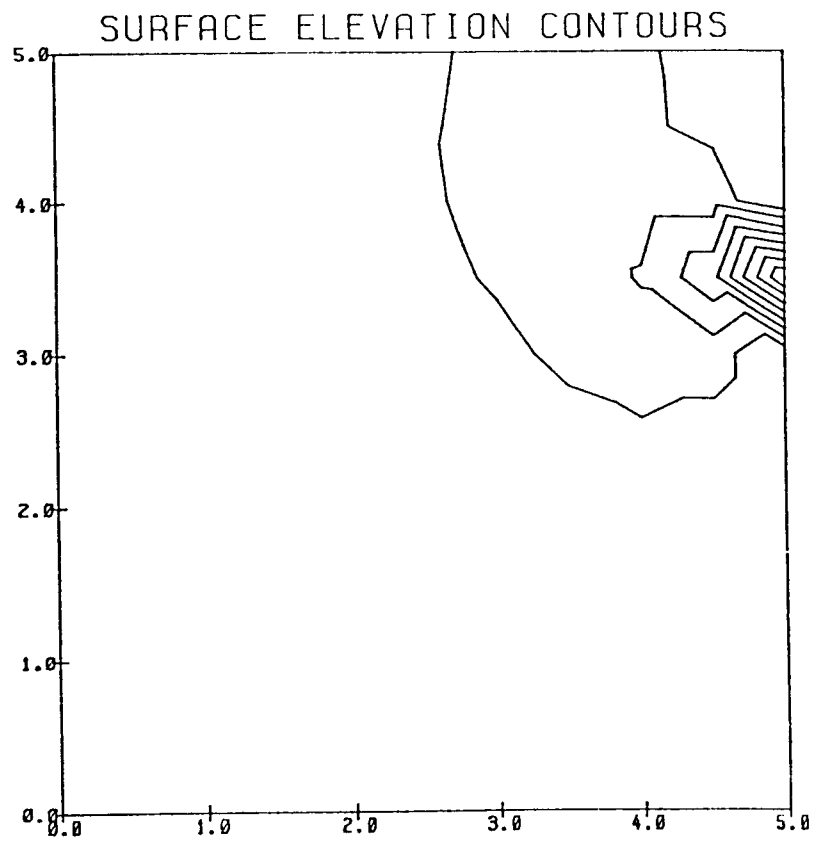


Figure 13c

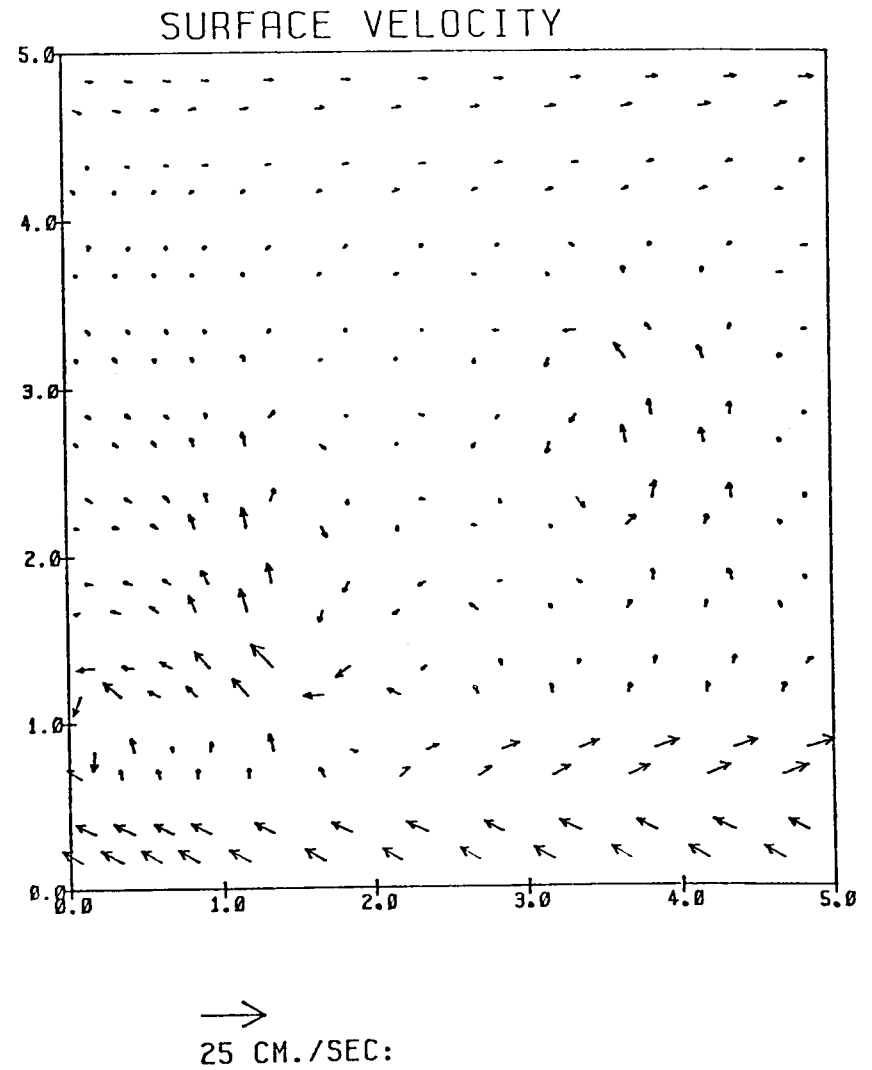


Figure 14a

S14

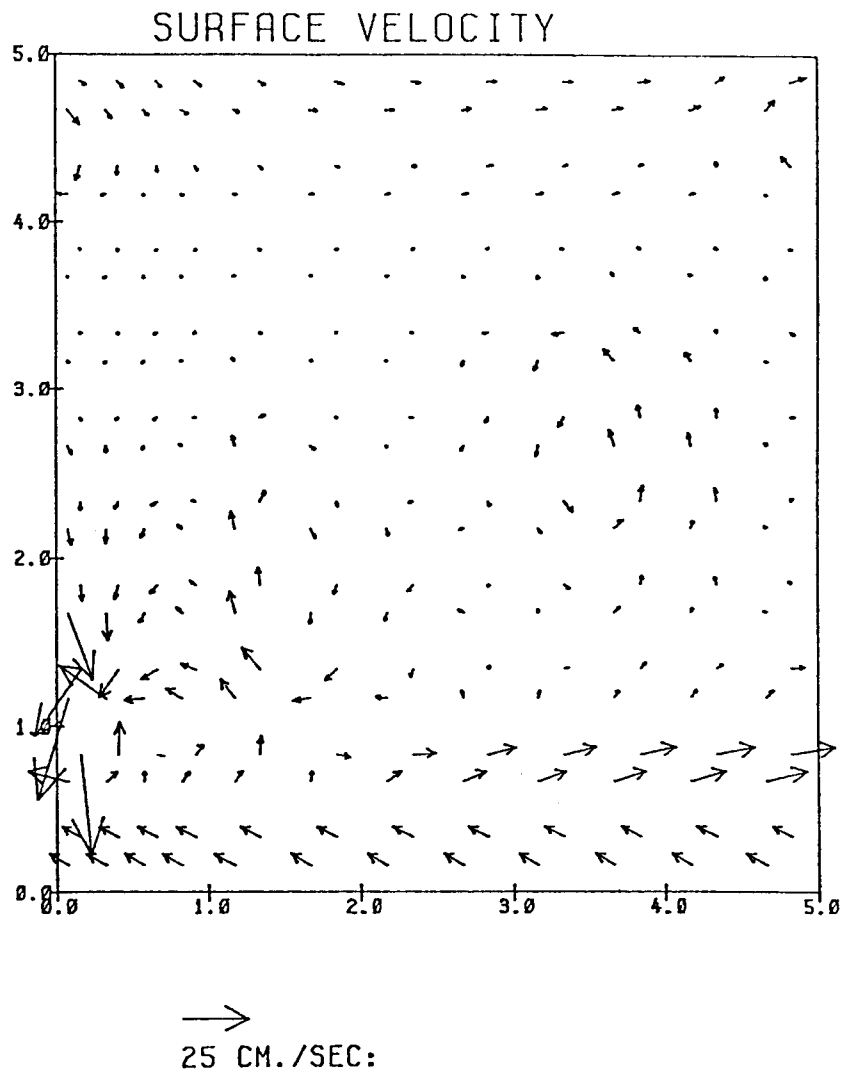


Figure 14b

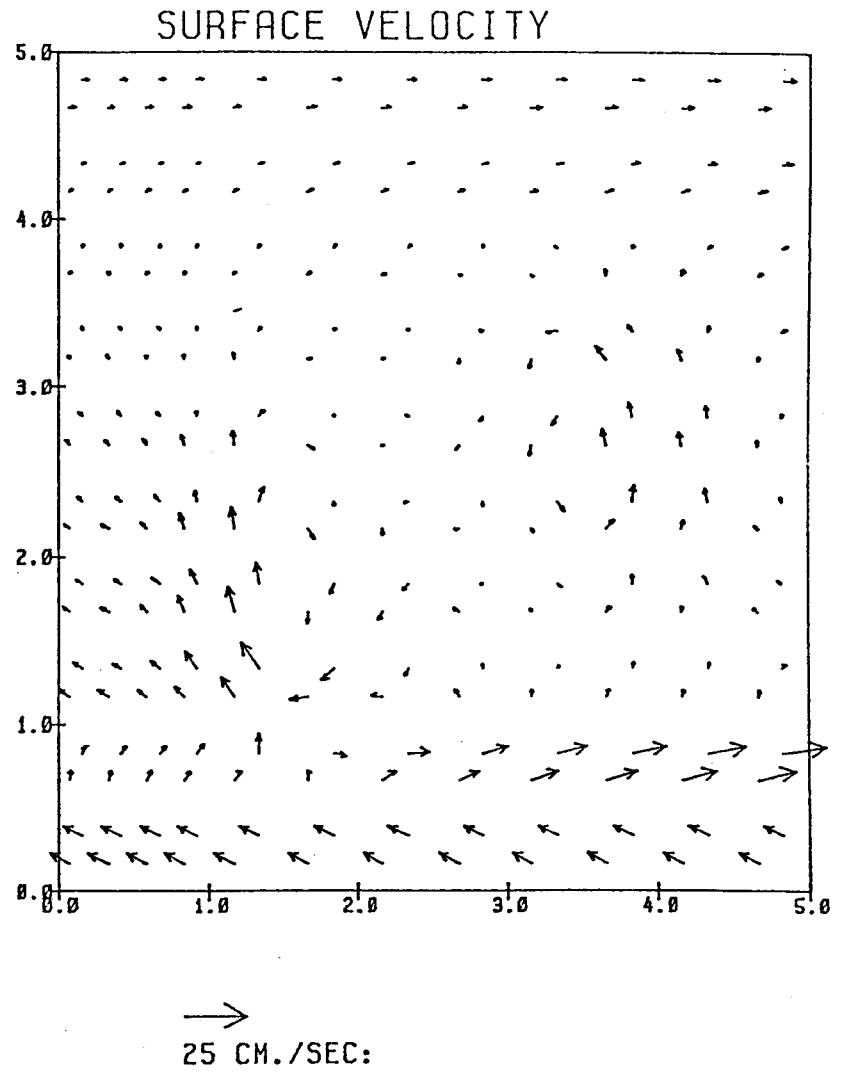
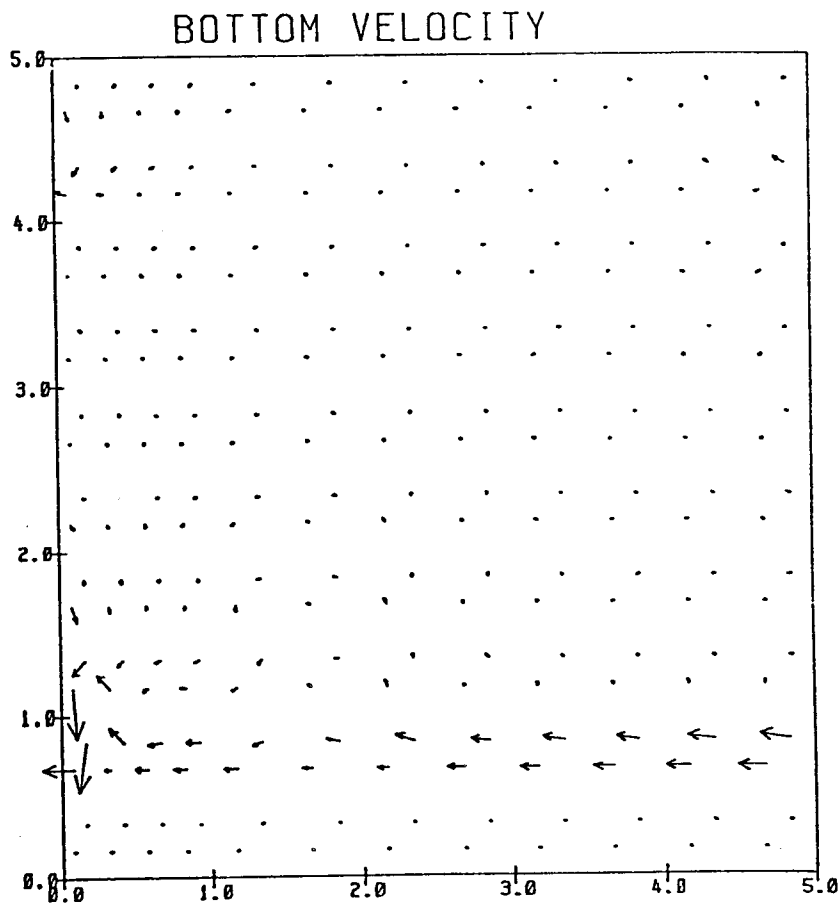


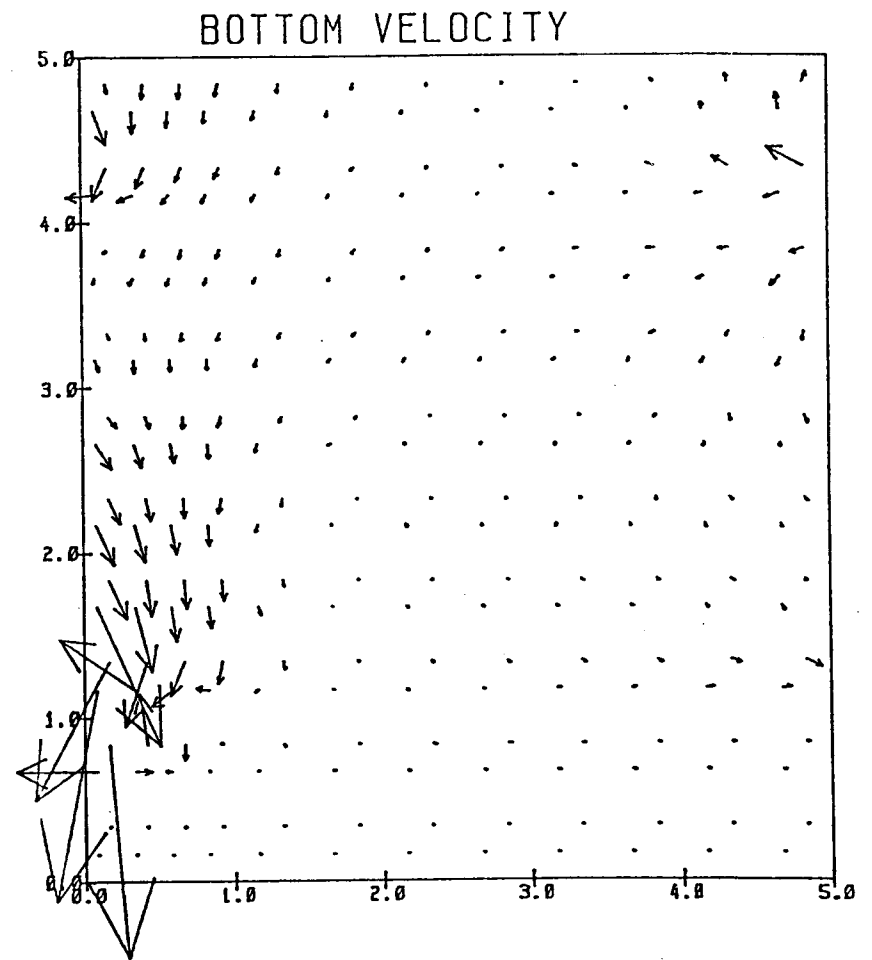
Figure 14c

515



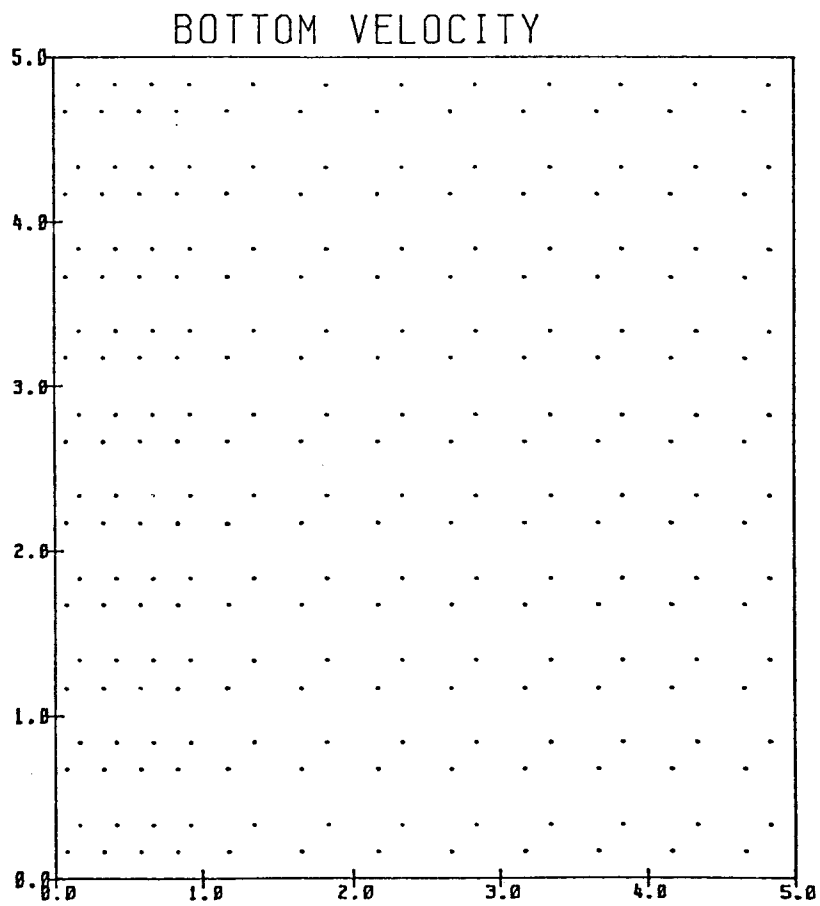
→
25 CM./SEC:

Figure 15a



→
25 CM./SEC:

Figure 15b



→
25 CM./SEC:

Figure 15c

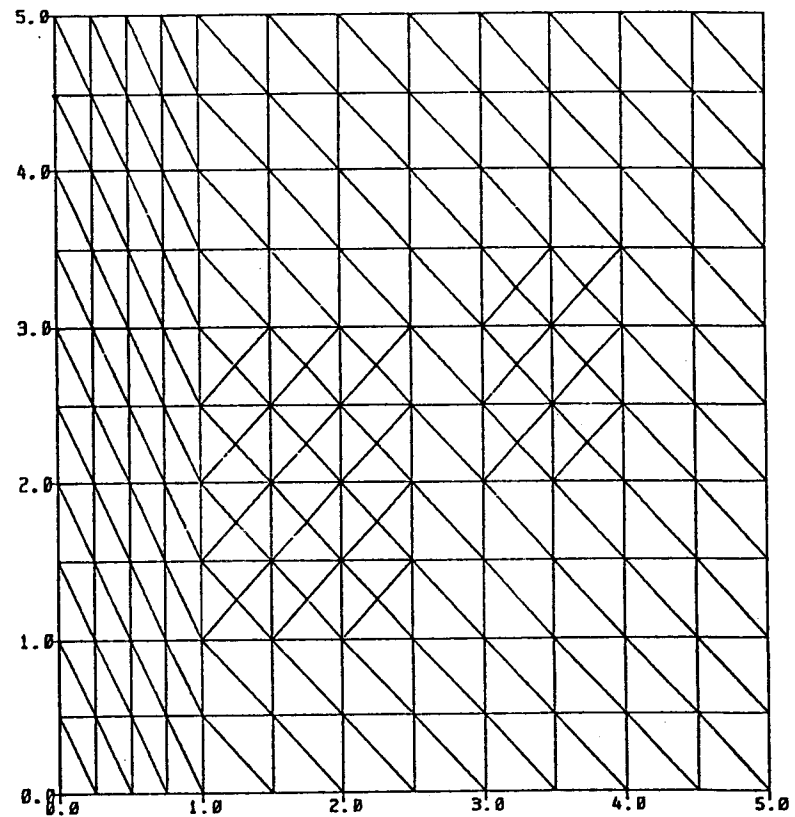


Figure 16

517

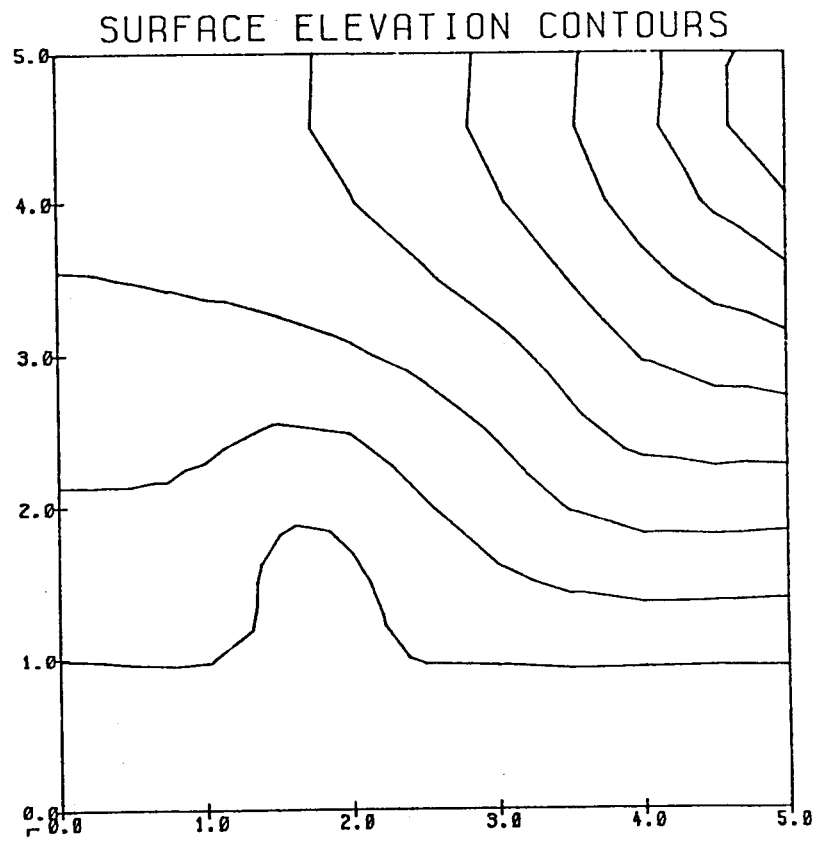


Figure 17a

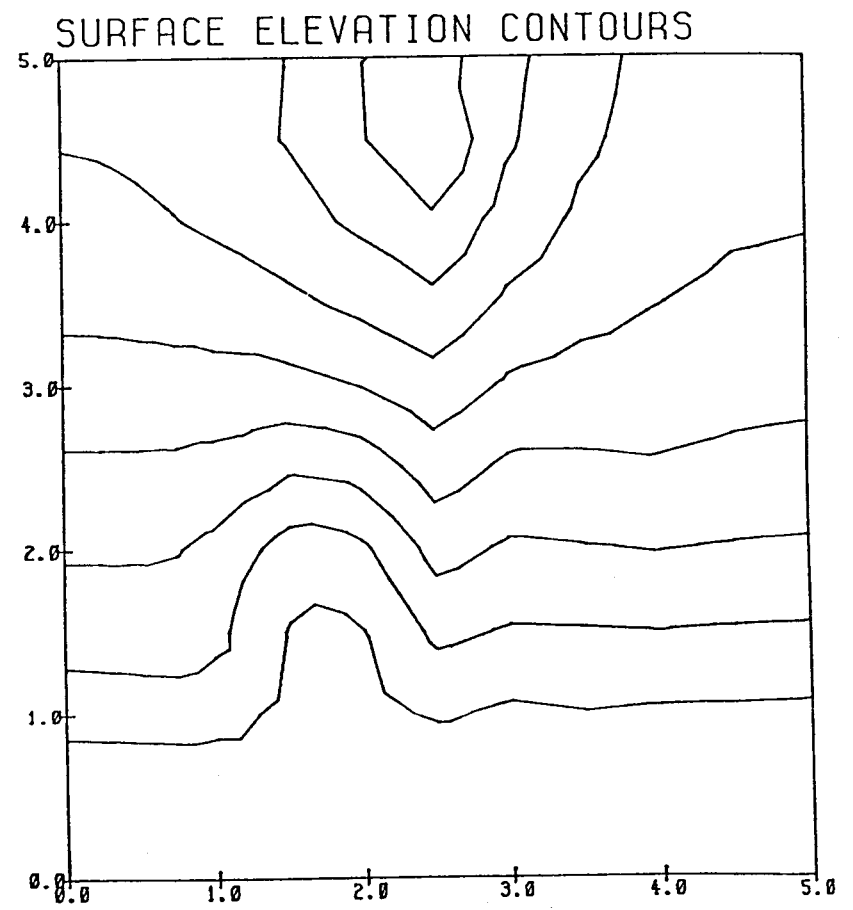


Figure 17b

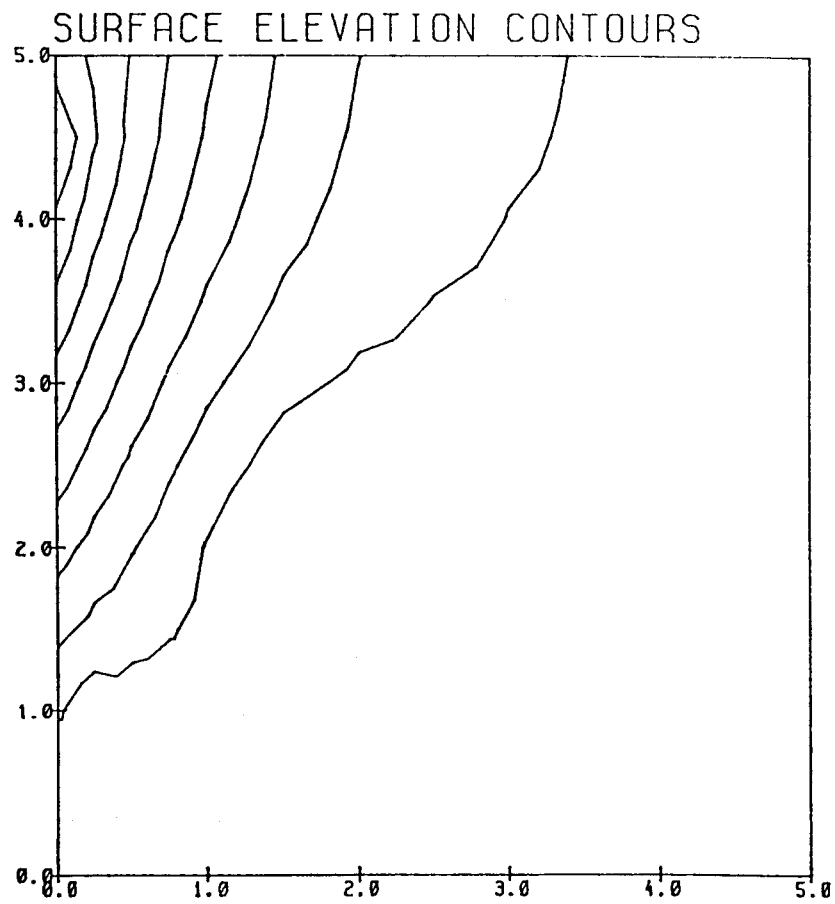


Figure 17c

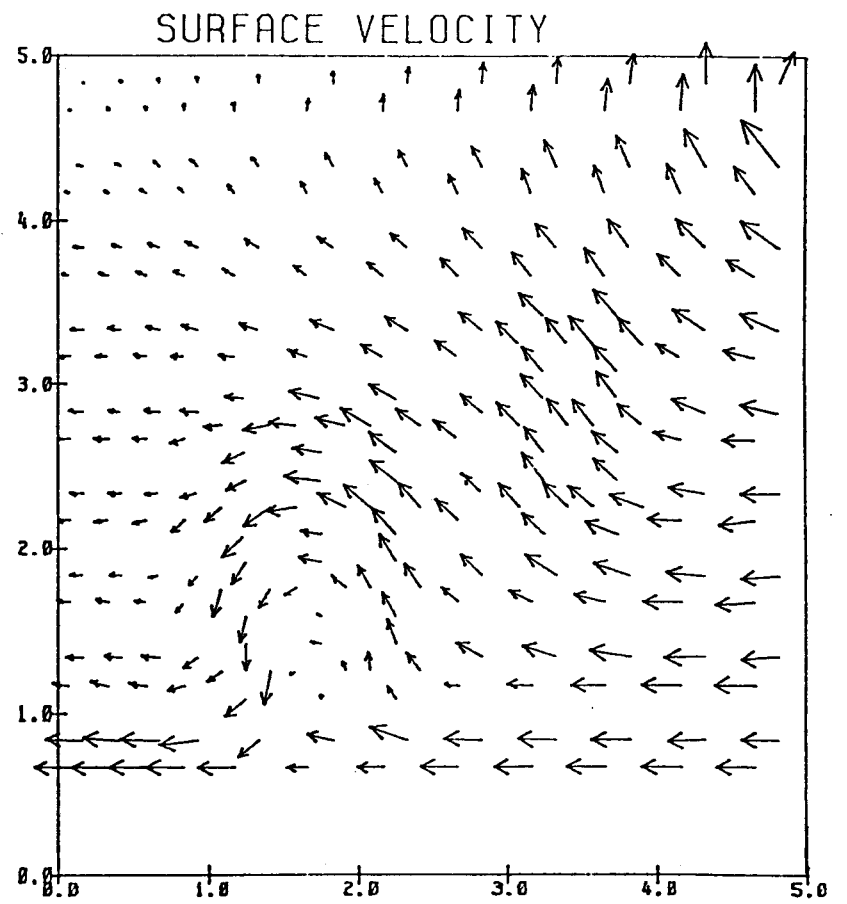
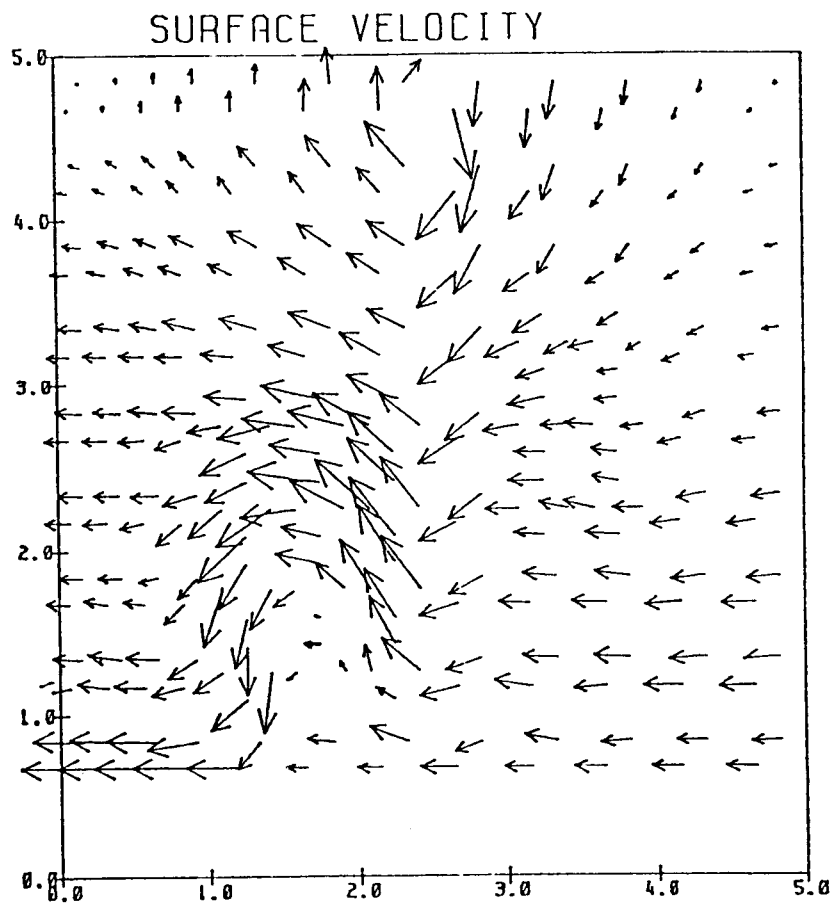
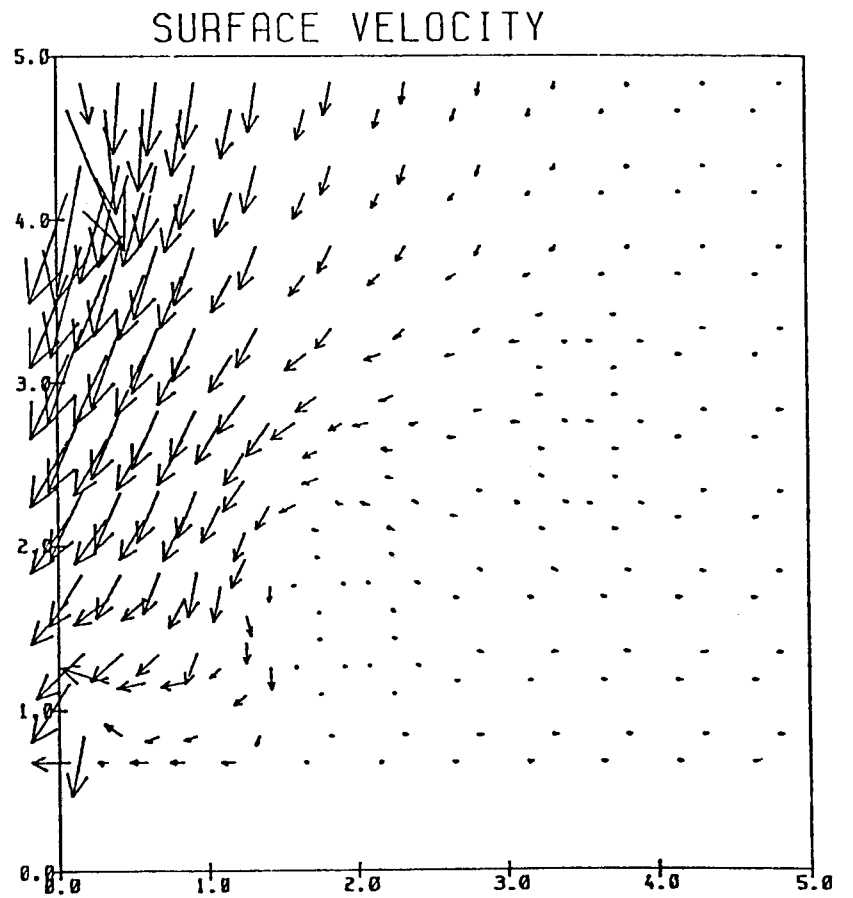


Figure 18a




 5 CM./SEC.:

Figure 18b




 5 CM./SEC.

Figure 18c

520

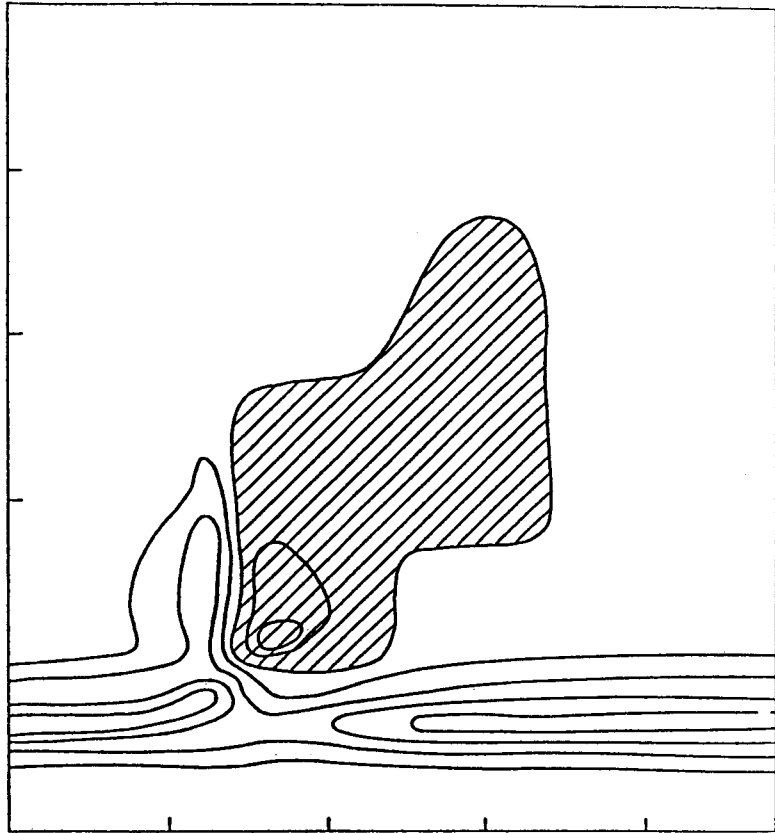


Figure 19

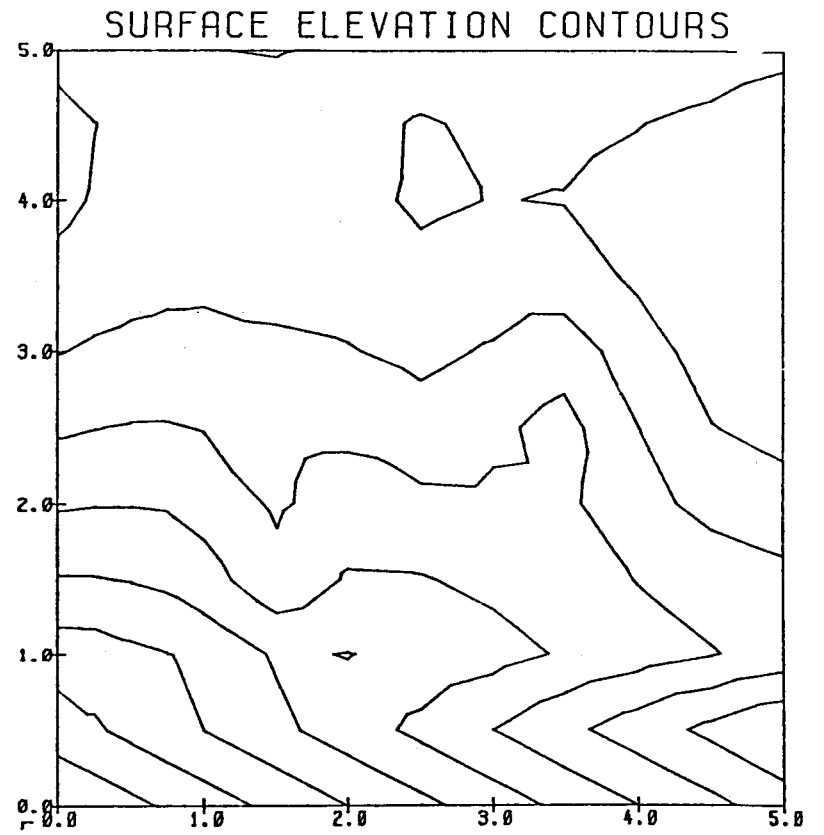
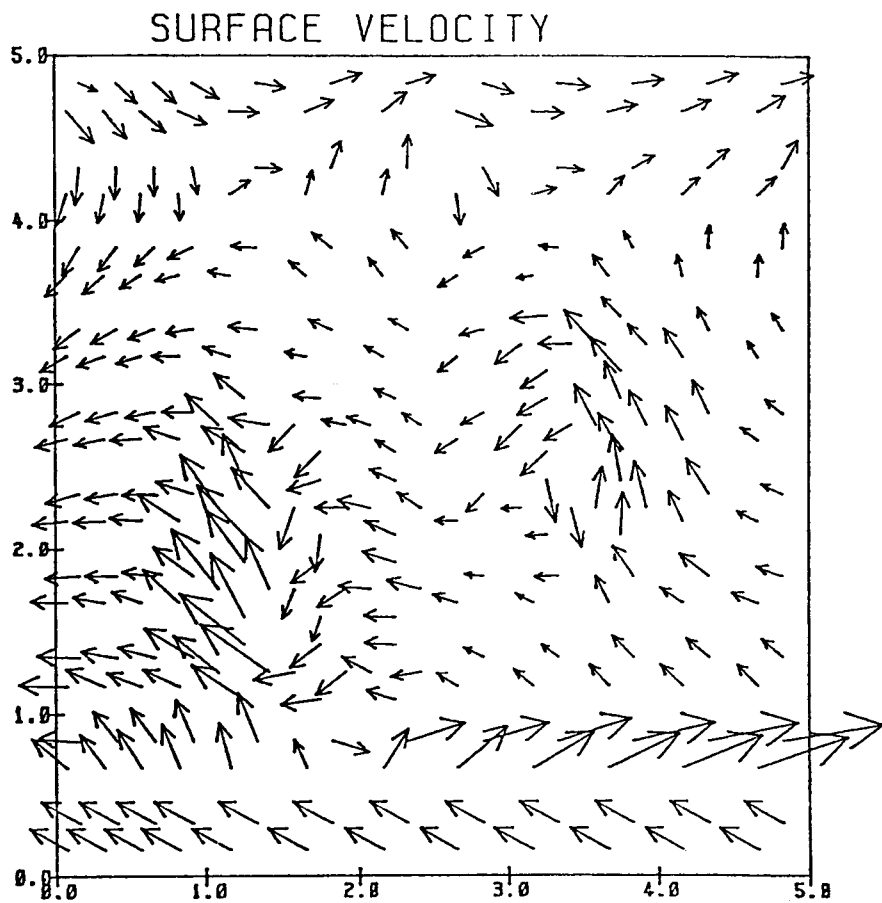


Figure 20a

521



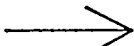

25 CM./SEC.

Figure 20b

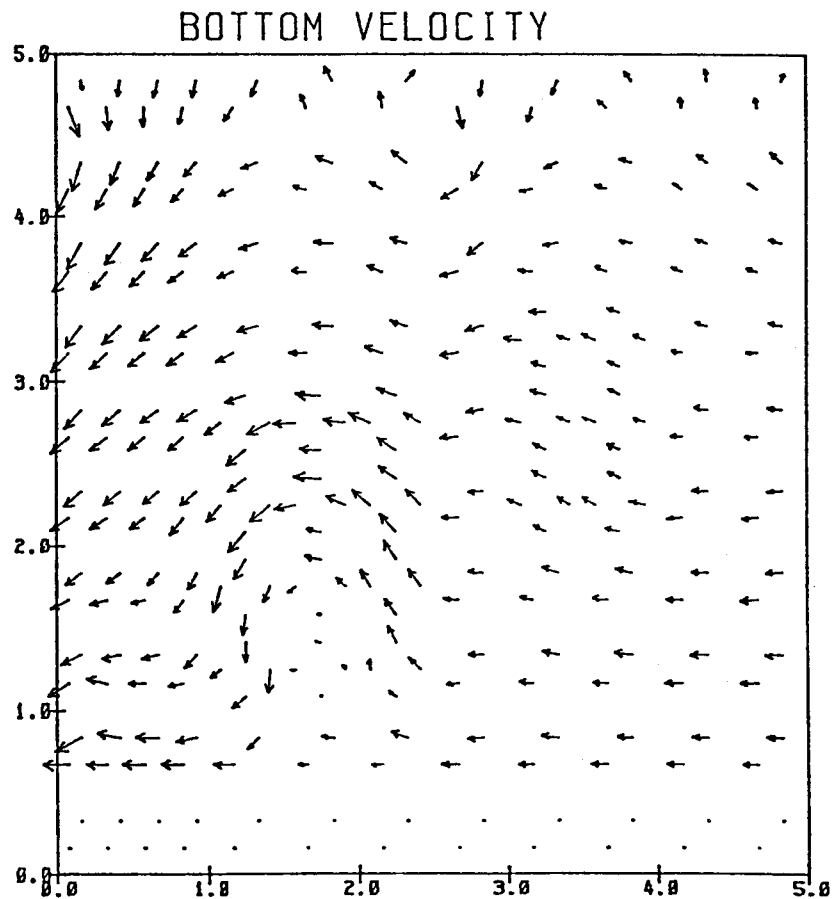


Figure 20c

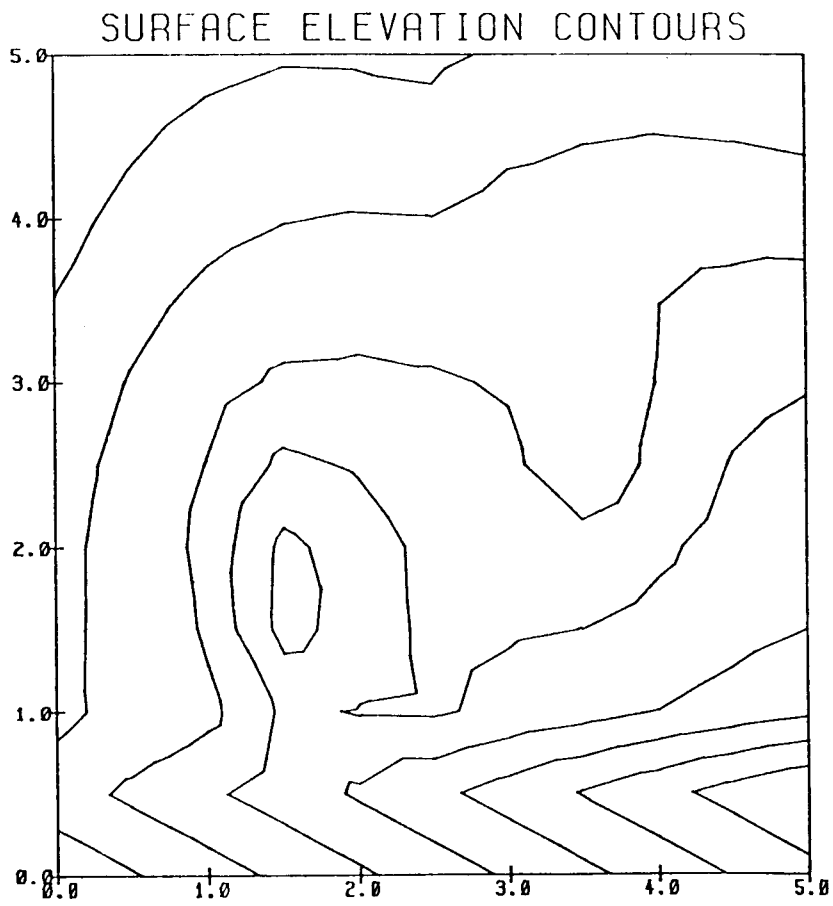
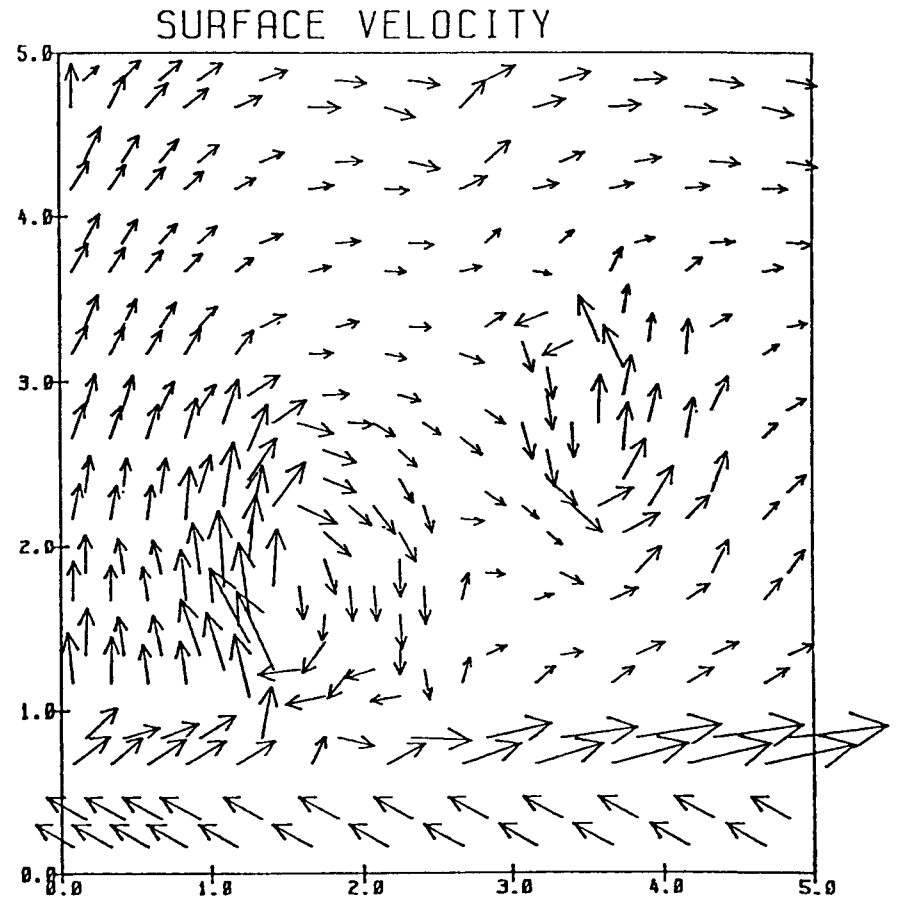


Figure 21a



→
25 CM./SEC.

Figure 21b

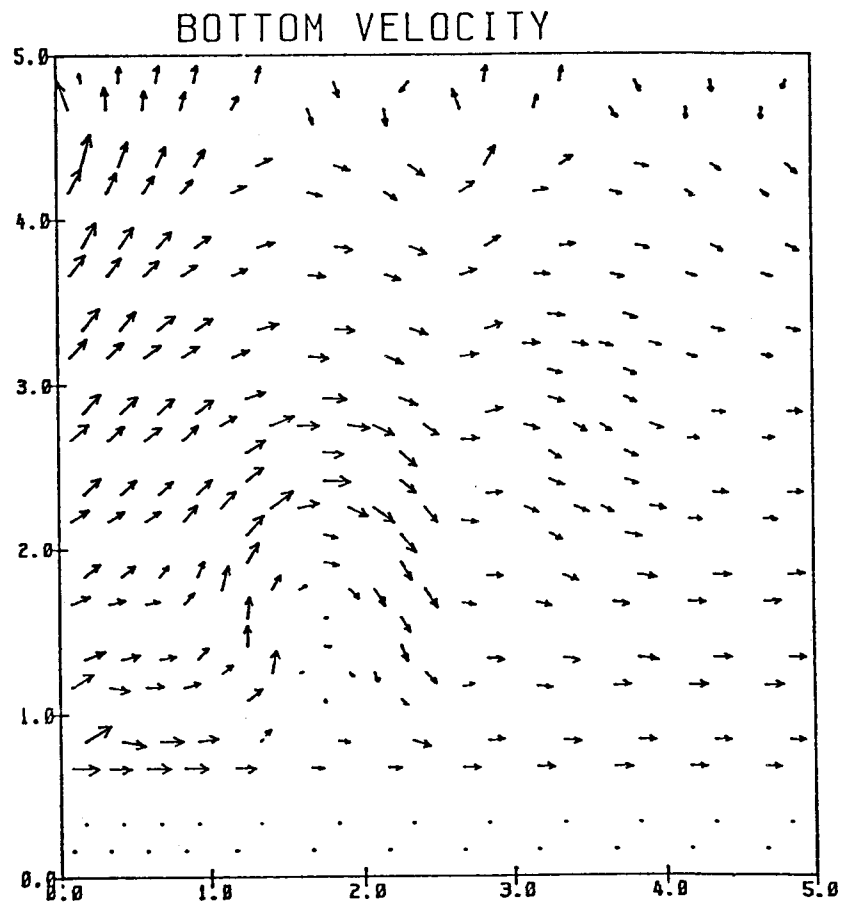
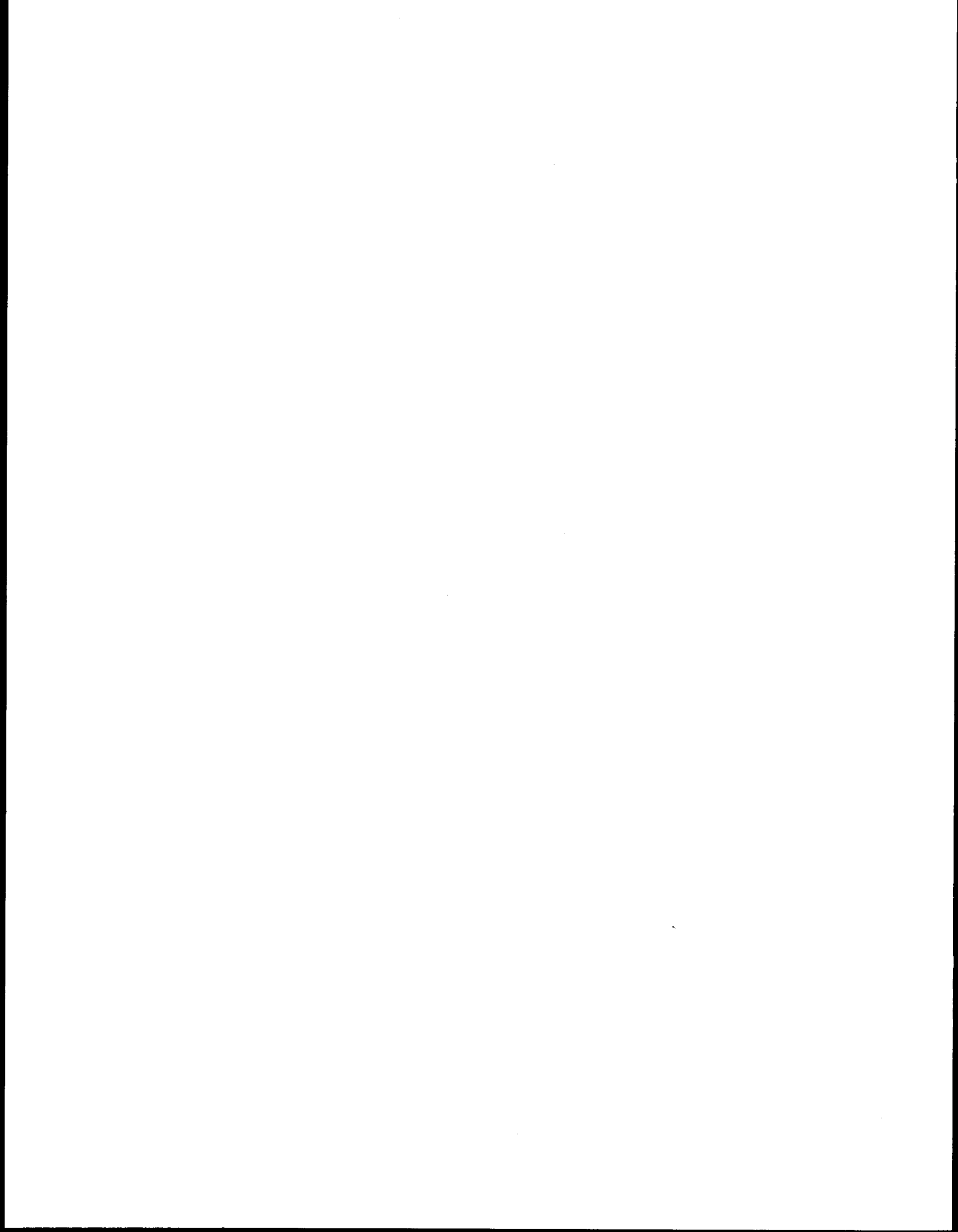


Figure 21c



APPENDIX D

A Synoptic Climatology for Surface Winds
Along the Southern Coast of Alaska

by

J. E. Overland and T. R. Hiester

September 1978

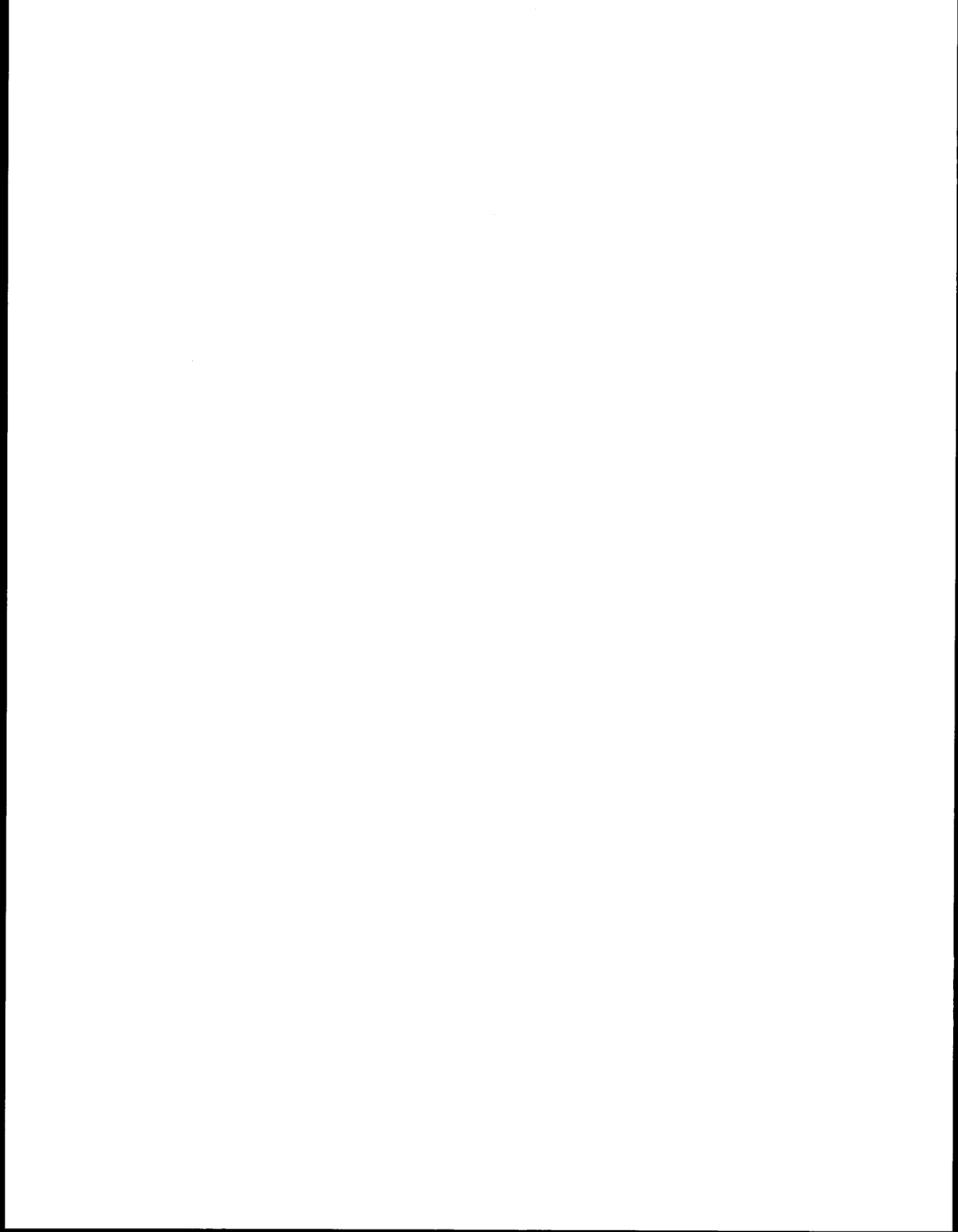
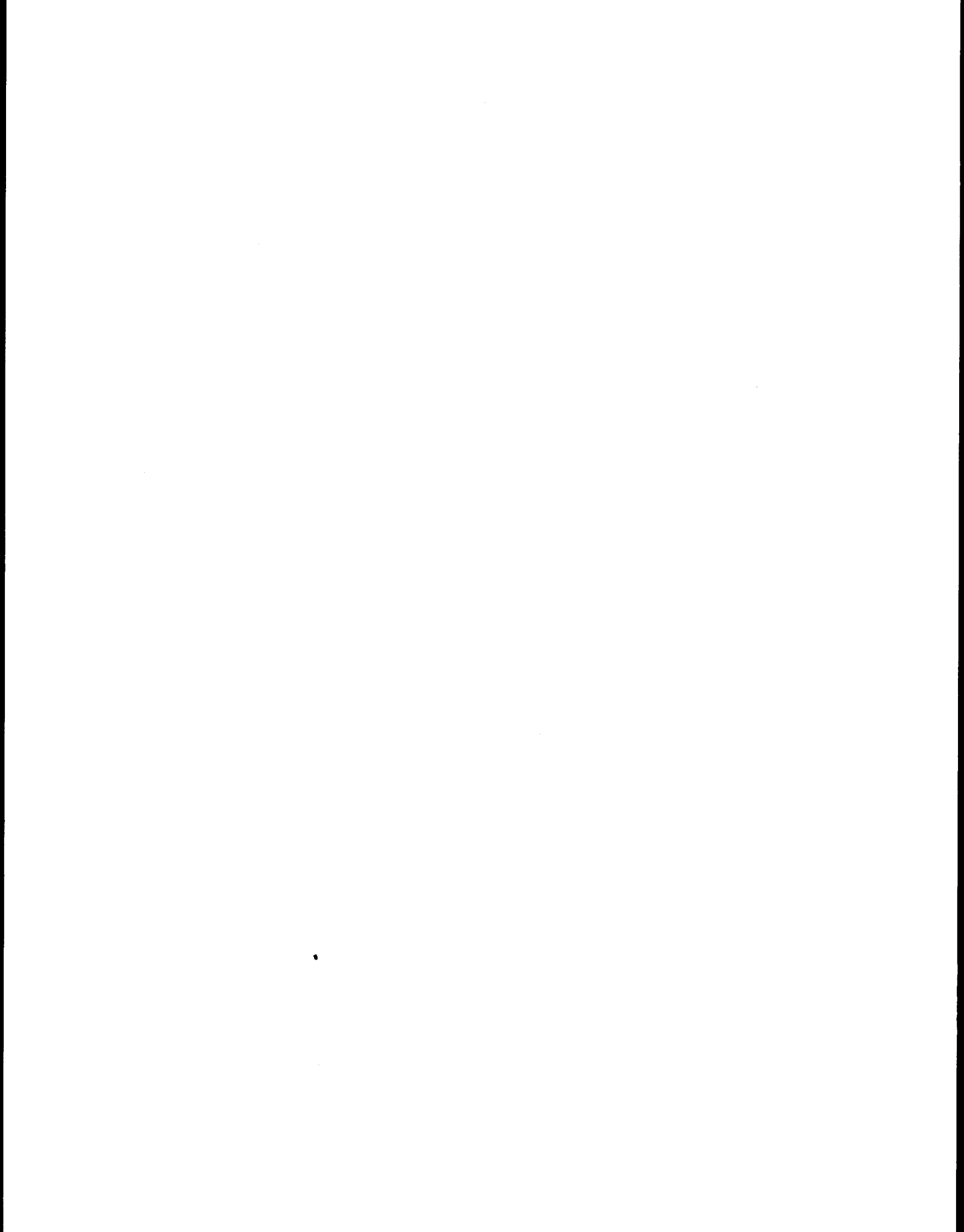


TABLE OF CONTENTS

	Page
1. INTRODUCTION.	529
2. SUBJECTIVE WEATHER PATTERNS FOR COASTAL GULF OF ALASKA.	534
2.1 Technique.	534
2.2 The Six Surface Weather Type Patterns.	536
2.3 Pattern Climatology.	541
3. AUTOMATED WEATHER TYPING.	545
3.1 Methodology and Results.	545
3.2 Comparison With the Subjective Types	546
4. LOCAL WIND FIELDS FOR NORTHEAST GULF OF ALASKA.	550
4.1 Procedure.	550
4.2 Description of Local Wind Fields	564
4.3 Evaluation	568
REFERENCES.	574
APPENDIX A. Subjective Pattern Types	575
APPENDIX B. Automated Pattern Types.	591
APPENDIX C. Local Wind Fields for Each Subjective Subtype.	601



1. Introduction

This report assembles a synoptic climatology to estimate surface winds over the water along the southern coast of Alaska from Yakutat to Kodiak Island. A synoptic climatology is a collection of generalized quasi-steady states of the atmosphere which are frequently observed or a continuum of states along particular storm tracks. The following classification is based upon sea level pressure analyses. Weather types aim to maintain the range of synoptic variability while grouping daily weather maps which have the same basic meteorological structure but slightly different locations or intensities. A synoptic climatology differs from calculation of means in that it specifies specific type patterns, such as a high or low pressure center, which could occur on any given day rather than forming an average over several possibly different sequential daily maps.

It should be recalled that atmospheric modes are continuous in time and that synoptic systems differ in size and intensity throughout their individual life cycle and from one storm to the next. Given the assumption that classification is possible, our approach regards patterns of weather circulation as implicit functions of the static sea level pressure distribution (Barry and Perry, 1973). It differs from a kinematic approach in which synoptic weather maps are classified in terms of principal storm tracks. The former approach is most appropriate in regions where a proportion of features form and/or decay in situ or are persistent. Since the Gulf of Alaska is often the decay center for storms in the Pacific, the static approach is taken as a working hypothesis. Western Europe and the East Coast of the United States are examples where a kinematic approach would be more appropriate.

This study was initiated as part of the Outer Continental Shelf Environmental Assessment Project (OCSEAP) to provide local winds to an oil spill trajectory model, coupled with the ability to provide frequency of occurrence information from the meteorological record. The intent is to retain the influence of a daily wind variability on the dispersion of trajectories as part of a climatological assessment.

There are two approaches to map typing which can be referred to as objective (or at least automated) and subjective. Objective typing can be considered a pattern recognition problem involving digitized weather maps. Such techniques are generally based upon principal component analysis, factor analysis and their close relatives (Kendall and Stuart, 1975) or pattern correlation techniques (Lund, 1963). General objective techniques are being investigated as a companion study to the research reported here. The subjective approach involves assigning daily weather maps into different categories by a synoptic meteorologist. A rationale for subjective typing is that in order for patterns to be successful the underlying meteorological processes leading to these patterns should be recognizable.

This report establishes six subjectively derived weather types which are subdivided into twelve subtypes for the Northeast Gulf of Alaska (NEGOA) - Kodiak Island region. These six patterns were derived from combining and modifying patterns from two previous studies by Sorkina (1963) and Putnins (1966), subjective analysis of fall 1977 - summer 1978 sea level pressure charts from the National Meteorological Center, and post modification of patterns based upon daily typing of candidate patterns. Post analysis indicated the necessity of including subtypes. Subtypes

within a type contain the same general distribution of features and meteorological basis but represent slight variations in locations of features which cause changes in the orientation of the geostrophic wind at the central location of the NEGOA coastline. These types are developed in chapter 2.

An additional resource for this study is the digitized sea level pressure grids for the northern hemisphere produced by the National Meteorological Center (Jenne, 1975). These fields are available for 1968-1975. Each subjective subtype was digitized on the same mesh as the Meteorological Center grid for twenty-four common points (figure 1). A daily map may then be quickly typed by computing its correlation with each of the subjective types. Such a procedure forms the basis for percent coverage and transition probability calculations for the various types.

The second approach to typing considered in this report consists of applying the pattern correlation technique (Lund, 1963) to the digitized daily weather maps. The pattern correlation technique consists of forming the correlation of each day with all other days during the year. The day with the highest number of correlations greater than a prescribed cut off value as type A. All days that correlate greater than the cut off value with type A are removed and the procedure is repeated to find type B; the analysis is continued until the data is exhausted. This procedure is applied to NEGOA as an independent check on the subjective typing and documented in chapter 3.

The relation of the surface wind fields over coastal waters of Alaska to geostrophic winds is complicated by coastal blocking, extensive air mass modification and mesoscale features induced by coastal topography. The available density of station data does not provide the resolution of the

spatial variation of the wind field over the water for input to trajectory calculations. As an alternative we have developed local wind fields on a $7\frac{1}{2}$ minute latitude by 15 minute longitude grid which are the assumed local winds that occur with each synoptic scale subtype. These local patterns use a single point planetary boundary layer model proposed by Cardone (1969) to compute surface stress from the geostrophic wind, including corrections for thermal influence, and modify the near shore wind field based upon the field program of Reynolds, et al. (1978).

NMC OCTAGONAL GRID

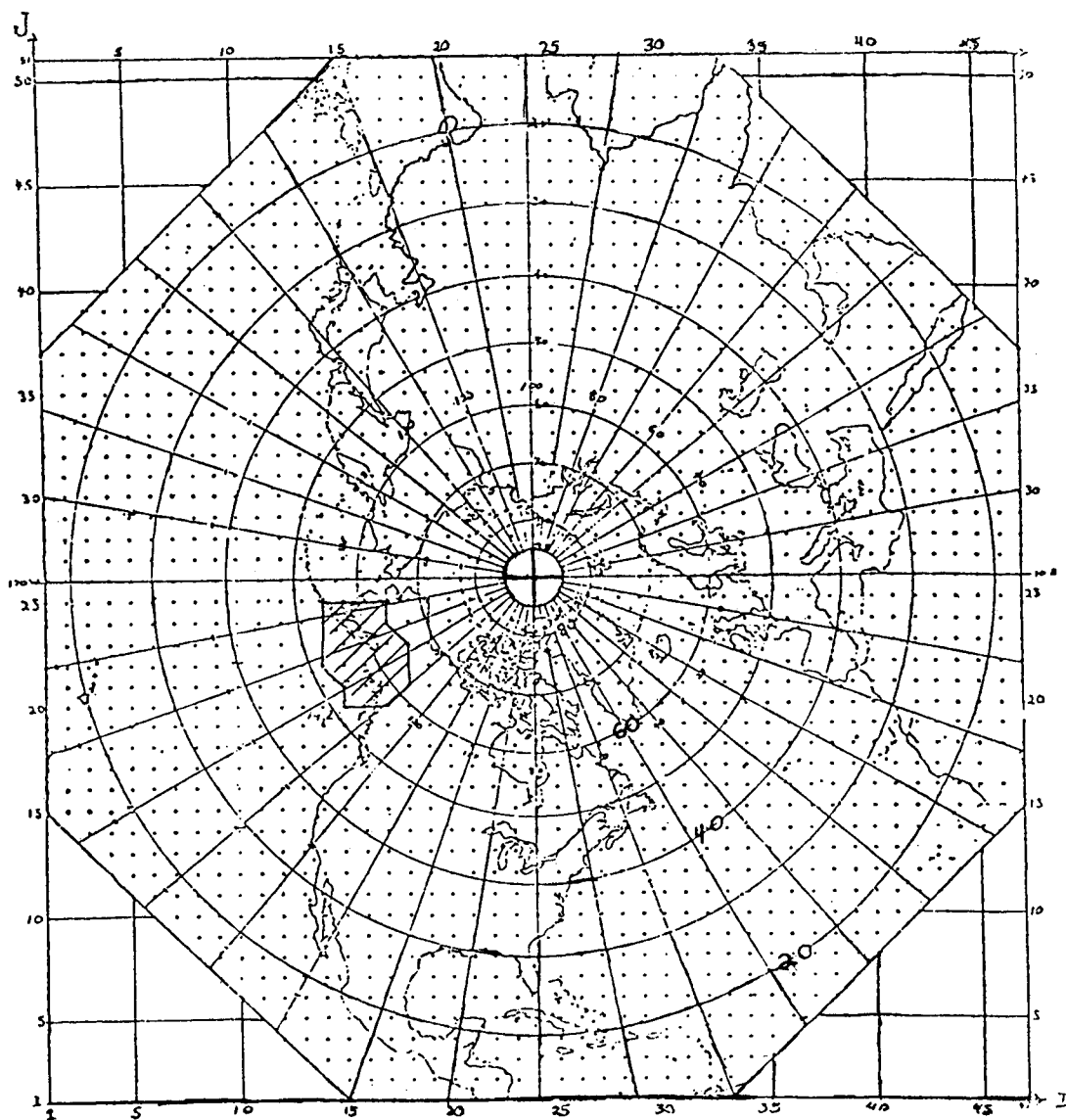


Figure #1 NMC 47 x 51 grid. There are 1,977 points in the entire grid. The subset of 24 points used in this study are shown by a lined region.

2. Subjective Weather Patterns for Coastal Gulf of Alaska

2.1 Technique

The two previous studies to find type patterns, duration, and transition probabilities which cover southern Alaska are Sorkina (1963) and Putnins (1966). Our six patterns result from modifying Putnins' patterns in the following ways:

- a) combining like patterns
- b) modifying them according to Sorkina's patterns
- c) using fall, winter and spring of 77-78 sea level pressure analyses from the National Meteorological Center to test the patterns and to modify them accordingly.

Sorkina (1963) provides a description of the surface circulation patterns over the entire North Pacific Ocean. Fifteen patterns are obtained based on 16,000 daily synoptic maps spanning 47 years (1899-1939, 1954-1959). Each pattern is subjectively justified upon meteorological grounds. Seasonal duration and transitional probability statistics are established. Three underlying regional physical processes are evident which can be combined and rearranged to make each pattern. These are zones of cyclogenesis, high pressure regions, and regions for stagnation of lows. The horizontal temperature contrast between the northwest Pacific and the adjacent continent gives rise to the arctic front, a region of active cyclogenesis, which is oriented SW-NE near Japan in the mean. The newly formed cyclones travel rapidly toward the northeast. The curved coastline of Alaska is a region where low pressure centers stagnate. High pressure areas and zones of cyclogenesis tend to alternate at mid-latitudes, while regions of stagnation and zonal bands of rapid movement for lows alternate at higher latitudes. Sorkina

shows that each of her patterns is seasonally persistent and tends to lead to specific other patterns.

Sorkina's patterns were applied to a new data set, the daily Pacific surface analyses at 1800 GMT from September 1977 to December 1977, prepared by the Ocean Services Unit of the Weather Service Forecast Office in Seattle. An analysis of map sequences for the middle and eastern North Pacific showed that the daily maps would closely resemble one of Sorkina's patterns in general character for a day or two, followed by three or four days of less identifiable character as the cyclones moved rapidly from cyclongenesis regions to stagnation regions where the maps would again closely resemble a type pattern for another few days.

Sorkina (1963) provided a very useful reference; unfortunately, her type patterns cover the whole northern Pacific and do not adequately resolve the comparatively small and peripheral coastal Gulf of Alaska. Putnins' patterns are on a more applicable scale. However, Sorkina excels Putnins in establishing physical bases for her patterns and was used as a general guideline for deciding the final six type patterns.

Putnins' twenty-two patterns were also obtained from a large data set. Weather maps, both surface and 500 mb, for the period 1 January 1945 to 31 March 1963 were used to determine types "in such a way that for every date of this period a specific baric weather pattern could be assigned." Duration and transition frequencies were also found. The 500 mb patterns were used to assign either a 'cyclonic', 'anticyclonic' or 'mixed' designation to the flow pattern aloft. Most of Putnins' patterns can be related to one or another of Sorkina's patterns. Representative daily maps are shown by Putnins as examples of each type. However, little physical discussion is

given of each type and several of the infrequently occurring types seem arbitrary. Furthermore, his patterns apply to all of Alaska so that the difference between any two patterns is sometimes due to a difference occurring far from the coastal Gulf of Alaska. Thus many of these patterns have been grouped and redrawn to be more useful for Gulf of Alaska studies.

2.2 The Six Surface Weather Type Patterns

The six types (Table 1) represented by twelve subtype patterns are shown in Appendix A as figures A1 - A12. All 22 of Putnins' patterns can be incorporated into these slightly more general patterns, and most of the 77-78 surface maps subjectively resemble one or another of the twelve. Subtypes consider the same meteorological conditions as the parent type, but represent slight variation in location of pressure centers which result in large wind direction changes over NEGOA. For example, the major subtypes for Type 1 are relocating the low center along the coast as seen in figure 2.

An example of how these patterns were obtained is given for the common case of a stagnating low pressure system tucked into the center of the coastal Gulf of Alaska. The underlying broad pattern, Sorkina's 4c, is shown in figure 3. Putnins' type patterns A₁ and A' shown in figures 4 and 5 reveal more of the necessary details and the effect of the orientation of the land and ocean on the isobar pattern. Type pattern 1, figure 2, was thus determined concentrating on the orientation of the geostrophic wind along the coastal Gulf of Alaska.

Type pattern 1 (Figure A1 - A4) is a manifestation of the natural stagnation region for cyclones provided in fall, winter and spring by the higher elevation, relatively cooled land to the north. Cold air in the interior

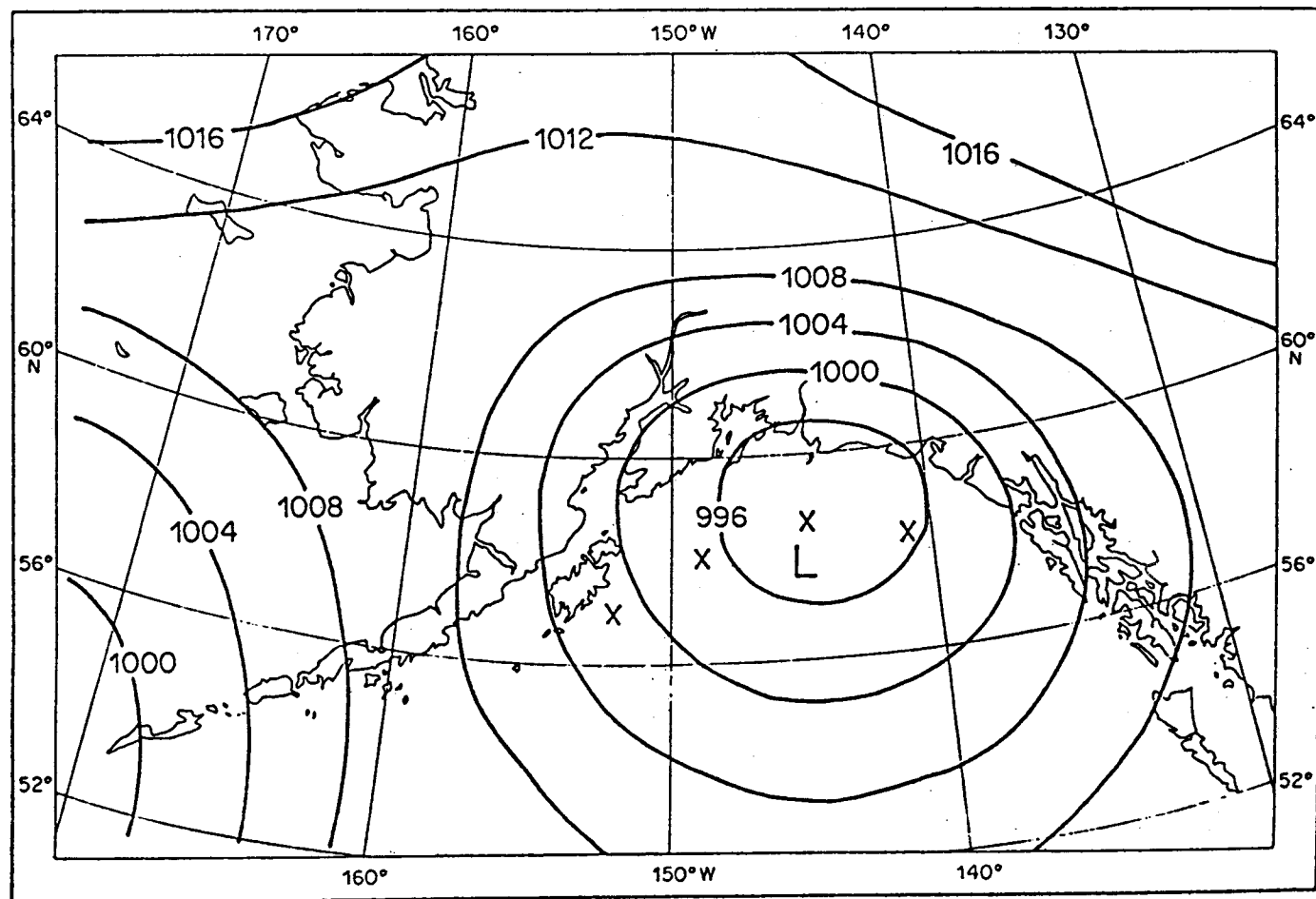
TABLE 1

Type	Description	Sorkina Type	Putnins Type	Dominant Season
I	Low in Gulf of Alaska	4c	A', A ₁ , G, H	Winter
II	Aleutian Low	5b	A, C, E, A _c	Winter, Spring, Fall
III	High pressure in Alaskan Interior	6a	D, B, D	Winter
IV	Low pressure center over Central Alaska	1a	A'', A ₃ , F	Summer
V	Pacific Anticyclone	1b, 5a	A''', A ₂ , E', E' ₁	Summer
VI	Stagnating low off of Queen Charlotte Islands	7a	D', E'', E ₁ , F ₁	Spring, Fall

of Alaska creates a very stable anticyclone over the Yukon, which can dominate the coast in the absence of cyclones, as typified by pattern 3 (Figure A7). In both cases the coastal mountains tend to contain the cold air while the relatively warmer water constitutes a good substrate for cyclonic conditions, making for closely packed isobars parallel to the coast.

Type pattern 2 (A5 and A6) represents the average position of cyclones as they are transported in the westerlies to eventually die out in the northeastern Gulf. However, cyclones often linger over the central Aleutian Islands. This frequented position is associated with an Aleutian low at 500 mb as the disturbances align vertically in old age. Subtype 2.0 is more typical of winter and subtype 2.1 is more typical of summer and fall when the Aleutian low is adjacent to a strong east Pacific high pressure area.

In the summer the comparatively cool northeast Pacific Ocean surface provides for a well developed anticyclone. This often encroaches on the region and is the basis of type pattern 5 (A8 and A9). Subtypes 5.0 and 5.1 represent an east and west location for the main axis of the pressure ridge. In this milder part of the year, the equator to pole temperature gradient



1.0

+

Figure 2. Subjective weather type 1.0. The "x" indicate locations of the low center for the four subtypes comprising type 1.0.

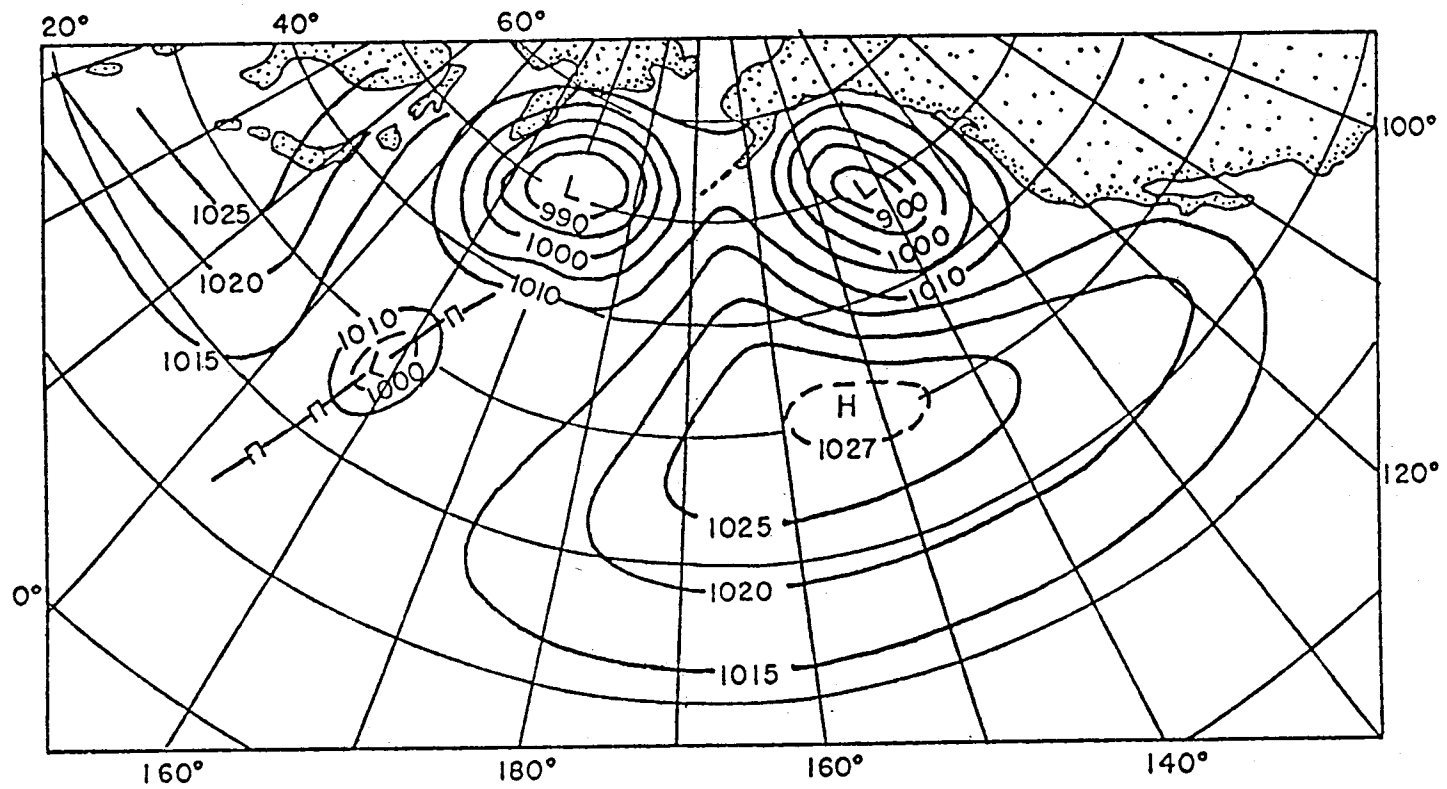


Figure 3. Sorkina's weather type 4c.

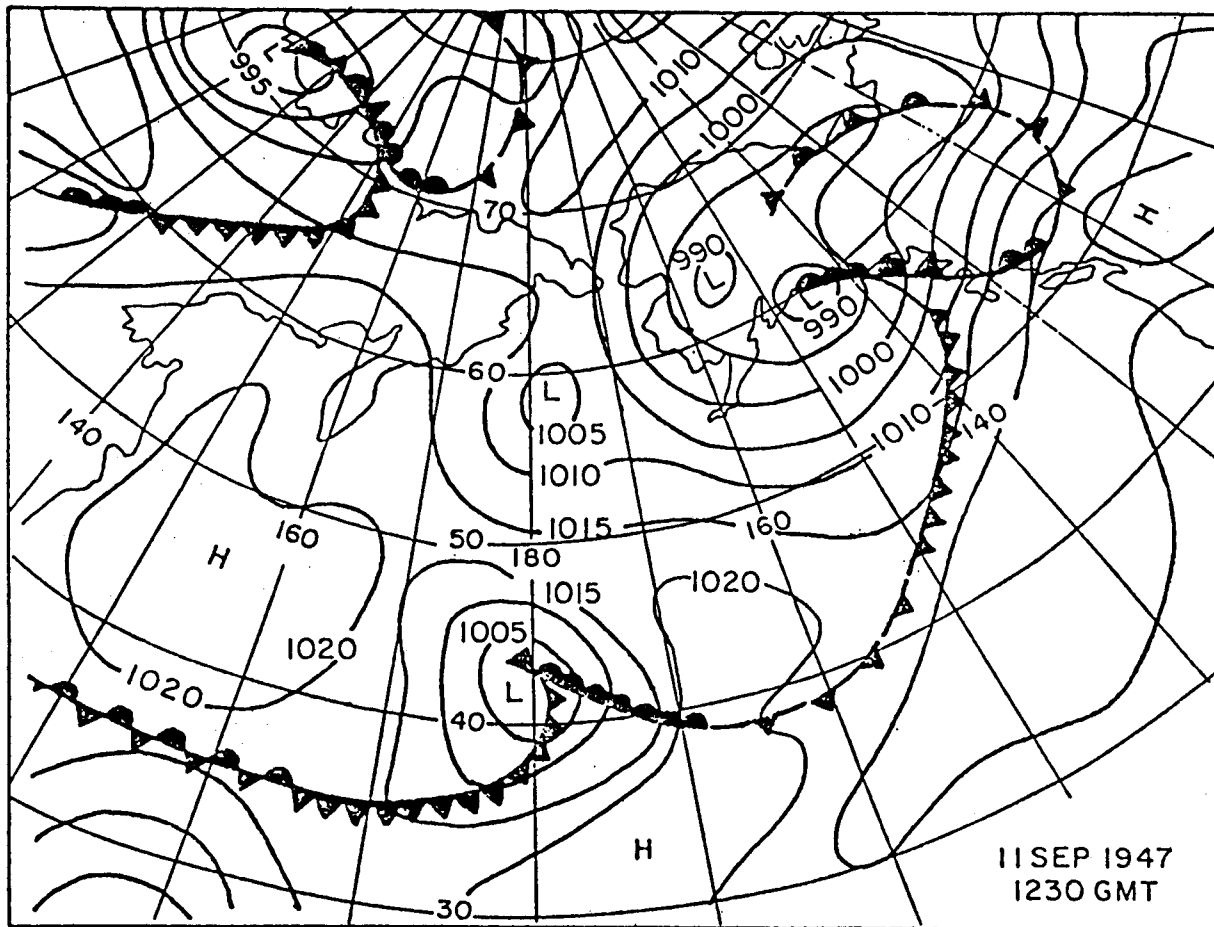


Figure 4. Putnins' weather type A_1 .

lessens and cyclonic systems become weaker and are found farther to the north. Lows tend to move through the Alaska mainland, frequently being observed as shown in patterns 4.0 and 4.1 (A_{10} and A_{11}).

Another commonly observed pattern, type 6 (A_{12}), shows a cyclone positioned near the Queen Charlotte Islands, with a high over northeast Alaska and the Bering Sea. This occurs when cyclogenesis occurs farther to the east and south than for the lows observed in the other cases. The cyclone often retrogrades towards the central Gulf coast or may travel northeast

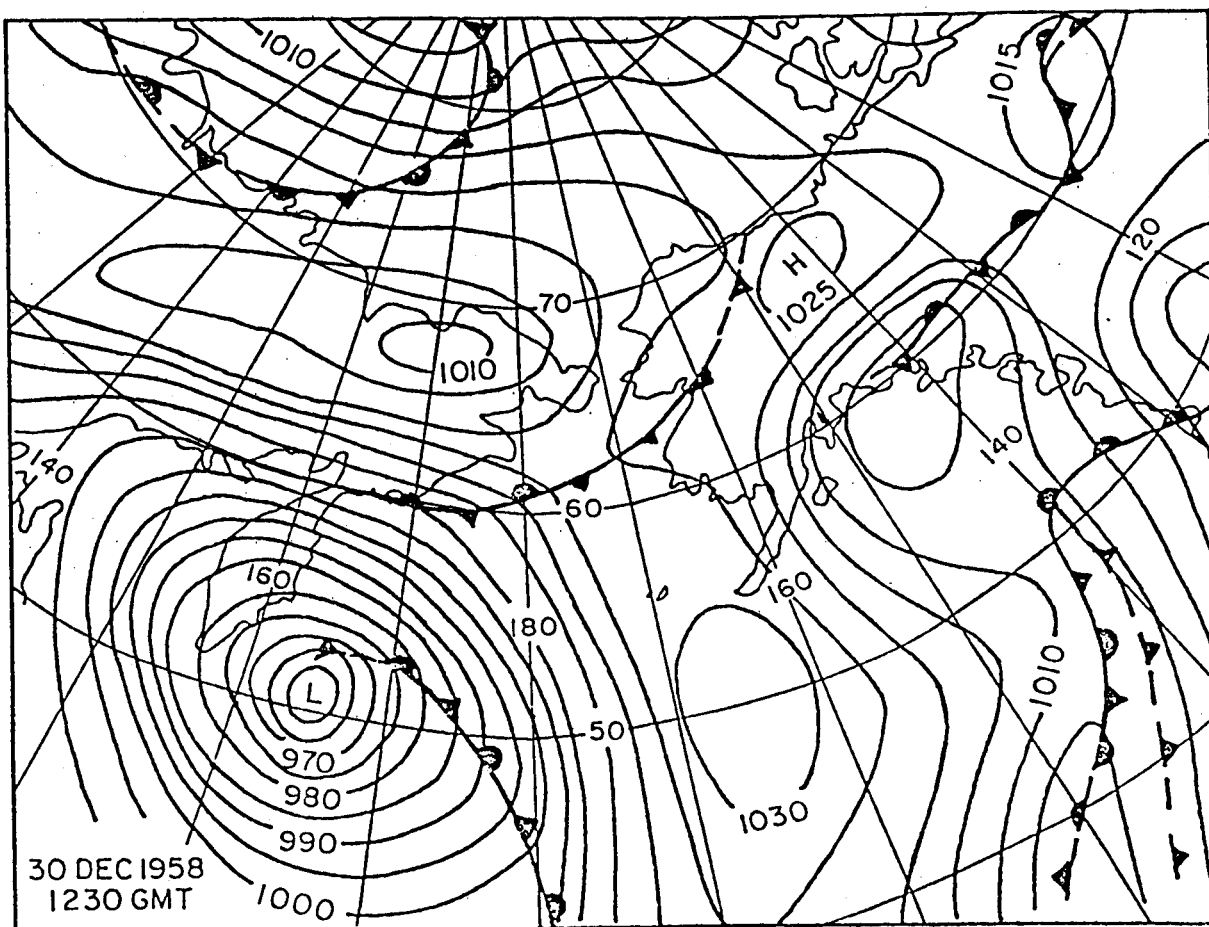


Figure 5. Putnins' weather type A'.

onto the continent, usually to die.

Each of the six patterns are listed in table 1 with the season it is commonly associated, the Putnins' patterns from which it is derived and the underlying Sorkina pattern.

2.3 Pattern Climatology

Automated sea level pressure analyses on a polar stereographic grid over the northern hemisphere produced at the National Meteorological Center (NMC) were obtained for 1968-1975. The mesh length is 381 km at 60° north

latitude. Since 1972 the analysis has consisted of fitting Hough functions to observed data (Flattery, 1970). Hough functions are solutions to Laplace's tidal equations, which imply a geostrophic relation between the wind and mass fields. The analysis is spectral in character fitting the entire atmosphere at once with 24 wave numbers in latitude and longitude and seven layers in the vertical. Prior to this time the analysis consisted of a local interpolation to grid points based upon Cressman (1959). Analyses are performed twice a day with a data receipt cutoff of ten hours after observation. It should be recalled that the analyses maps are dependent upon the availability of ship observations on a given day and are subject to interpolation and smoothing errors introduced by the analysis procedures. This was particularly noticeable as a lack of packing of the isobars along the coastlines in weather maps representing Type 1 synoptic conditions.

A subset of 24 grid points was extracted from each 12 hour map for the NEGOA region (figure 1). Each subjective subtype was also digitized to provide sea level pressure values at each of the 24 grid point locations. The correlation was then computed between each map and the twelve subtypes to determine the pattern for each 12 hour weather map:

$$r_{it} = \frac{\sum_{m=1}^{24} P_{im} P_{tm}}{\left(\sum_{m=1}^{24} P_{im}^2 \sum_{m=1}^{24} P_{tm}^2 \right)^{-1/2}}$$

where P_{im} and P_{tm} represent the deviation of pressures from the map average for data i and type t at grid point m . The weather type with the largest correlation is assigned to that map. The magnitude of the correlation is recorded along with the type.

The percent of occurrence of each type by year and season are listed in Table 2 and graphed in Figure 6. Percent of occurrence of each subtype

TABLE 2

TRANSITIONS FROM INITIAL TYPE TO FOLLOWING TYPE

Based on 12 Hourly Analyses 1968-1974

	Initial Type	% Occurrence of Initial Type	% of Initial Type Followed by Following Type					
			1	2	3	4	5	6
Y E A R	1	16	47	17	6	13	2	15
	2	31	12	71	6	7	3	1
	3	9	14	15	56	1	1	13
	4	18	8	11	-0	60	16	5
	5	12	-0	24	1	15	59	1
	6	14	15	3	9	8	3	62
W I N T E R	1	23	57	15	6	6	1	15
	2	26	13	71	8	6	1	1
	3	19	10	10	70	-0	1	9
	4	7	19	14	1	42	13	11
	5	4	0	29	5	14	52	0
	6	21	14	2	9	4	1	70
S P R I N G	1	16	43	17	6	16	1	17
	2	37	11	73	6	7	2	1
	3	8	16	21	47	0	0	16
	4	16	8	14	1	54	16	7
	5	9	0	35	1	10	52	1
	6	14	16	4	8	10	4	58
S U M M E R	1	8	34	20	4	27	5	10
	2	30	8	68	5	9	8	2
	3	3	27	20	29	2	7	15
	4	26	4	7	0	67	20	2
	5	27	-0	19	0	12	68	1
	6	6	14	7	4	15	7	52
F A L L	1	18	45	18	6	14	1	16
	2	30	15	68	6	8	2	1
	3	8	16	18	43	3	1	19
	4	22	9	12	-0	60	13	6
	5	7	1	27	0	34	37	1
	6	15	15	2	10	9	3	61

is listed in Appendix A. The Aleutian low (pattern 2) is dominant in all seasons. Pattern 3 (high in interior of Alaska) is confirmed as a winter pattern and the east Pacific high pressure as a summer pattern. Lows to the north (pattern 4) peak in summer and lows to the southeast (pattern 6) peak in winter. The same tables also list transition probabilities. The large diagonal components, many over 50% are an indication of persistence of each pattern.

Figure 7 plots the percentage of days from the 1969-74 record which could be typed by at least one of the patterns at a given threshold value

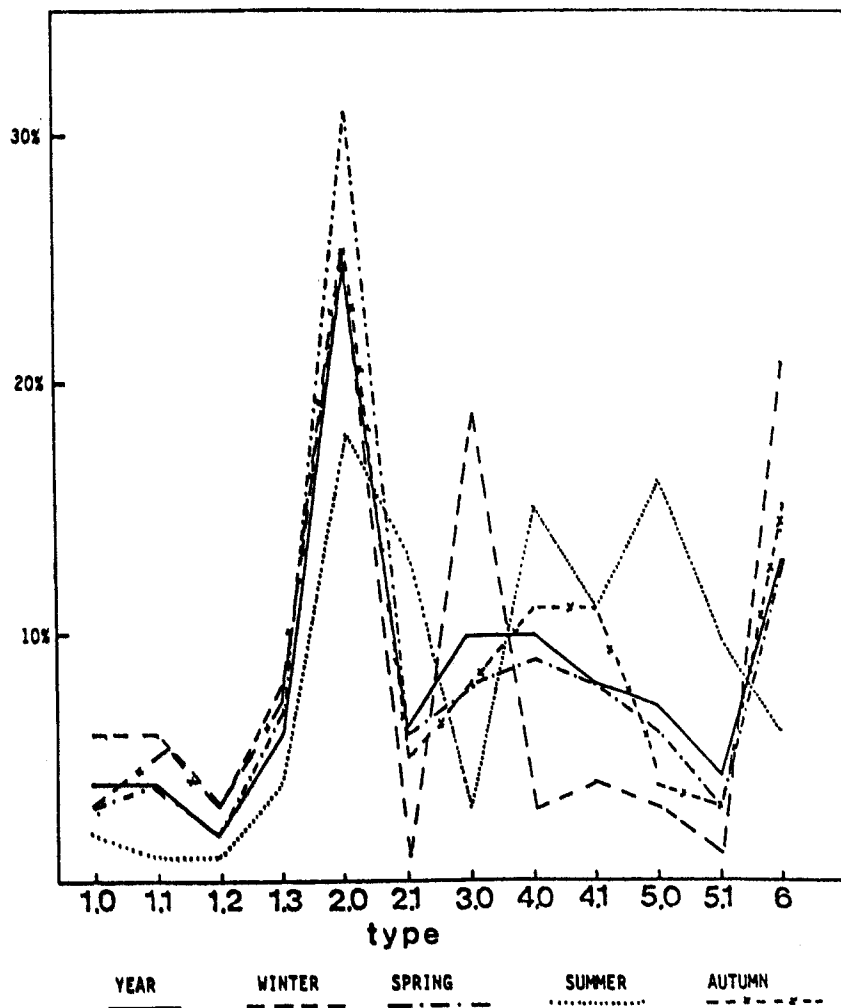


Figure 6. Percentage occurrence of synoptic weather type by season.

SUBJECTIVE TYPES AGAINST 1968-1974 DATA
STATISTICS FOR YEAR

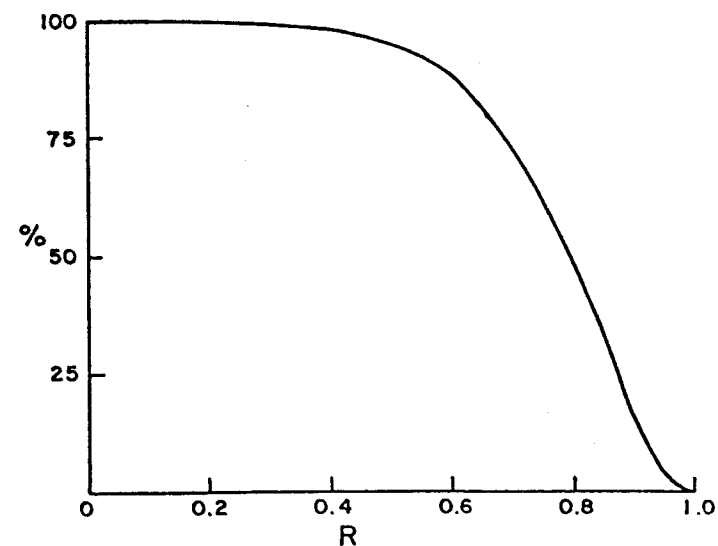


Figure 7. Percentage of 12-hour NMC pressure fields from 1968 to 1973 typed by at least one subtype at a given threshold.

of the correlation coefficient. Approximately 75% of the record can be typed with a correlation of 0.7 or better.

3. Automated Weather Typing

3.1 Methodology and Results

This section discusses an independent approach to map typing to compare with the subjective typing in the last chapter. The technique used is the pattern correlation technique (Lund, 1963, Basing, 1975, Singh et al, 1978). The procedure is as follows.

1) Correlation coefficients are computed for each existing 00 GMT map and all others for the year 1974. Accounting for missing data, this formed a correlation matrix of 354 x 354 elements.

2) The correlation matrix is examined to determine which daily map is highly correlated with the greatest number of other maps. For this purpose highly correlated implies values greater than a cutoff value, r_c . The chart having the maximum number of correlations exceeding the threshold value is classified as type A.

3) All maps which correlated greater than r_c with type A are removed from the analysis.

4) The procedure is repeated to find type B, C, . . . until either all days are classified or they do not correlate with any remaining map. We designate that a type must have a minimum of ten members.

In following the above procedure certain arbitrary criteria are adopted in picking r_c . Too high a cutoff may produce a large number of types while too low a value may provide lumping of synoptically distinct patterns. Thus the procedure is automated, but not necessarily unique.

Table 3 shows the number of maps removed (out of 354) at each step of the procedure. The second column gives the percent of the 354 maps

TABLE 3
NUMBER OF DAYS FIT BY EACH PATTERN TYPE

Type	Cutoff = 0.8		Type	Cutoff = 0.7		Type	Cutoff = 0.6	
	No. of Fits	% of Occurrence		No. of Fits	% of Occurrence		No. of Fits	% of Occurrence
A	77	24	AA	102	23	AAA	132	27
B	34	11	BB	49	15	BBB	63	18
C	29	10	CC	42	9	CCC	55	14
D	26	10	DD	44	15	DDD	31	11
E	24	13	EE	19	13	EEE	22	13
F	18	6	FF	17	12	FFF	14	17
G	14	10	GG	13	8	GGG	14	17
H	12	9	HH	10	5			
I	10	7						

which correlate the greatest with each of the patterns. It accounts for some days that were removed by an early step of the procedure but correlate highest with a latter pattern. Appendix B shows the days picked for cutoff of 0.8 and 0.7.

3.2 Comparison With the Subjective Types

Table 4 lists the date selected for each objective type A-I (0.8 cutoff) and its correlation with each subjective subtype. Table 5 is a similar format for the 0.7 cutoff. Type A and AA are March and September dates which correlate strongly with type 2. This case is the Aleutian low pressure center which has the highest percent of occurrence (25%, Appendix A) in the 1968-74 record of any weather type. Subjective subtype 6.0, the second most frequent type, was closest to the second pick with the 0.7 cutoff and third with the 0.8 cutoff. Type B from early September is dissimilar to any of our patterns. It contains a migrating low in the central Gulf

TABLE 4

Type	Date	1.0	1.1	1.2	1.3	2.0	2.1	3.0	4.0	4.1	5.0	5.1	6.0	Closest Fit
A	3-23-74	.03	.35	-.05	.70	<u>.96</u>	.50	.63	.09	-.78	.07	-.72	-.35	2
B	9-08-74	.39	.73	.26	<u>.90</u>	.69	-.12	<u>.90</u>	-.51	-.71	-.78	-.95	.51	1 or 3
C	1-16-74	.65	.67	.53	.40	-.12	-.53	.33	-.50	.09	-.89	-.33	<u>.82</u>	6
D	7-19-74	.06	-.24	-.00	-.64	-.87	-.11	-.85	.41	<u>.86</u>	.26	.83	-.05	4
E	8-08-74	-.24	-.25	-.30	-.09	.33	<u>.76</u>	-.32	.76	-.07	<u>.84</u>	.19	-.94	5
F	7-04-74	-.39	-.61	0.38	-.74	-.51	.36	-.87	.76	.52	<u>.88</u>	.84	-.70	5
G	4-14-74	.43	.70	.07	<u>.78</u>	.69	.38	.43	.29	-.52	-.23	-.65	-.12	1
H	1-13-74	.32	.44	.47	.44	.19	-.67	.74	-.89	-.29	-.83	-.55	<u>.87</u>	6
I	10-03-74	.51	.14	.68	-.28	-.56	-.60	-.21	-.28	<u>.73</u>	-.28	.40	.51	4

TABLE 5

Type	Date	1.0	1.1	1.2	1.3	2.0	2.1	3.0	4.0	4.1	5.0	5.1	6.0	Closest Fit
AA	9-20-74	.13	.53	-.07	.86	<u>.94</u>	.48	.69	-.00	-.83	-.19	-.86	-.17	2
BB	9-09-74	.55	.69	.51	.57	.18	-.65	.70	-.63	-.29	-.94	-.60	<u>.88</u>	6
CC	6-23-74	.19	-.22	.17	-.65	-.77	-.06	-.85	.49	<u>.92</u>	.36	.85	-.19	4
DD	8-08-74	-.24	-.25	-.30	-.09	.33	.76	-.32	.76	.07	<u>.84</u>	.19	-.94	5
EE	1-02-74	-.08	.18	.06	.51	.80	.04	.78	-.34	-.78	-.07	-.66	.01	2
FF	2-21-74	.70	.41	.69	-.05	-.47	-.62	-.11	-.18	.60	-.52	.20	.65	1
GG	4-21-74	.57	.72	.18	.59	.25	.19	.14	.29	-.11	-.38	-.38	.08	1
HH	7-04-74	-.39	-.61	-.38	-.74	-.51	.36	-.87	.76	.52	<u>.88</u>	.84	-.70	5

south of our region. Types F and DD, and D and CC consists of summer cases similar to our couplets 4.0 and 5.0 versus 4.1 and 5.1. Subtypes 4.0 and 5.0 are high pressure to the southeast and 4.1 and 5.1 have high pressure to the southwest. Type 4 patterns have weak lows over interior Alaska. The automated typing sees the east or west orientation of the pressure gra-

dient as more important than the inclusion of the weak low pressure centers.

After pattern DD, the number of fits for 0.7 drops by more than half. Pattern EE is half way between type 2 and 3. Type FF and GG pick up pattern 1 while type HH is similar to an earlier type DD. Type G picks up pattern 1. Pattern H is much closer to our type 6 than pattern C. Pattern I is between our pattern 1 and 4 while pattern C lies between our 1 and 6.

All approaches, the two automated and subjective, point to four primary patterns, the Aleutian low, low over the southeast Gulf of Alaska, and east and west high pressure ridge orientation. The subjective approach and the 0.7 cutoff place low pressure centers in similar locations to produce the remaining types. After the first four primary patterns, the 0.8 cutoff also adds various low pressure centers to the basic group of four patterns, but has a different regional location from the other approaches, indicating a different grouping of migratory lows.

All digitized weather maps for 1968-73 were typed by comparison with the twelve subjective subtypes and the two automated sets of weather. In addition eight sets of ten maps were drawn at random from 1974, and used as weather types against the 1968-73 maps. Figure 8 shows that both automated types perform slightly better than the subjective classification scheme when compared to the NMC digitized sea level pressure grids.

12 SUBJ. 8 RANDOM. .8. AND .7 CUTS

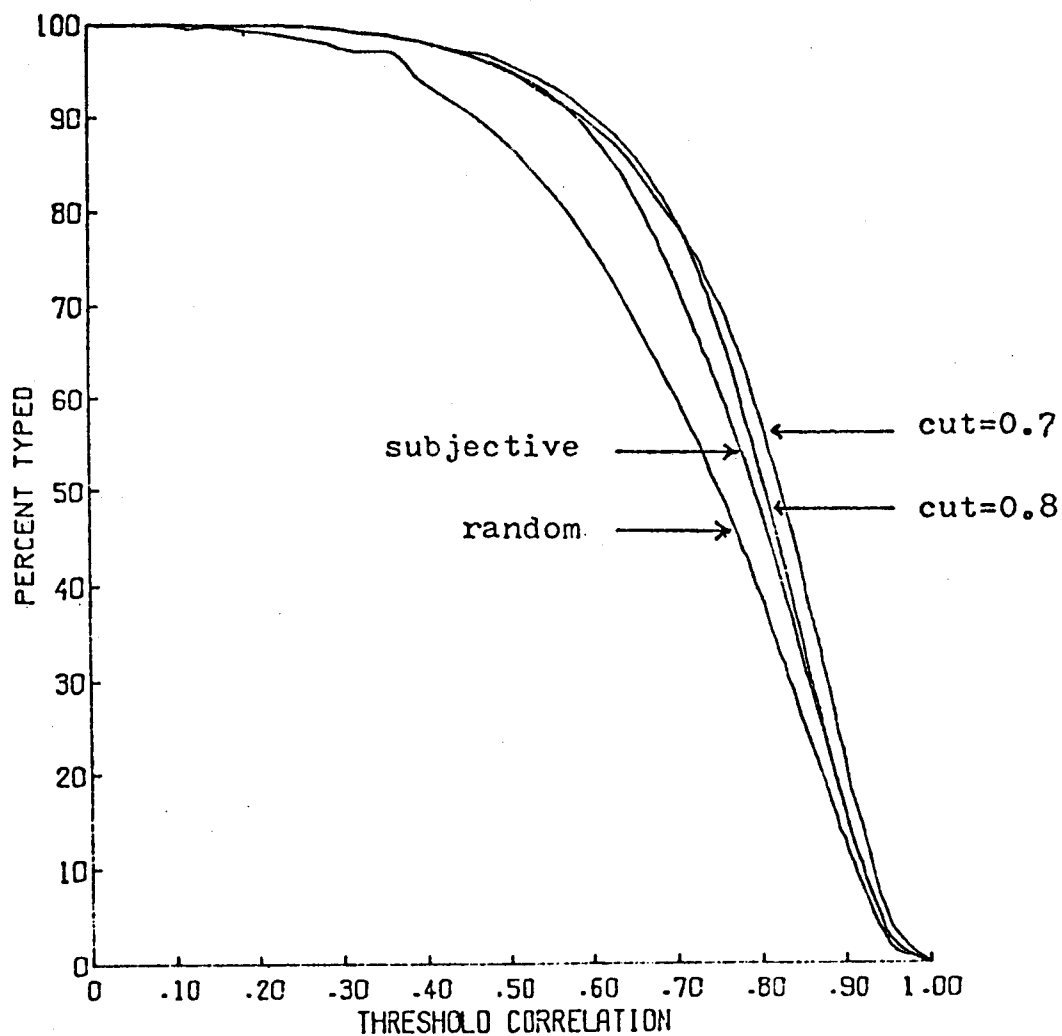


Figure 8. Percentage of 12 hour NMC pressure fields typed by the subjective approach, the two pattern correlation types and the average of eight sets of ten maps drawn at random from the NMC data set for 1974.

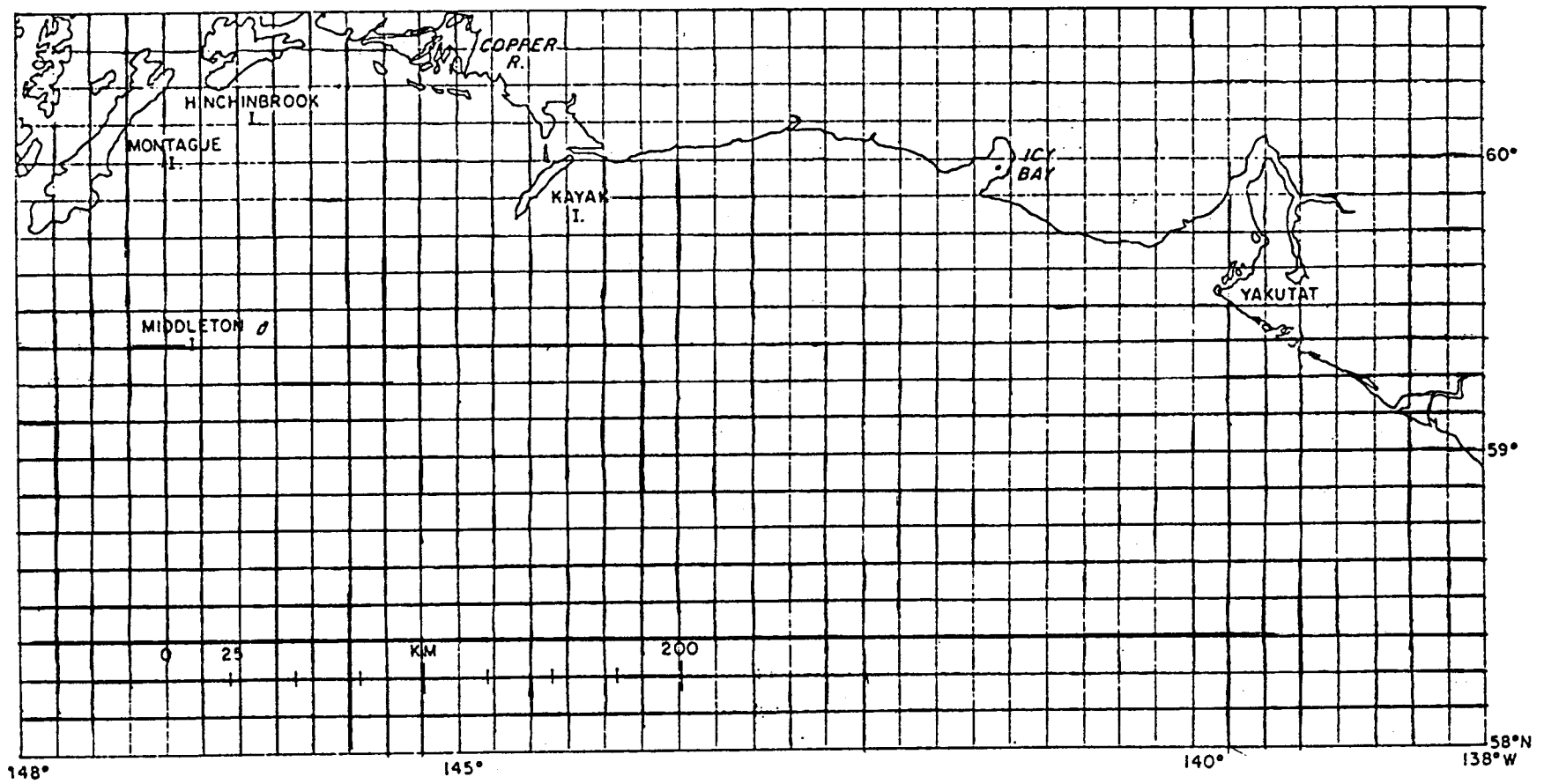
4. Local Wind Fields for NEGOA

4.1 Procedure

This section discusses the generation of local wind fields from surface pressure pattern types described in section 2. For use in the oil spill trajectory calculations all local wind speeds within a pattern will be scaled against an anemometer record. Therefore, the primary aim is to produce wind fields showing local direction and relative magnitude. Computation began by computing gradient wind speeds and directions from the patterns on a uniform set of grid points over the localized area shown in figure 9. The grid consisted of 800 boxes; each box was $7\frac{1}{2}$ minutes in latitude by 15 minutes in longitude. At 60°N the boxes were 13.89 km on a side. Boundary layer thermal structure and air-sea temperature differences were estimated for each pattern. Cardone's (1969) planetary boundary layer model was used to estimate cross isobar flow angles (α) and surface friction velocities (u_{*}) over open ocean. Within 50 to 100 km of the coast data from coastal measurements and descriptions of coastal processes were used to modify Cardone's model output. The friction velocities were then converted to equivalent 10 m elevation neutral surface layer winds. The wind field away from the coast was smoothed and a final diagnostic check of the divergence field was made.

Since local winds will be scaled against an anemometer, the magnitude of the geostrophic wind within each pattern is of secondary importance. However, with higher wind speed cases the nonlinear effects of inertia on surface winds are important, causing larger relative variations in wind speed. Therefore, in computing local wind fields we biased the analysis toward the higher wind speed cases. Geostrophic wind speeds typically were taken between 10 and 20 m/sec with some 25 m/sec values where isobars are packed

GRID FOR WIND



551

Figure 9. Grid network for estimating local winds.

along the coast. Gradient wind speed corrections were applied to regions of isobaric curvature.

We assumed a thermal structure for the marine planetary boundary layer (PBL) so that the baroclinicity of the PBL was consistent with an ideal storm structure and climatology. For example, pattern type 1 (figure 2) represents the stagnated low pressure center in the Gulf of Alaska. Our ideal storm consists of warm air advection behind a warm front and cold advection well behind the cold front. Nearshore, where offshore flow occurs we assume large horizontal air temperature gradients. The climatology for the winter months when storm type 1 prevails shows a mean surface air temperature distribution which reflects the large duration of pattern type 1. Isotherms were drawn to reproduce the climatological large scale temperature gradient and then distorted to be consistent with storm structure, packing the isotherms in frontal zones. Actual fronts were not created so as not to over-specify the generalized storm. Figure 10 shows the isotherms used for type 1 along with the isobars. From the isotherms, the magnitude and direction (relative to the surface geostrophic wind) of the baroclinic field (thermal wind) were determined. Baroclinicity for the other map types were similarly computed.

The distribution of air-sea temperature difference was also assumed for each pattern, also drawing on idealized storm structure and climatology. Figure 11 portrays the climatological air-sea temperature difference distributions from the OCSEAP Gulf of Alaska Climatic Atlas (Brower, et. al, 1977). The climatic atlas covers several marine "areas" of which areas D and E are two. The western half of our grid is part of area D, and the eastern half is part of area E. During winter the mean air-sea temperature difference

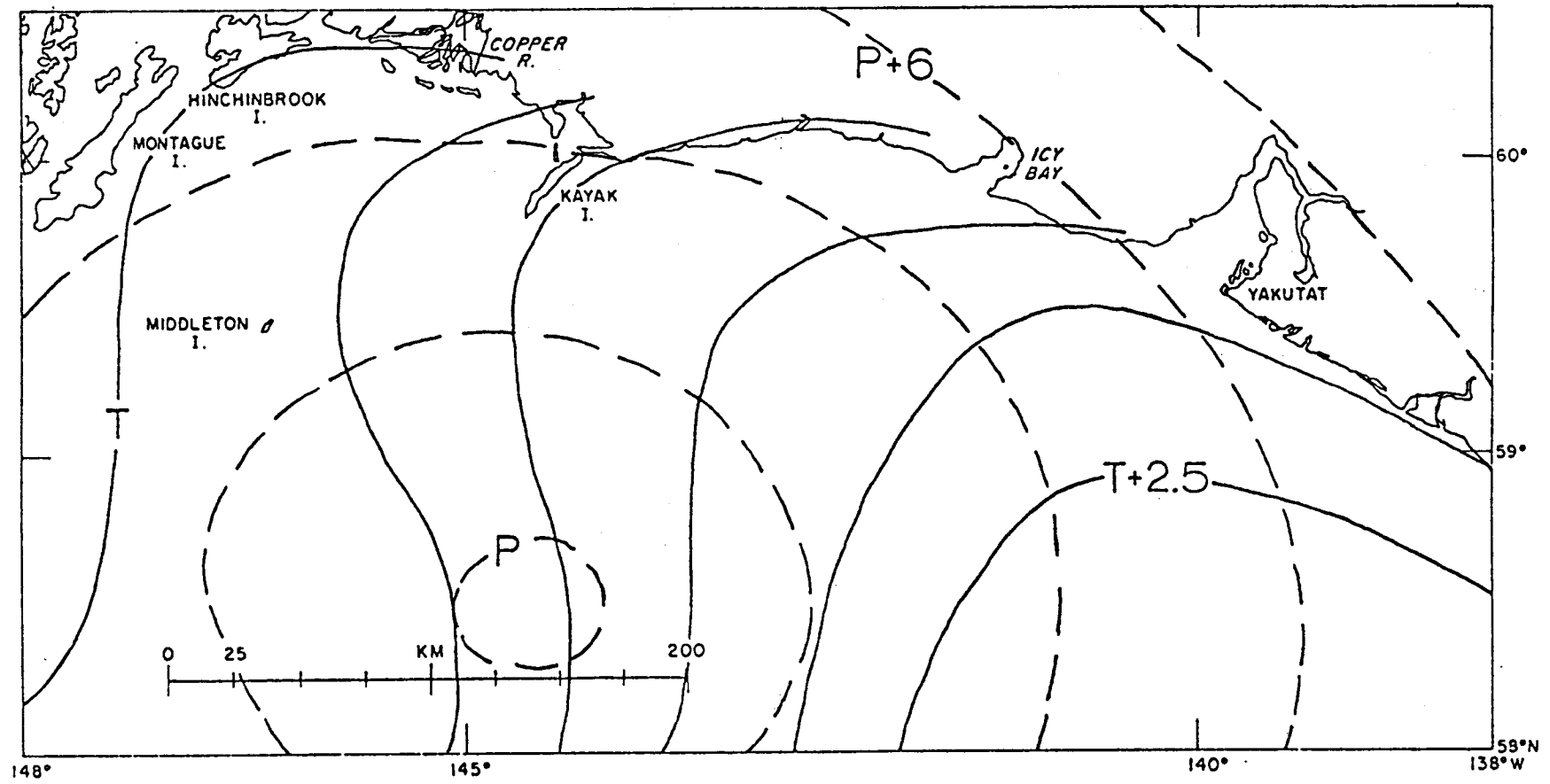


Figure 10. Isotherm pattern used to estimate local winds for pattern type 1.0.

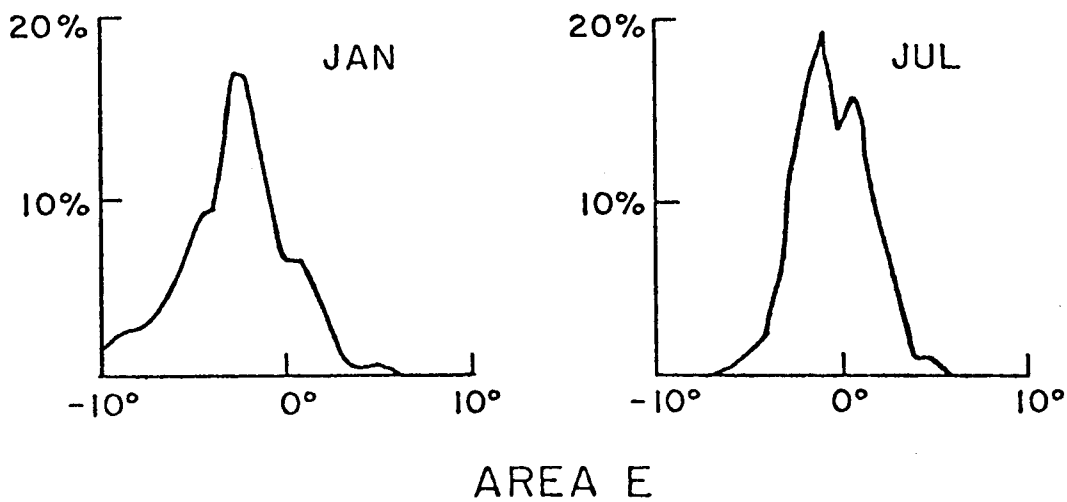
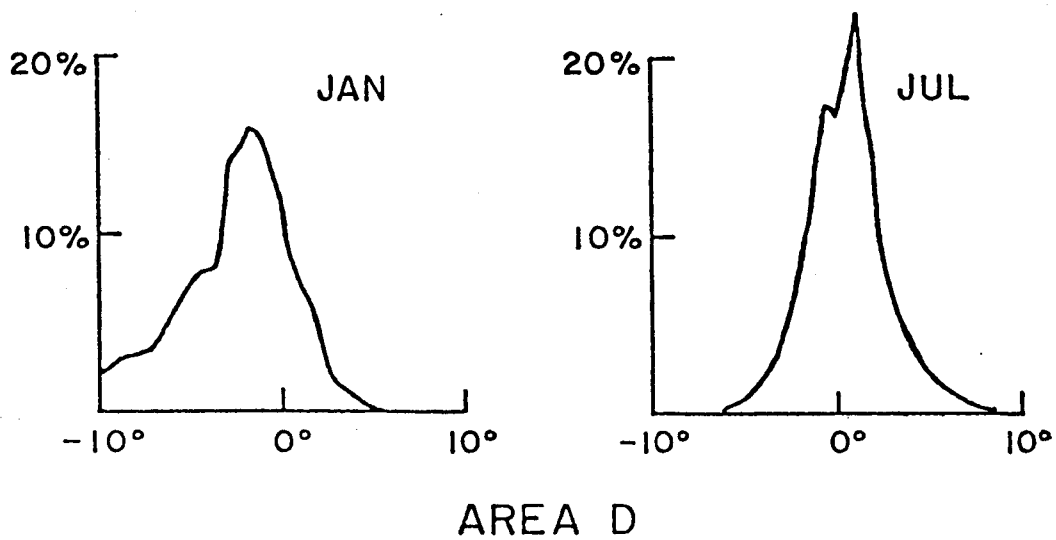


Figure 11. Climatological air-sea temperature distribution for the western Gulf of Alaska (D) and the eastern section (E). (After Brower et al. 1977).

is more negative and the distribution of air-sea temperature difference is broader, reflecting the vigorous temperature advection caused by the more severe winter storms. In area E, the air-sea temperature difference is more negative than in area D due to the advection of warm surface water into that region, and due to offshore flow of cool air. In the spatial distributions of air-sea temperature difference that we created, the means were commensurable with those in figure 11 and our most extreme deviations from the mean were generally within one standard deviation (based on figure 11) of the mean. Figure 12 shows the air-sea temperature differences used for type 1.

Cardone's (1969) Ekman layer model was used to provide the friction velocity u_* and cross isobar flow angle α . The inputs required are the gradient wind speed, G , the magnitude of the PBL horizontal temperature gradient, $\Delta\bar{T}$, the angle between the surface geostrophic wind and the thermal wind, η , and the air-sea temperature difference $\Delta\theta$. Values of drag coefficient and inflow angle were interpolated from a set of curves produced by running Cardone's model. Figure 13 shows the behavior of u_*/G versus G , η , $\sqrt{\Delta\bar{T}}$, and $\Delta\theta$. Likewise, figure 14 shows the behavior of α .

Surface stress, u_* , was converted to a neutral stratification 10 m surface layer wind speed. That is, a logarithmic wind profile was assumed with the roughness length, z_0 , depending on u_* as (as in Cardone's model, CGS units)

$$z_0 = 0.684/u_* + 4.285 \times 10^{-5} u_*^2 - 4.43 \times 10^{-2}$$

Only constant drag coefficients or drift factors should be used with these winds as wind speed and stability corrections are already included.

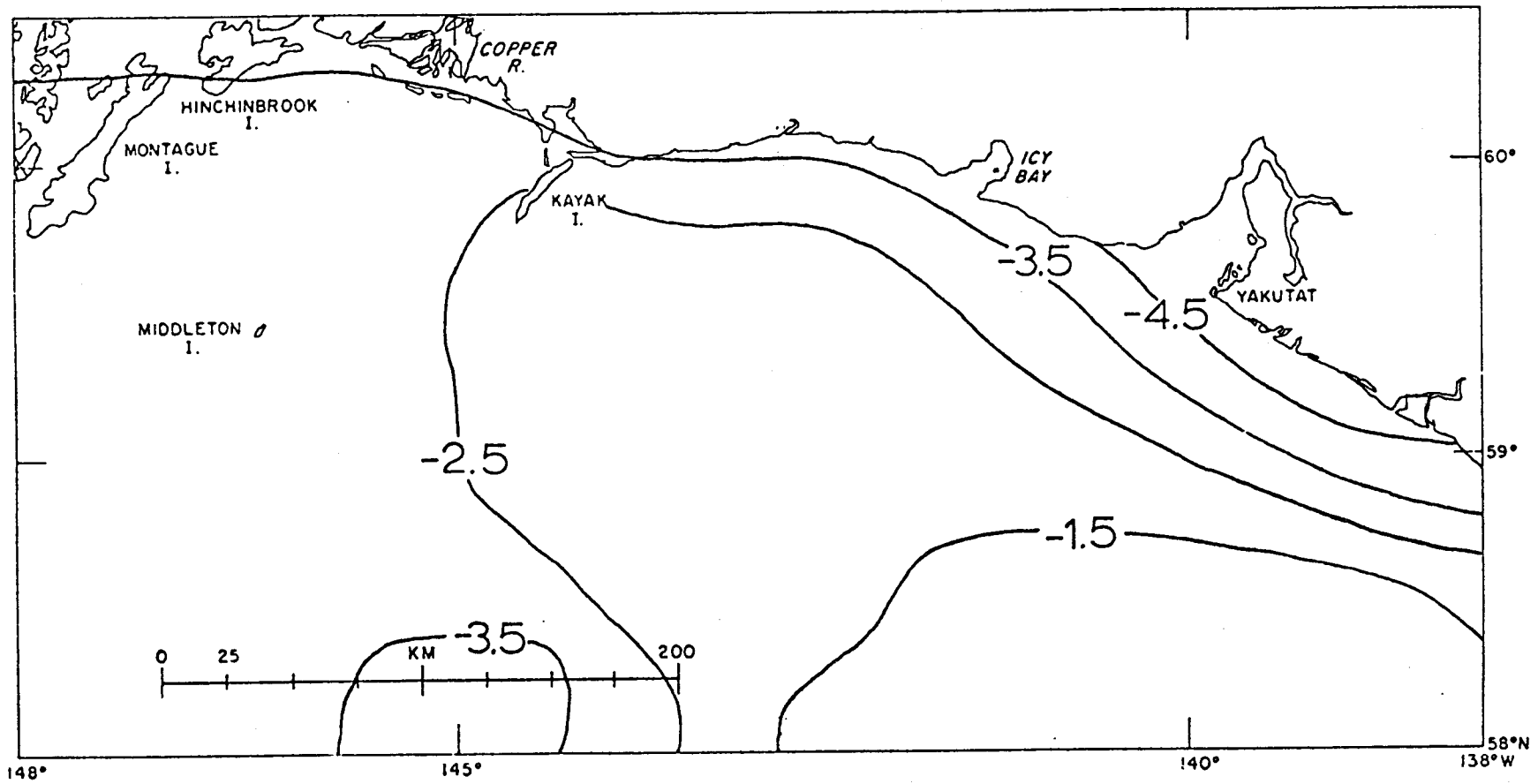


Figure 12. Air-sea temperature difference map used to estimate local winds for type 1.0.

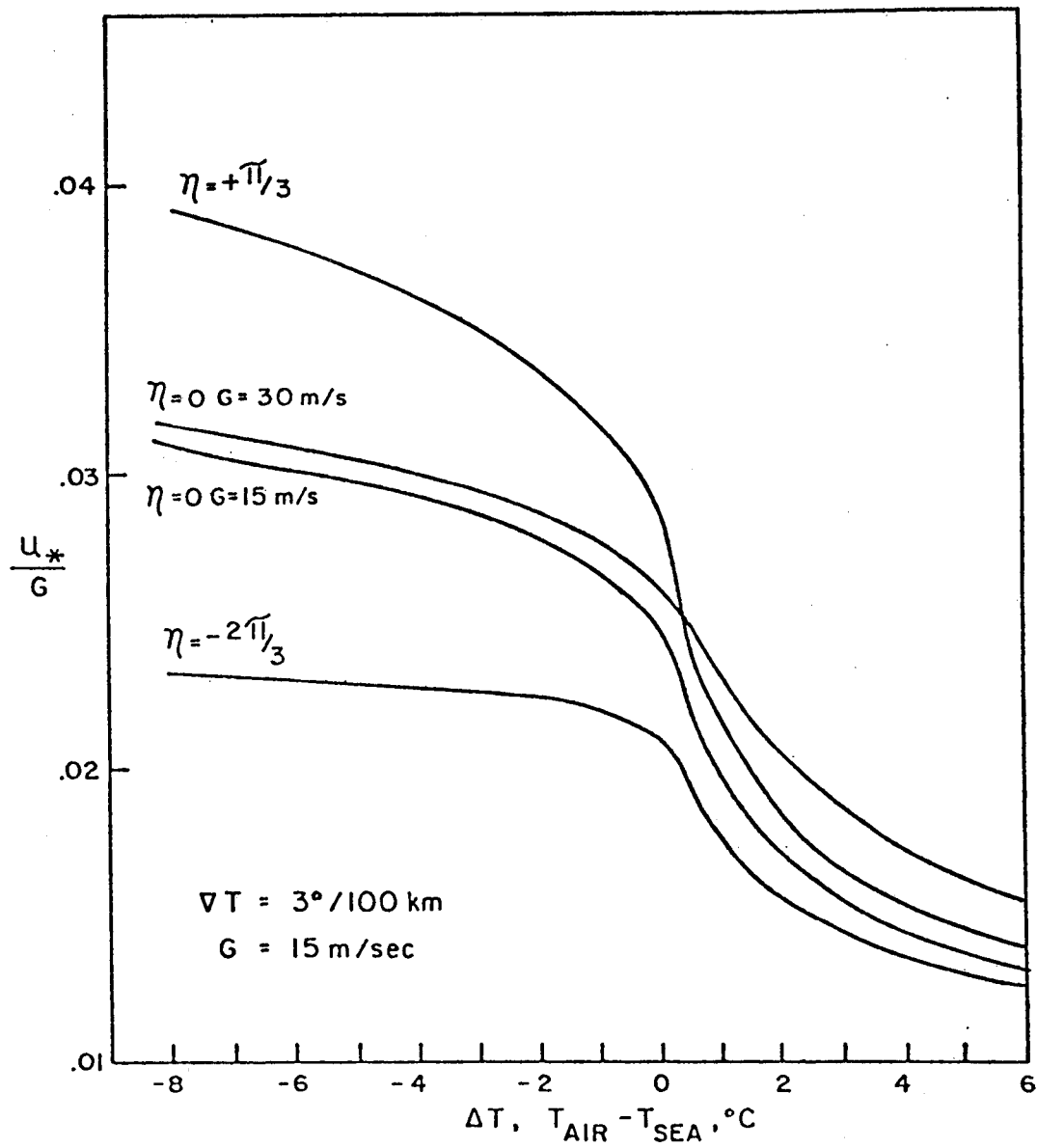


Figure 13. Geostrophic drag coefficient as a function of air-sea temperature difference for Cardone's model. The parameter η is the angle between the geostrophic and thermal wind; G is the gradient wind speed.

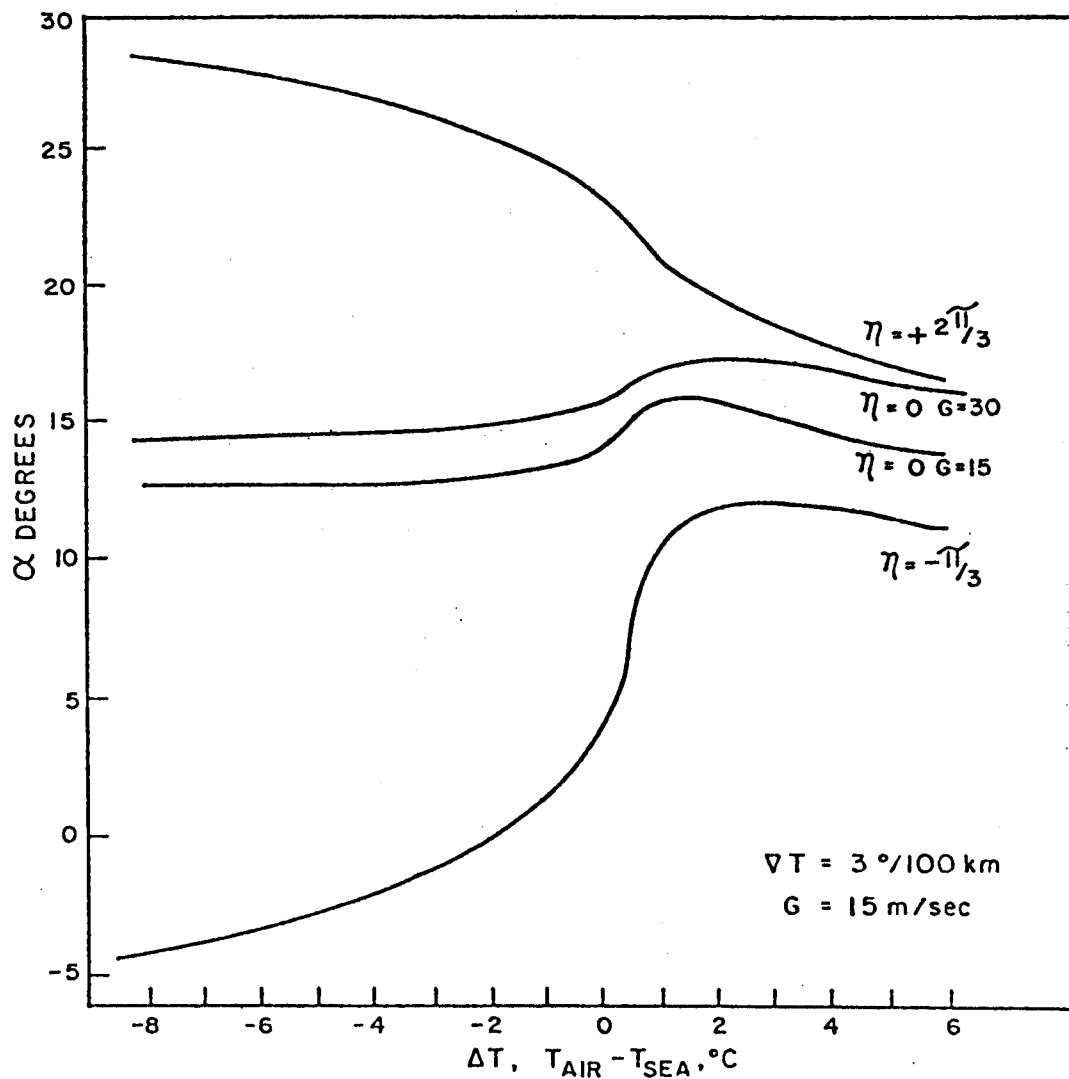


Figure 14. Similar to 13, but for inflow angle (angle of the surface wind to the left of the geostrophic direction).

By comparing the baroclinic, stability dependent 10 m wind field with a wind field based on a constant $u_* / G = 0.025$ for pattern type 1.0, the effects of stability and baroclinicity are about 15%.

Within 50 - 100 km of the coast where Cardone's model is inappropriate, primary guidance was taken from actual measurements and descriptions of coastal processes reported in the draft NOAA Technical Report, "Coastal Meteorology in the Gulf of Alaska, Icy Bay to Yakutat Bay" (Reynolds, Hiester, Macklin, 1978). That report dealt only with the Icy Bay to Yakutat coastline but the following principles of that area were applied to the remainder of the NEGOA coastline.

Planetary boundary layer air piles up against the sides of coastal mountains when the incident winds are obliquely onshore. A pressure gradient forms normal to the coastline which establishes a longshore geostrophic flow. This orographic forcing is part of the reason that low pressure systems stagnate in the Gulf of Alaska. The length scale of the seaward extent that this deviation from the incident geostrophic flow is discernible is poorly understood. The length scale probably depends on the angle between the initial geostrophic flow and the coast, and the speed of an impinging pressure system. There are indications that this length scale is on the order of 100 km.

Near the surface and nearshore, the winds are not in geostrophic balance and blow at an angle to the coastline. Within 20 km of the coast, the winds can have an offshore katabatic component due to drainage of denser air from the mountain valleys and glaciers. This is an almost permanent feature in winter but occurs mainly at night in the summer. Winds nearshore also respond to the coastal discontinuity in frictional drag creating an offshore wind

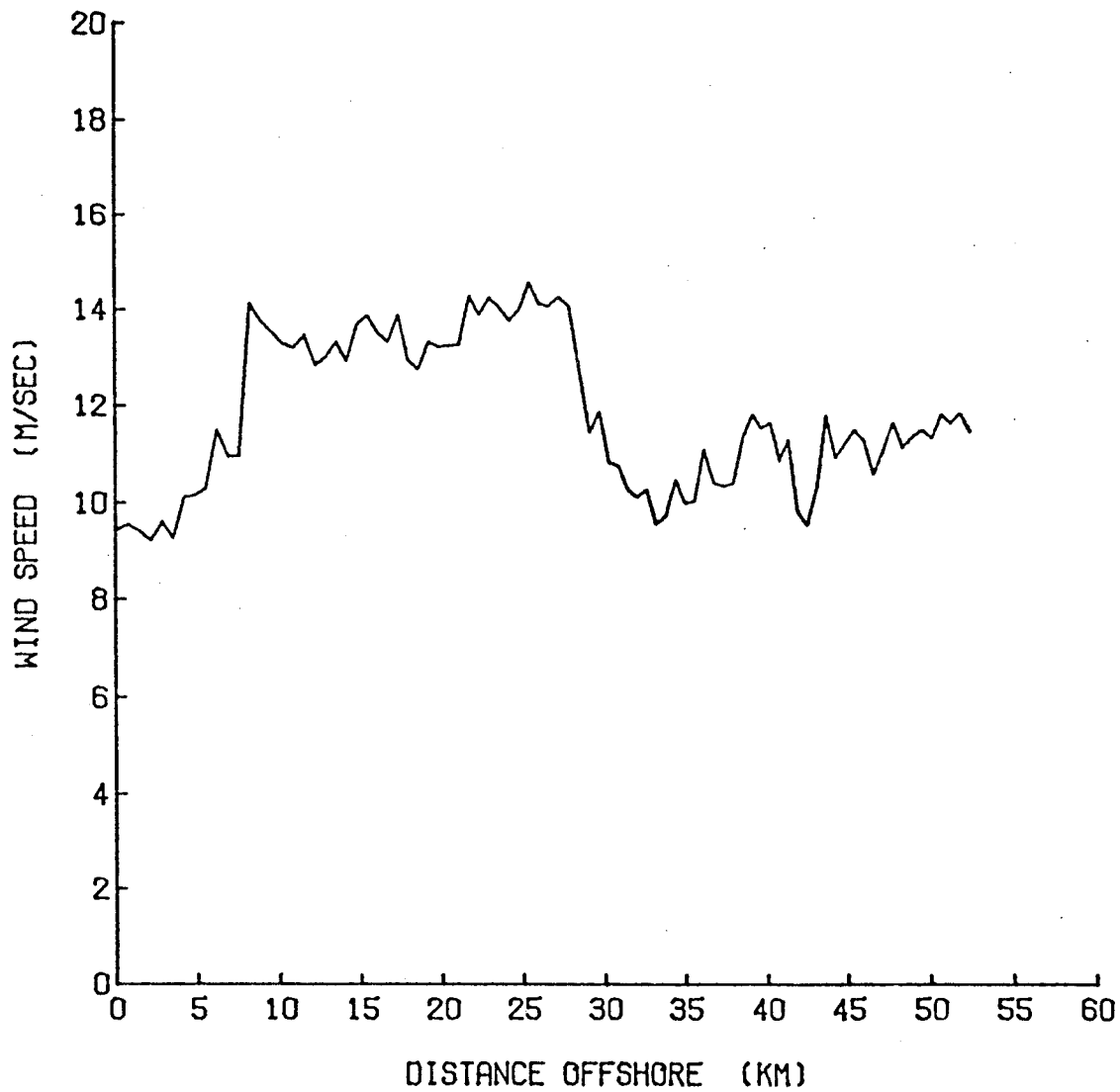


Figure 15a. Wind speed as a function of offshore distance.

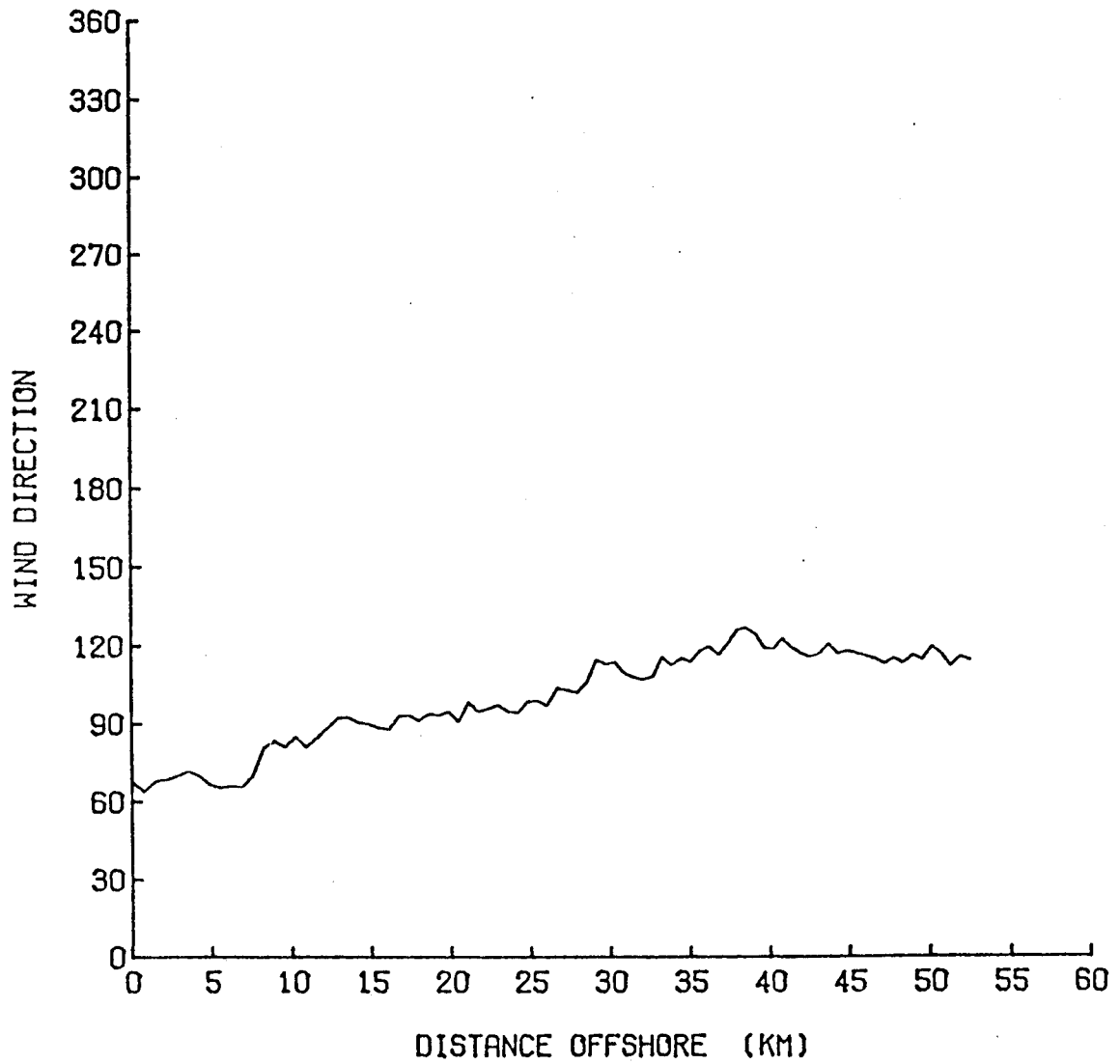


Figure 15b. Direction of the 30 meter wind as a function of offshore direction.

component when there are longshore easterlies in NEGOA and an onshore component for longshore westerlies.

Figure 15 shows the wind speed and direction measured from an aircraft in a line directly offshore of the Malaspina Glacier. Nearshore winds were blowing from the NNE, slightly offshore and out of Yakutat Bay, while 50 km offshore, the winds were from the SE. Where the offshore and the onshore winds merged, the flow accelerated and formed a coastal jet 10 to 30 km offshore and parallel to the shore. That was the best example measured, but we believe the jet is a frequently occurring feature. The sensitivity of the jet to variations in meteorological parameters remains unknown.

In winter the winds nearshore are persistently offshore but in summer the drainage winds are weak and easily overcome by an onshore push. There is a deceleration as the shore is approached. Data from EB-70, EB-43, and an anemometer at Pt. Riou (on the shore at the western tip of the Malaspina Glacier) were used to scale these decelerations.

After using the above principles to modify the coastal winds, the wind fields were smoothed. A nine point smoother was used on all grid boxes that were at least one box away from the shore. The filter smooths the effects of the interpolation and truncation error.

Finally, the divergence at each grid point was computed for every wind field. The contours of the divergence field ($\times 10^5$) for type 1.0 are shown in figure 16. The values at the coastline cannot be taken too literally as the wind vectors only represent the over water wind. The figure provides confidence in the overall method. There is convergence (of sensible magnitude) at the center of the storm, divergence behind the cold front, and convergence just off the coast where onshore flow meets katabatic flow.

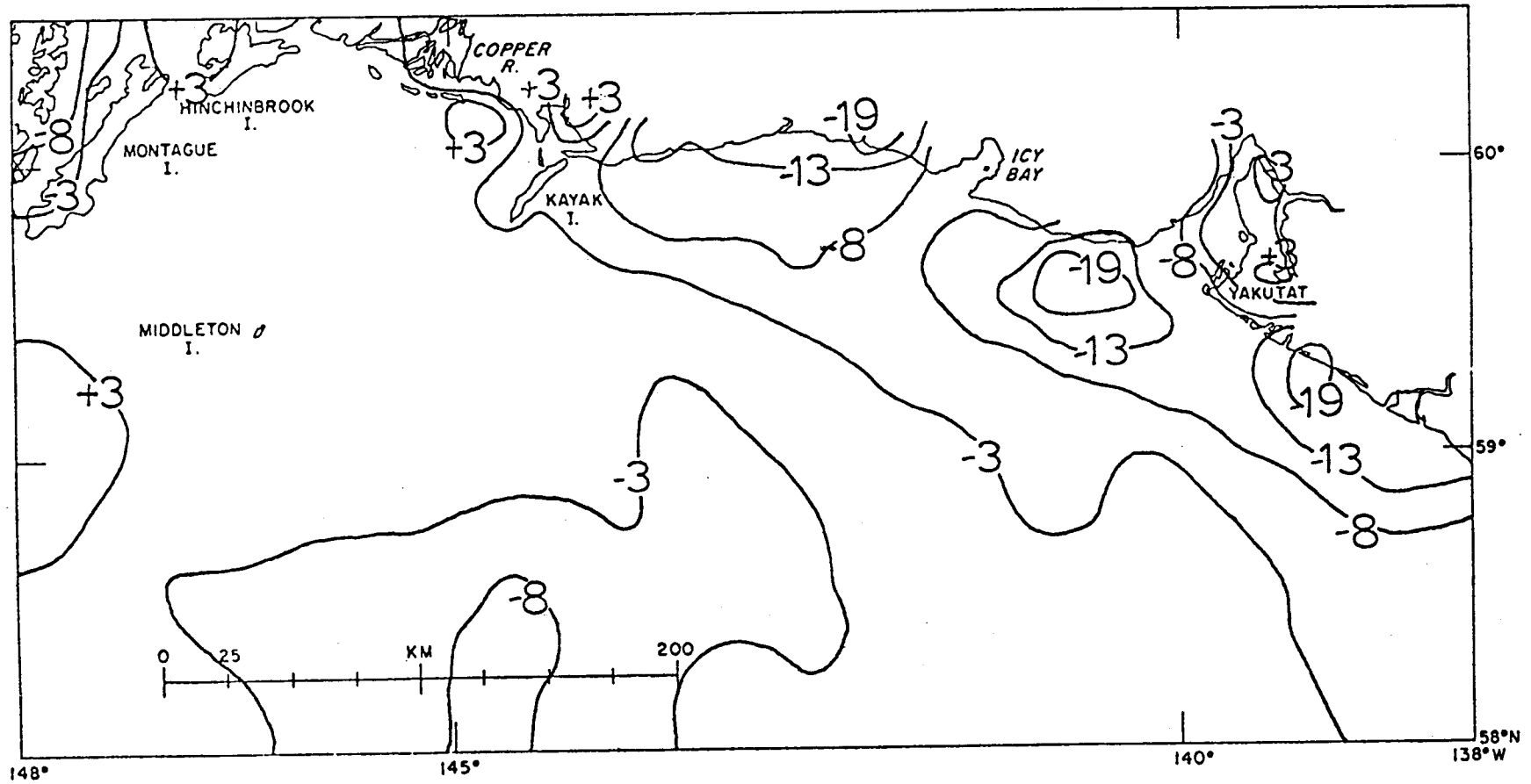


Figure 16. Divergence field calculated from the local wind field for type 1.0.

4.2 Description of Local Wind Fields

This section presents thirteen velocity fields for the synoptic subtypes described in section 2. Arrow plots are contained in Appendix C. A velocity vector applies only to the over water portion of a box that spans the coastline. The length of each arrow is a measure of the relative wind speed, and each arrow points downwind.

Synoptic pattern 1 (figure 2) represents a low pressure system contained within the Gulf of Alaska by coastal mountains. This pattern was broken down into four subtypes corresponding to four positions of the storm center as it migrates through the Gulf. Figure C4 is the vector plot for type 1.3 with the storm center at $57^{\circ}\text{N } 152^{\circ}\text{W}$, just east of Kodiak Island. The topographical forcing of the boundary layer is not yet strong so the flow near shore, in the mid to western portions of our grid, is onshore. Near the shoreline and at the surface (not necessarily representative of the entire depth of the PBL) there is offshore katabatic flow. Fed by surrounding tributaries, the drainage flow is deeper in the estuaries such as Yakutat Bay and hence dominates the wind fields in those regions. Whenever flow encounters land it decelerates and turns toward lower pressure. For example, the winds that blow across Kayak Island are retarded and deflected to the south. The air accelerates around the southern tip of the island to rejoin undisturbed flow on the lee side. The winds are also generally slowed by the landforms at the entrances to the Copper River Delta and Prince William Sound, however some passes channel and accelerate the flow.

Figure C2 is the wind field for type 1.1 when the storm is centered

at about 50°N 148°W . The considerations are similar to those documented for type 1.3.

The archetype for this series, type 1.0 with the storm as shown in figure A1, is given in figure C1. As the storm moves eastward into this position the orographic forcing of the PBL becomes strong, especially in the Yakutat to Kayak Island region. There the offshore flow (katabatically, frictionally and topographically forced) meets the onshore flow and the two form an alongshore jet. The winds blowing offshore in the western portion of the grid accelerate from their nearshore speeds up to their open ocean speeds, causing some divergence there.

Figure C3 shows the wind field for type 1.2. The storm is at its eastern extreme; at about 58°N 141°W . The alongshore jet is mostly east of our grid region but is visible entering the region at the eastern border. The jet quickly dissipates in the diffluent region in the northwest quadrant of the storm.

Type 2 represents an Aleutian low as shown in figure A5. The local wind field is shown in figure C5. There is also an alongshore jet for this type. Since the flow in the eastern part of the grid is roughly alongshore, there is no alongshore acceleration there. The jet forms between Icy Bay and Kayak Island where the geostrophic flow is more directly onshore. The confluence at the mouth of the Yakutat Bay and the deceleration windward of Kayak Island cause those areas to be convergence centers. There is relief behind Kayak Island where the winds turn northward to almost be in geostrophic-frictional balance before encountering the drainage winds in the Copper River area. The winds are slowed by the land masses in the Cape Hinchinbrook region but are not blocked by them. Figure C6

represents an autumn case of type 2.1 with a remnant of high pressure to the east.

We have split the synoptic type 3 (figure A7) into two cases. Type 3.0 (figure C7) is the usual case where the anticyclone over the Yukon dominates the NEGOA area. This is typically a time of clear skies. Radiational cooling of the land surfaces causes katabatic flow, especially off of the Bering, Malaspina, and Hubbard Glaciers. East of Yakutat, the winds accelerate offshore making it a region of divergence. From Yakutat Bay to Kayak Island there is convergence of katabatic and alongshore winds. West of the Bering Glacier is another region of divergence. The winds blowing from the Copper River delta hit Hinchinbrook and Montague Islands quite obliquely, so we show the air blowing roughly parallel to those shores and around the islands to the south rather than making the more energy consuming trip over the tops as in the previously described types. The eastern shores of these islands are therefore in a convergent region.

Type 3.1 (figure C8) allows for the reported cases of very strong (50 to 100 knots) winds near shore along the NEGOA coast. The surface pressure pattern is virtually indistinguishable from that of type 3.0. The air northeast of the coastal mountains is very cold throughout a very deep layer; i.e., the 1000-500 mb thickness is less northeast of the mountains than in the Gulf. When the reservoir of cold air gets deep enough, the cold air spills through the mountain passes like water over a dam. The low temperature is somewhat maintained (against adiabatic warming during descent) by flow over the radiationally cooled icefields. Large velocities build up as the air drains out of the prominent valleys. We have allowed strong winds to blow out of the Alsek River Valley, Yakutat Bay, Icy Bay, off the

Bering Glacier, and from the Copper River Valley.

The Icy Bay winds are strongest and actually blow off the Malaspina Glacier just east of Icy Bay. Guidance for this location came from a run of the regional meteorological model described by Overland et al. (1978). We assumed the core of strong winds would totally mix with the ambient air about 100 km downstream of the shore. Most cores turn to the right as they mix with the ambient flow. The Bering Glacier and Copper River winds meet and mutually interfere.

Synoptic pattern 4 (figure A8 and A9) is a summertime case when a large low pressure system over central Alaska dominates with the Pacific high retreating to the south. It is also observed if the Aleutian Low (type 2) drifts north. In the local wind fields (figure C9 and C10) we weaken the katabatic flow off the ice (the land surfaces may be warmer than the ocean), and the land-sea frictional differences encourage onshore flow. The winds also blow up estuaries, unlike previously described cases.

Synoptic pattern 5 (figure A10 and A11) represent the predominate summer case of the Pacific anticyclone. The local wind fields, shown in figure C11 and C12 were treated similarly to type 4. There is some topographical forcing, however, as the isobars are slightly packed on the eastern side of the high. The central area of the high is divergent with the onshore flow at the coast being convergent.

Synoptic type 6 (figure A12) represents the low pressure center west of the Queen Charlotte Islands. Frequently this low stagnates and fills in place, but it also may move NNW into the Gulf of Alaska and become type 1.2. The local wind field (figure C13) is divergent over most of the NEGQA grid. Guidance in scaling the small horizontal variations for this pattern was

taken from aircraft measurements made under similar synoptic conditions, reported in the Reynolds et al. report.

4.3 Evaluation

July-August 1974 and February-March 1975 were visually typed from the hand drawn sea level pressure analyses from the National Meteorological Center every twelve hours through these periods (Table 6 and 7).

Figure 17 shows the direction of the local wind (meteorological) at Middleton Island for each weather type as inferred from figures C1 - C13. For comparison the anemometer record at Middleton Island during the sample periods was stratified by synoptic type. Vector mean winds were then computed within each type and plotted for the winter period on figure 17 and for the summer period in figure 18. A similar plot for winter at EB-33 is shown in figure 18. Middleton winds show good agreement with the subjective types. Figure 18 indicates that EB-33 contained more of an alongshore component to the winds than inferred subjectively.

TABLE 6. SUBJECTIVE TYPING--WINTER

DAY	TIME (GMT)	TYPE	DAY	TIME (GMT)	TYPE	DAY	TIME (GMT)	TYPE
<u>FEBRUARY, 1975</u>								
1	00	6.0	23	00	2.0	16	00	3.0
1	12	6.0	23	12	5.0	16	12	1.3
2	00	6.0	24	00	4.0	17	00	1.3
2	12	6.0	24	12	2.1	17	12	6.0
3	00	6.0	25	00	1.3	18	00	6.0
3	12	6.0	25	12	2.0	18	12	6.0
4	00	6.0	26	00	1.3	19	00	6.0
4	12	5.1	26	12	2.0	19	12	1.0
5	00	5.1	27	00	4.0	20	00	5.0
5	12	5.1	27	12	2.1	20	12	4.0
6	00	3.0	28	00	5.0	21	00	2.1
6	12	6.0	28	12	5.0	21	12	4.0
7	00	6.0				22	00	4.1
7	12	1.2				22	12	1.2
8	00	2.0				23	00	1.1
8	12	2.0				23	12	1.1
9	00	4.1				24	00	1.1
9	12	6.0				24	12	4.0
10	00	6.0				25	00	4.1
10	12	6.0				25	12	4.1
11	00	6.0				26	00	1.3
11	12	1.0				26	12	1.3
12	00	1.0				27	00	2.0
12	12	1.0				27	12	2.0
13	00	1.1				28	00	2.0
13	12	1.1				28	12	3.0
14	00	1.1				29	00	2.0
14	12	2.0				29	12	4.1
15	00	4.0				30	00	5.1
15	12	4.0				30	12	5.0
16	00	5.0				31	00	1.3
16	12	2.0				31	12	5.0
17	00	1.3						
17	12	4.0						
18	00	2.0						
18	12	2.1						
19	00	2.0						
19	12	4.1						
20	00	4.0						
20	12	4.1						
21	00	2.0						
21	12	2.0						
22	00	2.0						
22	12	4.0						
<u>MARCH, 1975</u>								
			1	00	6.0			
			1	12	6.0			
			2	00	5.1			
			2	12	3.0			
			3	00	6.0			
			3	12	5.0			
			4	00	2.1			
			4	12	2.0			
			5	00	1.3			
			5	12	1.0			
			6	00	1.0			
			6	12	1.2			
			7	00	6.0			
			7	12	6.0			
			8	00	5.1			
			8	12	1.2			
			9	00	1.0			
			9	12	2.0			
			10	00	3.0			
			10	12	2.0			
			11	00	2.0			
			11	12	4.0			
			12	00	5.0			
			12	12	2.0			
			13	00	3.0			
			13	12	2.0			
			14	00	1.3			
			14	12	1.2			
			15	00	1.3			
			15	12	1.1			

TABLE 7. SUBJECTIVE TYPING--SUMMER

DAY	TIME (GMT)	TYPE	DAY	TIME (GMT)	TYPE	DAY	TIME (GMT)	TYPE
<u>JULY, 1974</u>								
1	00	1.3	23	00	1.3	13	00	5.1
1	12	1.3	23	12	2.1	13	12	5.1
2	00	4.1	24	00	1.1	14	00	5.1
2	12	2.1	24	12	4.0	14	12	5.1
3	00	4.1	25	00	4.0	15	00	5.1
3	12	4.0	25	12	1.1	15	12	5.1
4	00	5.0	26	00	5.0	16	00	5.1
4	12	5.1	26	12	5.1	16	12	5.0
5	00	5.1	27	00	5.1	17	00	5.1
5	12	1.1	27	12	5.1	17	12	5.1
6	00	1.1	28	00	5.0	18	00	1.0
6	12	5.1	28	12	5.0	18	12	4.1
7	00	5.1	29	00	4.0	19	00	5.1
7	12	5.0	29	12	5.0	19	12	5.1
8	00	5.1	30	00	5.1	20	00	4.1
8	12	5.0	30	12	5.1	20	12	1.1
9	00	5.1	31	00	5.1	21	00	4.1
9	12	5.1	31	12	4.0	21	12	4.0
10	00	5.1	<u>AUGUST, 1974</u>			22	00	4.0
10	12	1.1	1	00	3.0	22	12	4.0
11	00	1.1	1	12	2.0	23	00	1.1
11	12	1.3	2	00	1.3	23	12	4.1
12	00	1.1	2	12	1.3	24	00	4.1
12	12	1.1	3	00	1.1	24	12	5.0
13	00	2.1	3	12	1.1	25	00	1.3
13	12	2.0	4	00	1.1	25	12	1.3
14	00	4.0	4	12	6.0	26	00	1.0
14	12	5.1	5	00	5.0	26	12	4.0
15	00	5.1	5	12	4.0	27	00	2.1
15	12	5.1	5	12	4.0	27	12	2.0
16	00	4.0	6	00	2.1	28	00	2.1
16	12	5.1	6	12	2.1	28	12	2.1
17	00	4.1	7	00	2.1	29	00	2.1
17	12	5.1	7	12	1.3	29	12	2.1
18	00	5.0	8	00	1.1	30	00	2.1
18	12	4.0	8	12	4.0	30	12	2.1
19	00	4.0	9	00	5.0	31	00	5.1
19	12	2.1	9	12	5.0	31	12	4.0
20	00	2.1	10	00	5.0			
20	12	2.0	10	12	5.1			
21	00	2.0	11	00	5.1			
21	12	1.3	11	12	5.1			
22	00	1.3	12	00	5.1			
22	12	1.1	12	12	5.1			

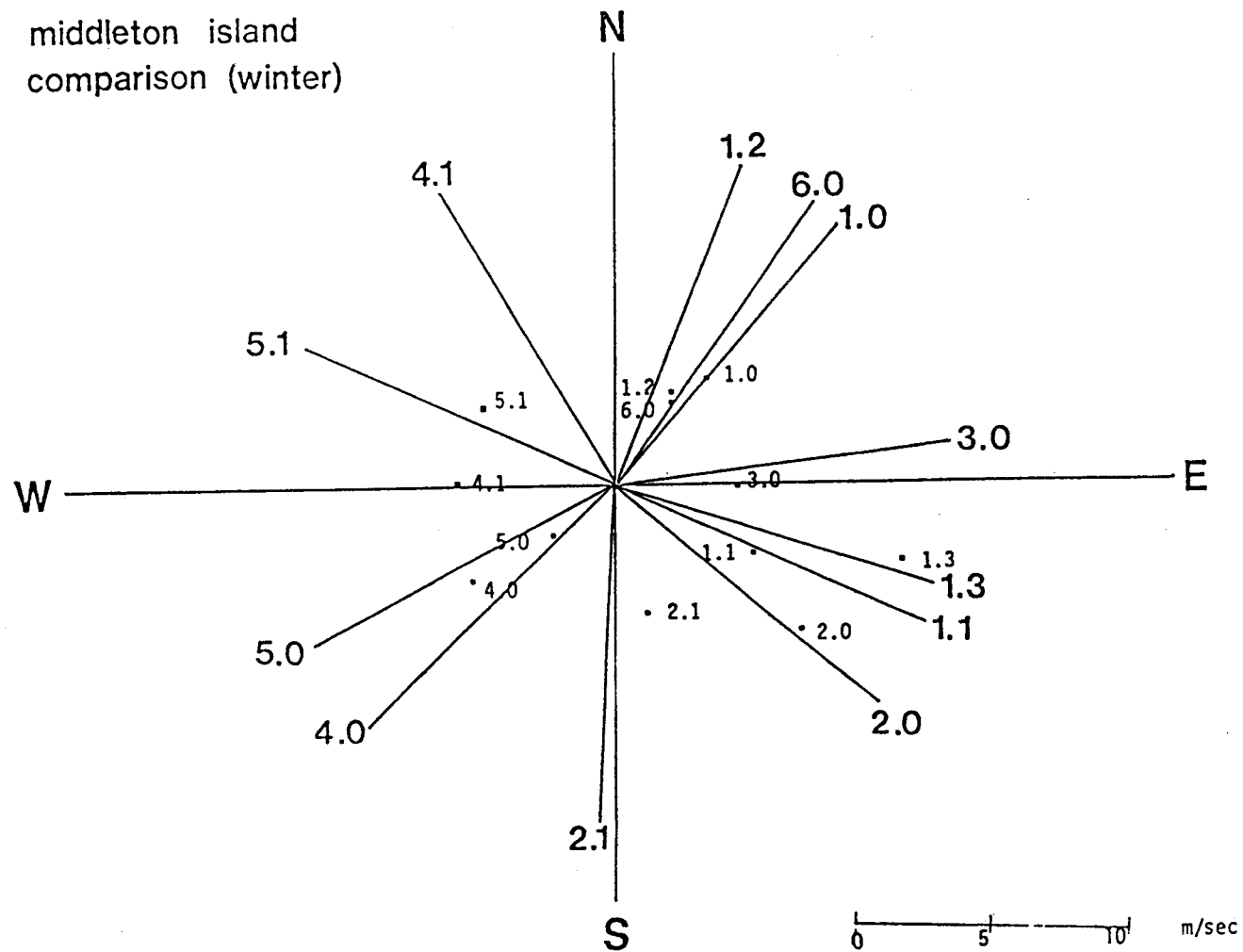


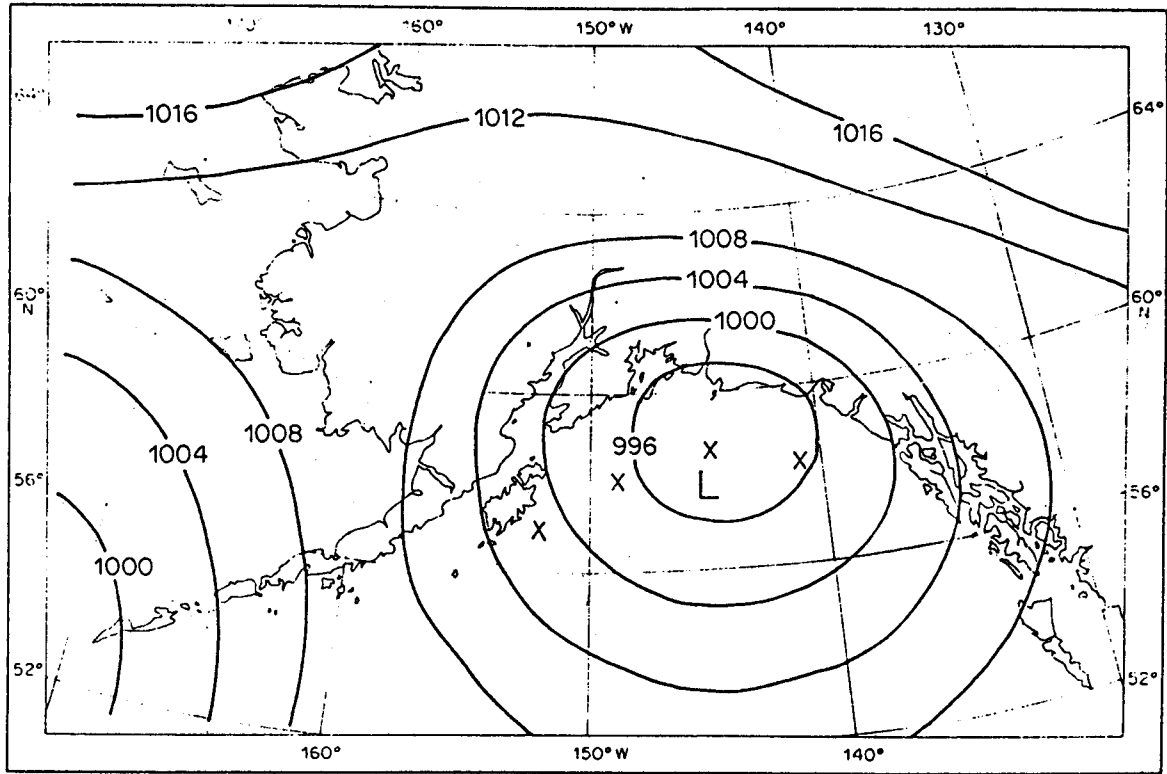
Figure 17. Direction of local wind types at Middleton Island. Dots represent the vector mean observed wind at Middleton stratified by subtypes for the February - March 1975 period.

REFERENCES

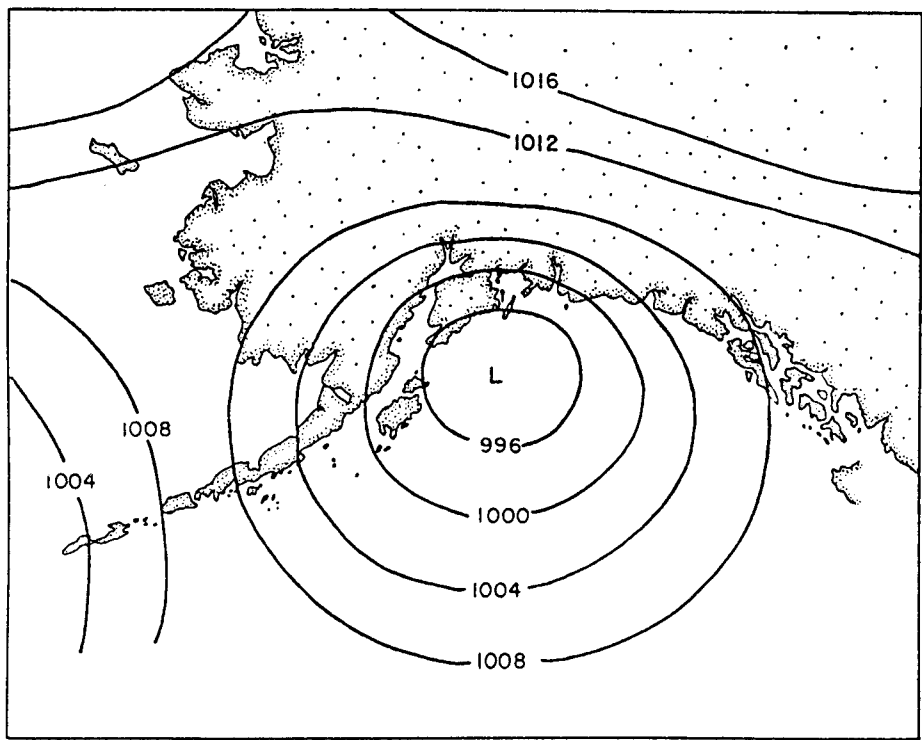
- Barry, R.G., and A.H. Perry. Synoptic Climatology, Methods and Application. London: Methuen & Co., 1973, 553 pp.
- Blasing, T.J. A comparison of map patterns correlation and principal component eigenvector methods for analyzing climate anomaly patterns, in Preprints Fourth Conf. Probability and Statistics in the Atmospheric Sciences, Amer. Meteor. Soc. 1975 p. 96-101.
- Brower, J.R.W.A., Diaz H.F., Prechtel A.S. Searby, H.W. and J.L. Wise. Climatic Atlas of the Outer Continental Shelf waters and coastal Regions of Alaska: Vol. 1 Gulf of Alaska, National Climate Center, Environmental Data Service, NOAA, Ashville N.C. 1977, 439 pp.
- Cardone, V.J. Specification of the wind distribution in the marine boundary layer for wave forecasting. Report GSL TR69-1 New York University School of Engineering and Science. 1969, 131 pp.
- Cressman, G.P. An operational objective analysis system. Mon. Wea. Rev. 1959 87, 367-374.
- Flattery, T.W. Spectral Models for global analysis and forecasting. in Proceedings sixth AWS Technical Exchange Conference, AWS Tech Rept. 242, Scott AFB, Ill., 1970, pp. 42-54.
- Jenne, R.L. Data sets for meteorological research. NCAR Tech Note NCAR-TN/1A-111 1975, 194 pp.
- Kendall, M.G. and A. Stewart. The Advanced Theory of Statistics Vol. 3. New York N.Y.: Hafner Press, 1975. 585 pp.
- Lund, I.A. Map pattern classification by statistical methods. J. Appl. Meteor. 2 1963, p. 56-65.
- Overland, J.E. Hitchman M.H. and Y.J. Han A Regional Surface Wind Model for Mountainous Coastal Areas PMEL/ERL/NOAA Tech Report (In Press) 1978
- Putnins, P. The sequence of baric pressure patterns over Alaska. Studies on the meteorology of Alaska 1st Interim Report Washington. D.C. Environmental Data Service ESSA, 1966. 57 pp.
- Reynolds, R.M. Hiester, T.R. and S.A. Macklin. Coastal Meteorology of the Gulf of Alaska Icy Bay to Yakutat Bay. PMEL/ERL/NOAA Tech Report (In press) 1978.
- Singh, S.V., Mooley D.A., and R.H. Kripalani Synoptic Climatology of the Daily 700mb Summer Monsoon Flow Patterns over India. Mon. Wea. Rev. 106 1978 510-525.
- Sorkina A.I. Tipy atmosfernoj tsirkuliatsii Israel Program for Scientific Translations, Jerusalem 1963. pp. 247.

APPENDIX A

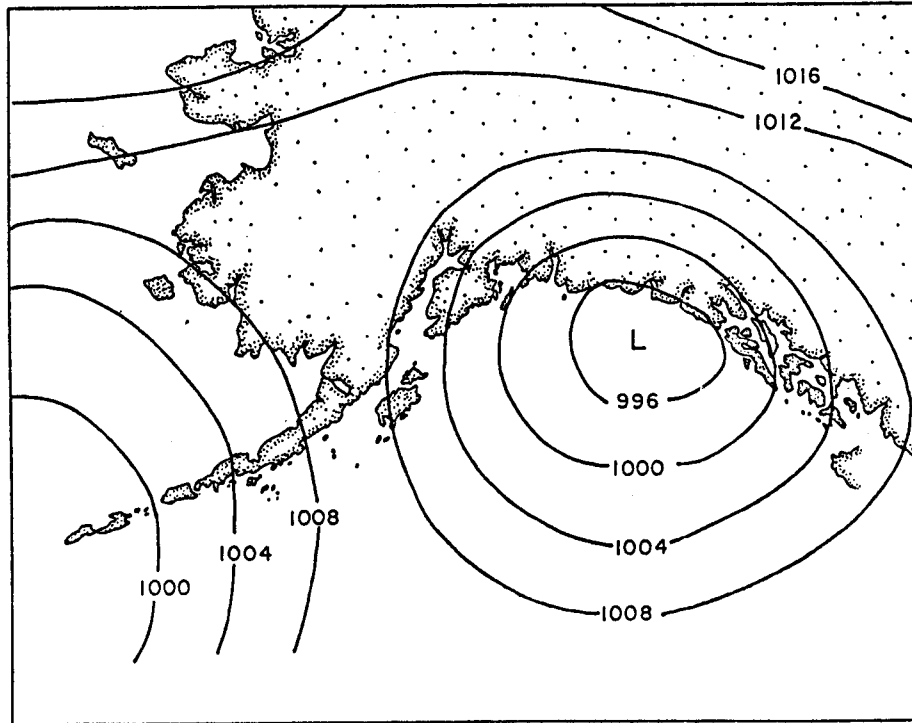
1. Subjective Subtype Patterns 1.0-6.0 (Hand Drawn)
2. Subjective Subtype Patterns 1.0-6.0 (Machine Drawn)
3. Percent of Occurrence and Transition Probabilities for Subtypes
4. Correlation Matrix Between Subjective Types



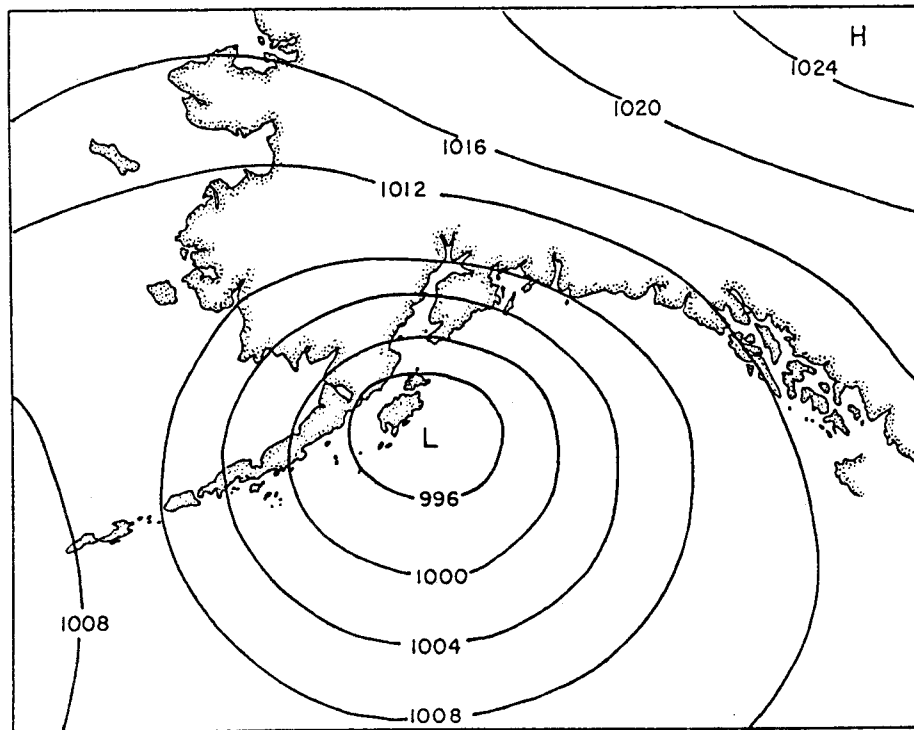
1.0



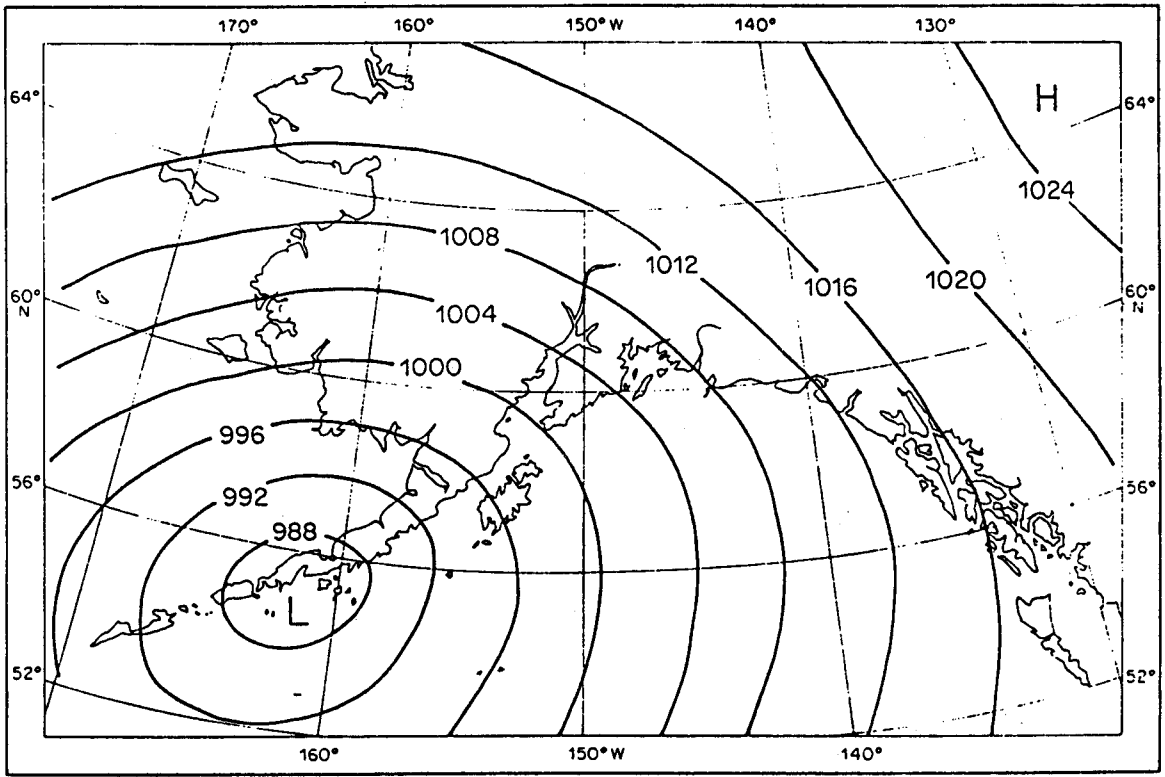
1.1



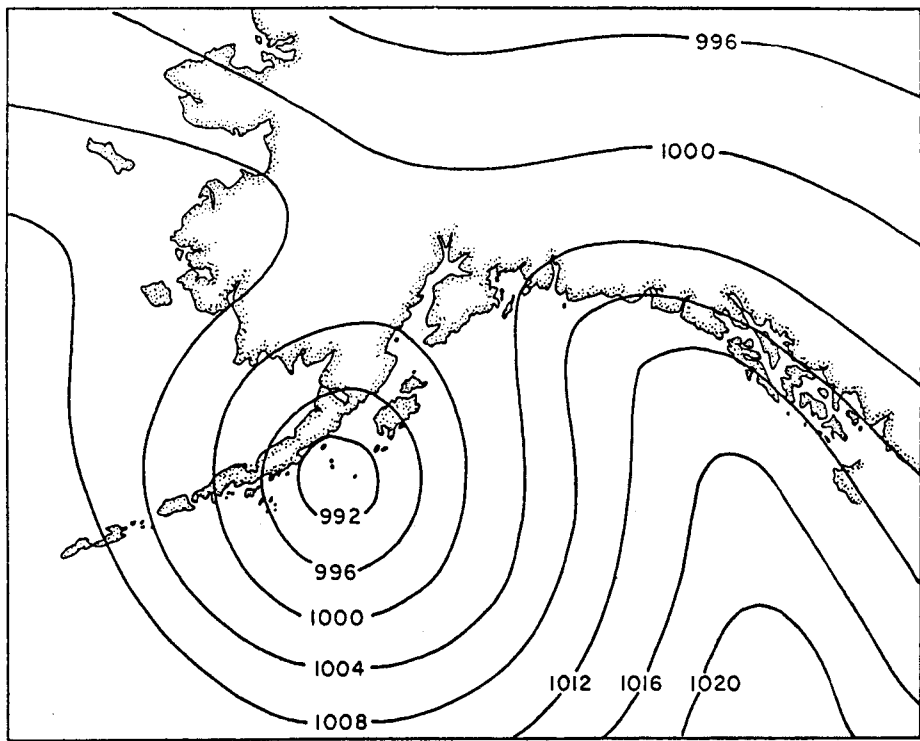
1.2



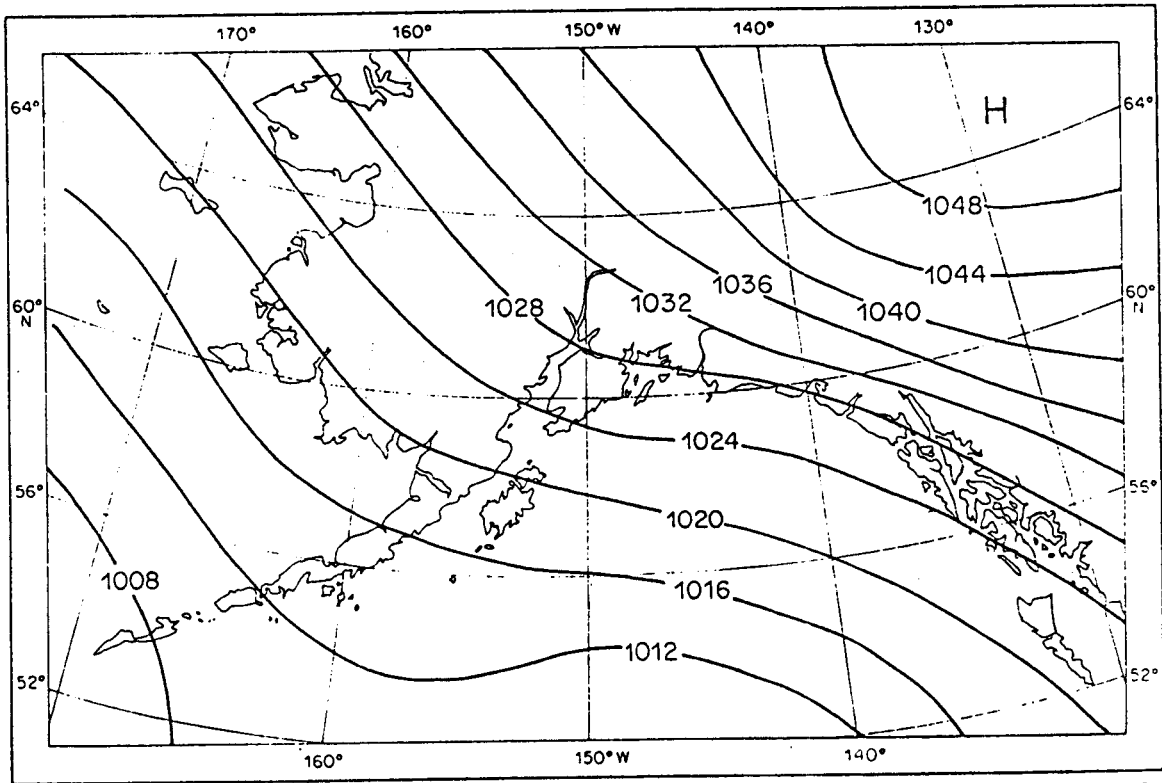
1.3



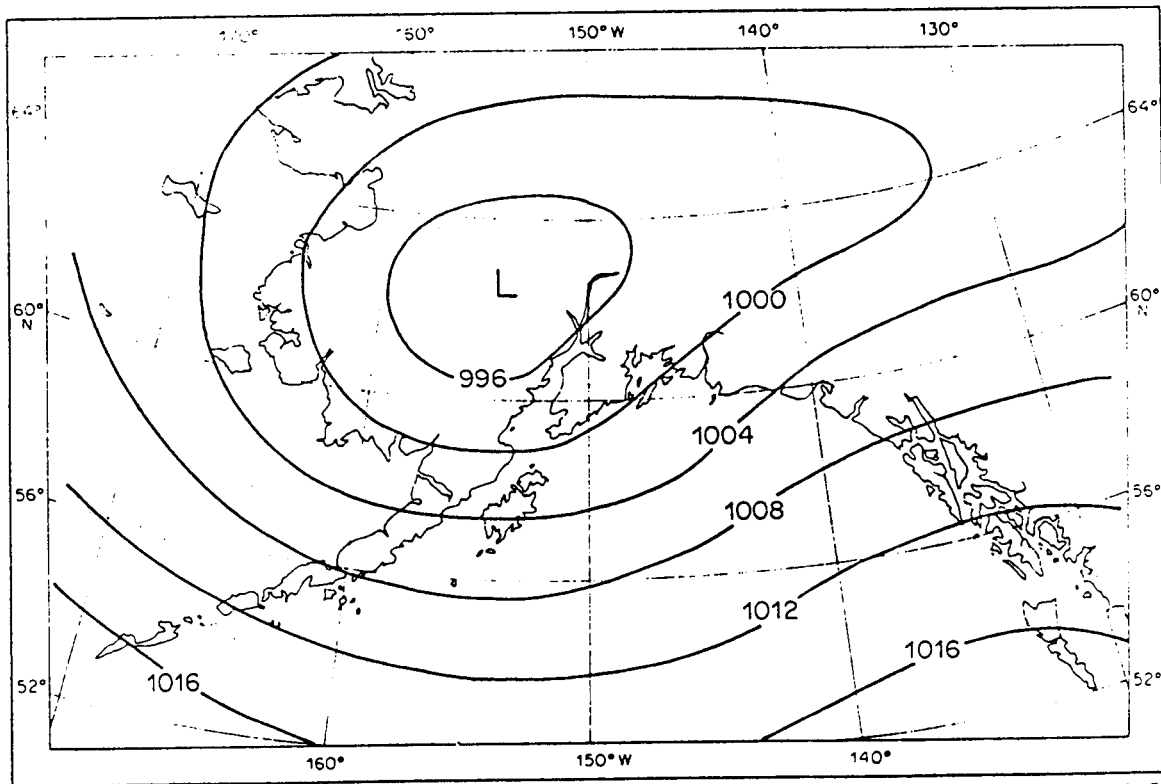
2.0



2.1

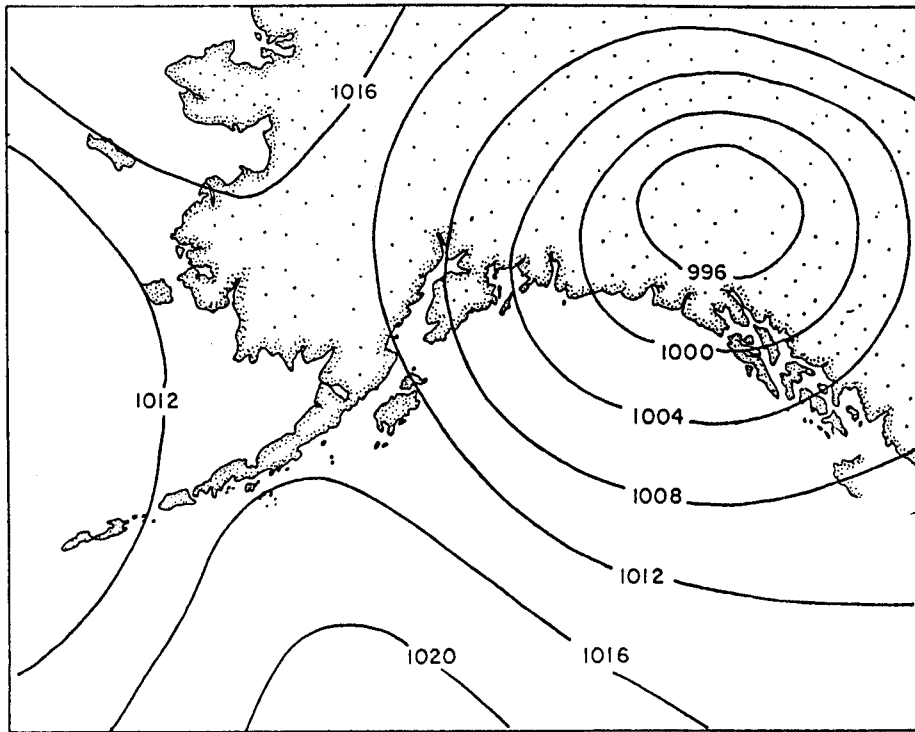


3.0

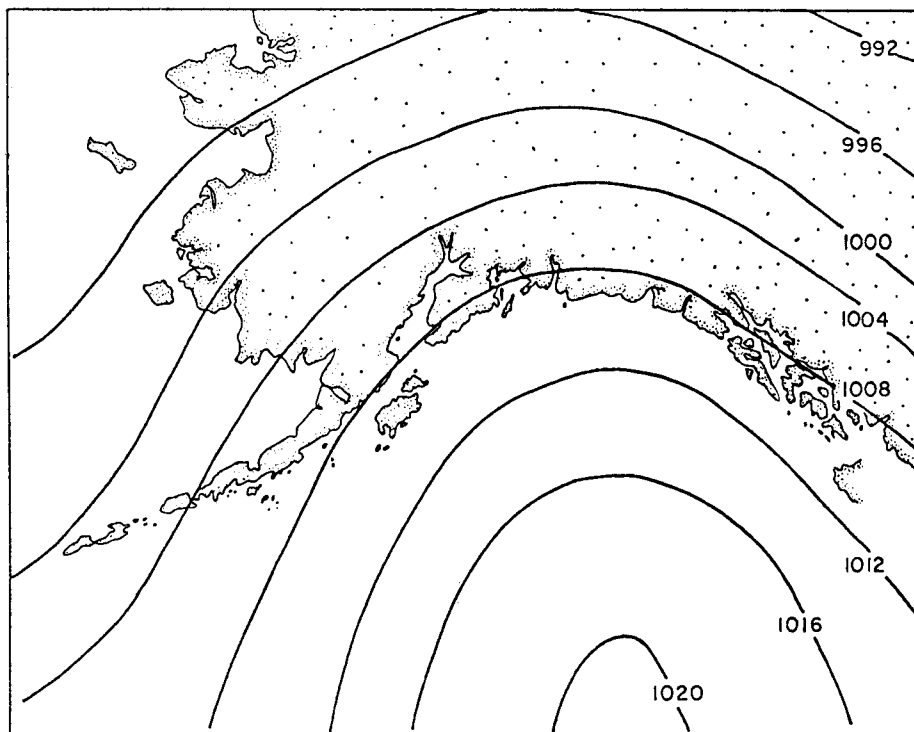


4.0

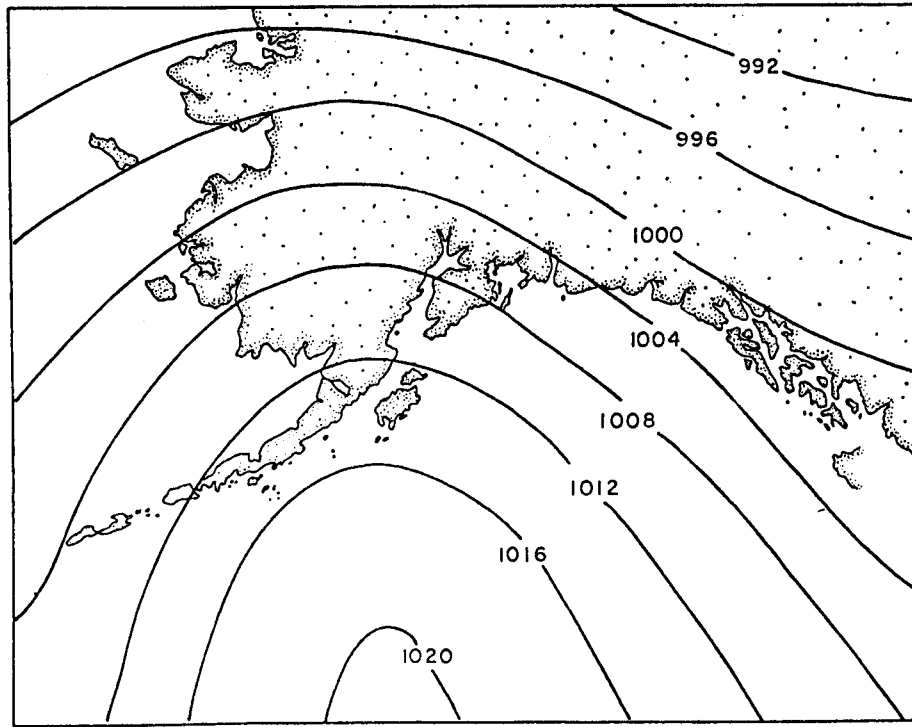
+



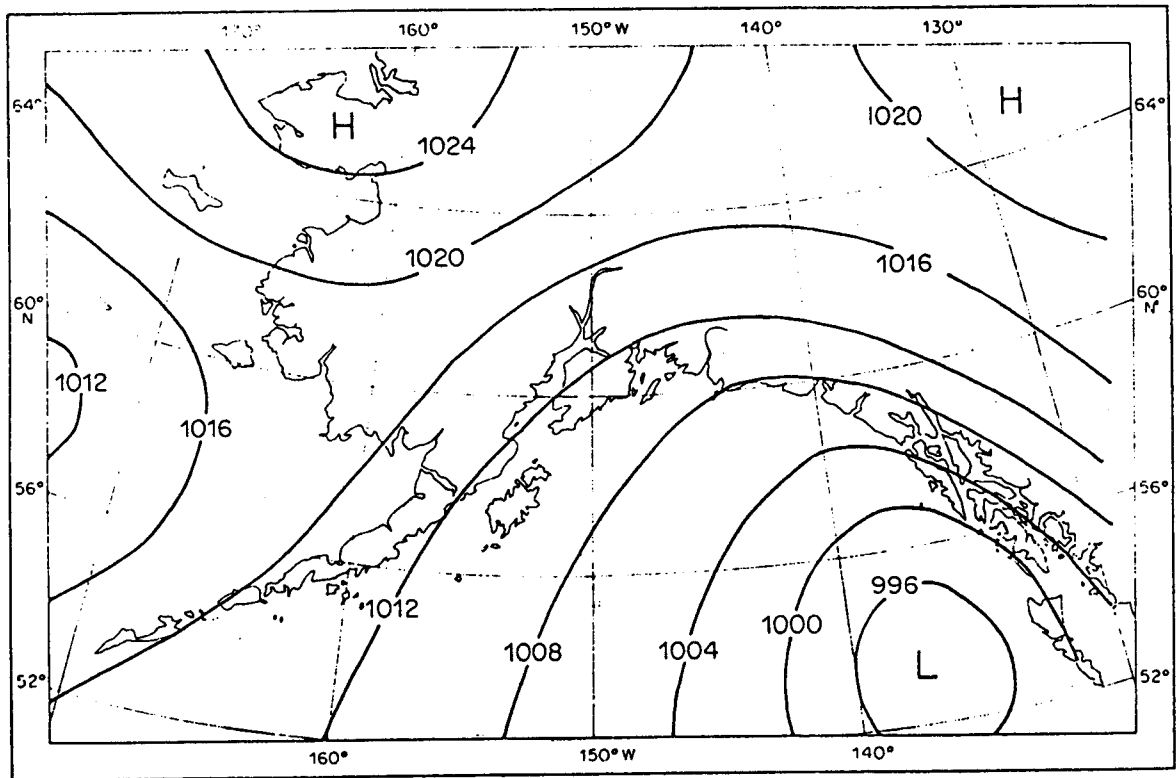
4.1



5.0



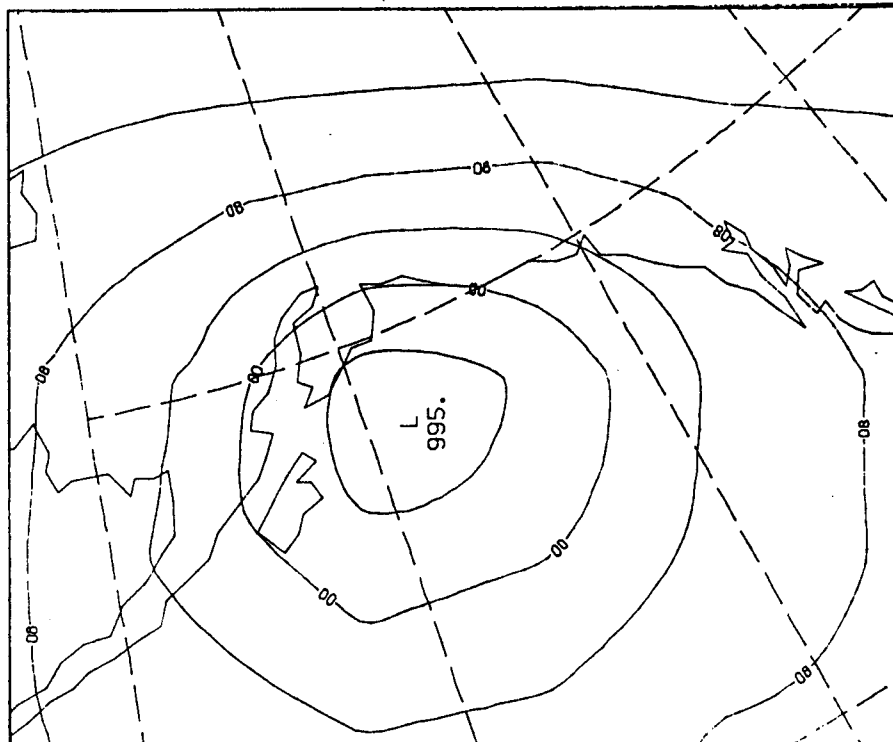
5.1



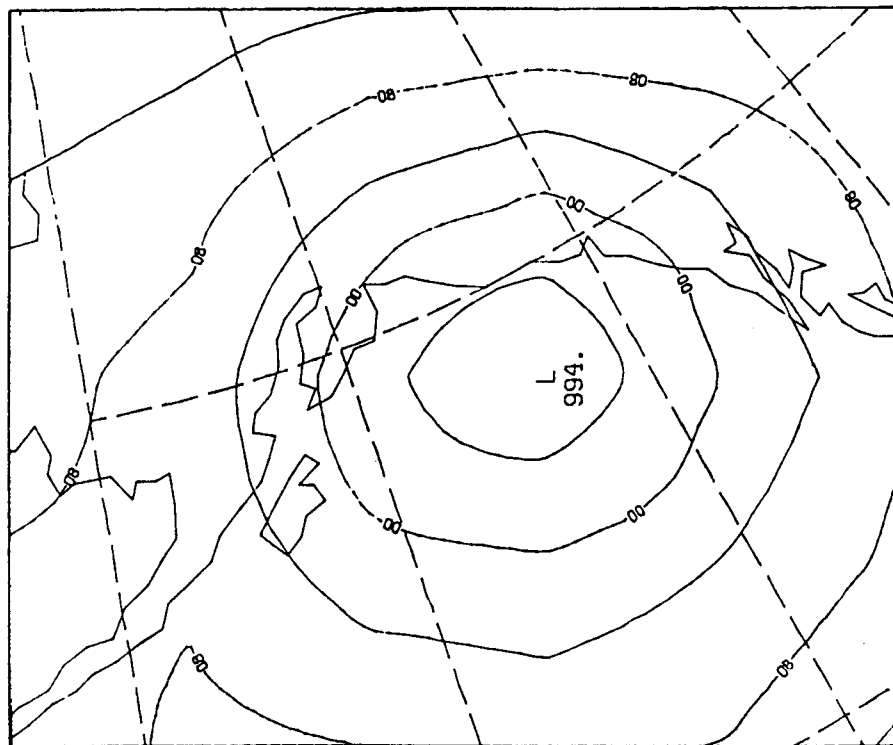
6.0

+

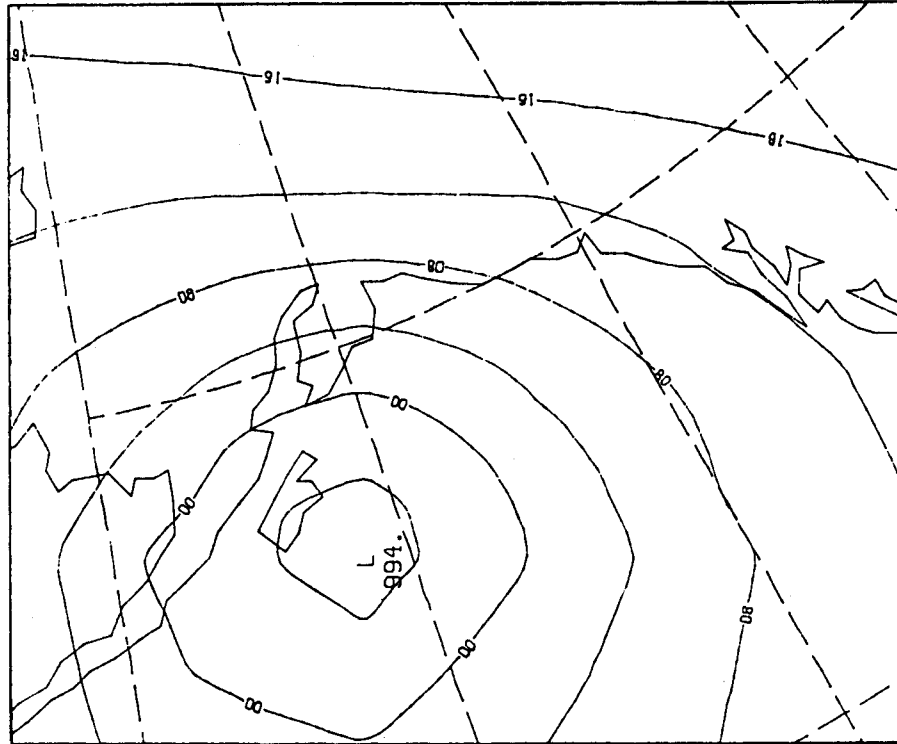
CLIMATE 11



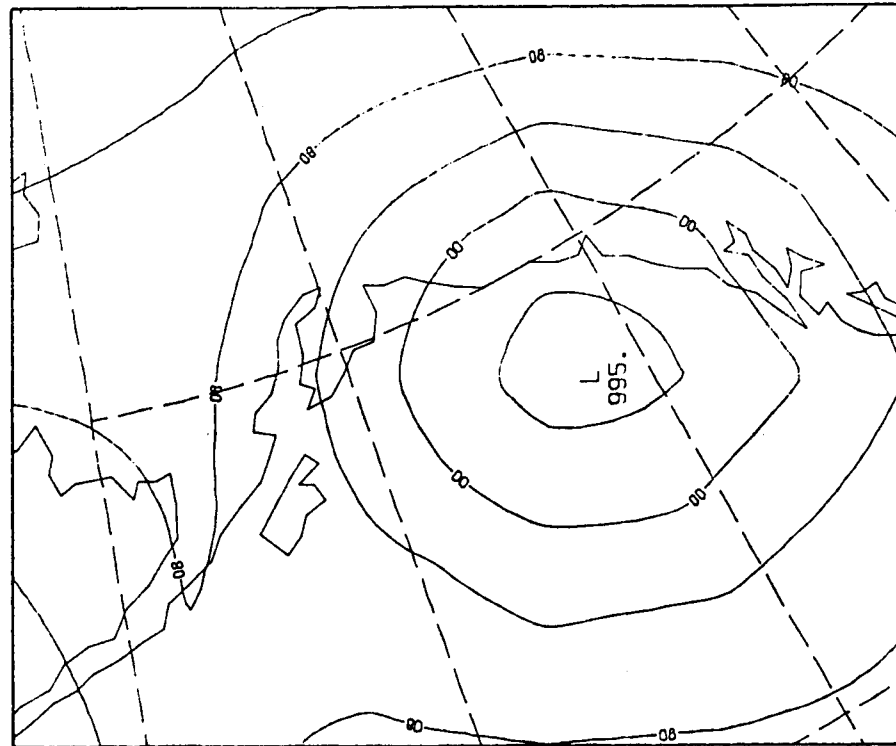
CLIMATE 10



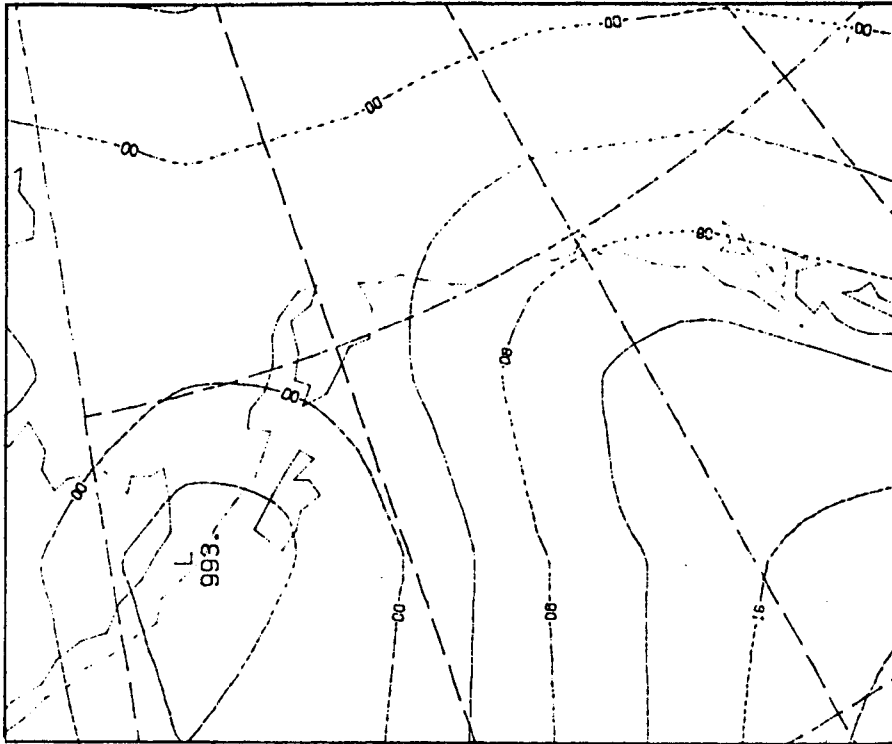
CLIMATE 13



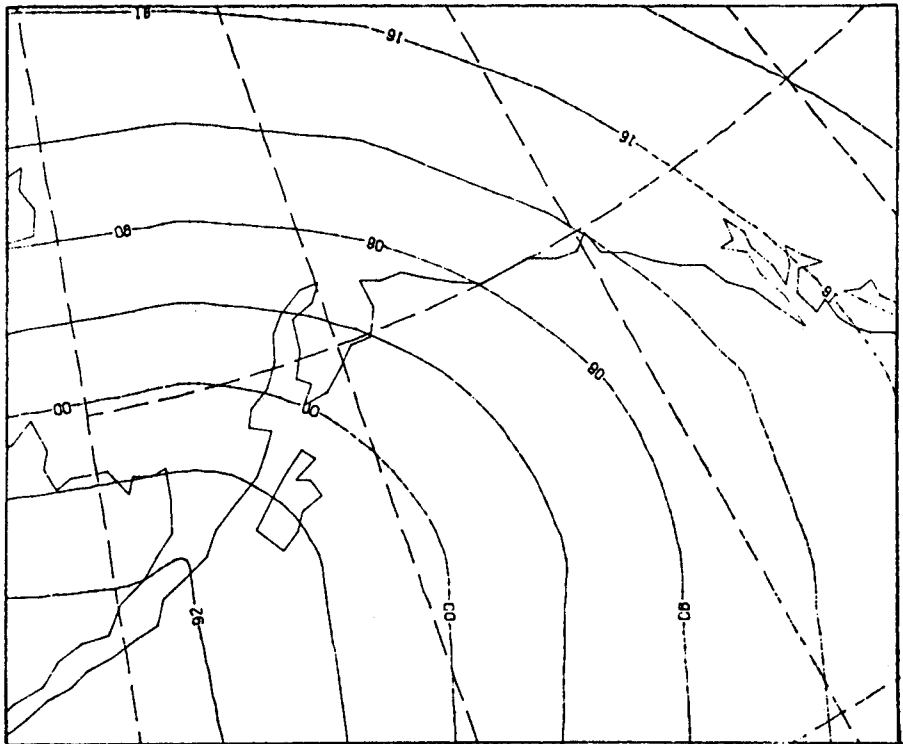
CLIMATE 12



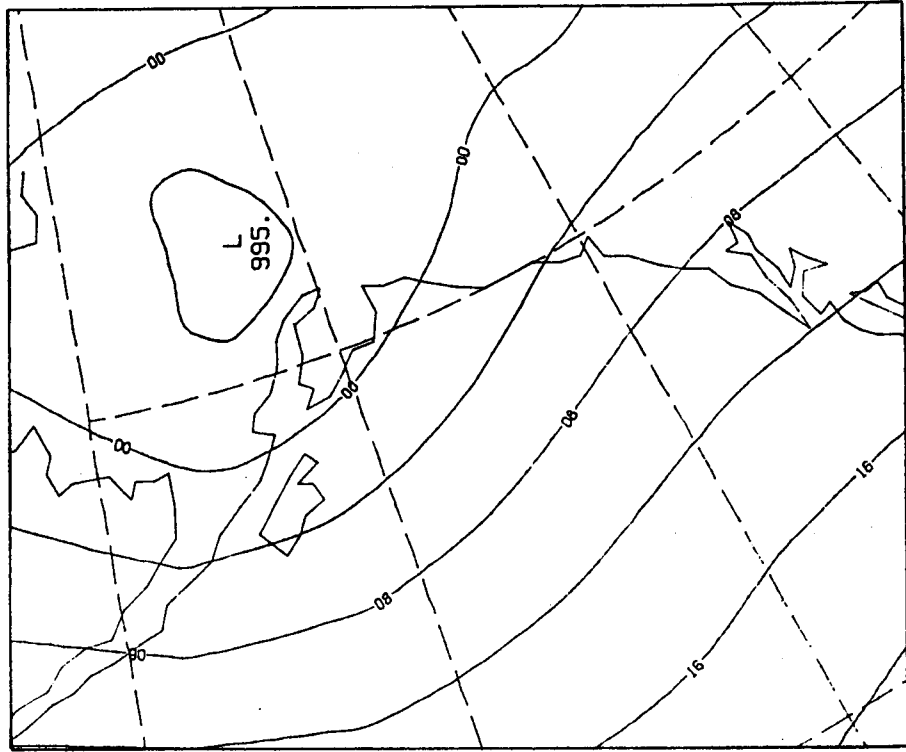
CLIMATE 21



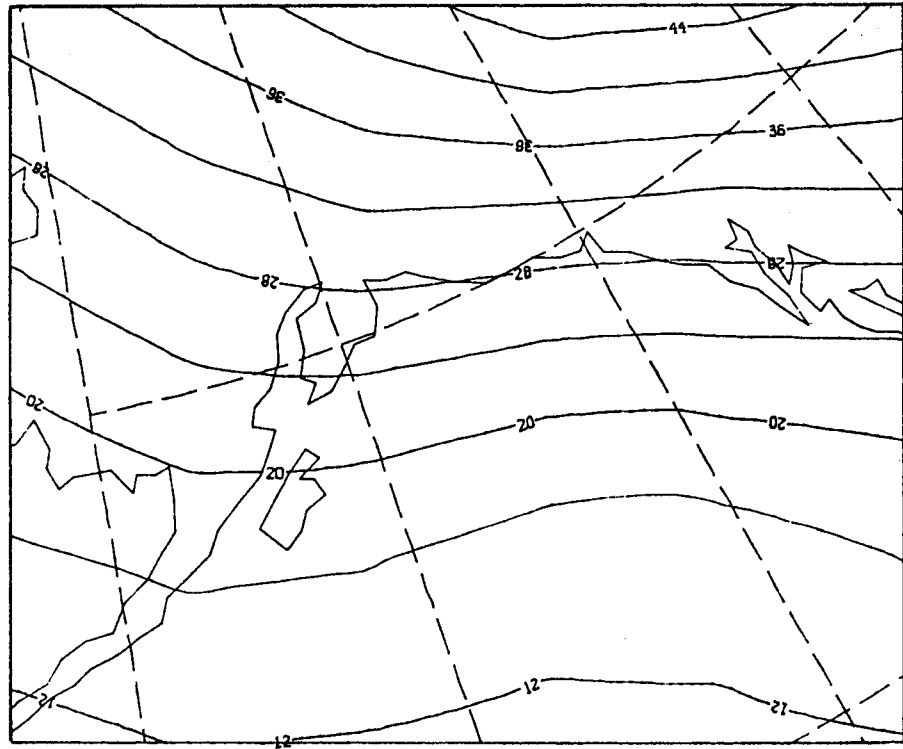
CLIMATE 20



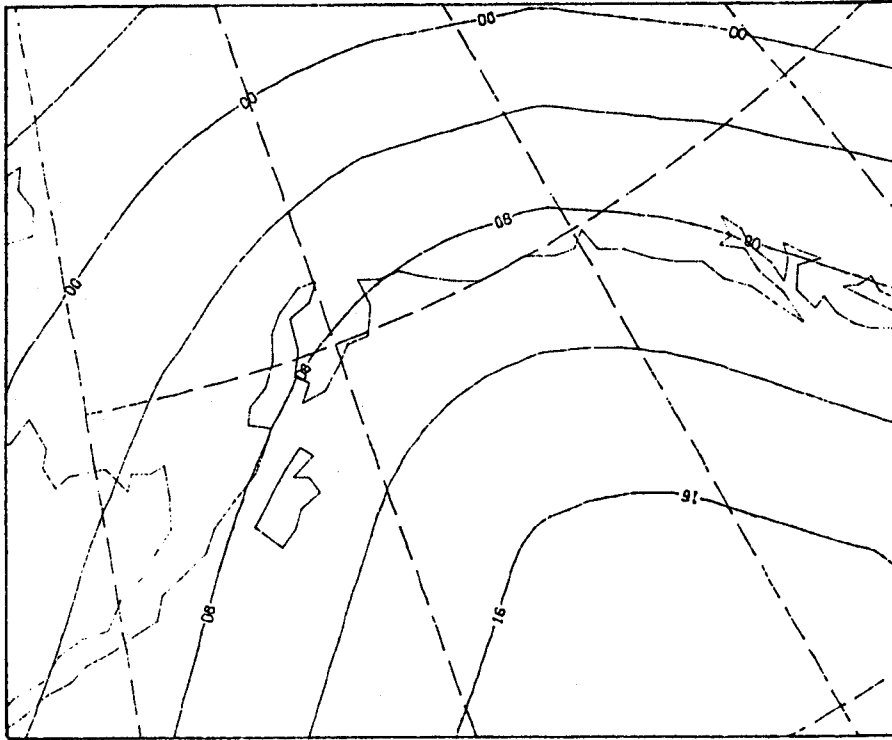
CLIMATE 40



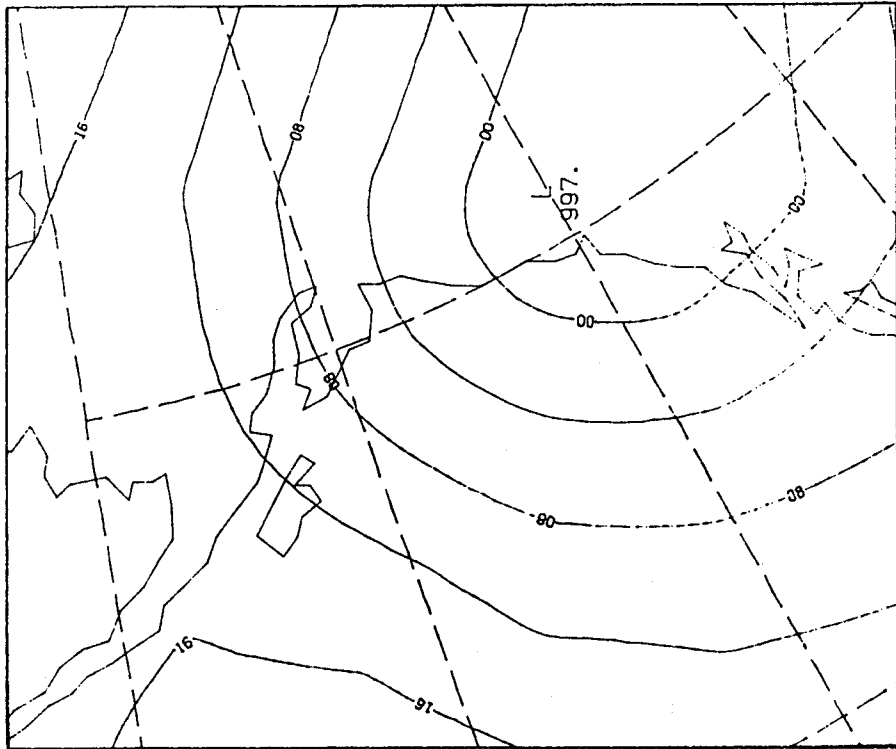
CLIMATE 30



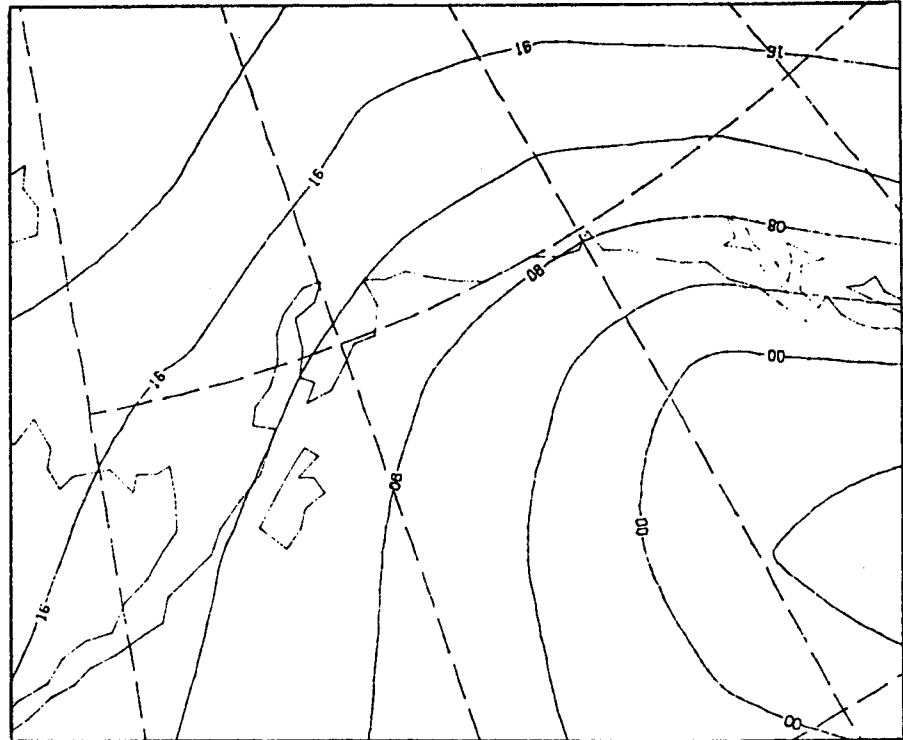
CLIMATE 50



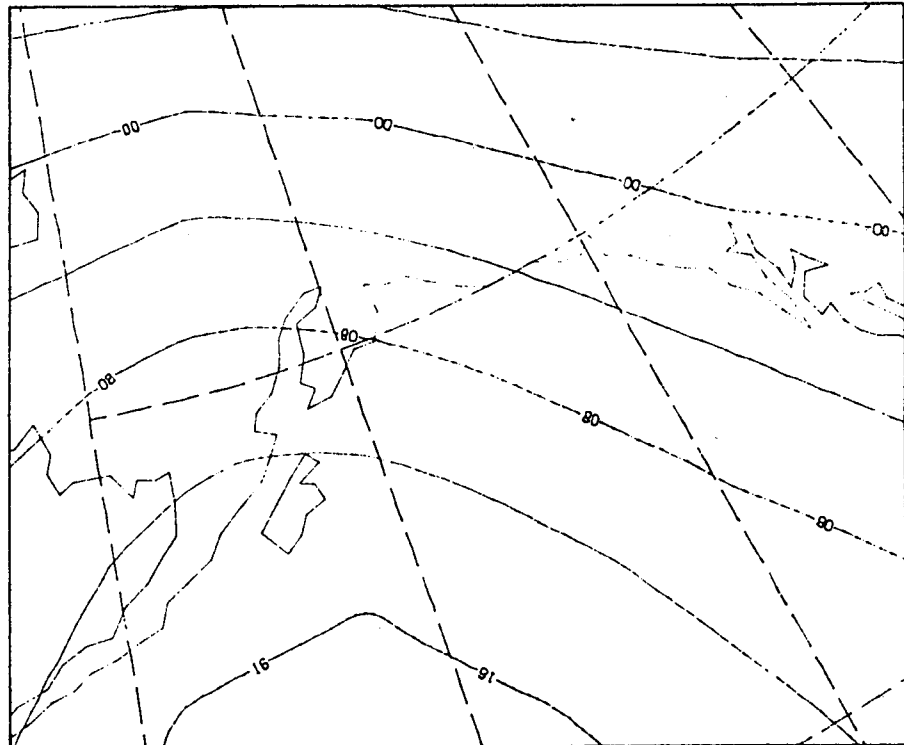
CLIMATE 41



CLIMATE 60



CLIMATE 51



TRANSITIONS FROM INITIAL TYPE TO FOLLOWING TYPE
Based on 12 Hourly Analyses 1968-1974

	Initial Type	% of Occurrence of Initial Type	% of Initial Type Followed by Following Type											
			1.0	1.1	1.2	1.3	2.0	2.1	3	4.0	4.1	5.0	5.1	6
Y E A R	1.0	4	28	5	8	0	8	5	2	10	18	1	0	15
	1.1	4	14	23	2	10	7	1	3	9	7	1	1	22
	1.2	2	3	4	18	4	32	3	12	3	2	6	2	11
	1.3	6	5	18	1	31	15	4	8	5	1	0	5	12
	2.0	25	1	1	0	9	69	4	7	5	0	3	0	1
	2.1	6	1	2	1	9	24	35	2	17	1	5	1	2
	3	10	1	4	1	8	15	0	57	0	0	1	0	13
	4.0	10	3	2	0	1	6	8	0	50	9	11	8	2
	4.1	8	4	1	5	1	4	3	0	5	55	5	9	8
	5.0	7	0	0	0	0	19	16	1	7	0	52	4	1
5.1	4	0	0	0	0	3	1	0	9	19	18	49	1	
6	14	5	4	5	1	3	0	9	1	7	1	2	62	
W I N T E R	1.0	6	39	5	12	0	8	4	1	4	8	0	0	19
	1.1	6	16	35	4	12	7	0	3	1	3	0	0	19
	1.2	3	0	0	21	5	36	0	11	3	0	3	3	18
	1.3	8	5	20	2	38	14	0	10	2	1	0	0	8
	2.0	25	1	1	0	10	70	2	9	5	0	1	0	1
	2.1	1	0	0	12	18	40	12	0	18	0	0	0	0
	3	19	0	3	0	6	10	0	71	0	0	1	0	9
	4.0	3	14	0	3	0	12	8	0	24	13	13	8	5
	4.1	4	10	0	10	0	4	4	2	2	45	2	4	17
	5.0	3	0	0	0	0	33	3	7	10	0	44	3	0
5.1	1	0	0	0	0	8	0	0	0	25	33	34	0	
6	21	6	6	2	0	2	0	9	0	3	0	0	71	
S P R I N G	1.0	3	11	11	6	0	9	6	0	11	32	0	0	14
	1.1	4	9	19	0	11	7	2	2	11	9	2	0	28
	1.2	2	0	10	25	5	15	5	10	5	0	5	0	20
	1.3	7	4	16	0	32	19	4	10	4	0	0	0	11
	2.0	31	2	2	0	7	71	3	7	5	0	2	0	1
	2.1	6	0	0	0	15	34	25	0	18	1	4	0	3
	3	8	1	6	0	9	19	2	47	0	0	0	0	16
	4.0	9	2	1	0	1	10	10	1	48	5	10	8	4
	4.1	8	6	1	5	0	3	3	0	4	53	9	6	10
	5.0	6	0	0	0	0	29	19	3	1	1	43	3	1
5.1	3	0	0	0	0	6	0	0	3	25	31	35	0	
6	13	5	5	4	2	4	0	8	1	8	1	2	60	

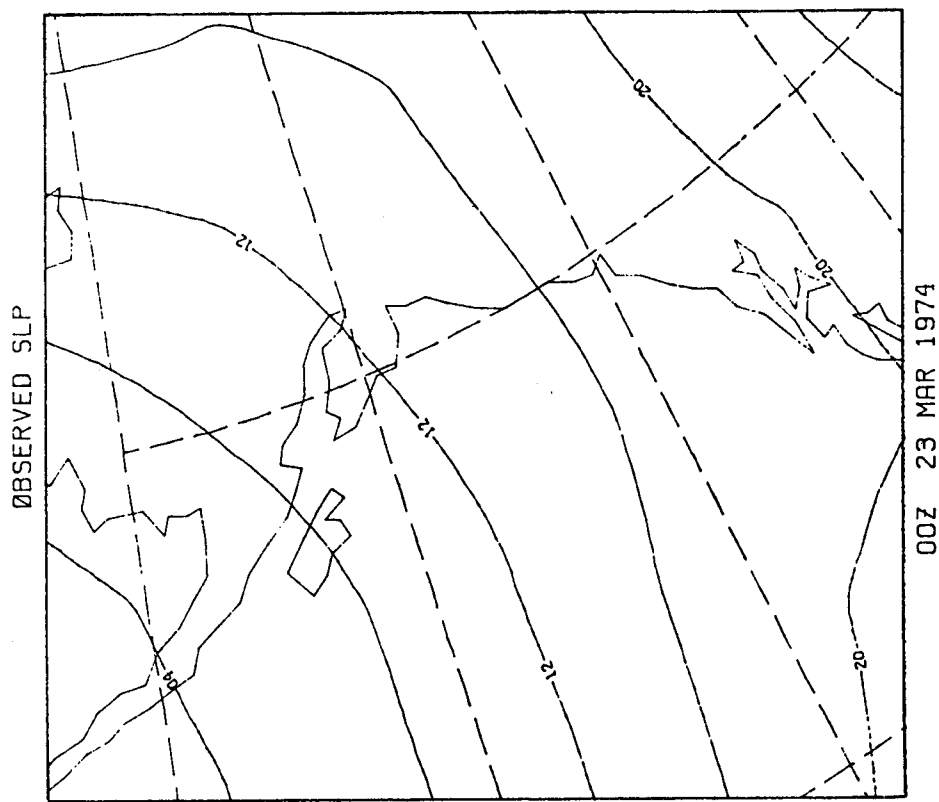
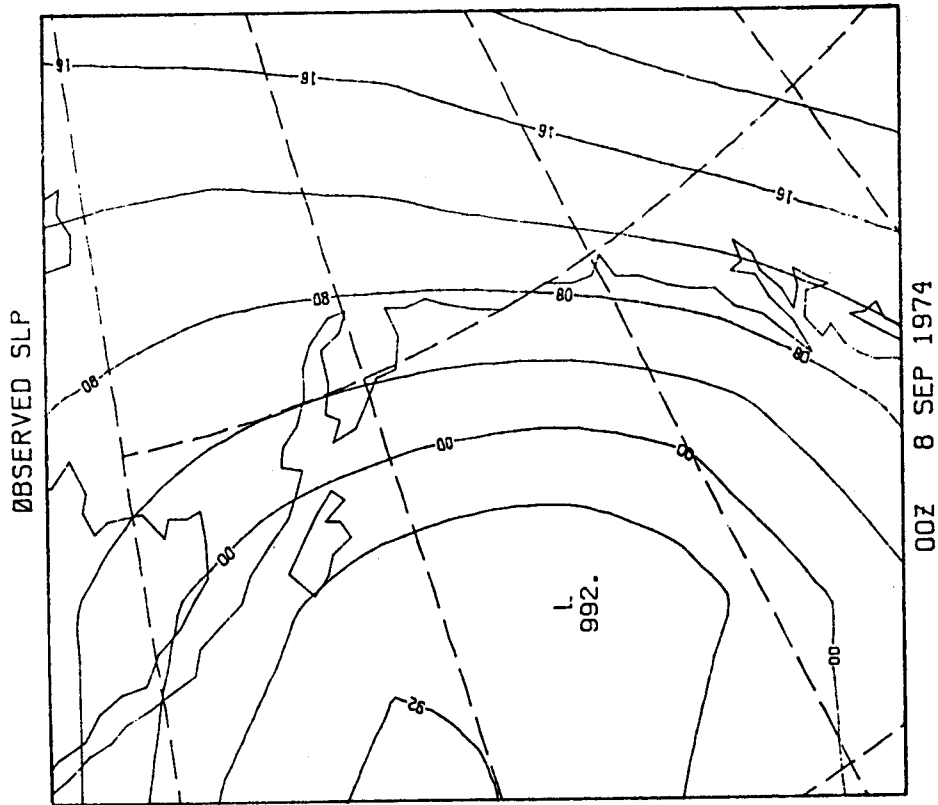
TRANSITIONS FROM INITIAL TYPE TO FOLLOWING TYPE (Cont.)
Based on 12 Hourly Analyses 1968-1974

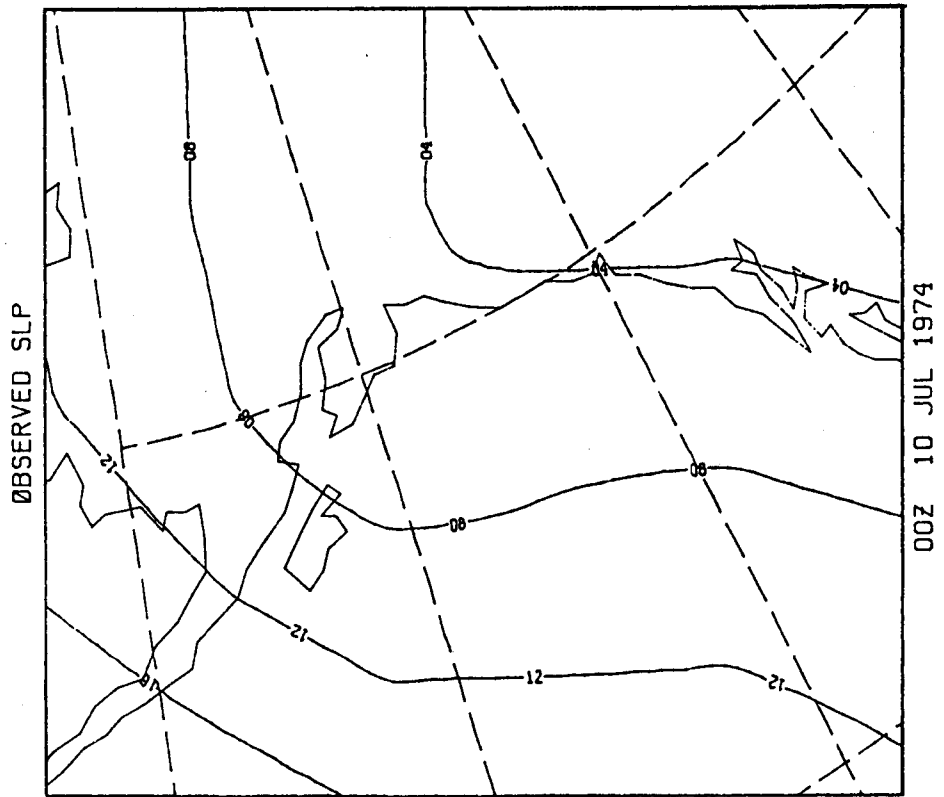
Initial Type	% of Occurrence of Initial Type	% of Initial Type Followed by Following Type											
		1.0	1.1	1.2	1.3	2.0	2.1	3	4.0	4.1	5.0	5.1	6
S U M M E R	1.0	24	0	4	0	8	8	0	16	32	4	0	4
	1.1	14	7	0	7	0	0	0	37	14	0	7	14
	1.2	1	0	16	0	15	15	15	8	8	15	0	0
	1.3	4	6	8	0	27	13	13	4	10	2	0	2
	2.0	18	0	0	0	8	65	9	7	2	0	7	0
	2.1	13	1	1	0	6	13	47	3	17	1	7	2
	3	3	5	5	7	10	20	0	29	0	2	7	0
	4.0	15	1	2	0	1	3	7	0	57	6	12	10
	4.1	11	2	1	2	0	1	1	0	11	60	3	15
	5.0	16	0	0	0	0	12	18	0	4	0	61	5
	5.1	10	0	0	1	0	1	2	0	9	13	15	57
6	6	7	1	4	1	6	1	4	0	16	1	6	
F A L L	1.0	27	3	5	0	8	3	5	15	19	0	0	15
	1.1	16	20	2	7	7	2	4	11	9	0	0	22
	1.2	3	6	6	14	3	43	0	13	0	3	6	3
	1.3	7	6	24	0	25	14	2	6	5	1	0	0
	2.0	25	0	0	12	67	4	7	6	0	2	0	0
	2.1	5	0	5	2	11	39	23	2	16	0	0	0
	3	8	1	2	0	13	18	0	43	2	1	1	0
	4.0	11	3	3	0	1	5	8	1	49	14	9	5
	4.1	11	1	1	7	2	7	4	0	1	57	4	7
	5.0	4	2	0	0	0	23	15	0	26	0	32	2
	5.1	3	0	0	0	0	9	3	0	14	31	11	29
6	15	3	2	10	1	2	1	9	2	7	1	2	

Type	1.0	1.1	1.2	1.3	2.0	2.1	3.0	4.0	4.1	5.0	5.1	6.0
1.0	1.00	.81	.89	.46	.18	-.32	.28	-.08	.22	-.50	-.26	.40
1.1	.81	1.00	.57	.84	.50	-.10	.58	-.12	-.27	-.62	-.66	.38
1.2	.89	.57	1.00	.25	.10	-.52	.30	-.31	.31	-.45	-.14	.48
1.3	.46	.84	.25	1.00	.82	.17	.81	-.23	-.68	-.55	-.92	.24
2.0	.18	.50	.10	.82	1.00	.38	.76	-.10	-.78	-.15	-.84	-.13
2.1	-.32	-.10	-.52	.17	.38	1.00	-.23	.58	-.22	.57	-.05	-.80
3.0	.28	.58	.30	.81	.76	-.23	1.00	-.62	-.76	-.66	-.93	.47
4.0	-.08	-.12	-.31	-.23	-.10	.58	-.62	1.00	.22	.73	.44	-.78
4.1	.22	-.27	.31	-.68	-.78	-.22	-.76	.22	1.00	.24	.82	-.01
5.0	-.50	-.62	-.45	-.55	-.15	.57	-.66	.73	.24	1.00	.62	-.88
5.1	-.26	-.66	-.14	-.92	-.84	-.05	-.93	.44	.82	.62	1.00	-.32
6.0	.40	.38	.48	.24	-.13	-.80	.47	-.78	-.01	-.88	-.32	1.00

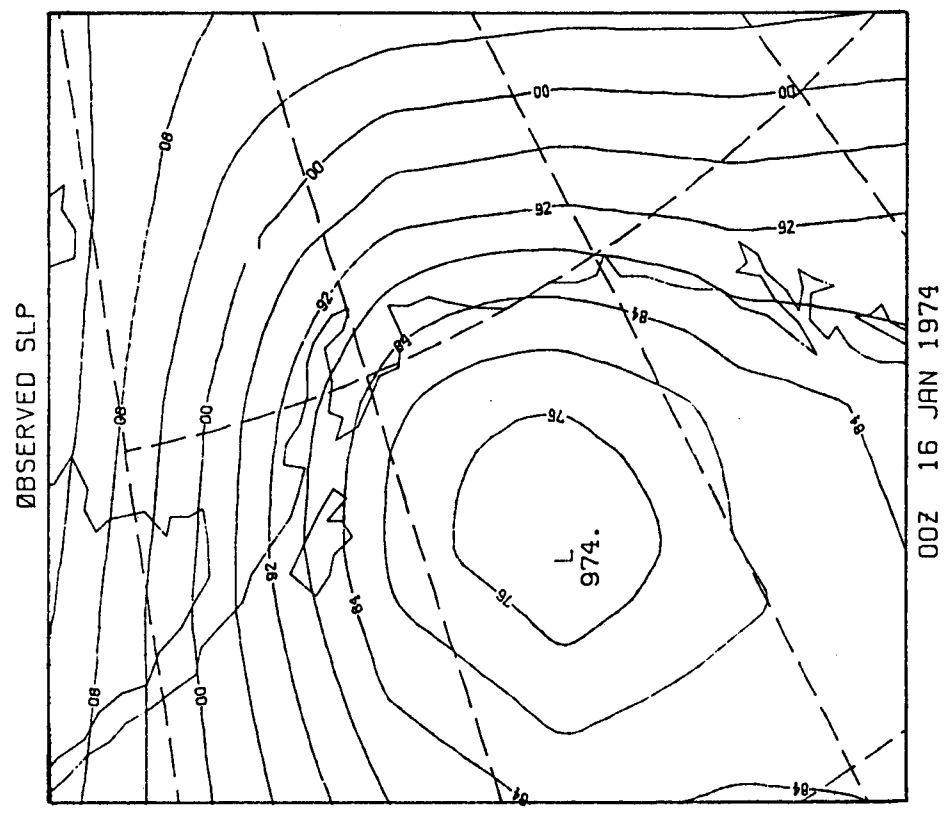
APPENDIX B

1. Objective Patterns A-I (correlation cutoff = 0.8)
2. Objective Patterns AA-HH (correlation cutoff = 0.7)

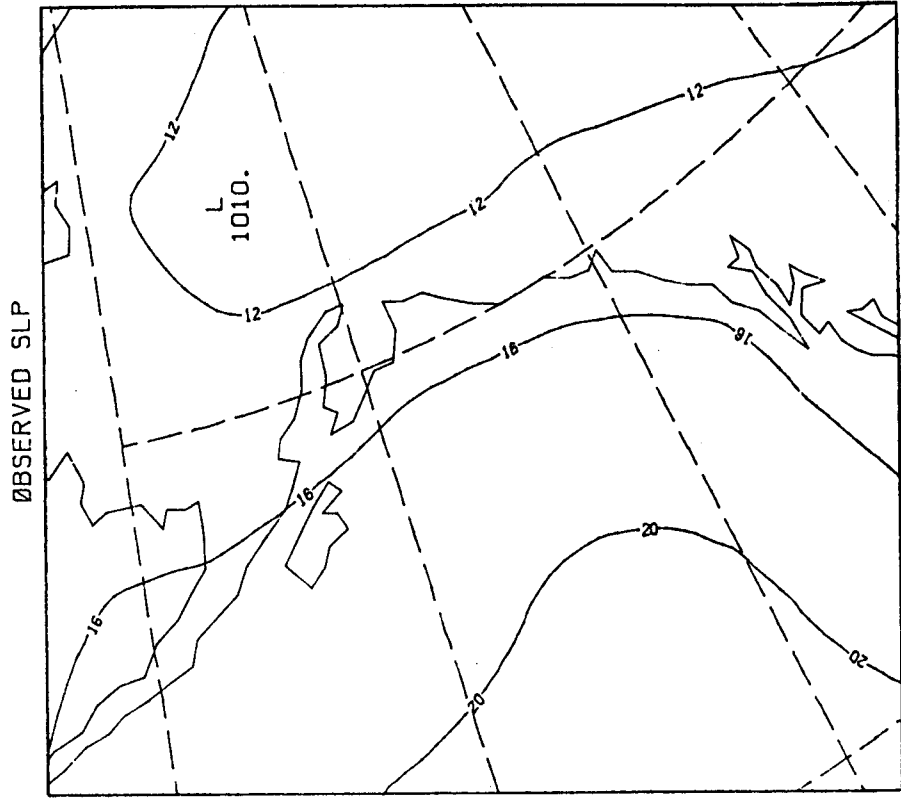




Type D

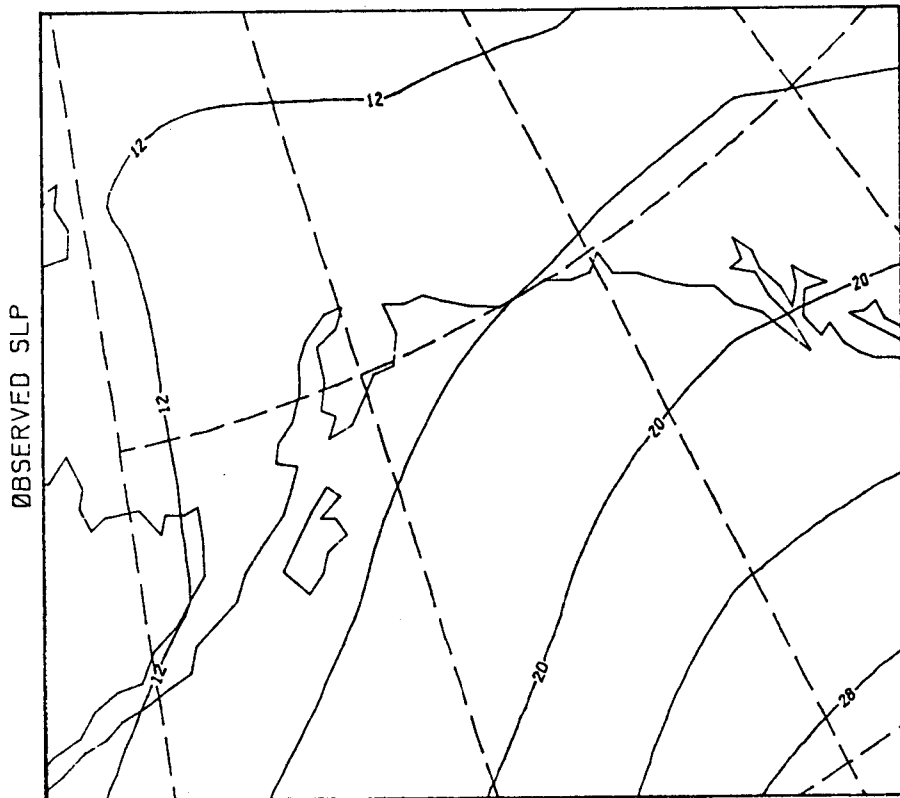


Type C



00Z 4 JUL 1974

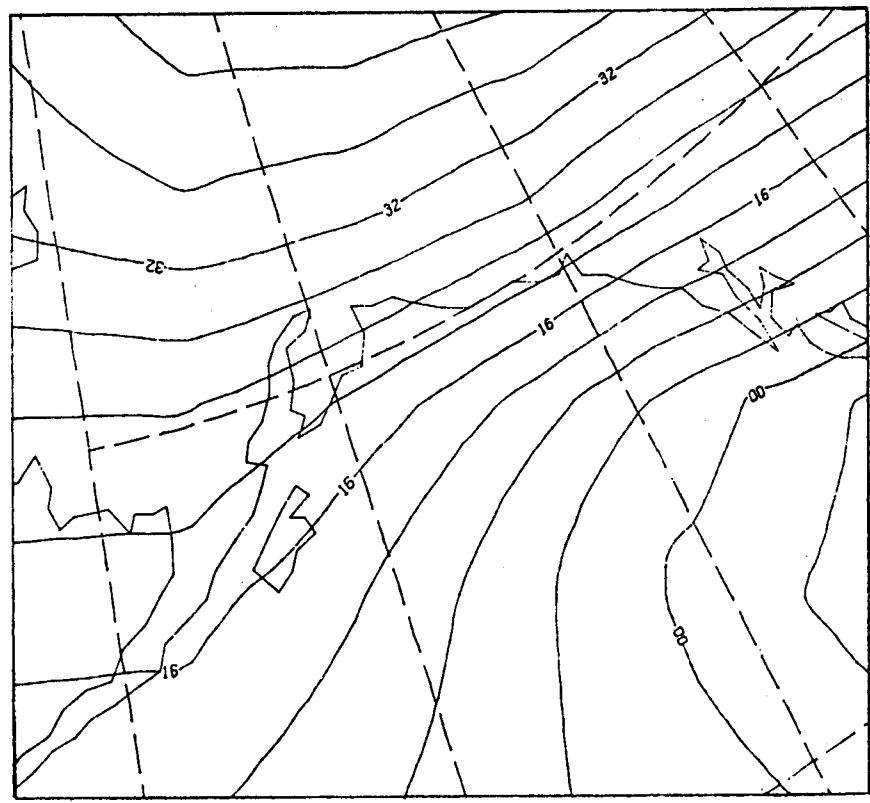
Type F



00Z 8 AUG 1974

Type E

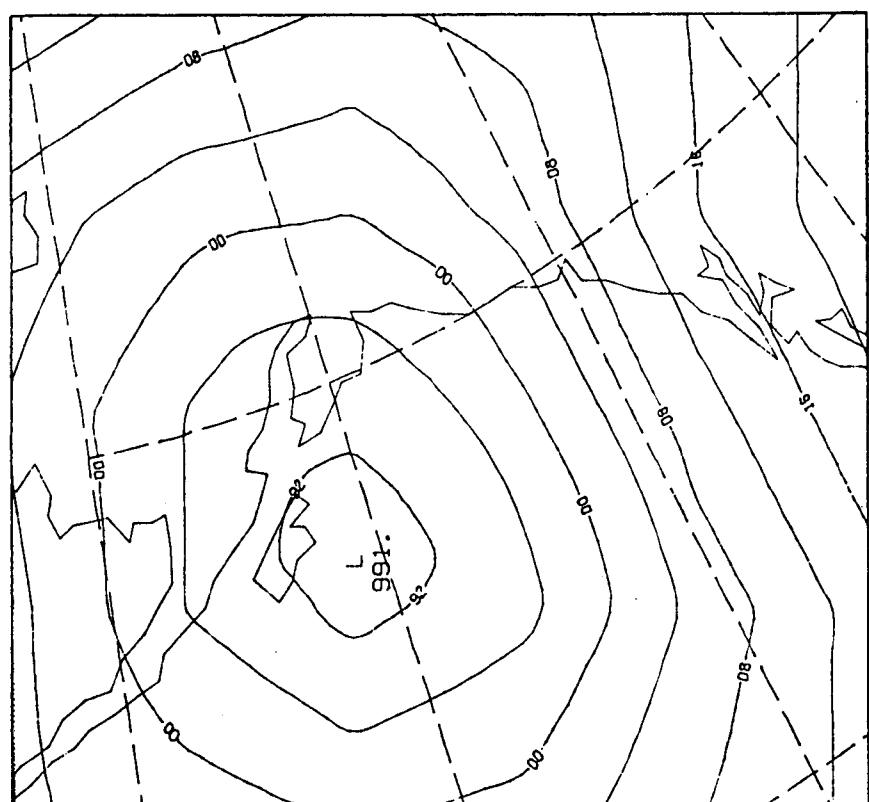
ØBSERVED SLP



00Z 13 JAN 1974

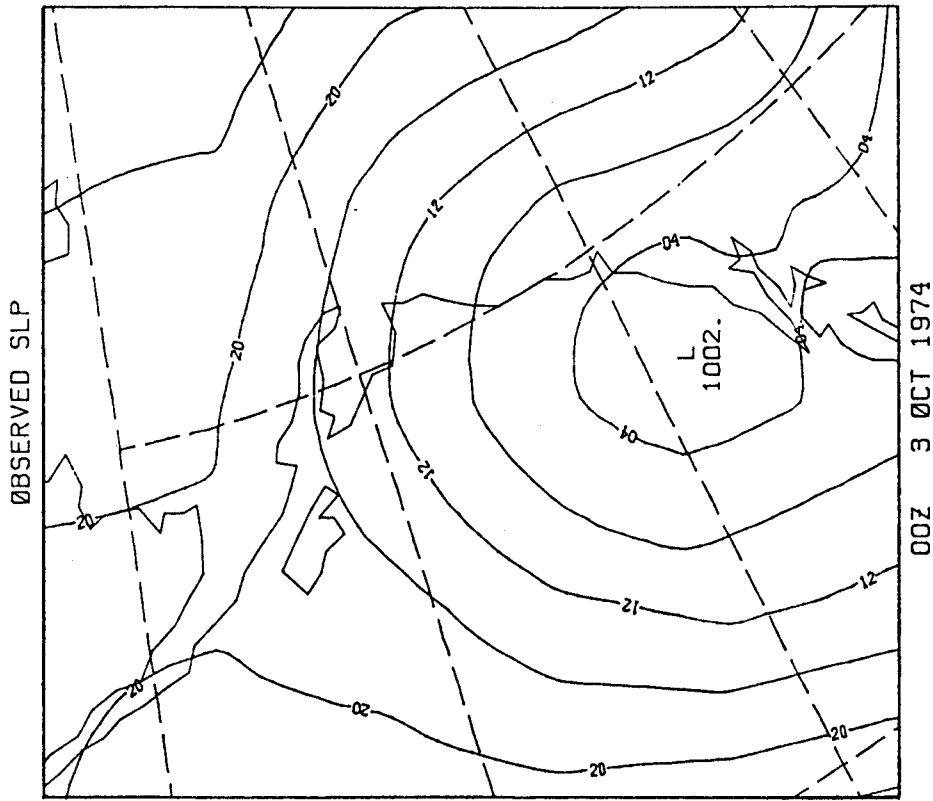
Type H

ØBSERVED SLP



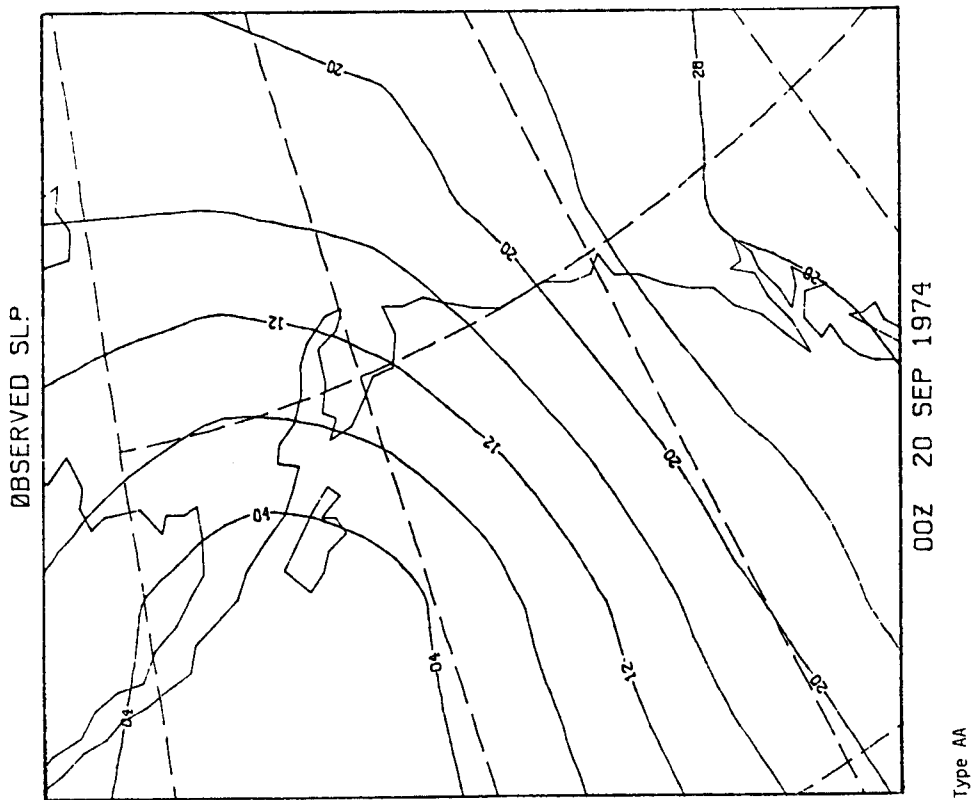
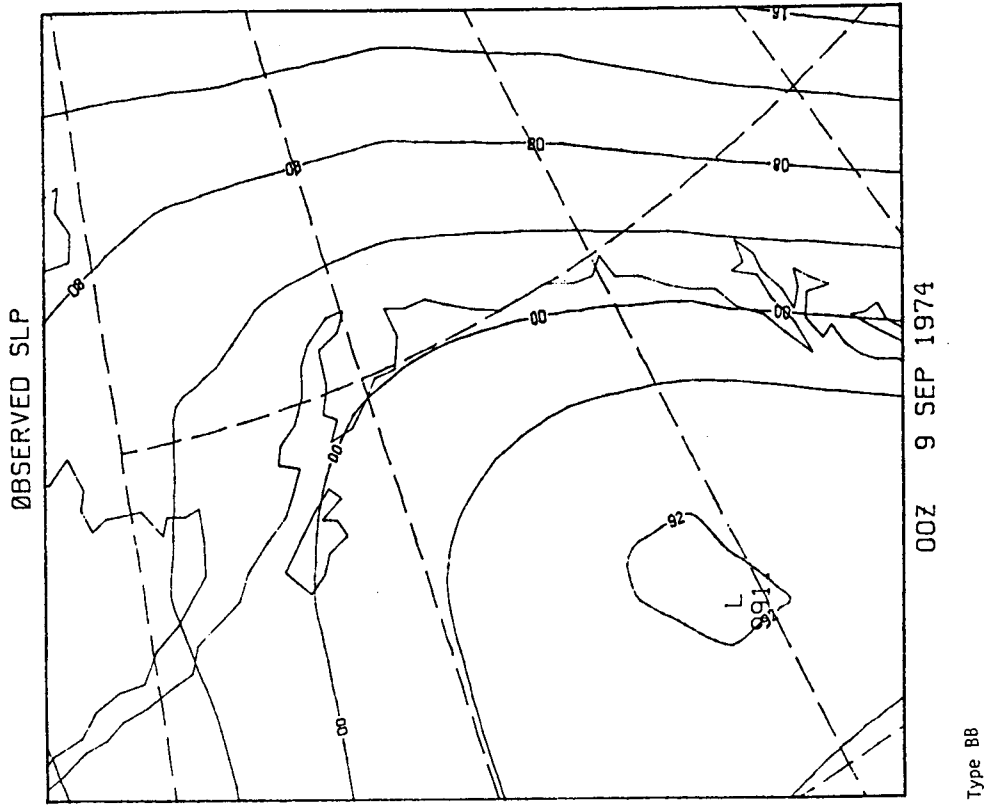
00Z 14 APR 1974

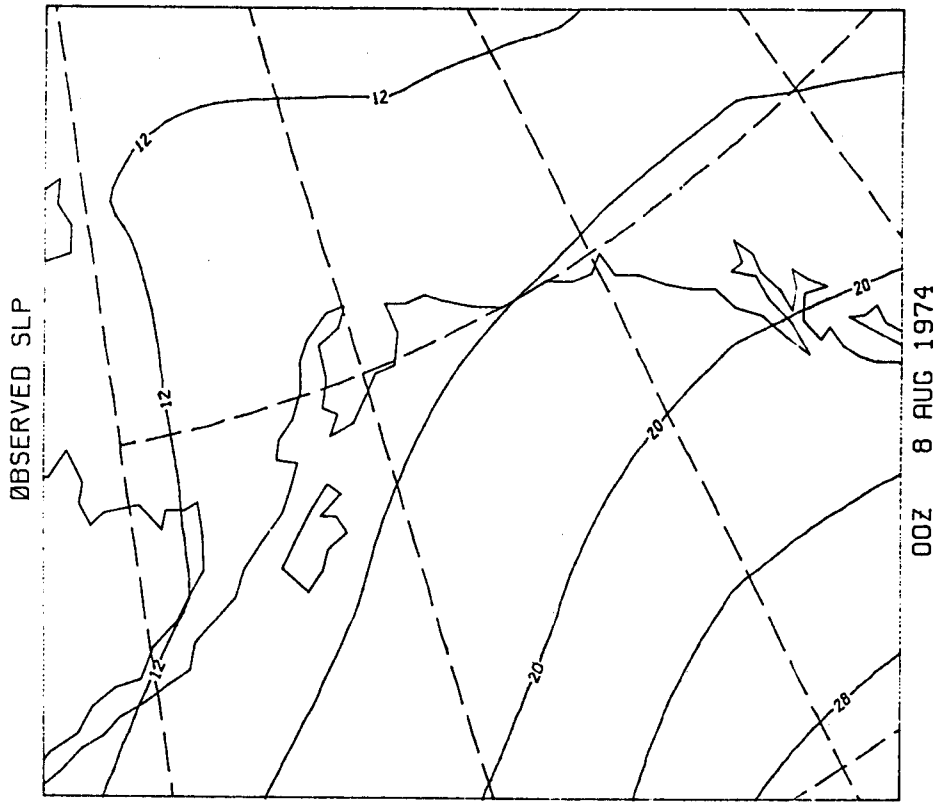
Type G



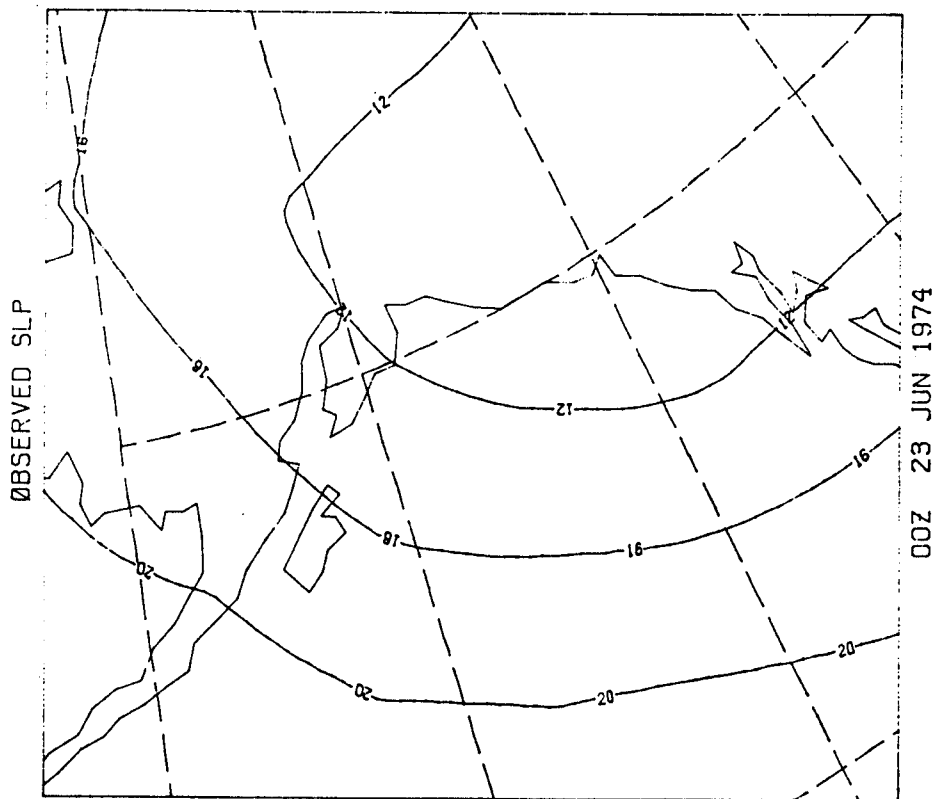
Type 1

Cutoff = 0.7

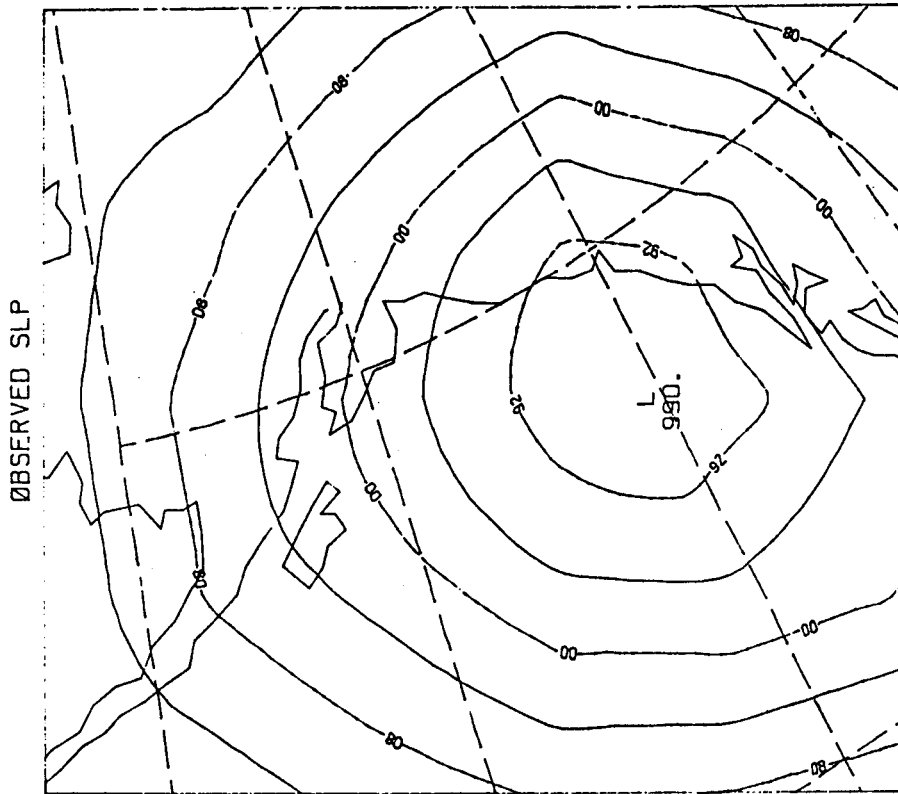




Type DD

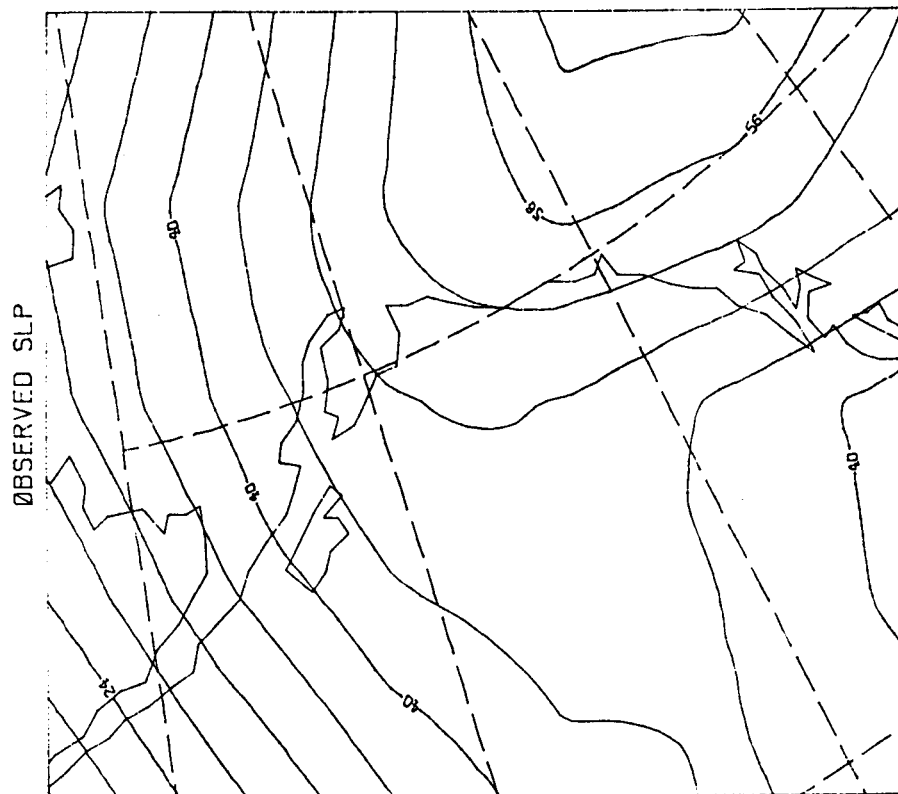


Type CC



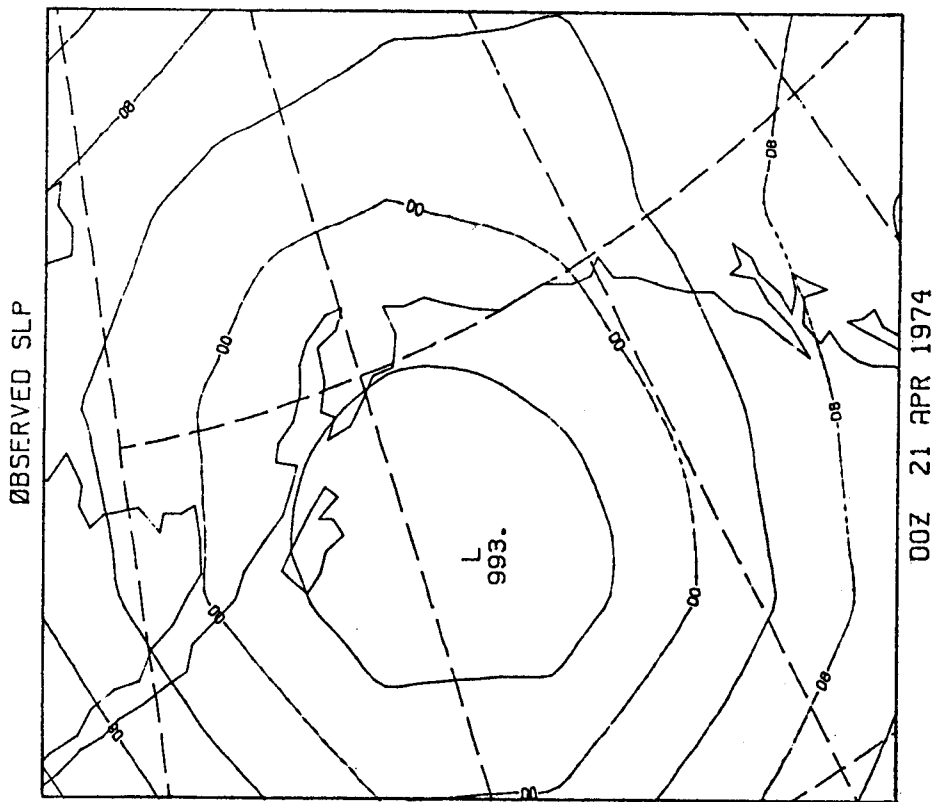
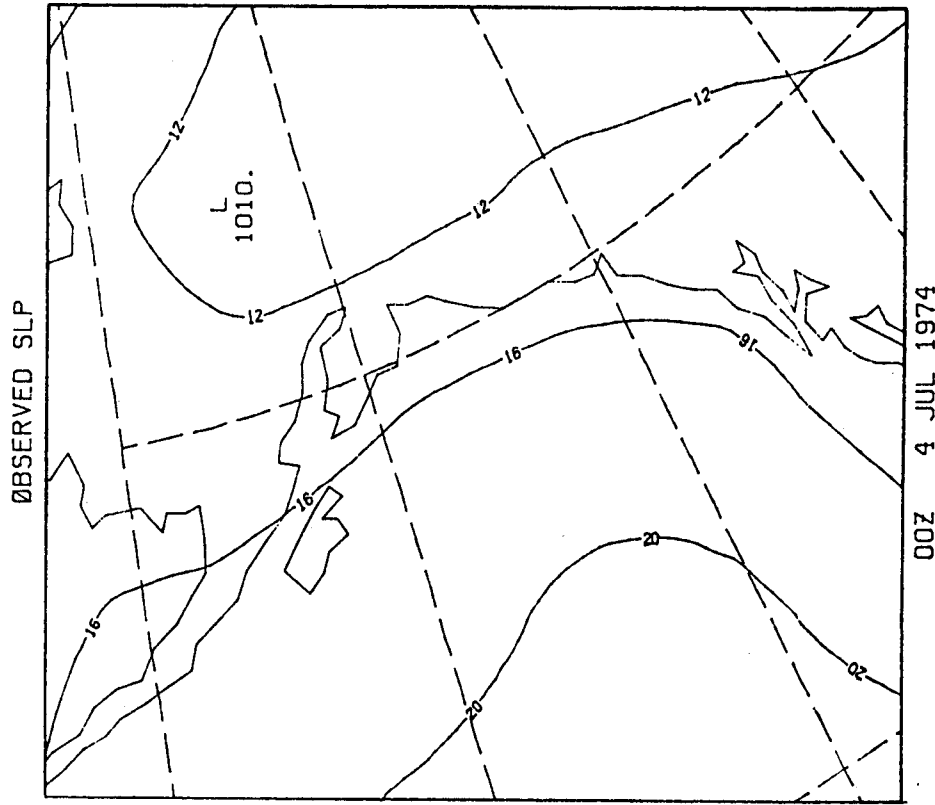
00Z 21 DEC 1974

Type FF



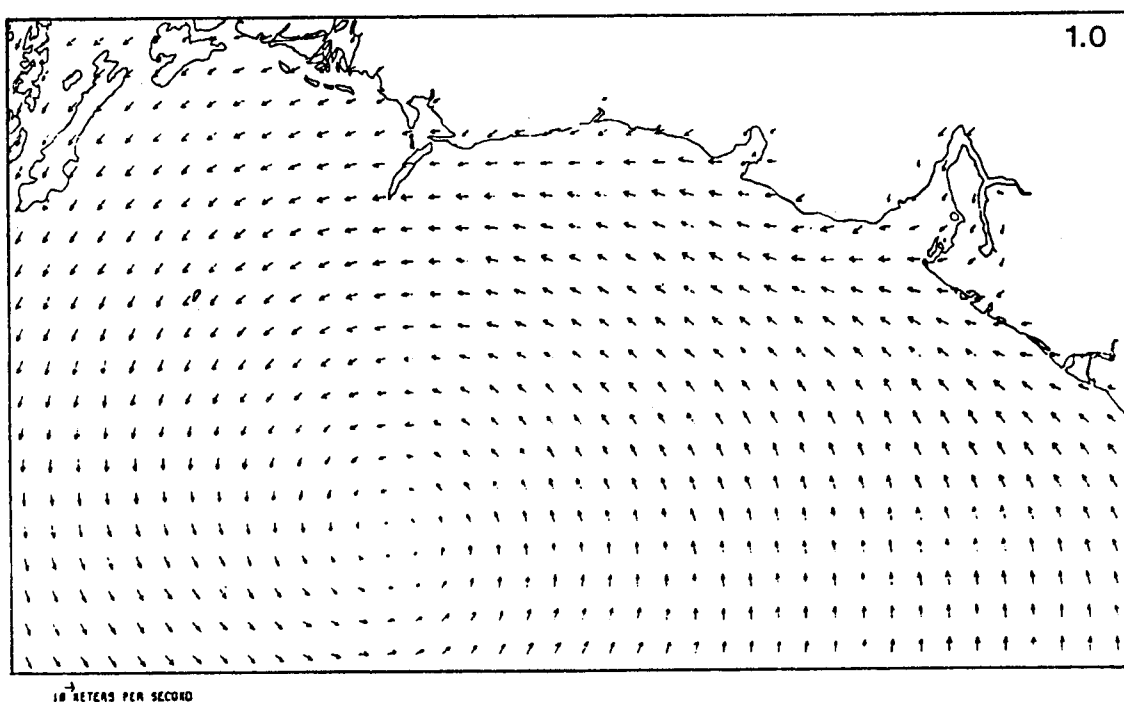
00Z 2 JAN 1974

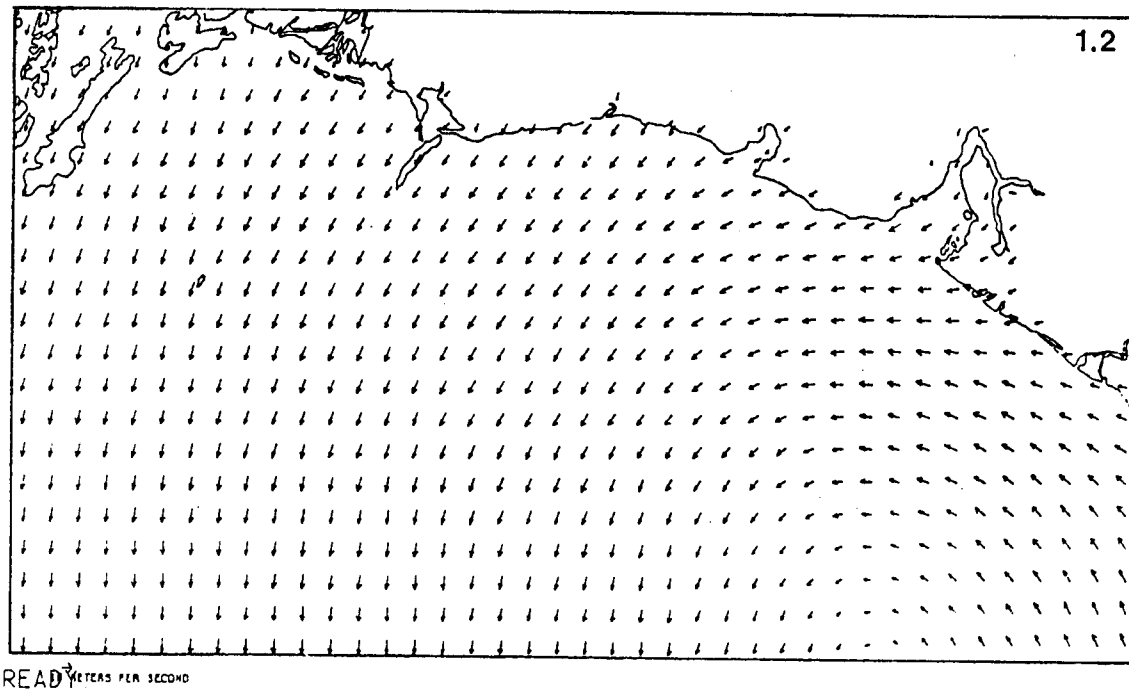
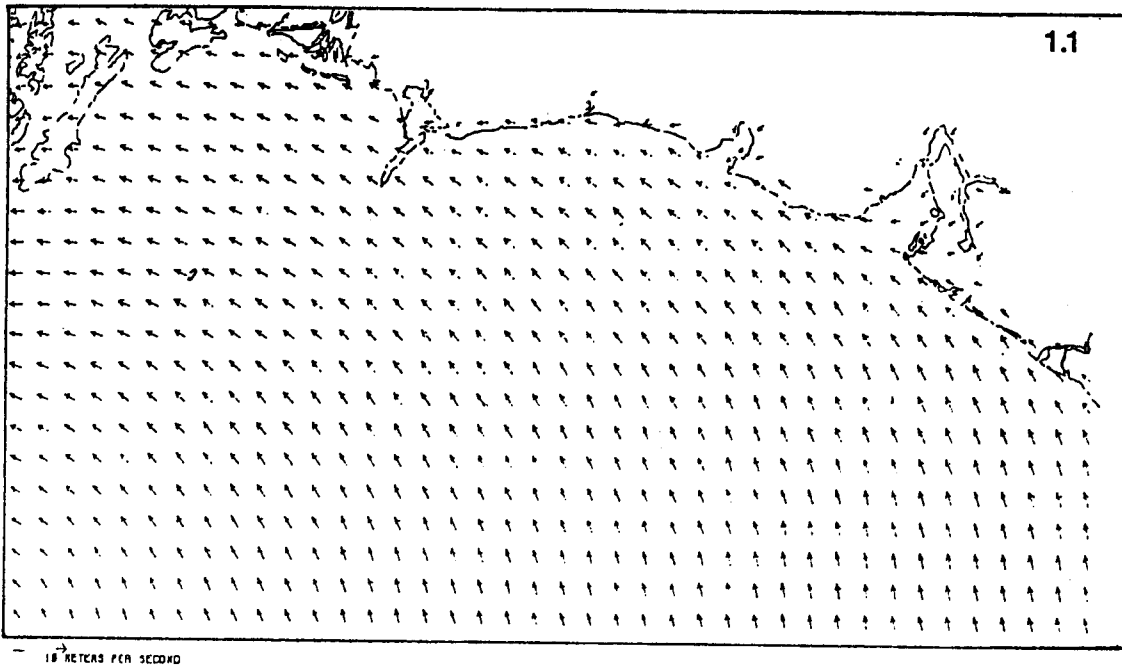
Type EE

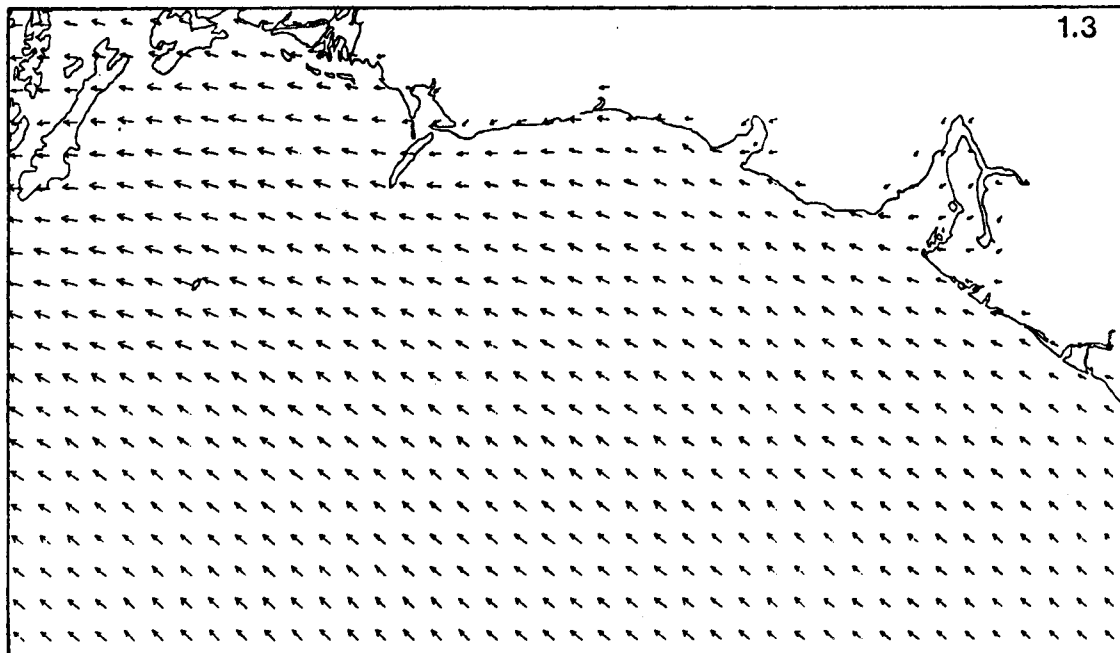


APPENDIX C

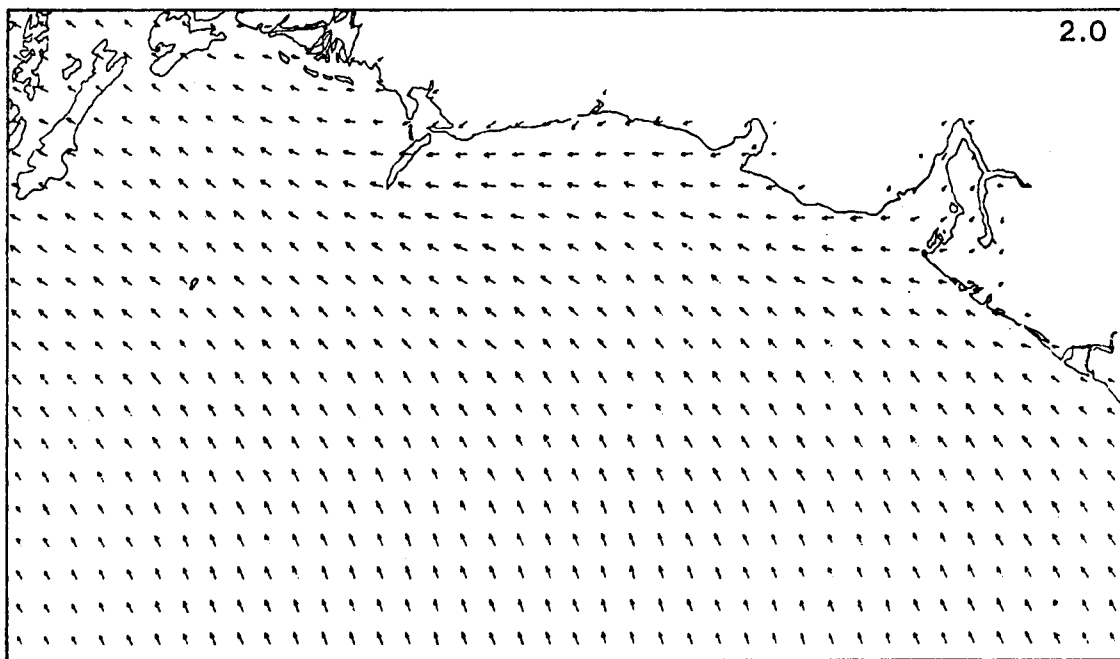
1. Local Wind Patterns for Subtypes 1.0-6.0.



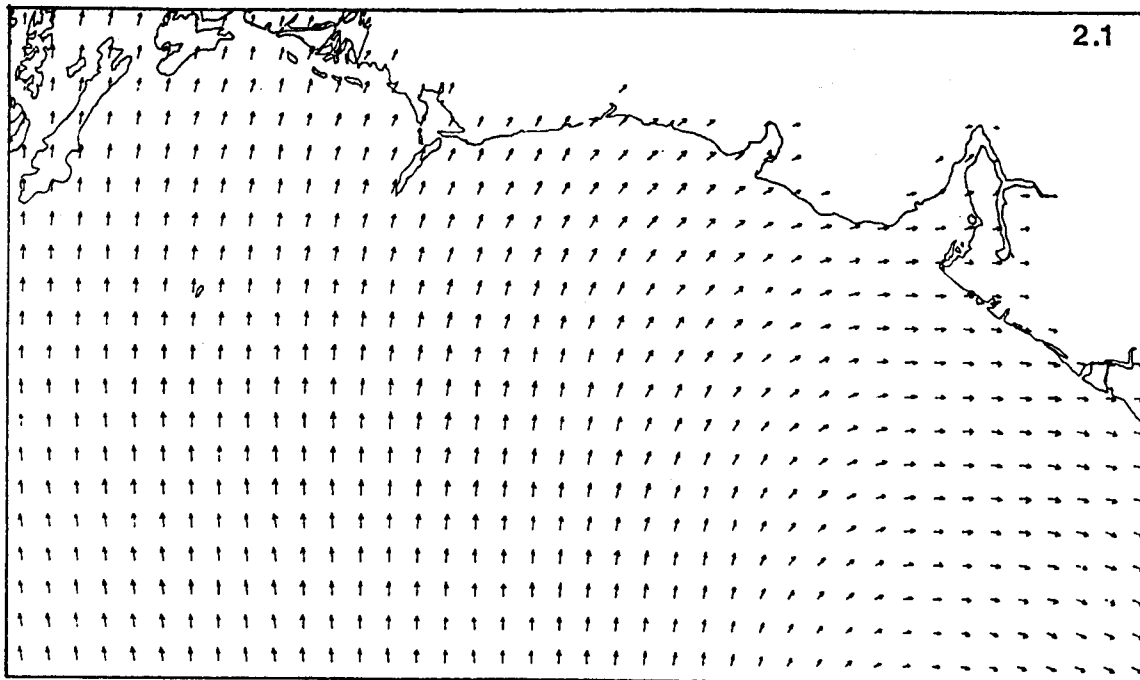




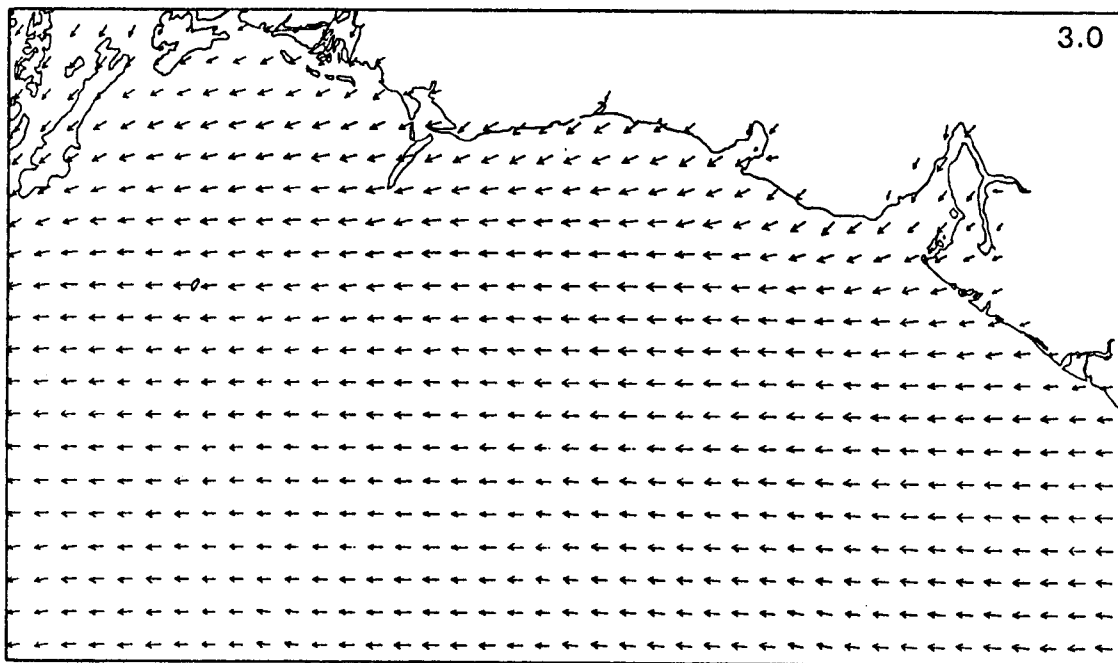
10 METERS PER SECOND



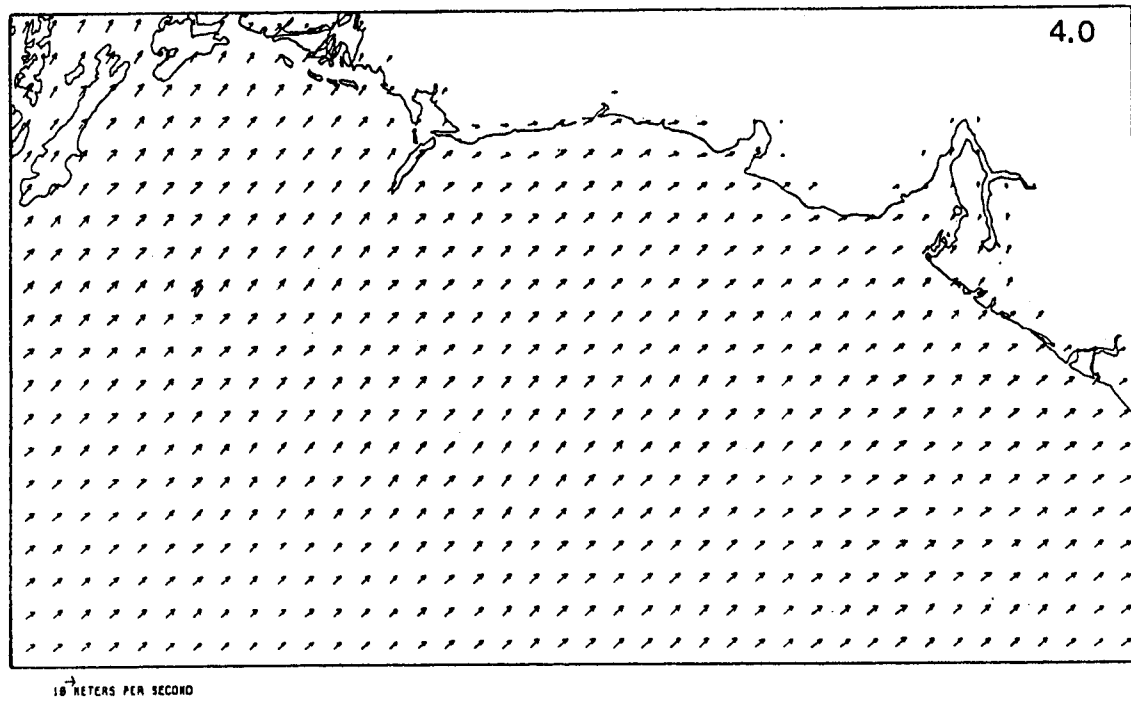
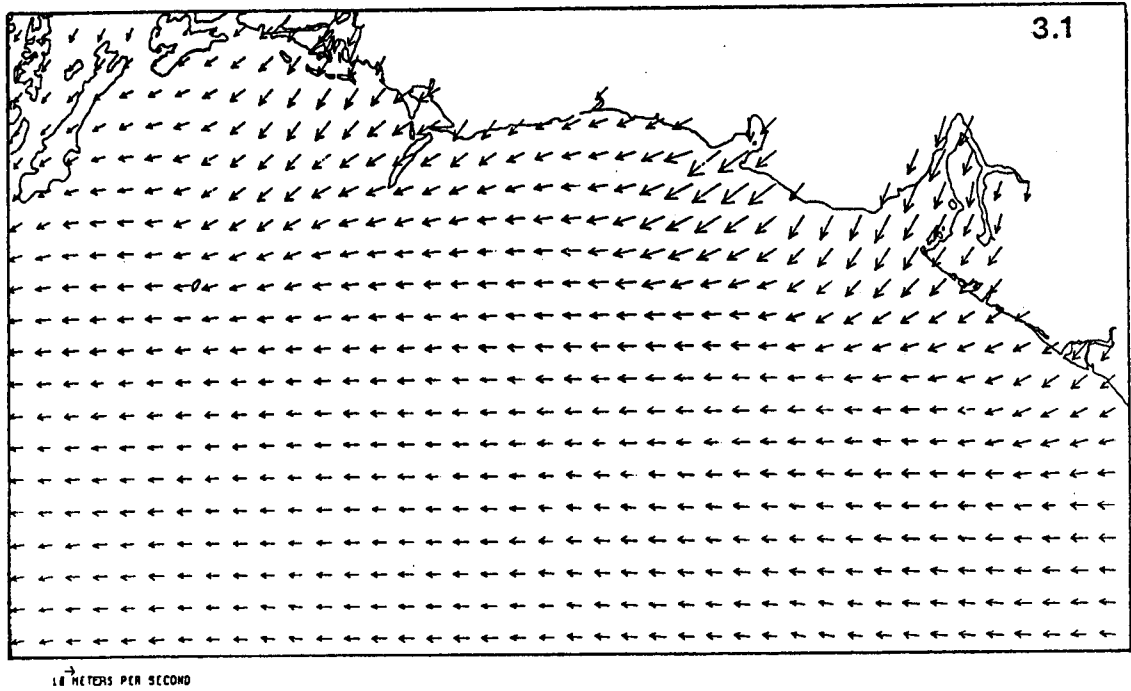
10 METERS PER SECOND

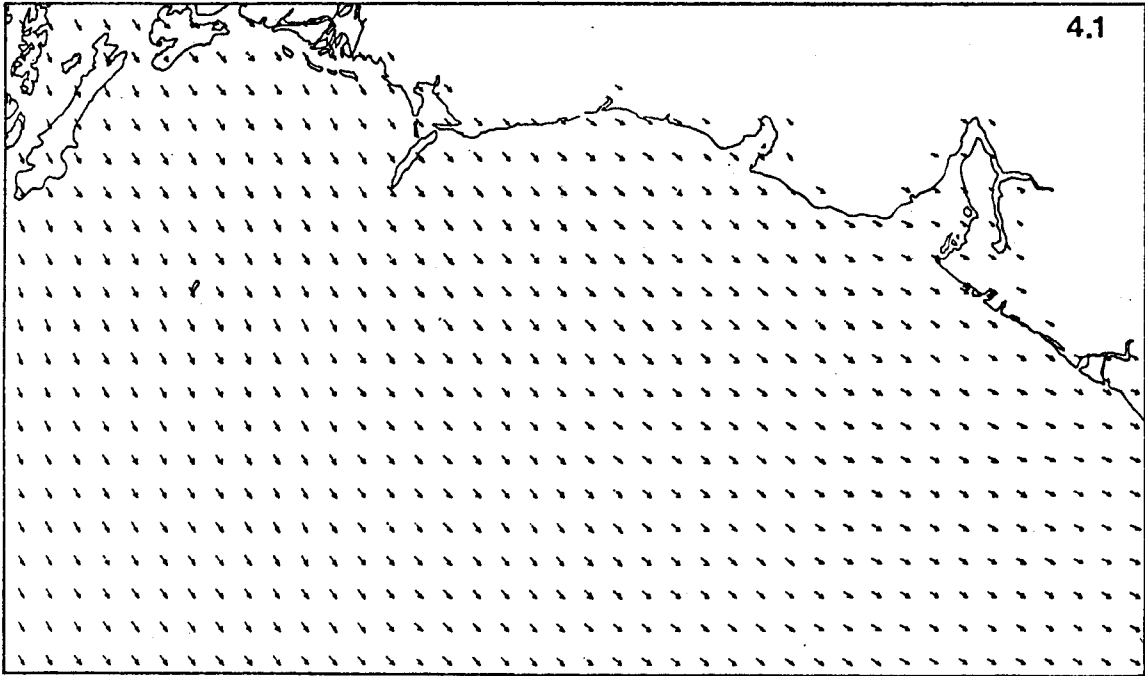


10 METERS PER SECOND

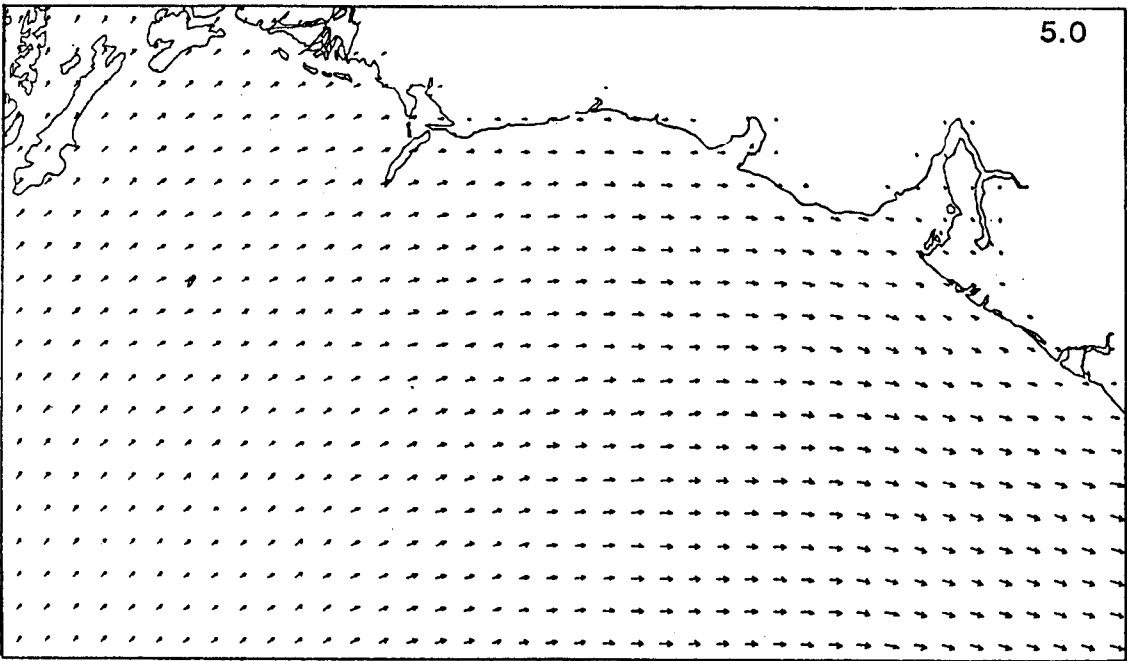


10 METERS PER SECOND

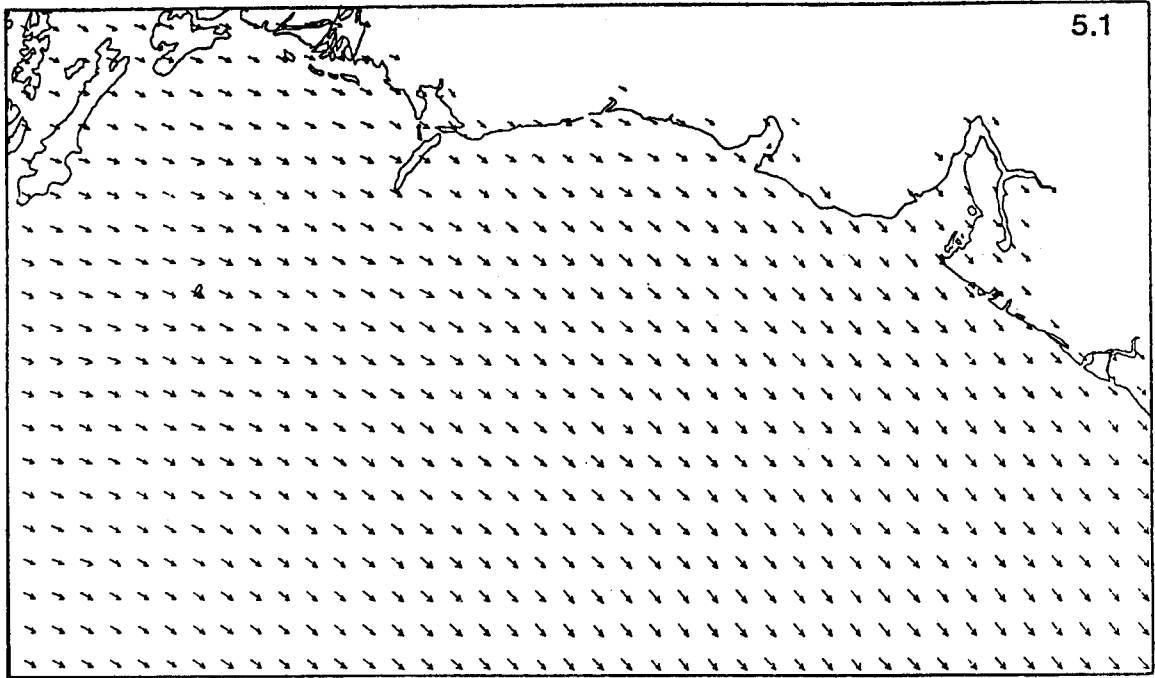




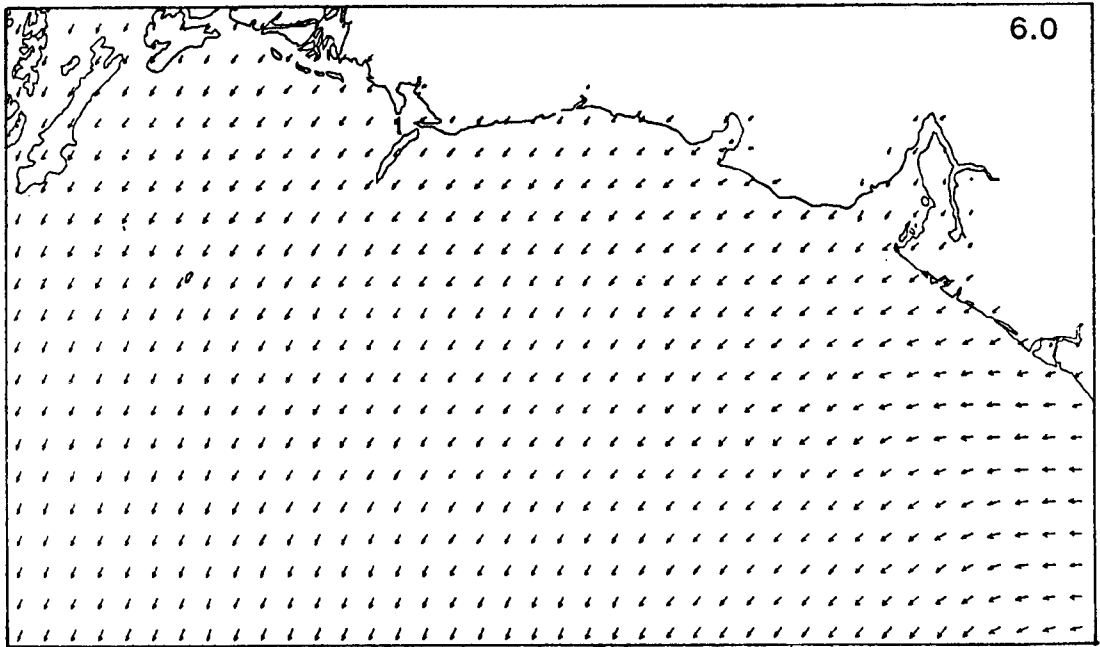
10 METERS PER SECOND



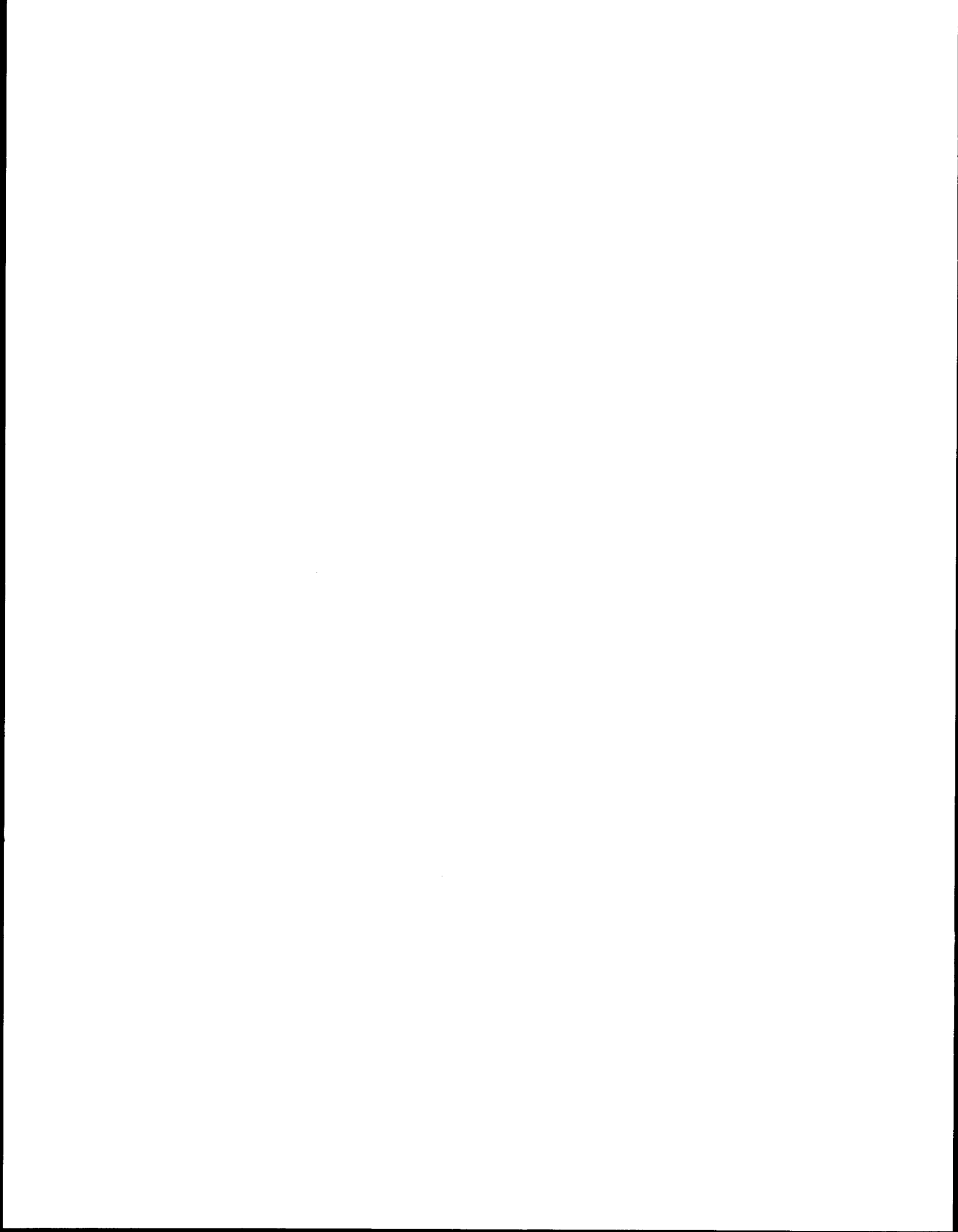
10 METERS PER SECOND



10 METERS PER SECOND



10 METERS PER SECOND



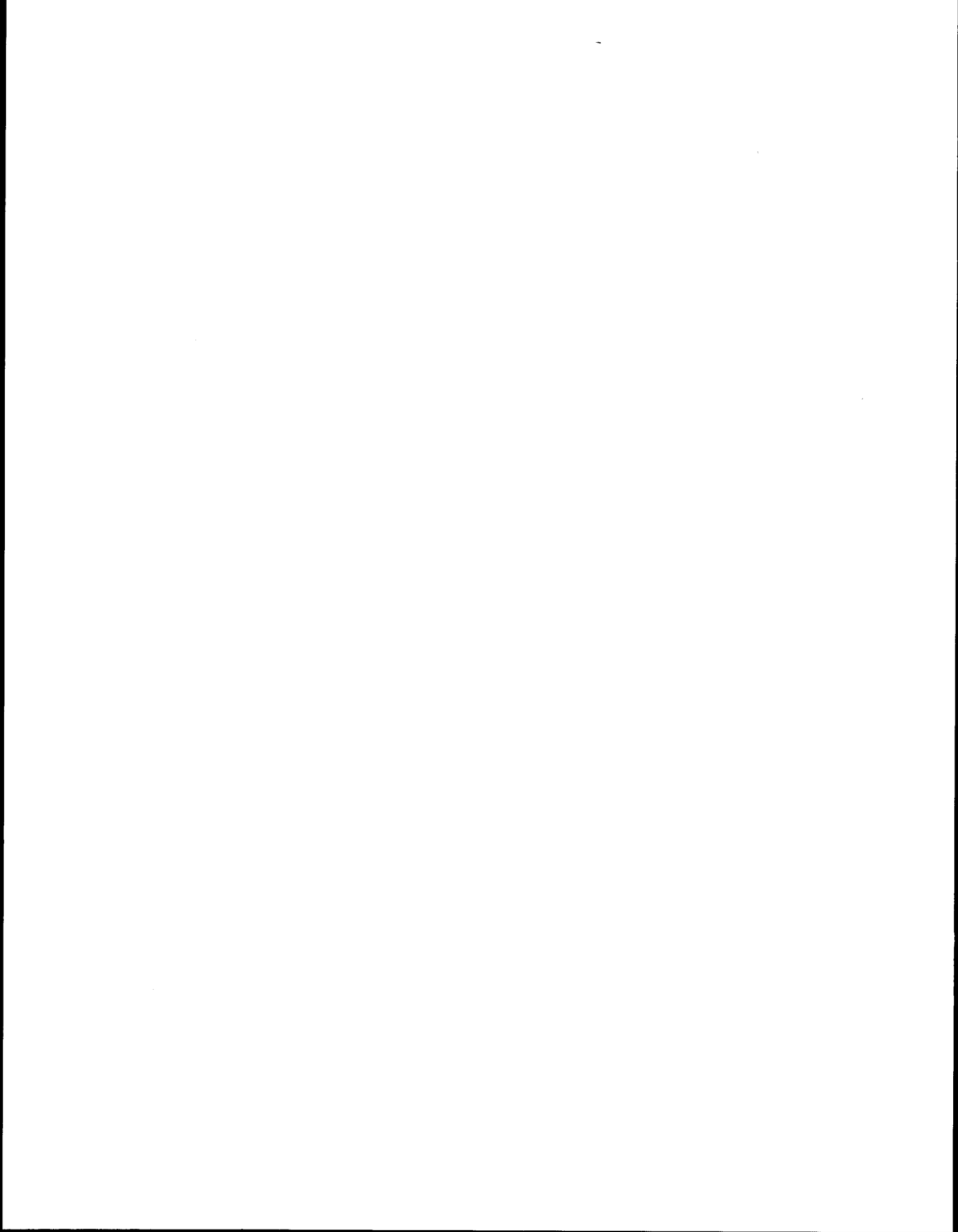
APPENDIX E

The Regional Meteorological Model Status Report

by

James E. Overland

September 1978



A major limitation of pollutant trajectory modeling is the inadequate specification of the local wind field at the spatial resolution necessary to resolve wind drift. Typically, this is due to difficulty of estimating nearshore wind fields directly from large scale synoptic patterns or widely scattered and often unrepresentative wind measurements. Near the coastline of Alaska topography and discontinuities in surface roughness and heating give rise to significant mesoscale variations.

A numerical meteorological model has been developed for use in conjunction with a field measurement program to ascertain the magnitude of mesoscale modification and aid in determining regional wind patterns. A full description of the model is given in the attached PMEL Technical Report (in press). Within the context of its formulation, the model can be used to assess the implications of changes in large scale flow, surface parameters, and assumed dynamics on the wind pattern in a limited region. A major goal is the ability to infer local winds and small scale spatial variations in wind fields from the large scale flow pattern for locations where long term direct observations are not practical.

The model chosen is an adaptation of one proposed by Lavoie which consists of fairly general conservation statements for mass, momentum, and heat. Lavoie treats the planetary boundary layer (PBL), typically 0.5 to 2 km deep, as a one layer, vertically integrated primitive equation model. The model solves for the two components of horizontal velocity, boundary layer height, and potential temperature throughout a limited region. Large scale geostrophic wind, surface elevation, temperature, and the stability of the air in the layer above the PBL are specified as boundary conditions. Air temperature and PBL height are specified along the inflow boundaries. The local response is calculated by specifying smooth initial values of wind,

temperature and PBL height and then time stepping the equations of continuity, momentum, and heat conservation until an equilibrium state is obtained. The system is free to estimate mesoscale wind variations caused by contrasts in heating and roughness of land and water, modification of the down wind environment by advection and channeling by topography. The equilibrium state is considered to give the local winds which occur in conjunction with the given large scale pressure pattern.

The model consists of only one layer processes which depend upon vertical structure that cannot be directly resolved; however, the model is well suited to estimating wind patterns in mountainous regions with strong orographic control. For example, questions remain on the adequacy of the model to represent sea breeze circulation without explicitly resolving return flow aloft or katabatic flows that occur within a planetary boundary layer.

The Puget Sound - Strait of Juan de Fuca region in northwest Washington State was used as a test basin as a fairly comprehensive data set was obtained for initial comparison. Complete description of three case studies is also included in the Technical Report. In applying the model to Puget Sound it was determined that the model was very well suited for studying the interaction of inertia and orographic channeling; specifically the continuity balance resulting from air coming into the basin from two directions and ability to resolve mesoscale eddies shed by headlands. There were two shortcomings of the model. The first is that air stability (the restoring force in the model) is applied only at the top of the boundary layer. Several synoptic situations consisted of continuously stratified conditions. These can be simulated (as opposed to modeled) by a very shallow PBL with a strong jump at the top. The other problem is treating open boundary conditions along and edge that contains a land-water transition. The PBL height must be

a priori along an open boundary and it is not known ahead of time what the PBL modification is for onshore flow. This problem was solved in part by iteration. To resolve stable atmospheric cases, making the model more complicated in terms of number of layers, adding mass entrainment across the top of the PBL, etc., would have an adverse impact upon resolving the dominant physics of channeling and treatment and initialization of open boundaries. In summary, the model is very good at looking at certain dominant meteorological features (which we think are important) but not all features. However, more complicated models are not the answer to providing better winds as certain meteorological processes cannot be effectively modeled simultaneously.

The first application of the regional meteorological model (RMM) to Alaska was for the Icy Bay - Yakutat vicinity (Figure 1). It showed extensive channeling over the mountains and a transition of the coastal flow to the offshore geostrophically balanced winds. It was less successful in explaining thermodynamically driven features and suffered from questions of what were the appropriate boundary conditions along the eastern edge of the model. About this time the format for the winds input to the trajectory calculations were finalized. The region was all of NEGOA at a scale coarser than the RMM. As the preliminary runs of the RMM were supportive of the general conclusions of Reynolds (RU #367) on the offshore extent of the coastal zone and the katabatic zone, further runs of the RMM were not necessary. Establishing these length scales was adequate spatial information on coastal wind modification for the trajectory model.

Attention was then turned to applying the RMM to Kodiak Island and Lower Cook Inlet (LCI). This has been accomplished. Figures 2 and 3 show two arrow plots for two geostrophic offshore wind directions of 155° and 180° . Kodiak Island is in the lower part of the figure. Points denoted by

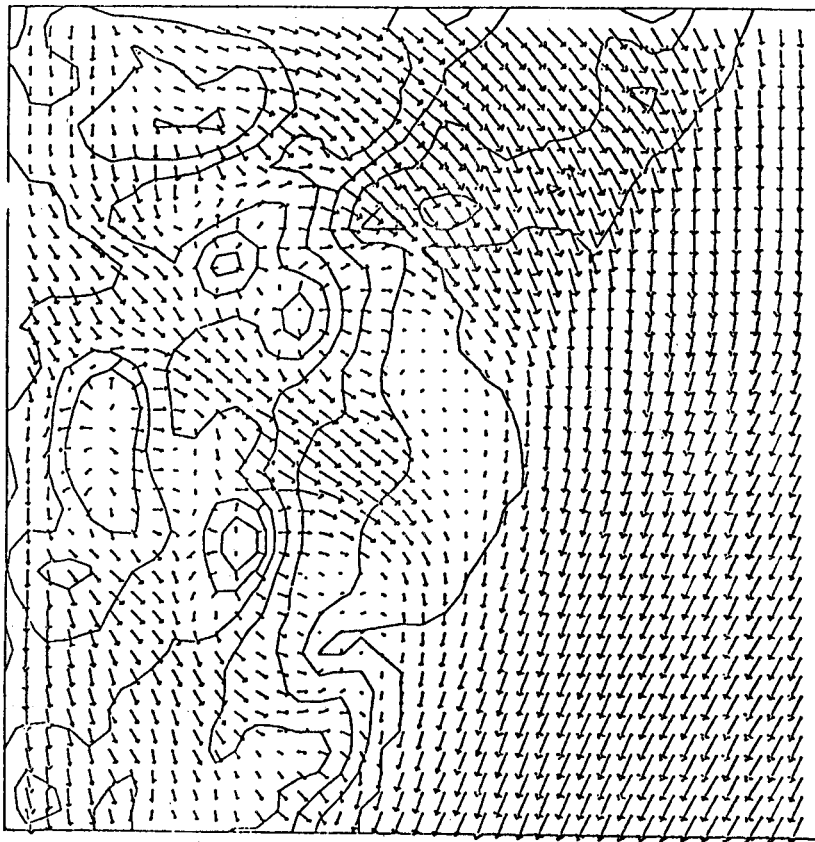


Figure 1

an "x" imply that the ground elevation is higher than the marine planetary boundary layer. The high steep mountains make an ideal location for the RMM. Figure 2 has a piling up of air along the open coast and at the entrance to Shelikov Strait (lower left). This causes channeling into the Strait at a large angle to the incident wind from the southeast. The jet formed at the eastern coast continues halfway into LCI under the influence of inertia. Figure 3 has the incident wind rotated 25° to the south relative to Figure 2. Flow in upper Cook Inlet. Figure 4 shows a sample arrow plot for the Kodiak grid. It has many of the same advantages for the RMM as LCI.

The RMM is at the stage for both LCI and Kodiak to be an aid in interpreting the field measurements with RU #367 in a comprehensive review of LCI.

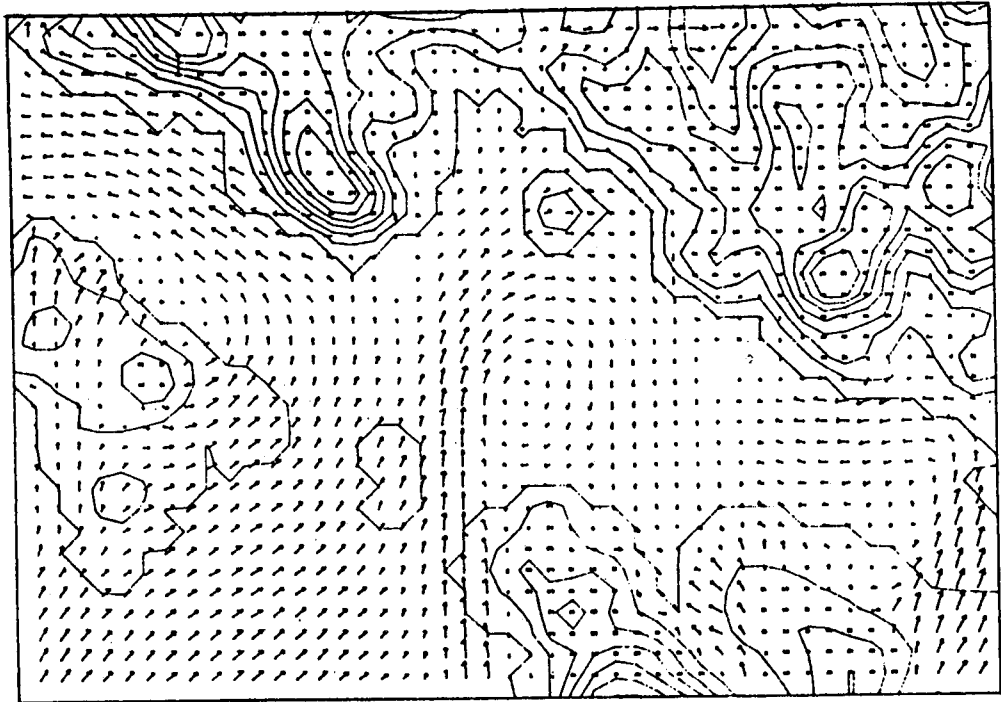


Figure 2

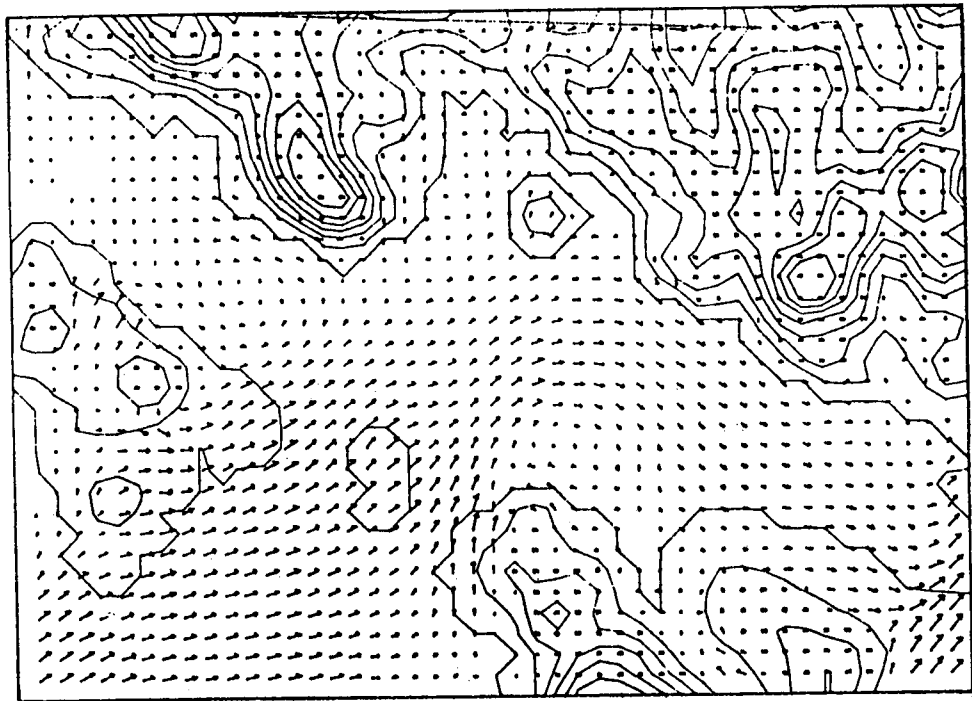


Figure 3

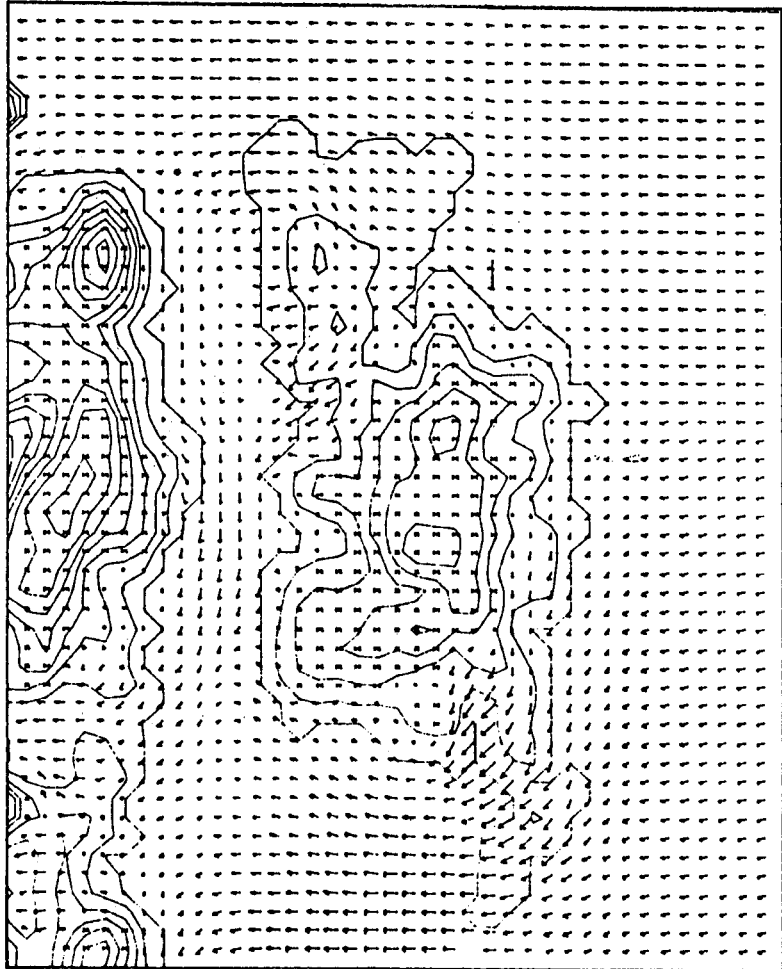


Figure 4

A Regional Surface Wind Model
for Mountainous Coastal Areas

by

James E. Overland, Matthew H. Hitchman,
and Young June Han

(Contribution No. 366 from the NOAA/ERL
Pacific Marine Environmental Laboratory.)

1978

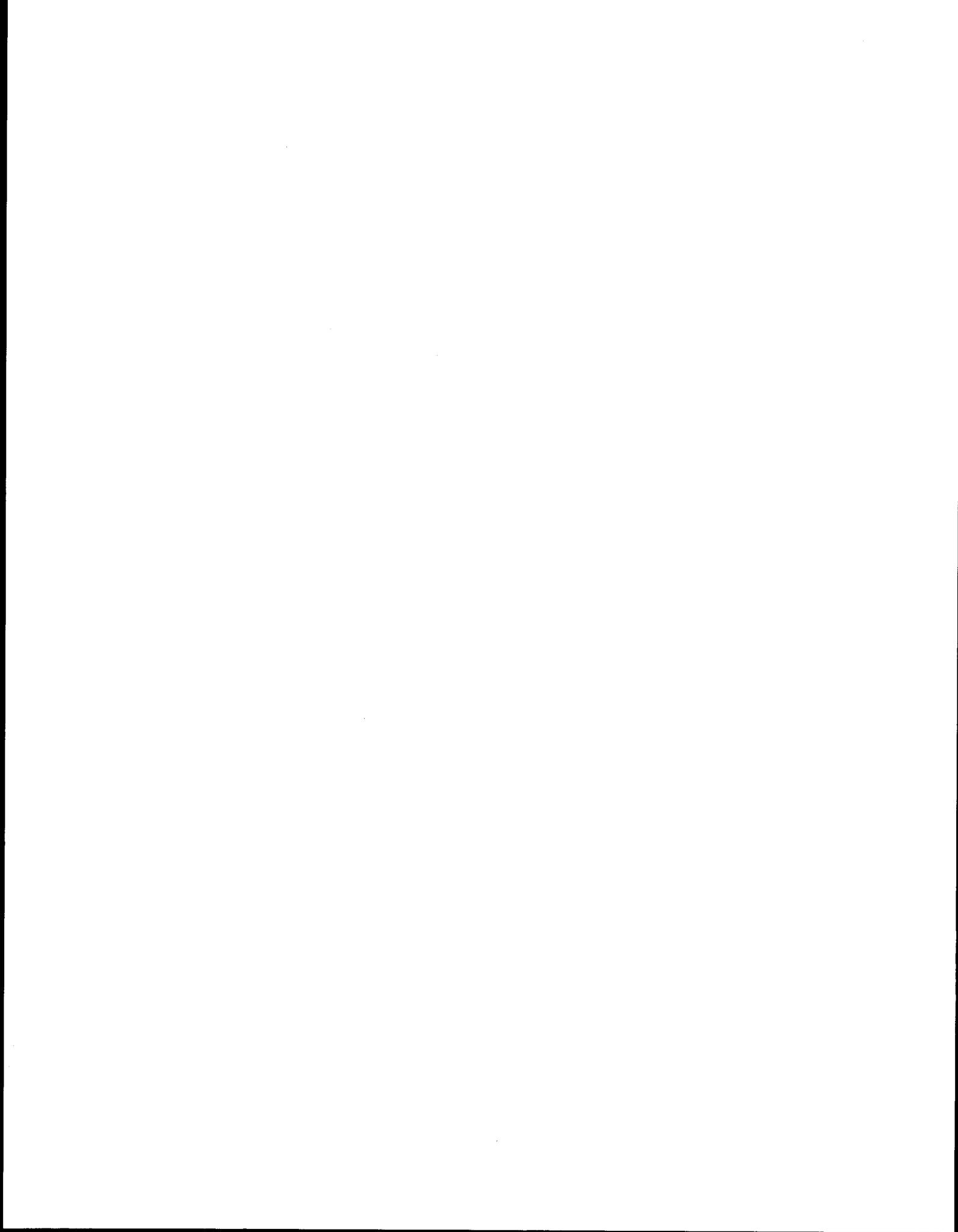
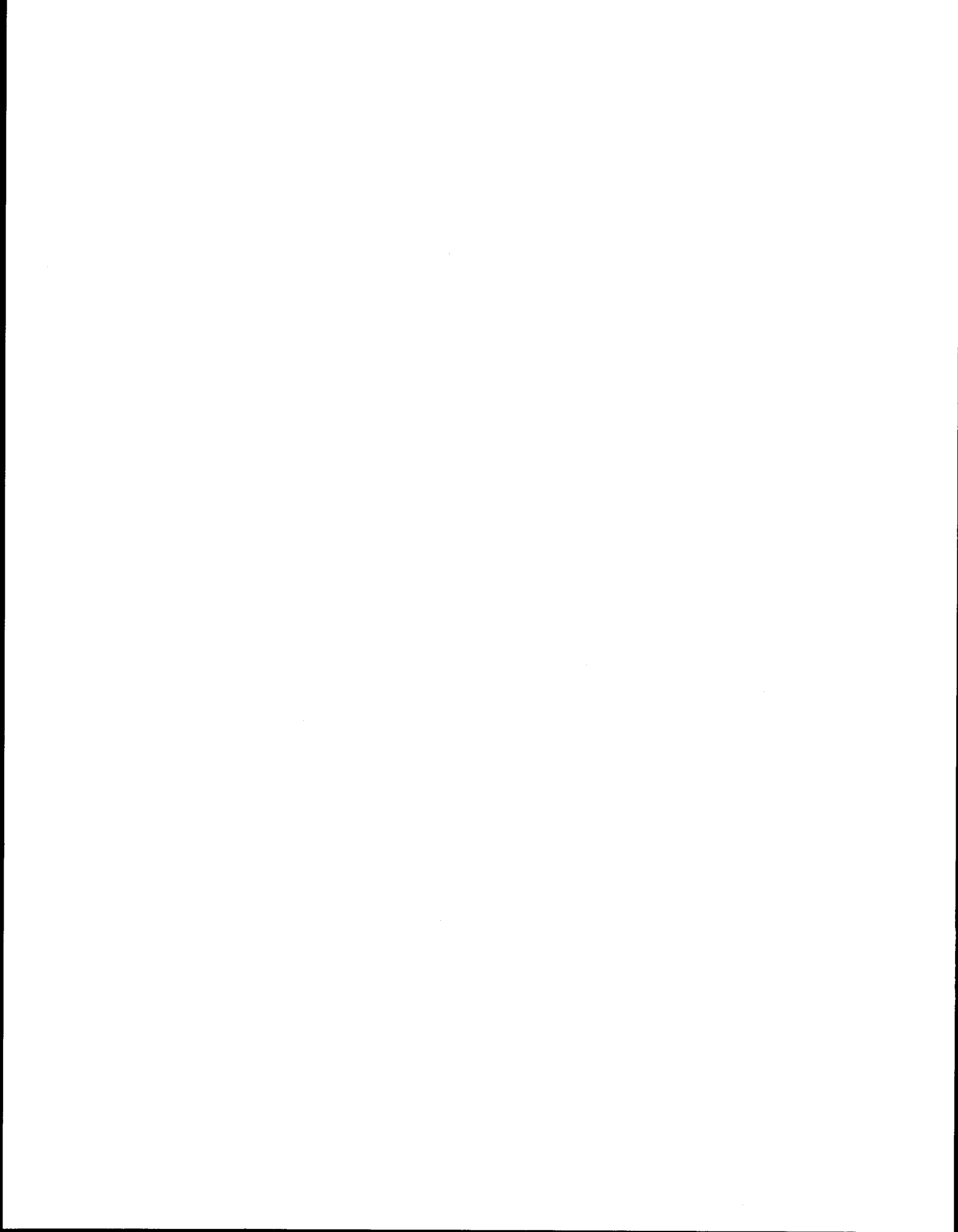


TABLE OF CONTENTS

	Page
ABSTRACT.	621
1. INTRODUCTION.	622
2. THE MODEL	625
3. DETAILS	628
3.1 Finite Difference Form	628
3.2 Boundary Conditions.	628
3.3 Flooding	629
3.4 Entrainment.	630
3.5 Initialization	630
4. SIMPLE EXPERIMENTS.	631
5. SIMULATION FOR PUGET SOUND-STRAIT OF JUAN DE FUCA	637
5.1 Regional Description	638
5.2 Data Sources	640
5.3 Meteorological Case Discussion	642
6. ACKNOWLEDGEMENTS.	649
7. REFERENCES.	650
APPENDIX A: Derivation of Boundary Layer Equations	651
FIGURES	654



ABSTRACT. The Mesoscale Numerical Model of the Planetary Boundary Layer (PBL) which Lavoie applied to lake-effect snowstorms is modified for maritime application in orographically dominated regions along the west coast of the United States and along the coast of southern Alaska. The model treats the PBL as a one-layer primitive equation system solving for the two components of horizontal velocity, boundary layer height, and potential temperature throughout a limited region, subject to specification of the large-scale geostrophic wind pattern and the stability of the air above the PBL.

Experiments with a cross-section version of the model are performed to assess the model's response to variable terrain, differential heating, and differential roughness at the coast for a domain containing both a flat coastal plain and low coastal mountains such as the shore along Oregon.

The complete model is applied to three quite dissimilar synoptic situations for the Puget Sound-Strait of Juan de Fuca system in northwest Washington State. The model is specifically useful in suggesting the dynamic and kinematic causes of the complex flow patterns observed in each regime, particularly the relative role of inertia and topography.

1. INTRODUCTION

A major limitation of coastal marine meteorology is the inadequate specification of the local wind field at the spatial resolution necessary to resolve wind drift, local waves, and vessel or oil spill leeway. Typically, this is due to the difficulty of estimating nearshore wind fields directly from large-scale synoptic patterns or from widely scattered and often unrepresentative wind measurements. Near the coastline, topography and discontinuities in surface roughness and heating give rise to significant mesoscale variations. For example, Figure 1 shows reported regions of anomalous wind speed and direction along the Alaskan coast. The Alaska region of the National Weather Service compiled Figure 1 from a survey of the Coast Guard and other groups operating vessels in Alaskan waters. Strong ageostrophic winds exist in the passes of the southeast Alaskan coast and are attributed to channeling around islands. The open coast is also subject to anomalous winds caused by high coastal mountains. Of particular importance are winds blowing off the land, called katabatic winds, forced by the contrast of warm ocean temperatures and cold temperatures 50-100 km inland. Further south, in the Puget Sound Basin of the State of Washington, forecasters are aware of a quiet zone of reduced winds in the lee of the Olympic Mountains. This zone changes location as a function of the offshore wind direction. Sea breeze circulation is an additional example of coastal modification.

This report documents a numerical meteorological model for use in conjunction with a field measurement program to determine regional wind patterns. Within the context of its formulation, the model can be used to assess the implications of changes in large-scale flow, surface parameters,

and assumed dynamics on the wind pattern in a limited region. A major goal is the ability to infer local winds and small-scale spatial variations in wind fields from the large-scale flow pattern for locations where long-term observations are not practical.

We have chosen to adapt a model proposed by Lavoie (1972, 1974; see also Keyser and Anthes, 1977) which consists of fairly general conservation statements for mass, momentum, and heat. Lavoie treats the planetary boundary layer (PBL), typically 0.5-2 km deep, as a one-layer, vertically integrated primitive equation model. The model solves for the two components of horizontal velocity, boundary layer height, and potential temperature throughout a limited region. Large-scale geostrophic wind, surface elevation, temperature, and the stability of the air in the layer above the PBL are specified as boundary conditions. Air temperature and PBL height are specified along the inflow boundaries. The local response is calculated by specifying smooth initial values of wind, temperature, and PBL height and then time-stepping the equations of continuity, momentum, and heat conservation until an equilibrium state is obtained. The system allows estimation of mesoscale wind variations caused by contrasts in heating and roughness of land and water, modification of the down-wind environment by advection and channeling by topography. The equilibrium state is considered to provide the local winds which occur in conjunction with the given large-scale pressure patterns. Since the model consists of only one layer, processes which depend upon vertical structure cannot be directly resolved. For example, questions remain on the adequacy of the model to represent sea breeze circulation without explicitly resolving return flow aloft. However, the model is well suited

to estimating wind patterns in mountainous regions with strong orographic control.

We proceed with the formulation and initial testing of the model. The Puget Sound-Strait of Juan de Fuca region in northwest Washington is used as a test basin because there was a fairly comprehensive data set available for comparison. Since the model is quickly dominated by complex topography, several cases with simple geometry are included in Section 4 to build confidence in interpreting more complicated results. The question of the type and quality of large-scale pressure field input is also addressed by comparison of hand-drawn analyses with machine-prepared analyses from the National Meteorological Center.

2. THE MODEL

The atmosphere is represented by three layers defined by changes in the lapse rate of potential temperature, as shown in Figure 2. The layer in contact with the surface is a constant stress or surface layer assumed to be represented by a logarithmic velocity profile. The upper limit of this layer is taken to be 50 m. Above the surface layer is the planetary boundary layer (PBL), represented by vertically integrated values of velocity and potential temperature, capped by a density discontinuity, which parameterizes the restoring force of an inversion layer of stable air above the PBL. The PBL layer, then, is the only layer which is explicitly modeled. The model specifies four dependent variables: the PBL height, h , identified with the inversion base in unstable or neutral stratification; the PBL potential temperature, θ ; and the two components of the vertically integrated wind velocity within the PBL, \vec{v} . The governing equations for conservation of mass, momentum and heat result from vertically integrating the primitive equations for the PBL, treating the lower atmosphere as a Boussinesq system. Interactions with the surface layer and upper atmosphere are parameterized. The resulting equations (see Appendix A) reduce to:

$$\frac{\partial h}{\partial t} + \nabla \cdot (h-D) \vec{v} = E, \quad (1)$$

$$\begin{aligned} \frac{\partial (h-D) \vec{v}}{\partial t} + \nabla \cdot (h-D) \vec{v} \vec{v} + (h-D) f \vec{k} \times \vec{v} = \\ -(h-D) \vec{F}_i + \frac{g(h-D) \Delta \theta}{\theta_0} \nabla h + \frac{\alpha (h-D)^2}{2\theta_0} \nabla \theta + E \vec{v}_+ - C_D |\vec{v}| \vec{v}, \end{aligned} \quad (2)$$

$$\frac{\partial (h-D) \theta}{\partial t} + \nabla \cdot (h-D) \vec{v} \theta = E \theta_+ - C_H |\vec{v}| (\theta - \theta_s). \quad (3)$$

The right side of the mass conservation equation (1) represents the recruitment of mass into the PBL through entrainment of the overlying fluid at rate E . The height of the top of the surface layer above sea level is indicated by D , so that $h-D$ is the local PBL thickness. In the momentum equation (2), the second term is inertia; f is the Coriolis parameter; g is gravity; θ_0 is a reference temperature; \vec{v}_+ is the velocity at the base of the inversion layer (entrained into the PBL at rate E), and C_D is the surface drag parameter. The temperature increase between the PBL and the inversion layer is $\Delta\theta$. The air stability associated with the inversion is thus modeled as a jump condition in density. \vec{F}_i represents the uniform pressure gradient associated with the background large-scale flow (the major meteorological input to the model), while the next two terms consider pressure gradients developed by the model induced by the local variations in PBL height and temperature. In the absence of mesoscale variation, (2) reduces to a geostrophic balance modified by surface drag. The right-hand side of the heat equation (3) indicates that the PBL can be warmed by entrainment at the top of the PBL (θ_+ being the temperature at the base of the inversion) or by surface heating proportional to the difference between the PBL air temperature and surface temperature, θ_s .

The wind velocity \vec{v} is an average for the entire PBL. Since almost all wind shear is confined to the surface layer, the model wind can be taken as nearly equal to the wind at 50 m elevation. At this level the wind speed is approximately 20% greater than the wind measured at the normal anemometer height of 10 m. Corrected for height in this manner, the model winds should correspond to 10-min averaged anemometer winds which are not unduly influenced by surface features smaller than the mesh length of the model for a well-mixed PBL.

For domain sizes on the order of several hundred kilometers it is important to emphasize the gravitationally controlled circulation, which requires specification of either boundary layer height or inflow velocity. Along inflow boundaries over the ocean, we have chose to specify constant PBL height, h_i , and air temperature θ_i . These values are held fixed for all time. Inflow boundaries over land specify the PBL height and temperature as

$$h = h_i + aD, \quad a = 0.5$$

$$\theta = \theta_i \tag{4}$$

subject to a minimum PBL height. This minimum is now 300 m. After the h values are set by (4), they are smoothed twice by a 1-2-1 smoother to remove the influence of rapid variations in the ground elevation D . Presently, the model needs to be rerun on a case-by-case basis adjusting the constant "a" to minimize the influence of the open boundary on the height field at interior points. The authors are currently experimenting with setting the PBL height along inflow boundaries from the results of a 1-D model. At outflow boundaries we follow Lavoie by setting the PBL height and potential temperature at their upstream values.

3. DETAILS

3.1 Finite Difference Form

The chosen grid is a single Richardson lattice (Figure 3) in which the two velocity components are staggered relative to the height field and each other, with u and v components midway between height points along the x and y axes respectively. This approach is optimal for gravity waves. This lattice also eliminates overspecification of boundary conditions, a difficulty with Lavoie's original formulation. The flux form of the advective terms maintains conservation of scalar quantities. Upstream values instead of centrally averaged values for advected quantities are chosen to maintain the transportive property, which guarantees one-way flow of information.

3.2 Boundary Conditions

Specification of boundary conditions for limited area integrations of the primitive equations is a formidable task. One advantage of the present approach is that constant values on the boundaries can be specified, with the integration run until all the ringing of the time-dependent modes is frictionally damped.

Specifying the momentum flux through the open boundaries for the non-linear advection terms in the momentum equations must be done with care, since advection in a limited domain scale is significant. Several options for inflow velocities were investigated, including specifying the laterally homogeneous solution for the given geostrophic wind and drag coefficient. This proved unsatisfactory because the imbalance between the boundary values and the internal values influenced by orography caused severe geostrophic adjustment problems throughout the model domain and resulted in large deviations in the height field. Our final choice is to assume zero gradient conditions on the velocity components at the inflow boundary. This assumption results in determination of the values at the first interior point by the local dynamic balance. This decision is consistent with the limited data input available and the desire to resolve orographic control interior to the model. Since upstream differencing is used for momentum advection, only minor difficulties are encountered at outflow boundaries.

3.3 Flooding

In the presence of high mountains or low mean velocities, the top of the marine inversion layer may actually intersect the topography. In terms of the vertically integrated model, this is equivalent to forming an island.

In the cases studied by Lavoie it was not necessary to resolve this feature, but it becomes important to resolve for Puget Sound and especially for the high Alaskan coastal mountains. In the present model flooding is accomplished by selectively removing a grid point if the PBL depth falls below a preset value, and adding points if the surrounding PBL heights are great enough to increase the PBL depth above a minimum. Since adding or dropping points creates new internal boundary conditions, flooding increases the relaxation time to steady state by a factor of three.

3.4 Entrainment

Even in the absence of topography, determination of the PBL height is a complex problem. For unstable boundary layers the height cannot be explicitly determined, but is governed by a rate equation which considers free and forced convection, large-scale subsidence, shear instabilities, and solar radiation. The importance of entrainment is problem-dependent and we can suppose that it is more significant in the winter Gulf of Alaska case with cold air outbreaks over warm water than for the Puget Sound case.

In our initial application to mountainous regions we will assume that an oceanic PBL height can be specified *a priori* and, for the time interval necessary for a parcel to flow through the domain of the model, that no significant modification is contributed directly through entrainment, i.e., E is set to zero. Entrainment can be added to this type of model (Stull, 1976, for example), but represents a major complication and is of secondary importance relative to the influence of large topographic features.

3.5 Initialization

The values of parameters and input conditions in Table 1 are used in subsequent model runs.

The background large-scale pressure gradient, \vec{F}_i , is calculated to balance the specified geostrophic wind, V_g . The PBL height is initialized by h_i and velocities are initialized by 70% of the geostrophic wind.

4. SIMPLE EXPERIMENTS

In the sections to follow, complex topography dominates the flow field through the overlapping influence of several mountains and land/water contrasts. These all contribute to local modification of the wind field. To aid in interpretation of more complex results, this section describes several experiments with simple topography, isolating particular physical processes. The examples use a one-dimensional version of the model (i.e., north-south derivatives are set to zero) with the parameters given in Table 1. Topography consists of either a flat coastal plain or coastal mountain 700 m in elevation. The latter topography runs west-east and is roughly comparable to a slice through the Coast Range and Willamette Valley in Oregon. The total domain is large (300 km) to reduce the influence of the inflow or outflow boundaries. The grid mesh is 3 km. While most of the conclusions in this section can be derived from analytic solutions or scale analysis, we take the numerical approach consistent with development of the 2-D model.

Figure 4a shows the simplest case of onshore flow for a flat coastline. Geostrophic wind approaches from 270° at 13.0 m/s with a boundary layer height of 600 m and no land/water temperature contrast. Seaward, the horizontally homogeneous solution matches the analytical solution for a momentum integral (Brown, 1974) with the boundary layer wind 0.96 of geostrophic and an inflow angle of 17° . Coastal influence begins near the shoreline and, inland, results in a PBL height increase of 260 m and a reduction in wind speed to 9.0 m/s. One measure of the relaxation distance for the flow to return to a near geostrophic-frictional balance is given by the ratio of the magnitude of the inertia terms ($u\partial u/\partial x$, etc.) to the large-scale pressure gradient force ($f\vec{v}_g$). This ratio is given as the top curve in Figure 4a; it is largest just landward of the coast and is 0.1 inland a distance of 100 km. Near the outflow boundary the solution again fits Brown's solution with the increased drag coefficient over land. For mass continuity in a 1-D model with no entrainment, the product of the u-velocity component and the PBL depth must be constant throughout the model domain. In the example of Figure 4a, conservation is satisfied to better than 0.2%.

The importance of momentum advection is further illustrated by contrasting 4a with 4b. In Figure 4b, the same conditions are specified as in 4a, except that the momentum advection terms are set to zero, leaving large-scale and locally induced pressure gradients and friction as the only forces. The seaward extent of coastal influence is much greater. The main feature is a coastal jet induced by the rise in the PBL height of 14.5 m/s from 226° , nearly a 65° change from the offshore direction. The second main feature is a nearly complete frictional equilibrium landward of the coastline. Clearly, in the absence of heating and mountains, inertia dominates onshore flow resulting in almost no modification of the marine wind until right at the coastline. The third example (Figure 4c) is a "sea breeze" with a background geostrophic wind of 3.0 m/s from 290° . The land temperature is 291° K, 10° warmer than the ocean. The temperature equilibrates to 90% of the temperature contrast 100 km inland from the coast. There is little variation in direction except for a delayed frictional turning inland. The wind speed is maximum at the coastline in response to pressure gradient induced by the land-water temperature difference. Continuity in this model requires a lowering of the PBL height in the vicinity of the coast as a result of the increased velocity; the resulting slope of the PBL height influences the winds 40 km seaward of the coast. An interesting feature is the double peak in the magnitude of the inertia terms.

Figure 5a shows an offshore wind for the same parameters as in 4a. There is acceleration across the coastline with a maximum 6 km offshore. Acceleration terms still account for 20% of the magnitude of the geostrophic term at the limit of the model, 180 km seaward of the coast. Velocities over land are in frictional equilibrium but they gradually increase offshore to a super-geostrophic magnitude of 14.6 m/s at a distance of 110 km from the coast. A gradual decline is indicated near the limit of the model domain. For an overwater drag coefficient of 1.5×10^{-3} , the boundary layer has only begun to equilibrate with surface friction within the model domain. One can project that coastal influences of offshore flow extend seaward at least 300-500 km. This length scale is further substantiated by the "land breeze" case shown in 5b, in which the ocean is 10°K warmer than the land. The air temperature increases only 3°K over a distance of 180 km. The contribution of the land breeze increase over the background flow is of order 1 m/s, compared to the sea breeze-induced increase of 3 m/s. The length scale for thermal equilibrium of a coastal temperature discontinuity is well beyond the domain of the model even for modest advective velocities on the order of 4 m/s.

The case of a coastal mountain, Figure 6, shows onshore flow for three options of offshore PBL height and no temperature contrast. Even for moderate terrain the results are qualitatively very dissimilar to the flat coastal plain. All three cases show similar patterns of a coastal influence zone that extends from 50 km to 100 km offshore. The offshore transition is not gradual, but is marked by a sharp front at the seaward limit as seen in the PBL height and magnitude of the advective terms. Within this "offshore coastal zone" the winds are reduced by as much as 40% with a minimum approximately 20-40 km offshore. The winds veer to the southwest as they approach the coastline and accelerate toward a minimum in the PBL height on the lee side of the mountain. They then recover to a near-frictional balance within 50 km of the PBL minimum. Figure 7 shows the influence of the presence of the mountain on sea breeze circulation (10°K land/sea temperature contrast). In this formulation the mountain acts as an effective barrier to development and emphasizes the importance of low-level valleys in the mountain range for the development of sea breeze circulation. In addition to temperature contrasts, flows through valleys would be enhanced by the high pressure/low pressure contrast on the windward/leeward side of the ridge. Figures 8 and 9 show offshore flow and land breeze for a low coastal mountain. Unlike the onshore flow case with constant friction on the lee side of the mountain, a pronounced minimum in the PBL height does not occur when there is a reduction in friction on the seaward side of the mountain. This case strongly contrasts with the offshore flow case for flat topography in that there is virtually no variation in velocity seaward of the coastline. In the land breeze case, the temperature contrast reinforces the down slope flow resulting in a wind speed maximum of 9 m/s at the coast, reducing to 4 m/s at 20 km offshore.

Several important qualitative results can be inferred from the 1-D model runs. First, the length scale for frictional and thermodynamic equilibrium over water is several 100's of kilometers; this is consistent with observations of wintertime cold continental air outbreaks over the Atlantic Ocean along the northeast coast of the United States. Second, in the vicinity of discontinuities, advective effects are very important. Third, the presence of even modest orography modifies the offshore flow pattern. One can anticipate that alongshore variations in topography are also important. Finally, except for certain special cases, observations made right at the coast should be, at best, only qualitatively similar to the offshore flow field.

5. SIMULATION FOR PUGET SOUND - STRAIT OF JUAN DE FUCA

A matter of primary importance is the determination of the transport mechanism of petroleum if spilled into the waters of Puget Sound and Southeast Alaska. Since winds have a sizeable effect upon surface drift, direct measurements of winds over the water are being made as part of coastal assessment programs. A goal of the regional meteorological model is to extend the usefulness of these observational data sets and to enhance the understanding of the mesoscale atmospheric response.

We have selected three generalized meteorological flow conditions for the Puget Sound system, corresponding to typical summer and winter regimes. In the summer months, anticyclonic flow around a well-developed semi-permanent high pressure cell to the west of the region causes prevailing northwest winds offshore along the western coasts of Washington and Vancouver Island. Midwinter is characterized by a series of cyclonic storms with strong winds from the southwest carrying warm moist air inland over Western Washington. A frequent winter case is the lull between storms with high pressure to the east of the region giving easterly winds along the Strait of Juan de Fuca and relatively light winds elsewhere.

5.1 Regional Description

The area investigated is comprised of Western Washington, the southern end of Vancouver Island, and Southwest British Columbia. Major features are: the offshore ocean, Puget Sound, and the Straits of Juan de Fuca and Georgia (Figure 10a). This region spans the coordinates 121°W to 126°W and 46°N to 56°N. Topographic data for the model were obtained from a master tape at the National Center for Atmospheric Research (NCAR). The mesh is a 5-minute of latitude-longitude grid with an average elevation computed for each square. The NCAR elevation data were smoothed in both directions with a 1-2-1 type smoother (Shuman, 1957). Figure 10b presents a view of the smoothed topographic grid as seen from the southwest.

The Cascade Mountains form a north-south barrier to the east ranging from a low elevation of 916 m at Snoqualmie Pass to a high of 4392 m at Mt. Rainier, with an average height of 1800 m. The Olympic Mountains in the center of the region rise gradually from the south and west to 2428 m at the summit of Mt. Olympus, with an average height of 1600 m, descending rapidly to the north and east. A significant area of higher elevation to the south is the Willapa Hills 300-600 m high between the Columbia River and the Chehalis River Valley. Vancouver Island is primarily mountainous, with heights averaging 900 m, reaching 1200 m in several locations.

This topography establishes one main north-south low level passage-way extending from the Columbia River Valley through Puget Sound, and two low level east-west passages between the central basin and the Pacific Ocean, the Strait of Juan de Fuca and the Grays Harbor Inlet-Chehalis River Valley. To the northwest, Puget Sound opens out into the San Juan Islands and the Georgia Strait. The flat land to the east of Georgia Strait narrows eastward as the Fraser River Valley.

5.2 Data Sources

We wished to obtain a set of data which would adequately represent the regional wind field during November and December of 1976 and January of 1977. This set included routine meteorological station reports supplemented by an array of recording anemometers at strategic locations. Figure 11 and Table 2 provide station location, source and National Weather Service station symbols. Teletype data for National Weather Service Offices and Coast Guard Stations were obtained from the Ocean Services Unit of the Seattle Weather Service Forecast Office. The Weather Service Offices and ships from the northeast Pacific typically report every 6 hours. The Coast Guard Stations usually report every 3 hours, but most do not report during the night. Three MRI Model 7092 Anemometers were set out by the authors. These yielded strip charts, which were converted to 1-hour averages and plotted every 6 hours. Data from 3 vector averaging anemometers in the Strait of Juan de Fuca were provided by Jim Holbrook as part of the Puget Sound MESA project. It should be noted that stations in Table 1 designated as 10-17 are well inland, and thus local microtopography affects the air movement at these more than at the shore stations, and are less indicative of the general flow. Station wind reports were mapped every 6 hours from 0000 Greenwich Mean Time (GMT) on November 27, 1976 to 1800 GMT on January 26, 1977. From these regional maps, examples of typical weather events were selected.

For each case selected, large-scale synoptic pressure maps centered on Western Washington were prepared from North Pacific synoptic charts. In addition objective sea level pressure analyses on the Limited Area Fine Mesh Model (LFM) grid were obtained for the region from the National Meteorological Center. Our intent is to compare the objective analyses on the 160-km mesh to the hand-drawn charts to determine if LFM input is adequate for the regional model.

Upper-air sounding data were available from Quillayutte (station) on the Washington coast; weather ship PAPA located at 50°N, 145°W; SEATAC airport, south of Seattle; and Portage Bay in Seattle.

The pressure analyses have pressure given in millibars, written out on isobars to the units place and to the tenths place at stations (deleting the first two digits), e.g. 236 = 1023.6 mb. Wind is given on these maps as barbs (one full barb = 10 knots). On the local wind maps, direction and speed are also given at stations, e.g. 3408 = wind from true north direction 340, speed at 08 kn.

5.3 Meteorological Case Discussion

Two basic regimes describe the general weather characteristics of Decembers in Western Washington. As is typical of the latitude, a succession of frontal passages from the west, varying in number and intensity, dominates the flow patterns providing strong winds from the southwest. Between storms, high pressure builds up near the area, often in the continental interior, bringing clear skies and relatively low winds lasting for several days to a week or more. The fall and winter of 1976 were unusual in that a persistently recurring ridge of high pressure over the northeastern Pacific at 500 mb, frequently extending almost to the pole, allowed only an occasional weakened frontal passage through the area. Surface high pressure associated with the 500-mb pattern, but displaced eastward over the continent, dominated the Puget Sound Basin.

A good example of this situation is 0000 GMT on December 1, 1976. For several days prior to and succeeding this time, high pressure prevailed over southeastern British Columbia, extending north and south over the interior plateau (Figure 12). In the absence of topography, widely spaced isobars would suggest a weak flow outward from the high pressure center westward over the area. However, the local wind shown in Figure 13 reveals a complex pattern with easterly winds at the coast and calm or light northerly winds in the Puget Sound. A very interesting feature is seen in the Strait of Juan de Fuca. In sharp contrast to the weak and variable winds elsewhere on the inland waters, there is a strong flow out the Strait, reaching 20 kn at Cape Flattery. This isolated jet was reported on by Reed (1931) but is not specifically mentioned in more recent literature. Associated with these low level wind vectors are temperature soundings over the area revealing a strongly stratified regime throughout the planetary boundary layer. The SEATAC sounding for November 30, 1976 at 1610 GMT is shown in Figure 14. Lines of constant potential temperature are also shown indicating stable stratification throughout the boundary layer.

On the objective analyses from the National Meteorological Center, the absence of horizontal air flow seen at 850 mb in Figure 15 for December 1, 0000 GMT contrasts with the surface pattern (Figure 16) which shows a light pressure gradient east-west through the region in agreement with the hand-drawn map. The spacing on the surface LFM map is 1 mb, approximately equivalent to the 10-geopotential meter spacing of the 850-mb LFM map. The decoupling of the 850 mb and surface layer is consistent with the strong vertical stratification observed at SEATAC. Stability restricts the flow to regions below the mountain tops where the air is accelerated along the east-west pressure gradient out through the Strait of Juan de Fuca and west through the Cowlitz Valley south of the Olympic Mountains. The winds can be explained as stronger in the Strait than along the southern Washington coast because the down gradient acceleration is uninhibited by surface friction. Another curious feature is that the winds in Puget Sound proper flow south in the opposite direction to an inferred surface geostrophic wind. A second example of winds under the high pressure regime is seen in Figures 17 and 18, where high pressure has built up rather rapidly between frontal passages. The local stations again reflect the widely spaced isobars with easterly winds on the coast, calm in the Sound and acceleration along the Strait of Juan de Fuca.

Figure 19 shows the wind pattern generated by the model which corresponds to the December 1, 1976 case. While the boundary layer is not well mixed as assumed in section 2, we considered that we could simulate the forced channeling for the east wind case by assuming a very shallow PBL in the model capped by very strong stability. Input parameters are summarized in Table 3. The model was initialized by a geostrophic wind of 4.8 ms^{-1} from 144° and a low PBL height of 0.5 km as representative of stable conditions throughout the lower troposphere. The major features are: light winds in the central basin, weak easterly flow along the coast, and accelerating easterly flow down gradient through the Strait of Juan de Fuca, similar to Figures 13 and 17. As the flow in all channels is out of the Puget Sound Basin, this case could not be run to steady state. In the prototype the outflowing air is replaced by subsidence associated with the synoptic high pressure. Subsidence is not included in the model to balance the falling PBL height; Figure 19 is the model-estimated wind field when the interior PBL height reached 400 m after 4 hours and was falling at a constant velocity. To increase the resolution in the main area of interest, the Strait of Juan de Fuca, the grid length was reduced to one half of its previous value in the north-south direction, while the domain was also reduced to see if the model could be sectionalized (Figure 20). Good agreement is obtained in the Straits. Contrary to the inferred flow from observations, at the east end of the Strait a more geostrophic flow is allowed by not resolving the southern end of Puget Sound.

The front that approached the coast at 0000 GMT, December 8, 1976 (Figure 21) turned into a cold front of respectable energy as the high retreated far to the south. This case of even isobars and southwesterly geostrophic flow is a good example of the typical situation before the passage of a cold front. From the local wind vectors (Figure 22), one first notices that the flow is channeled by the Olympic and Cascade Mountains. Winds over Puget Sound are stronger and more southerly than offshore. A region of light winds is evident in the lee of the Olympic Mountains. There is also general steering of the flow along the axis of Georgia Strait, more than a 90° deflection from the geostrophic wind. The December 7 1605 GMT temperature sounding at SEATAC shows a relatively moist, deep, well-mixed PBL with near-neutral stability (Figure 23). This is illustrated further by the fact that the 850-mb flow is very similar to the surface flow on the LFM maps (see Figures 24 and 25). The hand-drawn and LFM surface maps agree well. Figures 26 and 27 for 0000 GMT, December 15, show an additional example of strong winds from the southwest.

The corresponding storm situation of December 8, 1976, is simulated by a model run in Figures 28 and 29 for a PBL height of 1800 m and 900 m, respectively. Geostrophic wind is 14.7 m/s^{-1} from 251° . The overall wind pattern for the observed PBL height (1800 m) is much smoother than that suggested by observations. The lower height, however, shows the approximate amount of detail. A relative eddy has formed at the east end of the Strait of Juan de Fuca near Port Angeles to various degrees in both simulations. The PBL height deviations show a gentle rise over the windward side of the mountains with a pronounced lee wave trough on the downwind side of the Olympics and Vancouver Island. With a low inversion height, increased winds flow through the low point in the mountains of Vancouver Island and spill out over the inland waters. Observed winds in the east end of the Strait of Juan de Fuca are less intense and more westerly than either model run suggests. It may be that the position of the eddy and the magnitude of the pressure gradient that develops along the axis of the Strait of Juan de Fuca are very sensitive to the volume of air channeled through Puget Sound, which depends in turn on the orientation of the offshore flow. Inflow along the southern boundary is not handled satisfactorily by arbitrary specification of inversion height, especially at the land-water interface. However, this does not appear to unduly influence the flow in the central basin.

In the previous section it was noted that inertia plays a dominant role in mesoscale circulations. In contrasting the two model runs, the main differences are between allowing the flow to go over the mountain or forcing it around the mountain. Since observations resemble more the case with a lower inversion, perhaps the effective cross-sectional height of the mountains is higher than the model-assumed average elevations; the light stable stratification of the PBL shown in the SEATAC sounding may contribute to increased channeling.

The front depicted in Figure 17 was the weakest of four crossing the region in December 1976. For a day following the December 22 front and a day following the December 8 front, a cell of high pressure existed off the coast of Oregon and Northern California which brought strong northwesterly winds through Washington as part of an anticyclonic circulation. Except for temperature effects, this pattern is typical of summertime conditions in the region. The hand-drawn pressure map of December 23, 1976, 1800 GMT shows a relatively uniform pressure gradient from offshore inland to Vancouver, B.C. (Figure 30). The local anemometers (Figure 31) reveal the effect of topography on a northwesterly geostrophic wind. Strong channeling is indicated in the Strait of Juan de Fuca with variable winds in the lee of the Olympic Mountains. It is interesting that for this case and for December 9, 1976, 1200 GMT (Figures 32 and 33), there is a southerly flow in the lower Puget Sound in the lee of the Olympics, but only on the surface. Figure 34 shows the December 9, 1400 GMT, McChord AFB wind sounding and the Quillayutte temperature sounding. The LFM maps (Figures 35 and 36) concur with the hand analysis in showing a northwesterly geostrophic flow.

Figure 37 shows the model velocity field for northwest winds. Channeling is indicated in the Strait of Juan de Fuca and especially in the Strait of Georgia. Height deviations are less intense than for the southwest wind case, although the velocity field indicates that the lee wave eddy is still a major feature. A southerly tendency is indicated in the lower Puget Sound trough where the flow is parallel to the pressure gradient below the ridge crests.

In contrasting the wind and height fields for NW and SW winds, northwest winds tend to flow fairly closely to the orientation of the ridge line. Southwest winds funnel the flow into Puget Sound, but farther north inertia carries the major volume flux (velocity multiplied by PBL depth) across topographic contours through the low points in the ridge crest. This cross-contour flow induces a major local response in the height field and eddies.

6. ACKNOWLEDGEMENTS

This study was supported jointly by the Puget Sound Marine Ecosystems Analysis (MESA) Project and the Outer Continental Shelf Environmental Assessment Program (OCSEAP) to assist in providing wind fields for oil spill trajectory calculations, and the Marine Services Program at PMEL in support of National Weather Service marine prediction along the west coast and Gulf of Alaska.

We wish to thank Robert Anderson and his colleagues at the Seattle National Weather Service Forecast Office for their collaboration in the field program and in compiling the routine observation data sets.

7. REFERENCES

- Brown, R. A. (1974): A simple momentum integral model. J. Geophys. Res. 79:4076-4079.
- Keyser, D., and Anthes, R. (1977): The applicability of a mixed-layer model of the planetary boundary layer to real-data forecasting. Mon. Wea. Rev. 105:1351-1371.
- Lavoie, R. (1972): A mesoscale numerical model of lake-effect storms. J. Atmos. Sci. 29:1025-1040.
- Lavoie, R. (1974): A numerical model of tradewind weather on Oahu. Mon. Wea. Rev. 102:630-637.
- Ogura, Y., and N. W. Phillips (1962): Scale analysis of deep and shallow convection in the atmosphere. J. Atmos. Sci. 19:173-179.
- Reed, J. (1931): Gap winds of the Strait of Juan de Fuca. Mon. Wea. Rev. 59:373-376.
- Stull, R. B. (1976): Mixed-layer depth model based upon turbulent energetics. J. Atmos. Sci. 33:1268-1278.

Appendix

DERIVATION OF BOUNDARY LAYER EQUATIONS

We shall write the equations of motion for deviation from a steady reference state. If the reference state changes only very little with height, it is possible to use the Boussinesq approximation, but with potential temperature as the thermal variable (Ogura and Phillips, 1962).

The momentum equation is:

$$\frac{\partial \vec{v}}{\partial t} + \vec{v} \cdot \nabla \vec{v} = w \frac{\partial \vec{v}}{\partial z} + f \vec{k} \times \vec{v} + c_p \theta_0 \nabla \pi = - \frac{\partial}{\partial z} (\vec{v}' w') \quad (\text{A1})$$

where

$$\pi \equiv \left(\frac{p}{p_0} \right)^\chi, \quad \chi = R/c_p.$$

The hydrostatic equation is:

$$c_p \theta \frac{\partial \pi}{\partial z} = -g. \quad (\text{A2})$$

The equation of continuity is:

$$\nabla \cdot \vec{v} + \frac{\partial w}{\partial z} = 0. \quad (\text{A3})$$

The first law of thermodynamics is approximated by:

$$\frac{\partial \theta}{\partial t} + \vec{v} \cdot \nabla \theta + w \frac{\partial \theta}{\partial z} = - \frac{\partial}{\partial z} (w' \theta'). \quad (\text{A4})$$

In these equations \vec{v} is Reynolds' averaged horizontal velocity vector, \vec{v}' is the deviation velocity, θ is potential temperature, and θ_0 is the potential temperature of the reference state (constant). The other terms are defined in the usual meteorological sense.

We simplify the hydrostatic equation (A2) in the following way:

$$c_p \frac{\partial \pi}{\partial z} = - \frac{g}{\theta} \approx -g \frac{1}{\theta_0} \left(1 - \frac{\theta''}{\theta_0} \right),$$

where $\theta'' = \theta - \theta_0$.

If we define π_0 such that

$$c_p \frac{\partial \pi_0}{\partial z} = -\frac{g}{\theta_0}$$

then

$$c_p \frac{\partial \pi''}{\partial z} = \frac{g}{\theta_0} \frac{\theta''}{\theta_0}, \text{ where } \pi'' = \pi - \pi_0.$$

Since π_0 is a function of z only, we can rewrite Eqn. (A1):

$$\frac{\partial \vec{v}}{\partial t} + \vec{v} \cdot \nabla \vec{v} + w \frac{\partial \vec{v}}{\partial z} + f \vec{k} \times \vec{v} + c_p \theta_0 \nabla \pi'' = -\frac{\partial}{\partial z} (\overline{\vec{v}'w'}) \quad (\text{A6})$$

We shall use equations (A3), (A4), (A5), and (A6) for describing the flow field in the well-mixed layer.

We now integrate (A4) and (A6) through the mixed layer. The basic equations then become:

$$\frac{\partial \vec{v}}{\partial t} + \vec{v} \cdot \nabla \vec{v} + f \vec{k} \times \vec{v} + \frac{c_p \theta_0}{h-D} \int_D^h \nabla \pi'' dz = -(\overline{\vec{v}'w'}_h - \overline{\vec{v}'w'}_s)/(h-D) \quad (\text{A7})$$

$$\frac{\partial \theta}{\partial t} + \vec{v} \cdot \nabla \theta = -(\overline{w'\theta'}_h - \overline{w'\theta'}_s)/(h-D) \quad (\text{A8})$$

In addition, the mass continuity equation, by definition, can be written:

$$\frac{\partial h}{\partial t} + \nabla \cdot (h-D)\vec{v} = E, \quad (\text{A9})$$

where E is the net entrainment rate at which the well-mixed layer gains mass from the free atmosphere.

Using hydrostatic equation, we evaluate the vertically integrated pressure gradient force:

$$-\frac{c_p \theta_0}{(h-D)} \int_D^h \nabla \pi'' = -c_p \theta_0 \nabla \pi''_H + \frac{g}{\theta_0} (H-h) \nabla \theta''_H - \frac{g}{\theta_0} (\theta''_h - \theta'') \nabla h + \frac{g}{\theta_0} \frac{1}{2} (h-D) \nabla \theta'' \quad (\text{A10})$$

where subscript H denotes the top of the model atmosphere.

For the convenience of finite differencing, Eqn. (A8) is written in a flux form:

$$\frac{\partial}{\partial t} (h-D)\theta + \nabla \cdot (h-D)\vec{v}\theta - \theta E = -(\overline{w'\theta'})_h + (\overline{w'\theta'})_s \quad (\text{A11})$$

In deriving the equation, Eqn. (A9) was used.

Integrating Eqns. (A1) and (A4) across the jump between the PBL and inversion layer using Leibnitz' rule, we obtain relations:

$$(\overline{\vec{v}'w'})_h = -E\Delta\vec{v} \quad (\text{A12})$$

$$(\overline{w'\theta'})_h = -E\Delta\theta \quad (\text{A13})$$

where $\Delta\vec{v} = \vec{v}_+ - \vec{v}_-$ and $\Delta\theta = \theta_+ - \theta_-$.

Equations (A7), (A9), and (A11) with equations (A10), (A12), and (A13) form a closed set of equations, if the entrainment rate can be parameterized in terms of the mixed layer variables.

FIGURE CAPTIONS

- Figure 1. Regions of anomalous winds as reported by vessels operating in Alaskan waters.
- Figure 2. Model-defined parameters of height, velocity and potential temperature. In application $\gamma=0$ and $\theta_H \approx \theta_+$.
- Figure 3. Staggered mesh for primary variables.
- Figure 4a. Onshore flow with flat coastline.
- Figure 4b. Onshore flow with flat coastline with acceleration terms set to zero.
- Figure 4c. Sea breeze circulation with a flat coastline.
- Figure 5a. Offshore wind with flat coastline.
- Figure 5b. Land breeze circulation with flat coastline.
- Figure 6a. Onshore flow with coastal mountain; offshore PBL = 500 m.
- Figure 6b. Onshore flow with coastal mountain; offshore PBL = 900 m.
- Figure 6c. Onshore flow with coastal mountain; offshore PBL = 1500 m.
- Figure 7. Sea breeze circulation with coastal mountain.
- Figure 8. Offshore flow with coastal mountain.
- Figure 9. Land breeze with coastal mountain.
- Figure 10a. Location map for the Puget Sound Basin.
- Figure 10b. Topographic grid used in the computations as viewed from the southwest.
- Figure 11. Location map for anemometer stations collected for December 1976 - January 1977.
- Figure 12. Sea level pressure analysis 1 DEC 76, 0000GMT.
- Figure 13. Local wind observations 1 DEC 76, 0000GMT.
- Figure 14. Atmospheric sounding for SEATAC 30 NOV 76, 1610GMT.
- Figure 15. Objective analysis of 850-mb heights 1 DEC 76, 0000GMT.
- Figure 16. Objective analysis of sea level pressure 1 DEC 76, 0000GMT.

FIGURE CAPTIONS (continued)

- Figure 17. Second example of high pressure to the northeast of Puget Sound, 21 DEC 76, 1800GMT.
- Figure 18. Local wind observations for pressure field shown in Figure 17.
- Figure 19. Model run for east wind case.
- Figure 20. Model run for east wind case with increased north-south resolution.
- Figure 21. Sea level pressure chart 8 DEC 76, 0000GMT.
- Figure 22. Local wind observations 8 DEC 76, 0000GMT.
- Figure 23. SEATAC sounding 7 DEC 76, 1605GMT.
- Figure 24. Objective analysis of 850-mb heights 8 DEC 76, 0000GMT.
- Figure 25. Objective analysis of sea level pressure, 8 DEC 76, 0000GMT.
- Figure 26. Second example of strong onshore flow from southwest, 15 DEC 76, 1800GMT.
- Figure 27. Local wind observations for Figure 26.
- Figure 28. Model winds for southwest flow with offshore PBL height of 1800 m.
- Figure 29. Model winds for southwest flow with offshore PBL height of 900 m.
- Figure 30. Sea level pressure chart, 23 DEC 76, 0800GMT.
- Figure 31. Local wind observations, 23 DEC 76, 1800GMT.
- Figure 32. Sea level pressure chart 9 DEC 76, 1200GMT.
- Figure 33. Local wind observations 9 DEC 76, 1200GMT.
- Figure 34. Temperature sounding at Quillayute (Washington coast) and McChord AFB (Puget Sound) for 1200 and 1400GMT, 9 DEC 76.
- Figure 35. Objective analysis of 850-mb heights, 9 DEC 76, 1200GMT.
- Figure 36. Objective analysis of sea level pressure, 9 DEC 76, 1200GMT.
- Figure 37. Model winds for northwest flow.

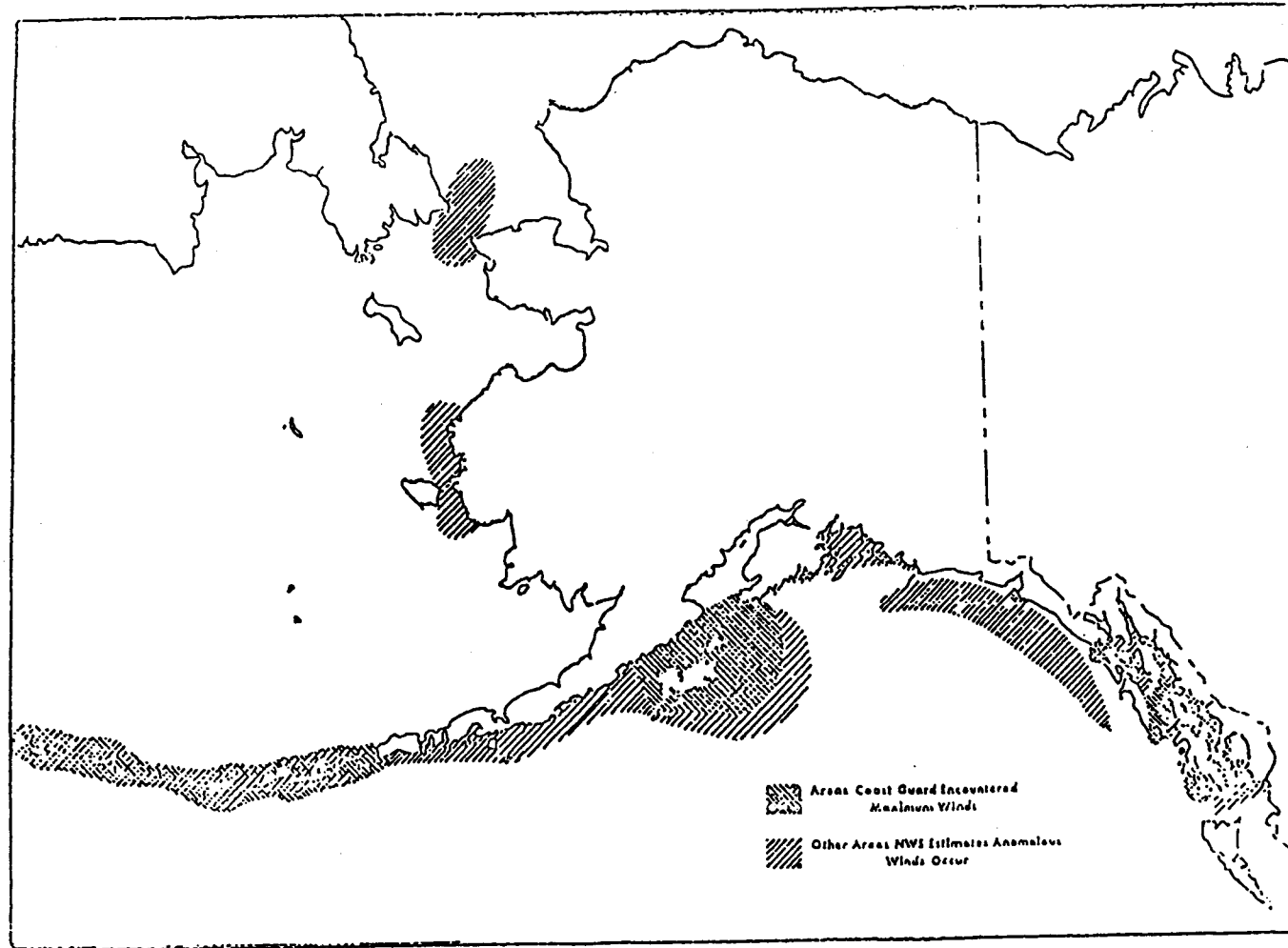


Figure 1.

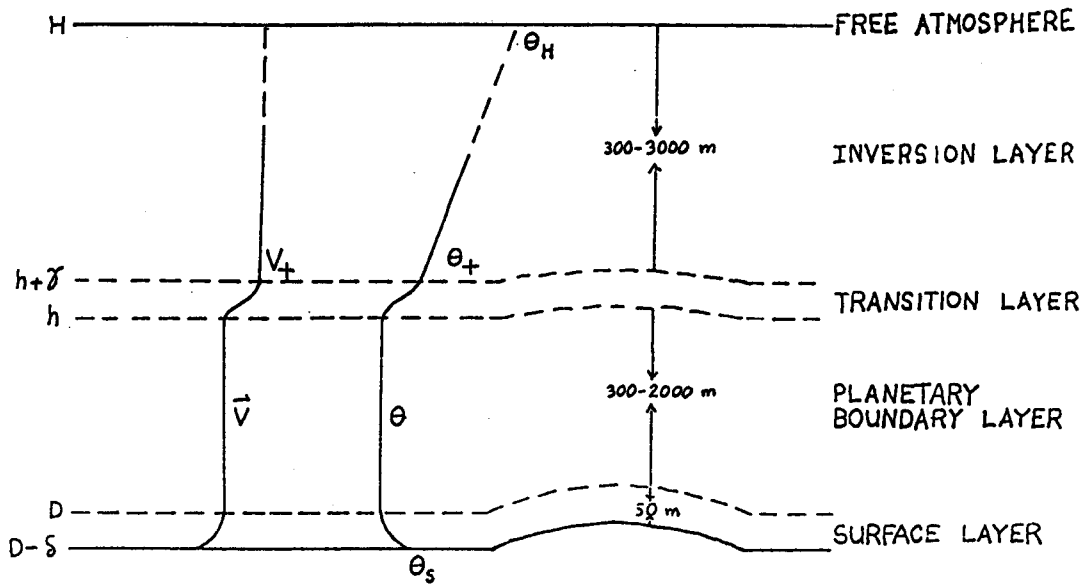


Figure 2.

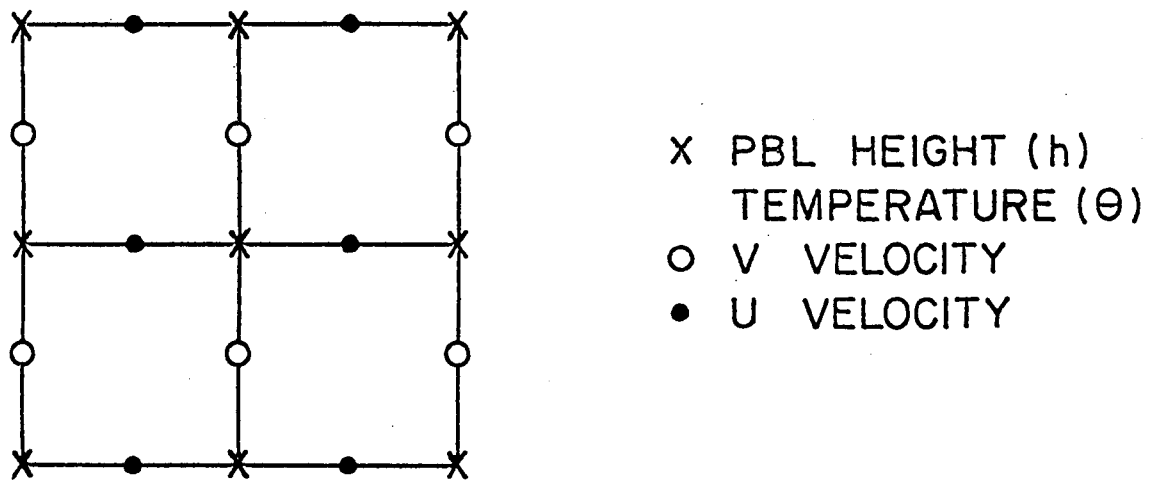


Figure 3.

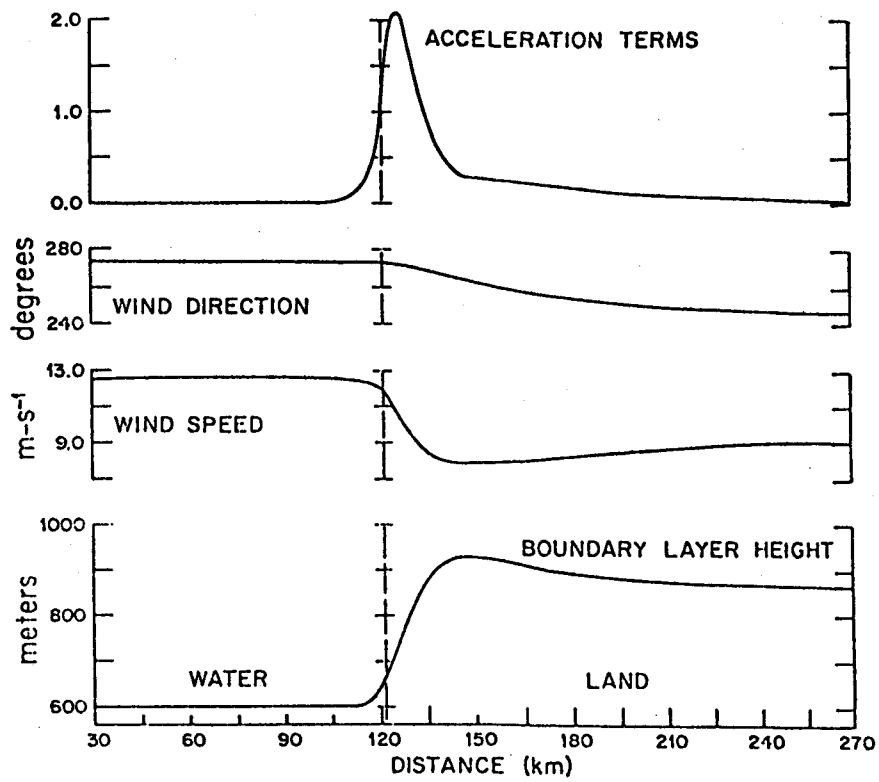


Figure 4a.

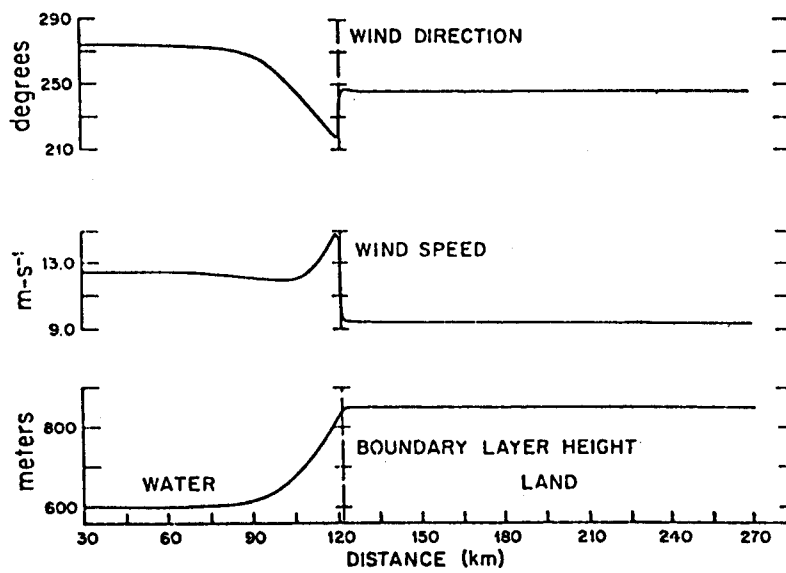


Figure 4b.

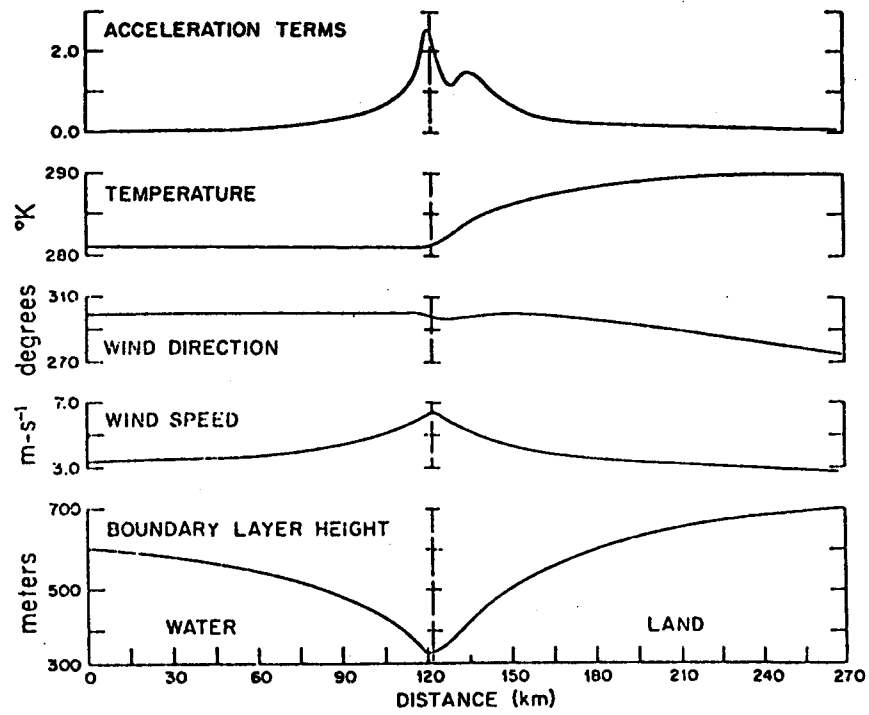


Figure 4c.

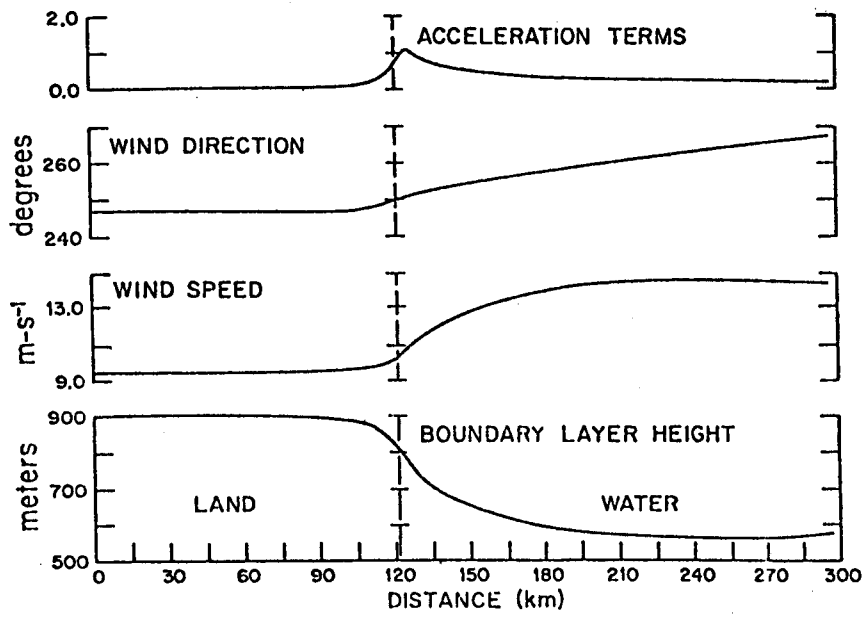


Figure 5a.

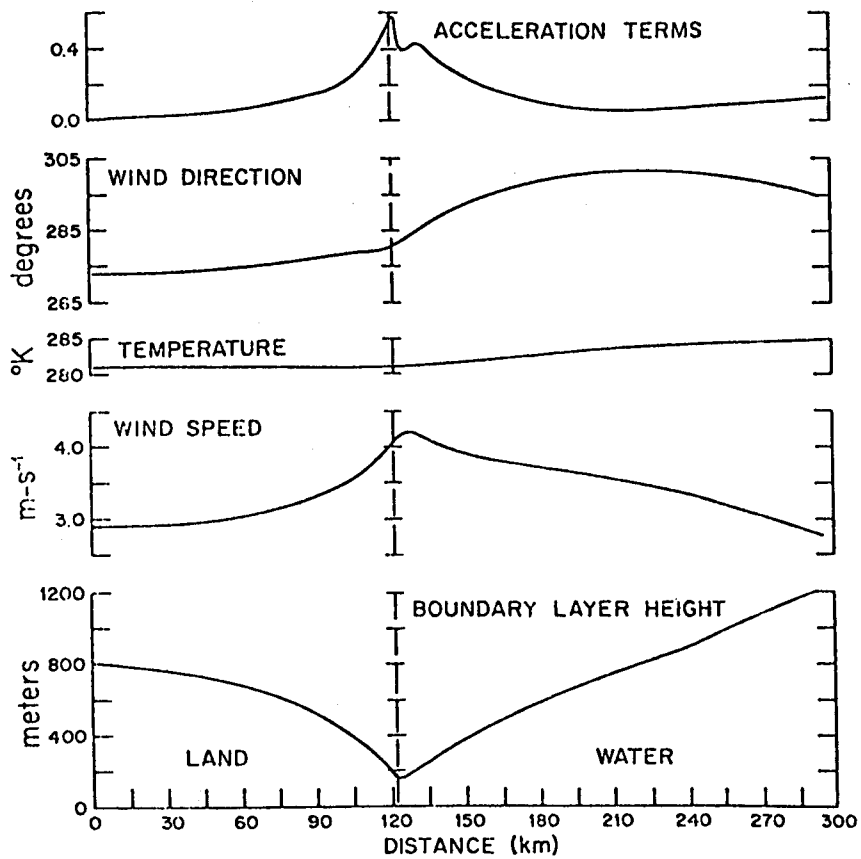


Figure 5b.

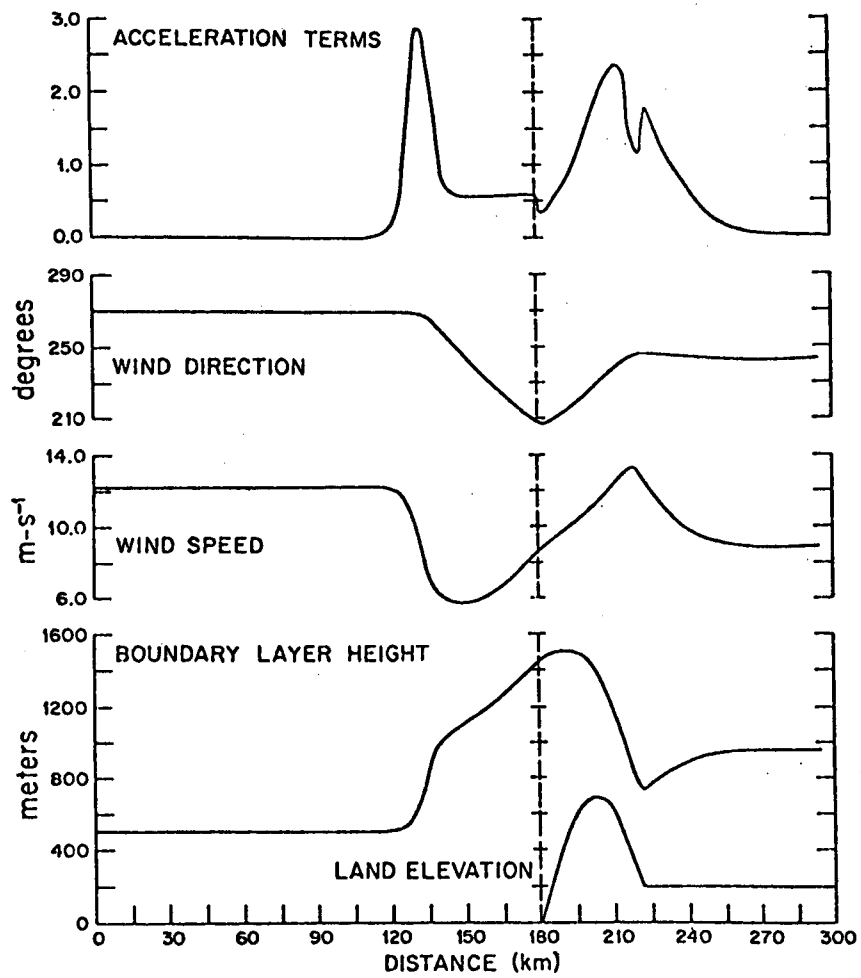


Figure 6a.

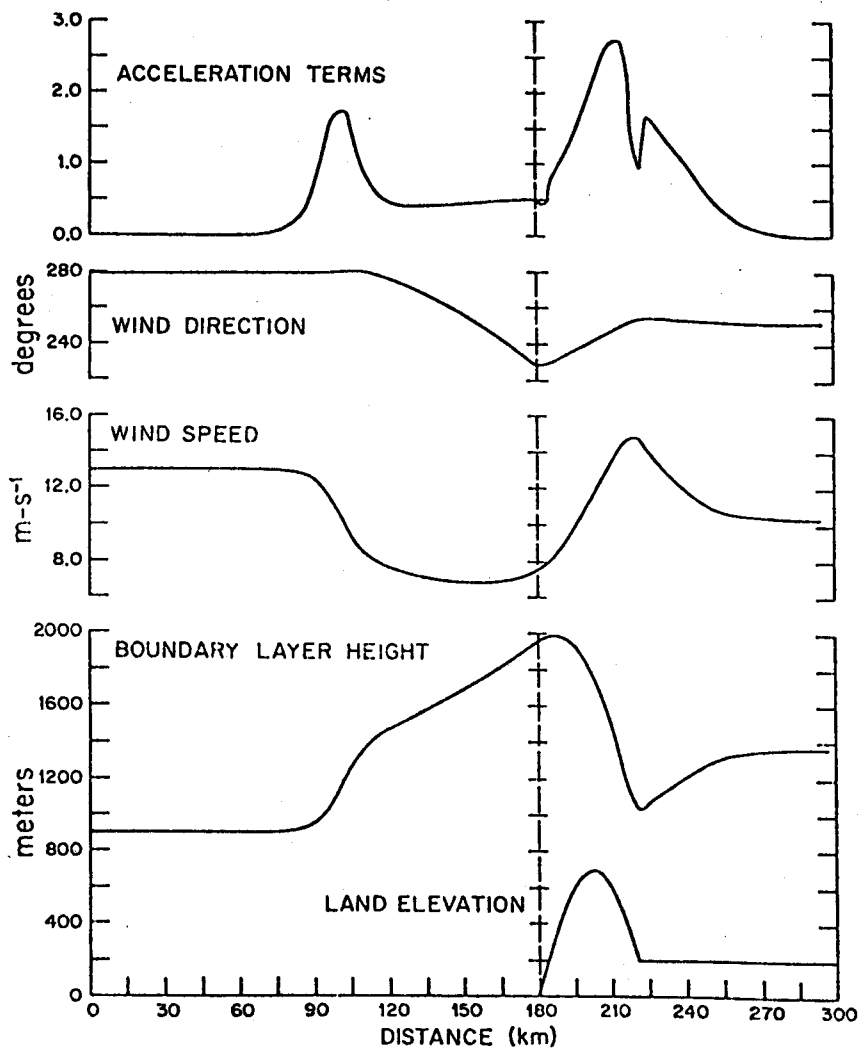


Figure 6b.

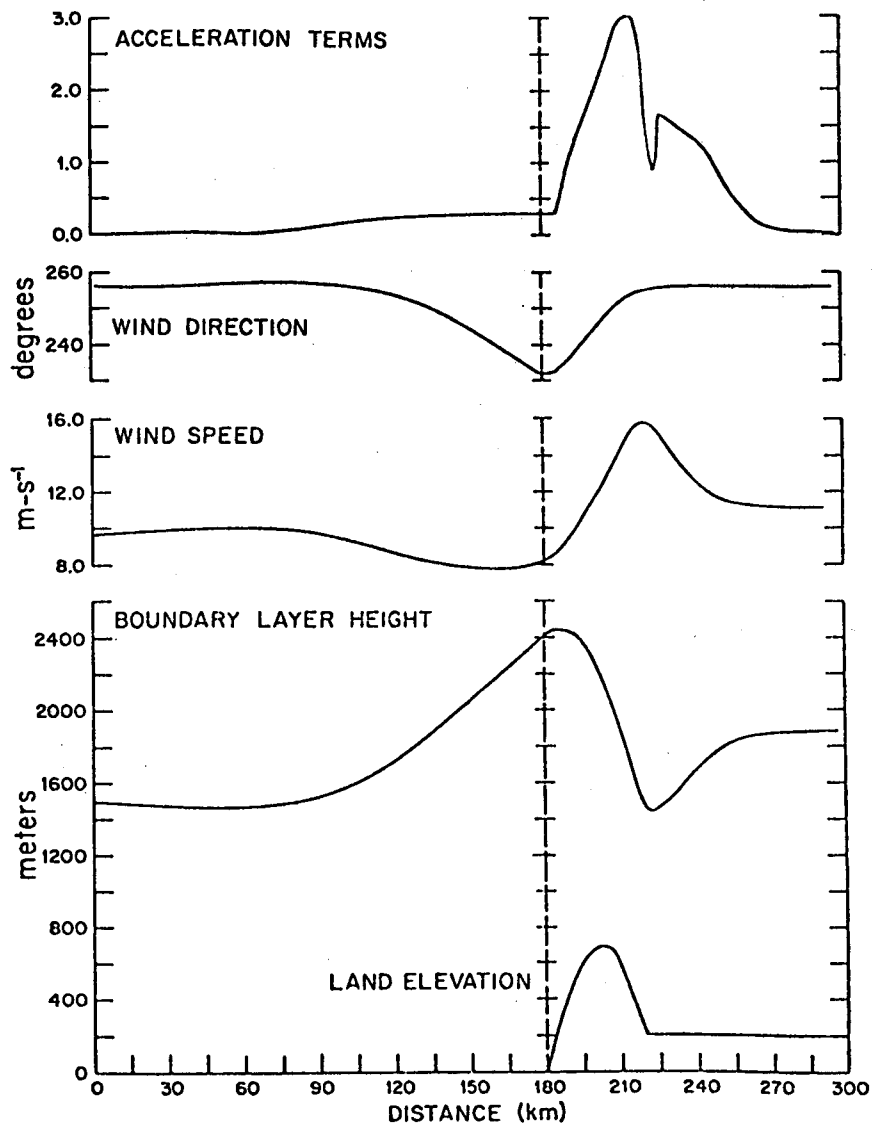


Figure 6c.

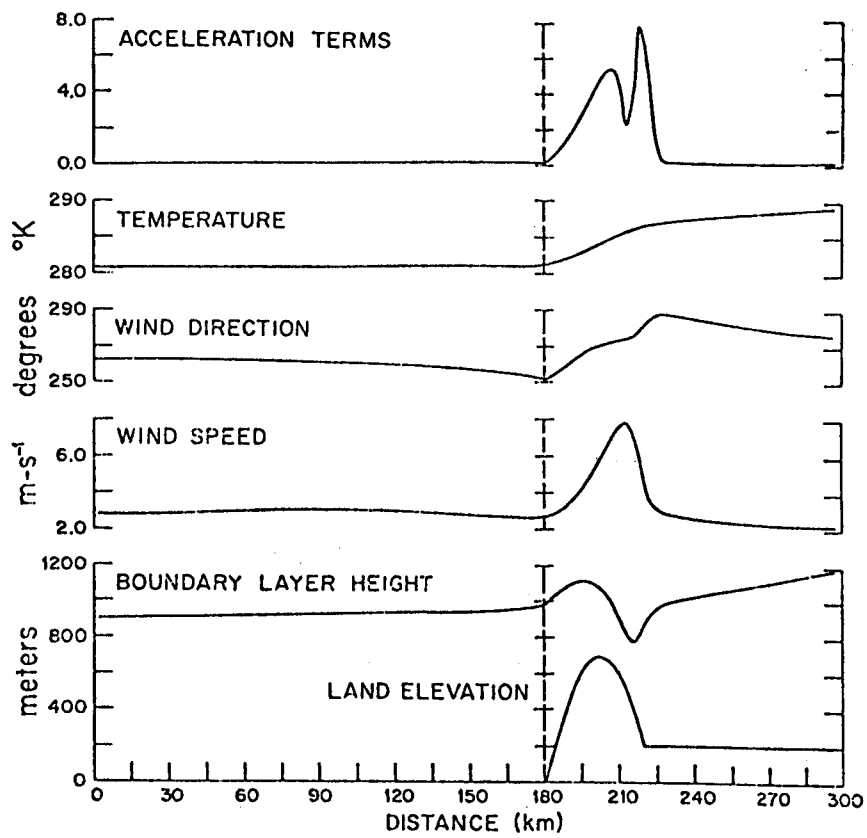


Figure 7.

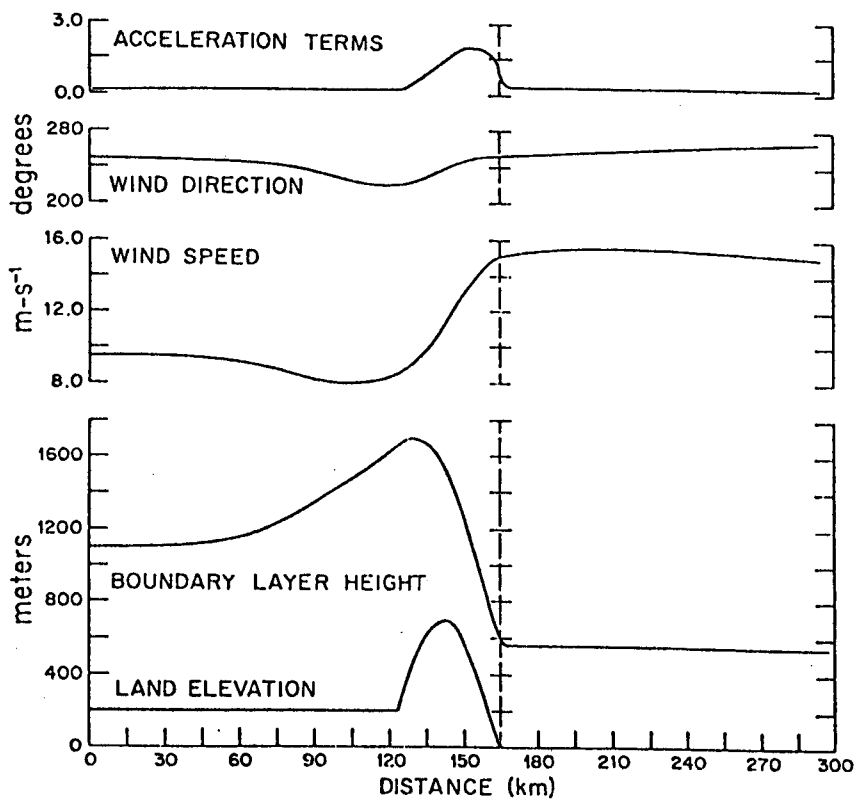


Figure 8.

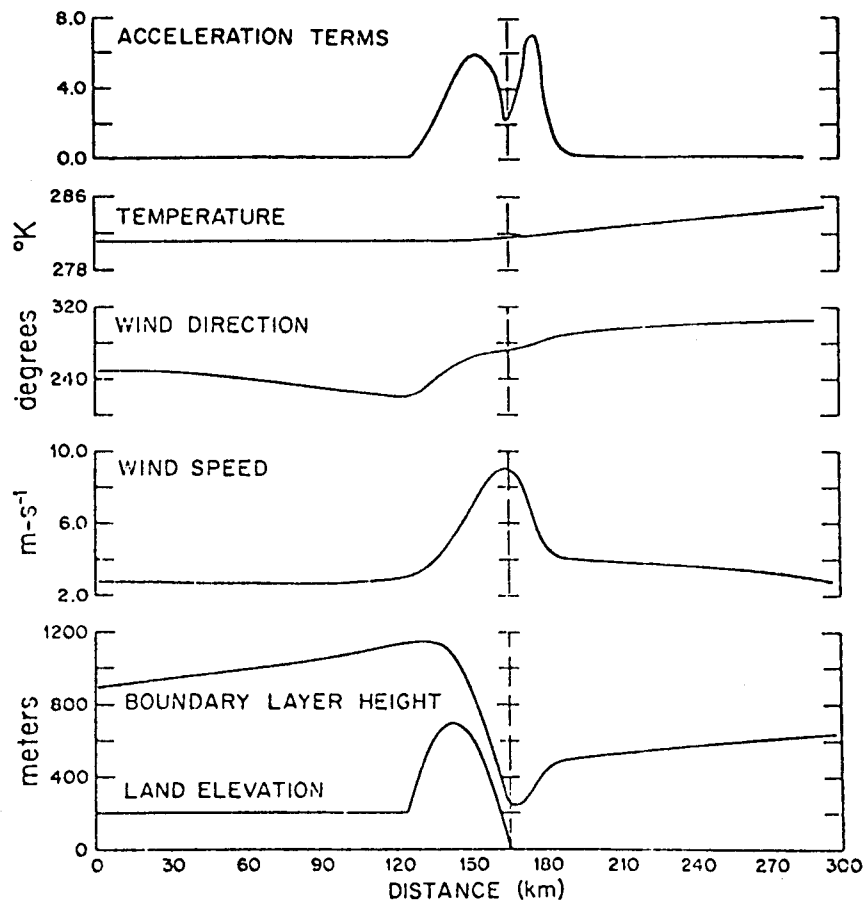


Figure 9.

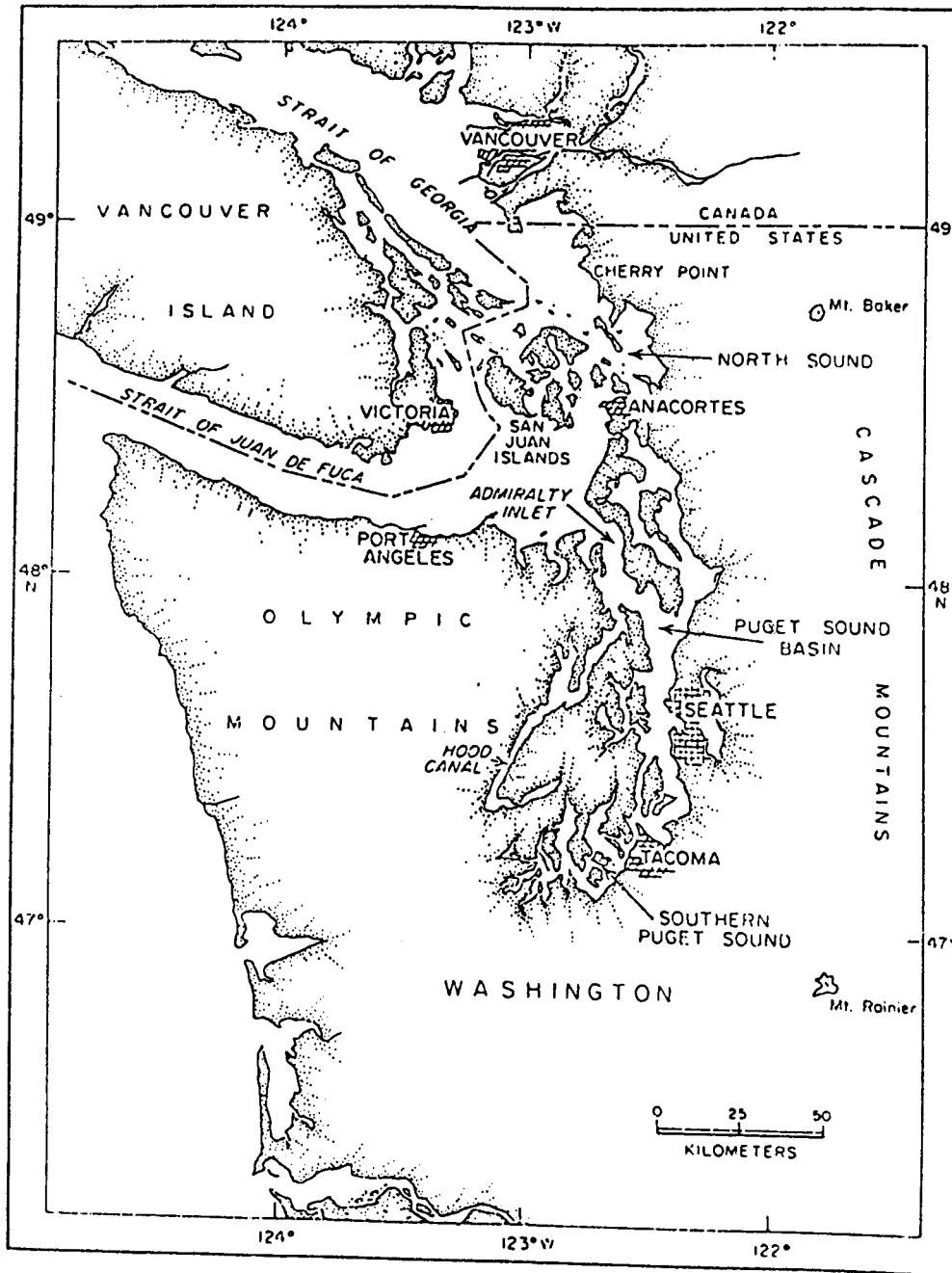


Figure 10a.

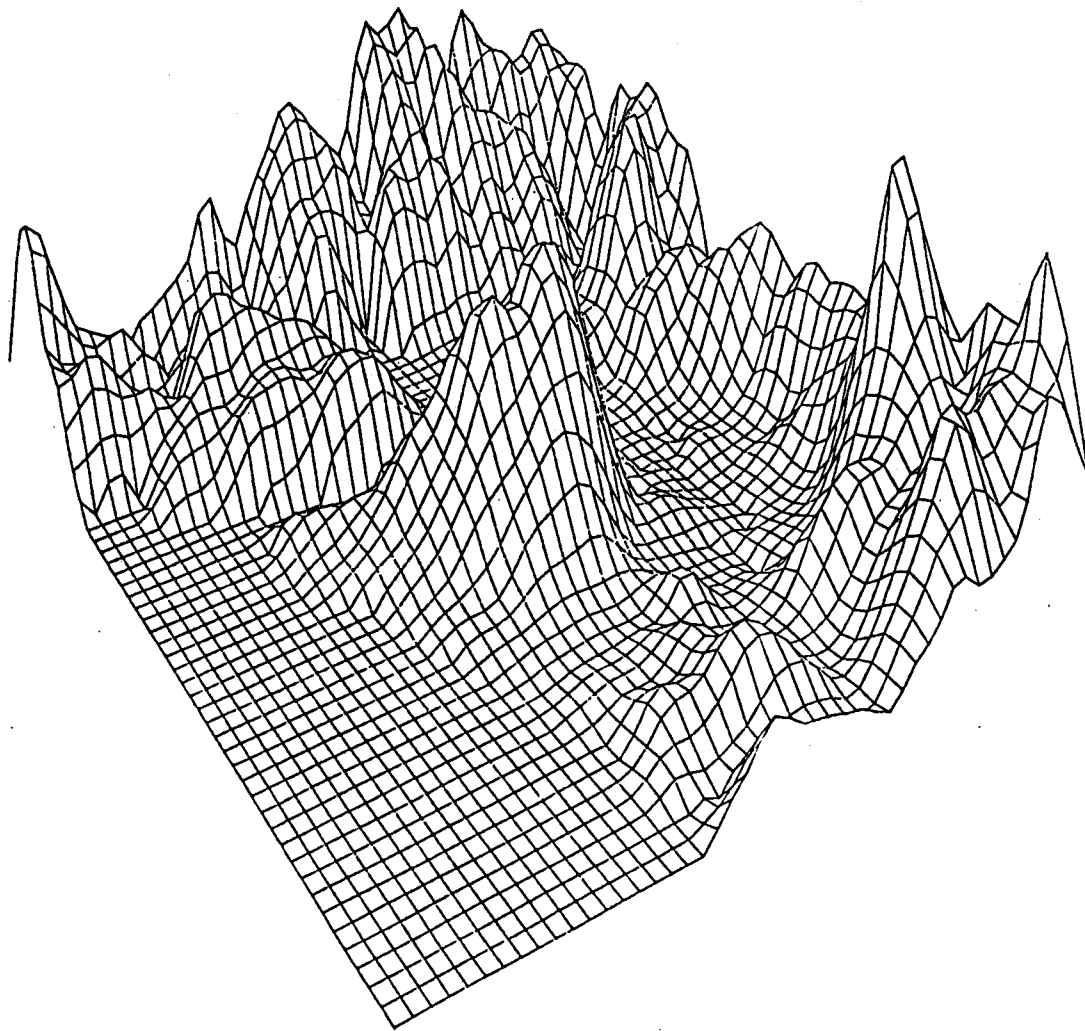


Figure 10b.

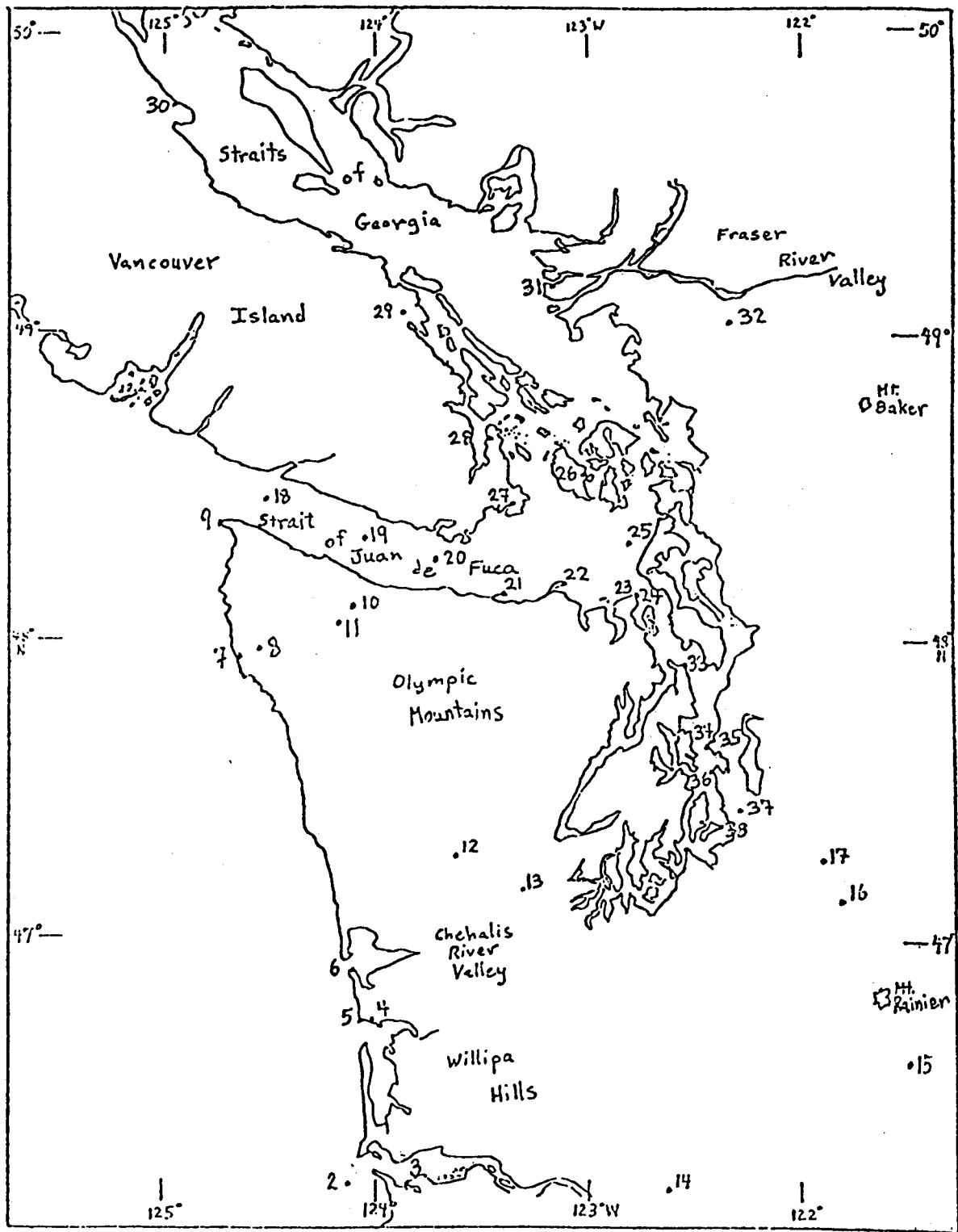


Figure 11.

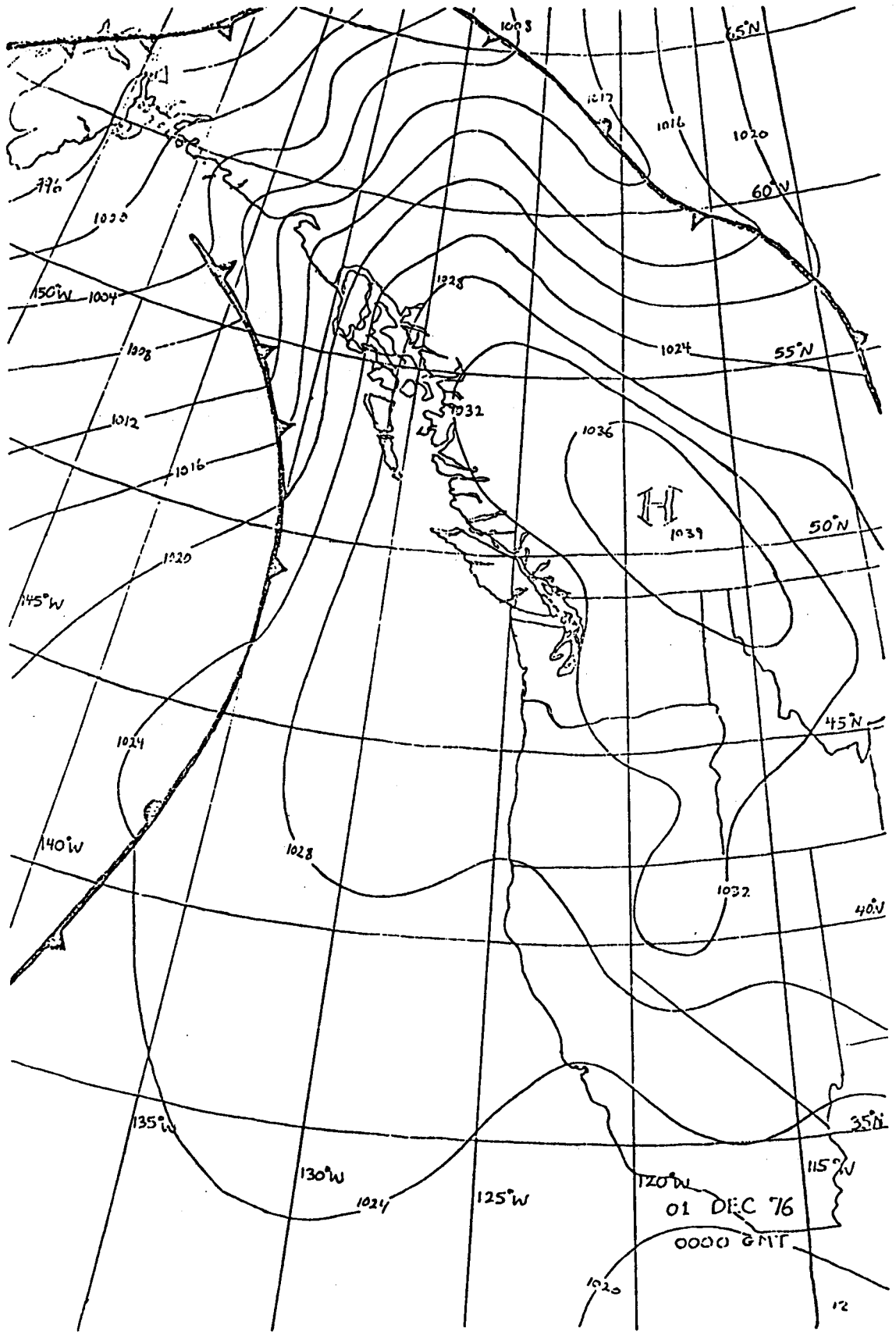


Figure 12.

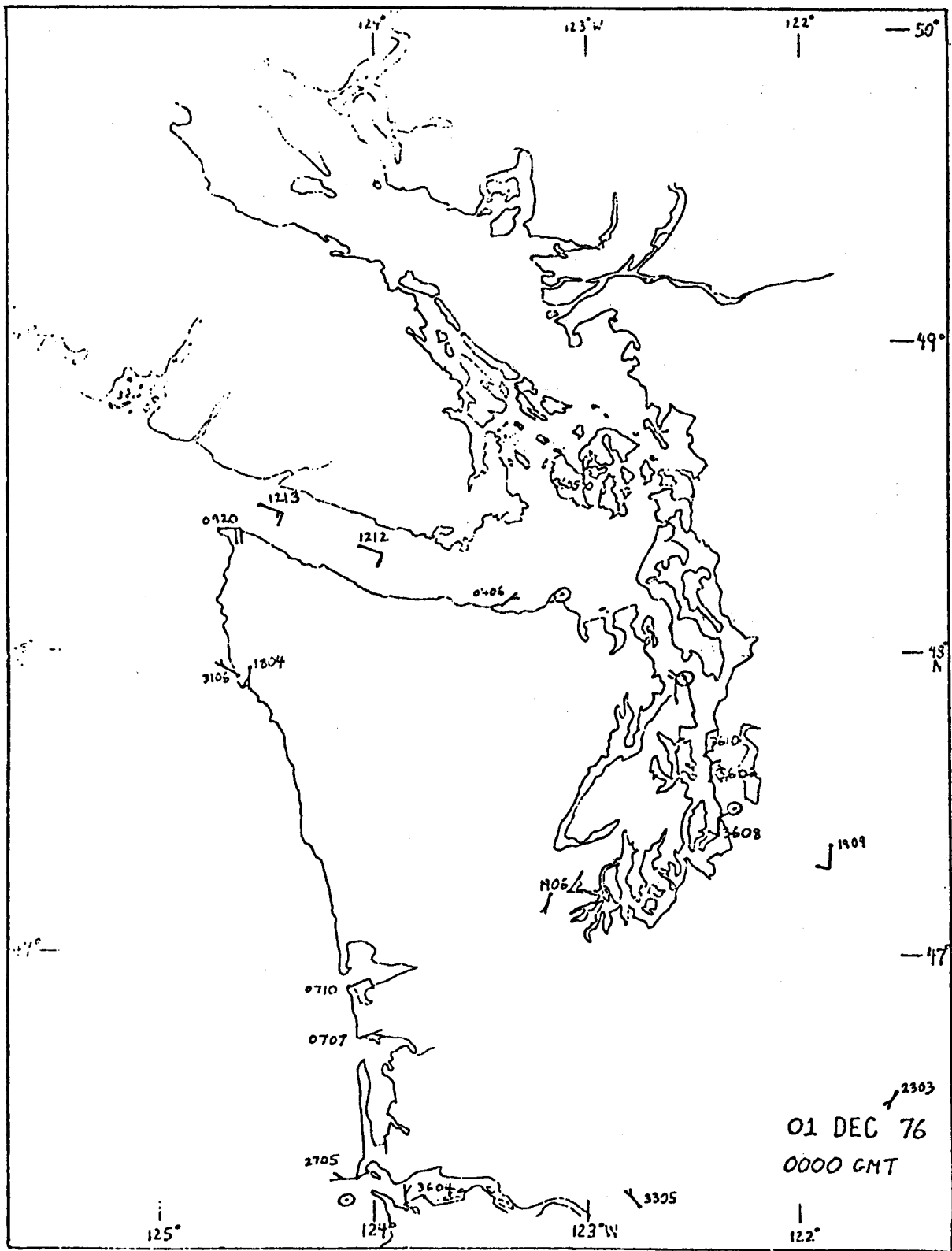


Figure 13.

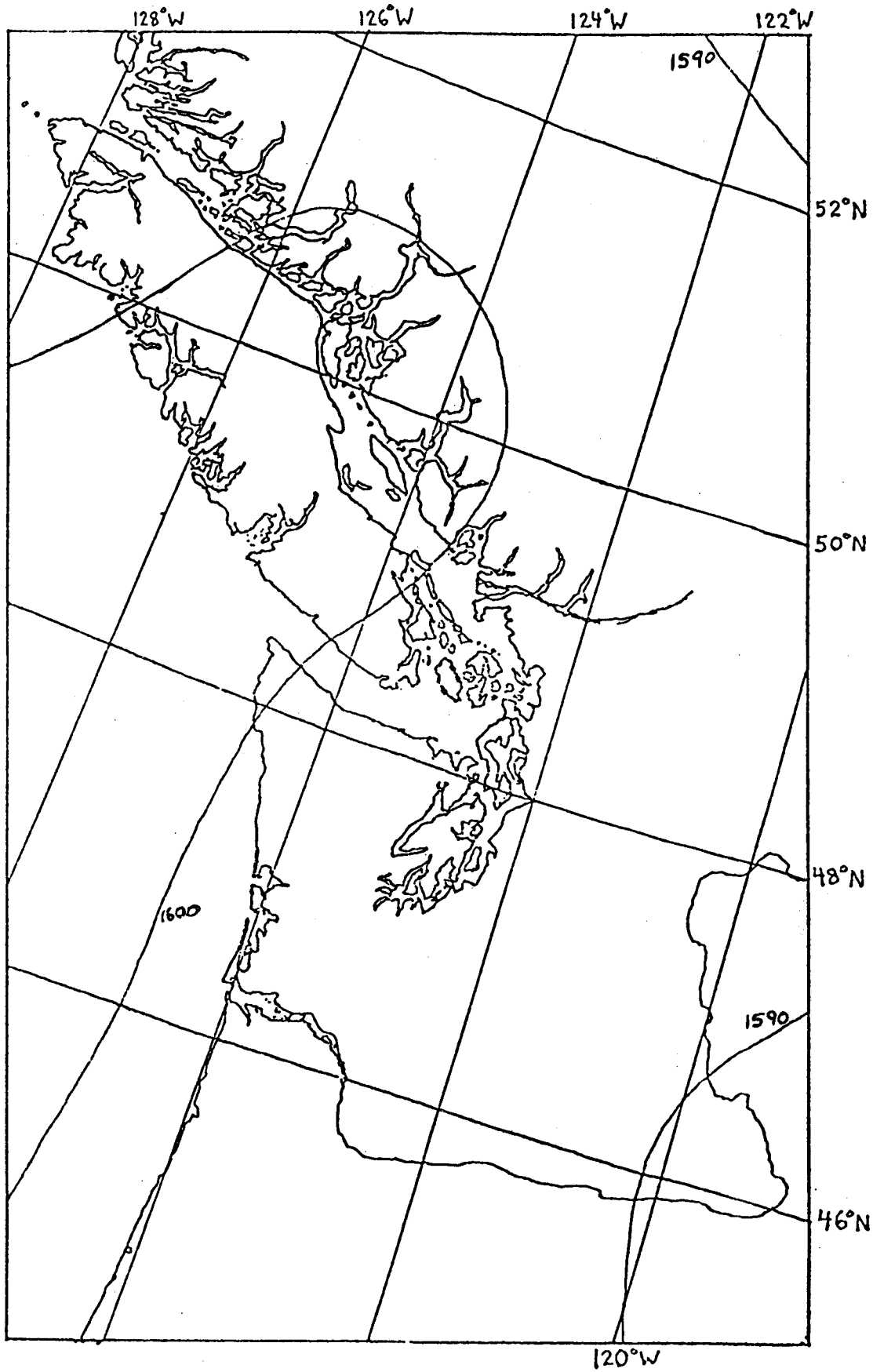


Figure 15.

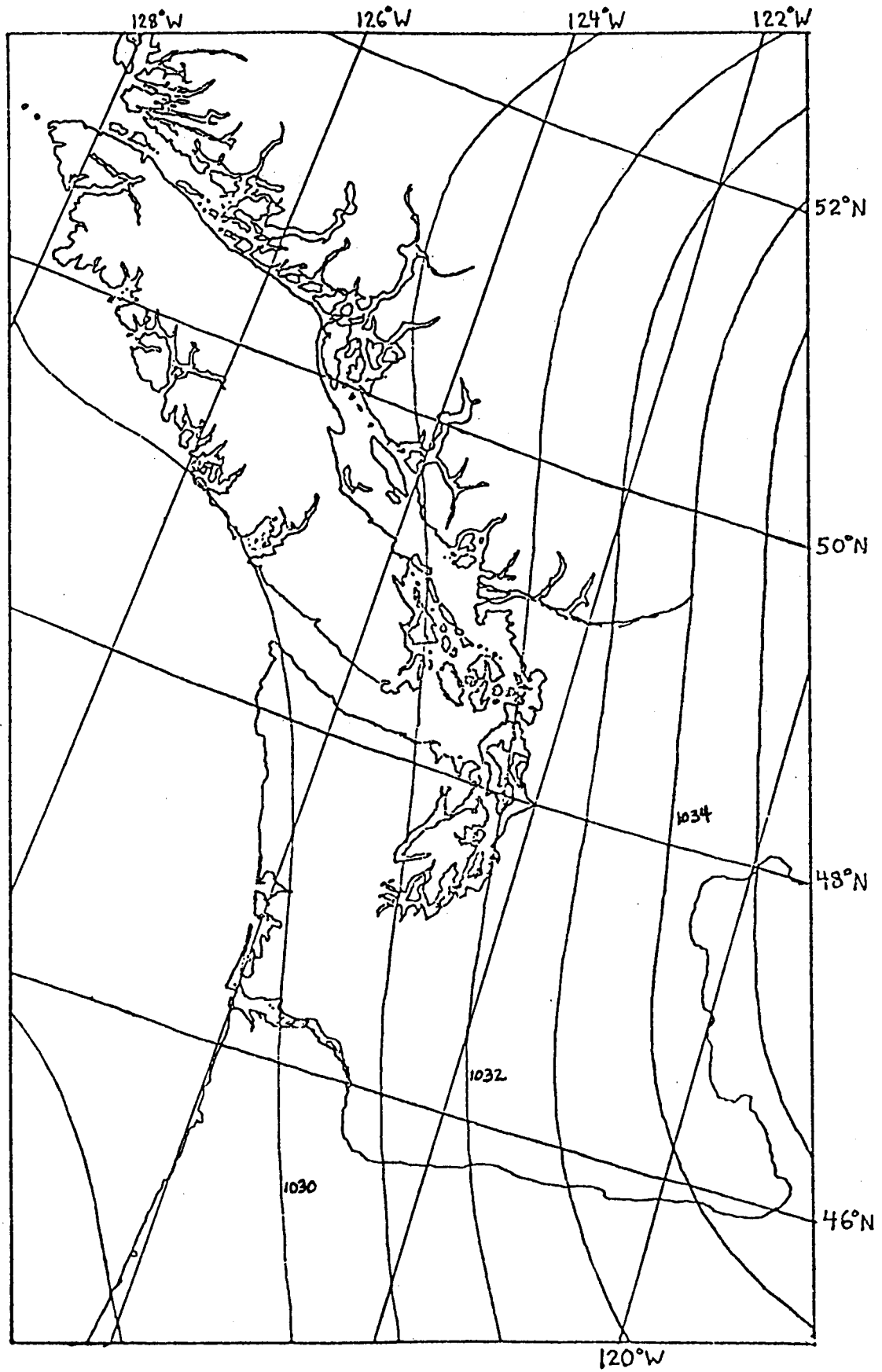


Figure 16.

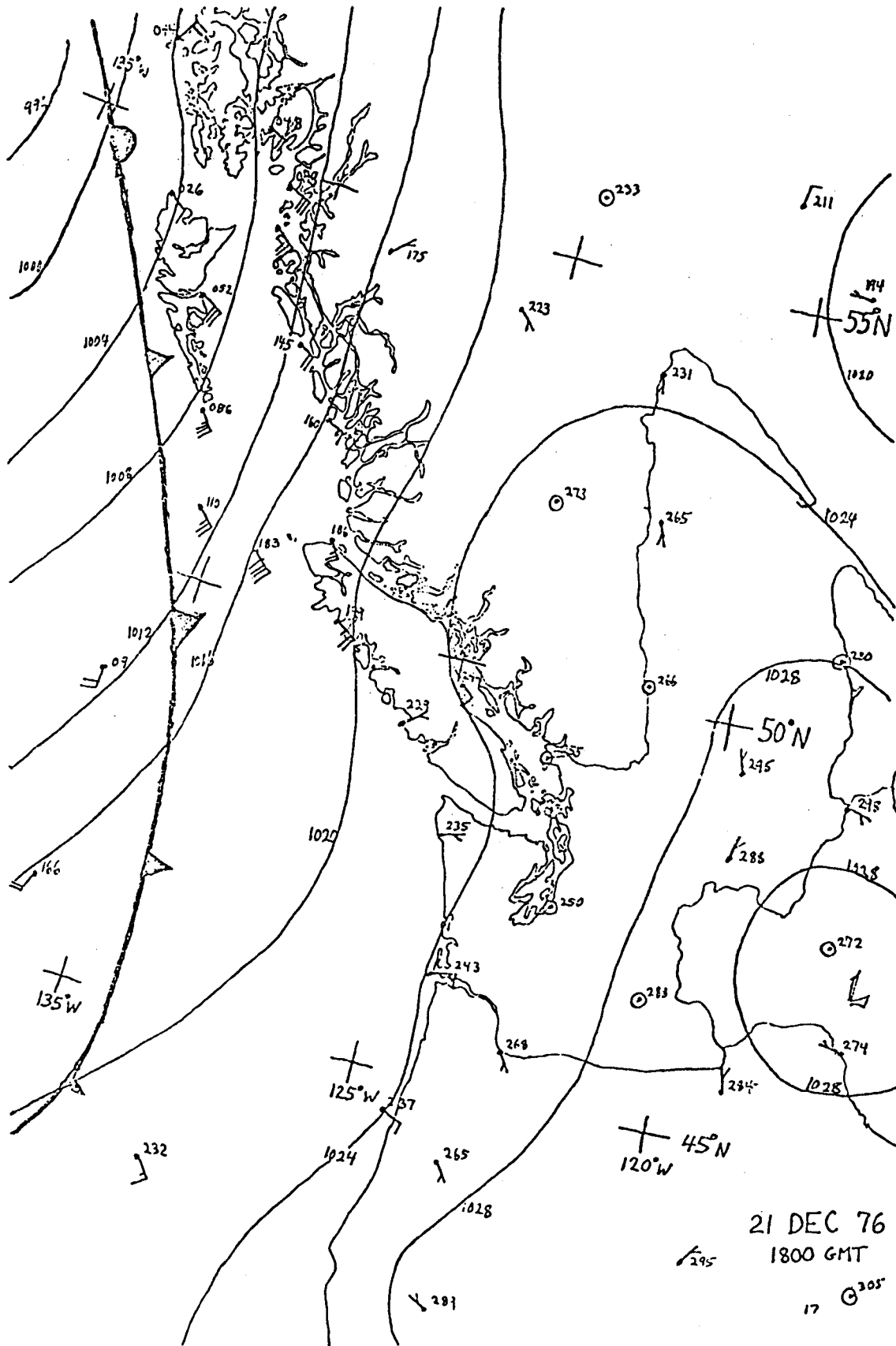


Figure 17.

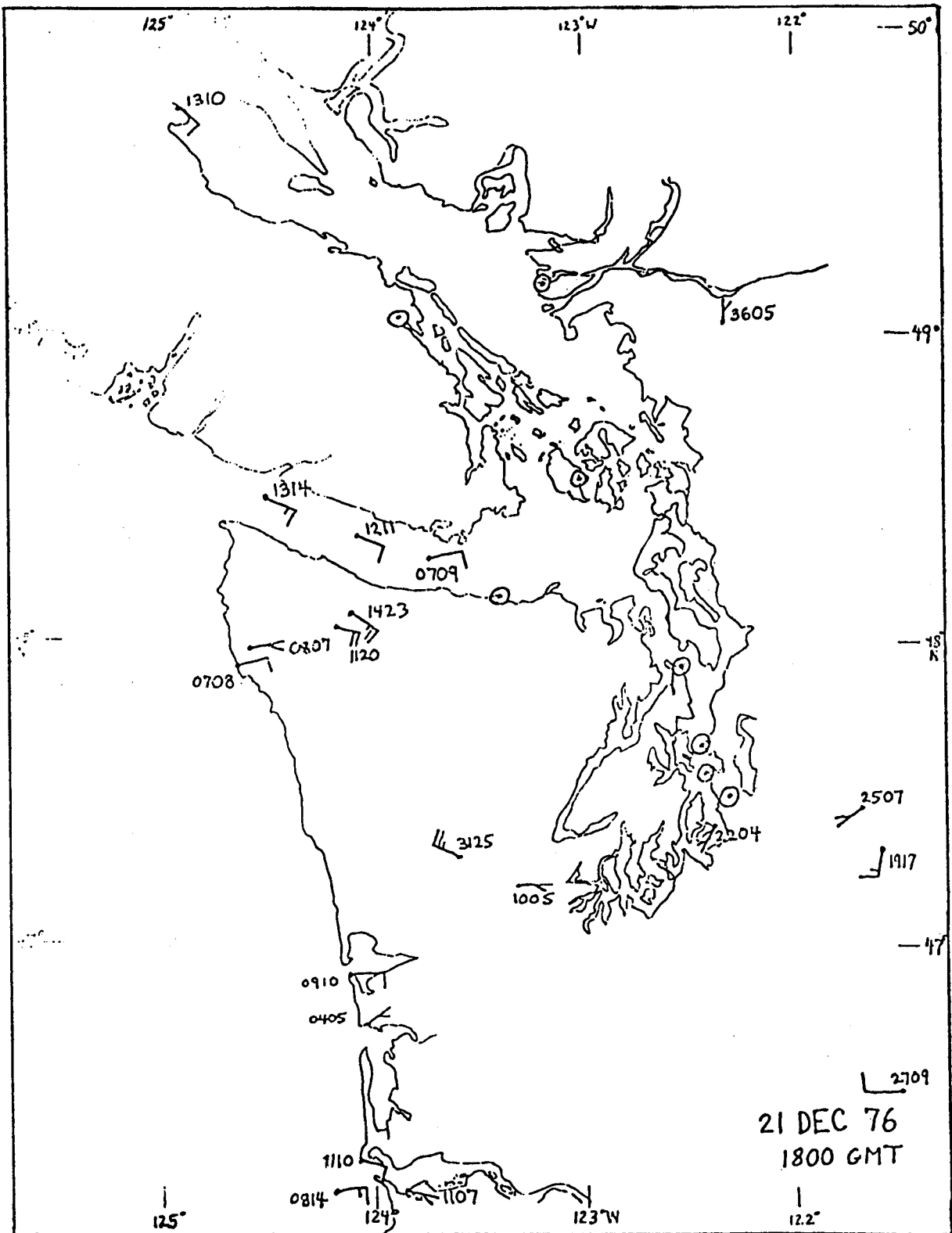
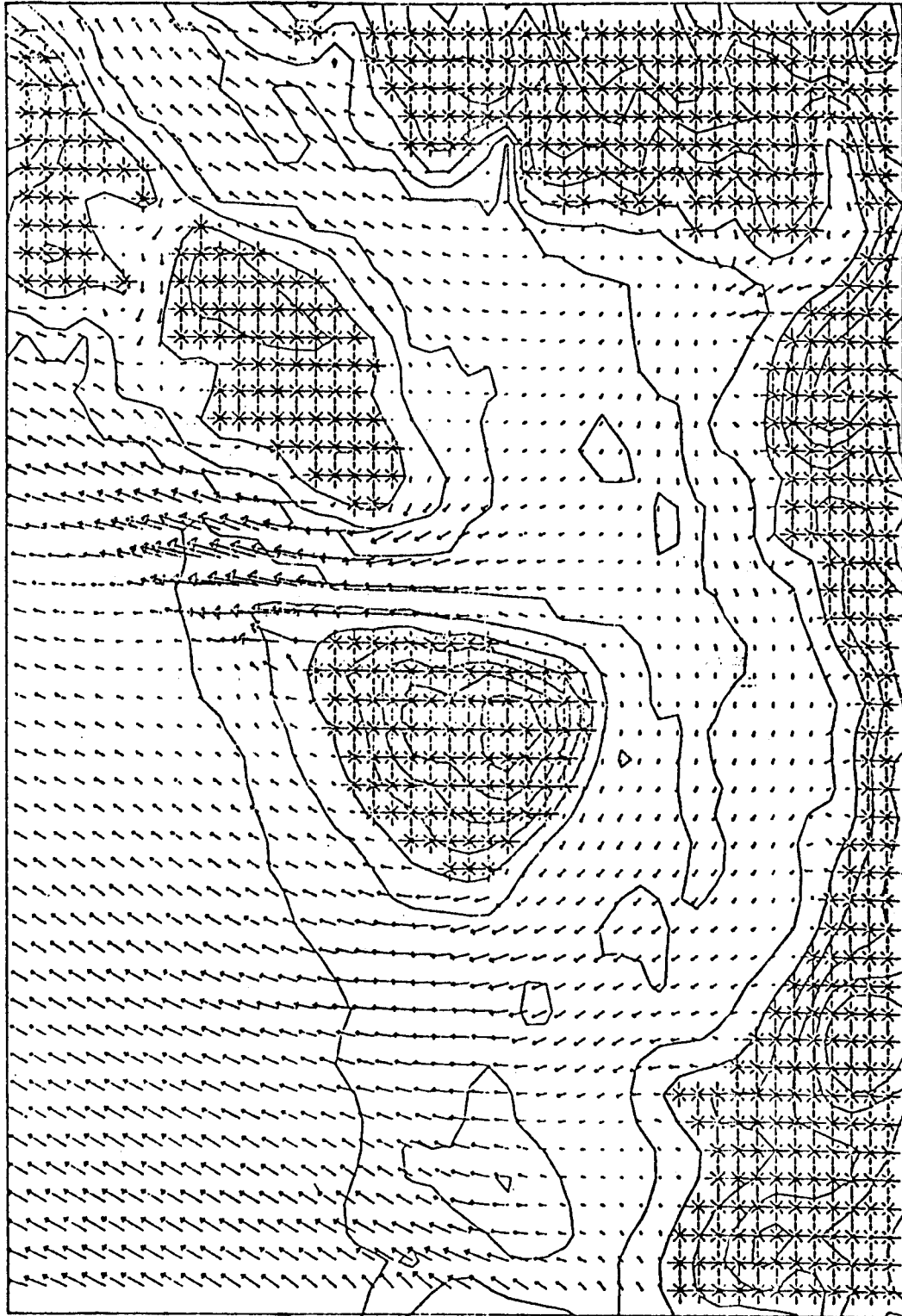


Figure 18.

VELOCITY VECTOR PLOT



10 METERS PER SECOND

Figure 19.

VELOCITY VECTOR PLOT

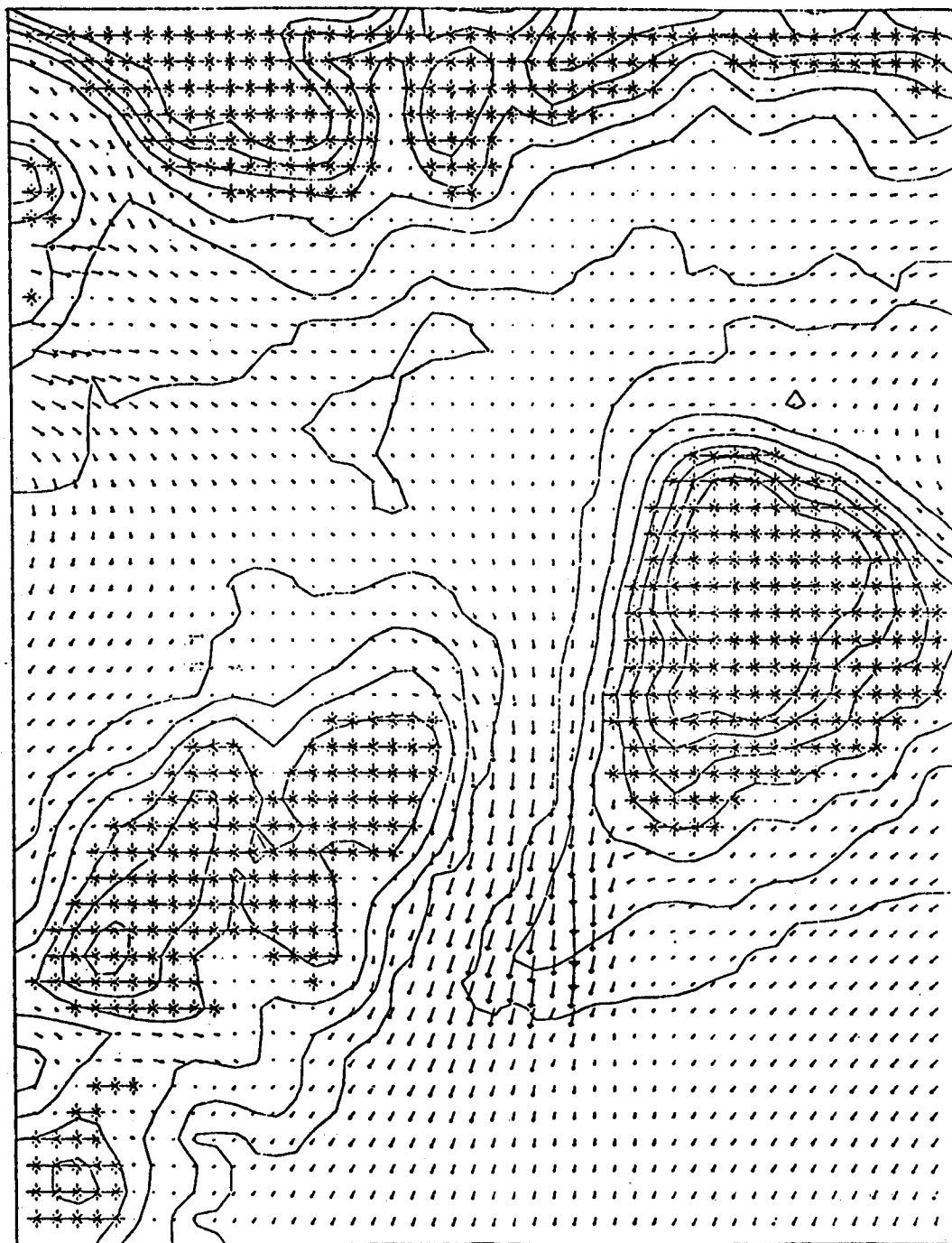


Figure 20.

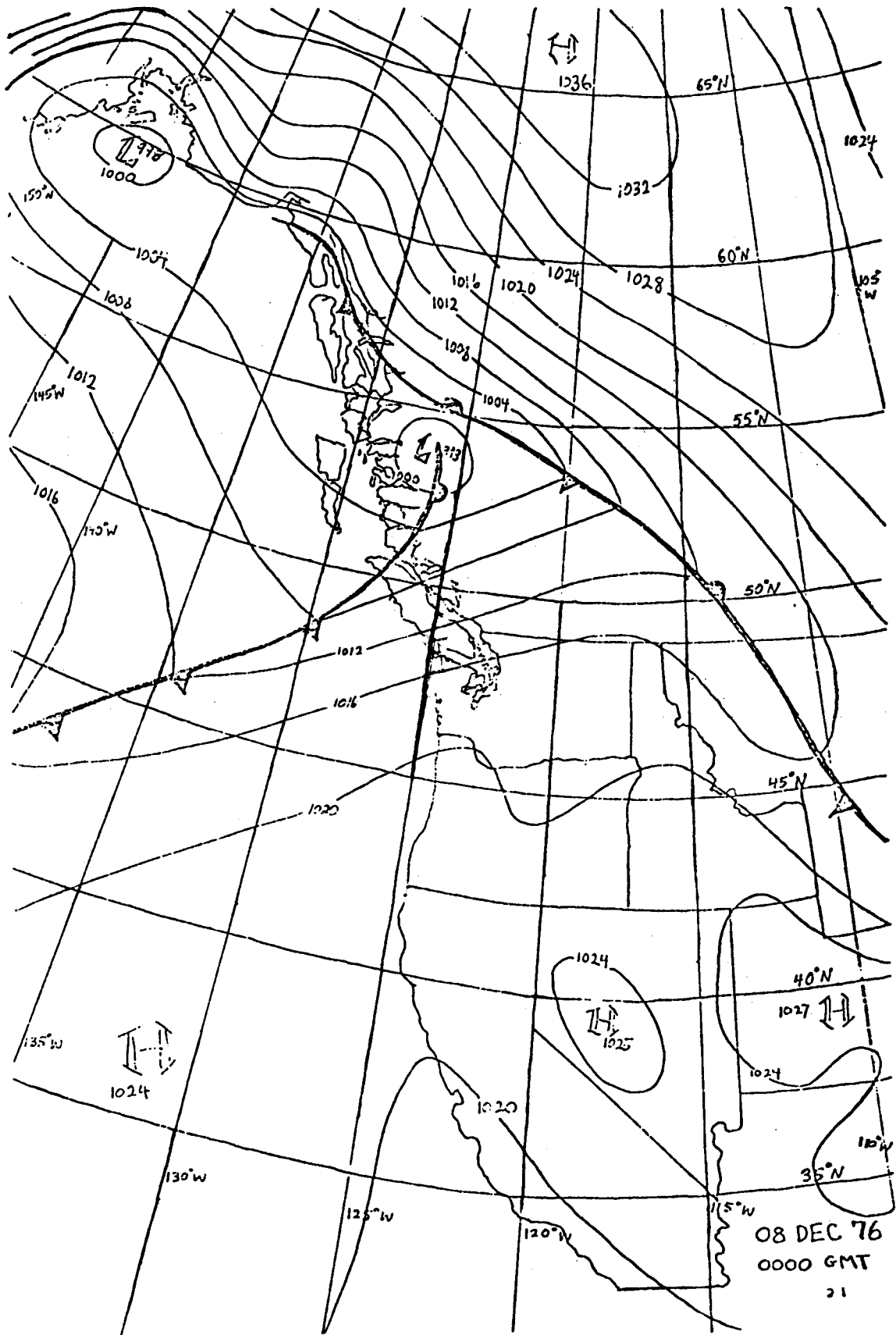


Figure 21.

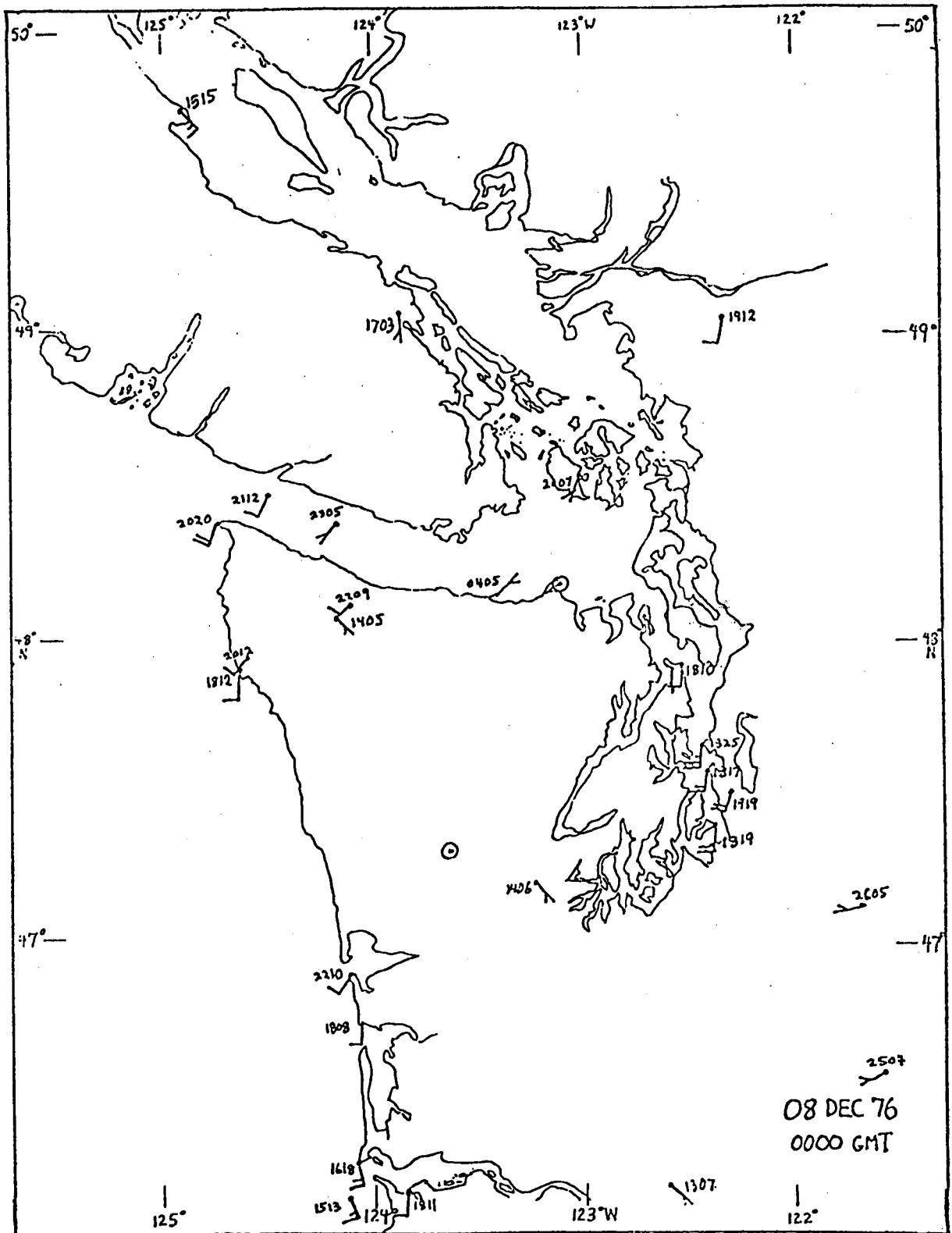


Figure 22.

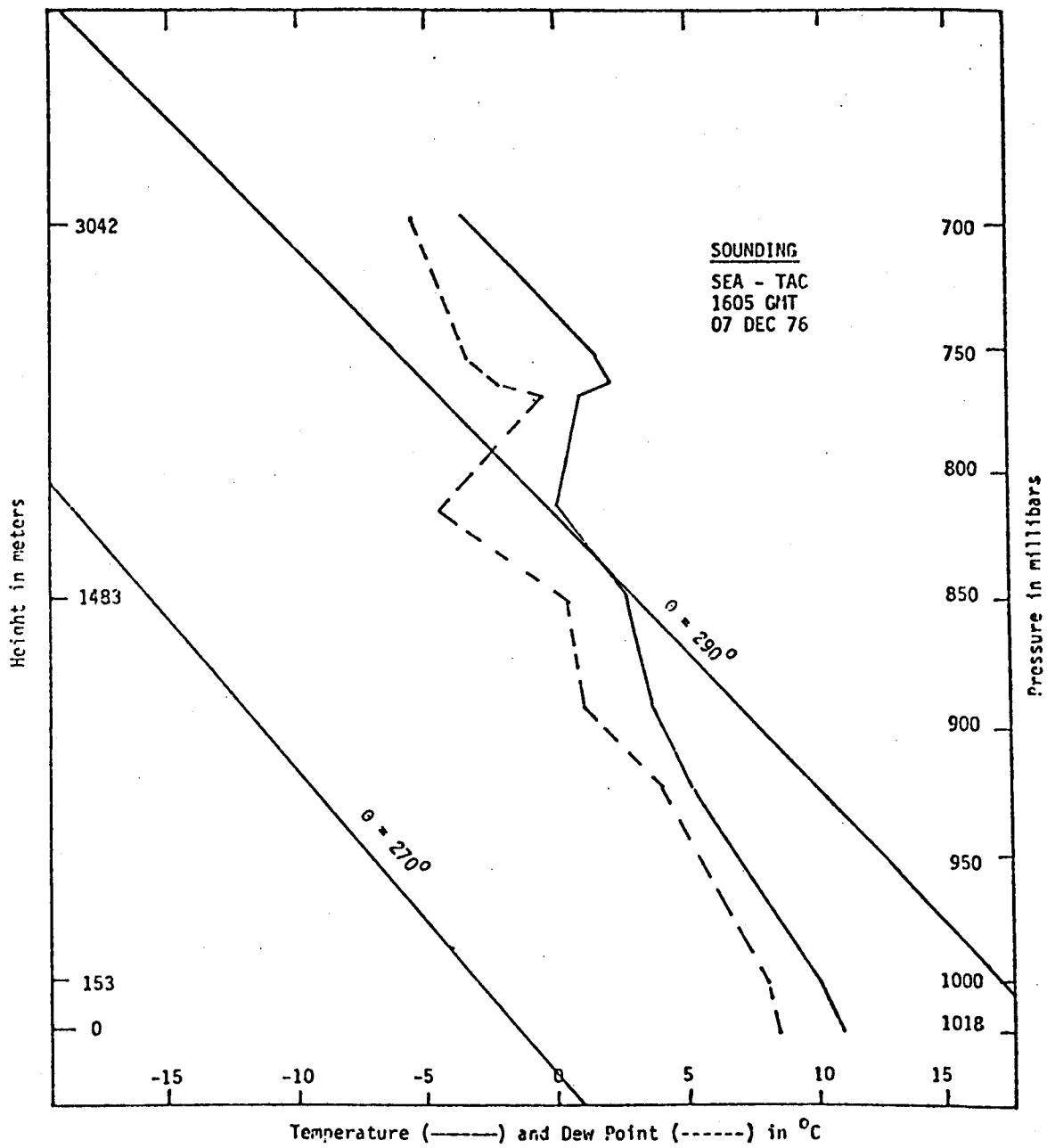


Figure 23.

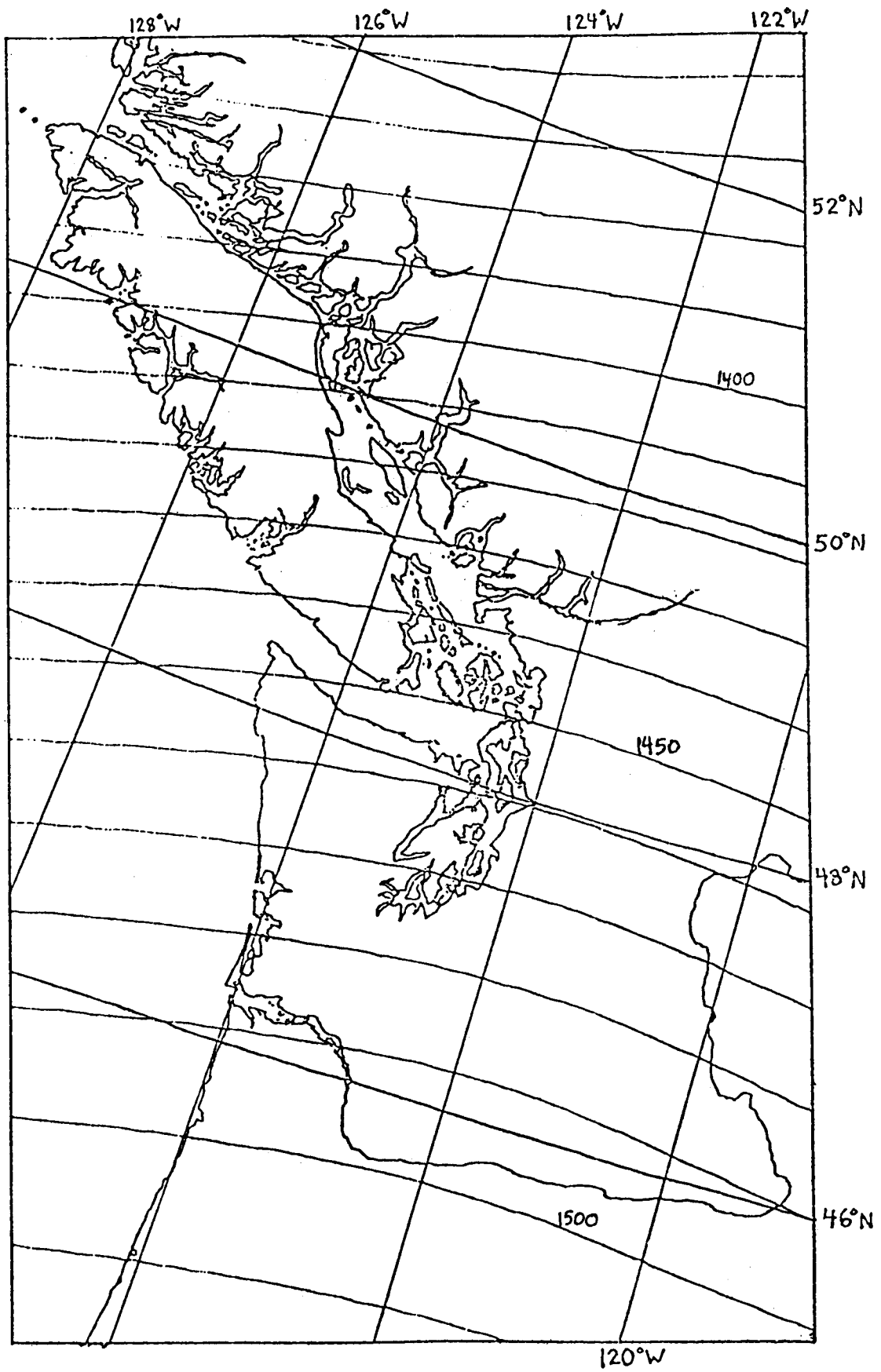


Figure 24.

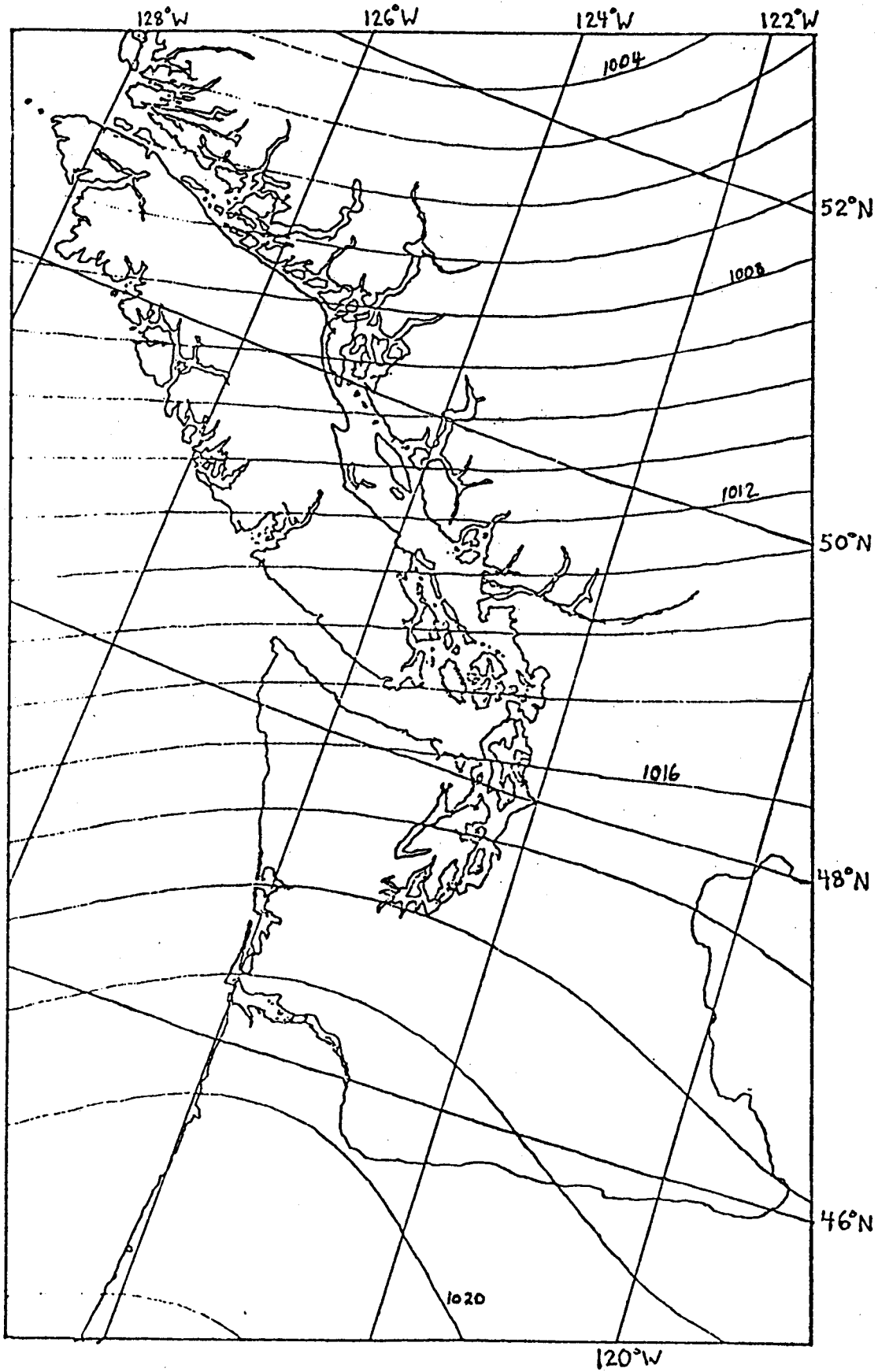


Figure 25.

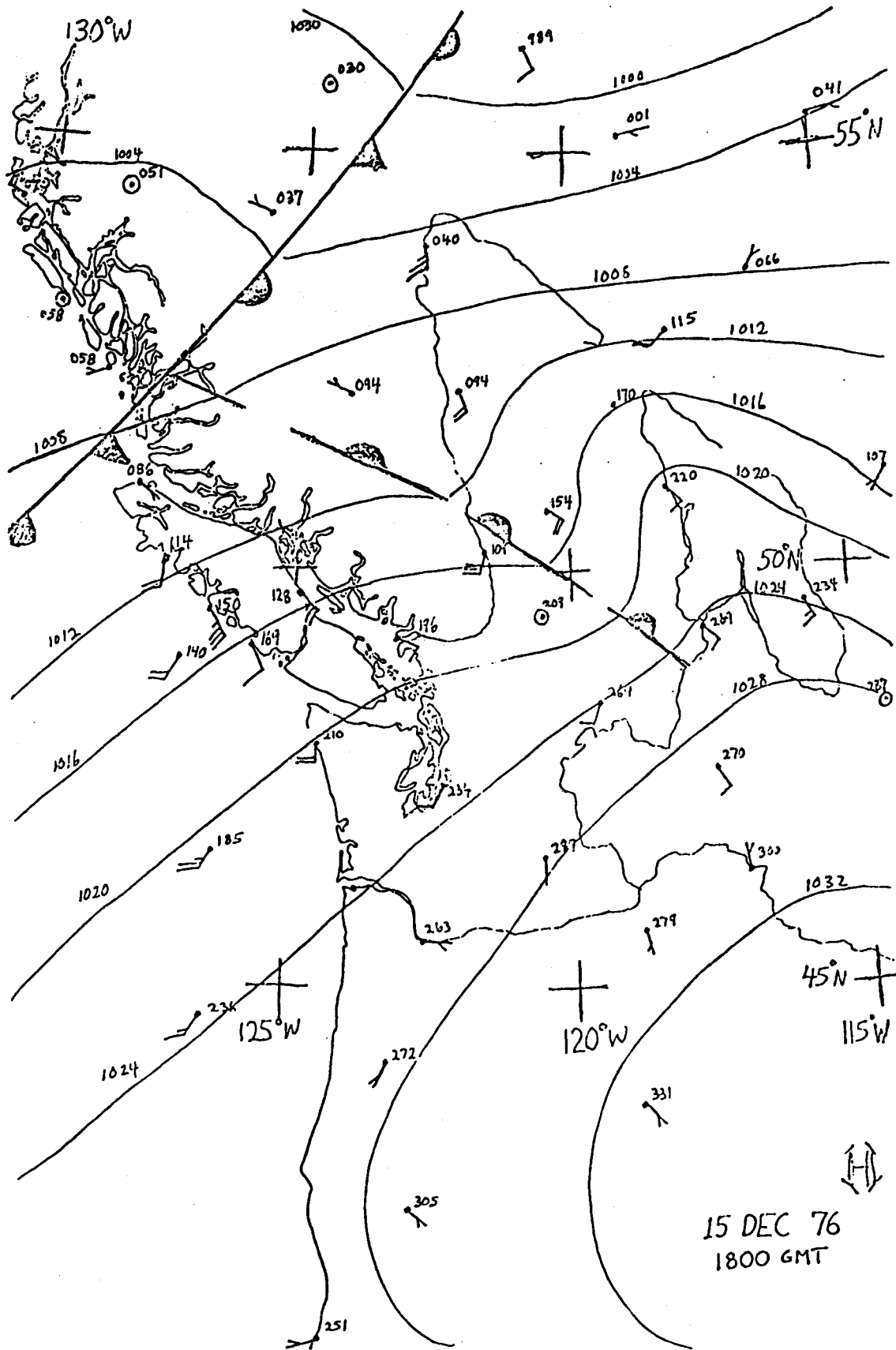


Figure 26.

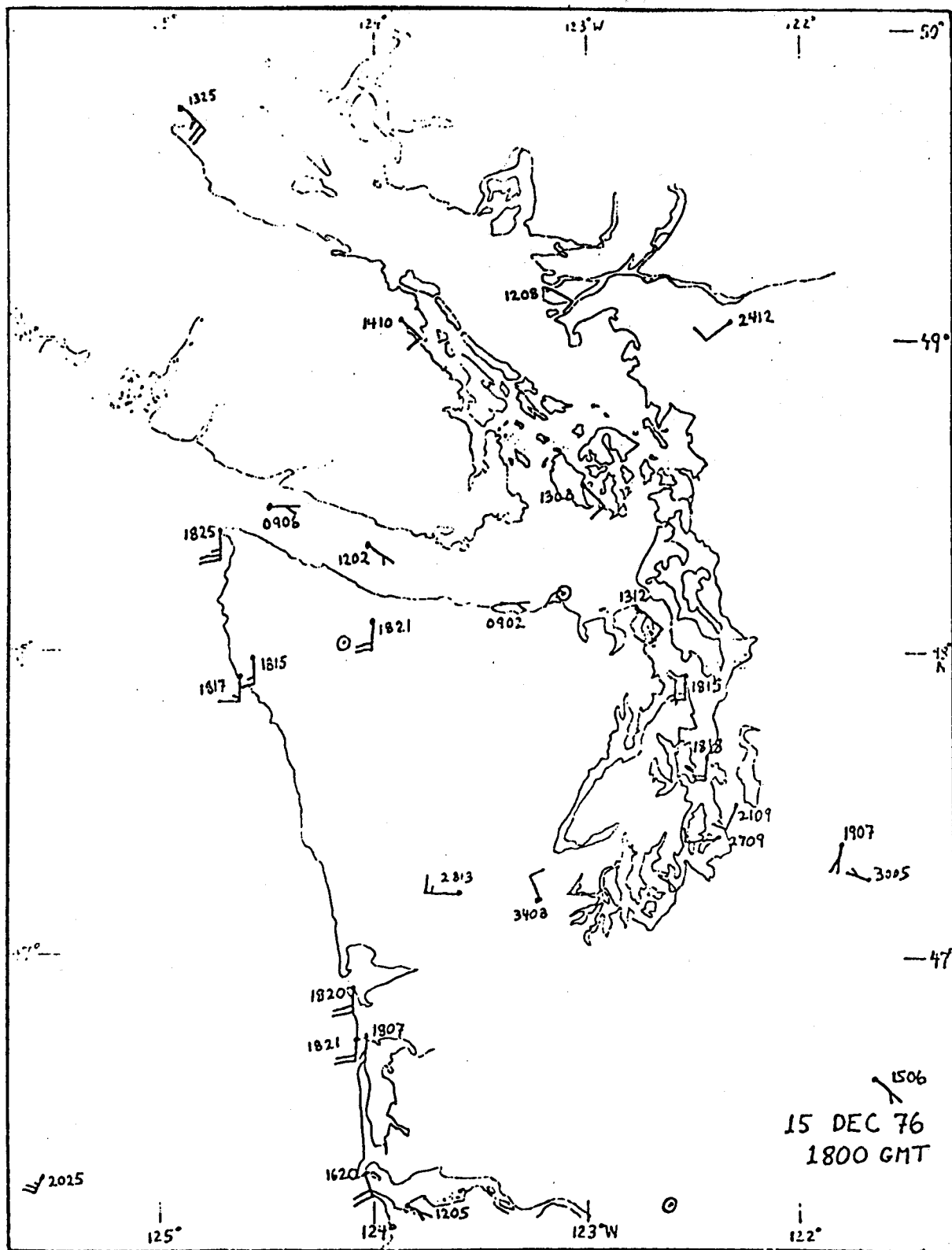
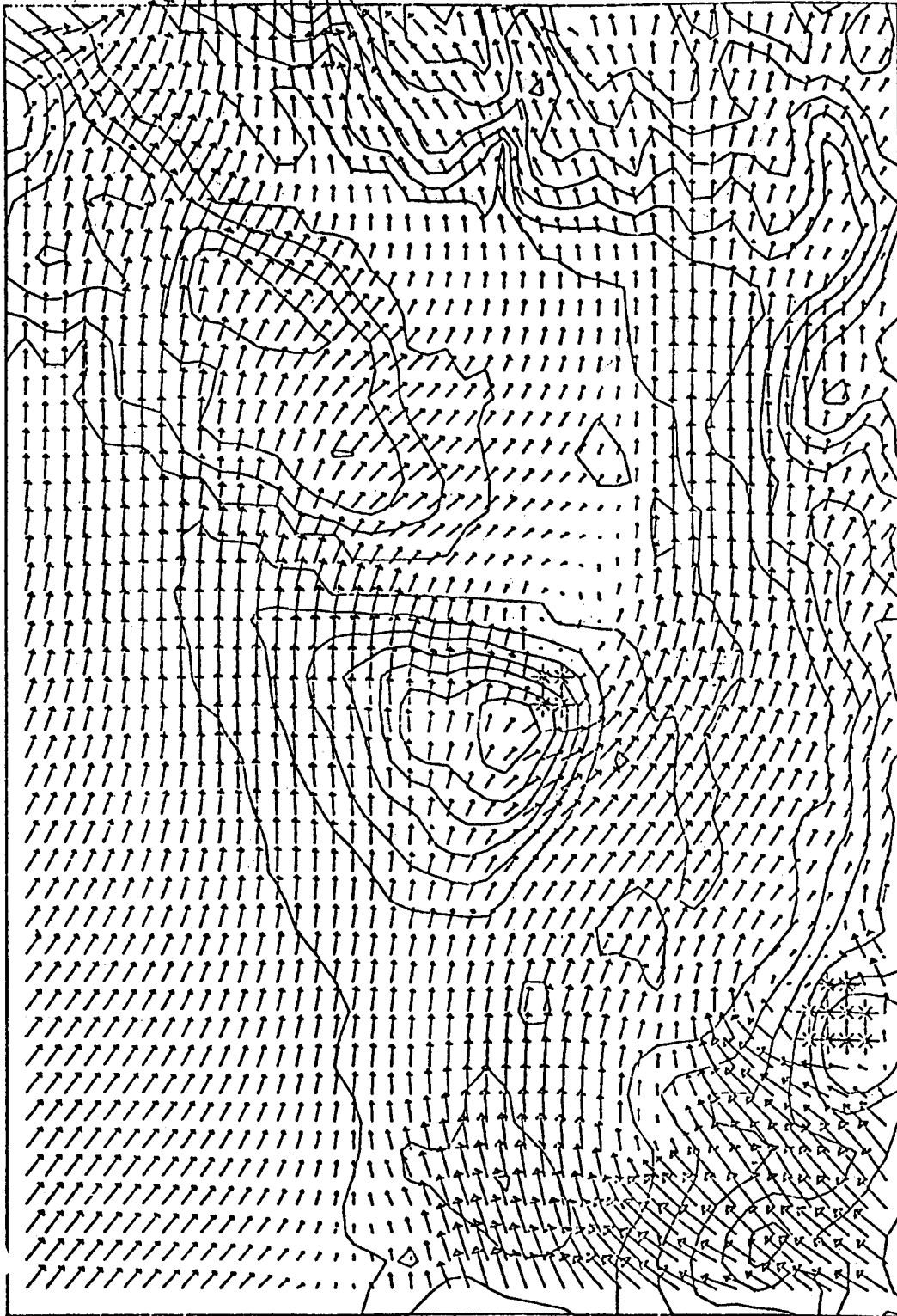


Figure 27.

VELOCITY VECTOR PLOT

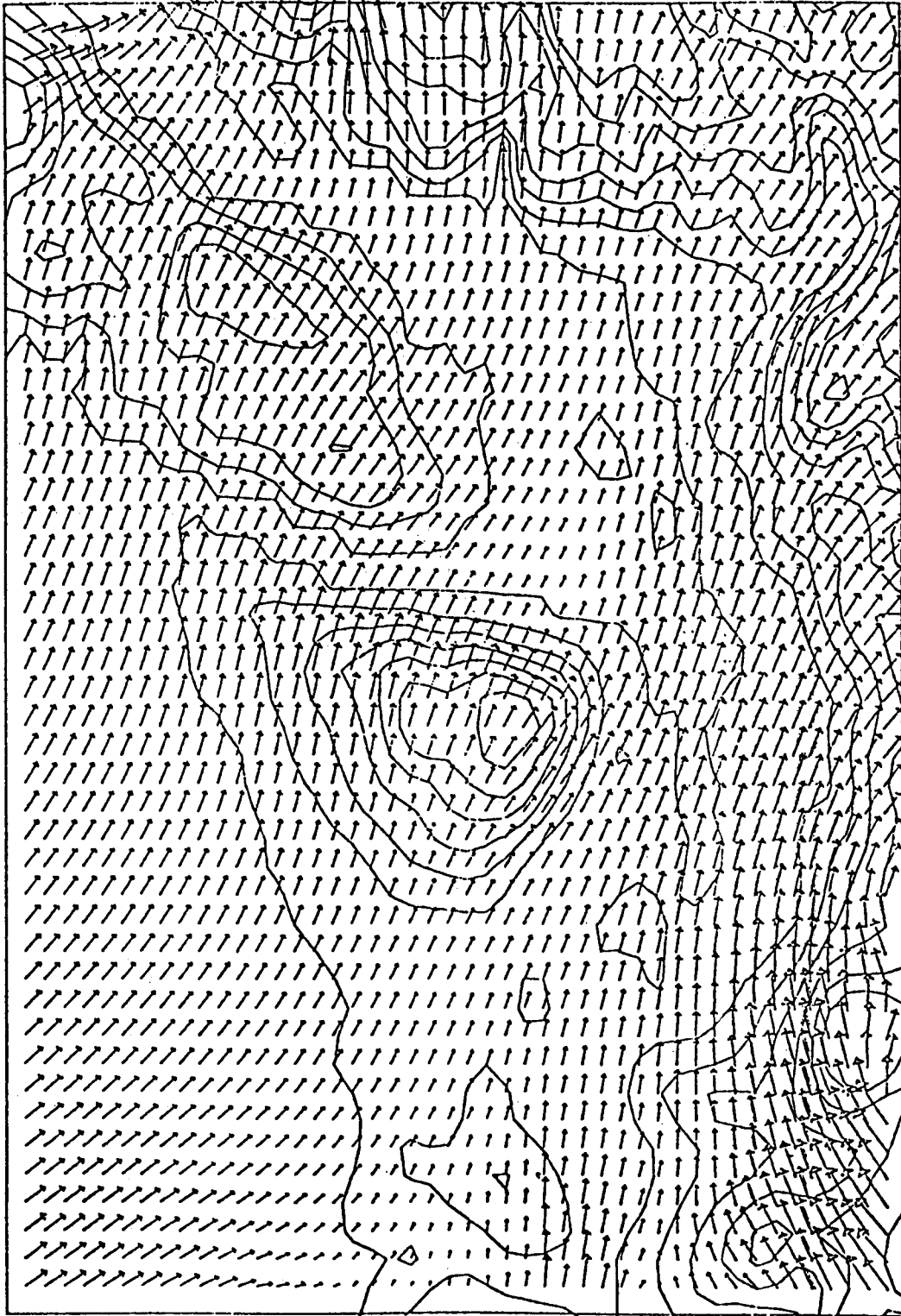


→

10 METERS PER SECOND

Figure 28.

VELOCITY VECTOR PLOT



10 METERS PER SECOND

Figure 29.

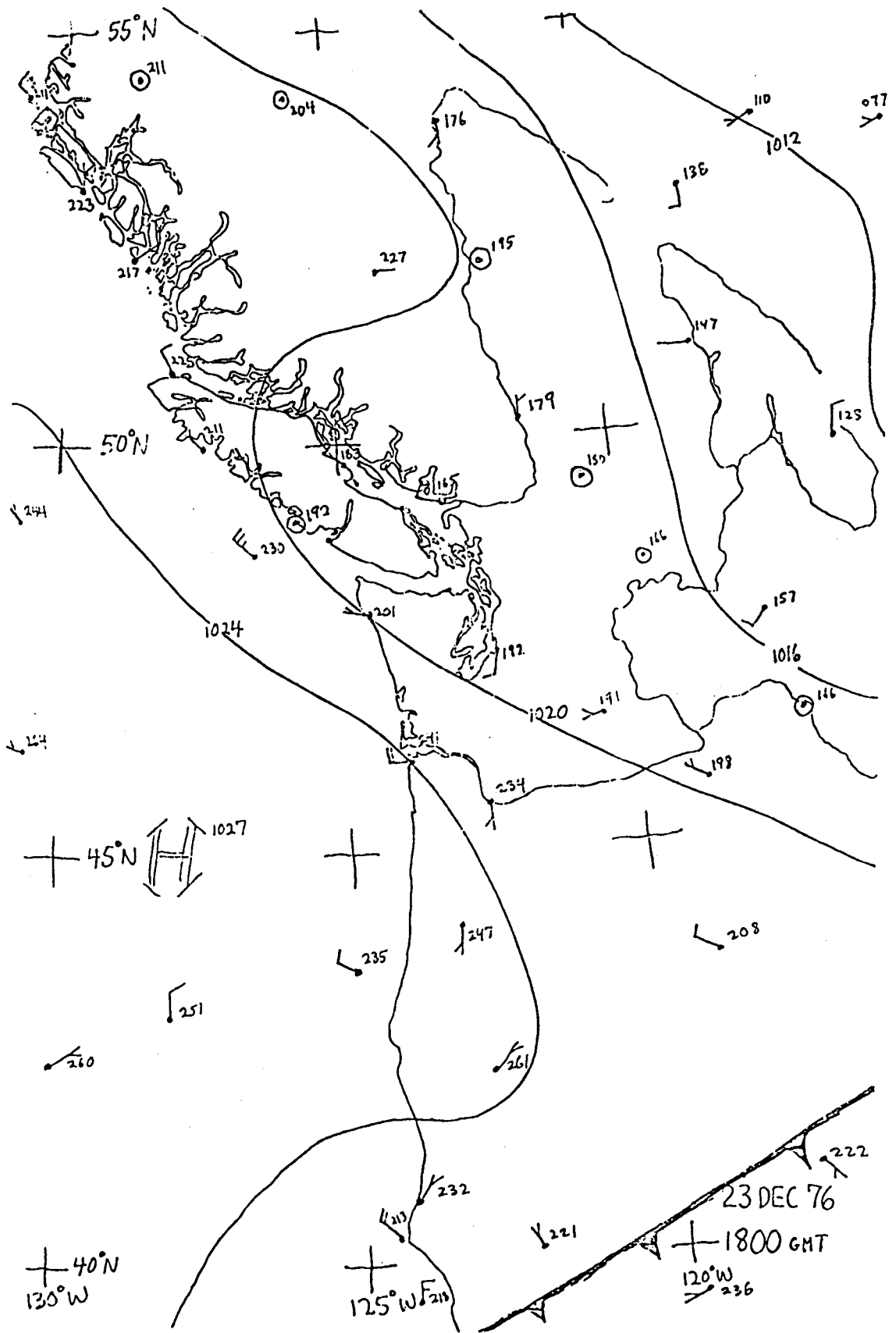


Figure 30.

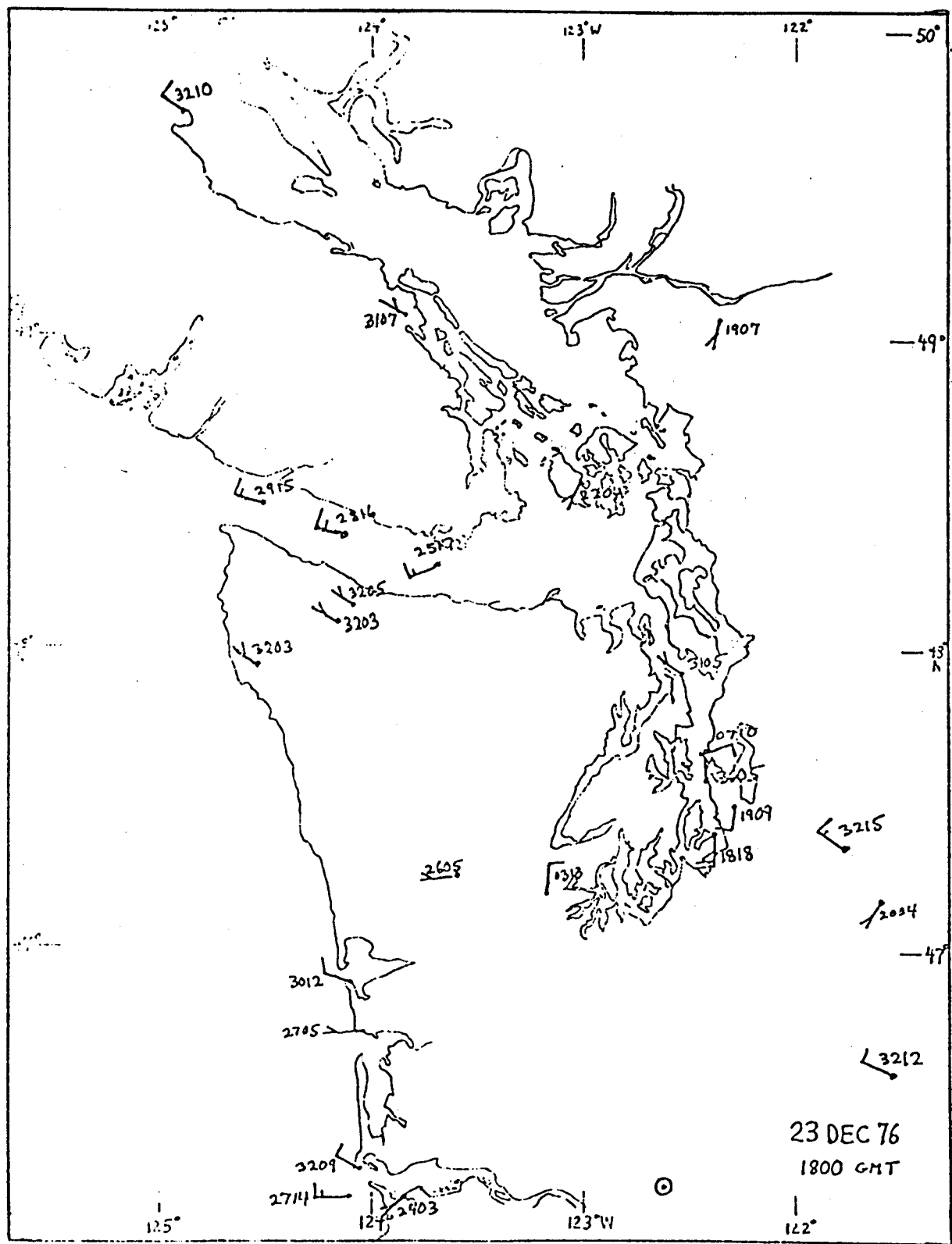


Figure 31.

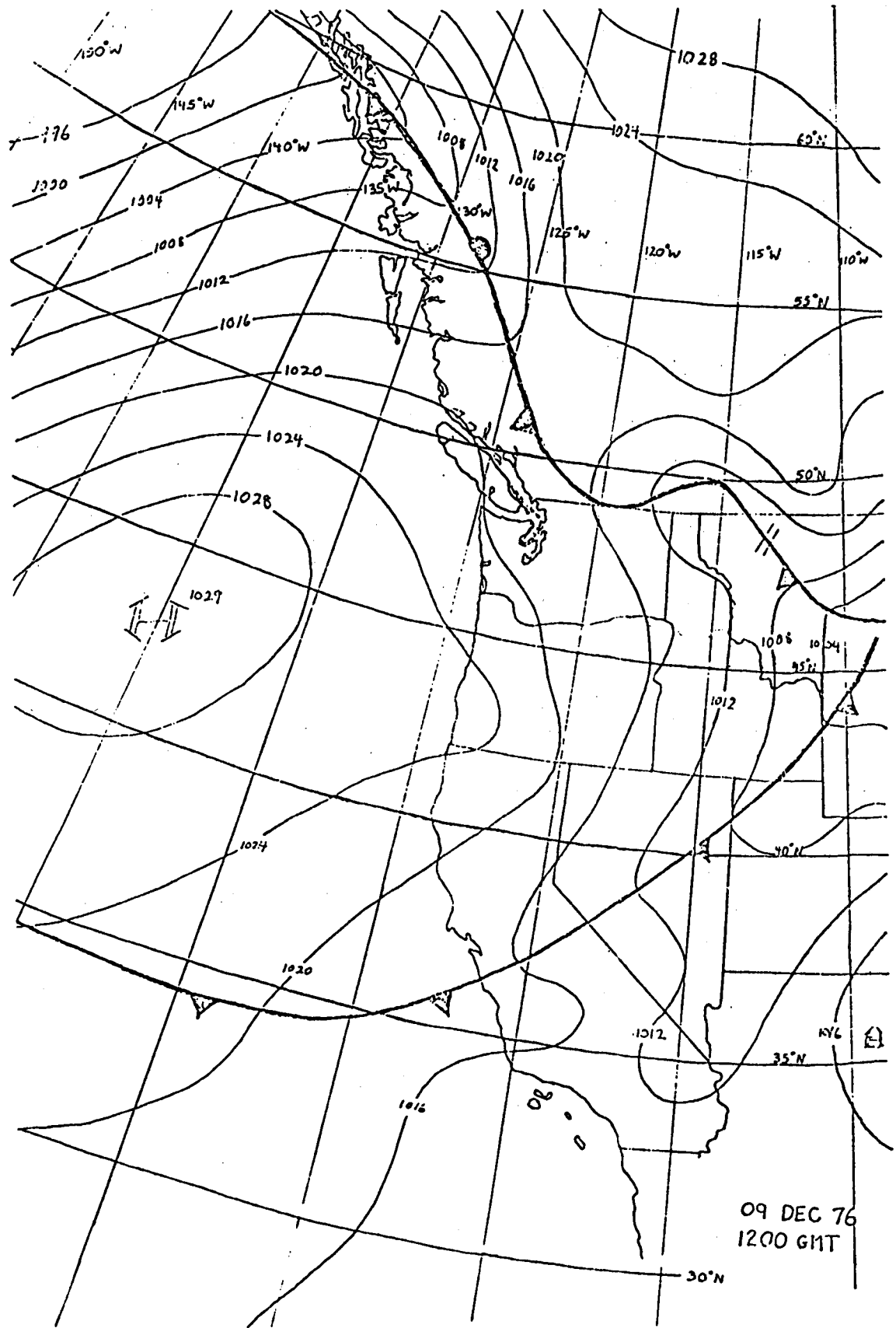


Figure 32.

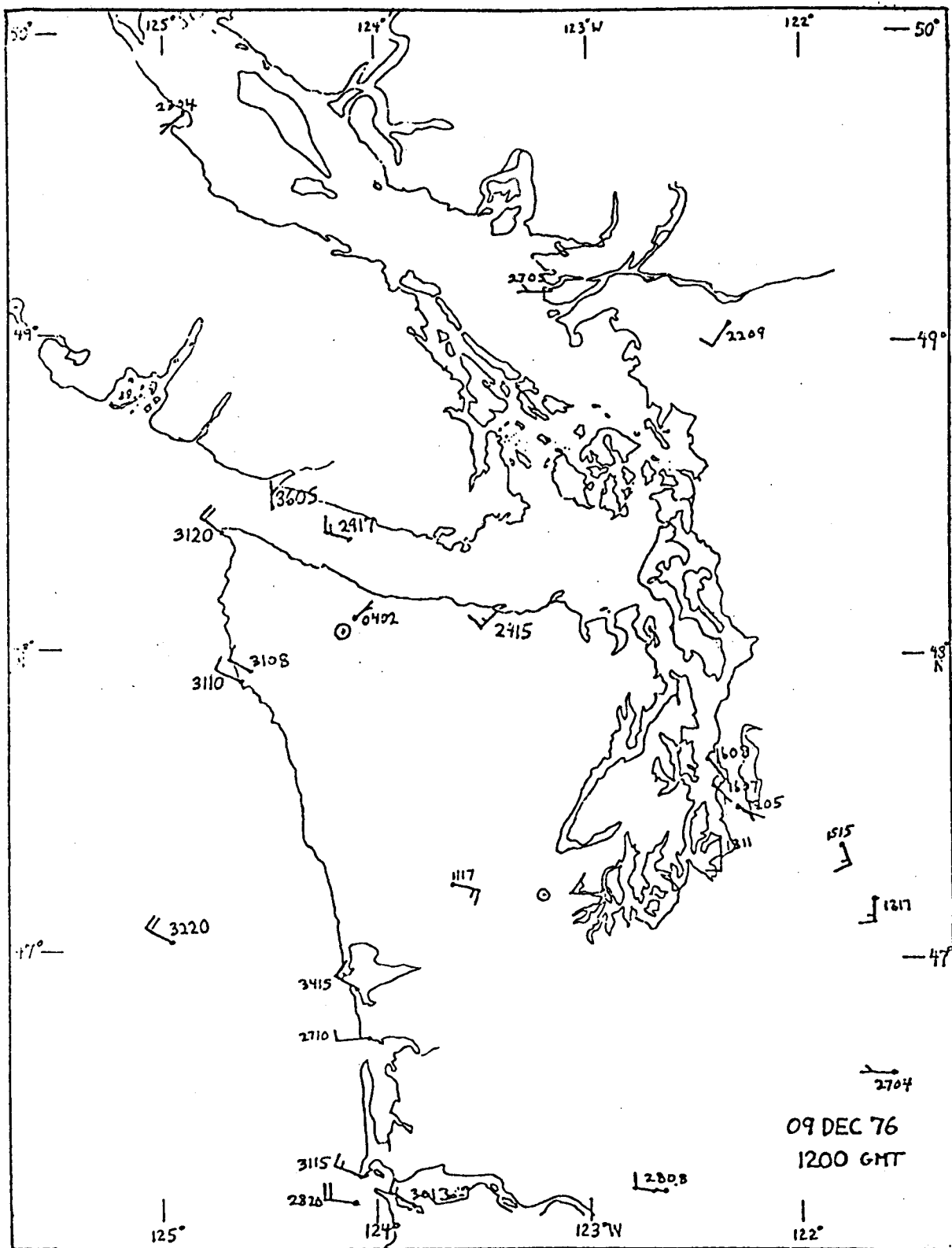


Figure 33.

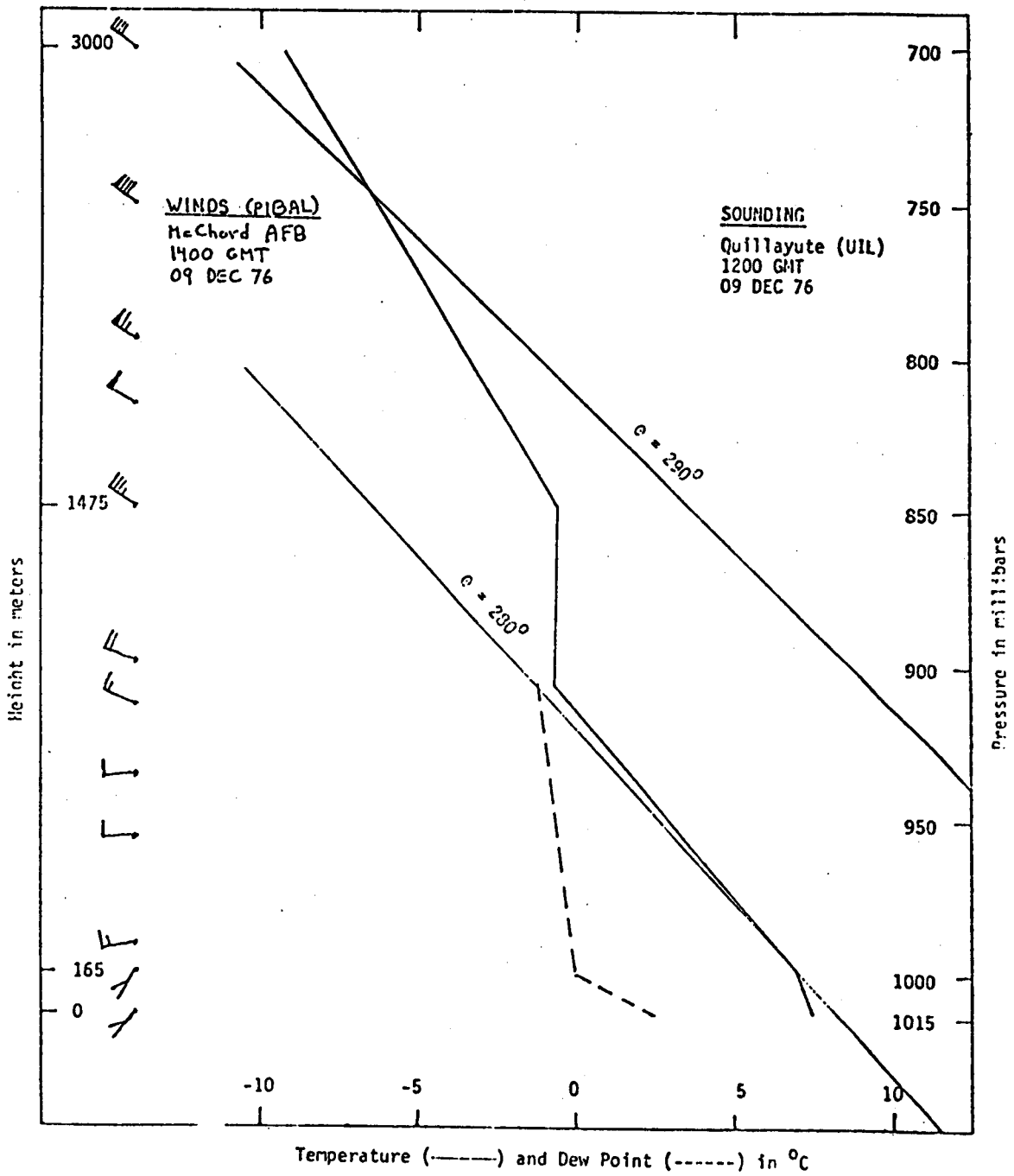


Figure 34.

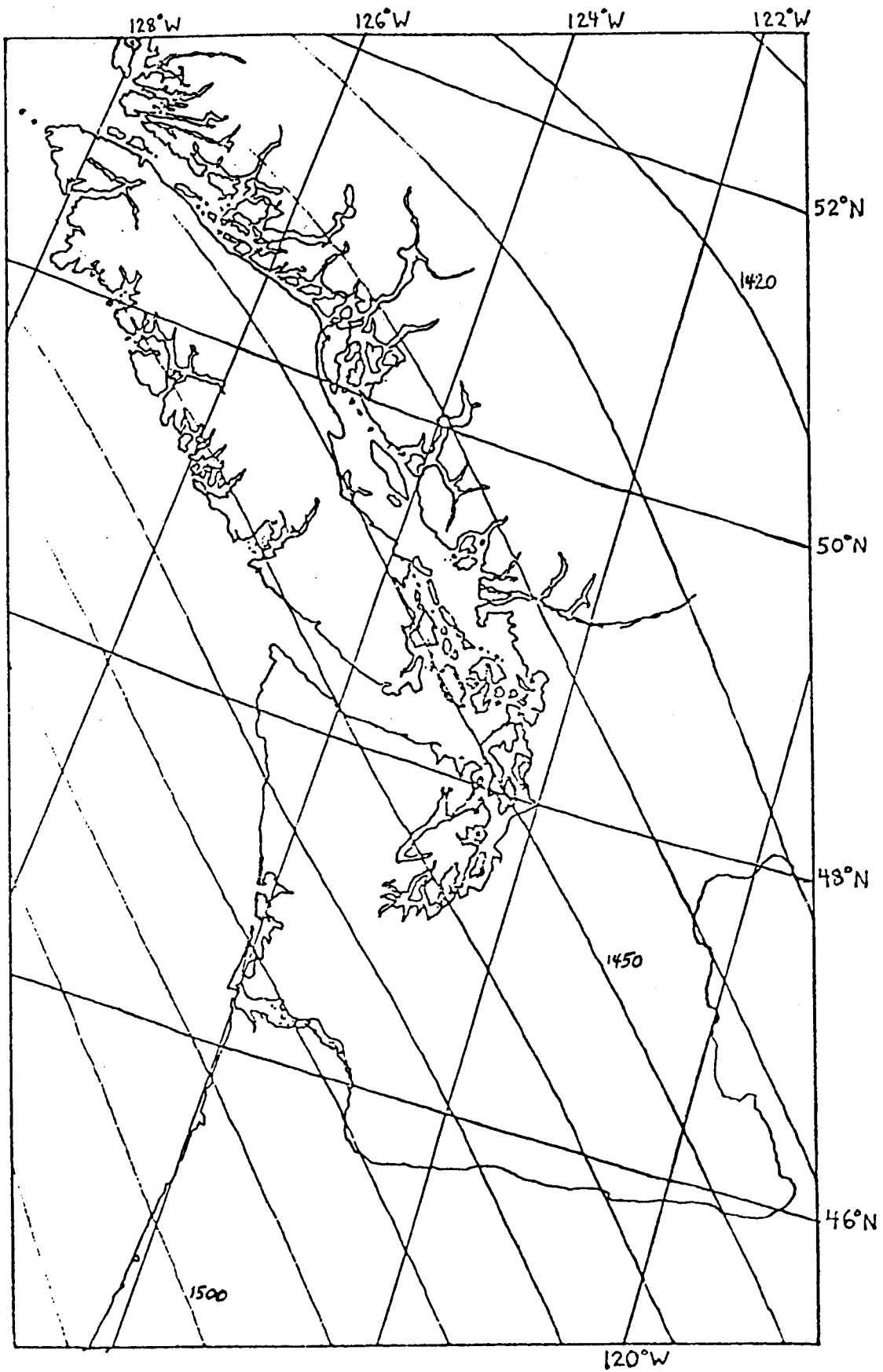


Figure 35.

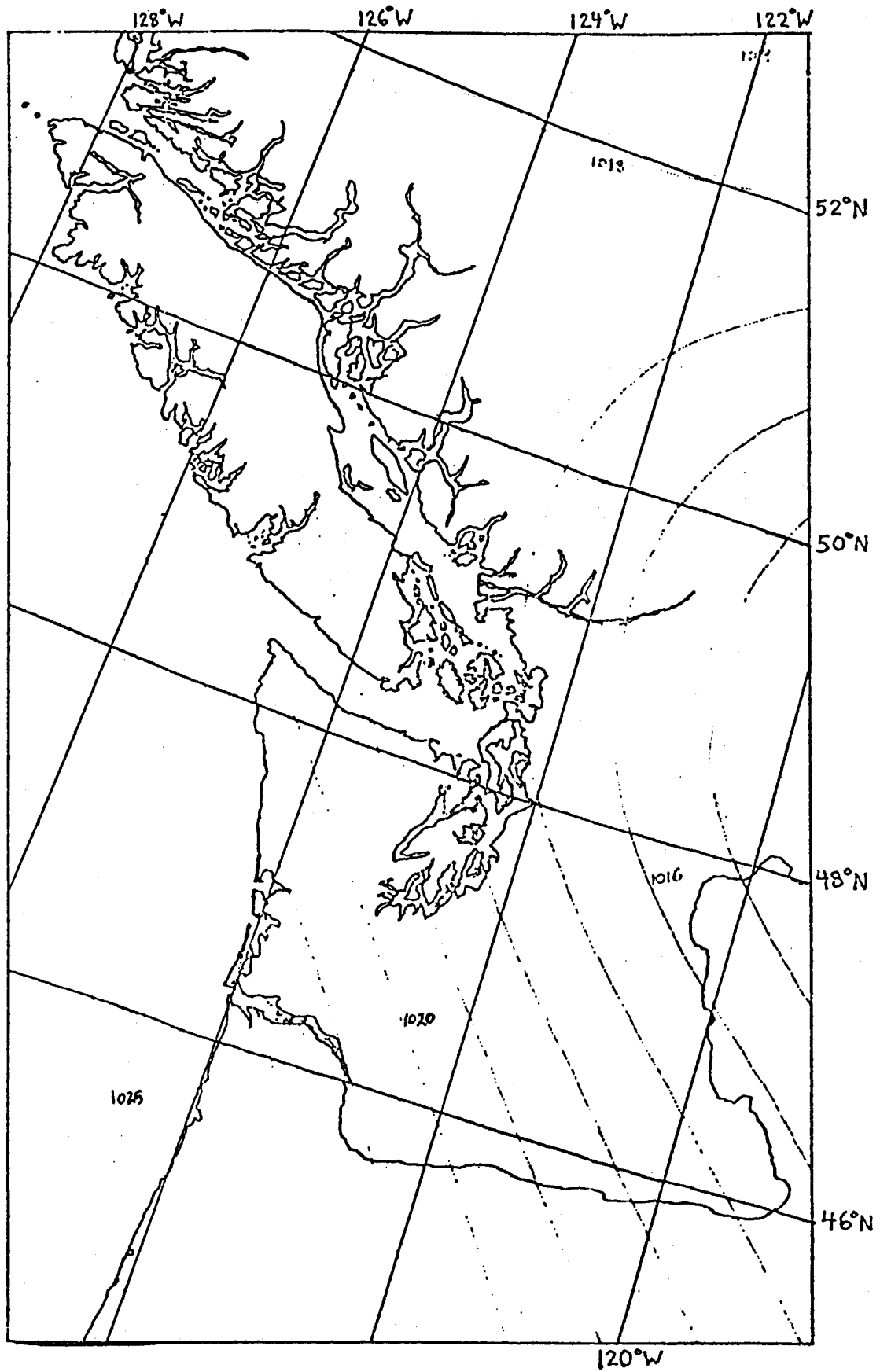
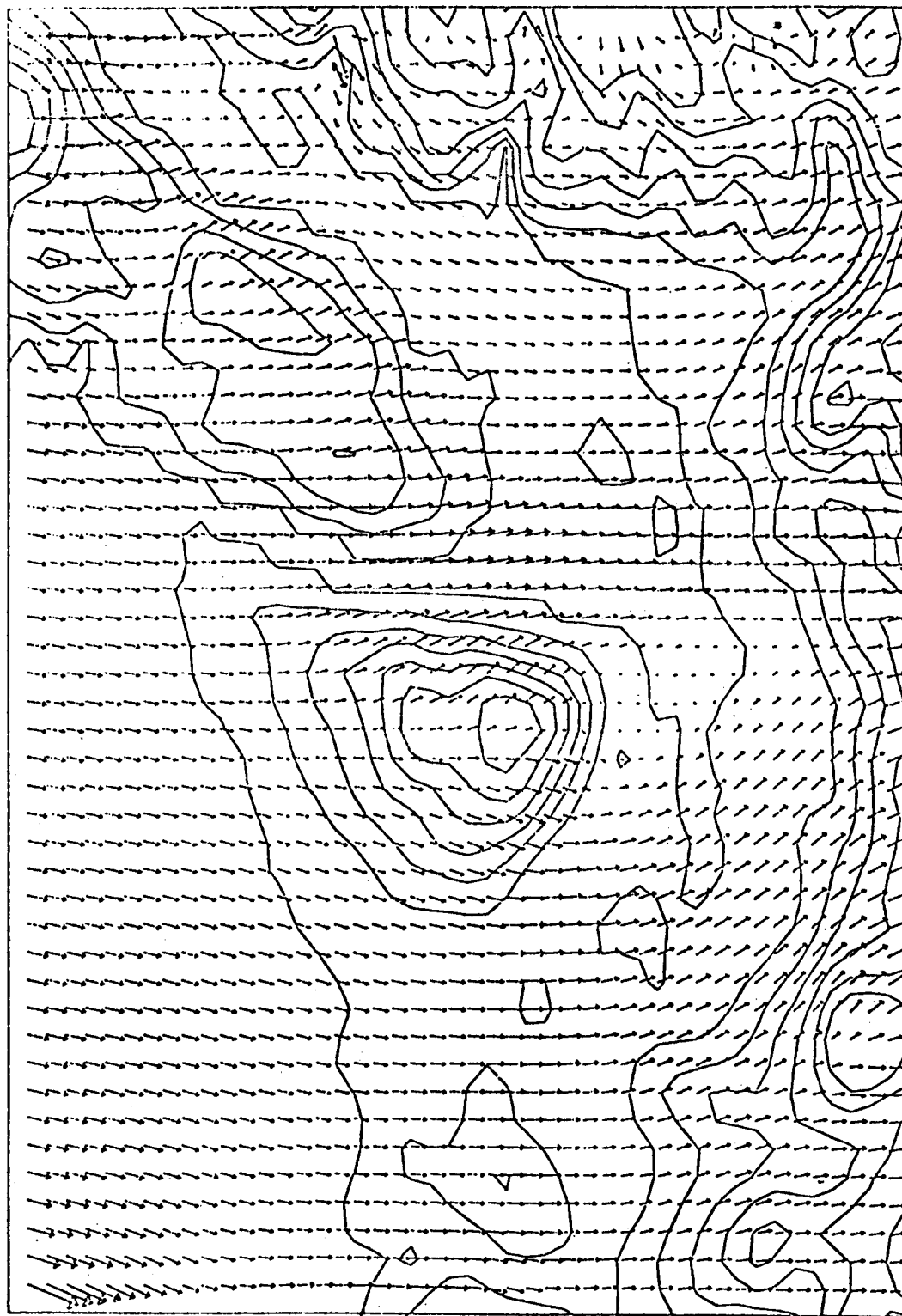


Figure 36.

VELOCITY VECTOR PLOT



→

10 METERS PER SECOND

Figure 37.

APPENDIX F

A Numerical Investigation of the Bering Sea
Circulation Using a Linear Homogenous Model

by

Y.-J. Han* and J. A. Galt

(Contribution No. 375 from the NOAA/ERL
Pacific Marine Environmental Laboratory.)

September 1978

*Present affiliation: Department of Atmospheric Sciences
Oregon State University,
Corvallis, OR 97331

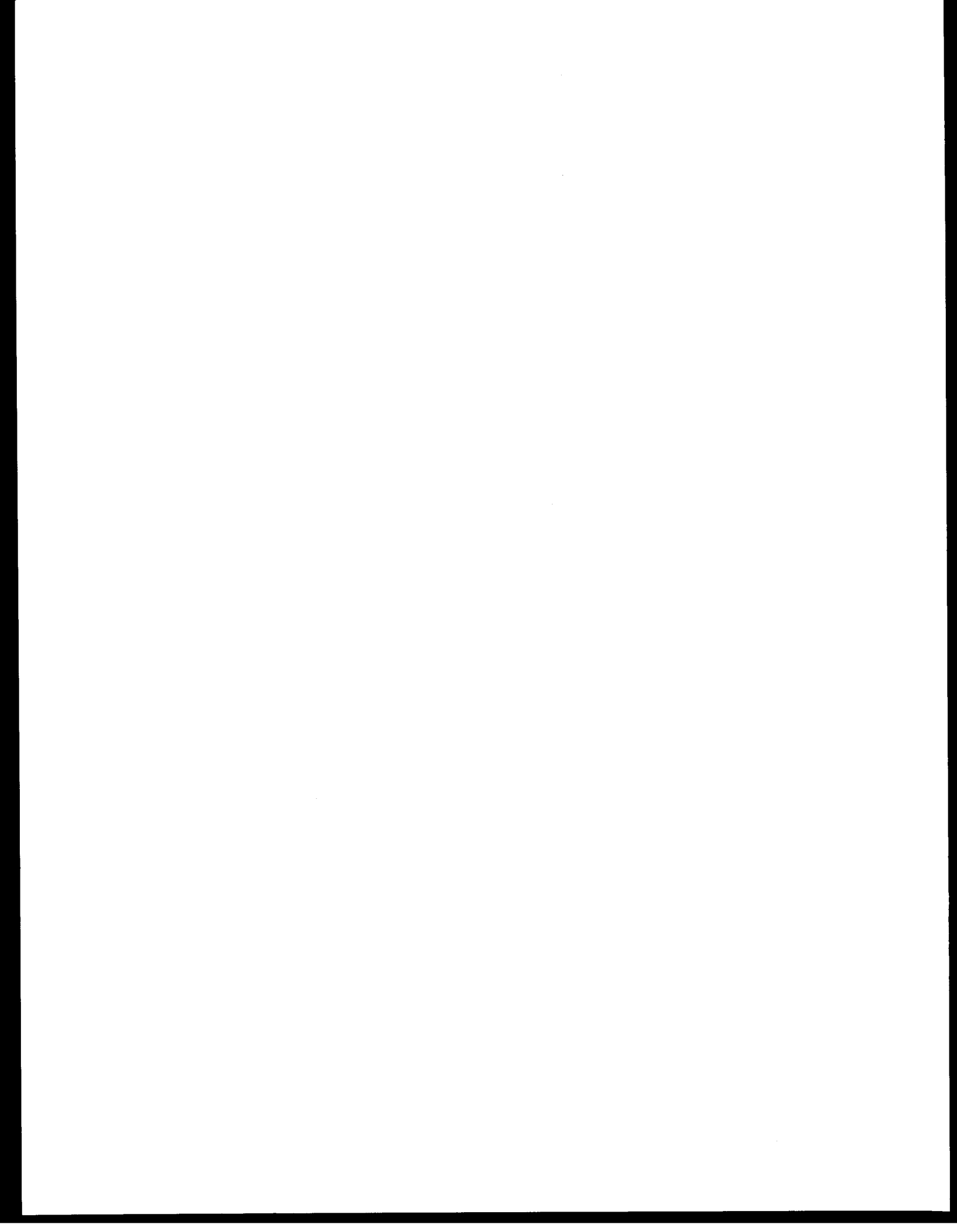


TABLE OF CONTENTS

	Page
ABSTRACT.	699
1. INTRODUCTION.	699
2. THE MATHEMATICAL MODEL AND BOUNDARY CONDITIONS.	702
2.1 The Model.	702
2.2 Surface Wind Stress and Open Boundary Conditions	705
2.3 Numerical Procedures	708
3. RESULTS	713
4. SUMMARY AND SUGGESTIONS	716
5. REFERENCES.	718
TABLE 1	719
FIGURES	720



Abstract. A linear diagnostic model was constructed to simulate the Bering Sea circulation. Monthly mean wind stresses along with lateral water mass exchanges were used as model-forcing functions. The numerical solutions obtained for the case of annual mean wind stress generally agreed with an existing view about the cyclonic circulation of the sea water. The solutions obtained for each twelve-month period, however, revealed significant seasonal differences in both magnitudes and flow patterns. Additional controlled experiments indicated that the winter circulation regime was strongly influenced by wind stresses as well as lateral water mass exchanges, whereas the summer circulation regime was basically controlled by the latter. The model results also showed that the circulation is strongly bathymetry-dependent.

1. INTRODUCTION

There is currently a significant focus of scientific interest on the Bering Sea. This area has always been of particular concern to investigators supporting fisheries research in both the United States and Japan. More recently a large scale environmental assessment program sponsored by the Outer Continental Shelf office of the Bureau of Land Management has concentrated attention on potential oil development areas in Bristol Bay. This study contains a number of components covering many scientific disciplines which require supportive circulation information. Within the immediate future, planned expansion of the OCS study will extend the investigations to the north, including most of the eastern continental shelf area as far as Norton Sound and through the Bering Strait. In addition to these studies, a second large scale study, PROBES

(Productivity and Resources of the Bering Shelf), is being planned, which will concentrate on the trophic level exchange in the incredibly rich fisheries located along the shelf break; this ecologically based study will also require circulation information.

Due largely to technical difficulties in oceanographic observations, our present knowledge of the Bering Sea circulation is fragmentary. The presently available observational data reveals only uncertain knowledge of the surface current velocities and very little about the deep basin circulation. Recently Arsen'ev (1967), Hughes et al. (1972) and Takenouti et al. (1972) compiled rather extensive field data, and proposed a number of alternative current schemes. Although they all shared an existing view about the cyclonic circulation of the sea waters, they disagreed in all the other respects: the number, location, size and even the direction of rotation of gyres depicted.

In the present study we attempted to explore fundamental physical processes of the sea using an oceanic general circulation model. A number of oceanic general circulation models have already been developed and have successfully simulated many of the observed large-scale features of the ocean currents. We have begun our study by adopting one such model (Semtner, 1974) in a simplified form.

Gurikova et al., (1964) carried out a numerical study of the Bering Sea circulation using a linear diagnostic model. They assumed a flat-bottomed, laterally closed basin, and thus investigated only a wide-driven circulation. The model results, however, confirmed the presence of a cyclonic circulation of the sea waters.

Lately Bacon (1973) applied the barotropic model of Galt (1973) to the Bering Sea, and examined a typical seasonal response of the western deep basin circulation. He was also able to identify, by making a series of controlled experiments, some of the important effects such as wind stress, lateral boundary forcing, and bathymetry.

The Bering Sea studies above are essentially two-dimensional and do not take into account the thermohaline component of the circulation. It would seem that any serious attempt to simulate a realistic circulation must eventually include the thermohaline effect. Accordingly, our main effort has been to model the Bering Sea in a three-dimensional way. This study is still in progress and will soon be published in part II of this series of technical reports. Meanwhile we have constructed and tested a two-dimensional diagnostic model as an initial step toward the three-dimensional modeling efforts. We have applied this simple model to the Bering Sea; this report reviews the model and its results. Section 2 contains a brief discussion of the mathematical model and the numerical procedure, together with the model boundary conditions. The results and their implications are discussed in sections 3 and 4.

2. THE MATHEMATICAL MODEL AND BOUNDARY CONDITIONS

2.1 The Model

The equations of motion for horizontal non-accelerated flow with a constant vertical eddy coefficient are:

$$-fv\rho_0 = -\frac{1}{a \cos\phi} \frac{\partial p}{\partial \lambda} + \rho_0 \kappa \frac{\partial^2 u}{\partial z^2} \quad (1)$$

$$fu\rho_0 = -\frac{1}{a} \frac{\partial p}{\partial \phi} + \rho_0 \kappa \frac{\partial^2 v}{\partial z^2} \quad (2)$$

The hydrostatic equation and the mass continuity equations are:

$$\frac{\partial p}{\partial z} = -g\rho_0 \quad (3)$$

$$\frac{1}{a \cos\phi} \frac{\partial u}{\partial \lambda} + \frac{1}{a \cos\phi} \frac{\partial}{\partial \phi} (v \cos\phi) + \frac{\partial w}{\partial z} = 0 \quad (4)$$

In these equations spherical coordinates are used, with λ , ϕ , and z representing longitude, latitude, and height. The fluid is contained between the surface $z = \eta$ and the bottom $z = -H(\lambda, \phi)$. The model specifies two horizontal velocities and pressure. The model assumes the fluid is homogeneous; thus the density ρ_0 is a constant ($\rho_0 = 1$).

The boundary conditions are:

$$\kappa\rho_0 \frac{\partial u}{\partial z} = \tau_\lambda; \quad \kappa\rho_0 \frac{\partial v}{\partial z} = \tau_\phi \quad \text{and} \quad W = \left(\frac{u}{a \cos\phi} \frac{\partial \eta}{\partial \lambda} + \frac{v}{a} \frac{\partial \eta}{\partial \phi} \right) \quad \text{at} \quad z = \eta \quad (5)$$

$$\kappa\rho_0 \frac{\partial u}{\partial z} = \tau_b; \quad \kappa\rho_0 \frac{\partial v}{\partial z} = \tau_b^\phi \quad \text{and} \quad W = -\left(\frac{u}{a \cos\phi} \frac{\partial H}{\partial \lambda} + \frac{v}{a} \frac{\partial H}{\partial \phi} \right) \quad \text{at} \quad z = -H(\lambda, \phi) \quad (6)$$

In equations (5) and (6) η is the free surface elevation; H is the depth of the sea; and τ_b^λ , τ_b^ϕ are the bottom stress components. Assuming that $\eta/H \ll 1$, we impose the boundary condition (5) at $z = 0$.

Then the momentum equations (1) and (2) are vertically averaged to yield:

$$-f\bar{v} = -\frac{\rho_0 g}{a \cos \phi} \frac{\partial \eta}{\partial \lambda} + \frac{1}{H} (\tau_o^\lambda - R\bar{u}), \quad (7)$$

$$f\bar{u} = -\frac{\rho_0 g}{a} \frac{\partial \eta}{\partial \lambda} + \frac{1}{H} (\tau_o^\phi - R\bar{v}) \quad (8)$$

where

$$\bar{u} = \frac{1}{H} \int_0^0 \rho_o u dz \quad (9)$$

$$\bar{v} = \frac{1}{H} \int_{-H}^0 \rho_o v dz \quad (10)$$

In equations (7) and (8) the component bottom stresses are taken as $R\bar{u}$ and $R\bar{v}$ where R is the coefficient of friction ($R = 0.02$ m/s). Integration of the continuity equation (4) with boundary conditions (5) and (6) yields:

$$\frac{1}{a \cos \phi} \frac{\partial}{\partial \lambda} \left(\int_{-H}^0 u dz \right) + \frac{1}{a \cos \phi} \frac{\partial}{\partial \phi} \left(\cos \phi \int_{-H}^0 v dz \right) = 0 \quad (11)$$

Equation (11) simply states that the vertically integrated flow is horizontally nondivergent, which guarantees the existence of a transport stream function ψ such that

$$\bar{u} = \frac{1}{H} \int_{-H}^0 \rho_0 u dz = -\frac{1}{a} \frac{1}{H} \frac{\partial \psi}{\partial \phi} \quad (12)$$

$$\bar{v} = \frac{1}{H} \int_{-H}^0 \rho_0 v dz = \frac{1}{H} \frac{1}{a \cos \phi} \frac{\partial \psi}{\partial \lambda} \quad (13)$$

Substituting equations (12) and (13) into (7) and (8), and applying the cur_z^1 operator, defined by

$$\text{cur}_z^1 (q_1, q_2) = \frac{1}{a \cos \phi} \left[\frac{\partial p_2}{\partial \lambda} - \frac{\partial}{\partial \phi} (q_1 \cos \phi) \right] \quad (14)$$

and simplifying by eliminating a factor of $1/(a^2 \cos \phi)$, we get:

$$\begin{aligned} R \left[\frac{\partial}{\partial \lambda} \left(\frac{1}{H \cos \phi} \frac{\partial \psi}{\partial \lambda} \right) + \frac{\partial}{\partial \phi} \left(\frac{\cos \phi}{H^2} \frac{\partial \psi}{\partial \phi} \right) \right] + \frac{\partial}{\partial \phi} \left(\frac{f}{H} \right) \frac{\partial \psi}{\partial \lambda} - \frac{\partial}{\partial \lambda} \left(\frac{f}{H} \right) \frac{\partial \psi}{\partial \phi} \\ = \frac{\partial}{\partial \lambda} \left(\frac{a \tau_0^\phi}{H} \right) - \frac{\partial}{\partial \phi} \left(\frac{a \cos \phi}{H} \tau_0^\lambda \right) \end{aligned} \quad (15)$$

Equation (15) is an inhomogeneous, linear, elliptic, second-order partial differential equation for the stream function ψ . For a given bathymetry $H(\lambda, \phi)$ and a prescribed surface stress distribution $\tau_0^\lambda(\lambda, \phi)$ and $\tau_0^\phi(\lambda, \phi)$, the stream function ψ can be obtained by inverting the second order differential operator. It is necessary to specify boundary conditions for this inversion. If the domain is singly connected, an arbitrary value can be specified as the value of the stream function on the boundary in general. However, the domain of ψ will be a multiple connected region whose boundary consists of a primary continent and several islands.

On the chosen continent, ψ can be held constant, but on the islands ψ must be obtained as a part of the total solution. In order to obtain the ψ on the islands, we use the method of "hole relaxation" by Takano (1974). Since the surface elevation η is a single valued function, a line integral of $\nabla \eta$ around the coast line of each island should vanish. By applying this condition in integrating equations (7) and (8) around each island, the following equation is obtained to predict the ψ on the island:

$$\oint \frac{1}{H} \left(\tau_o^\lambda + \frac{R}{aH} \frac{\partial \psi}{\partial \phi} \right) a \cos \phi \, d\lambda + \oint \frac{1}{H} \left(\tau_o^\phi - \frac{R}{H a \cos \phi} \frac{\partial \psi}{\partial \lambda} \right) a \, d\phi = 0 \quad (16)$$

In the above, the fact that ψ is spatially constant along the coastline eliminates any contribution from the Coriolis terms.

We solve equations (15) and (16) simultaneously by the "successive over-relaxation method." It should be mentioned, however, that the highest order terms in equation (15) involve a small friction parameter R , and thus special care must be taken to maintain stability of the numerical methods. This plus the numerical procedure for solving Equation (15) and (16) will be discussed in section 2.3.

2.2 Surface Wind Stress and Open Boundary Conditions

Wind stress can be estimated by conventional drag law methods if the surface wind is known. Unfortunately, wind measurements over the Bering Sea are very sparse in space and time, since they generally come from a handful of ship stations. Therefore, for the numerical models,

wind stress is computed from surface pressure data. First, monthly mean pressure data provided by the National Climate Center were interpolated quadratically from a $5^{\circ} \times 5^{\circ}$ grid mesh onto the model grid mesh of 2° (long.) \times 1° (lat.). The interpolated pressure data were then used to estimate the geostrophic wind velocity, and the wind velocity at anemometer height was obtained by multiplying the geostrophic wind speed by a factor γ and changing the geostrophic wind direction by angle α (the constant γ is .07: α is 19°). Strictly speaking, one should use synoptic maps in estimating wind stress because the variable part of the pressure could increase the wind stress estimate through the non-linearity of the drag law. In fact, the studies by Aagaard (1970) and Fissel et al. (1977) strongly suggest that the stress computed from the monthly mean pressure could be easily underestimated by a factor of 2 or 3. On the basis of this study, we multiplied the monthly mean stress by 3.0 for the model calculation.

The annual mean wind stress was computed by averaging 12 months of wind stress data. This is shown in Figure 1. The computed monthly mean wind stress patterns for January through December are shown in Figures 2-13. The January map shows a typical winter pattern characterized by the northeasterly stress associated with a strong high pressure center over Siberia and low pressure center over the North Pacific Ocean. The stress pattern in August, on the other hand, shows a very weak stress over most of the sea and somewhat stronger southwesterly stress over the southeast part of the basin. In general, the wind forcing in summer

is weaker by one order of magnitude than in winter. This significantly large winter-to-summer change in the wind stress might lead to large annual signals in the resulting currents. Recent work by Kinder, et al. (1975) has suggested that variations in the wind stress may result in planetary wave patterns that control the current structure along the Bering Sea shelf break. Although the present model does not include any such wave dynamics in its steady state formulations, the time-dependent problem is of considerable theoretical interest. For this reason the complete annual cycle by months has been included. To the authors' knowledge the analysis of these monthly mean pressure data to yield sequential stress patterns is not available elsewhere; We hope that this effort will help stimulate productive consideration of the more complete time-dependent problem. In addition to stress fields, the model requires boundary conditions.

At the open boundaries of the grid, estimates of vertically integrated transports were required. The model has four open boundaries along the Aleutian - Commander Island Arc: Kamchatka Strait, Commander - Near Strait, Central Aleutian Pass and Western Aleutian Pass. The Bering Strait also modelled as an open boundary. The widths and depths of the open boundaries are adjusted to match the observed bathymetry within the limits imposed by grid resolutions. Integrated volume transport values on the open sections are chosen from various estimates presently available. It should be mentioned, however, that at the present stage there are many uncertainties in transport estimates at the various passes.

The chosen values of (annual mean) transports are given in Table 1. A net transport of 18 sv (1 sv = $10^6 \text{ m}^3/\text{s}$.) outward through the Kamchatka Strait is in close agreement with an estimate of 18.4 sv by Arsen'ev (1967) and summer values (20sv) by Hughes et al. (1974). A net transport of 14sv inward across the Commander - Near Strait, taken from Arsen'ev (1967), is greater than an estimate (10sv) by Favorite (1974) but less than Hughes et al. (25sv). The total inflows through the Western and Central Aleutian are based on the estimates made by Arsen'ev (1967). For the Bering Strait, the total transport (1sv) outward was chosen from the estimate (1.1sv) by Arsen'ev (1967).

2.3 Numerical Procedures

The basic equations (15) and (16) for the volume flux stream function ψ are solved numerically by finite-difference methods. The Bering Sea domain is approximated by a collection of rectangles, each having horizontal dimensions corresponding to increments $\Delta\lambda$ and $\Delta\phi$ in longitude and latitude. The boundary grid is chosen so as to best approximate the coastline (Fig. 14).

We write the basic equation (15) in a compact form using Cartesian coordinates:

$$R \nabla^2 \psi + A \frac{\partial \psi}{\partial x} + B \frac{\partial \psi}{\partial y} = \phi . \quad (17)$$

where A, B and ϕ are functions of bottom slope, planetary vorticity gradient and the wind stress distribution.

Let the nodes (Fig. 15) be labeled $x = i$, $x + d = i + 1$, $x - d =$

$i - 1, y = j, y + d = j + 1, y - d = j - 1$. Then at the nodes (i, j) , Equation (17) has the finite difference form:

$$R \left[\frac{1}{d^2} (\psi_{i+1,j} + \psi_{i,j+1} + \psi_{i-1,j} + \psi_{i,j-1} - 4\psi_{i,j}) \right] + \frac{A}{2d} (\psi_{i+1,j} - \psi_{i-1,j}) + \frac{B}{2d} (\psi_{i,j+1} - \psi_{i,j-1}) = \phi_{i,j} \quad (18)$$

Solving for $\psi_{i,j}$ leads to

$$4\frac{R}{d^2} \psi_{i,j} = \left(\frac{R}{d^2} + \frac{A}{2d}\right) \psi_{i+1,j} + \left(\frac{R}{d^2} + \frac{B}{2d}\right) \psi_{i,j+1} + \left(\frac{R}{d^2} - \frac{A}{2d}\right) \psi_{i-1,j} + \left(\frac{R}{d^2} - \frac{B}{2d}\right) \psi_{i,j-1} - \phi_{i,j} \quad (19)$$

Thus ψ is defined at each grid point in terms of ψ at four neighboring grid points, each weighted by a factor related to the grid size, depth, bottom slope and wind stress.

Approximating the differential equation (17) by the finite difference equation (19), we obtain a system of linear algebraic equations. One efficient method of solving this type of equation is that of "successive over-relaxation." For solution convergence, however, the matrix of equation (19) must be diagonally dominant, i.e., the sum of the off diagonal elements in any row of the coefficient matrix must be less than or equal to the diagonal element in that row. The condition to be met here is:

$$\left| \frac{R}{d^2} + \frac{A}{2d} \right| + \left| \frac{R}{d^2} + \frac{B}{2d} \right| + \left| \frac{R}{d^2} - \frac{A}{2d} \right| + \left| \frac{R}{d^2} - \frac{B}{2d} \right| \leq 4 \frac{R}{d^2} \quad (20)$$

This condition will be met if:

$$|A| \leq \frac{2R}{d}, \quad (21)$$

$$|B| < \frac{2R}{d}. \quad (22)$$

Thus, three factors are critical in obtaining a converging solution: bottom slope, friction coefficient and grid size. Clearly conditions (21) and (22) can always be satisfied by making d small enough. In practice, however, the number of iterations and the storage requirements increase as d decreases.

Sarkisian (1976) recognized this difficulty and proposed an alternative; the "method of directional differences." We used this method for the present study. The essence of the method is quite simple: Depending on the sign of the coefficients, forward or backward finite differences are used for the first-order derivatives in such a way that diagonal terms possess the maximum weights. For instance, in Equation (17), following Sarkisian's notation, we substitute the derivative with respect to x by the directional difference relation in the following way:

$$d\left(\frac{\partial \chi}{\partial x}\right) = \delta_1 \psi_{i+1,j} + (1 - 2\delta_1) \psi_{i,j} + (\delta_1 - 1) \psi_{i-1,j} \quad (23)$$

where $\delta_1 = 0$ for $A_{i,j} < 0$

$\delta_1 = 1$ for $A_{i,j} > 0$

Similarly,

$$d\left(\frac{\partial \psi}{\partial y}\right) = \delta_2 \psi_{i,j+1} + (1 - 2\delta_2) \psi_{i,j} + (\delta_2 - 1) \psi_{i,j-1} \quad (24)$$

where $\delta_2 = 0$ for $B_{i,j} < 0$

$\delta_2 = 1$ for $B_{i,j} > 0$

If we write the finite-difference analogue of the sum $A \frac{\partial \psi}{\partial x} + B \frac{\partial \psi}{\partial y}$, then $\psi_{i,j}$ has the coefficient $[|A_{i,j}| + |B_{i,j}|]$ in this sum. Thus the diagonal predominance is present in the system of algebraic equations obtained, independent of the signs of the coefficients A and B. The Laplace operator is written as in equation (18). Then we obtain the following difference approximation of equation (17):

$$\begin{aligned} & \frac{R}{d^2} [\psi_{i-1,j} + \psi_{i+1,j} + \psi_{i,j-1} + \psi_{i,j+1} - 4\psi_{i,j}] \\ & + A_{i,j} \frac{\delta_1 \psi_{i+1,j} + (1 - 2\delta_1) \psi_{i,j} + (\delta_1 - 1) \psi_{i-1,j}}{d} \\ & + B_{i,j} \frac{\delta_2 \psi_{i,j+1} + (1 - 2\delta_2) \psi_{i,j} + (\delta_2 - 1) \psi_{i,j-1}}{d} = \phi_{i,j} \quad (25) \end{aligned}$$

The computation of the stream function on islands remains to be discussed. Rather than construct a finite difference version of equation (16) directly, we use an indirect approach which is based on a finite-difference form of Stokes theorem (see Semtner (1974)). This theorem applies to any area A covered by a collection of rectangles and having a perimeter P of rectangle edges. If arbitrary values of two fields q_1 and q_2 are defined at the corners of rectangles, the following can be shown to hold:

$$\sum_A \sum \left[\frac{\partial}{\partial x} (\bar{q}_2^y) - \frac{\partial}{\partial y} (\bar{q}_1^x) \right] \Delta x \Delta y$$

$$= \sum_p (\bar{q}_1^x \Delta x + \bar{q}_2^y \Delta y) \quad (26)$$

where $\bar{q}_1^x = \frac{q_1(x) + q_1(x+d)}{2}$

$$\bar{q}_2^y = \frac{q_1(y) + q_1(y+d)}{2}$$

To compute the value of the island stream function, a line integral of equations (7) and (8) is required. The curl of those equations is already available in equation (25). By virtue of the Stokes theorem above, we can equivalently take the area sum of equation (25). (We can arbitrarily set the values of stress to be zero at the interior corners of rectangles, then the area sum will pick up non-zero at the interior corners of rectangles on the margin of the area.) The resulting area sum gives an algebraic relation between the value of ψ for an island and all the values of ψ immediately surrounding the island. This relation is solved simultaneously with equation (25) at each grid point in the Bering Sea domain.

3. RESULTS

Solutions were obtained first for the case of annual mean wind stress (Fig. 1) and mean mass flux conditions (Table 1) specified at the open passes. Solutions for each twelve-month period were also obtained, but due to the lack of data, monthly variations of the lateral boundary mass fluxes were not taken into account; an annual mean flux condition was used in the calculations. Additional model parameters are given in Appendix B.

With the annual mean wind stress from the general direction of northeast, contours of the stream function for the whole Bering Sea (Fig. 16) show a strong cyclonic gyre in the western half of the basin, and a somewhat complicated but much weaker flow (less than 2 sv.) in the eastern shelf region. More specifically, the Pacific Ocean waters entering through the open passes along the Aleutian Islands chain first move eastward along the Aleutians, and then turn northwestward along the shelf break to form a broad cross basin flow. A little south of Cape Navarin this cross basin current branches into two parts: the main part flows southwest, the second part flows toward the Bering Strait. The southwest-bound current moving parallel to Koryak Coast and Shirshov Ridge finally flows through the Kamchatka Strait into the Pacific Ocean.

The mass transport vectors computed from Equation (12) and Equation (13) for the annual mean case are shown in Figure 17. To show a clearer picture of the circulation pattern in the deep basin, that portion was magnified and is shown in Figure 18. The flow pattern, of course, is consistent with the stream function field described above. It must be

remembered, however, that the transport velocity vectors do not characterize the motion of the water particles but give only a picture of the overall water transport in the whole vertical column of the layer. In other words, the actual current pattern at a certain level could be substantially different from the transport pattern. Nonetheless, the results obtained are of definite importance for establishing the nature of the mean circulation of the sea.

To illustrate the monthly average characteristics of the total current, transport stream functions for January through December were calculated. Judging from these maps, the average, longterm current in the deep basin is basically cyclonic, which agrees with the annual mean case. There are, however, significant differences in both magnitudes and flow patterns between the winter regime and the summer regime.

In the winter season, the flow in the deep basin is characterized by three strong cyclonic subgyres. These subgyres are established in November and retained through the winter months (November-March) reaching a maximum strength in February (Fig. 19). The strong cross-basin transport along the shelf break is another characteristic of the winter regime. It extends from the southeast corner of the basin to the south of Cape Navarin. The flow in the shelf region appears to be quite complicated; it even shows an anticyclonic gyre in the Gulf of Anadyr. Unfortunately, due to a wide coverage of pack ice over the shelf in winter, there are no field data available to verify the model results. We might conjecture at most that the flow under the ice sheet probably resembles the model result, but this is not certain.

The transition to summer is characterized by weakening of both the subgyres in the deep basin and the cross-basin transport along the shelf break. The subgyres completely disappear in May and reappear in October. The pattern for August is seen in Figure 20. The deep basin circulation becomes weaker and tends to confine itself in the vicinity of the source-sink region as the season progresses. The seasonal differences of the flow regime in the present study must be attributed to seasonal variation of the wind stress since the model assumed a fixed mass flux boundary condition. This was further investigated in a series of controlled experiments; one with wind forcing only (fig. 21), and the other with a source-sink only (Fig. 22). Evidently, the summer circulation closely resembles the one with the source-sink only. This might indicate that the circulation in summer, is primarily driven by the mass source-sink specified along the boundary mainly due to the absence of strong wind. On the other hand, the closed gyres of the deep basin in winter are direct consequences of wind forcing, which showed up clearly in the experiment with wind forcing only.

4. SUMMARY AND SUGGESTIONS

The present diagnostic study attempts to establish a basis for a three-dimensional prognostic modeling of the Bering Sea. The model performances are very encouraging; a simple model such as this can be valuable for exploring some fundamental physical processes in the Bering Sea. The results obtained generally agree with the existing flow features as inferred from the climatological hydrographic data. Seasonal characteristics of the model flow, however, are yet to be verified with the observational data.

Furthermore, the present study provides us with invaluable information on the range of model parameters such as bottom topography, wind stress, etc. This information has already been used in our initial calibration of a three-dimensional model.

Based on the analysis of the present study, we propose a few suggestions:

- 1) A numerical model with a finer grid resolution is needed to handle the narrow passage along the Aleutian chain and to adequately resolve the bottom topography of the sea. There is a strong indication that the model flow depends upon the prescribed boundary mass flux conditions and upon the details of bottom topography. Doubling the present grid resolution (100 X 100 km) should improve the results significantly.

- 2) A more accurate estimate of wind stress over the Bering Sea is certainly necessary. The present study indicates a sensitivity of flow features to both the intensity and the pattern of driving stress. For

example, seasonal characteristics of the model flow are entirely due to seasonal variation of the imposed wind stresses. Reliable synoptic pressure maps are required in order to eliminate the use of stress multipliers with mean pressure maps. (This has been under investigation and will be reported elsewhere.)

The effect of seasonal variation of boundary mass flux on the sea circulation must be taken into account in future studies. The controlled experiment shows that the summer flow regime is very similar to that with the boundary mass forcing only, thus indicating the importance of boundary conditions in determining the summer regime. Future field work directed toward measuring lateral boundary conditions will improve simulation of the interior flow.

3) Finally, the two-dimensionality of the present model -- probably the weakest point of the model--allows only vertically averaged mass circulations. These results, however, are difficult to verify with field data obtained at a fixed level because there is usually a rapid variation of magnitude and direction of the flow with depth in the real sea.

In order to simulate more realistic circulation in the Bering Sea, three-dimensional modeling based on complete equations is necessary.

5. REFERENCES

- Aagaard, K. 1970: Wind-driven transports in the Greenland and Norwegian Seas, Deep-Sea Res. 17, 281-291.
- Arsen'ev, V.S., 1967: Currents and Water Masses of the Bering Sea, Izd. Nauka, Moscow. (Transl., 1968, Nat. Mar. Fish. Serv., Northwest Fish. Center, Seattle, Wash.). 135 pp.
- Bacon, J.C., 1963: Numerical investigation of Bering Sea dynamics, M.S. Dissertation, Naval Postgraduate School.
- Favorite, F., 1974: Flow into the Bering Sea through Aleutian island passes, Oceanography of the Bering Sea, Hood, D.W. and E.J. Kelly, Ed., 3-37.
- Fissel, D., S. Pond and M. Miyake, 1977: Computation of surface fluxes from climatological and synoptic data, Monthly Weather Review 105, 26-36.
- Galt, J.A., 1973: A numerical investigation of Arctic Ocean dynamics, Journal of Physical Oceanography.
- Gurikova, K.F., T.T. Vinokurova, and V.V. Natarov, 1964: A model of the wind-driven currents in the Bering Sea in August 1958 and 1960. (Transl., 1968, in Soviet fisheries investigations in the Northeastern Pacific, Part 2, pp 48-77, avail. Nat. Tech. Inf. Serv., Springfield, VA, TT 67-51204).
- Hughes, F.W., L.K. Coachman and K. Aagaard, 1974: Circulation, transport and water exchange in the Western Bering Sea, Oceanography of the Bering Sea, Hood, D.W. and W.J. Kelly, Ed. 59-98.
- Kinder, T.H., L.K. Coachman and J.A. Galt (1975): The Bering Slope Current, Journal of Physical Oceanography, 5(2), pp 231-244.
- Sarkisian, A.S., 1976: The diagnostic calculations of a large-scale Oceanic circulation, The Sea, Vol. 6, Goldberg, E.D., Ed., 363-458.
- Semtner, A.J., 1974: An oceanic general circulation model with bottom topography, Numerical simulation of Weather and Climate, Technical Report No. 9, Department of Meteorology, University of California, Los Angeles, 99 pp.
- Takano, K., 1974: A general circulation model for the world ocean Numerical simulation of weather and climate, Technical Report No. 8 Department of Meteorology, University of California, Los Angeles, 47 pp.
- Takenouti, A.Y. and K. Ohtani, 1974: Currents and water masses in the Bering Sea: A review of Japanese work, Oceanography of the Bering Sea, Hood, D.W. and E.J. Kelly, Ed., 39-57.

Table 1.

Mass transport at open boundaries

Kamchatka Strait	- 18sv.*
Commander - Near Strait	+ 14sv.*
Western Aleutian Pass	+ 4sv.
Central Aleutian Pass	+ 1sv.
Bering Strait	- 1sv.

* - Outward

+ Inward

FIGURE CAPTIONS

- Figure 1. Annual mean wind stress (dyne/cm^2) computed from 12 monthly mean wind stresses
- Figure 2. January mean wind stress computed from the monthly mean pressure map
- Figure 3. February mean wind stress computed from the monthly mean pressure map
- Figure 4. March mean wind stress computed from the monthly mean pressure map
- Figure 5. April mean wind stress computed from the monthly mean pressure map
- Figure 6. May mean wind stress computed from the monthly mean pressure map
- Figure 7. June mean wind stress computed from the monthly mean pressure map
- Figure 8. July mean wind stress computed from the monthly mean pressure map
- Figure 9. August mean wind stress computed from the monthly mean pressure map
- Figure 10. September mean wind stress computed from the monthly mean pressure map
- Figure 11. October mean wind stress computed from the monthly mean pressure map
- Figure 12. November mean wind stress computed from the monthly mean pressure map
- Figure 13. December mean wind stress computed from the monthly mean pressure map
- Figure 14. Bering sea configuration and the finite difference approximation of the Basin. Contours of depth are superimposed.
- Figure 15. Location of variables in the horizontal grid
- Figure 16. Annual mean mass transport stream functions. Contour intervals are 2 sv (____) and 0.2 sv (---)
- Figure 17. Velocity vectors which correspond to Figure 16
- Figure 18. Velocity vectors for the deep basin

FIGURE CAPTIONS (cont.)

- Figure 19. February mean mass transport stream function
- Figure 20. Same as Figure 19 except for August
- Figure 21. Annual mean stream functions computed with the annual mean wind stress forcing only.
- Figure 22. Annual mean stream functions computed with the prescribed lateral mass source-sink only.

WINDSTRESS VECTOR PLOT

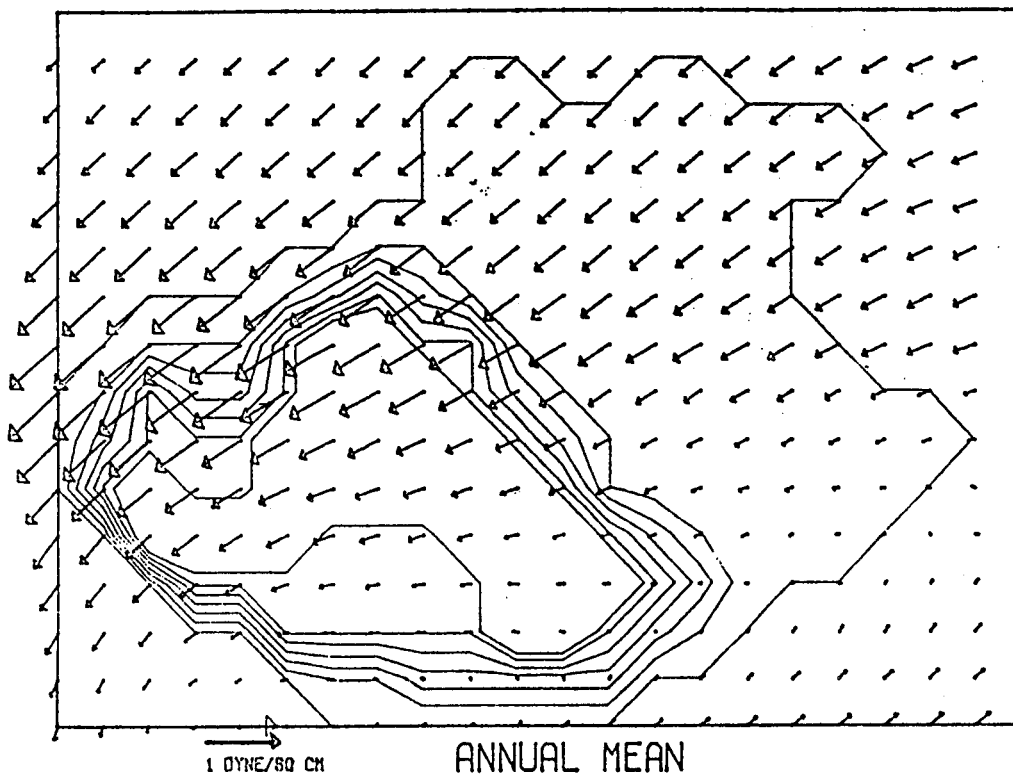


Figure 1

WINDSTRESS VECTOR PLOT

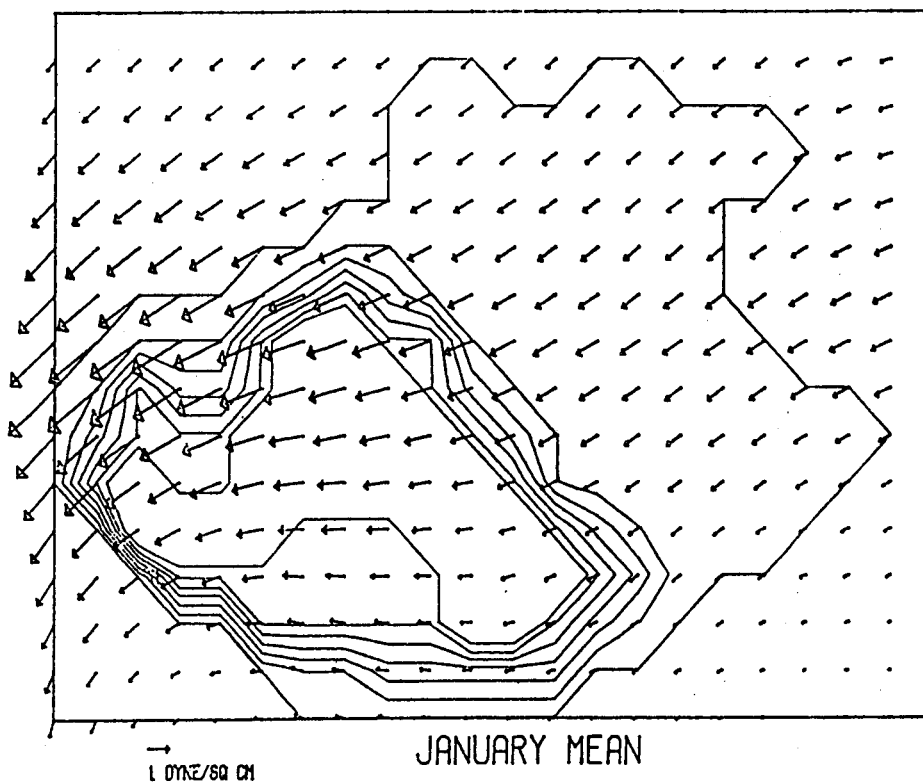


Figure 2

WINDSTRESS VECTOR PLOT

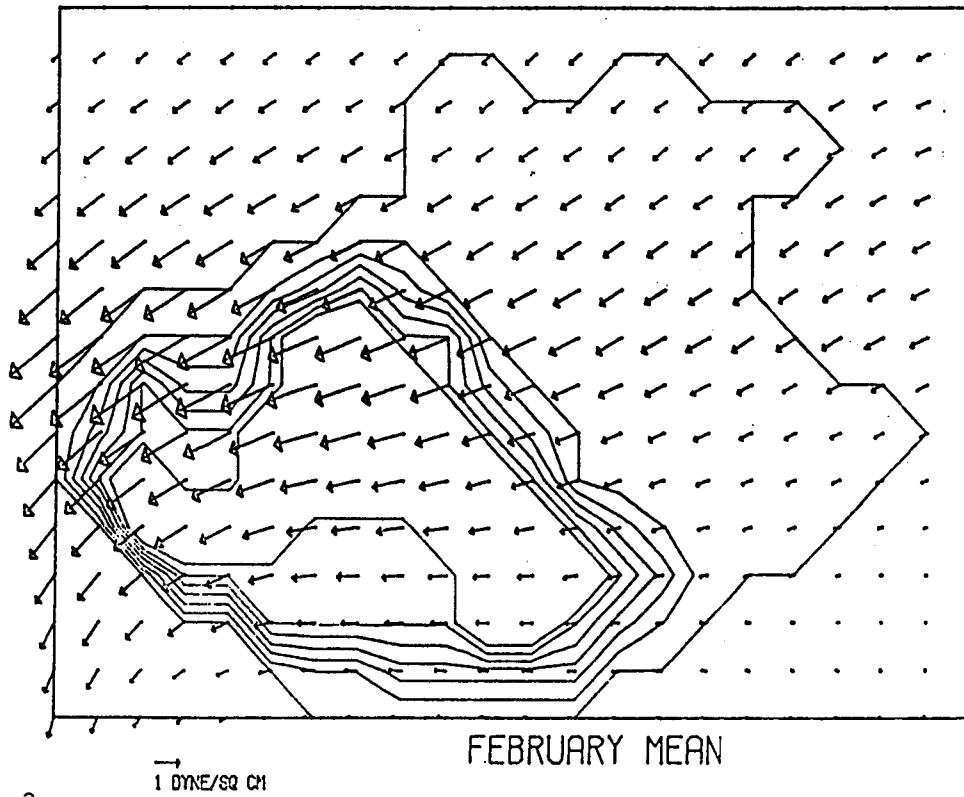


Figure 3

WINDSTRESS VECTOR PLOT

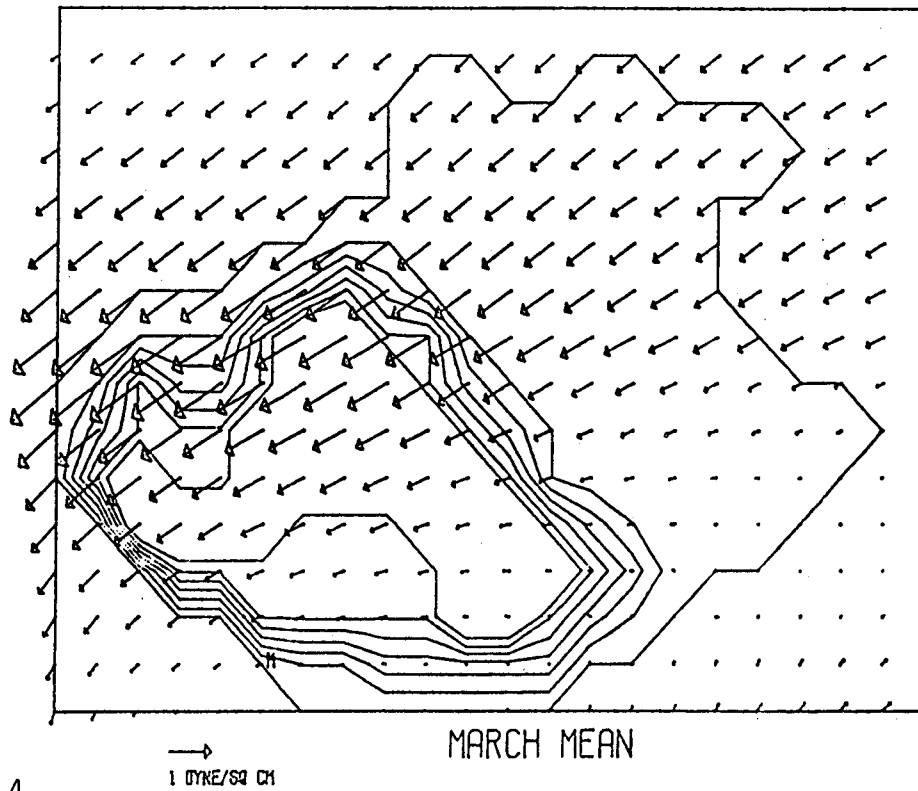


Figure 4

WINDSTRESS VECTOR PLOT

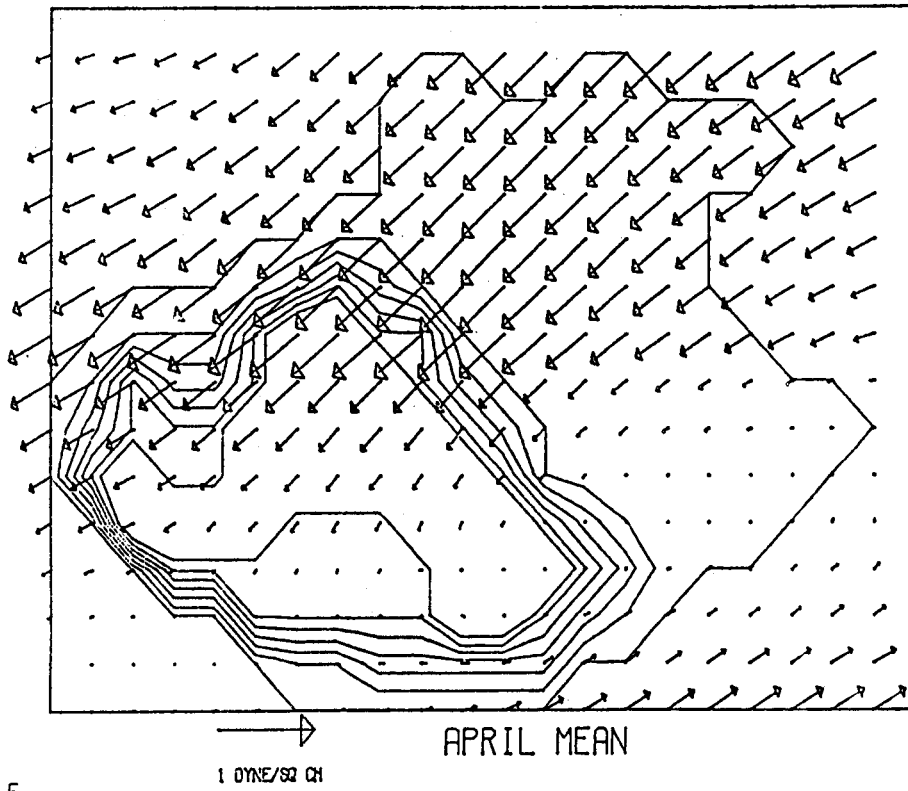


Figure 5

WINDSTRESS VECTOR PLOT

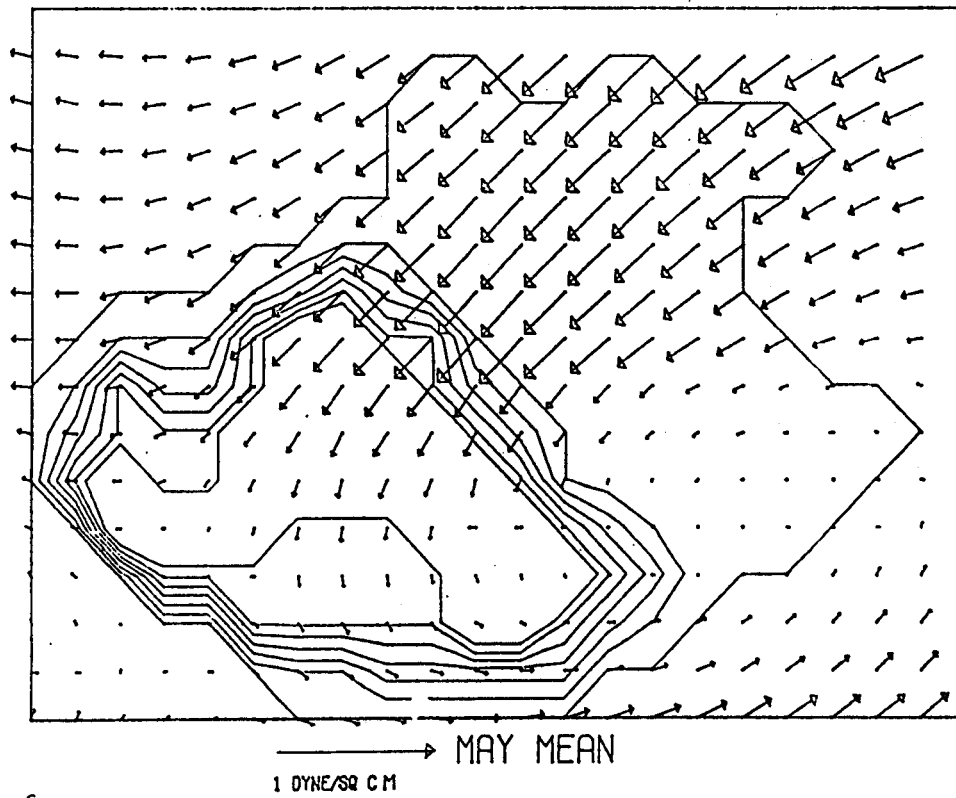


Figure 6

WINDSTRESS VECTOR PLOT

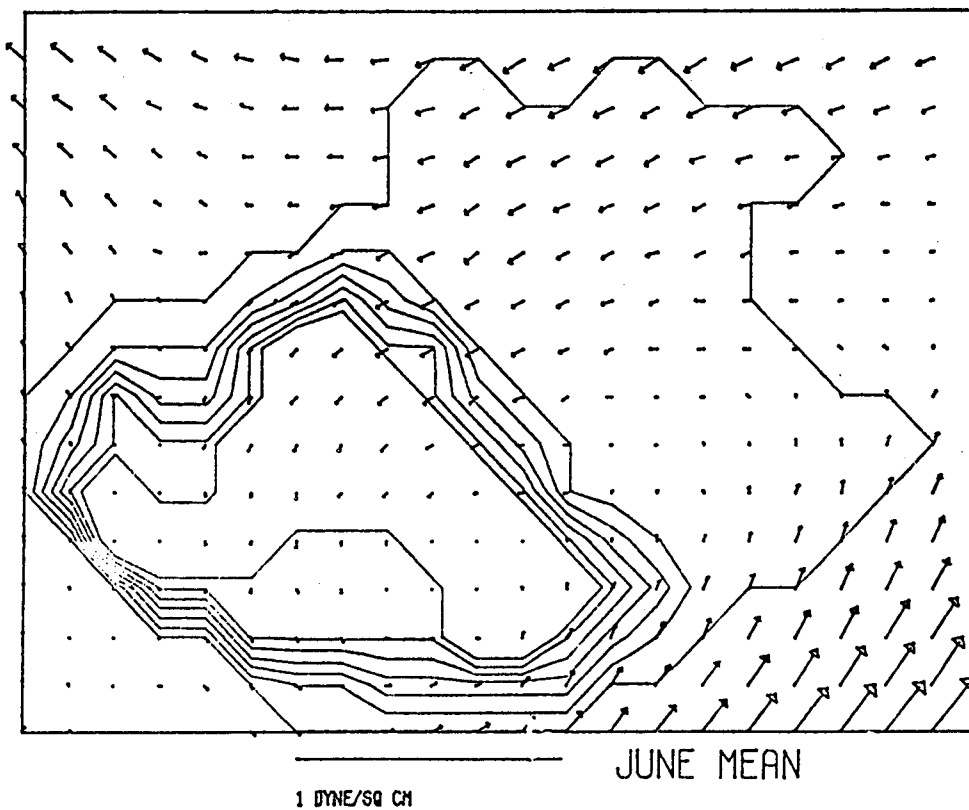


Figure 7

WINDSTRESS VECTOR PLOT

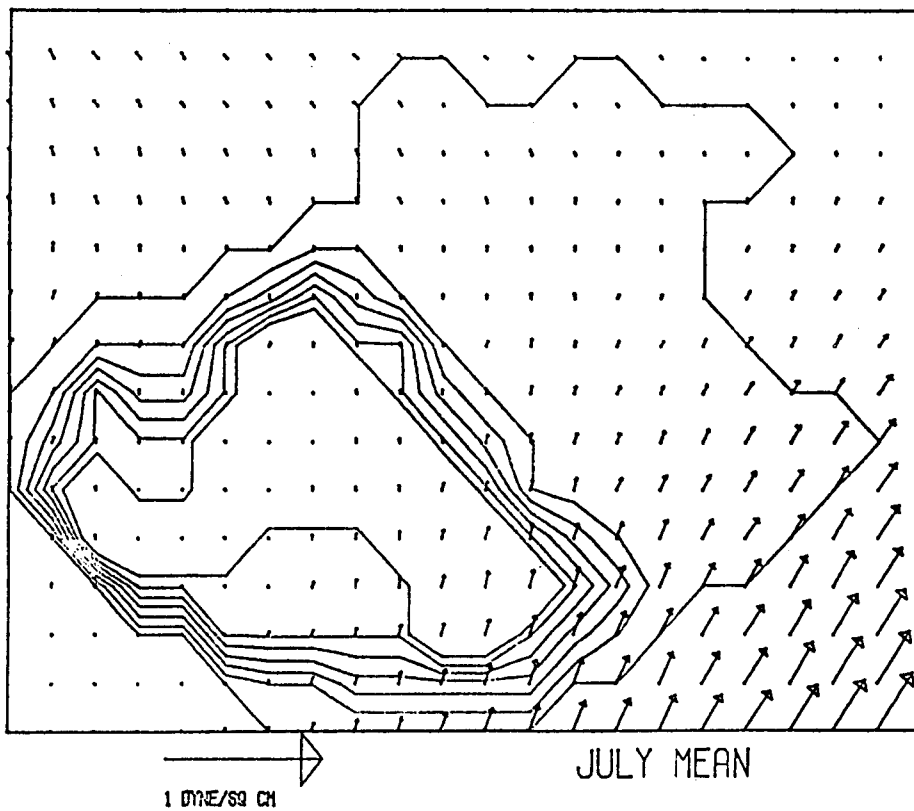


Figure 8

WINDSTRESS VECTOR PLOT

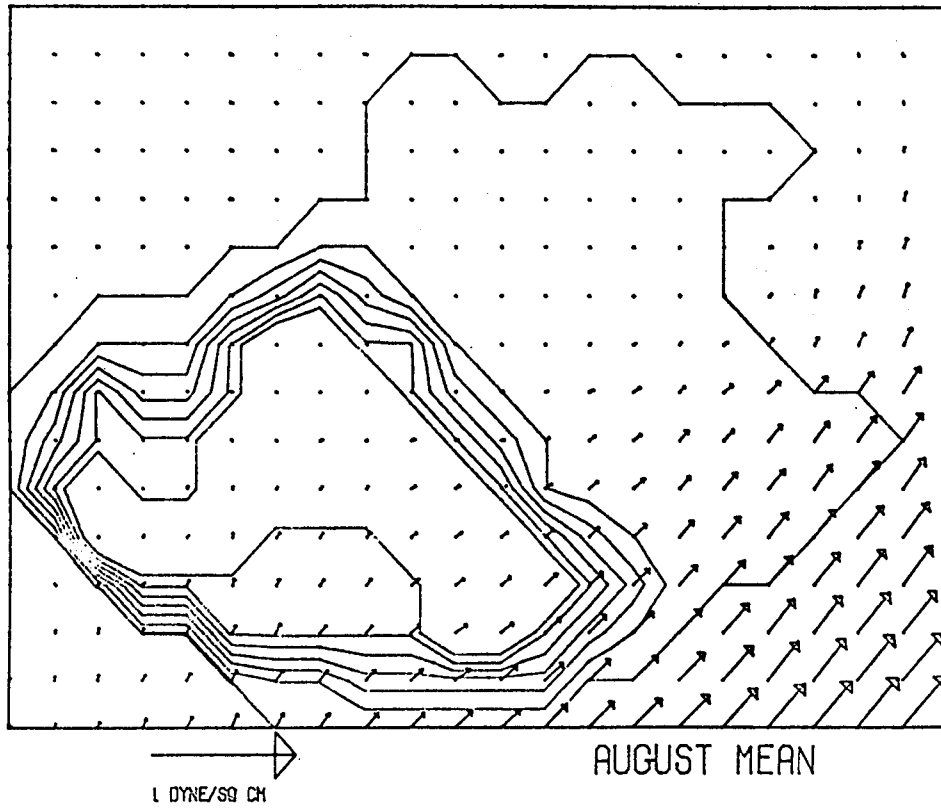


Figure 9

WINDSTRESS VECTOR PLOT

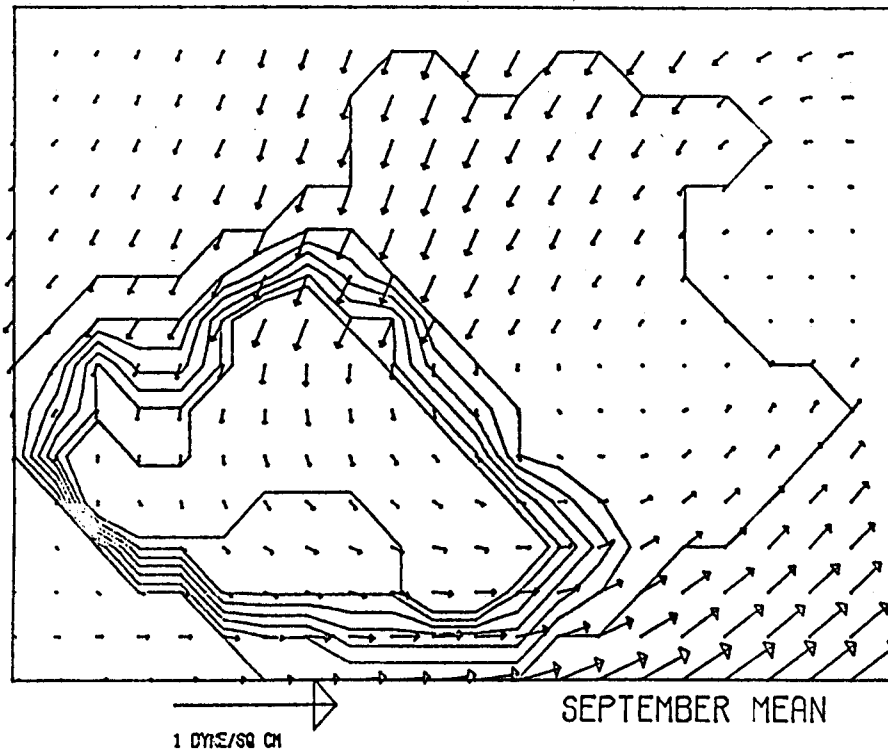


Figure 10

WINDSTRESS VECTOR PLOT

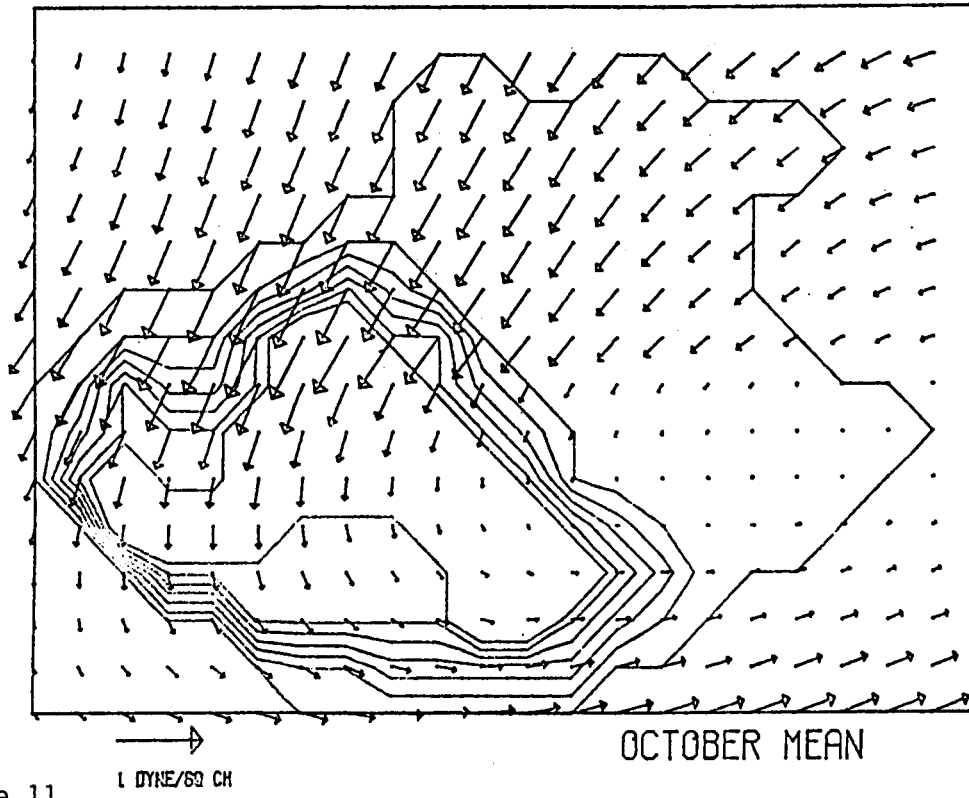


Figure 11

WINDSTRESS VECTOR PLOT

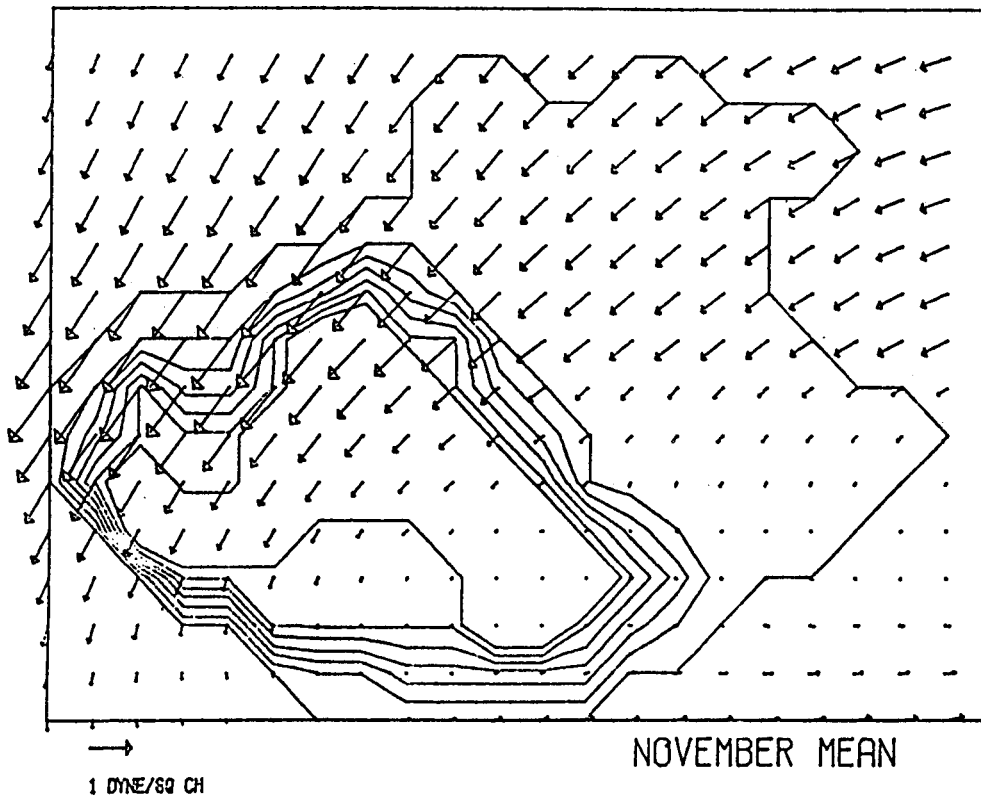


Figure 12

WINDSTRESS VECTOR PLOT

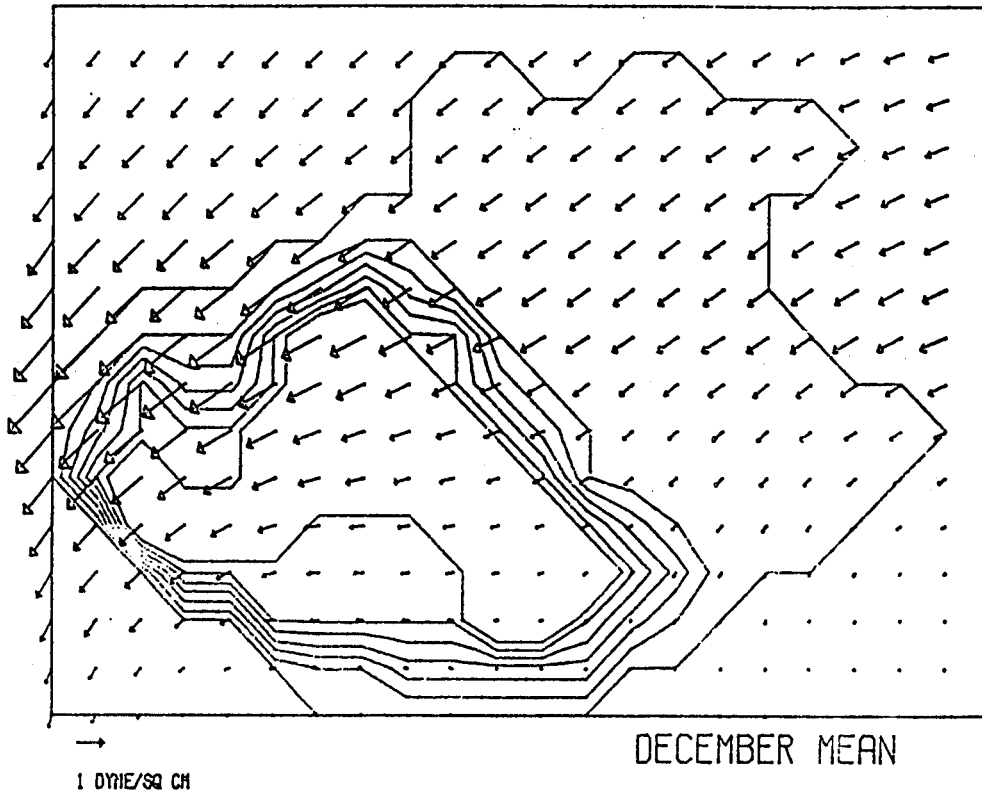


Figure 13

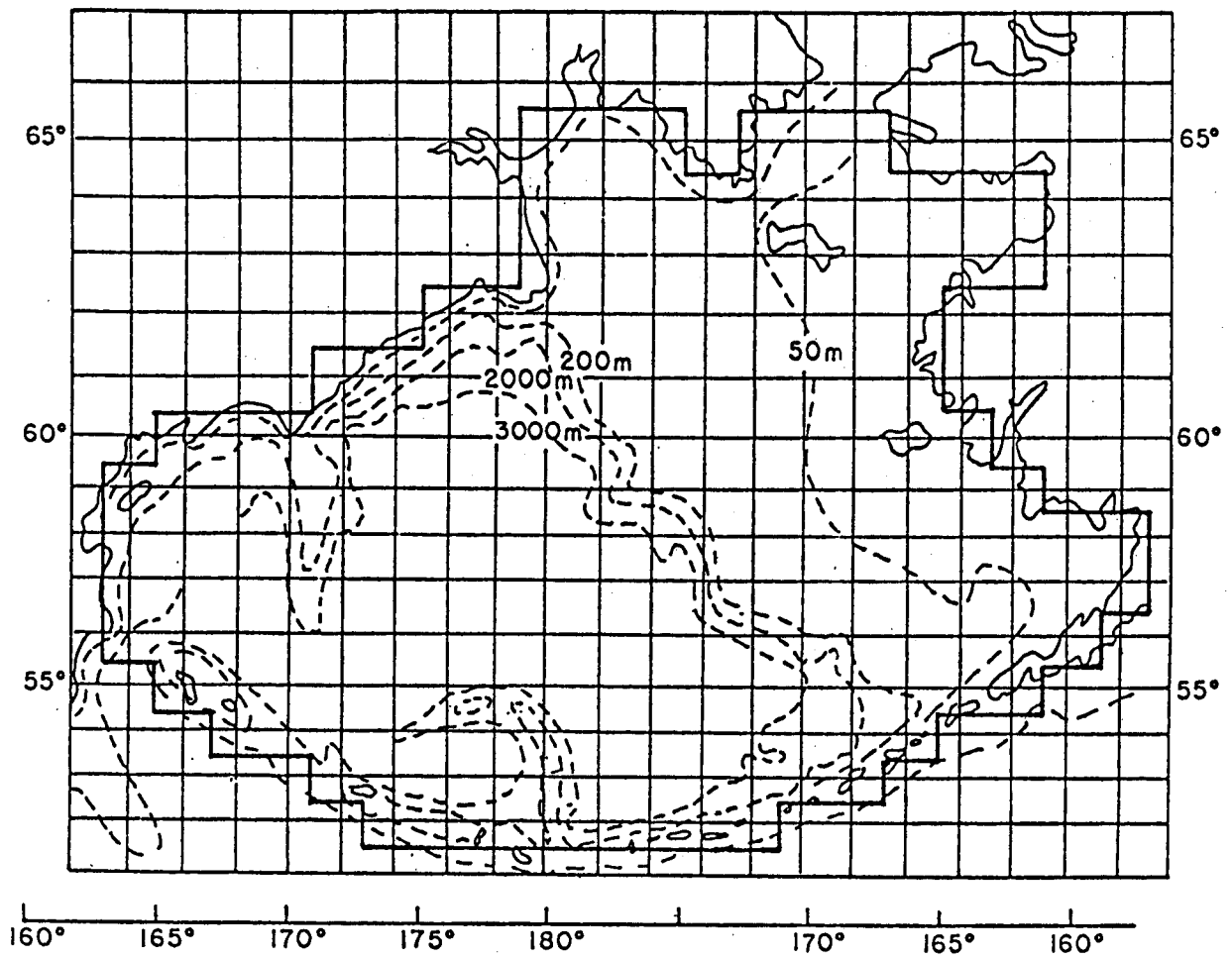


Figure 14

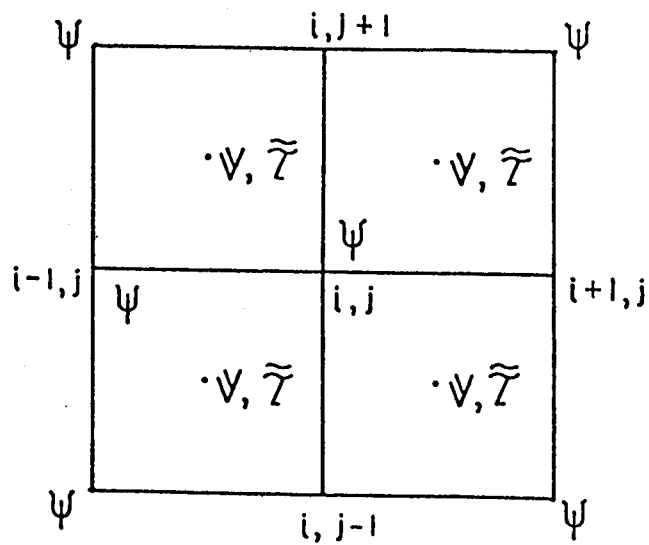


Figure 15

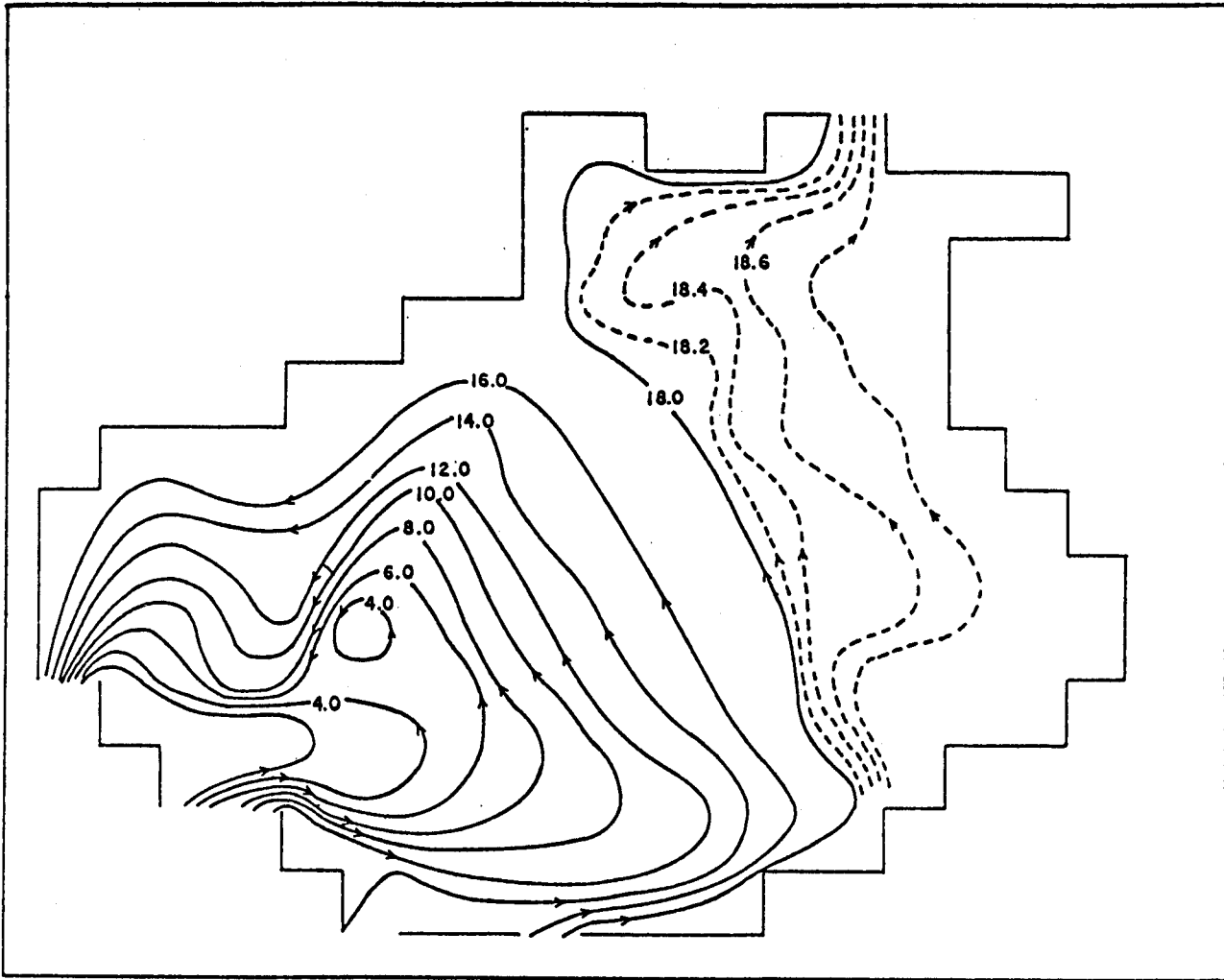


Figure 16

VELOCITY VECTOR PLOT

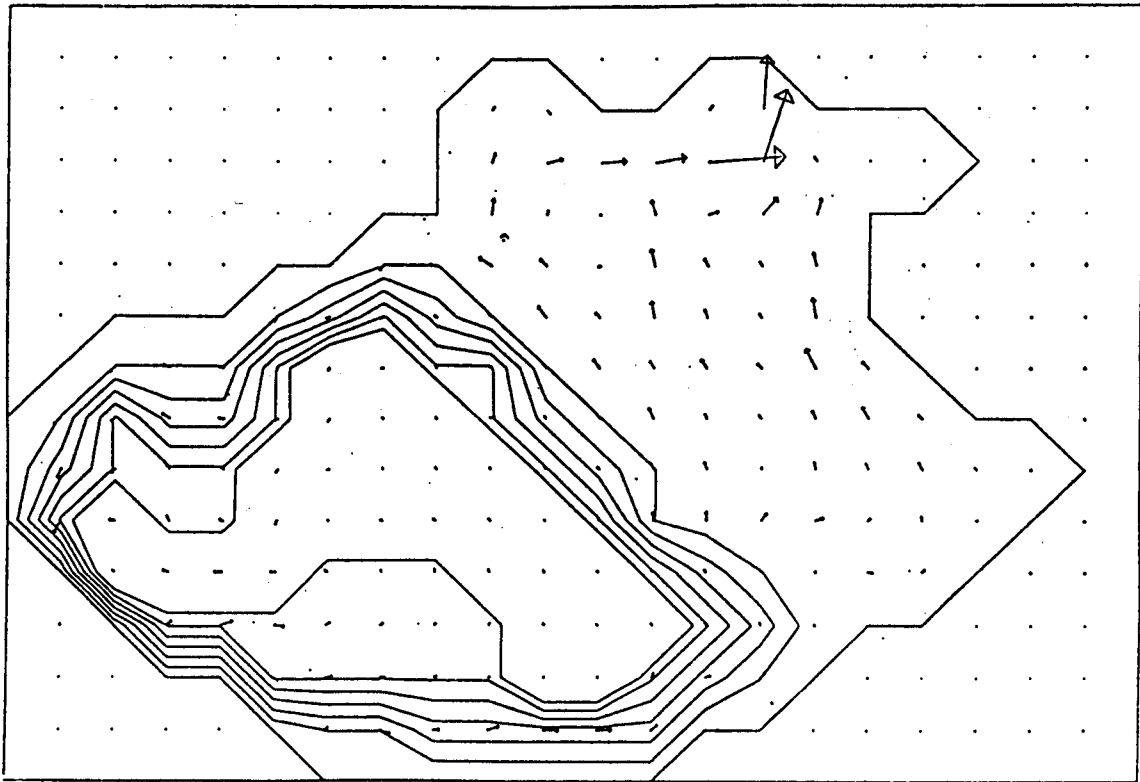


Figure 17 10 (cm/sec)

VELOCITY VECTOR PLOT

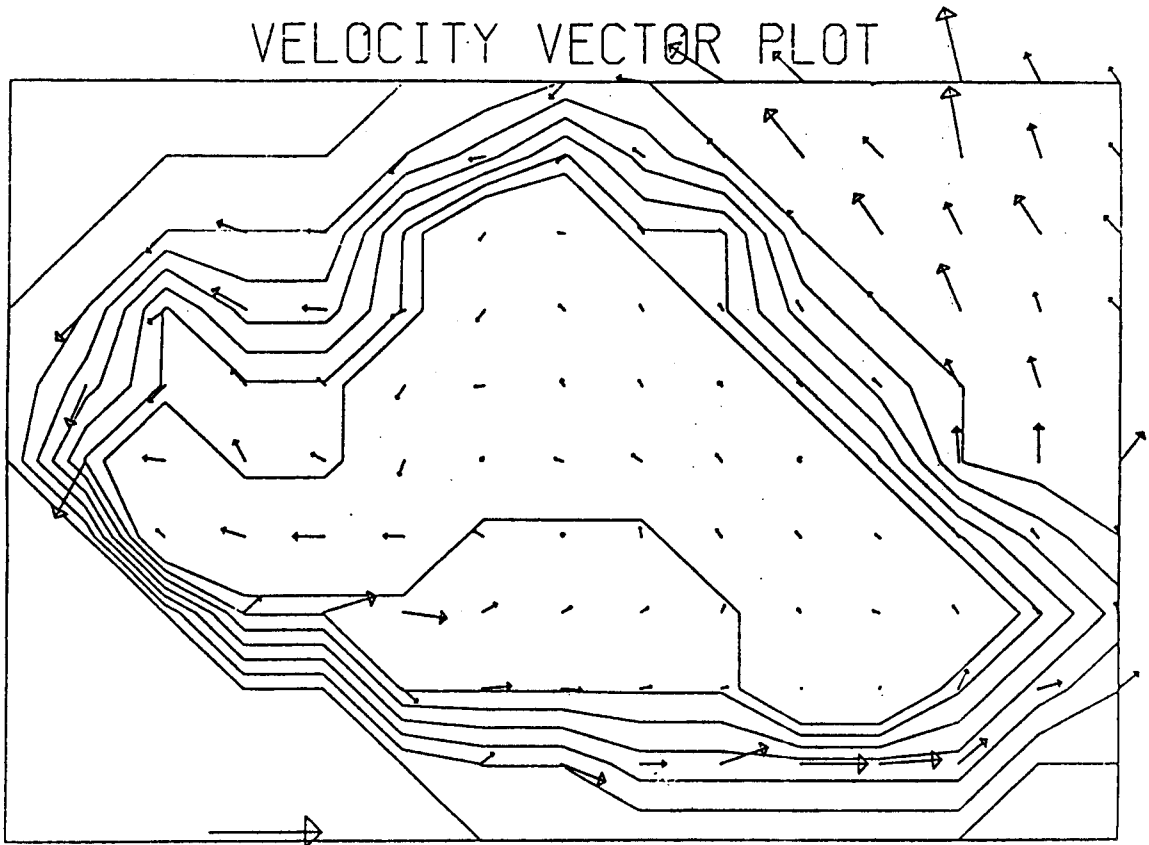


Figure 18

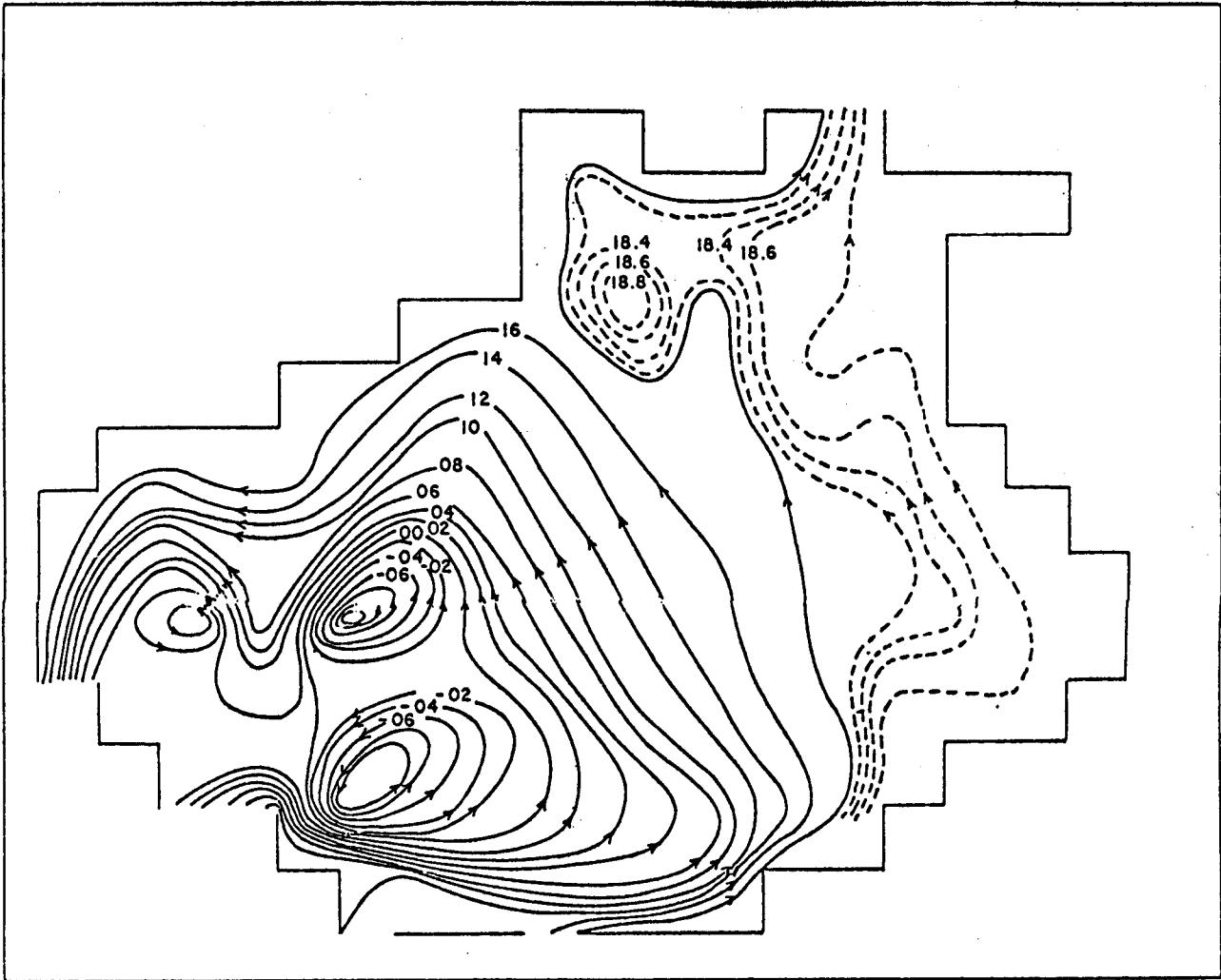


Figure 19

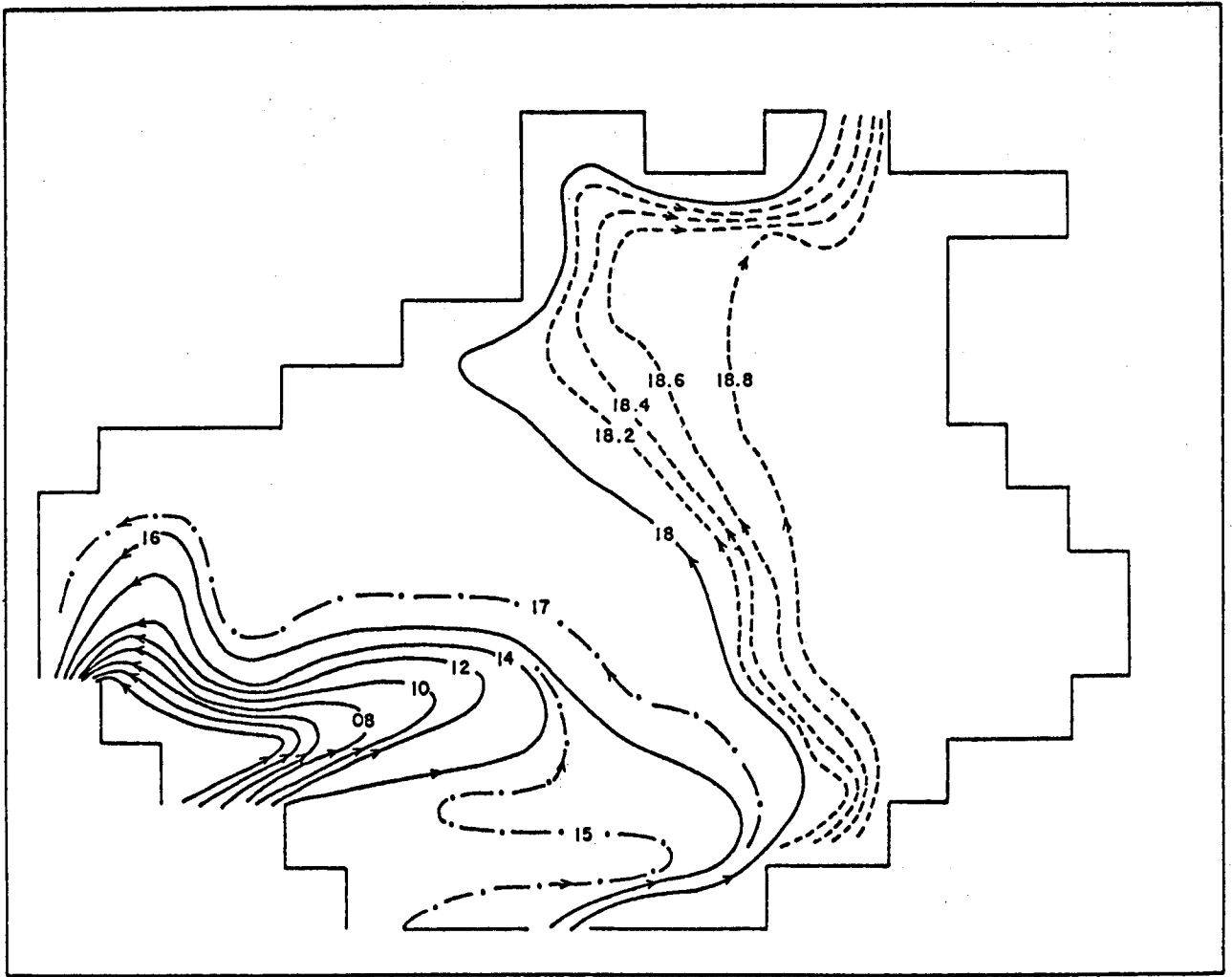


Figure 20

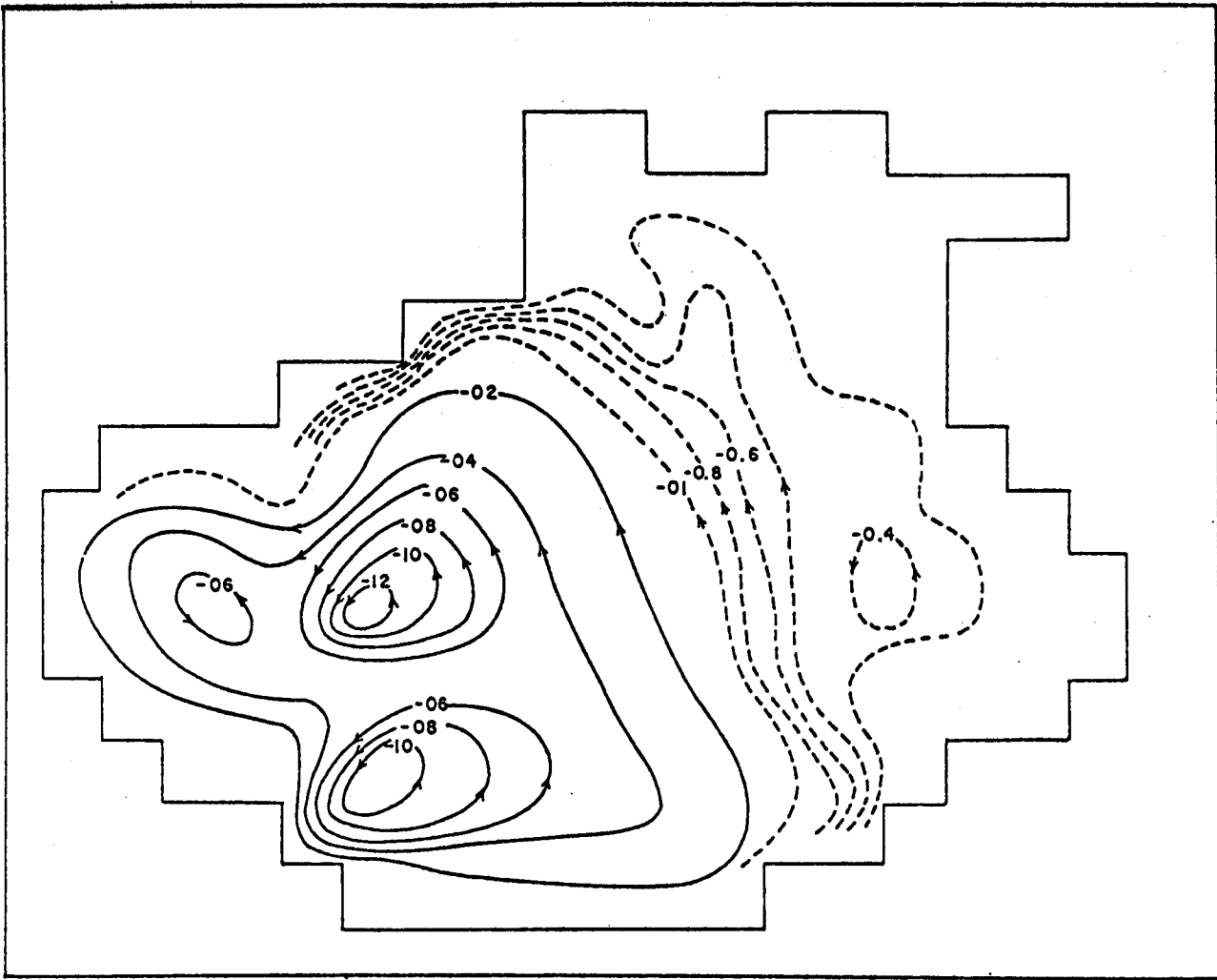


Figure 21

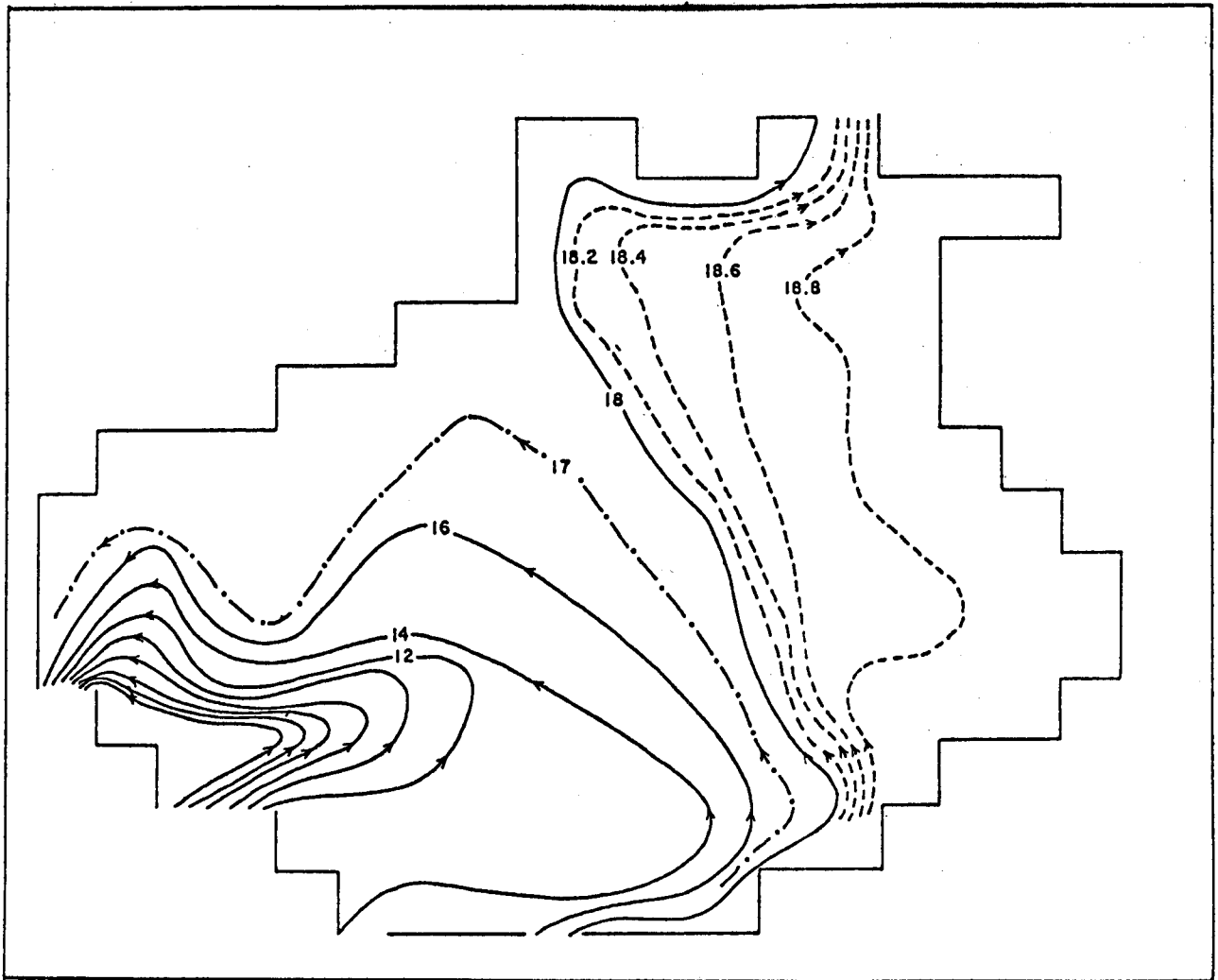


Figure 22



APPENDIX G
Trajectory Model Listing

September 1978

This appendix contains a listing of the trajectory model used to generate the trajectories presented in this report. The code was designed by R.J. Stewart for the NEGQA region and utilizes the environmental library described in the main body of the report.

```

PROGRAM MCTRAJ(INPUT,OUTPUT,TAPE5=INPUT,TAPE6=OUTPUT,
*TAPE1,TAPE2,TAPE3,TAPE8,TAPE9,TAPE17,TAPE23,TAPE29)
      BE CAREFUL TO RESERVE BUFFERS ONLY FOR THOSE FILES BEING USED.
      SUBROUTINES
CNUWND: CALLED BY MCTRAJ,DECODES INTEGER REPRESENTATION OF
      WIND VECTOR(M/S)
CNUCUR: CALLED BY MCTRAJ,DECODES INTEGER REPRESENTATION OF
      CURRENT VECTOR(M/S)

      FUNCTIONS
AVMAG: RETURNS TWELVE HOURLY AVERAGE MAGNITUDE
DEGPKM: RETURNS DEGREES LONGITUDE PER KILOMETER
      AT LATITUDE SPECIFIED IN ARGUMENT

      INPUT DATA SETS
PATSEQ = SEQUENCE OF WIND PATTERNS, APPENDED TO END OF TAPE3
      AND TAPE4.
WMI694 = MID IS HOURLY DATA JUN-SEP 1974 (INTEGER CODED)
WMI135 = TAPE3, MID IS HOURLY DATA JAN-MAR 1975 (INTEGER CODED)
WB125 = EB33 HOURLY DATA JAN-FEB 1975 (INTEGER CODED)
RUNPFG = TAPE5, INPUT DATA FOR THE MAIN PROGRAM(CARDS,TERM)
CURM62 = TAPE9, STATION 62 CURRENT METER DATA FEB 1975(INTEGER CODED)
CURM60 = TAPE9, STATION 60 CURRENT METER DATA JUL 1974(INTEGER CODED)
WINDXY = TAPE17, WIND PATTERNS FOR NEGOA, 13 TYPES (INTEGER CODED)
CURRXY = TAPE23, CURRENT PATTERN FOR NEGOA, 13 BAROTROPIC,
      2 BAROCLINIC (INTEGER CODED)
MAP = TAPE29, DIGITAL COASTLINE REPRESENTATION (0 IS WATER)

      OUTPUT DATA SETS
NDATAN = TAPE2, SPILL TRAJECTORY POSITIONS FOR PLOT VIA PICTUR
OUTS = TAPE6, LISTING OF PROGRAM

COMMON/WNDATA/WINDTM
REAL NCLAT,ECLONG,SCLAT,WCLONG
INTEGER WINDTM,CURRTM
DIMENSION MSTIND(3,14)
INTEGER STRTDA,STRTHR
INTEGER WINDXY,CURRXY
DIMENSION TWLTLG(2,2)
DIMENSION TCLTLG(2,2)
DIMENSION WINDTM(24,90),CURRTM(24,90)
DIMENSION MAP(80,40)
DIMENSION IWNDSEQ(2,90)
DIMENSION WINDXY(40,20,13),CURRXY(60,30,13)
DIMENSION X(960),Y(960),YLAT(960),XLONG(960)
DIMENSION IBAROC(60,30)
DIMENSION UVCTRW(2,2,13),UVCTRC(2,2,13)
DIMENSION WMGSTN(13),CMGSTN(13)
DIMENSION UWSTN(13)
DIMENSION VWSTN(13)
DIMENSION UCSTN(13)
DIMENSION VCSTN(13)
DATA WDNFAC/.03/
DATA NCLAT/60.50/,ECLONG/138.00/,SCLAT/58.00/,WCLONG/148.00/
DATA TWLTLG/59.43,146.33,58.50,141.00/
DATA TCLTLG/59.55,142.27,60.03,145.85/
DATA X/960*9999./, Y/960*0.0/

```

```

C           AT THE BEGINNING OF THE PROGRAM AND THE DATA STATEMENTS.
C
DO 10 I=1,90
  READ(3,1040)(WINDTM(J,I),J=1,12)
  READ(3,1040)(WINDTM(J,I),J=13,24)
  READ(9,1045)(CURRTM(J,I),J=1,8)
  READ(9,1045)(CURRTM(J,I),J=9,16)
  READ(9,1045)(CURRTM(J,I),J=17,24)
10 CONTINUE
1040 FORMAT(12I6)
1045 FORMAT(8I8)
C
C           THE LAST RECORDS IN THE WIND TIME SERIES CONTAIN THE
C           PATTERN SEQUENCE
C
  READ(3,1090)((IWNDSEQ(K,J),K=1,2),J=1,30)
  READ(3,1090)((IWNDSEQ(K,J),K=1,2),J=31,60)
  READ(3,1090)((IWNDSEQ(K,J),K=1,2),J=61,90)
1090 FORMAT(30I2)
C
C           THE FOLLOWING ARRAY CONTAINS THE 13 WIND FIELDS
C
DO 15 K=1,13
  DO 14 J=1,20
    DO 13 LL=1,4
      LLO=(LL-1)*10+1
      LHI=LLO+9
      READ(17,2000)(WINDXY(L,J,K),L=LLO,LHI)
13      CONTINUE
14      CONTINUE
15      CONTINUE
2000 FORMAT(10I6)
C
C           THE FOLLOWING ARRAY CONTAINS THE 13 BAROTROPIC CURRENT FIELDS
C
DO 23 K=1,13
  DO 22 J=1,30
    DO 21 LL=1,6
      LLO=(LL-1)*10+1
      LHI=LLO+9
      READ(23,2002)(CURRXY(L,J,K),L=LLO,LHI)
21      CONTINUE
22      CONTINUE
23      CONTINUE
2002 FORMAT(10I8)
C
C           THE ARRAY IBAROC CONTAINS THE BAROCLINIC COMPONENT OF THE CURRENT
C           FIELD. IT IS ASSUMED CONSTANT OVER THE SIMULATION PERIOD.
C
  IREAD = 0
27 DO 29 J=1,30
  DO 28 LL=1,6
    LLO = (LL-1)*10+1
    LHI = LLO+9
    READ(23,2002)(IBAROC(L,J),L=LLO,LHI)
28      CONTINUE

```

```

IYRBN = MSTIND(IROW,1)
IMOBN = MSTIND(IROW,2)
IDABGN = MSTIND(IROW,3)
IHRBN = MSTIND(IROW,4)
IYREND = MSTIND(IROW,5)
IMOEND = MSTIND(IROW,6)
IDAEND = MSTIND(IROW,7)
IHREND = MSTIND(IROW,8)
LASTDA = MSTIND(IROW,11)
NOWSTN = MSTIND(IROW,12)
NOCSTN = MSTIND(IROW,13)
NBAROC = MSTIND(IROW,14)

```

C
C
C
C
C

```

CHECK IF START IS EARLIER THEN DATA
IF(STRTDA.LT.MSTIND(IROW,8))GOTO 490

```

```

NOW WRITE ALL PERTINENT DATA READ FROM TAPE 5 AT TOP OF NEW PAGE
ON TAPE 6.

```

```

WRITE(6,1010)
WRITE(6,1017)MSTIND(IROW,1),MSTIND(IROW,2),MSTIND(IROW,3),
1 MSTIND(IROW,4)
WRITE(6,1018)MSTIND(IROW,5),MSTIND(IROW,6),MSTIND(IROW,7),
P 2 MSTIND(IROW,8)
WRITE(6,1027)IDASEP,IHRSEP
WRITE(6,1067)STRTDA,STRTHR
WRITE(6,991)MSTIND(IROW,9),MSTIND(IROW,10)
991 FORMAT(1X,*EARLIEST START POSSIBLE*,3X,* STRTDA = *,
1 I2,2X,*STRTHR = *,I2)
WRITE(6,1068)LASTDA
WRITE(6,1037)SRCLAT,SRCLNG
WRITE(6,1072)NOWSTN,TWLTG(1,NOWSTN),TWLTG(2,NOWSTN)
WRITE(6,1073)NOCSTN,TCLTLG(1,NOCSTN),TCLTLG(2,NOCSTN)
WRITE(6,1074)NBAROC
1010 FORMAT(1H1,* SIMULATION DATA CHOSEN IS: /*)
1015 FORMAT(4(1X,I2))
1017 FORMAT(* IYRBN = *,I2,2X,*IMOBN = *,I2,2X,*IDABGN = *,
* I2,2X,*IHRBN = *,I2)
1018 FORMAT(* IYREND = *,I2,2X,*IMOEND = *,I2,2X,*IDAEND = *,
* I2,2X,*IHREND = *,I2)
1025 FORMAT(7X,2(I2,1X))
1027 FORMAT(27X,* IDASEP = *,I2,
12X,*IHRSEP = *,I2)
1037 FORMAT(1X,F7.4,4X,F8.4)
1037 FORMAT(* SRCLAT = *,F7.4,2X,*SRCLNG = *,F8.4)
1067 FORMAT(5X,*FOR THIS RUN*,10X,* STRTDA = *,I2,2X,
1 *STRTHR = *,I2)
1068 FORMAT(5X,*LAST POSSIBLE DATE*,4X,*LASTDA = *,I2)
1070 FORMAT(2X,3(I2,2X))
1072 FORMAT(* WIND STATION NO = *,I2,* (MID IS = 1, EB33 = 2)*,
*2X,*AT LAT = *,F7.3,2X,*LONG = *,F7.3)
1073 FORMAT(* CURRENT STATION NO = *,I2,1X,* (62 = 1, 60 = 2)*,
*2X,*AT LAT = *,F7.3,2X,*LONG = *,F7.3)
1074 FORMAT(* INDEX OF BAROCLINIC FIELD = *,I2,5X,
** (1 = JULY 1974, 2 = FEBRUARY 1975)*)

```

C THE FOLLOWING ARRAYS CONTAIN THE CURRENT AND WIND TIME SERIES. THE
C VARIABLE TAPE NUMBER IDENTIFIES THE SOURCE PER THE COMMENTS

```

DATA MSTIND/74,75,75,06,01,01,07,01,01,00,00,00,
1      74,75,75,09,03,03,04,31,31,00,24,24,
2      26,33,33,05,22,01,86,90,59,
3      01,01,02,02,01,01,01,02,02/

```

```

C
C CONVENTION FOR INDEXING SPATIAL ARRAYS IS THAT THE
C FIRST INDEX IS EAST-WEST. ALL INDEXING IS BASED ON AN
C ORIGIN AT THE SW CORNER.
C THE NE AND SW CORNERS OF THE COMPUTATIONAL AREA ARE SPECIFIED BY
C NCLAT,ECLONG,SCLAT,AND WCLONG.
C THE OIL-WIND-CURRENT INTERACTION IS MODELED AS A SIMPLE
C VECTORIAL SUM. THE WIND VELOCITY IS SCALED BY
C WDNFAC, TYPICALLY .03.
C

```

```

C DEGPKM IS A STATEMENT FUNCTION WITH ARGUMENT SLAT
C DEGPKM(SLAT) = DGPKM/COS(SLAT*.0174533)
C DGPKM = 1.0/111.12
C

```

```

C RGN TO END SPECIFIES PERIOD UNDER STUDY.
C TIME SIMULATION PERIODS INCLUDE THE FOLLOWING
C

```

PERIOD	STRTDA	STRTHR	LASTDA	NOWSTN	NOCSTN	NBAROC
6/7/74-9/4/74	26	5	86	1	2	1
1/1/75-3/31/75	33	22	90	1	1	2
1/1/75-3/31/75	33	1	59	2	1	1

```

C IN GENERAL, ONLY A FRACTION OF THESE PERIODS HAVE SIMULTANEOUS
C DENSITY FIELD, WIND, AND CURRENT MEASUREMENTS
C

```

```

C INPUT START DATA
C SIMULATION PERIOD
C READ(5,1025)IROW
C IDASEP DETERMINES THE TIME SEPARATING TRAJECTORY RUNS
C READ(5,1025)IDASEP,IHRSEP
C TIME TO START IS SPECIFIED WITH STRTDA,STRTHR
C READ(5,1025)STRTDA,STRTHR
C CURRENT DATA FOR TIME SERIES IS OBTAINED EITHER FROM
C STATION 62 OR STATION 60
C STN 62 = LAT 59.55N LONG 142.27W; NOCSTN = 1
C STN 60 = LAT 60.03N LONG 145.85W; NOCSTN = 2
C THIS DATA IS STORED IN TCLTLG.
C THE TIME STEADY BAROCLINIC CURRENTS ARE BASED ON
C DENSITY DATA FROM
C JULY 1974; NBAROC = 1
C FEB 1975; NBAROC = 2
C SRCLAT AND SRCLNG SPECIFY THE SPILL SITE.
C READ(5,1035)SRCLAT,SRCLNG
C WIND DATA FOR TIME SERIES IS OBTAINED EITHER FROM
C MIDDLETON ISLAND OR EB33.
C MID IS = LAT 59.43N LONG 146.33W; NOWSTN = 1
C EB33 = LAT 58.50N LONG 141.00W; NOWSTN = 2
C THIS DATA IS STORED IN TWLTLG
C EQUATE VARIABLES TO MASIND
C

```

```

29 CONTINUE
  IREAD = IREAD+1
  IF(IREAD.EQ.1.AND.NBAROC.EQ.2)GOTO 27
  DO 31 J=1,40
    READ(29,2050)(MAP(I,J),I=1,80)
31 CONTINUE
  WRITE(6,2060)
  DO 32 J=1,40
    JJ=41-J
    WRITE(6,2055)(MAP(I,JJ),I=1,80)
32 CONTINUE
2050 FORMAT(80I1)
2055 FORMAT(1X,80I1)
2060 FORMAT(20X,*MAP*)
C
C      CALCULATE INDICES OF WIND AND CURRENT METER STATIONS
C
  JWSTN = IFIX((TWLTLG(1,NOWSTN)-SCLAT)*20/(NCLAT-SCLAT))+1
  IWSTN = IFIX((WCLONG-(TWLTLG(2,NOWSTN)))*40/(WCLONG-ECLONG))+1
  JCSTN = IFIX((TCLTLG(1,NOCSTN)-SCLAT)*30/(NCLAT-SCLAT))+1
  ICSTN = IFIX((WCLONG-(TCLTLG(2,NOCSTN)))*60/(WCLONG-ECLONG))+1
  WRITE(6,2074)
2074 FORMAT(1H0,* INDICES OF WIND AND CURRENT METER STNS ARE: *//)
  WRITE(6,2075)IWSTN,JWSTN,ICSTN,JCSTN
2075 FORMAT(* IWSTN =*,I2,2X,*JWSTN =*,I2,2X,*ICSTN =*,
  *      I2,2X,*JCSTN =*,I2)
C
C      CALCULATE THE NOMINAL WIND AND CURRENT VELOCITIES FOR THE 13
C      PATTERN TYPES AT THE WIND AND CURRENT METER STATIONS.
C      ALSO DETERMINE THE WIND AND CURRENT MAGNITUDES AND THE
C      REQUIRED LONGITUDINAL AND TRANSVERSE UNIT VECTORS.
C
  WRITE(6,2079)
  CALL CNVCUR(IBAROC(ICSTN,JCSTN),UBCSTN,VBCSTN)
  WRITE(6,5050)UBCSTN,VBCSTN
5050 FORMAT(* UBCSTN = *,E12.4,2X,* VBCSTN = *,E12.4)
  DO 50 J=1,13
    CALL CNVWND(WINDXY(IWSTN,JWSTN,J),UWSTN(J),VWSTN(J))
    CALL CNVCUR(CURRXY(ICSTN,JCSTN,J),UCSTN(J),VCSTN(J))
    WIND AND CURRENT VECTOR MAGNITUDE
    WMGSTN(J) = SQRT((UWSTN(J)**2)+(VWSTN(J)**2))
    CMGSTN(J) = SQRT((UCSTN(J)**2)+(VCSTN(J)**2))
    WIND UNIT VECTOR ARRAY
    UVCTRW(1,1,J) = UWSTN(J)/WMGSTN(J)
    UVCTRW(2,1,J) = VWSTN(J)/WMGSTN(J)
    UVCTRW(1,2,J) = -VWSTN(J)/WMGSTN(J)
    UVCTRW(2,2,J) = UWSTN(J)/WMGSTN(J)
    CURRENT UNIT VECTOR ARRAY
    UVCTRC(1,1,J) = UCSTN(J)/CMGSTN(J)
    UVCTRC(2,1,J) = VCSTN(J)/CMGSTN(J)
    UVCTRC(1,2,J) = -VCSTN(J)/CMGSTN(J)
    UVCTRC(2,2,J) = UCSTN(J)/CMGSTN(J)
2079 FORMAT(1H0,* WIND AND CURRENT PATTERN DATA AT STATIONS *//)
  WRITE(6,2080)J,WINDXY(IWSTN,JWSTN,J),
  *      CURRXY(ICSTN,JCSTN,J)

```

```

      WRITE(6,2082)UWSTN(J),VWSTN(J),
*          UCSTN(J),VCSTN(J),
*          WMGSTN(J),CMGSTN(J)
50 CONTINUE
  WRITE(6,2090)
  DO 51 I=1,13
    WRITE(6,2092)((UVCTRW(1,K,I),K=1,2),
*              (UVCTRC(1,K,I),K=1,2))
    WRITE(6,2092)((UVCTRW(2,K,I),K=1,2),
*              (UVCTRC(2,K,I),K=1,2))
51 CONTINUE
  CALL CNVCUR(IBAROC(ICSTN,JCSTN),UBCSTN,VBCSTN)
2080 FORMAT(* J=*,I2,5X,*WINDXY=*,I6,2X,*CURRXY=*,I8)
2082 FORMAT(* UWSTN=*,E12.4,2X,*VWSTN=*,E12.4,2X,* UCSTN=*,E12.4,
*          2X,*VCSTN=*,E12.4,2X,* WMGSTN=*,E12.4,2X,*CMGSTN=*,E12.4)
2090 FORMAT(20X,* WIND AND CURRENT UNIT VECTOR ARRAY*)
2092 FORMAT(1X,4(E12.4,2X))
C
  WRITE(2,2093)SCLAT,WCLONG,NCLAT,ECLONG
2093 FORMAT(4(1X,F9.4))
C
C      INITIALIZE TIME COUNTER
  IHR = STRTHR
  IDA = STRTDA
100 ISEQNM = 1
  ISEQDA = IDA
C
C      BEGIN TRAJECTORY CALCULATIONS
C
  IF(IHR.LE.6.OR.IHR.GT.18)GOTO 101
  ISEQNM = 2
  GOTO 104
101 IF(IHR.LE.6)GOTO 104
  ISEQDA = IDA + 1
104 WNDMAG = AVMAG(ISEQNM,ISEQDA)
  XLONG(1) = SRCLNG
  YLAT(1) = SRCLAT
  X(1) = (WCLONG-SRCLNG)/DEGPKM(SRCLAT)
  Y(1) = (SRCLAT-SCLAT)/DGPKM
  WRITE(6,2999)
2999 FORMAT(1H0,* TRAJECTORY DATA *//)
  WRITE(6,3000)X(1),Y(1),XLONG(1),YLAT(1)
3000 FORMAT(* X=*,F8.2,1X,*Y=*,F8.2,1X,*XLONG=*,F8.2,1X,*YLAT=*,F8.2)
  KOUNTI = 1
C
C      THE PROBLEM IS NOW INITIALIZED.  BEGIN CALCULATING
C      CONSECUTIVE POSITIONS
C
  DO 120 I=2,959
  IW = IFIX(((WCLONG-XLONG(I-1))*40)/(WCLONG-ECLONG))+1
  JW = IFIX(((YLAT(I-1)-SCLAT)*20)/(NCLAT-SCLAT))+1
  ICR = IFIX(((WCLONG-XLONG(I-1))*60)/(WCLONG-ECLONG))+1
  JCR = IFIX(((YLAT(I-1)-SCLAT)*30)/(NCLAT-SCLAT))+1
  IMAP = IFIX(((WCLONG-XLONG(I-1))*80)/(WCLONG-ECLONG))+1

```

```

JMAP = IFIX(((YLAT(I-1)-SCLAT)*40)/(NCLAT-SCLAT))+1
WRITE(6,3020)IW,JW,ICR,JCR,IMAP,JMAP,IDA,IHR
3020 FORMAT(* IW=*,I2,2X,*JW=*,I2,2X,*ICR=*,I2,2X,*JCR=*,I2,2X,
*          *IMAP=*,I2,2X,*JMAP=*,I2,2X,*IDA =*,I3,2X,*IHR=*,I2)
C
C      GROUNDING CHECK
C      IF(MAP(IMAP,JMAP).NE.0) GOTO 140
C      WIND ARRAY CHECK
C      IF(WINDXY(IW,JW).LT.0) GOTO 140
C      CURRENT ARRAY CHECK
C      IF(CURRXY(ICR,JCR).LT.0) GOTO 140
C      DETERMINE IF BAROCLINIC CURRENT IS KNOWN
C      IF(IBAROC(ICR,JCR).LT.0) GOTO 140
C      DETERMINE LOCAL BAROCLINIC CURRENT VELOCITY
C      CALL CNVCUR (IBAROC(ICR,JCR),BCUC,BCVC)
C      CHECK FOR BAD DATA
C      IF(IWINDSEQ(ISEQNM,ISEQDA).LT.0)GOTO 450
C      LOOK-UP PATTERN NUMBER TYPE
C      NUMSEQ = IWINDSEQ(ISEQNM,ISEQDA)
C      DETERMINE LOCAL BAROTROPIC CURRENT VELOCITY
C      CALL CNVCUR(CURRXY(ICR,JCR,NUMSEQ),BTUC,BTVC)
C      DETERMINE LOCAL WIND VELOCITY
C      CALL CNVWIND(WINDXY(IW,JW,NUMSEQ),WUC,WVC)
C      DETERMINE STRENGTH OF WIND FIELD
C      FLDSTR = WNDMAG/WMGSTN(NUMSEQ)
C      CHECK FOR BAD DATA
C      IF(WINDTM(IHR,IDA).LT.0)GOTO 450
C      DETERMINE HOURLY WIND VELOCITY AT WIND STATION
C      CALL CNVWIND(WINDTM(IHR,IDA),UWHR,VWHR)
C      DETERMINE WIND PERTURBATION VELOCITY AT WIND STATION
C      UWPERT = UWHR - FLDSTR*UWSTN(NUMSEQ)
C      VWPERT = VWHR - FLDSTR*VWSTN(NUMSEQ)
C      DECOMPOSE INTO ALONG AND LEFT PERPENDICULAR COMPONENTS
C      WALNGU = UVCTRW(1,1,NUMSEQ)*UWPERT + UVCTRW(2,1,NUMSEQ)*VWPERT
C      WLEFTU = UVCTRW(1,2,NUMSEQ)*UWPERT + UVCTRW(2,2,NUMSEQ)*VWPERT
C      DETERMINE LOCAL WIND SPEED FOR TURBULENCE SCALE
C      WMGLOC = SQRT((WUC**2) + (WVC**2))
C      TRBSCL IS NOW THE FOLLOWING RATIO OF THE UNWEIGHTED FIELD VARIABLES
C      TRBSCL = WMGLOC/WMGSTN(NUMSEQ)
C      WALNGU = WALNGU*TRBSCL
C      WLEFTU = WLEFTU*TRBSCL
C      CALCULATE X,Y COMPONENTS OF ROTATED PERTURBATION VELOCITY
C      UWPERT = (WALNGU*WUC/WMGLOC) - (WLEFTU*WVC/WMGLOC)
C      VWPERT = (WALNGU*WVC/WMGLOC) + (WLEFTU*WUC/WMGLOC)
C      DETERMINE SYNTHESIZED LOCAL HOURLY WIND VELOCITY
C      WU = FLDSTR*WUC + UWPERT
C      WV = FLDSTR*WVC + VWPERT
C      CHECK FOR BAD DATA
C      IF(CURRTM(IHR,IDA).LT.0)GOTO 450
C      DETERMINE HOURLY CURRENT VELOCITY AT CURRENT STATION
C      CALL CNVCUR(CURRTM(IHR,IDA),UCHR,VCHR)
C      DETERMINE CURRENT PERTURBATION VELOCITY AT CURRENT STATION
C      UCPERT = UCHR - UBCSTN - (FLDSTR**2)*UCSTN(NUMSEQ)
C      VCPERT = VCHR - VBCSTN - (FLDSTR**2)*VCSTN(NUMSEQ)
C      DECOMPOSE INTO ALONG AND LEFT PERTURBATION COMPONENTS

```

```

CALNGU = UVCTRC(1,1,NUMSEQ)*UCPERT + UVCTRC(2,1,NUMSEQ)*VCPERT
CLEFTU = UVCTRC(1,2,NUMSEQ)*UCPERT + UVCTRC(2,2,NUMSEQ)*VCPERT
C   DETERMINE LOCAL BAROTROPIC CURRENT MAGNITUDE
CMGLOC = SQRT((BTUC**2) + (BTVC**2))
TRBSCL = CMGLOC/CMGSTN(NUMSEQ)
C   DETERMINE SCALED PERTURBATION COMPONENTS
CALNGU = TRBSCL*CALNGU
CLEFTU = TRBSCL*CLEFTU
C   CALCULATE SYNTHESIZED LOCAL CURRENT PERTURBATION
UCPERT = (CALNGU*BTUC/CMGLOC) - (CLEFTU*BTVC/CMGLOC)
VCPERT = (CALNGU*BTVC/CMGLOC) + (CLEFTU*BTUC/CMGLOC)
C   DETERMINE SYNTHESIZED LOCAL CURRENT VELOCITY.
C   THE BAROCLINIC AND PERTURBATION COMPONENTS ARE SCALED
C   ALREADY, BUT THE BAROTROPIC PORTION STILL REQUIRES AMPLIFICATION
CU = BCUC + UCPERT + (FLDSTR**2)*BTUC
CV = BCVC + VCPERT + (FLDSTR**2)*BTVC
C   STORE VELOCITY DATA IN TAPE8 FOR STICK VECTOR DRAWINGS
U1=UCHR*100.
U2=BCUC*100.
U3=CU*100.
V1=VCHR*100.
V2=BCVC*100.
V3=CV*100.
WRITE(8,3029)U1,V1,UWHR,VWHR,U2,V2,U3,V3,WU,WV
3029 FORMAT(10F8.3)
C   WRITE MISC. VARIABLES FOR DEBUG.
C   WRITE(6,3030)CU,CV,WU,WV,BCUC,BCVC,BTUC,BTVC,
C   *   CALNGU,CLEFTU,TRBSCL,FLDSTR
C3030 FORMAT(1X,12E10.3)
C   NOW UPDATE POSITION
X(I) = X(I-1) + 3.6*(CU + WNDFAC*WU)
Y(I) = Y(I-1) + 3.6*(CV + WNDFAC*WV)
YLAT(I) = YLAT(I-1) + (Y(I)-Y(I-1))*DGPKM
XLONG(I) = XLONG(I-1) - (X(I)-X(I-1))*DEGPKM(YLAT(I))
C   UPDATE KOUNTI TO INDICATE NEW POSITION DATA
KOUNTI = I
C   NOW UPDATE TIME
IHR = IHR + 1
IF(IHR.LE.24) GOTO 110
IDA = IDA + 1
IHR = IHR - 24
110 IF(IDA.GT.LASTDA) GOTO 140
IF(IDA.EQ.LASTDA.AND.IHR.GT.18) GOTO 140
WRITE(6,3040)X(I),Y(I),I
3040 FORMAT(1X,*X(I)=*,F8.2,2X,*Y(I)=*,F8.2,2X,*I=*,I3)
IF(IHR.NE.7) GOTO 112
ISEQNM = 2
WNDMAG = AVMAG(ISEQNM,ISEQDA)
GOTO 120
112 IF(IHR.NE.19)GOTO 120
ISEQNM = 1
ISEQDA = IDA + 1
WNDMAG = AVMAG(ISEQNM,ISQDA)
120 CONTINUE
140 WRITE(6,3044)
3044 FORMAT(1H0,* FORMATTED LISTING OF TAPE2 DATA *//)

```

```

WRITE(6,3045)SCLAT,WCLONG,NCLAT,ECLONG
3045 FORMAT(1X,*SCLAT=*,F8.2,2X,*WCLONG=*,F8.2,2X,*NCLAT=*,F8.2,2X,
*
*ECLONG=*,F8.2)
KOUNTI = KOUNTI + 1
DO 142 I=1, KOUNTI
WRITE(2,3050)X(I),Y(I)
WRITE(6,3055)X(I),Y(I)
3050 FORMAT(2(1X,F8.2))
3055 FORMAT(1X,*X(I)=*,F8.2,2X,*Y(I)=*,F8.2)
142 CONTINUE
STRTHR = STRTHR + IHRSEP
STRTDA = STRTDA + IDASEP
IF(STRTHR.LE.24) GO TO 143
STRTDA = STRTDA + 1
STRTHR = STRTHR - 24
143 IF((STRTDA.GT.LASTDA).OR.(STRTDA.EQ.LASTDA.AND.STRTHR.GT.18))
* GO TO 500
IDA = STRTDA
IHR = STRTHR
DO 144 I=1,960
X(I) = 9999.
Y(I) = 0.0
144 CONTINUE
GOTO 100

C
C
450 WRITE(6,4010)
4010 FORMAT(1X,* TIME SERIES DATA ERROR SEE LISTING *)
WRITE(6,4020)ISEQNM,ISEQDA,IHR,IDA
4020 FORMAT(1H0,* ISEQNM *,I4,* ISEQDA *,I4,* IHR *,
1 I4,* IDA *,I4/)
C PPRINT OUT DATA FIELDS
DO 455 I=1,90
WRITE(6,4030)(WINDTM(J,I),J=1,12)
WRITE(6,4030)(WINDTM(J,I),J=13,24)
455 CONTINUE
DO 460 I=1,90
WRITE(6,4040)(CURRTM(J,I),J=1,8)
WRITE(6,4040)(CURRTM(J,I),J=9,16)
WRITE(6,4040)(CURRTM(J,I),J=17,24)
460 CONTINUE
4030 FORMAT(1X,12I6)
4040 FORMAT(1X,8I8)
WRITE(6,4050)
4050 FORMAT(1H0,* WIND SEQUENCE ONE *//)
WRITE(6,4060)(IWNDSEQ(1,J),J=1,30)
WRITE(6,4060)(IWNDSEQ(1,J),J=31,60)
WRITE(6,4060)(IWNDSEQ(1,J),J=61,90)
4060 FORMAT(1X,30I2)
WRITE(6,4070)
4070 FORMAT(1H0,* WIND SEQUENCE TWO *//)
WRITE(6,4060)(IWNDSEQ(2,J),J=1,30)
WRITE(6,4060)(IWNDSEQ(2,J),J=31,60)

GOTO 500
490 WRITE(6,5000)

```

```

5000 FORMAT(1H0,* START DAY IS BEFORE DATA */)
500 STOP
END

```

```

REAL FUNCTION AVMAG(ILO,IDA)
INTEGER WINDTM
DIMENSION U(12),V(12)
COMMON/WNDATA/WINDTM(24,90)
DATA U,V/12*0.0,12*0.0/
DATA XNSAM/12.0/
IF(ILO.EQ.2)GOTO 20
DO 15 I = 1,6
    IF(WINDTM(IDA-1,I+18).LT.0)XNSAM = XNSAM-1
    IF(WINDTM(IDA-1,I+18).LT.0)GOTO 11
    CALL CNVWND(WINDTM(IDA-1,I+18),U(I),V(I))
11    IF(WINDTM(IDA,I).LT.0)XNSAM = XNSAM-1
    IF(WINDTM(IDA,I).LT.0)GOTO 15
    CALL CNVWND(WINDTM(IDA,I),U(I+6),V(I+6))
15 CONTINUE
GOTO 50
20 DO 25 I = 1,12
    IF(WINDTM(IDA,I+6).LT.0)XNSAM = XNSAM-1
    IF(WINDTM(IDA,I+6).LT.0)GOTO 25
    CALL CNVWND(WINDTM(IDA,I+6),U(I),V(I))
25 CONTINUE
50 AVMAG = 0.0
DO 60 I = 1,12
    AVMAG = AVMAG + SQRT((U(I)**2)+(V(I)**2))/XNSAM
60 CONTINUE
RETURN
END

```

```

SUBROUTINE CNVWND(IVEL,UW,VW)
VSUR = FLOAT(IVEL-1000*IFIX(.001*FLOAT(IVEL)))
USUR = (FLOAT(IVEL)-VSUR)*.001
UW = USUR*.1 - 50.0
VW = VSUR*.1 - 50.0
RETURN
END

```

```

SUBROUTINE CNVCUR(ICUR,UC,VC)
VSUR = FLOAT(ICUR-10000*IFIX(.0001*FLOAT(ICUR)))
USUR = (FLOAT(ICUR)-VSUR)*.0001
UC = (USUR-5000)*0.1
VC = (VSUR-5000)*0.1
C    THIS RECREATES CURRENT IN ITS ORIGINAL UNITS WHICH WAS
C    CM/SEC. NOW CONVERT TO M/SEC FOR USE BY PROGRAM.
UC = UC*1.0E-2
VC = VC*1.0E-2
RETURN
END

```

**U. S. DEPARTMENT OF COMMERCE
NATIONAL OCEANIC AND ATMOSPHERIC ADMINISTRATION**

**NOS/OMA/OAD—Alaska Office
701 C Street, P.O. Box 56
Anchorage, Alaska 99513**

**POSTAGE AND FEES PAID
U.S. DEPARTMENT OF COMMERCE
COM-210**



PRINTED MATTER

CLASS OF POSTAL SERVICE

**OFFICIAL BUSINESS
PENALTY FOR PRIVATE USE, \$300**

BARRARA J. SOKOLOV
ARCTIC ENVIRON INFO AND DATA CTR
UNIVERSITY OF ALASKA
707 A STREET
ANCHORAGE, AK 99501

See NDM 61-50 for Class of Postal Service